Proceedings of

RAGtime 8/9: Workshops on black holes and neutron stars

15–19/19–21 September '06/'07
Hradec nad Moravicí, Opava,
Czech Republic

Editors
S. Hledík
Z. Stuchlík

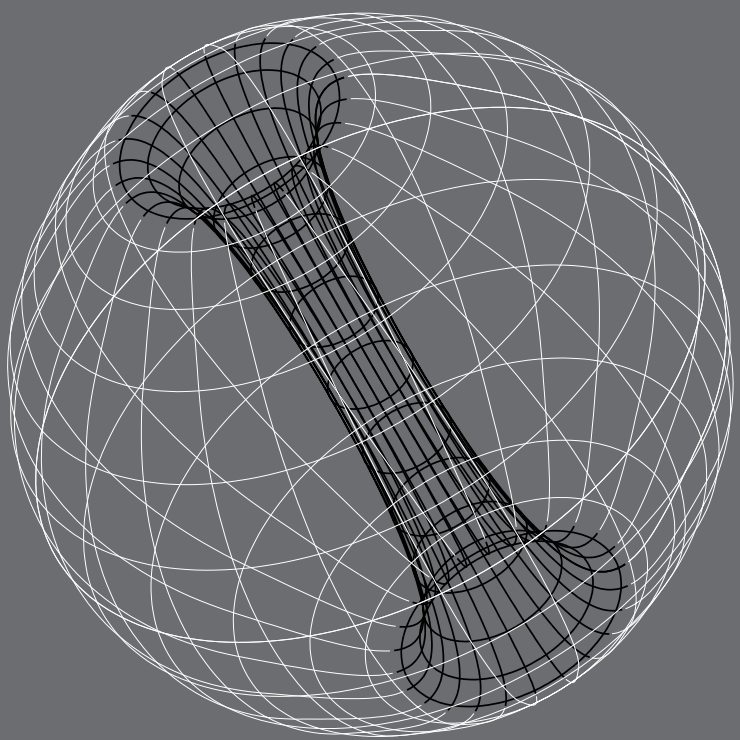

SILESIAN UNIVERSITY IN OPAVA

Publications of the Institute of Physics No. 5

RAG time 8

WORKSHOP ON BLACK HOLES AND NEUTRON STARS, 15-19TH SEPT 2006

Relativistic Astrophysics Group
at the Institute of Physics
Faculty of Philosophy & Science
Silesian University in Opava
Bezručovo nám. 13, CZ-746 01
Opava, Czech Republic

http://www.physics.cz/rag/time8/

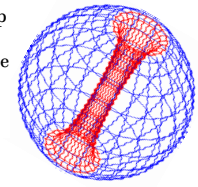

RAG time 9

WORKSHOP ON BLACK HOLES AND NEUTRON STARS, 19TH-21ST SEPT 2007

Relativistic Astrophysics Group
at the Institute of Physics
Faculty of Philosophy & Science
Silesian University in Opava
Bezručovo nám. 13, CZ-746 01
Opava, Czech Republic

http://www.physics.cz/ragtime/

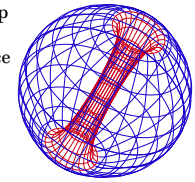

Supported by

Czech Institutional Research Grant
MSM 4781305903

Cargo Design/Ing. Vít Škrobánek:
Conversions, extensions and
adaptations of lorries

http://www.czechcontact.com/CARGO_DESIGN_SKROBANEK

Proceedings of RAGtime 8/9: Workshops on black holes and neutron stars 15–19/19–21 September 2006/2007 Hradec nad Moravicí, Opava Czech Republic

S. Hledík and Z. Stuchlík, editors

Opava 2007

Annotation: In this Proceedings, the talks presented during workshops *RAGtime 8/9: Workshops on black holes and neutron stars, 15–19/19–21 September 2006/2007, Hradec nad Moravicí, Opava, Czech Republic* are collected.

ISBN 978-80-7248-419-5

PREFACE

Relativistic Astrophysics Group (RAG) at the Institute of Physics, the Faculty of Philosophy and Science of the Silesian University in Opava, started a series of Workshops on Black Holes and Neutron Stars called *RAGtime* in 1999. The purpose of the workshops was to provide an opportunity for the presentation and discussion of recent developments in the field of relativistic astrophysics related to accretion processes onto black holes and neutron stars, and to general physical phenomena connected to the properties of black holes and their vicinity, and the internal structure of neutron stars or quark stars, as they were obtained by collaborating research groups at the Silesian University in Opava, the Faculty of Mathematics and Physics of Charles University in Prague, the International School for Advanced Studies in Trieste, the Institute of Astrophysics at University of Oxford, the Department of Astrophysics of Göteborg University, the Institute of Physics at the University of Bergen, the Institute of Astronomy of the Polish Academy of Science, and other remarkable institutes.

The *RAGtime* workshops are also vitally important for students of theoretical physics and/or astrophysics at the Silesian University in Opava, because they have a unique opportunity to be regularly in direct contact with the most recent results of relativistic astrophysics and they also have a possibility to discuss problems with leading astrophysicists of worldwide reputation like Marek Abramowicz, John Miller, Jeff McClintock, Ron Remillard, Włodzimierz Kluźniak, Shoji Kato, Luciano Rezzolla, Vladimír Karas, Petr Hadrava and others.

We would like to thank all the authors for careful preparation of their contributions. We are also indebted to the Ministry of Education of the Czech Republic for providing financial support in the framework of the Grant MSM 4781305903, and all other sponsors for their contributions to the successful course of the last RAGtime meetings.

Opava, December 2007

S. Hledík and Z. Stuchlík
editors

CONTENTS

Proceedings of *RAGtime 8/9, 15–19/19–21 September, 2006/2007, Hradec nad Moravicí, Opava, Czech Republic*
S. Hledík and Z. Stuchlík, editors, Silesian University in Opava, 2007, pp. 1–10

Dipole magnetic field on a Schwarzschild background and related epicyclic frequencies

Pavel Bakala[a], Eva Šrámková, Zdeněk Stuchlík and Gabriel Török

Institute of Physics, Faculty of Philosophy & Science, Silesian University in Opava, Bezručovo nám. 13, CZ-746 01 Opava, Czech Republic
[a]pavel.bakala@fpf.slu.cz

ABSTRACT
Several models of the X-ray flux modulation observed in the low-mass X-ray binaries (LMXBs), in particular the neutron star LMXBs, deal with Keplerian and epicyclic frequencies of geodesic orbital motion. We discuss non-geodesic corrections to the orbital and epicyclic frequencies of charged test particles caused by presence of a neutron star magnetic field. The magnetic field is considered to be generated by an intrinsic static dipole magnetic moment of a neutron star represented by the Schwarzschild geometry. We present fully general relativistic formulae for the orbital and epicyclic frequencies, obtained using the appropriate equations governing perturbations of the circular motion. The most significant correction arises for the radial epicyclic frequency. The zero point of the corrected radial epicyclic frequency defines radius of the effective innermost stable circular orbit "(EISCO)." The dipole magnetic field also violates equality of the orbital and vertical epicyclic frequencies corresponding to the spherical symmetry of the Schwarzschild geometry.

Keywords: X-ray – neutron stars – binaries – accretion discs – QPOs – magnetic field

1 INTRODUCTION

The RXTE earth satellite has provided during the past decade a large amount of the X-ray timing measurements to the astrophysical community. Among other facts these measurements have revealed existence of nearly periodic modulations of X-ray flux detected from several low-mass X-ray binaries (LMXBs), so called quasi-periodic oscillations (QPOs).

Two main branches of oscillations are observed in LMXBs – the low ($\sim$ 1–10 Hz) and high ($\sim$ 200–1200 Hz), named also "kHz" frequency QPOs (see van der Klis, 2006 for a review). The kHz oscillations often come in pairs consisting of the so called lower and upper QPO mode with frequencies $\nu_{\rm L}$, $\nu_{\rm U}$. Notably, the frequencies $\nu_{\rm L}$, $\nu_{\rm U}$ roughly correspond to Keplerian periods in the close vicinity of the binary compact object.

Miscellaneous orbital QPO models have been proposed. In particular, the relativistic precession model (in next RP model) introduced by Stella and Vietri (1998) relates the

978-80-7248-419-5

upper and lower kHz QPOs to the Keplerian and periastron precession frequency on a geodesic orbit inside the inner part of the accretion disc.[1]

In neutron star sources the frequencies $\nu_{\rm L}$, $\nu_{\rm U}$ vary in a range of hundreds of Hertzs on time scales of several hours. The observed frequencies $\nu_{\rm L}$, $\nu_{\rm U}$ are rather well correlated, always keeping a nearly linear pattern in a frequency-frequency plane. The pattern (frequency correlation) is specific for a given source. It has been noticed that, in general, correlation $\nu_{\rm U}(\nu_{\rm L})$ is qualitatively well fitted by the RP model prediction (see, e.g., Stella and Vietri, 1999, 2002; Belloni et al., 2007; Török et al., 2007b).

Nevertheless, when modelling individual frequency relations from the RP model or its generalization to the total precession model in the framework of Hartle–Thorne geometry (Stuchlík et al., 2007b), the mass and angular momentum relevant to the best fits are questionably high ($M \sim 2$–$3\,{\rm M}_\odot$, $j \sim 0.2$–0.4; e.g., Stella and Vietri, 2002; Boutloukos et al., 2006; Török et al., 2007a).

Also the quality of the fits is not satisfactory with χ^2 indicating a systematic deviation between the expected and empirical trend.

It has been discussed within the framework of the RP model that the above discrepancies could be connected to non-geodesic corrections to the orbital and epicyclic frequencies, most likely originating in the presence of a neutron star magnetic field (Stella and Vietri, 1999, 2002; Stuchlík et al., 2007a; Török et al., 2007a). Notice that the formulae describing the orbital motion appear in several QPO models, and the corrections should therefore be valid also to these models, and not only to the particular RP model. When considering a dominant influence of the central compact object magnetic field, two main kinds of such corrections play a role. The first kind is connected to diamagnetic effects in hot plasma (see, e.g., Stella and Vietri, 1999), while the second kind arises when assuming a specific charge of the accreted plasma, caused, e.g., by interaction of a binary partner stellar wind with the magnetic field.

In the present paper we discuss in detail the latter kind of non-geodesic corrections using a fully general relativistic approach. We consider a magnetic field generated by an intrinsic static dipole magnetic moment of a neutron star on a background of the Schwarzschild geometry. We calculate the relevant frequencies of the non-geodesic charged test particle motion, and discuss some implications following for the hot spot and disc oscillation models of the X-ray flux modulation.

2 CIRCULAR ORBITAL MOTION IN A DIPOLE MAGNETIC FIELD ON THE SCHWARZSCHILD BACKGROUND

The line element in the Schwarzschild spacetime has the familiar form

$$ {\rm d}s^2 = -\eta(r)^2\,{\rm d}t^2 + \frac{{\rm d}r^2}{\eta(r)^2} + r^2({\rm d}\theta^2 + \sin^2\theta\,{\rm d}\phi^2)\,, \qquad (1) $$

[1] The same model relates the low frequency QPO branch to the "Lense–Thirring" orbit precession.

where $\eta(r)$ is given by

$$\eta(r) \equiv \left(1 - \frac{2M}{r}\right)^{1/2} .$$

We have adopted here geometric units, $c = G = 1$, that we use throughout the paper, if not stated otherwise.

Solving the vacuum Maxwell equations

$$F^{\mu\nu}{}_{;\mu} = 0 , \qquad ({}^*F^{\mu\nu}{}_{;\mu} = 0) ,$$

on the background of the spacetime geometry (1) for a static magnetic dipole moment μ, parallel to the rotational axis of the star, one obtains formula for an exterior ($r > R$, where R is the neutron star radius) electromagnetic four-potential A_μ (e.g., Wasserman and Shapiro, 1982; Braje and Romani, 2001),

$$A_\alpha = -\delta^\phi_\alpha f(r) \frac{\mu \sin^2\theta}{r} , \tag{2}$$

which has the form of the flat space result, multiplied by a "relativistic correction" function $f(r)$ given by

$$f(r) = \frac{3r^3}{8M^3}\left[\log\eta(r)^2 + \frac{2M}{r}\left(1 + \frac{M}{r}\right)\right] . \tag{3}$$

In case of potential (2), the Maxwell tensor $F_{\mu\nu}$, connected to the four-potential A_μ through the relation

$$F_{\mu\nu} = \frac{\partial A_\nu}{\partial x^\mu} - \frac{\partial A_\mu}{\partial x^\nu} ,$$

has only two independent non-vanishing components,

$$F_{r\phi} = \frac{\mu \sin^2\theta\,(f(r) - r f'(r))}{r^2} , \quad F_{\theta\phi} = -\frac{\mu f(r) \sin 2\theta}{r} , \tag{4}$$

which are related to the components of the magnetic field three-vector B as follows:

$$F_{r\phi} = B^\theta , \quad F_{\theta\phi} = -B^r .$$

Note that "coma" in Eq. (4) denotes partial derivative with respect to the radial coordinate r.

In a curved spacetime with the presence of an electromagnetic field, the equation of motion for a charged test particle of mass m and charge q reads

$$\frac{\mathrm{d}U^\mu}{\mathrm{d}\tau} + \Gamma^\mu_{\alpha\beta} U^\alpha U^\beta = \tilde{q} F^\mu_\nu U^\nu , \tag{5}$$

where U^μ is the four-velocity and $\tilde{q} \equiv q/m$ is the specific charge of the particle.

Symmetry properties of the spacetime geometry (1) and electromagnetic field (2) allow charged test particle motion which is restricted to the equatorial plane $\theta = \pi/2$. Throughout this paper we confine ourselves to studying only circular equatorial motion.[2] The

[2] See (Kovář et al., 2007) for a discussion of the existence of non-equatorial, so called "halo," orbits.

four-velocity then has only two non-vanishing components, $U^\mu = (U^t, 0, 0, U^\phi)$. Solving the radial component of Eq. (5) together with the normalization condition $U^\mu U_\mu = -1$ for metric (1) and potential (2) we obtain the non-zero components of U^μ in the form

$$U^t = \sqrt{\frac{r - \tilde{q}\mu\Phi(r)U^\phi}{(r-3M)}}\,, \tag{6}$$

$$U^\phi = \frac{\Upsilon(r,\tilde{q},\mu)}{2r^3\,(r-3M)}\,, \tag{7}$$

and the angular velocity defined as $\Omega = U^\phi/U^t$ then reads

$$\Omega = \frac{\Upsilon(r,\tilde{q},\mu)}{r^{3/2}\sqrt{4r^4\,(r-3M) - 2\tilde{q}\mu\Phi(r)\Upsilon(r,\tilde{q},\mu)}}\,. \tag{8}$$

Here $\Phi(r)$, $\chi(r)$, $\Psi(r)$ and $\Upsilon(r,\tilde{q},\mu)$ are given by

$$\begin{aligned}
&\Phi(r) \equiv f(r) - rf'(r)\,,\\
&\chi(r) \equiv (r-2M)\,\Phi(r)\\
&\Psi(r) \equiv \sqrt{4Mr^4(r-3M) + (\tilde{q}\mu\chi(r))^2}\,,\\
&\Upsilon(r,\tilde{q},\mu) \equiv \Psi(r) - \tilde{q}\mu\chi(r)\,.
\end{aligned}$$

2.1 Epicyclic frequencies

The nodal precession, precession of periastron, and associated phenomena can be understood in terms of the epicyclic frequencies of a test particle in a stable circular orbit.

Formulae for the radial and vertical epicyclic frequencies of a charged test particle in the presence of a general electromagnetic field have been derived by Aliev and Galtsov (1981); Aliev (2006). One may obtain the formulae by perturbing the particle's position around the circular orbit $(r,\theta) = (r_0, \pi/2)$, i.e., by presuming that $x^\mu(\tau) = z^\mu(\tau) + \xi^\mu(\tau)$ where $\xi^\mu(\tau)$ is a small perturbation. Substituting this into the equation of motion (5) and restricting to first order terms in ξ^μ one arrives at the relation for ξ^μ that takes the form of an equation for a linear harmonic oscillator,

$$\frac{\mathrm{d}^2\xi^a}{\mathrm{d}t^2} + \omega_a^2\xi^a = 0\,, \quad a \in (r,\theta)\,.$$

Using the general formulae (Aliev, 2006), the explicit expressions for the epicyclic frequencies in the spacetime geometry (1) and magnetic field (2) are given by

$$\begin{aligned}
\omega_r^2 = \Big\{ &\left(U^\phi\right)^2 r^6(3r-8M) + 2M(M-r)r^3\left(U^t\right)^2 + \tilde{q}\mu\Big[\Phi(r)\Big(2U^\phi r^3(3r-7M)+\\
&+\tilde{q}\mu\chi(r)\Big) + U^\phi r^5(r-2M)f''(r)\Big]\Big\}\Big/ r^7\left(U^t\right)^2\,,
\end{aligned} \tag{9}$$

$$\omega_\theta^2 = \frac{U^\phi\left(U^\phi r^3 - 2\tilde{q}\mu f(r)\right)}{(U^t)^2\,r^3}\,. \tag{10}$$

One can easily check that in the absence of the Lorentz force ($\mu = 0$ or $\tilde{q} = 0$) the expressions for the orbital (8) and epicyclic (9), (10) frequencies merge into the well-known formulae for geodesic motion in the Schwarzschild geometry:

$$\Omega = \omega_\theta = \sqrt{M/r^3}\,, \quad \omega_r = \sqrt{M(r-6M)}/r^2\,.$$

3 MAGNETIC FIELD CORRECTIONS TO ORBITAL AND EPICYCLIC FREQUENCIES

Consider now an astrophysically relevant situation of a rather slowly rotating neutron star described by the Schwarzschild geometry that possesses a dipole magnetic field. Our interest is focused to LMXBs with evidence of an accretion disc exhibiting the kHz QPOs. We restrict our consideration to the approach of a thin accretion disc that is assumed to consist of test particles moving along nearly circular geodesics in the equatorial plane.

Intrinsic magnetic dipole moment of the star can be obtained from the presumed magnetic field strength at the star surface. A locally measured magnetic field strength is defined as a projection of the Maxwell tensor into an orthonormal basis of a static observer on the surface of the star. For such an observer located at the equator of the star with radius R, the

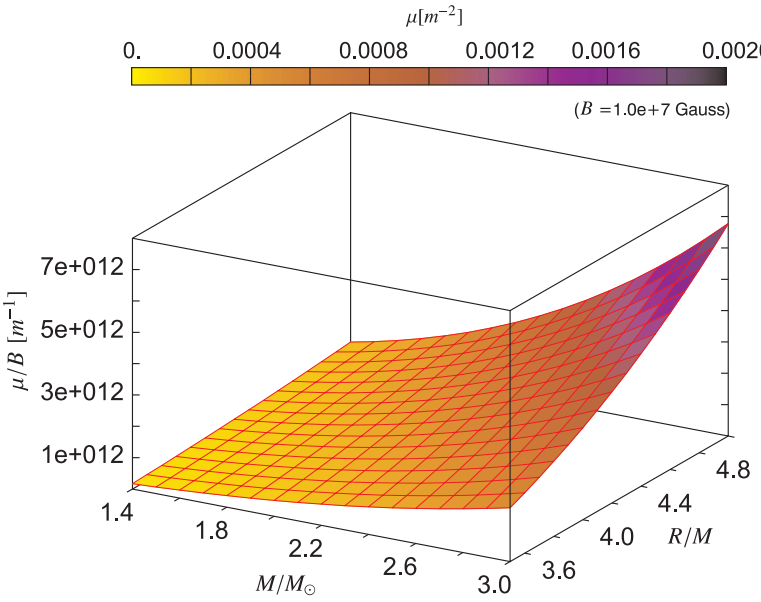

Figure 1. Intrinsic magnetic dipole moment μ of the star as a function of the star radius R and mass M for a fixed magnetic field strength B at the star surface. The z-axis is scaled in relative units of μ/B, while the colour scaling at the 3D-plot surface shows values of μ for $B = 10^7$ Gauss $= 2.875 \times 10^{-16}\,\mathrm{m}^{-1}$.

magnetic field three-vector has only one non-zero component,

$$B^{\hat{\theta}} = F_{\hat{r}\hat{\phi}} = \frac{\eta(R)}{R} F_{r\phi} \,.$$

Therefore, using Eqs (3) and (4), one may write

$$\mu = \frac{4M^3 R^{3/2}\sqrt{R-2M}}{6M(R-M) + 3R(R-2M)\,\log \eta\,(R)^2}\, B^{\hat{\theta}} \,.$$

The behaviour of μ as a function of M and R for fixed B on the star equator is illustrated in Fig. 1. For a neutron star with a rather weak magnetic field strength, $B = 10^7$ Gauss $= 2.875\times10^{-16}\,\mathrm{m}^{-1}$, mass $M = 1.5\,\mathrm{M}_\odot$ and radius $R = 4M$, we have $\mu = 1.06\times10^{-4}\,\mathrm{m}^{-2}$.

We have investigated behaviour of the orbital and epicyclic frequencies for various parameters of the considered magnetic field, and present the resulted frequencies for the above value of μ and two different values of $\tilde{q}$, $\tilde{q} = 5.555 \times 10^{10}$ and $\tilde{q} = 1.111 \times 10^{12}$. Both of these values are still very low in comparison with the value $\tilde{q} = 1.111 \times 10^{18}$ corresponding to matter purely consisting of ions of hydrogen. Note that the Lorentz force in the considered equation of motion, and consequently the described effects, depend on the product of μ and $\tilde{q}$, and therefore varying μ results in a similar effect on the investigated properties as varying the specific charge $\tilde{q}$.

The left panel of Fig. 2, made for $\tilde{q} = 5.555 \times 10^{10}$, shows a high sensitivity of the radial epicyclic frequency keeping qualitatively the same profile that is however shifted to lower values and away from the central object. The influence on the orbital and vertical epicyclic frequency is considerably smaller, and becomes more relevant for higher values of $\tilde{q}$ (see the right panel of Fig. 2 corresponding to $\tilde{q} = 1.111 \times 10^{12}$). Generally speaking, in the presence of the assumed Lorentz force the radial epicyclic frequency dramatically decreases,

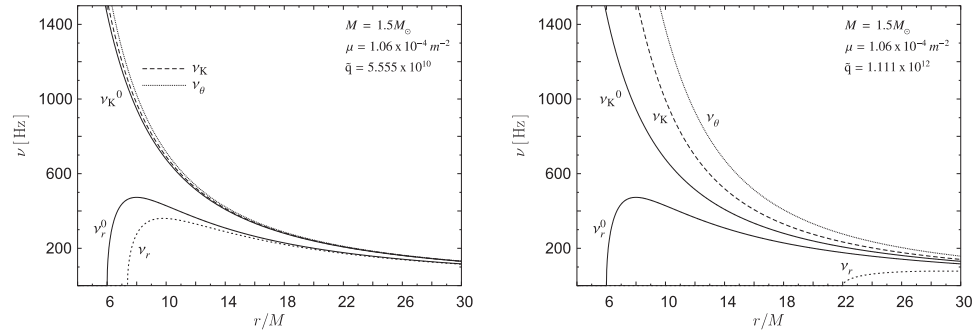

Figure 2. *Left:* An illustration of the radial epicyclic, $\nu_r^0 = \omega_r^0/(2\pi)$, vertical epicyclic, $\nu_\theta^0 = \omega_\theta^0/(2\pi)$, and orbital, $\nu_\mathrm{K}^0 = \Omega_\mathrm{K}/(2\pi) = \nu_{\theta^0}$, frequency behaviour in the Schwarzschild geometry in a pure geodesic case compared to case with a presence of an intrinsic external dipole magnetic field $B = 10^7$ Gauss on the surface of the star with $M = 1.5\,\mathrm{M}_\odot$ and $R = 4M$ (quantities ν_K, ν_θ and ν_r without a superscript). *Right:* The same comparison but for a higher value of the specific charge $\tilde{q}$. Note the much larger difference between the geodesic and corrected frequencies and the major shift of the point where the radial frequency goes to zero, compared to the left panel.

while the orbital and vertical epicyclic frequencies rather slightly increase. Described behaviour is qualitatively in accordance with what one would expect, as the considered Lorentz force acting on the particles moving in the equatorial plane has only radial non-zero component.

4 EFFECTIVE INNERMOST STABLE CIRCULAR ORBIT (EISCO)

The presence of the Lorentz force naturally alters the location of a charged test particle's innermost stable circular orbit. For such an effective innermost stable circular orbit we

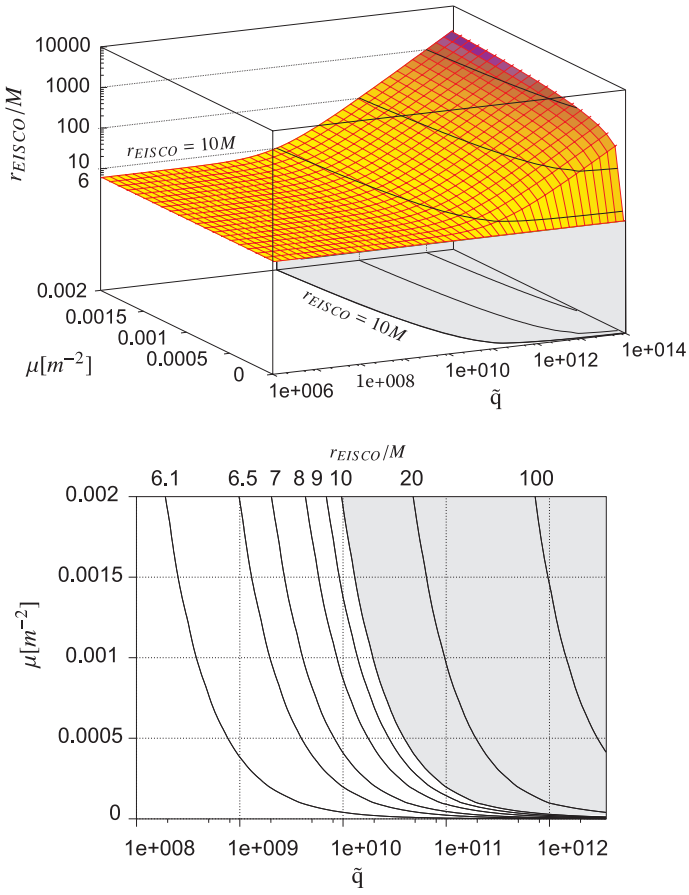

Figure 3. *Top:* Location of EISCO as a function of the test particle specific charge $\tilde{q}$ and the intrinsic magnetic dipole moment μ of the star. The curves at the 3D-plot surface and their projections into the μ-$\tilde{q}$ plane denote $r_{\rm EISCO} = 10\,M$, $100\,M$, $1000\,M$. *Bottom:* Astrophysically relevant region of the μ-$\tilde{q}$ plane with distinctive values of $r_{\rm EISCO}$.

introduce a new abbreviation term – "EISCO" – as an equivalent to a commonly used term "ISCO" in the purely geodesic case. Standard methods for obtaining the location of the innermost stable circular orbit are based on investigation of the properties of the particle's effective potential (e.g., Misner et al., 1973). One may as well use the requirement that the radial epicyclic frequency defined at this location must go to zero, as a small radial perturbation of such particle's position would induce its direct infall towards the gravitational centre. Therefore the condition for $r_{\rm EISCO}$ may be written as

$$\omega_r(r_{\rm EISCO}) = 0\,. \tag{11}$$

We present a numerical solution of the above equation in Fig. 3, which shows a high sensitivity of $r_{\rm EISCO}$ to $\tilde{q}$. With growing values of $\tilde{q}$ it rapidly draws apart from the well-known radius of ISCO in the Schwarzschild geometry, $r_{\rm ISCO} = 6\,M$. In case of $\mu = 1.06\times10^{-4}\,{\rm m}^{-2}$ corresponding to Fig. 2 we find that for $\tilde{q} = 5.555\times10^{10}$ there is $r_{\rm EISCO} = 7.39\,M$, while for $\tilde{q} = 1.111\times10^{12}$ we obtain $r_{\rm EISCO} = 22.16\,M$. For the extremal specific charge $\tilde{q} = 1.111\times10^{18}$ the location of EISCO orbit flies away onto $r_{\rm EISCO} = 177864.76\,M$.

5 CONCLUSIONS

Orbital motion and the related epicyclic frequencies have been considered by several authors as a key agent in their models of the high frequency QPOs. These models mostly assume geodesic motion, although some non-geodesic corrections have been studied in the past, e.g., due to pressure gradient forces (Blaes et al., 2007), or due to diamagnetic forces in hot plasma interacting with a central compact object magnetic field (e.g., Stella and Vietri, 1999).

Non-geodesic corrections arising from the interaction of the central magnetic field with a test particle specific charge (i.e., the Lorentz force) have, however, not been considered in this context so far, and the formulae derived above therefore represent a first attempt to describe the appropriate problem within a fully general relativistic regime. [3]

As demonstrated in Figs 2 and 3, the magnetic field influence on the orbital motion may be very significant. Even for astrophysically very low values of $\tilde{q}$ the calculated correction to the radial epicyclic frequency and the associated location of the effective innermost stable circular orbit (EISCO) is notably large, see Fig. 3. In other words, presence of the Lorentz force strongly affects the location of the inner edge of the thin accretion disc.

The presence of the dipole magnetic field also violates the $\nu_{\rm K} = \nu_\theta$ equality corresponding to spherical symmetry of the background Schwarzschild geometry. However, as seen in Fig. 3, the corrections to the orbital and vertical epicyclic frequency are much less significant than the correction to the radial epicyclic frequency. In fact, these two "vertical" corrections become relevant only for $\tilde{q}$ matching a situation with a shift of ISCO inconsistent with the present astrophysical view of LMXBs. Notice that the vertical epicyclic frequency exceeds

[3] We restrict here ourselves by the following assumptions: the frame-dragging effects are not considered; the neutron star magnetic field is fully dominant over the magnetic field generated by the currents in the disc.

the Keplerian frequency, contrary to the case of rotating axially symmetric spacetimes, e.g., Kerr spacetimes (Aliev and Galtsov, 1981). Hence, in the lowest approximation, the influence of the specific charge of the accreted matter should enter the orbital QPO models in the form of a corrected radial epicyclic frequency (9).

ACKNOWLEDGEMENTS

This work has been supported by the Czech grants LC06014 (P. B., E. S.) and MSM 4781305903 (Z. S., G. T.). The authors (G. T., P. B., E. S.) would like to thank the fishermen community in Derítő-Tó, Tata, Hungary for a royal hospitality and inspiring atmosphere for the research.

REFERENCES

Aliev, A. N. (2006), Epicyclic Frequencies and Resonant Phenomena Near Black Holes: The Current Status, arXiv: `astro-ph/0612730`.

Aliev, A. N. and Galtsov, D. V. (1981), Radiation from relativistic particles in non-geodesic motion in a strong gravitational field, *Gen. Relativity Gravitation*, **13**, pp. 899–912.

Belloni, T., Méndez, M. and Homan, J. (2007), On the kHz QPO frequency correlations in bright neutron star X-ray binaries, *Monthly Notices Roy. Astronom. Soc.*, **376**(3), pp. 1133–1138, arXiv: `astro-ph/0702157`.

Blaes, O. M., Šrámková, E., Abramowicz, M. A., Kluźniak, W. and Torkelsson, U. (2007), Epicyclic Oscillations of Fluid Bodies. Paper III. Newtonian Non-Slender Torus, *Astrophys. J.*, **665**, pp. 642–653, arXiv: `0706.4483`, URL `http://adsabs.harvard.edu/abs/2007ApJ...665..642B`.

Boutloukos, S., van der Klis, M., Altamirano, D., Klein-Wolt, M., Wijnands, R., Jonker, P. G. and Fender, R. P. (2006), Discovery of twin kHz QPOs in the peculiar X-ray binary Circinus X-1, *Astrophys. J.*, **653**, pp. 1435–1444, arXiv: `astro-ph/0608089v2`.

Braje, T. M. and Romani, R. W. (2001), Magnetospheric scattering and emission in millisecond pulsars, *Astrophys. J.*, **550**, pp. 392–396.

Kovář, J., Stuchlík, Z. and Karas, V. (2007), On existence of halo orbits in Kerr–Newman spacetimes, pp. 125–138, this volume.

Misner, C. W., Thorne, K. S. and Wheeler, J. A. (1973), *Gravitation*, W. H. Freeman and Co, New York, San Francisco.

Stella, L. and Vietri, M. (1998), Lense–Thirring Precession and Quasi-periodic Oscillations in Low-Mass X-Ray Binaries, *Astrophys. J. Lett.*, **492**, pp. L59–L62, arXiv: `astro-ph/9709085`.

Stella, L. and Vietri, M. (1999), kHz Quasiperiodic Oscillations in Low-Mass X-Ray Binaries as Probes of General Relativity in the Strong-Field Regime, *Phys. Rev. Lett.*, **82**(1), pp. 17–20.

Stella, L. and Vietri, M. (2002), Strong Field Gravity and Quasi-Periodic Oscillations from Low Mass X-Ray Binaries, in V. G. Gurzadyan, R. T. Jantzen and R. Ruffini, editors, *The Ninth Marcel Grossmann Meeting. Proceedings of the MGIXMM Meeting held at The University of Rome "La Sapienza," 2–8 July 2000*, volume A, p. 426, World Scientific Publishing.

Stuchlík, Z., Bakala, P. and Török, G. (2007a), in preparation.

Stuchlík, Z., Török, G. and Bakala, P. (2007b), On a multi-resonant origin of high frequency quasiperiodic oscillations in the neutron-star X-ray binary 4U 1636−53, submitted to Astronomy and Astrophysics, arXiv: `0704.2318`.

Török, G., Bakala, P., Stuchlík, Z. and Šrámková, E. (2007a), On a multi-resonant origin of high frequency QPOs in the atoll source 4U 1636−53, pp. 489–499, this volume, URL `http://xmm.esac.esa.int/external/xmm_science/workshops/2007_science/presentations/P2.6.pdf`.

Török, G., Stuchlík, Z. and Bakala, P. (2007b), A remark about possible unity of the neutron star and black hole high frequency QPOs, *Central European J. Phys.*, **5**(4), pp. 457–462.

van der Klis, M. (2006), Rapid X-ray Variability, in W. H. G. Lewin and M. van der Klis, editors, *Compact Stellar X-Ray Sources*, pp. 39–112, Cambridge University Press, Cambridge.

Wasserman, I. and Shapiro, S. L. (1982), Masses, radii and magnetic fields of pulsating X-ray sources: Is the standard model self-consistent?, *Astrophys. J.*, **265**, p. 1036.

Proceedings of *RAGtime 8/9, 15–19/19–21 September, 2006/2007, Hradec nad Moravicí, Opava, Czech Republic*
S. Hledík and Z. Stuchlík, editors, Silesian University in Opava, 2007, pp. 11–20

Modulation of high-frequency QPOs

Michal Bursa

Astronomical Institute, Czech Academy of Sciences, Boční II 1401/1a, CZ-141 31 Praha 4, Czech Republic
bursa@astro.cas.cz

ABSTRACT
We study strong-gravity effects on modulation of radiation emerging from accreting compact objects as a possible mechanism for flux modulation in QPOs. We construct a toy model of an oscillating torus in the slender approximation assuming thermal bremsstrahlung for the intrinsic emissivity of the medium and we compute observed (predicted) radiation signal including contribution of indirect (higher-order) images and caustics in the Schwarzschild spacetime. We show that the simplest oscillation mode in an accretion flow, axisymmetric up-and-down motion at the meridional epicyclic frequency, may be directly observable when it occurs in the inner parts of accretion flow around black holes. Together with the second oscillation mode, an in-and-out motion at the radial epicyclic frequency, it may then be responsible for the high-frequency modulations of the X-ray flux observed at two distinct frequencies (twin HF-QPOs) in micro-quasars.

Keywords: black hole physics – gravitation – X-rays: variability – quasi-periodic oscillations (high frequency) – ray-tracing

1 INTRODUCTION

X-ray radiation coming from accreting black hole binary sources can show quasi-periodic modulations at two distinct high frequencies (> 30 Hz), which appear in the $3:2$ ratio (McClintock and Remillard, 2004). Observations show that the solely presence of a thin accretion disk is not sufficient to produce these HFQPO modulations, because they are exclusively connected to the spectral state, where the energy spectrum is dominated by a steep power law with some weak thermal disk component. We have shown recently (Bursa et al., 2004) that significant temporal variations in the observed flux can be accomplished by oscillations in the geometrically thick flows, fluid tori, even if they are axially symmetric. Here we propose that the QPO variations in the energetic part of the spectrum may come from such very hot and optically thin torus terminating the accretion flow, which exhibits two basic oscillating modes.

Relativistic tori will generally oscillate in a mixture of internal and global modes. Internal modes cause oscillations of the pressure and density profiles within the torus. The outgoing flux is therefore directly modulated by changes in the thermodynamical properties of the gas, while the shape of the torus is nearly unchanged, which is off our interest here. Global modes, on the other hand, alter mainly the spatial distribution of the material. Because light

978-80-7248-419-5

rays do not follow straight lines in a curved spacetime, these changes can be displayed out by effects of gravitational lensing and light bending.

In this paper we summarize extended results of numerical calculations and show how simple global oscillation modes of a gaseous torus affect the outgoing flux received by an static distant observer in the asymptotically flat spacetime and how the flux modulation depends on the geometry and various parameters of the torus. In Section 2 we briefly summarise the idea of the slender torus model and the equations, which are used to construct the torus and to set its radiative properties. In Section 3 we let the torus to execute global oscillations and using a numerical ray-tracing we inspect how these oscillations modulate the observed flux. Then we provide a comparison of our model with complex MHD simulations. If not stated otherwise, we use geometrical units $c = G = 1$ throughout this paper.

2 SLENDER TORUS MODEL

Observations show that the solely presence of a thin accretion disc is not sufficient to produce the HFQPO oscillations, because they are exclusively connected to the spectral state, where the energy spectrum is dominated by a steep power law with some weak thermal disc component. A model is more appropriate, where an outer cool disc is continuously transitioned into or sandwiched by a hot, thick, but optically thin flow (Esin et al., 1998). An optically thin advectiondominated accretion flow (ADAF) is mostly transparent for photons, and therefore general relativistic light bending and lensing effects may gain a particular importance. Significant temporal variations in the observed flux can then be accomplished by global oscillations of such geometrically thick flow, fluid tori.

In order to explore, whether it is possible to obtain some flux modulation just by effects of strong gravity, we set up a model of a possible accretion configuration, largely simplified to a presence of a hot and optically thin luminous torus, optionally surrounded by a cool opaque disc. The torus is considered in a *slender approximation*.

The equipotential structure of a torus is given by the solution of the Euler equation, for which we assume a polytropic flow with purely azimuthal motion and an uniform specific angular momentum ℓ. In the slender approximation, the solution can be expressed in

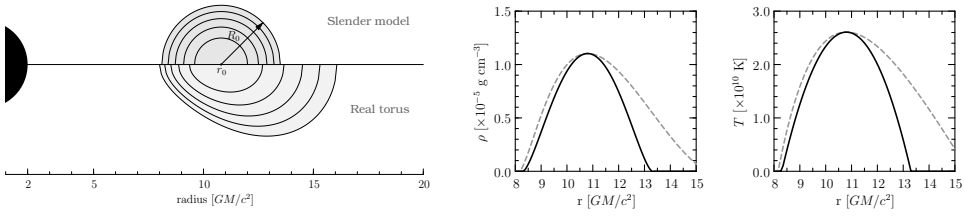

Figure 1. *Left:* An illustration of the equipotential structure of a real relativistic torus (lower part) and of our circular slender torus model (upper part) surrounding a black hole. *Right:* The density and temperature profiles of a polytropic gas forming an accretion torus with the centre at $r_0 = 10.8\,M$. Solid lines represent the slender model with radius $R_0 = 2\,M$ and dashed lines represent the real torus filling the potential well of the same depth.

terms of second derivatives of the effective potential and it turns out that the torus has an elliptical cross-section with semi-axes in the ratio of epicyclic frequencies (Abramowicz et al., 2006). For the model used here, we make even greater simplification and use only the expansion at $r = r_0$ in the z-direction to obtain a slender torus with a circular cross-section of equipotential surfaces (Fig. 1). For the emissivity we assume the torus to be filled with an optically thin gas radiating by the bremsstrahlung cooling.

3 STRONG GRAVITY EFFECTS ON LIGHT MODULATION FROM AN OSCILLATING SLENDER TORUS

Relativistic tori can generally oscillate in a mixture of internal and global modes. Internal modes invoke pressure and density waves within the torus, while its shape remains nearly unchanged. The outgoing flux is therefore directly modulated by variations in the profiles of thermodynamical properties and by the corresponding change of the local emissivity in the optically thin medium. In this case, lensing or any general relativistic effect on the radiation transport is not important, which is off our interest here. Global modes, on the other hand, alter mainly the topological structure and spatial distribution of the material. Because light rays do not follow straight lines in a curved spacetime, these changes can be displayed out by effects of gravitational lensing and light bending.

So far, a certain level of non-axisymmetry has been preferred in proposed models, as it was thought that a non-axisymmetry is a necessary condition for the X-ray flux modulation in black-hole QPOs. Here we show that gravitational bending of the photon trajectories in the vicinity of a black hole suffices to appreciably modulate the flux observed at infinity even if the source of radiation is axially symmetric.

3.1 Oscillation of a slender torus

We impose on the slender torus rigid and axisymmetric ($m = 0$) sinusoidal oscillations in the vertical direction, i.e., parallel to its axis, as well as in the perpendicular radial direction. Such assumption will serve us to model the possible basic global modes found by Abramowicz et al. (2006). In our model, the torus is rigidly displaced from its equilibrium, so that the position of the central circle of maximal pressure varies in time as

$$r(t) = r_0 + \delta r \, \sin(\omega_r t) \,, \qquad z(t) = \delta z \, \sin(\omega_z t) \,,$$

where $\omega_z = \Omega_{\rm K} = \left(M/r_0^3\right)^{1/2}$ is the vertical epicyclic frequency, in Schwarzschild geometry equal to the Keplerian orbital frequency, and $\omega_r = \Omega_{\rm K}\left(1 - 6r_{\rm g}/r_0\right)^{1/2}$ is the radial epicyclic frequency. The torus is placed at the distance $r_0 = 10.8\,M$ so that the oscillation frequency ratio $\omega_z : \omega_r$ is $3:2$, but the choice is arbitrary and only serves to mimic the observed frequency ratio. In the default configuration, the cross-section radius is $R_0 = 2.0\,M$ and amplitudes of the both vertical and radial motion are set to $\delta z = \delta r = 0.1 R_0$.

Two modes are assumed in numerical calculations: *incompressible* and *compressible* mode. In the incompressible mode, the equipotential structure, the thermodynamical quantities describing the torus and in particular its size are fixed and *do not vary* in time as the torus moves. This helps to identify and fully understand the effects of light bending

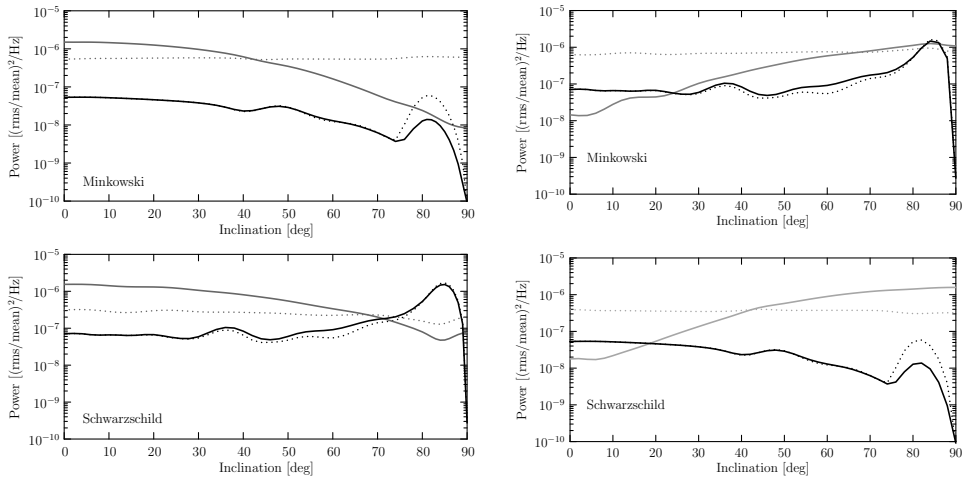

Figure 2. The inclination dependence of powers in the radial (*red*) and the vertical (*blue*) oscillations. Top panel shows calculations in the flat spacetime, bottom panel shows powers as computed in the curved Schwarzschild spacetime. Dashed lines represent the same calculations done with switched-off g-factor ($g \equiv 1$).

on observed lightcurves and power spectra. The compressible mode, which is more close to a real situation, allows for the redistribution of gas in the torus in a response to changes in the radial distance of the torus centre.

Figure 2 compares the dependence of the radial and vertical oscillation powers on changing inclination if the torus is incompressible (left) or compressible (right). We can see that the power in the vertical oscillation stays unchanged, while the radial power is largely affected, particularly if inclination is changed. There is a clear difference between the red curve progression in the left and right panel in Fig. 2. It is caused by the inversion of the luminosity dependence on the torus displacement, which in combination with the effect of g-factor results in a reverse trend of the ω_r power.

3.2 Effect of spacetime geometry

In the Newtonian limit and when the speed of light $c \to \infty$, the only observable periodicity is the radial oscillation (illustrated in Fig. 3). There is no sign of any modulation at the ω_z frequency in the lightcurve, although the torus is moving vertically. This is clear and easy to understand, because the $c \to \infty$ limit suppresses the time delay effects and causes photons from all parts of the torus to reach an observer at the same instant of time, so it is really seen as rigidly moving up and down giving no reason for modulation at the vertical frequency.

When the condition of the infinite light speed is relaxed, the torus is no longer seen as a rigid body. The delays between photons, which originate at different parts of the torus body, significantly alter its image. Those emerging from the front and back at the same coordinate time will be detected at different instants separated by some short amount of time, which is maximal for an edge-on view ($i = \pi/2$) and compared to the Keplerian orbital it can make

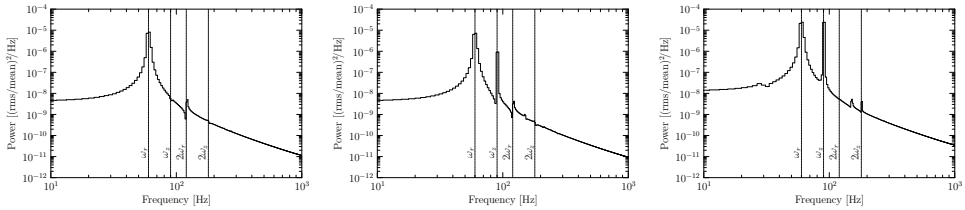

Figure 3. Power spectra of an oscillating torus calculated in the Newtonian limit (*left*), Minkowski spacetime (*middle*) and the Schwarzschild spacetime (*right*). Viewing angle is 70°.

up to about 10 % at $r_0 = 10.8\,M$. The torus is seen from distance as an elastic ring, which modulates its brightness also at the vertical oscillation frequency ω_z due to the time delay effect and the seeming volume change.

Curved spacetime adds the effect of light bending. Photons are focused by the central mass' gravity, which leads to a magnification of any vertical movement. Black hole is not a perfect lens, so that parallel rays do not cross in a single point, but rather form a narrow focal furrow behind it. When the torus trench the furrow (at high viewing angles), its oscillations are greatly magnified by the lensing effect. This is especially significant in the case of the vertical oscillation, as the bright centre of the torus periodically passes through the focal line.

3.3 Effects of changing inclination, torus size, distance, and surrounding disc position

The effect of inclination is probably the most featured, in spite of it is difficult to be directly observationally determined. Changing the line of sight affect the power in the radial/vertical oscillation frequencies, because different effects are important at different angles. When the torus is viewed face-on (i.e., from the top), we expect the amplitude of ω_r to be dominant, as the radial pulsations of the torus can be nicely seen and light rays passing through the gas are not yet strongly bent. When viewed almost edge-on, the Doppler effect reduces the power of ω_r, while gravitational lensing amplifies the power in ω_z. Thus we expect the vertical oscillation to overpower the radial one. Figure 2 (left) shows the inclination dependence of oscillation powers in the Minkowski spacetime (top panel) and in the curved Schwarzschild spacetime (bottom panel).

The effect of the size of the torus is important to study, because it can be directly tested against observational data. Other free model parameters tend to be fixed for a given source (like inclination), but the torus size may well vary for a single source as a response to temporal changes in the accretion rate. The power in the radial oscillation is correlated with its amplitude, which is set to $\delta r = 0.1\,R_0$ and grows with the torus size. It is therefore evident, that the radial power will be proportional to R_0 squared. If the amplitude was constant or at least independent of R_0, the ω_r power would be independent of R_0 too. Thus the non-trivial part of the torus size dependence will be incurred by vertical movements of the torus. Figure 4 (left) shows the PDS power profiles of both the radial and vertical oscillations for several different inclinations. Indeed, the radial power has a quadratic

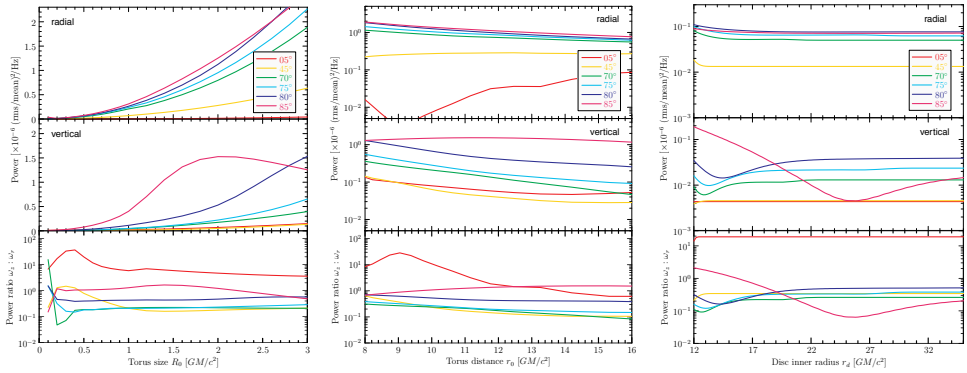

Figure 4. Powers in the radial and vertical oscillations and their ratio as a function of the torus size (*top*), distance from the graviting centre (*middle*) and as a function of an opaque disc distance (*bottom*). Different viewing angles are plotted.

profile and is more dominant for lower viewing angles, which follows from the previous paragraph. The power in the vertical oscillation is at low inclinations also quadratic and similar to the radial one, but the reason is different. The time delay effect causes apparent deformations from the circular cross-section as the torus moves up and down, i.e., to and from the observer in the case of a face-on view. The torus is squeezed along the line of sight at the turning points and stretched when passing the equatorial plane.

The distance of the torus from the gravity centre also affects the intensity of modulation in observed lightcurves (Fig. 4, middle). The power in the radial oscillation is either increasing or decreasing, depending on the inclination. Looking face-on, the g-factor is dominated by the redshift component and the power in ω_r is increasing with the torus distance being less dumped. When the view is more inclined, the Doppler component starts to be important and the oscillation looses power with the torus distance. The critical inclination is about 70°. The power of vertical oscillation generally decreases with the torus distance. It is made visible mainly by the time delay effect and because with the increasing distance of the torus the oscillation period also increases, the effect is loosing on importance. An exception is when the inclination is very high. The large portion of visible relativistic images causes the vertical power first to increase up to some radius, beyond which it then decays. Both small and large tori do not have much of visible secondary images, because they are either too compact or they are too far. The ideal distance is about $11\,r_{\rm g}$ – this is the radius, where the torus has the largest portion of higher-order images, corresponding to the maximum of the vertical power.

There can likely be an outer cool disc surrounding the torus, from which the torus is formed, and which can as well have a substantial effect on light modulation. The Shakura––Sunyaev disc is optically thick and blocks propagation of photons crossing the equatorial plane beyond its terminal radius. Most of the stopped photons has been strongly bent and has carried information predominantly about the vertical mode, thus the presence or not-presence of an opaque disc may be important for the power distribution in QPO modes, namely the vertical one. The disc is considered as a geometrically thin and non-transparent

body. It lies in the the equatorial plane (at $z = 0$) and goes from infinity down to some terminal radius $r_{\rm d}$, which is a parameter of the model. For the purpose of this example, the torus is put somewhat closer to the black hole, with its inner edge near the marginally stable orbit. Its centre is at $r_0 = 9.4\,r_{\rm g}$, its size is $R_0 = 3.0\,r_{\rm g}$, and oscillation amplitudes are $\delta r = \delta z = 0.2\,r_{\rm g}$. The disc can extend as close as to the torus, but does not penetrate into it ($r_{\rm d} > r_0 + R_0 + \delta r$). Figure 4 (right) shows how powers in the oscillation modes are changed if an opaque disc is present. The presence of a thin disc is important, if the disc does not end far from the torus, but rather within a distance of ~ 5 gravitational radii from it, and when the viewing angle is moderate to high. Under these conditions the effect of the torus obscuration by an optically thick medium is capable to substantially change powers in oscillations, and in particular in the vertical mode.

3.4 Comparison with numerical 3D MHD accretion flow simulations

Although the model of an oscillating slender torus is greatly simplified, it shows the possibility of radiation modulation by acting of strong gravity on emerging photons. Due to the level of abstraction, the obtained results are only qualitative. Nonetheless, they may be compared with results obtained by numerical ray-tracing from a more realistic three-dimensional magneto-hydrodynamic simulation of an accretion flow. Such a simulation has been performed by M. Machida (Machida et al., 2005, 2006).

The initial state of the magnetohydrodynamical simulation is an equilibrium polytropic ($\gamma = 5/3$) torus located at $r_0 = 70\,r_{\rm g}$ with a nearly Keplerian distribution of angular momentum, $L = L_0(r_0)\,(r/r_0)^{0.46}$. The torus is threaded by a weak toroidal magnetic field (Okada et al., 1989) with the initial gas to magnetic pressure ratio $\beta \simeq 100$. The presence of the strong gravitational field is simulated by using the pseudo-Newtonian potential (Paczyński and Wiita, 1980) of a $10\,{\rm M}_\odot$ black hole. The self-gravity of the gas and the radiative cooling are neglected.

The initial torus is lead to evolve and after several orbital periods the magnetic field is amplified by number of MHD instabilities together with the differential rotation. The magnetorotational instability (MRI) driven turbulence develops and the torus deforms itself into an accretion disc by transporting angular momentum outwards by Maxwell stress. In the inner part, the matter accretes to the centre, while the disc is expanded radially by gaining some angular momentum in the outer part. The radial angular momentum distribution is very slightly sub-Keplerian, but because the efficiency of the angular momentum transport rate is $\alpha \lesssim 0.01$, it becomes almost constant in the region $10\,r_{\rm g} < r < 22\,r_{\rm g}$ and a small transitional constant angular momentum torus is created at about $16\,r_{\rm g}$. The existence of such tori appears to be a robust feature of many global magnetohydrodynamic simulations (cf. DeVilliers et al., 2003).

The inner torus is an eccentric and time-varying structure. As a response to an event of enhanced mass accretion, a crescent-like density fluctuation develops in the torus sustained by a strong magnetic field. The fluctuation can persist several rotational periods, but is finally destroyed by a magnetic reconnection between the lower and higher density regions. The degree of eccentricity of the torus fluctuates in the response to variations in the mass accretion rate being more pronounced after an increased mass inflow and the development of the crescent.

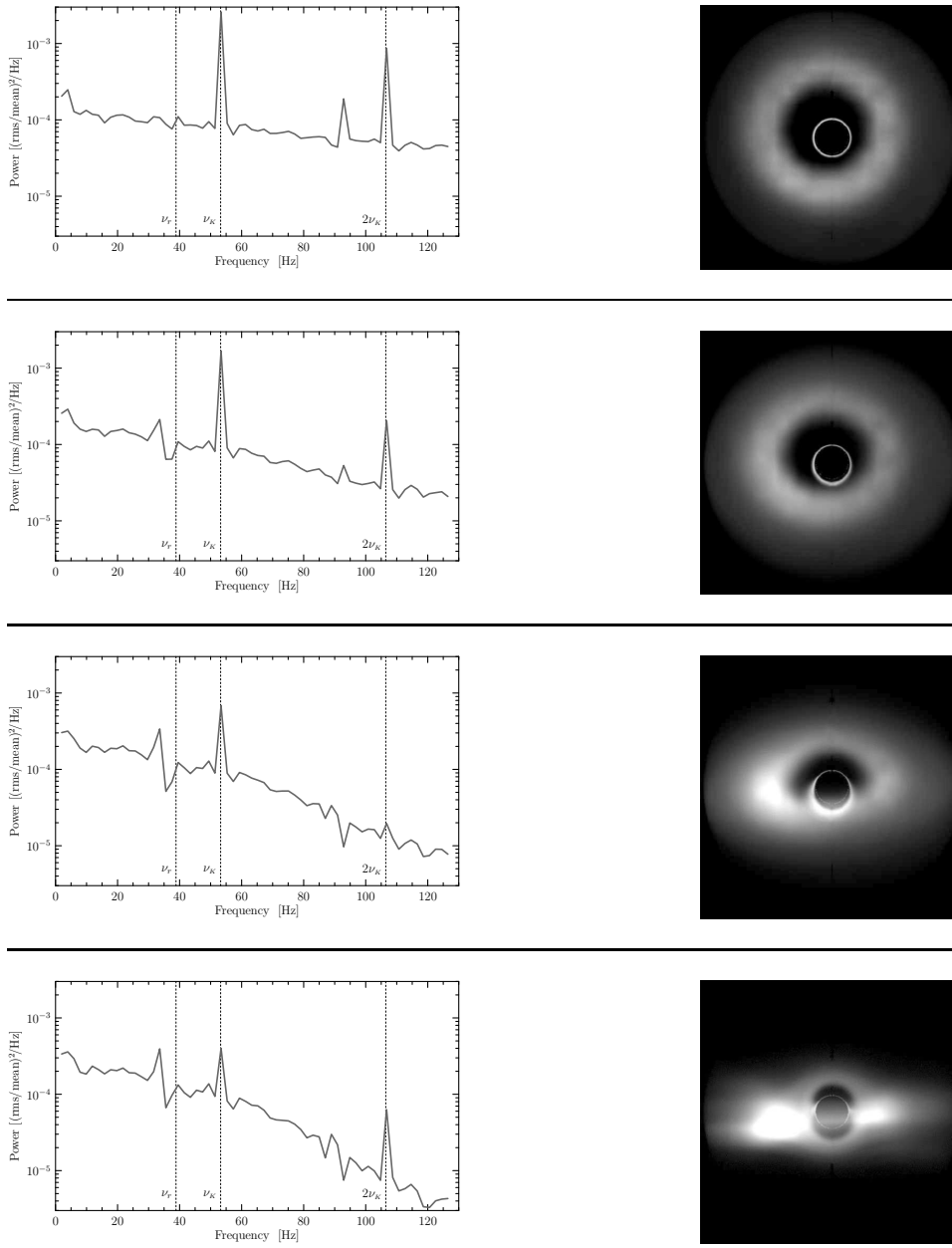

Figure 5. Instant snapshots and power spectra of a MHD accretion flow simulation by M. Machida viewed from different positions (from top): 5°, 30°, 60° and 85°.

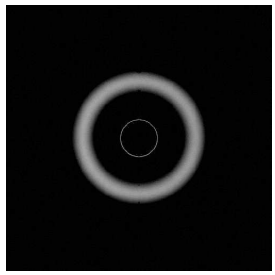
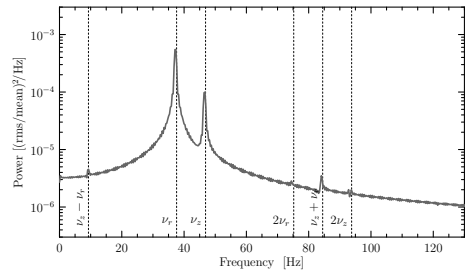

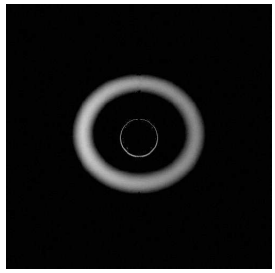
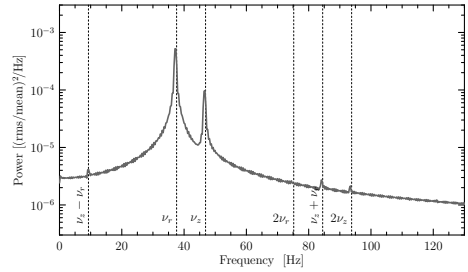

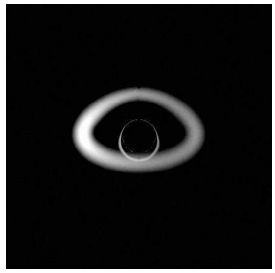
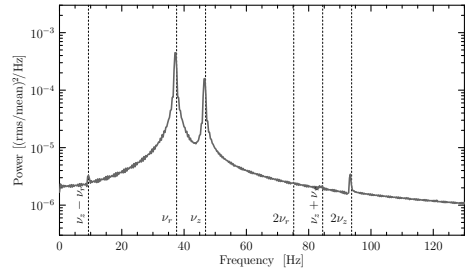

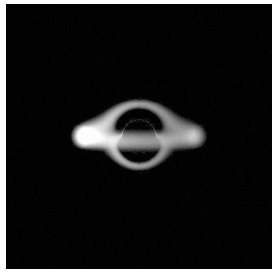
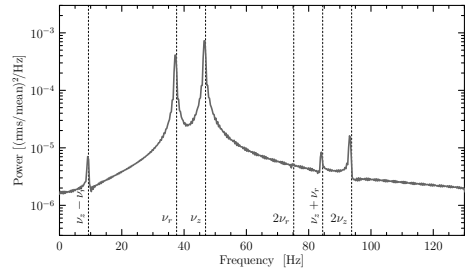

Figure 6. Instant snapshots and power spectra of a slender torus model at $16\,r_{\rm g}$ viewed from different positions (from top): 5°, 30°, 60° and 85°.

The outputs of the simulation are used to analyse the X-ray emission from the inner region of the simulated accretion flow within $40\,r_{\rm g}$ from the central black hole. Figure 5 shows the resulting power spectra and instant snapshot images of the transient torus calculated for several different inclinations. They may be compared with similar panels in Fig. 6, where power spectra and snapshots of a slender torus model are shown. The parameters of the model are chosen such that they resemble the size and distance of the torus in the MHD simulation. The model, however, stays axi-symmetric and oscillates radially and vertically at epicyclic frequencies, as it has been considered throughout this chapter. Despite of this difference, the power spectra reflect a similar pattern of changing power of different peaks depending on the observer's inclination. An additional similarity between the model and the simulated flow may be found, namely that the transient torus oscillates in the vertical direction as well, but not in the rigid mode as the model does. The vertical oscillation frequency is equal to the orbital frequency in the spherically symmetric spacetime, so that the vertical oscillation consequently tilts the torus a little off the equatorial plane. This effect may be seen in the bottom panel in Fig. 5.

ACKNOWLEDGEMENTS

The work was supported by Centre for Theoretical Astrophysics (ref. LC06014). The Astronomical Institute is operated under the project AV0Z10030501.

REFERENCES

Abramowicz, M. A., Blaes, O. M., Horák, J., Kluźniak, W. and Rebusco, P. (2006), Epicyclic oscillations of fluid bodies: Paper II. Strong gravity, *Classical Quantum Gravity*, **23**(5), pp. 1689–1696, arXiv: `astro-ph/0511375`.

Bursa, M., Abramowicz, M. A., Karas, V. and Kluźniak, W. (2004), The Upper Kilohertz Quasi-periodic Oscillation: A Gravitationally Lensed Vertical Oscillation, *Astrophys. J.*, **617**, p. L45.

DeVilliers, J.-P., Hawley, J. F. and Krolik, J. H. (2003), Magnetically Driven Accretion Flows in the Kerr Metric. I. Models and Overall Structure, *Astrophys. J.*, **599**, pp. 1238–1253.

Esin, A. A., Narayan, R., Cui, W., Grove, J. E. and Zhang, S.-N. (1998), Spectral Transitions in Cygnus X-1 and Other Black Hole X-Ray Binaries, *Astrophys. J.*, **505**, pp. 854–868.

Machida, M., Nakamura, K. and Matsumoto, R. (2005), Global Structures of Optically Thin Black Hole Accretion Flows Obtained from Direct Magnetohydrodynamic Simulations, *Publ. Astronom. Soc. Japan*, **56**(4), pp. 671–679.

Machida, M., Nakamura, K. and Matsumoto, R. (2006), Formation of Magnetically Supported Disks during Hard-to-Soft Transitions in Black Hole Accretion Flows, *Publ. Astronom. Soc. Japan*, **58**(1), pp. 193–202, arXiv: `astro-ph/0511299`.

McClintock, J. E. and Remillard, R. A. (2004), Black Hole Binaries, in W. H. G. Lewin and M. van der Klis, editors, *Compact Stellar X-Ray Sources*, Cambridge University Press, Cambridge, arXiv: `astro-ph/0306213`.

Okada, R., Fukue, J. and Matsumoto, R. (1989), A model of astrophysical tori with magnetic fields, *Publ. Astronom. Soc. Japan*, **41**, pp. 133–140.

Paczyński, B. and Wiita, P. J. (1980), Thick accretion disks and supercritical luminosities, *Astronomy and Astrophysics*, **88**(1–2), pp. 23–31, URL `http://adsabs.harvard.edu/abs/1980A\%26A...88...23P`.

Proceedings of *RAGtime 8/9, 15–19/19–21 September, 2006/2007, Hradec nad Moravicí, Opava, Czech Republic*
S. Hledík and Z. Stuchlík, editors, Silesian University in Opava, 2007, pp. 21–25

The timescale of encircling light

Michal Bursa[1], Marek A. Abramowicz[2,3], Vladimír Karas[1], Włodek Kluźniak[3,4] and Alexander Schwarzenberg-Czerny[3]

[1]Astronomical Institute, Czech Academy of Sciences, Boční II 1401/1a, CZ-141 31 Praha 4, Czech Republic
[2]Department of Physics, Göteborg University, S-412 96 Göteborg, Sweden
[3]Copernicus Astronomical Centre, Bartycka 18, PL-00-716 Warszawa, Poland
[4]Department of Physics and Astronomy, Uniwersytet Zielonogórski, ul. Lubuska 2, PL-65-265 Zielona Góra, Poland

ABSTRACT
We show that in some astronomical sources containing black holes, the signature of the circular photon orbit may be detected by searching for the shortest timescale in the variability data. A positive detection would provide the direct empirical support for Einstein's general relativity in its super-strong field limit, relevant to black holes.

Keywords: Kerr–de Sitter spacetime – black hole – naked singularity – test particle – cosmological constant – spin dynamics – equilibrium

1 INTRODUCTION

Whenever a possibly relativistic object is discovered, one of the first questions astrophysicists ask is *what is its compactness*, i.e., what mass is enclosed in what volume. While several methods can be used to measure the mass, knowing the object size is a greater challenge and observers often deduce it from observed variability of the object, providing an upper limit to its physical dimensions from the shortest characteristic timescale found in the lightcurve (or using other approaches like, e.g., a cross-correlation analysis). Thus, the related question to the one given above is *what is the shortest time scale of strong gravity that may be measured by astronomical observations?*

In the context of thin-disk black hole accretion, a well known timescale is that connected to the marginally stable orbit (ISCO). At this boundary, the almost circular motion of matter changes into an almost free-fall and the matter looses contact with the outer accretion flow. The Keplerian orbital period at the ISCO is therefore the shortest timescale that may be associated with the orbital motion in thin accretion disks. In the case of non-rotating neutron stars and black holes, the ISCO is characterised by[1]

$$R_{\rm ms} = 6\,, \quad T_{\rm ms} = 2\pi\sqrt{6^3} \simeq 92.3\,. \tag{1}$$

[1] For an object with the mass M, gravity defines natural scales for length, $R_{\rm G} = GM/c^2$, and time, $T_{\rm G} = R_{\rm G}/c$, which are conveniently used throughout this paper to express any length or time of interest, e.g., radius, orbital time, etc. To recover physical units, one only needs to multiply by $R_{\rm G} = 1.477 \times 10^3\,(M/{\rm M}_\odot)$ meters, or by $T_{\rm G} = 4.926 \times 10^{-6}\,(M/{\rm M}_\odot)$ seconds.

When hydrodynamical stresses in the accretion flow are important, accretion forms a thick disk and the inner edge of the flow may move closer to the black hole, up to the marginally bound orbit. Again, in the Schwarzschild spacetime this boundary is characterised by

$$R_{\rm mb} = 4\,, \quad T_{\rm mb} = 2\pi\sqrt{4^3} \simeq 50.3\,. \tag{2}$$

Thus, formally, $T_{\rm mb}$ gives a (much) shorter time scale than $T_{\rm ms}$; it is, however, not clear whether $T_{\rm mb}$ actually defines any *observable* time scale. In a more physically realistic picture of thick accretion flows, magnetic stresses and in particular the MHD turbulence are far more important than those of hydrodynamical origin, and the situation is very much different. On the basis of numerical simulations, Krolik and Hawley (2002) argue that the location of the inner edge in the MHD thick disks cannot be well defined, the flow is non-axisymmetric and unsteady, so that no characteristic timescale could be identified.

For these reasons, it is generally believed that in the case of thin steady accretion disks, $T_{\rm ms}$ is a relevant observable time scale of strong gravity, while shorter scales, like $T_{\rm mb}$, are not practically observable.

But there is still another, yet much shorter and more fundamental, timescale that is not connected to the accretion flow, but to the strong gravity itself. Close to the black hole horizon, spacetime curvature becomes so strong that photons are able to make loops around the black hole. For a static black hole, the timescale corresponding to the photon orbit loop is

$$R_{\rm ph} = 3\,, \quad T_{\rm ph} = 6\pi g(R_{\rm ph}) \simeq 32.6\,, \tag{3}$$

where $g(R_{\rm ph}) = (1 - 2/R_{\rm ph})^{-1/2}$ is the relevant g-factor for an observer at infinity.

If the conditions are right, signal from some transient events in accretion disk, e.g., random short-lived flares, may reach the observer repeatedly with delays corresponding to the travel time around the photon orbit and still with a sufficient intensity to be practically detected. In this article we report about an ongoing theoretical research on the conditions of detectability of photon orbit patterns by the cross-correlation analysis of the variability data.

2 THE SHORTEST VARIABILITY

Radiation from flaring events, which occur close to the black hole, can reach a distant observer following several different paths. Depending on the source geometry, properties and the surrounding environment, some of these possible ways may be obscured or light can be scattered or absorbed and re-emitted. Most of the radiation is usually concentrated in the direct image, but due to the light bending effect of strong gravity, the same event may also be seen somewhat delayed in the indirect image (on the opposite side of the black hole) or in higher-order images, which make at least one full loop around the photon orbit. The interval between the arrival of individual images depends on geometry and on the mass of the central object only (for the moment we assume zero or small spin of the black hole), thus providing us with a possibility of direct mass measurements.

In the next section we take a closer look at one possible scenario – a thin accretion disk with flares on its surface.

3 DISK FLARES

In systems, in which the thermal-dominated central black hole is surrounded by a thin steady accretion disk terminated near the marginally stable orbit, the geometry is such that first and second order photons from an event come to an observer with a delay that is in most cases close to the photon orbital timescale $T_{\rm ph}$.

We consider flares above the surface of the accretion disk, which may spring up as a result of magnetic reconnection similar to solar eruptions. Flares arise on both sides of the disk, but since the accretion flow is opaque, radiation from the reverse side can only reach the observer through looped photons and therefore much weakened. Thus we consider merely flares on the side of the disk facing the observer (see Fig. 1). Light from those will reach the observer's eye directly, but he will have a chance to see also photons, which wind around the black hole once and only after that escape to infinity. The delay between these two arrivals can then be recovered from the lightcurve, as described in the following section.

Figure 2 shows calculated time delays between photons following the two distinct trajectories, and how this delay depends on the orientation of the system with respect to the observer. We can see that in the area close to ISCO, from which we get the strongest response in the looped image, the delay stays in the narrow interval ~ 35–$45\ T_{\rm G}$, and thus the time of arrival depends only a little on the place of emission.

4 SIGNAL DETECTABILITY & ANALYSIS

Important factors for the detectability of the looped events are the signal-to-noise ratio, timing resolution of the detector, and the ratio of observed intensities between first, second, and higher order images.

While not much can be done about the detector resolution, an appropriate source selection may be crucial for a successful detection. Table 1 summarises the relevant observational properties of different types of black-holes sources. Active galactic nuclei come out far best from the comparison, followed by galactic microquasars and intermediate-mass ULXs. The

Table 1. A summary of typical luminosities, distances, count rates, short variability timescales, and expected detection rate of counts per timescale period for various types of compact sources: active galactic nuclei, ultra-luminous X-ray sources, and galactic black holes. Since the physical picture of ULXs is not known, this type of sources is listed twice with different assumed masses: lines [1] and [2] represent intermediate-mass and stellar-mass black holes, respectively.

	luminosity [erg/s]	distance [kpc]	count rate [cts/s]	timescale [s]	cts/timescale [cts]
AGN	10^{41}–10^{43}	10^{3}–10^{4}	10^{0} –10^{2}	10^{2} –10^{4}	10^{2} –10^{5}
ULX[1]	10^{39}–10^{41}	10^{3}–10^{4}	10^{-2}–10^{0}	10^{-2}–10^{-1}	10^{-4}–10^{-1}
ULX[2]	10^{39}–10^{41}	10^{3}–10^{4}	10^{-2}–10^{0}	10^{-4}–10^{-3}	10^{-6}–10^{-3}
GBH	10^{36}–10^{38}	10^{0}–10^{1}	10^{1} –10^{3}	10^{-4}–10^{-3}	10^{-3}–10^{0}

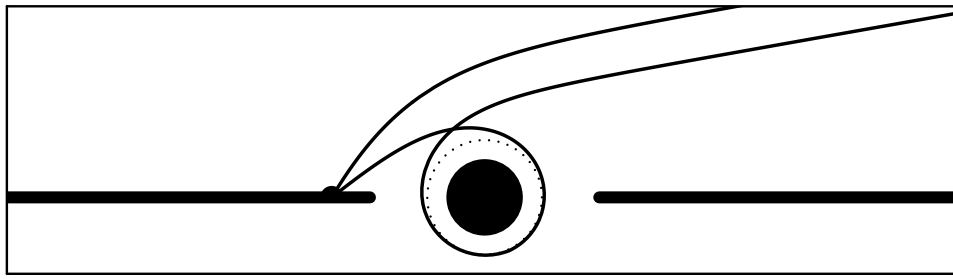

Figure 1. Trajectories of direct and looped photons emerging from a flare on the surface of an accretion disk.

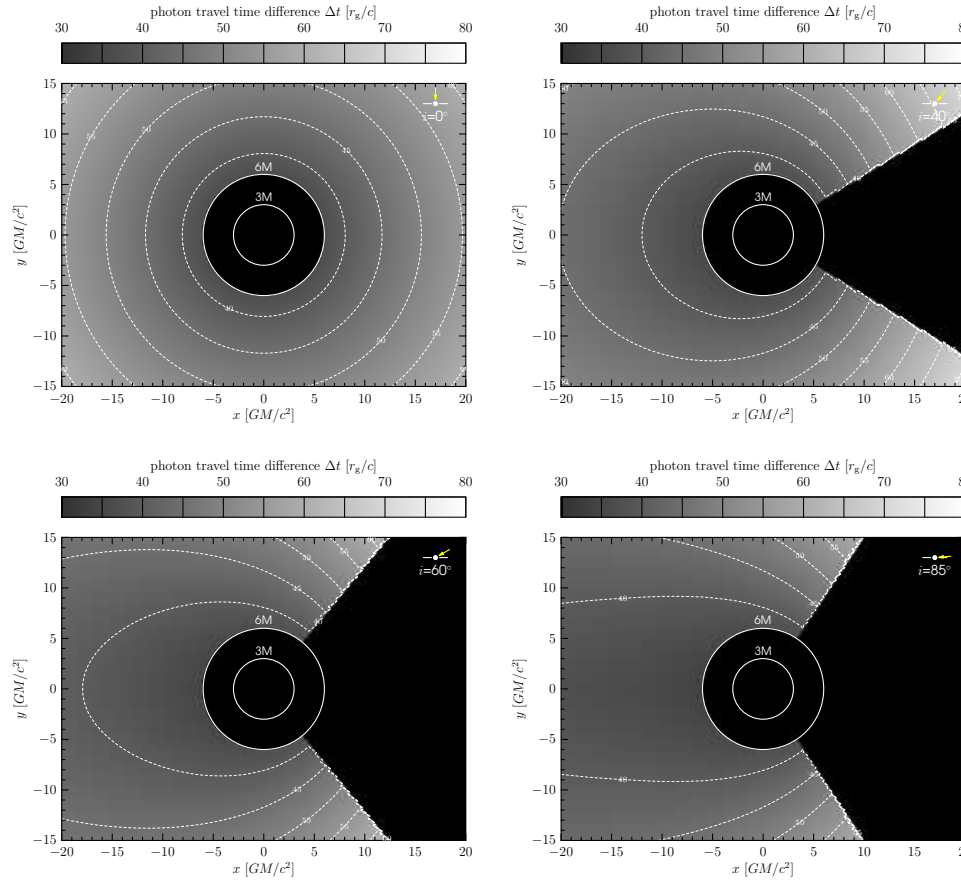

Figure 2. Map of time delay between direct and looped next order image in the disk geometry. Different panels show different inclinations.

situation is much worse for stellar-mass ULXs not only because of low signal level but also due to strong beaming of outgoing radiation and short photon mean free path.

The ratio of observed intensities of looped images can be deduced from the asymptotic expansion of the elliptic function driving the photon trajectory with periastron close to the critical photon orbit (Luminet, 1979),

$$I_{n+1}/I_n \propto \mathrm{e}^{-2\pi} \simeq 1:500\,. \tag{4}$$

Thus, only the first higher order image is sufficiently strong to be practically detected. Its intensity ratio with respect to the direct image can be up to $1:100$.

Due to the fact that we can detect at most two images from each flare that are shifted in time by approximately the interval of photon loop period T_{ph}, the suggested tool for the lightcurve analysis is the autocorrelation function (ACF). Autocorrelation is useful for finding repeating patterns in a signal, such as determining the presence of a periodic signal, which has been buried under noise, or to quantifying how much is an observation related to an adjacent observation. By a convolution of the signal with the time-shifted copy of itself over a sufficiently long time interval, we can obtain a sign of the photon-orbit variability manifested as an excess in ACF at very small time-shifts. Integration over a long interval will erase all randomness in the lightcurve, while looped events will sum up and unfold. The more narrow the spread of photon delays is, the more significant the excess in the autocorrelation will be.

5 CONCLUSIONS

If the delay in arrival time from the vicinity of a black hole between "direct" and "looped" photons (see Fig. 2) could indeed be found in the light curves of AGNs or microquasars, it would not only provide an excellent tool to measure the mass and spin of the black hole, but it would also provide direct evidence for the existence of (nearly) circular photon orbits. In this way one would demonstrate the validity of an important prediction of general relativity in the regime of extremely strong gravitational field.

ACKNOWLEDGEMENTS

The work was supported by Centre for Theoretical Astrophysics (ref. LC06014) and by the GAAV grant KJB300030703. The Astronomical Institute is operated under the project AV0Z10030501.

REFERENCES

Krolik, J. H. and Hawley, J. F. (2002), Where Is the Inner Edge of an Accretion Disk around a Black Hole?, *Astrophys. J.*, **573**(2), pp. 754–763, arXiv: `astro-ph/0203289`.

Luminet, J.-P. (1979), Image of a spherical black hole with thin accretion disk, *Astronomy and Astrophysics*, **75**, p. 228.

Proceedings of *RAGtime 8/9, 15–19/19–21 September, 2006/2007, Hradec nad Moravicí, Opava, Czech Republic*
S. Hledík and Z. Stuchlík, editors, Silesian University in Opava, 2007, pp. 27–33

Thin accretion disks in the Paczyński–Wiita pseudo-potential

Marta Czapla[1] and Włodzimierz Kluźniak[1,2,a]

[1] Department of Physics and Astronomy, Uniwersytet Zielonogórski, ul. Lubuska 2, PL-65-265 Zielona Góra, Poland
[2] Copernicus Astronomical Centre, Bartycka 18, PL-00-716 Warszawa, Poland
[a] wlodek@camk.edu.pl

ABSTRACT
As first shown by Urpin (1984), thin accretion disks exhibit backflows. Using the expansion formalism of Kluźniak and Kita (2000), we investigate the structure of a thin polytropic disk in the Paczyński–Wiita pseudo-potential. Close to the equatorial plane the radial velocity changes sign at a certain distance from the black hole. As expected, the velocity profile corresponds to backflow at large distances and a strong inflow close to the inner edge of the disk. The inner edge of the accretion disk turns out to be at three Schwarzschild radii ($r = 6MG/c^2$).

Keywords: Black holes – accretion disks – hydrodynamics –equilibrium

1 THIN ACCRETION DISKS

Thin accretion disks are present in many astronomical systems, but cannot at present be described by MHD simulations. However, they are fluid systems very nearly in hydrostatic equilibrium, and this makes them amenable to an approximate description in hydrodynamics. Here, we present an analytic solution to the three-dimensional structure of an accretion disk in the Paczyński–Wiita Newtonian model of the Schwarzschild metric (Paczyński and Wiita, 1980).

Mathematical treatment of thin accretion disks around black holes began with the paper of Shakura and Sunyaev (1973), who solved a system of (simplified) equations of hydrodynamics for a viscous fluid assumed to be very close to hydrostatic equilibrium in the Newtonian gravitational field of a point mass. Self-gravity of the disk can safely be neglected for accreting white dwarfs, neutron stars, and black holes in binary systems. We are not going to concern ourselves here with the treatment of radiation, which was also discussed extensively by Shakura and Sunyaev. However, we assume a state of radiative efficiency, which allows the disk to be cool (relative to the virial temperature), and hence to be thin in the direction perpendicular to the equatorial plane.

The Shakura and Sunyaev (SS) thin disk is rotationally supported by orbital motion, and is in vertical hydrostatic equilibrium. Shakura and Sunyaev showed that the latter condition relates the ratio of disk thickness, h, to the radius r (of a given annulus) to the ratio of the speed of sound c_s to the Keplerian velocity $r\Omega_K$. This ratio, $\varepsilon \equiv c_s/(r\Omega_K) \approx h/r$ defines a small parameter in the problem, which we will exploit later. The presence of

978-80-7248-419-5

dissipation leads to the transport of angular momentum outwards (away from the source of gravity), and a concomitant inflow of matter (accretion) on a timescale much longer than the orbital timescale.

Postulating that the leading viscous stress term, the r-ϕ component of the stress tensor, $\eta r\, \partial\Omega/\partial r$, is proportional to the pressure, Shakura and Sunyaev were able to solve the vertically integrated equations of motion, under the boundary condition that the viscous torque vanishes at a certain radius, taken to be equal to the radius of the innermost stable circular orbit around a black hole, $6GM/c^2$ in the Schwarzschild metric. Later, this boundary condition in a Newtonian calculation was shown (Muchotrzeb and Paczyński, 1982) to be a very good approximation to the correct one of transonic flow in the Kerr metric (Stoeger, 1976). The nature of accretion flow through the inner boundary in the Kerr metric was elucidated in a study of the differential topology of accretion disks by Abramowicz et al. (1978) who found that one of the isobaric surfaces has an inner cusp.

Urpin (1984) showed that asymptotically (at large radial distances from the inner edge) the velocity field in a thin disk is qualitatively different from its average over the disk thickness. In particular, close to the equatorial plane the flow is directed more or less radially outwards. Only further away from the disk mid-plane (i.e., at higher values of the z co-ordinate) is the flow directed radially inwards, as one may expect for an accreting black hole. The global flow pattern in a thin disk was found by Kluźniak and Kita (2000), see Fig. 1, below.

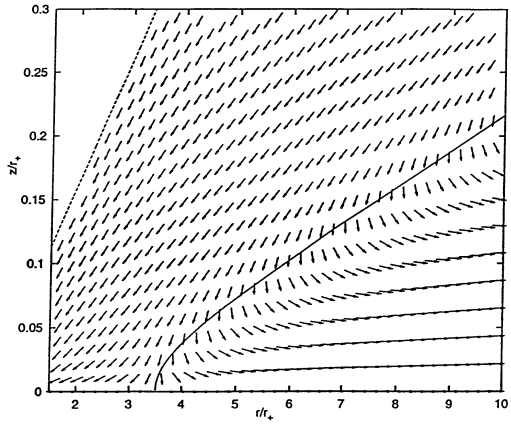

Figure 1. The general character of flow in a thin accretion disk. This figure (Fig. 6a of Kluźniak and Kita, 2000) shows the meridional cross-section of the inner parts of an accretion disk. The abscissa is the cylindrical radial r co-ordinate in units of the inner edge of the disk, the ordinate is the cylindrical z co-ordinate in the same units. Note that the vertical scale is greatly expanded, the actual z/r ratio is less than 0.1. The direction of velocity vectors is indicated. Close to the surface of the disk, the velocity of the fluid is directed towards the inner edge of the disk. The continuous line is the locus of points where the direction of flow is vertical (perpendicular to the plane of the disk, and directed towards it). To the left of this line, the flow is inwards, to the right of this line the flow is directed outwards. A stagnation point (here at an abscissa of ~ 3.5) is present in the equatorial plane. Note that the magnitude of velocity is not plotted, i.e., the velocity vectors are normalized to unity in the figure.

Kluźniak and Kita's (KK) analytic calculation, just like Shakura and Sunyaev's, was carried out for a Newtonian $1/R$ potential, and with the same inner boundary condition of vanishing torque at a certain prescribed radius. This leads to well known divergencies at the inner edge, which are an artifact of the boundary condition. As a first step to finding the three-dimensional structure of an accretion disk in the Kerr metric, we repeat the KK calculation in the Paczyński–Wiita (PW) pseudopotential. This will allow us discard the inner boundary condition of the SS disk.

For motion in the PW potential

$$\psi = -\frac{GM}{R - r_{\rm S}}\,, \tag{1}$$

where $r_{\rm S} = 2GM/c^2$ is the Schwarzschild radius, the role of Keplerian angular velocity is played by $\Omega_{\rm g} \equiv \Omega_{\rm K}/(1 - r/r_{\rm S})$, with r the cylindrical radial co-ordinate, and $R = (r^2 + z^2)^{1/2}$. However, the correct Schwarzschild radial position of the ISCO is reproduced, $r_{\rm ms} = 6MG/c^2$ (Paczyński and Wiita, 1980).

2 THE EQUATIONS AND THE KK EXPANSION

To obtain the structure of a thin accretion disk, we solve the equation of continuity and the (generalized) Navier–Stokes equation

$$\frac{\partial \rho}{\partial t} + \boldsymbol{\nabla} \cdot (\rho \boldsymbol{V}) = 0\,, \tag{2}$$

$$\frac{\partial \boldsymbol{V}}{\partial t} + (\boldsymbol{V} \cdot \boldsymbol{\nabla})\boldsymbol{V} = -\frac{1}{\rho}\,\boldsymbol{\nabla} P - \boldsymbol{\nabla}\psi + \frac{1}{\rho}\,\boldsymbol{\nabla} \cdot \sigma \tag{3}$$

with a viscous stress tensor

$$\sigma_{ik} = \eta \left(\frac{\partial v_i}{\partial x_k} + \frac{\partial v_k}{\partial x_i} - \frac{2}{3}\delta_{ik}\frac{\partial v_l}{\partial x_l} \right) + \xi \delta_{ik} \frac{\partial v_l}{\partial x_l}\,, \tag{4}$$

under the following assumptions. The system (disk) is

1. time independent,
2. azimuthally symmetric,
3. reflection-symmetric in $z = 0$ plane,
4. thin, $z/r \ll 1$,
5. subject to an alpha-like viscosity,
6. described by a polytropic e.o.s., $n = 3$,
7. in the Paczyński–Wiita potential.

Assumption 5 requires a comment. For comparison with the SS solution of the height-integrated equations, we would like to have a similar viscosity model. However, unlike SS, we use all the components of the stress tensor, and we need to specify the coefficient of viscosity, $\eta = \nu\rho$. To lowest order (the only one we need for this coefficient) we use

$$\nu_0(r, z) = \alpha \left(1 + \frac{1}{n} \right)^{-1} \frac{c_{\rm s0}^2(r, z)}{\Omega_0}\,, \tag{5}$$

which yields an r-ϕ component of the stress tensor similar in value to the SS one. As it turns out, all terms involving the bulk viscosity, ξ, are third order or higher in ε, so we do not need to specify the bulk viscosity, except to say that it is of the same order as η, or higher.

Assumption 6 is one of convenience only. We model an efficiently cooled disk with a polytrope. However, the effects we describe are dynamic. As shown by Regev and Gitelman (2002), the KK results for the flow pattern are reproduced when the polytrope of assumption 6 is replaced by an ideal-gas e.o.s., with radiative transfer treated numerically.

Assumption 7 is the only new ingredient of the calculation, which otherwise follows closely the KK paper. The method of solution is the Kluźniak and Kita expansion in z/r, whereby the equations are solved order by order in the small parameter, after all quantities are scaled with their characteristic values and then expanded systematically:

$$u \equiv \frac{v_r}{\tilde{c}_\mathrm{s}} = u_0 + \varepsilon u_1 + \varepsilon^2 u_2 + \cdots , \tag{6}$$

$$v \equiv \frac{v_z}{\tilde{c}_\mathrm{s}} = v_0 + \varepsilon v_1 + \varepsilon^2 v_2 + \cdots , \tag{7}$$

$$\frac{c_\mathrm{s}}{\tilde{c}_\mathrm{s}} = c_{\mathrm{s}0} + \varepsilon c_{\mathrm{s}1} + \varepsilon^2 c_{\mathrm{s}2} + \cdots , \tag{8}$$

$$\frac{\Omega}{\Omega_\mathrm{g}} = \Omega_0 + \varepsilon \Omega_1 + \varepsilon^2 \Omega_2 + \cdots , \tag{9}$$

$$\frac{\rho}{\tilde{\rho}} = \rho_0 + \varepsilon \rho_1 + \varepsilon^2 \rho_2 + \cdots , \tag{10}$$

$$\frac{\eta}{\tilde{\eta}} = \eta_0 + \varepsilon \eta_1 + \varepsilon^2 \eta_2 + \cdots . \tag{11}$$

For example, the equation of continuity will now have the form

$$\frac{\varepsilon}{r}\frac{\partial}{\partial r}(r\rho u) + \frac{\partial}{\partial z}(\rho v) = 0 , \tag{12}$$

reflecting the fact that in a thin disk radial gradients are suppressed by a factor of ε relative to the vertical ones. An immediate consequence of Eq. (12) is that the z component of velocity is of higher order in ε than the radial component. However, "higher order" is not the same as "always smaller." The KK solution to the e.o.m. reveals a surface within the disk through which flow is purely vertical (perpendicular to the equatorial plane), see Fig. 1, and the same is true for the solution discussed here.

3 BOUNDARY CONDITIONS

We take the density to vanish sufficiently far above (or below) the mid-plane of the disk. For a polytrope, of course, the density goes to zero at a definite height. With this b.c., the azimuthal component of the e.o.m.,

$$\rho \frac{v_r}{r^2}\frac{\partial}{\partial r}(r^2\Omega) + \rho v_z \frac{\partial \Omega}{\partial z} = \frac{1}{r^3}\frac{\partial}{\partial r}\left(\eta r^3 \frac{\partial \Omega}{\partial r}\right) + \frac{\partial}{\partial z}\left(\eta \frac{\partial \Omega}{\partial z}\right) ,$$

can be integrated vertically and radially to yield

$$\dot{m}(j - j_+) = -r^3 \int_{-\infty}^{+\infty} \eta \, \mathrm{d}z \frac{\partial \Omega}{\partial r} \,, \tag{13}$$

where, $\dot{m}$ is the (scaled) mass accretion rate, j is the vertical average of angular momentum per unit mass, $r^2\Omega$, and j_+ is a constant of integration. The SS and KK disks (in the Newtonian $1/R$ potential) extend down to a radius where $j = j_+$, and hence the height of the disk goes to zero there. This is the zero-torque assumption of SS, discussed in Section 1 above. Here, in the PW potential this assumption is no longer necessary.

4 THE SOLUTION

To present the flavour of the calculation, let us discuss the radial component of the e.o.m.

$$v_r \frac{\partial v_r}{\partial r} + v_z \frac{\partial v_r}{\partial z} - \Omega^2 r = -\frac{\partial \psi}{\partial r} - \frac{1}{\rho}\frac{\partial P}{\partial r} + \frac{1}{\rho} F_r \,, \tag{14}$$

with

$$F_r = \frac{2}{r}\frac{\partial}{\partial r}\left(\eta r \frac{\partial v_r}{\partial r}\right) - \frac{2\eta v_r}{r^2} + \frac{\partial}{\partial z}\left[\eta\left(\frac{\partial v_r}{\partial z} + \frac{\partial v_z}{\partial r}\right)\right] + \frac{\partial}{\partial r}\left[\left(\xi - \frac{2}{3}\eta\right)(\boldsymbol{\nabla}\cdot\boldsymbol{V})\right] .$$

The scaled version is

$$\begin{aligned}
\varepsilon^2 u \frac{\partial u}{\partial r} + \varepsilon v \frac{\partial u}{\partial z} - \Omega^2 r = &-\left[1 + \varepsilon^2\left(\frac{z}{r}\right)^2\right]^{-1/2}\left\{r\left[1 + \varepsilon^2\left(\frac{z}{r}\right)^2\right]^{1/2} - r_{\mathrm{g}}\right\}^{-2} \\
&- \varepsilon^2 n \frac{\partial c_{\mathrm{s}}^2}{\partial r} + \frac{\varepsilon^3}{\rho r}\frac{\partial}{\partial r}\left(2\eta r \frac{\partial u}{\partial r}\right) + \frac{\varepsilon}{\rho}\frac{\partial}{\partial z}\left(\eta \frac{\partial u}{\partial z}\right) + \frac{\varepsilon^2}{\rho}\frac{\partial}{\partial z}\left(\eta \frac{v}{r}\right) \\
&- \frac{\varepsilon^3}{\rho}\frac{2\eta u}{r^2} + \frac{\varepsilon^3}{\rho}\frac{\partial}{\partial r}\left[\left(\xi - \frac{2}{3}\eta\right)\frac{1}{r}\frac{\partial}{\partial r}(ru)\right] + \frac{\varepsilon^2}{\rho}\frac{\partial}{\partial r}\left[\left(\xi - \frac{2}{3}\eta\right)\frac{\partial v}{\partial z}\right] .
\end{aligned} \tag{15}$$

In zeroth order all terms disappear, except for the last term on the left side and for the first term on the RHS of Eq. (14), with the solution

$$\Omega_0 = r^{-3/2}\left(1 - \frac{r_{\mathrm{g}}}{r}\right)^{-1} . \tag{16}$$

To this order, the equation simply states that the lowest order azimuthal velocity is equal to the orbital velocity of a test particle in circular orbit, $\Omega = \Omega_{\mathrm{g}}$.

In higher orders we are not so lucky. The second order (in ε) equations form a system as complicated as can be – we have to solve coupled, partial, second order differential equations. Luckily, an ansatz may be used (KK), which converts the system to algebraic equations.

The solution for angular velocity is qualitatively similar to that of KK. Close to the inner edge of the disk Ω is superKeplerian, while for $r \gg r_S$ it is subKeplerian. The solution for radial velocity is considerably more interesting:

$$u_1(r,z) = \alpha\Omega_0 \frac{h^2}{r} \left\{ \frac{\frac{11}{8} + \frac{r_S}{r}\left(1-\frac{r_S}{r}\right)^{-1}\left[\frac{7}{3} + \frac{r_S}{r}\left(1-\frac{r_S}{r}\right)^{-1}\right]}{\frac{72\alpha^2}{25} + \left[\frac{1}{2} - \frac{r_S}{r}\left(1-\frac{r_S}{r}\right)^{-1}\right]} \right.$$
$$\left. \times \left[\frac{6}{5}\left(1 - \frac{z^2}{h^2}\right) + \frac{\frac{72\alpha^2}{25}}{\frac{1}{2} - \frac{r_S}{r}\left(1-\frac{r_S}{r}\right)^{-1}} \right] - \frac{\mathrm{d}\ln h}{\mathrm{d}\ln r}\left[\frac{\frac{3}{2} + \frac{r_S}{r}\left(1-\frac{r_S}{r}\right)^{-1}}{\frac{1}{2} - \frac{r_S}{r}\left(1-\frac{r_S}{r}\right)^{-1}}\right] \right\}. \quad (17)$$

The radial velocity is of the order $\varepsilon^2\Omega r$ and proportional to the viscosity coefficient. In the limit of $r_S \to 0$ the solution goes over to that of KK, as the PW potential goes over to the Newtonian one. However, for $r_S \neq 0$ the last two denominators in Eq. (17) go to zero at $r = 3\,r_S$, and so the radial velocity becomes divergent (and negative), indicating supersonic inflow close to the position of the ISCO, at $r = 3\,r_S = 6MG/c^2$. On the other hand, for $r \gg r_S$, where $\mathrm{d}h/\mathrm{d}r \sim h/r$, the last term is no longer dominant in the mid-plane of the disk and the radial velocity is positive, corresponding to outflow near the midplane of the disk, as in Fig. 1.

5 CONCLUSIONS

It is possible to solve equations of viscous hydrodynamics in 3D analytically for the vertical structure of an accretion disk. A non-trivial flow pattern in the meridional plane appears even for an axisymmetric disk, including a backflow. Close to the inner edge of the disk the fluid flows inwards at all heights within the disk. In the mid-plane of the disk a stagnation point separates the region of inflow and backflow (Kluźniak and Kita, 2000).

We have obtained an analytic solution for a thin accretion disk in the Paczyński–Wiita Newtonian model of black-hole gravity, without imposing an inner boundary condition. The solution exhibits supersonic inflow close to the radius of the innermost (marginally) stable circular orbit, i.e., at $r = 6MG/c^2$.

REFERENCES

Abramowicz, M. A., Jaroszyński, M. and Sikora, M. (1978), Relativistic accreting disks, *Astronomy and Astrophysics*, **63**(1–2), pp. 221–224, URL `http://adsabs.harvard.edu/abs/1978A\%26A....63..221A`.

Kluźniak, W. and Kita, D. (2000), Three dimensional structure of an alpha accretion disk, arXiv: `astro-ph/0006266`, (KK).

Muchotrzeb, B. and Paczyński, B. (1982), Transonic accretion flow in a thin disk around a black hole, *Acta Astronom.*, **32**, p. 1.

Paczyński, B. and Wiita, P. J. (1980), Thick accretion disks and supercritical luminosities, *Astronomy and Astrophysics*, **88**(1–2), pp. 23–31, (PW).

Regev, O. and Gitelman, L. (2002), Asymptotic models of meridional flows in thin viscous accretion disks, *Astronomy and Astrophysics*, **396**, p. 623.

Shakura, N. I. and Sunyaev, R. A. (1973), Black holes in binary systems. Observational appearance, *Astronomy and Astrophysics*, **24**, p. 337, (SS).

Stoeger, W. R. (1976), Boundary-condition modification of the Novikov–Thorne accretion-disc models and velocity matching across the inner edge, *Astronomy and Astrophysics*, **53**, p. 267.

Urpin, V. A. (1984), Hydrodynamic flows in accretion disks, *Astronom. Zh.*, **61**, pp. 84–90, (also 1984, *Soviet Astronom.*, **28**, p. 50).

Proceedings of *RAGtime 8/9, 15–19/19–21 September, 2006/2007, Hradec nad Moravicí, Opava, Czech Republic*
S. Hledík and Z. Stuchlík, editors, Silesian University in Opava, 2007, pp. 35–44

Low angular momentum[1] accretion flow model of Sgr A* activity

Bożena Czerny[1,a], Monika Mościbrodzka[1], Daniel Proga[2], Tapas K. Das[3] and Aneta Siemiginowska[4]

[1]Copernicus Astronomical Centre, Bartycka 18, PL-00-716 Warszawa, Poland
[2]Department of Physics, University of Nevada, Las Vegas, NV 89154, USA
[3]Harish Chandra Research Institute, Allahabad-211 019, India
[4]Harvard-Smithsonian Center for Astrophysics, 60 Garden Street, Cambridge MA 02138, USA
[a]bcz@camk.edu.pl

ABSTRACT
Sgr A* is a source of strongly variable emission in several energy bands. It is generally agreed that this emission comes from the material surrounding the black hole which is either falling in or flowing out. The activity must be driven by accretion but the character of accretion flow in this object is an open question. We suggest that the inflow is dominated by the relatively low angular momentum material originating in one of the nearby group of stars. Such material flows in directly towards the black hole up to the distance of order of ten Schwarzschild radii or less, where it hits the angular momentum barrier which leads naturally to a flow variability. We study both the analytical and the numerical solutions for the flow dynamics, and we analyze the radiation spectra in both cases using the Monte Carlo code to simulate the synchrotron, bremsstrahlung and the Compton scattering. Our model roughly reproduces the broad band spectrum of Sgr A* and its variability if we allow for a small fraction of energy to be converted to non-thermal population of electrons. It is also consistent (for a range of viewing angles) with the strong constraints on the amount of circumnuclear material imposed by the measurements of the Faraday rotation.

Keywords: Sgr A* – black hole – accretion – radiation spectra

1 INTRODUCTION

The character of the accretion flow onto a black hole depends on the initial angular momentum of the material. This angular momentum is specified by the outer boundary conditions which depend on the relative motion of the donor with respect to the black hole. This angular momentum corresponds to a certain circularization radius, i.e., the radius where this angular momentum is equal to the local Keplerian value. In binary systems the material

[1] See Introduction for specification of what we mean by low angular momentum.

978-80-7248-419-5

comes from the secondary star and in general is possess high angular momentum due to the orbital motion. In Low mass X-ray binaries the flow proceeds through an inner Lagrange point and the circularization radius is a significant fraction of a Roche radius around a black hole, of order of $10^4\ R_{\rm g}$ ($R_{\rm g} = GM/c^2$). In high mass X-ray binaries the accretion flow comes from the intercepted focused wind, so the circularization radius is smaller but still large, of order of $10^3\ R_{\rm g}$. In such case the inflowing material form an accretion disk around a black hole and the inflow proceeds due to the angular momentum transfer. Apart from the outermost region and the region close to the ISCO (innermost stable circular orbit), the distribution of the angular momentum is relatively smooth and not much different from the Keplerian law. The exact departures from Keplerian motion depends on the disk temperature (or more exactly, on the pressure distribution).

In active galactic nuclei (AGN) the source of material is less specified. The material comes either from the stars (in the form of stellar winds) or from the gaseous phase of the galactic material. Bright AGN (quasars, Seyfert 1 galaxies) show the presence of accretion disks similar to the disks in binary systems so we can conclude that the angular momentum reaching the galactic center is high. In sources showing water maser activity we observe the outer parts of the disk directly, and in most sources the motion of the disk material is Keplerian. However, in weakly active galaxies like Sgr A* or giant elliptical galaxies we see no direct evidence of a disk. In Sgr A* the presence of the cold disk is actually excluded by the lack of eclipses of the stars which move very close to the central black hole and are systematically monitored since several years.

Since in weakly active galaxies there are no direct observational arguments for any value of the angular momentum of the donated material and the location of material sources, three types of models are being considered:

- high angular momentum flow, with circularization radius of order of hundreds-thousands of $R_{\rm g}$;
- low angular momentum flow, with circularization radius of order of a few $R_{\rm g}$;
- spherical and quasi-spherical accretion, without angular momentum barrier.

The high angular momentum flow solutions for weakly active galaxies generally belong to ADAF (advection dominated accretion flow) family (Ichimaru, 1977; Narayan and Yi, 1994), with possibly additional effects like outflows (Blandford and Begelman, 1999) and convection. In this case the flow is not exactly Keplerian since the pressure gradients are important, but the local ratio of the angular momentum to the Keplerian angular momentum in most part of the flow is not wildly different from unity, and the angular momentum transfer (through viscosity) or angular momentum loss (through magnetic wind) at all radii is essential. Stationary solutions usually exist, and asymptotically the density of the flow approaches zero at infinity.

In spherical and quasi-spherical flow there is no angular momentum barrier so the loss of angular momentum is not the necessary condition for the accretion to occur. Examples of such solutions are: purely spherical Bondi flow or flows where the angular momentum density is below the minimum angular momentum at the circular orbit around a black hole which is given by

$$l_{\rm min} = 3\sqrt{3}\,GM/c^2 \tag{1}$$

in case of Schwarzschild black hole; more general formula for a Kerr black hole can be found in Bardeen et al. (1972). In Bondi solution (Bondi, 1952; Baganoff et al., 2003) the outer boundary condition are specified by the density and the temperature of the uniform medium surrounding black hole at large distances. The flow velocity is zero at infinity, the inflow becomes transonic at the Bondi radius, and the supersonic flow reaches the black hole horizon. The Bondi radius depends significantly on the gas properties (e.g., polytropic index; Bondi radius is of order of thousands of $R_{\rm g}$ for relativistic flow with $\gamma = 4/3$ but is approaches zero if $\gamma \rightarrow 5/3$, typical for perfect fluid non-relativistic solution), but the accretion rate is much less sensitive to those assumptions. Purely Bondi flow has generally very low radiative efficiency so it cannot reproduce the observed luminosity in most weakly active galaxies (Moscibrodzka, 2006). If the accreting material at the outer boundary condition has certain angular momentum $l < l_{\rm min}$, the dynamics of the flow is slightly modified in comparison with Bondi flow and the flow is not spherically symmetric any more but the stationary solution for the flow always exists.

The intermediate case of low angular momentum the situation is the most complex as initially the flow behaves as the Bondi flow but close to the black hole the flow starts suddenly to feel the angular momentum barrier (Abramowicz and Zurek, 1981). In this case analytical stationary solutions frequently do not exist. In numerical solutions the flow is variable and does not reach a stationary solution in the computing time. If the angular momentum of the donated material is also a subject of changes (e.g., the result of the stellar motion), a truly stationary solution indeed can never be reached for physical reasons.

In the case of Sgr A* the available spatial resolution is the highest and we can have the best insight into the sources of material (Genzel and Karas, 2007). Therefore, in the present paper we concentrate specifically on this source and we argue that the low angular momentum flow is an interesting and promising option for the flow description.

2 SGR A* SURROUNDING AND THE SOURCE OF MATERIAL

At the central parts of our Galaxy there are a few stellar populations and each of them provides stellar winds. The closest O/B stars (at distances of a small fraction of a parsec) used for the mass measurements have moderate winds; much stronger winds come from more evolved stars being at distances up to a few parsecs. If a single star dominates as a donor star, and the wind velocity is larger than the stellar orbital velocity, there is a zero angular momentum line joining the donor star and the black hole, so the net angular momentum flowing in is likely to be low (Loeb, 2004; Mościbrodzka et al., 2006). Estimates of the ram pressure indicate that a single source, IRS 13E (the compact group of Wolf–Rayet stars) with the strongest wind (e.g., Rockefeller et al., 2004) indeed dominates independently from the relatively large distance from the central black hole (Mościbrodzka et al., 2006).

Although the ram pressure argument strongly depends on the adopted wind outflow rate and wind velocity, the additional argument against the dominance of the nearby young O/B stars comes from the lack of obvious correlation between the activity level and stellar passages. On the other hand, un-modulated flow can come from stars forming a mysterious ring-like structure at a distance of a parsec scale (Paumard et al., 2006). In this case the

material might have very large angular momentum, and even a cold disk may form, as postulated by Nayakshin and Sunyaev (2003). However, the periodicity seemed to be seen in the NIR and X-ray flares (Genzel et al., 2003; Bélanger et al., 2006) and the absence of eclipses does not seem to support cold disk scenario. The motion of IRS 13E differs from that of other stars and seems to be significantly eccentric. Detailed studies of the observational consequences of all scenarios are necessary to solve the issue.

3 ANALYTICAL SOLUTIONS FOR THE DYNAMICS

Analytical solutions can be obtained if the description of the flow is simplified: outflow and viscosity are neglected, the flow is polytropic and the gravity is described by pseudo-Newtonian potential. The problem was studied in numerous papers following the idea of Abramowicz and Zurek (1981).

3.1 Transonic solutions with and without shocks

The existence and the character of solution depends critically on the interplay of the solution parameters: polytropic index, energy density and angular momentum density (e.g., Das et al., 2003). The equations usually show the presence of three critical points: the outer one is direct generalization of the Bondi radius, the inner one describes the expected transition to the supersonic flow below the ISCO and the intermediate point is unphysical (in a sense it is not of the saddle type and the flow cannot pass there smoothly from subsonic to supersonic solution). Usually the flow passes from subsonic flow at infinity to supersonic flow close to horizon either at the outer *or* at the inner critical point. For a certain range of the parameters, it is also possible to find a second solution, with a shock (satisfying the standard Rankine–Hugoniot conditions) located between the outer and the inner sonic point. Such a shock *may*, but *not must*, form.

The eventual shock development is likely to be related to the past state of the accretion flow. For a fixed value of polytropic index and energy, there is a specific value of the angular momentum density at which the solution changes from transonic at outer to transonic at inner critical points. This change of flow properties is dramatic, and therefore the flow slowly crossing this angular momentum border is likely to develop a shock instead of following a new shock-less solution since this allows for a slow and continuous change in the flow properties (shock is initially weak). The discussion of this issue will be presented elsewhere (Das, Czerny & Mościbrodzka, in preparation).

For large enough angular momentum there is no analytical solution which extends down to the black hole even if a shock is allowed, and in this case the dynamics can be described analytically only, e.g., down to a few a a few tens of $R_{\rm g}$ (Mościbrodzka et al., 2006). This part of the flow is likely to be stationary while the inner part must form a kind of unstable ring.

3.2 Exemplary spectra

The radiation spectra were calculated with the code described in Moscibrodzka (2006) and later generalized to non-spherical distribution of the inflowing material (Mościbrodzka

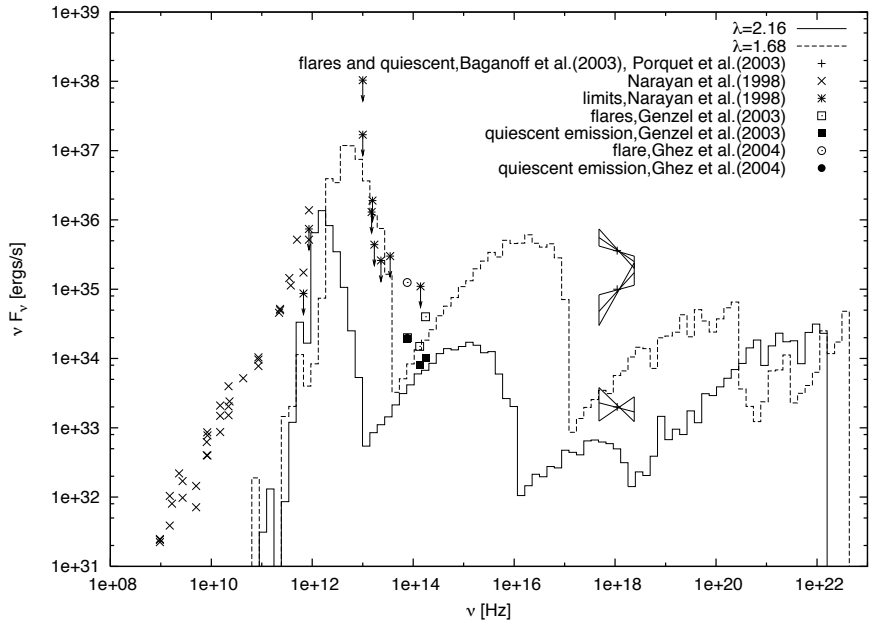

Figure 1. The two exemplary spectra models of Sgr A* for two values of the angular momentum density in analytical model. One of the solutions extends only down to 20 $R_{\rm g}$ and correspond naturally to the weakly variable part of the flow. Thermal distribution of electrons was assumed. Dots mark the data points or upper limits in radio and NIR, and three representative levels of radio emission from Chandra are marked as power laws with slope errors.

et al., 2006). The emission processes taken into account include synchrotron radiation, bremsstrahlung and Compton scattering.

Two examples of the spectra are shown in Fig. 1. The spectra reproduce the NIR peak although are short of the data points at long wavelengths. The level of the continuous emission in X-rays is reproduced by the higher angular momentum model, so we can speculate that the emission of the innermost unstable ring, not described by a stationary solution, may account for the strongly variable part of the X-ray flux.

4 MHD SIMULATIONS OF THE FLOW DYNAMICS

4.1 Flow description

Exploratory phase of the use of MHD simulations for modelling Sgr A* time-dependent spectra made use of the simulations which were performed by Proga and Begelman (2003). The setup assumed the almost Bondi flow. The input of material was set at 1.2 $R_{\rm B}$ (where $R_{\rm B}$ is the Bondi radius), which in turn was equal to 2×10^3 $R_{\rm g}$, and the angular momentum of the new material was $4R_{\rm g}c$ at the equatorial plane. The time-dependent computations

were performed for a few dynamical timescales at the outer radius which gave the time-dependent distribution of the energy density, velocity and the magnetic field. The flow was strongly time-dependent, with large scale fluctuations seen at the end of the computer run as well. The inflow was accompanied by a significant outflow. The computations never fully reached the exact stationarity condition in a sense that the inflow rate was not quite balanced by the outflow and accretion rate. However, in reality the flow also may not have time to reach equilibrium since the donor star moves (long term effects) and the Wolf–Rayet stellar winds show considerable clumpiness and overall variability (short timescale effects).

Time-dependent electron temperature distribution was obtained by assuming several channels of energy transmission: (i) Coulomb coupling between the ions and electrons, (ii) direct heating of electrons due to compression, (iii) electron radiative cooling, and (iv) electron advection. Optionally, we also allowed a fraction of energy to be in a form of non-thermal electrons. In order to simplify the computations, at each moment the flow was assumed to be stationary, i.e., time-dependent solutions for the flow dynamics were treated as frozen frames (for a detailed description, see Mościbrodzka et al., 2007).

4.2 Spectral variability

Flow variability was reflected in variability of the broad band spectra. Exemplary states are shown in Fig. 2. We see that the pure thermal electron distribution cannot represent the X-ray variability. The variable emission comes from the inner region of the flow in the

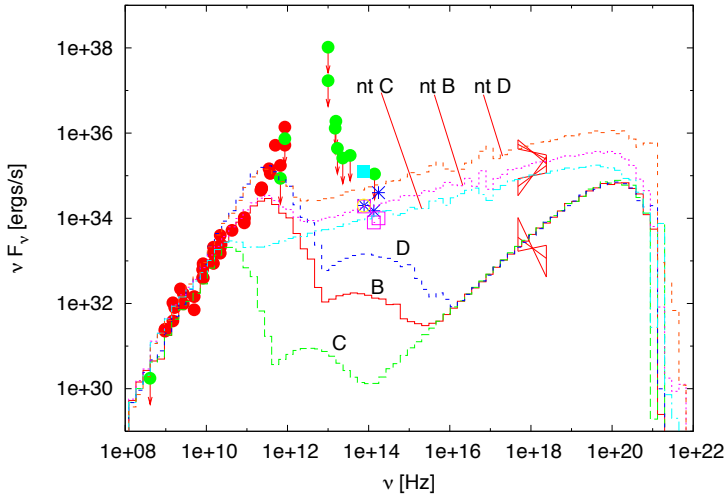

Figure 2. MHD simulations: the exemplary broad band spectra of Sgr A* for four different time moments labelled as A,B,C and D. Dots mark the data points or upper limits in radio and NIR, and three representative levels of radio emission from Chandra are marked as power laws with slope errors. Lower lines represent solutions with only thermal electrons, upper lines show solutions with a fraction of energy in a population of non-thermal electrons.

form of synchrotron emission, and for thermal electrons this component does not extend to X-rays. Bremsstrahlung emission, and Compton scattered emission comes from more extended region where variability is weaker and/or smeared. Therefore, the presence of non-thermal population is essential.

The amplitude of the variability in the timescales recorded in MHD simulations (a day) was very large, over an order of magnitude so the variability in the overall accretion rate (one order of magnitude) is additionally enhanced at some wavelengths (particularly at NIR) by the spectral effects.

The relation between the dynamics and the spectra is rather complex as it is strongly non-linear. There is no one-to-one correspondence between the accretion state and the predicted spectrum. For example, two states with similar accretion rates at the inner edge can have different spectra, or two states with different accretion rates can have similar spectra.

The specific issue is the description of the outer parts of the flow. Bremsstrahlung dominates there, and the measured flux depends on the size of the emitting region. Since the spatial resolution available in X-ray band is low in comparison with the modelled region (even in Sgr A*) this is an additional problem in comparing the models to the data.

4.3 Faraday rotation measure

The strongest observational constraint for the models comes from the estimates of the Faraday rotation measure towards Sgr A*. The observed polarization and the change of its angle indicate very low density plasma along the line of sight to the source. Our MHD model allows to calculate the integrated expected rotation measure as a function of the line

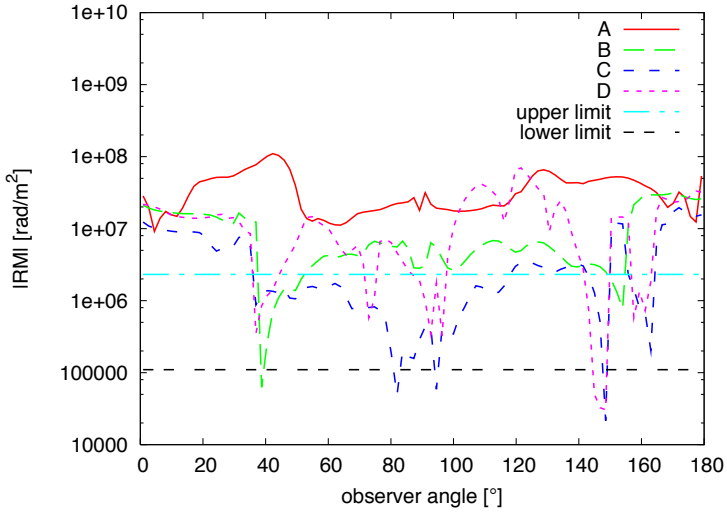

Figure 3. The determination of the Faraday rotation measure from the model, as a function of the viewing angle of an observer, for the same four different time moments labelled as A,B,C and D. Horizontal lines show the upper and the lower limit from the measurements of Marrone et al. (2006).

of sight. The result is shown in Fig. 3. For some inclination angles the model is consistent with the observational limits.

5 RECENT DEVELOPMENTS

5.1 GR effects

The computations presented in previous sections did not include the effects of General Relativity properly – either purely Newtonian approach was used (with GR effects mimicked by the flow cut-off at $6R_{\rm g}$) or pseudo-Newtonian potential was adopted. Since the black hole in Sgr A* is likely to be rotating, more appropriate approach would be useful, or at least some estimates must be performed of an error to the spectrum due to the negligence of GR effects.

Analytical solutions for the low angular momentum flow in the Kerr metric are well known (Barai et al., 2004) and can be used to determine the flow dynamics. Spectral computations using the Monte Carlo code require computing millions of photons so ray tracing for each of them is too time consuming if a number of models is to be calculated. However, we can calculate the escape probability of a photon as a function of radius, for a given Kerr parameter and we can test whether it depends significantly on the motion of the emitter (i.e., the solution for the flow dynamics).

The computations are done in a standard way (see, e.g., Schee et al., 2005 and the references therein) by integrating the photon paths for 100,000 photons emitted isotropically within the frame of the emitter at a given radius, and the calculations are performed for several radial points.

This work is still in progress, but in Fig. 4 we show an example for a specific dynamical solution with a shock. For a comparison, in the lower panel we also show the result for the

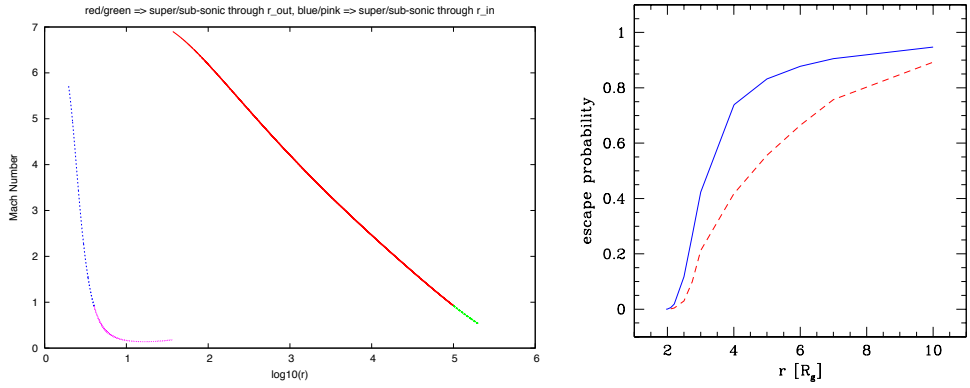

Figure 4. The radial dependence of the Mach number for a solution with the shock and the corresponding escape probability; Kerr parameter $a = 0.3$. Dashed line in the lower panel shows the escape probability for a solution without a shock, with much larger radial velocity of the emitter in the innermost part of the flow.

solution without a shock (dashed line). We see that the material effective emissivity is much higher in the case with shock, even without the shock emission included. Therefore, the GR effects should be estimated separately for each dynamical solution.

5.2 New dynamical simulations

Also the dynamical MHD simulations used in the previous study was not fully satisfactory from the point of view of Sgr A* modelling. First of all, the results of the simulations were not recorded densely enough in time to allow us to follow as fast time variability as 17 minutes seen in QPO-like events. New simulations, better suited for the centre of our Galaxy, are currently being performed (Mościbrodzka & Proga, in preparation). The preliminary results show that indeed the shortest timescale variability is seen in the dynamical simulations.

6 CONCLUSIONS

Low angular momentum accretion flow is a promising scenario for the accretion onto Sgr A* due to its natural variability pattern. The flow is slightly more energetically efficient than the purely spherical Bondi flow and can reproduce both the required level of the luminosity and is consistent with the data on Faraday rotation measure. The overall broad band spectra are also roughly reproduced if a fraction of energy is allowed to be converted the non-thermal population of electrons. The current results are therefore encouraging, and the further work is in progress.

ACKNOWLEDGEMENTS

The present work was supported by the Polish Grant 1P03D 008 29 and the Polish Astroparticle Network 621/E-78/SN-0068/2007.

REFERENCES

Abramowicz, M. A. and Zurek, W. H. (1981), Rotation-induced bistability of transonic accretion onto a black hole, *Astrophys. J.*, **246**, pp. 314–320.

Baganoff, F. K., Maeda, Y., Morris, M., Bautz, M. W., Cui, W., Doty, J. P., Brandt, W. N., Feigelson, E. D., Garmire, G. P., Pravdo, S. H., Ricker, G. R. and Townsley, L. K. (2003), Chandra X-Ray Spectroscopic Imaging of Sagittarius A* and the Central Parsec of the Galaxy, *Astrophys. J.*, **591**, pp. 891–915, arXiv: `astro-ph/0102151`.

Barai, P., Das, T. K. and Wiita, P. J. (2004), The Dependence of General Relativistic Accretion on Black Hole Spin, *Astrophys. J. Lett.*, **613**, pp. L49–L52, arXiv: `astro-ph/0408170`.

Bardeen, J. M., Press, W. H. and Teukolsky, S. A. (1972), Rotating black holes: locally nonrotating frames, energy extraction, and scalar synchrotron radiation, *Astrophys. J.*, **178**, pp. 347–369.

Bélanger, G., Terrier, R., De Jager, O., Goldwurm, A. and Melia, F. (2006), Periodic modulations in an X-ray flare from Sagittarius A*, *Journal of Physics: Conf. Series*, **54**, pp. 420–426, arXiv: `astro-ph/0604337`.

Blandford, R. D. and Begelman, M. C. (1999), On the fate of gas accreting at a low rate on to a black hole, *Monthly Notices Roy. Astronom. Soc.*, **303**, pp. L1–L5, arXiv: astro-ph/9809083.

Bondi, H. (1952), On spherically symmetrical accretion, *Monthly Notices Roy. Astronom. Soc.*, **112**, p. 195.

Das, T. K., Pendharkar, J. K. and Mitra, S. (2003), Multitransonic Black Hole Accretion Disks with Isothermal Standing Shocks, *Astrophys. J.*, **592**, pp. 1078–1088, arXiv: astro-ph/0301189.

Genzel, R. and Karas, V. (2007), The Galactic Center, in V. Karas and G. Matt, editors, *Black Holes from Stars to Galaxies – Across the Range of Masses*, volume 238 of *Proceedings of IAU Symposium*, pp. 173–180, International Astronomical Union, Cambridge University Press, Cambridge, UK, ISSN 1743-9213.

Genzel, R., Schödel, R., Ott, T., Eckart, A., Alexander, T., Lacombe, F., Rouan, D. and Aschenbach, B. (2003), Near-infrared flares from accreting gas around the supermassive black hole at the Galactic Centre, *Nature*, **425**, pp. 934–937, arXiv: astro-ph/0310821.

Ichimaru, S. (1977), Bimodal behavior of accretion disks – Theory and application to Cygnus X-1 transitions, *Astrophys. J.*, **214**, pp. 840–855.

Loeb, A. (2004), Direct feeding of the black hole at the Galactic Centre with radial gas streams from close-in stellar winds, *Monthly Notices Roy. Astronom. Soc.*, **350**, pp. 725–728, arXiv: astro-ph/0311512.

Marrone, D. P., Moran, J. M., Zhao, J.-H. and Rao, R. (2006), Interferometric Measurements of Variable 340 GHz Linear Polarization in Sagittarius A*, *Astrophys. J.*, **640**, pp. 308–318, arXiv: astro-ph/0511653.

Moscibrodzka, M. (2006), Spherical accretion in nearby weakly active galaxies, *Astronomy and Astrophysics*, **450**, pp. 93–103, arXiv: astro-ph/0512527.

Mościbrodzka, M., Das, T. K. and Czerny, B. (2006), The pattern of accretion flow on to Sgr A*, *Monthly Notices Roy. Astronom. Soc.*, **370**, pp. 219–228, arXiv: astro-ph/0604516.

Mościbrodzka, M., Proga, D., Czerny, B. and Siemiginowska, A. (2007), Accretion of low angular momentum material onto black holes: radiation properties of axisymmetric MHD flows, *Astronomy and Astrophysics*, **474**, p. 1, arXiv: 0707.1403.

Narayan, R. and Yi, I. (1994), Advection-dominated accretion: A self-similar solution, *Astrophys. J.*, **428**, pp. L13–L16, arXiv: astro-ph/9403052.

Nayakshin, S. and Sunyaev, R. (2003), Close stars and an inactive accretion disc in Sgr A*: eclipses and flares, *Monthly Notices Roy. Astronom. Soc.*, **343**, pp. L15–L19, arXiv: astro-ph/0302084.

Paumard, T., Genzel, R., Martins, F., Nayakshin, S., Beloborodov, A. M., Levin, Y., Trippe, S., Eisenhauer, F., Ott, T., Gillessen, S., Abuter, R., Cuadra, J., Alexander, T. and Sternberg, A. (2006), The Two Young Star Disks in the Central Parsec of the Galaxy: Properties, Dynamics, and Formation, *Astrophys. J.*, **643**, pp. 1011–1035, arXiv: astro-ph/0601268.

Proga, D. and Begelman, M. C. (2003), Accretion of low angular momentum material onto black holes: two-dimensional magnetohydrodynamic case, *Astrophys. J.*, **592**, pp. 767–781, arXiv: astro-ph/0303093.

Rockefeller, G., Fryer, C. L., Melia, F. and Warren, M. S. (2004), Diffuse X-Rays from the Inner 3 Parsecs of the Galaxy, *Astrophys. J.*, **604**, pp. 662–670, arXiv: astro-ph/0309497.

Schee, J., Stuchlík, Z. and Juráň, J. (2005), Light escape cones and raytracing in Kerr geometry, in S. Hledík and Z. Stuchlík, editors, *Proceedings of RAGtime 6/7: Workshops on black holes and neutron stars, Opava, 16–18/18–20 September 2004/2005*, pp. 143–155, Silesian University in Opava, Opava, ISBN 80-7248-334-X.

Proceedings of *RAGtime 8/9, 15–19/19–21 September, 2006/2007, Hradec nad Moravicí, Opava, Czech Republic*
S. Hledík and Z. Stuchlík, editors, Silesian University in Opava, 2007, pp. 45–59

Variation of the primary and reprocessed radiation in the flare-spot model

Michal Dovčiak,[1,a] Vladimír Karas,[1] Giorgio Matt[2] and René W. Goosmann[1]

[1] Astronomical Institute, Czech Academy of Sciences, Boční II 1401/1a, CZ-141 31 Praha 4, Czech Republic
[2] Dipartimento di Fisica, Università degli Studi "Roma Tre," Via della Vasca Navale 84, I-00146 Roma, Italy
[a] dovciak@astro.cas.cz

ABSTRACT
We study light curves and spectra (equivalent widths of the iron line and some other spectral characteristics) which arise by reprocessing on the surface of an accretion disc, following its illumination by a primary off-axis source – an X-ray "flare," assumed to be a point-like source just above the accretion disc. We consider all general relativity effects (energy shifts, light bending, time delays, delay amplification due to the spot motion) near a rotating black hole. For some sets of parameters the observed reflected flux exceeds the observed flux from the primary component. We show that the orbit-induced variations of the equivalent width with respect to its mean value can be as high as 30 % for an observer's inclination of 30°, and much more at higher inclinations. We calculate the ratio of the reflected flux to the primary flux and the hardness ratio which we find to vary significantly with the spot phase mainly for small orbital radii. This offers the chance to estimate the lower limit of the black hole spin if the flare arises close to the black hole. We show the results for different values of the flare orbital radius.

Keywords: Line: profiles – relativity – galaxies: active – X-rays: galaxies

1 INTRODUCTION

X-ray spectral measurements of the iron line and the underlying continuum provide a powerful tool to study accretion discs in active galactic nuclei (AGN) and Galactic black holes (for a review, see Fabian et al., 2000; Reynolds and Nowak, 2003). If a line originates by reflection of the primary continuum, then its observed characteristics may reveal rapid orbital motion and light bending near the central black hole. Spectral characteristics can be employed to constrain the black hole mass and angular momentum. A particularly important role is played by the equivalent width (EW), which reflects the intensity of the line versus the continuum flux as well as the role of general relativity effects in the source.

978-80-7248-419-5

In order to reduce the ambiguity of the results one needs to perform spectral fitting with self-consistent models of both the line and continuum.

Some AGN are known to exhibit iron lines with an EW greater than expected for a "classical" accretion disc. Enhanced values for the EW can be obtained by assuming an anisotropical distribution of the primary X-rays (Ghisellini et al., 1991), significant ionization of the disc matter (Matt et al., 1993) or iron overabundance (George and Fabian, 1991). Martocchia and Matt (1996) and Martocchia et al. (2000) found, using an axisymmetric lamp-post scheme, an anticorrelation between the intensity of the reflection features and the primary flux. When the primary source is at a low height on the disc axis, the EW can be increased by up to an order of magnitude with respect to calculations neglecting general relativity effects. When allowing the source to be located off the axis of rotation, an even stronger enhancement is expected (Dabrowski and Lasenby, 2001). Miniutti et al. (2003) and Miniutti and Fabian (2004) have realised that this so-called light bending model can naturally explain the puzzling behaviour of the iron line of MCG-6-30-15, when the line saturates at a certain flux level and then its EW starts decreasing as the continuum flux increases further. Niedźwiecki and Życki (2007) point out that the illumination by radiation which returns to the disc (following the previous reflection of the primary emission) also contributes significantly to formation of the line profile in some cases. This results into the line profile with a pronounced blue peak unless the reflecting material is absent within the innermost 2–3 gravitational radii.

In our previous paper (Dovčiak, 2004), we have proposed that the orbiting spot model could explain the origin of transient narrow lines, which have been reported in some AGN X-ray spectra (Turner et al., 2002; Guainazzi, 2003; Yaqoob et al., 2003) and widely discussed since then. The main purpose of the current paper is to present accurate computations of time-dependent EWs and other spectral characteristics within the framework of the flare-spot model, taking into account a consistent scheme for the local spectrum reprocessing. The main difference from previous papers is that the current one combines the primary source power-law continuum with the reprocessed spectral features. Both components are further modified by relativistic effects as the signal propagates towards an observer.

In a parallel paper (Dovčiak et al., 2007), we study general relativistic effects and spectral characteristics (EWs, hardness ratio, etc.) for the flare-spot model in two model setups – the Schwarzschild black hole with a flare arising at radius $7\,r_{\rm g}$ and extremally rotating black hole with a flare at $3\,r_{\rm g}$. In the current paper we would like to present the results of our computations for more values of the flare orbital radius. We also show that for a given flare radius the resultant spectra do not differ much for different spins of the black hole.

In Section 2 we describe the model and the approximation used and in Section 3 we present the results of our calculations. For a more detailed description of the model and for the equations used we refer the reader to the paper Dovčiak et al. (2007).

2 MODEL APPROXIMATIONS AND LIMITATIONS

We examine a system composed by a black hole, an accretion disc and a co-rotating flare with the spot underneath (Collin et al., 2003), see Fig. 1. The gravitational field is described in terms of the Kerr metric (Misner et al., 1973). Both static Schwarzschild and rotating

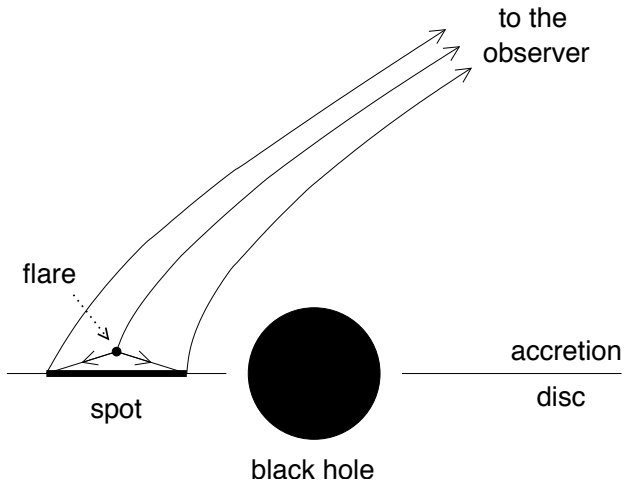

Figure 1. A sketch of the model geometry (not to scale). A localized flare occurs above the disc, possibly due to magnetic reconnection, and creates a spot by illuminating the disc surface. The resulting "hot spot" co-rotates with the disc and contributes to the final observed signal by reprocessing the primary X-rays.

Kerr black holes are considered. The co-rotating Keplerian accretion disc is geometrically thin and optically thick, therefore we take into account only photons coming from the equatorial plane directly to the observer. We further assume that the matter in the accretion disc is cold and neutral.

A flare is supposed to arise in the disc corona due to a magnetic reconnection event (Galeev et al., 1979; Poutanen and Fabian, 1999; Merloni and Fabian, 2001). Details of the formation of the flare and its structure are not the subject of the present paper, instead we assume that the flare is an isotropic stationary point source with a power-law spectrum, located very near above the disc. It co-rotates with the accretion disc. We also assume that a single flare dominates the intrinsic emission for a certain period of time.

The spot represents the flare-illuminated part of the disc surface. We consider the spot to be a rigid two dimensional circular feature, with its centre directly below the flare. Thus the spot does not share the differential rotation with the disc material. However, the matter in the disc lit by the flare is in Keplerian motion at the corresponding radii, and so it has different velocities at different parts of the spot (which is important when calculating the transfer function for the observer in the infinity). Because the flare is very close to the disc, the spot does not extend far from below the flare. We approximate the photon trajectories between the flare and the spot by straight lines and we do not consider the energy shift and abberation due to the different motion of the flare and matter illuminated by it. Furthermore we neglect the time delay between the photon's emission from the flare and its later re-emission from the spot.

The intrinsic (local) spectra from the spot were computed by Monte Carlo simulations considering multiple Compton scattering and iron line fluorescence in a cold, neutral, con-

stant density slab with solar iron abundance. We used the NOAR code for these computations, see Section 5 of Dumont et al. (2000) and Chapter 5 of Goosmann (2006). The local flux depends on the local incident and local emission angles, hence the flux changes across the spot. Here and elsewhere in the text we refer to the quantities measured in the local frame co-moving with the matter in the disc as "local."

The local flux consists of only two components – the flux from the primary source (the flare) and the reflected flux from the spot. The latter one consists of the reflection continuum (with the Compton hump and the iron edge as the main features) and the neutral Kα and Kβ iron lines. No other emission is taken into account. The spectral properties of the local emission (the local EW, ratio of the reflected flux to the primary one and hardness ratio) are shown in Figs 2 and 3.

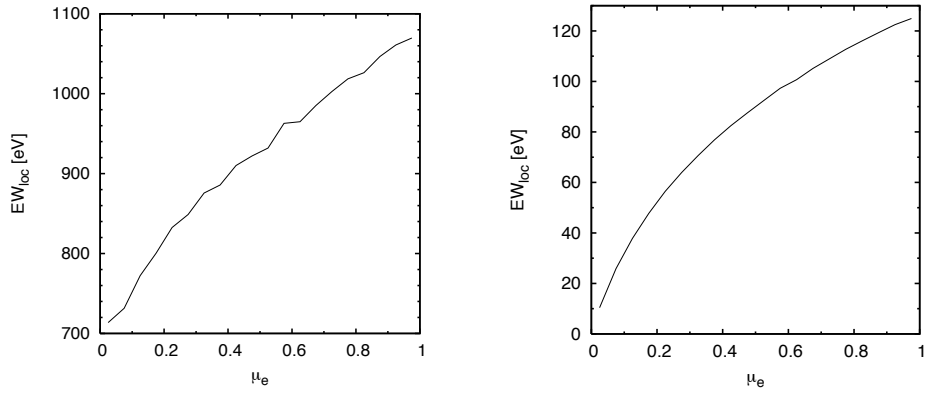

Figure 2. *Left:* The local equivalent width without taking the primary flux into account as a function of the direction of emission. *Right:* The same as in the left panel but with the flux from the primary source included.

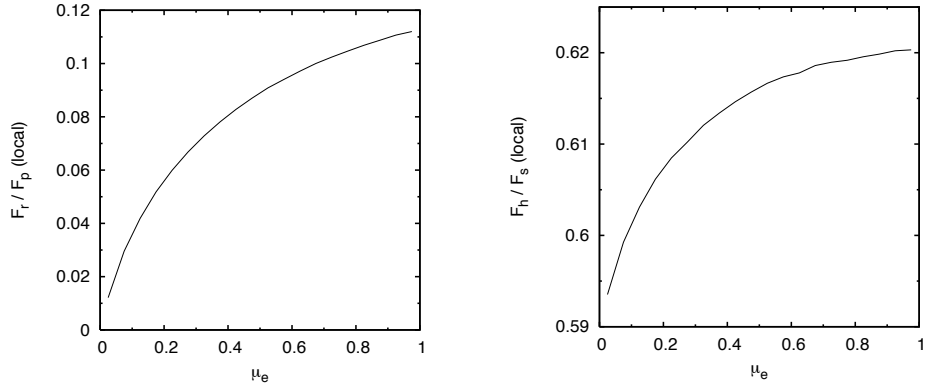

Figure 3. *Left:* The ratio of the locally emitted energy flux in the direction μ_e to the primary flux. The fluxes are integrated in the energy range 3–10 keV. *Right:* The local hardness ratio of the fluxes in the ranges 6.5–10 keV (F_h) and 3–6.5 keV (F_s).

As far as the photon trajectories from the spot to the observer are concerned, all general relativistic effects – energy shift, aberration, light bending, lensing and relative time delays – are taken into account. We assume that only the gravity of the central black hole influences the photons on their path from the disc to the observer. This allows us to define a relatively simple scheme in which different intervening effects remain under full control and can be well identified.

3 SPECTRAL CHARACTERISTICS OF THE OBSERVED SIGNAL

The observed light curves computed for the spot in the vicinity of the extremally spinning Kerr black hole ($a = 0.998\,GM/c^3$) and the Schwarzschild black hole ($a = 0\,GM/c^3$) in the 3–10 keV energy range for different orbital radius can be seen in Figs 4 and 5. The light curves are influenced mainly by the overall amplification factor, consisting of transfer function and delay amplification (see paper Dovčiak et al., 2007 for details), and by the dependence of the local flux on the emission angle. The primary emission dominates the observed flux as expected, meanwhile the reflected flux in the Fe lines from the spot contributes less. There is an exception in this behaviour, though, for some parts of the orbit close to the black hole (see top row of Fig. 4). The reflected flux from the spot exceeds the flux of the primary for the orbital radius $r = 3\,GM/c^2$ and for the inclinations $\theta_\mathrm{o} = 60°$ and 85°. The variations of the flux decrease with the orbital radius as expected. Note, that the amplification of the emission due to the lensing effect is still relevant as far as $100\,GM/c^2$ for large inclination angles (85°).

Figures 6 and 7 shows the mean spectra taken over the whole orbit. The line is smeared when taken over the whole orbit. As it is well known (Iwasawa et al., 1996) in the Schwarzschild case, if we assume that the emission comes mainly from above the innermost stable orbit, the line stays above 3 keV, while in the Kerr case it can be shifted even below this energy (as is the case for all shown inclinations for the spot orbit below $4\,GM/c^2$). The iron edge is smeared in all studied cases and the dominance of the primary emission is evident. As we expect the line is less shifted with the increasing orbital radius but it is still substantially broadened even at the radius $100\,GM/c^2$ due to the large orbital velocity of the spot.

In order to quantify the properties of the observed spectra let us look at the equivalent width, ratio of the observed reflected and primary components, and the hardness ratio (Figs 8 and 9).

A closer look at the EW, see the left panels in Figs 8 and 9, reveals that it does not much differ from its local value (Fig. 2), i.e., $EW(t) \approx EW_\mathrm{loc}(\mu_\mathrm{e}(t))$ (for the dependence $\mu_\mathrm{e}(t)$ for some radii see Dovčiak et al., 2007). This is not, however, true for the case of the low orbital radius with an observer inclination of 85° when the EW is magnified due to the lensing effect. For the spot close to the black hole ($r = 3\,GM/c^2$) the EW is changing with respect to its mean value by 30% even for a low inclination angle 30°. For an almost edge-on disc it can vary by as much as 200 %. Similar to the flux variations at the larger radii the variation of the EW decreases. This is true also for all the other studied spectral characteristics.

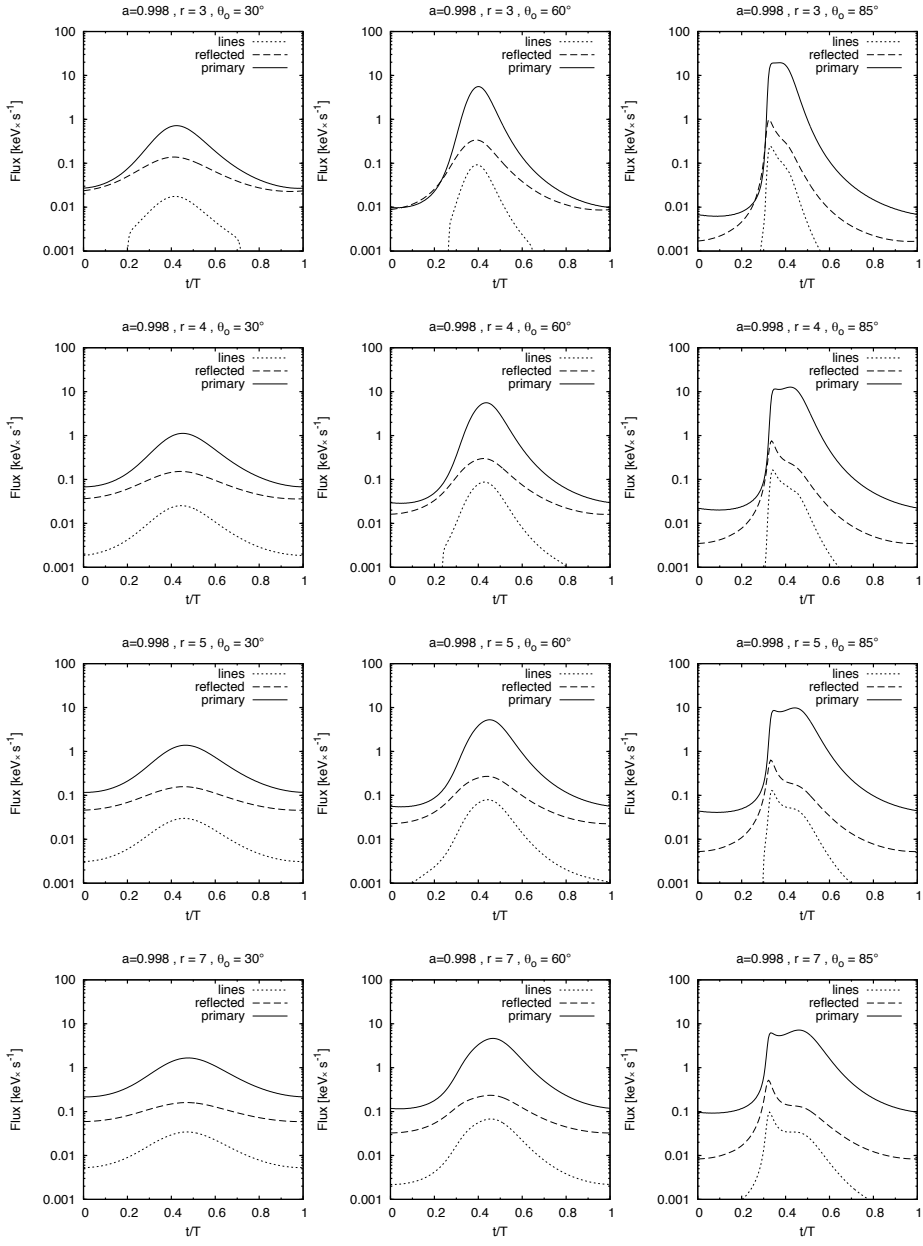

Figure 4. The light curves of the observed emission from the flare and the spot for the energy range 3–10 keV for the Kerr black hole with the spin $0.998\,GM/c^3$, the spot orbital radii 3, 4, 5 and $7\,GM/c^2$ (from top to bottom) and the observer's inclination angles 30°, 60° and 85° (from left to right). The primary emission, spot's continuum emission and spot's emission in Kα and Kβ lines are denoted by solid, dashed and dotted graphs, respectively.

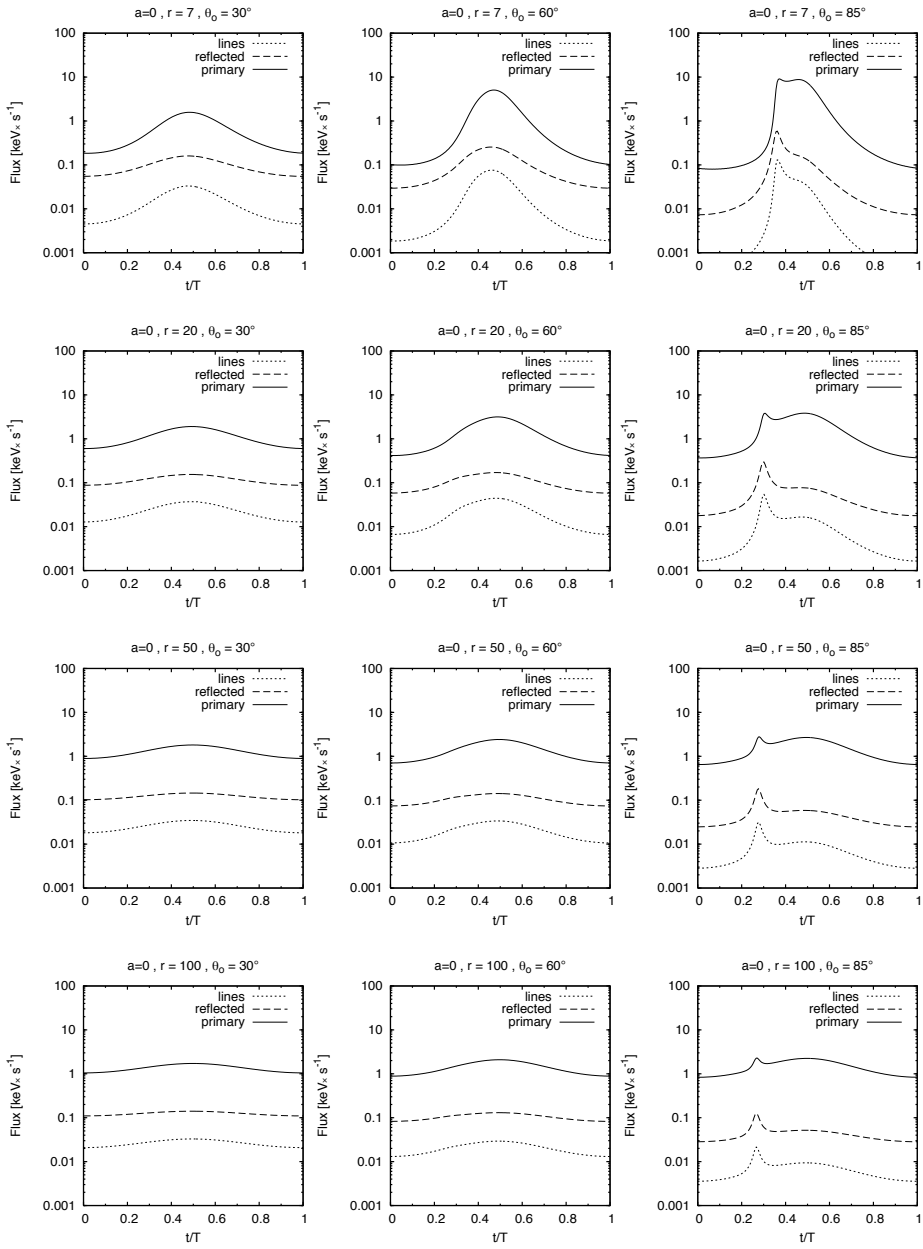

Figure 5. The same as in Fig. 4 but for the Schwarzschild black hole and the spot orbital radii 7, 20, 50 and 100 GM/c^2 (from top to bottom).

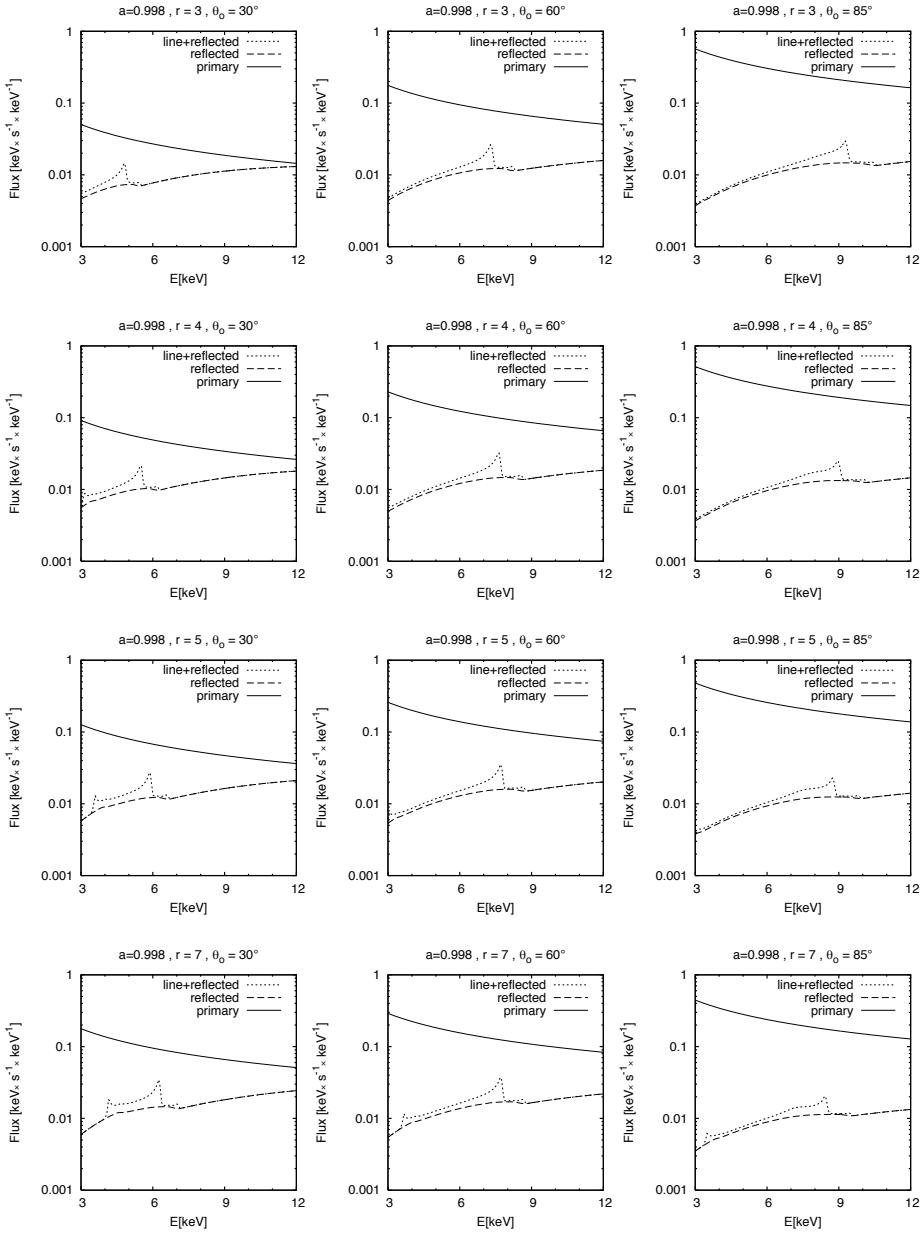

Figure 6. The observed spectra averaged over one orbit computed for the same set of parameters as in Fig. 4. Here, the observed line flux is shown on top of the spot continuum emission.

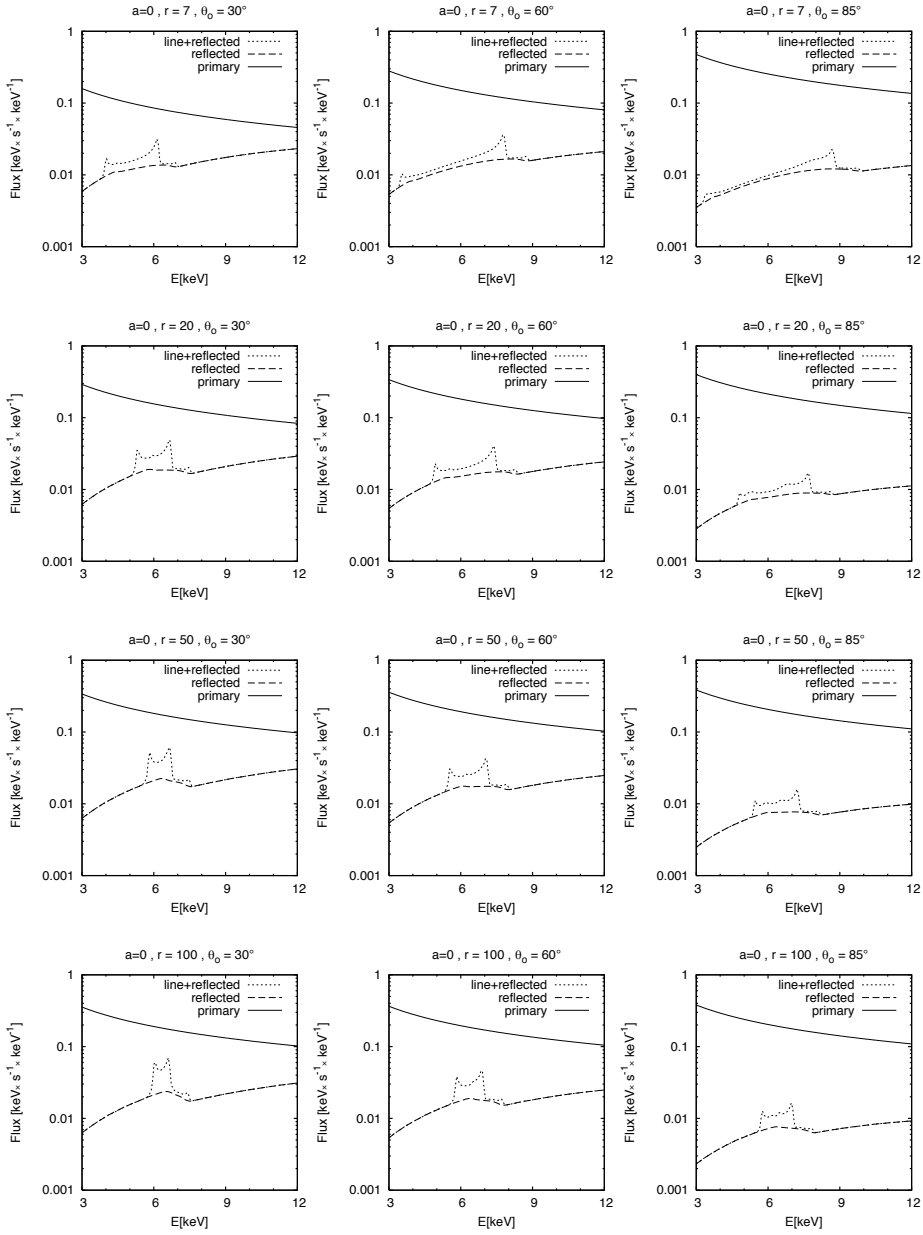

Figure 7. The observed spectra averaged over one orbit computed for the same set of parameters as in Fig. 5. Here, the observed line flux is shown on top of the spot continuum emission.

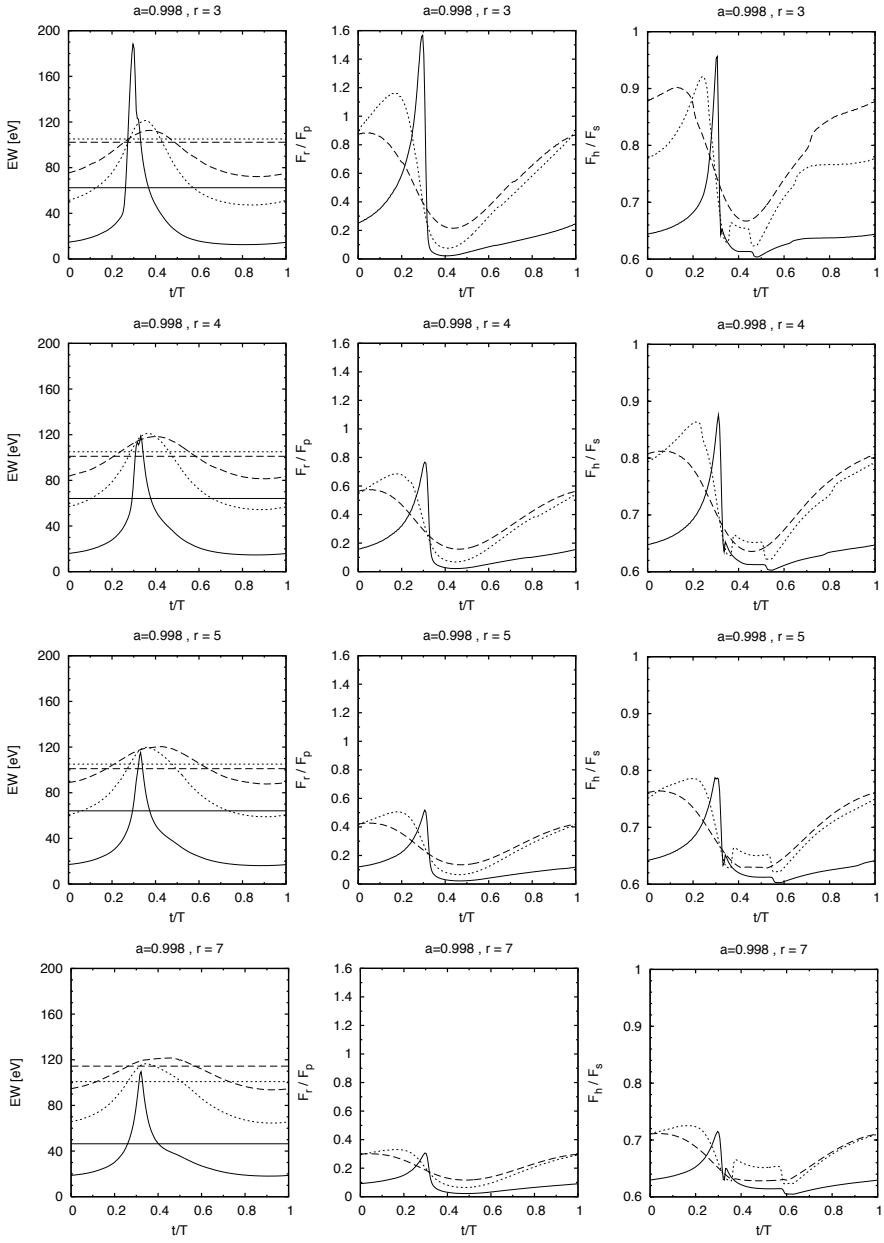

Figure 8. *Left:* The time variation of the observed EW of the Kα line. The integrated EW is shown in horizontal lines. *Middle:* The ratio of the observed reflected emission to the observed primary emission. The fluxes are integrated in the 3–10 keV energy range. *Right:* The hardness ratio of the hard flux $F_{\rm h}$ (6.5–10 keV) to the soft flux $F_{\rm s}$ (3–6.5 keV). The flux in the Fe lines is also included. The dashed, dotted and solid lines correspond to the inclinations 30°, 60° and 85°.

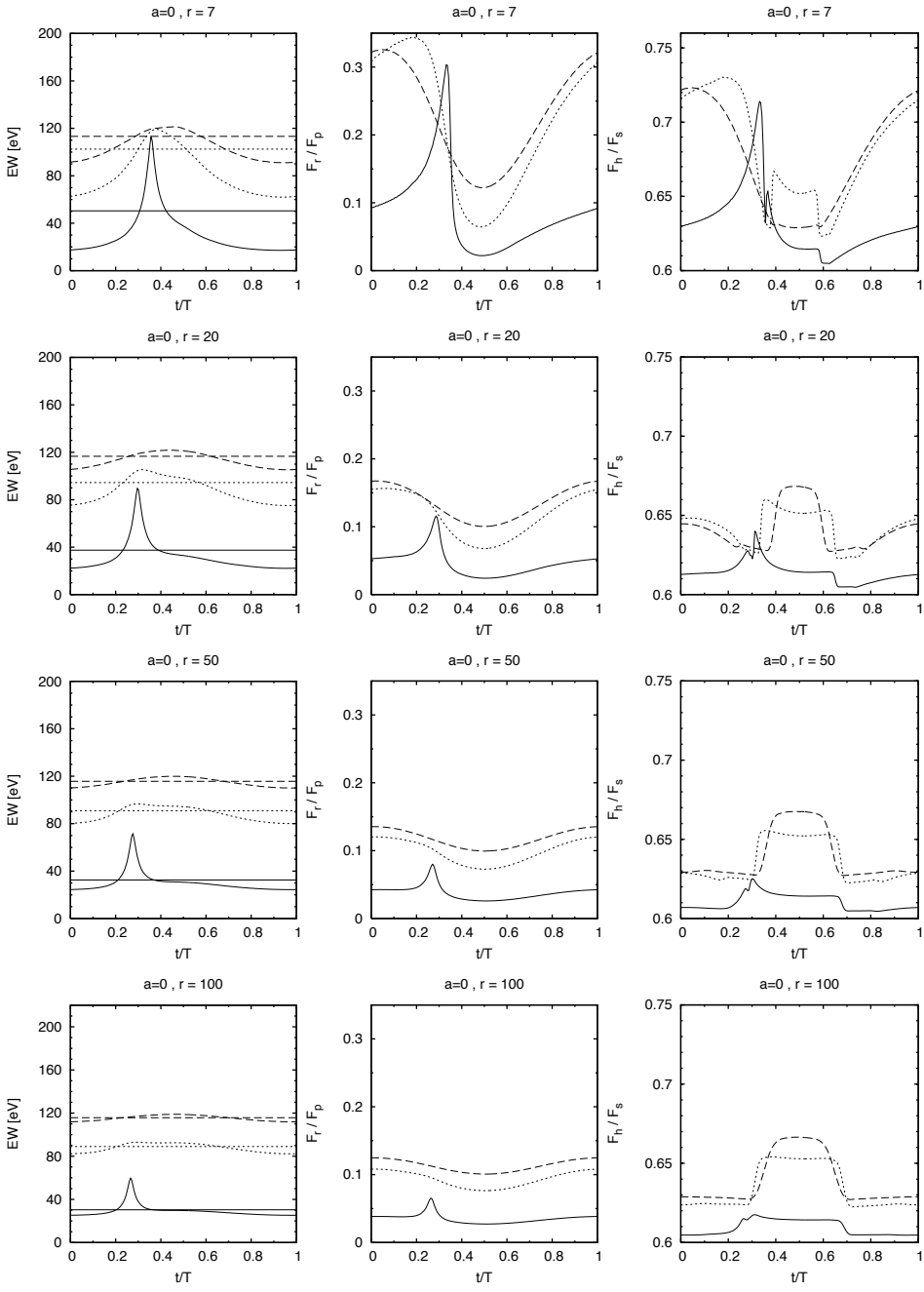

Figure 9. The same as in Fig. 8 but for the Schwarzschild black hole and the spot orbital radii 7, 20, 50 and 100 GM/c^2 (from top to bottom).

The observed ratio of the reflected flux to the primary flux is amplified when compared to the local one, see the middle panels in Figs 8 and 9 and the left panel in Fig. 3. The amplification is the highest for the lowest orbital radius and highest inclination angle – the ratio in this case is increased by more than one order of magnitude. Note that in the Kerr case with the orbital radius $3\,GM/c^2$ and for the inclinations 60° and 85° the ratio of the observed reflected flux to the observed primary flux is larger than unity, meaning the reflected component prevails over the primary one in a certain part of the orbit.

To evaluate the hardness ratio we compared the fluxes in between 3–6.5 keV (soft component, F_s) and 6.5–10 keV (hard component, F_h). The hardness ratio is also amplified

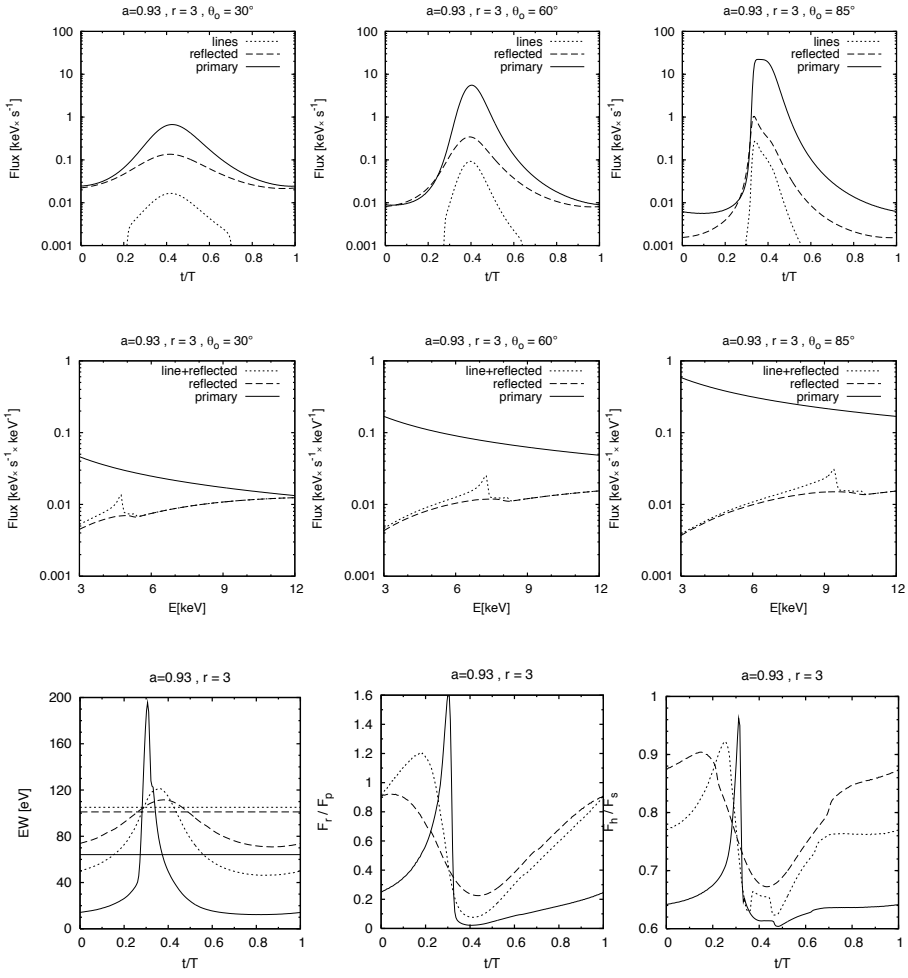

Figure 10. The same as in Figs 4, 6, and 8 top rows (i.e., the spot orbital radius $3\,GM/c^2$) but for the Kerr black hole with the spin $0.93\,GM/c^3$.

when we compare it with the local hardness ratio (the right panels in Figs 8, 9 and 3). As in other spectral characteristics, the amplification and the variation of the hardness ratio is the largest for the lowest orbital radius in the extremally rotating Kerr case and they decrease with the increasing orbital radius.

To see how the different values of the spin parameter influence the studied properties of the observed signal we can compare the results for the same radius, see the bottom panels of Figs 4, 6 and 8 for the extremally rotating Kerr black hole and compare them with the top panels of Figs 5, 6 and 9 for the Schwarzschild black hole. For the closer radius, $r = 3\,GM/c^2$, we have computed the results for the spin $a = 0.93\,GM/c^3$ (the spin cannot be lower if the spot should be above the innermost stable circular orbit), see Fig. 10 and compare it with the top panels in Figs 4, 6 and 8. It is clear from all of these comparisons that if we fix the orbital radius our results do not depend on the spin of the black hole.

4 CONCLUSIONS

We have studied the light curves, spectra and several spectral characteristics in the flare-spot model for different orbital radii of the flare. The primary flux was included and the mutual normalizations of the primary and reflected emission were treated within the framework of a simple yet self-consistent scheme. About half of the isotropic primary flux hits the disc below the flare and is reprocessed there, creating a radiating spot. A part of the reprocessed radiation is re-emitted towards the observer. The radiation is influenced by the relativistic effects before reaching the observer.

We can sum up our results in several conclusions:

(1) The EW, apart for the extreme cases of high inclinations, does not differ significantly from the local EW. However, close to the black hole it varies even for low inclination of 30° by up to 30 % when compared with its mean value for the whole orbit. The EW could be significantly amplified in our model only if the primary emission were beamed towards the disc, thus decreasing the observed primary emission.

(2) Both the ratio of the observed reflected to the observed primary flux and the hardness ratio are amplified when compared to the values for the intrinsic (local) emission.

(3) The variations of all of the studied spectral characteristics are the highest for close orbits and higher inclination angles.

(4) The spin of the black hole affects significantly our results only as far as it determines the location of the marginal stable orbit.

Here, we would like to remind the reader, that these results apply for a flare arising very near above the disc and thus they can heavily differ from the results of the light-bending model by Miniutti and Fabian (2004) where the flare orbits far above the disc and the resulting spot is much larger.

It follows from our results that the studied flux ratios could be used for estimating the lower limit of possible values of the spin parameter if the flare arises in the close vicinity of the black hole.

ACKNOWLEDGEMENTS

This research is supported by the ESA PECS project No. 98040. MD and VK gratefully acknowledge support from the Czech Science Foundation grants 205/05/P525 and 202/06/0041. GM acknowledges financial support from Agenzia Spaziale Italiana (ASI). RG is grateful for financial support to the Centre of Theoretical Astrophysics (LC06014).

REFERENCES

Collin, S., Coupé, S., Dumont, A.-M., Petrucci, P.-O. and Różańska, A. (2003), Evolution of the X-ray spectrum in the flare model of Active Galactic Nuclei, *Astronomy and Astrophysics*, **400**, pp. 437–449.

Dabrowski, Y. and Lasenby, A. N. (2001), Reflected iron line from a source above a Kerr black hole accretion disc, *Monthly Notices Roy. Astronom. Soc.*, **321**, pp. 605–614.

Dovčiak, M. (2004), *Radiation of accretion discs in strong gravity*, Ph.D. thesis, Charles University at Prague, Faculty of Mathematics and Physics, Prague, arXiv: `astro-ph/0411605`.

Dovčiak, M., Karas, V., Matt, G. and Goosmann, R. (2007), Variation of the primary and reprocessed radiation from an orbiting spot around a black hole, *Monthly Notices Roy. Astronom. Soc.*, accepted.

Dumont, A.-M., Abrassart, A. and Collin, S. (2000), A code for optically thick and hot photoionized media, *Astronomy and Astrophysics*, **357**, pp. 823–838.

Fabian, A. C., Iwasawa, K., Reynolds, C. S. and Young, A. J. (2000), Broad Iron Lines in Active Galactic Nuclei, *Publ. Astronom. Soc. Pacific*, **112**, pp. 1145–1161.

Galeev, A. A., Rosner, R. and Vaiana, G. S. (1979), Structured coronae of accretion disks, *Astrophys. J.*, **229**, pp. 318–326, URL `http://adsabs.harvard.edu/abs/1979ApJ...229..318G`.

George, I. M. and Fabian, A. C. (1991), X-ray reflection from cold matter in active galactic nuclei and X-ray binaries, *Monthly Notices Roy. Astronom. Soc.*, **249**, pp. 352–367.

Ghisellini, G., George, I. M., Fabian, A. C. and C., D. (1991), Anisotropic inverse Compton emission, *Monthly Notices Roy. Astronom. Soc.*, **248**, pp. 14–19.

Goosmann, R. W. (2006), *Accretion and Emission close to supermassive Black Holes in Quasars and AGN: Modeling the UV-X-spectrum*, Ph.D. thesis, Universität Hamburg, Germany.

Guainazzi, M. (2003), The history of the iron Kα line profile in the Piccinotti AGN ESO 198-G24, *Astronomy and Astrophysics*, **401**, pp. 903–910.

Iwasawa, K., Fabian, A. C., Reynolds, C. S., Nandra, K., Otani, C., Inoue, H., Hayashida, K., Brandt, W. N., Dotani, T., Kunieda, H., Matsuoka, M. and Tanaka, Y. (1996), The variable iron K emission line in MCG-6-30-15, *Monthly Notices Roy. Astronom. Soc.*, **282**, pp. 1038–1048.

Martocchia, A., Karas, V. and Matt, G. (2000), Effects of Kerr space-time on spectral features from X-ray illuminated accretion discs, *Monthly Notices Roy. Astronom. Soc.*, **312**, pp. 817–826.

Martocchia, A. and Matt, G. (1996), Iron K-alpha line intensity from accretion discs around rotating black holes, *Monthly Notices Roy. Astronom. Soc.*, **282**, pp. L53–L57.

Matt, G., Fabian, A. C. and Ross, R. R. (1993), Iron K_α lines from X-ray photoionized accretion discs, *Monthly Notices Roy. Astronom. Soc.*, **262**(1), pp. 179–186.

Merloni, A. and Fabian, A. C. (2001), Accretion disc coronae as magnetic reservoirs, *Monthly Notices Roy. Astronom. Soc.*, **321**, pp. 549–552.

Miniutti, G. and Fabian, A. C. (2004), A light bending model for the X-ray temporal and spectral properties of accreting black holes, *Monthly Notices Roy. Astronom. Soc.*, **349**, pp. 1435–1448.

Miniutti, G., Fabian, A. C., Goyder, R. and Lasenby, A. N. (2003), The lack of variability of the iron line in MCG-6-30-15: general relativistic effects, *Monthly Notices Roy. Astronom. Soc.*, **344**, pp. L22–L26.

Misner, C. W., Thorne, K. S. and Wheeler, J. A. (1973), *Gravitation*, W. H. Freeman and Co, New York, San Francisco.

Niedźwiecki, A. and Życki, P. T. (2007), On variability and spectral distortion of the fluorescent iron lines from black-hole accretion discs, *Monthly Notices Roy. Astronom. Soc.*, arXiv: `0710.5578v1`.

Poutanen, J. and Fabian, A. C. (1999), Spectral evolution of magnetic flares and time lags in accreting black hole sources, *Monthly Notices Roy. Astronom. Soc.*, **306**, pp. L31–L37, arXiv: `astro-ph/9811306`.

Reynolds, C. S. and Nowak, M. A. (2003), Fluorescent iron lines as a probe of astrophysical black hole systems, *Phys. Rep.*, **377**, pp. 389–466.

Turner, T. J., Mushotzky, R. F., Yaqoob, T., George, I. M., Snowden, S. L., Netzer, H., Kraemer, S. B., Nandra, K. and Chelouche, D. (2002), Narrow Components within the Fe Kα Profile of NGC 3516: Evidence of the Importance of General Relativistic Effects?, *Astrophys. J.*, **574**, pp. L123–L127.

Yaqoob, T., George, I. M., Kallman, T. R., Padmanabhan, U., Weaver, K. A. and Turner, T. J. (2003), Fe XXV and Fe XXVI Diagnostics of the Black Hole and Accretion Disk in Active Galaxies: Chandra Time-resolved Grating Spectroscopy of NGC 7314, *Astrophys. J.*, **596**, pp. 85–104.

Proceedings of *RAGtime 8/9, 15–19/19–21 September, 2006/2007, Hradec nad Moravicí, Opava, Czech Republic*
S. Hledík and Z. Stuchlík, editors, Silesian University in Opava, 2007, pp. 61–69

Modelling the polarization dichotomy of Active Galactic Nuclei

René W. Goosmann

Astronomical Institute, Czech Academy of Sciences, Boční II 1401/1a, CZ-141 31 Praha 4, Czech Republic
goosmann@astro.cas.cz

ABSTRACT
I present polarization modelling of Active Galactic Nuclei in the optical/UV range. The modelling is conducted using the Monte-Carlo radiative transfer code Stokes, which self-consistently models the polarization signature of a complex model arrangement for an active nucleus. In this work I include three different scattering regions around the central source: an equatorial electron scattering disk, an equatorial obscuring dusty torus, and polar electron scattering cones. I investigate the resulting dependencies of the V-band polarization for different optical depths of the scattering cones, different dust compositions inside the torus, and various half-opening angles of the torus/polar cones. The observed polarization dichotomy can be successfully reproduced by the model.

Keywords: Galaxies: active – radiative transfer – polarization

1 INTRODUCTION

The research of Active Galactic Nuclei (AGN) started with the discovery of separate types of objects that nowadays we gather under the AGN-class: Seyfert galaxies, radio galaxies, quasars, blazars, etc. . . An important common property among the various types is the very strong luminosity produced inside a small spatial region at the centre of the host galaxy. The standard model of the AGN phenomenon assumes accretion onto a supermassive black hole as the fundamental mechanism for producing the strong radiation. The central black hole and the accretion flow are surrounded by several additional media such as the broad line and narrow line regions. A key assumption of this so-called *unified scheme* for AGN is the existence of a dusty torus (see, e.g., Antonucci, 1993). It divides AGN into two classes: "type-1" objects, which are seen close to face-on, and "type-2" objects seen rather edge-on. In type-1 AGN the central energy source and the broad line region can be seen directly, whilst in type-2 AGN the torus blocks the view toward the centre.

Current observational technology in the optical and UV waveband does not allow to resolve the inner regions of AGN. However, the light of AGN is polarized over a broad wavelength range, which allows to put important constraints on the geometry of the emitting and scattering regions. When light is scattered, the angle of polarization depends on

978-80-7248-419-5

the direction of the last scattering, so one expects the angle of polarization to be related to the structure of the AGN. Stockman et al. (1979) made the seminal discovery that for low-polarization, high optical luminosity, radio-loud AGN, the optical polarization position angles tend to align *parallel* to the large-scale radio structure. Antonucci (1982) pointed out that whilst many radio galaxies showed a similar parallel alignment of the polarization and radio axes, there was, unexpectedly, a population showing a *perpendicular* relationship. It was subsequently shown (Antonucci, 1983) that relatively-radio-quiet Seyfert galaxies show a similar dichotomy between the predominantly, but not exclusively, parallel polarization in face-on type-1 Seyferts and the perpendicular polarization of type-2 Seyferts (see Antonucci, 1993, 2002 for reviews).

Applying the radiative transfer code Stokes, we have presented theoretical modelling of individual scattering regions in AGN (Goosmann and Gaskell, 2007; Goosmann et al., 2007a,b). In these papers, we considered dusty torii, polar electron cones, and equatorial scattering wedges individually calculating their polarization signatures for various viewing angles. For the present proceedings note I expand on this type of modelling combining the individual regions to obtain an approach to the unified scheme of AGN. With Stokes such modelling is done consistently as the code automatically includes the effects of multiple scattering. In Section 2, I briefly summarize the basic properties of Stokes. In Section 3, I describe the model setup. The modelling results are then presented in Section 4 and discussed in Section 5.

2 THE RADIATIVE TRANSFER CODE "STOKES"

The computer program Stokes performs simulations of radiative transfer, including the treatment of polarization, for AGN and related objects. The code is publicly available and 100 % shareware.[1] It is based on the Monte Carlo method and follows single photons inside the source region through various scattering processes until they become absorbed or escape from the model region (Fig. 1).

Photons are created inside the source regions, which can be defined by different geometries. The continuum radiation is set by the index α of an $F_\nu \propto \nu^{-\alpha}$ power law. The Stokes vectors of the emitted photons are initially set to the values of completely unpolarized light. Various scattering regions can be arranged around the source regions. The program offers, e.g., toroidal, cylindrical, spherical or conical shapes. These regions can contain free electrons or dust consisting of "astronomical silicate" and graphite. A photon works its way through the model region and generally undergoes several scattering events. The emission directions, path lengths between scattering events, and the scattering angles are sampled by Monte Carlo routines based on classical intensity distributions. During each scattering event the Stokes vector is changed by multiplication with the corresponding Mueller matrix. For dust scattering, absorption is important, and a large fraction of the photons does not reach the virtual observer. The relevant cross sections and matrix elements for dust scattering and absorption are computed on the basis of Mie theory applied to size distributions of spherical graphite and silicate grains.

[1] `http://www.stokes-program.info/`

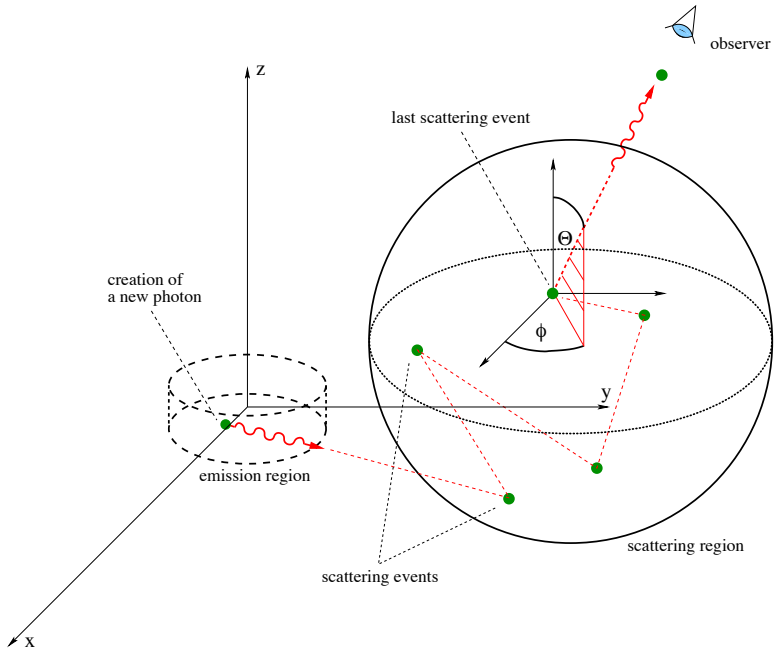

Figure 1. A photon working its way through the model space.

When a photon escapes from the model region, it is registered by a web of virtual detectors arranged in a spherical geometry around the source. The flux and polarization information of each detector is obtained by adding up the Stokes parameters of all detected photons. If the model is completely axially symmetric these can be azimuthally integrated and, if there is plane symmetry, the top and bottom halves are combined. The object can be analyzed in total flux, in polarized flux, percentage of polarization, and the position angle at each viewing angle.

3 MODELLING THE UNIFIED SCHEME

Our setup for the united model of AGN is shown in Fig. 2. We include the equatorial dusty torus and the polar electron scattering cones. In addition to that an equatorial electron scattering wedge is defined. Such a region produces the correct (parallel) polarization of type-1 AGN. The polarization properties of flat equatorial scattering disks have been investigated in a series of papers by Young (2000) and Smith et al. (2002, 2004, 2005) as well as in Goosmann and Gaskell (2007).

We assume that the central source of the AGN is point-like and emits a flat intrinsic spectrum around $\lambda = 5500\,\text{Å}$. We define a half-opening angle, θ_{disk}, of the flared electron disk of $\theta_{\text{disk}} = 25°$. For this half-opening angle a high percentage of type-1 polarization is expected (Goosmann and Gaskell, 2007). The radial Thomson optical depth of the wedge

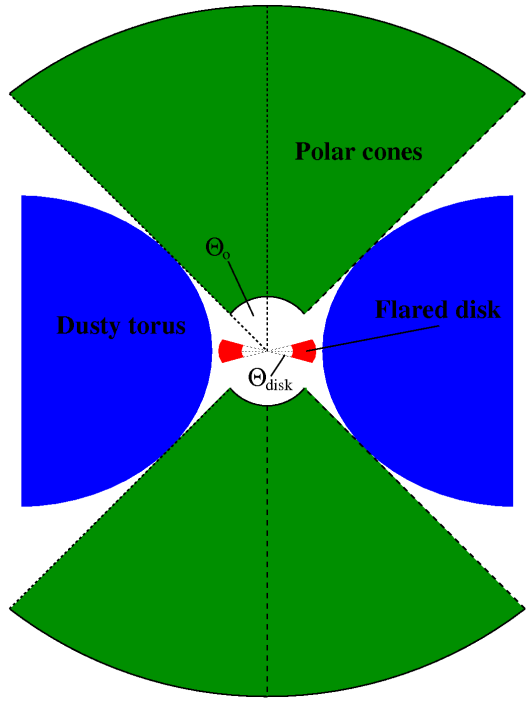

Figure 2. Illustration of the setup for a unified scheme model of AGN. The central source is surrounded by a flared electron scattering disk (wedge), a dusty torus, and by polar electron cones.

Table 1. Parameterization of the dust models.

Type	Graphite	Silicate	a_{min}	a_{max}	α_{s}
Galactic	62.5 %	37.5 %	0.005 µm	0.250 µm	−3.5
AGN	85 %	15 %	0.005 µm	0.200 µm	−2.05

is set to unity. The half-opening angles θ_0 of the torus and the cone are set equal, which corresponds to the interpretation that the ionized outflow is collimated by the torus. We consider two cases for the Thomson optical depth of the scattering cones, which is measured along the symmetry axis of a single cone and set to $\tau_{\mathrm{cone}} = 0.01$ and $\tau_{\mathrm{cone}} = 0.1$ respectively. The radial optical depth of the dusty torus in the equatorial plane is set to 750 for the V-band. The dust models (Table 1) assume a mixture of graphite and "astronomical silicate" and a grain radii distribution $n(a) \propto a_{\mathrm{s}}^{\alpha}$ between a_{min} and a_{max}.

The "Galactic dust" model reproduces the interstellar extinction for $R_{\mathrm{V}} = 3.1$ whilst the "AGN dust" parameterization is obtained from quasar extinction curves derived by Gaskell et al. (2004). This latter dust type favours larger grain sizes. Using Stokes we consistently

model the resulting polarization spectrum of the entire model setup for various inclinations, i, of the observer and for four different values of θ_0 between 30° and 45°.

4 RESULTS

We investigate the dependence of the polarization in the visual band on the half-opening angle of the dusty torus/polar cones. In Fig. 3 and Fig. 4 we show the resulting percentage of polarization, P, versus i for the two values of τ and for the two types of dust. The relation has a similar shape for all cases shown and reproduces the observed type-1/type-2 polarization dichotomy: the polarization position angle is oriented parallel to the projected symmetry axis when the line of sight is above the horizon of the torus, i.e., for $i < \theta_0$, and switches to a perpendicular orientation for $i > \theta_0$. In the figures, the two different orientations of the polarization vector are denoted by negative (type-1) and positive (type-2) values of P. The type-1 values of P are moderate and reach maximum absolute values of $\sim 2.5\,\%$. They rise with i until the polarization vector switches to the type-2 orientation. In the type-2 case P continues to increase with i and saturates for edge-on viewing angles at a level that depends on θ_0.

The combined effect of all scattering regions on the total polarization value can be partly understood from the results we obtained when modelling the individual regions in Goosmann and Gaskell (2007). However, the fact that all regions are radiatively coupled adds more complexity to the model. The polar scattering regions have a strong impact on the result, in particular for type-2 viewing angles. With increasing θ_0 the resulting type-2 polarization becomes lower because it is averaged over a broader distribution of polarization position angles. An increasing optical depth of the cones raises P for the type-2 case because more photons are scattered by the cones.

For nearly face-on viewing directions, the polar cones have less impact as they cause mainly forward or backward scattering producing low polarization. In these cases the resulting polarization is mainly determined by the geometry and optical depth of the equatorial scattering disk. However, these two regions compete against each other, as they produce different orientations of the polarization vector. For higher optical depth the impact of the polar cones becomes stronger and lowers the resulting type-1 polarization, as can be seen when comparing the top with the bottom panels in Figs 3 and 4.

In the central parts of the model region, the optically thick torus, and the scattering wedge are strongly interconnected by multi-scattering. This explains the significant impact of the dust composition and grain size distribution on the resulting polarization profile. For AGN dust the obtained type-2 polarization percentages for intermediate viewing angles are lower than for the Galactic dust torus. For this range of i the reflection off the torus has an important influence while toward edge-on values of i the polar scattering is again more important.

5 SUMMARY AND DISCUSSION

In this proceedings note, we have investigated the optical polarization imprint of an active nucleus. Our model is geared toward the unified scheme of AGN including equatorial and

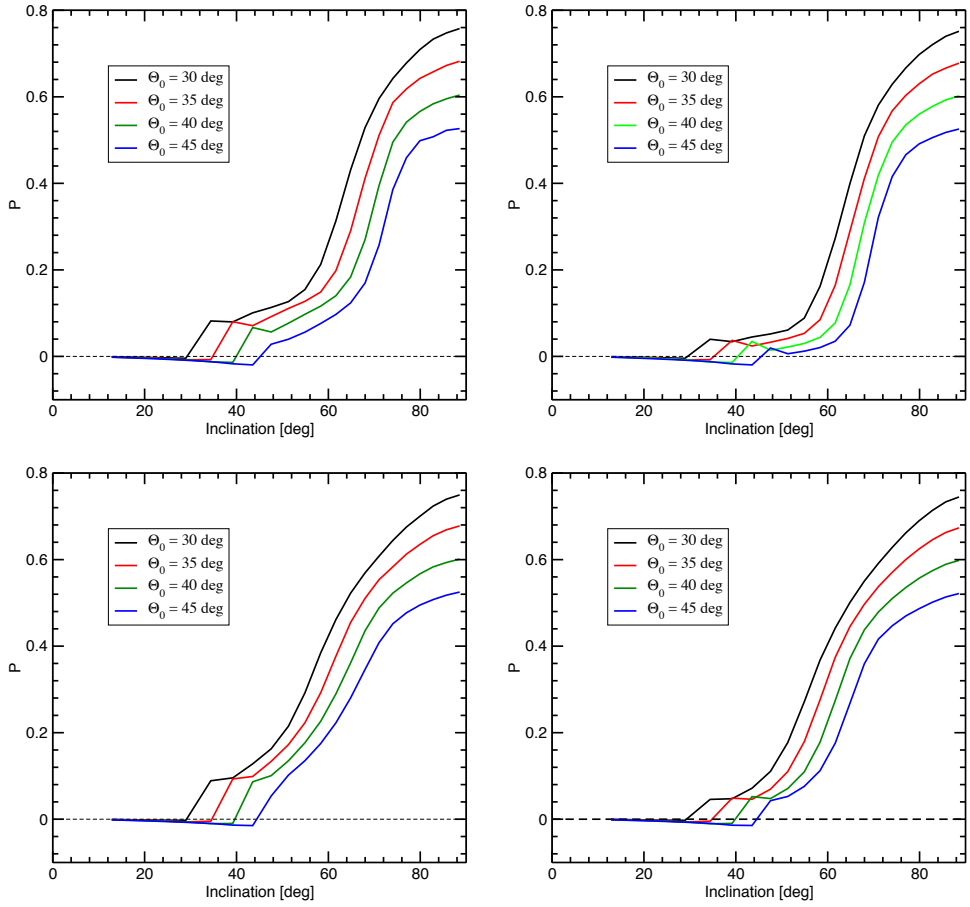

Figure 3. Polarization degree P at 5500 Å as a function of the disk inclination i. The upper panels denote an optical depth $\tau = 0.01$ of the polar electron cones, the lower ones denote $\tau = 0.1$. On the left side, the results for a torus with Galactic dust are given, on the right side the results are for AGN dust. From left to write the four curves of each panel mark increasing half-opening angles θ_0 of the system. Positive values of the polarization degree denote an orientation of the polarization position angle, which is perpendicular to the symmetry axis, negative values stand for parallel polarization.

polar electron scattering regions and an obscuring dusty torus. Evaluating the polarization percentage and position angle for various disk inclinations we succeed to reproduce the observed polarization dichotomy between type-1 and type-2 AGN. However, the presence of the dichotomy is sensitive to the model parameters, as it is the result of the competing type-1 polarization produced by the equatorial wedge on the one hand, and the type-2 polarization caused by the torus and the polar cones on the other.

Smith et al. (2004) pointed out that the competition between the equatorial and polar scattering explains the special population of Seyfert-1 galaxies that shows type-2 polariza-

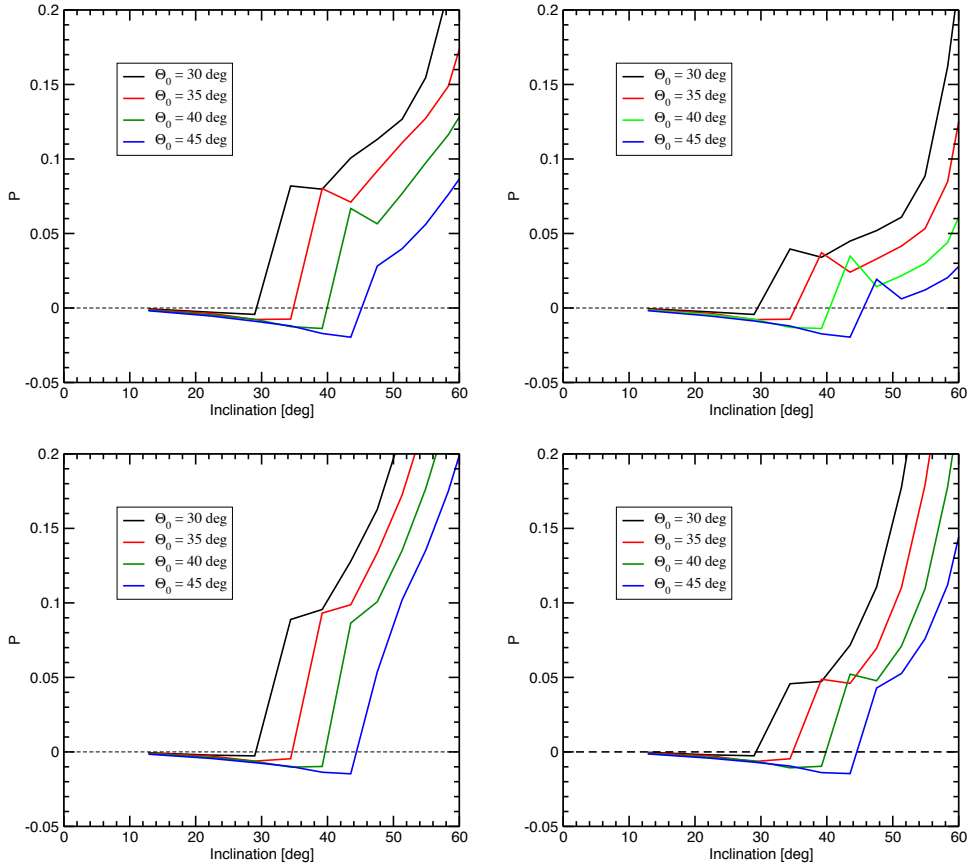

Figure 4. Same as in Fig. 3 but zoomed in and limited to disk inclinations of 60°.

tion. They are considered to be dominated by polar instead of equatorial scattering. In our model, we have set the half-opening angle and the optical depth of the equatorial wedge in such a way that a maximum type-1 polarization percentage is obtained. We then vary the optical depth of the polar scattering cones. The resulting distribution of the polarization position angle as a function of the inclination must correspond to the observed number densities of Seyfert-1 galaxies that are dominated by polar and by equatorial scattering. In principle, it is thus possible to put constraints on the optical depth of the polar cones.

But our modelling shows that there is also a significant impact of the dusty torus on the resulting polarization, especially for intermediate viewing angles. The resulting polarization changes with the dust type. From the given number density of AGN with different spectral and polarization types it is thus not straightforward to find relations between the properties of the various scattering regions. It rather requires more detailed modelling over a broader spectral range and within a larger parameter space than presented here. We intend to conduct such investigations in the future.

ACKNOWLEDGEMENTS

This work was supported by the Centre for Theoretical Astrophysics through research grant LC06014.

REFERENCES

Antonucci, R. R. J. (1982), Optical polarization position angle versus radio source axis in radio galaxies, *Nature*, **299**, pp. 605–606, URL http://adsabs.harvard.edu/abs/1982Natur.299..605A.

Antonucci, R. R. J. (1983), Optical polarization position angle versus radio structure axis in Seyfert galaxies, *Nature*, **303**, pp. 158–159, URL http://adsabs.harvard.edu/abs/1983Natur.303..158A.

Antonucci, R. (1993), Unified models for active galactic nuclei and quasars, *Annual Review of Astronomy and Astrophysics*, **31**, pp. 473–521, URL http://adsabs.harvard.edu/abs/1993ARA\%26A..31..473A.

Antonucci, R. (2002), Polarization insights for active galactic nuclei, in J. Trujillo-Bueno, F. Moreno-Insertis and F. Sánchez, editors, *Astrophysical Spectropolarimetry*, pp. 151–175, URL http://adsabs.harvard.edu/abs/2002apsp.conf..151A.

Gaskell, C. M., Goosmann, R. W., Antonucci, R. R. J. and Whysong, D. H. (2004), The Nuclear Reddening Curve for Active Galactic Nuclei and the Shape of the Infrared to X-Ray Spectral Energy Distribution, *Astrophys. J.*, **616**, pp. 147–156, arXiv: astro-ph/0309595, URL http://adsabs.harvard.edu/abs/2004ApJ...616..147G.

Goosmann, R. W. and Gaskell, C. M. (2007), Modeling optical and UV polarization of AGNs. I. Imprints of individual scattering regions, *Astronomy and Astrophysics*, **465**, pp. 129–145, URL http://adsabs.harvard.edu/abs/2007A\%26A...465..129G.

Goosmann, R. W., Gaskell, C. M. and Shoji, M. (2007a), AGN polarization modeling with Stokes, in V. Karas and G. Matt, editors, *Black Holes from Stars to Galaxies – Across the Range of Masses*, volume 238 of *Proceedings of IAU Symposium*, pp. 375–376, International Astronomical Union, Cambridge University Press, Cambridge, UK, ISSN 1743-9213, URL http://adsabs.harvard.edu/abs/2007IAUS..238..375G.

Goosmann, R. W., Gaskell, C. M. and Shoji, M. (2007b), Modeling the Polarization of Dusty Scattering Cones in Active Galactic Nuclei, *ArXiv Astrophysics e-prints*, arXiv: astro-ph/0701163, URL http://adsabs.harvard.edu/abs/2007astro.ph..1163G.

Smith, J. E., Robinson, A., Alexander, D. M., Young, S., Axon, D. J. and Corbett, E. A. (2004), Seyferts on the edge: polar scattering and orientation-dependent polarization in Seyfert 1 nuclei, *Monthly Notices Roy. Astronom. Soc.*, **350**, pp. 140–160, arXiv: astro-ph/0401496, URL http://adsabs.harvard.edu/abs/2004MNRAS.350..140S.

Smith, J. E., Robinson, A., Young, S., Axon, D. J. and Corbett, E. A. (2005), Equatorial scattering and the structure of the broad-line region in Seyfert nuclei: evidence for a rotating disc, *Monthly Notices Roy. Astronom. Soc.*, **359**, pp. 846–864, arXiv: astro-ph/0501640, URL http://adsabs.harvard.edu/abs/2005MNRAS.359..846S.

Smith, J. E., Young, S., Robinson, A., Corbett, E. A., Giannuzzo, M. E., Axon, D. J. and Hough, J. H. (2002), A spectropolarimetric atlas of Seyfert 1 galaxies, *Monthly Notices Roy. Astronom. Soc.*, **335**, pp. 773–798, arXiv: astro-ph/0205204, URL http://adsabs.harvard.edu/abs/2002MNRAS.335..773S.

Stockman, H. S., Angel, J. R. P. and Miley, G. K. (1979), Alignment of the optical polarization with the radio structure of QSOs, *Astrophys. J. Lett.*, **227**, pp. L55–L58, URL `http://adsabs.harvard.edu/abs/1979ApJ...227L..55S`.

Young, S. (2000), A generic scattering model for AGN, *Monthly Notices Roy. Astronom. Soc.*, **312**, pp. 567–578, URL `http://adsabs.harvard.edu/abs/2000MNRAS.312..567Y`.

Proceedings of *RAGtime 8/9, 15–19/19–21 September, 2006/2007, Hradec nad Moravicí, Opava, Czech Republic*
S. Hledík and Z. Stuchlík, editors, Silesian University in Opava, 2007, pp. 71–78

Optical spectroscopy of Cyg X-1

Petr Hadrava

Astronomical Institute, Czech Academy of Sciences, Boční II 1401/1a, CZ-141 31 Praha 4, Czech Republic
had@sunstel.asu.cas.cz

ABSTRACT
The star HDE 226868 known as an optical counterpart of the black hole candidate Cyg X-1 has been observed in H_α region using spectrograph at Ondřejov 2-m telescope. The orbital parameters are determined from He I-line by means of the author's method of Fourier disentangling. Preliminary results are also presented of disentangling the H_α-line into a P-Cyg profile of the (optical) primary and an emission profile of the circumstellar matter (and a telluric component).

1 INTRODUCTION

The bright X-ray source Cyg X-1 has been identified with the star denoted as HDE 226868, V1357 Cyg or BD+34°3815 etc. An improvement of instrumentation of the Ondřejov 2-m telescope enabled to start with systematic observations of this target of magnitude $V \simeq 8.9$, $B \simeq 9.6$. With coordinates $\alpha_{2000} = 19^{\rm h}58^{\rm m}21.7^{\rm s}$, $\delta_{2000} = +35°12'6''$ it is well observable from Ondřejov mainly at summer.

It is known to be an interacting binary with period $P \simeq 5.6$ d. The primary component is a supergiant of spectral type classified as B0 (or O9.7) Iab with temperature $T_{\rm eff} = 30400 \pm 500$ K and $\log g = 3.31 \pm 0.07$. This primary, which nearly fills its Roche lobe, shows signs of variable strong stellar wind and an overabundace of He and heavier elements (cf., e.g., Karitskaya et al., 2007).

The secondary component invisible in optical radiation is a compact object, most probably a black hole. This companion, or its neighborhood emits a variable X-radiation, which is supposed to originate from an accretion disk fed by the stellar wind from the primary.

The X-radiation switches chaotically between two states. In the low/hard state the total X-ray flux is low and the spectrum is flat, so that the hard tail of X-radiation prevails. In the high/soft state the soft radiation is enhanced more, and consequently the spectrum has a steeper decrease toward the higher energies and hence the radiation is softer in the mean. Some intermediate states may also appear temporarily.

The X-ray flux is anticorrelated with the strength of emission in the H_α -line of the primary: in the X-low/hard state the H_α emission is strong, while in the X-high/soft state the H_α emission is weak.

The aim of the observational campaign at Ondřejov observatory was to improve orbital parameters of the system, to check a possible spectroscopic features connected with the

978-80-7248-419-5

circumstellar matter (either accretion disk around the black hole, gaseous streams or stellar wind) or with a possible third body, and to get line-profiles enabling a quantitative comparison with a model of the atmosphere and stellar wind of the primary. The first part of obtained spectra was provided for a study on Cyg X-1 organized in a wide international collaboration, the results of which should appear in Gies et al. (2007). In the present contribution, results obtained using the author's method of spectra disentangling from the same set of Ondřejov spectra are given. A more detailed study taking into account also recently obtained spectra is in progress.

2 OBSERVATIONAL DATA

The set of spectra used here consists of 24 exposures obtained with CCD in the focus of 700 mm camera of Coudé spectrograph of the Ondřejov 2-m telescope between April 1st and September 21st, 2003. A typical resolution is about 0.25 Å per pixel. The rough data have been processed by M. Šlechta according to Škoda and Šlechta (2002).

The observational period covers a transition of Cyg X-1 from the low to high state and back, as it can be seen from the RXTE X-ray light-curve in Fig. 1.

Examples of obtained spectra in both states are given in Fig. 2. It is obvious here that the upper spectrum taken at April before the high-state episode has a strong emission in the whole H_α line profile, while in August the emission remains in the long-wavelength wing of the line only and the short-wavelength side of the line-profiles reveals an absorption, as it is typical in the P-Cyg line-profiles of stars losing mass via a stellar wind. The strength of the emission can be quantified by the equivalent width of the line, i.e., by an integral across the

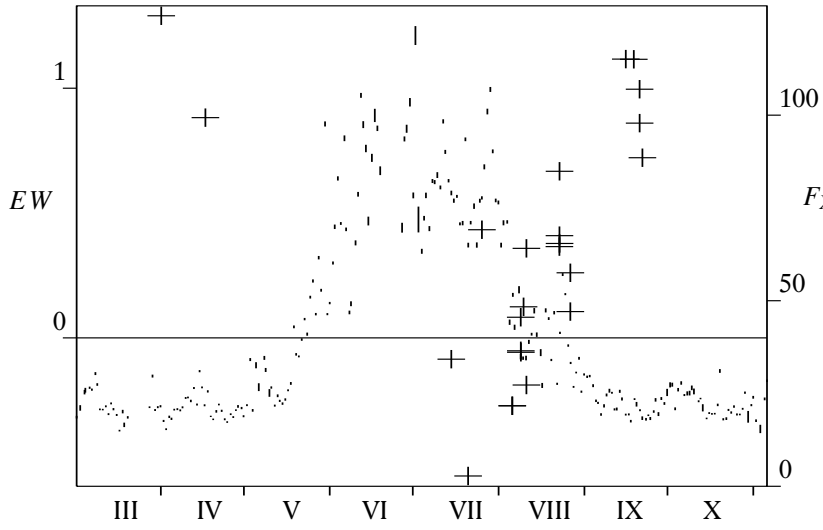

Figure 1. The equivalent width of H_α emission (in Å, crosses) in 2003 and ASM/RXTE one-day averages of sum-band intensity (in counts/s, error-bars).

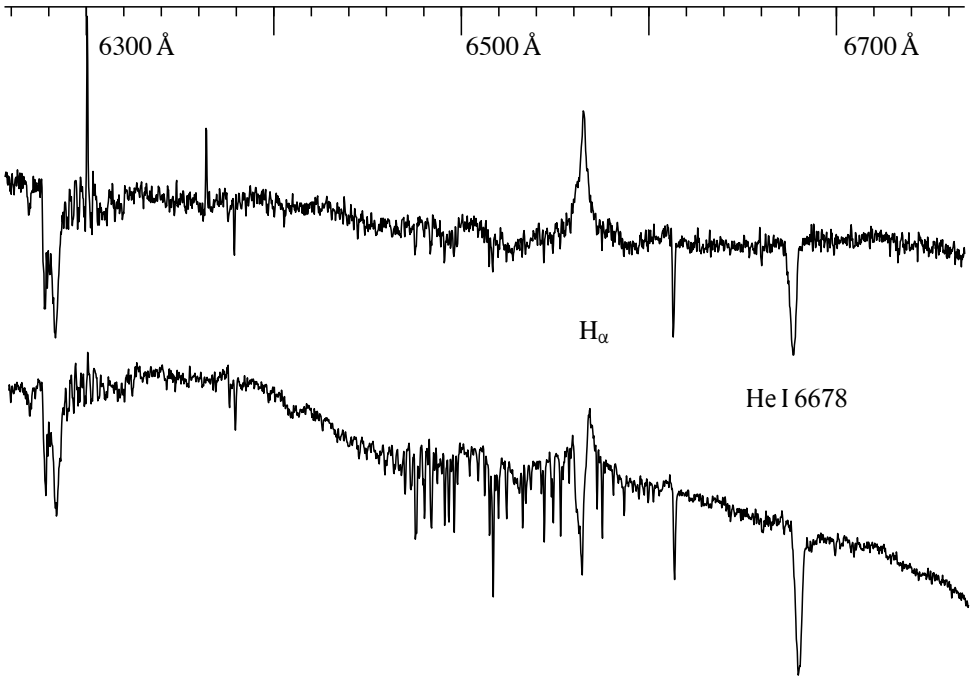

Figure 2. Spectra of Cyg X-1 taken with Ondřejov 2-m telescope on April 1st (upper curve) and August 5th (lower curve), 2003.

line of the intensity rectified to the continuum. These values are plotted for each exposure in Fig. 1 which confirms the above mentioned anticorrelation with the X-ray flux.

The He I-line 6678 Å is practically free of emission in both states. It means that this line may enable to measure reliably radial velocities of the primary component to get a constraint on the orbital parameters of the system.

3 SPECTRA DISENTANGLING

Despite the radial velocities of the He I-line 6678 Å could be measured using some standard method, it is advantageous to use the author's method of Fourier spectra disentangling (cf. Hadrava, 1995, 1997, 2004), which makes the procedure efficient and provides directly the orbital parameters. The principle of the method (in the version of 1997 used here) consists in least-squares fitting of all the spectra I observed at various times t as a superposition of unknown spectra I_j of the components in the form

$$I(x,t;\,p) = \sum_{j=1}^{n} I_j(x) * s_j(t)\delta(x - v_j(t;\,p))\,. \tag{1}$$

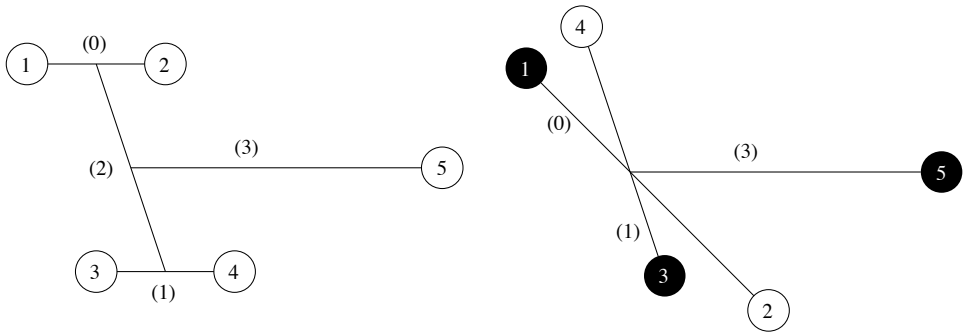

Figure 3. Hierarchical structure of a multiple stellar system supposed in KOREL-code (left) and its use for H_α-line of Cyg X-1 (right).

Here $x = c \ln \lambda$ is a logarithmic wavelength, v_j are instantaneous radial velocities of each component (or logarithms of redshift g-factors for a general relativistic case), s_j are factors fitting possibly variable strengths of lines, p are the orbital parameters to be found. Fourier transform

$$\tilde{I}(y, t; p) = \sum_{j=1}^{n} \tilde{I}_j(y) \, \tilde{\Delta}_j(y, t, p) \tag{2}$$

of Eq. (1) separates the solving for I_j into individual modes; similarly for s_j one gets a set of linear equations, while p can be found by some numerical method of optimization (e.g., simplex method in the author's code KOREL). Here $\Delta_j = s_j \delta(x - v_j)$ in the present calculation, but generally it could also characterize some general broadening function.

The method can generally provide intrinsic spectra of n sources, if more than n observed spectra taken at different values v_j are on input. Karas and Kraus (1996) suggested a possibility to disentangle in this way contributions of several spots to a line-profile of an accretion disk. The author's code KOREL should be modified for such a purpose, because it is designed for applications to systems of binary or multiple stars. A hierarchical structure of the system is supposed (cf. Fig. 3, left), in which two pairs of close binaries (denoted $1 + 2$ and $3 + 4$) are orbiting around their common centre of mass, which may be on an even wider orbit with respect to another component (Nr. 5). To be able to treat simpler systems, spectrum of each component can be switched on or off, and the higher orbits (denoted by numbers in parenthesis in Fig. 3) may be chosen degenerated. At the same time, this model is general enough to enable solving some more complicated cases, e.g., just like a presence of circumstellar matter in a binary.

As already mentioned, there are seen no traces of the companion or of the circumstellar matter in the He I-line for Cyg X-1. Consequently, one could take the extremally simple case $n = 1$ of the disentangling (with only the component 1 and orbit (0) switched on – cf. Fig. 3, right) for the spectral region around 6678 Å. However, because some weak telluric lines are also present in this region, $n = 2$ was used instead, with the component 5 corresponding to the telluric lines and orbit (3) to the annual motion. Results of the disentangling are

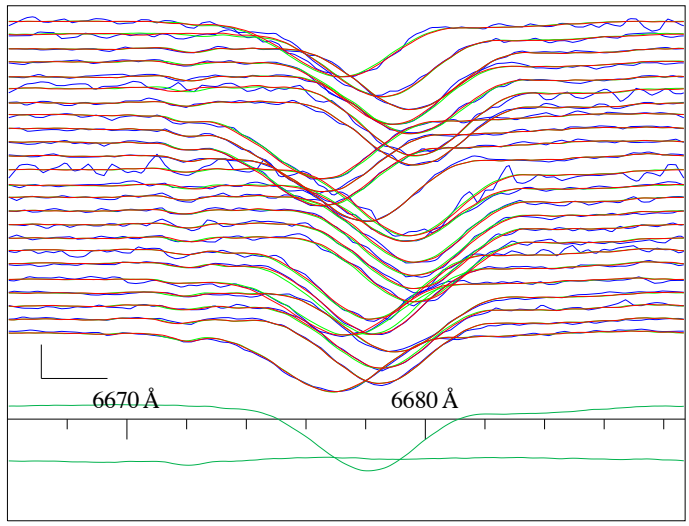

Figure 4. Disentangled line He I 6678 Å.

Table 1. Disentangled orbital parameters of Cyg X-1.

Line	He I	H_α	H_α – wind
Period		5.599829 d	
Periastron epoch	52872.83	52873.01	52875.41
Eccentricity		0.0	
Periastron long.		−90°	
K_1 [km/s]	71.94	71.26	60.78

shown in Fig. 4. In the upper part of this standard output from the KOREL-code, we can see superimposed the 24 observed line-profiles (rectified to the continuum) and their reconstructions from the disentangled line-profiles, which are plotted as the two bottom curves. The disentangled values of orbital parameters (the epoch and the amplitude of the radial-velocity curve) are given in Table 1.

4 DOPPLER MAPPING AND DISENTANGLING OF CIRCUMSTELLAR MATTER

Unlike the He I-line, the H_α shows the above mentioned irregular emission, revealing a presence of strongly variable circumstellar matter in the system. The variability of line-profile of the emission component, which is frequent in many emission-line systems, obviously violates the assumption on constancy of component spectra I_j in Eq. (1) and makes the use of disentangling for such systems questionable. On the other hand, one can always try, if

a violation of underlying assumptions is not an effect of second order, and if a mean behaviour of the system cannot be approximated neglecting this effect, or if the effect cannot be modelled as some additional perturbation.

If the distribution of emissivity of the circumstellar matter in the velocity space is stable on a time-scale longer than the orbital period, it can be mapped by methods of Doppler tomography. The links between this method and the spectra disentangling have been discussed by Hadrava (2001). Unlike the disentangling, where a few components may have a general intrinsic spectrum and changes of velocity, the Doppler imaging assumes locally delta-function line-profile of a smooth distribution of matter in a rigidly rotating velocity-space. However, in some cases both methods can provide an equivalent description of the observed phase-locked line-profile variations of binaries.

Several attempts have been done by the author to fit discrepancies between observed spectra of different binaries with circumstellar matter (e.g., Be-stars or algols) and their reconstructions from disentangled spectra. The method consists in fixing the period of orbit (1) equal to that of orbit (0) but converging either epochs or periastron longitudes of both orbits together with the radial-velocity amplitudes (K) as independent quantities. If the component 1 and 2 correspond to the primary and secondary star, the component 3 may also be switched on, to correspond to (either emission or absorption) features of the circumstellar matter. The amplitude and phase-shift of this component are then correspond to the absolute value and orientation of the superposition of the orbital and intrinsic velocity of the circumstellar matter with respect to the center of mass of the system. In principle, up to five component spectra corresponding to different features corotating in the orbital plane of a binary may be treated using KOREL, if the periods of all four orbits are fixed equal. Such a disentangling always improved formally the fit, but usually it did not provide a fully satisfactory explanation of a long-lasting series of line-profiles. This may be explained by variations of the motion and emissivity of the circumstellar matter on time-scales shorter then the orbital period.

Sowers et al. (1998) used the method of Doppler mapping to interpret the line-profiles of the H_α line of Cyg X-1. They found a good agreement with observations if an emission source attributed to a focused stellar wind is involved. Recently Jingzhi Yan (2007) suggested to disentangle this focused stellar wind and the primary component from the H_α line of Cyg X-1. The preliminary results reported here are obtained by switching on the components 1, 3 and 5 for the primary, the focused wind and telluric water-vapor lines (which are quite strong here), resp. The period of orbit (1) is set equal to that of orbit (0), orbit (3) is the annual motion and orbit (2) is degenerated (cf. Fig. 3, right).

The results are shown in Fig. 5 and Table 1. The profiles reconstructed from the disentangled components are again superimposed on the observed 24 line-profiles plotted in the chronological order from the top. The agreement of these curves is surprisingly better than the one obtained for some other interacting binaries with much less pronounced variability. The agreement is a bit worse for the first two exposures taken before the X-high episode, also compared to the last exposures, where X-emission was low again and H_α emission high (cf. Fig. 4), but still with the P-Cyg profile. The mean line-profile of the primary has a P-Cyg shape, the component attributed to the focused stellar wind is a broad emission. The disentangled spectrum of telluric lines is partly contamined with the H_α emission, but again much less than for many other emission-line binaries. Both the primary and wind

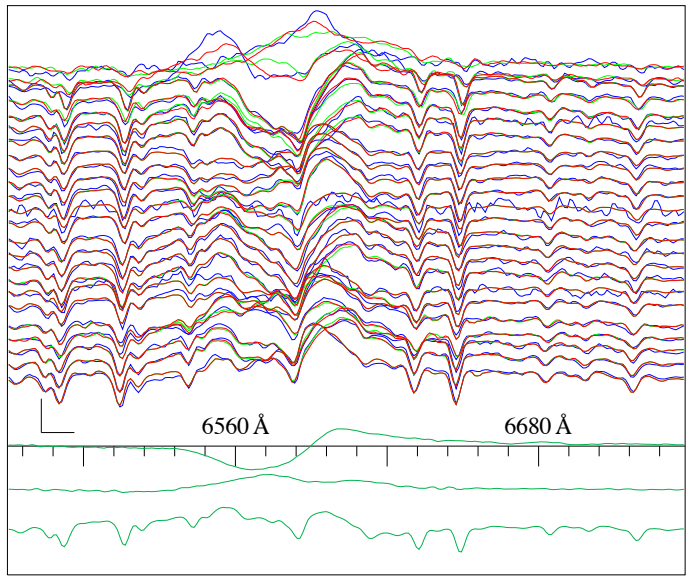

Figure 5. Disentangled H_α-line.

components are varying in strength, but the analysis of this variability is postponed to a next study based on more spectra disentangled with constrained telluric component as described by Hadrava (2006a,b).

The orbital parameters for the primary disentangled from H_α are in good agreement with those obtained from He-line here as well as in other studies. The radial-velocity amplitude $K_{\rm wind} = 60.78\,{\rm km\,s^{-1}}$ and the phase shift $\phi_0 = 0.46$ (with respect to the He-line) of the wind component is not in a complete agreement with results given in text of (Sowers et al., 1998, p. 428) who obtained $K_{\rm wind} = 68\,{\rm km\,s^{-1}}$ and $\phi_0 = 0.86$ using the tomographic method. Such a disagreement is not surprising, because in spite of some similarities, both methods are different, particularly in taking into account the line-strength variability or the telluric lines. Also the long-term stability of the focused-wind component should be tested by additional spectra. However, the present results indicate, that the velocity-distribution of this component does not vary substantially before and during the episode od high X-ray state.

ACKNOWLEDGEMENTS

This work has been done in the framework of the Center for Theoretical Astrophysics (ref. LC06014) with a support of grant GAČR 202/06/0041. It is based on observational data obtained using Ondřejov 2-m telescope and ASM at RXTE satellite. The work of teams at both these instruments is highly appreciated.

REFERENCES

Gies, D. R., Bolton, C. T., Blake, M., Caballero-Nieves, S. M., Crenshaw, D. M., Hadrava, P., Herrero, A., Hillwig, T. C., Howell, S. B., Huang, W., Kaper, L., Koubský, P., McSwain, M. V. and Melymuk, L. (2007), Stellar wind variations during the X-ray high and low states of Cygnus X-1, *Astrophys. J.*, submitted.

Hadrava, P. (1995), Orbital elements of multiple spectroscopic stars, *Astronom. Astrophys. Suppl. Ser.*, **114**, pp. 393–396.

Hadrava, P. (1997), Relative line photometry of eclipsing binaries, *Astronom. Astrophys. Suppl. Ser.*, **122**, pp. 581–584.

Hadrava, P. (2001), The method of spectra disentangling and its links to Doppler tomography, in H. M. J. Boffin, D. Steeghs and J. Cuypers, editors, *Astrotomography, indirect imaging methods in observational astronomy*, volume 573 of *Lecture notes in physics*, pp. 261–268, Springer.

Hadrava, P. (2004), KOREL – User's guide, *Publ. Astron. Inst. ASCR*, **92**, pp. 15–35.

Hadrava, P. (2006a), Disentangling of the spectra of binary stars – Principles, results and future development, *Astrophys. Space Sci.*, **304**, pp. 337–341.

Hadrava, P. (2006b), Disentangling telluric lines in stellar spectra, *Astronomy and Astrophysics*, **448**, pp. 1149–1152.

Jingzhi Yan (2007), private communication.

Karas, V. and Kraus, P. (1996), Doppler tomography of relativistic accretion disks, *Publ. Astronom. Soc. Japan*, **48**, pp. 771–775.

Karitskaya, E. A., Shimanskii, V. V., Bochkarev, N. G., Sakhibullin, N. A., Galazutdinov, G. A. and Lee, B.-C. (2007), Properties of the Cyg X-1 Optical Component, *IAU Symp.*, **240**, p. 130.

Škoda, P. and Šlechta, M. (2002), Reduction of spectra exposed by the 700mm CCD camera of the Ondřejov telescope coudé spectrograph, *Publ. Astron. Inst. ASCR*, **90**, pp. 22–35.

Sowers, J. W., Gies, D. R., W. G. Bagnuolo, Jr., Shafter, A. W., Wiemker, R. and Wiggs, M. S. (1998), Tomographic analysis of Hα profiles in HDE 226868/Cygnus X-1, *Astrophys. J.*, **506**, pp. 424–430.

Proceedings of *RAGtime 8/9, 15–19/19–21 September, 2006/2007, Hradec nad Moravicí, Opava, Czech Republic*
S. Hledík and Z. Stuchlík, editors, Silesian University in Opava, 2007, pp. 79–87

Disc instability as an energy source for quasi-periodic oscillations

Jiří Horák

Astronomical Institute, Czech Academy of Sciences, Boční II 1401/1a, CZ-141 31 Praha 4, Czech Republic

ABSTRACT
We discuss a scenario, in which the energy for quasi-periodic oscillations comes from instabilities of the accretion disc. We demonstrate this mechanism on the interaction among stable and unstable modes of oscillations in slender accretion tori. In our model, the unstable non-axisymmetric corotation modes are nonlinearly coupled to stable acoustic modes of torus oscillations. The increasing energy of corotation modes is advected to the acoustic modes by the means of parametric instability. The stable modes may reach substantial amplitudes even if they are damped according to the linear theory.

Keywords: Black hole physics – accretion discs – instabilities

1 INTRODUCTION

It has been proposed that a nonlinear resonance among two accretion disc oscillations is responsible for observed quasiperiodic oscillations (QPOs) in both black-hole and neutron-star sources (see Kluźniak, 2005 for a review). In earlier versions of the resonance model, the two QPOs were connected to the orbital and radial epicyclic motion. More recently, QPOs has been interpreted as radial and vertical epicyclic oscillations of the accreted matter at the position of the 3:2 parametric resonance (Kluzniak and Abramowicz, 2002).

The source of energy for the oscillations has not been identified yet. In the parametric-resonance models the vertical oscillations are excited and fed by the radial oscillations. If the feedback of vertical to radial oscillations is taken into account, the two modes periodically exchange the energy keeping the total energy constant. In order to solve this problem, two possible sources of energy has been proposed: (1) external periodic forcing, e.g., by spinning central neutron star and (2) internal stochastic forcing by hydrodynamic or magnetohydrodynamic turbulence. The former process was proposed by Lee et al. (2004) and was largely motivated by an observation that in the two millisecond pulsars showing QPOs the QPO frequency difference is always close to the observed spin frequency or half of it (Wijnands et al., 2003; Linares et al., 2005). The latter was recently examined by Brandenburg (2005) and Arras et al. (2006) in the shearing-box simulations and by Vio et al. (2006) in the simplified model of stochastic excitation of test-particle epicyclic motion.

978-80-7248-419-5

In this work we propose an alternative mechanism in addition to these two scenarios. In our view the QPOs are fed by a linear instability of the accretion disc through a nonlinear modal coupling. As an example of this process we start to examine nonlinear interactions among stable and unstable modes of slender accretion tori. The source of the energy is Papaloizou-Pringle instability. The plan of the paper is the following. Growth rates and eigen-functions of the unstable modes are summarized in Section 2. The mechanism of nonlinear interactions among stable and unstable modes is outlined in Section 3. In Section 4 we show that the two necessary conditions for these interactions (a particular combination of eigenfrequencies of the modes and non-zero coupling coefficient) are satisfied in slender tori. Finally, Section 5 is devoted to a discussion and conclusions.

2 LINEAR INSTABILITY OF SLENDER TORI

An important class of torus oscillations is represented by corotation modes, for which the mode pattern corotates with the fluid at a particular radius inside the torus (corotation radius). According to classical works in the subject (e.g., Goldreich et al., 1986), these modes are suspected to be unstable. Indeed, in the limit of infinitely slender tori these modes are just marginally stable. They are described by eigenfunctions and eigenfrequencies of the form

$$W_0 = \mathrm{C}_0 \mathrm{e}^{\mathrm{i}m_0\phi}\,, \quad w_0 = m_0\Omega_0\,, \tag{1}$$

where C_0 is a normalization constant, m_0 is an integer azimuthal wavenumber and Ω_0 is the flow angular velocity at the maximal pressure radius that coincides with the local Keplerian frequency, $\Omega_0 = \Omega_{\mathrm{K}}(r_0)$. The perturbation quantity W is connected to the Eulerian pressure perturbation by $\delta p = (w - m_0\Omega)\rho W$. The slender torus corresponds to the limit $\beta \sim \Delta r/r \to 0$ (Δr is the radial size of the torus).

The modal eigenfrequencies and eigenfunctions of larger tori can be found using a perturbative expansion in β (Blaes, 1985; Blaes et al., 2007). For tori with constant angular momentum distribution this procedure gives

$$\begin{aligned} w_0 &= m_0\Omega_0 + \mathrm{i}\sqrt{2}\, m_0 b\beta + \mathcal{O}(\beta^2)\,, \\ W_0 &= \mathrm{C}_0 \mathrm{e}^{\mathrm{i}m_0\phi}\left\{1 + m_0^2\beta^2\left[a^2\bar{x}^2 - b^2\bar{y}^2\frac{4\sqrt{2}\,\mathrm{i}b}{\bar{\omega}_r^2}\bar{x} + \frac{\bar{\omega}_r^2 b^2 - \bar{\omega}_z^2 a^2}{2(n+1)\bar{\omega}_r^2\bar{\omega}_z^2}\right] + \mathcal{O}(\beta^3)\right\}\,, \end{aligned} \tag{2}$$

where the coefficients a and b are given by

$$a^2 \equiv \frac{4(1+2n) + \bar{\omega}_r^2}{4(1+n)\bar{\omega}_r^2}\,, \quad b^2 \equiv \frac{4 - \bar{\omega}_r^2}{4(1+n)\bar{\omega}_r^2}\,. \tag{3}$$

The eigenfunctions are expressed using "slender" coordinates $\bar{x}$ and $\bar{y}$ contracting with the torus as $\beta \to 0$ (see Blaes et al., 2006 for a definition). The corotation mode of the slender torus splits into two modes. The positive or negative values of b give the unstable or stable mode, respectively, where the unstable mode corresponds to the principal mode of the Papaloizou–Pringle instability (Blaes, 1985).

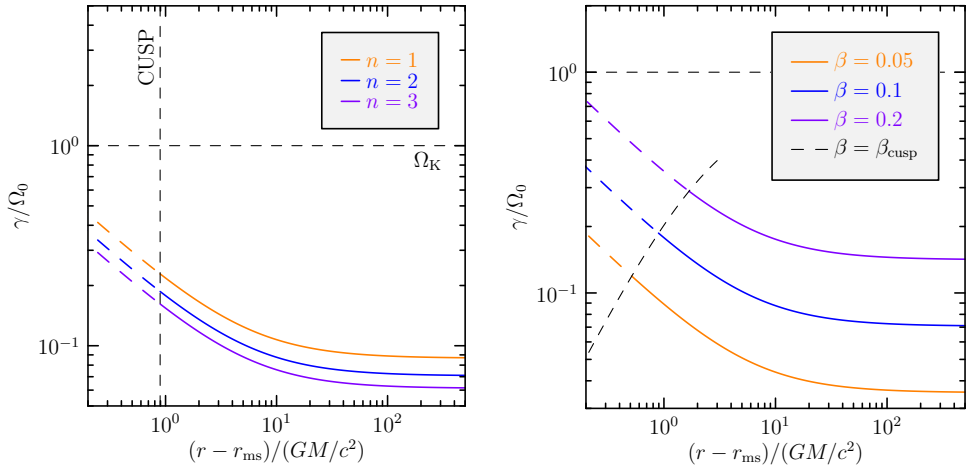

Figure 1. The growth-rate of the Papaloizou–Pringle instability normalized by the local Keplerian angular velocity Ω_0 as function of the location of the torus centre for different values of the polytropic index (*left*) and of the torus thickness β (*right*). The limiting cases of the torus with cusp are denoted by the dashed line.

The external gravitational potential comes into the above formulae only through the normalized radial and vertical epicyclic frequencies $\bar{\omega}_r = \omega_r/\Omega_0$ and $\bar{\omega}_z = \omega_z/\Omega_0$. In the spherically symmetric Newtonian gravitation field both epicyclic frequencies equal to the Keplerian orbital frequency, $\bar{\omega}_r = \bar{\omega}_z = 1$ and we recover Eqs (4.11) and (4.13) of Blaes (1985).

The growth-rates of the instability (given by the imaginary part of w_0) as functions of the location of the torus are shown in Fig. 1 for different values of the polytropic index n and the thickness of the torus β. In this case, we consider the pseudo-Newtonian potential (Paczyński and Wiita, 1980) $\Phi = GM/(r - r_s)$ with $r_s \equiv 2GM/c^2$ being the Schwarzschild gravitational radius. The instability is stronger when the torus approaches the location of the marginally stable circular orbit r_{ms}. For a given value of β, however, there exists a limiting radius bellow which the matter in the torus starts to accrete onto the black hole and the assumption about stationary equilibrium breaks down.

Our results have been obtained for constant angular momentum tori that are violently unstable. The instability is largely reduced for steep angular momentum distributions (e.g., if $q > \sqrt{3}$, where the flow angular velocity is parameterized as $\Omega \propto r^{-q}$).

3 INTERACTIONS AMONG STABLE AND UNSTABLE MODES

When the amplitude of the corotation mode is sufficiently large, nonlinear processes become important. In principle, growth of the instability can be even halted by nonlinear interaction with other oscillation modes, if they are damped significantly. The energy of the unstable mode is advected to the damped modes, where it is dissipated. This process

likely plays a key role in limiting amplitudes of the pulsations of ZZ Ceti stars, dwarf-type variables and some δ Scuti stars (Dziembowski, 1982; Nowakowski, 2005; and references therein). It also seems to be important for the saturation of the r-mode instability in neutron stars (Arras et al., 2003).

The mechanism of this process is as follows. Let us consider two stable damped modes ("daughter" modes) whose eigenfrequencies and excitation rates are ω_1, ω_2 and $\gamma_1, \gamma_2 < 0$ (the complex eigenfrequencies are given by $w_i = \omega_i + \mathrm{i}\gamma_i$). They will form a resonant triple with the unstable ("parent") mode with frequency ω_0 and excitation rate $\gamma_0 > 0$ if the condition of a combination resonance,

$$\omega_1 + \omega_2 + \omega_0 \equiv \delta\omega \approx 0\,, \tag{4}$$

is satisfied. Neglecting any influence of the other modes, the oscillations can be described by the Lagrangian displacement

$$\boldsymbol{\xi}(t, \boldsymbol{x}) = \Re\left[A_0(t)\mathrm{e}^{-\mathrm{i}\omega_0 t}\boldsymbol{\xi}_0(\boldsymbol{x}) + A_1(t)\mathrm{e}^{-\mathrm{i}\omega_1 t}\boldsymbol{\xi}_1(\boldsymbol{x}) + A_2(t)\mathrm{e}^{-\mathrm{i}\omega_2 t}\boldsymbol{\xi}_2(\boldsymbol{x})\right], \tag{5}$$

where $\boldsymbol{\xi}_i(\boldsymbol{x})$ are the Lagrangian eigenfunctions of the interacting modes. The resonance causes a slow modulation of the phases ϕ_i and amplitudes a_i of the oscillations that can be described by slowly varying dimensionless complex amplitudes $A_i = a_i\mathrm{e}^{\mathrm{i}\phi_i}$. Their time-behaviour is given by the amplitude equations of the form

$$\dot{A}_1 = \gamma_1 A_1 + \mathrm{i}\omega_1\kappa^* A_2^* A_0^* \mathrm{e}^{\mathrm{i}\delta\omega t}\,, \tag{6}$$
$$\dot{A}_2 = \gamma_2 A_2 + \mathrm{i}\omega_2\kappa^* A_1^* A_0^* \mathrm{e}^{\mathrm{i}\delta\omega t}\,, \tag{7}$$
$$\dot{A}_0 = \gamma_0 A_0 + \mathrm{i}\omega_0\kappa^* A_1^* A_2^* \mathrm{e}^{\mathrm{i}\delta\omega t}\,, \tag{8}$$

where κ is the three-mode coupling coefficient determined by the eigenfunctions of the modes.

The generic behaviour of the amplitudes is illustrated by three examples in Fig. 2. The solutions are obtained by numerical integration of Eqs (6)–(8) for different values of the parameters γ_i and $\delta\omega$. Initially, they behave according to the linear theory – the amplitude of the parent mode grows exponentially while the daughter modes are exponentially damped. Nonlinear effects become important after the amplitude A_0 overcomes certain threshold. The energy accumulated in the parent mode is then transferred to the daughter modes by means of the parametric instability. The threshold can be derived from Eqs (6)–(8) assuming that the amplitudes A_1 and A_2 are much smaller than the amplitude of the parent mode, so that their influence on the parent mode can be neglected (Dziembowski, 1982; Nowakowski, 2005). In that case we may suppose that $A_0(t) \propto \mathrm{e}^{\gamma_0 t}$ and both $A_1(t)$ and $A_2(t)$ are proportional to $\mathrm{e}^{\nu t}$. The real part of ν is positive when

$$A_0 \gtrsim A_{\mathrm{crit}} = \frac{1}{Q_1 Q_2 |\kappa|^2}\left[1 + \left(\frac{\delta\omega + \gamma_0}{\gamma_1 + \gamma_2}\right)^2\right], \tag{9}$$

with $Q_i \equiv \omega_i/\gamma_i$ being quality factors of the daughter modes.

Some fraction of the energy transferred from the parent mode is dissipated in the daughter modes, the rest of it flows back to the parent mode. Depending on the excitation rate γ_0,

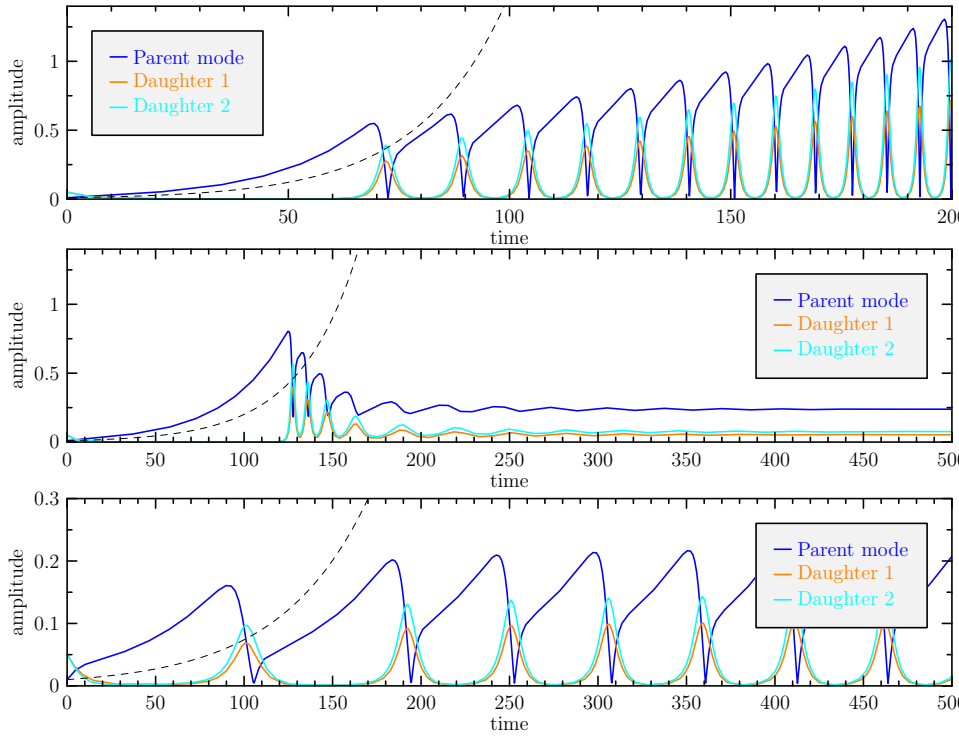

Figure 2. Evolution of the amplitudes in a resonant triple. While the parent mode is unstable, the two daughter modes are damped. Three types of possible evolution are shown: *Top:* The damping rates are too small compared to the growth-rate of the instability so that the daughter modes are not able to saturate the unstable parent mode. *Middle:* The energy from the instability is dissipated by the daughter modes and the system reach a steady state. *Bottom:* The accumulated energy of the parent mode is periodically advected to the daughter modes where it is dissipated.

damping rates γ_1, γ_2 and on the frequency detuning $\delta\omega$, the whole process may lead to an unsaturated growth of all three modes, to a steady state or to periodic limit cycles. The unsaturated grow (Fig. 2a) occurs when $\gamma_1 + \gamma_2 \lesssim \gamma_0$, e.g., when the daughter modes are not able to dissipate the energy coming to the system from the instability. The instability is saturated by reaching the steady state (Fig. 2b) or by executing periodic limit cycles (Fig. 2c) when the total damping slightly overcome the excitation. The type of the saturation depends on the frequency detuning $\delta\omega$ (Wersinger et al., 1980; Dziembowski, 1982). Properties of the limit cycles in dependence of the system parameters were discussed in great details by Moskalik (1985). In particular, the period of the cycles is mostly influenced by the excitation rate, $T \sim |\gamma_0|^{-1}$.

In practical situations, there can be several pairs of modes that satisfy the resonance condition (4). Recently, the resonant interactions among the unstable parent mode and N pairs of damped daughter modes have been studied by Nowakowski (2005). In this case,

the necessary condition for the saturation is natural generalization of that for the single pair,

$$\sum_{i=1}^{N}(\gamma_{i,1}+\gamma_{i,2}) \geq \gamma_0\,, \tag{10}$$

where $\gamma_{i,1}$ and $\gamma_{i,2}$ are the damping rates of the daughter modes in i-th pair. When $N > 2$ it is impossible to reach the steady-state and the amplitudes are always strongly variable. For large N the amplitude of the parent mode suffers random changes and the system reach some kind of a statistical equilibrium.

4 PARAMETRIC INSTABILITY IN SLENDER TORI

Is the scenario described in the previous section relevant for the nonlinear behaviour of the Papaloizou–Pringle instability of accretion tori? Essential is a presence of the daughter modes that are resonantly coupled to the unstable corotation mode. In this section we examine the necessary conditions for the existence of the coupled modes. The important question whether they are able to saturate the instability or not will be addressed in future.

Let us consider tori with $\beta = 0$. The eigenfunctions and eigenfrequencies of the non-axisymmetric modes can be expressed as

$$W_\alpha = \tilde{W}_\alpha \mathrm{e}^{\mathrm{i}m_\alpha\phi}\,, \quad \omega_\alpha = m_\alpha\Omega_0 + \tilde{\omega}_\alpha\,, \tag{11}$$

where $\tilde{W}_\alpha$ and $\tilde{\omega}_\alpha$ are the eigenfunction and eigenfrequency of the axisymmetric mode with $m_\alpha = 0$ (Blaes et al., 2006). The pattern speed of the mode is given by $\omega_{\mathrm{p},\alpha} = \omega_\alpha/m = \Omega_0 + \tilde{\omega}_\alpha/m_\alpha$. The daughter modes may be identified with modes whose patterns propagate with the same speed in the opposite direction with respect to the flow

$$\omega_1 = m_1\Omega_0 + \tilde{\omega}\,, \quad \omega_2 = m_2\Omega_0 - \tilde{\omega}\,. \tag{12}$$

The azimuthal wavenumbers m_1 and m_2 may be different. Combining the Eqs (1) and (12), we find that

$$\delta\omega \equiv \omega_1 + \omega_2 + \omega_0 = 0 \quad \Leftrightarrow \quad m_1 + m_2 + m_0 = 0\,. \tag{13}$$

Our discussion may be extended to thicker tori by means of the perturbative expansion in β-parameter. The main effect is change of the eigenfrequencies due to the pressure corrections. These corrections are of the order of β^2 and depends also on the azimuthal wavenumber, because the pressure gradients in the azimuthal direction become important. The result is detuning of the perfect resonance whose magnitude is $\delta\omega \sim \beta^2$.

Next, we examine a coupling among these modes. The coupling coefficient for the interaction is given by the integral over the volume of the torus,

$$\kappa = \int_V f(\boldsymbol{\xi}_0, \boldsymbol{\xi}_1, \boldsymbol{\xi}_2)\,\mathrm{d}V\,, \tag{14}$$

where f is a multi-linear function in all its arguments. Except for eigenfunctions $\boldsymbol{\xi}_i$, f depends only on the quantities describing the equilibrium and there is no explicit dependence on the coordinates (Schenk et al., 2002). Because the equilibrium configuration is

axially and equatorial-plane symmetric and the eigenfunctions depend on the azimuthal angle as $\boldsymbol{\xi}_\alpha \propto \exp(\mathrm{i}m_\alpha\phi)$, we find that the coupling coefficient may be nonzero only when

$$m_1 + m_2 + m_0 = 0\,. \tag{15}$$

We obtain the same selection rule as it is needed by the resonance condition (13), which implies that the resonant interaction is indeed possible. Finally, let us examine effects of two other symmetries. Because the corotation mode eigenfunction is even with respect to reflection and $\bar{y} \leftrightarrow -\bar{y}$ the daughter modes have to have the same parity with respect to this symmetry. Otherwise f is an odd function of z and the coupling coefficient vanishes.

5 DISCUSSION & CONCLUSIONS

According to the general discussion given in Section 3 stable oscillation modes of a fluid body may reach substantial amplitudes if they are nonlinearly coupled to a linearly unstable mode. In this work we have examined this process for the particular case of slender tori that are unstable with respect to the Papaloizou–Pringle instability. We have demonstrated that two necessary conditions for the resonance coupling: the frequency condition of a combination resonance and the selection rule imposed on the azimuthal wavenumbers are satisfied by many pairs of torus modes in the infinitely slender tori. A finite thickness of the torus cause a detuning of the perfect resonance which is of order of β^2. Careful analysis of the modal eigenfrequencies and eigenfunctions similar to that of (Blaes et al., 2007) for epicyclic modes is needed in order to decide what modes are in the resonance in thicker tori.

The mechanism described above is unable to saturate the instability if the daughter modes are not sufficiently damped. This occurs in inviscid slender tori, where the instability leads to a fragmentation (Goodman et al., 1987). One possible source of damping may be a viscosity of the flow. Preliminary study shows that if the standard α-prescription is assumed the modes with significant pressure gradients are damped on the time-scale $t_{\mathrm{damp}} \sim (\alpha\Omega_0)^{-1}$ (the timescale for the epicyclic modes is comparable with that of the secular evolution of the torus $\beta^{-2}(\alpha\Omega_0)^{-1}$). Comparing it with the timescale of the instability growth, we realize that the corotation mode may be saturated if $\beta \lesssim \alpha$.

The other possible source of damping is accretion. It has been shown that the growth of the instability is reduced significantly because the reflection of the waves at the inner edge of the torus is not perfect (Blaes, 1987). Likely, the same effect causes damping of other oscillation modes.

ACKNOWLEDGEMENTS

The work was supported by Center for Theoretical Astrophysics (ref. LC06014) and by Grant Agency of the Czech Republic (ref. 205/06/P415).

REFERENCES

Arras, P., Blaes, O. and Turner, N. J. (2006), Quasi-periodic Oscillations from Magnetorotational Turbulence, *Astrophys. J. Lett.*, **645**, pp. L65–L68, arXiv: astro-ph/0602275, URL http://adsabs.harvard.edu/abs/2006ApJ...645L..65A.

Arras, P., Flanagan, E. E., Morsink, S. M., Schenk, A. K., Teukolsky, S. A. and Wasserman, I. (2003), Saturation of the r-Mode Instability, *Astrophys. J.*, **591**, pp. 1129–1151, arXiv: astro-ph/0202345, URL http://adsabs.harvard.edu/abs/2003ApJ...591.1129A.

Blaes, O. M. (1985), Oscillations of slender tori, *Monthly Notices Roy. Astronom. Soc.*, **216**, pp. 553–563, URL http://adsabs.harvard.edu/abs/1985MNRAS.216..553B.

Blaes, O. M. (1987), Stabilization of non-axisymmetric instabilities in a rotating flow by accretion on to a central black hole, *Monthly Notices Roy. Astronom. Soc.*, **227**, pp. 975–992, URL http://adsabs.harvard.edu/abs/1987MNRAS.227..975B.

Blaes, O. M., Arras, P. and Fragile, P. C. (2006), Oscillation modes of relativistic slender tori, *Monthly Notices Roy. Astronom. Soc.*, **369**, pp. 1235–1252, arXiv: astro-ph/0601379, URL http://adsabs.harvard.edu/abs/2006MNRAS.369.1235B.

Blaes, O. M., Šrámková, E., Abramowicz, M. A., Kluźniak, W. and Torkelsson, U. (2007), Epicyclic Oscillations of Fluid Bodies. Paper III. Newtonian Non-Slender Torus, *Astrophys. J.*, **665**, pp. 642–653, arXiv: 0706.4483, URL http://adsabs.harvard.edu/abs/2007ApJ...665..642B.

Brandenburg, A. (2005), Turbulence and its parameterization in accretion discs, *Astronom. Nachr.*, **326**, pp. 787–797, arXiv: astro-ph/0510015, URL http://adsabs.harvard.edu/abs/2005AN....326..787B.

Dziembowski, W. (1982), Nonlinear mode coupling in oscillating stars. I. – Second order theory of the coherent mode coupling, *Acta Astronom.*, **32**, pp. 147–171, URL http://adsabs.harvard.edu/abs/1982AcA....32..147D.

Goldreich, P., Goodman, J. and Narayan, R. (1986), The stability of accretion tori. I. – Long-wavelength modes of slender tori, *Monthly Notices Roy. Astronom. Soc.*, **221**, pp. 339–364, URL http://adsabs.harvard.edu/abs/1986MNRAS.221..339G.

Goodman, J., Narayan, R. and Goldreich, P. (1987), The stability of accretion tori. II. – Non-linear evolution to discrete planets, *Monthly Notices Roy. Astronom. Soc.*, **225**, pp. 695–711, URL http://adsabs.harvard.edu/abs/1987MNRAS.225..695G.

Kluźniak, W. (2005), High frequency QPOs, nonlinear oscillations in strong gravity, *Astronom. Nachr.*, **326**, pp. 820–823, arXiv: astro-ph/0510725, URL http://adsabs.harvard.edu/abs/2005AN....326..820K.

Kluzniak, W. and Abramowicz, M. A. (2002), Parametric epicyclic resonance in black hole disks: QPOs in micro-quasars, *ArXiv Astrophysics e-prints*, arXiv: astro-ph/0203314, URL http://adsabs.harvard.edu/abs/2002astro.ph..3314K.

Lee, W. H., Abramowicz, M. A. and Kluźniak, W. (2004), Resonance in Forced Oscillations of an Accretion Disk and Kilohertz Quasi-periodic Oscillations, arXiv: astro-ph/0402084, URL http://adsabs.harvard.edu/abs/2004ApJ...603L..93L.

Linares, M., van der Klis, M., Altamiro, D. and Markwardt, C. B. (2005), Discovery of Kilohertz Quasi-periodic Oscillations and Shifted Frequency Correlations in the Accreting Millisecond Pulsar XTE J1807−294, *Astrophys. J.*, **634**(2), pp. 1250–1260, arXiv: astro-ph/0509011, URL http://adsabs.harvard.edu/abs/2005ApJ...634.1250L.

Moskalik, P. (1985), Modulation of amplitudes in oscillating stars due to resonant mode coupling, *Acta Astronom.*, **35**, pp. 229–254, URL http://adsabs.harvard.edu/abs/1985AcA....35..229M.

Nowakowski, R. M. (2005), Multimode Resonant Coupling in Pulsating Stars, *Acta Astronom.*, **55**, pp. 1–41, arXiv: astro-ph/0501510, URL http://adsabs.harvard.edu/abs/2005AcA...55....1N.

Paczyński, B. and Wiita, P. J. (1980), Thick accretion disks and supercritical luminosities, *Astronomy and Astrophysics*, **88**(1–2), pp. 23–31, URL http://adsabs.harvard.edu/abs/1980A\%26A...88...23P.

Schenk, A. K., Arras, P., Flanagan, É. É., Teukolsky, S. A. and Wasserman, I. (2002), Nonlinear mode coupling in rotating stars and the r-mode instability in neutron stars, *Phys. Rev. D*, **65**(2), p. 024001, arXiv: gr-qc/0101092, URL http://adsabs.harvard.edu/abs/2002PhRvD..65b4001S.

Vio, R., Rebusco, P., Andreani, P., Madsen, H. and Overgaard, R. V. (2006), Stochastic modeling of kHz quasi-periodic oscillation light curves, *Astronomy and Astrophysics*, **452**, pp. 383–386, URL http://adsabs.harvard.edu/abs/2006A\%26A...452..383V.

Wersinger, J.-M., Finn, J. M. and Ott, E. (1980), Bifurcation and "strange" behavior in instability saturation by nonlinear three-wave mode coupling, *Phys. Fluids*, **23**, pp. 1142–1154, URL http://adsabs.harvard.edu/abs/1980PhFl...23.1142W.

Wijnands, R., van der Klis, M., Homan, J., Chakrabarty, D., Markwardt, C. B. and Morgan, E. H. (2003), Quasi-periodic X-ray brightness fluctuations in an accreting millisecond pulsar, *Nature*, **424**, pp. 44–47, arXiv: astro-ph/0307123, URL http://adsabs.harvard.edu/abs/2003Natur.424...44W.

Proceedings of *RAGtime 8/9, 15–19/19–21 September, 2006/2007, Hradec nad Moravicí, Opava, Czech Republic*
S. Hledík and Z. Stuchlík, editors, Silesian University in Opava, 2007, pp. 89–97

Relativistic gyratons

Hedvika Kadlecová

Institute of Theoretical Physics, Faculty of Mathematics and Physics, Charles University in Prague,
V Holešovičkách 2, CZ-180 00 Praha 8 – Holešovice, Czech Republic
Hedvika.Kadlecova@centrum.cz

ABSTRACT
We investigate the non-vacuum gyraton metric in 4-dimensional spacetime. We show that it belongs to the Kundt class of spacetimes (generalized pp-waves). We demostrate that the gyraton metric belongs also to the VSI spacetimes which are special subclasses of the Kundt class of spacetimes. Thanks to that fact we have showed that algebraical type of the gyraton metric in flat spacetime and those metrics which are conformally related to them is III or more special.

Keywords: Kundt's class – curvature invariants – generalized pp-waves – spin coefficients – gyratons

1 INTRODUCTION

The history of studies of gravitational fields of beams and pulses of light is quite long. Tolman (1934) obtained solutions for the gravitational field of beams of radiation and pulses of light in the linear approximation. The exact solutions of the non-linear Einstein equations were found by Peres (1959, 1960) and Bonnor (1969). These solutions belong to the pp-wave class and reduce to Aichelburg–Sexl metric (Aichelburg and Sexl, 1971) when we consider the infinitely small cross-section of the beam and the delta-type distribution of the light-pulse in time. Furthermore, Bonnor (1970) generalized these 4-dimensional solutions to the case the matter of beam (null fluid) is charged or spinning.

Recently, Frolov and Fursaev (2005) and Frolov et al. (2005) found higher dimensional generalization of previous solutions to the case where the beam of radiation carries angular momentum. The solution describes a pulsed beam of radiation with negligible radius of cross-section, finite duration in time and with finite both energy E and angular momentum J. The ultra-relativistic source with these characteristics is called a *gyraton*.

Typical example of a gyraton is a pulse of circular polarized light or a modulated beam of ultrarelativistic particles with spin. The gravitational field of the gyraton is determined by a number of arbitrary functions of the retarded time u. They describe profiles of the energy density and angular momenta distributions of the gyraton. The gyratons propagating in asymptotically flat D-dimensional spacetime were published in Frolov and Fursaev (2005); Frolov et al. (2005). In these papers, it was shown that gyratons propagating in flat spacetime have two very important features. First, the gyraton metric belongs to a class

978-80-7248-419-5

of metrics for which all scalar invariants constructed from the curvature and its covariant derivatives vanish identically in any dimension (Frolov et al., 2005). The second property is that the Einstein–Maxwell field equations in D-dimensional spacetime reduce to a set of linear equations in the Euclidean $(D-2)$-dimensional space.

Generalized gyraton solutions containing electric charge were presented in Frolov and Zelnikov (2006). Also a generalization of electrically charged gyratons to the theory of supergravity was found in Frolov and Feng-Li (2006).

The results were also generalized to the asymptotically AdS spacetime (Frolov and Zelnikov, 2005). Here they obtained exact solutions for the gyraton propagating in an asymptotically AdS background. The gyratons in AdS are perturbatively exact in string theory.

There were also found supersymmetric gyraton solutions in minimal gauged theory in five dimensions in Caldarelli et al. (2007).

Nowadays, the gravitational field generated by gyratons is important for studies of mini-black hole production in colliders (the Large Hadron Collider in CERN) or for cosmic ray experiments. The mini-black hole formation in high energy particle collisions is an important issue of TeV gravity scenarios. in Yoshino et al. (2007) head-on collisions of two gyratons and black hole formations are studied in these processes.

In this paper, we review and further investigate the four dimensional gyraton metric in flat spacetime. In Section 2 we review some important features about the Kundt class (Stephani et al., 2003; Pravda et al., 2002). In Section 3 basic theory about the gyratons in flat 4-dimensional spacetimes is mentioned. In Section 4 we apply the theory of the Kundt class spacetimes to the gyratons from Section 3 and we demonstrate that the gyraton metric belong to the VSI spacetimes.

2 THEORY AROUND KUNDT'S CLASS

The Kundt class of spacetimes has shear-free, non-expanding, non-twisting geodesics null congruence. We will review shortly the Kundt class as in Stephani et al. (2003), for more see also (Kundt, 1961). The non-twisting null vector field may be chosen to be a gradient field, and coordinates u and v are then naturally introduced by

$$\boldsymbol{e}_4 = k^i \partial_i = \partial_v \,, \quad \boldsymbol{\omega}^3 = -k_i \,\mathrm{d}x^i = \mathrm{d}u \,. \tag{1}$$

As coordinates in the null hypersurfaces $u = \text{const}$ we use the affine parameter v and two spacelike coordinates x^1, x^2. With this choice, the line element has the form

$$\mathrm{d}s^2 = g_{AB}\,\mathrm{d}x^A \mathrm{d}x^B - 2\,\mathrm{d}u\,(\mathrm{d}v + m_A\,\mathrm{d}x^A + H\,\mathrm{d}u)\,, \quad A, B = 1, 2\,. \tag{2}$$

The functions in the metric $g_{AB}(u, x^1, x^2, v)$, $m_A(u, x^1, x^2, v)$ and $H(u, x^1, x^2, v)$ are real. The spin coefficients ρ and σ are then

$$\begin{aligned} \rho &= -k_{a;b}\, m^a \overline{m}^b = -\tfrac{1}{2} g_{ab,v}\, m^a \overline{m}^b = -\tfrac{1}{2} g_{AB,v}\, m^A \overline{m}^B \,, \\ \sigma &= -k_{a;b}\, m^a m^b = -\tfrac{1}{2} g_{ab,v}\, m^a m^b = -\tfrac{1}{2} g_{AB,v}\, m^A m^B \,, \\ \kappa &= -k_{a;b}\, m^a k^b \,. \end{aligned} \tag{3}$$

Hence

$$\rho = \sigma = 0 \tag{4}$$

leads to $g_{AB,v} = 0$. And it can be calculated directly that

$$\kappa = 0\,. \tag{5}$$

Performing a coordinate transformation $x^{A'} = x^{A'}(x^B, u)$, and with complex coordinates

$$\zeta = \frac{1}{\sqrt{2}}\left(x^1 + \mathrm{i}x^2\right)\,, \quad \bar{\zeta} = \frac{1}{\sqrt{2}}\left(x^1 - \mathrm{i}x^2\right)\,, \tag{6}$$

the line element (2) can be written in the form

$$\mathrm{d}s^2 = 2P^{-2}\,\mathrm{d}\zeta\mathrm{d}\bar{\zeta} - 2\,\mathrm{d}u\,(\mathrm{d}v + W\,\mathrm{d}\zeta + \overline{W}\,\mathrm{d}\bar{\zeta} + H\,\mathrm{d}u)\,, \tag{7}$$

and

$$P(u, \zeta, \bar{\zeta})_{,v} = 0\,. \tag{8}$$

It could be written equivalently as

$$\mathrm{d}s^2 = 2\boldsymbol{\omega}^1\boldsymbol{\omega}^2 - 2\boldsymbol{\omega}^3\boldsymbol{\omega}^4\,, \tag{9}$$

where the tetrad components are

$$\boldsymbol{\omega}^1 = \frac{\mathrm{d}\zeta}{P}\,, \quad \boldsymbol{\omega}^2 = \frac{\mathrm{d}\bar{\zeta}}{P}\,, \quad \boldsymbol{\omega}^3 = \mathrm{d}u\,, \quad \boldsymbol{\omega}^4 = \mathrm{d}v + W\,\mathrm{d}\zeta + \overline{W}\,\mathrm{d}\bar{\zeta} + H\,\mathrm{d}u\,, \tag{10}$$

where the functions $P(u, \zeta, \bar{\zeta})$ and $H(u, \zeta, \bar{\zeta}, v)$ are real. The function $W(u, \zeta, \bar{\zeta}, v)$ is complex.

It is useful to perform a null rotation with respect to k and use the rotated tetrad instead of (10). The basis of one-forms is

$$\boldsymbol{\omega}^1 = \frac{\mathrm{d}\zeta}{P} - P\overline{W}\,\mathrm{d}u\,,\ \boldsymbol{\omega}^2 = \frac{\mathrm{d}\bar{\zeta}}{P} - PW\,\mathrm{d}u\,,\ \boldsymbol{\omega}^3 = \mathrm{d}u\,,\ \boldsymbol{\omega}^4 = \mathrm{d}v + (H + P^2W\overline{W})\,\mathrm{d}u\,, \tag{11}$$

and corresponding tetrad vectors

$$\boldsymbol{e}_1 = P\partial_\zeta\,,\ \boldsymbol{e}_2 = P\partial_{\bar{\zeta}}\,,\ \boldsymbol{e}_3 = \partial_u + P^2(\overline{W}\partial_\zeta + W\partial_{\bar{\zeta}}) - (H + P^2W\,\overline{W})\partial_v\,,\ \boldsymbol{e}_4 = \partial_v\,. \tag{12}$$

The rotated tetrad (11) and (12) are useful in calculating the Riemann tensor in the Newman–Penrose formalism.

The coordinate transformations preserving the form (7) of the metric and the associated transformations of metric functions P, H and W are

(i) $$\zeta' = f(\zeta, u)\,, \quad P'^2 = P^2 f_{,\zeta}\bar{f}_{,\bar{\zeta}}\,, \quad W' = W/f_{,\zeta} + \bar{f}_u/P^2 f_{,\zeta}\bar{f}_{,\bar{\zeta}}\,, \tag{13}$$
$$H' = H - \left(f_{,u}\bar{f}_{,u}/P^2 + Wf_{,u}\bar{f}_{,\bar{\zeta}} + \overline{W}\,\bar{\zeta}_{,u}f_{,\zeta}\right)/(f_{,\zeta}\bar{f}_{,\bar{\zeta}})\,,$$

(ii) $$v' = v + g(\zeta, \bar{\zeta}, u)\,, \quad P' = P\,, \quad W' = W - g_{,\zeta}\,, \quad H' = H - g_{,u}\,, \tag{14}$$

(iii) $$u' = h(u)\,, \quad v' = v/h_{,u}\,, \tag{15}$$
$$P' = P\,, \quad W' = W/h_{,u}\,, \quad H' = (H + vh_{,uu}/h_{,u})/(h_{,u})^2\,.$$

Let us mention some further properties of the Kundt class. If $(\ln P)_{\zeta\bar{\zeta}} = 0$, then it is always possible to transform P to

$$P = 1\,. \tag{16}$$

The condition

$$W_{,v} = 0 \tag{17}$$

is invariant under the transformations (13), (14) and (15), and so characterizes a special subclass of metrics. The 2-surfaces $u, v = \text{const}$ with metric $2\,\mathrm{d}\zeta\mathrm{d}\bar{\zeta}/P^2$ are called *wave surfaces*. The tetrad vector fields $\boldsymbol{e}_1 = P\partial_\zeta$ and $\boldsymbol{e}_1 = P\partial_{\bar{\zeta}}$ are surface-forming, i.e., their commutator is a linear combination of themselves. They are tangent to the wave surfaces, whereas the vector fields $\boldsymbol{e}_1 = P(\partial_\zeta - W\partial_v)$ and $\boldsymbol{e}_2 = P(\partial_{\bar{\zeta}} - \overline{W}\partial_v)$ associated with the basis (10) are *not*.

The existence of (spacelike) 2-surfaces orthogonal to $\boldsymbol{k}$ implies $\omega = 0$. The spacetime geometry uniquely determines the null congruence $\boldsymbol{k}$ and the wave surfaces. The Gaussian curvature

$$K = 2P^2(\ln P)_{,\zeta\bar{\zeta}} \tag{18}$$

of the wave surfaces is a spacetime invariant.

In the next paragraph, we will mention a few words about spacetimes with vanishing curvature invariants (VSI). The VSI spacetimes represent an important subclass of spacetimes in the Kundt class of spacetimes. It was proved in Pravda et al. (2002) that all Lorentzian spacetimes for which all curvature invariants of all orders are zero satisfy the next theorem:

Theorem 1 *All curvature invariants of all orders vanish if and only if the following two conditions are satisfied:*

(A) The spacetime possesses a non-diverging shear-free geodesics null congruence.
(B) Relative to the above null congruence, all curvature scalars with non-negative boost weight vanish.

The analytic form of condition (A), expressed relative to any spin basis where $\boldsymbol{k}$ is aligned with the null congruence in question, is simply

$$\kappa = \rho = \sigma = 0 \tag{19}$$

and the analytic form of condition (B) is

$$\Psi_0 = \Psi_1 = \Psi_2 = 0\,, \tag{20}$$
$$\Phi_{00} = \Phi_{01} = \Phi_{02} = \Phi_{11} = 0\,, \tag{21}$$
$$\Lambda_{\mathrm{NP}} = 0\,. \tag{22}$$

Previous equations are expressed in terms of quantities used in the Newman–Penrose formalism. Spacetimes that satisfy condition (A) belong to Kundt's class (Stephani et al.,

2003). Condition (B) implies that the spacetime is of Petrov type III, N or O (see Eq. (20)) with the Ricci tensor restricted by (21) and (22). We note here that $\Lambda_{\rm NP}$ is Ricci scalar up to a constant factor. Non-vacuum spacetimes with a covariantly constant null vector are often referred to as generalized pp-wave.

3 THE RELATIVISTIC GYRATON IN FLAT 4D SPACETIME

The gyraton metric in 4-dimensional spacetime has a form

$$\mathrm{d}s^2 = -2\,\mathrm{d}u\mathrm{d}v + \mathrm{d}z^2 + \mathrm{d}x^2 + \Phi(u,x,z)\,\mathrm{d}u^2 + 2[A_z(u,x,z)\,\mathrm{d}z + A_x(u,x,z)\,\mathrm{d}x]\,\mathrm{d}u\,. \quad (23)$$

The functions Φ (gravitoelectric potential) and A_a (gravitomagnetic potential) can be considered as a scalar and a vector field in the 2-dimensional Euclidean space with Cartesian coordinates x, z. The functions do not depend on v. The metric (23) reduces to Minkowski metric for $A = \Phi = 0$.

The null Killing vector is $\boldsymbol{k} = k^\mu \partial_\mu = \partial_v$. Instead of u, v we also use coordinates t, ξ given by $u = (t - y)/\sqrt{2}$, $v = (t + y)/\sqrt{2}$. The metric (23) describes an object moving with the velocity of light in the ξ direction. The coordinates x and z are coordinates of an 2-dimensional space which is transverse to the direction of motion.

We introduce the antisymmetric tensor in the 2-transversal plane with the only independent component

$$F_{zx} = \partial_z A_x - \partial_x A_z\,. \quad (24)$$

It can be shown that the null Killing vector $\boldsymbol{k}$ is covariantly constant, i.e.,

$$k_{\mu;\nu} = 0\,. \quad (25)$$

It means that the spacetime admit a covariantly constant null vector field.

The Einstein equations reduce to two sets of equations in 2-dimensional flat space (Frolov et al., 2005)

$$F_{ab}{}^{:b} = J_a\,, \quad (26)$$

$$\Phi^{:a}_{:a} = -J + \tfrac{1}{2} F_{ab}F^{ab} + 2\partial_u(A^{:a}_{a})\,, \quad (27)$$

where $J_a = \kappa T_{ua}$, $J = \kappa T_{uu}$. Here $()_{:a}$ denotes the covariant derivative with respect to the flat metric in the transverse space, the indices a, b could be x and z. The first set of equations (26) formally coincides with the Euclidean Maxwell equations in 2 dimensions where J_a plays the role of the current. We need to find the static magnetic potential A_a created by the gyraton source. The second equation (27) is similar to the equation for the electric potential Φ with the important difference that in addition to the charge distribution J it contains an extra source proportional to $F_{ab}F^{ab}$. We obtain vacuum solution when we set $J = J_a = 0$. It describes a solution outside the source of gyraton.

4 RESULTS

In this section, we will show that the gyraton metric in flat spacetime belongs to the subclass of the Kundt class of spacetimes. Then we will calculate spin coefficients, the Ricci scalars and the Weyl scalars to demonstrate that the gyraton metric belong also to the VSI spacetimes. Furthermore, we will determine the algebraical type of that metric.

First, we compare the gyraton metric (23) with the general Kundt metric (2). We observe that they can be compared and the functions could be identified as

$$g_{11} = g_{22} = 1\,,\ g_{12} = g_{21} = 0\,,\ m_1 = -A_x\,,\ m_2 = -A_z\,,\ H = -\Phi/2,\ P = 1\,. \tag{28}$$

We choose $x^1 = x, x^2 = z$, then the complex coordinates read

$$\zeta = \frac{1}{\sqrt{2}}(x + \mathrm{i}z)\,, \quad \bar{\zeta} = \frac{1}{\sqrt{2}}(x - \mathrm{i}z)\,, \tag{29}$$

and the inverse transformation

$$x = \frac{1}{\sqrt{2}}(\bar{\zeta} + \zeta)\,, \quad z = \frac{\mathrm{i}}{\sqrt{2}}(\bar{\zeta} - \zeta)\,. \tag{30}$$

The gyraton metric can be rewritten in complex coordinates by (30) to the Kundt form (7)

$$\mathrm{d}s^2 = 2\,\mathrm{d}\zeta\,\mathrm{d}\bar{\zeta} - 2\,\mathrm{d}u\,(\mathrm{d}v + W\,\mathrm{d}\zeta + \overline{W}\,\mathrm{d}\bar{\zeta} + H\,\mathrm{d}u)\,, \tag{31}$$

where

$$\begin{aligned} W &= \frac{1}{\sqrt{2}}(m_1 - \mathrm{i}m_2) = -\frac{1}{\sqrt{2}}\left(\widetilde{A}_x - \mathrm{i}\widetilde{A}_z\right)\,, \\ \overline{W} &= \frac{1}{\sqrt{2}}(m_1 + \mathrm{i}m_2) = -\frac{1}{\sqrt{2}}\left(\widetilde{A}_x + \mathrm{i}\widetilde{A}_z\right)\,, \\ H &= -\tfrac{1}{2}\widetilde{\Phi}\,, \quad P = 1\,, \end{aligned} \tag{32}$$

and we observe that condition (8) for P is trivially satisfied. We have denoted the functions $\widetilde{A}_a(u,\zeta,\bar{\zeta}) = A_a(u,x,z)$ and $\widetilde{\Phi}(u,\zeta,\bar{\zeta}) = \Phi(u,x,z)$. In the following we use mainly the coordinates (v,x,z,u) and we evaluate everything in them. We substitute the transformation (32) into the rotated tetrad (11), (12). The basis of one-forms are

$$\begin{aligned} &\boldsymbol{\omega}^1 = \frac{1}{\sqrt{2}}\left[\mathrm{d}x + \mathrm{i}\,\mathrm{d}z - (A_x + \mathrm{i}A_z)\,\mathrm{d}u\right],\ \boldsymbol{\omega}^2 = \frac{1}{\sqrt{2}}\left[\mathrm{d}x - \mathrm{i}\,\mathrm{d}z - (A_x - \mathrm{i}A_z)\,\mathrm{d}u\right], \\ &\boldsymbol{\omega}^3 = \mathrm{d}u\,, \quad \boldsymbol{\omega}^4 = \mathrm{d}v - \tfrac{1}{2}\left(\Phi - A_x^2 - A_z^2\right)\mathrm{d}u\,, \end{aligned} \tag{33}$$

and corresponding tetrad vectors

$$\begin{aligned} &\boldsymbol{e}_1 = \frac{1}{\sqrt{2}}(\partial_x + \mathrm{i}\partial_z)\,, \quad \boldsymbol{e}_2 = \frac{1}{\sqrt{2}}(\partial_x - \mathrm{i}\partial_z)\,, \\ &\boldsymbol{e}_3 = \partial_u - (A_x\partial_x + A_z\partial_z) + \tfrac{1}{2}\left(\Phi - A_x^2 - A_z^2\right)\partial_v\,, \quad \boldsymbol{e}_4 = \partial_v\,. \end{aligned} \tag{34}$$

We will discuss the transformations preserving the form of the metric (31). The transformation (13) can not be used, because $P = 1$. The transformation (14) reads:

$$v' = v + \widetilde{g}(z, x, u)\,, \quad P' = P = 1\,, \quad A'_a = A_a + \widetilde{g}_{,a}\,, \quad \Phi' = \Phi + 2\widetilde{g}_{,u}\,, \tag{35}$$

where $\widetilde{g}(z, x, u) = g(\zeta, \bar{\zeta}, u)$. Then in the transformation (15) we choose the function $h(u)$ to be linear function of u, $h(u) = bu$; $b \neq 0$:

$$u' = bu\,, \quad v' = v/b\,, \quad P' = P = 1\,, \quad A'_a = A_a/b\,, \quad \Phi' = \Phi/b^2\,, \tag{36}$$

which is in agreement with (Frolov et al., 2005).

The 2-surfaces $u, v = \text{const}$ with the metric $\mathrm{d}x^2 + \mathrm{d}z^2$ are called *wave surfaces*. The vector fields $\boldsymbol{e}_1$, $\boldsymbol{e}_2$ are surface-forming. The Gaussian curvature (18) is $K = 0$ since $P = 1$ here. The functions in the gyraton metric (28) does not depend on coordinate v, so the condition (17) characterizes a special subclass of metrics. These non-vacuum gyraton solutions in flat spacetime with covariantly constant null field (25) are often called generalized pp-waves. The vacuum gyraton solutions in flat spacetime could be transformed to the standard pp-wave solutions in 4D. We can get vacuum pp-wave metric by deleting A-terms in the gyraton metric by transformation (35).

Now, we derive spin coefficients, Ricci scalars and Weyl scalars with respect to the tetrad (33), (34). The spin coefficients are

$$\begin{aligned}
&\kappa = \sigma = \rho = \tau = \pi = \epsilon = \alpha = \beta = 0\,,\\
&\lambda = \tfrac{1}{2}[(\partial_x + \mathrm{i}\partial_z)A_x - (\partial_z - \mathrm{i}\partial_x)A_z]\,,\\
&\nu = \frac{1}{2\sqrt{2}}\,[(\partial_x + \mathrm{i}\partial_z)\Phi - A_x(\partial_x + \mathrm{i}\partial_z)A_x - A_z(\partial_x + \mathrm{i}\partial_z)A_z]\,,\\
&\mu = \tfrac{1}{2}(\partial_x A_x + \partial_z A_z)\,,\\
&\gamma = \tfrac{1}{4}\mathrm{i}F_{zx}\,,
\end{aligned} \tag{37}$$

and the Ricci scalars are:

$$\begin{aligned}
&\Phi_{00} = \Phi_{01} = \Phi_{02} = \Phi_{11} = 0\,,\\
&\Phi_{12} = -\frac{1}{4\sqrt{2}}\,(\partial_z + i\,\partial_x)F_{zx}\,,\\
&\Phi_{22} = \frac{1}{4}\left[F_{zx}^2 - \left(\partial_z^2 + \partial_x^2\right)\Phi + 2\partial_u\,(\partial_x A_x + \partial_z A_z) - 2\,(A_z\partial_x - A_x\partial_z)\,F_{zx}\right].
\end{aligned} \tag{38}$$

The Weyl scalars are

$$\begin{aligned}
\Psi_0 =&\Psi_1 = \Psi_2 = 0\,,\\
\Psi_3 =&\frac{1}{4\sqrt{2}}(\partial_z - \mathrm{i}\partial_x)F_{zx}\,,\\
\Psi_4 =&\tfrac{1}{4}(\partial_z - \mathrm{i}\partial_x)^2\Phi - \tfrac{1}{2}A_x(\partial_z - \mathrm{i}\partial_x)F_{zx}\\
&- \tfrac{1}{2}A_z(\partial_x + \mathrm{i}\partial_z)F_{zx} - \tfrac{1}{2}\partial_u(\partial_z - \mathrm{i}\partial_x)A_x + \tfrac{1}{2}\partial_u(\partial_x + \mathrm{i}\partial_z)A_x\,,\\
\Lambda_{\mathrm{NP}} =&\tfrac{1}{24}R = 0\,.
\end{aligned} \tag{39}$$

We compare our results (37), (38) and (39) with the Theorem 1, the analytical equivalents of conditions (A) and (B), cf. (19), (21), (20) and (22) are satisfied. Therefore the metric (23) belongs to the VSI spacetimes. It is valid in any dimension (Frolov et al. 2005, for more information about VSI class of spacetimes see, e.g., Pravda et al. 2002 in 4D and Coley et al. 2004 in higher dimensions). Furthermore, the condition (B) of the Theorem 1 determine the algebraical type of gyraton metric. Their type is III or more special.

Let us recall that the Weyl tensor is invariant under the conformal transformations. It means that the Weyl tensors for gyraton metric in flat and in conformally related spacetime are the same. Then we have determined algebraical type for the gyraton in four dimensional flat spacetime and for any conformally related metrics. An example of such a conformally related metric in the gyraton metric in AdS (Frolov and Zelnikov, 2005). An important subfamily of the gyraton metric in AdS was first described in Siklos (1985) and also studied in Podolský (1998).

To conclude this section, we have shown that the non-vacuum gyraton metric in flat 4D spacetime belongs to the Kundt class of spacetimes and also to its VSI subclass. Particularly, it belongs to the generalized pp-waves. We have applied the theory of the Kundt spacetimes on the gyraton metric. Moreover, we have determined the algebraical type of the gyraton metric in flat spacetime and those metrics which are conformally related to them.

5 CONCLUSIONS

We have shown that the non-vacuum gyraton metric (23) in 4-dimensional spacetime belongs to the Kundt class of spacetimes, specifically, to their subclass-generalized pp-wave spacetimes. The metric (23) could be rewritten to the standard Kundt form of metric (7) by the complex transformation (30). We have calculated spin coefficients, Ricci scalars and Weyl scalars and thanks to the Theorem 1 in the Section 2 we have demonstrated that the gyraton metric belongs to the VSI spacetimes which are special subclasses of the Kundt class of spacetimes. Thanks to that fact we have showed the algebraical type of the gyraton metric in flat spacetime and those metrics which are conformally related to them is III or more special.

In the future work, we want to investigate the higher dimensional Kundt class of spacetimes and to study other conformally related spacetimes to the gyratons in flat spacetimes and find their higher dimensional generalization. The very interesting assignment is to find a connection between the gyratons in AdS and the AdS/CFT correspondence.

ACKNOWLEDGEMENTS

The work was supported by the Czech Science Foundation under grant 205/03/H144.

REFERENCES

Aichelburg, P. C. and Sexl, R. U. (1971), On the Gravitational Field of a Massless particle, *Gen. Relativity Gravitation*, **2**, p. 303.

Bonnor, W. B. (1969), The gravitational field of light, *Comm. Math. Phys.*, **13**, p. 163.

Bonnor, W. B. (1970), Charge moving with the speed of light in Einstein-Maxwell theory, *Internat. J. Theoret. Phys.*, **3**, p. 57.

Caldarelli, M. M., Klemm, D. and Zorzan, E. (2007), Supersymmetric gyratons in five dimensions, *Classical Quantum Gravity*, **24**, pp. 1341–1357.

Coley, A., Milson, R., Pravda, V. and Pravdová, A. (2004), Vanishing scalar invariant spacetimes in higher dimensions, *Classical Quantum Gravity*, **21**, pp. 5519–5542.

Frolov, V. P. and Feng-Li, L. (2006), String gyratons in supergravity, *Phys. Rev. D*, **73**, p. 104028.

Frolov, V. P. and Fursaev, D. V. (2005), Gravitational field of a spinning radiation beam-pulse in higher dimensions, *Phys. Rev. D*, **71**, p. 104034.

Frolov, V. P., Israel, W. and Zelnikov, A. (2005), Gravitational field of relativistic gyratons, *Phys. Rev. D*, **72**, p. 084031.

Frolov, V. P. and Zelnikov, A. (2005), Relativistic gyratons in asymptotically AdS spacetime, *Phys. Rev. D*, **72**, p. 104005.

Frolov, V. P. and Zelnikov, A. (2006), Gravitational field of charged gyratons, *Classical Quantum Gravity*, **23**, p. 2119.

Kundt, W. (1961), The Plane-fronted Gravitatational Waves, *Zeischrifft für Physik*, **163**, pp. 77–86.

Peres, A. (1959), Some Gravitational Waves, *Phys. Rev. Lett.*, **3**, p. 571.

Peres, A. (1960), *Phys. Rev. D*, **118**, p. 1105.

Podolský, J. (1998), Interpretation of the Siklos solutions as exact gravitational waves in the anti-de Sitter universe, *Classical Quantum Gravity*, **15**, p. 719.

Pravda, V., Pravdová, A., Coley, A. and Milson, R. (2002), All spacetimes with vanishing curvature invariants, *Classical Quantum Gravity*, **19**, pp. 6213–6236.

Siklos, S. T. C. (1985), *Galaxies, Axisymmetric Systems and Relativity*, Cambridge University Press, Cambridge.

Stephani, H., Kramer, D., Maccallum, M., Hoenselaers and Herlt, E. (2003), *Exact Solutions to Einstein's Field Equations*, Cambridge University Press, Cambridge.

Tolman, R. C. (1934), *Relativity, Thermodynamics, and Cosmology*, Clarendon Press, Oxford.

Yoshino, H., Zelnikov, A. and Frolov, V. (2007), Apparent horizon formation in the head-on collision of gyratons, *Phys. Rev. D*, **74**, p. 044003, arXiv: `gr-qc/0703127`.

Proceedings of *RAGtime 8/9, 15–19/19–21 September, 2006/2007, Hradec nad Moravicí, Opava, Czech Republic*
S. Hledík and Z. Stuchlík, editors, Silesian University in Opava, 2007, pp. 99–108

Flares from spiral waves by lensing and time-delay amplification?

Vladimír Karas[1], Michal Dovčiak[1], Andreas Eckart[2,3] and Leonhard Meyer[2]

[1]Astronomical Institute, Czech Academy of Sciences, Boční II 1401/1a, CZ-141 31 Praha 4, Czech Republic
[2]I. Physikalisches Institut, Universität zu Köln, Zülpicher Str. 77, D-50937 Köln, Germany
[3]Max-Planck-Institut für Radioastronomie, Auf dem Hügel 69, D-53121 Bonn, Germany

ABSTRACT

Episodically accreting black holes are thought to produce flares when a chunk of particles is accelerated to high velocity near the black hole horizon. This also seems to be the case of Sagittarius A* in the Galactic Center, where the broad-band radiation is produced, likely via the synchrotron self-Compton mechanism. It has been proposed that strong-field gravitational lensing magnifies the flares. The effect of lensing is generally weak and requires a fine-tuned geometrical arrangement, which occurs with only a low probability. However, there are several aspects that make Sagittarius A* a promising target to reveal strong gravity effects. Unlike type II (obscured) active galaxies, chances are that a flare is detected at high inclination, which would be favourable for lensing. Time delays can then significantly influence the observed flare duration and the form of light-curve profiles.

Here we discuss an idea that the impact of lensing amplification should be considerably enhanced when the shape of the flaring clump is appropriately elongated in the form of a spiral wave or a narrow filament, rather than a simple (circular) spot which we employed previously within the phenomenological "orbiting spot model." By parameterizing the emission region in terms of the spiral shape and contrast, we are able to extend the spot model to more complicated sources. In the case of spirals, we notice a possibility that more photons reach a distant observer at the same moment because of interplay between lensing and light-travel time. The effect is not symmetrical with respect to leading versus trailing spirals, so in principle the source geometry can be constrained. In spite of this, the spot model seems to provide entirely adequate framework to study the currently available data.

Keywords: Black holes – Galactic center (Sgr A*) – accretion – gravitational lensing

1 INTRODUCTION

Temporal changes of the radiation flux are frequently reported in active galactic nuclei (AGN) as well as Galactic black-hole candidates, i.e., two categories of objects that contain accreting black holes (for reviews of AGN variability, see, e.g., McHardy and Czerny, 1987;

978-80-7248-419-5

Lawrence and Papadakis, 1993; Done, 2002; Gaskell and Klimek, 2003; Vaughan et al., 2005). Especially X-rays vary a lot and on short time-scales. Variability time-scales extend down to the shortest resolvable intervals and seem to scale with the black hole mass (Mirabel and Rodríguez, 1998; Papadakis, 2004; Done and Gierliński, 2005). Persisting fluctuations are occasionally dominated by more substantial increases of the radiation flux. These events have been dubbed "flares" and often attributed to instabilities/shocks operating in black-hole accretion flows (Haardt et al., 1994; Poutanen and Fabian, 1999; Życki, 2002; Czerny et al., 2004; Goosmann et al., 2006). One can expect that fast bulk (orbital) motion and lensing play a role in amplification of the flaring signal.

In the dynamical center of our Galaxy, a peculiar radio source, Sagittarius A* (Sgr A*), is located (e.g., Eckart et al., 2005). It is very compact and presumably contains a supermassive black hole. Given a relatively small distance ($D \simeq 8\,\mathrm{kpc}$) and a large mass of the black hole ($M_\bullet \simeq 3\text{–}4 \times 10^6\,\mathrm{M}_\odot$), a silhouette of Sgr A* should draw a circle of diameter $\simeq 10.4\, r_\mathrm{g}/D \simeq 42\,\mu$arcsec on the sky. Furthermore, a gaseous torus is not detected in Sgr A*, and so the central region can be viewed at high inclination, something which is quite impossible in obscured AGN.

In spite of a very low level of its activity, flares of duration $\simeq t_\mathrm{K}(r_\mathrm{ms})$ have been reported also from the Galactic Center (Baganoff et al., 2001; Genzel et al., 2003; Marrone et al., 2006; Bélanger et al., 2005, 2006). Duration of short flares is comparable with Keplerian orbital period near the marginally stable orbit, $t_\mathrm{K}(r_\mathrm{ms})$, and it is not much longer than the light-crossing time across one gravitational radius: $t_\mathrm{c} \equiv r_\mathrm{g}/c$, $r_\mathrm{g} \equiv GM_\bullet/c^2 \approx 1.5 \times 10^{11}\, M_6\,\mathrm{cm}$, $M_6 \equiv M_\bullet/10^6\,\mathrm{M}_\odot$.

The flares occur about once per day from within a few milli-arcseconds of Sgr A* radio position. Because of short time-scales they cannot be explained in terms of viscous processes in the standard accretion disc with some appreciable accretion rate (as already mentioned, there is no evidence for a standard-type axially symmetric accretion regime); Sgr A* is accreting at a highly sub-Eddington rate. Nonetheless, recent millimeter, infrared and X-ray observations have confirmed these irregular outbursts lasting between $\simeq 20$ minutes and about 2 hours. They are probably generated by relativistic acceleration of electrons in the innermost region, where synchrotron radiation emerges followed by inverse Compton mechanism (Markoff et al., 2001; Yuan et al., 2003; Liu Siming et al., 2006). There are indications for 17–20 min quasi-periodicities to be present in light curves of some of these flares (Genzel et al., 2003; Eckart et al., 2004). The influences of relativistic lensing and Doppler effects have been considered in connection with Sgr A* since more than a decade ago (see, e.g., Hollywood and Melia, 1995; Melia et al., 2001). These effects are now of imminent interest because of growing amount of new data gathered in different wavebands.

The model of a bright spot orbiting near a black hole (Bao and Stuchlík, 1992; Cunningham and Bardeen, 1972, 1973; Karas et al., 1992) has been fairly successful in explaining the observed Sgr A* modulation (Broderick and Loeb, 2005, 2006; Meyer et al., 2006a,b; Noble et al., 2007). It has been argued that the flare lightcurves can be understood as a region of enhanced emission, a.k.a. "spot," that performs a co-rotational bulk motion near above the innermost stable orbit, $r = r_\mathrm{ms}$. The observed signal is modulated by relativistic effects. According to this idea, Doppler and gravitational lensing influence the observed radiation flux and this can be computed by ray-tracing methods (Dovčiak et al., 2004b,a).

The original idea and the interpretation of the "spot" origin have to be adapted to the conditions appropriate for Sgr A*. To this aim, the phenomenological model of the source is a way of parametrizing the intensification of the signal. This approach can be extended to more complicated geometry of the emission region, like standing shocks and spiral waves, which is what we discuss here. For example, spiral waves as an agent of light modulation have discussed and compared with the spot model by Varnière and Blackman (2005) in the context of quasi-periodic oscillations from accretion discs. On a more physical level it is still not possible to calculate the intrinsic emissivity from first principles, i.e., without enlarging the number of free parameters beyond and reasonable limit.

2 TIME DELAYS FROM SGR A* VICINITY

2.1 Model setup

It is quite likely that the geometrical shape of the flare emission region is deformed by shearing due to strong tidal fields of the black holes, magnetohydrodynamic instabilities operating in the plasma, as well as by the influence of stars passing nearby. Under such circumstances the emission area can be better described as a transient pattern extending in both radial and azimuthal directions. Relativistic effects from spiral waves and standing shocks have been previously invoked to explain spectral features from black-hole accretions discs (Karas et al., 2001; Hartnoll and Blackman, 2002; Machida and Matsumoto, 2003; Fukumura and Tsuruta, 2004). Although the Doppler boosting is visible even at a moderate value of the inclination angle, much stronger enhancement can occur via gravitational lensing, provided that a rather precise geometrical alignment with the caustic position is satisfied (e.g., Rauch and Blandford, 1994; Bozza et al., 2005).

It has been proposed that a kind of this instability could play a role in forming Sgr A* flares (Tagger et al., 1990; Tagger and Melia, 2006) and since then the idea of spiral perturbations has been greatly advanced (Falanga et al., 2007). Here we put forward a simple argument (based on Karas et al., 2001) that relativistic effects together with finite light travel time from different elements of the spiral source may add up together and enhance the observed flare signal from Sgr A*. For suitable spiral shapes, $r \equiv r(\phi)$, the enhancement can reach quite significant levels. Lightcurve profiles depend on observer inclination, $\theta_{\rm o}$, and the emission radius as the principal parameters, which in turn may depend on the black hole spin a through $r_{\rm ms}(a)$ dependency.

Let us assume that a perturbation of local emissivity structure develops on length-scales of $\simeq 10$–$20\,r_{\rm g}$ extending along a logarithmic spiral pattern $r \equiv r(\phi)$ (Karas et al., 2001). The spirals become active either by their intrinsic synchrotron emission and Compton upscattering or the illumination from a primary source. Although our model is a phenomenological one, such kind of spirals are expected to arise by several mechanisms in accretion discs: spiral waves represent large-scale structures (size comparable with the radius) that can be induced by non-axisymmetric instability mechanisms.[1] Also, a pattern resembling a

[1] Most of the attention towards gaseous spiral waves has been originally motivated by studies of cataclysmic variables. It has been recognized that the variation of the density profile and of the ionization structure of accretion

single-armed spiral is produced from an extended spot after its decay due to shearing (Karas et al., 1992) or it may be produced by debris in the wake of a tidally captured and disrupted satellite (e.g., Gomboc and Čadež, 2005).

One should emphasize that the physical conditions leading to the spiral-shaped source of X-rays must be very different from those envisaged by the orbiting spot model, although, on the phenomenological level the two models do not appear to be that much different (they can be treated by similar numerical schemes). The spot model has been built on the standard disc, which is illuminated by coronal flares; otherwise it remains almost intact. Spots are merely the reflection features that come into existence only by flares and they cease as soon as the irradiation is diminished. On the other hand, the existence of extended spirals probably requires that the base flow is non-axisymmetric and, hence, profoundly different from a standard disc – self-gravity, external forcing by another body, or MHD processes must be invoked to create the spirals and calculate their form. They light up themselves by the synchrotron mechanism.

2.2 Time-delay calculations and the signal enhancement

We calculated the light-travel time from the equatorial disc around a Kerr black hole to a distant observer. Apart from the central mass $M_\bullet$, the situation is characterized by parameters a (dimension-less black hole spin) and θ_o (inclination angle).[2] The complexities of primary X-ray reprocessing can be hidden by parameterizing the emissivity in the form of a logarithmic spiral wave. The emission region extent and shape are then defined by the spiral-wave pitch angle and the emissivity contrast – two variables that can be fitted to actual data.

Adopting the phenomenological approach does not merely hide the unknown physics. It also allows us to distinguish the principal difference of the two models, i.e., their geometry, while the "physical" models in reality rely on a number of free input parameters that have to be set.

We first estimate the light-crossing time across the spiral-wave extent. It comes out of the order of $t_c \approx 10 M_6$ sec. On the other hand, the orbital, thermal, sound-crossing, and viscous time-scales are typically longer than t_c. Radiation arrives at the observer from different regions of the source, so that individual light rays experience variable time lags. Time intervals get longer very near to the hole because of gravitational delays predicted by general relativity, including the frame-dragging effect near a rotating black hole, which we also take into account.

---

flows, predicted by numerical and semi-analytical methods, is followed by temperature modulation and, therefore, a change in the gas (thermal) emissivity within the spirals. A similar effect is expected for the X-ray irradiated accretion flows in AGN. Sanbuichi et al. (1994) first considered the spirals extending close to a Schwarzschild black hole and they showed examples of relativistically distorted spectra where the effects of general relativity play a role.

[2] We employ standard notation for the Kerr spacetime in Boyer–Lindquist coordinates and geometrized units ($c = G = 1$, e.g., Misner et al., 1973). All lengths and times are made dimensionless by expressing them in units of the typical mass of the central black hole. Radius is supposed to be greater than the marginally stable orbit, i.e., $r_{ms} = 3\, r_g$ for a non-rotating black hole ($a = 0$), and $r_{ms} = 1\, r_g$ for a maximally rotating black hole ($a = 1$).

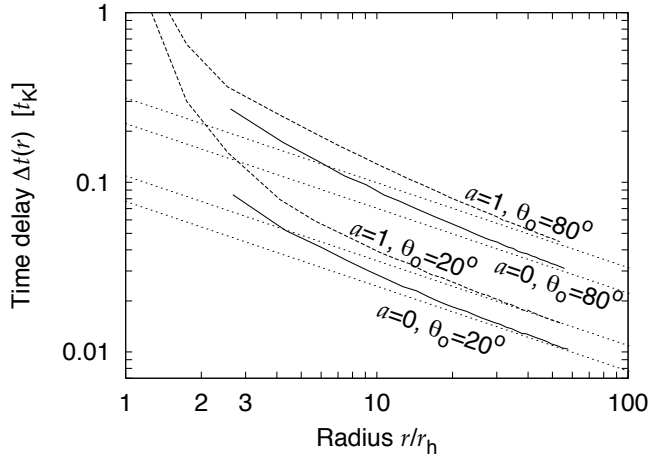

Figure 1. Graphs of the maximum time delay $\Delta t(r)$ for photons originating from an $r = \text{const}$ ring rotating in the black-hole equatorial plane. The delay is plotted in units of the Keplerian orbital period, $t_k \simeq 31(r^{3/2} + a)M_6$ sec. Radius is expressed in $r_h = [1 + (1 - a^2)^{1/2}]^{1/2} r_g$. Four cases are shown with different spin a of the black hole and inclination θ_o of the observer. The Euclidean estimate is plotted by dotted lines of $-1/2$ slope. Towards low radius the relativistic delay grows more rapidly than the estimate because of fast motion and strong gravity.

The geometrical time lag (along different rays) can be characterized by the maximum value $\Delta t(r)$, which also indicates whether the Euclidean formula gives a correct value of the light-travel time with an acceptable precision. Figure 1 shows Δt for a source located near $r = r_{ms}$. Solid curves represent the delay values in Kerr spacetime, while the dotted lines show the approximation in flat space. Relativistic corrections are increasingly important for $r \lesssim 5r_g$, where $\Delta t(r)$ increases sharply. On the other hand, the difference between the exact value of Δt and its Euclidean approximation is less than 10 % for a source location $\gtrsim 5r_g$ (see Karas et al., 2001).

Figure 2 shows contours of relative time delay between a ray coming from a given radius in the equatorial plane ($\theta = 90^o$), and an (arbitrarily chosen) reference ray. In this figure, time delay was calculated in Kerr metric. Clearly, the contours are progressively deformed and even split as the emission radius approaches the black-hole horizon. Reference values quoted with the contours of this figure can be transformed to physical time units (measured by a distant observer) by the relation $\bar{t}\,[\text{sec}] \approx 10M_6\, t$. Furthermore, contours of constant redshift $g(r, \phi) = \text{const}$ are over-plotted in Fig. 2. Radiation flux is enhanced (or diminished) by factor g^4 as it originates from the regions approaching (receding) the observer.

Figure 2 once again suggests the main grounds for the enhancement of the observed signal. The enhancement occurs when photons emitted at different points of the rotating source reach the observer similar time. This is possible near the black hole ($r \lesssim 6r_g$), where $t(r, \phi) = \text{const}$ contours are bent significantly. The actual shape of the spiral supporting the signal enhancement depends also on the pattern rotation, i.e., not solely on the spacetime

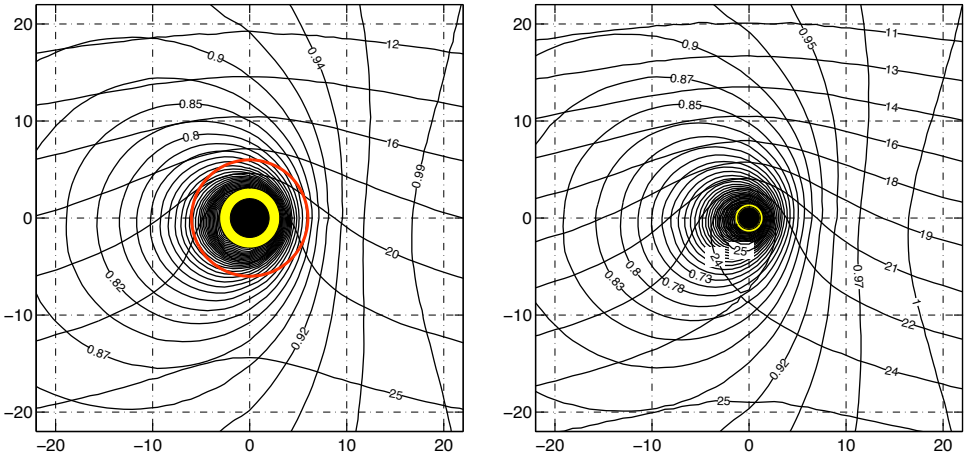

Figure 2. Levels of light-travel time $t\,(r, \phi) = \text{const}$ (approximately horizontal direction of the contour lines) are plotted together with levels of the redshift function $g(r, \phi) = \text{const}$ (roundish shape of the latter). The contours are constructed in the equatorial plane of Kerr black hole for two cases: a non-rotating hole ($a = 0$, left panel) and for a maximally rotating hole ($a = 1$, right panel). Observer is located towards top of the figure (at the inclination of $\theta_{\rm o} = 20°$). The argument of this paper assumes that the spiral pattern crosses $t = \text{const}$ contours and the signal varies thanks to their deformation and thanks to lensing near the horizon. Geometrical units are used for time t (conversion to physical units as in the previous figure caption); redshift function g is dimensionless and it attains values around unity ($g > 1$ corresponds to the blue-shift, i.e., observed energy of photons higher than the rest-frame energy). Three circles are plotted around the center: the horizon radius ($r = r_{\rm h}$, black), the circular photon orbit ($r = r_{\rm ph}$, yellow), and the marginally stable orbit ($r = r_{\rm ms}$, red). The circles coincide with each other in the extremely rotating case: $r_{{\rm h}|a=1} = r_{\rm g}$.

geometry. Needless to say, the effect combines with the lensing and Doppler amplification as the source crosses the lensing caustics in $g > 1$ region.

Obviously the effect grows with spin of the black hole and attains maximum at $a = 1$, a theoretical upper limit for Kerr black hole. The difference from the canonical $a = 0.998$ case is rather minimal, except for a small shift of $r_{\rm ms}(a)$ radius. That shift can prove to be important for the disc emission though, provided that the inner edge of the disc is attached to $r = r_{\rm ms}$.

3 DISCUSSION

As mentioned above, the interplay of lensing and the Doppler boosting was discussed by many authors within the orbiting spot model, whereas the influence of time-delays has not been emphasized to such detail. The effect is noticeable when watching the well-known animations of an orbiting spot at a large view-angle inclination (e.g., Fig. 3 in Eckart et al., 2007): the signal is sharply enhanced at the moment when the large spot moves behind the black hole. In the case of a spiral-shaped emission region the effect is expected to be even more pronounced thanks to the elongated size of the source.

The amplification is not symmetrical between leading and trailing spirals of otherwise the same geometry and the intrinsic emissivity. Put in a different way, the timing properties of the flare lightcurves can in principle constrain the ratio of v_r/v_ϕ of the spiral pattern producing them. In particular, for $v_r = 0$, $v_\phi = v_{\rm K}$ the model is effectively reduced to the orbiting spot model, whereas for $l = \text{const}$ (constant angular momentum of the gas), $v_r < 0$, $v_\phi < v_{\rm K}$ the case goes over to the falling spot model. Very exciting is now the possibility of having an extended source which can be incorporated within the spiral model. On the other hand the effects of lensing and the delay amplification should not be so important in the case of a low-angular momentum inflow ($v_\phi \ll v_{\rm K}$), which has been also widely applied in the context of Sgr A* (Proga and Begelman, 2003; Mościbrodzka et al., 2007 and references cited therein).

Further, it has been recognized that relativistic effects can strongly influence the observed signal and enable us to measure physical parameters of Sgr A* black hole. The simultaneous near-infrared and X-ray flares as well as the steady microwave emission from Sgr A* may be important probes of the gas dynamics and space-time metric of the black hole. The enhancement of the signal discussed in the present paper should be seen in all wavelengths as long as the approximation of geometrical optics is satisfied.

We have argued that the emitting region is likely to be twisted into a shape more complex than a simple spot. The spiral pattern is a physically sound possibility for the flaring region, in which the effect of relativistic modulation is more pronounced. The enhancement of the main peak of the lightcurve takes place roughly on time-scale of the spiral pattern crossing the equal-time curves. In other words the duration of the event can be significantly shorter that the pattern rotation period (it depends on the spiral shape and its rotation law). On the other hand, the pattern orbital speed is still relevant for the estimation of the flare periodicity over the entire cycle.

Given a specific mechanism to generate the spiral waves, certain freedom remains in the model parameters, so the actual form of the spiral profile can vary. Because for an ideal geometrical alignment of the spiral a rather sharp enhancement of the observed signal is foreseen (i.e., stronger than the spot model would predict), we can expect occasional strong flares with amplitudes exceeding the more frequent and currently known flares from Sgr A*.

4 CONCLUSIONS

Albeit physically substantiated, the model of an extended emission region suffers from a practical disadvantage in comparison with the spot model. The spiral model is more complex and the number of parameters describing the source is greater. Therefore, the fitting procedure will need better quality of future data. The spiral model assumes mechanisms beyond the standard disc scheme play a major role and form these non-axisymmetric structures. This may or may not be true. After all, the two scenarios – spots versus spirals – can be relevant for different categories of objects and different regimes of accretion. To this uncertainty refers the question mark in the title of the paper. The advent of simultaneous X-ray and IR detections of Sgr A* flares and the improving temporal and polarimetric resolution offer a promising potential to remove ambiguities that still hamper the association between physical models and real data.

ACKNOWLEDGEMENTS

The Czech authors thank the ESA PECS program (ref. 98040) and the Center for Theoretical Astrophysics (ref. LC06014) for the continued support.

REFERENCES

Baganoff, F., Bautz, M. W., Brandt, W. N., Chartas, G., Feigelson, E. D., Garmire, G. P., Maeda, Y., Morris, M., Ricker, G. R., Townsley, L. K. and Walter, F. (2001), Rapid X-ray flaring from the direction of the supermassive black hole at the Galactic Centre, *Nature*, **413**, p. 45.

Bao, G. and Stuchlík, Z. (1992), Accretion disk self-eclipse – X-ray light curve and emission line, *Astrophys. J.*, **400**, pp. 163–169.

Bélanger, G., Goldwurm, A., Melia, F., Ferrando, P., Grosso, N., Porquet, D., Warwick, R. and Yusef-Zadeh, F. (2005), Repeated X-ray flaring activity in Sagittarius A*, *Astrophys. J.*, **635**, p. 1095.

Bélanger, G., Terrier, R., De Jager, O., Goldwurm, A. and Melia, F. (2006), Periodic modulations in an X-ray flare from Sagittarius A*, *Journal of Physics: Conf. Series*, **54**, pp. 420–426, arXiv: `astro-ph/0604337`.

Bozza, V., de Luca, F., Scarpetta, G. and Sereno, M. (2005), Analytic Kerr black hole lensing for equatorial observers in the strong deflection limit, *Phys. Rev. D*, **72**, p. 083003.

Broderick, A. E. and Loeb, A. (2005), Imaging bright-spots in the accretion flow near the black hole horizon of Sgr A*, *Monthly Notices Roy. Astronom. Soc.*, **363**, p. 353.

Broderick, A. E. and Loeb, A. (2006), Imaging optically-thin hotspots near the black hole horizon of Sgr A* at radio and near-infrared wavelengths, *Monthly Notices Roy. Astronom. Soc.*, **367**, p. 905.

Cunningham, C. T. and Bardeen, J. M. (1972), The optical appearance of a star orbiting an extreme Kerr black hole, *Astrophys. J.*, **173**, p. L137.

Cunningham, C. T. and Bardeen, J. M. (1973), The Optical Appearance of a star orbiting an extreme Kerr black hole, *Astrophys. J.*, **183**, pp. 237–264.

Czerny, B., Różańska, A., Dovčiak, M., Karas, V. and Dumont, A.-M. (2004), The structure and radiation spectra of illuminated accretion disks in AGN. II. Flare/spot model of X-ray variability, *Astronomy and Astrophysics*, **420**, pp. 1–16, arXiv: `astro-ph/0402394`.

Done, C. (2002), Accretion flows in X-ray binaries, *Philos. Trans. Roy. Soc. London Ser. A*, **360**, p. 1967.

Done, C. and Gierliński, M. (2005), Scaling variability from stellar to supermassive black holes, *Monthly Notices Roy. Astronom. Soc.*, **364**, p. 208.

Dovčiak, M., Karas, V., Martocchia, A., Matt, G. and Yaqoob, T. (2004a), An XSPEC model to explore spectral features from black-hole sources, in S. Hledík and Z. Stuchlík, editors, *Proceedings of RAGtime 4/5: Workshops on black holes and neutron stars, Opava, 14–16/13–15 October 2002/2003*, pp. 33–73, Silesian University in Opava, Opava, ISBN 80-7248-242-4, arXiv: `astro-ph/0407330`.

Dovčiak, M., Karas, V. and Yaqoob, T. (2004b), An extended scheme for fitting X-Ray data with accretion disk spectra in the strong gravity regime, *Astrophys. J. Suppl.*, **153**, pp. 205–221.

Eckart, A., Baganoff, F. K., Morris, M., Bautz, M. W., Brandt, W. N., Garmire, G. P., Genzel, R., Ott, T., Ricker, G. R., Straubmeier, C., Viehmann, T., Schödel, R., Bower, G. C. and Goldston, J. E. (2004), First simultaneous NIR/X-ray detection of a flare from Sgr A*, *Astronomy and Astrophysics*, **427**, p. 1.

Eckart, A., Schödel, R., Meyer, L., Straubmeier, C., Dovčiak, M., Karas, V., Morris, M. R. and Baganoff, F. K. (2007), Variable and polarized emission from Sgr A*, in V. Karas and G. Matt, editors, *Black Holes from Stars to Galaxies – Across the Range of Masses*, volume 238 of *Proceedings of IAU Symposium*, p. 181, International Astronomical Union, Cambridge University Press, Cambridge, UK, ISSN 1743-9213.

Eckart, A., Schödel, R. and Straubmeier, C. (2005), *The Black Hole at the Center of the Milky Way*, Imperial College Press, London.

Falanga, M., Melia, F., Tagger, M., Goldwurm, A. and Bélanger, G. (2007), General relativistic flux modulations from disk instabilities in Sagittarius A*, *Astrophys. J.*, **662**, p. L15.

Fukumura, K. and Tsuruta, S. (2004), Iron Kα fluorescent line profiles from spiral accretion flows in active galactic nuclei, *Astrophys. J.*, **613**, p. 700.

Gaskell, C. M. and Klimek, E. S. (2003), Variability of active galactic nuclei from optical to X-ray regions, *AAT*, **22**, p. 661.

Genzel, R., Schödel, R., Ott, T., Eckart, A., Alexander, T., Lacombe, F., Rouan, D. and Aschenbach, B. (2003), Near-infrared flares from accreting gas around the supermassive black hole at the Galactic Centre, *Nature*, **425**, pp. 934–937, arXiv: `astro-ph/0310821`.

Gomboc, A. and Čadež, A. (2005), Effects of a black hole's gravitational field on the luminosity of a star during a close encounter, *Astrophys. J.*, **625**, p. 278.

Goosmann, R. W., Czerny, B., Mouchet, M., Ponti, G., Dovčiak, M., Karas, V., Różańska, A. and Dumont, A.-M. (2006), The structure and X-ray radiation spectra of illuminated accretion disks in AGN. III. Modeling fractional variability, *Astronomy and Astrophysics*, **454**, p. 741.

Haardt, F., Maraschi, L. and Ghisellini, G. (1994), A model for the X-ray and ultraviolet emission from Seyfert galaxies and galactic black holes, *Astrophys. J.*, **432**, p. 95.

Hartnoll, S. A. and Blackman, E. G. (2002), Iron line profiles from black hole accretion discs with spiral velocity structure, *Monthly Notices Roy. Astronom. Soc.*, **332**, p. L1.

Hollywood, J. M. and Melia, F. (1995), The effects of redshifts and focusing on the spectrum of an accretion disk in the galactic center black hole, *Astrophys. J.*, **443**, p. L17.

Karas, V., Martocchia, A. and Šubr, L. (2001), Variable line profiles due to non-axisymmetric patterns in an accretion disc around a rotating black hole, *Publ. Astronom. Soc. Japan*, **53**, p. 189.

Karas, V., Vokrouhlický, D. and Polnarev, A. G. (1992), In the vicinity of a rotating black hole – A fast numerical code for computing observational effects, *Monthly Notices Roy. Astronom. Soc.*, **259**, pp. 569–575.

Lawrence, A. and Papadakis, I. (1993), X-ray variability of active galactic nuclei – A universal power spectrum with luminosity-dependent amplitude, *Astrophys. J.*, **414**, p. L85.

Liu Siming, Melia, F. and Petrosian, V. (2006), Stochastic electron acceleration during the near-infrared and X-ray flares in Sagittarius A*, *Astrophys. J.*, **636**, p. 798.

Machida, M. and Matsumoto, R. (2003), Global three-dimensional magnetohydrodynamic simulations of black hole accretion disks: X-ray flares in the plunging region, *Astrophys. J.*, **585**, p. 429.

Markoff, S., Falcke, H., Yuan, F. and Biermann, P. L. (2001), The nature of the 10 kilosecond X-ray flare in Sgr A*, *Astronomy and Astrophysics*, **379**, p. L13.

Marrone, D. P., Moran, J. M., Zhao, J.-H. and Rao, R. (2006), Interferometric Measurements of Variable 340 GHz Linear Polarization in Sagittarius A*, *Astrophys. J.*, **640**, pp. 308–318, arXiv: `astro-ph/0511653`.

McHardy, I. M. and Czerny, B. (1987), Fractal X-ray time variability and spectral invariance of the Seyfert galaxy NGC5506, *Nature*, **325**, p. 696.

Melia, F., Bromley, B. C., Liu, S. W. and Christopher, K. (2001), Measuring the Black Hole Spin in Sagittarius A*, *Astrophys. J.*, **554**, p. L37.

Meyer, L., Eckart, A., Schödel, R., Duschl, W. J., Mužić, K., Dovčiak, M. and Karas, V. (2006a), Near-infrared polarimetry setting constraints on the orbiting spot model for Sgr A* flares, *Astronomy and Astrophysics*, **460**, p. 15.

Meyer, L., Schödel, R., Eckart, A., Karas, V., Dovčiak, M. and Duschl, W. J. (2006b), K-band polarimetry of an Sgr A* flare with a clear sub-flare structure, *Astronomy and Astrophysics*, **458**, p. L25.

Mirabel, I. F. and Rodríguez, L. F. (1998), Microquasars in our Galaxy, *Nature*, **392**, pp. 673–676.

Misner, C. W., Thorne, K. S. and Wheeler, J. A. (1973), *Gravitation*, W. H. Freeman and Co, New York, San Francisco.

Mościbrodzka, M., Proga, D., Czerny, B. and Siemiginowska, A. (2007), Accretion of low angular momentum material onto black holes: radiation properties of axisymmetric MHD flows, *Astronomy and Astrophysics*, **474**, p. 1, arXiv: `0707.1403`.

Noble, S. C., Leung Po Kin, Gammie, C. F. and Book, L. G. (2007), Simulating the emission and outflows from accretion discs, *Classical Quantum Gravity*, **24**, p. S259.

Papadakis, I. E. (2004), The scaling of the X-ray variability with black hole mass in active galactic nuclei, *Monthly Notices Roy. Astronom. Soc.*, **348**, p. 207.

Poutanen, J. and Fabian, A. C. (1999), Spectral evolution of magnetic flares and time lags in accreting black hole sources, *Monthly Notices Roy. Astronom. Soc.*, **306**, pp. L31–L37, arXiv: `astro-ph/9811306`.

Proga, D. and Begelman, M. C. (2003), Accretion of low angular momentum material onto black holes: two-dimensional magnetohydrodynamic case, *Astrophys. J.*, **592**, pp. 767–781, arXiv: `astro-ph/0303093`.

Rauch, K. P. and Blandford, R. D. (1994), Optical caustics in a Kerr space-time and the origin of rapid X-ray variability in active galactic nuclei, *Astrophys. J.*, **421**, p. 46.

Sanbuichi, K., Fukue, J. and Kojima, Y. (1994), Emission-line profiles of accretion disks with a non-axisymmetric pattern, *Publ. Astronom. Soc. Japan*, **46**, p. 605.

Tagger, M., Henriksen, R. N., Sygnet, J. F. and Pellat, R. (1990), Spiral waves and instability in magnetized astrophysical disks, *Astrophys. J.*, **353**, p. 654.

Tagger, M. and Melia, F. (2006), A possible Rossby wave instability origin for the flares in Sagittarius A*, *Astrophys. J.*, **636**, p. 33.

Varnière, P. and Blackman, E. G. (2005), Flux modulation from non-axisymmetric structures in accretion discs, *New Astronomy*, **11**, p. 43.

Vaughan, S., Fabian, A. C. and Iwasawa, K. (2005), Rapid X-Ray variability of Seyfert 1 galaxies, *Astrophys. Space Sci.*, **300**, p. 119.

Yuan, F., Quataert, E. and Narayan, R. (2003), Nonthermal electrons in radiatively inefficient accretion flow models of Sagittarius A*, *Astrophys. J.*, **598**, p. 301.

Życki, P. T. (2002), Predictions for Fourier-resolved X-ray spectroscopy from the model of magnetic flare avalanches above an accretion disc with hot ionized skin, *Monthly Notices Roy. Astronom. Soc.*, **333**, p. 800.

Proceedings of *RAGtime 8/9, 15–19/19–21 September, 2006/2007, Hradec nad Moravicí, Opava, Czech Republic*
S. Hledík and Z. Stuchlík, editors, Silesian University in Opava, 2007, pp. 109–123

Test particle motion in brany black hole spacetimes with a nonzero cosmological constant

Martin Kološ, Zdeněk Stuchlík and Stanislav Hledík

Institute of Physics, Faculty of Philosophy & Science, Silesian University in Opava,
Bezručovo nám. 13, CZ-746 01 Opava, Czech Republic

ABSTRACT
In the framework of the brany cosmology, the influence of the bulk spacetime on the black holes in the brane can be described by the so called tidal charge, which has a character similar to the charge parameter in the standard black-hole solutions, but can be both positive and negative. We discuss the influence of the tidal charge on the test particle and photon motion in the spherically symmetric spacetimes with a nonzero cosmological constant using the analysis realised in the case of Reissner–Nordström–(anti-)de Sitter spacetimes. We concentrate on the properties of circular geodesics as they play an important role in determining the brane properties of both thin and thick accretion discs. Some implications of the tidal charge influence are outlined.

Keywords: Brany black hole – tidal charge – Kerr–Newman–(anti-)de Sitter – Reissner–Nordström–(anti-)de Sitter – black hole – test particle motion – cosmological constant

1 INTRODUCTION

The Brane models of the Universe (Randall and Sundrum, 1999a,b), are studied intensive today since they could give an effective description of multidimensional theories of physical interactions. Roughly said, the brane model represent a five-dimensional spacetime – bulk, where the brane – our Universe is placed. Basical information about the brane models can be found in Maartens (2004); Majumdar and Mukherjee (2005). Recent cosmological tests indicate presence of a nonzero (but very small) repulsive cosmological constant ($\Lambda > 0$) responsible for the observed present acceleration of the expansion of our universe (Riess et al., 2004). Therefore, some attemption was denoted to the studies of the influence of $\Lambda > 0$ in astrophysical situations related to supermasive black holes (Stuchlík, 2002, 2005). Both test particles or photons and test fluid were studied in the field of spherically symmetric (Stuchlík and Hledík, 1999) or rotating black holes (Hledík, 2002; Stuchlík and Slaný, 2004) with $\Lambda > 0$. Since the brany black holes could be described by standard

978-80-7248-419-5

metrics with a single additional brany parameter b, called tidal charge because of representing non-local, i.e., tidal, gravitational effects of the bulk we extend our studies to the case of brany black holes with repulsive cosmological constant. Here we restrict our attention to the case of spherically symmetric black holes by the spacetimes of the Reissner–Nordström––(anti-)de Sitter type.

In this article we use tilde $\widetilde{\ }$ for the five-dimensional quantities, while the standard notation is used for the four-dimensional quantities on the brane. From the five-dimensional Einstein field equations, governing the whole bulk spacetime

$$\widetilde{G}_{AB} = -\widetilde{\Lambda}\tilde{g}_{AB}\tilde{\kappa}^2 + \widetilde{T}_{AB}\,, \tag{1}$$

we can express the effective four dimensional Einstein field equations (see Shiromizu et al., 1999; Majumdar and Mukherjee, 2005) in the form

$$G_{\mu\nu} = -\Lambda g_{\mu\nu} + \kappa^2 T^{\mathrm{eff}}_{\mu\nu} = -\Lambda g_{\mu\nu} + \kappa^2 T_{\mu\nu} + 6\frac{\kappa^2}{\epsilon}S_{\mu\nu} - E_{\mu\nu}\,. \tag{2}$$

Here ϵ is the brane tension, $\kappa^2 = \epsilon\tilde{\kappa}^4/6$ is the effective coupling constant, $\Lambda = (\widetilde{\Lambda}+\kappa^2\epsilon)/2$ is the effective cosmological constant, $E_{\mu\nu}$ is the brane projection of the five-dimensional Weyl tensor determining non-local gravitational effect of the bulk, while $S_{\mu\nu}$ is made up of energy momentum tensor $T_{\mu\nu}$ and represent the local gravitational effect. These tensors can be expressed in the form (Shiromizu et al., 1999)

$$S_{\mu\nu} = -\tfrac{1}{4}T^{\alpha}_{\mu}T^{\alpha}{}_{\nu} + \tfrac{1}{12}T^{\alpha}{}_{\alpha}T_{\mu\nu} - \tfrac{1}{24}g_{\mu\nu}\left[3T_{\alpha\beta}T^{\alpha\beta} - (T^{\alpha}{}_{\alpha})^2\right], \tag{3}$$

$$E_{\mu\nu} = -\frac{6}{\kappa^2\epsilon}\left[U(u_\mu u_\nu + \tfrac{1}{3}h_{\mu\nu})P_{\mu\mu} + 2Q_{(\mu}u_{\nu)}\right]. \tag{4}$$

where U represents energy density of the so called dark radiation and P represents dark pressure.

From the Bianchi identities $\nabla^\nu G_{\mu\nu} = 0$ it follows thus $\nabla^\nu T^{\mathrm{eff}}_{\mu\nu} = 0$. If matter on the brane is conserved, then $\nabla^\nu T_{\mu\nu} = 0$. It is clear, that is such a situation

$$\nabla^\mu E_{\mu\nu} = \frac{6\kappa^2}{\epsilon}\nabla^\mu S_{\mu\nu}\,. \tag{5}$$

2 AXIALLY SYMMETRIC SPACETIMES WITH TIDAL CHARGE

We shall now demonstrate how can we construct a stationary and axisymmetric metric, which is asymptotically (anti-)de Sitter, that can describe a rotating black-hole. Following the original approach of Kerr (Kerr and Schild, 1965) we can use the Kerr–Schild ansatz (for $\Lambda \neq 0$, see Carter, 1973; Gibbons et al., 2004), this means that the metric around a rotating black hole is represented by a linear approximation around the (anti-)de Sitter metric. For the spacetime interval we thus assume

$$\mathrm{d}s^2 = g_{\mu\nu}\,\mathrm{d}x^\mu\mathrm{d}x^\nu = \bar{g}_{\mu\nu}\,\mathrm{d}x^\mu\mathrm{d}x^\nu + H(k_\mu\,\mathrm{d}x^\mu)^2\,, \tag{6}$$

where k_μ is a null vector in both $g_{\mu\nu}$ and $\bar{g}_{\mu\nu}$, $H = H(r)$ is an arbitrary scalar function. The (anti-)de Sitter metric $\bar{g}_{\mu\nu}$ can we taken in the from

$$\mathrm{d}\bar{s}^2 = -\frac{(1-yr^2)\Delta_\theta\,\mathrm{d}\tau^2}{1+ya^2} + \frac{\rho^2\,\mathrm{d}r^2}{(1-yr^2)(r^2+a^2)} + \frac{\rho^2\,\mathrm{d}\theta}{\Delta_\theta} + \frac{(r^2+a^2)\sin^2\theta\,\mathrm{d}\phi^2}{1+ya^2}\,, \tag{7}$$

$$\rho^2 = r^2 + a^2\cos^2\theta\,, \quad \Delta_\theta = 1 + ya^2\cos^2\theta\,. \tag{8}$$

We introduced $y = \Lambda/3$, where Λ is the effective cosmological constant. The null vector field is then given in the form

$$k_\mu = \frac{\Delta_\theta\,\mathrm{d}\tau}{1+ya^2} + \frac{\rho^2\,\mathrm{d}r}{(1-yr^2)(r^2+a^2)} - \frac{a\sin^2\theta\,\mathrm{d}\phi}{1+ya^2}\,. \tag{9}$$

With a coordinate transformation (see Gibbons et al., 2004)

$$\mathrm{d}\tau = \frac{\mathrm{d}t}{1+ya^2} + \frac{\hat{H}\,\mathrm{d}r}{(1-yr^2)\Delta_r}\,, \qquad \mathrm{d}\phi = \mathrm{d}\phi - ay\frac{\mathrm{d}t}{1+ya^2} + \frac{a\hat{H}\,\mathrm{d}r}{(r^2+a^2)\Delta_r}\,, \tag{10}$$

where

$$\Delta_r = (1-yr^2)(r^2+a^2) - \hat{H}\,; \qquad \hat{H} \equiv H\rho^2\,, \tag{11}$$

we can give the axially symmetric metric in the standard Boyer–Lindquist like coordinates

$$\begin{aligned}\mathrm{d}s^2 = &-\frac{\Delta_r}{(1+ya^2)^2\rho^2}(\mathrm{d}t - a\sin^2\theta\,\mathrm{d}\phi)^2 + \frac{\rho^2}{\Delta_r}\,\mathrm{d}r^2 \\ &+ \frac{\rho^2}{\Delta_\theta}\,\mathrm{d}\theta^2 + \frac{\Delta_\theta\sin^2\theta}{(1+ya^2)^2\rho^2}[a\,\mathrm{d}t - (r^2+a^2)\,\mathrm{d}\phi]^2\,.\end{aligned} \tag{12}$$

The trace of the Einstein field equations (2) in vacuum $T_{\mu\nu} = 0$ can be expressed in a very simply form $R = 4\Lambda$ (because $E^\alpha{}_\alpha = 0$), in case of our metric (12) we are going to get, after some calculation, a differential equation $\mathrm{d}\hat{H}/\mathrm{d}r = 0$. An ordinary solution for $\hat{H}$ is

$$\hat{H} = 2Mr - b\,, \tag{13}$$

where M and b are constant.

The axially symmetric spacetime with tidal charge given by (12) and (13) has the character of Kerr–Newman–(anti-)de Sitter spacetime, although here b (tidal charge) – can be both positive or negative, contrary to the standard electromagnetic case of $Q^2 > 0$. For $y = 0, a = 0$, the metric is of the Reissner–Nordström form (see Dadhich et al., 2000), and for the case $y = 0$, $a \neq 0$ the Kerr–Newman form (see Aliev and Gümrükçüoğlu, 2005). For $a = 0$ and $y \neq 0$, we obtain metric of the Reissner–Nordström–(anti-)de Sitter form describing brany spherically symmetric black holes with $\Lambda \neq 0$.

The tidal charge b arises from the projection of the gravitational field in the bulk on to the brane – it is an imprint of the extra dimension. Negative b strengthens the gravitational field, positive b weakens the gravitational field.

Non-zero components of the "tidal" tensor $E_{\mu\nu}$ tensor are

$$E_t{}^t = -E_\phi{}^\phi = -\frac{b}{\rho^6}\left[\rho^2 - 2(r^2+a^2)\right], \tag{14}$$

$$E_r{}^r = -E_\theta{}^\theta = \frac{b}{\rho^2}, \tag{15}$$

$$E_\phi{}^t = -(r^2+a^2)\sin^2\theta\, E_t{}^\phi = -\frac{2\beta a}{\rho^6}(r^2+a^2)\sin^2\theta\,. \tag{16}$$

This type of $E_{\mu\nu}$ has the same form ($b \to Q^2/8\pi$) as energy momentum tensor $T_{\mu\nu}$ for the classical Kerr–Newman metric (Aliev and Gümrükçüoğlu, 2005). This type of $E_{\mu\nu}$ obey the conservation condition (5), ie $\nabla^\mu E_{\mu\nu}$, as the $S_{\mu\nu}$ tensor vanishes in the vacuum case ($T_{\mu\nu} = 0$).

3 SPHERICALLY SYMMETRIC SPACETIMES WITH THE TIDAL CHARGE AND NONZERO COSMOLOGICAL CONSTANT

We would like to examine geodetical structure of the axially symmetric spacetime with the tidal charge (12), but hereinafter we focus our attention to the simplest case of the spherically symmetric spacetime with $a = 0$. Thus the metric (12) has the form (SdS with a tidal charge)

$$\mathrm{d}s^2 = A(r)\,\mathrm{d}t^2 + A^{-1}(r)\,\mathrm{d}r^2 + r^2(\mathrm{d}\theta^2 + \sin^2\,\mathrm{d}\phi^2), \quad A(r) = 1 - \frac{2M}{r} - \frac{1}{3}\Lambda r^2 + \frac{b}{r^2}. \tag{17}$$

The tidal charge metric (17) has same form as the Reissner–Nordström metric with nonzero cosmological constant with the exception that the tidal charge b of arbitrary sign is replaced with non-negative square of electrical charge Q^2. Thus, the Reissner–Nordström metric represents a special case ($b > 0$) of metric (17).

In article (Stuchlík and Hledík, 2002) geodetical structure of Reissner–Nordström spacetime with cosmological constant is discussed, and we are going to use the same approach for examination of metric with tidal charge (17). All equations from (Stuchlík and Hledík, 2002) can be used only with substitution $Q^2 \to b$ (or $e^2 \to x$). Therefore we are going to write here only main steps; much more detailed discussion can be found in Stuchlík and Hledík (2002).

It is convenient to introduce a dimensionless cosmological parameter $y \equiv \Lambda M^2/3$, and dimensionless tidal charge $x \equiv bM^{-2}$ and dimensionless coordinates $t \to t/M, r \to r/M$.

The event horizons of the metric (17) are determined by the condition

$$-g_{tt} \equiv 1 - \frac{2}{r} + \frac{x}{r^2} - yr^2 = 0\,. \tag{18}$$

We are going to express position of the event horizons as solutions of the equation

$$y = y_{\mathrm{h}}(r; x) \equiv \frac{r^2 - 2r + x}{r^4}\,; \tag{19}$$

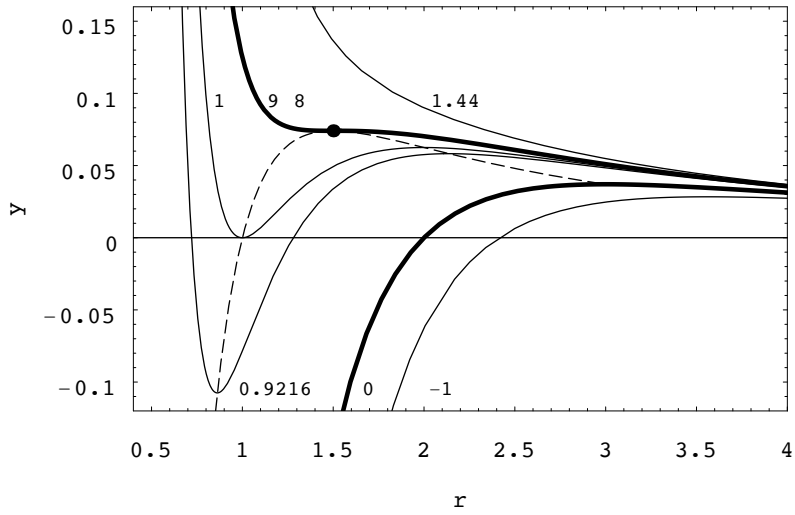

Figure 1. The loci of the event horizons in the tidal charge spacetimes. The functions $y_{\rm h}(r;x)$ are labelled by the corresponding value of the parameter x – the asymptotic behaviour is $y_{\rm h}(r\to\infty,x)\to 0$. We distinguish three different class of behaviour $y_{\rm h}(r,x)$, $x<0$, $0<x<9/8$ and $9/8<x$. The loci of the local extrema are emphasised by the dashed curve.

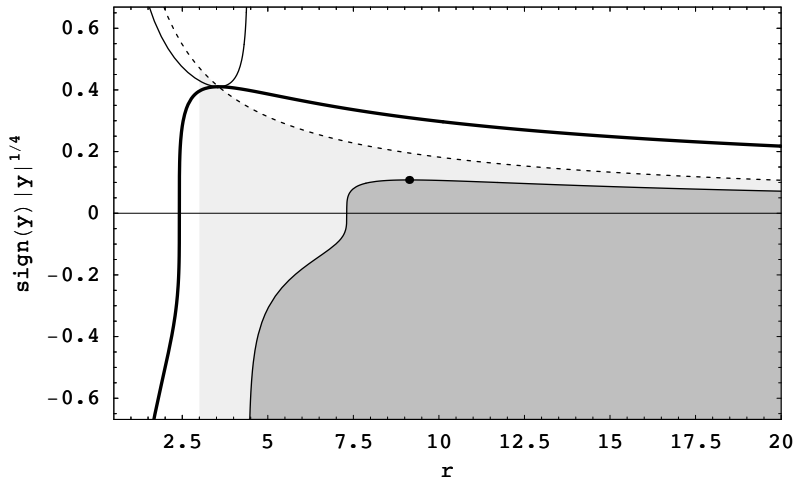

Figure 2. Properties of the circular geodesics in the tidal charge spacetime for $x=-1$. Determined by the function $y_{\rm h}(r;x)$ (thick solid line), giving event horizons , $y_{\rm ms}(r;x)$ (thin solid line), giving marginally stable circular orbits, and $y_{\rm s}(r;x)$ (dotted line), giving so called static radii, where particles with zero angular momentum remain at an equilibrium position. Regions admitting existence of circular geodesics are shaded. If the orbits are unstable, a low level of gray is used, while the regions of stable circular geodesics are emphasised by a higher level of gray (compare with the Fig. 4 from Stuchlík and Hledík, 2002, where are cases $x>0$).

properties of the function $y_{\rm h}(r;x)$ determine distribution of black-hole and naked-singularity spacetimes in the parameter space x-y (see Figs 1 and 2).

First, we are going to inspect special cases. For the case $x = 0$ ((anti-)de Sitter metric) we are going to determine the loci of the event horizons from the equation $yr^3 - r + 2 = 0$, so black holes can exist for all $y \leq y_{\rm c} = 1/27$. For $y > 1/27$, naked singularity exist (see Stuchlík and Hledík, 1999).

For a special case $y = 0$ (tidal charge metrics see Dadhich et al., 2000) the loci of the event horizons can be expressed as a solution of the equation $r^2 - 2r + x = 0$. This implies that black-holes exist for all $x < x_{\rm c} = 1$, for $x > 1$ only naked singularity exist.

The zero points of the $y_{\rm h}(r;x)$ are given by the relation determining horizons of black holes with tidal charge

$$x = x_{\rm z(h)} \equiv 2r - r^2 \,. \tag{20}$$

Its local extrema are given by the equation

$$x = x_{\rm e(h)} \equiv \tfrac{1}{2}(3r - r^2) \,. \tag{21}$$

At the local extrema, the cosmological parameter takes the values

$$y_{\rm h(max)}(x) \equiv \frac{r_{\rm e(h)+} - x}{r^4_{\rm e(h)+}} \,, \qquad y_{\rm h(min)}(x) \equiv \frac{r_{\rm e(h)-} - x}{r^4_{\rm e(h)-}} \,, \tag{22}$$

where

$$r_{\rm e(h)\pm} = \frac{3}{2}\left[1 \pm \left(1 - \frac{8x}{9}\right)^{1/2}\right] . \tag{23}$$

Equation (23) determinate position of the black-hole horizons. The black holes with tidal charge have two black-hole horizons $r_{\rm b-} < r_{\rm b+}$ for $0 < x < 9/8$ and only one horizon $r_{\rm b+}$ for $x < 0$. The asymptotically de Sitter black-holes has one extra horizon – the so called cosmological horizon $r_{\rm b+} < r_{\rm c}$. The stationary parts of the Reissner–Nordström–(anti-)de Sitter geometry are located at $r_{\rm b+} < r < r_{\rm c}$ and $0 < r_{\rm b-}$ (if $r_{\rm b-} > 0$), and dynamic at $r > r_{\rm c}$ and $r_{\rm b-} < r < r_{\rm b+}$.

4 GEODETICAL MOTION

Motion of uncharged test particles and photons is governed by the geodetical structure of the spacetime. The geodesic equation reads

$$\frac{{\rm D}p^\mu}{{\rm d}\lambda} = 0 \,, \tag{24}$$

where $p^\mu \equiv {\rm d}x^\mu/{\rm d}\lambda$ is the four-momentum of a test particle (photon) and λ is the affine parameter related to the proper time τ of a test particle by $\tau = \lambda/m$. The normalisation condition reads $p^\mu p_\mu = -m^2$, where m is the rest mass of the particle; $m = 0$ for photons.

It follows from the central symmetry of the geometry (17) that the geodetical motion is allowed in the central planes only. Two constants of the motion must exist

$$p_t = g_{t\mu}p^\mu = -\mathcal{E}\,, \qquad p_\phi = g_{\phi\mu}p^\mu = \Phi\,. \tag{25}$$

In the spacetimes with $\Lambda \neq 0$, the constants of motion $\mathcal{E}$ and Φ cannot be interpreted as energy and axial component of the angular momentum at infinity since the geometry is not asymptotically flat. It is convenient to introduce specific energy E, specific axial angular momentum L and impact parameter ℓ by the relations

$$E = \frac{\mathcal{E}}{m}\,, \quad L = \frac{\Phi}{m}\,, \quad \ell = \frac{\Phi}{\mathcal{E}}\,. \tag{26}$$

Choosing the plane of the motion to be the equatorial plane, we find that the motion of test particles ($m \neq 0$) can be determined by an "effective potential" of the radial motion (see Fig. 3)

$$V^2_{\rm eff}(r; L, y, x) \equiv \left(1 - \frac{2}{r} + \frac{x}{r^2} - yr^2\right)\left(1 + \frac{L^2}{r^2}\right)\,. \tag{27}$$

Since $(u^r)^2 = (\mathrm{d}r/\mathrm{d}\tau)^2 = E^2 - V^2_{\rm eff}(r; L, y, x)$, the motion is allowed where

$$E^2 \geq V^2_{\rm eff}(r; L, y, x)\,, \tag{28}$$

and the turning points of the radial motion are determined by the condition

$$E^2 = V^2_{\rm eff}(r; L, y, x)\,. \tag{29}$$

The radial motion of photons ($m = 0$) is determined by a "generalised effective potential" $\ell^2_{\rm R}(r; y, x)$ related to the impact parameter ℓ (see Fig. 4). The motion is allowed, if

$$\ell^2 \leq \ell^2_{\rm R}(r; y, x) \equiv \frac{r^4}{r^2 - 2r + x - yr^4}\,, \tag{30}$$

the condition $\ell^2 = \ell^2_{\rm R}(r, y, x)$ gives the turning points of the radial motion.

The special case of $x = 0$ has been extensively discussed in Stuchlík and Hledík (1999). Therefore, we concentrate our discussion on the case $x \neq 0$. The effective potentials $V^2_{\rm eff}(r; L, y, x)$ and $\ell^2_{\rm R}(r; y, x)$ define turning points of the radial motion at the static regions of the tidal charge spacetimes. (At the dynamic regions, where the inequalities $V_{\rm eff}(r; L, y, x) < 0$ and $\ell^2_{\rm R}(r; y, x) < 0$ hold, there are no turning points of the radial motion). $V^2_{\rm eff}$ is zero at the horizons, while ℓ^2 diverges there. At $r = 0$, $V^2_{\rm eff} \to +\infty$, while $\ell^2_{\rm R} = 0$. Circular orbits of uncharged test particles correspond to local extrema of the effective potential ($\partial V_{\rm eff}/\partial r = 0$). Maxima ($\partial^2 V_{\rm eff}/\partial r^2 < 0$) determine circular orbits unstable with respect to radial perturbations, minima ($\partial^2 V_{\rm eff}/\partial r^2 > 0$) determine stable circular orbits. The specific energy and specific angular momentum of particles on a circular orbit,

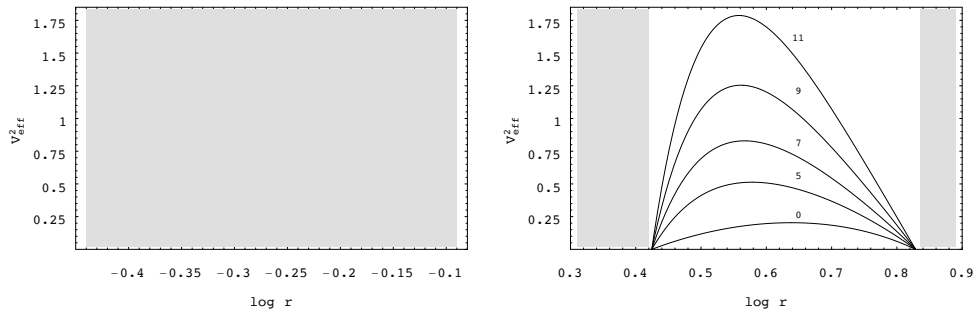

(a) dS-NS-5: $y = 0.09, x = -1$

(b) dS-BH-2: $y = 0.015, x = -1$

(c) dS-BH-1: $y = 0.00001, x = -1$

(d) adS-BH-1: $y = -0.0005, x = -1$

Figure 3. The effective potential $V^2_{\rm eff}(r;\, x,\, y,\, L)$ of the test-particle geodetical motion in tidal charge spacetimes, for $x < 0$. There are four qualitatively different types of the behaviour of $V^2_{\rm eff}$ subsequently illustrated in the cases (a) through (d). The curves giving the effective potential are labelled by the values of the particle's angular momentum L. The dynamic regions of the spacetimes, where $V^2_{\rm eff}$ is not properly defined, are shaded (compare with the Fig. 5 from Stuchlík and Hledík, 2002).

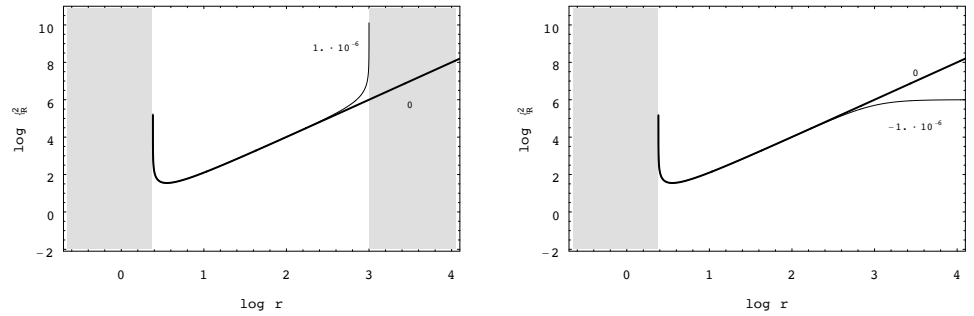

(a) dS-BH-1: $y \in \{0, 0.000001\}, x = -1$

(b) adS-BH-1: $y \in \{0, -0.000001\}, x = -1$

Figure 4. The effective potential $\ell^2_{\rm R}(r;\, x,\, y)$ of the photon geodetical motion in tidal charge spacetimes.The dynamic regions of the spacetimes, where $\ell^2_{\rm eff}$ is not properly defined, are shaded (compare with the Fig. 6 from Stuchlík and Hledík, 2002).

at a given r, are determined by the relations

$$E_{\mathrm{c}}(r;\, y, x) = \frac{1 - \frac{2}{r} + \frac{x}{r^2} - yr^2}{\left(1 - \frac{3}{r} + \frac{2x}{r^2}\right)^{1/2}}\,, \tag{31}$$

$$L_{\mathrm{c}}(r;\, y, x) = \left(\frac{r - x - yr^4}{1 - \frac{3}{r} + \frac{2x}{r^2}}\right)^{1/2}\,. \tag{32}$$

(The minus sign for L_{c} is equivalent to the plus sign in spherically symmetric spacetimes, therefore, we do not give the minus sign explicitly here and in the following.)

At $r = r_{\mathrm{ph}+}$, and $r = r_{\mathrm{ph}-}$, where

$$r_{\mathrm{ph}\pm}(x) = \frac{3}{2}\left[1 \pm \left(1 - \frac{8x}{9}\right)^{1/2}\right]\,, \tag{33}$$

both E_{c} and L_{c} diverge – photon circular orbits exist at these radii. The photon circular orbits are determined by the local extrema of the function $\ell^2_{\mathrm{R}}(r;\, y, x)$, which are located at $r = r_{\mathrm{ph}\pm}(x)$ independently of the cosmological parameter y. Of course, the impact parameter of the photon circular orbits depends on y; there is

$$\ell^2_{\mathrm{c}\pm}(y, x) = \frac{r^4_{\mathrm{ph}\pm}}{r^2_{\mathrm{ph}\pm} - 2r_{\mathrm{ph}\pm} + x - yr^4_{\mathrm{ph}\pm}}\,. \tag{34}$$

The loci of photon circular orbits can be implicitly given by the equation $x = x_{\mathrm{ph}}(r) = x_{\mathrm{e(h)}}$. Because $r_{\mathrm{ph}\pm}(x) = r_{\mathrm{e(h)}\pm}(x)$, where $r_{\mathrm{e(h)}\pm}(x)$ determine local extrema of the function $y_{\mathrm{h}}(r;\, x)$ governing horizons of the tidal charge spacetimes, we can directly conclude that two photon circular orbits can exist at the naked-singularity spacetimes with $y < y_{\mathrm{h(min)}}(x)$, while one photon circular orbit at $r_{\mathrm{ph}+}(x) > r_{\mathrm{b}+}(x)$ exists in the black-hole spacetimes with $y_{\mathrm{h(min)}}(x) < y < y_{\mathrm{h(max)}}(x)$. If no local extrema of $y_{\mathrm{h}}(r;\, x)$ exist, i.e., for $x \leq 9/8$ and $y > y_{\mathrm{h(max)}}(x)$, and for $x > 9/8$ and y arbitrary, no photon circular geodesics are admitted in the corresponding naked-singularity spacetimes.

The circular geodesics are allowed at regions, where the denominator of both (31) and (32) is real, i.e., at

$$r < r_{\mathrm{ph}-} \quad \text{and} \quad r > r_{\mathrm{ph}+}\,. \tag{35}$$

However, we have to add the condition given by reality of the numerator in (32):

$$r - x - yr^4 \geq 0\,. \tag{36}$$

The equality at (36) determines so called static radii r_{s}, where $L_{\mathrm{c}}(r_{\mathrm{s}};\, y, x) = 0$.

The static radii are given by the condition

$$y = y_{\mathrm{s}}(r;\, x) \equiv \frac{r - x}{r^4}\,. \tag{37}$$

The asymptotic behaviour of $y_{\rm s}(r, x)$ is determined by relations (see also Fig. 2)

$$y_{\rm s}(r \to 0, x) \to -\infty, \quad y_{\rm s}(r \to \infty, x) \to 0\,. \tag{38}$$

The function $y_{\rm s}(r; x)$ has its zero point at $r = x$ and its local maximum is at $r = 4x/3$, where

$$y_{\rm s(max)}(x) = \frac{27}{256x^3}\,. \tag{39}$$

The conditions (35) and (36) limiting radii of circular geodetical motion have to be considered simultaneously. We arrive at the conclusion that the geodetical circular orbits are allowed at radii

$$r_{\rm s1} < r < r_{\rm ph-}\,, \quad r_{\rm ph+} < r < r_{\rm s2}\,. \tag{40}$$

The stable circular geodesics are limited by the relation

$$4yr^6 - 15yr^5 + 12yxr^4 - r^3 + 6r^2 - 9xr + 4x^2 \le 0\,. \tag{41}$$

Radii of the marginally stable circular geodesics, given by the equality in (41), can be expressed in the form

$$y = y_{\rm ms}(r; x) \equiv \frac{r^3 - 6r^2 + 9xr - 4x^2}{r^4\left(4r^2 - 15r + 12x\right)}\,. \tag{42}$$

The asymptotic behaviour of the function $y_{\rm ms}(r; x)$ is given by the relations $y_{\rm ms}(r \to 0, x) \to -\infty$, $y_{\rm ms}(r \to \infty, x) \to 0$ (see also Fig. 2). The zero points of $y_{\rm ms}(r; x)$, determining marginally stable circular geodesics of the Reissner–Nordström spacetimes, are given by the relation

$$x = x_{\rm z(ms)}(r) \equiv \frac{9r \pm r\sqrt{16r - 15}}{8}\,, \tag{43}$$

while its divergent points are located at $r = 0$, where $y_{\rm ms}(r \to 0, x) \to -\infty$, and at radii implicitly determined by the relation

$$x = x_{\rm d(ms)}(r) \equiv \frac{15r - 4r^2}{12}\,. \tag{44}$$

Both functions $x_{\rm z(ms)}(r)$ and $x_{\rm d(ms)}(r)$ are illustrated in Fig. 5.

Local extrema of $y_{\rm ms}(r; x)$ determine the extremal values $y_{\rm ms(max)}(x)$ and $y_{\rm ms(min)}(x)$ of spacetimes that admit existence of stable circular geodesics. These local extrema are determined by the equation

$$(2x - 3r + r^2)(16x^2 - 28xr + 15r^2 - 2r^3) = 0\,. \tag{45}$$

In the special case of $x = 0$, we find $r_{\rm max} = 15/2$ and $y_{\rm ms(max)} = 12/15^4 \approx 0.000237$; further, there is $r_{\rm min} = 3$ and $y_{\rm ms(min)} = 1/27$, which is irrelevant for timelike geodesics (see Stuchlík and Hledík, 1999 for details).

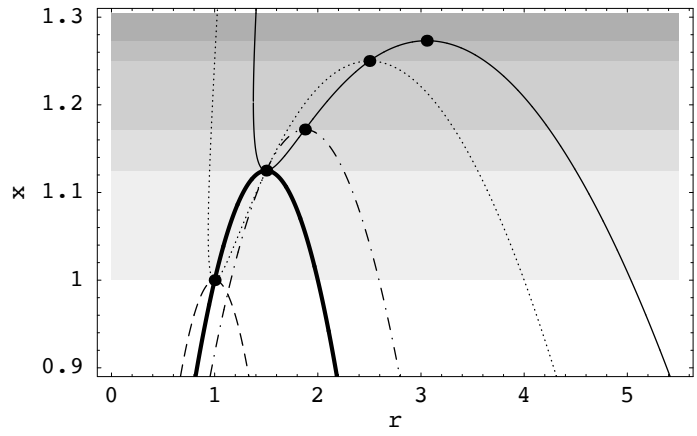

Figure 5. The characteristic functions governing the test-particle geodetical motion in the tidal charge spacetimes. Properties of the The function $x_{\mathrm{z(h)}}(r)$ (represented by the dashed curve) governs the zero points (event horizons of tidal charge ($\Lambda = 0$) black holes) and the characteristic function $x_{\mathrm{e(h)}}(r)$ (represented by the bold solid curve) governs the local extrema of the function $y_{\mathrm{h}}(r; x)$ determining the event horizons of the tidal charge spacetimes. Their respective local maxima are located at the points $(1, 1)$ and $(3/2, 9/8)$. The characteristic functions $x_{\mathrm{z(ms)}\pm}(r)$ (represented by the dotted curve) govern the zero points of $y_{\mathrm{ms}}(r; x)$ determining the marginally stable circular geodesics, the characteristic function $x_{\mathrm{d(ms)}}(r)$ (represented by the dashed-dotted curve) governs the divergent points of $y_{\mathrm{ms}}(r; x)$, and the characteristic functions $x_{\mathrm{e(ms)}\pm}(r)$ (represented by the thin solid curve) govern the local extrema of the function $y_{\mathrm{ms}}(r; x)$. Their respective local maxima are located at the points $(5/2, 5/4)$ (on the "$-$" branch), $(15/8, 75/64)$ and $(55/18, 275/216)$ (on the "$-$" branch). The local minimum of the function $x_{\mathrm{z(ms)}\pm}(r)$ (the "$-$" branch) coincides with the local maximum of the function $x_{\mathrm{z(h)}}(r)$ at (1,1), the local minimum of the function $x_{\mathrm{e(ms)}\pm}(r)$ (the "$-$" branch) coincides with the local maximum of the function $x_{\mathrm{e(h)}}(r)$ at $(3/2, 9/8)$. The extrema of characteristic functions governing the test-particle geodetical motion divide the our graph into six subintervals, each of them implying different behaviour of the functions $y_{\mathrm{h}}(r; x)$ and/or $y_{\mathrm{ms}}(r; x)$. The extrema are in the $x > 0$ part of our graph, here are no new cases, different from (Stuchlík and Hledík, 2002).

The common points of $y_{\mathrm{ms}}(r; x)$ and $y_{\mathrm{h}}(r; x)$ are located at $r = r_{\mathrm{ph}+}$ and $r = r_{\mathrm{ph}-}$, where both $y_{\mathrm{ms}}(r; x)$ and $y_{\mathrm{h}}(r; x)$ have local extrema, because of the first bracket of Eq. (45); these are also common points with the function $y_{\mathrm{s}}(r; x)$. Other local extrema of $y_{\mathrm{ms}}(r; x)$ are determined by the term in the second bracket in (45). They can be given by the relation

$$x = x_{\mathrm{e(ms)}\pm}(r) \equiv \frac{7r - r\sqrt{8r - 11}}{8}\,. \tag{46}$$

The function $x_{\mathrm{e(ms)}\pm}(r)$ is, again, illustrated in Fig. 5. Inspecting Fig. 5 we can conclude that the local extrema of $y_{\mathrm{ms}}(r; x)$, determined by (46), govern only one local extreme of $y_{\mathrm{ms}}(r; x)$ in the spacetimes with black-hole horizons ($x < 9/8$), while they govern three local extrema in naked-singularity spacetimes with $9/8 < x < 275/216$.

5 CONCLUSIONS

Analysis of the characteristic functions $y_{\mathrm{h}}(r;x)$, $y_{\mathrm{s}}(r;x)$, $y_{\mathrm{ms}}(r;x)$ shows that there are fifteen types of the tidal charge spacetimes with qualitatively different behaviour of the effective potential of the geodetical motion (and the circular orbits), see Fig. 6.

Spacetimes for $x > 0$

Standard Reissner–Nordström–(anti-)de Sitter spacetime (see Stuchlík and Hledík, 2002):

dS-BH-1 One region of circular geodesics at $r > r_{\mathrm{ph+}}$ with unstable then stable and finally unstable geodesics (for radius growing).[1]

[1] Type dS-BH-1 means asymptotically de Sitter black-hole spacetime of type 1, etc. . .

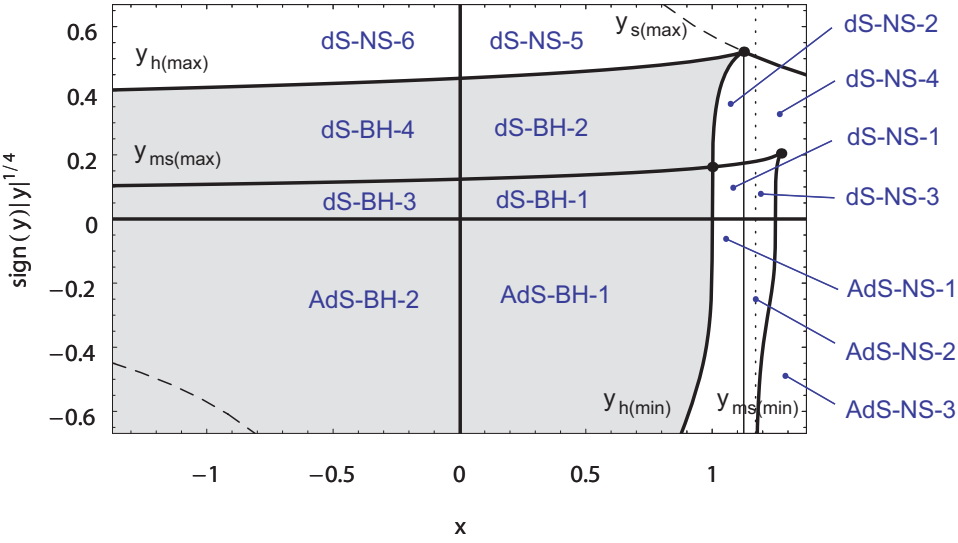

Figure 6. The classification of the tidal charge spacetimes according to properties of the effective potential of the test-particle geodetical. The functions $y_{\mathrm{h(min)}}(x)$ and $y_{\mathrm{h(max)}}(x)$ limit the region of black-hole spacetimes (shaded) in the parameter space x-y. Outside that region, merely naked-singularity spacetimes exist. The function $y_{\mathrm{s(max)}}(x)$ (represented by the dashed curve in the region, where it is irrelevant for the classification) marks the local maxima of the function $y_{\mathrm{s}}(r;x)$ governing the static radii. The functions $y_{\mathrm{ms(min)}}(x)$ and $y_{\mathrm{ms(max)}}(x)$ separate the asymptotically de Sitter black-hole spacetimes containing a region of stable circular orbits allowing accretion processes in the disk regime (dS-BH-1), (dS-BH-3) from those with unstable circular orbits only (dS-BH-2), (dS-BH-4) and the naked-singularity spacetimes with two regions of stable circular orbits from those with one region of stable circular orbits From behaviour of the characteristic functions $y_{\mathrm{h}}(r;x)$, $y_{\mathrm{s}}(r;x)$, $y_{\mathrm{ms}}(r;x)$ we can see that there are eleven different types of the spacetimes (compare with Fig. 3 in Stuchlík and Hledík, 2002).

dS-BH-2 One region of circular geodesics at $r > r_{\mathrm{ph}+}$ with unstable geodesics only.
dS-NS-1 Two regions of circular geodesics, the inner region consists of stable geodesics only, the outer one contains subsequently unstable, then stable and finally unstable circular geodesics.
dS-NS-2 Two regions of circular orbits, the inner one consist of stable orbits, the outer one of unstable orbits.
dS-NS-3 One region of circular orbits, subsequently with stable, unstable, then stable and finally unstable orbits.
dS-NS-4 One region of circular orbits with stable and then unstable orbits.
dS-NS-5 No circular orbits allowed.
AdS-BH-1 One region of circular geodesics at $r > r_{\mathrm{ph}+}$ with unstable and then stable geodesics.
AdS-NS-1 Two regions of circular geodesics, the inner one ($r < r_{\mathrm{ph}-}$) consists of stable geodesics only, the outer one ($r > r_{\mathrm{ph}+}$) contains both unstable and then stable circular geodesics.
AdS-NS-2 One region of circular orbits, subsequently with stable, then unstable and finally stable orbits.
AdS-NS-3 One region of circular orbits with stable orbits exclusively.

New type of the spacetime ($x < 0$)

Pure brany case:

dS-BH-3 One region of circular geodesics at $r > r_{\mathrm{ph}+}$ with unstable then stable and finally unstable geodesics.
dS-BH-4 One region of circular geodesics at $r > r_{\mathrm{ph}+}$ with unstable geodesics only.
dS-NS-6 No circular orbits allowed. There is no region where $V^2_{\mathrm{eff}}(r; L, y, x)$ is properly defined.
AdS-BH-2 One region of circular geodesics at $r > r_{\mathrm{ph}+}$ with unstable and then stable geodesics.

The tidal charge black holes have two non-cosmological $r_{\mathrm{b}-} < r_{\mathrm{b}+}$ horizons for $0 < x < 9/8$ and only one $r_{\mathrm{b}+}$ for $x < 0$. For black hole spacetimes with $b < 0$ there is no inner horizon, but this is irrelevant for the geodetical motion. So we thing that influence of $b < 0$ on the spacetime structure is quantitative, not qualitative.

If we calculate binding energy $(1 - E_{\mathrm{ms}})$, we can see that it decreases with decreasing tidal charge b.

Finally, we could note that is of some fundamental interest, to what extend the combined influence of both the tidal charge and cosmological constant could influence quasiperiodic oscillations in accretion discs that could enable relatively precise determination of the black hole parameters (Török et al., 2005). It seem that the quasiperiodic oscillations observed near the galaxy centre black hole source Sgr A* give information (Aschenbach, 2004; Török, 2005a,b) that could be used to test the brany models Stuchlík and Kotrlová (2007).

ACKNOWLEDGEMENTS

The present work was supported by Czech Grants MSM 4781305903, GAČR 205/03/H144. One of the authors (Z. S.) would like to express his gratitude to Czech Committee for collaboration with CERN for support and CERN Theory Division for perfect hospitality.

REFERENCES

Aliev, A. N. and Gümrükçüoğlu, A. E. (2005), Charged Rotating Black Holes on a 3-Brane, *Phys. Rev. D*, **71**(10), p. 104027, arXiv: `hep-th/0502223v2`.

Aschenbach, B. (2004), Measuring mass and angular momentum of black holes with high-frequency quasi-periodic oscillations, *Astronomy and Astrophysics*, **425**, pp. 1075–1082, arXiv: `astro-ph/0406545`.

Carter, B. (1973), Black hole equilibrium states, in C. D. Witt and B. S. D. Witt, editors, *Black Holes*, pp. 57–214, Gordon and Breach, New York–London–Paris.

Dadhich, N., Maartens, R., Papadopoulos, P. and Rezania, V. (2000), Black holes on the brane, *Phys. Rev. B*, **487**, arXiv: `hep-th/0003061v3`.

Gibbons, G. W., Lu, H., Page, D. N. and Pope, C. N. (2004), The General Kerr–de Sitter Metric in All Dimensons, *J. Geom. Phys.*, **53**, pp. 49–73, arXiv: `hep-th/0404008v3`.

Hledík, S. (2002), Optical geometry, inertial forces, and embedding diagrams, in Semerák et al. (2002), pp. 161–192.

Kerr, R. P. and Schild, A. (1965), Some algebraically degenerate solutions of Einstein's gravitational field equations, in R. Finn. American Math. Soc., editor, *Proc. Sym. in Applied Math.*, volume XVII, pp. 199–209, Providence, Rhode Island.

Maartens, R. (2004), Brane-world gravity, *Living Rev. Rel.*, **7**, arXiv: `gr-qc/0312059v2`.

Majumdar, A. S. and Mukherjee, N. (2005), Braneworld black holes in cosmology and astrophysics, *Internat. J. Modern Phys. D*, **14**, arXiv: `astro-ph/0503473v2`.

Randall, L. and Sundrum, R. (1999a), A Large Mass Hierarchy from a Small Extra Dimension, *Phys. Rev. D*, **83**(2), pp. 3370–3373, arXiv: `hep-ph/9905221`.

Randall, L. and Sundrum, R. (1999b), An Alternative to Compactification, *Phys. Rev. D*, **83**(2), pp. 4690–4693, arXiv: `hep-th/9906064`.

Riess, A. G., Strolger, L.-G., Tonry, J. et al. (2004), Type Ia Supernova Discoveries at $z > 1$ From the Hubble Space Telescope: Evidence for Past Deceleration and Constraints on Dark Energy Evolution, *Astrophys. J.*, **607**, pp. 665–687, arXiv: `astro-ph/0402512v2`.

Semerák, O., Podolský, J. and Žofka, M., editors (2002), *Gravitation: Following the Prague Inspiration (A Volume in Celebration of the 60th Birthday of Jiří Bičák)*, World Scientific, New Jersey, London, Singapore, Hong Kong, ISBN 981-238-093-0.

Shiromizu, T., Maeda, K. and Sasaki, M. (1999), The Einstein Equations on the 3-Brane World, *Phys. Rev. D*, **62**, p. 024012, arXiv: `gr-qc/9910076`.

Stuchlík, Z. (2002), The role of a repulsive cosmological constant in astrophysical processes, in Semerák et al. (2002), pp. 27–83.

Stuchlík, Z. (2005), Influence of the Relict Cosmological Constant on Accretion Discs, *Modern Phys. Lett. A*, **20**(8), pp. 561–575.

Stuchlík, Z. and Hledík, S. (1999), Some properties of the Schwarzschild–de Sitter and Schwarzschild–anti-de Sitter spacetimes, *Phys. Rev. D*, **60**(4), p. 044006 (15 pages).

Stuchlík, Z. and Hledík, S. (2002), Properties of the Reissner–Nordström spacetimes with a nonzero cosmological constant, *Acta Phys. Slovaca*, **52**(5), pp. 363–407, ISSN 0323-0465/02, erratum notice can be found at `http://www.acta.sav.sk/acta02/no6/`, URL `http://www.acta.sav.sk/acta02/no5/`.

Stuchlík, Z. and Kotrlová, A. (2007), Orbital resonance model of QPOs in braneworld Kerr black hole spacetimes, pp. 323–361, this volume.

Stuchlík, Z. and Slaný, P. (2004), Equatorial circular orbits in the Kerr–de Sitter spacetimes, *Phys. Rev. D*, **69**, p. 064001, ISSN 1094-1622, arXiv: `gr-qc/0307049`.

Török, G. (2005a), A possible 3 : 2 orbital epicyclic resonance in QPO frequencies of Sgr A*, *Astronomy and Astrophysics*, **440**(1), pp. 1–4, arXiv: `astro-ph/0412500`.

Török, G. (2005b), QPOs in microquasars and Sgr A*: measuring the black hole spin, *Astronom. Nachr.*, **326**(9), pp. 856–860, arXiv: `astro-ph/0510669`.

Török, G., Abramowicz, M. A., Kluźniak, W. and Stuchlík, Z. (2005), The orbital resonance model for twin peak kHz quasi periodic oscillations in microquasars, *Astronomy and Astrophysics*, **436**(1), pp. 1–8, arXiv: `astro-ph/0401464`.

Proceedings of *RAGtime 8/9, 15–19/19–21 September, 2006/2007, Hradec nad Moravicí, Opava, Czech Republic*
S. Hledík and Z. Stuchlík, editors, Silesian University in Opava, 2007, pp. 125–138

On existence of halo orbits in Kerr–Newman spacetimes

Jiří Kovář[1,a] Zdeněk Stuchlík[1] and Vladimír Karas[2]

[1] Institute of Physics, Faculty of Philosophy & Science, Silesian University in Opava, Bezručovo nám. 13, CZ-746 01 Opava, Czech Republic
[2] Astronomical Institute, Czech Academy of Sciences, Boční II 1401/1a, CZ-141 31 Praha 4, Czech Republic
[a] Jiri.Kovar@fpf.slu.cz

ABSTRACT
Being inspired by existence of non-equatorial circular (halo) stable orbits of charged particles in composite of gravitational, dipole magnetic and co-rotational electric fields near some planets, we find possible existence of these orbits in strong gravitational fields described by the Kerr–Newman geometry. By using the general relativistic inertial forces formalism combined with the effective potential approach, we show that the stable halo orbits do exist there. But it seems that they are out of the astrophysical importance, being hidden under the inner black-hole horizon, or appearing in the naked singularity spacetimes.

Keywords: Kerr–Newman spacetime – black hole – naked singularity – charged particle – magnetic field – halo orbits

1 INTRODUCTION

Investigation of charged particle motion in strong gravitational and electromagnetic fields ranks among the elementary exercises in theoretical physics and astrophysics related to black holes or neutron stars (Prasanna, 1980; Karas and Vokrouhlický, 1991; Vokrouhlický and Karas, 1991). The test particle motion analysis is usually restricted to the motion along symmetry axis (Bičák et al., 1989), and to the equatorial (Balek et al., 1989) or spherical motion (Johnston and Ruffini, 1974), and to the special case of particles freely falling from rest at infinity (Stuchlík et al., 1999). The general off-equatorial motion in the field of rotating black holes represents an interesting open problem deserving attention. We would like to tackle this problem focusing on the case of the so-called halo orbits, i.e., off-equatorial circular orbits, which could be interesting from the astrophysical point of view as well as the equatorial circular orbits.

As a partial motivation of our work, we mention an investigation of the charged dust grains motion in magnetosphere of some planets (see, e.g., Howard et al., 1999, where the halo orbits and their stability are discussed near Saturn). Some later general studies of the problem are presented in Dullin et al. (2002).

Of course, the natural question appears. Could such halo orbits survive in strong gravitational field near a compact object with additional magnetic field? Clearly, there are many, say "strong-filed" configuration, corresponding to the situation near the magnetized planets, i.e., a central spherically (axially) symmetric gravitational field and rotating dipole magnetic field. We can mention, e.g., neutron stars, and static or rotating black holes with plasma rings in the equatorial plane, as sources of the dipole magnetic fields. In this cases, exact investigations require knowledge of solutions of the Einstein–Maxwell equations, in order to described present magnetic (electric) and gravitational fields well. Naturally, the magnetic field can be considered to be the test field only, which is usually sufficient in many cases, and acceptable within the general relativistic approaches. On the other hand, there is well-known solution of the Einstein–Maxwell equations, describing the required field configuration. It is the Kerr–Newman solution, describing axially symmetric spacetimes of rotating and charged black holes (naked singularities), where the electromagnetic field is internally related to the spacetimes, originating from the rotating charged sources.

In the case of Kerr–Newman spacetimes, the answer for our question concerning the existence of halo orbits, has been partly found in de Felice (1979); Calvani et al. (1982), where the authors conclude that under some circumstances, the halo orbits do exist in Kerr–Newman spacetimes. Nevertheless, because of many input parameters characterizing the central object and particle motion itself, the detailed discussion of the halo orbits existence and their stability is not presented by those authors. Moreover, the later paper (Stuchlík and Hledík, 1998), dealing with a similar problem, i.e., with the stability of charged spherical shells in Kerr–Newman spacetimes, could suggest that the existence of the halo orbits can be restricted to the hypothetical naked-singularity spacetimes only, which holds for the stable configuration of the shells.

Our discussion of halo orbits existence is based on the inertial forces analysis of the charged test particle motion (Aguirregabiria et al., 1996), which, in combination with the standard approach based on the analysis of an 2D effective potential of the particle motion, gives understandable and semi-analytic discussible condition on the halo orbits existence. Note that in general the inertial forces formalism, defined in the general relativity in the framework of the so-called optical reference geometry (Abramowicz et al., 1995), turned out to be very effective in relativistic dynamics when dealing with problems concerning the circular motion (Kovář and Stuchlík, 2006, 2007).

2 KERR–NEWMAN SPACETIME

The Kerr–Newman spacetime is stationary and axially symmetric solution of the Einstein–Maxwell equations, with the Killing vector fields $\eta^i = \delta^i_t$ and $\xi^i = \delta^i_\phi$, related to the standard Boyer-Linquist coordinates (t, r, ϕ, θ). In the geometrical units ($c = G = 1$), the line element of the spacetime geometry takes the form (Misner et al., 1973)

$$\mathrm{d}s^2 = -\frac{\Delta}{\rho^2}(\mathrm{d}t - a\sin\theta\,\mathrm{d}\phi)^2 + \frac{\sin^2\theta}{\rho^2}[(r^2+a^2)\,\mathrm{d}\phi - a\,\mathrm{d}t]^2 + \frac{\rho^2}{\Delta}\,\mathrm{d}r^2 + \rho^2\,\mathrm{d}\theta^2\,, \qquad (1)$$

where

$$\Delta = r^2 - 2Mr + a^2 + e^2\,, \quad \rho^2 = r^2 + a^2\sin^2\theta\,, \qquad (2)$$

and M, a and e are the mass, angular momentum and charge parameters of the spacetime. As the standard practise is, we use the dimensionless quantities, such as $r \to r/M$, $a \to a/M, e \to e/M$, etc.

Pseudo-singularities of the solution (1), given by the relation $\Delta = 0$, determine positions of two black hole horizons when $a^2 + e^2 < 1$, coalescing for $a^2 + e^2 = 1$ at the radius $r = 1$, and vanishing for $a^2 + e^2 \geq 1$ when the naked singularities appear. Between the horizons, i.e., in the region where $\Delta < 0$, the particles are forced to move inward to the inner black-hole horizon. The spacetime is called dynamical in that region. On the other hand, both the remaining parts of the spacetime, i.e., above the outer horizon and under the inner horizon, are stationary, and called outer and inner stationary regions. The naked-singularity spacetimes are stationary everywhere.

The electromagnetic field associated to the Kerr–Newman spacetimes can be simply expressed by using the vector potential in the form

$$A = -\frac{er}{\rho^2}(\mathrm{d}t - a\sin^2\theta\,\mathrm{d}\phi)\,, \tag{3}$$

determining the electromagnetic field tensor $F_{ij} = A_{j,i} - A_{i,j}$. Its non-zero components read

$$F_{rt} = -F_{tr} = \frac{e(r^2 - a^2\cos^2\theta)}{\rho^4}\,, \tag{4}$$

$$F_{r\phi} = -F_{\phi r} = \frac{-ae\sin^2\theta(r^2 - a^2\cos^2\theta)}{\rho^4}\,, \tag{5}$$

$$F_{\theta t} = -F_{t\theta} = \frac{-a^2 er\sin 2\theta}{\rho^4}\,, \tag{6}$$

$$F_{\theta\phi} = -F_{\phi\theta} = \frac{aer\sin 2\theta(r^2 + a^2)}{\rho^4}\,. \tag{7}$$

3 EFFECTIVE POTENTIAL

In any electromagnetic field, the "super Hamiltonian" for the motion of a test particle of charge q and mass m, parametrized by the affine parameter $\lambda = \tau/m$ (τ is the proper time), reads (Misner et al., 1973)

$$\mathcal{H} = \tfrac{1}{2}g^{ij}(\pi_i - qA_i)(\pi_j - qA_j)\,, \tag{8}$$

where π_i is the generalized 4-momentum. The first Hamilton equation implies $dx^i/d\lambda = \pi^i - qA^i \equiv p^i$. The second Hamilton equation ensures that the momenta

$$\pi_t = p_t + qA_t \equiv -E\,, \tag{9}$$

$$\pi_\phi = p_\phi + qA_\phi \equiv L \tag{10}$$

are conserved.

The effective potential for the motion of a particle with the specific charge $\tilde{q} = q/m$, deduced from the Hamiltonian (8), or from the Carter equations (Carter, 1968), takes the form (Misner et al., 1973)

$$W_{\mathrm{eff}} = \frac{\beta + \sqrt{\beta^2 - \alpha\gamma}}{\alpha}\,, \tag{11}$$

where

$$\alpha = (r^2 + a^2)^2 - \Delta a^2 \sin^2\theta\,, \tag{12}$$
$$\beta = (\tilde{L}a + \tilde{q}er)(r^2 + a^2) - \tilde{L}a\Delta\,, \tag{13}$$
$$\gamma = (\tilde{L}a + \tilde{q}er)^2 - \Delta\tilde{L}^2/\sin^2\theta - \Delta\rho^2 \tag{14}$$

and $\tilde{L} = L/m$ is the conserved specific angular momentum (axial component).

4 PROJECTION OF LORENTZ EQUATION AND INERTIAL FORCES FORMALISM

Investigation of the effective potential behaviour is though to be the standard routine for the circular orbits determination. However, in the Kerr–Newman spacetime, this "method of effective potential" itself does not seem to be convenient and effective enough for investigation of the charged particle motion. It is helpful to combine it with the "forces approach" (Abramowicz et al., 1988).[1] We define the inertial and real forces by projecting the Lorentz equation of motion for a particle with 4-velocity u^i (Abramowicz et al., 1995; Aguirregabiria et al., 1996)

$$mu^k\nabla_k u_j = qF_{jk}u^k\,, \tag{15}$$

into the space (hypersurface) of the zero angular momentum (ZAMO) observers (in the locally non-rotating frames), eliminating as much as possible the influence of the rotational effects of the spacetime (Bardeen et al., 1972).

We start with the decomposition of the particle 4-velocity into the form

$$u^i = \gamma(n^i + v\tau^i)\,, \tag{16}$$

where the 4-velocity field n^i (here considered to be the 4-velocity of the ZAMO) satisfies the conditions

$$n^k n_k = -1\,, \quad n^i\nabla_i n_k = \nabla_k\Phi\,, \quad n_{[i}\nabla_j n_{k]} = 0\,, \tag{17}$$

and the vector τ^i is the unit spacelike vector orthogonal to it, along which the spatial 3-velocity with magnitude v is aligned. The 4-velocity field n^i can be chosen in the form

$$n^i = \mathrm{e}^{-\Phi}\iota^i\,, \quad \Phi = \tfrac{1}{2}\ln(-\iota^i\iota_i)\,, \tag{18}$$

[1] It was shown that the force analysis of circular geodesics seems to be much more effective and straightforward in comparison with the effective potential approach (Kovář and Stuchlík, 2007).

thus it corresponds to 4-velocity field of stationary observers (here ZAMO), parallel to a timelike vector field ι^i. Now, we can express the left-hand side of the Lorentz equation (15) in the form

$$ma_k = m[\gamma^2\nabla_k\Phi + \gamma^2 v(n^i\nabla_i\tau_k + \tau^i\nabla_i n_k) + \gamma^2 v^2\tau^i\nabla_i\tau_k + (v\gamma)^{\cdot}\tau_k + \dot{\gamma}n_k]\,, \tag{19}$$

where $(v\gamma)^{\cdot} = u^i\nabla_i(\gamma v)$. By using the projection tensor h^i_k related to the directly projected geometry

$$h_{ik} = g_{ik} + n_i n_k\,, \tag{20}$$

we obtain the uniquely decomposed 4-force (19) in the form

$$ma^{\perp}_j = mh^k_j a_k = -G_j - Z_j - C_j - E_j\,, \tag{21}$$

where

$$G_j = -m\nabla_j\Phi\,, \tag{22}$$
$$Z_j = -m(\gamma v)^2\tilde{\tau}^i\tilde{\nabla}_i\tilde{\tau}_j\,, \tag{23}$$
$$C_j = -m\gamma^2 v X_j\,, \tag{24}$$
$$L_j = -m\dot{V}\tilde{\tau}_j \tag{25}$$

can be interpreted as the gravitational, centrifugal, Coriolis and Euler inertial forces (Abramowicz et al., 1995). In the above relations $X_j = n^i(\nabla_i\tau_j - \nabla_j\tau_i)$ and $\dot{V} = -u^i\nabla_i(\iota^k u_k v)$. The vector $\tilde{\tau}^i = e^{\Phi}\tau^i$, with its covariant form $\tilde{\tau}_i = e^{-\Phi}\tau_i$, is the spacelike unit vector parallel to τ^i in the so-called optical reference geometry, defined by the relation

$$\tilde{h}_{ik} = \mathrm{e}^{-2\Phi}h_{ik}\,. \tag{26}$$

Projecting the right-hand side of the Lorentz equation (15), we obtain the equation

$$qh^i_j F_{ik}u^k = E_j + M_j\,, \tag{27}$$

where

$$E_j = q\gamma F_{jk}n^j\,, \tag{28}$$
$$M_j = q\gamma v(F_{jk}\tau^k + n_j F_{kl}n^k\tau^l) \tag{29}$$

are the electric and magnetic forces, respectively.

4.1 Circular motion in Kerr–Newman spacetimes

In the Kerr–Newman spacetimes, it is convenient to consider n^i to be 4-velocity ZAMO observers, i.e.,

$$n^i = \mathrm{e}^{-\Phi}(\eta^i + \Omega_{\mathrm{ZAMO}}\xi^i)\,, \tag{30}$$
$$\Phi = \frac{1}{2}\ln\left[-(\eta^i + \Omega_{\mathrm{ZAMO}}\xi^i)(\eta_i + \Omega_{\mathrm{ZAMO}}\xi_i)\right]\,, \tag{31}$$

where $\Omega_{\mathrm{ZAMO}} = -\eta^i \xi_i / \xi^j \xi_j$. Considering a uniform circular motion of particle at a constant radius and a constant latitude, i.e.,

$$\tau^i = (\xi^k \xi_k)^{-1/2} \, \xi^i \,, \tag{32}$$

the mass and velocity independent parts of the non-zero radial and latitudinal components of the forces (22)–(25) take in the Kerr–Newman spacetimes the form:

$$\mathcal{G}_r = \frac{-4r}{\mu} - \frac{(a^2+r^2)[(r-1)(a^2+r^2) - 2r\Delta]}{\Delta\nu} + \frac{r}{\rho^2} \,, \tag{33}$$

$$\mathcal{Z}_r = \frac{-4r}{\mu} - \frac{2(a^2+r^2)[(r-1)(a^2+r^2) - 2r\Delta]}{\Delta\nu} + \frac{r-1}{\Delta} \,, \tag{34}$$

$$\mathcal{C}_r = 2a \sin\theta \left\{ \frac{2(a^2+r^2)[(2r-1)(a^2+r^2) - a^2(r-1)\sin^2\theta]}{\mu\nu\sqrt{\Delta}} - \frac{r(3a^2+4r^2+a^2\cos 2\theta)\Delta}{\mu\nu\sqrt{\Delta}} \right\} \,, \tag{35}$$

$$\mathcal{G}_\theta = \frac{1}{2} a^2 \sin 2\theta \left(\frac{4}{\mu} - \frac{\Delta}{\nu} - \frac{1}{\rho^2} \right) \,, \tag{36}$$

$$\mathcal{Z}_\theta = \cot\theta + \frac{2a^2 \sin 2\theta}{\mu} - \frac{a^2 \sin 2\theta \Delta}{\nu} \,, \tag{37}$$

$$\mathcal{C}_\theta = \frac{4a^3 \cos\theta \sin^2\theta (\Delta - a^2 - r^2)\sqrt{\Delta}}{\mu\nu} \,, \tag{38}$$

where

$$\mu = a^2 + 2r^2 + a^2 \cos 2\theta \,, \quad \nu = (a^2+r^2)^2 - \Delta a^2 \sin^2\theta \,. \tag{39}$$

The Euler force L_k vanishes because of the uniformity of the motion. The charge and velocity independent parts of the non-zero electric and magnetic force components (28)–(29) are given by the relations

$$\mathcal{E}_r = \frac{e(a^2+r^2)(r^2 - a^2\cos^2\theta)}{\rho^3\sqrt{\nu\Delta}} \,, \tag{40}$$

$$\mathcal{M}_r = \frac{ae \sin\theta (a^2\cos^2\theta - r^2)}{\rho^3\sqrt{\nu}} \,, \tag{41}$$

$$\mathcal{E}_\theta = \frac{-2a^2 er\sqrt{\Delta}\sin 2\theta}{\mu\rho\sqrt{\nu}} \,, \tag{42}$$

$$\mathcal{M}_\theta = \frac{2aer\cos\theta(r^2+a^2)}{\rho^3\sqrt{\nu}} \,. \tag{43}$$

5 HALO ORBITS EXISTENCE AND STABILITY

For a uniform circular motion of a particle at constant radius and latitude, and with the velocity v (measured by ZAMO), we can write two force equations

$$-\mathcal{G}_r - (\gamma v)^2 \mathcal{Z}_r - \gamma^2 v \mathcal{C}_r = \tilde{q}\gamma(\mathcal{E}_r + v\mathcal{M}_r)\,, \tag{44}$$

$$-\mathcal{G}_\theta - (\gamma v)^2 \mathcal{Z}_\theta - \gamma^2 v \mathcal{C}_\theta = \tilde{q}\gamma(\mathcal{E}_\theta + v\mathcal{M}_\theta)\,, \tag{45}$$

where the Lorentz factor $\gamma = (1 - v^2)^{1/2}$.

Eliminating $\tilde{q}$ from Eqs (44), (45) and assuming that $0 < \theta < \pi/2$, i.e., omitting stationary equilibrium points on the axis of symmetry (Bičák et al., 1989) and circular orbits in the equatorial plane (Balek et al., 1989), we obtain a cubic equation

$$Av^3 + Bv^2 + Cv + D = 0\,, \tag{46}$$

where

$$A = \mathcal{M}_\theta(\mathcal{G}_r - \mathcal{Z}_r) + \mathcal{M}_r(\mathcal{Z}_\theta - \mathcal{G}_\theta)\,, \tag{47}$$

$$B = \mathcal{E}_r(\mathcal{G}_r - \mathcal{Z}_r) + \mathcal{E}_r(\mathcal{Z}_\theta - \mathcal{G}_\theta) + \mathcal{C}_\theta\mathcal{M}_r - \mathcal{C}_r\mathcal{M}_\theta\,, \tag{48}$$

$$C = \mathcal{C}_\theta\mathcal{E}_r - \mathcal{C}_r\mathcal{E}_\theta + \mathcal{G}_\theta\mathcal{M}_r - \mathcal{G}_r\mathcal{M}_\theta\,, \tag{49}$$

$$D = \mathcal{E}_r\mathcal{G}_\theta - \mathcal{E}_\theta\mathcal{G}_r\,. \tag{50}$$

This gives three, in general complex, solutions $v_{\rm I}(r, \theta; a, e)$, $v_{\rm II}(r, \theta; a, e)$ and $v_{\rm III}(r, \theta; a, e)$ for possible orbital velocities of charged particles moving along the halo orbits. Although the three roots can be expressed in analytical form, we do not present them here because of their complexity, and perform further a numerical analysis.

Considering the velocity candidates $v_{\rm I}$, $v_{\rm II}$ and $v_{\rm III}$ to be parameterized by the spin a and latitude θ, we can investigate the validity of the condition for them to be the relevant velocity, i.e., $v_i \in R$ and $-1 < v_i < 1$ ($i = {\rm I}, {\rm II}, {\rm III}$), in the plane $(r \times e)$[2]. Our numerical analysis of v_i confirms the existence of halo orbits in the Kerr–Newman naked-singularity spacetimes as well as in both the inner and outer stationary regions of the black-hole spacetimes (see Fig. 1).

We conclude our study of halo orbits existence by the discussion of their stability, namely by seeking for stable circular orbits. which remain locked in the region entirely outside the equatorial plane. For this purpose, we can use Eq. (44) and express the specific charge $\tilde{q}_h$ of the particle moving along the expected halo orbit at velocity v by the relation

$$\tilde{q}_h = \frac{\mathcal{G}_r(v^2 - 1) - v(\mathcal{C}_r + v\mathcal{Z}_r)}{(\mathcal{E}_r + v\mathcal{M}_r)\sqrt{1 - v^2}}\,, \tag{51}$$

The condition (51) provides three possible values $\tilde{q}_{h,i}$ related to v_i. By using relation (10), the metric coefficients (1) and the 4-velocity decomposition (16), we can write for the specific angular momentum of particles at halo orbits

$$\tilde{L}_h = \gamma v\sqrt{g_{\phi\phi}} + \tilde{q}_h A_\phi\,, \tag{52}$$

[2] The natural parameterization a and e, and following investigation of conditions in the plane $(r \times \theta)$ is not so illustrative.

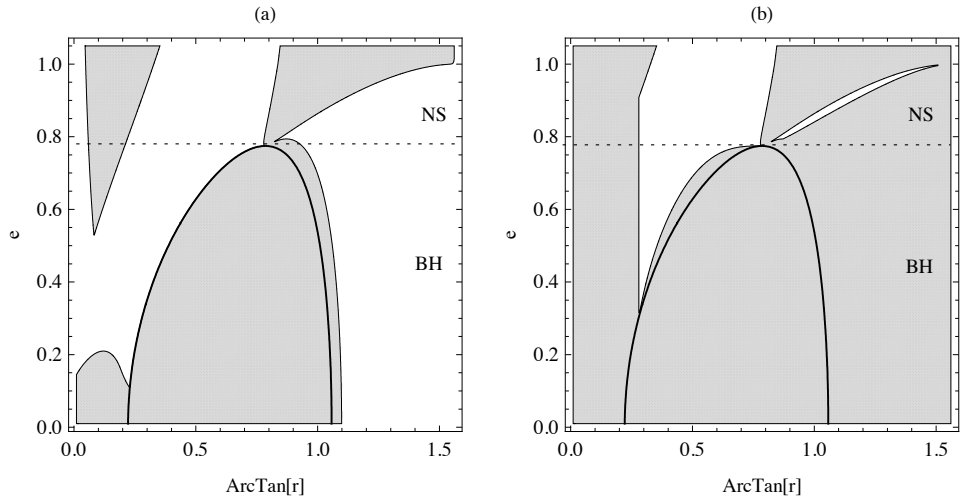

Figure 1. Existence of halo orbits in Kerr–Newman black-hole (BH) and naked-singularity (NS) spacetimes. Positions of horizons are denoted by the thick curve. *Left:* White areas correspond to the regions where the root v_i is real and $-1 < v_i < 1$, i.e., where the halo orbits occur. We present here result of investigation of the typical (a) v_{I} behaviour ($a^2 = 0.4$, $\theta = 1.1$), (c) v_{II} behaviour ($a^2 = 0.7$, $\theta = 1.4$), and (e) v_{III} behaviour ($a^2 = 0.4$, $\theta = 0.15$), allowing the existence of halo orbits in the NS spacetimes as well as in the BH spacetimes in the inner and outer stationary regions. *Right:* White areas correspond to the regions where the stationary points of the effective potential W_{eff}, corresponding to the values of v, are minima, i.e., where the halo orbits are stable. We present here result of investigation of the typical (b) $W_{\mathrm{eff\text{-}I}}$ behaviour ($a^2 = 0.4$, $\theta = 1.1$), related to the values of v_{I} (see part (a) of figure), (d) $W_{\mathrm{eff\text{-}II}}$ behaviour ($a^2 = 0.7, \theta = 1.4$), related to the values of v_{II} (see part (c) of figure), and (f) $W_{\mathrm{eff\text{-}III}}$ behaviour ($a^2 = 0.4, \theta = 0.15$), related to the values of v_{III} (see part (e) of figure), allowing the existence of stable halo orbits only in the NS spacetimes and in the inner stationary region of the BH spacetimes.

obtaining three possible values $\tilde{L}_{h,i}$ related to $\tilde{q}_{h,i}$ and v_i.

The stable halo orbits must satisfy the conditions of effective potential minima, i.e.,

$$\partial_r^2 W_{\mathrm{eff}}(r, \theta; a, e, \tilde{L} = \tilde{L}_h, \tilde{q} = \tilde{q}_h) > 0\,, \tag{53}$$

$$\partial_\theta^2 W_{\mathrm{eff}}(r, \theta; a, e, \tilde{L} = \tilde{L}_h, \tilde{q} = \tilde{q}_h) > 0\,, \tag{54}$$

which we analyze in a numerical way in the plane $(r \times e)$, considering the parametrization by a and θ, for all three pairs of $\tilde{L}_{h,i}$ and $\tilde{q}_{h,i}$. Going through a large number of related $(r \times e)$ plots for combinations of a and θ in the intervals $0 < a < 1$ and $0 < \theta < \pi/2$ (see Fig. 1), we have not found any combination of parameters allowing the existence of stable halo orbits in the outer stationary region of the Kerr–Newman black-hole spacetimes[3]. Because

[3] From the conceptional point of view, it is certainly better to discuss the conditions for the stable halo orbits (53)–(54) having the specific angular momentum $\tilde{L}_h$ and charge $\tilde{q}_h$ available from the conditions $\partial_r W_{\mathrm{eff}} = 0$

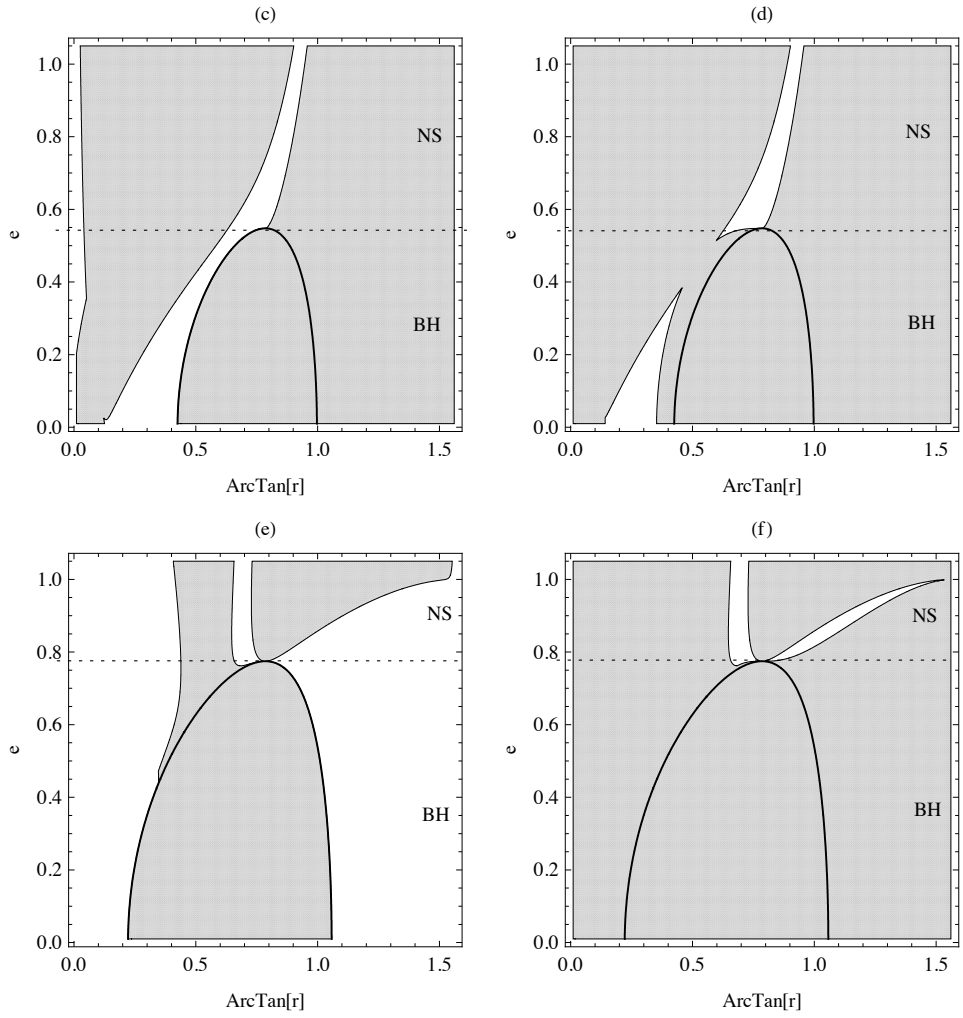

Figure 1. Continued from page 132.

of this, we presume to state that there are no such orbits. On the other hand, the inner stationary region of the black-hole spacetimes and the naked-singularity spacetimes do exhibit stable halo orbits. We give illustrative cases of the behaviour of the effective potential for motion of charged particles in Figs 2–3.

and $\partial_\theta W_{\rm eff} = 0$, which are equivalent to the force equations (44)–(45). But it seems that it is not possible to express the quantities $\tilde{L}_h$ and $\tilde{q}_h$ so easy as from the force equations, i.e., by using only three, in general, complex, but analytical roots for $\tilde{L}_h$ and related three roots for $\tilde{q}_h$. Because of this, there are more additional cases to be discussed in the following numerical routines.

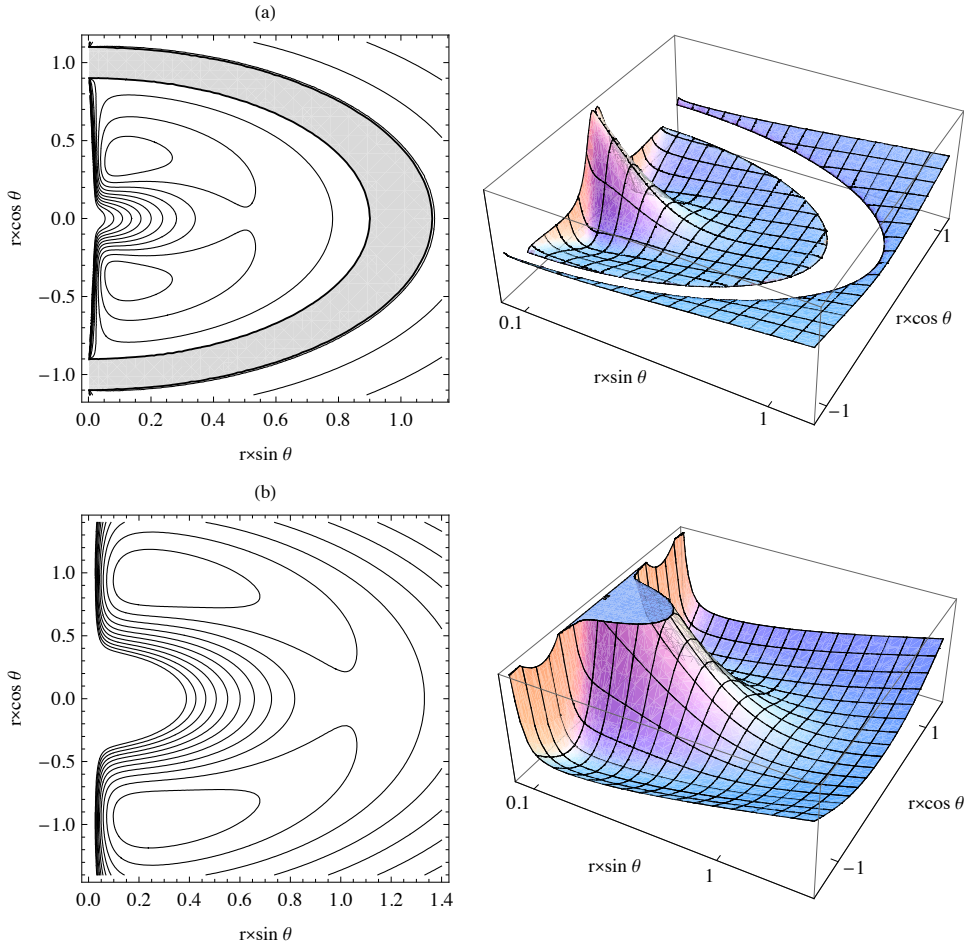

Figure 2. Effective potential $W_{\rm eff}$ and its contours for motion of charged particles with $\tilde{L} = 1$ and $\tilde{q} = -5$ (in geometric units) in the Kerr–Newman (a) black-hole spacetime with $a^2 = 0.04$ and $e^2 = 0.95$; (b) naked-singularity spacetime with $a^2 = 0.6$ and $e^2 = 0.95$. Positions of stable halo orbits correspond to the potential minima. Concomitant equatorial circular orbit, stable in radial direction, corresponds to the saddle point in the equatorial plane. The effective potential $W_{\rm eff}$ is not relevant in the region between the event horizons (gray), where $\Delta < 0$. Clearly, the stable halo orbits located under the inner horizon become accessible after transforming into the naked-singularity spacetime.

6 CONCLUSIONS

As expected, our study has confirmed the results of (Calvani et al., 1982). The halo orbits can appear in strong gravitational fields in the vicinity of compact objects endowed with an additional magnetic fields of dipole character, such as Kerr–Newman black holes or naked

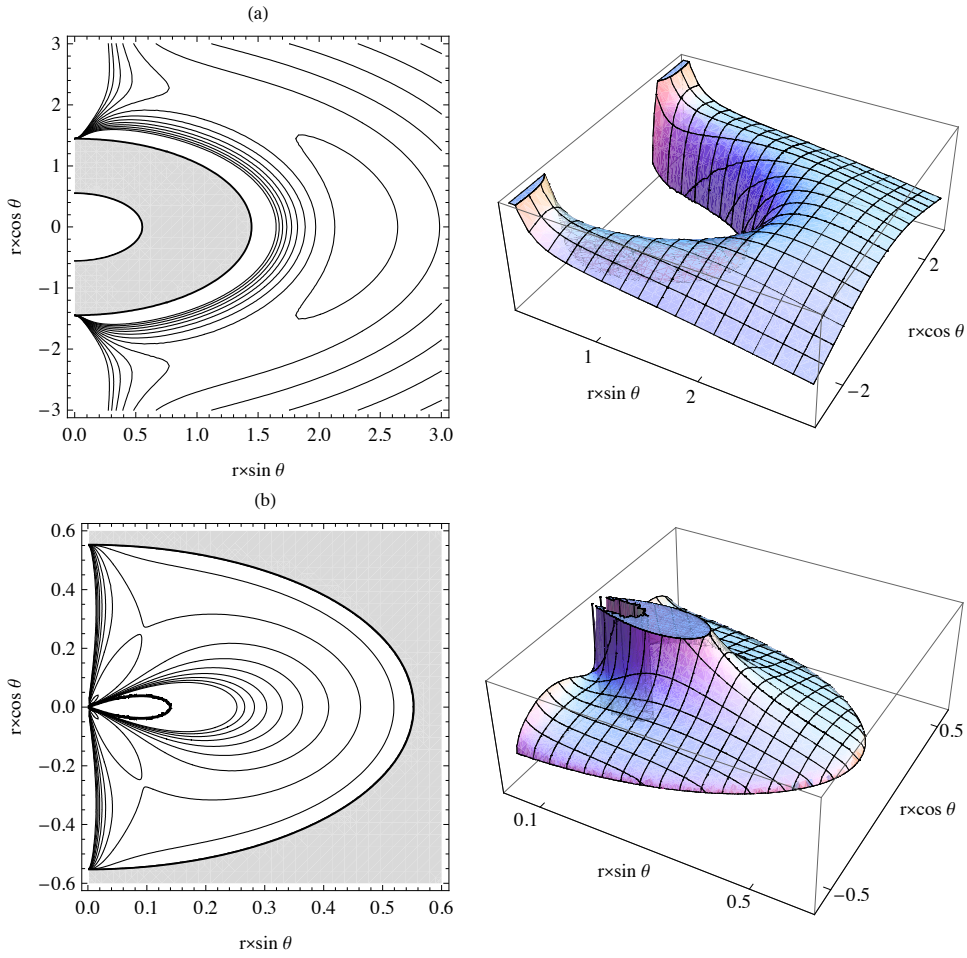

Figure 3. Effective potential $W_{\rm eff}$ and its contours for motion of charged particles with $\tilde{L} = 0.1$ and $\tilde{q} = 2.9$ (in geometric units) in the Kerr–Newman black-hole spacetime with $a^2 = 0.5$ and $e^2 = 0.3$, in the regions (a) above the outer event horizon; (b) under the inner event horizon. Positions of unstable stable halo orbits correspond to the saddle points of the potential. Concomitant equatorial unstable circular orbit corresponds to the potential maximum in the equatorial plane. The effective potential $W_{\rm eff}$ is not relevant in the region between the event horizons (gray), where $\Delta < 0$.

singularities. In addition, our investigation suggests that there are no stable halo orbits in the field of Kerr–Newman black holes above the outer horizon. It seems that the connection of the electromagnetic field with the spin of the spacetime causes impossibility of the halo orbits stability outside the black hole, and only unstable halo orbits are allowed there. On the other hand, the combinations of spacetime parameters allow existence of stable halo orbits under the inner horizon of black holes and in the naked-singularity spacetimes. These

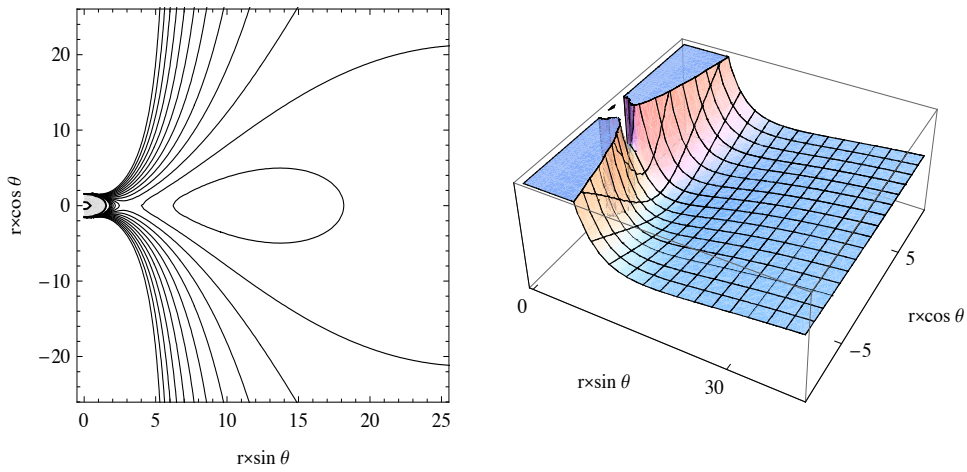

Figure 4. Effective potential $W_{\rm eff}$ and its contours for motion of charged particles with $\tilde{L} = 8$ and $\tilde{q} = -5$ (in geometric units) in the region above the outer event horizon of the Kerr–Newman black-hole spacetime with $a^2 = 0.2$ and $e^2 = 0.5$. The potential minimum corresponds to the stable equatorial circular orbit. The effective potential $W_{\rm eff}$ is not relevant in the region between the event horizons (gray), where $\Delta < 0$. In all numerically tested cases, no stable halo orbits have been found, only the stable equatorial circular orbits were confirmed.

conclusions of our semi-analytic analysis, are consistent with the results of pure analytic study of the situation on the axis of symmetry, where the circular motion degenerates to the equilibrium positions of the particle. There, only unstable positions exist above the outer event horizon. The stable positions occur only under the inner horizon or in the naked-singularity spacetimes (Bičák et al., 1989). Thus, in the Kerr–Newman black-hole spacetimes, the only astrophysically relevant stable circular orbits at constant radius and latitude are those in the equatorial plane (Dadhich and Kale, 1977) as depicted in Fig. 4.

High frequency kilohertz quasiperiodic oscillations (QPOs) observed in some microquasars and binary systems with compact stars are frequently explained by variety of models based on the equatorial quasicircular motion, with characteristic orbital Keplerian and epicyclic frequencies. Most promising seems to be the relativistic precession model (Stella and Vietri, 1999), and the orbital resonance model (Kluźniak and Abramowicz, 2001; Aliev and Galtsov, 1981) or its generalization to the orbital multiresonant model (Stuchlík and Kotrlová, 2007; Stuchlík et al., 2007c) for both binary systems with black holes (microquasars) and neutron stars; in the case of near-extreme Kerr black-hole candidates (e.g., well known GRS 1915+105 microquasar) the complex high frequency QPOs patterns could be explained using the extended resonance model with the so-called hump-induced oscillations, additional to the orbital epicyclic oscillations (Stuchlík et al., 2007b,a). The orbital resonance model seems to be relevant even for the intermediate and galactic nuclei (Sgr A*) black-hole accretion disk (Török, 2005b,a; Kluźniak et al., 2007). Using the orbital resonance models, black hole parameters, especially, the spin could be determined.

The halo orbits in the magnetic field of neutron stars and black holes (Kovář et al., 2007) could in principle be related to the oscillatory motion with "halo" radial and vertical frequencies, which could be considered as complementary model of the QPOs observed in the binary system of neutron stars and microquasars.

ACKNOWLEDGEMENTS

This work was supported by the Czech grants MSM 4781305903, LC06014 and GAČR 202/06/0041. V. K. thanks the Czech Science Foundation (GAČR 205/07/0052).

REFERENCES

Abramowicz, M. A., Carter, B. and Lasota, J. (1988), Optical reference geometry for stationary and static dynamics, *Gen. Relativity Gravitation*, **20**, p. 1173.

Abramowicz, M. A., Nurowski, P. and Wex, N. (1995), Optical reference geometry for stationary and axially symmetric spacetimes, *Classical Quantum Gravity*, **12**(6), pp. 1467–1472, URL `http://www.iop.org/EJ/abstract/0264-9381/12/6/012`.

Aguirregabiria, J. M., Chamorro, A., Nayak, K. R., Suinaga, J. and Vishveshwara, C. V. (1996), Equilibrium of a charged test particle in the Kerr–Newman spacetime: force analysis, *Classical Quantum Gravity*, **13**(8), pp. 2179–2189, URL `http://www.iop.org/EJ/abstract/0264-9381/13/8/013`.

Aliev, A. N. and Galtsov, D. V. (1981), Radiation from relativistic particles in non-geodesic motion in a strong gravitational field, *Gen. Relativity Gravitation*, **13**, pp. 899–912.

Balek, V., Bičák, J. and Stuchlík, Z. (1989), The motion of the charged particles in the field of rotating charged black holes and naked singularities – II. The motion in the equatorial plane, *Bull. Astronom. Inst. Czechoslovakia*, **40**(3), pp. 133–165.

Bardeen, J. M., Press, W. H. and Teukolsky, S. A. (1972), Rotating black holes: locally nonrotating frames, energy extraction, and scalar synchrotron radiation, *Astrophys. J.*, **178**, pp. 347–369.

Bičák, J., Stuchlík, Z. and Balek, V. (1989), The motion of charged particles in the field of rotating charged black holes and naked singularities – I. The general features of the radial motion and the motion along the axis of symmetry, *Bull. Astronom. Inst. Czechoslovakia*, **40**(2), pp. 65–92.

Calvani, M., de Felice, F., Fabbri, R. and Turolla, R. (1982), Off-equatorial orbits in the Kerr–Newman space-time, *Nuovo Cimento B*, **67**, p. 1.

Carter, B. (1968), Global Structure of the Kerr Family of Gravitational Fields, *Phys. Rev.*, **174**(5), pp. 1559–1571.

Dadhich, N. and Kale, P. P. (1977), Equatorial circular geodesics in the Kerr–Newman geometry, *J. Math. Phys.*, **18**, pp. 1727–1728.

de Felice, F. (1979), On the non-existence of non-equatorial circular geodesics with constant latitude in the Kerr metric, *Phys. Lett. A*, **69**, p. 307.

Dullin, H. R., Horányi, M. and Howard, J. E. (2002), *Physica D*, **171**, pp. 178–195.

Howard, J. E., Horányi, M. and Stewart, G. R. (1999), *Phys. Rev. Lett.*, **83**(20), p. 3993.

Johnston, M. and Ruffini, R. (1974), Generalized Wilkins effect and selected orbits in a Kerr–Newman geometry, *Phys. Rev. D*, **10**, p. 2324.

Karas, V. and Vokrouhlický, D. (1991), Dynamics of charged particles near a black hole in a magnetic field, *J. Physique*, **1**, p. 1005.

Kluźniak, W. and Abramowicz, M. A. (2001), Strong-Field Gravity and Orbital Resonance in Black Holes and Neutron Stars – kHz Quasi-Periodic Oscillations (QPO), *Acta Phys. Polon. B*, **32**, pp. 3605–3612, URL `http://th-www.if.uj.edu.pl/acta/vol32/abs/v32p3605.htm`.

Kluźniak, W., Abramowicz, M. A., Bursa, M. and Török, G. (2007), QPOs and resonance in accretion disks, *Rev. Mexicana Astronom. Astrofís. and (Serie de Conferencias)*, **27**, pp. 18–25.

Kovář, J. and Stuchlík, Z. (2006), Forces in Kerr space-times with a repulsive cosmological constant, *Internat. J. Modern Phys. A*, **21**, pp. 4869–4897, arXiv: `gr-qc/0611152`.

Kovář, J. and Stuchlík, Z. (2007), Optical reference geometry and inertial forces in Kerr–de Sitter spacetimes, *Classical Quantum Gravity*, **24**, pp. 565–594.

Kovář, J., Stuchlík, Z. and Karas, V. (2007), Off-equatorial orbits in strong gravitational fields near compact objects, *being reviewed in Phys. Rev. D*.

Misner, C. W., Thorne, K. S. and Wheeler, J. A. (1973), *Gravitation*, W. H. Freeman and Co, New York, San Francisco.

Prasanna, A. R. (1980), General-relativistic analysis of charged-particle motion in electromagnetic fields surrounding black holes, *Riv. Nuovo Cimento*, **3**, p. 1.

Stella, L. and Vietri, M. (1999), kHz Quasiperiodic Oscillations in Low-Mass X-Ray Binaries as Probes of General Relativity in the Strong-Field Regime, *Phys. Rev. Lett.*, **82**(1), pp. 17–20.

Stuchlík, Z., Bičák, J. and Balek, V. (1999), The shell of incoherent charged matter falling onto a charged rotating black hole, *Gen. Relativity Gravitation*, **31**(1), pp. 53–71, ISSN 0001-7701.

Stuchlík, Z. and Hledík, S. (1998), Stationary spherical shells around Kerr–Newman naked singularities, *Acta Phys. Slovaca*, **48**(5), pp. 549–562, ISSN 0323-0465/98.

Stuchlík, Z. and Kotrlová, A. (2007), Orbital resonance model of QPOs in braneworld Kerr black hole spacetimes, pp. 323–361, this volume.

Stuchlík, Z., Slaný, P. and Török, G. (2007a), Humpy LNRF-velocity profiles in accretion discs orbiting almost extreme Kerr black holes – A possible relation to quasi-periodic oscillations, *Astronomy and Astrophysics*, **463**(3), pp. 807–816, arXiv: `astro-ph/0612439`.

Stuchlík, Z., Slaný, P. and Török, G. (2007b), LNRF-velocity hump-induced oscillations of a Keplerian disc orbiting near-extreme Kerr black hole: A possible explanation of high-frequency QPOs in GRS 1915+105, *Astronomy and Astrophysics*, **470**(2), pp. 401–404, arXiv: `0704.1252v2`.

Stuchlík, Z., Török, G. and Bakala, P. (2007c), On a multi-resonant origin of high frequency quasiperiodic oscillations in the neutron-star X-ray binary 4U 1636−53, submitted to Astronomy and Astrophysics, arXiv: `0704.2318`.

Török, G. (2005a), A possible 3 : 2 orbital epicyclic resonance in QPO frequencies of Sgr A*, *Astronomy and Astrophysics*, **440**(1), pp. 1–4, arXiv: `astro-ph/0412500`.

Török, G. (2005b), QPOs in microquasars and Sgr A*: measuring the black hole spin, *Astronom. Nachr.*, **326**(9), pp. 856–860, arXiv: `astro-ph/0510669`.

Vokrouhlický, D. and Karas, V. (1991), Motion of charged particles around a black hole in a magnetic field, *Astronomy and Astrophysics*, **243**, p. 165.

Proceedings of *RAGtime 8/9, 15–19/19–21 September, 2006/2007, Hradec nad Moravicí, Opava, Czech Republic*
S. Hledík and Z. Stuchlík, editors, Silesian University in Opava, 2007, pp. 139–149

Geodesic motion and test fields in the background of higher-dimensional black holes[1]

Pavel Krtouš

Institute of Theoretical Physics, Faculty of Mathematics and Physics, Charles University in Prague,
V Holešovičkách 2, CZ-180 00 Praha 8 – Holešovice, Czech Republic
Pavel.Krtous@utf.mff.cuni.cz

ABSTRACT
In a series of papers, we recently investigated properties of geodesic motion and test scalar fields in the background of generic rotating higher-dimensional black holes. In this contribution, we briefly discuss the integrability of geodesic motion, the construction of constants of motion, and the relation to the separability of the Hamilton–Jacobi equation. We also present a class of algebraically special test electromagnetic fields which generalize the electromagnetic field of a charged black hole in four dimensions. It will be, however, shown that in higher dimensions such fields cannot be easily modified in such a way that they would satisfy full Maxwell––Einstein equations.

Keywords: Black holes – higher dimensions – geodesic motion – integrability and separability – test fields

1 INTRODUCTION

Spacetimes of higher dimensions ($D > 4$) have become much studied as a result of their role in unification theories, such as the string/M theory. One important class of such spacetimes is a sequence of higher-dimensional black-hole metrics of greater and greater generality that have been discovered over the years.

The first such higher-dimensional black-hole spacetime was the metric for a nonrotating black hole in $D > 4$ (the generalization of the 1916 Schwarzschild solution), found in Tangherlini (1963). Next was the metric for a rotating black hole in higher dimensions (the generalization of the 1963 Kerr metric in four dimensions), discovered in Myers and Perry (1986) in the case of zero cosmological constant. Then in 1999 Hawking, Hunter and Taylor-Robinson (Hawking et al., 1999) found the general $D = 5$ version of the $D = 4$ rotating black hole with a cosmological constant (called also the Kerr–(anti-)de Sitter metric). In 2004 Gibbons, Lü, Page and Pope (Gibbons et al., 2004, 2005) discovered the general

[1] This contribution is a review of the results which have been obtained together with Don N. Page, Valeri Frolov, David Kubizňák, and Muraari Vasudevan last and this year and have been published in the papers (Page et al., 2007; Frolov et al., 2007; Krtouš et al., 2007a,b; Krtouš, 2007).

978-80-7248-419-5

Kerr–de Sitter metrics in all higher dimensions, and in 2006 Chen, Lü and Pope (Chen et al., 2006) put these into a simple form similar to that of Carter (1968a,b) and were able to add a NUT parameter (though not electric charge) to get the general Kerr–NUT–(a)dS metrics for all D. The properties of these metrics have been extensively studied in recent years. In the following, we give overview of some of these results.

One of the key spacetime properties is the nature of the corresponding geodesic motion. In our papers (Page et al., 2007; Krtouš et al., 2007b) we have found a full set of D conserved quantities for geodesic motion and demonstrated that this motion is completely integrable. The constants of motion have been constructed with help of the principal Killing–Yano tensor – an important geometrical structure that has been thoroughly investigated in (Krtouš et al., 2007a).

Closely related to the integrability of the geodesic motion is the separability of the Hamilton–Jacobi equation. It was proved, together with the separability of the Klein–Gordon equation (in Frolov et al., 2007).

Finally, we will discuss a test electromagnetic field specially aligned with the high-dimensional black hole background which was found in (Krtouš 2007; cf. also Chen and Lü 2007) and a no-go theorem for "charging" the rotating black hole in higher dimensions with the electromagnetic field of this type. Let us note that another no-go theorem for "accelerating" black holes in a way analogous to the four dimensional case has been presented in Kubizňák and Krtouš (2007).

In the following sections, we will revisit these topics in more detail. For simplicity, we will concentrate on the case of even dimensions. However, all discussed properties are valid also in odd dimensions – see the originals papers for corresponding expressions and modifications.

2 METRIC OF A GENERALLY ROTATING BLACK HOLE IN HIGHER DIMENSIONS

The metric of the general Kerr–NUT–(anti-)de Sitter spacetime in $D = 2n$ dimensions discovered by Chen et al. (2006) can be written

$$\boldsymbol{g} = \sum_{\mu=1}^{n} \left[\frac{U_\mu}{X_\mu}\, \boldsymbol{d}x_\mu^2 + \frac{X_\mu}{U_\mu} \left(\sum_{k=0}^{n-1} A_\mu^{(k)}\, \boldsymbol{d}\psi_k \right)^2 \right] . \tag{1}$$

Here, the coordinates x_μ ($\mu = 1, \dots, n$) correspond to (Wick rotated) radial and latitudinal directions, ψ_k ($k = 0, \dots, n-1$) to temporal and azimuthal directions. The metric functions U_μ, $A_\mu^{(k)}$, together with auxiliary functions $A^{(k)}$, are given by

$$U_\mu = \prod_{\substack{\nu=1 \\ \nu\neq\mu}}^{n} \left(x_\nu^2 - x_\mu^2 \right) , \quad A_\mu^{(k)} = \sum_{\substack{\nu_1,\dots,\nu_k=1 \\ \nu_1<\dots<\nu_k,\, \nu_i\neq\mu}}^{n} x_{\nu_1}^2 \cdots x_{\nu_k}^2 , \quad A^{(k)} = \sum_{\substack{\nu_1,\dots,\nu_k=1 \\ \nu_1<\dots<\nu_k}}^{n} x_{\nu_1}^2 \cdots x_{\nu_k}^2 . \tag{2}$$

Each of the remaining metric functions X_μ is a function of a single variable x_μ and their exact form is given by the Einstein equations. However, most of the properties discussed below are independent of the exact form of the metric functions X_μ.

It is useful to rewrite the metric in a diagonal form

$$\boldsymbol{g} = \sum_{\mu=1}^{n} (\boldsymbol{e}^{\mu}\boldsymbol{e}^{\mu} + \boldsymbol{e}^{\hat{\mu}}\boldsymbol{e}^{\hat{\mu}}) \tag{3}$$

introducing an orthonormal frame of 1-forms $\{\boldsymbol{e}^{\mu}, \boldsymbol{e}^{\hat{\mu}}\}$ and the dual vector frame $\{\boldsymbol{e}_{\mu}, \boldsymbol{e}_{\hat{\mu}}\}$, with $\mu = 1, \ldots, n$ and $\hat{\mu} = \mu + n$:

$$\begin{aligned} \boldsymbol{e}^{\mu} &= \left(\frac{U_\mu}{X_\mu}\right)^{1/2} \boldsymbol{d}x_\mu\,, & \boldsymbol{e}_{\mu} &= \left(\frac{X_\mu}{U_\mu}\right)^{1/2} \boldsymbol{\partial}_{x_\mu}\,, \\ \boldsymbol{e}^{\hat{\mu}} &= \left(\frac{X_\mu}{U_\mu}\right)^{1/2} \sum_{k=0}^{n-1} A_\mu^{(k)}\, \boldsymbol{d}\psi_k\,, & \boldsymbol{e}_{\hat{\mu}} &= \left(\frac{1}{X_\mu U_\mu}\right)^{1/2} \sum_{k=0}^{n-1} \left(-x_\mu^2\right)^{n-1-k} \boldsymbol{\partial}_{\psi_k}\,. \end{aligned} \tag{4}$$

It was derived in Hamamoto et al. (2007) that the Ricci tensor is also diagonal in this frame

$$\boldsymbol{Ric} = -\sum_{\mu=1}^{n} r_\mu (\boldsymbol{e}^{\mu}\boldsymbol{e}^{\mu} + \boldsymbol{e}^{\hat{\mu}}\boldsymbol{e}^{\hat{\mu}})\,, \tag{5}$$

with the component r_μ given by

$$r_\mu = \frac{1}{2}\frac{X_\mu''}{U_\mu} + \sum_{\substack{\nu=1 \\ \nu\neq\mu}}^{n} \frac{1}{U_\nu} \frac{x_\nu X_\nu' - x_\mu X_\mu'}{x_\nu^2 - x_\mu^2} - \sum_{\substack{\nu=1 \\ \nu\neq\mu}}^{n} \frac{1}{U_\nu} \frac{X_\nu - X_\mu}{x_\nu^2 - x_\mu^2}\,. \tag{6}$$

The scalar curvature then is

$$\mathcal{R} = -\sum_{\nu=1}^{n} \frac{X_\nu''}{U_\nu}\,. \tag{7}$$

Enforcing the vacuum Einstein equations we have to solve the conditions $r_\mu = 0$. It turns out that the general solution is

$$X_\mu = b_\mu x_\mu + \sum_{k=0}^{n-1} c_k \left(-x_\mu^2\right)^{n-1-k}\,. \tag{8}$$

The constants b_μ and c_k are related to the mass, NUT parameters, angular momenta and cosmological constant (for details, see Gibbons et al., 2005; Chen et al., 2006).

3 PRINCIPAL KILLING–YANO TENSOR

Inspecting the metric, we immediately see that the metric has n Killing vectors $\boldsymbol{\partial}_{\psi_k}$. However, it also possesses hidden symmetries which can be demonstrated by the existence of the so-called *principal* Killing–Yano tensor $\boldsymbol{f}$

$$\boldsymbol{f} = \sum_{\mu=1}^{n} x_\mu \underbrace{\boldsymbol{e}^1 \wedge \cdots \wedge \boldsymbol{e}^D}_{\boldsymbol{e}^{\mu}, \boldsymbol{e}^{\hat{\mu}} \text{ skipped}}\,. \tag{9}$$

Its Hodge dual gives the second-rank closed conformal Killing–Yano tensor

$$\boldsymbol{h} = \sum_{\mu=1}^{n} x_\mu \boldsymbol{e}^\mu \wedge \boldsymbol{e}^{\hat{\mu}} \,. \tag{10}$$

The conformal Killing–Yano tensor (CKYT) was first proposed by Kashiwada (1968) and Tachibana (1969) as a generalization of the Killing–Yano tensors (Yano, 1952). Since then both these tensors found wide applications in physics related to hidden (super)symmetries, conserved quantities, symmetry operators, or separation of variables. Let us recall that CKYT of a general rank r is an antisymmetric r-form $\boldsymbol{f}$ the covariant derivative of which can be split into an antisymmetric part and a divergence part

$$\nabla \boldsymbol{f} = \mathcal{A} \nabla \boldsymbol{f} + \mathcal{T} \nabla \boldsymbol{f} \,. \tag{11}$$

Here $\mathcal{A}$ is the standard anti-symmetrization and $\mathcal{T}$ is the projection onto the "trace" part of the tensor of rank $r+1$ which is antisymmetric in the last r indices,

$$\mathcal{T}\, A_{aa_1\ldots a_r} = \frac{r}{D-r+1} g_{a[a_1} A^{e}{}_{|e|a_2\ldots a_r]} \,. \tag{12}$$

The divergence part $\mathcal{T} \nabla \boldsymbol{f}$ thus depends only on the divergence $\nabla_e f^e{}_{ab\ldots}$. The operations $\mathcal{A}$ and $\mathcal{T}$ satisfy $\mathcal{A}^2 = \mathcal{A}$, $\mathcal{T}^2 = \mathcal{T}$, and $\mathcal{T}\,\mathcal{A} = \mathcal{A}\,\mathcal{T} = 0$. The condition (11) implies that $\nabla \boldsymbol{f}$ does not have a harmonic part (given by the complement of the $\mathcal{A}$ and $\mathcal{T}$ projectors), i.e., $\boldsymbol{f}$ does not have a part for which both $\boldsymbol{d}\boldsymbol{f}$ and $\nabla \cdot \boldsymbol{f}$ vanishes. A CKYT transforms into a CKYT under the Hodge duality. The antisymmetric part $\mathcal{A} \nabla \boldsymbol{f}$ transforms into the divergence part $\mathcal{T} \nabla * \boldsymbol{f}$ and vice versa.

A Killing–Yano tensor $\boldsymbol{f}$ is such a CKYT for which the divergence part is missing, i.e., $\nabla \boldsymbol{f} = \mathcal{A} \nabla \boldsymbol{f}$. The dual of a Killing–Yano tensor is a closed CKYT, i.e., an r-form obeying $\nabla \boldsymbol{f} = \mathcal{T} \nabla \boldsymbol{f}$.

In our case, the principal CKYT $\boldsymbol{h}$ is the crucial geometrical structure which allows us to construct additional conserved quantities for geodesic motion and which is closely related to the separability of the Hamilton–Jacobi equation.

4 INTEGRABILITY OF GEODESIC MOTION

Let us now investigate geodesic motion in the spacetime given by the metric (1) with unspecified metric functions X_μ. For such a motion, the non-normalized velocity plays the role of momentum $\boldsymbol{p}$. Its norm

$$w = \boldsymbol{p} \cdot \boldsymbol{p} \tag{13}$$

is conserved along the motion. Having n Killing vectors $\boldsymbol{\partial}_{\psi_k}$, we can construct n conserved quantities linear in momentum

$$L_j = \boldsymbol{\partial}_{\psi_j} \cdot \boldsymbol{p} \,, \qquad j = 0, \ldots, n-1 \,. \tag{14}$$

The remaining $n-1$ independent constants of motion can be constructed starting from the generating function written in terms of the Killing–Yano tensor and momentum

$$W(\beta) = \det\left(\boldsymbol{I} - \sqrt{\beta}\,\boldsymbol{h}\cdot\boldsymbol{P}\right) . \tag{15}$$

Here, $\boldsymbol{P}$ is a projector on the directions orthogonal to the momentum $\boldsymbol{p}$. It was shown in Krtouš et al. (2007a) that $W(\beta)$ is conserved for any value of β. The independent constants of motion can be extracted as coefficients in the β-expansion

$$W(\beta) = \frac{1}{w}\sum_j C_j \beta^j , \tag{16}$$

leading to $C_0 = w$ and

$$C_j = \sum_{\mu=1}^{n} A_\mu^{(j)} \left(\bar{p}_\mu^2 + \bar{p}_{\hat{\mu}}^2\right) , \qquad j = 0, \ldots, n-1 , \tag{17}$$

where $\bar{p}_\mu$, $\bar{p}_{\hat{\mu}}$ are components of momentum in the frame $\boldsymbol{e}^\mu$, $\boldsymbol{e}^{\hat{\mu}}$,

$$\boldsymbol{p} = \sum_{\mu=1}^{n} \left(\bar{p}_\mu \boldsymbol{e}^\mu + \bar{p}_{\hat{\mu}} \boldsymbol{e}^{\hat{\mu}}\right) . \tag{18}$$

We have shown in Page et al. (2007); Krtouš et al. (2007b) that the constants L_j and C_j are not only independent, but that they are also in involution

$$\{L_k, L_l\} = \{L_k, C_l\} = \{C_k, C_l\} = 0 . \tag{19}$$

These are sufficient conditions for the motion to be completely integrable (see, e.g., Arnol'd, 1989).

5 SEPARABILITY OF THE HAMILTON–JACOBI AND KLEIN–GORDON EQUATIONS

Both the complete integrability and the existence of the Killing–Yano tensor are closely related to the separability of the Hamilton–Jacobi equation (see, e.g., Arnol'd, 1989; Floyd, 1973; Penrose, 1973; Benenti and Francaviglia, 1979, 1980).

The separability of the Hamilton–Jacobi equation for geodesic motion

$$\frac{\partial S}{\partial \tau} + \boldsymbol{d}S \cdot \boldsymbol{g} \cdot \boldsymbol{d}S = 0 \tag{20}$$

can be demonstrated assuming

$$S = -\tau w + \sum_{\mu=1}^{n} S_\mu(x_\mu) + \sum_{i=0}^{n-1} L_i \psi_i ,$$

with $S_\mu(x_\mu)$ being functions of a single variable only. Substituting into (20), we obtain an ordinary differential equation for S_μ (Frolov et al., 2007)

$$S_\mu'^2 = \frac{1}{X_\mu}\sum_{i=0}^{n-1} C_i \left(-x_\mu^2\right)^{n-1-i} - \frac{1}{X_\mu^2}\left[\sum_{i=0}^{n-1} L_i \left(-x_\mu^2\right)^{n-1-i}\right]^2 , \tag{21}$$

which can be solved by quadratures.

Identifying the gradient $\boldsymbol{d}S$ with the momentum $\boldsymbol{d}S = \boldsymbol{p}$, we find that the separability constants w, L_j, and C_j are exactly those defined in the previous section in (13), (14), and (17), L_j being linear in momentum and C_j quadratic.

Similarly, it was also demonstrated in Frolov et al. (2007), that the massive Klein–Gordon equation for a scalar field

$$\left[\Box - m^2\right]\Phi = 0 \tag{22}$$

can be solved by the separability ansatz

$$\Phi = \prod_{\mu=1}^{n} R_\mu(x_\mu) \prod_{k=0}^{m} \exp\left(\mathrm{i}\Psi_k \psi_k\right) . \tag{23}$$

It leads to differential equations for R_μ

$$\left(X_\mu R_\mu'\right)' - \left[\frac{1}{X_\mu}\left(\sum_{k=0}^{n-1} \Psi_k (-x_\mu^2)^{n-1-k}\right)^2 + \sum_{k=0}^{n-1} \Xi_k \left(-x_\mu^2\right)^{n-1-k}\right] R_\mu = 0 , \tag{24}$$

with Ψ_j and Ξ_k arbitrary separation constants.

6 ALGEBRAICALLY SPECIAL TEST ELECTROMAGNETIC FIELD

Following Krtouš (2007), we will discuss now a special kind of test electromagnetic fields on the background given by the metric (1). We are looking for a field that would share the explicit symmetry of the metric (it would be independent of ψ_j) and that would be aligned with the hidden symmetry of the spacetime, namely, its Maxwell tensor $\boldsymbol{F}$ would have the same eigenspaces as the principal conformal Killing–Yano tensor $\boldsymbol{h}$. We thus require

$$\boldsymbol{F} = \sum_{\mu=1}^{n} f_\mu \boldsymbol{e}^\mu \wedge \boldsymbol{e}^{\hat{\mu}} , \quad f_\mu = f_\mu(x_1, \ldots, x_n) . \tag{25}$$

The Maxwell tensor is generated by the vector potential, $\boldsymbol{F} = \boldsymbol{d}\boldsymbol{A}$. As a consequence of the assumption (25), we find that the vector potential can be written as

$$\boldsymbol{A} = \sum_{\mu=1}^{n} g_\mu \left(\frac{x_\mu}{U_\mu}\right)^{1/2} \boldsymbol{e}^{\hat{\mu}} , \tag{26}$$

where g_μ are functions of a *single variable* only, $g_\mu = g_\mu(x_\mu)$. Evaluating the Maxwell tensor, we get the components f_μ:

$$f_\mu = \frac{g_\mu}{U_\mu} + \frac{x_\mu g'_\mu}{U_\mu} + 2x_\mu \sum_{\substack{\nu=1 \\ \nu\neq\mu}}^{n} \frac{1}{U_\nu} \frac{x_\nu g_\nu - x_\mu g_\mu}{x_\nu^2 - x_\mu^2} \,. \tag{27}$$

Alternatively, we could apply directly the first Maxwell equation $\boldsymbol{dF} = 0$ to find that f_μ are generated by an auxiliary potential ϕ,

$$f_\mu = \phi_{,\mu} \,, \tag{28}$$

which satisfies the equation

$$\phi_{,\mu\nu} = 2\frac{x_\nu \phi_{,\mu} - x_\mu \phi_{,\nu}}{x_\mu^2 - x_\nu^2} \quad \text{for} \quad \mu \neq \nu \,. \tag{29}$$

The field (26) is generated by the potential

$$\phi = \sum_{\nu=1}^{n} \frac{g_\nu x_\nu}{U_\nu} \,. \tag{30}$$

Calculating the source $\boldsymbol{J}$ of the electromagnetic field using the second Maxwell equation $\boldsymbol{J} = -\boldsymbol{\nabla} \cdot \boldsymbol{F}$, we obtain

$$\boldsymbol{J} = \sum_{\mu=1}^{n} j_\mu \left(\frac{x_\mu}{U_\mu}\right)^{1/2} \boldsymbol{e}_{\hat{\mu}} \,, \tag{31}$$

with

$$j_\mu = -\frac{1}{x_\mu} \frac{\partial}{\partial x_\mu} \left(\phi - x_\mu^2 \sum_{\nu=1}^{n} x_\nu^{-1} \phi_{,\nu} \right) \,. \tag{32}$$

Substituting (30), we finally obtain

$$j_\mu = \frac{1}{x_\mu} \frac{\partial}{\partial x_\mu} \left(\sum_{\nu=1}^{n} \frac{x_\nu^2 g'_\nu}{U_\nu} \right) \,. \tag{33}$$

We are interested in source-free electromagnetic fields, so we require $\boldsymbol{J} = 0$. Using the special form of the sum in the square brackets in (33) we find that g'_μ are given by a single polynomial of order $(n-1)$ in variable x_μ^2. Integrating once more, we find

$$g_\mu x_\mu = e_\mu x_\mu + \sum_{k=0}^{n-1} a_k \left(-x_\mu^2\right)^{n-1-k} \,. \tag{34}$$

Substituting into the vector potential (26) or the scalar potential (30), we find that the terms containing the constants a_k are gauge-trivial and they can be ignored.

We have thus found that an algebraically special electromagnetic field (i.e., a field of the form (25)) satisfies Maxwell equations on the background described by the metric (1) if and only if it is generated by the vector potential

$$\boldsymbol{A} = \sum_{\mu=1}^{n} e_\mu \left(\frac{x_\mu}{U_\mu}\right)^{1/2} \boldsymbol{e}^{\hat{\mu}} . \tag{35}$$

The components f_μ of the Maxwell tensor are easily determined by (28) from the auxiliary potential

$$\phi = \sum_{\mu=1}^{n} \frac{e_\mu x_\mu}{U_\mu} , \tag{36}$$

and they read

$$f_\mu = \frac{e_\mu}{U_\mu} + 2x_\mu \sum_{\substack{\nu=1 \\ \nu\neq\mu}}^{n} \frac{1}{U_\nu} \frac{x_\nu e_\nu - x_\mu e_\mu}{x_\nu^2 - x_\mu^2} . \tag{37}$$

Here, e_μ are constants that can be related to the electric and magnetic charges of the field using the Gauss and Stokes theorems.

If we set all charges except for one, say e_ν, to zero, the Maxwell tensor $\boldsymbol{F}$ corresponds to the harmonic form $\boldsymbol{G}^{(\nu)}_{(2)}$ recently found and verified for particular cases in Chen and Lü (2007).

The surprising property of our field is that it satisfies Maxwell equations independently of the specific form of metric functions X_μ. Moreover, the stress-energy tensor corresponding to the field (25) has a form consistent with the structure of the Ricci (and Einstein) tensor (5). These facts open up a possibility that we could solve the full Einstein–Maxwell equations: modifying the metric functions X_μ, we could construct a spacetime in which the stress-energy tensor $\boldsymbol{T}$ would be a source for the Einstein equations, and the electromagnetic field would still satisfy Maxwell equations.

7 NO-GO THEOREM FOR CHARGING THE KERR–NUT–(A)DS METRIC

Indeed, this goal can be achieved in the physical dimension $D = 4$. In this case metric (1) with metric functions X_μ given by (8) corresponds to the uncharged black-hole solution in the form found by Carter (1968a,b) and elaborated by Plebański and Demiański (1976). However, if we modify the metric functions by adding constant terms $-e_1^2$ and $-e_2^2$,

$$\begin{aligned} X_1 &= c_0 + c_1 x_1^2 + c_2 x_1^4 + 2b_1 x_1 - e_1^2 , \\ X_2 &= c_0 + c_1 x_2^2 + c_2 x_2^4 + 2b_2 x_2 - e_2^2 , \end{aligned} \tag{38}$$

the metric (1) together with the electromagnetic field (35) solve the full Einstein–Maxwell equations – it corresponds to the Carter's charged black-hole solution.

In a generic dimension, we first evaluate the stress-energy tensor $\boldsymbol{T}$ of the electromagnetic field (25):

$$8\pi\boldsymbol{T} = \sum_{\mu=1}^{n} \left(2f_\mu^2 - f^2\right)\left(\boldsymbol{e}^\mu\boldsymbol{e}^\mu + \boldsymbol{e}^{\hat{\mu}}\boldsymbol{e}^{\hat{\mu}}\right) . \tag{39}$$

Its trace is

$$8\pi T = 2(2-n)f^2 , \tag{40}$$

where the function f^2 is defined as

$$f^2 = \sum_{\nu=1}^{n} f_\nu^2 . \tag{41}$$

We explicitly see that the trace of the stress-energy is non-vanishing for $D \neq 4$ which is related to the fact that the electromagnetic field is not conformally invariant in a general dimension.

Now we would like to solve the Einstein equations $\boldsymbol{Ric} - \frac{1}{2}\mathcal{R}\boldsymbol{g} + \Lambda\boldsymbol{g} = 8\pi\boldsymbol{T}$. The trace gives the condition

$$\mathcal{R} = 2\frac{D}{D-2}\Lambda + 2\frac{D-4}{D-2}f^2 . \tag{42}$$

However, the scalar curvature has the form (7) and it immediately follows that

$$\frac{\partial^{2n-2}}{\partial x_\mu^{2n-2}}(U_\mu\mathcal{R}) = -X_\mu^{[2n]} , \tag{43}$$

which is a function of x_μ only. Applying this to the right-hand-side of (42), we obtain the condition:

$$\frac{\partial^{2n-2}}{\partial x_\mu^{2n-2}}\left(U_\mu f^2\right) \quad \text{must be a function of } x_\mu \text{ only.} \tag{44}$$

This condition does not hold for the electromagnetic field given by (37), at least for the lowest non-trivial values of n. It seems that the main problem is that $\mathcal{R}$ behaves as $\sum h_\mu/U_\mu$ while f^2 as a square of such sums.

We can thus conclude that in a generic even dimension the electromagnetic field of the form (25), (37) cannot couple to the metric given by (1).

8 SUMMARY

In this contribution, we have reviewed some properties of the general higher-dimensional rotating black-hole spacetimes given by the metric (1). We have discussed the complete

integrability of geodesic motion and explicitly found the full set of constants of motion. We have seen that the "nontrivial" constants are generated using the principal conformal Killing–Yano tensor and that they are quadratic in momenta and thus correspond to rank-2 Killing tensors (Krtouš et al., 2007a).

The complete integrability of the geodesic motion is related to the issue of separability of the Hamilton–Jacobi equation, which has been reviewed next. It was demonstrated that the separability constants for the Hamilton–Jacobi equation are the same as those constructed directly for geodesic motion.

Finally, we have presented an algebraically special test electromagnetic field. It depends on $n = D/2$ constants e_μ related to the global electric and magnetic charges. It generalizes the field known on the background of the Carter's black-hole solution in $D = 4$ dimensions. In this case, the metric functions can be modified in such a way that the field and the metric solve the full Einstein–Maxwell equations. Unfortunately, an analogous modification is not possible in a generic dimension.

ACKNOWLEDGEMENTS

This work was supported by the grant GAČR 202/06/0041 and by the Czech Ministry of Education under the project LC06014. The author would like to thank Don N. Page, Valeri P. Frolov, David Kubizňák, and Jiří Podolský for numerous discussions, and Martin Žofka for reading the manuscript.

REFERENCES

Arnol'd, V. I. (1989), *Mathematical methods of classical mechanics*, volume Graduate texts in mathematics, Springer, New York, 2nd edition, ISBN 0-387-96890-2, originally published by Nauka, Moscow, 1974.

Benenti, S. and Francaviglia, M. (1979), Remarks on certain separability structures and their applications to general relativity, *Gen. Relativity Gravitation*, **10**(1), pp. 79–92.

Benenti, S. and Francaviglia, M. (1980), *The theory of separability of the Hamilton–Jacobi equation and its applications to general relativity*, chapter 13, Lecture Notes in Mathematics, Plenum Press, New York.

Carter, B. (1968a), A new family of Einstein spaces, *Phys. Lett. A*, **26**, pp. 399–400.

Carter, B. (1968b), Hamilton–Jacobi and Schrödinger separable solutions of Einstein's equations, *Comm. Math. Phys.*, **10**, pp. 280–310.

Chen, W. and Lü, H. (2007), Kerr–Schild structure and harmonic 2-forms on (a)dS–Kerr–NUT metrics, arXiv: `0705.4471`.

Chen, W., Lü, H. and Pope, C. N. (2006), General Kerr–NUT–adS metrics in all dimensions, *Classical Quantum Gravity*, **23**, pp. 5323–5340, arXiv: `hep-th/0604125`.

Floyd, R. (1973), *The dynamics of Kerr fields*, Ph.D. thesis, London University.

Frolov, V. P., Krtouš, P. and Kubizňák, D. (2007), Separability of Hamilton–Jacobi and Klein–Gordon equations in general Kerr–NUT–adS spacetimes, *Journal High Energy Phys.*, **02**, p. 005, arXiv: `hep-th/0611245`.

Gibbons, G. W., Lü, H., Page, D. N. and Pope, C. N. (2004), Rotating black holes in higher dimensions with a cosmological constant, *Phys. Rev. Lett.*, **93**, p. 171102, arXiv: `hep-th/0409155`.

Gibbons, G. W., Lü, H., Page, D. N. and Pope, C. N. (2005), The general Kerr–de Sitter metrics in all dimensions, *J. Geom. Phys.*, **53**, pp. 49–73, arXiv: `hep-th/0404008`.

Hamamoto, N., Houri, T., Oota, T. and Yasui, Y. (2007), Kerr-NUT-de Sitter curvature in all dimensions, *J. Phys. A*, **40**, pp. F177–F184, arXiv: `hep-th/0611285`.

Hawking, S. W., Hunter, C. J. and Taylor-Robinson, M. M. (1999), Rotation and the adS/cft correspondence, *Phys. Rev. D*, **59**, p. 064005, arXiv: `hep-th/9811056`.

Kashiwada, T. (1968), On conformal Killing tensors, *Phys. Rev. D*, **19**, pp. 67–74.

Krtouš, P. (2007), Electromagnetic field in higher-dimensional black-hole spacetimes, *Phys. Rev. D*, **76**, p. 084035, arXiv: `0707.0002`.

Krtouš, P., Kubizňák, D., Page, D. N. and Frolov, V. P. (2007a), Killing–Yano tensors, rank-2 Killing tensors, and conserved quantities in higher dimensions, *Journal High Energy Phys.*, **2**, p. 004, arXiv: `hep-th/0612029`.

Krtouš, P., Kubizňák, D., Page, D. N. and Vasudevan, M. (2007b), Constants of geodesic motion in higher-dimensional black-hole spacetimes, *Phys. Rev. D*, **76**, p. 084034, arXiv: `0707.0001`.

Kubizňák, D. and Krtouš, P. (2007), On conformal Killing–Yano tensors for Plebański–Demiański family of solutions, *Phys. Rev. D*, **76**, p. 084036, arXiv: `0707.0409`.

Myers, R. C. and Perry, M. J. (1986), Black holes in higher dimensional space-times, *Ann. Physics (N. Y.)*, **172**, pp. 304–347.

Page, D. N., Kubizňák, D., Vasudevan, M. and Krtouš, P. (2007), Integrability of geodesic motion in general Kerr–NUT–adS spacetimes, *Phys. Rev. Lett.*, **98**, p. 061102, arXiv: `hep-th/0611083`.

Penrose, R. (1973), Naked singularities, *Ann. N. Y. Acad. Sci.*, **224**, pp. 125–134.

Plebański, J. and Demiański, M. (1976), Rotating charged and uniformly accelerated mass in general relativity, *Ann. Physics (N. Y.)*, **98**, pp. 98–127.

Tachibana, S. (1969), On conformal Killing tensor in a Riemannian space, *Tôhoku Math. J.*, **21**, p. 56.

Tangherlini, F. R. (1963), Schwartzschild field in n dimensions and the dimensionality of space problem, *Nuovo Cimento A*, **27**, p. 636.

Yano, K. (1952), Some remarks on tensor fields and curvature, *Ann. of Math.*, **55**, pp. 328–347.

Proceedings of *RAGtime 8/9, 15–19/19–21 September, 2006/2007, Hradec nad Moravicí, Opava, Czech Republic*
S. Hledík and Z. Stuchlík, editors, Silesian University in Opava, 2007, pp. 151–165

Evidence for relativistic iron lines in AGN

Giorgio Matt

Dipartimento di Fisica, Università degli Studi Roma Tre, Via della Vasca Navale 84,
I-00146 Roma, Italy
matt@fis.uniroma3.it

ABSTRACT
Iron lines emitted in the innermost regions of the accretion disc in Active Galactic Nuclei (and Galactic Black Hole candidates) are one of the best tools to probe strong gravity effects in the close vicinity of a Black Hole. In this contribution I review the basic theory on "relativistic lines" and the observational evidence for them in Active Galactic Nuclei.

Keywords: Iron lines – General Relativity – active galactic nuclei – X-rays

1 INTRODUCTION

In the 90's, X-ray missions carrying on-board high sensitivity, moderate energy resolution instruments working at energy bands including the iron line complex ($\sim$ 6–7 keV) were launched, the first of them being ASCA, then followed by *Beppo SAX* (both of them are no longer operating). Then *Chandra*, *XMM-Newton* and *Suzaku* joined (all three still operating as for late 2007). With these missions, probing General Relativity (GR) effects on iron emission lines has became possible, and it is now a relevant part of the studies on Active Galactic Nuclei (AGN) as well as on Galactic Black Hole systems (GBH) and also on X-ray binaries with neutron stars, if accretion occurs via a disc (e.g., Di Salvo et al., 2005).

In this paper I will review the main GR effects on the iron line emitted in the innermost regions of the accretion disc (often referred to as "relativistic lines") and I will discuss the observational evidence for them. The paper is organized as follows: in Section 2 the basic concepts concerning Black Holes, of relevance for understanding GR effects on line emission, are summarized. In Section 3 line emission from a relativistic accretion disc is presented, while Section 4 is devoted to the discussion of the strenghts and weaknesses of methods, based on iron emission lines, to measure the mass and spin of the Black Hole. Present observational evidence for relativistic lines in AGN are discussed in Section 5, while conclusions are given in Section 6.

2 BLACK HOLES

A Black Hole (BH) is fully characterized by only three quantities: its mass M, angular momentum J and electric charge Q, which is usually assumed to be negligible for astrophys-

978-80-7248-419-5

ically relevant Black Holes. The space time around a BH is described by the Kerr–Newman metric which, when $Q = 0$, reduces to the slightly simpler Kerr metric. If also J is null, than the metric is the much simpler Schwarzschild one. While the static solution was found by Karl Schwarzschild in 1916 (i.e., only one year after the publication by Einstein of the theory of General Relativity), the rotating solution was found by Roy Kerr only in the sixties (Kerr, 1963), a delay probably due more to the lack of interest in the field rather than to the mathematical difficulties of the problem.

All relevant General Relativity effects around a BH are scale invariant, i.e., do not depend on the BH mass. It is therefore convenient to measure all distances in units of the so-called gravitational radius, $r_{\rm g} = GM/c^2$. It is also customary to introduce the adimensional angular momentum per unit mass, $a = Jc/GM^2$, called for simplicity "spin" hereinafter.

In Boyer–Lindquist spherical coordinates (namely t, r, ϕ, θ, with the usual meaning of symbols), the Kerr metric can be written as:

$$\mathrm{d}s^2 = -\left(1 - \frac{2r}{\Sigma}\right)\mathrm{d}t^2 - \left(\frac{4ar\sin^2\theta}{\Sigma}\right)\mathrm{d}t\mathrm{d}\phi + \left(\frac{\Sigma}{\Delta}\right)\mathrm{d}r^2 + \Sigma\,\mathrm{d}\theta^2 + \left(r^2 + a^2 + \frac{2a^2 r\sin^2\theta}{\Sigma}\right)\sin^2\theta\,\mathrm{d}\phi^2\,, \tag{1}$$

where

$$\Sigma = r^2 + a^2\cos^2\theta\,, \quad \Delta = r^2 - 2r + a^2\,.$$

(If the Black Hole electric charge is not null, then $\Delta = r^2 - 2r + a^2 + Q^2$). For $a = 0$, the Schwarzschild metric is obtained:

$$\mathrm{d}s^2 = -\left(1 - \frac{2}{r}\right)\mathrm{d}t^2 + \left(1 - \frac{2}{r}\right)^{-1}\mathrm{d}r^2 + r^2(\mathrm{d}\theta^2 + \sin^2\theta\,\mathrm{d}\phi^2)\,. \tag{2}$$

The radius of the Event Horizon, i.e., the surface of "no return," is given by $R_{\rm EH} = 1 + \sqrt{1 - a^2}$. This implies that $0 \le a \le 1$, i.e., that there is a maximum value for the spin. When $a = 1$ the BH is said to be maximally rotating; in this case the radius of the Event Horizon is equal to the gravitational radius, while it is $2r_{\rm g}$ (the "Schwarzschild radius") for a static ($a = 0$) BH.[1] It is interesting to note that the Schwarzschild radius corresponds, in a pure Newtonian calculation, to the radius a star should have in order for its escape velocity to be equal to c. Indeed, Black Holes (or invisible stars, as they were called at the time) were predicted in this way more than two centuries ago by Michell (1784) and Laplace (1796), even if of course they could not know that from such objects nothing, not only the light, could escape.

[1] It is important to recall here that Thorne (1974) has shown that in the standard accretion disc model the radiation emitted by the disc and swallowed by the BH produces a counteracting torque which limits the spin to a maximum value of ~ 0.988, corresponding to $R_{\rm EH} \sim 1.23$. Different values can be found for different assumptions on the accretion flow (see Agol and Krolik, 2000).

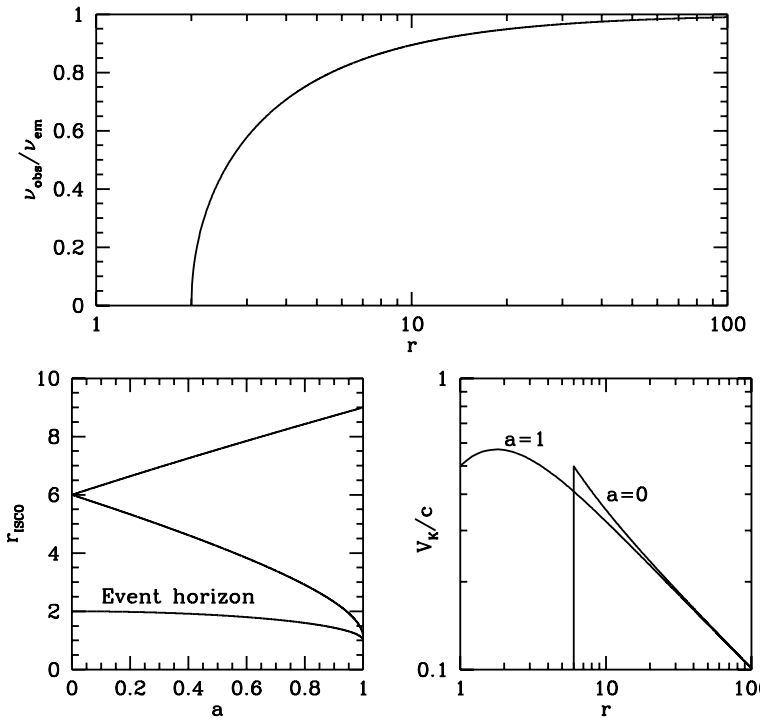

Figure 1. *Upper panel:* the ratio between the observed and emitted frequency of a photon ("gravitational redshift") in Schwarzschild metric as a function of the radius at which the photon is emitted. *Lower-left panel:* the radius of the Innermost Stable Circular Orbit as a function of the BH spin. The lower (upper) curve refers to a co- (counter-) rotating disc. The radius of the Event Horizon is also shown for comparison. *Lower-right panel:* the Keplerian velocity (in the LNRF) in the equatorial plane as a function of radius, for a static and a maximally rotating BH.

An important General Relativity effect is the gravitational redshift. Photons can get out of the gravitational potential of the BH only at the expense of their energy, and therefore frequency. In Schwarzschild metric

$$\frac{\nu_{\rm obs}}{\nu_{\rm em}} = \sqrt{1-\frac{2}{r}}\,, \tag{3}$$

where $\nu_{\rm em}$ and $\nu_{\rm obs}$ are the emitted and observed (at infinity) frequencies of the photon, and r the emission radius (see also Fig. 1). In Kerr metric, a similar formula can be written only for the photons emitted on the rotation axis, where it reads

$$\frac{\nu_{\rm obs}}{\nu_{\rm em}} = \sqrt{1-\frac{2r}{r^2+a^2}}\,. \tag{4}$$

For any other point, the "dragging of the inertial frame," i.e., the corotation of the space-time with the BH spin makes gravitational and Doppler shifts not separable.

3 LINE EMISSION FROM ACCRETION DISCS

3.1 General remarks

Accretion onto Black Holes, at least for luminous systems, is believed to occur via an accretion disc, where gravitational energy can be efficiently dissipated and eventually converted into radiation. Accretion discs are very complicated systems, and the details of the physical processes are far from being fully understood. Fortunately, for what follows we only have to make a few assumptions, and forget about details. The assumptions are: that the disc is geometrically thin (i.e., its height is always much smaller than its radius at any radius), so that it may be approximated with a thin slab on the equatorial plane; that it is homogenous enough in order that clumpiness does not affect much the line emissivity; and that it is optically thick, so that iron line fluorescent emission can be efficient.

I also assume that the iron line is due to fluorescent emission after illumination by an external source of X-rays. George and Fabian (1991) and Matt et al. (1991) discussed in detail the properties of the fluorescent line for neutral matter (rest frame energy of 6.4 keV[2]), while Matt et al. (1993a,b, 1996); Nayakshin and Kallman (2001), A. C. Fabian, R. R. Ross and collaborators in a series of papers (Ross and Fabian, 2005 and references therein) discussed the case of ionized matter (rest frame energies up to $\sim$7 keV).

GR effects on the radiation emitted by an accretion disc were first studied by Cunningham (1975), while Fabian et al. (1989) and Chen et al. (1989) were the first to model line emission from relativistic discs and compare calculations with observations. Different groups (too many to be quoted here; further references can be found in: Fabian et al., 2000; Reynolds and Nowak, 2003; Fabian and Miniutti, 2005; Karas, 2006) have since then performed calculations of line profiles under different assumptions and physical conditions, stimulated by the *GINGA* discovery that iron lines are almost ubiquitous in the X-ray spectra of AGN (e.g., Nandra and Pounds, 1994). Precise and fast models for fitting real data are now available (e.g., Dovčiak et al., 2004b,d).

3.2 Line emission from relativistic discs

The inner radius of the accretion disc cannot be smaller than the Innermost Stable Circular Orbit (ISCO). This of course does not mean that there is no matter at radii lower than the ISCO; simply, the matter must spiral in (see Krolik and Hawley, 2002 for different definitions of the "edge" of the disc). The ISCO depends on the BH spin and on whether the disc is co- or counter-rotating with the BH (see Fig. 1):

$$r_{\rm ISCO} = 3 + Z_2 \pm [(3 - Z_1)(3 + Z_1 + 2Z_2)]^{1/2}\,, \tag{5}$$

where

$$Z_1 = 1 + (1 - a^2)^{1/3}[(1 + a)^{1/3} + (1 - a)^{1/3}] \quad Z_2 = (3a^2 + Z_1^2)^{1/2}\,.$$

[2] This line is actually a doublet, with energies of 6.4055 and 6.3916 keV and a branching ratio of $\sim$2 : 1 (Palmeri et al., 2003). As the broadening effects we are discussing here are much larger than the $\sim$ 14 eV intrinsic separation, we will assume a single narrow line with a weighted mean energy of 6.4 keV.

The $-$ (+) sign applies to co- (counter-) rotating discs. The decrease of the ISCO with a (for a corotating disc) is usually used to estimate the spin (see next Section).

Motion of matter in accretion discs is supposed to be dominated by the gravitational potential of the BH, and then rotation to be Keplerian. Close to the BH the Keplerian velocity, $v_{\rm K}$, becomes very large, reaching a significant fraction of the velocity of light. In the Locally Non-Rotating Frame (LNRF), i.e., the reference frame "rotating with the Black Hole" (Bardeen et al., 1972), we have (see also Fig. 1):

$$v_{\rm K}/c = \frac{r^2 - 2a\sqrt{r} + a^2}{(r^2 + a^2 - 2r)^{1/2}(r^{3/2} + a)} \,. \tag{6}$$

It is interesting to note that $v_{\rm K}$ can be a significant fraction of the velocity of light, implying that the Doppler shift and boosting may be very prominent.[3] At these velocities, the fully relativistic Doppler effect must be considered, as the transverse Doppler effect (i.e., the redshift of photons when matter has only a transverse component of the velocity) is by no means negligible.

In General Relativity, photon geodesics are no longer straight lines (the so-called "light bending"). In Schwarzschild metric they still lie on a plane, and therefore the equation of the orbit can be written in terms of only two coordinates, the radius and the azimuthal angle,

[3] Doppler boosting is the brightening/dimming of the flux when the matter is approaching/receding. It is a Special Relativity aberration effect due to the fact that I_ν/ν^3 is a Lorentz invariant.

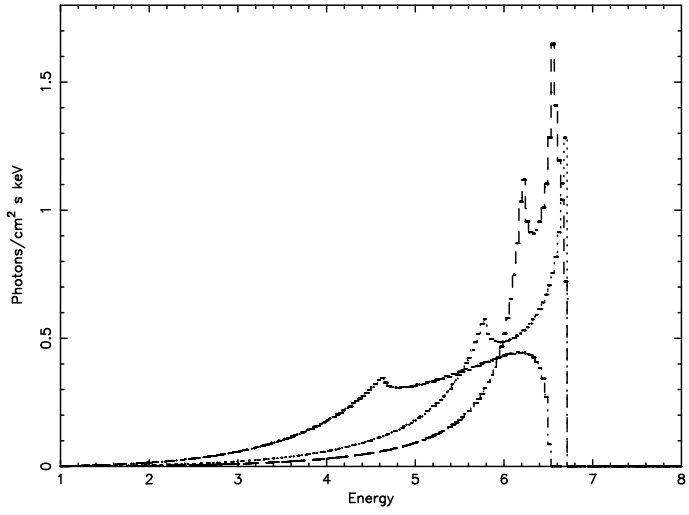

Figure 2. Iron line profiles for a maximally rotating BH, extending from the ISCO to 400, 50 and 10 $r_{\rm g}$ (from top to bottom) with a 30° inclination angle and the index of the emissivity law $q = 2$ (see footnote #4). Here and in the next figure profiles have been calculated with the code kyrline (Dovčiak et al., 2004b,d) in the XSPEC software package.

Φ, on the plane of the trajectory (Misner et al., 1973):

$$\frac{\mathrm{d}^2 u}{\mathrm{d}\Phi^2} = 3u^2 - u \,, \tag{7}$$

where $u = 1/r$. In Kerr metric the orbits are fully tridimensional, and the equation of motion much more complex (Carter, 1968). As a result of light bending, geodesics of photons emitted in the far side of the disc are strongly curved, and the disc appears "bended" towards the observer (see, e.g., Luminet, 1979, 1992).

All these effects strongly modify the properties of emission lines. Let us for simplicity neglect natural and thermal line broadening, so that the line profile, in the matter reference frame, is a δ-function. Let us also assume that the line is the neutral iron Kα at 6.4 keV. Their resulting line profile has a characteristic doubled-horned shape, with the blue peak brighter than the red peak due to Doppler Boosting, and an extended red wing due to both Doppler Transverse and Gravitational redshift. In Fig. 2 profiles obtained for different outer radii are shown. Many more examples, illustrating the dependence of the profile on the various parameters (spin, inner and outer radii, inclination angle, emissivity laws[4] can be found in the literature (see, e.g., references in Matt, 2006; Karas, 2006).

4 MEASURING THE SPIN AND MASS OF BLACK HOLES USING IRON LINES

Iron line profiles from relativistic accretion discs provides potentially very powerful methods to measure the mass and the spin of the Black Holes in Active Galactic Nuclei. Pros and cons of these methods are now briefly discussed in the following paragraphs.

4.1 Spin

Methods to measure the Black Hole spin usually make use of the dependence of the ISCO on a. Methods based on the iron line make no exception. The smaller the inner disc radius, the lower (due to gravitational redshift) the energy to which the profile extends. In Fig. 3, left panel, profiles from accretion discs around a static and a maximally rotating Black Holes, in both cases extending down to the ISCO, are shown. The advantage of this method is that it is very simple and straightforward, at least conceptually. Moreover, no detailed physical modelling of the line emission is required: the spin is measured from the low end of the profile, independently of the exact form of the profile itself (once the inclination angle is determined).

[4] A crucial ingredient in shaping the line profile is the radial emissivity law, ξ. For the iron fluorescent line, which is emitted following external illumination (e.g., George and Fabian, 1991; Matt et al., 1991), ξ depends mainly on the geometry of the system. It is customary to assume a power law emissivity law, $\xi \propto r^{-q}$. If $q < 2$, the outer regions dominate the emissivity, while the inner regions prevail for $q > 2$. Actually, the emissivity law is likely to be more complex than a simple power law. Even in the simplest case, the so-called "lamp-post" model in which the primary emitting region is a small cloud on the BH axis (as in aborted jet models, e.g., Ghisellini et al., 2004), the emissivity law is, *neglecting GR effects and radiative transfer subtleties*, given by: $\xi \propto (h^2 + r^2)^{-3/2}$, where h is the height of the emitting point; ξ is then a power law ($q = 3$) only for large radii. Once the effects on the emissivity of the incident angle (Matt et al., 1991) and, especially, of GR (light bending, gravitational shift) are included, the emissivity is significantly modified (e.g., Martocchia and Matt, 1996; Martocchia et al., 2000, 2002).

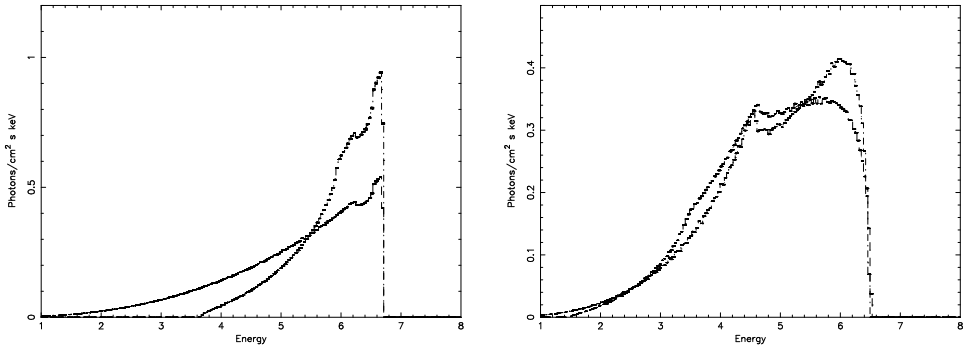

Figure 3. *Left panel:* iron line profiles for a maximally rotating BH and a static BH, extending from the ISCO to $400\,r_{\rm g}$, with a 30° inclination angle. Note that the profile for the spinning BH extends to much lower energies. *Right panel:* iron line profiles for a maximally rotating BH and a static BH, extending from $r = 2$ to $10\,r_{\rm g}$, with a 30° inclination angle, to illustrate the differences due to the metric.

There are, however, also some limitations and caveats to this method that must be taken into account. First of all, strictly speaking the method provides only a lower limit to the spin, because the disc (or at least the iron line emitting region) could in principle not extend down to the ISCO (see next section). Technically, zero-intensity energies are far from trivial to be measured. Finally, even if the disc (properly said) stops at the ISCO, the region within the ISCO (the so-called plunging region) in not empty, and line emission may arise from the matter free-falling onto the Black Hole (Reynolds and Begelman, 1997; Krolik and Hawley, 2002 ,for different definitions of the "edge" of the disc), even if matter is likely to be significantly ionized there. If the inner radius results to be smaller than 2, there is of course no ambiguity. Otherwise, one could in principle rely to the differences in the profiles due to the metrics themselves (Fig. 3, right panel) which, at least for small radii, are subtle but not entirely negligible and will be hopefully exploited by the next generation of large area X-ray satellites.

4.2 Mass

Iron Kα reverberation mapping of structures in the profile (Stella, 1990) or of integrated quantities (Equivalent Width, centroid energy and width, Matt and Perola, 1992) has been suggested, in analogy with the method routinely used for optical broad lines, as a tool to measure the BH mass in AGN (this technique is practically inapplicable in Galactic Black Hole systems because of the very short time scales involved, and the much lower typical flux per light-crossing time). It is a conceptually simple but technically very difficult technique. First of all, it requires a large number of photons. Worst than that, the Transfer Function, which describes how the line follows variations of the illuminating continuum, is strongly geometry-dependent. With respect to the reverberation mapping of optical broad lines, one here has the advantage that the geometry of the illuminated region can be assumed a priori (i.e., the accretion disc), but has the disadvantage that the geometry of the illuminating

region is unknown. In fact, in the optical lines case a point-like source is a safe assumption, given the much larger distance of the illuminated matter. For the iron lines, instead, the illuminating and illuminated regions are likely of comparable sizes.

On the other hand, if the iron line is emitted in a small spot on the accretion disc (corotating with the disc at the Keplerian velocity), the BH mass could be easily and precisely measured, once the spot radius is known (Dovčiak et al., 2004a, 2007). Such a hot spot may be due to a localized flare, possibly of magnetic origin, just above the disc surface.

A spot on the accretion disc at a radius r has an orbital period (as measured by an observer at infinity) given by

$$T_{\rm orb} = 310 \left(r^{3/2} + a\right) M_7 \,[\rm sec]\,, \tag{8}$$

where M_7 is the mass of the black hole in units of 10^7 solar masses. If the spot radius and the BH spin can be estimated, the measurement of the orbital period immediately provides the Black Hole mass (note that the spin is relevant only for small radii; when $r \gg 1$, when the spin is hard to measure, it fortunately becomes irrelevant).

There is some observational evidence (albeit still controversial) for spot-like emission in AGN (e.g., Turner et al., 2002; Dovčiak et al., 2004a; Iwasawa et al., 2004; Pecháček et al., 2005, and references therein), but confirmations and the full exploitation of the method have to wait for the next generation of X-ray satellites.

5 OBSERVATIONAL EVIDENCE FOR RELATIVISTIC LINES IN AGN

5.1 The innermost regions of (radio-quiet) AGN

The standard scenario for the innermost regions of AGN is shown in Fig. 4. The UV thermal photons emitted by the accretion disc are Comptonized by hot ($T \sim 100$–200 keV) electrons in an optically thin corona. The resulting X-ray spectrum is, in the very first approximation, a power law with a high energy cut-off, as indeed is observed (Petrucci et al., 2001; Perola

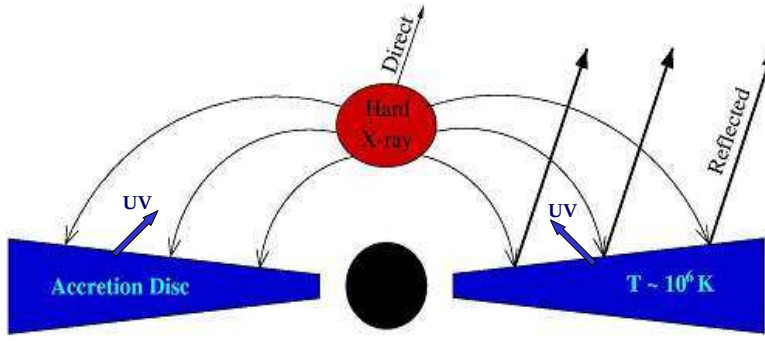

Figure 4. Schematic view of the innermost region of a radio-quiet AGN. UV photons from the accretion disc are Comptonized in a hot corona, producing the primary continuum, part of which is in turn reprocessed by the disc itself. Adapted from (Dabrowski, 1998).

et al., 2002). The primary X-ray emission illuminates the accretion disc, producing the so-called Compton reflection component (Lightman and White, 1988; Guilbert and Rees, 1988; George and Fabian, 1991; Matt et al., 1991) plus several fluorescent emission lines, by far the most prominent of them being the iron line (Reynolds et al., 1995). This two–phase scenario was first discussed in detail by Haardt and Maraschi (1991). While the aspects regarding the reprocessing are now well established, the origin and geometry of the hot corona are still far from clear.

The spectrum of the reflection component is determined by the competition between photoelectric absorption and Compton scattering. For neutral matter, the former dominates $\ll$ 10 keV, the latter above this energy. Combined with the Compton downscattering, a characteristic bump at 20–30 keV is produced. If the matter is ionized, photoabsorption is reduced, and the albedo below 10 keV increases (Ross and Fabian, 1993; Matt et al., 1993a; Nayakshin and Kallman, 2001; Ross and Fabian, 2005).

5.2 Relativistic lines

Among the fluorescent lines, the Fe Kα is often the only detectable. On the other hand, its presence is almost ubiquitous. It may originate both in the innermost regions of the accretion disc or in more distant matter like the "torus." In the first case, its profile is broadened by the Special and General Relativity effects, discussed above. In the latter case, it is unresolved at the energy resolution of present detectors.

Relativistic lines have been discovered by ASCA in the spectra of several AGN, firstly and most notably in the Seyfert galaxy MCG-6-30-15 (Tanaka et al., 1995). XMM-Newton observations have confirmed the presence of the relativistic iron line in this source (Wilms et al., 2001; Fabian et al., 2002) as well as in other sources (e.g., Turner et al., 2002; Balestra et al., 2004; Piconcelli et al., 2006), but in many bright sources the line is definitely narrow (i.e., unresolved at the energy resolution of the CCDs, e.g., Matt et al., 2001, 2006; Pounds et al., 2003; Bianchi et al., 2004; Vaughan et al., 2004, see Fig. 5). Indeed, a narrow iron line is almost always present, independently of the presence of the broad one.

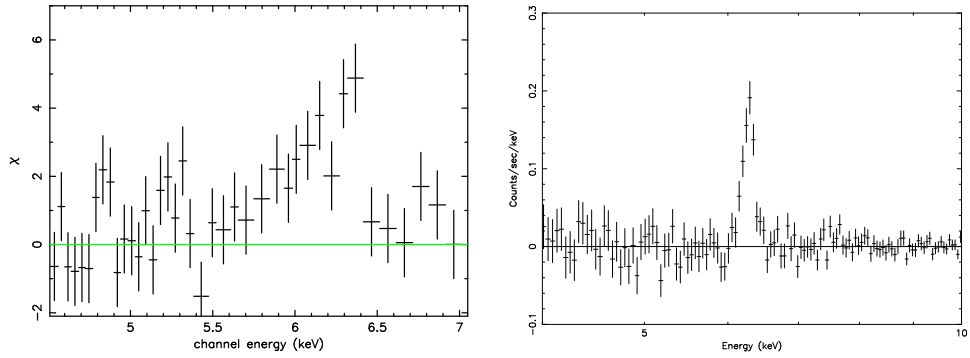

Figure 5. Examples of sources with (*left panel:* 4U 1344-60 Piconcelli et al., 2006) and without (*right panel:* MCG–8-11-11, Matt et al., 2006) the relativistic line.

What is the fraction of AGN with a relativistic line? Guainazzi et al. (2006) and Nandra et al. (2007) analyzed the XMM-Newton spectra of bright Seyfert galaxies available in the public archive. The two groups find similar results, i.e., that this fraction is about 30–40 %. Unfortunately, the number of sources which are bright enough, and/or have been observed with sufficient exposure time, is relatively small, and moreover the samples are neither complete nor, probably, entirely fair. A firm conclusion, however, can already been drawn: relativistic lines are relatively common but definitely not ubiquitous. Possible explanations are now discussed.

5.2.1 Why are relativistic lines not ubiquitous?

In the standard disc-corona scenario, relativistic lines are expected, and the fact that they are not always present is puzzling. A few explanations (none of them fully satisfactory) are now briefly mentioned.

A first possibility is that the matter in the disc is ionized. Some degree of ionization is indeed likely, especially for large accretion rates. A strong reduction of the line flux is expected for moderate (due to resonant trapping) and very large (due to full ionization) degrees of ionization, at least in the constant density model (Matt et al., 1993a, 1996). Hydrostatic equilibrium models (Nayakshin and Kallman, 2001) predict a strong reduction in the line flux with ionization. For a given black hole mass, the ionization parameter (L/nr^2) increases with the accretion rate, hence with luminosity. On the other hand, for a given accretion rate (or, better, Eddington ratio), the ionization parameter decreases with the Black Hole mass, and therefore with luminosity. It would be very important, therefore, to search for a correlation between the presence of the relativistic line and the luminosity or accretion rate. At present, the number of sources in which the relativistic line can be profitably searched for is too limited, but hopefully it will increase in the next years.

Another possibility is that the disc is truncated well before the last stable orbit, therefore producing a less intense and narrower line. Accretion discs are believed to be truncated in the low/hard state of Galactic Black Hole systems (Fender et al. 2004; but the issue is controversial, e.g., Miller et al. 2006). Recently, possible evidence for disc truncation has been found in a quasar, Q0056-383 (Matt et al., 2005). This quasar was observed by XMM-Newton in 2000 and 2003. In the second observation, the UV to X-ray ratio was lower, the soft X-ray emission fainter, the hard X-ray emission flatter, and the iron line EW halved. All these results can be explained, at least qualitatively, if in the second observation the disc is truncated to a much larger radius than in the first observation.

A third possibility is that the line is so broad to be hardly recognizable, at least in relatively faint objects. This may happen if line emission is confined to the innermost regions of an accretion disc around a Kerr Black Hole. Indeed, in MCG-6-30-15 this is what seems to occur (Wilms et al., 2001), either due to enhanced energy dissipation very close to the Black Hole (Wilms et al., 2001) or to geometrical effects (Martocchia et al., 2002; Miniutti et al., 2003). The problem with this solution is that the line EW is expected to be very large (Martocchia and Matt, 1996), as indeed is the case for MCG-6-30-15. Bianchi et al. (2004) analyzed a sample of bright Seyferts observed simultaneously by BeppoSAX and XMM-Newton, and found rather tight upper limits to such lines in all sources.

5.2.2 The light bending model

MCG-6-30-15 is definitely the best source to study the relativistic line, because it is relatively bright and with a very intense iron line. Indeed it has been extensively observed by all major satellites. One of most puzzling result on this source is that the line varies much less than the continuum (Fabian et al., 2002), contrary to what expected in the simple disc-corona model. Miniutti et al. (2003) proposed a model in which the primary emission is due to a small region close to the Black Hole axis (as expected in models like the aborted jets, Ghisellini et al., 2004). As the emitting region goes up and down, the primary emission appears to vary due to variations in the gravitational redshift and light bending, while the reflection has been shown to vary less, at least in a wide range of parameters. This model reproduces rather well the variability pattern in this and other sources. It is also interesting to note that Dovčiak et al. (2004c) made clear predictions on the polarization properties from the reflection component in such a situation. It would be very exciting, for this and many other reasons, to have an X-ray polarimeter on-board a future mission, now that sensitive enough polarimeters do exist (Costa et al., 2006).

6 CONCLUSIONS

Iron lines are probably the best tools to probe GR effects in the vicinity of Black Holes. Spectral distortions are much easier to study in lines then in continua, because of their intrinsic narrowness – broadening can be safely assume to arise mainly, if not exclusively, from such effects. Even if many important observational results have already been obtained, much work is still to be done, especially in using iron lines to estimate the mass and the spin of the Black Hole. Relativistic iron lines are definitely still a major scientific driver for next generation, large area X-ray satellites.

ACKNOWLEDGEMENTS

It is a pleasure to thank the RAGtime organizers for inviting me to this very interesting conference. This contribution owes much to the work of, and the discussions with, my collaborators, and in particular S. Bianchi, M. Dovčiak, M. Guainazzi and V. Karas. I acknowledge financial support from ESA PECS 98040.

REFERENCES

Agol, E. and Krolik, J. H. (2000), Magnetic Stress at the Marginally Stable Orbit: Altered Disk Structure, Radiation, and Black Hole Spin Evolution, *Astrophys. J.*, **528**, p. 161.

Balestra, I., Bianchi, S. and Matt, G. (2004), The reprocessing features in the X-ray spectrum of the NELG MCG-5-23-16, *Astronomy and Astrophysics*, **433**, p. 65.

Bardeen, J. M., Press, W. H. and Teukolsky, S. A. (1972), Rotating black holes: locally nonrotating frames, energy extraction, and scalar synchrotron radiation, *Astrophys. J.*, **178**, pp. 347–369.

Bianchi, S., Matt, G., Balestra, I., Guainazzi, M., Perola, G. C., and and (2004), X-ray reprocessing in Seyfert galaxies: Simultaneous XMM-Newton/BeppoSAX observations, *Astronomy and Astrophysics*, **422**, p. 65.

Carter, B. (1968), Global Structure of the Kerr Family of Gravitational Fields, *Phys. Rev.*, **174**(5), pp. 1559–1571.

Chen, K., Halpern, J. P. and Filippenko, A. V. (1989), Kinematic evidence for a relativistic Keplerian disk – ARP 102B, *Astrophys. J.*, **339**, p. 742.

Costa, E. et al. (2006), Opening a New Window to Fundamental Physics and Astrophysics: X-ray Polarimetry, in F. Favata and Gimenez, editors, *Proc. 39th ESLAB Symposium, Noordwijk, 19–21 April 2005, SP-588*, pp. 141–149, ESA internal publication, Noordwijk, The Netherlands.

Cunningham, C. T. (1975), The effects of redshifts and focusing on the spectrum of an accretion disk around a Kerr black hole, *Astrophys. J.*, **202**, pp. 788–802.

Dabrowski, Y. (1998), Spinning Black Holes in Active Galactic Nuclei, in *First XMM workshop*, volume XX, ESTEC, Noordwijk, arXiv: `astro-ph/9810494`, URL `http://xmm.vilspa.esa.es/external/xmm_science/workshops/1st_workshop/ws1_papers.shtml`.

Di Salvo, T. et al. (2005), A Broad Iron Line in the Chandra High Energy Transmission Grating Spectrum of 4U 1705−44, *Astrophys. J.*, **623**, p. L121.

Dovčiak, M., Bianchi, S., Guainazzi, M., Karas, V. and Matt, G. (2004a), Relativistic spectral features from X-ray-illuminated spots and the measure of the black hole mass in active galactic nuclei, *Monthly Notices Roy. Astronom. Soc.*, **350**, pp. 745–755.

Dovčiak, M., Karas, V., Martocchia, A., Matt, G. and Yaqoob, T. (2004b), An XSPEC model to explore spectral features from black-hole sources, in S. Hledík and Z. Stuchlík, editors, *Proceedings of RAGtime 4/5: Workshops on black holes and neutron stars, Opava, 14–16/13–15 October 2002/2003*, pp. 33–73, Silesian University in Opava, Opava, ISBN 80-7248-242-4, arXiv: `astro-ph/0407330`.

Dovčiak, M., Karas, V. and Matt, G. (2004c), Polarization signatures of strong gravity in active galactic nuclei accretion discs, *Monthly Notices Roy. Astronom. Soc.*, **355**, pp. 1005–1009.

Dovčiak, M., Karas, V., Matt, G. and Goosmann, R. (2007), Variation of the primary and reprocessed radiation from an orbiting spot around a black hole, *Monthly Notices Roy. Astronom. Soc.*, accepted.

Dovčiak, M., Karas, V. and Yaqoob, T. (2004d), An extended scheme for fitting X-Ray data with accretion disk spectra in the strong gravity regime, *Astrophys. J. Suppl.*, **153**, pp. 205–221.

Fabian, A. C., Iwasawa, K., Reynolds, C. S. and Young, A. J. (2000), Broad Iron Lines in Active Galactic Nuclei, *Publ. Astronom. Soc. Pacific*, **112**, pp. 1145–1161.

Fabian, A. C. and Miniutti, G. (2005), The X-ray spectra of accreting Kerr black holes, eprint, part of book Fab:2005:XSpectraKerrBOOK, arXiv: `astro-ph/0507409`.

Fabian, A. C., Rees, M. J., Stella, L. and White, N. E. (1989), X-ray fluorescence from the inner disc in Cygnus X-1, *Monthly Notices Roy. Astronom. Soc.*, **238**, p. 729.

Fabian, A. C. et al. (2002), A long hard look at MCG-6-30-15 with XMM-Newton, *Monthly Notices Roy. Astronom. Soc.*, **335**, p. L1.

Fender, R. P., Belloni, T. M. and Gallo, E. (2004), Towards a unified model for black hole X-ray binary jets, *Monthly Notices Roy. Astronom. Soc.*, **355**, p. 1105.

George, I. M. and Fabian, A. C. (1991), X-ray reflection from cold matter in active galactic nuclei and X-ray binaries, *Monthly Notices Roy. Astronom. Soc.*, **249**, pp. 352–367.

Ghisellini, G., Haardt, F. and Matt, G. (2004), Aborted jets and the X-ray emission of radio-quiet AGNs, *Astronomy and Astrophysics*, **413**, p. 535.

Guainazzi, M., Bianchi, S. and Dovčiak, M. (2006), Statistics of relativistically broadened Fe Kα lines in AGN, *Astronom. Nachr.*, **327**, p. 1028.

Guilbert, P. W. and Rees, M. J. (1988), 'Cold' material in non-thermal sources, *Monthly Notices Roy. Astronom. Soc.*, **233**, p. 475.

Haardt, F. and Maraschi, L. (1991), A two-phase model for the X-ray emission from Seyfert galaxies, *Astrophys. J.*, **380**, p. L5.

Iwasawa, K., Miniutti, G. and Fabian, A. C. (2004), Flux and energy modulation of redshifted iron emission in NGC 3516: implications for the black hole mass, *Monthly Notices Roy. Astronom. Soc.*, **355**, p. 1073.

Karas, V. (2006), Theoretical aspects of relativistic spectral features, *Astronom. Nachr.*, **327**, p. 961.

Kerr, R. P. (1963), Gravitational Field of a Spinning Mass as an Example of Algebraically Special Metrics, *Phys. Rev. Lett.*, **11**, p. 237.

Krolik, J. H. and Hawley, J. F. (2002), Where Is the Inner Edge of an Accretion Disk around a Black Hole?, *Astrophys. J.*, **573**(2), pp. 754–763, arXiv: `astro-ph/0203289`.

Laplace, P. S. (1796), *Exposition du systeme du monde*, Imprimerie du Cercle Social, Paris, an iv edition.

Lightman, A. P. and White, T. R. (1988), Effects of cold matter in active galactic nuclei – A broad hump in the X-ray spectra, *Astrophys. J.*, **335**, p. 57.

Luminet, J.-P. (1979), Image of a spherical black hole with thin accretion disk, *Astronomy and Astrophysics*, **75**, p. 228.

Luminet, J.-P. (1992), *Black Holes*, Cambridge University Press, Cambridge.

Martocchia, A., Karas, V. and Matt, G. (2000), Effects of Kerr space-time on spectral features from X-ray illuminated accretion discs, *Monthly Notices Roy. Astronom. Soc.*, **312**, pp. 817–826.

Martocchia, A. and Matt, G. (1996), Iron K-alpha line intensity from accretion discs around rotating black holes, *Monthly Notices Roy. Astronom. Soc.*, **282**, pp. L53–L57.

Martocchia, A., Matt, G. and Karas, V. (2002), On the origin of the broad, relativistic iron line of MCG-6-30-15 observed by XMM-Newton, *Astronomy and Astrophysics*, **383**, p. L23.

Matt, G. (2006), General Relativity effects and line emission, *Astronom. Nachr.*, **327**, p. 949.

Matt, G., Bianchi, S., de Rosa, A., Grandi, P. and Perola, G. C. (2006), XMM-Newton observation of the bright Seyfert 1 galaxy, MCG+8-11-11, *Astronomy and Astrophysics*, **377**, p. L31.

Matt, G., Fabian, A. C. and Ross, R. R. (1993a), Iron K_α lines from X-ray photoionized accretion discs, *Monthly Notices Roy. Astronom. Soc.*, **262**(1), pp. 179–186.

Matt, G., Fabian, A. C. and Ross, R. R. (1993b), X-Ray Photoionized Accretion Discs – Ultraviolet and X-Ray Continuum Spectra and Polarization, *Monthly Notices Roy. Astronom. Soc.*, **264**, p. 839.

Matt, G., Fabian, A. C. and Ross, R. R. (1996), Iron K fluorescent lines from relativistic, ionized discs, *Monthly Notices Roy. Astronom. Soc.*, **278**, p. 1111.

Matt, G. and Perola, G. C. (1992), The iron K-alpha response in an X-ray illuminated relativistic disc and a black hole mass estimate, *Monthly Notices Roy. Astronom. Soc.*, **259**, p. 433.

Matt, G., Perola, G. C. and Piro, L. (1991), The iron line and high energy bump as X-ray signatures of cold matter in Seyfert 1 galaxies, *Astronomy and Astrophysics*, **247**, pp. 25–34.

Matt, G. et al. (2001), The complex iron line of NGC 5506, *Astronomy and Astrophysics*, **377**, p. L31.

Matt, G. et al. (2005), A changing inner radius in the accretion disc of Q0056-363?, *Astronomy and Astrophysics*, **435**, p. 857.

Michell, J. (1784), On the Means of Discovering the Distance, Magnitude, etc. of the Fixed Stars, in Consequence of the Diminution of the Velocity of Their Light, in Case Such a Diminution Should be Found to Take Place in any of Them, and Such Other Data Should be Procured from Observations,

as Would be Farther Necessary for That Purpose, *Phyl. Trans. Roy. Soc. London*, **74**, p. 35.

Miller, J. M. et al. (2006), A Long, Hard Look at the Low/Hard State in Accreting Black Holes, *Astrophys. J.*, **653**, p. 525.

Miniutti, G., Fabian, A. C., Goyder, R. and Lasenby, A. N. (2003), The lack of variability of the iron line in MCG-6-30-15: general relativistic effects, *Monthly Notices Roy. Astronom. Soc.*, **344**, pp. L22–L26.

Misner, C. W., Thorne, K. S. and Wheeler, J. A. (1973), *Gravitation*, W. H. Freeman and Co, New York, San Francisco.

Nandra, K., O'Neill, P. M., George, I. M. and Reeves, J. N. (2007), An XMM-Newton survey of broad iron lines in Seyfert galaxies, *Monthly Notices Roy. Astronom. Soc.*, in press.

Nandra, K. and Pounds, K. A. (1994), GINGA Observations of the X-Ray Spectra of Seyfert Galaxies, *Monthly Notices Roy. Astronom. Soc.*, **268**, p. 405.

Nayakshin, S. and Kallman, T. R. (2001), Accretion Disk Models and Their X-Ray Reflection Signatures. I. Local Spectra, *Astrophys. J.*, **546**, p. 406.

Palmeri, P., Mendoza, C., Kallman, T. R., Bautista, M. A. and Melendez, M. (2003), Modeling of iron K lines: Radiative and Auger decay data for Fe II–Fe IX, *Astronomy and Astrophysics*, **410**, p. 359.

Pecháček, T., Dovčiak, M., Karas, V. and Matt, G. (2005), The relativistic shift of narrow spectral features from black-hole accretion discs, *Astronomy and Astrophysics*, **441**, pp. 855–861.

Perola, G. C. et al. (2002), Compton reflection and iron fluorescence in BeppoSAX observations of Seyfert type 1 galaxies, *Astronomy and Astrophysics*, **389**, p. 802.

Petrucci, P. O. et al. (2001), Testing Comptonization Models Using BeppoSAX Observations of Seyfert 1 Galaxies, *Astrophys. J.*, **556**, p. 716.

Piconcelli, E. et al. (2006), 4U 1344−60: a bright intermediate Seyfert galaxy at $z = 0.012$ with a relativistic Fe Kα emission line, *Astronomy and Astrophysics*, **453**, p. 839.

Pounds, K. A. et al. (2003), A simultaneous XMM-Newton and BeppoSAX observation of the archetypal broad line Seyfert 1 galaxy NGC 5548, *Monthly Notices Roy. Astronom. Soc.*, **341**, p. 953.

Reynolds, C. S. and Begelman, M. C. (1997), Iron Fluorescence from within the Innermost Stable Orbit of Black Hole Accretion Disks, *Astrophys. J.*, **488**, p. 109.

Reynolds, C. S., Fabian, A. C. and Inoue, I. (1995), ASCA observations of the Seyfert 1 galaxies MRK 1040 and MS 0225.5+3121, *Monthly Notices Roy. Astronom. Soc.*, **276**, p. 1311.

Reynolds, C. S. and Nowak, M. A. (2003), Fluorescent iron lines as a probe of astrophysical black hole systems, *Phys. Rep.*, **377**, pp. 389–466.

Ross, R. R. and Fabian, A. C. (1993), The effects of photoionization on X-ray reflection spectra in active galactic nuclei, *Monthly Notices Roy. Astronom. Soc.*, **261**, p. 74.

Ross, R. R. and Fabian, A. C. (2005), A comprehensive range of X-ray ionized-reflection models, *Monthly Notices Roy. Astronom. Soc.*, **358**, p. 211.

Stella, L. (1990), Measuring black hole mass through variable line profiles from accretion disks, *Nature*, **344**, p. 747.

Tanaka, Y., Nandra, K., Fabian, A. C., Inoue, H., Otani, C., Dotani, T., Hayashida, K., Iwasawa, K., Kii, T., Kunieda, H., Makino, F. and Matsuoka, M. (1995), Gravitationally Redshifted Emission Implying an Accretion Disk and Massive Black-Hole in the Active Galaxy MCG-6-30-15, *Nature*, **375**, p. 659.

Thorne, K. S. (1974), Disk-accretion onto a black hole. II. Evolution of the hole, *Astrophys. J.*, **191**, pp. 507–520.

Turner, T. J. et al. (2002), Narrow Components within the Fe Kα Profile of NGC 3516: Evidence of the Importance of General Relativistic Effects?, *Astrophys. J.*, **574**, p. L123.

Vaughan, S. et al. (2004), An XMM-Newton observation of Ark 120: the X-ray spectrum of a 'bare' Seyfert 1 nucleus, *Monthly Notices Roy. Astronom. Soc.*, **351**, p. 193.

Wilms, J., Reynolds, C. S., Begelman, M. C., Reeves, J., Molendi, S., Staubert, R. and Kendziorra, E. (2001), XMM-EPIC observation of MCG-6-30-15: direct evidence for the extraction of energy from a spinning black hole?, *Monthly Notices Roy. Astronom. Soc.*, **328**, p. L27.

Proceedings of *RAGtime 8/9, 15–19/19–21 September, 2006/2007, Hradec nad Moravicí, Opava, Czech Republic*
S. Hledík and Z. Stuchlík, editors, Silesian University in Opava, 2007, pp. 167–176

Ideas in relativistic hydrodynamics

John Miller

SISSA, International School for Advanced Studies, Via Beirut 2–4, I-34014, Trieste, Italy
INFN, Trieste, Italy
Department of Physics (Astrophysics), University of Oxford, England
miller@sissa.it

ABSTRACT
The talks of which these notes provide a written version were intended to introduce a range of basic ideas in relativistic hydrodynamics to an audience having a background in relativity theory but perhaps not being familiar with this particular material. Following some preliminaries, the basic equations of relativistic hydrodynamics were first introduced in a general form and then some applications to problems with spherical symmetry were discussed, concerning cosmological expansion, gravitational collapse and hydrostatic equilibrium (applicable for relativistic stellar models).

1 PRELIMINARIES

1.1 Going from Newtonian theory to Special Relativity

In going from Newtonian theory to Special Relativity (SR), we move from a picture in which we have three dimensions of space plus a separate one-dimensional time to a picture with a unified four-dimensional space-time in which the three dimensions of space and the one of time are brought together and are seen to be inextricably inter-related. Using rectangular Cartesian coordinates, the formula for the distance between adjacent points in Newtonian theory

$$\mathrm{d}s^2 = \mathrm{d}x^2 + \mathrm{d}y^2 + \mathrm{d}z^2 \tag{1}$$

goes over, in SR, to the 4D space-time interval

$$\mathrm{d}s^2 = \mathrm{d}x^2 + \mathrm{d}y^2 + \mathrm{d}z^2 - c^2\,\mathrm{d}t^2 \tag{2}$$

with $\mathrm{d}s^2$ being invariant under transformations from one inertial frame to another. It is a key point that all four dimensions appear in this. In the *rest frame* of an observer, we have

$$\mathrm{d}s^2 = -c^2\,\mathrm{d}t^2 \quad \rightarrow \quad -c^2\,\mathrm{d}\tau^2\,, \tag{3}$$

where τ is the *proper time* measured by that observer using a co-moving standard clock. Since $\mathrm{d}s^2$ is an invariant, we can then write

$$c^2\,\mathrm{d}\tau^2 = c^2\,\mathrm{d}t^2 - \mathrm{d}x^2 - \mathrm{d}y^2 - \mathrm{d}z^2 \tag{4}$$

978-80-7248-419-5

for non-comoving frames, giving

$$\left(\frac{\mathrm{d}\tau}{\mathrm{d}t}\right)^2 = 1 - \frac{\mathrm{d}x^2 + \mathrm{d}y^2 + \mathrm{d}z^2}{c^2\,\mathrm{d}t^2} \quad \rightarrow \quad 1 - \frac{v^2}{c^2}\,, \tag{5}$$

where v is the three-velocity. This then leads to

$$\frac{\mathrm{d}t}{\mathrm{d}\tau} = \frac{1}{\sqrt{1 - v^2/c^2}} = \gamma \tag{6}$$

with γ being the *Lorentz factor*.

1.2 The position vector in Special Relativity

In Newtonian theory, the position vector (still using rectangular Cartesian coordinates) is given by

$$\boldsymbol{x} \equiv (x, y, z)\,. \tag{7}$$

In Special Relativity (SR) we have two choices. If the interval is written as

$$\mathrm{d}s^2 = \mathrm{d}x^2 + \mathrm{d}y^2 + \mathrm{d}z^2 + \mathrm{d}(\mathrm{i}ct)^2\,, \tag{8}$$

we then have the corresponding position vector

$$\boldsymbol{x} \equiv (x, y, z, \mathrm{i}ct)\,. \tag{9}$$

However, if instead we write the interval as

$$\mathrm{d}s^2 = \mathrm{d}x^2 + \mathrm{d}y^2 + \mathrm{d}z^2 - \mathrm{d}(ct)^2\,, \tag{10}$$

this corresponds to

$$\boldsymbol{x} \equiv (x, y, z, ct) \tag{11}$$

but with also the introduction of the idea of a *metric tensor*. The first approach is often convenient in SR, not only because it avoids the need to introduce the metric tensor at this stage but also because it is then possible to continue using the well-known ideas of Cartesian tensors, just extended from 3D to 4D.

1.3 The Special Principle of Relativity

This says that physical laws should be the same in all inertial frames, embodying the idea of *covariance*. Mathematically, covariance is ensured if we write our physical laws in terms of scalars, vectors and tensors, with the vectors and tensors having the same dimensionality as the space concerned (i.e., four dimensions for the space-time of SR).

1.4 Velocity in Special Relativity

In order to get a velocity, we need to differentiate the position vector with respect to time, but the differentiation of our position 4-vector must be with respect to a *scalar* measure of time in order to produce another 4-vector. Our scalar measure of time is the proper time τ, and so for the 4-velocity we have

$$\boldsymbol{u} \equiv \frac{\mathrm{d}}{\mathrm{d}\tau}(\boldsymbol{x}) \quad \rightarrow \quad \frac{\mathrm{d}t}{\mathrm{d}\tau} \cdot \frac{\mathrm{d}}{\mathrm{d}t}(x, y, z, \mathrm{i}ct) \quad \rightarrow \quad \gamma(v_x, v_y, v_z, \mathrm{i}c) \,. \tag{12}$$

Having introduced these basic ideas, we now move on to our discussion of relativistic hydrodynamics.

2 THE SYSTEM OF EQUATIONS DESCRIBING A RELATIVISTIC FLUID

Our system of equations needs to include

- conservation of mass,
- an energy equation,
- a momentum equation.

In the following, we will see how the expressions for these in relativity theory differ from the corresponding ones in Newtonian theory.

2.1 Conservation of mass

We will begin this subsection with a purely *Newtonian* discussion and will then generalise it. We focus on an imaginary fixed three-dimensional box of unit volume through which the fluid is able to flow freely. Since the box has unit volume, the amount of mass inside it at any time is equal to the *mass density* ρ, and the time rate of change of this is given by the Newtonian equation

$$\frac{\partial \rho}{\partial t} = -\nabla \cdot (\rho \boldsymbol{v}) \,, \tag{13}$$

which says just that the rate of change of the amount of mass contained in the box is equal to the negative of the net mass flux out of it. Writing this in components (again using rectangular Cartesian coordinates), we have

$$\frac{\partial \rho}{\partial t} = -\frac{\partial}{\partial x}(\rho v_x) - \frac{\partial}{\partial y}(\rho v_y) - \frac{\partial}{\partial z}(\rho v_z) \,. \tag{14}$$

Bringing all of the terms onto the left-hand side and re-arranging gives

$$\frac{\partial}{\partial x}(\rho v_x) + \frac{\partial}{\partial y}(\rho v_y) + \frac{\partial}{\partial z}(\rho v_z) + \frac{\partial}{\partial t}(\rho) = 0 \,. \tag{15}$$

Now we make a move which is completely allowed but very non-intuitive when viewed in a Newtonian context: we make the replacement

$$\frac{\partial}{\partial t}(\rho) \quad \rightarrow \quad \frac{\partial}{\partial(\mathrm{i}ct)}(\rho \mathrm{i}c) \,. \tag{16}$$

Using this, Eq. (15) can be rewritten in the compact form

$$\sum_j \frac{\partial}{\partial x_j}(\rho v_j) = 0\,, \tag{17}$$

where

$$x_j \equiv (x, y, z, \mathrm{i}ct) \tag{18}$$

and

$$v_j \equiv (v_x, v_y, v_z, \mathrm{i}c) \equiv \frac{\partial}{\partial t}(x_j)\,. \tag{19}$$

This is *Newtonian theory* written in an unusual way. In order to go to SR, it is necessary to replace $v_j \equiv \partial x_j/\partial t$ with $u_j \equiv \partial x_j/\partial \tau$ since the quantity representing the velocity needs to be a 4-vector in order to have covariance. Also, ρ now has to be specified as being the *rest-mass density*. Next, we use the *summation convention* (implied summation over repeated indices):

$$\sum_j \frac{\partial}{\partial x_j}(\rho u_j) \quad \rightarrow \quad \frac{\partial}{\partial x_j}(\rho u_j) \tag{20}$$

and introduce the comma notation for partial derivatives

$$\frac{\partial}{\partial x_j}(\rho u_j) \quad \rightarrow \quad (\rho u_j)_{,j}\,. \tag{21}$$

The mass conservation equation (17) then becomes

$$(\rho u_j)_{,j} = 0 \tag{22}$$

which is *Lorentz covariant* for flat space-time (SR). For the curved space-time of General Relativity (GR), we need to replace the partial derivative with a covariant derivative in order to give a tensor quantity, and then we have

$$(\rho u^\mu)_{;\mu} = 0 \tag{23}$$

which is *generally covariant* as necessary for GR. In making this step, we also move to an *indefinite metric*, using $x^0 = ct$ rather than $x_4 = (\mathrm{i}ct)$ as the time component of the position vector, and this then requires making a distinction between contravariant and covariant vectors. Under these circumstances, we follow the convention of using Greek letters for indices rather than Latin ones.

2.2 The energy equation

In the previous subsection, we considered an imaginary box of unit volume which was fixed with respect to the coordinate system being used. For the discussion in this subsection, we

shift to considering a different imaginary box which is now *co-moving* with the matter flow and contains unit mass (rest-mass) of the medium which we take to be a perfect fluid (i.e., no viscosity, heat transfer, etc). The change in the internal energy of the matter in the box, as it is expanded or compressed, is given by the first law of thermodynamics:

$$\mathrm{d}\varepsilon = -p\,\mathrm{d}V\,, \tag{24}$$

where ε is the specific internal energy, p is the pressure and V is the volume (proper volume) of the box. Since we have unit mass in the box, $\rho V = 1$ and $V = 1/\rho$, so that

$$\mathrm{d}\varepsilon = -p\,\mathrm{d}\left(\frac{1}{\rho}\right)\,. \tag{25}$$

Next, we introduce the total energy density

$$e = \rho c^2 + \rho\varepsilon = \rho(c^2 + \varepsilon)\,. \tag{26}$$

Up to this point, the discussion in this subsection has been the same for Newtonian theory and in relativity (as long as rest mass and proper volume are used when appropriate) but this step moves strictly to relativity with the introduction of the rest-mass energy (using $E = mc^2$). Next, we look at the variation of the energy density as the box expands or contracts; we have

$$\begin{aligned}
\mathrm{d}e &= (c^2 + \varepsilon)\,\mathrm{d}\rho + \rho\,\mathrm{d}\varepsilon \\
&\rightarrow (c^2 + \varepsilon)\,\mathrm{d}\rho - p\rho\,\mathrm{d}\left(\frac{1}{\rho}\right) \\
&\rightarrow (c^2 + \varepsilon)\,\mathrm{d}\rho + \frac{p}{\rho}\,\mathrm{d}\rho \\
&\rightarrow \left(c^2 + \varepsilon + \frac{p}{\rho}\right)\,\mathrm{d}\rho \\
&\rightarrow \frac{e+p}{\rho}\,\mathrm{d}\rho\,.
\end{aligned} \tag{27}$$

Note here the appearance of the enthalpy density $(e + p)$. Eq. (27) links the changes of e and ρ and can also be written in terms of the co-moving (Lagrangian) derivatives of these quantities:

$$\mathrm{D}_t e = \frac{e+p}{\rho}\,\mathrm{D}_t\rho\,, \tag{28}$$

where the relativistic expression for D_t gives

$$\mathrm{D}_t e \equiv u^\mu e_{,\mu} = \frac{\partial e}{\partial x^\mu}\,\frac{\mathrm{d}x^\mu}{\mathrm{d}\tau} = \frac{\mathrm{d}e}{\mathrm{d}\tau} \tag{29}$$

(similarly for $\mathrm{D}_t\rho$). From the mass equation (23)

$$(\rho u^\mu)_{;\mu} = 0 \quad \rightarrow \quad u^\mu\rho_{,\mu} + \rho u^\mu{}_{;\mu} = 0 \tag{30}$$

and so

$$\mathrm{D}_t \rho \equiv u^\mu \rho_{,\mu} = -\rho u^\mu{}_{;\mu} \,. \tag{31}$$

The energy equation (28) can then be written in the alternative form

$$u^\mu e_{,\mu} + (e + p) u^\mu{}_{;\mu} = 0 \,. \tag{32}$$

2.3 The momentum equation

Following on from the discussion in Section 2.1, the general form for a relativistic conservation equation is

$$\left(X u^\mu\right)_{;\mu} = 0 \,, \tag{33}$$

where X is the density of the quantity being conserved. Compare this with the Newtonian form

$$\frac{\partial X}{\partial t} = -\boldsymbol{\nabla} \cdot (X \boldsymbol{v}) \,. \tag{34}$$

In this subsection, we will look at conservation of momentum, setting X equal to the momentum density ρu^ν (but bearing in mind that momentum is only conserved if there are no forces acting). Expanding out the expression coming from the left hand side of Eq. (33) then gives

$$(\rho u^\nu u^\mu)_{;\mu} = u^\nu{}_{;\mu} (\rho u^\mu) + u^\nu (\rho u^\mu)_{;\mu} \,. \tag{35}$$

The second term on the right hand side is zero, by conservation of rest mass, and so

$$(\rho u^\nu u^\mu)_{;\mu} = \rho u^\mu u^\nu{}_{;\mu} = \rho \, \mathrm{D}_t u^\nu \,. \tag{36}$$

If there are no forces acting, $\rho \, \mathrm{D}_t u^\nu \to 0$ and momentum is then conserved, as expected. We now introduce the *energy-momentum tensor* as

$$T^{\mu\nu} \equiv \rho u^\mu u^\nu \tag{37}$$

and, if there are no forces acting, we have

$$T^{\mu\nu}{}_{;\nu} = 0 \,. \tag{38}$$

(Note that $T^{\mu\nu}$ has dimensions of *energy density*.) When there *are* forces acting, as is typically the case, the right hand side would be non-zero if the energy-momentum tensor continued to be defined as above, but it turns out to be more convenient to absorb the forces into the definition of $T^{\mu\nu}$ so that Eq. (38) continues to hold. We are focusing here on the case of a *perfect fluid* with energy density e and pressure p (which is an internal force). How should we then modify $T^{\mu\nu}$? If there were no pressure, then it would just be necessary to replace ρ by e/c^2 and this suggests writing

$$T^{\mu\nu} = \frac{e}{c^2} u^\mu u^\nu + p S^{\mu\nu} \,, \tag{39}$$

where $S^{\mu\nu}$ is the most general second-rank tensor that can be constructed from quantities associated with the fluid:

$$S^{\mu\nu} = ku^\mu u^\nu + \ell g^{\mu\nu} . \tag{40}$$

We need to check whether this is, in fact, reasonable and to determine the values of the constants k and ℓ. Projecting $T^{\mu\nu}{}_{;\nu} = 0$ along the direction of motion of the fluid element (i.e., taking $u_\mu T^{\mu\nu}{}_{;\nu} = 0$) gives the energy equation and we already know what that should be from Section 2.2. It is easy to check that $u_\mu T^{\mu\nu}{}_{;\nu} = 0$ *does* reduce to Eq. (32) *if* $\ell = kc^2 = 1$. Therefore, we have

$$T^{\mu\nu} = \frac{e+p}{c^2}\, u^\mu u^\nu + p g^{\mu\nu} \tag{41}$$

for a perfect fluid. Finally, using this in $T^{\mu\nu}{}_{;\nu} = 0$ leads to the *Euler equation*:

$$\mathrm{D}_t u^\mu \equiv u^\nu u^\mu{}_{;\nu} = -\frac{p_{,\nu}}{e+p}\left(g^{\mu\nu}c^2 + u^\mu u^\nu\right) . \tag{42}$$

The *mass equation*, the *energy equation* and the *Euler equation* form the full set of hydrodynamical equations for a perfect fluid in a given space-time. However, we need the *Einstein field equations* to tell us about the space-time curvature produced by a given source.

2.4 The full set of relativistic hydro equations for a perfect fluid

To summarise, our set of hydrodynamical equations written in Lagrangian form (i.e., using time derivatives which are projections of the partial or covariant derivatives along the fluid world-lines) are

$$\mathrm{D}_t \rho = -\rho u^\mu{}_{;\mu} , \tag{43}$$

$$\mathrm{D}_t e = \frac{e+p}{\rho}\,\mathrm{D}_t \rho , \tag{44}$$

$$\mathrm{D}_t u^\mu = -\frac{p_{,\nu}}{e+p}\left(g^{\mu\nu}c^2 + u^\mu u^\nu\right) , \tag{45}$$

while in Eulerian form we have

$$\left(\rho u^\mu\right)_{;\mu} = 0 , \tag{46}$$

$$u^\mu e_{,\mu} + (e+p)u^\mu{}_{;\mu} = 0 , \tag{47}$$

$$u^\nu u^\mu{}_{;\nu} + \frac{p_{,\nu}}{e+p}\left(g^{\mu\nu}c^2 + u^\mu u^\nu\right) = 0 . \tag{48}$$

Note that the 4-acceleration $\mathrm{D}_t u^\mu$ is zero if there is no pressure and Eq. (45) then reduces to the geodesic equation. The gravity is contained inside the 4-acceleration: in the following, it will be convenient to write

$$\mathrm{D}_t u^\mu = u^\nu u^\mu{}_{;\nu} = u^\nu\left(\frac{\partial u^\mu}{\partial x^\nu} + \Gamma^\mu_{\nu\lambda}\, u^\lambda\right) \quad \rightarrow \quad \frac{\mathrm{d}u^\nu}{\mathrm{d}\tau} + \Gamma^\mu_{\nu\lambda}\, u^\nu u^\lambda , \tag{49}$$

where the term $\Gamma^\mu_{\nu\lambda}\, u^\nu u^\lambda$ represents the "gravitational part."

3 SOME APPLICATIONS TO PROBLEMS WITH SPHERICAL SYMMETRY

3.1 The equation of motion

Up to now, our treatment has been general in the sense that no particular symmetry has been assumed. In this section, we will restrict attention to spherical symmetry but will include self-gravity of the fluid. The equation of motion for the fluid elements can then be written (see Misner and Sharp, 1964 and many subsequent authors) as:

$$\frac{\mathrm{d}U}{\mathrm{d}\tau} = -\frac{\Gamma^2 c^2}{e+p}\,\frac{\partial p}{\partial R} - \frac{Gm}{R^2} - 4\pi R\frac{G}{c^2}p\,, \tag{50}$$

where

R is the Schwarzschild circumference coordinate,

$U = \mathrm{D}_t R\,,$

$$m = \int_0^R 4\pi R^2 (e/c^2)\,\mathrm{d}R\,,$$

$$\Gamma^2 = 1 - \frac{2Gm}{Rc^2} + \frac{U^2}{c^2}\,.$$

and a diagonal metric is being used with co-moving coordinates. The derivation of Eq. (50) involves the Euler equation (45) together with the Einstein field equations. We will now consider applications of it in two particular cases.

3.2 Case 1: A homogeneous medium

We consider here a medium for which the energy density e and the pressure p are the same everywhere at any particular value of the coordinate time but can change with time. A well-known example of this is in the Friedmann–Robertson–Walker cosmological models. For a medium of this type, Eq. (50) can be written as

$$\frac{\mathrm{d}U}{\mathrm{d}\tau} = -\frac{G}{c^2}\left(\tfrac{4}{3}\pi R e + 4\pi R p\right) \quad \rightarrow \quad -\frac{4\pi}{3}\,\frac{G}{c^2}\,R(e+3p)\,. \tag{51}$$

Defining

$$\frac{\mathrm{d}U}{\mathrm{d}\tau} \equiv \ddot{R}\,, \tag{52}$$

Eq. (51) can then be written as

$$\ddot{R} + \frac{4\pi}{3}\,\frac{G}{c^2}\,R(e+3p) = 0\,, \tag{53}$$

which is the *Friedmann acceleration equation*. This applies for either expansion (as in the case of the universe, at least at present) or contraction (as in gravitational collapse). When used for collapse, it gives the basis for the *Oppenheimer–Snyder* solution (Oppenheimer and Snyder, 1939), where the pressure is set to zero.

Suppose now that we have a *false vacuum* present in addition to the matter. A property of a false vacuum is that it has constant energy density $e_{\rm v}$ at all places and at all times. The energy equation (44) for this component then gives

$$\mathrm{D}_t e_{\rm v} = -(e_{\rm v} + p_{\rm v})\, u^{\mu}{}_{;\mu} \to 0\,, \tag{54}$$

where $u^{\mu}{}_{;\mu}$ is the expansion of the worldlines of the standard component, and this implies

$$p_{\rm v} = -e_{\rm v}\,. \tag{55}$$

Adding this to the standard component

$$e \to e + e_{\rm v}\,, \tag{56}$$

$$p \to p + p_{\rm v} = p - e_{\rm v}\,, \tag{57}$$

and Eq. (53) then becomes

$$\ddot{R} + \frac{4\pi}{3}\frac{G}{c^2}R(e+3p) = \frac{8\pi}{3}\frac{G}{c^2}Re_{\rm v} \quad \to \quad \frac{1}{3}R\Lambda c^2\,, \tag{58}$$

where $\Lambda = 8\pi G e_{\rm v}/c^4$ is the *cosmological constant*.

3.3 Case 2: Hydrostatic equilibrium

For a configuration in hydrostatic equilibrium, both the velocity U and the acceleration $\mathrm{d}U/\mathrm{d}\tau$ are zero everywhere. Eq. (50) then gives

$$\frac{\partial p}{\partial R} = -\frac{G\left[m + 4\pi R^3 p/c^2\right]\left[(e+p)/c^2\right]}{R\left[R - 2Gm/c^2\right]}\,. \tag{59}$$

This is the Tolman–Oppenheimer–Volkoff (TOV) equation which is used for calculating the equilibrium structure of spherical relativistic stars (e.g., *neutron stars*). The equivalent equation in Newtonian theory is

$$\frac{\partial p}{\partial R} = -\frac{Gm\rho}{R^2} \tag{60}$$

and it is interesting to check on how important an effect is produced by the relativistic corrections in each of the sets of square brackets in the TOV equation (59). Curves of total mass plotted against radius are shown in Fig. 1 for sequences of neutron star models calculated with the rather typical Bethe–Johnson equation of state (Bethe and Johnson, 1974), using different versions of the equation of hydrostatic equilibrium: the dotted curves were calculated with the Newtonian equation (60); for the short-dashed curves, this was modified by including the correction term in the first set of square brackets in Eq. (59), i.e., $4\pi R^3 p/c^2$ was added to m; for the long-dashed curves, the pressure correction term in the second set of square brackets was also included (ρ was put equal to e/c^2 for the Newtonian calculation); for the solid curves, the full form of Eq. (59) was used. It can be seen that for neutron stars near to the canonical mass of $1.4\,\mathrm{M}_\odot$, the subtraction of $2Gm/c^2$ from R in the denominator has overwhelmingly the most significant effect but for the models with the highest masses, all of the correction terms are very important. The differences between the Newtonian and relativistic higher-mass models are enormous.

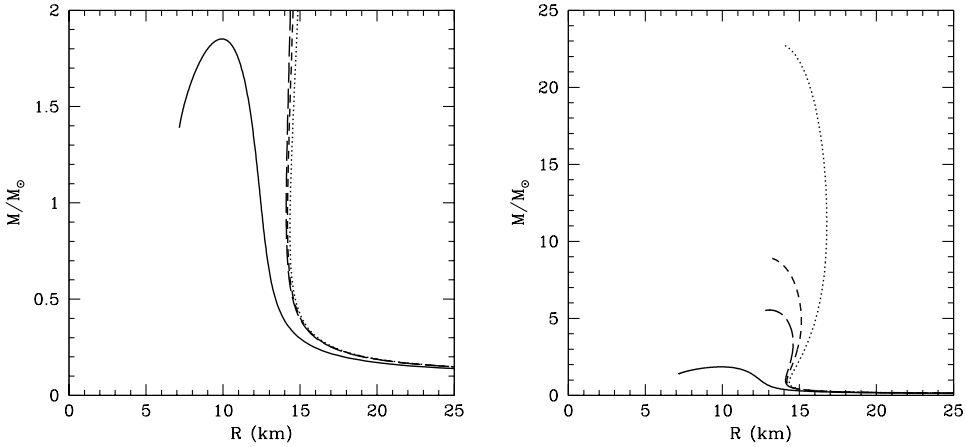

Figure 1. The relation between the gravitational mass M and radius R of neutron star models calculated using different forms of the equation of hydrostatic equilibrium. See text for details.

REFERENCES

Bethe, H. and Johnson, M. B. (1974), Dense baryon matter calculations with realistic potentials, *Nuclear Phys. A*, **230**, p. 1.

Misner, C. W. and Sharp, D. H. (1964), Relativistic equations for adiabatic, spherically symmetric gravitational collapse, *Phys. Rev.*, **136**, p. B571.

Oppenheimer, J. R. and Snyder, H. (1939), On continued gravitational contraction, *Phys. Rev.*, **56**, p. 455.

Proceedings of *RAGtime 8/9, 15–19/19–21 September, 2006/2007, Hradec nad Moravicí, Opava, Czech Republic*
S. Hledík and Z. Stuchlík, editors, Silesian University in Opava, 2007, pp. 177–187

Modelling an accretion disc stochastical variability

Tomáš Pecháček and Vladimír Karas

Astronomical Institute, Czech Academy of Sciences, Boční II 1401/1a, CZ-141 31 Praha 4, Czech Republic

ABSTRACT
Hot spots residing on the surface of an accretion disc have been considered as a model of short-term variability of active galactic nuclei. In this paper we apply the theory of random point processes to model the observed signal from an ensemble of randomly generated spots. The influence of general relativistic effects near a black hole is taken into account and it is shown that typical features of power spectral density can be reproduced. Connection among spots is also discussed in terms of Hawkes' process, which produces more power at low frequencies. We derive a semi-analytical way to approximate the resulting power-spectral density.

Keywords: Black holes – accretion – variability

1 INTRODUCTION

Radiation from accreting black holes varies on different timescales (Gaskell et al., 2006). In X-rays, the observed light-curve, $f \equiv f(t)$, is a complicated noisy curve that can be represented by a broad-band power spectrum (Uttley et al., 2002). It has been proposed (Abramowicz et al., 1991; Wiita et al., 1992) that "hot spots" are a possible contributor to this variability. These spots are supposed to occur on the surface of an accretion disc following its irradiation by coronal flares (Galeev et al., 1979; Merloni and Fabian, 2001; Czerny et al., 2004). A model light-curve can be constructed as a sum of contributions from many point-like sources that are orbiting above an underlying accretion disc. The observed signal is modulated by relativistic effects as photons propagate towards a distant observer.

In order to characterise the light curves we need to introduce some appropriate estimator of the source variability. In a mathematical sense, one applies a functional: $f \rightarrow \mathcal{S}[f]$, where $\mathcal{S}[.]$ is a map from functions defined on $\mathbb{R}$ to functions on $\mathbb{R}^k$ ($k \geq 0$). The variability estimator can be a single number (for example, the mean flux or the "rms" characteristic), or function of one variable (power spectrum density or probability distribution) or of many variables (poly-spectra, rms-flux relation, etc). A signal of such a spotted accretion disc should be intrinsically stochastical. Hence, the variability estimator $\mathcal{S}[f]$, derived from a piece of the light-curve, is a random value, too.

Various schemes have been proposed in which spots are mutually interconnected in some way (Poutanen and Fabian, 1999; Życki and Niedźwiecki, 2005). We want to investigate

978-80-7248-419-5

this type of models within a common mathematical basis. Other authors have developed different approaches to the problem (Mineshige et al., 1994; Lyubarskii, 1997).

2 SPOT MODELS AND THE ACCRETION DISC VARIABILITY

2.1 Model assumptions and variables

Let us have K samples of the observed light-curves from the same source, f_j. The law of large numbers ensures that

$$\frac{1}{K}\sum_{j=1}^{K}\mathcal{S}\left[f_j\right] \to \mathrm{E}\left[\mathcal{S}\left[f\right]\right], \quad K \to \infty, \tag{1}$$

where E[.] is the mean value operator. The average value of the functional is formally defined

$$\mathrm{E}\left[\mathcal{S}\left[f\right]\right] \equiv \sum_{\{\text{All possible } f_j(t)\}} \left(\text{Probability of } f_j\right) \times \mathcal{S}\left[f_j\right], \tag{2}$$

where the sum goes over all possible light-curves generated by this model. We will show how to define and parameterise "the space of all possible light-curves" and how to perform the averaging when the functional is the power spectrum.

The general model is constrained only by the following three assumptions about the creation and evolution of spots:

(i) Each spot is described by its time and place of birth (t_j, r_j and ϕ_j) on the disc surface.
(ii) Every new occurrence starts instantaneously; afterwards the emissivity decays gradually to zero. The total emitted radiation energy is finite.
(iii) The intrinsic emissivity can be fully determined by a finite number of parameters which form a vector $\boldsymbol{\xi}_j$.

For a simple demonstration of this concept see Fig. 1. The disc itself has a passive role in our present considerations. We will treat it as a geometrically thin, optically thick layer lying in the equatorial plane.

2.2 Random point processes

The concept of point processes is a generalisation of well-known random processes which were developed as a description of time-dependent random values (Bendat and Piersol, 2000). Point processes are used as statistical description of configurations of some randomly distributed points in space $\mathbb{R}^n$.

One way of describing a configuration of points is by their counting measure, $N(A)$, which for every $A \subset \mathbb{R}^n$ gives a number of points lying in A. One defines the intensity measure,

$$M_1(A) = \mathrm{E}\left[N(A)\right]. \tag{3}$$

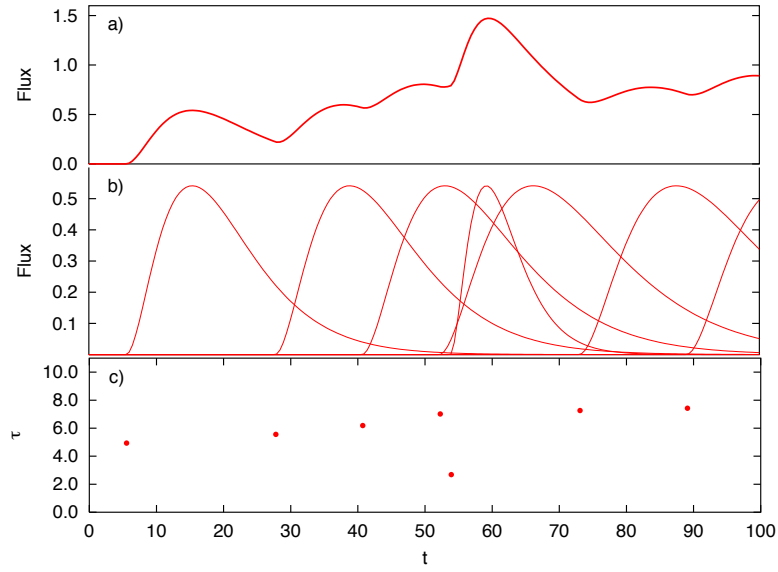

Figure 1. The model curve (*panel a*) is obtained as a sum of elementary events (*panel b*). Profile of each individual event is assumed to be $I(t,\tau) = (t/\tau)^2 \exp(-t/\tau)\,\theta(t)$, as described in the text. Their normalization is assumed to be identical. The final light-curve is fully determined by the form of the individual contributions together with a set of points in t-τ plane (*panel c*), which represent pairs of ignition times and temporal constants τ of each event.

Similarly to random processes, the point process can be characterised by its *mean value* and *moments*. For every $A \subset \mathbb{R}^n$, $M_1(A)$ is the mean number of points lying in A. The second-order moment measure is defined in the same way on the Cartesian product of spaces $\mathbb{R}^n \times \mathbb{R}^n$:

$$M_2(A \times B) = \mathrm{E}\left[N(A)N(B)\right] . \tag{4}$$

Let $\{x_i\}_N$ be one possible configuration of points, i.e., the support of some $N(.)$ For the functions $f(x)$ and $g(x,y)$ on $\mathbb{R}^n$ and $\mathbb{R}^{2n}$, respectively, it follows (Campbell, 1909; Daley and Vere-Jones, 2003)

$$\mathrm{E}\left[\sum_{\{x_i\}_N} f(x_i)\right] = \mathrm{E}\left[\int_{\mathbb{R}^n} f(x)N(\mathrm{d}x)\right] = \int_{\mathbb{R}^n} f(x)M_1(\mathrm{d}x)\,, \tag{5}$$

$$\mathrm{E}\left[\sum_{\substack{\{x_i\}_N \\ \{y_i\}_N}} g(x_i,y_i)\right] = \mathrm{E}\left[\int_{\mathbb{R}^{2n}} g(x,y)N(\mathrm{d}x)N(\mathrm{d}y)\right] = \int_{\mathbb{R}^{2n}} g(x,y)M_2(\mathrm{d}x\times\mathrm{d}y)\,. \tag{6}$$

The concept of point process can be further generalised in the following way. We add a *mark* κ_i from the mark set $\mathcal{K}$ to each coordinate x_i from $\{x_i\}_N$. Marks carry additional

information. The resulting point process on the set $\mathbb{R}^n \times \mathcal{K}$ is called the "marked point process" if for every $A \subset \mathbb{R}^n$ it fulfils the condition $N_{\rm g}(A) \equiv N(A \times \mathcal{K}) < \infty$.

The random measure $N_{\rm g}(A)$ represents the *ground process* of the marked process N. When the dynamics of the process is governed only by the ground process and marks are mutually independent and identically distributed random values with the distribution functions $G(\mathrm{d}\kappa)$, then the process intensity and the second order measure fulfil

$$M_1(\mathrm{d}x \times \mathrm{d}\kappa) = M_{1\rm g}(\mathrm{d}x)G(\mathrm{d}\kappa)\,, \tag{7}$$

$$M_2(\mathrm{d}x_1 \times \mathrm{d}\kappa_1 \times \mathrm{d}x_2 \times \mathrm{d}\kappa_2) = M_{\rm g2}(\mathrm{d}x_1 \times \mathrm{d}x_2)G(\mathrm{d}\kappa_1)G(\mathrm{d}\kappa_2)\,. \tag{8}$$

2.3 Relationship between point processes and spots

Let us assume a surface element orbiting at radius r with constant emissivity I and orbital frequency $\Omega(r)$. This should represent an infinitesimally small spot. For the flux measured by an observer at inclination $\theta_{\rm o}$ we find

$$f(t) = I\,F(t, r, \theta_{\rm o})\,. \tag{9}$$

The periodical modulation of the signal is determined by relations

$$F(t(\phi), r, \theta_{\rm o}) = F(\phi, r, \theta_{\rm o})\,, \tag{10}$$

$$t(\phi) = \frac{\phi}{\Omega(r)} + \delta t(\phi, r, \theta_{\rm o})\,, \tag{11}$$

where $F(\phi, r, \theta_{\rm o})$ is the transfer function describing the total amplification of signal emitted from then disc surface element on the coordinates r and ϕ. The function $\delta t(\phi, r, \theta_{\rm o})$ is the time delay of the signal (hereafter we will omit $\theta_{\rm o}$ in the argument of F for simplicity). Now, we consider a process consisting of statistically dependent events,

$$f(t) = \sum_j I(t - \delta_j, \boldsymbol{\xi}_j)F(t - \delta_{{\rm p}j}, r_j)\,, \tag{12}$$

where: $I(t, \boldsymbol{\xi}) = \theta(t)g(t, \boldsymbol{\xi})$ is the profile of a single event; $\delta_j = t_j + t_{0j}$ is time offset; $\delta_{{\rm p}j} = \delta_j + t_{{\rm p}j}$ is the phase offset; $\theta(t)$ is the Heaviside function; and $g(t, \boldsymbol{\xi})$ is non-negative function of $k+1$ variables t and $\boldsymbol{\xi} = (\xi^1, \ldots, \xi^k)$, which is on the interval $\langle 0, \infty)$ integrable in the variable t for all values of parameters $\boldsymbol{\xi} \in \Xi$. The set Ξ is some measurable subset of $\mathbb{R}^k$. For a fixed value of r, $F(t, r)$ is a periodical function of t, with the angular frequency $\Omega(r)$.

Quantities $\boldsymbol{\xi}_j, t_j, r_j, t_{{\rm p}j}$ and t_{0j} are random values. The vector $\boldsymbol{\xi}_j$ determines the duration and shape of each event, t_j is time of ignition of the j-th event, and t_{0j} the corresponding initial time-offset. Parameter $t_{{\rm p}j}$ determines the initial phase of the periodical modulation. Processes of this kind and their power spectra were mathematically studied by Brémaud and Massoulié (2002); Brémaud et al. (2005).

Power spectral function of a stationary stochastic process $X(t)$ is

$$S(\omega) = \lim_{T\to\infty} \frac{1}{2T}\,\mathrm{E}\left[|\mathcal{F}_T[X(t)](\omega)|^2\right]\,, \tag{13}$$

where $\mathcal{F}_T[\,]$ is the incomplete Fourier transform,

$$\mathcal{F}_T[X(t)] = \int_{-T}^{T} X(t)\,\mathrm{e}^{-\mathrm{i}\omega t}\,\mathrm{d}t\,. \tag{14}$$

This can be evaluated by using the complete Fourier transform,

$$\int_{-T}^{T} X(t)\,\mathrm{e}^{-\mathrm{i}\omega t}\,\mathrm{d}t = \int_{-\infty}^{\infty} X(t)\chi_{\langle -T,\,T\rangle}(t)\,\mathrm{e}^{-\mathrm{i}\omega t}\,\mathrm{d}t = 2\,\frac{\sin(T\omega)}{\omega} \star \mathcal{F}[X(t)](\omega)\,, \tag{15}$$

where $\chi_A(x)$ is the characteristic function of set A, which equals 1 for $x \in A$ and 0 for $x \notin A$. Symbol $\star$ denotes the convolution operation.

By applying this transformation on the process (12) we find

$$\mathcal{F}_T[f(t)](\omega) = \frac{2\sin(T\omega)}{\omega} \star \sum_j \mathcal{F}[I(t-\delta_j, \boldsymbol{\xi}_j)F(t-\delta_{\mathrm{p}j}, r_j)](\omega)\,. \tag{16}$$

The Fourier transform of a single event $I(t-\delta_j, \boldsymbol{\xi}_j)F(t-\delta_{\mathrm{p}j}, r_j)$ is then

$$\mathcal{F}[I(t-\delta_j, \boldsymbol{\xi}_j)F(t-\delta_{\mathrm{p}j}, r_j)](\omega) = \mathrm{e}^{-\mathrm{i}\omega\delta_j}\,\mathcal{F}[I(t, \boldsymbol{\xi}_j)] \star \mathcal{F}[F(t+t_{\mathrm{p}j}, r_j)]\,. \tag{17}$$

Function $F(t, r)$ is periodical in time, and so it can be expanded:

$$F(t, r) = \sum_{k=-\infty}^{\infty} c_k(r)\,\mathrm{e}^{\mathrm{i}k\Omega(r)t}\,, \tag{18}$$

where $\Omega(r)$ is the frequency of $F(t, r)$. We find

$$\mathcal{F}\left[F(t_{\mathrm{p}}, r)\right](\omega) = \sum_{k=-\infty}^{\infty} c_k(r)\,\mathrm{e}^{\mathrm{i}k\Omega(r)t_{\mathrm{p}}}\delta\left(\omega - k\Omega(r)\right)\,, \tag{19}$$

$$\mathcal{F}\left[I(t, \boldsymbol{\xi})\right] \star \mathcal{F}\left[F(t+t_{\mathrm{p}}, r)\right] = \sum_{k=-\infty}^{\infty} c_k(r)\,\mathrm{e}^{\mathrm{i}k\Omega(r)t_{\mathrm{p}}}\mathcal{F}\left[I(t, \boldsymbol{\xi})\right](\omega - k\Omega(r))\,. \tag{20}$$

The above given formulation of the problem falls perfectly within the mathematical framework of point processes.

2.4 The case of independent decaying spots (Poisson process)

Knowing the incomplete Fourier transform of $f(t)$ we can now calculate its squared absolute value and perform the averaging over all realizations of the process. Between $-T$ and T the process is influenced by all events ignited during the preceding interval $\langle -\infty, T\rangle$, however (because of fast decay of every single event), this can be restricted onto $\langle -(T+C), T\rangle$,

where C is a sufficiently large positive constant. Therefore, every realization of the process $f(t)$ on the interval $\langle -T, T\rangle$ can be described by set of points in $(k+4)$-dimensional space $(t_j, t_{0j}, t_{\mathrm{p}j}, r_j, \boldsymbol{\xi}_j)$, where $t_j \in \langle -(T+C), T\rangle$.

Equation (12) represents a very general class of random processes. However, in all reasonable models of spotted accretion discs the values of initial time delay and phase are functions of initial position of each spot (r and ϕ), i.e.,

$$t_0 = \delta t(r,\phi), \qquad t_{\mathrm{p}} = \frac{\phi}{\Omega(r)} + t_0\,. \tag{21}$$

Fourier transform of the resulting signal can be then simplified,

$$\begin{aligned}\mathcal{F}[I(t-t_{0j},\boldsymbol{\xi}_j)F(t-t_{0j}+t_{\mathrm{p}j},r_j)](\omega)\\ = \sum_{k=-\infty}^{\infty} c_k(r)\,\mathrm{e}^{\mathrm{i}k\phi}\mathcal{F}\left[I(t-\delta t(r,\phi),\boldsymbol{\xi})\right](\omega - k\Omega(r))\,.\end{aligned} \tag{22}$$

Every realization of this process is completely determined by set of points $(t_j, \phi_j, r_j, \boldsymbol{\xi}_j)$ from some subset of $\mathbb{R}^{k+3}$.

For the sum of K complex numbers z_i it follows

$$\left|\sum_{i=1}^{K} z_i\right|^2 = \left(\sum_{i=1}^{K} z_i\right)\left(\sum_{i=1}^{K} z_i\right)^* = \left(\sum_{i=1}^{K} z_i\right)\left(\sum_{i=1}^{K} z_i^*\right) = \sum_{i=1}^{K}\sum_{j=1}^{K} z_i z_j^*\,. \tag{23}$$

Defining the function $s(t,\phi,r,\boldsymbol{\xi};\omega)$ as

$$s(t,\phi,r,\boldsymbol{\xi};\omega) = \frac{2\sin(T\omega)}{\omega} \star \left(\mathrm{e}^{-\mathrm{i}\omega t}\sum_{k=-\infty}^{\infty} c_k(r)\,\mathrm{e}^{\mathrm{i}k\phi}\mathcal{F}\left[I(t-\delta t,\boldsymbol{\xi})\right](\omega - k\Omega(r))\right)\,. \tag{24}$$

According to (23) we can write

$$\begin{aligned}|\mathcal{F}_T[f(t)](\omega)|^2 &= \left|\sum_j s(t_j,\phi_j,r_j,\boldsymbol{\xi}_j;\omega)\right|^2\\ &= \sum_j\sum_l s(t_j,\phi_j,r_j,\boldsymbol{\xi}_j;\omega)\,s^*(t_l,\phi_l,r_l,\boldsymbol{\xi}_l;\omega)\,.\end{aligned} \tag{25}$$

Due to Campbell's theorem (6),

$$\begin{aligned}\mathrm{E}\left[|\mathcal{F}_T[f(t)](\omega)|^2\right] &= \mathrm{E}\left[\sum_j\sum_l s(t_j,\phi_j,r_j,\boldsymbol{\xi}_j;\omega)\,s^*(t_l,\phi_l,r_l,\boldsymbol{\xi}_l;\omega)\right]\\ &= \int\limits_{A\times A'} s(t,\phi,r,\boldsymbol{\xi};\omega)\,s^*(t',\phi',r',\boldsymbol{\xi}';\omega)\,m_2(t,\phi,r,\boldsymbol{\xi},t',\phi',r',\boldsymbol{\xi}')\,\mathrm{d}A\mathrm{d}A'\,,\end{aligned} \tag{26}$$

where m_2 is density of the second-order moment measure corresponding to the random point process of $(t_j, \phi_j, r_j, \boldsymbol{\xi}_j)$. The set A is a Cartesian product of sets,

$$A = \langle -(T + C), T\rangle \times \langle 0, 2\pi\rangle \times \langle r_{\min}, r_{\max}\rangle \times \Xi \,. \tag{27}$$

Now we can perform the limit (13). It can be shown that the result is independent on the value of C. In order to obtain an explicit formula for the power spectral density we have to specify the form of $M_2(.)$. In the simplest case we assume events that are mutually independent with uniformly distributed ignition times. The process can be described as a marked point process with a Poissonian process as the ground process. The intensity and the second-order measure for the ground process are:

$$M_{\mathrm{g}1}(\mathrm{d}t) = n\,\mathrm{d}t \,, \tag{28}$$

$$M_{\mathrm{g}2}(\mathrm{d}t\mathrm{d}t') = \left[n^2 + n\delta(t - t')\right] \mathrm{d}t\mathrm{d}t' \,, \tag{29}$$

where n is the mean rate of events. Other parameters are treated as independent marks with common distribution $G(\mathrm{d}\phi\,\mathrm{d}r\,\mathrm{d}\boldsymbol{\xi})$. The second-order measure of the process has a form

$$M_2(\mathrm{d}t\,\mathrm{d}\phi\,\mathrm{d}r\,\mathrm{d}\boldsymbol{\xi}\,\mathrm{d}t'\,\mathrm{d}\phi'\,\mathrm{d}\boldsymbol{\xi}') = \Big[n^2 G(\mathrm{d}\phi\,\mathrm{d}r\,\mathrm{d}\boldsymbol{\xi}) G(\mathrm{d}\phi'\,\mathrm{d}r'\,\mathrm{d}\boldsymbol{\xi}') + nG(\mathrm{d}\phi\,\mathrm{d}r\,\mathrm{d}\boldsymbol{\xi}) \times \delta(t - t')\delta(\phi - \phi')\delta(r - r')\delta(\boldsymbol{\xi} - \boldsymbol{\xi}')\Big] \mathrm{d}t\mathrm{d}t' \,. \tag{30}$$

For the power spectrum we obtain this general formula,

$$S(\omega) = 4\pi^2 n \sum_{k=-\infty}^{\infty} \sum_{l=-\infty}^{\infty} \int_{\mathcal{K}} c_k(r) c_l^*(r)\, \mathrm{e}^{\mathrm{i}(l-k)\phi} \mathcal{F}\left[I(t - \delta t(r, \phi), \boldsymbol{\xi})\right](\omega - k\Omega(r)) \times \mathcal{F}^*\left[I(t - \delta t(r, \phi), \boldsymbol{\xi})\right](\omega - l\Omega(r))\, G(\mathrm{d}\phi\,\mathrm{d}r\,\mathrm{d}\boldsymbol{\xi}) \,. \tag{31}$$

2.5 Introducing a relationship among spots (Hawkes process)

The assumption that the spots are mutually statistically independent seems to be a reasonable first approximation, however, the actual ignition times and spot parameters should probably depend on the history of a real system. As an example of such non-Poissonian process, we calculated the power-spectral density (PSD) for a model in which the spot ignition times are distributed according to the Hawkes (1971) process.

The Hawkes process consists of two types of events. Firstly, new events are generated by Poisson process operating with the intensity λ. Secondly, an existing event with ignition time t_a can give birth to new event at time t according to Poisson process with varying intensity $\mu(t - t_a)$. So the mean number of events found at time t is

$$m(t) = \lambda + \sum_{i, t_i < t} \mu(t_i) = \lambda + \int \mu(t) N(\mathrm{d}t) \,. \tag{32}$$

For a stationary process the first moment density is constant. Averaging both sides of the previous equation we find,

$$m_1 = \frac{\lambda}{1-\nu}\,, \quad \nu = \int_{-\infty}^{\infty} \mu(t)\,\mathrm{d}t\,. \tag{33}$$

Stationarity of the process implies, that the second-order measure density can depend only on the difference of its arguments. It can be proven (Daley and Vere-Jones, 2003) that

$$m_{\mathrm{g}2}(t,t') = c(t-t') + m_{\mathrm{g}1}^2 + m_{\mathrm{g}1}\delta(t-t')\,, \tag{34}$$

where the $c(t)$ is an even function. Thus, for the corresponding marked process with independent marks we find $M_2(\mathrm{d}t\,\mathrm{d}\phi\,\mathrm{d}r\,\mathrm{d}\boldsymbol{\xi}\,\mathrm{d}t'\,\mathrm{d}\phi'\,\mathrm{d}\boldsymbol{\xi}')$:

$$\begin{aligned} M_2 = \Bigg[&\left(\frac{\lambda^2}{(1-\nu)^2} + c(t-t') \right) G(\mathrm{d}\phi\,\mathrm{d}r\,\mathrm{d}\boldsymbol{\xi}) G(\mathrm{d}\phi'\,\mathrm{d}r'\,\mathrm{d}\boldsymbol{\xi}') \\ &+ \frac{\lambda}{1-\nu} G(\mathrm{d}\phi\,\mathrm{d}r\,\mathrm{d}\boldsymbol{\xi}) \delta(t-t')\delta(\phi-\phi')\delta(r-r')\delta(\boldsymbol{\xi}-\boldsymbol{\xi}') \Bigg]\,\mathrm{d}t\mathrm{d}t'\,. \end{aligned} \tag{35}$$

This second-order measure is almost identical to that of the Poissonian process (there is only one additional term associated with the function $c(t)$). The resulting PSD is

$$\begin{aligned} S(\omega) = 4\pi^2 \frac{\lambda}{1-\nu} &\sum_{k=-\infty}^{\infty} \sum_{l=-\infty}^{\infty} \int_{\mathcal{K}} \mathrm{e}^{\mathrm{i}(l-k)\phi} c_k(r) c_l^*(r) \mathcal{F}\left[I(t-\delta t(r,\phi),\boldsymbol{\xi})\right](\omega - k\Omega(r)) \\ &\times \mathcal{F}^*\left[I(t-\delta t(r,\phi),\boldsymbol{\xi})\right](\omega - l\Omega(r))\, G(\mathrm{d}\phi\,\mathrm{d}r\,\mathrm{d}\boldsymbol{\xi}) + 4\pi^3 \mathcal{F}\left[c(t)\right](\omega) \\ &\times \sum_{k=-\infty}^{\infty} c_k(r) \int_{\mathcal{K}} \mathrm{e}^{-\mathrm{i}k\phi} \mathcal{F}\left[I(t-\delta t(r,\phi),\boldsymbol{\xi}')\right](\omega - k\Omega(r))\, G(\mathrm{d}\phi\,\mathrm{d}r\,\mathrm{d}\boldsymbol{\xi}) \\ &\times \sum_{l=-\infty}^{\infty} \int_{\mathcal{K}'} \mathrm{e}^{\mathrm{i}l\phi'} c_l^*(r') \mathcal{F}^*\left[I(t-\delta t(r',\phi'),\boldsymbol{\xi})\right](\omega - l\Omega(r'))\, G(\mathrm{d}\phi'\,\mathrm{d}r'\,\mathrm{d}\boldsymbol{\xi}')\,. \end{aligned} \tag{36}$$

The function $c(t)$ can be calculated from the mean number of secondary events $\mu(t)$. Assuming $\mu(t) = \nu\alpha\exp(-\alpha t)\theta(t)$ we obtain

$$c(t) = \frac{\lambda\alpha\nu(1-\nu/2)}{(1-\nu)^2} \exp(-\alpha(1-\nu)|t|)\,. \tag{37}$$

It is interesting to notice that the above-given formal approach can actually provide a useful analytical formula to approximate the power spectrum. Figure 2 shows exemplary PSD which were obtained by (i) direct computations of the light-curve and the resulting PSD, and by (ii) the semi-analytical approach with Poissonian and Hawkes processes.

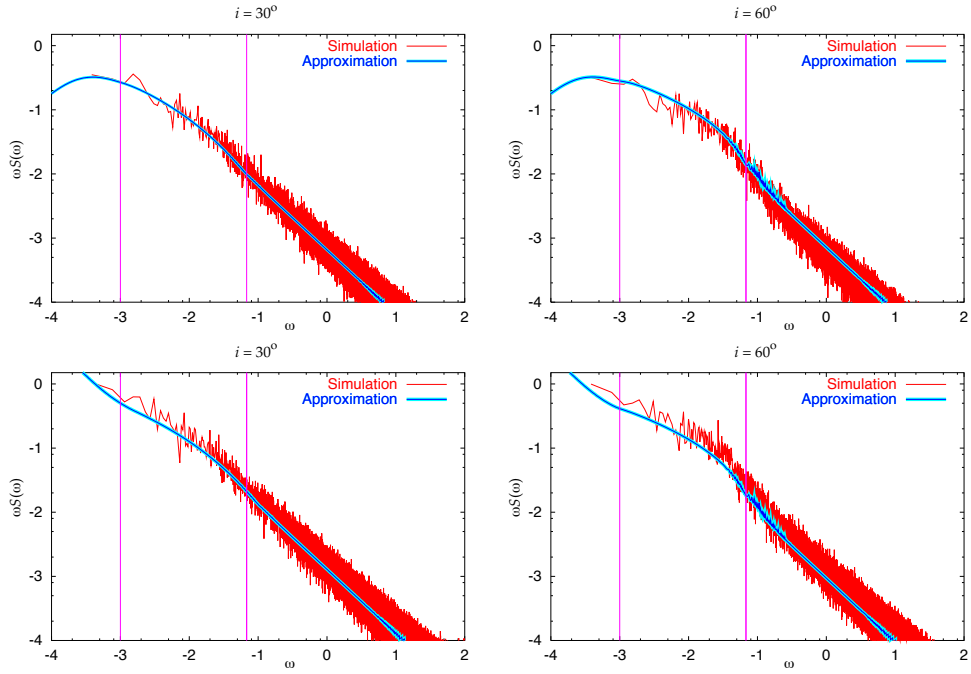

Figure 2. Power spectra from the spot model driven by the Poisson process (*top row*) and the Hawkes process (*bottom row*), calculated for spots orbiting and evolving on the surface of a thin accretion disc ($r_{\rm in} = 6$, $r_{\rm out} = 100$ gravitational radii). Two values of observer's inclination $\theta_{\rm o}$ are shown for comparison. The red (thin, noisy) curve is a result of direct numerical simulation. Blue (thick, continuous) curves are the analytical approximations based on Eqs (31) and (36), respectively. We assumed probability density function $\rho(\tau) \propto 1/\tau$. The magenta (vertical) lines denote the Keplerian orbital frequency $\Omega(r)$ at the inner and the outer edges of the disc. One can see that the Hawkes' process tends to enhance the low-frequency part of PSD and shift the break frequency towards lower values, below $\Omega(r_{\rm out})$.

3 CONCLUSIONS

We have studied the properties of power spectral density within the model of accretion disc variability driven by orbiting spots. The origin and evolution of spots were described in terms of Poissonian and Hawkes' processes. The latter belongs to a category of avalanche models. We developed an analytical approximation of PSD and compared it with our numerical results from light-curve simulations. In this way we were able to demonstrate the precision of formulae (31) and (36). The analytical approximation evaluates very fast and provides the main trend of the PSD shape while avoiding the noisy form of the numerically simulated spectra. Our approach allows us to investigate the resulting PSD as a function of the assumed type of process, which describes creation of parent spots and the subsequent cascades of daughter spots. In particular, we can investigate the predicted PSD slope at different frequency ranges and we can locate the break frequency depending on the model parameters.

The resulting PSD can be approximated by a broken power-law. For every stationary process the quantities $S(0)$ and $\int_0^\infty S(\omega)\,\mathrm{d}\omega$ are finite. Therefore, the function $S(\omega)$ flattens ($S(\omega) \approx \omega^0$) near $\omega = 0$ and it must decrease faster than $1/\omega$ at high frequencies. Power-spectra generated by the spot model behave in this way. The low-frequency limit is a constant, whereas the-high frequency behaviour depends mainly on the shape of the spot emission profile, $I(t, \boldsymbol{\xi}_j)$. In our calculations the emissivity was a decaying exponential and the slope was equal to -2 at high frequencies. The most interesting part of the spectra in between those two limits is influenced by both the emissivity profile and the underlying process.

ACKNOWLEDGEMENTS

We thank the Workshop participants for helpful comments and the Academy of Sciences for financial support (grant GAAV 300030510).

REFERENCES

Abramowicz, M. A., Bao, G., Lanza, A. and Zhang, X. (1991), X-ray variability power spectra of active galactic nuclei, *Astronomy and Astrophysics*, **245**, pp. 454–456, URL `http://adsabs.harvard.edu/abs/1991A\%26A...245..454A`.

Bendat, J. S. and Piersol, A. G. (2000), *Random Data: Analysis and Measurement Procedures*, Wiley, 3rd edition, ISBN 978-0-471-31733-3.

Brémaud, P. and Massoulié, L. (2002), Power spectra of general shot noises and Hawkes point processes with a random excitation, *Adv. in Appl. Probab.*, **34**(1), pp. 205–222.

Brémaud, P., Massoulié, L. and Ridolfi, A. (2005), Power spectra of random spike fields and related processes, *Adv. in Appl. Probab.*, **37**(4), pp. 1116–1146.

Campbell, N. R. (1909), The study of discontinuous phenomena, *Proc. Cambridge Philos. Soc.*, **15**, pp. 117–136.

Czerny, B., Różańska, A., Dovčiak, M., Karas, V. and Dumont, A.-M. (2004), The structure and radiation spectra of illuminated accretion disks in AGN. II. Flare/spot model of X-ray variability, *Astronomy and Astrophysics*, **420**, pp. 1–16, arXiv: `astro-ph/0402394`.

Daley, D. J. and Vere-Jones, D. (2003), *An Introduction to the Theory of Point Processes. Volume I: Elementary Theory and Methods*, Springer, ISBN 978-0-387-95541-4.

Galeev, A. A., Rosner, R. and Vaiana, G. S. (1979), Structured coronae of accretion disks, *Astrophys. J.*, **229**, pp. 318–326, URL `http://adsabs.harvard.edu/abs/1979ApJ...229..318G`.

Gaskell, C. M., McHardy, I. M., Peterson, B. M. and Sergeev, S. G. (2006), AGN Variability from X-Rays to Radio Waves, in *Proceedings of the conference held at Crimean Astrophysical Observatory*, Astronomical Society of the Pacific, San Francisco.

Hawkes, A. G. (1971), Spectra of Some Self-Exciting and Mutually Exciting Point Processes, *Biometrika*, **58**, pp. 83–90.

Lyubarskii, Y. E. (1997), Flicker noise in accretion discs, *Monthly Notices Roy. Astronom. Soc.*, **292**, pp. 679–685, URL `http://adsabs.harvard.edu/abs/1997MNRAS.292..679L`.

Merloni, A. and Fabian, A. C. (2001), Thunderclouds and accretion discs: a model for the spectral and temporal variability of Seyfert 1 galaxies, *Monthly Notices Roy. Astronom. Soc.*, **328**, pp. 958–968, URL `http://adsabs.harvard.edu/abs/2001MNRAS.328..958M`.

Mineshige, S., Ouchi, N. B. and Nishimori, H. (1994), On the generation of $1/f$ fluctuations in X-rays from black-hole objects, *Publ. Astronom. Soc. Japan*, **46**, pp. 97–105, URL `http://adsabs.harvard.edu/abs/1994PASJ...46...97M`.

Poutanen, J. and Fabian, A. C. (1999), Spectral evolution of magnetic flares and time lags in accreting black hole sources, *Monthly Notices Roy. Astronom. Soc.*, **306**, pp. L31–L37, arXiv: `astro-ph/9811306`.

Uttley, P., McHardy, I. M. and Papadakis, I. E. (2002), Measuring the broad-band power spectra of active galactic nuclei with RXTE, *Monthly Notices Roy. Astronom. Soc.*, **332**, pp. 231–250, arXiv: `astro-ph/0201134`.

Wiita, P. J., Mangalam, A. V. and Chakrabarti, S. K. (1992), Rapid variability in AGN and accretion disk hot-spots, in *American Institute of Physics Conference Series*, volume 254 of *American Institute of Physics Conference Series*, pp. 251–254, URL `http://adsabs.harvard.edu/abs/1992AIPC..254..251W`.

Życki, P. T. and Niedźwiecki, A. (2005), On the influence of relativistic effects on X-ray variability of accreting black holes, *Monthly Notices Roy. Astronom. Soc.*, **359**, pp. 308–314, arXiv: `astro-ph/0409425`.

Proceedings of *RAGtime 8/9, 15–19/19–21 September, 2006/2007, Hradec nad Moravicí, Opava, Czech Republic*
S. Hledík and Z. Stuchlík, editors, Silesian University in Opava, 2007, pp. 189–192

Stationary observers on the symmetry axis of rotating supermassive black holes

Martin Petrásek and Stanislav Hledík

Institute of Physics, Faculty of Philosophy & Science, Silesian University in Opava,
Bezručovo nám. 13, CZ-746 01 Opava, Czech Republic

ABSTRACT
Generalizing the results obtained by Semerák, O. (1993), Stationary Frames in the Kerr Field, *Gen. Relativity Gravitation*, **10**(1045), an interesting difference between the Kerr and Kerr–de Sitter geometries has been found. In the case of freely falling stationary observers located on the axis of symmetry, rotating supermassive black holes (not necessarily fast rotating) behave differently from the same bodies for which the present value of cosmological constant is not included. An interesting family of "freely falling stationary observers" is described.

1 KERR–DE SITTER GEOMETRY AND STATIONARY FRAMES

The line element of the Kerr–de Sitter geometry reads

$$\begin{aligned} \mathrm{d}s^2 = &- \frac{\Delta_r}{(1+\alpha)^2\rho^2}\,(\mathrm{d}t - a\sin^2\theta\,\mathrm{d}\phi)^2 \\ &+ \frac{\Delta_\theta \sin^2\theta}{(1+\alpha)^2\rho^2}\,[a\,\mathrm{d}t - (r^2+a^2)\,\mathrm{d}\phi]^2 + \frac{\rho^2}{\Delta_r}\,\mathrm{d}r^2 + \frac{\rho^2}{\Delta_\theta}\,\mathrm{d}\theta^2\,, \end{aligned} \tag{1}$$

where

$$\begin{aligned} &\Delta_r \equiv (r^2+a^2)\left(1-\frac{\alpha r^2}{a^2}\right) - 2Mr\,, \quad \Delta_\theta \equiv 1+\alpha\cos^2\theta\,, \\ &\rho^2 \equiv r^2 + a^2\cos^2\theta\,, \quad \alpha \equiv \tfrac{1}{3}\Lambda a^2\,. \end{aligned} \tag{2}$$

The Kerr geometry is a stationary axially symmetric vacuum solution to the Einstein's field equation (Misner et al., 1973; Bardeen et al., 1972). The Kerr–de Sitter geometry is a more general solution to the Einstein's field equations of the space in the sense that it includes a non-zero cosmological constant (Hledík, 2002; Stuchlík, 2002). From the Kerr–de Sitter metric expressed in Boyer–Lindquist coordinates (1) and (2) one can derive all important properties which leads to the clear description of stationary frames, particularly, the tetrads and 4-acceleration derived directly from metric coefficients (Stuchlík and Hledík, 2000; Stuchlík and Slaný, 2004; Kovář and Stuchlík, 2004, 2006, 2007).

We shall study only those cases for which the cosmological constant has a small positive value.

978-80-7248-419-5

1.1 Stationary frames

Stationary observers are formed by the class of observers which move along worldline of constant r and θ with a uniform angular velocity ω. Only those observers can perceive an unchanging geometry of the space-time in their vicinity. Those observers are considered to be "stationary" with respect to the local geometry (Misner et al., 1973; Bardeen et al., 1972). The simplest class of stationary frames are those with zero angular velocity $\omega = 0$. These observers are called static observers, because they appear static for distant observers.

However, one can distinguish four specific classes of stationary observers, namely, Static Observers ($\omega = 0$), Zero Angular Momentum Observers (ZAMO, $\omega = \omega_{\rm k}$), Carter's Observers ($\omega_{\rm CO}$) and Freely Orbiting Observers ($\omega_{\rm FOO\pm}$). There can also be found another classes of stationary observers as follows.

2 FREELY FALLING STATIONARY OBSERVERS

A very interesting class can be found using the definition of *4-acceleration*. We looked for freely falling stationary observers – those stationary observers whose 4-acceleration is zero which can be found in the equatorial plane or on the axis of symmetry.

We can find similar conditions as for the Kerr case for the existence of stationary observers in the equatorial plane, which is (due to small value of cosmological constant) almost indistinguishable from the pure Kerr case. But on the symmetry axis a new solution, not present in the Kerr geometry, emerges. The condition for *freely falling stationary observer* on the symmetry axis in case of the Kerr geometry reads $r = \pm a$ (hence, under the outer horizon), in the case of Kerr–de Sitter geometry there is one pair of solutions under the outer horizon as in the Kerr geometry, and another pair of solutions is located above the outer horizon. The condition arises from $a^\mu = 0$, and because $a^t = a^\theta = a^\phi = 0$ implicitly, it reads (we put $c = G = M = 1$ and denote $y = \frac{1}{3}\Lambda$)

$$a^r(\theta = \{\pi, 0\}) = \frac{r^2 - a^2}{(r^2 + a^2)^2} - ry\,.$$

We can cast this problem in the form

$$y(r; a) = \frac{r^2 - a^2}{r(r^2 + a^2)^2}\,, \tag{3}$$

which results in the plots in Fig. 1.

3 CONCLUSIONS

The physical meaning of the existence of another solution for stationary observers on the symmetry axis of the Kerr–de Sitter black hole arises from a simple concept. The observer has to be freely falling, consequently, no force can influence its fall onto the horizon. This shows that in case of Kerr geometry with even small repulsive cosmological constant, there exists a point on the symmetry axis where vector sum of forces vanishes (Stuchlík and

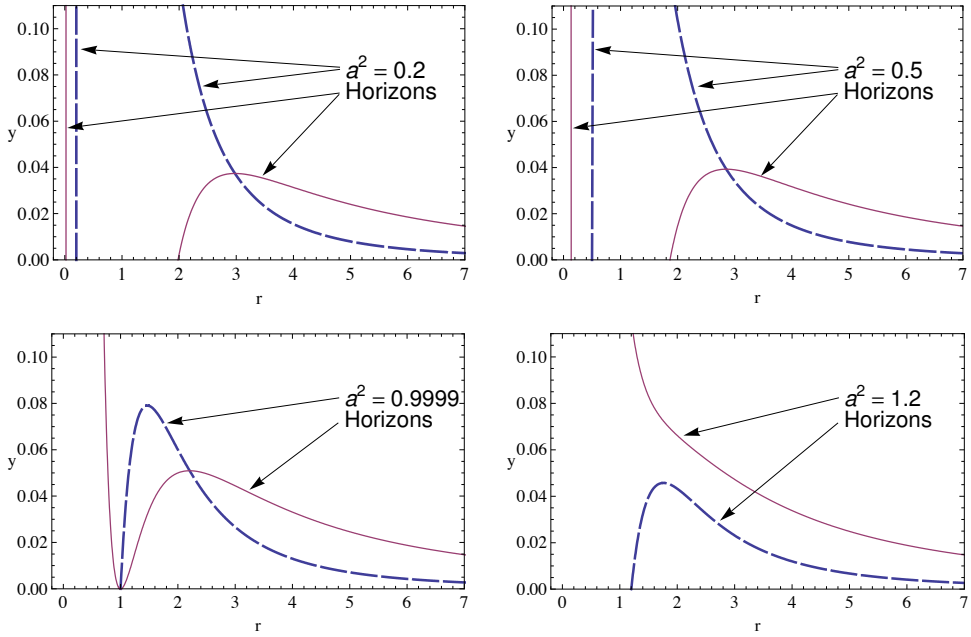

Figure 1. Plots of Eq. (3) for Freely Falling Stationary Observers on the axis of symmetry of the Kerr–de Sitter black hole for various values of of the black hole rotational parameter. The values $a^2 = 0.2$, $a^2 = 0.5$, $a^2 = 0.9999$, $a^2 = 1.2$ are used (in common reading order).

Kovář, 2006). Unfortunately this point is in cases of real values of cosmological constant too far from the outer horizon of the black hole, but not beyond the cosmological horizon. Only in the cases of very massive black holes or in cases of non-realistic, very large value of the cosmological constant, this point is shifted near the black hole as presented in Fig. 1. Different behaviour of forces for Kerr and Kerr–de Sitter black holes can also influence processes on the axis of symmetry (or near it) of very massive black holes which could lead to observable effects, for example in observation of collimation of relativistic jets (Slaný and Stuchlík, 2005; Stuchlík, 2005).

ACKNOWLEDGEMENTS

This work was supported by the Czech grants MSM 4781305903, GAČR 205/03/H144 and GAČR 202/06/0041.

REFERENCES

Bardeen, J. M., Press, W. H. and Teukolsky, S. A. (1972), Rotating black holes: locally nonrotating frames, energy extraction, and scalar synchrotron radiation, *Astrophys. J.*, **178**, pp. 347–369.

Hledík, S. (2002), Optical geometry, inertial forces, and embedding diagrams, in Semerák et al. (2002), pp. 161–192.

Kovář, J. and Stuchlík, Z. (2004), Inertial forces in Kerr–de Sitter spacetimes, in S. Hledík and Z. Stuchlík, editors, *Proceedings of RAGtime 4/5: Workshops on black holes and neutron stars, Opava, 14–16/13–15 October 2002/2003*, pp. 111–134, Silesian University in Opava, Opava, ISBN 80-7248-242-4.

Kovář, J. and Stuchlík, Z. (2006), Forces in Kerr space-times with a repulsive cosmological constant, *Internat. J. Modern Phys. A*, **21**, pp. 4869–4897, arXiv: `gr-qc/0611152`.

Kovář, J. and Stuchlík, Z. (2007), Optical reference geometry and inertial forces in Kerr–de Sitter spacetimes, *Classical Quantum Gravity*, **24**, pp. 565–594.

Misner, C. W., Thorne, K. S. and Wheeler, J. A. (1973), *Gravitation*, W. H. Freeman and Co, New York, San Francisco.

Semerák, O. (1993), Stationary Frames in the Kerr Field, *Gen. Relativity Gravitation*, **10**(1045).

Semerák, O., Podolský, J. and Žofka, M., editors (2002), *Gravitation: Following the Prague Inspiration (A Volume in Celebration of the 60th Birthday of Jiří Bičák)*, World Scientific, New Jersey, London, Singapore, Hong Kong, ISBN 981-238-093-0.

Slaný, P. and Stuchlík, Z. (2005), Relativistic thick discs in the Kerr–de Sitter backgrounds, *Classical Quantum Gravity*, **22**, pp. 3623–3651, URL `http://www.iop.org/EJ/abstract/-search=44947255.2/0264-9381/22/17/019`.

Stuchlík, Z. (2002), The role of a repulsive cosmological constant in astrophysical processes, in Semerák et al. (2002), pp. 27–83.

Stuchlík, Z. (2005), Influence of the Relict Cosmological Constant on Accretion Discs, *Modern Phys. Lett. A*, **20**(8), pp. 561–575.

Stuchlík, Z. and Hledík, S. (2000), Equatorial photon motion in the Kerr–Newman spacetimes with a non-zero cosmological constant, *Classical Quantum Gravity*, **17**(21), pp. 4541–4576, ISSN 0264-9381/00, URL `http://www.iop.org/EJ/abstract/0264-9381/17/21/312`.

Stuchlík, Z. and Kovář, J. (2006), Equilibrium conditions of spinning test particles in Kerr–de Sitter spacetimes, *Classical Quantum Gravity*, **23**, pp. 3935–3949, arXiv: `gr-qc/0611153`.

Stuchlík, Z. and Slaný, P. (2004), Equatorial circular orbits in the Kerr–de Sitter spacetimes, *Phys. Rev. D*, **69**, p. 064001, ISSN 1094-1622, arXiv: `gr-qc/0307049`.

Proceedings of *RAGtime 8/9, 15–19/19–21 September, 2006/2007, Hradec nad Moravicí, Opava, Czech Republic*
S. Hledík and Z. Stuchlík, editors, Silesian University in Opava, 2007, pp. 193–200

On privileged stationary observers in the Kerr–de Sitter geometry

Martin Petrásek[a] and Stanislav Hledík

Institute of Physics, Faculty of Philosophy & Science, Silesian University in Opava,
Bezručovo nám. 13, CZ-746 01 Opava, Czech Republic
[a]martin.petrasek@fpf.slu.cz

ABSTRACT
We focus on main differences between stationary frames in the Kerr geometry and the Kerr–de Sitter geometry. This comparison leads to new solutions on the symmetry axis and in the equatorial plane. This solution can clearly be described and physically interpreted. The most interesting is the case of freely falling stationary observers on the symmetry axis. We found a solution which can show that rotating supermassive black holes (not necessary fast rotating) could differ in a certain way from the same bodies for which the present value of the cosmological constant is not included. We show that an interesting family of "freely falling stationary observers" can be found. We found stationary observers in the equatorial plane, which can become (at a particular radius) counter rotating if they previously co rotated and vice versa. We also describe and compare stationary observers in the equatorial plane between themselves, showing how depends their angular velocity ω at the radius with chosen cosmological parameter $y = \Lambda/3$ and rotational parameter a.

1 KERR–DE SITTER GEOMETRY

The line element of the Kerr–de Sitter geometry reads

$$\begin{aligned} \mathrm{d}s^2 = &- \frac{\Delta_r}{(1+\alpha)^2\rho^2}\,(\mathrm{d}t - a\sin^2\theta\,\mathrm{d}\phi)^2 \\ &+ \frac{\Delta_\theta \sin^2\theta}{(1+\alpha)^2\rho^2}\,[a\,\mathrm{d}t - (r^2+a^2)\,\mathrm{d}\phi]^2 + \frac{\rho^2}{\Delta_r}\,\mathrm{d}r^2 + \frac{\rho^2}{\Delta_\theta}\,\mathrm{d}\theta^2\,, \end{aligned} \tag{1}$$

where

$$\begin{aligned} &\Delta_r \equiv (r^2+a^2)\left(1 - \frac{\alpha r^2}{a^2}\right) - 2Mr\,, \quad \Delta_\theta \equiv 1 + \alpha\cos^2\theta\,, \\ &\rho^2 \equiv r^2 + a^2\cos^2\theta\,, \quad \alpha \equiv \tfrac{1}{3}\Lambda a^2\,. \end{aligned} \tag{2}$$

The Kerr geometry is a stationary axially symmetric vacuum solution to the Einstein's field equation (Misner et al., 1973). The Kerr–de Sitter geometry is a more general solution to the

978-80-7248-419-5

Einstein's field equations of the space in the sense that it includes a non-zero cosmological constant (Hledík, 2002; Stuchlík, 2002). From Kerr–de Sitter metric written in Boyer–Lindquist coordinates (1), (2) one can derive important properties which lead to clear description of stationary frames, particularly tetrads and 4-acceleration derived directly from metric coefficients (Stuchlík and Hledík, 2000).

In our case, we will study only those cases for which the cosmological constant has an arbitrary positive value.

1.1 Horizons

The event horizons are given by the pseudo-singularities of the line element (1) by the condition

$$\Delta_r = (r^2 + a^2)\left(1 - \frac{\alpha r^2}{a^2}\right) - 2Mr = 0\,.$$

Introducing cosmological parameter $y = \frac{1}{3}\Lambda$, the loci of the event horizons are determined by the relation (Stuchlík and Slaný, 2004)

$$a^2 = a_{\rm h}^2(r;\, y) \equiv \frac{r^2 - 2r - yr^4}{yr^2 - 1}\,. \tag{3}$$

The 3D-plot of dependence between r, y, a described by Eq. (3) is shown in Fig. 1. This plot shows how the Kerr geometry is modified by the presence of the cosmological constant. For $\Lambda = 0$, there are apparently two inner horizons and no cosmological horizon. For any other $\Lambda \neq 0$ there is also a cosmological horizon which approaches to the inner horizons if cosmological parameter y increases.

2 STATIONARY FRAMES

Stationary observers move along world line of constant r and θ with uniform angular velocity ω. Only those observers could see an unchanging geometry of the space-time in their vicinity, being considered to be "stationary" in the reference to their local geometry (Misner et al., 1973). The most simple class of stationary frames are those with zero angular velocity $\omega = 0$. These observers are called static observers, because they appear static for distant observers.

There are four specific classes of stationary observers: Static Observers ($\omega = 0$), Zero Angular Momentum Observers ($\omega = \omega_{\rm K}$), Carter's Observers ($\omega_{\rm CO}$) and Freely Orbiting Observers ($\omega_{\rm FOO\pm}$), however, there can also be found other classes of stationary observers.

2.1 Zero Angular Momentum Observers (Locally Non-Rotating Frames)

Placing a rigid, circular mirror ("ring mirror") at fixed r around a black hole, and letting observer at r with angular velocity Ω emit a flash of light, some of the photons will get caught by the mirror and will skim along its surface, circumnavigating the black hole in the

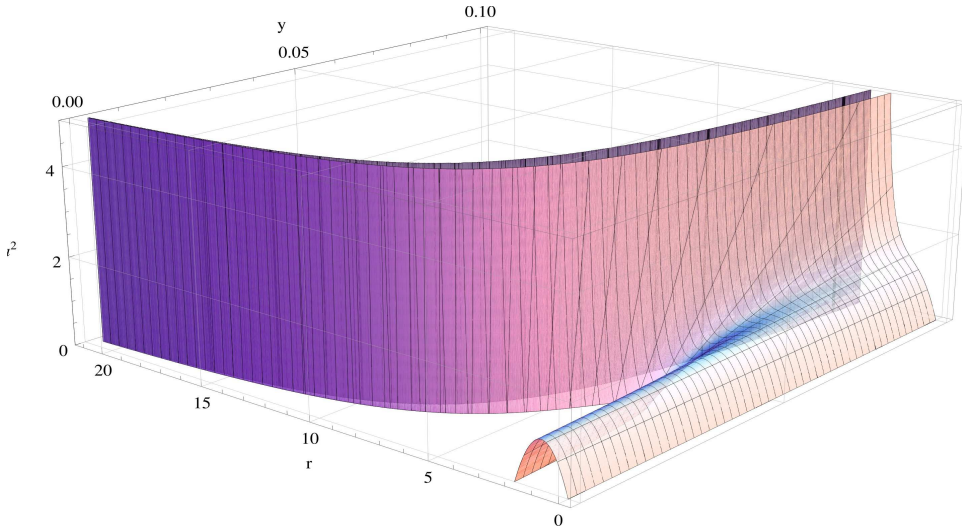

Figure 1. Horizons of Kerr–de Sitter geometry, dependence on r, y, a.

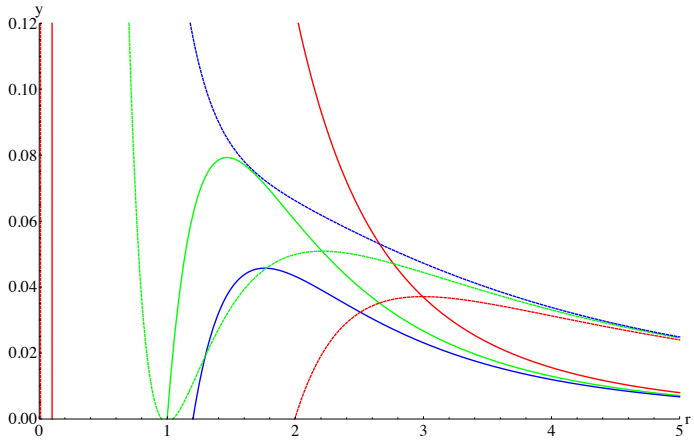

Figure 2. Resulting plot for Freely falling stationary observers on the symmetry axis of Kerr–de Sitter black hole for different values of angular velocity of the black hole. The solid red line marks the loci of freely falling stationary observers ($a^2 = 0.1$), the red dashed line marks the associated horizon. The solid green line marks the loci of freely falling stationary observers $a^2 = 0.999$, the green dashed line marks the associated horizon. The solid blue line marks the loci of freely falling stationary observers $a^2 = 1.2$ and blue dashed line marks the associated horizon.

positive-ϕ direction. Others will get caught and will skim along in the negative-ϕ direction. Then, only the observer with Keplerian angular velocity ω_{K} (the co-moving angular velocity) will receive emitted photons in the same moment. Only such an observer regard the $+\phi$ and $-\phi$ directions are equivalent in terms of local geometry:

$$\omega = \omega_{\mathrm{K}} = -\frac{g_{t\phi}}{g_{\phi\phi}} = \frac{2a\left[(a^2+r^2)\Delta_\theta - \Delta_r\right]}{(a^2+r^2)\Delta_\theta - a^2\sin^2\theta\,\Delta_r}\,.$$

2.2 Carter Observers (Carter Frames)

Carter Observers are specific class of observers connected with PNC (principal null congruence) photons. We can find such a class of observers for which 3-velocity will appear only radial (in terms of local geometry). These observers are Carter observers and are connected with their Carter local frames.

Angular velocity ω_{CO} for Kerr and Kerr–de Sitter geometry is same:

$$\omega_{\mathrm{CO}} = \frac{a}{a^2+r^2}\,.$$

2.3 Static Observers (Static Frames)

Another privileged local frame system is connected to "static observers." These observers occupy constant space coordinates. In other words, their are stationary and also satisfy the condition

$$\omega_{\mathrm{SO}} = 0\,.$$

2.4 Freely Falling Stationary Observers

The most interesting class we can find using the definition of *4-acceleration*. We looked for freely falling stationary observers – those stationary observers whose 4-acceleration is zero, we found them on the equatorial plane or on the symmetry axis.

We can find as similar conditions as apply for the Kerr case for existence of stationary observers on the equatorial plane, which is (due to small value of cosmological constant) almost unrecoverable from the pure Kerr case. But on the symmetry axis a new solution emerges. This solution is not present in Kerr geometry at all. As the condition for *freely falling stationary observer* on the symmetry axis reads $r = \pm a$ (hence, under the outer horizon), in case of the Kerr–de Sitter geometry there is one pair of solutions under the outer horizon as in the Kerr geometry, and another pair of solutions is above the outer horizon. The condition arises from $a^\mu = 0$, and because $a^t = a^\theta = a^\phi = 0$ implicitly, it reads (we put $c = G = M = 1$ and denote $y = \frac{1}{3}\Lambda$)

$$a^r(\theta \in \{\pi, 0\}) = \frac{r^2 - a^2}{(a^2+r^2)^2} - ry\,.$$

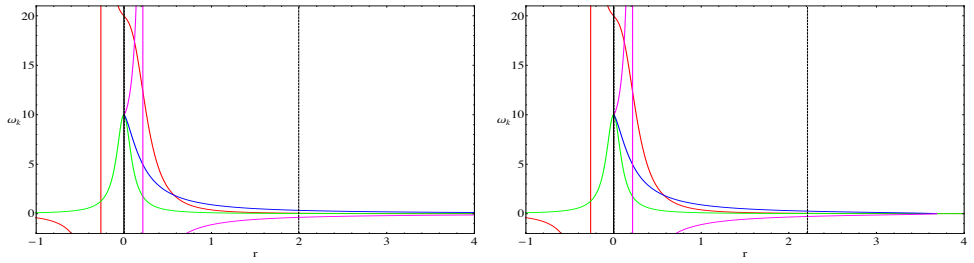

Figure 3. KdS black hole in the equatorial plane $\theta = \pi/2$, $a = 0.1$: where $y = 0$ left and $y = 0.02$ right.

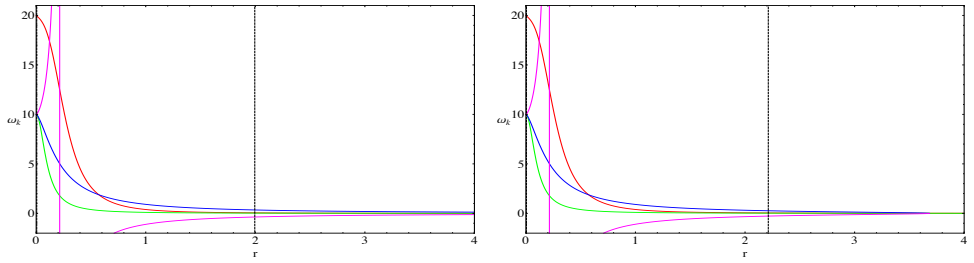

Figure 4. The same but zoomed region of KdS black hole in the equatorial plane $\theta = \pi/2$, $a = 0.1$: where $y = 0$ left and $y = 0.02$ right.

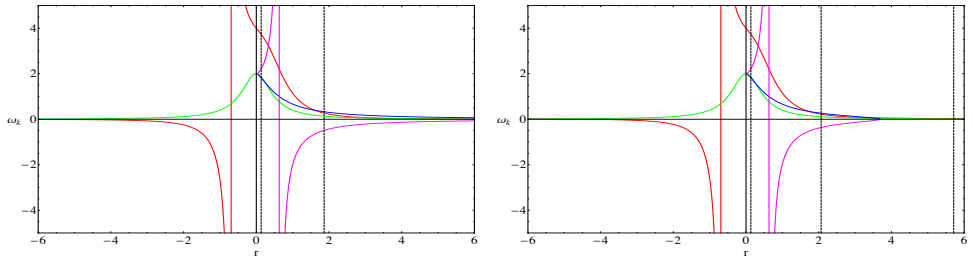

Figure 5. KdS black hole in the equatorial plane $\theta = \pi/2$, $a = 0.5$: where $y = 0$ left and $y = 0.02$ right.

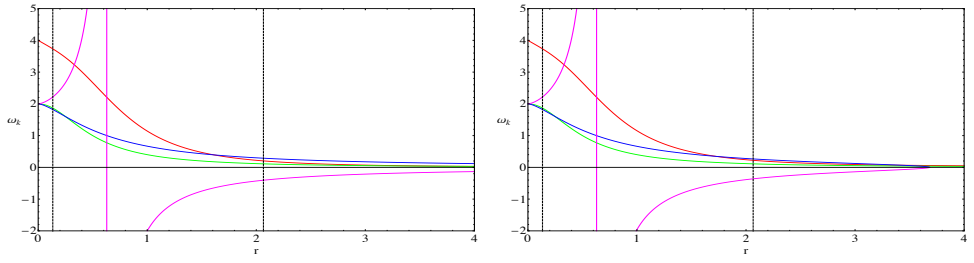

Figure 6. The same but zoomed region of KdS black hole in the equatorial plane $\theta = \pi/2$, $a = 0.5$: where $y = 0$ left and $y = 0.02$ right.

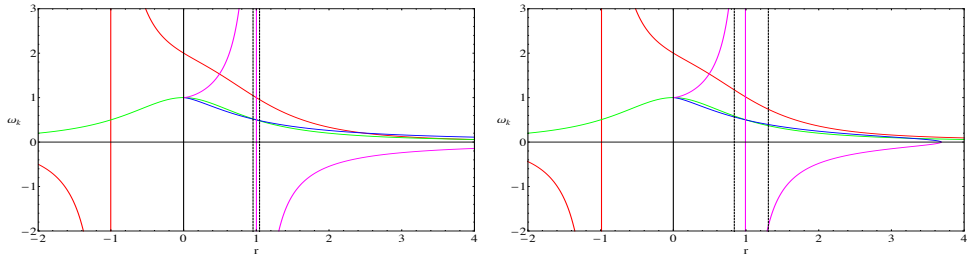

Figure 7. Near extremal KdS black hole in the equatorial plane $\theta = \pi/2$, $a = 0.999$: where $y = 0$ left and $y = 0.02$ right.

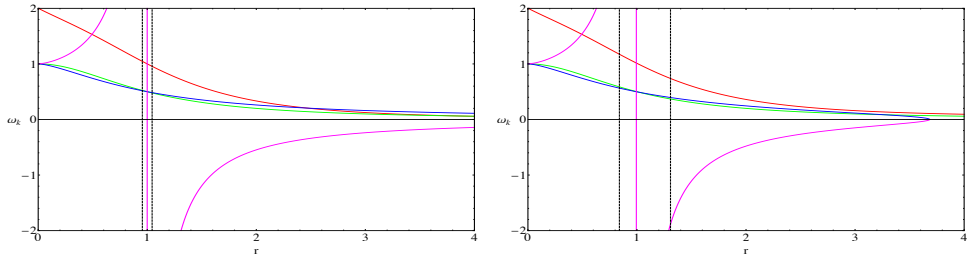

Figure 8. The same but zoomed region of the near extremal KdS black hole in the equatorial plane $\theta = \pi/2$ $a = 0.999$: where $y = 0$ left and $y = 0.02$ right.

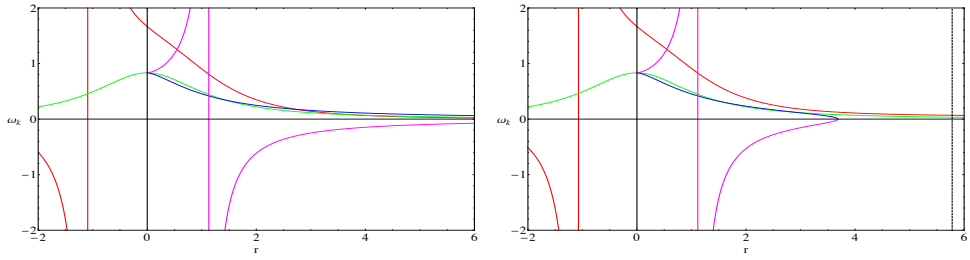

Figure 9. KdS naked singularity in the equatorial plane $\theta = \pi/2$, $a = 1.2$: where $y = 0$ left and $y = 0.02$ right.

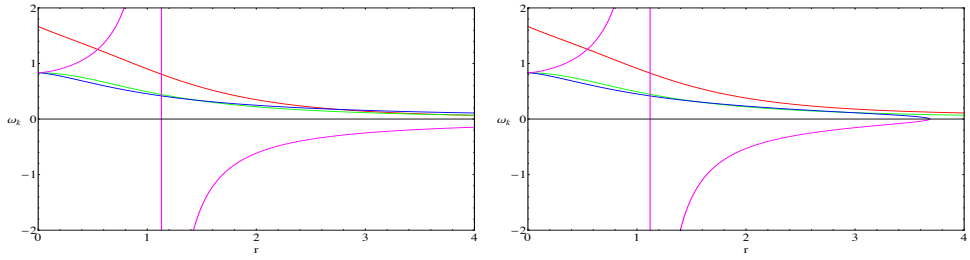

Figure 10. The same but zoomed region of KdS naked singularity in the equatorial plane $\theta = \pi/2$, $a = 1.2$: where $y = 0$ left and $y = 0.02$ right.

We can cast this problem in the form

$$y(r;a) = \frac{r^2 - a^2}{r(a^2 + r^2)^2},$$

which results in the plot (see Fig. 2).

3 COMPARISON OF STATIONARY FRAMES

Comparison of stationary frames has been done for Kerr geometry and Kerr–de Sitter geometry and between angular velocities ω_{K} of each stationary frames in dependence on their radii. Due to simplicity, we compared equatorial angular velocities and we have chosen only few typical parameters of rotational parameter a and cosmological parameter $y = \Lambda/3$. Resulting comparison is displayed in Figs 3–10. In all figures, red line is connected to the ZAMO's, green line describes Carter observers, blue line co-rotating freely orbiting observers (FOO+), and purple line shows counter-rotating freely orbiting observers (FOO−).

4 CONCLUSIONS

We can conclude that two key points exist in comparison of stationary frames between Kerr and Kerr–de Sitter geometry. The first one lies in existence of freely falling observers which simultaneously satisfy the condition of stationarity. The second one is a coalescence of co-rotating and counter-rotating Freely falling stationary observers in the equatorial plane for all positive values of cosmological parameter y and all values of rotating parameter a. In comparison with work of Stuchlík and Kovář (2006) it appears that positions of these stationary frames correspond to the so-called static radius located at $r = y^{-1/3}$.

Unfortunately, for realistic values of present cosmological constant these solutions are too far from outer horizon of the black hole, but still not behind the cosmological horizon. Only in cases of very massive black holes or in cases of very high value of cosmological constant we should "see" this point as it is presented on the (Fig. 2) near the black hole. Different behaviour of forces between Kerr and Kerr–de Sitter black holes can influence also processes on (or near to) the symmetry axis of very massive black holes which could lead to observable effects, for example in observation of collimation of relativistic jets (Slaný and Stuchlík, 2005).

ACKNOWLEDGEMENTS

This work was supported by the Czech grants MSM 4781305903, GAČR 205/03/H144 and GAČR 202/06/0041.

REFERENCES

Hledík, S. (2002), Optical geometry, inertial forces, and embedding diagrams, in Semerák et al. (2002), pp. 161–192.

Misner, C. W., Thorne, K. S. and Wheeler, J. A. (1973), *Gravitation*, W. H. Freeman and Co, New York, San Francisco.

Semerák, O., Podolský, J. and Žofka, M., editors (2002), *Gravitation: Following the Prague Inspiration (A Volume in Celebration of the 60th Birthday of Jiří Bičák)*, World Scientific, New Jersey, London, Singapore, Hong Kong, ISBN 981-238-093-0.

Slaný, P. and Stuchlík, Z. (2005), Relativistic thick discs in the Kerr–de Sitter backgrounds, *Classical Quantum Gravity*, **22**, pp. 3623–3651, URL `http://www.iop.org/EJ/abstract/-search=44947255.2/0264-9381/22/17/019`.

Stuchlík, Z. (2002), The role of a repulsive cosmological constant in astrophysical processes, in Semerák et al. (2002), pp. 27–83.

Stuchlík, Z. and Hledík, S. (2000), Equatorial photon motion in the Kerr–Newman spacetimes with a non-zero cosmological constant, *Classical Quantum Gravity*, **17**(21), pp. 4541–4576, ISSN 0264-9381/00, URL `http://www.iop.org/EJ/abstract/0264-9381/17/21/312`.

Stuchlík, Z. and Kovář, J. (2006), Equilibrium conditions of spinning test particles in Kerr–de Sitter spacetimes, *Classical Quantum Gravity*, **23**, pp. 3935–3949, arXiv: `gr-qc/0611153`.

Stuchlík, Z. and Slaný, P. (2004), Equatorial circular orbits in the Kerr–de Sitter spacetimes, *Phys. Rev. D*, **69**, p. 064001, ISSN 1094-1622, arXiv: `gr-qc/0307049`.

Proceedings of *RAGtime 8/9, 15–19/19–21 September, 2006/2007, Hradec nad Moravicí, Opava, Czech Republic*
S. Hledík and Z. Stuchlík, editors, Silesian University in Opava, 2007, pp. 201–208

Accretion disk atmoshperes: soft X-ray excess and Compton shoulder

Agata Różańska[1,a] and Jerzy Madej[2]

[1]Copernicus Astronomical Centre, Bartycka 18, PL-00-716 Warszawa, Poland
[2]Warsaw University Observatory, Al. Ujazdowskie 4, PL-00-478 Warsaw, Poland
[a]agata@camk.edu.pl

ABSTRACT
We have developed the set of model atmosphere equations, corresponding to an accretion disk around a supermassive black hole irradiated by hard X-ray lamp with power-law spectrum. Model equations allow for multiple Compton scattering of radiation on free electrons, and for large relative photon-electron energy exchange. We present spectra of specific intensities integrated over the disk radii. Outgoing intensity spectra show soft X-ray excess below 1 keV, and distinct K_α and K_β fluorescent lines of low ionized iron. We demonstrate the existence of the Compton shoulder on the red-wing side of K_α line. Our models exhibit very strong and steep temperature increase in the outermost layer of irradiated disk atmospheres which cause the effect of limb-brightening in reflected X-rays.

Keywords: Accretion disks – galaxies: active – radiative transfer – scattering – line: profiles

1 INTRODUCTION

X-ray spectra of many active galactic nuclei (AGN) exhibit effects of reprocessing of an external radiation originating either from the point like lamp or an accretion disk corona. We present a quite consistent and numerically exact modeling of an accretion disk atmosphere simultaneously with reprocessing of the external radiation field. The calculations of a vertical structure and an outgoing spectra are done for 8 neighboring rings, and than are integrated over disk radii.

Our equations include effects of multiple Compton scattering of radiation on free electrons in relativistic thermal motion, and rich set of bound-free and free-free monochromatic opacities. We allow for a large relative photon-electron energy exchange at the time of Compton scattering, and therefore we are able to reconstruct Compton scattering of photons with energy approaching or even exceeding the electron rest mass.

We present numerical results which are based on rigorous methods of the theory of stellar atmospheres. All existing opacity sources, both true absorption and non-thermal Compton down-scattering, are treated equivalently in the single model atmosphere code.

978-80-7248-419-5

Our opacities are supplemented by formulae describing emission fluorescent K_α and K_β lines of low ionized of iron. External hard X-rays interact most eagerly with electrons bound in the deepest K-shell of iron and cause ionization of iron atoms leaving a hole in the K-shell. An electron from the higher shell immediately fills the hole and with some probability, fluorescent yield, cause emission of the photon in the K_α line (electron from L-shell) or K_β line (electron from M-shell). Energy of Auger electrons and other radiation-less processes are ignored in our equations.

Full set of model stellar atmosphere equations with account of Compton scattering, but without fluorescent lines was already presented in Madej and Różańska (2004). Now we added terms which correspond to the fluorescent K_α and K_β lines of iron, adjusted to accretion disk geometry and assumed that the external irradiation from a point X-ray lamp has the power-law spectral distribution.

2 THE STRUCTURE OF AN ACCRETION DISK

We divide our disk onto 8 concentric rings situated at different distance from the supermassive black hole at mass $M = 10^7\,\mathrm{M}_\odot$. We assume constant moderate value of accretion rate in each ring, equal $\dot{m} = 0.03$ in units of Eddington accretion rate with accreting efficiency $\eta = 1/12$ suitable for Schwarzschild black hole.

In the first step, at each radius, we have computed vertical structure of non-illuminated disk using the method described in Różańska et al. (1999). We integrated equations of the disk vertical structure (equation of the hydrostatic equilibrium, equation of state, equation of vertical energy generation, transfer in diffusion approximation) assuming that viscosity is proportional to the total pressure, i.e., $P_{\rm tot} = P_{\rm rad} + P_{\rm gas}$. As the result, for each ring, we derived the effective temperature, and vertical gravity which affects the atmosphere, and we adopted those values for further advanced radiative transfer computations. All disk parameters used in further computations are summarized in Table 1.

Furthermore, we assumed that the disk is irradiated by an external point like X-ray lamp of the power-law spectrum $I_{\rm ext} \sim \nu^{-\alpha}$, with spectral index $\alpha = 0.9$. The lamp was located

Table 1. Parameters of eight neighboring rings (cgs units).

Ring No.	$r/r_{\rm Schw}$	$T_{\rm eff}$	$\log g$
1	3.478×10^0	1.018×10^5	5.5300
2	4.134×10^0	1.073×10^5	5.5740
3	5.204×10^0	1.020×10^5	5.4700
4	6.552×10^0	9.238×10^4	5.3010
5	8.248×10^0	8.181×10^4	5.1010
6	1.038×10^1	7.152×10^4	5.1820
7	1.385×10^1	5.976×10^4	5.594
8	1.847×10^1	4.950×10^4	5.596

above the first innermost ring at the height $h_{\rm lamp} = 5\,r_{\rm Schw}$, and the X-ray luminosity equal $L_{\rm X} = 10^{43}$ erg s^{-1}. We are comparing the results of power-law irradiation to the case when X-rays emitted by the same lamp are in the form of black-body with temperature 10^8 K and the same luminosity.

3 RADIATIVE TRANSFER EQUATION

The radiative transfer equation for the specific intensity, I_ν, solved in our research is as follows:

$$\mu \frac{{\rm d}I_\nu}{{\rm d}\tau_\nu} = I_\nu - \frac{j_\nu}{\kappa_\nu + \sigma_\nu} = I_\nu - S_\nu \,, \tag{1}$$

where S_ν is the frequency dependent source function, ${\rm d}\tau_\nu = -(\kappa_\nu + \sigma_\nu)\rho\,{\rm d}z$ is a monochromatic optical depth, ρ is density, and z is the geometrical depth scale in plane-parallel geometry. Variables j_ν, κ_ν and σ_ν denote frequency dependent emission, absorption and scattering coefficients for 1 gram, respectively. In this paper we use the LTE absorption κ_ν (local thermodynamic equilibrium), whereas coefficients of emission j_ν and scattering σ_ν include nonLTE terms.

Emission coefficient j_ν is the sum of three terms, $j_\nu = j_\nu^{\rm th} + j_\nu^{\rm sc} + j_\nu^{\rm fl}$, which represent thermal emission, Compton scattering emission and the emission in iron fluorescent lines, respectively. Full description of emission coefficient taking into account intensity of the external irradiation U_ν is given by

$$\begin{aligned} j_\nu = {} & \kappa_\nu B_\nu + \sigma_\nu J_\nu - \sigma_\nu J_\nu \int_0^\infty \Phi_1(\nu, \nu')\,{\rm d}\nu' \\ & + \sigma_\nu \int_0^\infty (J_{\nu'} + U_{\nu'})\Phi_2(\nu, \nu')\,{\rm d}\nu' + E_\alpha^{\rm fl}\varphi_\nu^\alpha + E_\beta^{\rm fl}\varphi_\nu^\beta \,. \end{aligned} \tag{2}$$

Thermal emission is proportional to the Planck function B_ν. The coefficient of true absorption κ_ν, is the sum of bound-free absorption from numerous levels of hydrogen, helium and iron atoms and ions, plus free-free absorption from all ions. We also included absorption of 4 lowest lines of fundamental series of helium-like iron and of similar 4 lowest lines of hydrogen like iron, all formed in LTE by assumption. We ignored here the presence of other heavy elements and their fluorescence lines.

Compton scattering cross sections were computed following the paper by Guilbert (1981). Functions Φ_1 and Φ_2 are properly weighted angle-averaged Compton redistribution functions for photons both incoming or outgoing of frequency ν after scattering in thermal electron gas (Madej and Różańska, 2004).

Fluorescence of low-ionized iron gas was approximated by two emission lines, $\rm K_\alpha$ line (transitions from L to K shells) and $\rm K_\beta$ line (transitions from M to K shells), $E_\alpha^{\rm fl}$ and $E_\beta^{\rm fl}$ denote the integrated intensity of $\rm K_\alpha$ and $\rm K_\beta$ emission lines, respectively. Frequency dependent variables φ_ν^α and φ_ν^β define profiles of fluorescent lines, both normalized to unity. Iron $\rm K_\alpha$ fluorescent line is a doublet line and such a structure was reproduced by our code. The $\rm K_\beta$ line was approximated by a singlet line. Profiles of all three lines are modelled as the convolution of natural and Doppler profiles.

Together with the radiative transfer equation we solve hydrostatic and radiative equilibrium equations, and take into account standard equation of state for ideal gas. Details of the transfer equation and the method of solution by partial ionization are presented in Madej and Różańska (2004).

4 RESULTS

Our computer code is very powerful and allowed us to compute the structure of disk atmospheres over very large range of electron scattering optical depth starting from $\tau_{\rm es} = 10^{-8}$ up to $\tau_{\rm es} = 10^4$. We were able to reproduce both the overall continuum spectrum from hard X-rays of 400 keV down to deep infrared of 0.4 eV. Our results include also details of some selected spectral line profiles, all of them were computed simultaneously.

We present our spectra as energy dependent outgoing specific intensities I_ν, which are suitable for disk geometry. We reject presentation of monochromatic fluxes since they are only relevant to spherical geometry.

Figure 1 presents temperature structure of several rings. In both cases of power-low or black-body external irradiation we note the existence of very hot outermost atmospheric layer (Nayakshin et al., 2000; Ballantyne et al., 2001; Różańska et al., 2002). The effective temperature of all rings, resulted from the accretion rate and non-zero viscosity, is slightly less or equal to 10^5 K. However, the temperature of the outermost hot skin approaches 3×10^6 K. For deeper layers external irradiation practically does not cause any changes of temperature.

Figures 2–4 present outgoing intensity spectra of the whole accretion disk at various aspect angles. The spectra were obtained by integration over eight rings located at different radii, see Table 1. Particular lines in Figs 2–4 correspond to different angles between the direction to the observer and the normal to the disk. Exact values of those eight angles and their cosines are given in Table 2. In further discussion we turn attention of the reader to

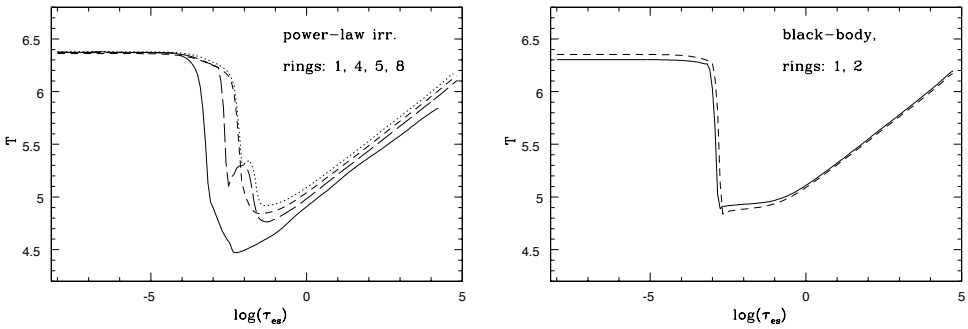

Figure 1. Temperature structure of an atmosphere for several rings. *Left panel* shows results for power-law irradiation (dotted line – first ring, short dashed – fourth ring, long dashed – fifth ring, and solid line – eight ring). *Right panel* shows irradiation of the black body shape (short dashed line – first ring, solid line – second ring).

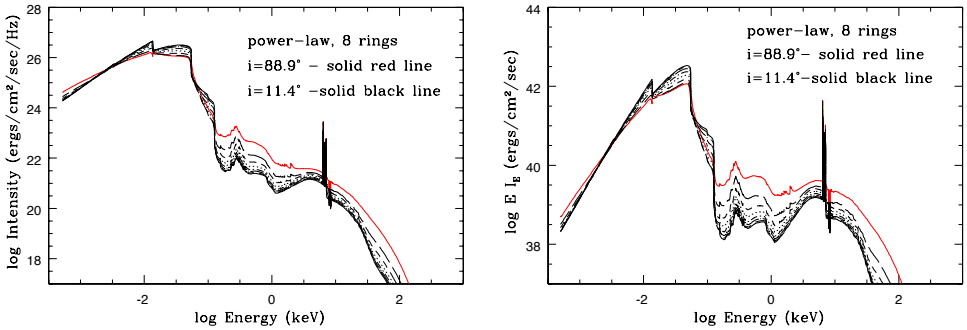

Figure 2. Outgoing intensity from the disk integrated over radii for eight different aspect angles. The product of $E\,I_{\rm E}$ versus energy is presented in the right panel.

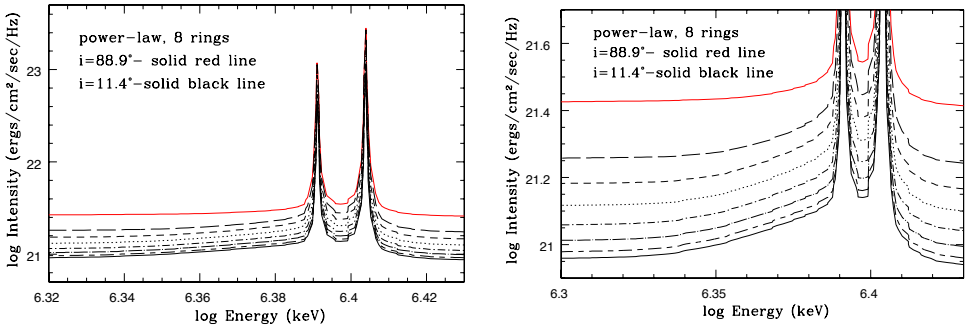

Figure 3. Outgoing intensity spectra from the disk integrated over radii for eight different aspect angles in the energy range around 6.4 keV. Compton shoulder is best seen for the vertical direction, $i = 11.4°$.

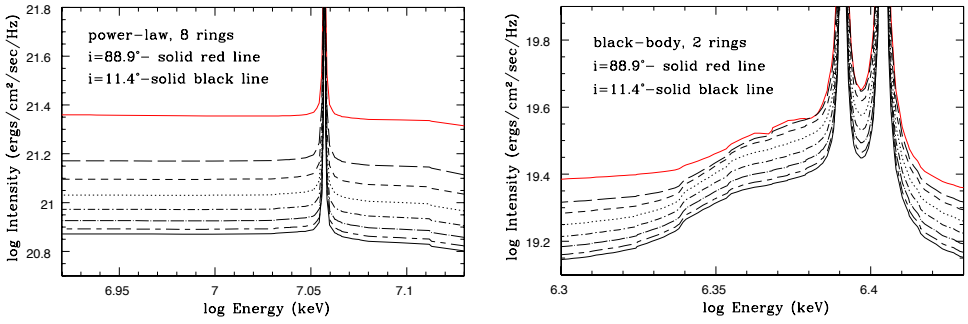

Figure 4. The profile of the fluorescent K_β line of iron (left panel), which is seen here without any apparent Compton shoulder. On the right panel we computed profiles of the K_α line for the case where the external irradiation has black body spectral distribution.

Table 2. Description of lines in Figs 2–4.

Type of a line	$\cos i$	i
solid black	0.980145	11.4°
short-long dashed	0.8983333	26.1°
long dashed dotted	0.7627662	40.3°
short dashed dotted	0.5917173	53.7°
dotted	0.4082827	65.9°
short dashed	0.2372338	76.3°
long dashed	0.1016668	84.2°
solid red	0.0198551	88.9°

the extreme angles: solid black line in Figs 2–4 represents almost vertical direction (face-on aspect), whereas the solid red line represents almost horizontal direction (edge-on aspect).

Figure 2 shows the overall spectra of our sample disk given either in specific intensity scale I_ν, or as the product of $E\,I_{\rm E}$. In both panels we observe the deficit of hard X-rays, which has been absorbed in a disk and suffered continuum Compton scattering. This caused the energy of hard X-rays has been redistributed to lower energies.

External irradiation generates two iron fluorescent lines: K_α (6.4 keV) and K_β (7.057 keV). Moreover, there exists a spectral bump below 1. keV, which is similar to the well know soft X-ray excess.

Both panels in Fig. 2 show the effect, that the intensity of radiation emerging almost horizontally to the disk ($i = 88.9°$) is greater than the intensity emerging almost vertically ($i = 11.4°$). This is valid in the whole X-ray energy band, from 0.1 keV up to 100 keV, and in the infrared. Such en effect of light-brightening was also presented by Goosmann et al. (2007), and should be attributed to the inversion of temperature in the irradiated disk atmospheres, see Fig. 1.

Figure 3 presents integrated intensity spectra just around the fluorescent K_α line of iron. We turn attention to the Compton shoulder which is most easily seen in the vertical direction (lower solid black line). Right panel in Fig. 3 is the enlargement of the left panel in the same figure, to emphasize properties of our synthetic Compton shoulder seen at different aspect angles.

Figure 4, left panel, demonstrates the profile of the fluorescent K_β line of iron, approximated here by a singlet line. Unfortunately, Compton shoulder of that line is not seen in our models. The most prominent Compton shoulder is visible in our results obtained for a black-body external irradiation, Fig. 4 right panel.

5 CONCLUSIONS

In this paper we presented computations of the radiation spectrum emerging from a sample accretion disk around the central supermassive black hole in an AGN. The disk was irradiated by an X-ray lamp located above the equatorial plane.

Reprocessing of external hard X-rays of power-law spectrum caused generation of a very hot external layer in the disk atmosphere where temperature T rises to millions K, whereas the structure of deeper atmospheric layers is not affected at all.

Outgoing intensity spectra of the disk exhibit the following important observable properties. First, external irradiation generates two fluorescent lines of iron, K_α and K_β. The former line appeared as the doublet and is located at the energy 6.4 keV. Compton scattering of line radiation on colder electron gas (below the hot disc skin) generates the Compton shoulder in the red side of the emission doublet K_α. The Compton shoulder modelled here differs from the Compton shoulder presented by Matt (2002), where the second is resulted during X-ray reflection from a constant density wall.

Second, Compton scattering of the external X-rays causes build-up of the soft X-ray excess below 1 keV. This excess is higher for the disk observed face-on, but still do low to explain observations.

Third, our results clearly demonstrate the effect of limb brightening of the disk radiation mostly in X-ray domain. This result can put new constrains on the geometry of the X-ray source and the reflecting disk atmosphere. We address this issue for further consideration.

ACKNOWLEDGEMENTS

The present work was supported by the Polish Committee for Scientific Research grant No. N N203 4061 33.

REFERENCES

Ballantyne, D. R., Ross, R. R. and Fabian, A. C. (2001), X-ray reflection by photoionized accretion discs, *Monthly Notices Roy. Astronom. Soc.*, **327**, pp. 10–22, URL `http://adsabs.harvard.edu/abs/2001MNRAS.327...10B`.

Goosmann, R. W., Mouchet, M., Czerny, B., Dovčiak, M., Karas, V., Różańska, A. and Dumont, A.-M. (2007), Iron lines from transient and persisting hot spots on AGN accretion disks, *ArXiv e-prints*, **709**, arXiv: `0709.1356`, URL `http://adsabs.harvard.edu/abs/2007arXiv0709.1356G`.

Guilbert, P. W. (1981), Numerical solution of time dependent Compton scattering problems by means of an integral equation, *Monthly Notices Roy. Astronom. Soc.*, **197**, pp. 451–460, URL `http://adsabs.harvard.edu/abs/1981MNRAS.197..451G`.

Madej, J. and Różańska, A. (2004), X-ray irradiated model stellar atmospheres – III. Compton redistribution of thermal external irradiation, *Monthly Notices Roy. Astronom. Soc.*, **347**, pp. 1266–1272, URL `http://adsabs.harvard.edu/abs/2004MNRAS.347.1266M`.

Matt, G. (2002), The iron K_α Compton shoulder in transmitted and reflected spectra, *Monthly Notices Roy. Astronom. Soc.*, **337**, pp. 147–150, URL `http://adsabs.harvard.edu/abs/2002MNRAS.337..147M`.

Nayakshin, S., Kazanas, D. and Kallman, T. R. (2000), Thermal Instability and Photoionized X-Ray Reflection in Accretion Disks, *Astrophys. J.*, **537**, pp. 833–852, URL `http://adsabs.harvard.edu/abs/2000ApJ...537..833N`.

Różańska, A., Czerny, B., Życki, P. T. and Pojmański, G. (1999), Vertical structure of accretion discs with hot coronae in active galactic nuclei, *Monthly Notices Roy. Astronom. Soc.*, **305**, pp. 481–491, URL `http://adsabs.harvard.edu/abs/1999MNRAS.305..481R`.

Różańska, A., Dumont, A.-M., Czerny, B. and Collin, S. (2002), The structure and radiation spectra of illuminated accretion discs in active galactic nuclei – I. Moderate illumination, *Monthly Notices Roy. Astronom. Soc.*, **332**, pp. 799–813, URL `http://adsabs.harvard.edu/abs/2002MNRAS.332..799R`.

Proceedings of *RAGtime 8/9, 15–19/19–21 September, 2006/2007, Hradec nad Moravicí, Opava, Czech Republic*
S. Hledík and Z. Stuchlík, editors, Silesian University in Opava, 2007, pp. 209–220

Spectral line profile of radiating ring orbiting a brany Kerr black hole

Jan Schee and Zdeněk Stuchlík

Institute of Physics, Faculty of Philosophy & Science, Silesian University in Opava,
Bezručovo nám. 13, CZ-746 01 Opava, Czech Republic

ABSTRACT
In the framework of the brany models, rotating black holes are described by the Kerr metric with a tidal charge representing the influence of the non-local gravitational (tidal) effects of the bulk space Weyl tensor onto the black hole spacetime. Here we study the influence of the tidal charge onto profiled spectral lines generated by radiating tori orbiting in vicinity of a rotating black hole. We show that with lowering the negative tidal charge of the black hole, the profiled line becomes to be flatter and wider.

1 INTRODUCTION

String theory and M-theory describing gravity as a truly higher-dimensional interaction becoming effectively 4D at low-enough energies inspired studies of the braneworld models, where the observable universe is a 3-brane (domain wall) to which the standard model (non-gravitational) matter fields are confined, while gravity field enters the extra spatial dimensions the size of which may be much larger than the Planck length scale $l_{\rm P} \sim 10^{-33}$ cm (Arkani-Hamed et al., 1998). Gravity can be localized near the brane at low energies even with a non-compact, infinite size extra dimension with the warped spacetime satisfying the 5D Einstein equations with negative cosmological constant (Randall and Sundrum, 1999).

The exact stationary and axisymmetric solutions describing rotating black holes localized in the Randall–Sundrum braneworld were derived in Aliev and Gümrükçüoğlu (2005). The solutions are determined by metric tensor of the Kerr–Newman form with a tidal charge describing the 5D correction term generated by the 5D Weyl tensor stresses. The tidal charge has an "electric" character and arises due to the 5D gravitational coupling between the brane and the bulk, reflected on the brane through the "electric" part of the bulk Weyl tensor (Aliev and Gümrükçüoğlu, 2005), in analogy with the spherically symmetric black-hole case (Dadhich et al., 2000). When the electromagnetic field is introduced, the non-vacuum solutions of the effective Einstein equations on the brane are much more complex in comparison with the standard Kerr–Newman solutions (Aliev and Gümrükçüoğlu, 2005).

978-80-7248-419-5

Here we consider optical phenomena in the Kerr–Newman type of solutions describing the brany rotating (Kerr) black holes with no electric charge, since in astrophysically relevant situations the electric charge of the black hole must be exactly zero, or very small (Misner et al., 1973). Then the results obtained in analysing the behaviour of test particles and photons or test fields around the Kerr–Newman black holes could be used assuming both positive and negative values of the brany tidal parameter b (used instead of charge parameter Q^2).

The information on the properties of strong gravitational fields in vicinity of compact objects, namely of black holes, is encoded into optical phenomena of different kind that enable us to make estimates of the black hole parameters, including its tidal charge, when predictions of the theoretical models are confronted with the observed data. From this point of view, the spectral profiles of accretion discs around the black holes in galactic binaries, e.g., in microquasars, are most promising (McClintock et al., 2007), along with profiled spectral lines in the X-ray flux (Bao and Stuchlík, 1992; Stuchlík and Bao, 1992; Laor, 1991; Matt et al., 1993; Zakharov, 2003; Zakharov and Repin, 2006). Important information could also be obtained from the quasiperiodic oscillations observed in the X-ray flux of some low-mass black hole binaries of Galactic origin (Remillard, 2005; Remillard and McClintock, 2006), some expected intermediate black hole sources (Strohmayer et al., 2007), or those observed in Galactic nuclei (Aschenbach, 2004, 2007). The most promising orbital resonance model then enables relative exact measurement of the black hole parameters (Török et al., 2005; Török, 2005a,b) that should be confronted with the predictions of the optical modelling (McClintock et al., 2007). In the case of our Galaxy centre black hole Sgr A*, we could be able to measure detailed optical phenomena, comparing the other sources, since it is the nearest supermassive black hole with mass estimated to be $\sim 4 \times 10^6\,\mathrm{M}_\odot$ (Ghez et al., 2005), enabling to measure the "silhouette" of the black hole and other subtle GR phenomena (Cunningham and Bardeen, 1973; Schee and Stuchlík, 2007; Schee et al., 2005).

Here we present an introductory study on the role of the brany tidal charge parameter in the optical phenomena related to profiled spectral lines generated by radiating tori in the brany Kerr black-hole backgrounds.

2 THE GEOMETRY OF BRANY KERR SPACETIME AND EQUATIONS OF MOTION FOR TEST PARTICLES AND PHOTONS

The solution of vacuum effective Einstein equations on the brane has been for rotating black holes given in Aliev and Gümrükçüoğlu (2005). The properties of the circular motion in brany Kerr spacetimes were discussed in Aliev and Gümrükçüoğlu (2005); Stuchlík and Kotrlová (2007).

2.1 Geometry

Using the standard Boyer–Linquist coordinates (t, r, θ, φ) and geometrical units ($c = G = 1$), we can write the line element of Kerr black-hole metric on the 3D-brane in the

form (Aliev and Gümrükçüoğlu, 2005)

$$\mathrm{d}s^2 = -\left(1 - \frac{2Mr - b}{\Sigma}\right)\mathrm{d}t^2 + \frac{\Sigma}{\Delta}\,\mathrm{d}r^2 + \Sigma\,\mathrm{d}\theta^2 + \frac{A}{\Sigma}\,\mathrm{d}\varphi^2 - 2\frac{2Mr - b}{\Sigma}\sin^2\theta\,\mathrm{d}t\mathrm{d}\varphi\,, \quad (1)$$

where

$$\Sigma = r^2 + a^2\cos^2\theta\,,$$
$$\Delta = r^2 - 2Mr + a^2 + b\,,$$
$$A = (r^2 + a^2)^2 - a^2\Delta\sin^2\theta\,.$$

M is the mass parameter, $a = J/M$ is the specific angular momentum, the brany parameter b is called *tidal charge* and represents the imprint of non-local (tidal) gravitational effects from the bulk space (Dadhich et al., 2000). The form of the metric (1) is the same as in the case of the Kerr–Newman metric, with the tidal charge being replaced by the squared electric charge, Q^2. The stress tensor on the brane $E_{\mu\nu}$ takes the form

$$E_t{}^t = -E_\varphi{}^\varphi = -\frac{b}{\Sigma^3}[\Sigma - 2(r^2 + a^2)]\,,$$
$$E_r{}^r = -E_\theta{}^\theta = -\frac{b}{\Sigma^2}\,,$$
$$E_\varphi{}^t = -(r^2 + a^2)\sin^2\theta\,E_t{}^\varphi = -\frac{2ba}{\Sigma^3}(r^2 + a^2)\sin^2\theta\,,$$

that is fully analogical ($b \to Q^2$) to the components of electromagnetic energy-momentum tensor for Kerr–Newman spacetimes in Einstein's general relativity (Aliev and Gümrükçüoğlu, 2005). For simplicity, we put $M = 1$ in the following, using thus dimensionless coordinates and parameters.

2.2 Carter's equations

In order to study the optical effects in brany Kerr spacetimes we have to solve equations of motion of photons. It is well known that photons move along null geodesics of the spacetime under consideration.

Using the Hamilton–Jacobi method, Carter found separated first order differential equations of motion (Carter, 1968), which in the case of brany Kerr spacetime read

$$\Sigma\frac{\mathrm{d}r}{\mathrm{d}w} = \pm\sqrt{R(r)}\,,$$
$$\Sigma\frac{\mathrm{d}\theta}{\mathrm{d}w} = \pm\sqrt{W(\theta)}\,,$$
$$\Sigma\frac{\mathrm{d}\varphi}{\mathrm{d}w} = -\frac{P_W}{\sin^2\theta} + \frac{aP_R}{\Delta}\,,$$
$$\Sigma\frac{\mathrm{d}t}{\mathrm{d}w} = -aP_W + \frac{(r^2 + a^2)P_R}{\Delta}\,,$$

where

$$R(r) = P_R^2 - \Delta(m^2 r^2 + K)\,,$$
$$W(\theta) = (K - a^2 m^2 \cos^2\theta) - \left(\frac{P_W}{\sin\theta}\right)^2\,,$$
$$P_R(r) = E(r^2 + a^2) - a\Phi\,,$$
$$P_W(\theta) = aE\sin^2\theta - \Phi\,.$$

E is the energy, Φ is the axial angular momentum and K is the constant of motion related to total angular momentum that is usually replaced by the constant $Q = K - (aE - \Phi)^2$, since for motion in the equatorial plane ($\theta = \pi/2$) there is $Q = 0$. For motion of photons, we put $m = 0$. Generally, these equations can be integrated and expressed in terms of elliptic integrals (Schee and Stuchlík, 2007). The analysis of photon motion in Kerr–Newman spacetime (Stuchlík, 1981) can be directly applied to the case of photon motion in brany Kerr spacetime. It is done in Schee and Stuchlík (2007); we shall use the results in the following.

3 ROTATING RING IN THE EQUATORIAL PLANE OF BRANY KERR BLACK HOLE

Following the Carter equations for the circular motion at a given radius r in the equatorial plane ($\theta = \pi/2, \mathrm{d}\theta/\mathrm{d}w = 0$), we find, solving simultaneously relations $R(r) = 0, \mathrm{d}R/\mathrm{d}r = 0$, the energy and angular momentum of the particle to be given by

$$E_\pm = \frac{r^2 - 2r + b \pm a\sqrt{r-b}}{Z_\pm}\,,$$
$$\Phi_\pm = \frac{(r^2 + a^2)\sqrt{r-b} \mp a(2r - b)}{Z_\pm}\,,$$

where

$$Z_\pm = r\sqrt{r^2 - 3r + 2b \pm 2a\sqrt{r-b}}\,.$$

The upper (lower) sign corresponds to the corotating (counter-rotating) orbits. The crucial limiting radii for existence of circular orbits correspond to the photon circular orbits given by the real positive roots of the equations

$$Z_\pm = 0\,, \quad r^2 - 3r + 2b \pm 2a\sqrt{r-b} = 0\,,$$

and to the marginally stable orbits ($\mathrm{d}^2 R/\mathrm{d}r^2 = 0$) given by Aliev and Gümrükçüoğlu (2005) in the form (see Fig. 1)

$$r(6r - r^2 - 9b + 3a^2) + 4b(b - a^2) \mp 8a(r-b)^{3/2} = 0\,.$$

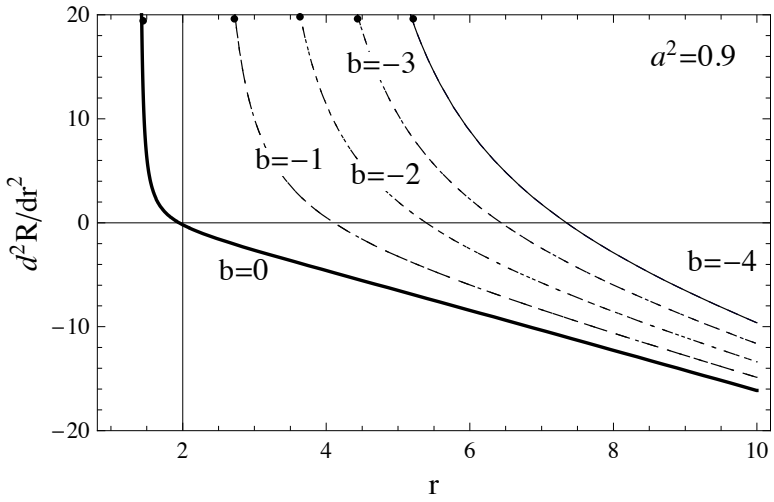

Figure 1. The plot of $\mathrm{d}^2R/\mathrm{d}r^2$ for four representative values of tidal charge $b = 0, -1, -2, -3, -4$ and rotational parameter$a^2 = 0.9$. The intersections of $\mathrm{d}^2R/\mathrm{d}r^2$ with 0 give the position of marginally stable orbit for specified parameters a and b.

We assume a bright rotating ring of particles following circular orbit to be located above the photon circular orbit or marginally stable orbit, respectively. The ring is composed of a large number of monochromatically radiating point sources which move along the circular orbit at the radial distance r_e and which radiate isotropically in their rest frame.

The angular velocity $\Omega = \mathrm{d}\varphi/\mathrm{d}t$ of such sources as measured by distant observers is given by

$$\Omega = \frac{\mathrm{d}\varphi}{\mathrm{d}t} = \frac{\sqrt{r-b}}{r^2 + a\sqrt{r-b}}\,. \tag{2}$$

4 THE SPECIFIC ENERGY FLUX OF PHOTONS

The observed specific energy flux is given by the formula

$$F_\mathrm{o}(\nu) = \int I_\mathrm{o}\,\mathrm{d}\Pi\,,$$

where I_o is observed specific intensity of the source and $\mathrm{d}\Pi$ is the solid angle subtended by the source on the observer sky. The observed specific intensity and its value at the rest frame of the source are related by the Liouville theorem

$$\frac{I_\mathrm{o}}{\nu_\mathrm{o}^3} = \frac{I_\mathrm{e}}{\nu_\mathrm{e}^3} = \mathrm{const}\,,$$

where index o (e) refers to the observer (emitter), $\nu_{\rm o}$ ($\nu_{\rm e}$) is the observed (emitted) frequency of photons. The observed specific flux then takes the form

$$F_{\rm o}(\nu) = \int I_{\rm e} g^3 \, {\rm d}\Pi \,, \tag{3}$$

where we introduced the frequency shift ratio of the observed frequency to the emitted one, $g = \nu_{\rm o}/\nu_{\rm e}$.

5 OPTICAL EFFECTS

The frequency shift and the focusing of the bundle of rays are the key phenomena that form the profile of the observed spectral line.

5.1 Frequency shift

The frequency shift g can be expressed as the ratio of observed photon energy $E_{\rm o}$ to emitted photon energy $E_{\rm e}$

$$g = \frac{E_{\rm o}}{E_{\rm e}} = \frac{k_\mu u^\mu_{\rm o}}{k_\mu u^\mu_{\rm e}}$$

where k_μ are covariant components of photon 4-momentum and $u^\mu_{\rm o}$ ($u^\mu_{\rm e}$, respectively) are contravariant components of the 4-velocity of the observer (emitter). In the case of static distant observer the 4-velocity reads $\boldsymbol{u}_{\rm o} = (1, 0, 0, 0)$. In the case of emitter following a circular geodesic at $r = r_{\rm e}$ in the equatorial plane of the brany Kerr black hole, the 4-velocity reads $\boldsymbol{u}_{\rm e} = (u^t_{\rm e}, 0, 0, u^\varphi_{\rm e})$; the components read

$$u^t_{\rm e} = \left[1 - \frac{2}{r_{\rm e}}(1 - a\Omega)^2 - (r_{\rm e}^2 + a^2)\Omega^2 + \frac{b}{r_{\rm e}^2}(1 - 2a\Omega)\right]^{-1/2} ,$$
$$u^\varphi_{\rm e} = \Omega u^t_{\rm e} \,,$$

where Ω is the angular velocity of the emitter as seen by distant observer and is given by Eq. (2). The total frequency shift, which includes gravitational and Doppler shifts, is finally given by

$$g = \frac{\left[1 - \frac{2}{r_{\rm e}}(1 - a\Omega)^2 - (r_{\rm e}^2 + a^2)\Omega^2 + \frac{b}{r_{\rm e}^2}(1 - 2a\Omega)\right]^{1/2}}{1 - \lambda\Omega} \,, \tag{4}$$

where $\lambda = -k_\varphi / k_t$ is the impact parameter of the photon being a constant of the photon motion; notice that g is explicitly independent of the second motion constant q. Of course, depending on the position of the emitter along the circular orbit, the motion constant of photons reaching a fixed distant observer will change periodically.

5.2 Focusing

For a distant observer, the solid angle $\mathrm{d}\Pi$ can be expressed in terms of observer's plane coordinates $[\alpha, \beta]$ (see Fig. 2)

$$\mathrm{d}\Pi = \frac{1}{d_{\mathrm{o}}^2}\,\mathrm{d}\alpha\mathrm{d}\beta\,.$$

The observer plane coordinates are in relations with photon's impact parameters λ and q given by formulae (Cunningham and Bardeen, 1973)

$$\alpha = -\frac{p^{(\varphi)}}{p^{(t)}} = -\frac{\lambda}{\sin\theta_{\mathrm{o}}}\,,$$

and

$$\beta = \frac{p^{(\theta)}}{p^{(t)}} = \pm\sqrt{q^2 + a^2\cos^2\theta_{\mathrm{o}} - \lambda^2\cot^2\theta_{\mathrm{o}}}\,.$$

and so one can switch the integration over λ and q. The solid angle $\mathrm{d}\Pi$ then reads

$$\mathrm{d}\Pi = \frac{1}{d_{\mathrm{o}}^2}\left|\frac{\partial(\alpha,\beta)}{\partial(\lambda,q)}\right|\mathrm{d}\lambda\mathrm{d}q\,.$$

where $|\partial\alpha, \beta/\partial\lambda, q|$ is the Jacobian of the transformation $(\alpha, \beta) \to (\lambda, q)$ and reads

$$\left|\frac{\partial(\alpha,\beta)}{\partial(\lambda,q)}\right| = \frac{q}{\sin\theta_{\mathrm{o}}\sqrt{q^2 + a^2\cos^2\theta_{\mathrm{o}} - \lambda^2\cot^2\theta_{\mathrm{o}}}}\,.$$

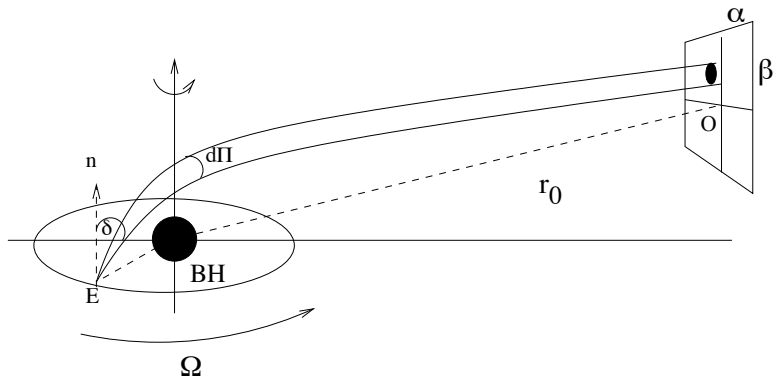

Figure 2. The emitter E emits isotropically in its rest frame. A photon is radiated at a directional angle δ. It is received by observer O at infinity, i.e., at sufficiently large distance. The coordinates of the received photon on the observer sky are $[\alpha, \beta]$.

The impact parameters λ and q can be expressed in terms of the frequency shift g and cosine of the directional angle δ defined by the normal $\boldsymbol{n}$ to the plane of the ring and photon 4-momentum $\boldsymbol{k}$, taken both at the emitter position. From (4) one finds the formula

$$\lambda = \frac{1}{\Omega}\left(1 - \frac{f}{g}\right),$$

where

$$f = \left[1 - \frac{2}{r_{\rm e}}(1 - a\Omega)^2 - (r_{\rm e}^2 + a^2)\Omega^2 + \frac{b}{r_{\rm e}^2}(1 - 2a\Omega)\right]^{1/2}.$$

The directional cosine of δ is given by the formula

$$\cos\delta = \frac{\boldsymbol{n}\cdot\boldsymbol{k}}{\boldsymbol{u}_{\rm e}\cdot\boldsymbol{k}}, \tag{5}$$

which, for normal $\boldsymbol{n} = (1/\sqrt{\Sigma})\partial_\theta$, leads to expression

$$\cos\delta = \frac{qg}{r_{\rm e}}.$$

By introducing $\chi \equiv \cos\delta$ the Jacobian of transformation $(\lambda, q) \to (g, \chi)$ reads

$$\left|\frac{\partial(\lambda, q)}{\partial(g, \chi)}\right| = \frac{r_{\rm e}}{\Omega}\frac{f}{g^3}.$$

The final formula for solid angle $\mathrm{d}\Pi$ then reads

$$\mathrm{d}\Pi = \frac{1}{d^2}\frac{r_{\rm e}^2\chi f}{\sin\theta_{\rm o} g^3\Omega\sqrt{r_{\rm e}^2\chi^2 + a^2g^2\cos^2\theta - \frac{1}{\Omega^2}(f-g)^2\cot^2\theta_{\rm o}}}\,\mathrm{d}g\mathrm{d}\chi. \tag{6}$$

6 PROFILED SPECTRAL LINE

We directly apply the results of the previous section to determine the spectral line profile of the bright ring in the equatorial plane of brany Kerr black hole.

Let the source radiates isotropically at a fixed frequency $\nu_{\rm e}$. The specific intensity $I_{\rm e}$ of the source is then given by

$$I_{\rm e}(\nu_{\rm e}) = \epsilon(r)\delta(\nu_{\rm e} - \nu_0), \tag{7}$$

where $\epsilon(r)$ is the local emissivity as a function of radial distance from the black hole, ν_0 is the rest frequency. Using (7) and (3) we arrive to the formula for the specific flux in the form

$$F_{\rm o}(\nu_{\rm o}) = \int \epsilon(r) g^4 \delta(\nu_{\rm o} - g\nu_0)\,\mathrm{d}\Pi.$$

Using Eq. (6) one finally arrives to

$$F_{\rm o}(\nu_{\rm o}) = \int \frac{g r_{\rm e}^2 \chi f}{d_{\rm o}^2 \sin\theta_{\rm o} \Omega \sqrt{r_{\rm e}^2\chi^2 + a^2 g^2 \cos^2\theta - \frac{1}{\Omega^2}(f-g)^2 \cot^2\theta_{\rm o}}} \, {\rm d}\chi \, . \tag{8}$$

In order to obtain the spectral line profile form (8), one must find all relevant pairs (λ, q), which are related to pairs of g and χ, by integrating the Carter equations schematically

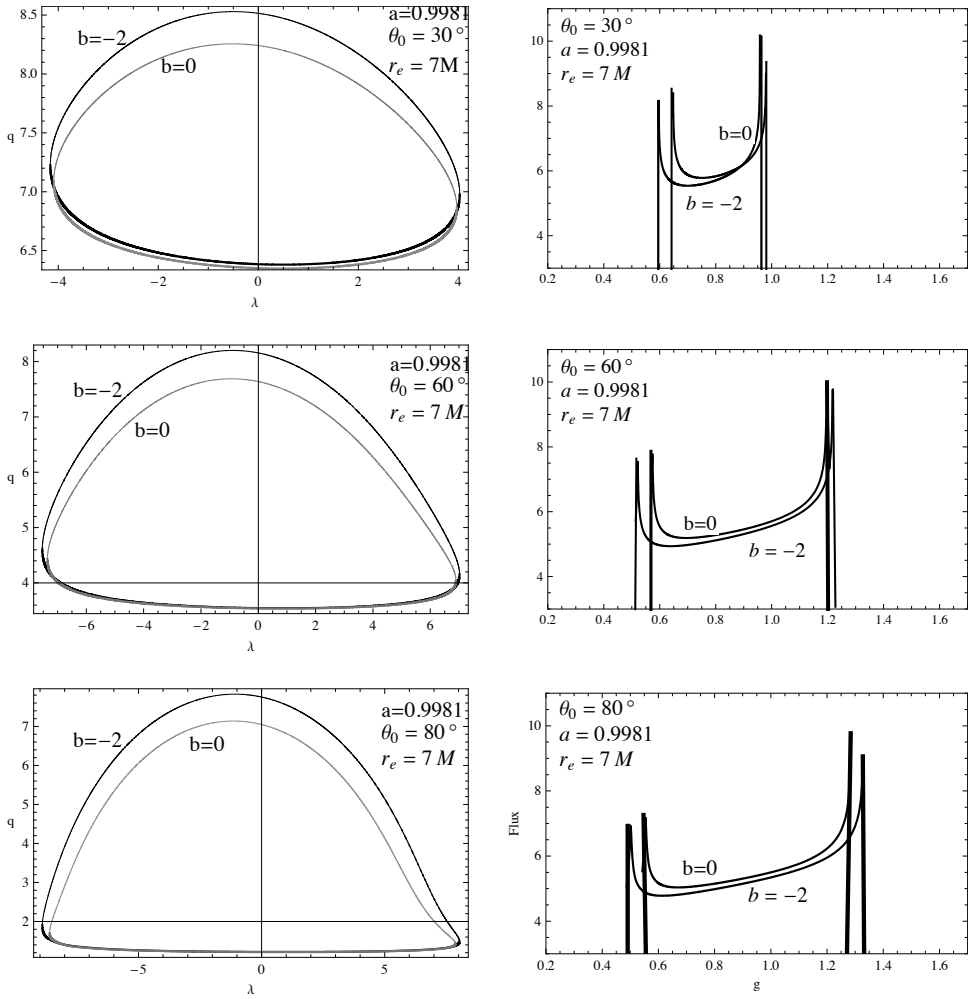

Figure 3. *Left:* The pairs of impact parameters λ and q are plotted for the rotational parameter $a = 0.9981$, radial coordinate of the emitter $r_{\rm e} = 7M$, two representative values of the tidal charge $b = -2, 0$ and three representative values of observer's inclination angle $\theta_0 = 30°, 60°$ and $80°$. *Right:* The plots of the profiled spectral lines of monochromatically radiating thin ring, plotted for the same parameters as the plots on the left.

given by the formula

$$\pm \int_{\theta e} \frac{1}{\sqrt{W(\theta)}}\,\mathrm{d}\theta = \pm \int_{re} \frac{1}{\sqrt{R(r)}}\,\mathrm{d}r\ .$$

The detailed calculation scheme in terms of the elliptic integrals can be found in Schee and Stuchlík (2007).

We plot the pairs (λ, q) for representative values of the rotation parameter $a = 0.9981$, tidal charge $b = -2$, radial coordinate of the emitter $r_{\mathrm{e}} = 7$ and latitudinal coordinate of the observer $\theta_{\mathrm{o}} = 30°\ (60°, 80°)$ in Fig. 3. The results obtained for the tidal charge $b = -2$ are compared with the case of pure Kerr black holes with $b = 0$. It is clear that in the case of the radiating ring there are two values of impact parameter $q_1(\chi_1)$, $q_2(\chi_2)$ for specified impact parameter $\lambda(g)$. Using the assumption that the source radiates isotropically, we can simply sum both contributions

$$F(g, \chi_1, \chi_2) = F(g, \chi_1) + F_2(g, \chi_2)\,.$$

Then the spectral line profiles can be immediately constructed. For some appropriately chosen values of the black hole parameters, the radiating source and the inclination angle of the observer, the typical results are plotted in Fig. 3.

7 CONCLUSIONS

In this paper we present some preliminary results concerning the study of the influence of negative tidal charge on the spectral line profile of bright, thin ring rotating in the equatorial plane of the brany Kerr black-hole. We have shown that with tidal charge decreasing to more negative values, the width of the spectral line is increasing. The profile of the line with decreasing value of (negatively-valued) b is flattened.

ACKNOWLEDGEMENTS

This work was supported by the Czech grants MSM 4781305903, LC06014 and GAČR 202/06/0041. One of the authors (Z. S.) would like to express his gratitude to Czech Committee for collaboration with CERN for support and CERN Theory Division for perfect hospitality.

REFERENCES

Aliev, A. N. and Gümrükçüoğlu, A. E. (2005), Charged Rotating Black Holes on a 3-Brane, *Phys. Rev. D*, **71**(10), p. 104027, arXiv: `hep-th/0502223v2`.

Arkani-Hamed, N., Dimopoulos, S. and Dvali, G. (1998), The Hierarchy Problem and New Dimensions at a Millimeter, *Phys. Lett. B*, **429**, pp. 263–272, arXiv: `hep-ph/9803315`.

Aschenbach, B. (2004), Measuring mass and angular momentum of black holes with high-frequency quasi-periodic oscillations, *Astronomy and Astrophysics*, **425**, pp. 1075–1082, arXiv: `astro-ph/0406545`.

Aschenbach, B. (2007), Measurement of Mass and Spin of Black Holes with QPOs, *Chinese Astronom. Astrophys.*, accepted for publication, arXiv: 0710.3454.

Bao, G. and Stuchlík, Z. (1992), Accretion disk self-eclipse – X-ray light curve and emission line, *Astrophys. J.*, **400**, pp. 163–169.

Carter, B. (1968), Global Structure of the Kerr Family of Gravitational Fields, *Phys. Rev.*, **174**(5), pp. 1559–1571.

Cunningham, C. T. and Bardeen, J. M. (1973), The Optical Appearance of a star orbiting an extreme Kerr black hole, *Astrophys. J.*, **183**, pp. 237–264.

Dadhich, N., Maartens, R., Papadopoulos, P. and Rezania, V. (2000), Black holes on the brane, *Phys. Rev. B*, **487**, arXiv: hep-th/0003061v3.

Ghez, A. M., Salim, S., Hornstein, S. D., Tanner, A., Lu, J. R., Morris, M., Becklin, E. E. and Duchêne, G. (2005), Stellar Orbits around the Galactic Center Black Hole, *Astrophys. J.*, **620**, pp. 744–757, arXiv: astro-ph/0306130.

Laor, A. (1991), Line profiles from a disk around a rotating black hole, *Astrophys. J.*, **376**, pp. 90–94.

Matt, G., Fabian, A. C. and Ross, R. R. (1993), Iron K_α lines from X-ray photoionized accretion discs, *Monthly Notices Roy. Astronom. Soc.*, **262**(1), pp. 179–186.

McClintock, J. E., Narayan, R. and Shafee, R. (2007), Estimating the Spins of Stellar-Mass Black Holes, in M. Livio and A. Koekemoer, editors, *Black Holes*, volume 707, Cambridge University Press, Cambridge, in press, to appear in 2008, arXiv: 0707.4492v1.

Misner, C. W., Thorne, K. S. and Wheeler, J. A. (1973), *Gravitation*, W. H. Freeman and Co, New York, San Francisco.

Randall, L. and Sundrum, R. (1999), An Alternative to Compactification, *Phys. Rev. D*, **83**(2), pp. 4690–4693, arXiv: hep-th/9906064.

Remillard, R. A. (2005), X-ray spectral states and high-frequency QPOs in black hole binaries, *Astronom. Nachr.*, **326**(9), pp. 804–807, arXiv: astro-ph/0510699.

Remillard, R. A. and McClintock, J. E. (2006), X-Ray Properties of Black-Hole Binaries, *Annual Review of Astronomy and Astrophysics*, **44**(1), pp. 49–92, arXiv: astro-ph/0606352.

Schee, J. and Stuchlík, Z. (2007), Optical effects in brany Kerr spacetimes, pp. 221–256, this volume.

Schee, J., Stuchlík, Z. and Juráň, J. (2005), Light escape cones and raytracing in Kerr geometry, pp. 143–155, this volume.

Strohmayer, T. E., Mushotzky, R. F., Winter, L., Soria, R., Uttley, P. and Cropper, M. (2007), Quasi-Periodic Variability in NGC 5408 X-1, *Astrophys. J.*, **660**, pp. 580–586, arXiv: astro-ph/0701390.

Stuchlík, Z. (1981), Null geodesics in the Kerr–Newman metric, *Bull. Astronom. Inst. Czechoslovakia*, **32**(6).

Stuchlík, Z. and Bao, G. (1992), Radiation from hot spots orbiting an extreme Reissner–Nordström black hole, *Gen. Relativity Gravitation*, **24**(9), pp. 945–957.

Stuchlík, Z. and Kotrlová, A. (2007), Orbital resonance model of QPOs in braneworld Kerr black hole spacetimes, pp. 323–361, this volume.

Török, G. (2005a), A possible 3 : 2 orbital epicyclic resonance in QPOs frequencies of Sgr A*, *Astronomy and Astrophysics*, **440**(1), pp. 1–4.

Török, G. (2005b), QPOs in microquasars and Sgr A*: measuring the black hole spin, *Astronom. Nachr.*, **326**(9), pp. 856–860, arXiv: astro-ph/0510669.

Török, G., Abramowicz, M. A., Kluźniak, W. and Stuchlík, Z. (2005), The orbital resonance model for twin peak kHz quasi periodic oscillations in microquasars, *Astronomy and Astrophysics*, **436**(1), pp. 1–8, arXiv: astro-ph/0401464.

Zakharov, A. F. (2003), The iron K_α line as a tool for analysis of black hole characteristics, *Publ. Astronom. Observator. Belgrade*, **76**, pp. 147–162, arXiv: `astro-ph/0411611`.

Zakharov, A. F. and Repin, S. V. (2006), Different types of Fe K_α lines from radiating annuli near black holes, *New Astronomy*, **11**, pp. 405–410, arXiv: `astro-ph/0510548`.

Proceedings of *RAGtime 8/9, 15–19/19–21 September, 2006/2007, Hradec nad Moravicí, Opava, Czech Republic*
S. Hledík and Z. Stuchlík, editors, Silesian University in Opava, 2007, pp. 221–256

Optical effects in brany Kerr spacetimes

Jan Schee[a] and Zdeněk Stuchlík

Institute of Physics, Faculty of Philosophy & Science, Silesian University in Opava,
Bezručovo nám. 13, CZ-746 01 Opava, Czech Republic
[a] schee@email.cz

ABSTRACT
In the framework of the brany models, rotating black holes are described by the Kerr metric with a tidal charge representing the influence of the shear effects of the bulk space Weyl tensor onto the black hole spacetime. Here we study the influence of the tidal charge onto some optical phenomena in rotating black hole spacetimes. The photon motion is given in terms of constants of the geodetical motion related to the spacetime symmetries and escape photon cones are given for special families of locally non-rotating, circular geodetical and radially freely-falling observers. The shadow of a rotating black hole and the shape of an equatorial thin accretion disk are given and classified in terms of the black hole rotational and tidal parameters.

1 INTRODUCTION

One way of realisation of the M-theory describing gravity as a truly higher-dimensional interaction becoming effectively 4D at low-enough energies is represented by the braneworld models, where the observable universe is a 3-brane (domain wall) to which the standard model (non-gravitational) matter fields are confined, while gravity field enters the extra spatial dimensions the size of which may be much larger than the Planck length scale $l_{\rm P} \sim 10^{-33}$ cm (Arkani-Hamed et al., 1998). Therefore, future collider experiments can test the braneworld models quite well, including the hypothetical mini black hole production on the TeV-energy scales (Emparan et al., 2002). On the other hand, the braneworld models could influence astrophysically important properties of black holes, enabling other tests of these models.

As shown in Randall and Sundrum (1999), gravity can be localized near the brane at low energies even with a non-compact, infinite size extra dimension with the warped spacetime satisfying the 5D Einstein equations with negative cosmological constant. Then an arbitrary energy-momentum tensor could be allowed on the brane (Shiromizu et al., 1999).

The Randall–Sundrum model gives 4D Einstein gravity in low energy limit, and the conventional potential of Newtonian gravity appears on the 3-brane with high accuracy (Randall and Sundrum, 1999). Significant deviations from the Einstein gravity occur at very high energies, e.g., in the very early universe, and in vicinity of compact objects (Maartens, 2004; Dadhich et al., 2000; Germani and Maartens, 2001; Aliev and Gümrükçüoğlu, 2005). Gravitational collapse of matter trapped on the brane results in black holes mainly localized on the brane, but their horizon could be extended into the extra dimension. The high-energy effects produced by the gravitational collapse are disconnected from the outside space by

978-80-7248-419-5

the horizon, but they could have a signature on the brane, influencing properties of black holes (Maartens, 2004). There are high-energy effects of local character influencing pressure in collapsing matter, and also non-local corrections of "backreaction" character arising from the influence of the Weyl curvature of the bulk space on the brane – the matter on the brane induces Weyl curvature in the bulk which makes influence on the structures on the brane due to the bulk graviton stresses (Maartens, 2004). The combination of high-energy (local) and bulk stress (nonlocal) effects alters significantly the matching problem on the brane, compared to the 4D Einstein gravity; for spherical objects, matching no longer leads to a Schwarzschild exterior in general (Maartens, 2004; Germani and Maartens, 2001). The Weyl stresses induced by bulk gravitons imply that the matching conditions do not have unique solution on the brane; in fact, knowledge of the 5D Weyl tensor is needed as a minimum condition for uniqueness (Germani and Maartens, 2001).[1] Some solutions for spherically symmetric black holes (Dadhich et al., 2000) and uniform density stars (Germani and Maartens, 2001) have been discussed. It is shown that in the black hole case the matching conditions could be satisfied and the bulk effects on the black hole spacetimes could be represented by a single "brany" parameter.

A promising way of generating exact localized solutions in the Randall–Sundrum braneworld models was initiated by Maartens and his coworkers (Maartens, 2004; Germani and Maartens, 2001; Dadhich et al., 2000). Assuming spherically symmetric metric induced on the 3-brane, the effective gravitational field equations on the brane could be solved, giving Reissner–Nordström static black hole solutions endowed with a brany parameter b having character of a "tidal" charge instead of the standard electric charge parameter Q^2 (Misner et al., 1973). The tidal charge reflects the effects of the Weyl curvature of the bulk space, i.e., from the 5D graviton stresses (Maartens, 2004) with the bulk graviton *tidal effects* giving the name of the charge. Note that the tidal charge can be both positive and negative, and there are some indications that negative tidal charge should properly represent the "backreaction" effects of the bulk space Weyl tensor on the brane (Dadhich et al., 2000).

The exact stationary and axisymmetric solutions describing rotating black holes localized in the Randall–Sundrum braneworld were derived in Aliev and Gümrükçüoğlu (2005), having the metric tensor of the Kerr–Newman form with a tidal charge describing the 5D correction term generated by the 5D Weyl tensor stresses. The tidal charge has an "electric" character again and arises due to the 5D gravitational coupling between the brane and the bulk, reflected on the brane through the "electric" part of the bulk Weyl tensor (Aliev and Gümrükçüoğlu, 2005), in analogy with the spherically symmetric case (Dadhich et al., 2000).

When both the tidal and electric charge are present in the brany black hole, its character is much more complex and usual Kerr–Newman form of the metric tensor is allowed only in limiting case of small values of the rotation parameter, when in the linear approximation in the rotation parameter a the metric arrives at the usual Boyer–Lindquist form describing charged and slowly rotating brany black holes (Aliev and Gümrükçüoğlu, 2005). For large enough rotation parameter, additional off-diagonal metric components $g_{r\varphi}$, g_{rt} are relevant along with the standard $g_{\varphi t}$ component, due to the combined effects of the local bulk on

[1] At present, no exact 5D solution in the braneworld model is known.

the brane and the dragging effect of rotation, which occur through the "squared" energy momentum tensor on the brane. This distorts the event horizon which becomes a stack of non-uniformly rotating null circles having different radii at fixed θ while going from the equatorial plane to the poles (Aliev and Gümrükçüoğlu, 2005). The uniformly rotating horizon is recovered for the small enough rotation parameter a. In the absence of rotation, the metric tensor reduces to the Reissner–Nordström form with correction term of non-local origin (Chamblin et al., 2001).

Here we restrict our attention to the Kerr–Newman type of solutions describing the brany rotating (Kerr) black holes with no electric charge, since in astrophysically relevant situations the electric charge of the black hole must be exactly zero, or very small (Misner et al., 1973). Then the results obtained in analysing the behaviour of test particles and photons or test fields around the Kerr–Newman black holes could be used assuming both positive and negative values of the brany tidal parameter b (used instead of charge parameter Q^2).

The information on the properties of strong gravitational fields in vicinity of a compact objects, namely of black holes, is encoded into optical phenomena of different kind that enable us to make estimates of the black hole parameters, including its tidal charge, when predictions of the theoretical models are confronted with the observed data. From this point of view, the spectral profiles of accretion discs around the black holes in galactic binaries, e.g., in microquasars, are most promising (Narayan et al., 2007; McClintock et al., 2007), along with profiled spectral lines in the X-ray flux (Laor, 1991; Bao and Stuchlík, 1992; Stuchlík and Bao, 1992; Karas et al., 1992; Matt et al., 1993). Important information could also be obtained from the quasiperiodic oscillations observed in the X-ray flux of some low-mass black hole binaries of Galactic origin (Remillard and McClintock, 2006), some expected intermediate black hole sources (Strohmayer et al., 2007), or those observed in Galactic nuclei (Aschenbach, 2004, 2007). In the case of our Galaxy centre black hole Sgr A*, we could be able to measure the optical phenomena in detailed form as compared with the other sources, since it is the nearest supermassive black hole with mass estimated to be $\sim 4 \times 10^6\,\mathrm{M}_\odot$ (Ghez, 2005), enabling to measure the "silhouette" of the black hole and other subtle GR phenomena (Bardeen, 1973; Cunningham and Bardeen, 1973).

In the present paper, we give an introductory study of the tidal charge influence on the optical phenomena near a rotating Kerr black hole. After summarising properties of brany gravitational field equations and their black hole solutions in Section 2, the effective potential of the photon motion in brany Kerr spacetimes is discussed in Section 3. Then in Section 4 the light escape cones are given for families of astrophysically interesting sources, namelly in locally non-rotating frames, and frames related to circular geodetical motion and radially free-falling sources (Schee et al., 2005). The silhouette of the black hole is determined in dependence of the black hole parameters in Section 5. Finally we discuss images of accretion discs in Section 6. Concluding remarks are presented in Section 7.

2 GRAVITATIONAL FIELD EQUATIONS ON THE BRANE

In the 5D warped space models of Randall and Sundrum, involving a non-compact extra dimension, the gravitational field equations in the bulk can be expressed in the form (Shir-

omizu et al., 1999; Dadhich et al., 2000)

$$\widetilde{G}_{AB} = \tilde{k}^2 \left[-\tilde{\Lambda} g_{AB} + \delta(\chi)(-\lambda g_{AB} + T_{AB}) \right] , \tag{1}$$

where the fundamental 5D Planck mass $\widetilde{M}_{\rm P}$ enters via $\tilde{k}^2 = 8\pi/\widetilde{M}_{\rm P}^3$, λ is the brane tension, and $\tilde{\Lambda}$ is the bulk cosmological constant. Denoting $\chi = x^4$ as the fifth dimension coordinate, $\chi = 0$ determines location of the brane in the bulk space, at the point of Z_2 symmetry; $g_{AB} = \tilde{g}_{AB} - n_A n_B$ is the induced metric on the brane, with n_A being the unit vector normal to the brane.

The effective gravitational field equations induced on the brane are determined by the bulk field Eq. (1), the Gauss–Codazzi equations and the generalised matching Israel conditions with Z_2-symmetry. They can be expressed as modified standard Einstein's equations containing additional terms reflecting bulk effects onto the brane (Shiromizu et al., 1999)

$$G_{\mu\nu} = -\Lambda g_{\mu\nu} + k^2 T_{\mu\nu} + \tilde{k}^2 S_{\mu\nu} - \mathcal{E}_{\mu\nu} , \tag{2}$$

where $k^2 = 8\pi/M_{\rm P}^2$, with $M_{\rm P}$ being the brany Planck mass. The relations of the energy scales and cosmological constants are given in the form

$$M_{\rm P} = \sqrt{\frac{3}{4\pi}} \left(\frac{\widetilde{M}_{\rm P}^2}{\sqrt{\lambda}} \right) \widetilde{M}_{\rm P} ; \quad \Lambda = \frac{4\pi}{\widetilde{M}_{\rm P}^3} \left[\tilde{\Lambda} + \left(\frac{4\pi}{3\widetilde{M}_{\rm P}^3} \right) \lambda^2 \right] . \tag{3}$$

Local bulk effects on the matter are determined by the "squared energy-momentum" tensor $S_{\mu\nu}$, where

$$S_{\mu\nu} = \tfrac{1}{12} T T_{\mu\nu} - \tfrac{1}{4} T_\mu{}^\alpha T_{\nu\alpha} + \tfrac{1}{24} g_{\mu\nu} \left(3T^{\alpha\beta} T_{\alpha\beta} - T^2 \right) , \tag{4}$$

while the non-local bulk effects are given by the tensor $\mathcal{E}_{\mu\nu}$ representing the bulk Weyl tensor $\widetilde{C}_{ABCD}$ projected onto the brane, whereas

$$\mathcal{E}_{AB} = \widetilde{C}_{ABCD} n^C n^D . \tag{5}$$

Symmetries of the Weyl tensor imply that $\mathcal{E}_{[AB]} = \mathcal{E}_A{}^A = 0$ and $\mathcal{E}_{AB} n^B = 0$. Therefore, on the brane $\chi \to 0$, there is $\mathcal{E}_{AB} \to \mathcal{E}_{\mu\nu} \delta_A{}^\mu \delta_B{}^\nu$. The $\mathcal{E}_{\mu\nu}$ tensor reflects influence of the non-local gravitational effects in the bulk, including the tidal ("Coulomb") and transverse traceless (gravitational wave) imprints of the free gravitational field of the bulk.

Here we consider vacuum (both bulk and brany) solutions of the gravitational field equations on the brane, assuming zero cosmological constant on the brane ($\Lambda = 0$) implying relation

$$\tilde{\Lambda} = -\frac{4\pi\lambda^2}{3\widetilde{M}_{\rm P}^2} . \tag{6}$$

In the absence of matter fields, there is $T_{\mu\nu} = 0 = S_{\mu\nu}$, i.e., we are not interested in the properties of the squared energy-momentum $S_{\mu\nu}$ representing local effects of the bulk. In the vacuum case, the effective gravitational field equations on the brane reduce to the form (Shiromizu et al., 1999)

$$R_{\mu\nu} = -\mathcal{E}_{\mu\nu} , \quad R_\mu{}^\mu = 0 = \mathcal{E}_\mu{}^\mu \tag{7}$$

implying divergence constraint (Shiromizu et al., 1999)

$$\nabla^{\mu}\mathcal{E}_{\mu\nu} = 0\,, \tag{8}$$

where ∇_{μ} denotes the brany covariant derivative.

Equation (8) represents Bianchi identities on the brane, i.e., an integrability condition for the field equations $R_{\mu\nu} = -\mathcal{E}_{\mu\nu}$. For stationary and axisymmetric (or static, spherically symmetric) solutions Eqs (7) and (8) form a closed system of equations on the brane.

Clearly, the 4D general relativity energy-momentum tensor $T_{\mu\nu}$ (with $T_{\mu}{}^{\mu} = 0$) can be formally identified to the bulk Weyl term on the brane due to the correspondence

$$k^2 T_{\mu\nu} \quad \longleftrightarrow \quad -\mathcal{E}_{\mu\nu}\,. \tag{9}$$

The general relativity conservation law $\nabla^{\mu}T_{\mu\nu} = 0$ then corresponds to the constraints equation on the brane Eq. (8). This behaviour indicates that Einstein–Maxwell solutions in general relativity should correspond to vacuum brany solutions. This was indeed shown in the case of Schwarzschild (R–N) (Maartens, 2004; Dadhich et al., 2000) and Kerr (K–N) spacetimes (Aliev and Gümrükçüoğlu, 2005). In both of these solutions the influence of the non-local gravitational effects of the bulk on the brane are represented by a single "brany" parameter b. The Coulomb-like behaviour in the Newtonian potential

$$\Phi = -\frac{M}{M_{\mathrm{P}}^2 r} + \frac{b}{2r^2} \tag{10}$$

inspired the name tidal charge.

Because of its symmetry properties, $\mathcal{E}_{\mu\nu}$ can be decomposed with respect to a 4-velocity field u^{μ} (Maartens, 2004)

$$\mathcal{E}_{\mu\nu} = -\left(\frac{\tilde{k}}{k}\right)^4 \left[U\left(u_{\mu}u_{\nu} + \tfrac{1}{3}h_{\mu\nu}\right) + P_{\mu\nu} + 2q_{(\mu}u_{\nu)}\right], \tag{11}$$

where $h_{\mu\nu} = g_{\mu\nu} + u_{\mu}u_{\nu}$ is the standard projection tensor. Here, three new characteristic quantities representing the influence of the non-local bulk effects are introduced. The effective energy density on the brane due to the tidal effects of the bulk

$$U = -\left(\frac{k}{\tilde{k}}\right)^4 \mathcal{E}_{\mu\nu}u^{\mu}u^{\nu}\,. \tag{12}$$

The effective anisotropic stress representing the spatially tracefree and symmetric part of the bulk influence

$$P_{\mu\nu} = -\left(\frac{k}{\tilde{k}}\right)^4 \left[h_{(\mu}{}^{\alpha}h_{\nu)}{}^{\beta} - \tfrac{1}{3}h_{\mu\nu}h^{\alpha\beta}\right]\mathcal{E}_{\alpha\beta}\,. \tag{13}$$

The effective energy flux from the free gravitational field in the bulk

$$q_{\mu} = \left(\frac{k}{\tilde{k}}\right)^4 h_{\mu}{}^{\alpha}\mathcal{E}_{\alpha\beta}u^{\beta}\,. \tag{14}$$

Assuming a static vacuum solution, and choosing u^μ along direction of time Killing vector field, we obtain $q_\mu = 0$, and the effective conservation law Eq. (8) is reduced to the form

$$\tfrac{1}{3} D_\mu U + \tfrac{4}{3} U a_\mu + D^\nu P_{\mu\nu} + a^\nu P_{\mu\nu} = 0\,, \tag{15}$$

where D_μ is u^μ-orthogonal projection of brany covariant derivative ∇_μ and 4-acceleration field $a_\mu = u^\nu \nabla_\nu u_\mu$. In static and spherically symmetric spacetimes

$$a_\mu = a(r) r_\mu\,, \quad P_{\mu\nu} = P(r)\left(r_\mu r_\nu - \tfrac{1}{3} h_{\mu\nu}\right)\,, \tag{16}$$

where r_μ is a unit radial vector, $a(r)$, $P(r)$ are functions of the radial coordinate only.

Under assumption of R–N field the solution of the conservation equation reads

$$U = \left(\frac{k}{\tilde{k}}\right)^4 \frac{B}{r^4} = -\frac{1}{2} P\,, \tag{17}$$

where the constant B is brany parameter representing the tidal effects of the bulk on the brane. Clearly, U represents an effective energy density of "radiation character," and sometimes is denoted as "dark radiation" energy density.

The spherically symmetric, static solution of the brany field equations takes a Reissner–Nordström form

$$\mathrm{d}s^2 = -\mathrm{e}^{2\Phi(r)}\,\mathrm{d}t^2 + \mathrm{e}^{2\Psi(r)}\,\mathrm{d}r^2 + r^2(\mathrm{d}\theta^2 + \sin^2\theta\,\mathrm{d}\varphi^2)\,, \tag{18}$$

with

$$\mathrm{e}^{2\Phi(r)} = \mathrm{e}^{-2\Psi(r)} = 1 - \frac{2M}{M_\mathrm{P}^2}\frac{1}{r} + \frac{B}{r^2}\,, \tag{19}$$

where M is the mass of the black hole and the bulk parameter B is named tidal charge. There is $\mathcal{E}_t{}^t = \mathcal{E}_r{}^r = -\mathcal{E}_\theta{}^\theta = -\mathcal{E}_\varphi{}^\varphi = B/r^4$.

Introducing a dimensionless brany parameter (tidal charge)

$$b = B\widetilde{M}_\mathrm{P}^2\,, \tag{20}$$

the spherically symmetric, brany black hole spacetime is characterized by the metric coefficients

$$-g_{tt} = g_{rr}^{-1} = 1 - \left(\frac{2M}{M_\mathrm{P}^2}\right)\frac{1}{r} + \left(\frac{b}{\widetilde{M}_\mathrm{P}^2}\right)\frac{1}{r^2}\,, \tag{21}$$

and by "energy-momentum" tensor

$$\mathcal{E}_{\mu\nu} = -\left(\frac{b}{\widetilde{M}_\mathrm{P}}\right)\frac{1}{r^4}(u_\mu u_\nu - 2r_\mu r_\nu + h_{\mu\nu})\,, \tag{22}$$

with black hole horizons given by the relation

$$r_\pm = \frac{M}{M_\mathrm{P}^2}\left(1 \pm \sqrt{1 - b\frac{M_\mathrm{P}^4}{M^2\widetilde{M}_\mathrm{P}^2}}\right)\,. \tag{23}$$

Contrary to the standard R–N solutions of general relativity, where $b = e^2 > 0$, the tidal charge b can be both positive and negative. For $b > 0$, there is $0 < r_- < r_+ < r_S = 2M/M_P^2$ and the black hole solutions are limited by the condition

$$b < b_{\max} \equiv \left(\frac{\widetilde{M}_P}{M_P}\right)^2 \left(\frac{M}{M_P}\right)^2 . \tag{24}$$

For $b < 0$, only one horizon exists, located above the Schwarzschild horizon

$$r_+ = \frac{M}{M_P^2}\left(1 - \sqrt{1 - b\frac{M_P^4}{M^2\widetilde{M}_P^2}}\right) > r_S . \tag{25}$$

Clearly, the physical singularity at $r = 0$ is then of spacelike character, contrary to the case of $b > 0$, where it is of timelike character (Misner et al., 1973). While $b > 0$ weakens the black hole gravitational field, negative tidal charge $b < 0$ *strengthens* the black hole field; the effective "dark energy" density U is then negative, in accord with the classical (Newtonian) result of negative energy density of isolated mass gravitational field (Dadhich et al., 2000). The gravitational field of the brany black hole acts in the fifth dimension as an attractive gravitational field with negative energy and the tidal acceleration measured by a static observer along the direction n^A reads

$$-\widetilde{R}_{ABCD}u^A n^B n^C n^D = \left(\frac{\tilde{k}}{k}\right)^4 U + \frac{1}{6}\tilde{k}\tilde{\Lambda} . \tag{26}$$

The negative bulk cosmological constant contributes to acceleration towards the brane, according its confining gravitational character. In order for U to reinforce confinement, it must be negative, and negative brany parameter $b < 0$ is physically more natural case (Dadhich et al., 2000).

Similar considerations hold in the case of the brany Kerr solutions discussed in Aliev and Gümrükçüoğlu (2005). Using representation of stationary and axially symmetric metric on the brane in the Kerr–Schild form, standard in derivation of the Kerr metric (Kerr, 1963), we are able to solve the gravitational equations on the brane. The Kerr–Schild ansatz assumes that the exact metric can be given in terms of its linear approximation around flat metric, i.e., in the form

$$\mathrm{d}s^2 = \eta_{ij}\,\mathrm{d}x^i\mathrm{d}x^j + H(l_i\mathrm{d}x^i)^2 , \tag{27}$$

where H is the characteristic scalar function and l_i is a geodetical null vector field in both flat and exact metric. There are two such vector fields, we call them ingoing and outgoing principal null congruences (Misner et al., 1973).

3 NULL GEODESIC IN KERR SPACETIME WITH A TIDAL CHARGE

3.1 Geometry

Following the work of Aliev and Gümrükçüoğlu (2005), and using the standard Boyer–Lindquist coordinates (t, r, θ, φ) and geometry units ($c = G = 1$) we can write the line

element of Kerr black-hole metric on the three-brane in the form

$$\mathrm{d}s^2 = -\left(1 - \frac{2Mr - b}{\Sigma}\right)\mathrm{d}t^2 + \frac{\Sigma}{\Delta}\,\mathrm{d}r^2 + \Sigma\,\mathrm{d}\theta^2 + \frac{A}{\Sigma}\,\mathrm{d}\varphi^2 - 2\frac{2Mr - b}{\Sigma}\sin^2\theta\,\mathrm{d}t\mathrm{d}\varphi\,, \quad (28)$$

where

$$\begin{aligned}
\Sigma &= r^2 + a^2\cos^2\theta\,,\\
\Delta &= r^2 - 2Mr + a^2 + b\,,\\
A &= (r^2 + a^2)^2 - a^2\Delta\sin^2\theta\,.
\end{aligned} \quad (29)$$

M is the mass parameter, $a = J/M$ is the specific angular momentum and the brany parameter b is the *tidal charge* representing imprint of non-local gravitational effects from the bulk space. The form of metric (28) is the same as the Kerr–Newman metric, where the tidal charge is replaced by squared electric charge. The stress tensor on the brane $E_{\mu\nu}$ takes the form

$$\begin{aligned}
E_t{}^t &= -E_\varphi{}^\varphi = -\frac{b}{\Sigma^3}[\Sigma - 2(r^2 + a^2)]\,,\\
E_r{}^r &= -E_\theta{}^\theta = -\frac{b}{\Sigma^2}\,,\\
E_\varphi{}^t &= -(r^2 + a^2)\sin^2\theta\,,\\
E_t{}^\varphi &= -\frac{2ba}{\Sigma^3}(r^2 + a^2)\sin^2\theta
\end{aligned}$$

that is fully analogical ($b \to Q^2$) to the components of energy-momentum tensor for Kerr–Newman spacetimes in Einstein's general relativity (Aliev and Gümrükçüoğlu, 2005).

Therefore, the photon motion analysis for the Kerr–Newman spacetimes can be directly used for brany Kerr spacetimes with a tidal charge. Of course, the brany parameter b can be both positive and *negative*, with the negative values being astrophysically more plausible (e.g., Dadhich et al., 2000).

The roots of $\Delta = 0$ identify the type of brany Kerr spacetime. There are two possibilities, a black hole or a naked singularity. By introducing $a^2/M^2 \to a^2$, $b/M^2 \to b$ and $r_+/M \to r_+$ and putting $M = 1$ we write the roots of $\Delta = 0$ in the form

$$r_+ = 1 + \sqrt{1 - a^2 - b}\,, \quad \text{(outer horizon)} \quad (30)$$

and

$$r_- = 1 - \sqrt{1 - a^2 - b}\,, \quad \text{(inner horizon)}. \quad (31)$$

The metric given by the line element Eq. (28) determines the geometry of rotating black hole in brany universe if

$$1 \geq a^2 + b\,. \quad (32)$$

The strong inequality refers to case of two horizons r_+ and r_-. For extreme black holes ($1 = a^2 + b$) there is $r_+ = r_- = 1$. It is clear that in the case of $b \geq 0$ the loci of the inner

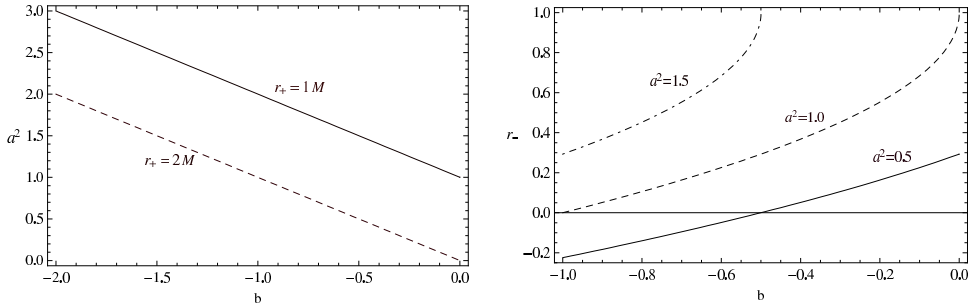

Figure 1. *Left*: The plot of a^2 as a function of tidal charge parameter b for fixed values of r_+. There are two curves for two representative values of outer horizon $r_+ = 1$ and $r_+ = 2$. *Right*: The plot of the inner horizon r_- as a function of tidal charge parameter b. There are there curves for three representative values of rotational parameter $a^2 = 0.5$, $a^2 = 1.0$ and $a^2 = 1.5$.

horizon r_- is always positive. But if the value of tidal parameter is $b < 0$, the loci of the inner horizon can also be at negative r, as illustrated in Fig. 1 (right). It is quite important that there is a crucial difference in between the spacetimes with $r_- > 0$ and $r_- < 0$, since in the first case ($r_- > 0$) the physical singularity is of time-like character, while in the second case ($r_- < 0$) it is of spacelike character, as stressed in Dadhich et al. (2000).

Writing the square of rotational parameter a^2 as a function of b one arrives from Eq. (30) to formula

$$a^2 = 1 - b - (-1 + r_+)^2 \,. \tag{33}$$

One can easily verify that we can have $a^2 > 1$ for particular choices of $b < 0$ and r_+, as illustrated in Fig. 1 (left). Notice that $a^2 > 1$ is not allowed for standard (non-brany) black holes (Misner et al., 1973).

The case of $1 < a^2 + b$ refers to the brany Kerr naked singularities. In this paper we focus on astrophysically interesting case of black holes, with emitting source and observer located above the outer horizon.

3.2 Carter's equations

In order to study the optical effects in brany Kerr spacetimes we have to solve equations of motion of photons. It is well known that photons move along null geodesics of the spacetime under consideration. The geodesic equation reads

$$\frac{\mathrm{D}k^\mu}{\mathrm{d}w} = 0 \,, \tag{34}$$

where $k^\mu = \mathrm{d}x^\mu/\mathrm{d}w$ is the wave vector, tangent to the null geodesic and w is the affine parameter. The geodesic equations can be found from the Lagrangian

$$\mathcal{L} = \frac{1}{2} g_{\mu\nu} \frac{\mathrm{d}x^\mu}{\mathrm{d}w} \frac{\mathrm{d}x^\nu}{\mathrm{d}w} \tag{35}$$

with the normalization condition

$$g_{\mu\nu}\frac{\mathrm{d}x^\mu}{\mathrm{d}w}\frac{\mathrm{d}x^\nu}{\mathrm{d}w} = g_{\mu\nu}k^\mu k^\nu = 0\,. \tag{36}$$

Equations (34) and (36) determine the motion of a photon unambiguously. Since the components of the metric tensor do not depend on φ and t coordinates, the following conjugate momenta

$$k_\varphi \equiv \frac{\partial\mathcal{L}}{\partial(\partial\varphi/\partial w)} = g_{\varphi\nu}k^\nu \equiv \Phi\,, \tag{37}$$

$$k_t \equiv \frac{\partial\mathcal{L}}{\partial(\partial t/\partial w)} = g_{t\nu}k^\nu \equiv -E\,, \tag{38}$$

are the integrals of motion. Carter found another integral of motion K as a separation constant when solving Hamilton–Jacobi equation

$$g^{\mu\nu}\frac{\mathrm{d}S}{\mathrm{d}x^\mu}\frac{\mathrm{d}S}{\mathrm{d}x^\nu} = 0\,, \tag{39}$$

where he assumed the action S in separated form

$$S = -E_t + \Phi\varphi + S_r(r) + S_\theta(\theta)\,. \tag{40}$$

Using Hamilton–Jacobi method, the equations of motion can be integrated and written separately in the form

$$\Sigma\frac{\mathrm{d}r}{\mathrm{d}w} = \pm\sqrt{R(r)}\,, \tag{41}$$

$$\Sigma\frac{\mathrm{d}\theta}{\mathrm{d}w} = \pm\sqrt{W(\theta)}\,, \tag{42}$$

$$\Sigma\frac{\mathrm{d}\varphi}{\mathrm{d}w} = -\frac{P_\mathrm{W}}{\sin^2\theta} + \frac{aP_\mathrm{R}}{\Delta}\,, \tag{43}$$

$$\Sigma\frac{\mathrm{d}t}{\mathrm{d}w} = -aP_\mathrm{W} + \frac{(r^2+a^2)P_\mathrm{R}}{\Delta}\,, \tag{44}$$

where

$$R(r) = P_\mathrm{R}^2 - \Delta K\,, \tag{45}$$

$$W(\theta) = K - \left(\frac{P_\mathrm{W}}{\sin\theta}\right)^2\,, \tag{46}$$

$$P_\mathrm{R}(r) = E(r^2+a^2) - a\Phi\,, \tag{47}$$

$$P_\mathrm{W}(\theta) = aE\sin^2\theta - \Phi\,. \tag{48}$$

It is useful to introduce integral of motion Q by the formula

$$Q = K - (E - a\varphi)^2\,. \tag{49}$$

The advantage of introducing this integral of motion comes from the fact that in the case of astrophysically most important motion in the equatorial plane there is $Q = 0$.

3.3 Radial and latitudinal motion

The photon motion (with fixed constants of motion E, Φ, Q) is allowed in regions where $R(r; E, \Phi, Q) \geq 0$ and $W(\theta; E, \Phi, Q) \geq 0$. The conditions $R(r; E, \Phi, Q) = 0$ and $W(\theta; E, \Phi, Q) = 0$ determine turning points of the radial and latitudinal motion, respectively, giving boundaries of the region allowed for the motion. Therefore, the analysis of the turning points of the r-motion and θ-motion is crucial for understanding properties of the photon motion. Detailed analysis of the θ-motion can be found in Bičák and Stuchlík (1976), while the radial motion was analysed (with restrictions implied by the θ-motion) in Stuchlík (1981a,b). Here we extend this detailed analysis to the case of $b < 0$.

To study the behaviour of null geodesics in the brany Kerr spacetimes we employ the Carter's equations. The radial and latitudinal Carter's equations read

$$\Sigma \left(\frac{\mathrm{d}r}{\mathrm{d}w}\right)^2 = \left[E(r^2 + a^2) - a\Phi\right]^2 - \Delta\left[L - 2a\Phi E + a^2E^2\right], \tag{50}$$

$$\Sigma \left(\frac{\mathrm{d}\theta}{\mathrm{d}w}\right)^2 = L + a^2E^2\cos^2\theta - \frac{\Phi^2}{\sin^2\theta}, \tag{51}$$

where the new motion constant $L = Q + \Phi^2$ has been introduced besides the fourth Carter's separation constant Q. It should be stressed that photon motion does not depend on E corresponding to the frequency of the photon due to equation $E = h\nu$. After rescaling the affine parameter w, Eqs (50) and (51) read

$$\Sigma \left(\frac{\mathrm{d}r}{\mathrm{d}w'}\right)^2 = \left[r^2 + a^2 - a\lambda\right]^2 - \Delta\left[\mathcal{L} - 2a\lambda + a^2\right], \tag{52}$$

$$\Sigma \left(\frac{\mathrm{d}\theta}{\mathrm{d}w'}\right)^2 = \mathcal{L} + a^2\cos^2\theta - \frac{\lambda^2}{\sin^2\theta} \tag{53}$$

where we have introduced impact parameters

$$\lambda = \frac{\Phi}{E}, \tag{54}$$

$$\mathcal{L} = \frac{L}{E^2} = \frac{Q + \Phi^2}{E^2} = q + \lambda^2, \tag{55}$$

and rescaled affine parameter

$$w' = Ew. \tag{56}$$

The reality conditions $(\mathrm{d}r/\mathrm{d}w')^2 \geq 0$ and $(\mathrm{d}\theta/\mathrm{d}w')^2 \geq 0$ lead to the restrictions on the impact parameter $\mathcal{L}$

$$\mathcal{L}_{\mathrm{min}} \leq \mathcal{L} \leq \mathcal{L}_{\mathrm{max}}, \tag{57}$$

where

$$\mathcal{L}_{\mathrm{max}} \equiv \frac{(a\lambda - 2r + b)^2}{\Delta} + r^2 + 2r - b, \tag{58}$$

and

$$\mathcal{L}_{\rm min} \equiv \begin{cases} \lambda^2 & \text{for } |\lambda| \geq a\,, \\ 2a|\lambda| - a^2 & \text{for } |\lambda| \leq a\,. \end{cases} \tag{59}$$

The upper constraint, $\mathcal{L}_{\rm max}$, comes from the radial-motion reality condition and the lower constraint, $\mathcal{L}_{\rm min}$, comes from the latitudinal-motion reality condition. The properties of the photon motion are determined by the behaviour of the surface $\mathcal{L}_{\rm max}(r;\lambda,a,b)$, as given by (58). The extrema of the surface $\mathcal{L}_{\rm max}$ (determined by the condition $\partial\mathcal{L}_{\rm max}/\partial r = 0$) are determined by

$$\lambda = \lambda_+ \equiv \frac{r^2 + a^2}{a}\,, \tag{60}$$

$$\lambda = \lambda_- \equiv \frac{r^2 - br - a^2 - r\Delta}{a(r-1)}\,. \tag{61}$$

The values of $\mathcal{L}_{\rm max}$ at these extreme points are given by

$$\mathcal{L}_+ = 2r^2 + a^2\,, \tag{62}$$

$$\mathcal{L}_- = \frac{2r\left(r^3 - 3r + 4b\right) + a^2\,(r+1)^2}{(r-1)^2}\,. \tag{63}$$

The character of the extrema follows from the sign of $\partial^2\mathcal{L}_{\rm max}/\partial r^2$. One finds that

$$\frac{\partial^2\mathcal{L}_{\rm max}}{\partial r^2} = \frac{8r^2}{\Delta} \quad \text{for } \lambda = \lambda_+\,, \tag{64}$$

$$\frac{\partial^2\mathcal{L}_{\rm max}}{\partial r^2} = \frac{8r^2}{\Delta} - \frac{8r}{(r-1)^2}\,, \quad \text{for } \lambda = \lambda_-\,. \tag{65}$$

Incorporating the restrictions given by the latitudinal Eq. (59), we determine where

$$\mathcal{L}_{\rm max} = \lambda^2 \quad \text{for } |\lambda| \geq a\,, \tag{66}$$

$$\mathcal{L}_{\rm max} = 2a|\lambda| - a^2 \quad \text{for } |\lambda| \leq a\,. \tag{67}$$

We find that

$$\mathcal{L}_{\rm max} = \lambda^2 \tag{68}$$

is fulfilled for

$$\lambda = \tilde{\lambda}_\pm \equiv \frac{a(b - 2r \pm r^2\sqrt{\Delta}\,)}{r^2 - 2r + b}\,, \tag{69}$$

while

$$\mathcal{L}_{\rm max} = 2a|\lambda| - a^2$$

is fulfilled for

$$\lambda = \bar{\lambda} \equiv \frac{1}{\Delta}\left[4r - r^2 - 2b - a^2 + 2\sqrt{\Delta(b-2r)}\right]. \tag{70}$$

The analysis of behaviour of curves $\lambda_\pm$, $\tilde{\lambda}_\pm$ and $\bar{\lambda}$ is used to classify the radial motion in brany Kerr spacetime. The extreme points of curves $\tilde{\lambda}_\pm$, which are also the intersection points of these curves with λ_-, are determined by the equation

$$f(r;a,b) \equiv r^4 - 6r^3 + (9+4b)r^2 - 4(3b+a^2)r + 4b(b+a^2) = 0\,. \tag{71}$$

The equation $f(r;a,b) = 0$ determines loci of the photon circular orbits; in an implicit form the radii are given by the condition

$$a^2 = a^2_{\mathrm{ph}\pm}(r;b) = \frac{r^2(r-3)^2 + 4b(r^2-3r+b)}{4(r-b)}\,. \tag{72}$$

The maxima of the curve $\bar{\lambda}$, which also determine the intersections of curves $\bar{\lambda}$ and λ_- are located on r satisfying the equation

$$2r^3 - (3+b)r^2 + 2br + a^2 = 0\,. \tag{73}$$

The brany Kerr spacetimes can be classified due to the properties of the photon motion determined by the behaviour of the functions $\lambda_\pm$, $\tilde{\lambda}_\pm$, $\bar{\lambda}$. The properties of these functions are given by their divergences (i.e., by existence of the horizons) and the local extrema

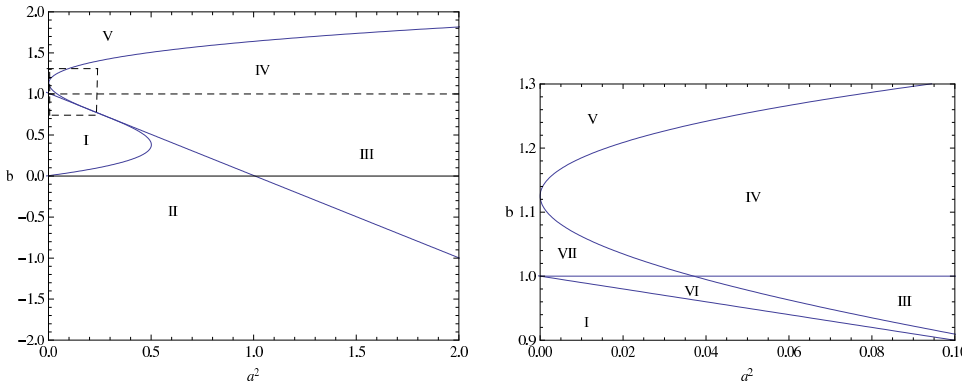

Figure 2. *Left*: classification of Kerr spacetime in Brany universe according to value of $a^2 + b$, b and n_{ext} (the number of extrema of the curves $\tilde{\lambda}_\pm$, which is also the number of circular photon orbits in the equatorial plane). The classification regions are: (I) for $a^2 + b \leq 1$ and $n_{\mathrm{ext}} = 2$, (II) for $a^2 + b \leq 1$ and $n_{\mathrm{ext}} = 4$, (III) $a^2 + b > 1$ and $b < 1$ and $n_{\mathrm{ext}} = 2$, (IV) for $a^2 + b > 1$ and $b > 1$ and $n_{\mathrm{ext}} = 2$, (V) for $a^2 + b > 1$ and $n_{\mathrm{ext}} = 0$, (VI) for $a^2 + b > 1$ and $b < 1$ and $n_{\mathrm{ext}} = 4$, (VII) for $a^2 + b > 1$ and $b > 1$ and $n_{\mathrm{ext}} = 4$. *Right*: zoom of the area in the dashed rectangle of the left plot, to uncover regions VI and VII.

determining equatorial photon circular orbits. There exist seven classes of the brany Kerr spacetimes, with the criteria of separation being $a^2 + b \lessgtr 1$, $b \lessgtr 1$ and the number of equatorial circular orbits. There are seven regions in (b, a^2) plot corresponding to different behaviour of curves $\lambda_\pm$, $\tilde{\lambda}_\pm$ and $\bar{\lambda}$ representing properties of the photon motion. The classification of the brany Kerr spacetime is represented in Fig. 2. There are two different classes of the black-hole spacetimes, differing by the presence of the photon circular orbits under the inner horizon. However, in the astrophysically relevant region outside the outer horizon, both the classes are of the same character, having two equatorial photon circular orbits, one corotating (at $r_{\rm ph1}$) and the other counter-rotating (at $r_{\rm ph2} > r_{\rm ph1}$).

Using the knowledge of the behaviour of $\mathcal{L}_{\rm max}$ and $\mathcal{L}_{\rm min}$, we can construct *the light escape cones*. In Figs 3, 4 and 5, we plot functions $\lambda_\pm$, $\tilde{\lambda}_\pm$ and $\bar{\lambda}$ for black hole spacetime parameters $a = 0.9$ and $b = -1.0$. In this case, taken as an example characterizing Kerr black holes, there exist ten significant values of λ:

- $\lambda_{\rm A} \equiv \lambda_-(r = \bar{r}) = \bar{\lambda}(r = \bar{r})$,
- $\lambda_{\rm B} \equiv \lambda_\pm(r = r_+) = \tilde{\lambda}_\pm(r = r_+) = \bar{\lambda}(r = r_+)$,
- $\lambda_{\rm C} \equiv \lambda_-(r = r_{\rm cph3}) = \tilde{\lambda}_+(r = r_{\rm cph3})$,
- $\lambda_{\rm D} \equiv \lambda_-(r = r_{\rm M})$,
- $\lambda_{\rm E} \equiv \lambda_-(r = r_-) = \tilde{\lambda}_-(r = r_-)$,
- $\lambda_{\rm F} \equiv \lambda_-(r = r_{\rm cph2}) = \tilde{\lambda}_+(r = r_{\rm cph2})$,
- $\lambda_{\rm G} \equiv \lambda_\pm(r = 0) = \tilde{\lambda}_\pm(r = 0)$,
- $\lambda_{\rm H} \equiv \lambda_-(r = r_{\rm cph1}) = \tilde{\lambda}_+(r = r_{\rm cph1})$,
- $\lambda_{\rm I} \equiv \lambda_-(r = \check{r}) = \bar{\lambda}(r = \check{r})$,
- $\lambda_{\rm J} \equiv \lambda_-(r = r_{\rm cph4}) = \tilde{\lambda}_+(r = r_{\rm cph4})$,

where $\bar{r}$ is the highest positive root of Eq. (73), $r_\pm$ are outer and inner horizons, $r_{\rm cph1}$–$r_{\rm cph4}$ are circular photon orbits in equatorial plane satisfying Eq. (71), $r_{\rm M} = 1 - (1 - a^2 - b)^{1/3}$ is the maximum of λ_- and $\check{r}$ is the negative root of Eq. (73). (Notice that above r_+, the behaviour is the same for all black-hole spacetimes.)

The behaviour of $\mathcal{L}_{\rm max} = \mathcal{L}_{\rm max}(r; \lambda)$ is qualitatively different in different intervals given by subsequent values of $\lambda_\mu (\mu \in A, \ldots, J)$. The plots of $\mathcal{L}_{\rm max}$ are depicted in Figs 6 and 7.

The allowed values of the impact parameter $\mathcal{L}$ lie between the limiting functions $\mathcal{L}_{\rm min}$ and $\mathcal{L}_{\rm max}$. If the minimum $\mathcal{L}^{\rm min}_{\rm max} \equiv \mathcal{L}_{\rm max}(r_{\rm min}, \lambda_0)$ of the limiting function $\mathcal{L}_{\rm max}$ is less than the value of the limiting function $\mathcal{L}_{\rm min}$, the incoming photon ($k^r < 0$) travelling from infinity will return back for all values of $\mathcal{L}_0 \in [\mathcal{L}_{\rm min}; \mathcal{L}_{\rm max}]$. If the value of the minimum $\mathcal{L}^{\rm min}_{\rm max}$ is greater than the value of limiting function $\mathcal{L}_{\rm min}$, the incoming photon ($k^r < 0$) travelling from infinity returns back if its impact parameter $\mathcal{L}_0$ satisfies the condition $\mathcal{L}_0 \geq \mathcal{L}^{\rm min}_{\rm max}$. The minimum $\mathcal{L}^{\rm min}_{\rm max}$ determines a photon spherical orbit, i.e., a sphere where photons move with $r = {\rm const.}$, but with varying latitude θ (and, of course, varying φ). When the condition $\mathcal{L}_0 = \mathcal{L}_{\rm min}$ is satisfied simultaneously, the spherical photon orbit is transformed to an equatorial photon circular orbit. Photons with $\mathcal{L}_0 = \mathcal{L}^{\rm min}_{\rm max}$ will wind up around the photon sphere. Using these limiting values of $\mathcal{L}_0$, we are able to construct light escape cones for any well defined family of local observers (radiating sources). Here we restrict our attention to the special sets of stationary observers, namely locally non-rotating observers, those following circular equatorial geodesics, and the radially free-falling observers.

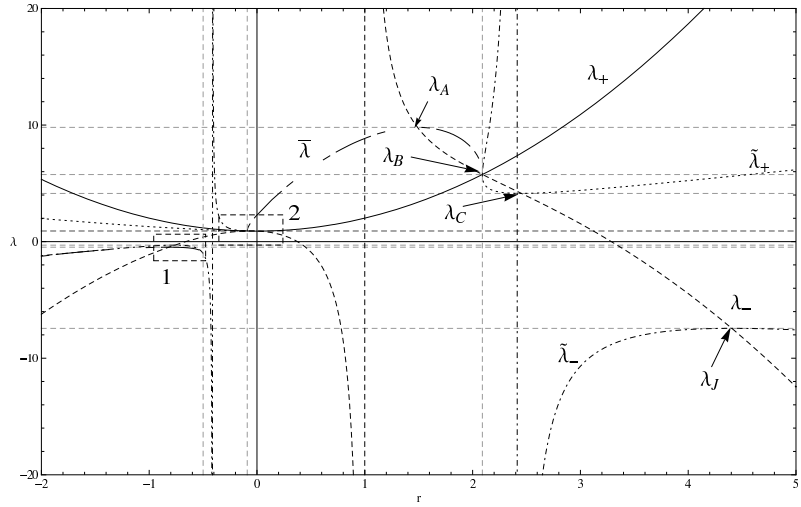

Figure 3. The graphs of $\lambda_\pm$, $\tilde{\lambda}_\pm$ and $\bar{\lambda}$ function are plotted for representative values of space parameters $a = 0.9$ and $b = -1.0$. The two dashed rectangle areas labelled with numbers 1 and 2 are zoomed in following figures. The horizontal gray dashed lines represents special values of the impact parameter λ, denoted due to the text as $\lambda_A, \ldots, \lambda_J$.

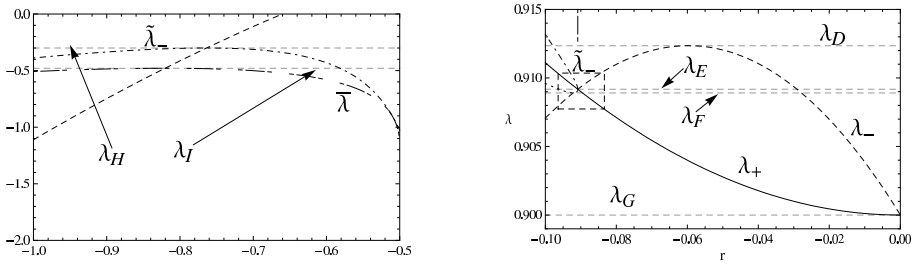

Figure 4. *Left panel:* the zoom of dashed area labelled 1 in the previous figure. *Right panel:* the zoom of dashed area labelled 2 in the previous figure. The dashed rectangle area here is zoomed in the next figure.

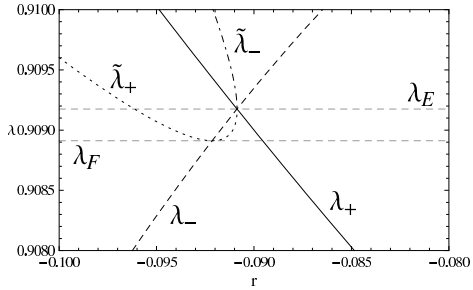

Figure 5. The zoom of the dashed rectangle area in the previous figure.

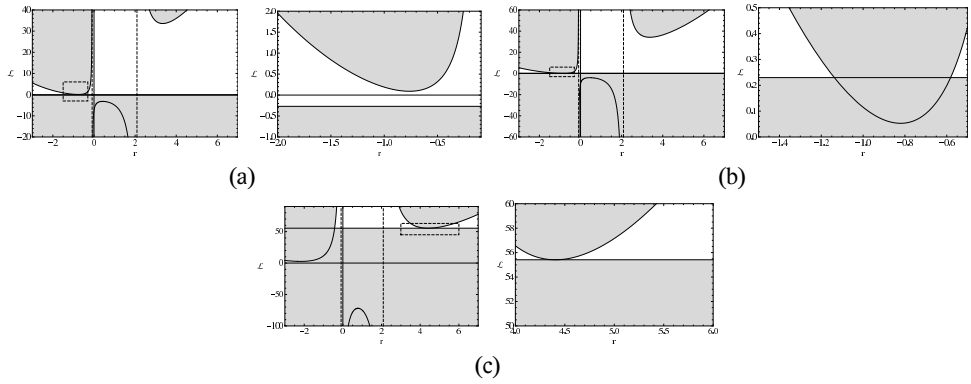

Figure 6. *Left images:* plots of $\mathcal{L} = \mathcal{L}(r; \lambda, a, b)$ are depicted for representative values of $a = 0.9$, $b = -1.0$ and λ: (a) $\lambda = \lambda_{\mathrm{G}}$, (b) $\lambda = \lambda_{\mathrm{H}}$, (c) $\lambda = \lambda_{\mathrm{I}}$. *Right images:* plots of zoomed area of relevant left plot.

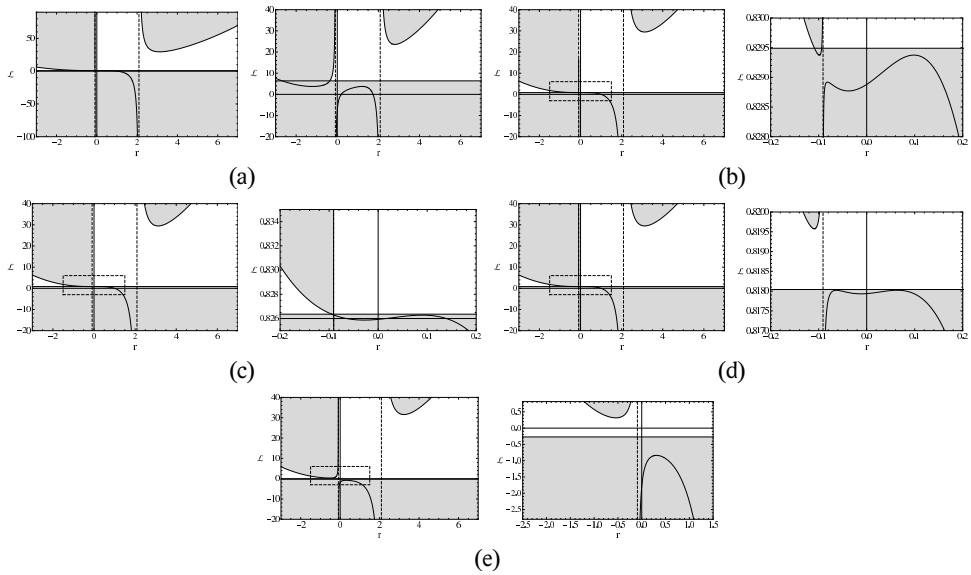

Figure 7. *Left images:* here we plots of $\mathcal{L} = \mathcal{L}(r; \lambda, a, b)$ are depicted for representative values of $a = 0.9$, $b = -1.0$ and λ: (a) $\lambda \in [\lambda_{\mathrm{B}}, \lambda_{\mathrm{A}}]$, (b) $\lambda \in [\lambda_{\mathrm{C}}, \lambda_{\mathrm{B}}]$, (c) $\lambda \in [\lambda_{\mathrm{D}}, \lambda_{\mathrm{C}}]$, (d) $\lambda \in [\lambda_{\mathrm{E}}, \lambda_{\mathrm{D}}]$, (e) $\lambda \in [\lambda_{\mathrm{F}}, \lambda_{\mathrm{E}}]$, (f) $\lambda \in [\lambda_{\mathrm{G}}, \lambda_{\mathrm{F}}]$. *Right images:* plots of zoomed area of relevant left plot.

4 CONSTRUCTION OF LIGHT ESCAPE CONES

We construct *light escape cones* of the brany Kerr black holes to filter out photons that after being radiated by a specific source at a given position characterized by the coordinates (r_0, θ_0) fall under the horizon from photons that after reaching a radial turning point return to infinity when the source is located above the photon circular orbit, or the photons escap-

ing to infinity from those being captured by the black hole after reaching a radial turning point when the source is located under the photon circular orbit. Here we apply the light escape cone construction developed and discussed in Schee et al. (2005).

Projection of a photon 4-momentum $\boldsymbol{k}$ onto the local tetrad of an observer is given by the formulae

$$k^{(t)} = -k_{(t)} = 1\,, \tag{74}$$
$$k^{(r)} = k_{(r)} = \cos\alpha_0\,, \tag{75}$$
$$k^{(\theta)} = k_{(\theta)} = \sin\alpha_0 \cos\beta_0\,, \tag{76}$$
$$k^{(\varphi)} = k_{(\varphi)} = \sin\alpha_0 \sin\beta_0\,, \tag{77}$$

where α_0, β_0 are directional angles of the photon in the local frame (see Fig. 8) and $\cos\gamma_0 = \sin\alpha_0 \sin\beta_0$. We use the impact parameters in the convenient way

$$\lambda \equiv \frac{\Phi}{E}\,, \quad q \equiv \frac{K - (\Phi - aE)^2}{E^2}\,, \quad \mathcal{L} \equiv q + \lambda^2\,. \tag{78}$$

In terms of the local tetrad components of the photon 4-momentum and the related directional angles, the conserved quantities, namely, the azimuthal momentum Φ and energy E read

$$\Phi = k_\varphi = -\omega^{(t)}{}_\varphi\, k^{(t)} + \omega^{(r)}{}_\varphi\, k^{(r)} + \omega^{(\theta)}{}_\varphi\, k^{(\theta)} + \omega^{(\varphi)}{}_\varphi\, k^{(\varphi)}\,, \tag{79}$$
$$E = -k_t = \omega^{(t)}{}_t\, k^{(t)} - \omega^{(r)}{}_t\, k^{(r)} - \omega^{(\theta)}{}_t\, k^{(\theta)} - \omega^{(t)}{}_\varphi\, k^{(\varphi)}\,, \tag{80}$$

and the third constant

$$K = \frac{1}{\Delta}\left\{\left[E(r^2 + a^2) - a\Phi\right]^2 - (\Sigma k^r)^2\right\}\,. \tag{81}$$

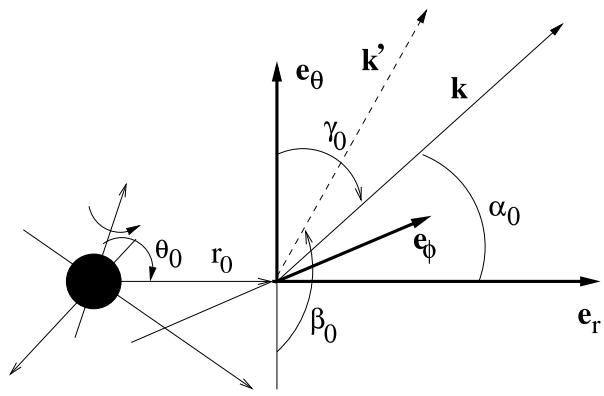

Figure 8. Definition of directional angles α_0, β_0 and γ_0 in a local frame. Vectors $\boldsymbol{e}_r$, $\boldsymbol{e}_\theta$, $\boldsymbol{e}_\varphi$ are the basic tetrad vectors. Position of the observer (source) is given by the coordinates (r_0, θ_0). Vector $\boldsymbol{k}$ represents a photon as observed by the observer in the given tetrad and vector $\boldsymbol{k}'$ is its projection into the plane $(\boldsymbol{e}_\theta, \boldsymbol{e}_\varphi)$.

The impact parameters λ and $\mathcal{L}$ are thus fully determined by any double, D, of angles from the set $M = [\alpha_0, \beta_0, \gamma_0]$.

4.1 Local frames of stationary and free-falling observers

There are four local frames we introduce here. The stationary frames, LNRF (Locally Nonrotatig Frame), SF (Static Frame), $\mathrm{GF}_{\pm}$ (Circular Geodesic Frame) and RFF (Radially Free-Falling Frame). All of the introduced frames are of direct astrophysical relevance. Especially the LNRF are of highest importance since the physical phenomena take the simplest form when expressed in such frames, because the rotational spacetime effects are maximally suppressed there (Bardeen, 1973; Misner et al., 1973). The $\mathrm{GF}_{\pm}$ are related to radiation of Keplerian accretion discs, both corotating and counterrotating, while RFF are related to free-falling spherical accretion. The SF, similarly to LNRF, correspond to accelerated frames fixed relative to distant observers.

The radial and latitudinal 1-forms of the three stationary frame tetrads are common for the all three stationary cases and read

$$\omega^{(r)} = \left\{0, \sqrt{\Sigma/\Delta}, 0, 0\right\} , \tag{82}$$

$$\omega^{(\theta)} = \left\{0, 0, \sqrt{\Sigma}, 0\right\} . \tag{83}$$

LNRF corresponds to observers with $\Phi = 0$ (zero angular momentum observers). Their time and azimuthal 1-forms read

$$\omega^{(t)} = \left\{\sqrt{\frac{\Delta\Sigma}{A}}, 0, 0, 0\right\} , \tag{84}$$

$$\omega^{(\varphi)} = \left\{-\Omega_{\mathrm{LNRF}}\sqrt{\frac{A}{\Sigma}}\sin\theta, 0, 0, \sqrt{\frac{A}{\Sigma}}\sin\theta\right\} . \tag{85}$$

where

$$\Omega_{\mathrm{LNRF}} = \frac{a(2r-b)}{A} \tag{86}$$

is the angular velocity of LNRF as seen by observers at infinity.

The tetrad of SF observers, i.e., observers with $\Omega = 0$ as seen by observers at infinity, is given by the formulae

$$\omega^{(t)} = \left\{\sqrt{1 - \frac{2r-b}{\Sigma}}, 0, 0, \frac{a(2r-b)\sin^2\theta}{\sqrt{\Sigma^2 - (2r-b)\Sigma)}}\right\} , \tag{87}$$

$$\omega^{(\varphi)} = \left\{0, 0, 0, \sqrt{\frac{\Delta\Sigma}{\Sigma - (2r-b)}}\sin\theta\right\} . \tag{88}$$

The $\mathrm{GF}_{\pm}$ observers move along φ coordinate in the equatorial plane with velocity $V_{\mathrm{GF}\pm}$ ($+$ denotes corotating, $-$ counterrotating) relative to the LNRF observers. In general,

formula for the velocity $V_{\mathrm{GF}\pm}$ reads

$$V_{\mathrm{GF}\pm} = \frac{U^{(\varphi)}}{U^{(t)}} = \frac{\omega^{(\varphi)}{}_{\mu} U^{\mu}}{\omega^{(t)}{}_{\mu} U^{\mu}}$$

and using the results of Bardeen et al. (1972), we arrive to

$$V_{\mathrm{GF}\pm} = \pm \frac{(r^2 + a^2)Y \mp a(2r - b)}{\sqrt{\Delta}(r^2 \pm aY)}, \tag{89}$$

where we have introduced $Y = \sqrt{r - b}$. The Lorentz transformation of LNRF to $\mathrm{GF}_{\pm}$ has the form

$$\Lambda(V) = \begin{pmatrix} \gamma & 0\ 0 & -\gamma V \\ 0 & 1\ 0 & 0 \\ 0 & 0\ 1 & 0 \\ -\gamma V & 0\ 0 & \gamma \end{pmatrix} \tag{90}$$

with $\gamma = 1/\sqrt{1 - V^2}$ and $V = V_{\mathrm{GF}\pm}$. Using Eq. (89), the Lorentz transformation of the LNRF tetrad gives the tetrad of $\mathrm{GF}_{\pm}$ in the form

$$\omega^{(t)}_{\pm} = \left\{ \frac{r^2 - 2r + b \pm aY}{Z_{\pm}}, 0, 0, \mp \frac{(r^2 + a^2)Y \mp a(2r - b)}{Z_{\pm}} \right\}, \tag{91}$$

$$\omega^{(\varphi)}_{\pm} = \left\{ \mp \frac{\sqrt{\Delta} Y}{Z_{\pm}}, 0, 0, \frac{\sqrt{\Delta(r^2 \pm aY)}}{Z_{\pm}} \right\}, \tag{92}$$

where

$$Z_{\pm} = r\sqrt{r^2 - 3r + 2b \pm 2aY}\,.$$

Note that the $\mathrm{GF}_{\pm}$ family of frames is restricted to the equatorial plane.

The RFF observers pass the LNRF with velocity

$$V_{\mathrm{RFF}} = \left\{ V^{(r)}, V^{(\theta)}, V^{(\varphi)} \right\} \tag{93}$$

as measured in LNRF, and in the case of radially free-falling (or free-escaping) observers starting at infinity there is $V^{(\theta)} = 0$ as they move with $\theta = \mathrm{const}$ and $V^{(\varphi)} = 0$. Using the results of Stuchlík et al. (1999), we find the velocity components of the free-falling frames in the LNRF frames

$$V^{(r)} = \pm\sqrt{1 - \frac{\Sigma\Delta}{A}}, \tag{94}$$

$$V^{(\theta)} = 0, \tag{95}$$

$$V^{(\varphi)} = 0. \tag{96}$$

Clearly, the free-falling (free-escaping) observers move only radially in the LNRF, representing thus generalisation of static observers and radially moving particles in static, Schwarzschild spacetimes (Stuchlík et al., 1999). The Lorentz transformation of the LNRF tetrad with the square of speed parameter $V^2 = (V^{(r)})^2$ has the form

$$\Lambda(V) = \begin{pmatrix} \gamma & -\gamma V & 0 & 0 \\ -\gamma V & \gamma & 0 & 0 \\ 0 & 0 & 1 & 0 \\ 0 & 0 & 0 & 1 \end{pmatrix} \tag{97}$$

where $\gamma = 1/\sqrt{1-V^2}$. For the radially free-falling sources, the tetrad components $\omega^{(\theta)}$ and $\omega^{(\varphi)}$ coincide with those of the LNRF tetrad, while $\omega^{(t)}$ and $\omega^{(r)}$ are transformed. The local Lorentz transformation of the LNRF to the RFF$_\pm$ tetrad thus yields

$$\omega_\pm^{(t)} = \left\{ \gamma \frac{\Delta\Sigma}{A}, \mp\sqrt{\frac{\Sigma}{\Delta}} V, 0, 0 \right\} , \tag{98}$$

$$\omega_\pm^{(r)} = \left\{ \mp\gamma \sqrt{\frac{\Delta\Sigma}{A}} V, \sqrt{\frac{\Sigma}{\Delta}} \gamma, 0, 0 \right\} , \tag{99}$$

$$\omega_\pm^{(\theta)} = \{0, 0, \sqrt{\Sigma}, 0\} , \tag{100}$$

$$\omega_\pm^{(\varphi)} = \left\{ -\Omega_{\mathrm{LNRF}} \sqrt{\frac{A}{\Sigma}} \sin\theta, 0, 0, \sqrt{\frac{A}{\Sigma}} \sin\theta \right\} . \tag{101}$$

4.2 Escape cones

In the situations related to accretion phenomena and their optical appearance, it is a crucial problem to calculate what portion of radiation emitted by a source moving in the black hole vicinity could escape to infinity (and, complementary, what portion is trapped by the black hole). For each direction of emission in the local frame of the source, there is a corresponding pair of values of the impact parameters λ and $\mathcal{L}$ which can be related to the directional cosines of the photon trajectory in the local frame at the position of the source. Of course, the analysis of the turning points of the radial motion of photons presented in the previous section is crucial in determining the local escape cones.

Having defined the source frame, we can construct light escape cones assuming fixed coordinates of the source r_0, θ_0. Their construction proceeds according to the following steps:

- for given D, say $D = [\alpha_0, \beta_0]$, we calculate $\lambda = \lambda(\alpha_0, \beta_0)$;
- λ determines the behaviour of $\mathcal{L}_{\max} = \mathcal{L}_{\max}(r; \lambda)$;
- from the analysis presented in the previous section we calculate minimum of $\mathcal{L}_{\max}$, which reads $\mathcal{L}_{\max}^{\min} = \mathcal{L}_{\max}(r_{\min}; \lambda)$;
- we search for such a double D which satisfies equation $\mathcal{L}_0(\alpha_0, \beta_0) = \mathcal{L}_{\max}(r_{\min}; \lambda)$.

We present in detail the construction of light escape cones in a particular case, namely of the LNRF observers. The procedure is analogous for the other stationary observers.

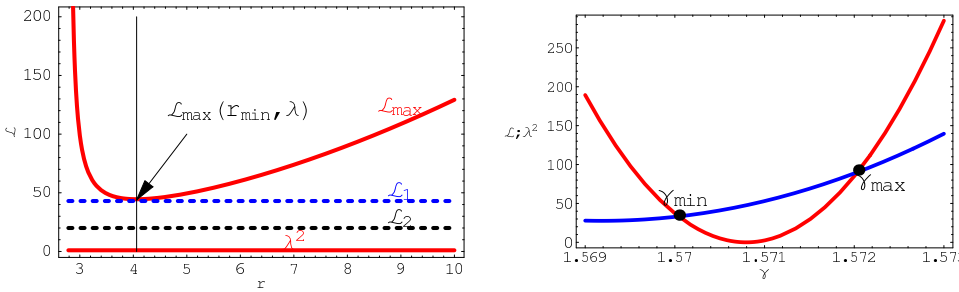

Figure 9. *Left:* The function $\mathcal{L}_{\max}$ and $\mathcal{L}_{\min} = \lambda_0^2$ are plotted together with representative constant functions $\mathcal{L}_1$ and $\mathcal{L}_2$ to demonstrate the construction of the photon escape cone. *Right:* The intersection of $\mathcal{L}_{\max}(\gamma_0)$ with $\lambda^2(\gamma_0)$ gives the interval of relevant values of $\gamma_0 \in [\gamma_{\min}; \gamma_{\max}]$.

One easily finds that impact parameter λ expressed in terms of the angle γ_0, related to the LNRF, reads

$$\lambda_0 = \frac{1}{\Omega_{\mathrm{LNRF0}} + \frac{\Sigma_0\sqrt{\Delta_0}}{A_0 \sin\theta_0 \cos\gamma_0}}\,, \tag{102}$$

where index '0' refers to the frame with coordinates $[r_0, \theta_0]$. The loci of minimum of $\mathcal{L}_{\max}$ is at

$$r_{\min} = \begin{cases} \sqrt{a\lambda - a^2} & \text{for } \lambda \geq \lambda_{\mathrm{G}} = a\,, \\ 1 - \frac{k_1}{k_2} + \frac{k_2}{3} & \text{for } \lambda < \lambda_{\mathrm{G}} = a\,, \end{cases} \tag{103}$$

where

$$k_1 = a^2 + 2b + a\lambda - 3\,, \tag{104}$$

$$k_2 = \left\{27(1 - a^2 - b) + 2\sqrt{3}\sqrt{27(1 - a^2 - b)^2 + k_1^3}\right\}^{1/3}\,. \tag{105}$$

The relevant values of $\mathcal{L}$ lie between $\mathcal{L}_{\max}$ and $\mathcal{L}_{\min}$ given by Eqs (58) and (59). The intersection of functions $\mathcal{L}_{\max} = \mathcal{L}_{\max}(\gamma_0)$ and $\mathcal{L}_{\min}(\gamma_0)$ gives the relevant interval of angles $\gamma \in [\gamma_{\min}, \gamma_{\max}]$ (see Fig. 9). For each γ from $[\gamma_{\min}, \gamma_{\max}]$ we calculate minimal value of the photon impact parameter $\mathcal{L}$, for which the photon reaches the turning point $r_{\min}$ and escapes to infinity. This minimal value is the minimum of $\mathcal{L}_{\max}$ which is located at $r_{\min}$, e.g., $\mathcal{L}_{\max} = \mathcal{L}_{\max}(r_{\min}; \lambda_0(\gamma_0), a, b)$, where $r_{\min}$ is given by (103). We now can calculate the value of α_0 using equation

$$\cos\alpha_0 = \frac{k^{(r)}}{k^{(t)}} = \frac{\omega^{(r)}_{\mathrm{LNRF}\,\mu} k^\mu}{\omega^{(t)}_{\mathrm{LNRF}\,\mu} k^\mu}\,. \tag{106}$$

We arrive to the formula

$$\cos\alpha_0 = \pm\sqrt{A_0}\,\frac{\sqrt{(r_0^2 + a^2 - a\lambda_0)^2 - \Delta_0(\mathcal{L}^{\min}_{\max} - 2a\lambda_0 + a^2)}}{-a(a\sin^2\theta_0 - \lambda_0)\Delta_0 + (r_0^2 + a^2)(r_0^2 + a^2 - a\lambda_0)}\,,$$

where $A_0 = A(r_0, \theta_0)$, $\Delta_0 = \Delta(r_0)$ and $\mathcal{L}^{\min}_{\max} = \mathcal{L}_{\max}(r_{\min}; \lambda_0, a, b)$. The angle β_0 can be calculated from the formula (77). In this way we obtain angles from the arc $\beta_0 \in \langle -\pi/2; \pi/2\rangle$. The remaining arc $\beta_0 \in \langle \pi/2; 3\pi/2\rangle$ can be obtained by turning the arc $\beta_0 \in \langle -\pi/2; \pi/2\rangle$ around the symmetry axis determined by angles $\beta_0 = -\pi/2$ and $\beta_0 = \pi/2$. This procedure can be done because photons released under angles β_0 and $\pi - \beta_0$ have the same constants of motion. Clearly, for sources under the radius corresponding to the corotating equatorial photon circular orbit, only outward directed photons with no turning point of the r-motion can escape. With radius of the source approaching the event horizon ($r_0 \to r_+$), the escape cone shrinks to infinitesimal extension, except the case of extreme black hole (see Bardeen, 1973). For the other frames considered here, the procedure of the related light escape cone construction can be directly repeated, but with the relevant tetrad 1-form components being used in the procedure. Some examples of behaviour of the escape cones in dependence of the brany parameter b are given in Fig. 10 for the LNRF and the geodetical frames. Clearly, for fixed rotation parameter a, the escape cone of the geodesic frames GF_+ becomes more symmetric relative to the outward radial direction with the negative brany parameter decreasing to the higher negative values.

Assuming astrophysically relevant sources in Keplerian accretion discs, their loci must be at orbits located above the marginally stable orbit r_{ms}, determined by the condition (Aliev and Gümrükçüoğlu, 2005; Stuchlík and Kotrlová, 2007)

$$a = a_{\mathrm{ms}}(r; b) \equiv \frac{4(r-b)^{3/2} \mp r\sqrt{3r^2 - 2r(1+2b) + 3b}}{3r - 4b}.$$

We demonstrate behaviour of the escape photon cones of the GF_+ illustrating the effects of the brany parameter in Fig. 11. We explicitly show the shift in the behaviour of the

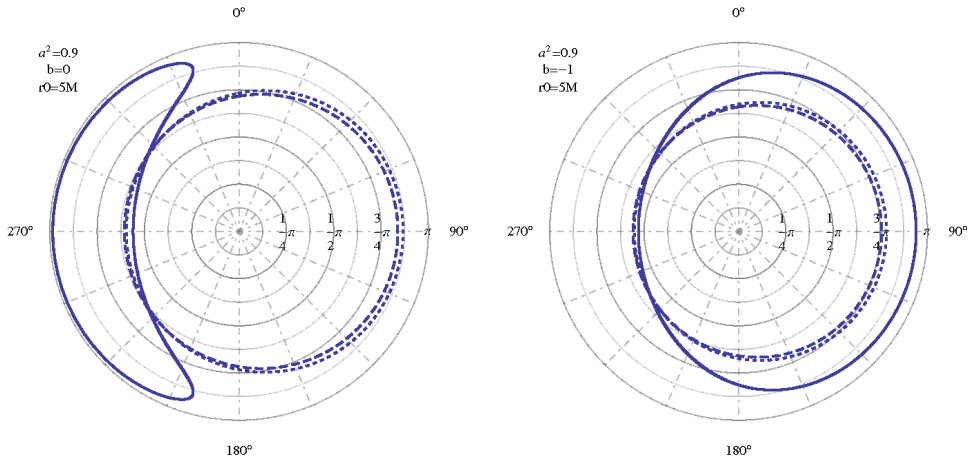

Figure 10. Two typical plots of the light escape cones for GF_+ (solid), LNRF (dashed) and SF (dot-dashed) sources in the equatorial plane of the black hole are given. The square of rotational parameter of the black hole is $a^2 = 0.9$ and the radial coordinate of the source is $r_0 = 5$ for both left and right images. The left image is plotted for brany parameter $b = 0$, while the right one is plotted for $b = -1$.

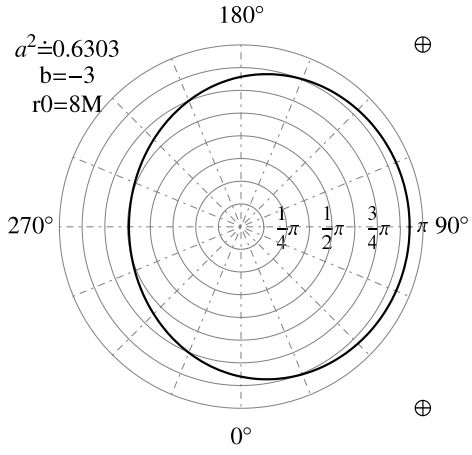

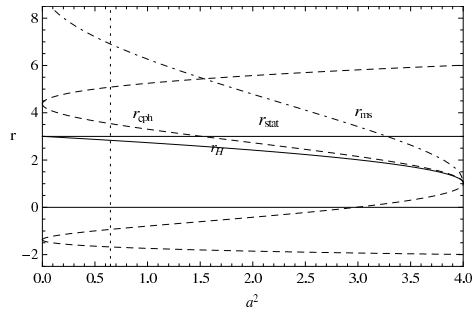

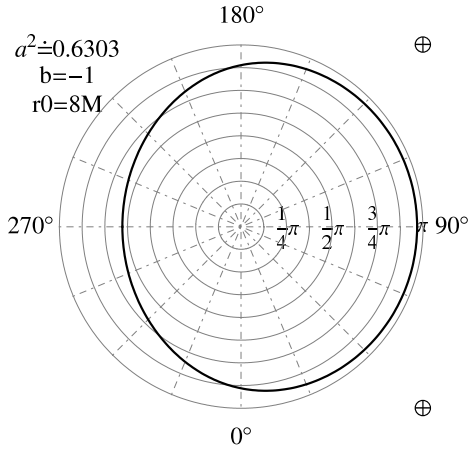

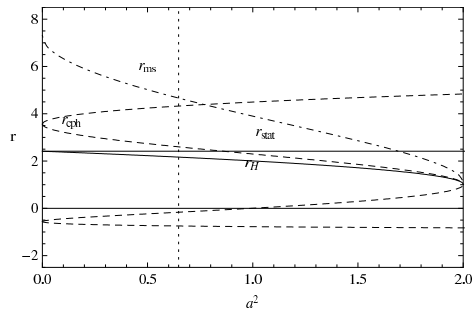

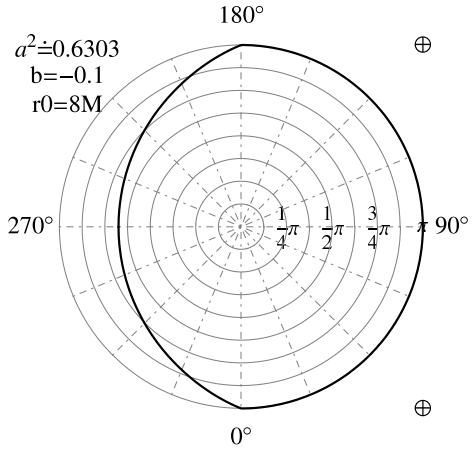

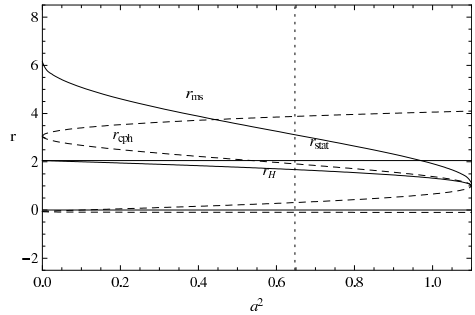

(continued on next page)

(continuation from previous page)

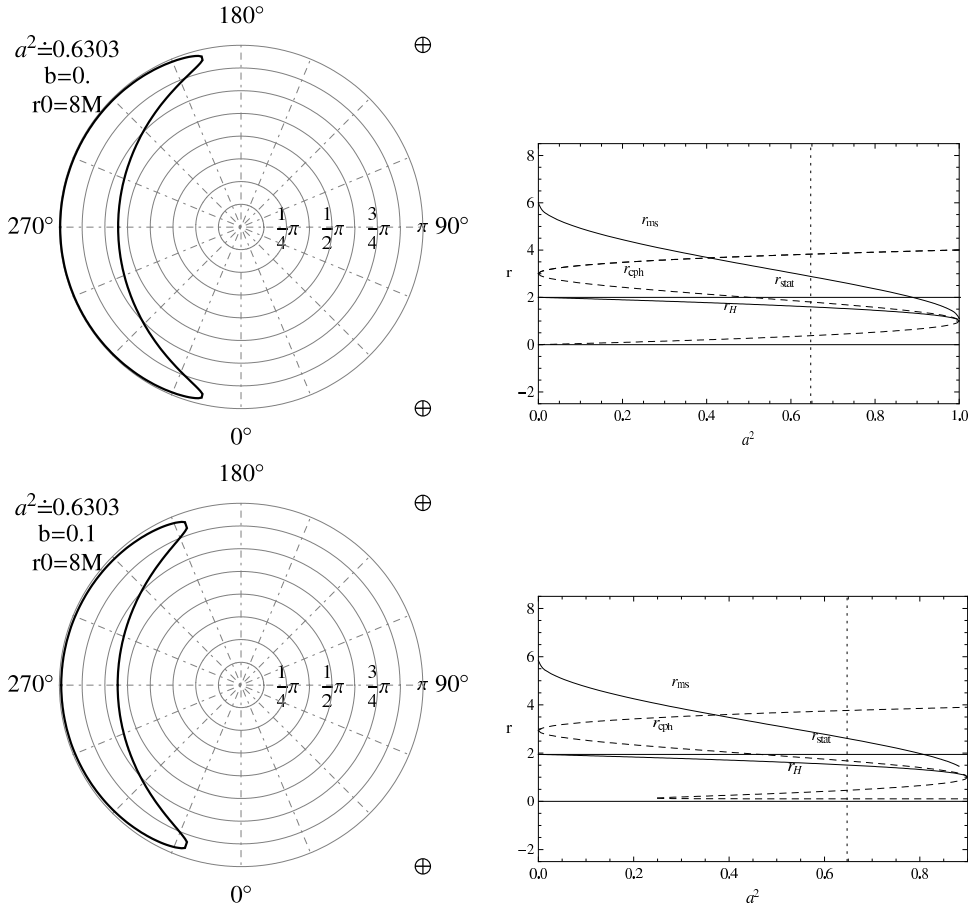

Figure 11. *Left*: The plots of light escape cones for the geodetical source following circular orbit at $r_0 = 8$ in the equatorial plane of brany Kerr black hole, plotted for the representative value of rotational parameter $a^2 = 0.6303$ and five representative values of brany parameter $b = -3, -1, -0.1, 0.0, 0.1$. The value of the rotational parameter a^2 was taken to demonstrate that for given brany parameter $b = -0.1$, the escaping emission angle $\alpha_0 = \pi$ represents the marginal value of α_0 for $\beta_0 = \pi/2$. For values $b \leq -0.1$ the photons that escape to infinity must be characterized by the angle doubles $[\alpha_0, \beta_0]$ located inside the area delimited by the bold curve, while for $b > -0.1$ the photons that escape to infinity must have the values of doubles $[\alpha_0, \beta_0]$ outside the area delimited by the bold curve. This particular marginal value of $b = -0.1$ holds for $a^2 = 0.6303$. *Right*: The plots of radii of circular photon orbits, $r_{\rm cph}$, marginally stable orbits of corotating observer, $r_{\rm ms}$, static radius in equatorial plane, $r_{\rm stat}$, and outer horizon of brany Kerr spacetime, $r_{\rm h}$, as functions of square of rotational parameter a^2 are constructed to show the position of the source relative to above mentioned radii, as their relations change substantially when b is changed for fixed a^2.

photon escape cone demonstrating explicitly the "conversion" case, when $\alpha_0 = \pi$ and $\beta_0 \in (0, \pi/2)$.

Clearly, at a fixed radius in spacetimes with fixed rotation parameter a^2, the rotational effects become stronger with growing of the brany parameter b, shifting the escape cone in the rotation direction.

5 SILHOUETTE OF A KERR BLACK HOLE IN BRANY UNIVERSE

In principle, it is of astrophysical importance to consider a black hole in front of a source of illumination whose angular size is large compared with the angular size of the black hole (Bardeen, 1973). A distant observer will see a silhouette of the black hole, i.e., a black hole in the larger bright source. The rim of the black hole silhouette corresponds to photon trajectories spiralling around the black hole many times before they reach the observer. Of course, the shape of the silhouette enables, in principle, determination of the black hole parameters. But we have to be aware of the strong dependence of the silhouette shape on the observer viewing angle; clearly the shape will be circular for observers on the black hole rotation axis, and its deformation grows with observer approaching the equatorial plane.

Assuming that distant observers measure photon directions relative to the symmetry centre of the gravitational field, the component of the angular displacement perpendicular to the symmetry axis is given by $-p^{(\varphi)}/p^{(t)}$ (for black hole rotating anticlockwise relative to distant observers), while for angular displacement parallel to the axis is given by $p^{(\theta)}/p^{(t)}$. These angles are proportional to $1/r_0$, therefore, it is convenient to use the impact parameters in the form independent of r_0 (Bardeen, 1973)

$$\tilde{\alpha} = -r_0 \frac{p^{(\varphi)}}{p^{(t)}} = -\frac{\lambda}{\sin\theta_0}\,, \tag{107}$$

and

$$\tilde{\beta} = r_0 \frac{p^{(\theta)}}{p^{(t)}} = \left(q + a^2\cos^2\theta_0 - \lambda^2\cot^2\theta_0\right)^{1/2} = \left(\mathcal{L} + a^2\cos^2\theta - \frac{\lambda^2}{\sin^2\theta_0}\right)^{1/2}. \tag{108}$$

Photon trajectories reaching the observer are represented by points in the $\tilde{\alpha}$-$\tilde{\beta}$ plane being a small portion of the celestial sphere of the observer.

The shape of the black hole silhouette is the boundary of the no-turning-point region, i.e., it is the curve $\mathcal{L} = \mathcal{L}_{\max}(\lambda)$ expressed in the $\tilde{\alpha}$-$\tilde{\beta}$ plane of impact parameters. For observers in the equatorial plane ($\theta_0 = \pi/2$), $\tilde{\alpha} = -\lambda$, $\tilde{\beta} = (\mathcal{L} - \lambda^2)^{1/2} = q^{1/2}$.

The marginal values of impact parameters λ_0 and $\mathcal{L}_0$ (q_0, respectively) are obtained from the light escape cone. Using the stationarity of the brany Kerr spacetime we "shoot out" virtual photons from observer (static frame at infinity or at very large distance r_0) and we are looking for the light escape cone of this virtual source (using the results of the previous section). The trapped light cone of this virtual source is constructed from the light escape cone of the virtual source by transformations of directional angle α_0 to $\bar{\alpha}_0 = \pi - \alpha_0$ and directional angle β_0 to $\bar{\beta}_0 = \beta_0$. In this way we get marginal directions for received photons from bright background behind the black hole. Then we can use the Eqs (79), (80) and (81)

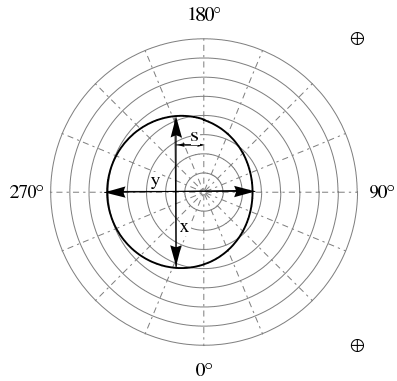

Figure 12. We define shift s and ellipticity $\epsilon = x/y$ parameters to evaluate the magnitude of distortion of Kerr black hole shadow shape in Brany universe.

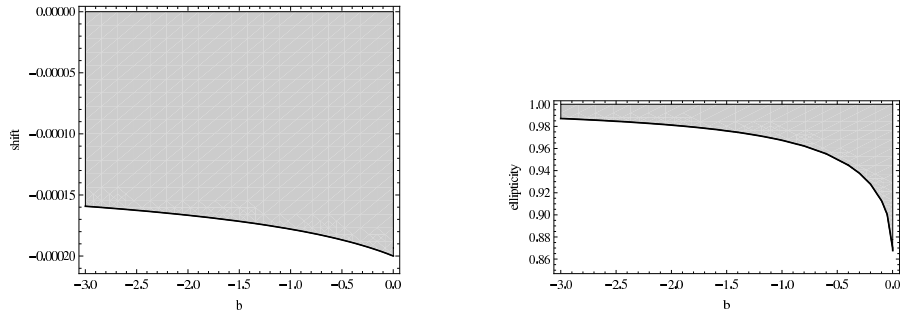

Figure 13. *Left:* the plot of $shift(b) = s(b; \theta_0 = 90°) - s(b; \theta_0 = 0°)$. *Right:* $ellipticity(b) = \epsilon(b; \theta_0 = 90°) - \epsilon(b; \theta_0 = 0°)$.

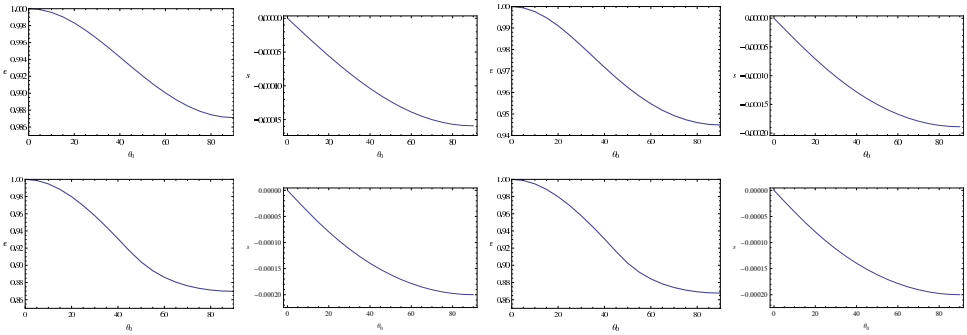

Figure 14. The plots are calculated for $r_0 = 10^4$ and $a^2 = 0.9995$. *Top figure (first and second):* the shift s as a function of θ_0 and the ellipticity ϵ as a function of θ_0 are plotted for $b = -3.0$. *Top figure(third and fourth):* the shift s as a function of θ_0 and the ellipticity ϵ as a function of θ_0 are plotted for $b = -0.4$. *Bottom figure(first and second):* the shift s as a function of θ_0 and the ellipticity ϵ as a function of θ_0 are plotted for $b = 0.0$. *Bottom figure(third and fourth):* the shift s as a function of θ_0 and the ellipticity ϵ as a function of θ_0 are plotted for $b = 0.0004$.

to calculate the marginal values of λ_0 and q_0 in order to obtain the silhouette of brany Kerr black hole in the plane $(\tilde{\alpha} - \tilde{\beta})$, i.e., the set of doubles $(\tilde{\alpha}_0, \tilde{\beta}_0)$ from Eqs (107) and (108). Here we plotted the silhouette directly from the trapped light cone $(\bar{\alpha}_0\,, \bar{\beta}_0)$ on the observer's sky $(\bar{\alpha}_0 \sin\bar{\beta}_0, \bar{\alpha}_0 \cos\bar{\beta}_0)$. Note that the angle $\bar{\alpha}_0$ is the radial coordinate and the angle $\bar{\beta}_0$ is the polar coordinate in the polar graph of the silhouette.

In order to characterize the influence of the tidal charge on the silhouette of a Kerr black hole we define *shift* s and *ellipticity* ϵ of the silhouette as quantities, in principle measurable

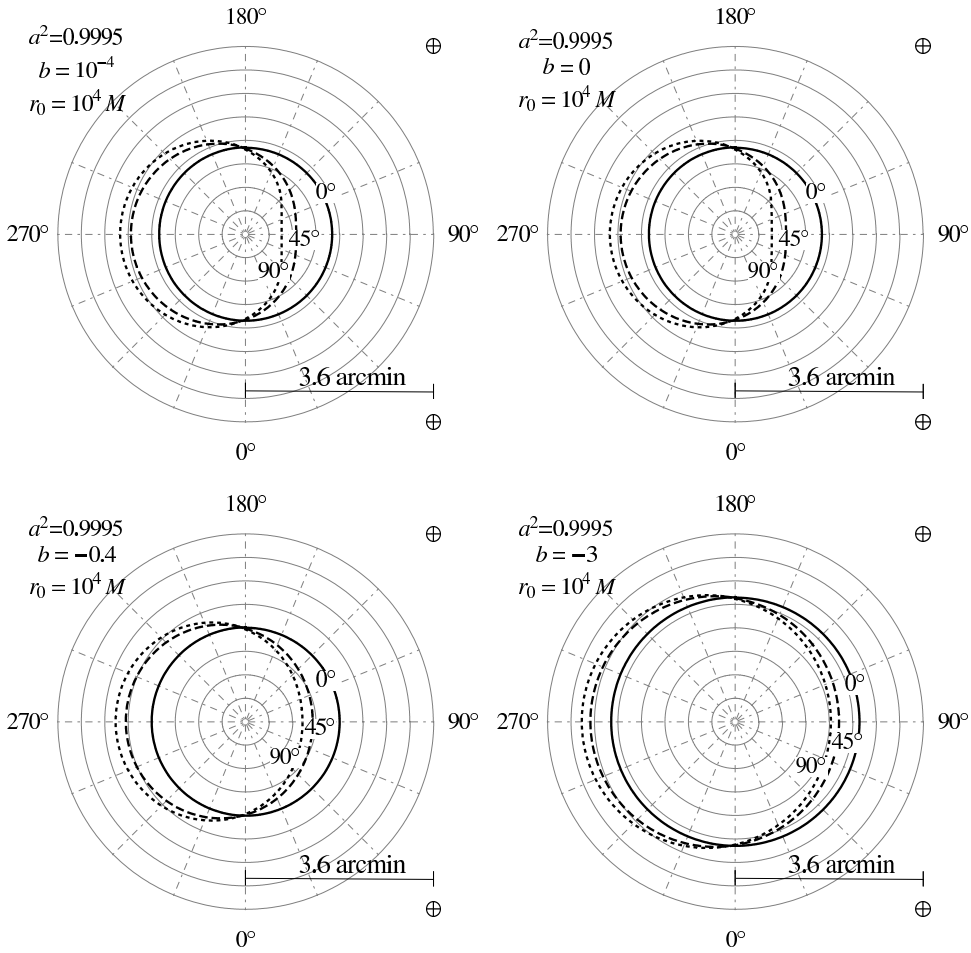

Figure 15. The silhouettes of rotating brany black hole on a bright background are plotted on four images on this figure. Each image contains three black hole shapes for three representative values of observer's inclination angle $\theta_0 = \{0°\text{(solid)}, 45°\text{(dashed)}, 90°\text{(dotted)}\}$, observer's radial coordinate $r_0 = 10^4$ and the rotational parameter $a^2 = 0.9995$. *Top left image:* $b = 0.0004$. *Top right image:* $b = 0.0$. *Bottom left image:* $b = -0.4$. *Bottom right image:* $b = -3.0$.

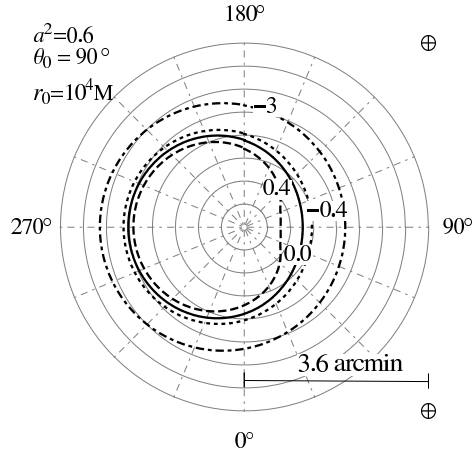

Figure 16. The $(\bar{\alpha}_0, \bar{\beta}_0)$ plots of silhouettes of brany Kerr black hole for rotational parameter $a^2 = 0.6$ and four representative values of tidal charge parameter $b = -3.0$, $b = -0.4$, $b = 0.0$ and $b = 0.4$. The observer is located at $r_0 = 10^4$ and $\theta_0 = 90°$.

by distant observers, in the form

$$s = \tilde{\alpha}(\beta_m)\sin(\beta_m - \pi)\,, \tag{109}$$

$$\epsilon = \frac{\tilde{\alpha}(\beta = 90°) + \tilde{\alpha}(\beta = 270°)}{2\tilde{\alpha}(\beta_m)\cos(\beta_m - \pi)}\,, \tag{110}$$

where β_m is defined by $\tilde{\alpha}(\beta_m)\sin(\beta_m - \pi) \geq \tilde{\alpha}(\beta)\sin(\beta - \pi)\ \forall\beta \in [\pi/2, 3/2\pi]$. In Fig. 12 the definition of *shift* s and *ellipticity* ϵ is depicted.

We calculated shift s and ellipticity ϵ as functions of tidal parameter b for the Kerr black hole with rotational parameter $a^2 = 0.9995$ see Fig. 13. The dependence on the viewing angle θ_0 is given in Figs 14 (top) and 14 (bottom).

The silhouettes of the Kerr black hole are plotted for three representative values of observer's inclination $\theta_0 = 0°$, 45° and 90° and four representative values of tidal parameter $b = -3, -0.4, 0.0$ with fixed $a^2 = 0.9995$ in Fig. 15. The rotational effect on the shape of the silhouette become strongest when viewed in the equatorial plane ($\theta_0 = \pi/2$), then the suppressing effect of the brany parameter is given in the most explicit form as demonstrated in Fig. 16.

The negative values of the brany parameter have the tendency to make the silhouette of a Kerr black hole (with a^2 fixed and for r_0, θ_0 fixed) spherical, suppressing thus the rotational effects.

6 DIRECT AND INDIRECT IMAGES OF ISORADIAL GEODESICS

The modelling of idealised situations like spectral line profiles of the thin bright rotating ring in the equatorial plane of brany Kerr black hole or light curve of the isotropically emitting

point source orbiting the brany Kerr black hole in the equatorial plane will give us information about the influence of the brany parameter b on such phenomena and subsequently the estimates of the influence of Kerr brany parameter in general astrophysically situations. We can then, at least in principle, obtain estimates on the astrophysical acceptable value of the brany parameter b.

Calculating images of the thin rotating ring in the equatorial plane of brany Kerr black hole is the first step to calculate mentioned optical phenomena. Generally one could obtain a direct and an indirect image (see Figs 17 and 18), but in special cases the situation could be much more complicated due to complicated latitudinal and azimuthal photon motion. Here we focus our attention to the direct and indirect images of isoradial geodesics.

In order to find all relevant positions of points forming the rotating ring on observer's sky, we have to find photon trajectories between the ring particles and the observer, i.e., we seek for such doubles of local observational angles $[\alpha_0, \beta_0]$ that satisfy the condition

$$I_{\mathrm{U}}(\alpha_0, \beta_0; n_u, u_{\mathrm{sgn}}) - I_{\mathrm{M}}(\alpha_0, \beta_0; n, p, s) = 0\,. \tag{111}$$

Here we introduced the modified radial coordinate $u = 1/r$ and cosine of latitudinal coordinate $\mu = \cos\theta$ (Rauch and Blandford, 1994). In the Eq. (111) n_u is the number of turning points in u coordinate, n is the number of turning points passed in μ coordinate, $p = \mathrm{mod}(n, 2)$, $s = (1 - \mu_{\mathrm{sgn}})/2$. In terms of u and μ we defined the functions I_{U} and I_{M} by

$$I_{\mathrm{U}}(\alpha_0, \beta_0; n_u, u_{\mathrm{sgn}}) \equiv \begin{cases} -u_{\mathrm{sgn}} \left(\int_{u_t}^{u_0} + \int_{u_t}^{u_e} \right) & \text{for } n_u = 1\,, \\ u_{\mathrm{sgn}} \int_{u_0}^{u_e} & \text{for } n_u = 0\,, \end{cases} \tag{112}$$

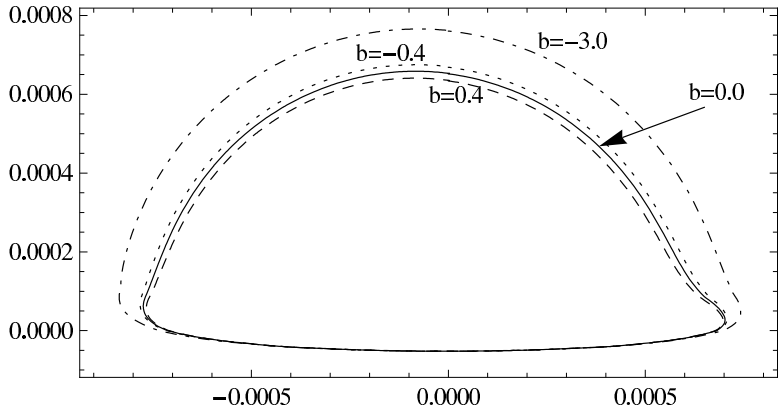

Figure 17. Four plots of *direct* image of the rotating ring in the equatorial plane at $r_{\mathrm{e}} = 6$ around brany Kerr black hole with rotational parameter $a^2 = 0.5$ for four representative values of tidal charge parameter $b = -3.0$, $b = -0.4$, $b = 0.0$ and $b = 0.4$. The observer is located at $r_0 = 10^4$ and $\theta_0 = 85°$.

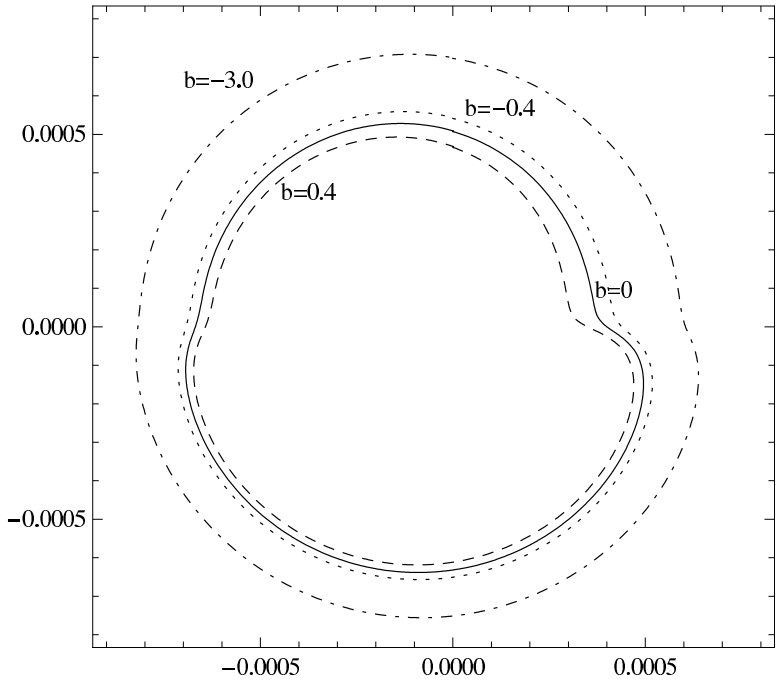

Figure 18. Four plots of *indirect* image of the rotating ring in the equatorial plane at $r_e = 6$ around brany Kerr black hole with rotational parameter $a^2 = 0.5$ for four representative values of tidal charge parameter $b = -3.0$, $b = -0.4$, $b = 0.0$ and $b = 0.4$. The observer is located at $r_0 = 10^4$ and $\theta_0 = 85°$.

and

$$I_M(\alpha_0, \beta_0; n, p, s) \equiv \mu_{\rm sgn}\left[\int_{\mu_0}^{\mu_+} + (-1)^{n+1}\int_{\mu_e}^{\mu_+} + \right.$$
$$\left. + (-1)^s[(1-p)n + p[(1-s)(n-1) + s(n+1)]]\int_{\mu_-}^{\mu_+}\right] \quad (113)$$

with

$$\int_{u_1}^{u_2} \equiv \int_{u_1}^{u_2} \frac{{\rm d}u}{\sqrt{U(u)}}\,, \quad (114)$$

$$U(u) = 1 + (a^2 - \lambda^2 - q)u^2 + 2[(\lambda^2 - a^2)^2 + q]u^3 - [q(a^2 + b) + b(a - l)^2]u^4 \quad (115)$$

and

$$\int_{\mu_1}^{\mu_2} \equiv \int_{\mu_1}^{\mu_2} \frac{{\rm d}\mu}{\sqrt{M(\mu)}}\,, \quad (116)$$

$$M(\mu) = q + (a^2 - l^2 - q)\mu^2 - a^2\mu^4\,. \quad (117)$$

6.1 Integration of photon trajectories

We express the integrals Eqs (114) and (116) in the form of the standard elliptic integrals of the first kind. Rauch and Blandford presented the tables of reductions of u-integrals and μ-integrals for the case of photons in Kerr geometry (Rauch and Blandford, 1994). Here we extended those reductions for the case of nonzero brany parameter b. Because the integration of the μ-integral does not depend on brany parameter b, the transformations are the same as in the case of Kerr metric (see Rauch and Blandford, 1994), we present here only tables of transformations of u-integral.

For distant observers we distinguish five relevant cases of the radial integral. These cases depend on the character of roots of the quartic equation $U(u) = 0$, i.e., on the number of turning points ($n_u = 0$ or $n_u = 1$) in the radial motion and the value of parameter $\tilde{q} = q(a^2 + b) + b(a - l)^2$. We have arranged those transformations into Table 1.

Denoting roots of the quartic equation $U(u) = 0$ by β_1, β_2, β_3 and β_4, the meaning of each of the five cases is the following:

The case I: four distinct real roots of $U(u) = 0$ forming the sequence $\beta_1 > \beta_2 > \beta_2 > 0$ and $\beta_4 < 0$. The value of modified constant of motion $\tilde{q} > 0$.

The case II: four real roots as in the case I but their values form the following order: $\beta_1 > \beta_2 > 0$ and $\beta_4 < \beta_3 < 0$. The value of modified constant of motion $\tilde{q} < 0$.

The case III: two real and two complex roots of $U(u) = 0$: β_1 being a complex root, $\beta_2 = \bar{\beta_1}$ and $\beta_4 < \beta_3 < 0$. The value of modified constant of motion $\tilde{q} < 0$.

The case IV: only complex roots: $\beta_2 = \bar{\beta_1}$ and $\beta_4 = \bar{\beta_3}$. The value of modified constant of motion $\tilde{q} < 0$.

The case V: two real and two complex roots of $U(u) = 0$: $\beta_1 > 0$, $\beta_4 < 0$, β_2 being a complex root and $\beta_3 = \bar{\beta_2}$.

Table 1. The reductions of $\int_{u_1}^{u} \mathrm{d}u'/\sqrt{U(u')} = I_{\mathrm{U}}$. (Kindly refer to Tables 2 and 3 on next page for definitions.)

Case	$\tan\Psi$	m	c_1	u_1
I	$\sqrt{\frac{(\beta_1-\beta_3)(u-\beta_4)}{(\beta_1-\beta_4)(\beta_3-u)}}$	$\frac{(\beta_1-\beta_2)(\beta_3-\beta_4)}{(\beta_1-\beta_3)(\beta_2-\beta_4)}$	$\frac{2}{\sqrt{\tilde{q}(b1-b3)(b2-b4)}}$	β_4
II	$\sqrt{\frac{(\beta_1-\beta_2)(u-\beta_3)}{(\beta_1-\beta_3)(\beta_2-u)}}$	$\frac{(\beta_2-\beta_3)(\beta_1-\beta_4)}{(\beta_1-\beta_2)(\beta_4-\beta_3)}$	$\frac{2}{\sqrt{-\tilde{q}(b1-b2)(b3-b4)]}}$	β_3
III	$\frac{2c_2(u)}{\lvert 1-c_2^2(u)\rvert}$	$\frac{4c_4c_5-(\beta_3-\beta_4)^2-c_4c_5}{4c_4c_5}$	$\frac{1}{\sqrt{-\tilde{q}c_4c_5}}$	β_3
IV	$\frac{u-c_3}{\Im(\beta_1)(1+c_2^2)+c_2(u-c_3)}$	$1-\left(\frac{c_4-c_5}{c_4+c_5}\right)^2$	$\frac{2}{(c_4+c_5)\sqrt{-\tilde{q}}}$	c_3
V	$\frac{2c_2(u)}{\lvert 1-c_2^2(u)\rvert}$	$1-\frac{(c_4+c_5)^2-(\beta_1-\beta_4)^2}{4c_4c_5}$	$\frac{1}{\sqrt{\tilde{q}c_4c_5}}$	β_4

Table 2. Definitions for Table 1.

Case	c_2	c_3
III	$\left[\frac{c5(u-\beta_3)}{c_4(u-\beta_4)}\right]^{1/2}$	–
IV	$\left\{\frac{4[\Im(\beta_1)]^2-(c_4-c_5)^2}{(c_4+c_5)^2-4[\Im(\beta_1)]^2}\right\}^{1/2}$	$\Re(\beta_1)+c_2\Im(\beta_1)$
V	$\left[\frac{c4(u-\beta_4)}{c_5(\beta_1-u)}\right]^{1/2}$	–

Table 3. Definitions for Tables 1 and 2.

Case	c_4	c_5
III	$\{[\Re(\beta_1)-\beta_3]^2+[\Im(\beta_1)]^2\}^{1/2}$	$\{[\Re(\beta_1)-\beta_4]^2+[\Im(\beta_1)]^2\}^{1/2}$
IV	$\{[\Re(\beta_1)-\Re(\beta_3)]^2+[\Im(\beta_1)+\Im(\beta_3)]^2\}^{1/2}$	$\{[\Re(\beta_1)-\Re(\beta_3)]^2+[\Im(\beta_1)-\Im(\beta_3)]^2\}^{1/2}$
V	$\{[\Re(\beta_2)-\beta_1]^2+[\Im(\beta_2)]^2\}^{1/2}$	$\{[\Re(\beta_2)-\beta_4]^2+[\Im(\beta_2)]^2\}^{1/2}$

Using presented transformations we can write the integral Eq. (114) in the form

$$\int_{u_1}^{u}\frac{1}{\sqrt{U(\tilde{u})}}\,\mathrm{d}\tilde{u}=c_1\mathcal{F}(\Psi;m)\,, \tag{118}$$

where $\mathcal{F}$ is the elliptic integral of the first kind and u_1 depends on the case of root distribution of quartic equation $U(u)=0$ as given in Table 1. If, in the cases III and V, the value of $1-c_2^2(u)<0$, we have to take instead of Eq. (118) the form

$$\int_{u_1}^{u}\frac{1}{\sqrt{U(\tilde{u})}}\,\mathrm{d}\tilde{u}=c_1(2\mathcal{K}(m)-\mathcal{F}(\Psi;m))\,, \tag{119}$$

where $\mathcal{K}$ is the complete elliptic integral of the first type. We consider two basic possibilities of trajectories, namely those corresponding to direct and indirect images (Figs 19 and 20).

6.2 Calculated images

It is useful to demonstrate the influence of the brany parameter on the shape of images of rings in the equatorial plane representing parts of Keplerian accretion discs. Of course, as well known from the Kerr (and even Schwarzschild) black holes, the images strongly depend on the latitude of the observer.

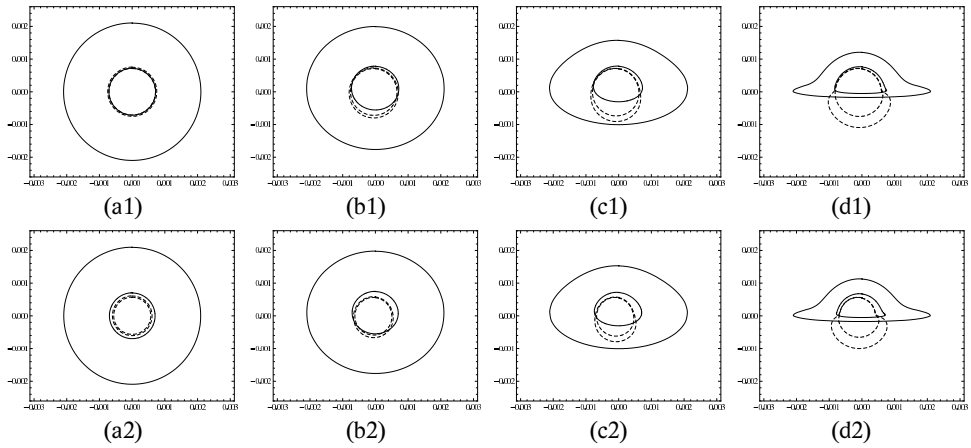

Figure 19. Two rings with radii $r_{\rm in} = 6$ and $r_{\rm out} = 20$ projected into observer's sky at $r_0 = 10^4$ are plotted on this figure for rotational parameter $a^2 = 0.5$ and representative values of tidal charge $b = -3$ (top plots), -0.4 (bottom plots) and observer's inclination $\theta_0 = 0°$, $30°$, $60°$ and $85°$ (plots from left to right). Direct (indirect) images are plotted with full (dashed) curves.

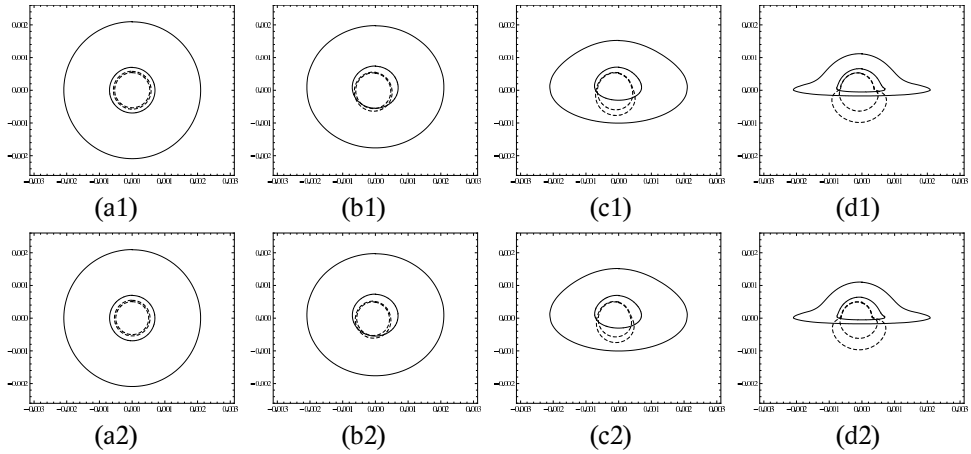

Figure 20. Two rings with radii $r_{\rm in} = 6$ and $r_{\rm out} = 20$ projected into observer's sky at $r_0 = 10^4$ are plotted on this figure for rotational parameter $a^2 = 0.5$ and representative values of tidal charge $b = 0.0$ (top plots), 0.4 (bottom plots) and observer's inclination $\theta_0 = 0°$, $30°$, $60°$ and $85°$ (plots from left to right).

We calculated the direct and indirect images of the flat disk in the equatorial plane around Kerr black hole with rotational parameter $a^2 = 0.5$ for four representative values of LNRF observer's inclination $\theta_0 = 0°$, $30°$, $60°$ and $85°$ and for four representative values of tidal parameter $b = -3.0, -0.4, 0.0$ and 0.4. The images are depicted in Figs 19 and 20.

7 CONCLUSIONS

One of the most promising ways of estimating influence of hypothetical hidden external dimensions, considered in the framework of the braneworld model with infinite external dimension, as developed by Randall and Sundrum (1999), seems to be investigation of the optical phenomena caused by the black hole backgrounds. It is because black holes represent the only case when the non-local influence of the bulk space on the brany space-time structure can be fully described by a single, brany parameter called tidal charge, with assumed negative value (Aliev and Gümrükçüoğlu, 2005; Dadhich et al., 2000).

Here we have shown how the brany tidal charge can effect the basic optical phenomena, especially the black-hole silhouette and the accretion disc shape. Generally, the rising negative value of the tidal charge leads to strengthening of the black hole field and suppressing of the rotational phenomena for the black-hole rotation parameter fixed. The black-hole silhouette is characterized by two parameters, shift of the centre and ellipticity, that could be in principle measurable in the Galactic Center black-hole system Sgr A*, after expected development of observational techniques.

Similarly, we can expect measurable phenomena due to spectral line profiles (Schee and Stuchlík, 2007)]. The optical tests have to be confronted with the data obtained from quasiperiodic oscillations observed in some special black-hole systems, namely microquasars (Remillard and McClintock, 2006)). The most promising orbital resonance model gives good estimates of the black-hole parameters (Török et al., 2005; Török, 2005a,b); this model has been recently generalized to the case of brany Kerr black holes (Stuchlík and Kotrlová, 2007), and it is shown that in the case of microquasar GRS 1915+105 and Galactic Center Sgr A* the negative brany parameters are allowed by the observational data.

We can also expect interesting relations of the optical phenomena in the field of neutron stars and the quasiperiodic oscillations observed in neutron-star binary systems, as discussed, e.g., in the case of 4U 1636+53 source (Török, 2007; Török et al., 2007).

ACKNOWLEDGEMENTS

This research was supported by the Czech grants MSM 4781305903, LC06014 and GAČR 202/06/0041. One of the authors (Z. S.) would like to express his gratitude to the Czech Committee for Collaboration with CERN for support.

REFERENCES

Aliev, A. N. and Gümrükçüoğlu, A. E. (2005), Charged Rotating Black Holes on a 3-Brane, *Phys. Rev. D*, **71**(10), p. 104027, arXiv: `hep-th/0502223v2`.

Arkani-Hamed, N., Dimopoulos, S. and Dvali, G. (1998), The Hierarchy Problem and New Dimensions at a Millimeter, *Phys. Lett. B*, **429**, pp. 263–272, arXiv: `hep-ph/9803315`.

Aschenbach, B. (2004), Measuring mass and angular momentum of black holes with high-frequency quasi-periodic oscillations, *Astronomy and Astrophysics*, **425**, pp. 1075–1082, arXiv: `astro-ph/0406545`.

Aschenbach, B. (2007), Measurement of Mass and Spin of Black Holes with QPOs, *Chinese Astronom. Astrophys.*, accepted for publication, arXiv: `0710.3454`.

Bao, G. and Stuchlík, Z. (1992), Accretion disk self-eclipse – X-ray light curve and emission line, *Astrophys. J.*, **400**, pp. 163–169.

Bardeen, J. M. (1973), Timelike and Null Geodesics in the Kerr Metric, in C. D. Witt and B. S. D. Witt, editors, *Black Holes*, p. 215, Gordon and Breach, New York–London–Paris.

Bardeen, J. M., Press, W. H. and Teukolsky, S. A. (1972), Rotating black holes: locally nonrotating frames, energy extraction, and scalar synchrotron radiation, *Astrophys. J.*, **178**, pp. 347–369.

Bičák, J. and Stuchlík, Z. (1976), On the Latitudinal and Radial Motion in the Field of a Rotating Black Hole, *Bull. Astronom. Inst. Czechoslovakia*, **27**(3), pp. 129–133.

Chamblin, A., Reall, H. S., Shinkai, H. and Shiromizu, T. (2001), Charged Brane-World Black Holes, *Phys. Rev. D*, **63**(6), p. 064015, arXiv: `hep-th/0008177`.

Cunningham, C. T. and Bardeen, J. M. (1973), The Optical Appearance of a star orbiting an extreme Kerr black hole, *Astrophys. J.*, **183**, pp. 237–264.

Dadhich, N., Maartens, R., Papadopoulos, P. and Rezania, V. (2000), Black holes on the brane, *Phys. Rev. B*, **487**, arXiv: `hep-th/0003061v3`.

Emparan, R., Masip, M. and Rattazzi, R. (2002), Cosmic Rays as Probes of Large Extra Dimensions and TeV Gravity, *Phys. Rev. D*, **65**, p. 064023, arXiv: `hep-ph/0109287`.

Germani, C. and Maartens, R. (2001), Stars in the braneworld, *Phys. Rev. D*, **64**, p. 124010, arXiv: `hep-th/0107011`.

Ghez, A. M. (2005), Stellar Orbits and the Supermassive Black Hole at the Center of Our Galaxy, *Bull. Amer. Astronom. Soc.*, **37**, p. 531.

Karas, V., Vokrouhlický, D. and Polnarev, A. G. (1992), In the vicinity of a rotating black hole – A fast numerical code for computing observational effects, *Monthly Notices Roy. Astronom. Soc.*, **259**, pp. 569–575.

Kerr, R. P. (1963), Gravitational Field of a Spinning Mass as an Example of Algebraically Special Metrics, *Phys. Rev. Lett.*, **11**, p. 237.

Laor, A. (1991), Line profiles from a disk around a rotating black hole, *Astrophys. J.*, **376**, pp. 90–94.

Maartens, R. (2004), Brane-world gravity, *Living Rev. Rel.*, **7**, arXiv: `gr-qc/0312059v2`.

Matt, G., Fabian, A. C. and Ross, R. R. (1993), Iron K_α lines from X-ray photoionized accretion discs, *Monthly Notices Roy. Astronom. Soc.*, **262**(1), pp. 179–186.

McClintock, J. E., Narayan, R. and Shafee, R. (2007), Estimating the Spins of Stellar-Mass Black Holes, in M. Livio and A. Koekemoer, editors, *Black Holes*, volume 707, Cambridge University Press, Cambridge, in press, to appear in 2008, arXiv: `0707.4492v1`.

Misner, C. W., Thorne, K. S. and Wheeler, J. A. (1973), *Gravitation*, W. H. Freeman and Co, New York, San Francisco.

Narayan, R., McClintock, J. E. and Shafee, R. (2007), Estimating the Spins of Stellar-Mass Black Holes by Fitting Their Continuum Spectra, in Y. F. Yuan, X. D. Li and D. Lai, editors, *Astrophysics of Compact Objects*, AIP, to appear, arXiv: `0710.4073v1`.

Randall, L. and Sundrum, R. (1999), An Alternative to Compactification, *Phys. Rev. D*, **83**(2), pp. 4690–4693, arXiv: `hep-th/9906064`.

Rauch, K. P. and Blandford, R. D. (1994), Optical caustics in a Kerr space-time and the origin of rapid X-ray variability in active galactic nuclei, *Astrophys. J.*, **421**, p. 46.

Remillard, R. A. and McClintock, J. E. (2006), X-Ray Properties of Black-Hole Binaries, *Annual Review of Astronomy and Astrophysics*, **44**(1), pp. 49–92, arXiv: `astro-ph/0606352`.

Schee, J. and Stuchlík, Z. (2007), Spectral line profile of radiating ring orbiting a brany Kerr black hole, pp. 209–220, this volume.

Schee, J., Stuchlík, Z. and Juráň, J. (2005), Light escape cones and raytracing in Kerr geometry, in S. Hledík and Z. Stuchlík, editors, *Proceedings of RAGtime 6/7: Workshops on black holes and neutron stars, Opava, 16–18/18–20 September 2004/2005*, pp. 143–155, Silesian University in Opava, Opava, ISBN 80-7248-334-X.

Shiromizu, T., Maeda, K. and Sasaki, M. (1999), The Einstein Equations on the 3-Brane World, *Phys. Rev. D*, **62**, p. 024012, arXiv: `gr-qc/9910076`.

Strohmayer, T. E., Mushotzky, R. F., Winter, L., Soria, R., Uttley, P. and Cropper, M. (2007), Quasi-Periodic Variability in NGC 5408 X-1, *Astrophys. J.*, **660**, pp. 580–586, arXiv: `astro-ph/0701390`.

Stuchlík, Z. (1981a), Evolution of Kerr naked singularities, *Bull. Astronom. Inst. Czechoslovakia*, **32**(2), pp. 68–72.

Stuchlík, Z. (1981b), Null geodesics in the Kerr–Newman metric, *Bull. Astronom. Inst. Czechoslovakia*, **32**(6).

Stuchlík, Z. and Bao, G. (1992), Radiation from hot spots orbiting an extreme Reissner–Nordström black hole, *Gen. Relativity Gravitation*, **24**(9), pp. 945–957.

Stuchlík, Z., Bičák, J. and Balek, V. (1999), The shell of incoherent charged matter falling onto a charged rotating black hole, *Gen. Relativity Gravitation*, **31**(1), pp. 53–71, ISSN 0001-7701.

Stuchlík, Z. and Kotrlová, A. (2007), Orbital resonance model of QPOs in braneworld Kerr black hole spacetimes, pp. 323–361, this volume.

Török, G. (2005a), A possible 3 : 2 orbital epicyclic resonance in QPO frequencies of Sgr A*, *Astronomy and Astrophysics*, **440**(1), pp. 1–4, arXiv: `astro-ph/0412500`.

Török, G. (2005b), QPOs in microquasars and Sgr A*: measuring the black hole spin, *Astronom. Nachr.*, **326**(9), pp. 856–860, arXiv: `astro-ph/0510669`.

Török, G. (2007), Reverse of twin peak QPO amplitude relationship in six atoll sources.

Török, G., Abramowicz, M. A., Kluźniak, W. and Stuchlík, Z. (2005), The orbital resonance model for twin peak kHz quasi periodic oscillations in microquasars, *Astronomy and Astrophysics*, **436**(1), pp. 1–8, arXiv: `astro-ph/0401464`.

Török, G., Stuchlík, Z. and Čermák, P. (2007), Reverse of twin peak kHz QPO inter relationship in the six atoll sources, pp. 511–522, this volume.

Proceedings of *RAGtime 8/9, 15–19/19–21 September, 2006/2007, Hradec nad Moravicí, Opava, Czech Republic*
S. Hledík and Z. Stuchlík, editors, Silesian University in Opava, 2007, pp. 257–265

Extended orbital resonance model applied to QPOs observed in three near-extreme Kerr black hole candidate systems

Petr Slaný[a] and Zdeněk Stuchlík[b]

Institute of Physics, Faculty of Philosophy & Science, Silesian University in Opava,
Bezručovo nám. 13, CZ-746 01 Opava, Czech Republic
[a]petr.slany@fpf.slu.cz
[b]zdenek.stuchlik@fpf.slu.cz

ABSTRACT
The "Extended Orbital Resonance Model," i.e., the idea of oscillations induced by the hump of the orbital velocity profile (related to the locally non-rotating frames – LNRF), which are proposed to excite the oscillations of Keplerian discs around near-extreme Kerr black holes with epicyclic frequencies, is used to estimate the mass and spin of three near-extreme Kerr black hole candidates GRS 1915+105, XTE J1650−500, and NGC 5408 X-1. The hump-induced oscillations are characterized by the so-called "humpy frequency," and a non-linear resonant coupling between these and epicyclic oscillations is expected. It it shown that the quasiperiodic variability (QPOs) observed in these sources can be matched with the proposals of the model, giving for the mass and spin of their black holes values consistent with the other observationally-established estimates.

Keywords: Black hole physics – relativity – accretion, accretion discs – X-rays: individual: GRS 1915+105, XTE J1650−500, NGC 5408 X-1

1 INTRODUCTION

The main goal is to show that perhaps in three black-hole candidates GRS 1915+105, NGC 5408 X-1, and XTE J1650−500 the observed quasi-periodic variability in their X-ray spectra could indicate the presence of so-called "Aschenbach effect" in their accretion discs, i.e., the discs in which a region with positive radial gradient of the LNRF-related orbital velocity exists, which further can be used to give the estimates on the mass and spin of the central Kerr black holes in the framework of so-called "Extended Orbital Resonance Model".

Detailed analysis of the X-ray variable Galactic binary system GRS 1915+105 reveals at least five high-frequency QPOs with centroid frequencies $\nu_1 = 27$ Hz (Belloni et al., 2001), $\nu_2 = 41$ Hz, $\nu_3 = 67$ Hz (Morgan et al., 1997; Strohmayer, 2001), $\nu_4 = 113$ Hz,

978-80-7248-419-5

$\nu_5 = 167\,\mathrm{Hz}$ (Remillard, 2004).[1] Moreover, careful and detailed analysis of the spectral continuum from GRS 1915+105 indicates the presence of a near-extreme Kerr black hole (McClintock et al., 2006) in the system. The black-hole mass has been restricted observationally to $M = (14.0 \pm 4.4)\,\mathrm{M}_\odot$ (see McClintock and Remillard, 2004; Remillard and McClintock, 2006).

The X-ray transient Galactic binary black hole XTE J1650−500 seems to reveal just one high-frequency QPO at 250 Hz, even if some other high-frequency features were also reported (Homan et al., 2003). Moreover, the broad, skewed Fe K_α line profile, being found by Miller et al. (2002) in the *XMM-Newton*/EPIC-pn spectrum from the XTE J1650−500, suggests that this source hosts a stellar-mass near-extreme Kerr BH in its centre. The R-band photometry enables to determine the optical mass-function, $f(M) = (2.73 \pm 0.56)\,\mathrm{M}_\odot$, and a lower limit to the inclination of the system of 50°, which both give an upper limit to the mass of the black hole in XTE J1650−500 of $M_{\mathrm{BH}} \lesssim 7.3\,\mathrm{M}_\odot$ (Orosz et al., 2004).

Recently, more than one quasi-periodic oscillation (QPO) have been found in the *XMM-Newton*/EPIC observations of the extra-Galactic ultra-luminous X-ray (ULX) source NGC 5408 X-1 (Strohmayer et al., 2007). The best evidence is for a 20 mHz QPO, but during the period when the 20 mHz QPO is the strongest, the 15 mHz QPO is also very strong, suggesting a possibility of resonance in the frequency ratio 4 : 3. Moreover, there is some evidence for the 3rd Lorentzian component at 27 mHz during the same period. Strohmayer et al. (2007) also gave some estimations on the mass of the central black hole. Comparing the timing and spectral properties of NGC 5408 X-1 with those of Galactic black hole systems revealing qualitatively similar behaviour, they inferred the BH mass of several $1000\,\mathrm{M}_\odot$, suggesting the presence of an intermediate-mass black hole (IMBH) in the system, even if some indications for a lower mass closer to $100\,\mathrm{M}_\odot$ are also discussed.

Accreting IMBHs with typical masses $(10^2$–$10^5)\,\mathrm{M}_\odot$, capable to explain inferred isotropic X-ray luminosities $L_{\mathrm{X}} \gtrsim 10^{39}\,\mathrm{erg\,s^{-1}}$, are favoured candidates as power-engines of most of ULXs observed in nearby galaxies (Miller and Colbert, 2004), even if there still remain many unresolved questions. Assuming multi-colour black-body radiation of a geometrically thin, optically thick accretion disc (in which each annulus of the disc radiates as a black body with radius-dependent temperature) – so-called Multi-Color Disc model (MCD), the temperature near the innermost stable circular orbit (ISCO) depends on the mass of the black hole M_{BH}, accretion rate $\dot{M}$ and location of the ISCO R_{in} as (Makishima et al., 2000)

$$kT_{\mathrm{in}} \propto (\alpha^2 M_{\mathrm{BH}}/\dot{M})^{-1/4}\,, \quad \alpha = R_{\mathrm{in}}/3R_{\mathrm{S}}\,, \tag{1}$$

where $R_{\mathrm{S}} = 2GM_{\mathrm{BH}}/c^2$ is the Schwarzschild radius, and $\alpha = 1$ for non-rotating (Schwarzschild) BH but $\alpha = 1/6$ for maximally rotating (extreme Kerr) BH and corotating disc.

In the case of NGC 5408 X-1, there is a general agreement (see, e.g., Soria et al., 2004; Wang et al., 2004; Strohmayer et al., 2007) that a soft thermal component of the energy spectrum corresponds to (0.13–0.15) keV. If this value represents the maximum colour

[1] Belloni et al. (2006), however, did not confirm the QPO at 113 Hz still referred, e.g., by Remillard and McClintock (2006).

temperature of the disc, $kT_{\rm in}$, it implies (for the standard accretion disc model with Eddington luminosity) the black-hole mass $M_{\rm BH} > 10^4\,{\rm M}_\odot$. Wang et al. (2004) used so-called Comptonized Multi-Color Disc model (CMCD), in which the accretion disc is described by the MCD model but an inverse-Compton scattering of X-ray photons from the disc in a corona is generated by Monte Carlo simulations, and obtained the mass estimate for a *non-spinning* black hole $M_{\rm BH} \simeq 10^{3.43}\,{\rm M}_\odot \doteq 2690\,{\rm M}_\odot$. If the black hole is rapidly rotating Kerr BH, its mass could be higher even by a factor of tens for the same $kT_{\rm in}$, see Eq. (1). Soria et al. (2004, 2006) argued that the X-ray and radio spectrum are consistent with an accreting BH of mass $M_{\rm BH} \gtrsim 10^2\,{\rm M}_\odot$. Note that it is still unclear whether the soft thermal component $kT_{\rm bb} \sim 0.1$ keV, typical for many ULXs, comes from the accretion disc or from the corona. King and Pounds (2003) suggested that these ULXs may be several $10\,{\rm M}_\odot$ accreting BHs during a super-Eddington accretion phase with the soft thermal component coming from the photosphere of an optically-(Compton)-thick radiatively-driven outflow from the accretion disc. If this is the case, the mass of the black hole in NGC 5408 X-1 should not exceed $50\,{\rm M}_\odot$, still consistent with a stellar origin (Soria et al., 2004).

2 EXTENDED ORBITAL RESONANCE MODEL – BASIC ASSUMPTIONS

In the case of very rapidly rotating Kerr BHs (with a dimensionless spin parameter $a_* = Jc/GM_{\rm BH}^2 > 0.9953$; J is the black-hole angular momentum), a test particle orbital velocity $\mathcal{V}^{(\varphi)}$, defined by appropriate projections of particle's 4-velocity U^μ onto the LNRF-tetrad (Bardeen et al., 1972),[2] reveals a non-monotonic profile in the equatorial plane (Aschenbach, 2004). Stuchlík et al. (2005) shown that the analogous humpy behaviour of $\mathcal{V}^{(\varphi)}$ takes place also for non-geodesic motion of test perfect fluid orbiting near-extreme Kerr BHs with $a_* > 0.9998$ in marginally stable thick discs (tori), characterized by uniform distribution of a specific angular momentum, $\ell(r,\theta) = -U_\varphi/U_t = {\rm const.}$[3] In both geometrically thin and thick accretion discs the positive part of $\partial\mathcal{V}^{(\varphi)}/\partial r$ is confined to the ergosphere around BH but located above the ISCO in the equatorial plane ($\theta = \pi/2$), see Fig. 1. Thus local processes in the inner part of accretion discs around near-extreme Kerr BHs could carry a signature of the orbital velocity hump.

Aschenbach (2004) introduced a characteristic (critical) frequency of any process connected with the velocity hump by the maximum positive slope of the orbital velocity $\mathcal{V}^{(\varphi)}$ as a function of BL radius r. Its coordinate-independent definition using the maximal positive rate of change of $\mathcal{V}^{(\varphi)}$ with proper radial distance $\tilde{r}$,

$$\nu^{\tilde{r}}_{\rm crit} = \left.\frac{\partial\mathcal{V}^{(\varphi)}}{\partial\tilde{r}}\right|_{\rm max}, \quad {\rm d}\tilde{r} = \sqrt{g_{rr}}\,{\rm d}r\,, \tag{2}$$

[2] In rotating spacetimes a rotation of the space, causing so-called "dragging of inertial frames," is superposed on the own orbital motion of a matter in the disc. Locally non-rotating frames (LNRF) are dragged along with the spacetime, thus the LNRF point of view should reveal local orbital properties of the disc in the clearest way, similarly as the static observers do in non-rotating spacetimes. LNRF is the frame of ZAMO (Zero Angular Momentum Observer).

[3] Standard Boyer–Lindquist (BL) coordinates (t, r, θ, φ) are used.

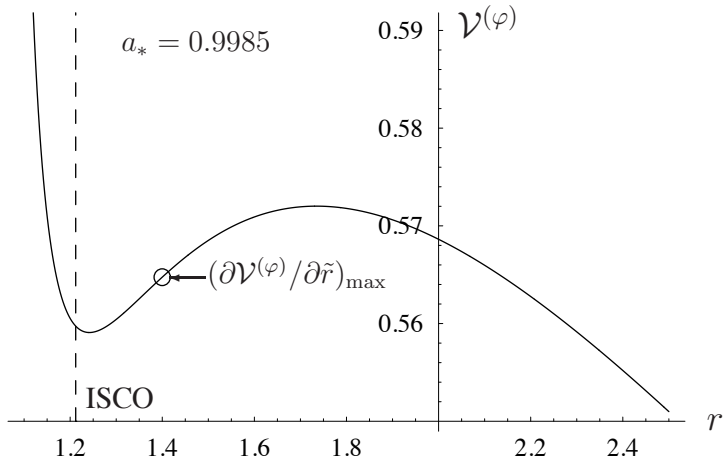

Figure 1. Test-particle orbital velocity profile determined by the locally non-rotating frames in the case of very rapidly rotating Kerr BH with a dimensionless spin $a_* = 0.9985$. The positive part of the radial gradient of $\mathcal{V}^{(\varphi)}$ is located close to but above the innermost stable circular orbit (ISCO). A circle denotes the orbit where the radial gradient of $\mathcal{V}^{(\varphi)}$ in terms of the proper radial distance reaches its maximal positive value used as the characteristic frequency of any local process triggered by the orbital velocity hump.

was given by Stuchlík et al. (2004). Relating this locally defined characteristic frequency $\nu^{\tilde{r}}_{\rm crit}$ to a static observer at infinity we get so-called "humpy frequency" (Stuchlík et al., 2007a)

$$\nu_{\rm h} = \sqrt{-(g_{tt} + 2\omega g_{t\varphi} + \omega^2 g_{\varphi\varphi})}\, \nu^{\tilde{r}}_{\rm crit}\,, \tag{3}$$

where $g_{\mu\nu}$ are metric coefficients of the Kerr geometry (in BL coordinates), and $\omega = -g_{t\varphi}/g_{\varphi\varphi}$ is the angular velocity of the LNRF (Bardeen et al., 1972).

Aschenbach (2004) also gave a heuristic assumption on possible excitation of particle's epicyclic motion in the inner part of Keplerian discs by the orbital velocity hump. The epicyclic motion is characterized by radial and vertical epicyclic frequencies $\nu_{\rm r},\ \nu_\theta$ (for their explicit definition see, e.g., Aliev and Galtsov (1981)). Stuchlík et al. (2007a) shown that for $a_* \to 1$ the ratios of the epicyclic frequencies to the humpy frequency, being evaluated at the so-called "humpy radius" (the definition BL radius of $\nu^{\tilde{r}}_{\rm crit}$), reach asymptotic, i.e., almost spin-independent, values $\nu_\theta : \nu_{\rm r} : \nu_{\rm h} \simeq 11 : 3 : 2$ suggesting an idea of resonant coupling between the hump-induced and epicyclic oscillations of Keplerian discs around near-extreme Kerr BHs. Moreover, in the region with positive slope of $\mathcal{V}^{(\varphi)}$ the resonant orbits $r_{3:1}$ and (for $a_* \gtrsim 0.996$) $r_{4:1}$, where the vertical and radial epicyclic frequencies are in ratios 3 : 1 and 4 : 1, are located (see Aschenbach, 2004; Stuchlík et al., 2007a) supporting the general idea of connection between the humpy profile of $\mathcal{V}^{(\varphi)}$ and epicyclic oscillations through resonant phenomena.

The "Extended Orbital Resonance Model" relies on the following assumptions (Stuchlík et al., 2007a):

• Excitation of epicyclic oscillation modes in accretion discs around near-extreme Kerr black holes by processes related to the velocity hump (and characterized by the humpy frequency);
• non-linear resonant phenomena are expected to be in play (as well as in the standard orbital resonance model of Kluźniak and Abramowicz (2001)).

3 APPLICATION OF THE EXTENDED RESONANT MODEL TO THE QUASI-PERIODIC VARIABILITY IN GRS 1915+105, XTE J1650−500, AND NGC 5408 X-1

3.1 GRS 1915+105

The model, in which the resonant coupling between the hump-induced and epicyclic oscillations is assumed, was first applied to the X-ray variable Galactic BH-source GRS 1915+105 (see Stuchlík et al., 2006, 2007b). The humpy frequency and excited radial epicyclic frequency (at the humpy radius $r_{\rm h}$) are identified with $\nu_2 = 41$ Hz and $\nu_3 = 67$ Hz QPOs, $\nu_2 \equiv \nu_{\rm h}$, $\nu_3 \equiv \nu_{\rm r}$, the only two QPOs observed simultaneously in GRS 1915+105 (Belloni et al., 2006), while the remaining three QPOs, $\nu_1 = 27$ Hz, $\nu_4 = 113$ Hz, and $\nu_5 = 167$ Hz, are explained, within the range of their errors being typically 1–5 Hz, by the combinational frequencies of the humpy frequency and both epicyclic frequencies evaluated at the same radius $r_{\rm h}$ ($\nu_\theta = 237$ Hz there), $\nu_1 \sim (\nu_{\rm r} - \nu_{\rm h})$, $\nu_4 \sim (\nu_{\rm r} + \nu_{\rm h})$, $\nu_5 \sim (\nu_\theta - \nu_{\rm r})$. Since the ratios of frequencies $\nu_2 : \nu_1$ and $\nu_5 : \nu_4$ are close to 3 : 2 ratio, $\nu_3 : \nu_2$ and $\nu_4 : \nu_3$ are close to 5 : 3 ratio, and $\nu_5 : \nu_2 \sim 4 : 1$, relatively strong resonant phenomena are expected to be in play. The model predicts near-extreme spin of the central BH, $a_* = 0.9998$, which is in a good agreement with results given by spectral continuum fits, $a_* > 0.98$, presented by McClintock et al. (2006), and the black-hole mass $M_{\rm BH} \sim 14.8\,{\rm M}_\odot$, being well inside the interval $(14.0 \pm 4.4)\,{\rm M}_\odot$ given by other observational methods (Remillard and McClintock, 2006). The results are summarized in Table 1 and Fig. 2.

Note that the orbital resonance model of Kluźniak and Abramowicz (2001) assumes non-linear resonant interaction between the orbital and/or epicyclic modes. When the parametric resonance between the vertical and radial epicyclic oscillations in the frequency ratio 3 : 2, represented by the uppermost pair of referred frequencies, 113 Hz and 167 Hz, is taken into account, the orbital resonance model also gives the spin $a > 0.98$, but for $M \simeq 18\,{\rm M}_\odot$ (Török, 2005). Moreover, the Extended Orbital Resonance Model seems

Table 1. Mass and spin of the Kerr black hole candidates following from the suggested applications of the Extended Orbital Resonance Model to quasi-periodic variabilities in their X-ray spectra.

BH-candidate	BH-mass	BH-spin
GRS 1915+105	$14.8\,{\rm M}_\odot$	0.9998
XTE J1650−500	$5.1\,{\rm M}_\odot$	0.9982
NGC 5408 X-1	$62 \times 10^3\,{\rm M}_\odot$	0.9985

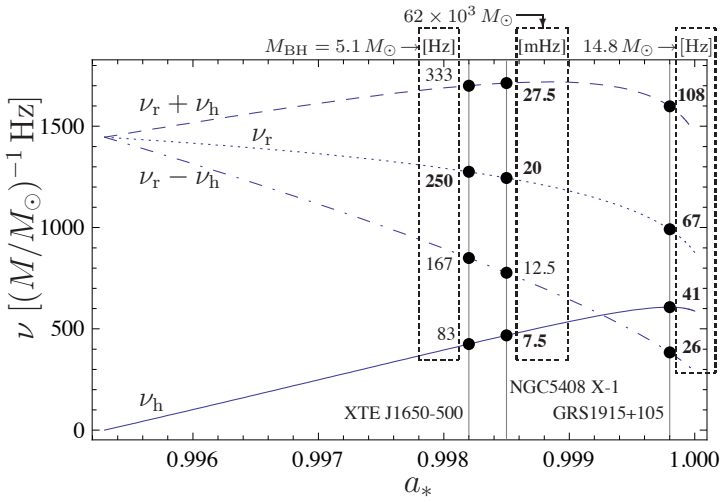

Figure 2. Spin dependence of the humpy and radial epicyclic frequency, $\nu_{\rm h}$ and $\nu_{\rm r}$, and their combinational frequencies $\nu_{\rm r} \pm \nu_{\rm h}$. All frequencies are calculated at the *same* radius, where the rate of change of the orbital velocity in terms of the proper radial distance reaches the maximal positive value for a given a_*. Moreover, the values of frequencies and corresponding black-hole mass and spin, implied by the "Extended Orbital Resonance Model," are presented for three sources: GRS 1915+105, NGC 5408 X-1 and XTE J1650−500. The bold-faced values of frequencies are comparable with centroid frequencies of previously referred QPOs for each source; see the text for concrete references. Note that from the point of view of the presented model, the humpy frequency at 7.5 mHz is observed through its first overtone at 15 mHz. Remaining values of frequencies are predicted by the model.

to be the first one able to match consistently the whole high-frequency pattern of the source (Aschenbach, 2007).

3.2 XTE J1650−500

As it was mentioned above, XTE J1650−500 belongs among the near-extreme Kerr BH candidates. Miller et al. (2002), analyzing profiles of the Fe K_α emission line, give the spin-estimate of $a_* \simeq 0.998$, which suggests that the effects of non-monotonic orbital velocity profile could take place in this source. Remarkably, for Keplerian discs and the spin $a_* = 0.9982$, the frequency ratio of the radial epicyclic frequency and the humpy frequency at the same, i.e., "humpy" radius is close to 3 : 1, thus the strong resonant coupling between the hump-induced and radial epicyclic oscillations is expected. Identifying the strong 250 Hz QPO with the radial epicyclic frequency which, for the spin $a_* = 0.9982$, reaches the value of 1275 $(M/\mathrm{M}_\odot)^{-1}$ Hz at the "humpy" radius, we get for the mass of the Kerr BH the value of $M_{\rm BH} \simeq 5.1\ \mathrm{M}_\odot$, in accordance with the proposed upper limit.

For completeness, the humpy and combinational frequencies, corresponding to the proposed radial epicyclic frequency and the resonant ratio $\nu_{\rm r} : \nu_{\rm h} = 3 : 1$, are given in Fig. 2. Although it is not necessary to observe them, note, however, that some broad high-frequency

features near the frequencies 80 Hz (Kalemci et al., 2003) and 168 Hz (Homan et al., 2003) were reported.

3.3 NGC 5408 X-1

In a spirit of application for GRS 1915+105, we suggest to match the strongest QPO at 20 mHz with the frequency of radial epicyclic oscillations of the Keplerian disc at the orbit where the proper radial gradient of the orbital velocity in the LNRF reaches the maximal positive value, corresponding to the humpy frequency $\nu_{\rm h} \simeq 7.5$ mHz. Next we suggest to match the 15 mHz QPO with the first overtone of the humpy frequency $\nu_{\rm h}$, i.e., $2\nu_{\rm h} \simeq 15$ mHz, and $\nu_{\rm r} \simeq 20$ mHz, both being determined at the same resonant orbit.

The ratio of suggested humpy and radial epicyclic frequencies, being well represented by the ratio of integer numbers, $\nu_{\rm r} : \nu_{\rm h} \sim 8:3$, is in accord with the predicted resonant coupling between the hump-induced and epicyclic oscillations (Stuchlík et al., 2007a). Because the ratio is given by relatively distant and high numbers, the resonance should be weak, and due to this fact a QPO at frequency ~ 7 mHz should be also weak to be directly observable. On the other hand, due to non-linear (anharmonic) oscillations expected in the system, the resonance at frequency being twice the basic humpy frequency $\nu_{\rm h}$, i.e., at $2\nu_{\rm h}$, could be strong, as the ratio of $\nu_{\rm r} : 2\nu_{\rm h} \sim 4:3$ is represented by close and small integers. Moreover, in non-linear oscillating systems the combinational frequencies are allowed as well (Landau and Lifshitz, 1976). Combining the humpy and radial epicyclic frequencies, in the lowest order we get $(\nu_{\rm r} + \nu_{\rm h}) \simeq 27.5$ mHz which is very close to the 3rd, not so strong as the previous ones, referred feature at 27 mHz, see Fig. 2. The same order of non-linearity admits also a combination $(\nu_{\rm r} - \nu_{\rm h}) \simeq 12.5$ mHz, which seems to be not directly observed, even though it is relatively close to the faint 11.4 mHz Lorentzian component in the best fit of the average power spectrum from all the data analysed by Strohmayer et al. (2007).

Presumed resonant coupling between the hump-induced and radial epicyclic oscillations, being represented by the 8 : 3 ratio, enables to determine the spin of the Kerr BH. If the both frequencies are expected to originate at the same radius $r_{\rm h}$, we get $a_* \simeq 0.9985$. Taking into account the $1/M$ scaling of the humpy frequency $\nu_{\rm h}$, we can also determine the black-hole mass. For the spin $a_* = 0.9985$, the humpy frequency $\nu_{\rm h} \doteq 468\ (M/{\rm M}_\odot)^{-1}$ Hz. Comparing it with the expected value 7.5 mHz we get $M_{\rm BH} \simeq 62 \times 10^3\ {\rm M}_\odot$, still consistent with the soft thermal component of the energy spectrum, $kT_{\rm in} \sim 0.15$ keV, related to the innermost part of the accretion disc in the system with near-extreme Kerr BH.

4 CONCLUSIONS

The "Extended Orbital Resonance Model," like other strong-gravity models, e.g., the "Relativistic Precession Model" of Stella et al. (1999) or the orbital resonance model of Kluźniak and Abramowicz (2001), is able to give the estimates for the mass and spin of the Kerr BH, if more than one frequency or one of the BH-parameters are known. The results are summarized in Table 1. Of course, the model can be applied only to near-extreme BH candidates, because only in this case the LNRF-related orbital velocity of the accretion disc reveals the non-monotonic behaviour in its inner part close to the ISCO.

ACKNOWLEDGEMENTS

The authors gratefully acknowledge the cooperation (the case of GRS 1915+105) and useful discussions (XTE J1650−500 and NGC 5408 X-1) with Gabriel Török. The presented work was supported by the Czech grant MSM 4781305903.

REFERENCES

Aliev, A. N. and Galtsov, D. V. (1981), Radiation from relativistic particles in non-geodesic motion in a strong gravitational field, *Gen. Relativity Gravitation*, **13**, pp. 899–912.

Aschenbach, B. (2004), Measuring mass and angular momentum of black holes with high-frequency quasi-periodic oscillations, *Astronomy and Astrophysics*, **425**, pp. 1075–1082, arXiv: `astro-ph/0406545`.

Aschenbach, B. (2007), Measurement of Mass and Spin of Black Holes with QPOs, *Chinese Astronom. Astrophys.*, accepted for publication, arXiv: `0710.3454`.

Bardeen, J. M., Press, W. H. and Teukolsky, S. A. (1972), Rotating black holes: locally nonrotating frames, energy extraction, and scalar synchrotron radiation, *Astrophys. J.*, **178**, pp. 347–369.

Belloni, T., Méndez, M. and Sánchez-Fernández, C. (2001), The high-frequency QPOs in GRS 1915+105, *Astronomy and Astrophysics*, **372**, pp. 551–556, arXiv: `astro-ph/0104019`.

Belloni, T., Soleri, P., Casella, P., Méndez, M. and Migliari, S. (2006), High-frequency quasi-periodic oscillations from GRS 1915+105 in its C state, *Monthly Notices Roy. Astronom. Soc.*, **369**(1), pp. 305–310.

Homan, J., Klein-Wolt, M., Rossi, S., Miller, J. M., Wijnands, R., Belloni, T., van der Klis, M. and Lewin, W. H. G. (2003), High-frequency quasi-periodic oscillations in the black hole X-ray transient XTE J1650−500, *Astrophys. J.*, **586**, pp. 1262–1267.

Kalemci, E., Tomsick, J. A., Rothschild, R. E., Pottschmidt, K., Corbel, S., Wijnands, R., Miller, J. M. and Kaaret, P. (2003), X-ray temporal properties of XTE J1650−500 during outburst decay, *Astrophys. J.*, **586**, pp. 419–426.

King, A. R. and Pounds, K. A. (2003), Black hole winds, *Monthly Notices Roy. Astronom. Soc.*, **345**, pp. 657–659.

Kluźniak, W. and Abramowicz, M. A. (2001), Strong-field gravity and orbital resonance in black holes and neutron stars – kHz quasi-periodic oscillations (QPO), *Acta Phys. Polon. B*, **32**, pp. 3605–3612.

Landau, L. D. and Lifshitz, E. M. (1976), *Mechanics*, volume I of *Course of Theoretical Physics*, Elsevier Butterworth-Heinemann, Oxford, 3rd edition, ISBN 0-7506-2896-0.

Makishima, K., Kubota, A., Mizuno, T., Ohnishi, T., Tashiro, M. and Aruga, Y. (2000), The Nature of Ultraluminous Compact X-Ray Sources in Nearby Spiral Galaxies, *Astrophys. J.*, **535**, pp. 632–643.

McClintock, J. E. and Remillard, R. A. (2004), Black Hole Binaries, in W. H. G. Lewin and M. van der Klis, editors, *Compact Stellar X-Ray Sources*, Cambridge University Press, Cambridge, arXiv: `astro-ph/0306213`.

McClintock, J. E., Shafee, R., Narayan, R., Remillard, R. A., Davis, S. W. and Li, L. (2006), The Spin of the Near-Extreme Kerr Black Hole GRS 1915+105, *Astrophys. J.*, **652**(2), pp. 518–539, arXiv: `astro-ph/0606076`.

Miller, J. M., Fabian, A. C., Wijnands, R., Reynolds, C. S., Ehle, M., Freyberg, M. J., van der Klis, M., Lewin, W. H. G., Sánchez-Fernández, C. and Castro-Tirado, A. J. (2002), Evidence of spin and energy extraction in a galactic black hole candidate: the *XMM-Newton*/EPIC-pn spectrum of XTE J1650−500, *Astrophys. J.*, **570**, pp. L69–L73.

Miller, M. C. and Colbert, E. J. M. (2004), Intermediate-Mass Black Holes, *Internat. J. Modern Phys. D*, **13**, pp. 1–64.

Morgan, E. H., Remillard, R. A. and Greiner, J. (1997), RXTE Observation of GRS 19115+105, *Astrophys. J.*, **482**, pp. 993–1010.

Orosz, J. A., McClintock, J. E., Remillard, R. A. and Corbel, S. (2004), Orbital parameters for the black hole binary XTE J1650−500, *Astrophys. J.*, **616**, pp. 376–382.

Remillard, R. A. (2004), *AIPC*, **714**, pp. 13–20.

Remillard, R. A. and McClintock, J. E. (2006), X-Ray Properties of Black-Hole Binaries, *Annual Review of Astronomy and Astrophysics*, **44**(1), pp. 49–92, arXiv: `astro-ph/0606352`.

Soria, R., Fender, R. P., Hannikainen, D. C., Read, A. M. and Stevens, I. R. (2006), A ULX microquasar in NGC5408?, *Monthly Notices Roy. Astronom. Soc.*, **368**, pp. 1527–1539.

Soria, R., Motch, C., Read, A. M. and Stevens, I. R. (2004), X-ray flares from the ultra-luminous X-ray source in NGC5408, *Astronomy and Astrophysics*, **423**, pp. 955–963.

Stella, L., Vietri, M. and Morsink, S. M. (1999), Correlations in the quasi-periodic oscillation frequencies of low-mass X-ray binaries and the relativistic precession model, *Astrophys. J.*, **524**, pp. L63–L66, arXiv: `astro-ph/9907346`.

Strohmayer, T. E. (2001), Discovery of a Second High-Frequency Quasi-periodic Oscillation from the Microquasar GRS 1915+105, *Astrophys. J.*, **554**, pp. L169–172.

Strohmayer, T. E., Mushotzky, R. F., Winter, L., Soria, R., Uttley, P. and Cropper, M. (2007), Quasi-Periodic Variability in NGC 5408 X-1, *Astrophys. J.*, **660**, pp. 580–586, arXiv: `astro-ph/0701390`.

Stuchlík, Z., Slaný, P. and Török, G. (2004), Marginally stable thick discs with gradient inversion of orbital velocity measured in locally non-rotating frames: A mechanism for excitation of oscillations in accretion discs?, in S. Hledík and Z. Stuchlík, editors, *Proceedings of RAGtime 4/5: Workshops on black holes and neutron stars, Opava, 14–16/13–15 October 2002/2003*, pp. 239–256, Silesian University in Opava, Opava, ISBN 80-7248-242-4.

Stuchlík, Z., Slaný, P. and Török, G. (2006), Humpy LNRF-velocity profiles in accretion discs orbiting rapidly rotating Kerr black holes: a possible relation to QPOs, in T. Belloni, editor, *Proceedings of the Sixth Microquasar Workshop – Microquasars and Beyond: From Binaries To Galaxies, Como, Italy, 18–22 September, 2006*, p. PoS(MQW6)095, Como, Italy, URL `http://pos.sissa.it/archive/conferences/033/095/MQW6_095.pdf`.

Stuchlík, Z., Slaný, P. and Török, G. (2007a), Humpy LNRF-velocity profiles in accretion discs orbiting almost extreme Kerr black holes – A possible relation to quasi-periodic oscillations, *Astronomy and Astrophysics*, **463**(3), pp. 807–816, arXiv: `astro-ph/0612439`.

Stuchlík, Z., Slaný, P. and Török, G. (2007b), LNRF-velocity hump-induced oscillations of a Keplerian disc orbiting near-extreme Kerr black hole: A possible explanation of high-frequency QPOs in GRS 1915+105, *Astronomy and Astrophysics*, **470**(2), pp. 401–404, arXiv: `0704.1252v2`.

Stuchlík, Z., Slaný, P., Török, G. and Abramowicz, M. A. (2005), Aschenbach effect: Unexpected topology changes in motion of particles and fluids orbiting rapidly rotating Kerr black holes, *Phys. Rev. D*, **71**, p. 024037 (9), arXiv: `gr-qc/0411091`.

Török, G. (2005), QPOs in microquasars and Sgr A*: measuring the black hole spin, *Astronom. Nachr.*, **326**(9), pp. 856–860, arXiv: `astro-ph/0510669`.

Wang, Q. D., Yao, Y., Fukui, W., Zhang, S. N. and Williams, R. (2004), XMM-Newton Spectra of Intermediate-Mass Black Hole Candidates: Application of a Monte-Carlo Simulated Model, *Astrophys. J.*, **609**, pp. 113–121.

Proceedings of *RAGtime 8/9, 15–19/19–21 September, 2006/2007, Hradec nad Moravicí, Opava, Czech Republic*
S. Hledík and Z. Stuchlík, editors, Silesian University in Opava, 2007, pp. 267–273

Humpy LNRF-related orbital velocity profiles of test-particle and perfect-fluid discs in Kerr–(anti-)de Sitter spacetimes

Petr Slaný[a] and Zdeněk Stuchlík[b]

Institute of Physics, Faculty of Philosophy & Science, Silesian University in Opava,
Bezručovo nám. 13, CZ-746 01 Opava, Czech Republic
[a]petr.slany@fpf.slu.cz
[b]zdenek.stuchlik@fpf.slu.cz

ABSTRACT
Humpy radial profiles of the LNRF-related orbital velocity was found for a circular motion of test particles and test perfect fluid orbiting near-extreme Kerr black holes and Kerr naked singularities. Preliminary results of an analogical study of the circular motion of test particles and fluid in the Kerr–(anti-)de Sitter spacetimes are presented.

Keywords: Black hole physics – relativity – accretion, accretion discs – cosmological constant

1 INTRODUCTION

Humpy radial profile of the LNRF-related orbital velocity[1] was found for a circular motion of test particles with Keplerian angular momentum distribution, orbiting near-extreme Kerr black holes (BH) with spin $a > 0.9953$ (Aschenbach, 2004). Subsequently, Stuchlík et al. (2005) showed that the same non-monotonic behaviour, being called "Aschenbach effect," takes place also for the Keplerian motion of test particles around Kerr naked singularities (NS) with spin $1 < a < 4.1942$, and for non-Keplerian motion with uniform (constant) specific angular momentum distribution, $\ell(r, \theta) = \text{const}$, in the Kerr backgrounds with $0.99964 < a < 1.5043$. Supposing that the $\ell = \text{const}$ motion corresponds to the angular momentum distribution in marginally stable barotropic perfect fuid tori, Stuchlík et al. (2005) shows that the Aschenbach effect is fully relevant for accretion discs around near-extreme Kerr BHs with $a \gtrsim 0.9998$.

Recently, it was shown in Stuchlík et al. (2007) that the Aschenbach effect in a Keplerian disc orbiting Kerr BH with mass $14.8\,\mathrm{M}_\odot$ and spin $a = 0.9998$ could be responsible for excitation of epicyclic oscillations in the X-ray variable binary black hole system

[1] LNRF means Locally Non-Rotating Frame (see, e.g., Bardeen et al., 1972 for its definition).

978-80-7248-419-5

GRS 1915+105; for more details and also for other applications of the idea of orbital-velocity-hump-induced oscillations see previous contribution of Slaný and Stuchlík in this volume.

Here, preliminary results of an analogical study of the circular motion of test particles and fluid in the Kerr–(anti-)de Sitter spacetimes are presented, including influence of the cosmological constant on the range of BH/NS spins, for which the Keplerian discs and marginally stable barotropic perfect fluid tori reveal humpy radial profiles of their orbital velocities in locally non-rotating frames.[2]

2 ORBITAL VELOCITY RELATED TO THE LNRF

In the Boyer–Lindquist coordinates (t, r, θ, ϕ) and geometrical units ($c = G = 1$) the Kerr–(anti-)de Sitter spacetime, characterized by the central-mass parameter M, rotational parameter (spin) $a > 0$ and cosmological constant Λ ($\Lambda > 0$ in asymptotically de Sitter backgrounds, and $\Lambda < 0$ in asymptotically anti-de Sitter backgrounds), is described by the line element

$$\mathrm{d}s^2 = -\frac{\Delta_r \Delta_\theta \rho^2}{I^2 A}\,\mathrm{d}t^2 + \frac{A \sin^2\theta}{I^2 \rho^2}(\mathrm{d}\phi - \omega\,\mathrm{d}t)^2 + \frac{\rho^2}{\Delta_r}\,\mathrm{d}r^2 + \frac{\varrho^2}{\Delta_\theta}\,\mathrm{d}\theta^2\,, \tag{1}$$

where

$$\begin{aligned} \Delta_r &= r^2 - 2Mr + a^2 - \tfrac{1}{3}\Lambda r^2(r^2 + a^2)\,, & \Delta_\theta &= 1 + \tfrac{1}{3}\Lambda a^2 \cos^2\theta\,, \\ \rho^2 &= r^2 + a^2\cos^2\theta\,, & A &= (r^2 + a^2)^2\Delta_\theta - a^2\Delta_r \sin^2\theta\,, \\ I &= 1 + \tfrac{1}{3}\Lambda a^2\,, & \omega &= \frac{a}{A}\left[(r^2 + a^2)\Delta_\theta - \Delta_r\right]. \end{aligned} \tag{2}$$

The orbital velocity of matter is given by appropriate projections of its 4-velocity $\boldsymbol{U}$ onto the tetrad of a locally non-rotating frame (LNRF) $\boldsymbol{e}^{(\mu)}$, and corresponds to the locally measured azimuthal component of 3-velocity in the LNRF

$$\mathcal{V}^{(\phi)} = \frac{U^\mu e^{(\phi)}_\mu}{U^\nu e^{(t)}_\nu} = \frac{A\sin\theta}{\rho^2\sqrt{\Delta_r \Delta_\theta}}(\Omega - \omega)\,, \tag{3}$$

where $\omega = -g_{t\phi}/g_{\phi\phi}$, given by (2), is the angular velocity of the LNRF, and

$$\Omega = -\frac{\ell g_{tt} + g_{t\phi}}{\ell g_{t\phi} + g_{\phi\phi}} \tag{4}$$

is the angular velocity of matter orbiting with the specific angular momentum $\ell = -U_\phi/U_t$.

Instead of Λ we introduce the "cosmological parameter"

$$y = \tfrac{1}{3}\Lambda M^2\,, \tag{5}$$

and reformulate relations (1)–(2) into the completely dimensionless form by putting $M = 1$ hereafter.

[2] Similar analysis has been done by Müller and Aschenbach (2007); a comment to their results can be found in Slaný and Stuchlík (2007).

2.1 Keplerian discs

Matter in the Keplerian disc follows stable circular geodesics in the equatorial plane ($\theta = \pi/2$), and is described by the "Keplerian" distribution of the specific angular momentum and corresponding Keplerian angular velocity (Stuchlík and Slaný, 2004; Slaný and Stuchlík, 2005)

$$\ell_{\mathrm{K}\pm}(r; a, y) = \pm\frac{(r^2+a^2)\sqrt{1-yr^3} \mp a\sqrt{r}[2+r(r^2+a^2)y]}{r\sqrt{r}[1-(r^2+a^2)y]-2\sqrt{r}\pm a\sqrt{1-yr^3}}\,, \tag{6}$$

$$\Omega_{\mathrm{K}\pm}(r; a, y) = \frac{1}{a \pm r\sqrt{r/(1-yr^3)}}\,, \tag{7}$$

where $\pm$ refers to two distinct families of orbits in the K(a)dS spacetimes. The minus-family represents retrograde orbits only (from the point of view of the LNRF) while the plus-family can be both the direct or retrograde.

The Keplerian orbital velocity is given by the relation

$$\mathcal{V}^{(\phi)}_{\mathrm{K}\pm}(r; a, y) = \frac{(r^2+a^2)\sqrt{1-yr^3} \mp a\sqrt{r}[2+r(r^2+a^2)y]}{\sqrt{\Delta_r}[a\sqrt{1-yr^3}\pm r\sqrt{r}]}\,. \tag{8}$$

For $y = 0$ the non-monotonic behaviour of $\mathcal{V}^{(\phi)}$ was found for the plus-family orbits (Aschenbach, 2004) therefore here (for $y \neq 0$) we restrict to this family only.

Spin-dependence of the Keplerian orbital velocity profile in KdS backgrounds is presented in Fig. 1 (left panel). The positive radial-gradient part of the Keplerian orbital velocity is located close to but above the marginally stable orbit of the given KdS spacetime. The analogical humpy behaviour near the marginally stable orbit is present also in KadS backgrounds where, nevertheless, an additional non-monotonicity in Keplerian orbital velocity profile is present independently of the spin a, see Fig. 1 (right panel). This local minimum

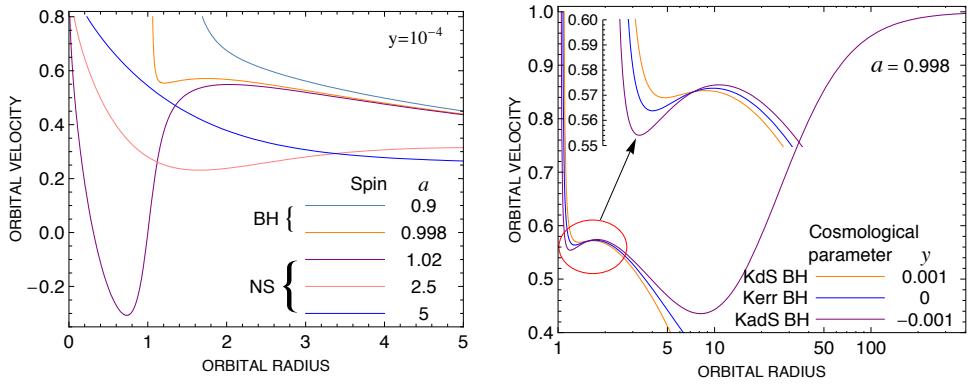

Figure 1. *Left:* Spin-dependence of the Keplerian orbital velocity profile in KdS backgrounds. *Right:* Λ-dependence of the Keplerian orbital velocity profile in K(a)dS backgrounds.

is given clearly by interplay between the cosmic attraction (represented by $\Lambda < 0$), increasing with increasing radius r, and gravitational attraction of the centre, increasing with decreasing radius r.

2.2 Marginally stable barotropic perfect fluid tori

Structure of test barotropic perfect-fluid tori with the uniform distribution of the specific angular momentum

$$\ell(r,\theta) = \text{const}\,, \tag{9}$$

in K(a)dS spacetimes is determined by the equipotential surfaces $W(r,\theta) = \text{const}$ (Slaný and Stuchlík, 2005), where

$$W(r,\theta) = \ln\left[\frac{\rho^2}{I^2}\frac{\Delta_r\Delta_\theta\sin^2\theta}{\Delta_\theta(r^2+a^2-a\ell)^2\sin^2\theta - \Delta_r(\ell - a\sin^2\theta)^2}\right]^{1/2}. \tag{10}$$

In all BH and most NS backgrounds closed equipotential surfaces, describing stationary tori, exist only if $\ell \in (\ell_{\rm ms}, \ell_{\rm mb})$ for $y \leq 0$, where $\ell_{\rm ms}$ ($\ell_{\rm mb}$) corresponds to the specific angular momentum of the marginally stable (marginally bound) equatorial circular geodesic, or $\ell \in (\ell_{\rm ms(i)}, \ell_{\rm ms(o)})$ for $y > 0$, where $\ell_{\rm ms(i)}$ ($\ell_{\rm ms(o)}$) are the specific angular momenta of the inner (outer) marginally stable equatorial circular geodesics. In NS backgrounds with spacetime-parameters being close to the extreme-BH case the situation is more complex, and in some cases the stationary tori exist even for $\ell \in (-\infty, +\infty)$ (see Slaný and Stuchlík, 2005 for details). A boundary of each torus is given by a concrete closed equipotential surface but there always exists a limit on the thickness and diameter of the disc orbiting particular black hole (naked singularity), which is given by the critical, marginally closed, equipotential surface, self-crossing in the cusp. When matter in the disc overfills this critical surface, it violates the hydrostatic equilibrium, and an outflow of matter through the cusp is necessary. In KdS backgrounds ($\Lambda > 0$), there are three types of stationary tori (Slaný and Stuchlík, 2005):

Accretion discs: the critical point (cusp) of the marginally closed equipotential surface is located in the equatorial plane at the inner edge of the disc,

Excretion discs: the critical point (cusp) of the marginally closed equipotential surface is located in the equatorial plane at the outer edge of the disc,

Marginally bound accretion discs: the critical marginally closed equipotential surface is self-crossing in both the inner and the outer cusps.

In Kerr and KadS backgrounds ($\Lambda \leq 0$) only the marginally closed equipotential surfaces with the inner cusps, exist.

The orbital velocity of the fluid with $\ell = \text{const}$ angular momentum distribution is determined by the relation:

$$\mathcal{V}^{(\phi)}_{\rm tor}(r,\theta;a,y,\ell) = \frac{\rho^2\ell\sqrt{\Delta_r\Delta_\theta}}{\{A - [\Delta_\theta(r^2+a^2) - \Delta_r]a\ell\}\sin\theta}\,. \tag{11}$$

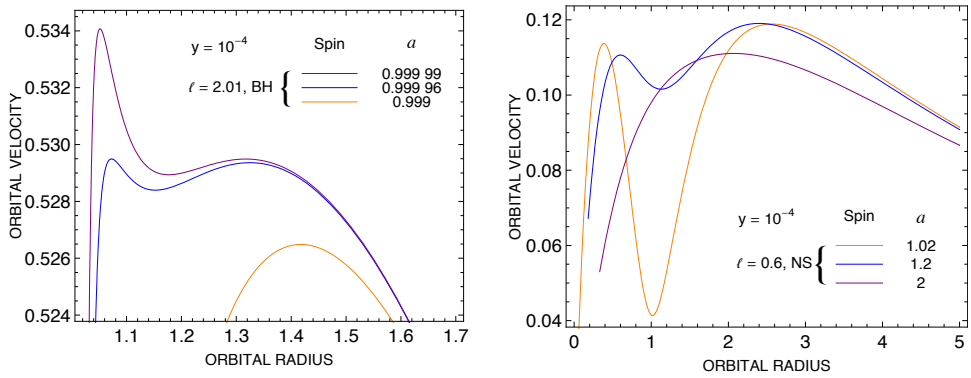

Figure 2. Spin-dependence of the $\ell = \text{const}$ orbital velocity profile in KdS black-hole (left panel) and naked-singularity (right panel) backgrounds.

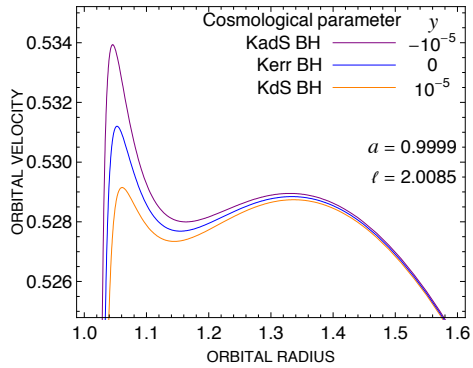

Figure 3. Λ-dependence of the $\ell = \text{const}$ orbital velocity profile in K(a)dS backgrounds.

Local extrema of the orbital velocity are given by the condition for the specific angular momentum

$$\ell = \ell_{\text{ex}}(r; a, y) \equiv a + \frac{r^2[(r^2+a^2)(r-1-yr(2r^2+a^2)) - 2r\Delta_r]}{ar[r-1-yr(2r^2+a^2)][2+yr(r^2+a^2)] + 2a\Delta_r(1-yr^3)}\,. \tag{12}$$

Here we restrict to the case $\ell > 0$ but there are also NS spacetimes with humpy profiles of $\mathcal{V}^{(\phi)}_{\text{tor}}$ for $\ell < 0$.

Spin-dependence of the $\ell = \text{const}$ orbital velocity profile in KdS backgrounds is presented in Fig. 2. The analogical behaviour can be found also in KadS backgrounds, see Fig. 3 where the Λ-dependence of the $\ell = \text{const}$ orbital velocity profile is shown.

3 KERR–(ANTI-)DE SITTER BACKGROUNDS WITH HUMPY ORBITAL VELOCITY PROFILES OF ACCRETION DISCS

Geometrically thin/thick accretion discs orbiting K(a)dS black holes (or even naked-singularities) are well represented by axisymmetric Keplerian/non-Keplerian circular motion of test particles/fluid in the particular black-hole (naked-singularity) background.

The range of spacetime parameters (a, y), for which the geometrically thin, i.e., Keplerian, accretion discs with humpy orbital velocity profiles exist, is presented graphically in Fig. 4 (left panel). Critical black-hole spin, for which the Aschenbach effect in Keplerian discs is getting to exist, increases with the cosmological parameter y (i.e., with the cosmological constant Λ) from $y_{\rm min} \doteq -0.01535$ up to the value of $y_{\rm c(ms+)} \doteq 0.06886$, corresponding to maximal value of the cosmological parameter which allows stable equatorial circular geodesics belonging to the plus-family in KdS spacetimes. In the range $y \in (-10^{-3}, 10^{-3})$ a Λ-dependence of this critical spin can be well described by the linear relation (Slaný and Stuchlík, 2007):

$$a_{\rm crit} = 0.99529 + 1.35395\,y = 0.99529 + 0.45132\,\Lambda\,. \tag{13}$$

In the case of geometrically thick accretion discs existence of the Aschenbach effect was studied for the marginally stable barotropic perfect fluid tori, i.e., the tori with uniformly distributed specific angular momentum $\ell(r, \theta) = \text{const}$. To recognize when the Aschenbach effect can be relevant for the torus in the given spacetime we compare the maximal extension of the disc in the spacetime, given by the critical marginally closed equipotential surface, with the positions of local minimum in the orbital velocity profile for given values of a, y, and ℓ. The critical black-hole spin, for which the marginally stable barotropic

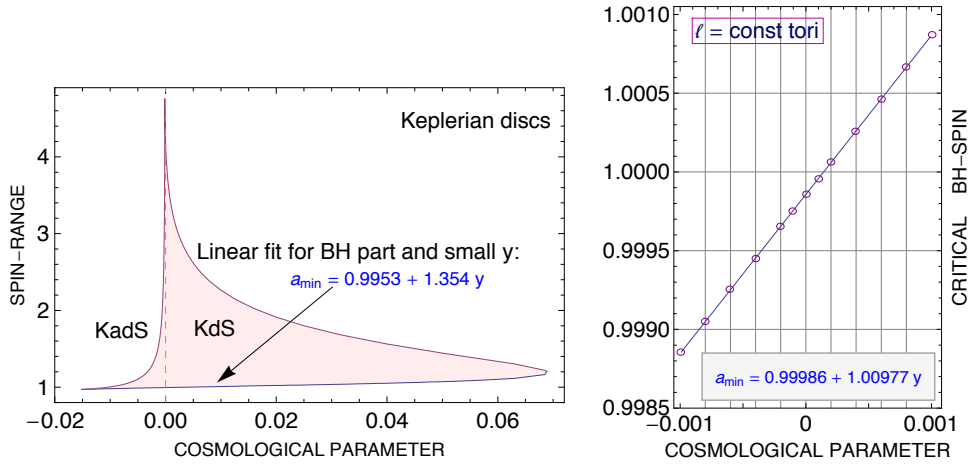

Figure 4. *Left:* Kerr–(anti-)de Sitter spacetimes in which the Keplerian discs with humpy LNRF-related orbital velocity profiles exist. *Right:* Critical black hole spin, for which the radial profile of the LNRF-related orbital velocity of marginally stable barotropic perfect fluid tori begins to contain positive radial gradient part for some physically relevant value of ℓ.

perfect fluid tori begin to contain the region with positive radial gradient of $\mathcal{V}^{(\phi)}$ in K(a)dS backgrounds with $y \in (-10^{-3}, 10^{-3})$, can be obtained from the linear relation

$$a_{\mathrm{crit}} = 0.99986 + 1.00977y = 0.99986 + 0.33659\Lambda \tag{14}$$

which describes the linear fit through numerically determined values presented in Fig. 4 (right panel).

4 CONCLUSIONS

Comparing radial profiles of the LNRF-related orbital velocity for a fixed value of the cosmological parameter y (i.e., for a fixed value of the cosmological constant Λ) and for a fixed spin a we conclude that in both cases of discussed angular momentum distributions, i.e., the Keplerian distribution and the uniform distribution, a decrease of the cosmological parameter y for a fixed value of the spin parameter a acts on the orbital velocity profile like an increase of a for a fixed value of y.

ACKNOWLEDGEMENTS

The presented work was supported by the Czech grant MSM 4781305903.

REFERENCES

Aschenbach, B. (2004), Measuring mass and angular momentum of black holes with high-frequency quasi-periodic oscillations, *Astronomy and Astrophysics*, **425**, pp. 1075–1082, arXiv: `astro-ph/0406545`.

Bardeen, J. M., Press, W. H. and Teukolsky, S. A. (1972), Rotating black holes: locally nonrotating frames, energy extraction, and scalar synchrotron radiation, *Astrophys. J.*, **178**, pp. 347–369.

Müller, A. and Aschenbach, B. (2007), Non-monotonic orbital velocity profiles around rapidly rotating Kerr–(anti-)de Sitter black holes, *Classical Quantum Gravity*, **24**(10), pp. 2637–2644, arXiv: `0704.3963`.

Slaný, P. and Stuchlík, Z. (2005), Relativistic thick discs in the Kerr–de Sitter backgrounds, *Classical Quantum Gravity*, **22**, pp. 3623–3651, URL `http://www.iop.org/EJ/abstract/-search=44947255.2/0264-9381/22/17/019`.

Slaný, P. and Stuchlík, Z. (2007), On non-monotonic orbital velocity profiles around rapidly rotating Kerr–(anti-)de Sitter black holes: A comment to the recently published results, arXiv: `0709.0803`.

Stuchlík, Z. and Slaný, P. (2004), Equatorial circular orbits in the Kerr–de Sitter spacetimes, *Phys. Rev. D*, **69**, p. 064001, ISSN 1094-1622, arXiv: `gr-qc/0307049`.

Stuchlík, Z., Slaný, P. and Török, G. (2007), LNRF-velocity hump-induced oscillations of a Keplerian disc orbiting near-extreme Kerr black hole: A possible explanation of high-frequency QPOs in GRS 1915+105, *Astronomy and Astrophysics*, **470**(2), pp. 401–404, arXiv: `0704.1252v2`.

Stuchlík, Z., Slaný, P., Török, G. and Abramowicz, M. A. (2005), The Aschenbach effect: unexpected topology changes in motion of particles and fluids orbiting rapidly rotating Kerr black holes, *Phys. Rev. D*, **71**, p. 024037 (9), arXiv: `gr-qc/0411091`.

Proceedings of *RAGtime 8/9, 15–19/19–21 September, 2006/2007, Hradec nad Moravicí, Opava, Czech Republic*
S. Hledík and Z. Stuchlík, editors, Silesian University in Opava, 2007, pp. 275–278

Oscillations of non-slender tori in Kerr metric

Odele Straub

Copernicus Astronomical Centre, Bartycka 18, PL-00-716 Warszawa, Poland
odele@camk.edu.pl

ABSTRACT
The innermost parts of accretion discs around black holes are subject to strong gravity and may be the realm where quasi periodic oscillations (QPOs) originate. Several X-ray binaries with known mass estimates show at high frequencies a stable QPO pair in a 3 : 2 ratio. We found that non-slender fluid tori around Kerr black holes oscillate for any given spin parameter a with lower epicyclic frequencies than free particles. These pressure corrected epicyclic frequencies of non-slender tori in Kerr metric were used to model the upper and lower QPO as a combination of radial and vertical epicyclic frequency with the Keplerian orbital frequency to estimate the black hole spin.

Keywords: Accretion discs – quasi periodic oscillations – Kerr metric – black hole spin

1 QPOS AND THE BLACK HOLE SPIN

Accretion discs are as manifold as their accreting central objects. We divide them roughly, depending on their radiative efficiency and their accretion flow, whether it is advection dominated (ADAF) or not, into different forms from geometrically thin discs to geometrically thick discs. Close to the innermost stable circular orbit (ISCO) where the gravitational field is strong, the accretion flow onto a black hole shows quasi periodic oscillations (QPOs). One way to describe such QPOs in the accretion flow is, that radial pressure gradients set up a fluid torus which supports discrete hydrodynamic modes (Abramowicz et al., 2006).

Several low mass X-ray binaries (LMXRB) show apart from broad low frequency QPOs at a few Hertz (Hz) narrow high frequency QPOs, which are observed in the kHz range and come with some remarkable properties (McClintock and Remillard, 2004). High frequency QPOs often appear in pairs of twin peaks which are, in the case of a black hole, in almost exact 3 : 2 ratio which in turn may indicate a resonance between two oscillation modes. As a matter of fact, this peculiar ratio may be explained as a non-linear resonance between two modes of disc oscillations (Kluźniak and Abramowicz, 2002). Another intriguing observation is that the very same high frequency QPOs reappear after years of quiescence in the binary system (Homan et al., 2005) after the disc has been rebuilt completely. QPO frequencies seem to be memorised and thus, are most likely determined by the central compact object.

978-80-7248-419-5

Black holes are rotating objects causing tremendous gravitational fields to literally drag space and time around themselves as they spin. Theory predicts that such astrophysical black holes are described by just two numbers: the mass M, and the angular momentum J. The dimensionless version of J,

$$a = \frac{Jc}{GM^2}\,, \tag{1}$$

is often called the black hole spin. Kerr metric describes the space-time geometry of rotating black holes in terms of these two parameters, M and $|a| < 1$. As we only observe black holes indirectly, examining from great distances radiation emitted by matter that is being accreted into a black hole, we encounter severe difficulties in accurately calculating the properties of the radiation emitted by accretion flows. And although radiation properties depend on the Kerr metric close to the black hole, and therefore contain an exact information on the black hole spin, important ingredients of the accretion physics, particularly viscosity and radiative transfer, remain not sufficiently known. Thus, estimating the black hole spin by spectral methods like fitting the observed K_α iron line profiles to these calculated (see, e.g., George and Fabian, 1991) or fitting the observed continuous electromagnetic spectra of micro-quasars when they are in quiescent states to these calculated (see, e.g., McClintock et al., 2006; Middleton et al., 2006) is not yet an affair of great precision.

We report here on a recent progress in sharpening theoretical tools needed in a very different method that is not influenced by details of the radiative transfer, but depends only on the orbital disc mechanics: fitting the observed QPO frequencies to those calculated from the QPO 3 : 2 resonance model (Abramowicz and Kluźniak, 2001; Török et al., 2005).

2 EPICYCLIC FREQUENCIES IN KERR METRIC

The relevant oscillation modes of the black hole accretion flow are the normal modes.[1] We consider the idealised configuration of a thick disc with a non-slender, constant angular momentum torus of a barotropic fluid in hydrostatic equilibrium (Blaes et al., 2007) in Kerr geometry. Slender tori behave like free particles and exhibit radial and vertical epicyclic frequencies. Non-slender tori have epicyclic frequencies which are likewise determined by linear perturbations of the stationary and axisymmetric torus equilibrium, receive however pressure corrections. The corresponding perturbation equation has been derived by Papaloizou and Pringle (1984) in Newtonian theory and by Abramowicz et al. (2006) in general relativity. In Kerr metric, the radial and vertical epicyclic frequencies for non-slender tori can be derived, as shown by Straub and Šrámková (2007), by rewriting the relativistic Papaloizou–Pringle equation as eigenvalue equation and expanding the eigenvalue problem around the torus centre in β, where

$$\beta^2 \equiv \frac{2(n+1)\,p_0}{A_0^2 r_0^2 \Omega_0^2 \rho_0} \tag{2}$$

[1] Blaes et al. (2006) derived the lowest order eigenfunctions and eigenfrequencies of relativistic slender tori.

is a dimensionless parameter which determines the thickness of the torus. The subscript zero refers to the pressure maximum located at the torus centre.

In lowest order the free particle solution is recovered, the first order vanishes and the second order adds negative corrections to both epicyclic frequencies. As a result the oscillation frequencies are for $0 < \beta \ll 1$ generally lower than for $\beta = 0$. For, e.g., a Schwarzschild black hole of ten solar masses the pressure corrected radial and vertical frequencies rise from the ISCO $\nu_r = \nu_z = 0$ to a maximum at $\nu_r(\beta) \approx 66$–72 Hz and $\nu_z(\beta) \approx 100$–180 Hz respectively, depending on the torus thickness, and then asymptotically go to the slender torus solution. The maximal thickness of the torus is the largest value of β for which the $3:2$ resonance between the oscillation modes occurs. Of course, the combination of modes responsible for the upper and lower QPO frequencies in ratio $\nu_{\rm U}:\nu_{\rm L} = 3:2$ has to be taken into account. It is obvious that with rising black hole spin both epicyclic frequencies rise but remain ever below the slender torus frequencies. Thus, a fairly thick torus around a very fast rotating black hole may have the same epicyclic frequencies as a rather slender torus around a slower spinning black hole.

3 BLACK HOLE SPIN ESTIMATION

Having these calculations in hand we can estimate the black hole spin for LMXRBs with well known black hole mass estimations. Based on the resonance model we assume that the higher and lower QPO peaks are composed of radial and vertical epicyclic frequencies and the Keplerian frequency. What we do not know, however, is the proper combination, such that we have to consider a set of plausible solutions. We studied behaviour of different combinations of radial epicyclic ω_r, vertical epicyclic ω_z and Keplerian $\omega_{\rm K}$ modes modelling the $\nu_{\rm U} : \nu_{\rm L} = 3 : 2$ resonance for a slender and slightly non-slender torus. We find that there is no combination of frequencies that would give the spin estimates consistent with the estimates obtained by the spectral fitting method. This may have two equally justifiable reasons: either we have not found the correct combination of modes yet, or the estimations are still not accurate enough. Bursa (2005) realised that the high frequency QPOs in micro-quasars are most likely due to the $3:2$ resonance between the axisymmetric vertical epicyclic mode and the one-arm non-axisymmetric radial mode, i.e., the combination $\omega_z/(\omega_{\rm K} - \omega_r)$. In this case and assuming a slightly (not maximally) non-slender torus, we predict for the micro-quasar GRO 1915+105 a black hole spin of $a = 0.5$–0.7. We conclude, however, that further investigations need to be done in what concerns the actually involved oscillation modes as well as the set-up for a thin accretion disc.

ACKNOWLEDGEMENTS

NORDITA Copenhagen/Stockholm provided two essential things: rooms and coffee for discussions with M. Abramowicz, O. Blaes and W. Kluźniak. And we acknowledge invaluable "brainstorming" with E. Šrámková, G. Török and P. Bakala. The research reported here was also supported by the Polish KBN grant N203 009 31/1466, and the Czech grant MSM 4781305903.

REFERENCES

Abramowicz, M. A., Blaes, O. M., Horák, J., Kluźniak, W. and Rebusco, P. (2006), Epicyclic oscillations of fluid bodies: Paper II. Strong gravity, *Classical Quantum Gravity*, **23**(5), pp. 1689–1696, arXiv: `astro-ph/0511375`.

Abramowicz, M. A. and Kluźniak, W. (2001), A precise determination of black hole spin in GRO J1655−40, *Astronomy and Astrophysics Lett.*, **374**, pp. L19–L21.

Blaes, O. M., Arras, P. and Fragile, P. C. (2006), Oscillation modes of relativistic slender tori, *Monthly Notices Roy. Astronom. Soc.*, **369**, pp. 1235–1252, arXiv: `astro-ph/0601379`, URL `http://adsabs.harvard.edu/abs/2006MNRAS.369.1235B`.

Blaes, O. M., Šrámková, E., Abramowicz, M. A., Kluźniak, W. and Torkelsson, U. (2007), Epicyclic Oscillations of Fluid Bodies. Paper III. Newtonian Non-Slender Torus, *Astrophys. J.*, **665**, pp. 642–653, arXiv: `0706.4483`, URL `http://adsabs.harvard.edu/abs/2007ApJ...665..642B`.

Bursa, M. (2005), High-frequency QPOs in GRO J1655−40: Constraints on resonance models by spectral fits, in S. Hledík and Z. Stuchlík, editors, *Proceedings of RAGtime 6/7: Workshops on black holes and neutron stars, Opava, 16–18/18–20 September 2004/2005*, pp. 39–45, Silesian University in Opava, Opava, ISBN 80-7248-334-X.

George, I. M. and Fabian, A. C. (1991), X-ray reflection from cold matter in active galactic nuclei and X-ray binaries, *Monthly Notices Roy. Astronom. Soc.*, **249**, pp. 352–367.

Homan, J., Miller, J. M., Wijnands, R. and Lewin, W. H. G. (2005), 2 Msec and counting: an unprecedented look at a black-hole transient in outburst, *Bull. Amer. Astronom. Soc.*, **37**(4), p. 1331, session 102.01.

Kluźniak, W. and Abramowicz, M. A. (2002), Parametric epicyclic resonance in black hole disks: QPOs in micro-quasars, arXiv: `astro-ph/0203314`.

McClintock, J. E. and Remillard, R. A. (2004), Black Hole Binaries, in W. H. G. Lewin and M. van der Klis, editors, *Compact Stellar X-Ray Sources*, Cambridge University Press, Cambridge, arXiv: `astro-ph/0306213`.

McClintock, J. E., Shafee, R., Narayan, R., Remillard, R. A., Davis, S. W. and Li, L. (2006), The Spin of the Near-Extreme Kerr Black Hole GRS 1915+105, *Astrophys. J.*, **652**(2), pp. 518–539, arXiv: `astro-ph/0606076`.

Middleton, M., Done, C., Gierliński, M. and Davis, S. W. (2006), Black hole spin in GRS 1915+105, *Monthly Notices Roy. Astronom. Soc.*, **373**(3), pp. 1004–1012, arXiv: `astro-ph/0601540v2`.

Papaloizou, J. C. B. and Pringle, J. E. (1984), *Monthly Notices Roy. Astronom. Soc.*, **208**, p. 721.

Straub, O. and Šrámková, E. (2007), Epicyclic Oscillations of Fluid Bodies: Non-Slender Torus in Kerr Metric, in preparation.

Török, G., Abramowicz, M. A., Kluźniak, W. and Stuchlík, Z. (2005), The orbital resonance model for twin peak kHz quasi periodic oscillations in microquasars, *Astronomy and Astrophysics*, **436**(1), pp. 1–8, arXiv: `astro-ph/0401464`.

Proceedings of *RAGtime 8/9, 15–19/19–21 September, 2006/2007, Hradec nad Moravicí, Opava, Czech Republic*
S. Hledík and Z. Stuchlík, editors, Silesian University in Opava, 2007, pp. 279–292

Trapping of neutrinos in brany extremely compact stars

Zdeněk Stuchlík[a], Jan Hladík and Martin Urbanec

Institute of Physics, Faculty of Philosophy & Science, Silesian University in Opava,
Bezručovo nám. 13, CZ-746 01 Opava, Czech Republic
[a] zdenek.stuchlik@fpf.slu.cz

ABSTRACT
Trapping of neutrinos in brany extremely compact stars is studied, using the simplest model with massless neutrinos and uniform-density star. The influence of bulk tension on the trapping is given for two solutions, namely with the Reissner–Nordström-type of geometry described by a single brany parameter, and the second one determined by the energy density of the star and the brane tension.

Keywords: Trapping of neutrinos – brany star – brany universe

1 INTRODUCTION

It is a well-known fact that in the internal Schwarzschild spacetimes of uniform energy density with radius $R < 3GM/c^2$ bound null geodetics exist, being concentrated around the stable circular null geodesic. Moreover, it follows from the behavior of the effective potential of null geodesics in the vacuum Schwarzschild spacetimes that any spherically symmetric, static interior spacetime with radius $R < r_{\rm ph} \equiv 3GM/c^2$ admits existence of bound null geodesics. Such objects are called *extremely compact objects*.

It is of considerable interest to look for possible existence of extremely compact objects and their astrophysical relevance in the case of brany universe. However, in the Randall–Sundrum II-type braneworld, the vacuum exterior of a spherical star is not in general a Schwarzschild spacetime; moreover, there are at least two solutions becoming asymptotically flat in the Schwarzschild-like way (Germani and Maartens, 2001).

Existence of bound null geodesics in extremely compact objects has astrophysical consequences. It was shown by Abramowicz et al. (1997) that the trapped modes of gravitational waves influence instabilities in such objects. There is also other interesting problem of trapped neutrinos in the strong gravitational field of extremely compact objects. This matter should be important for the following reasons. First, a distant observer can measure suppressed neutrino flow and secondly, trapped neutrinos in the interior of the extremely compact star can influence cooling processes of this star. Cooling process could be realized,

978-80-7248-419-5

as was pinpainted in Stuchlík et al. (2004), in a "two-temperature" regime. The temperature profile in the interior of the star with no trapped neutrinos differs from the profile established in the external layer with trapped neutrinos. We can cogitate for the neutrino dominated period of cooling process that in region where trapping of neutrinos reaches the highest efficiency (external layer near the radius of stable null circular geodesic) the temperature acquires higher values in comparison with the interior of the star. It is possible that such a non-uniformity leads to an inflow of heat from the external layer to the interior of the star. Such a process could influence the structure of the star. It can even end in developing of "self-organized" structures (Stuchlík et al., 2004). Therefore the standard picture given by Weber and Glendenning (1992) could be modified significantly.

Deep analysis of this idea requires sophisticated analytical estimates and numerical simulations. But the first step in our understanding of the role of trapped neutrinos in extremely compact stars is estimation of the efficiency of the trapping effect. This effect is determined by the ratio of trapped neutrinos to all neutrinos produced in the extremely compact object. The effect of trapping on neutrino luminosity of the star can be expressed by a luminosity trapping coefficient relating the total number of trapped neutrinos and the total number of radiated neutrinos, per unit time of distant observers. Influence on the cooling process can we rendered by a *local cooling trapping coefficient* and a *global cooling coefficient*. The first of them is given by ratio of trapped and radiated neutrinos at any radius where the trapping occurs, and the second one is given by ratio of trapped and radiated neutrinos (per unit time of distant observers) integrated over whole the region where trapping occurs.

The trapping and cooling coefficients were introduced in Stuchlík et al. (2004). They cogitated trapping in the internal Schwarzschild spacetime with uniform distribution of energy density and isotropic and uniform distribution of local neutrino luminosity. This work was complemented by estimation of the internal Schwarzschild–(anti-)de Sitter spacetimes in Stuchlík et al. (2005). Here we consider the trapping of neutrinos in the framework of the braneworld generalization of exact uniform-density solutions of effective Einstein's equations. We shall consider both of the known asymptotically flat solutions for uniform density stars (Germani and Maartens, 2001).

Section 2 contains a brief summary of the braneworld uniform density star properties. In Section 3, null geodesics of the spacetimes are given in terms of an effective potential. Section 4 is dedicated to determination of trapping neutrinos. Efficiency coefficients of the neutrino trapping are given in Section 5. In Section 6 concluding remarks are presented.

As the first approximation to solution of this problem we assume zero rest energy of neutrinos. We assume the period of evolution of the compact stars when the temperature is low enough to allow geodetical motion of neutrinos, i.e., we assume the neutrino free mean path larger than the dimension of the star R.

We shall use the high energy physics units, $\hbar = c = k_{\mathrm{B}} = 1$.

2 SPACETIME GEOMETRY

We consider stars in Randall–Sundrum II type braneworld. In the simplest case of static spherical star with uniform density the solution of effective field equations is given in Germani and Maartens (2001). The spherically symmetric metric in static Schwarzschild

coordinates reads (Misner et al., 1973)

$$\mathrm{d}s^2 = -A^2(r)\,\mathrm{d}t^2 + B^2(r)\,\mathrm{d}r^2 + r^2\,\mathrm{d}\Omega^2\,,$$

where

$$B^2(r) = \left[1 - \frac{2Gm(r)}{r}\right]^{-1}$$

and the mass function

$$m(r) = 4\pi \int_a^r \rho^{\mathrm{eff}}(r')r'^2\,\mathrm{d}r'\,,$$

while the integrating interval is taken from $a = 0$ for the interior solution and from $a = R$ for the exterior solution.

In the interior, considering the uniform distribution of energy density $\rho = \mathrm{const}$, we obtain

$$A^-(r) = \frac{\alpha}{\rho + p(r)}\,, \quad \text{where} \quad \alpha = \mathrm{const}\,.$$

Under the condition of uniform density, the interior mass function is reduced to

$$m^-(r) = M\left(1 + \frac{3M}{8\pi\lambda R^3}\right)\left(\frac{r}{R}\right)^3\,,$$

where $M = (4/3)\pi R^3\rho$. Thus

$$B^-(r) = 1/\Delta(r)\,,$$

where

$$\Delta(r) = \left[1 - \frac{2GM}{r}\left(\frac{r}{R}\right)^3\left(1 + \frac{\rho}{2\lambda}\right)\right]^{1/2}\,,$$

and the pressure radial profile is given by

$$\frac{p(r)}{\rho} = \frac{[\Delta(r) - \Delta(R)](1 + \rho/\lambda)}{3\Delta(R) - \Delta(r) + [3\Delta(R) - 2\Delta(r)]\rho/\lambda}\,,$$

with λ being the brane tension (Germani and Maartens, 2001).

There exist two exterior solutions having asymptotically the Schwarzschildian character. The first one is the Reissner–Nordström-like solution given by

$$(A^+)^2 = (B^+)^{-2} = 1 - \frac{2G\mathcal{M}}{r} + \frac{q}{r^2}\,.$$

The matching condition implies the brany parameter q to be given by (see Germani and Maartens, 2001)

$$q = -\frac{3GMR\rho}{\lambda}\,,$$

the effective gravitational mass

$$\mathcal{M} = M\left(1 - \frac{\rho}{\lambda}\right),$$

and

$$\alpha = \rho\Delta(R).$$

Since we require $\mathcal{M} > 0$, the condition on the brane tension in the form $\lambda > \rho$ must be satisfied.

The second exterior solution is given by (Germani and Maartens, 2001)

$$(A^+)^2 = 1 - \frac{2G\mathcal{N}}{r},$$

$$(B^+)^{-2} = (A^+)^2\left[1 + \frac{C}{\lambda(r - 3/2G\mathcal{N})}\right].$$

From the matching conditions we arrive to the expressions

$$\mathcal{N} = M\,\frac{1 + 2\rho/\lambda}{1 + 3GM\rho/R\lambda},$$
$$C = 3GM\rho\,\frac{1 - 3GM/2R}{1 + 3GM\rho/R\lambda},$$
$$\alpha = \frac{\rho\Delta(R)}{(1 + 3GM\rho/R\lambda)^{1/2}}.$$

3 NULL GEODESICS AND EFFECTIVE POTENTIAL

We assume free motion of massless neutrinos. Such neutrinos are moving along null geodesics. Their 4-momentum p^μ satisfies the equation

$$\frac{\mathrm{D}p^\mu}{\mathrm{d}\lambda} = 0$$

with the normalization condition

$$p^\mu p_\mu = 0.$$

The orbits in a central force field lie in a central plane. For a single particle it is reasonable to choose the equatorial plane ($\theta = \pi/2$ and $\mathrm{d}\theta/\mathrm{d}\lambda = 0$). Both the considered metrics are time independent and spherically symmetric. Each symmetry in the metric corresponds to a Killing vector field, i.e., the temporal ($\partial/\partial t$) vector field and the azimuthal one ($\partial/\partial\phi$). The related conserved quantities represent the projection of the neutrino 4-momentum

$$E = -p_t\,, \quad L = p_\phi\,,$$

where E is the energy and L is the axial angular momentum.

It is useful to describe null geodesics in terms of the *impact parameter*

$$\ell = \frac{L}{E}\,.$$

The relevant equation governing the radial motion then reads

$$(p^r)^2 = A^{-2}(r)B^{-2}(r)E^2\left(1 - A^2(r)\frac{\ell^2}{r^2}\right),$$

and the radial motion is restricted by an effective potential defined for the external and the internal spacetime separately

(1) for the Reissner–Nordström-like exterior solution

$$\ell^2 \leq \begin{cases} V_{\rm eff}^{\rm int} = \Delta^{-2}(R)r^2\left(1 + \frac{p(r)}{\rho}\right)^2 & \text{for} \quad r \leq R\,, \\ V_{\rm eff}^{\rm ext} = r^2\left\{1 - \frac{GM}{r}\left[2 - \frac{\rho}{\lambda}\left(2 - \frac{3R}{r}\right)\right]\right\}^{-1} & \text{for} \quad r > R\,, \end{cases}$$

(2) for the second exterior solution

$$\ell^2 \leq \begin{cases} V_{\rm eff}^{\rm int} = \Delta^{-2}(R)(1 + \frac{3GM}{R}\frac{\rho}{\lambda})r^2(1 + \frac{p(r)}{\rho})^2 & \text{for} \quad r \leq R\,, \\ V_{\rm eff}^{\rm ext} = r^2\left\{1 - \frac{2GM}{r}\left(\frac{1+\frac{2\rho}{\lambda}}{1+\frac{3GM}{R}\frac{\rho}{\lambda}}\right)\right\}^{-1} & \text{for} \quad r > R\,. \end{cases}$$

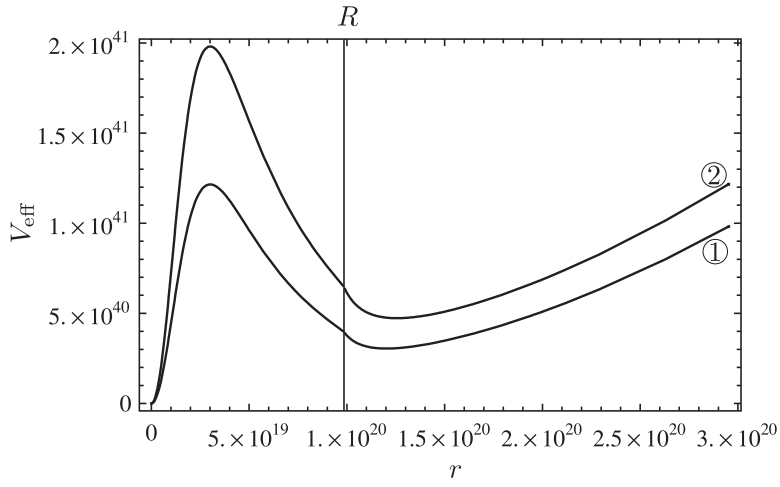

Figure 1. The behaviour of the effective potential for typical neutron star with $\rho \sim 10^9\,\mathrm{MeV}^4$, $M \sim 4 \times 10^{57}\,\mathrm{GeV}^4$, with the brane tension $\lambda = 1.3 \times 10^9\mathrm{MeV}^4$. The numbers 1 and 2 depict the type of the brany solution.

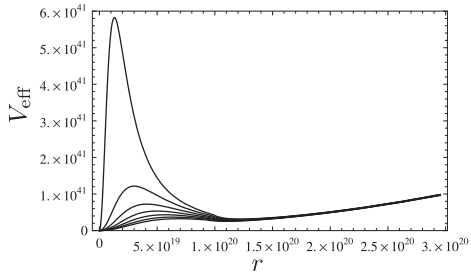

Figure 2. Behaviour of $V_{\rm eff}$ for the first type of the brany solution with $\lambda = 1.3 \times 10^9$ MeV^4, $\rho = 10^9$ MeV^4, $M \in (3.5\text{–}4.1) \times 10^{57}$ GeV^4.

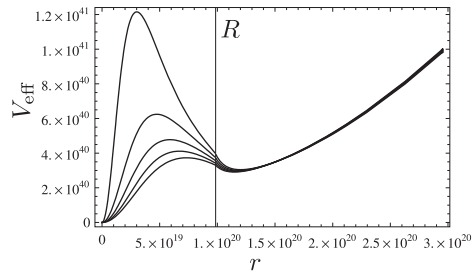

Figure 3. Behaviour of $V_{\rm eff}$ for the first type of the brany solution with $\lambda \in (1.3\text{–}1.7) \times 10^9$ MeV^4, $\rho = 10^9$ MeV^4, $M = 4 \times 10^{57}$ GeV^4.

Circular null geodesics are given by the local extrema of the effective potential $V_{\rm eff}$. Typical behaviour of the effective potential is depicted in Fig. 1. Figures 2 and 3 demonstrate the influence of varying values of the parameters M or λ on the behaviour of the effective potential $V_{\rm eff}$ in the Reissner–Nordström-like spacetimes.

4 TRAPPING OF NEUTRINOS

We can see that the stable bound null geodesics can exist in both spacetimes. Thus, some part of produced neutrinos is prevented from escaping such static objects. The stable circular null geodesics of the internal spacetime are located on the radius we denote $r_{\rm c(i)}$. The local minimum of $V_{\rm eff}^{\rm ext}$ at $r_{\rm c(e)}$ corresponds to the unstable circular null geodesic of the external spacetime, where we get for the related impact parameter the following prescriptions:

(1) for the Reissner–Nordström-like exterior solution

$$\ell_{\rm c(e)}^2 = \frac{\left[3GM(\lambda-\rho)+\sqrt{24GMR\rho\lambda+9G^2M^2(\lambda-\rho)^2}\right]^4}{8GM\lambda^2\left\{3GM(\lambda-\rho)^2+6R\rho\lambda+\sqrt{3GM[3GM(\lambda-\rho)^2+8R\lambda\rho]}(\lambda-\rho)\right\}},$$

(2) for the second exterior solution

$$\ell_{\rm c(e)}^2 = 27G^2M^2\left(\frac{1+2\frac{\rho}{\lambda}}{1+\frac{3GM}{R}\frac{\rho}{\lambda}}\right)^2.$$

4.1 Regions of trapping

In principle, bound neutrinos may appear outside the extremely compact objects, but they are trapped by the strong gravitational field of these objects and they enter them again. For this reason it is useful to divide the trapped neutrinos into two families (see Fig. 4).

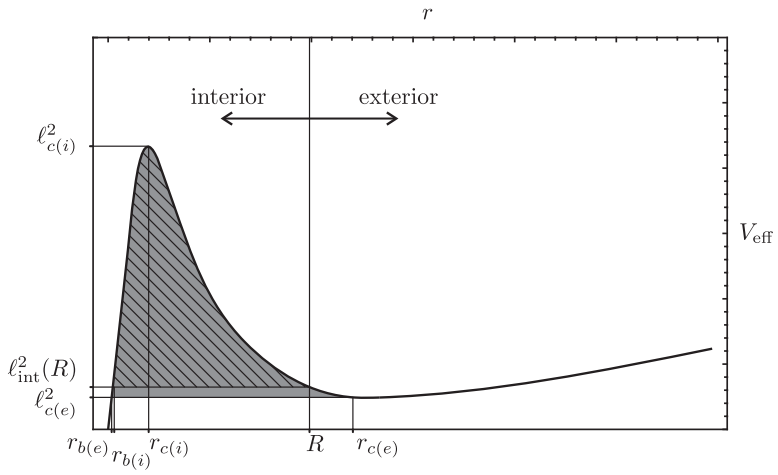

Figure 4. Illustrative scheme of the effective potential $V_{\rm eff}$ with parts corresponding to the trapped neutrinos.

(1) *Internal bound neutrinos:* Their motion is restricted inside the object; they correspond to the upper part of the shadow area in Fig. 4, having impact parameter between $\ell^2_{\rm int}(R)$ and $\ell^2_{\rm c(i)}$.

(2) *External bound neutrinos:* May leave the object, but they re-enter the object; depicted by the lower part of the shadow area in Fig. 4, having impact parameter between $\ell^2_{\rm c(e)}$ and $\ell^2_{\rm int}(R)$.

The cooling process can slow down by the bound neutrinos with mean free path higher than the radius R. From Weber and Glendenning (1992) we know that this condition is fulfilled in a few days old neutron stars. Of course, such neutrinos will be re-scattered due to finiteness of the mean free path.

The nature of re-scattering effect on the trapped neutrinos is a complex process. Numerical methods simulating such processes could be based on the Monte Carlo methods. This concerns only neutrinos produced above $r_{\rm b(e)}$ that can be re-scattered. Those produced below $r_{\rm b(e)}$ freely escape to infinity.

4.2 Directional angles

If we consider an equatorial motion, we can define the *directional angle* relative to the outward pointed radial direction measured in the emitter system (i.e., the local system of static observers in the internal spacetime) by the relations

$$\sin\psi = \frac{p^{(\phi)}}{p^{(t)}}\,, \quad \cos\psi = \frac{p^{(r)}}{p^{(t)}}\,,$$

where

$$p^{(\alpha)} = p^{\mu}\omega_{\mu}^{(\alpha)}\,, \quad p_{(\alpha)} = p_{\mu}e_{(\alpha)}^{\mu}$$

are the neutrino 4-momentum components as measured by static observers.[1] Because $p_\theta = 0$, there is

$$p^{(\phi)} = \frac{L}{r}\,, \qquad p^{(t)} = \frac{E}{A(r)}\,.$$

We obtain the directional angles in the form

$$\sin\psi = A(r)\,\frac{\ell}{r}\,, \quad \cos\psi = \pm(1-\sin^2\psi)^{1/2}\,.$$

The interval of relevant radii is $r \in (r_{\mathrm{b(e)}}, R)$. The impact parameter $\ell^2_{\mathrm{c(e)}}$ determines the directional angle limit for the bound neutrinos. For two metrics under consideration we get limiting angles

$$\sin\psi_{\mathrm{e}} = \frac{A(r)}{\sqrt{8GMr\lambda}} \times \frac{\left[3GM(\lambda-\rho)+\sqrt{24GMR\rho\lambda+9G^2M^2(\lambda-\rho)^2}\right]^2}{\left\{3GM(\lambda-\rho)^2+6R\rho\lambda+\sqrt{3GM[3GM(\lambda-\rho)^2+8R\lambda\rho]}\,(\lambda-\rho)\right\}^{1/2}}\,, \quad (1)$$

for the Reissner–Nordström-like solution and

$$\sin\psi_{\mathrm{e}} = \frac{A(r)}{r}\,3\sqrt{3}\,GM\,\frac{1+2\frac{\rho}{\lambda}}{1+\frac{3GM}{R}\frac{\rho}{\lambda}}\,. \quad (2)$$

for the second solution. Conspicuously, the condition $\psi_{\mathrm{i}} > \psi_{\mathrm{e}}$ holds at any given radius $r < R$.

4.3 Local escaped to produced neutrino ratio

We assume that neutrinos are locally produced by isotropically emitting sources. Then the escaped-to-produced-neutrinos ratio depends on geometrical argument only. This ratio is determined by the solid angle 2Ω corresponding to escaping neutrinos. Inward emitted neutrinos could not be omitted as they can be radiated away, as indicated in Fig. 5.

Labelling the number of produced, escaped and trapped neutrinos per unit time of an external static observer at infinity as N_{p}, N_{e} and N_{b}, we introduce the global correction factors by relations

$$\mathcal{E}(R,\lambda) \equiv \frac{N_{\mathrm{e}}(R,\lambda)}{N_{\mathrm{p}}(R,\lambda)}\,, \quad \mathcal{B}(R,\lambda) \equiv \frac{N_{\mathrm{b}}(R,\lambda)}{N_{\mathrm{p}}(R,\lambda)}\,.$$

[1] The tetrads of 1-forms $\omega_{\mu}^{(\alpha)}$ and 4-vectors $e_{(\alpha)}^{\mu}$ related to static observers have to be used (Hledík, 2002; Stuchlík, 2002).

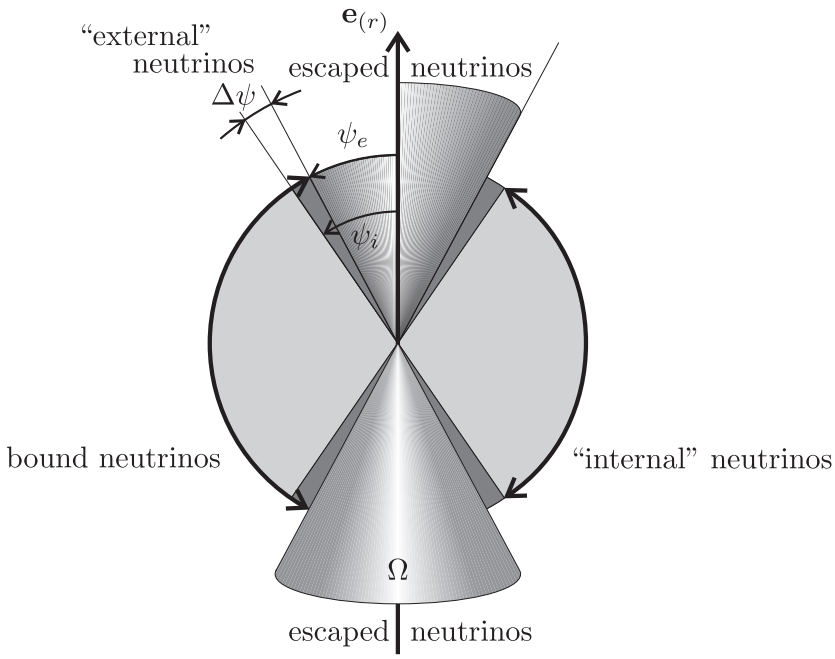

Figure 5. Guide illustration of the bound-escape ratio at radius $r \in (r_{\mathrm{b(e)}}, R)$ in the internal spacetime. Direction of the neutrino motion with respect to the static observers is related to $e_{(\mathrm{r})}$ giving the outward oriented radial direction. Figure taken from (Stuchlík et al., 2004).

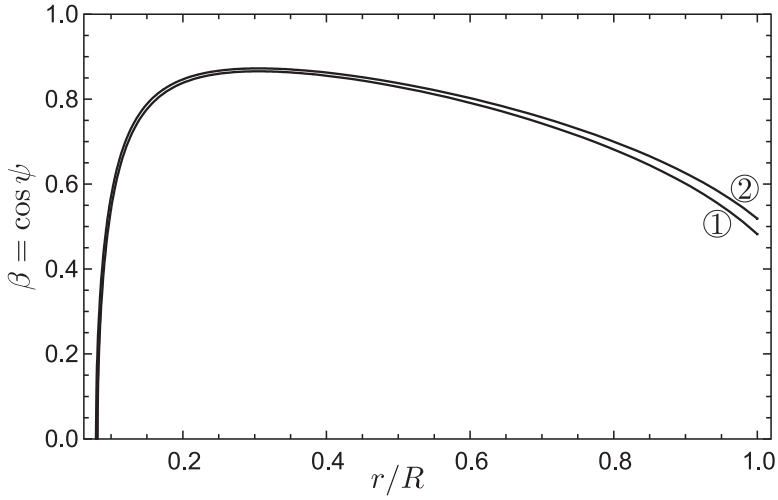

Figure 6. Local coefficient of cooling β; for typical neutron star $\rho \sim 10^9$ MeV^4, $M \sim 4 \times 10^{57}$ GeV^4; $\lambda = 1.3 \times 10^9$ MeV^4 for both spacetimes under consideration.

It is useful to introduce the local correction factor for escaping neutrinos at a given radius $r \in (r_{\mathrm{b(e)}}, R)$. The solid angle $2\Omega_{\mathrm{e}}(\psi_{\mathrm{e}})$ completely determines the ratio of escaped-produced neutrinos. In the case of non-isotropic emission of neutrinos it is reasonable to define this angle by relation

$$\Omega_{\mathrm{e}}(\psi_{\mathrm{e}}) = \int_0^{\psi_{\mathrm{e}}} \int_0^{2\pi} p(\psi) \sin\psi \, \mathrm{d}\psi \mathrm{d}\phi \,,$$

where $p(\psi)$ is directional function of emission (scattering) process.

In our approximation with isotropically emitting sources of neutrinos, the escape solid angle is given simply by

$$\Omega_{\mathrm{e}}(\psi_{\mathrm{e}}) = \int_0^{\psi_{\mathrm{e}}} \int_0^{2\pi} \sin\psi \, \mathrm{d}\psi \mathrm{d}\phi = 2\pi(1 - \cos\psi_{\mathrm{e}}) \,,$$

and the escaping correction factor reads

$$\epsilon(r, R, \lambda) = \frac{\mathrm{d}N_{\mathrm{e}}(r, \lambda)}{\mathrm{d}N_{\mathrm{p}}(r, \lambda)} = 1 - \cos\psi_{\mathrm{e}}(r, R, \lambda) \,.$$

The complementary factor for trapped neutrinos is given by

$$\beta(r, R, \lambda) = 1 - \epsilon(r, R, \lambda) = \frac{\mathrm{d}N_{\mathrm{b}}(r, \lambda)}{\mathrm{d}N_{\mathrm{p}}(r, \lambda)} = \cos\psi_{\mathrm{e}}(r, R, \lambda) \,.$$

The coefficient $\beta(r, R, \lambda)$ determines the local efficiency of the neutrino trapping. The local maxima of the function $\beta(r, R, \lambda)$ (with R, λ being fixed) are given by the condition $\partial\beta/\partial r = 0$ which is satisfied at radius $r = r_{\mathrm{c(i)}}$. This implies coincidence with the radius of the stable circular null geodesic.

Figure 6 demonstrates the behaviour of local cooling coefficient β for both estimated spacetimes.

4.4 Neutrino production rates

The neutrino production is a complex process depending on detailed structure of an extremely compact object. It is possible to express the locally defined neutrino production rate in the form

$$\ell(r\{\mathcal{A}\}) = \frac{\mathrm{d}N(r\{\mathcal{A}\})}{\mathrm{d}\tau(r)} \,,$$

where $\mathrm{d}N$ is the number of interactions at radius r, τ is the proper time of the static observer at the given r, $\{\mathcal{A}\}$ is the full set of quantities relevant for the production rate. The number of interactions can be written in the form

$$\mathrm{d}N(r) = n(r)\Gamma(r)\,\mathrm{d}V(r) \,,$$

where $n(r)$, $\Gamma(r)$ and $\mathrm{d}V(r)$ are the number density of particles entering the neutrino production processes, the neutrino production rate and the proper volume element at the

radius r, respectively. Functions $n(r)$ and $\Gamma(r)$ are given by detailed structure of the object, $\mathrm{d}V(r)$ is given only by the spacetime geometry.

We shall assume, considering the uniform density stars, the local production rate to be proportional to the energy density and therefore we can rewrite the local neutrino production rate to the form

$$\ell(r) = \frac{\mathrm{d}\mathcal{N}}{\mathrm{d}\tau} \propto \rho = \mathrm{const}\,.$$

The local neutrino production rate related to the distant static observers is given by the relation including the time-delay factor

$$I = \frac{\mathrm{d}N}{\mathrm{d}t} = \ell A(r)\,.$$

The number of neutrinos produced at a given radius in a proper volume $\mathrm{d}V$ per unit time of a distant static observer is given by the relation

$$\mathrm{d}N_{\mathrm{p}}(r) = I(r)\,\mathrm{d}V(r) = 4\pi\ell A(r)B(r)r^2\,\mathrm{d}r\,.$$

Integrating through the compact object, we arrive to the global neutrino production rate

$$N_{\mathrm{p}}(R) = 4\pi\ell\int_0^R [A^-(r)B^-(r)]r^2\,\mathrm{d}r\,,$$

and in an analogical way, we can give the expression for the global rates of escaping and trapping of the produced neutrinos in the form

$$N_{\mathrm{e}}(R) = 4\pi\ell\int_{r_{\mathrm{b(e)}}}^R (1-\cos\psi_{\mathrm{e}})[A^-(r)B^-(r)]\,r^2\,\mathrm{d}r + N_{\mathrm{p}}(r_{\mathrm{b(e)}})\,,$$

$$N_{\mathrm{b}}(R) = 4\pi\ell\int_{r_{\mathrm{b(e)}}}^R \cos\psi_{\mathrm{e}}[A^-(r)B^-(r)]\,r^2\,\mathrm{d}r\,.$$

5 EFFICIENCY OF NEUTRINO TRAPPING

To characterize the efficiency of neutrino trapping, we introduce some coefficients describing the trapping effect in connection to the total neutrino luminosity and the cooling process in the period of the evolution of the star corresponding to the geodetical motion of neutrinos.

5.1 Trapping coefficient of total neutrino luminosity

The influence of the trapping effect on the total neutrino luminosity can be appropriately given by the coefficient $\mathcal{B}_{\mathrm{L}}$ defined by the relation

$$\mathcal{B}_{\mathrm{L}} = \frac{N_{\mathrm{b}}}{N_{\mathrm{p}}}\,.$$

The coefficient relates the number of neutrinos produced inside the whole compact star during unit time of distant observer and the number of those of the produced neutrinos that will be captured by the gravitational field of the star.

The complementary "escaping" luminosity coefficient is then determined by

$$\mathcal{E}_{\mathrm{L}}(R) = 1 - \mathcal{B}_{\mathrm{L}}(R)\,.$$

It is useful, moreover, to define other global coefficients: for the "internal" neutrinos with motion restricted to the interior of the star by

$$\mathcal{Q}_{\mathrm{L}}(R) = \frac{N_{\mathrm{int}}}{N_{\mathrm{p}}}$$

and for the "external" neutrinos by a a complementary coefficient

$$\chi_{\mathrm{L}} = \frac{N_{\mathrm{ext}}}{N_{\mathrm{p}}} = \mathcal{B}_{\mathrm{L}} - \mathcal{Q}_{\mathrm{L}}\,.$$

After numerical calculation we get for typical neutron star ($\rho \sim 10^9\,\mathrm{MeV}^4$, $M \sim 4 \times 10^{57}\,\mathrm{GeV}^4$) with brany tension fixed at $\lambda = 1.3 \times 10^9\,\mathrm{MeV}^4$ the value $\mathcal{B}_{\mathrm{L}} = 0.644$ for the first type of spacetime solution and $\mathcal{B}_{\mathrm{L}} = 0.666$ for the second type of solution. What is really interesting is the strong dependence of $\mathcal{B}_{\mathrm{L}}$ and $\mathcal{Q}_{\mathrm{L}}$ on the brane tension λ (see Fig. 7). As mentioned in Germani and Maartens (2001), from the big bang nucleosynthesis we know that $\lambda \gtrsim 1\,\mathrm{MeV}^4$. Stronger bound arises from negative results of sub-millimetre tests of Newton's law $\lambda \gtrsim 10^8\,\mathrm{GeV}^4$. The existence of neutron stars leads us to put the value of λ somewhere between these limits.

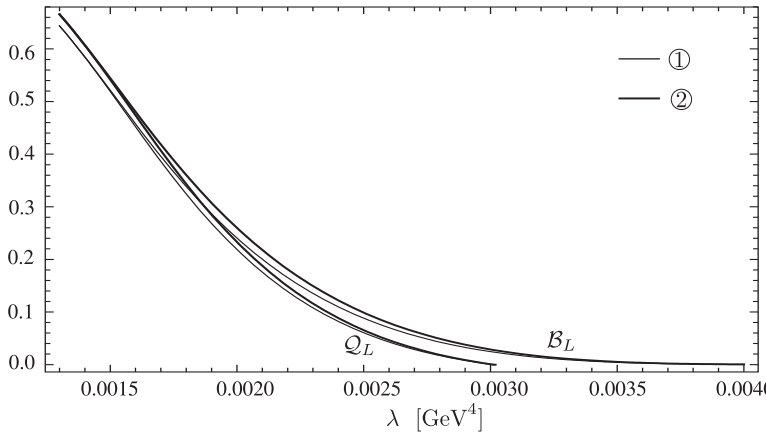

Figure 7. Dependence of $\mathcal{B}_{\mathrm{L}}$ and $\mathcal{Q}_{\mathrm{L}}$ on brane tension λ ($\rho \sim 10^9\,\mathrm{MeV}^4$, $M \sim 4 \times 10^{57}\,\mathrm{MeV}^4$) for both estimated spacetimes.

5.2 Trapping coefficient of neutrino cooling process

The efficiency of the influence of neutrino trapping on the cooling process is most effectively described by the local coefficient of trapping b_c relating the captured and produced neutrinos at a given radius of the star, i.e., we can define

$$b_c \equiv \beta(r; R) .$$

The behaviour of the local cooling coefficient is shown in Fig. 6. As intuitively expected, the maximum of $b_c(r; R)$ for a given R is located at the radius of the stable null circular geodesics.

The cooling process could be appropriately described likewise in a complementary manner by a global coefficient for trapping, restricted to the "active" zone, where the trapping of neutrino occurs.

6 CONCLUSION

We have demonstrated how the trapping effect by strong gravitational field of extremely compact stars can influence the total neutrino luminosity and cooling process. It is straightforward that the trapping of neutrinos can play an modified role in the case of Schwarzschild–(anti-)de Sitter spacetimes, as has been investigated in details by Stuchlík et al. (2005), as well as in the case of extremely compact stars in the brany universe. We used only "toy" model of real-world situation, but the working out foreshadows its relevance in realistic models of extremely compact objects. Especially, if we consider the cumulative nature of this phenomenon. Another step on this way should be accomplished by studying polytropic structures (Tooper, 1964; Stuchlík, 2002; Stuchlík and Hledík, 2005; Hledík et al., 2007; Mrázová et al., 2005).

We would like to give prominence to dependence of luminosity trapping coefficient on the value of brane tension. Today, we do not know its exact value. So it is a question if the trapping effect could be used for estimating the brany tension from future observations, but the subsequent task is how cooling process will be modified by cumulation of neutrinos in more realistic models of neutron or quark stars.

ACKNOWLEDGEMENTS

The presented work was supported by the Czech grants MSM 4781305903, LC06014 and GAČR 205/03/H144. One of the authors (Z. S.) would like to express his gratitude to Czech Committee for collaboration with CERN for support and CERN Theory Division for perfect hospitality.

REFERENCES

Abramowicz, M. A., Anderson, N., Bruni, M., Ghosh, P. and Sonego, S. (1997), Gravitational waves from ultracompact stars: the optical geometry view of trapped modes, *Classical Quantum Gravity*, **14**, p. L189.

Germani, C. and Maartens, R. (2001), Stars in the braneworld, *Phys. Rev. D*, **64**, p. 124010, arXiv: `hep-th/0107011`.

Hledík, S. (2002), Optical geometry, inertial forces, and embedding diagrams, in Semerák et al. (2002), pp. 161–192.

Hledík, S. and Stuchlík, Z., editors (2005), *Proceedings of RAGtime 6/7: Workshops on black holes and neutron stars, Opava, 16–18/18–20 September 2004/2005*, Silesian University in Opava, Opava, ISBN 80-7248-334-X.

Hledík, S., Stuchlík, Z. and Mrázová, K. (2007), Dynamical stability of fluid spheres in spacetimes with a nonzero cosmological constant, in M. Novello and S. Perez Bergliaffa, editors, *Proceedings of The Eleventh Marcel Grossmann Meeting on Recent Developments in Theoretical and Experimental General Relativity, Gravitation and Relativistic Field Theories, Berlin, Germany, 20–26 July 2006*, World Scientific, Singapore, ISBN 981-256-667-8 (Set), 981-256-980-4 (Part A), 981-256-979-0 (Part B), 981-256-978-2 (Part C), series Ed. R. Ruffini.

Misner, C. W., Thorne, K. S. and Wheeler, J. A. (1973), *Gravitation*, W. H. Freeman and Co, New York, San Francisco.

Mrázová, K., Hledík, S. and Stuchlík, Z. (2005), Games with polytropes and adiabates, in Hledík and Stuchlík (2005), pp. 109–117.

Semerák, O., Podolský, J. and Žofka, M., editors (2002), *Gravitation: Following the Prague Inspiration (A Volume in Celebration of the 60th Birthday of Jiří Bičák)*, World Scientific, New Jersey, London, Singapore, Hong Kong, ISBN 981-238-093-0.

Stuchlík, Z. (2002), The role of a repulsive cosmological constant in astrophysical processes, in Semerák et al. (2002), pp. 27–83.

Stuchlík, Z. and Hledík, S. (2005), Radial pulsations and dynamical stability of spherically symmetric perfect fluid configurations in spacetimes with a nonzero cosmological constant, in Hledík and Stuchlík (2005), pp. 209–222.

Stuchlík, Z., Török, G. and Hledík, S. (2004), Trapping of neutrinos in extremely compact stars, in S. Hledík and Z. Stuchlík, editors, *Proceedings of RAGtime 4/5: Workshops on black holes and neutron stars, Opava, 14–16/13–15 October 2002/2003*, pp. 257–269, Silesian University in Opava, Opava, ISBN 80-7248-242-4.

Stuchlík, Z., Urbanec, M. and Török, G. (2005), Trapping of neutrinos in the internal Schwarzschild–(anti-)de Sitter spacetimes, in Hledík and Stuchlík (2005), pp. 265–280.

Tooper, R. F. (1964), General relativistic polytropic fluid spheres, *Astrophys. J.*, **140**(2), pp. 434–459.

Weber, F. and Glendenning, N. K. (1992), Application of the improved Hartle method for the construction of general reletivistic rotating neutron star models, *Astrophys. J.*, **390**(2), pp. 541–549, ISSN 0004-637X, research supported by Max Kade Foundation, URL `http://adsabs.harvard.edu/abs/1992ApJ...390..541W`.

Proceedings of *RAGtime 8/9, 15–19/19–21 September, 2006/2007, Hradec nad Moravicí, Opava, Czech Republic*
S. Hledík and Z. Stuchlík, editors, Silesian University in Opava, 2007, pp. 293–322

Excitation of oscillations in accretion discs orbiting compact objects

Zdeněk Stuchlík[1], Sushan Konar[2], John C. Miller[3,4] and Stanislav Hledík[1]

[1] Institute of Physics, Faculty of Philosophy & Science, Silesian University in Opava, Bezručovo nám. 13, CZ-746 01 Opava, Czech Republic
[2] Centre for Theoretical Studies, Indian Institute of Technology, Kharagpur 721 302, India
[3] SISSA, International School for Advanced Studies and INFN, Via Beirut 2–4, I-34014, Trieste, Italy
[4] Department of Physics (Astrophysics), University of Oxford, Keble Road, Oxford OX1 3RH, England

ABSTRACT

High-frequency QPOs in neutron-star binary systems could be explained by models based on parametric or forced resonance between oscillation modes of the accretion disc around the neutron star (with frequencies related to the Keplerian and epicyclic frequencies of the disc) and the relative rotational motion between the disc material and either the neutron star or the binary companion.

Using Newtonian theory, we discuss the possibility of forced resonant phenomena being excited by means of gravitational perturbations coming from surface features on the neutron star and from the companion star. For each potential perturbation source, we have determined the Fourier decomposition of the gravitational perturbing forces acting on disc elements in the radial and vertical directions. The analysis presented for the binary companion can be applied also to black hole systems but the surface features would not be present in that case.

The oscillations induced by the binary partner are of a different character from those which would be induced by a mountain or by the accretion columns. In the case of symmetric accretion columns, the excitation frequency in the radial direction is twice that in the vertical direction and higher order modes could be relevant for parts of the disc very close to the neutron star. In this inner region, the influence of the accretion columns is greater than that of the binary companion for producing forced oscillations in both the radial and vertical directions; in the intermediate part, the vertical oscillations are induced by the accretion columns while the radial oscillations are excited by the binary partner (if appropriate conditions are fulfilled); sufficiently far from the neutron star, the binary companion has the greater effect. The limits on the magnitude of neutron star deformations given by the possibility to excite observable QPOs coincide with restrictions coming from (non-)observations of gravitational waves by LIGO.

Keywords: Neutron stars – binary systems – QPOs – accretion discs

978-80-7248-419-5

1 INTRODUCTION

Quasi-periodic oscillations (QPOs) of X-ray brightness have been observed in a number of accreting binary systems containing neutron stars (see van der Klis, 2000; Belloni et al., 2005; Homan et al., 2002; Barret et al., 2005 for a review) and black holes (Remillard, 2005; Remillard and McClintock, 2006) both at low frequencies (Hz) and at high frequencies (kHz). For the kHz QPOs, the spectrum often shows twin peaks at frequencies correlated with the X-ray intensity. The ratio of the twin peak frequencies observed in black-hole systems is exactly, or almost exactly 3 : 2 (Török, 2005b), while in the neutron star systems the ratio is concentrated around 3 : 2, but has a much wider range than for the black-hole systems. An anticorrelation effect has been noted for the neutron-star systems, giving an indication of the likely relevance of resonant phenomena (Abramowicz et al., 2005b). In each of the neutron-star systems, there is a linear relation between the upper and lower twin peak frequencies ($\nu_{\rm U}$ and $\nu_{\rm L}$)

$$\nu_{\rm U} = A\nu_{\rm L} + B\,, \tag{1}$$

and the slope A and the shift B are anti-correlated following the relation

$$A \approx \frac{3}{2} - \frac{B}{600\,\mathrm{Hz}}\,, \tag{2}$$

pointing to an intersection whose frequencies [~ 600 Hz, ~ 900 Hz] can be interpreted as the oscillation eigenfrequencies $\nu_{\rm U}^{\rm o}$, $\nu_{\rm L}^{\rm o}$ having the 3 : 2 ratio. The anticorrelation is predicted by the resonance model and is observed for the twelve neutron-star systems for which we have the relevant data (Abramowicz et al., 2005a,b).

Török discovered a significant effect concerning the relative energies of the upper and lower frequency oscillations that suggests a significant role for forced resonant phenomena (Török and Stuchlík, 2005b; Török et al., 2006; Török, 2007; Török and Barret, 2007). He showed that in the neutron star systems, the energy difference between the upper and lower twin peak oscillations (characterized by the rms amplitude difference between the twin peaks) is zero for the resonant frequency ratio 3 : 2 at a specific (lower) frequency $\nu_{\rm l}^{3:2}$ which is fixed for a particular system, while it is positive for frequencies below $\nu_{\rm l}^{3:2}$ and negative for frequencies above it with a dependence on the lower frequency given by the "Török curve" which has a sinusoidal shape. Up to now, Török curves have been determined for three neutron-star systems: 4U 1728−34, 4U 1608−522, 4U 1636−536 (Török et al., 2006). It is probably significant that when the energy difference is given in terms of the frequency ratio $\nu_{\rm U} : \nu_{\rm L}$ ($\nu_{\rm U} : \nu_{\rm L} \gtrless 3 : 2$ for $\nu_{\rm L} \lesseqgtr \nu_{\rm L}^{3:2}$) there seems to be an identical Török curve for all of the systems under consideration (Török and Barret, 2007), which is relatively well defined in the range $\nu_{\rm U} : \nu_{\rm L} \in (1.25, 1.7)$. This result, if confirmed by studies of other neutron-star systems, would indicate the general relevance both of the Török energy-switch effect at the frequency ratio $\nu_{\rm U} : \nu_{\rm L} = 3 : 2$, and of the functional dependence of the energy difference on the frequency ratio throughout the above interval. Therefore we could expect

the effectiveness of pumping energy into the upper and lower frequency oscillations by a forced resonance to be dependent on the frequency ratio (Török and Stuchlík, 2005a).[1]

In some black-hole sources, other small-integer frequency ratios have been observed (e.g., in microquasar GRS 1915+105 by Belloni et al. (2001); Strohmayer (2001); Remillard (2004) or extragalactic black hole NGC 5408 by Strohmayer et al. (2007)), but the evidence for them is usually not as clear as in the case of the 3 : 2 ratio (Abramowicz et al., 2004). The resonant oscillation model (Abramowicz and Kluźniak, 2001) seems to be promising for explaining QPOs in both black-hole and neutron-star systems (Abramowicz et al., 2005b; Török et al., 2005; Kluźniak et al., 2007) and even in Sgr A* (Török, 2005a). However, other possibilities, such as the relativistic precession model for neutron stars (Stella and Vietri, 1999), oscillations of a warped disc (Kato and Fukue, 1980; Kato, 2004a,b) or simple *p*-mode oscillations of fluid tori (Rezzolla, 2004; Rezzolla et al., 2003) also remain viable. Nevertheless, in all of the models, forcing of the oscillations should be addressed.

In order to initiate the oscillations and the resonance phenomena, it is necessary to have some internal and/or external perturbation mechanism. One example of an internal mechanism is the so-called Aschenbach effect, related to the presence of a hump in the velocity profile of the disc, as measured by locally non-rotating observers (Bardeen, 1973), which appears both for thin, Keplerian discs (Aschenbach, 2004, 2006) and for thick tori (Stuchlík et al., 2004, 2005, 2006, 2007a,b) orbiting extremely rapidly rotating black holes; the so-called extended resonant model is then able to explain all five high-frequency QPOs observed in GRS 1915+105 (Stuchlík et al., 2007c). The relevance of this effect still remains to be clarified by detailed studies, however. Other examples of internal mechanisms include oscillation modes of warped thin discs (Kato and Fukue, 1980) or turbulent motions in the disc. Possible external mechanisms include the effects of gravitational perturbations caused by the binary partner or, in the case of neutron-star systems, by asymmetries of the neutron star. Other possibilities include perturbations caused by an orbiting satellite or by a neutron-star magnetic field.

Here, we focus on neutron-star systems and on external perturbations caused by the binary partner or by asymmetries of the neutron star. These two types of perturbation clearly induce different behaviours: the frequency of the force arising from the influence of the binary partner (the difference between the rotational frequency of the disc and the orbital frequency of the binary partner) is essentially equal to the disc rotation-frequency, since this exceeds the orbital frequency by many orders of magnitude, whereas the frequency of the force caused by asymmetries of the neutron star is equal to the difference between the rotation frequencies of the disc and of the neutron star (Pétri, 2005). We give estimates on the forcing magnitude implied by the restrictions given by deformations of the neutron stars.

[1] Quite recently, it has been shown that multi-resonant phenomena could be relevant in the neutron star systems with resonant points in the frequency ratios 3 : 2 and 5 : 4 as shown by Török et al. (2007c); Stuchlík et al. (2007d,e) and Török et al. (2007a) for the 4U 1636−536 source. In some other sources (4U 1820−30 and 4U 1735−44), the frequency ratio 4 : 3 is relevant (Török, 2007). The relevance of the two resonant radii corresponding to the 3 : 2 and 5 : 4 frequency ratios has been shown also in the framework of the relativistic precession model (Stella and Vietri, 1999) by Török (2007).

2 BACKGROUND IDEAS ABOUT FORCED OSCILLATIONS

We summarise here some background ideas about forced oscillations which may not be well-known and which are fundamental for our discussion in this paper. We follow closely the presentation in Section 22 of Landau & Lifshitz *Mechanics* (Landau and Lifshitz, 1976). Consider first the idealised case of a test particle undergoing forced oscillations with the equation of motion being

$$\ddot{x} + \omega^2 x = F_{\rm p}(t)/m \,, \tag{3}$$

where x is the displacement from the mid-point of the oscillation, ω is the intrinsic oscillation frequency, m is the mass of the particle and $F_{\rm p}(t)$ is an external perturbative force which is varying with time t. We take $F_{\rm p}(t)$ to be a simple periodic function of time

$$F_{\rm p}(t) = f_{\rm p} \cos(\gamma t + \beta) \,, \tag{4}$$

where $f_{\rm p}$ is its amplitude, γ is its frequency and β is a phase constant. The motion of the particle is then given, in general, by

$$x = a \cos(\omega t + \varphi_0) + \left[\frac{f_{\rm p}}{m\left(\omega^2 - \gamma^2\right)} \right] \cos(\gamma t + \beta) \,, \tag{5}$$

where a and φ_0 are further constants whose values are fixed by the initial conditions. This is the general solution but it becomes indeterminate when *resonance* occurs ($\gamma = \omega$). To obtain the solution in that case, one can proceed by first rewriting Eq. (5) as

$$x = a \cos(\omega t + \varphi_0) + \frac{f_{\rm p}}{m} \left[\frac{\cos(\gamma t + \beta) - \cos(\omega t + \beta)}{\omega^2 - \gamma^2} \right] , \tag{6}$$

where a and φ_0 now take different values from before, and then applying l'Hôpital's rule to the contents of the square bracket to find its limit as $\gamma \to \omega$. The solution at resonance is then given by

$$x = a \cos(\omega t + \varphi_0) + \left(\frac{f_{\rm p}}{2m\omega} \right) t \, \sin(\omega t + \beta) \,, \tag{7}$$

which has a fundamentally different behaviour from the non-resonant solution, with the amplitude of the second term increasing cumulatively with time. This linear regime of forced resonance ends when the oscillation amplitude becomes large enough so that non-linear phenomena and/or dissipative processes become relevant (see Landau and Lifshitz, 1976).

We consider now the particular case of Keplerian orbital motion in the equatorial plane of a slowly-rotating compact object, with the motion being basically circular but with the possibility of having epicyclic oscillations around the circular path. We denote the frequency of the circular orbital motion at a general radius r by $\Omega_{\rm K}$ ($= \sqrt{GM/r^3}$) and write the epicyclic frequency as $\omega = \alpha \Omega_{\rm K}$ where α is, in principle, a known function of r for each particular type of epicyclic motion. If there is a periodic perturbing force acting, there will

clearly be some radius at which the frequency of the perturbing force will be in resonance with the epicyclic frequency and we focus here on that. Considering a time when the second term of Eq. (7) has grown to dominate over the first one, Eq. (7) can be re-written as

$$\left(\frac{x}{r}\right) = \frac{\pi}{\alpha}\left(\frac{f_{\rm p}}{f_0}\right)\left(\frac{t}{\tau_{\rm K}}\right)\sin(\omega t + \beta)\,, \tag{8}$$

where f_0 is the main gravitational force from the central object ($f_0 = GMm/r^2$, with M being the mass of the central object) and $\tau_{\rm K} = 2\pi/\Omega_{\rm K}$ is the period of the circular Keplerian motion. The time taken for the amplitude of the resonant oscillations $x_{\rm max}$ to grow to a particular value is then

$$t = \left(\frac{x_{\rm max}}{r}\right)\left(\frac{\alpha}{\pi}\right)\left(\frac{f_{\rm p}}{f_0}\right)^{-1}\tau_{\rm K}\,. \tag{9}$$

The discussion above is for test particle motion whereas for the context discussed in this paper one is dealing with *fluid elements* for which the situation becomes more complicated. Nevertheless, the above discussion gives an indication of how the mechanism works. For kilohertz QPOs, we are concerned with oscillations occurring in the very innermost parts of accretion discs around compact objects: we then have $\tau_{\rm K} \sim 10^{-3}$ s and also the α for radial epicyclic motion becomes small compared with unity as the marginally stable orbit is approached (this is well-known in the case of the Kerr metric and applies also in metrics appropriate for neutron stars (see, e.g., Stuchlík et al., 2007d). It then follows that the oscillation amplitude can rise rather rapidly to relevant values even when the force ratio $(f_{\rm p}/f_0)$ is quite small.

3 GRAVITATIONAL FORCE FROM THE PERTURBING SOURCES

In the case of an external excitation mechanism, the resonant phenomena are determined by coincidence of the frequency of the perturbing force, as observed in the frame comoving with the disc at a given radius, with the epicyclic frequency (radial or vertical), the orbital frequency, or a combination of these. Three kinds of resonance can be distinguished:

(1) *Corotating resonance*, when $\Omega_{\rm s} = \Omega_{\rm d}$ at some given radius r (where $\Omega_{\rm s}$ denotes the angular velocity of the gravitational perturbation source and $\Omega_{\rm d}(r)$ denotes the angular velocity profile of the accretion disc, both measured in the frame of stationary distant observers); $\Omega_{\rm s} = \Omega_{\rm ns}$ in the case where the perturbation comes from neutron-star asymmetries, $\Omega_{\rm s} \sim 0$ in the case where it comes from the binary partner of the neutron star or a black hole.

(2) *Forced (driven) resonance*, when at the given radius one of the epicyclic frequencies ω equals the frequency of some mode m of the gravitational perturbation, i.e.,

$$m|\Omega_{\rm d} - \Omega_{\rm s}| = \omega_{r(\theta)}\,.$$

Note that in the case of forced resonance, beat frequencies could also be observed (Landau and Lifshitz, 1976). If beat frequencies enter the resonance, the condition generalizes to the

form

$$m|\Omega_{\rm d} - \Omega_{\rm s}| = \frac{k}{l}\,\omega_{r(\theta)}\,,$$

where k and l are small integers.

(3) *Internal parametric resonance* related to a sinusoidally time-varying epicyclic frequency as described by the Mathieu equation (Landau and Lifshitz, 1976) and determined by the relation

$$m|\Omega_{\rm d} - \Omega_{\rm s}| = \frac{2}{n}\,\omega_{r(\theta)}\,,$$

with integer $n \geq 2$.

Naturally, the resonance conditions must be related to the restriction coming from the orbital angular velocity at the innermost stable circular orbit which determines (approximately) the inner boundary of the accretion disc if it is above the surface of the neutron star. Note that the current widely-accepted upper limit for observed neutron star rotation frequencies is $\nu_{\rm ns(max)} \sim 700$ Hz, while for the disc frequency $\nu_{\rm d(max)} \sim 1300$ Hz, and so the resonance conditions can easily be satisfied.

We assume a basically isotropic neutron star of mass $M_{\rm A}$ and radius $R_{\rm A}$ spinning about its rotation axis with angular velocity $\Omega_{\rm A}$ and with the symmetry plane of the accretion disc being orthogonal to the rotation axis, as can be expected out to radii $R \sim 10^3\,R_{\rm A}$ because of the Bardeen–Peterson effect (Bardeen and Peterson, 1975).

The neutron-star asymmetries are approximated as point-like sources with mass m located on the surface of the star at a position given by the latitudinal angle $\theta_{\rm A}$. We use spherical coordinates (R, θ, φ) with the origin of the coordinate system coinciding with the centre of the neutron star. The binary partner having mass $M_{\rm B}$ (radius $R_{\rm B}$) is assumed to be moving along an orbit with constant distance d from the neutron star and with its position given by the latitudinal coordinate $\theta_{\rm B}$; the situation for a single mountain is illustrated in Fig. 1 (we return later to the case of two mountains). For thin discs, the angular velocity profile is generally well-approximated as being Keplerian, i.e., $\Omega_{\rm d}(r) = \Omega_{\rm K}(r)$ (Novikov and Thorne, 1973; Abramowicz et al., 1992) but for thick (or slim) discs, there is a deviation away from this because of the action of pressure forces (Jaroszyński et al., 1980; Kozłowski et al., 1978). We here determine the radial and vertical components of the gravitational force produced by the perturbing sources in a purely Newtonian way. This is an approximation, but we do not expect that a relativistic analysis would greatly change the qualitative features of our results. For simplicity the force will be determined in the equatorial plane, i.e., in the symmetry plane of the disc; this is completely correct for the thin, Keplerian discs, and gives good estimates for slim discs. The time evolution of the perturbing force components will be determined for a fixed point on the disc characterized by the coordinates $(R, \theta = \pi/2, \varphi = \Omega_{\rm d} t)$, with the natural restriction put on the radial coordinate $R_{\rm A} < R < 10^3\,R_{\rm A}$. We treat separately the three cases (a single mountain, two symmetric mountains and the binary partner), giving both the exact formulae for the perturbing forces and also approximate results obtained under the conditions $d \gg R,\, R_{\rm B}; m \ll M_{\rm A},\, M_{\rm B}$. We give expressions both for the total forces and for their oscillatory parts.

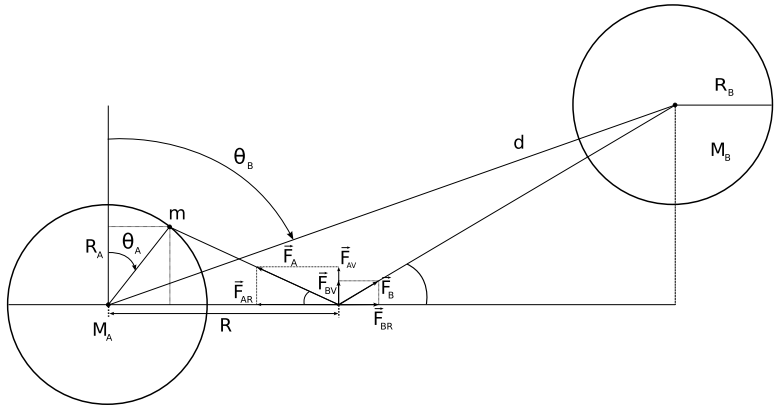

Figure 1. Schematic picture illustrating generation of a gravitational perturbative force in an equatorial accretion disc by a single mountain on the surface of a neutron star (M_A, R_A) or by a binary partner (M_B, R_B).

3.1 One mountain

Here, and in the following, we consider the force acting on a comoving unit mass element of the accretion disc located at a given radius R in the symmetry plane of the disc. The vertical component of the perturbing gravitational force F_{AV} is given by

$$F_{AV}(t) = \frac{Gm}{R_A^2}\left(\frac{R_A}{R}\right)^3 \cos\theta_A \left[1 - 2\frac{R_A}{R}\sin\theta_A \cos\omega_A t + \left(\frac{R_A}{R}\right)^2\right]^{-3/2}, \tag{10}$$

while the radial component is given by

$$F_{AR}(t) = \frac{Gm}{R_A^2}\left(\frac{R_A}{R}\right)^2 \left(1 - \frac{R_A}{R}\sin\theta_A \cos\omega_A t\right) \times \left[1 - 2\frac{R_A}{R}\sin\theta_A \cos\omega_A t + \left(\frac{R_A}{R}\right)^2\right]^{-3/2}, \tag{11}$$

where

$$\omega_A \equiv |\Omega_A - \Omega_d| \,. \tag{12}$$

The oscillations have an anharmonic character. Local extrema for both F_V and F_R are given by

$$\sin\omega_A t = 0 \,. \tag{13}$$

For the radial force F_R, there are additional extrema that occur only inside the neutron star and not in the disc, where $0 < x < 1$ ($R_A < R$). The relevance of these extrema inside the neutron star has been discussed by Stuchlík and Hledík (2005).

The vertical force has the mean value (given by Eq. (10) with $\cos\omega_{\rm A}t = 0$)

$$F_{\rm AV(mean)} = \frac{Gm}{R^2}\left(\frac{R_{\rm A}}{R}\right)^3 \cos\theta_{\rm A}\left[1+\left(\frac{R_{\rm A}}{R}\right)^2\right]^{-3/2} \tag{14}$$

and oscillates around this with frequency $\omega_{\rm A}$ and amplitude $A_{\rm V} \equiv F_{\rm AV(max)} - F_{\rm AV(mean)}$ given by the relation

$$A_{\rm V} = \frac{Gm}{R_{\rm A}^2}\left(\frac{R_{\rm A}}{R}\right)^3 \cos\theta_{\rm A}\left\{\left[1-2\frac{R_{\rm A}}{R}\sin\theta_{\rm A}+\left(\frac{R_{\rm A}}{R}\right)^2\right]^{-3/2} - \left[1+\left(\frac{R_{\rm A}}{R}\right)^2\right]^{-3/2}\right\}. \tag{15}$$

The behaviour of this amplitude is discussed in Stuchlík and Hledík (2005). The radial force oscillates around the mean value

$$F_{\rm AR(mean)} = \frac{Gm}{R_{\rm A}^2}\left(\frac{R_{\rm A}}{R}\right)^2\left[1+\left(\frac{R_{\rm A}}{R}\right)^2\right]^{-3/2}. \tag{16}$$

with frequency $\omega_{\rm A}$ and amplitude A_R given by

$$A_{\rm R} = \frac{Gm}{R_{\rm A}^2}\left(\frac{R_{\rm A}}{R}\right)^2\left\{\frac{1-\frac{R_{\rm A}}{R}\sin\theta_{\rm A}}{\left[1-2\frac{R_{\rm A}}{R}\sin\theta_{\rm A}+\left(\frac{R_{\rm A}}{R}\right)^2\right]^{3/2}} - \frac{1}{\left[1+\left(\frac{R_{\rm A}}{R}\right)^2\right]^{3/2}}\right\}. \tag{17}$$

The behaviour of $A_{\rm R}(x,\theta_{\rm A})$ is discussed in Stuchlík and Hledík (2005).

Note that the anharmonic oscillations given by Eqs (10) and (11) are strictly periodic. With a suitable choice of origin for the time axis, they can be Fourier decomposed to give

$$F_{\rm AV}(t) = \frac{Gm}{R_{\rm A}^2}\left(\frac{R_{\rm A}}{R}\right)^3 \cos\theta_{\rm A}\sum_{m=0}^{\infty} f_{\rm AV}^m\left(\frac{R_{\rm A}}{R},\sin\theta_{\rm A}\right)\cos(m\omega_{\rm A}t), \tag{18}$$

$$F_{\rm AR}(t) = \frac{Gm}{R_{\rm A}^2}\left(\frac{R_{\rm A}}{R}\right)^2 \sum_{m=0}^{\infty} f_{\rm AR}^m\left(\frac{R_{\rm A}}{R},\sin\theta_{\rm A}\right)\cos(m\omega_{\rm A}t), \tag{19}$$

where

$$f_{\rm AV}^m = \frac{1}{2\pi}\int_0^{2\pi/\omega_{\rm A}} \frac{\cos(m\omega_{\rm A}t)\,{\rm d}t}{\left[1-2\frac{R_{\rm A}}{R}\sin\theta_{\rm A}\cos\omega_{\rm A}t+\left(\frac{R_{\rm A}}{R}\right)^2\right]^{3/2}}, \tag{20}$$

$$f_{\rm AR}^m = \frac{1}{2\pi}\int_0^{2\pi/\omega_{\rm A}} \frac{\left(1-\frac{R_{\rm A}}{R}\sin\theta_{\rm A}\cos\omega_{\rm A}t\right)\cos(m\omega_{\rm A}t)\,{\rm d}t}{\left[1-2\frac{R_{\rm A}}{R}\sin\theta_{\rm A}\cos\omega_{\rm A}t+\left(\frac{R_{\rm A}}{R}\right)^2\right]^{3/2}}. \tag{21}$$

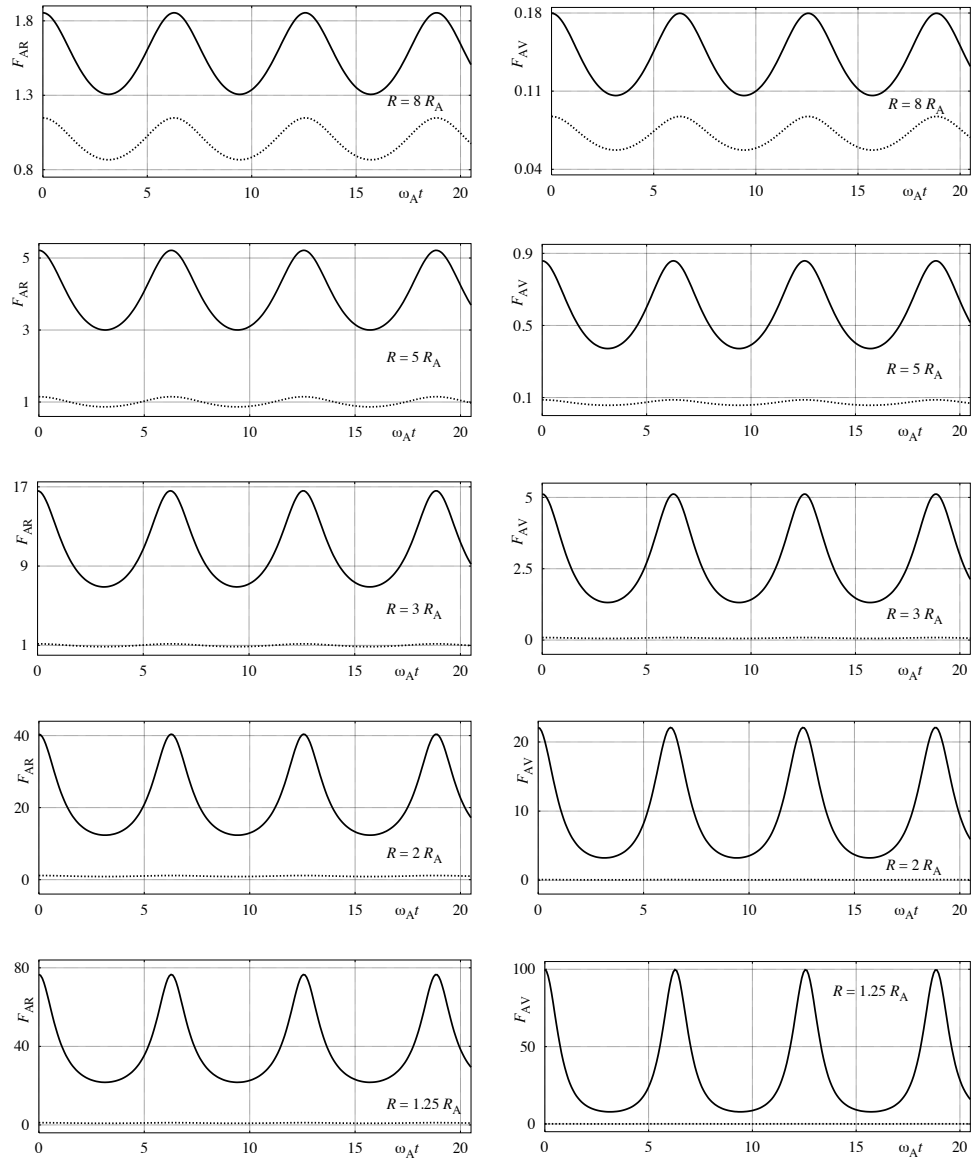

Figure 2. The oscillatory radial (*left column*) and vertical (*right column*) gravitational forces generated by a single "mountain" located on the surface of a rotating neutron star, and acting on elements of an encircling equatorial accretion disc. The mountain is assumed to be located at $\theta_A = 45°$. The oscillatory forces (at $R = 8\,R_A, 5\,R_A, 3\,R_A, 2\,R_A, 1.25\,R_A$ from top to bottom, full curves) are generally anharmonic and their behaviour is shown at some typical radii in the vicinity of the neutron star. These are compared with the behaviour of the forces at $R = 10\,R_A$ (dotted curves), where the oscillations approach a harmonic character. Notice that the vertical and radial force oscillations are mutually in phase and this does not change when approaching the surface $R = R_A$.

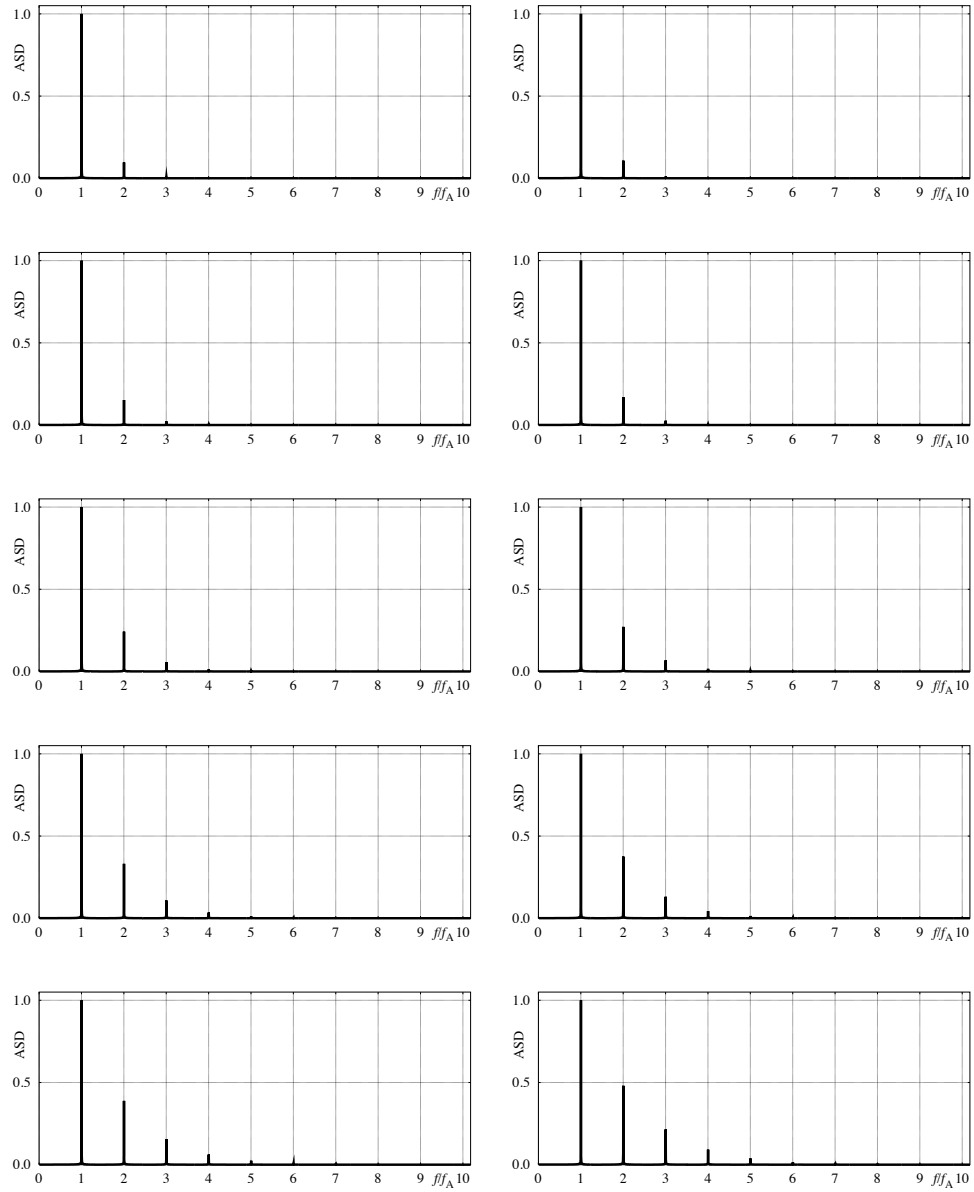

Figure 3. Fourier amplitude spectral density corresponding to oscillations of the radial component (*left column*) and vertical component (*right column*) of the gravitational force from an isolated mountain acting on the equatorial disc. From top to bottom, the frames refer to $R = 8\ R_{\rm A}, 5\ R_{\rm A}, 3\ R_{\rm A}, 2\ R_{\rm A}$ and $1.25\ R_{\rm A}$. The zero-frequency peak (corresponding to the constant part of the force) has been removed and the peaks are normalized to a maximum of 1. Higher harmonics become noticeable when approaching the stellar surface for both the radial and vertical forces, in accordance with the discussion of Fig. 2.

The Fourier components $f^m_{\rm AV}$ ($f^m_{\rm AR}$) determine the m-th mode of the force amplitude (see Figs 2 and 3).

3.2 Two symmetric mountains

We consider two symmetric diametrically-opposed mountains which we represent as equal point masses, each of mass $m_{\rm D}$, located at opposite ends of an axis tilted at angle $\theta_{\rm A}$ with respect to the rotation axis (see Fig. 4). We can use the results already obtained for a single isolated mountain with suitable modification. In fact, we can use the simple relations

$$F_{\rm DV}(t) = F_{\rm AaV}(t) - F_{\rm AbV}(t)\,, \qquad F_{\rm DR}(t) = F_{\rm AaR}(t) + F_{\rm AbR}(t)\,, \tag{22}$$

where $F_{\rm AaV}$, $F_{\rm AaR}$ ($F_{\rm AbV}$, $F_{\rm AbR}$) give the vertical and radial forces produced by the mountains above (and below) the equatorial plane. The values of the azimuthal angle φ in the expressions for the forces $F_{\rm Aa}$ and $F_{\rm Ab}$ are different by π. The vertical force is then given by

$$F_{\rm DV}(t) = \frac{Gm_{\rm D}}{R_{\rm A}^2}\left(\frac{R_{\rm A}}{R}\right)^3 \cos\theta_{\rm A}\left\{\left[1 - 2\frac{R_{\rm A}}{R}\sin\theta_{\rm A}\cos\omega_{\rm A}t + \left(\frac{R_{\rm A}}{R}\right)^2\right]^{-3/2} - \left[1 + 2\frac{R_{\rm A}}{R}\sin\theta_{\rm A}\cos\omega_{\rm A}t + \left(\frac{R_{\rm A}}{R}\right)^2\right]^{-3/2}\right\}\,, \tag{23}$$

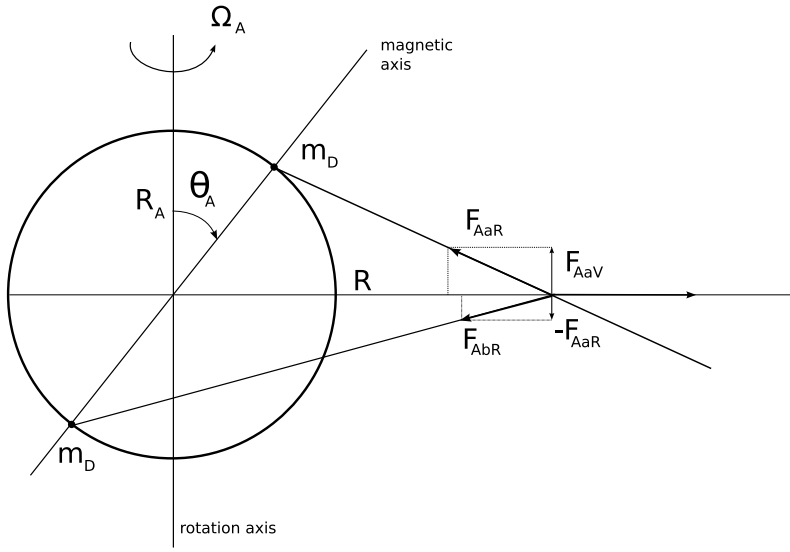

Figure 4. Schematic picture illustrating the generation of gravitational perturbation forces in an equatorial accretion disc by two symmetric diametrically-opposed mountains on the surface of a neutron star.

and the radial force

$$F_{\mathrm{DR}}(t) = \frac{Gm_{\mathrm{D}}}{R_{\mathrm{A}}^2}\left(\frac{R_{\mathrm{A}}}{R}\right)^2 \left\{ \frac{1 - \frac{R_{\mathrm{A}}}{R}\sin\theta_{\mathrm{A}}\cos\omega_{\mathrm{A}}t}{\left[1 - 2\frac{R_{\mathrm{A}}}{R}\sin\theta_{\mathrm{A}}\cos\omega_{\mathrm{A}}t + \left(\frac{R_{\mathrm{A}}}{R}\right)^2\right]^{3/2}} + \frac{1 + \frac{R_{\mathrm{A}}}{R}\sin\theta_{\mathrm{A}}\cos\omega_{\mathrm{A}}t}{\left[1 + 2\frac{R_{\mathrm{A}}}{R}\sin\theta_{\mathrm{A}}\cos\omega_{\mathrm{A}}t + \left(\frac{R_{\mathrm{A}}}{R}\right)^2\right]^{3/2}} \right\}. \tag{24}$$

Once again, these are anharmonically oscillating forces, but the frequency for the radial force is doubled because of the symmetry of the mountains.

The vertical force oscillates around the mean value $F_{\mathrm{DV(mean)}} = 0$ with frequency ω_{A} and amplitude

$$D_{\mathrm{V}} = \frac{Gm_{\mathrm{D}}}{R_{\mathrm{A}}^2}\left(\frac{R_{\mathrm{A}}}{R}\right)^3 \cos\theta_{\mathrm{A}} \left\{ \left[1 - 2\frac{R_{\mathrm{A}}}{R}\sin\theta_{\mathrm{A}} + \left(\frac{R_{\mathrm{A}}}{R}\right)^2\right]^{-3/2} - \left[1 + 2\frac{R_{\mathrm{A}}}{R}\sin\theta_{\mathrm{A}} + \left(\frac{R_{\mathrm{A}}}{R}\right)^2\right]^{-3/2} \right\}. \tag{25}$$

The radial force oscillates around the mean value

$$F_{\mathrm{DR(mean)}} = \frac{2Gm_{\mathrm{D}}}{R_{\mathrm{A}}^2}\left(\frac{R_{\mathrm{A}}}{R}\right)^2 \left[1 + \left(\frac{R_{\mathrm{A}}}{R}\right)^2\right]^{-3/2} \tag{26}$$

with frequency $\omega_{\mathrm{DR}} = 2\omega_{\mathrm{A}}$ and amplitude

$$D_{\mathrm{R}} = \frac{Gm_{\mathrm{D}}}{R_{\mathrm{A}}^2}\left(\frac{R_{\mathrm{A}}}{R}\right)^2 \left\{ \frac{1 - \frac{R_{\mathrm{A}}}{R}\sin\theta_{\mathrm{A}}}{\left[1 - 2\frac{R_{\mathrm{A}}}{R}\sin\theta_{\mathrm{A}} + \left(\frac{R_{\mathrm{A}}}{R}\right)^2\right]^{3/2}} - \frac{2}{\left[1 + \left(\frac{R_{\mathrm{A}}}{R}\right)\right]^{3/2}} + \frac{1 + \frac{R_{\mathrm{A}}}{R}\sin\theta_{\mathrm{A}}}{\left[1 + 2\frac{R_{\mathrm{A}}}{R}\sin\theta_{\mathrm{A}} + \left(\frac{R_{\mathrm{A}}}{R}\right)^2\right]^{3/2}} \right\}. \tag{27}$$

Again, the anharmonic forces can be Fourier decomposed in an analogous way as for Eqs (18) and (20) as shown in Figs 5 and 6.

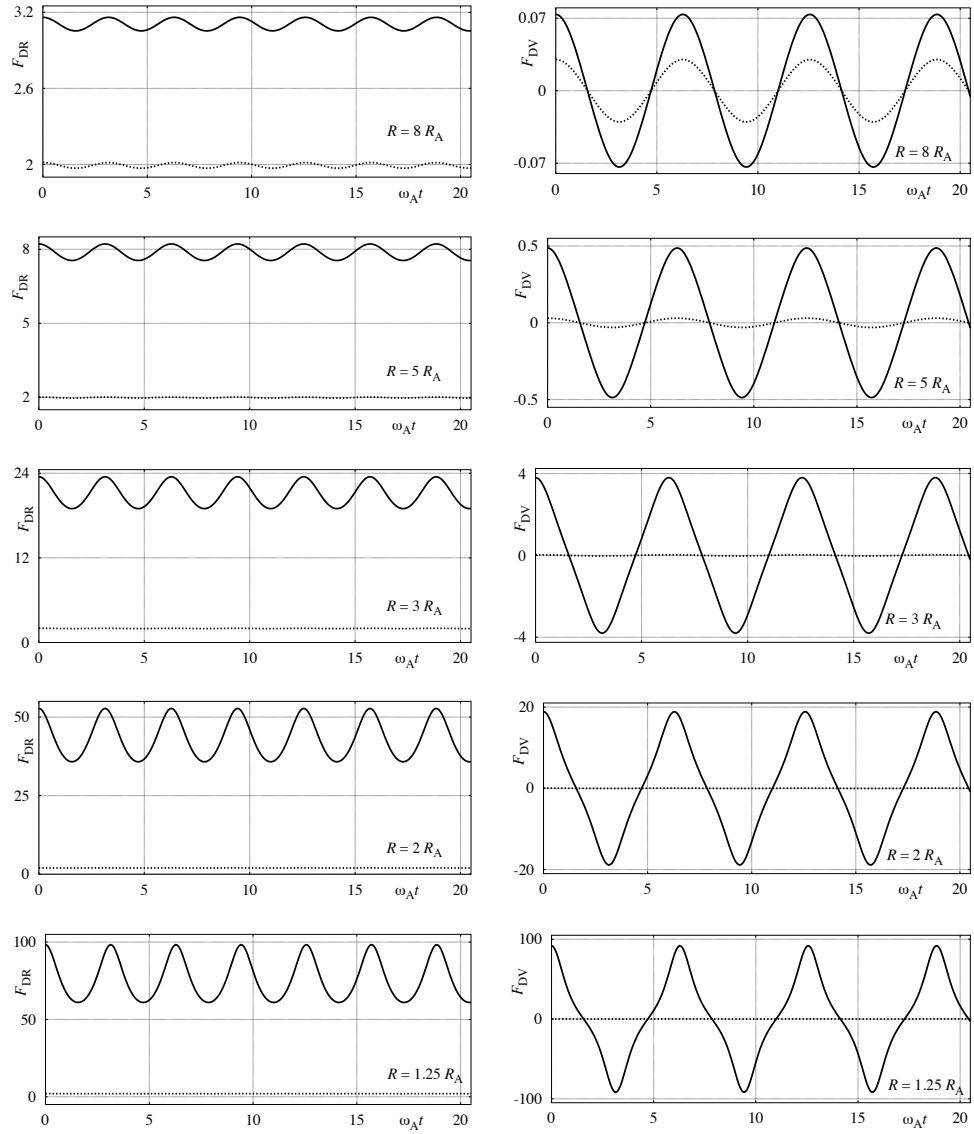

Figure 5. The oscillatory radial (*left column*) and vertical (*right column*) gravitational forces generated by two mountains of equal mass located at opposite ends of an inclined axis ($\theta_A = 45°, 135°$, and $\Delta\varphi_A = 180°$) on the surface of a rotating neutron star, and acting outside the star on elements of an equatorial accretion disc. The oscillatory forces are generally only slightly anharmonic; their behaviour is shown at some typical radii in the vicinity of the neutron star (at $R = 8\ R_A, 5\ R_A, 3\ R_A, 2\ R_A, 1.25\ R_A$ from top to bottom, full curves). In each case they are compared with the behaviour of the forces at $R = 10\ R_A$ (dotted curves), where the oscillations approach a harmonic character. Note the double frequency of the radial component compared with the vertical one, and that the phase does not change when approaching the surface $R = R_A$ from above.

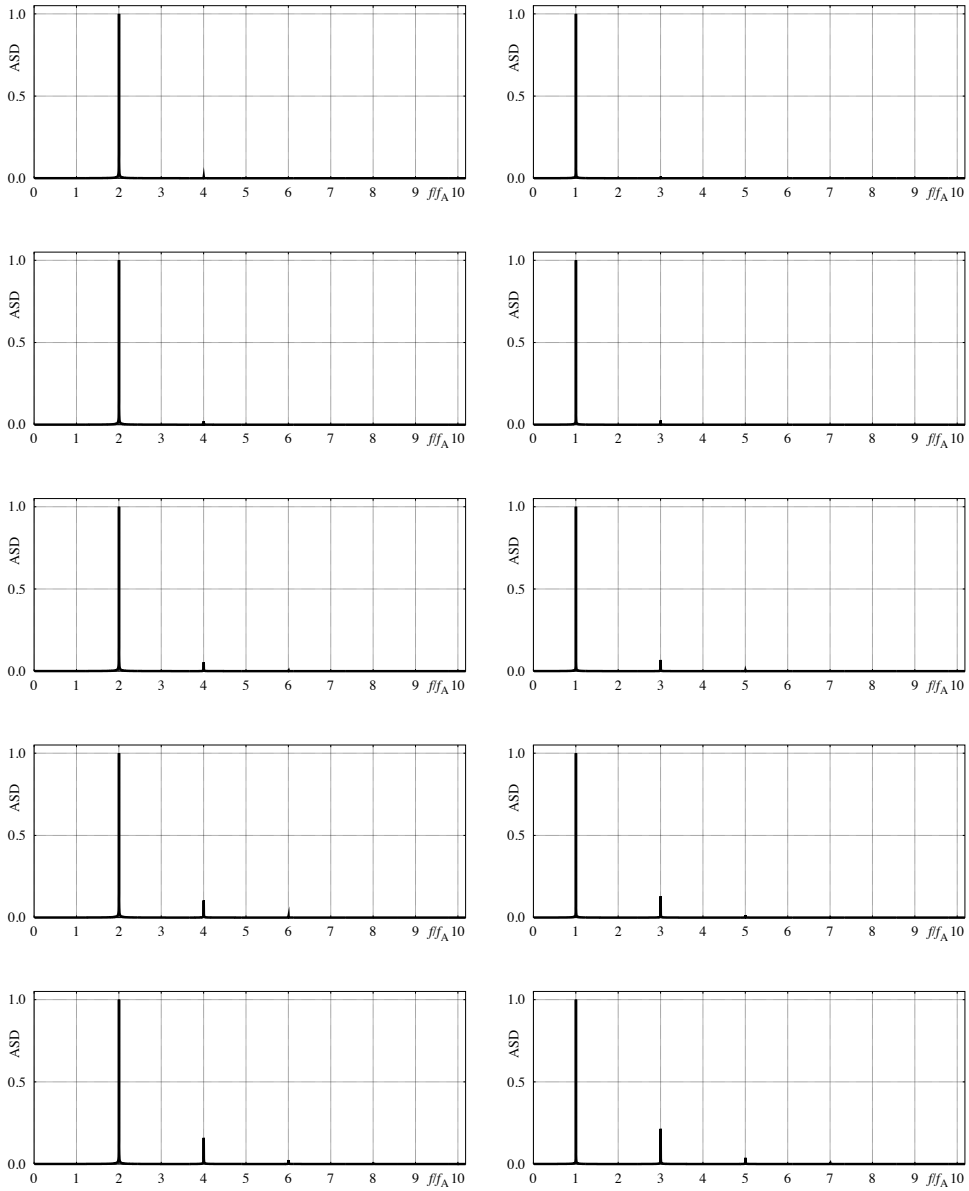

Figure 6. Fourier amplitude spectral density corresponding to oscillations of the radial component (*left column*) and vertical component (*right column*) of the gravitational force generated in the equatorial disc by symmetric accretion columns. From top to bottom, the frames refer to $R = 8\,R_{\rm A}, 5\,R_{\rm A}, 3\,R_{\rm A}, 2\,R_{\rm A}$ and $1.25\,R_{\rm A}$. The zero-frequency peak (corresponding to the constant part of the force) has been removed and the peaks are normalized to a maximum of 1. The symmetry of the columns makes the higher harmonics generally smaller than in the case of an isolated mountain. Note the frequency doubling of the radial force. This is in accordance with the discussion for Fig. 5.

3.3 Binary companion

In this section, we consider the influence of the binary companion which we take to be orbiting the neutron star at a constant distance d, with angular velocity $\Omega_{\rm B}$ (see Fig. 1). Of course, in the range of interest for accretion disc radii ($R_{\rm A} < R < 10^3\, R_{\rm A}$), we have $\Omega_{\rm d} \gg \Omega_{\rm B}$. The vertical component of the force on the accreting material caused by the binary companion is given by

$$F_{\rm BV}(t) = \frac{GM_{\rm B}}{d^2}\cos\theta_{\rm B}\left[1 - 2\left(\frac{R}{d}\right)\sin\theta_{\rm B}\cos\omega_{\rm B}t + \left(\frac{R}{d}\right)^2\right]^{-3/2}, \tag{28}$$

while the radial component of the force is

$$F_{\rm BR}(t) = \frac{GM_{\rm B}}{d^2}\frac{\sin\theta_{\rm B}\cos\omega_{\rm B}t - \frac{R}{d}}{\left[1 - 2\left(\frac{R}{d}\right)\sin\theta_{\rm B}\cos\omega_{\rm B}t + \left(\frac{R}{d}\right)^2\right]^{3/2}}, \tag{29}$$

where the angular velocity

$$\omega_{\rm B} = |\Omega_{\rm B} - \Omega_{\rm d}| \approx \Omega_{\rm d}\,. \tag{30}$$

Generally, these relations represent anharmonically oscillating forces. However, in the present case and for the relevant range of accretion disc radii, we can assume $R/d \ll 1$ and the resulting approximate formulae then correspond to harmonically oscillating forces:

$$F_{\rm BV}(t) \sim \frac{GM_{\rm B}}{d^2}\cos\theta_{\rm B}\left[1 + 3\left(\frac{R}{d}\right)\sin\theta_{\rm B}\cos\omega_{\rm B}t\right], \tag{31}$$

and

$$F_{\rm BR}(t) \sim \frac{GM_{\rm B}}{d^2}\left[\sin\theta_{\rm B}\cos\omega_{\rm B}t + \left(\frac{R}{d}\right)\left(-1 + 3\sin^2\theta_{\rm B}\cos^2\omega_{\rm B}t\right)\right]. \tag{32}$$

The vertical force oscillates around the mean value

$$F_{\rm BV(mean)} = \frac{GM_{\rm B}}{d^2}\cos\theta_{\rm B} \tag{33}$$

with frequency $\omega_{\rm B} = \Omega_{\rm d}$ and amplitude

$$B_{\rm V} \approx 3\frac{GM_{\rm B}}{d^2}\left(\frac{R}{d}\right)\cos\theta_{\rm B}\sin\theta_{\rm B}\,. \tag{34}$$

The radial force oscillates around the mean value

$$F_{\rm BR(mean)} \approx -\frac{GM_{\rm B}}{d^2}\left(\frac{R}{d}\right) \tag{35}$$

with frequency $\omega_{\rm B} \approx \Omega_{\rm d}$ and amplitude

$$B_{\rm R} \approx \frac{GM_{\rm B}}{d^2}\cos\Omega_{\rm B}\,. \tag{36}$$

4 NEUTRON-STAR ASYMMETRIES

We now turn to obtaining estimates for the effective values of the point masses which we are using to model the asymmetries of the neutron star, considering various possibly-relevant cases in turn. First, we consider a classical crystalline mountain on the surface of the neutron star and magnetically constrained accretion columns above its magnetic poles. Both of these are seen to be either inadequate or problematic for the present purposes. However, there are some different observationally-motivated scenarios in the literature, giving rise to misaligned quadrupole moments which could be relevant here, and we discuss these in the third subsection below.

4.1 Crystalline mountains

Here we assume that the basic nature of the mountain on the surface of the neutron star is the same as for mountains on planets. In other words, we assume the average density of the material in the mountain to be the same as the surface density of the neutron star. The condition for stability is that the pressure at the base of the mountain should be less than the shear stress of the surface material.

The pressure at the base of the mountain is given by

$$P_{\rm mnt} = \rho_{\rm mnt} g_{\rm ns} h_{\rm mnt} \,, \tag{37}$$

where $\rho_{\rm mnt}$ is the average density of the material in the mountain, $g_{\rm ns}$ is the surface gravity of the neutron star and $h_{\rm mnt}$ is the height of the mountain. The base of the mountain would be located at the outermost solid surface layer of the neutron star. The relevant density to take for this layer is rather uncertain but for our present rough calculation we will take it as being $\sim 10^6$ gm cm^{-3} and put $\rho_{\rm mnt}$ equal to that. The surface gravity is given by

$$g_{\rm ns} = \frac{G M_{\rm ns}}{R_{\rm ns}^2} \,, \tag{38}$$

where $M_{\rm ns}$ and $R_{\rm ns}$ are the mass and the radius of the neutron star. For a neutron star of mass 1.4 $M_\odot$ and radius 10 km, $g_{\rm ns}$ is typically 10^{14} cm s^{-2}.

Following Strohmayer et al. (1991), the shear modulus of the neutron star surface material is given by

$$\mu = \frac{0.1194}{1 + 1.781 \times (100/\Gamma)^2} \frac{n(Ze)^2}{a} \,, \tag{39}$$

where n is the ion number density, a is the inter-ionic distance, Z is the atomic number of the dominant ionic species, and Γ is the Coulomb coupling parameter ($\Gamma > 10^3$ for all practical purposes). The typical values of n, a, Z are as follows,

$$Z = 26 \,, \qquad n \simeq 10^{28}\,{\rm cm}^{-3} \,, \qquad a \simeq 7 \times 10^{-10}\,{\rm cm} \,;$$

assuming the dominant ionic species in the stellar surface to be Fe^{56}_{26}. The maximum shear strain in the surface of the neutron star has been calculated to be (Smoluchowski and Welch, 1970),

$$\Theta \sim 10^{-5}\text{–}10^{-3} \,, \tag{40}$$

although there are suggestions that it might also be as high as 10^{-2} (Ushomirsky et al., 2000). Taking the complete range, the shear stress on the surface of a typical neutron star would be

$$S = \mu\Theta \simeq 10^{18}\text{–}10^{21}\,\text{dynes}\,\text{cm}^{-2}\,. \tag{41}$$

The maximum height of a mountain on the surface of a neutron star is then obtained when $P_{\rm mnt} = S$, and is given by

$$h_{\rm mnt}^{\rm max} \simeq 0.01\text{–}10\text{cm}\,. \tag{42}$$

The maximum mass contained in such a mountain would be

$$M_{\rm mnt} \sim \rho_{\rm mnt}(h_{\rm mnt}^{\rm max})^3 \sim 10^9\,\text{g} \sim 10^{-24}\text{–}10^{-25}\,M_{\rm ns}\,, \tag{43}$$

which is very small compared with the total stellar mass $M_{\rm ns}$.

Of course, these estimates are made assuming an isolated, cold neutron star. If the star is accreting then the temperature of the surface regions would increase and may perhaps be sufficient to melt the topmost layers. In that case the possible height of any mountain and the total mass contained within it would even be smaller than the above estimates. However, Ushomirsky et al. (2000) estimated the maximum quadrupole in the accreting system due to horizontal temperature variations to be $Q/MR^2 < 10^{-8}$, which could represent a point mass of size $m \sim 10^{-8}\,\text{M}_\odot$.

4.2 Accretion columns

For an accreting neutron star with a strong enough magnetic field, accreting matter sufficiently close to the neutron star can be diverted away from the accretion disc by the magnetic field and form into accretion columns above the magnetic poles (Woosley and Wallace, 1982; Hameury et al., 1983). If the amount of matter in the columns is sufficiently large, this might then provide another significant source of neutron-star asymmetry which could again be modelled in terms of "mountains" on the neutron-star surface (probably two symmetric ones in this case). This may well be of significant interest for discussions of gravitational wave emission but its relevance in the present context is doubtful, particularly in view of the fact that a neutron star with a sufficiently strong magnetic field for producing the accretion columns seems unlikely to allow the presence of a nearly-Keplerian accretion disc reaching in to small radii, as would be required for our QPO model. Nevertheless, since this type of picture has been widely discussed and since the detailed physics involved in truncation of the disc is not very clearly established, we include a discussion here of the effective masses which might be involved.

The height of the columns above the neutron-star surface can be determined from the condition that the flow will develop a sideways component when the pressure of the material in the column becomes large enough to bend the magnetic field lines outwards. This typically becomes significant when the pressure of the matter in the column is about a hundred times greater than the magnetic pressure responsible for confining it (Brown and

Bildsten, 1998). Following Shapiro and Teukolsky (1983), the area of the polar cap can be estimated as

$$A_{\rm P} \sim 10^{10}\,{\rm cm}^2 \left(\frac{B_{\rm s}}{10^{12}\,{\rm G}}\right)^{-4/7} \left(\frac{M_{\rm ns}}{1.4\,{\rm M}_\odot}\right)^{1/7} \left(\frac{R_{\rm ns}}{10^6\,{\rm cm}}\right)^{9/7} \times \left(\frac{\dot{M}}{10^{-9}\,{\rm M}_\odot/{\rm yr}}\right)^{2/7}, \tag{44}$$

where $B_{\rm s}$ is the strength of the surface dipole field and $\dot{M}$ is the accretion rate.

The height of the accretion column is determined by the condition that the pressure at the bottom of the column should be ~ 100 times as large as the magnetic pressure, i.e.,

$$P_{\rm ac} \sim 4 \times 10^{24} \left(\frac{B_{\rm s}}{10^{12}\,{\rm G}}\right)^2 . \tag{45}$$

Hydrostatic equilibrium requires that this pressure should be the same as the pressure elsewhere in the crust (outside the polar cap) at the same distance from the centre of the neutron star as the bottom of the column. Fortunately, the pressure for the density range $10^6\,{\rm gm\,cm}^{-3} \le \rho \le 10^{10}\,{\rm gm\,cm}^{-3}$ can be expressed using the following fitting formula (Baym et al., 1971):

$$\log P = 13.65 + 1.45 \log \rho\,. \tag{46}$$

The relation between the field strength and the density at the bottom of the accretion column is then roughly given by

$$\left(\frac{\rho_{\rm bot}}{10^6\,{\rm gm\,cm}^{-3}}\right) \sim 35 \left(\frac{B_{\rm s}}{10^{12}\,{\rm G}}\right)^{1.38} \tag{47}$$

giving the scale height of the column, $h_{\rm ac}$, as

$$h_{\rm ac} \sim P_{\rm ac}/(\rho_{\rm bot}\, g_{\rm ns}) \sim 10^3 \left(\frac{B_{\rm s}}{10^{12}\,{\rm G}}\right)^{0.62} {\rm cm}\,. \tag{48}$$

The density profile within the column can be described by an "atmosphere" solution (Bildsten and Cutler, 1995). Using this, the total mass contained in the accretion column is given by

$$\begin{aligned} M_{\rm ac} &\sim A_{\rm P} \int_h^0 \rho_{\rm bot}\, e^{-x/h} dx \\ &\sim 2 \times 10^{-13}\, M_{\rm ns} \left(\frac{B_{\rm s}}{10^{12}\,{\rm G}}\right)^{1.43} \left(\frac{M_{\rm ns}}{1.4\,{\rm M}_\odot}\right)^{-6/7} \left(\frac{R_{\rm ns}}{10^6\,{\rm cm}}\right)^{9/7} \\ &\quad \times \left(\frac{\dot{M}}{10^{-9}\,{\rm M}_\odot/{\rm yr}}\right)^{2/7} . \end{aligned} \tag{49}$$

This is again a rather small number. We note that some recent work (Melatos and Payne, 2005) has suggested that magnetically constrained accretion columns might have masses much higher than those quoted above in the case of magnetars, with $M_{\rm ac} \sim 10^{-5}\, M_{\rm ns}$, but the continued existence of a Keplerian accretion disc down to small radii then becomes even more unlikely.

It should be mentioned here that in the discussion above we have assumed a symmetric dipolar magnetic field. However, a complex multipolar field near to the surface of the neutron star is not ruled out, as has been indicated by Gil and Mitra (2001). In the presence of a multipolar field structure that is asymmetric with respect to the two poles (still assuming the stellar field to be largely dipolar) the shapes and sizes of the accretion columns over the two poles may not remain equal. Such a situation would give rise to a further asymmetry over and above the mass quadrupole moment generated by a symmetric pair of accretion columns.

4.3 Quadrupole moments inferred from limiting pulsar spin rates

The mass estimates for the crystalline mountains are far too small to be of interest for our present purposes and the possibility of the magnetically-constrained accretion columns being relevant here is problematic, as discussed above. However, there are other scenarios advocated in the literature which look much more promising. Many accreting weakly-magnetised neutron stars in the galaxy are found to have spin frequencies in a rather narrow range around 300 Hz (van der Klis, 1998), which is a much lower frequency than that corresponding to centrifugal break-up. Since these objects are thought to have been accreting for long enough so as to gain sufficient angular momentum to reach the break-up limit, it seems that some mechanism is halting the spin-up. One possibility is that this may be due to magnetic braking but it has also been suggested (Bildsten, 1998) that it could have been halted because of the accretion torque becoming balanced by a gravitational-wave torque resulting from an asymmetry of the neutron star. Taking the asymmetry to be represented by an $l = m = 2$ perturbation, one finds that the magnitude of the misaligned quadrupole moment required for attaining this equilibrium at a frequency $\nu_{\rm s}$ is given by

$$Q_{\rm eq} = 3.5 \times 10^{37}\,{\rm g\,cm^2} \left(\frac{M_{\rm ns}}{1.4\,{\rm M}_\odot}\right)^{1/4} \left(\frac{R_{\rm ns}}{10^6\,{\rm cm}}\right)^{1/4} \times \left(\frac{\dot{M}}{10^{-9}\,{\rm M}_\odot/{\rm yr}}\right)^{1/2} \left(\frac{300\,{\rm Hz}}{\nu_{\rm s}}\right)^{5/2}, \tag{50}$$

where the accretion rate $\dot{M}$ is typically in the range 10^{-10}–$2 \times 10^{-8}\,{\rm M}_\odot/{\rm yr}$ for LMXBs. In terms of our simplified model of representing the asymmetry by means of point masses on the surface of an otherwise spherical neutron star, this corresponds to

$$M_{\rm quad} \sim 10^{-8}\, M_{\rm ns} \left(\frac{M_{\rm ns}}{1.4\,{\rm M}_\odot}\right)^{-3/4} \left(\frac{R_{\rm ns}}{10^6\,{\rm cm}}\right)^{-7/4} \times \left(\frac{\dot{M}}{10^{-9}\,{\rm M}_\odot/{\rm yr}}\right)^{1/2} \left(\frac{300\,{\rm Hz}}{\nu_{\rm s}}\right)^{5/2}, \tag{51}$$

for the canonical parameter values. Bildsten suggested that a quadrupole moment of the required size might be produced because of non-axisymmetric temperature variations in the outer crust leading to asymmetric electron captures and hence to density variations giving rise to the required quadrupole moment. A subsequent more detailed analysis by Ushomirsky et al. (2000) showed that temperature variations in the outer crust could not, in fact, produce a large enough quadrupole moment but that the mechanism could be effective for the *inner* crust although it would need the breaking strain to be very high in some cases. A further analysis by Haskell et al. (2006) included relativistic corrections and found that these enhanced the effect, raising the maximum values of the quadrupole moment by about an order of magnitude for the same breaking strain, easing the requirements for the latter. Another variant of this picture is that there may have been lateral composition gradients produced directly which could also produce a similar quadrupole moment. The considerations involved in all of this discussion are quite intricate and we refer the reader to the original papers for the details.

There are also other possibilities discussed in the literature for producing large misaligned quadrupole moments. One type of picture is concerned with strange quark matter either comprising the whole star or appearing in the cores of hybrid stars consisting of a strange quark core surrounded by an outer region of standard neutron-star matter (Glendenning, 1996). Within this context, Owen (2005) estimated maximum quadrupole moments corresponding to $M_{\rm quad} \sim 5 \times 10^{-6}\, M_{\rm ns}$ in the case of hybrid stars and $\sim 2 \times 10^{-4}\, M_{\rm ns}$ for pure strange stars. For crystalline, colour superconducting quark cores (Mannarelli et al., 2007), the corresponding values of $M_{\rm quad}$ might even reach as high as $\sim 10^{-3}\, M_{\rm ns}$ (see Haskell et al., 2007a) although, as the latter authors pointed out, such extreme values are already ruled out by current LIGO observations, at least for the galactic sources that we are discussing. Another possibility is that the quadrupole moment could be produced by a large internal magnetic field (Cutler, 2002; Haskell et al., 2007b). Depending on the circumstances, this might give $M_{\rm quad}/M_{\rm ns} \sim 10^{-12}$–$10^{-6}$. However, for interior magnetic fields sufficiently strong to give a value of $M_{\rm quad}$ interesting for our purposes, it is very doubtful whether the *external* field could be small enough to allow a nearly-Keplerian accretion disc to continue down to sufficiently small radii, giving a similar problem to that with the accretion columns.

Our point here is not to be specific about the process leading to the occurrence of the quadrupole deformation but rather to note that values of the deformation large enough to be capable of explaining the limiting pulsar spin rate may also be large enough for the present purposes: in the following, we take the value for the point mass given by Eq. (51), and check on whether this same value would *also* be large enough to be relevant for inducing the QPO behaviour. We note that, depending on the circumstances, this sort of asymmetry might be represented in terms of either a single point particle on the surface of the neutron star or by two diametrically-opposed point particles.

5 THE MAGNITUDES OF THE OSCILLATING FORCES

A first question to ask after the discussion of the preceding section is whether the magnitudes for the effective point masses calculated there would be sufficiently large to provide

a plausible explanation for the QPO phenomena. Recalling the discussion of Section 2, we showed there that the time taken for the amplitude $x_{\max}$ of resonant oscillations in our simplified picture to grow to a particular value is

$$t = \left(\frac{x_{\max}}{r}\right)\left(\frac{\alpha}{\pi}\right)\left(\frac{f_{\rm p}}{f_0}\right)^{-1}\tau_{\rm K}\,, \tag{52}$$

where $f_{\rm p}$ is the amplitude of the perturbing force, f_0 is the main gravitational force from the central object, $\tau_{\rm K} = 2\pi/\Omega_{\rm K}$ is the period of the circular Keplerian motion at the location being considered and the epicyclic frequency of the perturbation being excited is $\omega = \alpha\Omega_{\rm K}$. The dimensionless radial and vertical "epicyclic functions" satisfy $\alpha_{\rm R(V)}(r) < 1$ everywhere. At $r = r_{\rm ms}$, $\alpha_{\rm V} \sim 1$ but $\alpha_{\rm R} \to 0$ there and is small in the adjoining region, where some of the most important resonances occur, significantly raising the efficiency of the forced-resonant oscillation amplification. Note that since $\tau_{\rm K} \sim 10^{-3}$ s, the amplitude magnification in 1 second is $\sim 10^3$.

We consider here forces acting on an element of unit mass, so that $f_0 = GM_{\rm A}/R^2$ and $f_{\rm p}$ represents the oscillation amplitude of either the vertical or radial perturbing force, as calculated in Section 3. We denote these here as $f_{\rm V}$ and $f_{\rm R}$ respectively.

In the case of the influence of the binary partner, for the radial perturbing force

$$\frac{f_{\rm R}}{f_0} \sim \left(\frac{M_{\rm B}}{M_{\rm A}}\right)\left(\frac{R}{d}\right)^2 \sim 10^{-8}\frac{M_{\rm B}}{M_{\rm A}}\left(\frac{R}{10^6\,{\rm cm}}\frac{10^{10}\,{\rm cm}}{d}\right)^2\,. \tag{53}$$

In contact binary systems (e.g., 4U 1820), $d \sim 10^{10}$ cm, and in the inner part of the disc where $R \sim 10^6$ cm the dimensionless oscillation amplitude $x_{\max}/r$ would grow above 10^{-3} (as required in order for it to potentially explain the observed effect) in $\sim 10^3$ s if the binary companion has a mass of $\sim 0.1M_{\rm A}$ (with shorter times for higher mass companions). However, for the vertical perturbing force

$$\frac{f_{\rm V}}{f_0} \sim \left(\frac{M_{\rm B}}{M_{\rm A}}\right)\left(\frac{R}{d}\right)^3 \sim 10^{-12}\,\frac{M_{\rm B}}{M_{\rm A}}\left(\frac{R}{10^6\,{\rm cm}}\frac{10^{10}\,{\rm cm}}{d}\right)^3\,, \tag{54}$$

which gives the time for reaching $x_{\max}/r > 10^{-3}$ as $\sim 10^5$ s.

In the case of a single mountain on the neutron star surface, we have

$$\frac{f_{\rm R(V)}}{f_0} \sim \frac{m}{M_{\rm A}}\left(\frac{R_{\rm A}}{R}\right)^{3(4)} f_{\alpha(\beta)}\,, \tag{55}$$

where $f_{\alpha(\beta)}$ (with $\alpha = {\rm R, V}$) are anharmonicity factors which are of order unity for $R \gtrsim 10\,R_{\rm A}$ but grow rapidly as $R \to R_{\rm A}$. Taking $m \sim 10^{-8}\,M_{\rm A}$, as discussed in the previous section, the time for reaching $x_{\max}/r > 10^{-3}$ is then $\sim 10^2$ s in the inner parts of the disc for both radial and vertical oscillations. Timescales $\lesssim 10^3$ s are reasonable for our purposes (as we discuss later) and so this encourages further investigation of the scenario.

Clearly, these asymmetries of the neutron star tend to dominate the behaviour in the inner part of the disc while the effect of the binary partner is more significant further out. We now analyse the relative strengths of these perturbations in more detail. For

doing this, we can use the asymptotic forms of the amplitudes $A_{\rm V}$, $A_{\rm R}$, $D_{\rm V}$, $D_{\rm R}$, whenever $10\,R_{\rm A} < R < 10^3\,R_{\rm A}$, while for the binary companion, where $d \gg R$, the approximate formulae can always be used.

The ratio of the amplitudes of the oscillating forces is given by the following relations. For the ratio between the vertical oscillatory forces produced by the binary partner (with mass $M_{\rm B}$) and by a single mountain (with mass m), we obtain the relation

$$R_{\rm V(B/A)} = \frac{B_{\rm V}}{A_{\rm V}} = 3\left(\frac{M_{\rm B}}{\mathrm{M}_\odot}\right)\left(\frac{\mathrm{M}_\odot}{m}\right)\left(\frac{\mathrm{R}_\odot}{d}\right)^3\left(\frac{R_{\rm A}}{\mathrm{R}_\odot}\right)^3\left(\frac{R}{R_{\rm A}}\right)^4\frac{\cos\theta_{\rm B}\sin\theta_{\rm B}}{\cos\theta_{\rm A}}$$
$$\times\left\{\left[1-2\left(\frac{R_{\rm A}}{R}\right)\sin\theta_{\rm A}+\left(\frac{R_{\rm A}}{R}\right)^2\right]^{-3/2}-\left[1+\left(\frac{R_{\rm A}}{R}\right)^2\right]^{-3/2}\right\}^{-1}. \qquad (56)$$

This reduces to the approximate relation

$$\tilde{R}_{\rm V(B/A)} \sim \left(\frac{M_{\rm B}}{\mathrm{M}_\odot}\right)\left(\frac{\mathrm{M}_\odot}{m}\right)\left(\frac{\mathrm{R}_\odot}{d}\right)^3\left(\frac{R_{\rm A}}{\mathrm{R}_\odot}\right)^3\left(\frac{R}{R_{\rm A}}\right)^5\frac{\cos\theta_{\rm B}\sin\theta_{\rm B}}{\cos\theta_{\rm A}\sin\theta_{\rm A}} \qquad (57)$$

when $R \gg R_{\rm A}$. Here, and in an analogous way in the following, the approximate ratio $\tilde{R}_{\rm V(B/A)}$ relates the amplitudes $B_{\rm V}$ and $A_{\rm V}$ in situations where the oscillations of the force F_A can be considered as being harmonic, e.g. it can be used when $R > 10\,R_{\rm A}$. For the radial oscillatory force, we obtain

$$R_{\rm R(B/A)} = \frac{B_{\rm R}}{A_{\rm R}} = \left(\frac{M_{\rm B}}{\mathrm{M}_\odot}\right)\left(\frac{\mathrm{M}_\odot}{m}\right)\left(\frac{\mathrm{R}_\odot}{d}\right)^2\left(\frac{R_{\rm A}}{\mathrm{R}_\odot}\right)^2\left(\frac{R}{R_{\rm A}}\right)^2$$
$$\times\left\{\frac{1-\frac{R_{\rm A}}{R}\sin\theta_{\rm A}}{\left[1-2\frac{R_{\rm A}}{R}\sin\theta_{\rm A}+\left(\frac{R_{\rm A}}{R}\right)^2\right]^{3/2}}-\frac{1}{\left[1+\left(\frac{R_{\rm A}}{R}\right)^2\right]^{3/2}}\right\}^{-1}\sin\theta_{\rm B} \qquad (58)$$

giving the approximate expression

$$\tilde{R}_{\rm R(B/A)} \sim \frac{1}{2}\left(\frac{M_{\rm B}}{\mathrm{M}_\odot}\right)\left(\frac{\mathrm{M}_\odot}{m}\right)\left(\frac{\mathrm{R}_\odot}{d}\right)^2\left(\frac{R_{\rm A}}{\mathrm{R}_\odot}\right)^2\left(\frac{R}{R_{\rm A}}\right)^3\frac{\sin\theta_{\rm B}}{\sin\theta_{\rm A}}, \qquad (59)$$

when $R \gg R_{\rm A}$.

The ratio between the vertical oscillatory forces produced by the binary companion and by the two symmetric mountains (each with mass $m_{\rm D}$) is

$$R_{\rm V(B/D)} = \frac{B_{\rm V}}{D_{\rm V}} = 3\left(\frac{M_{\rm B}}{{\rm M}_\odot}\right)\left(\frac{{\rm M}_\odot}{m_{\rm D}}\right)\left(\frac{{\rm R}_\odot}{d}\right)^3\left(\frac{R_{\rm A}}{{\rm R}_\odot}\right)^3\left(\frac{R}{R_{\rm A}}\right)^4\frac{\cos\theta_{\rm B}\sin\theta_{\rm B}}{\cos\theta_{\rm A}} \times\left\{\left[1-2\left(\frac{R_{\rm A}}{R}\right)\sin\theta_{\rm A}+\left(\frac{R_{\rm A}}{R}\right)^2\right]^{-3/2} -\left[1+2\left(\frac{R_{\rm A}}{R}\right)\sin\theta_{\rm A}+\left(\frac{R_{\rm A}}{R}\right)^2\right]^{-3/2}\right\}^{-1}, \tag{60}$$

giving the approximate form

$$\tilde{R}_{\rm V(B/D)} \sim \frac{1}{2}\left(\frac{M_{\rm B}}{{\rm M}_\odot}\right)\left(\frac{{\rm M}_\odot}{m_{\rm D}}\right)\left(\frac{{\rm R}_\odot}{d}\right)^3\left(\frac{R_{\rm A}}{{\rm R}_\odot}\right)^3\left(\frac{R}{R_{\rm A}}\right)^5\frac{\cos\theta_{\rm B}\sin\theta_{\rm B}}{\cos\theta_{\rm A}\sin\theta_{\rm A}} \tag{61}$$

The ratio of the radial oscillatory forces for this case is then given by

$$R_{\rm R(B/D)} = \frac{B_{\rm R}}{D_{\rm R}} = \left(\frac{M_{\rm B}}{{\rm M}_\odot}\right)\left(\frac{{\rm M}_\odot}{m_{\rm D}}\right)\left(\frac{{\rm R}_\odot}{d}\right)^2\left(\frac{R_{\rm A}}{{\rm R}_\odot}\right)^2\left(\frac{R}{R_{\rm A}}\right)^2\sin\theta_{\rm B} \times\left\{\frac{1-\frac{R_{\rm A}}{R}\sin\theta_{\rm A}}{\left[1-2\frac{R_{\rm A}}{R}\sin\theta_{\rm A}+\left(\frac{R_{\rm A}}{R}\right)^2\right]^{3/2}}-\frac{2}{\left[1+\left(\frac{R_{\rm A}}{R}\right)^2\right]^{3/2}} +\frac{1+\frac{R_{\rm A}}{R}\sin\theta_{\rm A}}{\left[1+2\frac{R_{\rm A}}{R}\sin\theta_{\rm A}+\left(\frac{R_{\rm A}}{R}\right)^2\right]^{3/2}}\right\}^{-1}, \tag{62}$$

which reduces to the approximate form

$$\tilde{R}_{\rm R(B/D)} \sim \frac{1}{24}\left(\frac{M_{\rm B}}{{\rm M}_\odot}\right)\left(\frac{{\rm M}_\odot}{m_{\rm D}}\right)\left(\frac{{\rm R}_\odot}{d}\right)^2\left(\frac{R_{\rm A}}{{\rm R}_\odot}\right)^2\left(\frac{R}{R_{\rm A}}\right)^4\frac{\sin\theta_{\rm B}}{\sin^2\theta_{\rm A}} \tag{63}$$

when $R \gg R_{\rm A}$.

We now apply these formulae to a range of cases, again taking $R_{\rm A} \sim 10\,{\rm km}$, focusing on misaligned quadrupole moments which, following the discussion of Section 4.3, could be represented as either single or double effective mountains with masses of $\sim 10^{-8}\,{\rm M}_\odot$, and considering radii in the disc within the range $R_{\rm A} < R < 10^3\,R_{\rm A}$ for the reasons mentioned earlier.

For the case of a single mountain, the approximate expression Eq. (57) gives

$$\tilde{R}_{\rm V(B/A)} \sim 4\times10^{-7}\left(\frac{M_{\rm B}}{{\rm M}_\odot}\right)\left(\frac{{\rm R}_\odot}{d}\right)^3\left(\frac{R}{R_{\rm A}}\right)^5\frac{\sin 2\theta_{\rm B}}{\sin 2\theta_{\rm A}}\,. \tag{64}$$

According to Carroll and Ostlie (1996), the binary systems can for our purposes be classified into three groups: primordial systems, with the orbital separation of the stars ~ 70–$460\,\mathrm{R}_\odot$, intermediate systems, with orbital separation ~ 10–$65\,\mathrm{R}_\odot$, and gravitational wave radiating systems, with orbital separation ~ 0.2–$1.4\,\mathrm{R}_\odot$. Taking $d \sim 0.2\,\mathrm{R}_\odot$ and $R \sim 10^3\,R_\mathrm{A}$ at one extreme, and $d \sim 10^2\,\mathrm{R}_\odot$ and $R \sim R_\mathrm{A}$ at the other, we find that $\tilde{R}_{\mathrm{V(B/A)}} \sin 2\theta_\mathrm{A}/\sin 2\theta_\mathrm{B}$ ranges from $\sim 10^{12}$ down to $\sim 10^{-15}$ and so either one may dominate. (Note that the asymptotic formulae cease to be valid for $R < 10\,R_\mathrm{A}$ but we use them throughout the above range here so as to get a feel for the problem and return afterwards to a further discussion of this.)

For the radial forces, we arrive at the formula

$$\tilde{R}_{\mathrm{R(B/A)}} \sim 10^{-2} \left(\frac{M_\mathrm{B}}{\mathrm{M}_\odot}\right) \left(\frac{\mathrm{R}_\odot}{d}\right)^3 \left(\frac{R}{R_\mathrm{A}}\right)^5 \frac{\sin\theta_\mathrm{B}}{\sin\theta_\mathrm{A}} \tag{65}$$

which gives $\tilde{R}_{\mathrm{R(B/A)}} \sin\theta_\mathrm{A}/\sin\theta_\mathrm{B}$ in the range between $\sim 10^{17}$ and $\sim 10^{-8}$ again allowing for either type of perturbation to dominate. However, we note that in the inner parts of the disc, which are of most interest for high frequency QPOs, the perturbation from the mountain is always dominant.

For the two symmetric mountains, the situation is basically the same for the vertical perturbations but rather different for the radial ones. For the vertical perturbations we obtain the relation

$$\tilde{R}_{\mathrm{V(B/D)}} \sim 2 \times 10^{-7} \left(\frac{M_\mathrm{B}}{\mathrm{M}_\odot}\right) \left(\frac{\mathrm{R}_\odot}{d}\right)^3 \left(\frac{R}{R_\mathrm{A}}\right)^5 \frac{\sin 2\theta_\mathrm{B}}{\sin 2\theta_\mathrm{A}} \tag{66}$$

which is the same as Eq. (64) apart from a factor of two. However, for the radial perturbations, we have

$$\tilde{R}_{\mathrm{R(B/D)}} \sim 10^{-3} \left(\frac{M_\mathrm{B}}{\mathrm{M}_\odot}\right) \left(\frac{\mathrm{R}_\odot}{d}\right)^2 \left(\frac{R}{R_\mathrm{A}}\right)^4 \frac{\sin\theta_\mathrm{B}}{\sin^2\theta_\mathrm{A}}\,, \tag{67}$$

which gives $\tilde{R}_{\mathrm{R(B/D)}} \sin^2\theta_\mathrm{A}/\sin\theta_\mathrm{B}$ in the range between $\sim 10^5$ and $\sim 10^{-3}$. Again, we find that either mechanism can dominate but the neutron-star asymmetry is more important for the region close to the neutron star. A separate analysis would be needed for each particular binary system.

In making the above discussion, we have used the formulae in their asymptotic form appropriate for $R \gg R_\mathrm{A}$, when the forces are harmonic in character. This is convenient in order to get a feeling for the working of the problem but closer to the neutron star ($R < 10\,R_\mathrm{A}$), where the forces F_AR and F_DR are anharmonic, the amplitude of the perturbations coming from the neutron-star asymmetries grows substantially, while that from the binary partner continues to decrease. The effect of the anharmonic character of the oscillations for $R_\mathrm{A} < R < 10\,R_\mathrm{A}$ can again be represented by anharmonicity factors $f_{\alpha(\mathrm{B}/\beta)}$, now defined by the relation

$$R_{\alpha(\mathrm{B}/\beta)} = f^{-1}_{\alpha(\mathrm{B}/\beta)} \tilde{R}_{\alpha(\mathrm{B}/\beta)}\,, \tag{68}$$

where $\alpha = \mathrm{V}, \mathrm{R}$ and $\beta = \mathrm{A}, \mathrm{D}$. The anharmonicity factors $f_{\alpha(\mathrm{B}/\beta)}$ grow substantially when $R \to R_\mathrm{A}$; plots showing their behaviour are shown in Fig. 7.

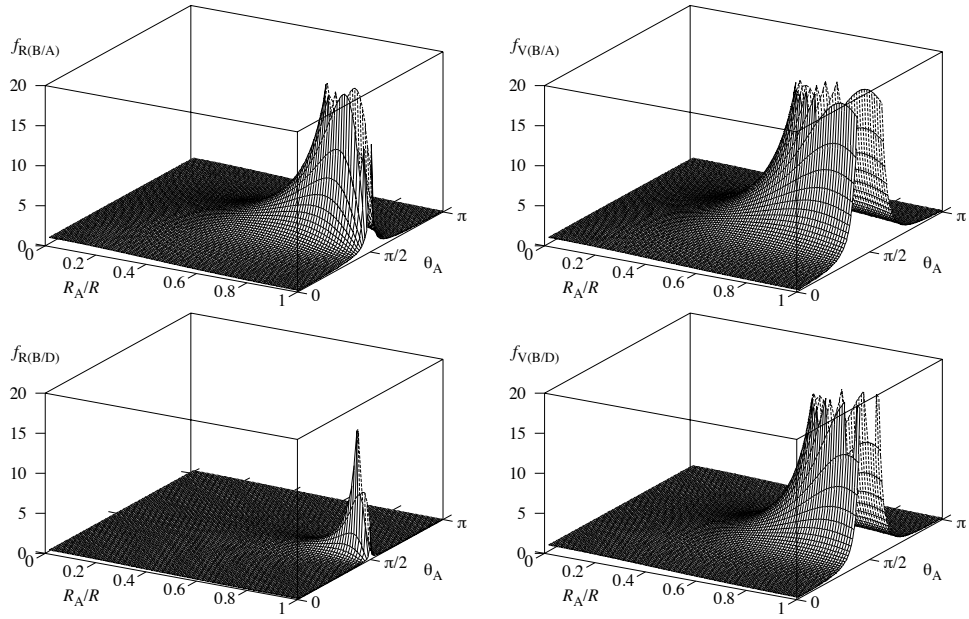

Figure 7. *Left column:* 3D plots of the anharmonicity factors for the ratio between the radial oscillatory forces produced by the binary partner and by the isolated mountain (top) and for the ratio between the radial oscillatory forces produced by the binary companion and by the symmetric accretion column (bottom). *Right column:* 3D plots of the anharmonicity factors for the ratio between the vertical oscillatory forces produced by the binary partner and by the isolated mountain (top) and for the ratio between the vertical oscillatory forces produced by the binary companion and by the symmetric accretion column (bottom).

6 CONCLUSIONS

From analysis of observational data for the neutron-star sources it seems that the high-frequency twin-peak QPO behaviour observed in some atoll (and Z) sources could be fitted well by the relativistic precession model (Stella and Vietri, 1999) or its generalization to the so-called total precession model (Stuchlík et al., 2007d), where an oscillatory quasi-circular orbital motion of a radiating blob is considered with resonant frequencies being a combination of the Keplerian frequency and the radial and vertical epicyclic frequencies.[2]

We expect that the resonances occur when the frequency ratios are close to small natural number ratios, corresponding to situations where the 3D blob trajectory becomes closed. Further, it has been shown (Stuchlík et al., 2007d; Bakala et al., 2007) that in the six

[2] The QPOs observed in the neutron star binary systems could also be explained by warped disc oscillations with resonating inertial/acoustic modes (Kato, 2004b): namely, the upper frequency $\nu_U = 2\nu_K - \nu_\theta$ and the lower frequency $\nu_L = \nu_K - \nu_r$ could fit quite well the data observed for the six atoll sources discussed above and the Z source Circinus X1 (Török et al., 2007b). Excitation of such oscillations and stability analysis of them was carefully discussed by Kato.

atoll sources discussed in the Introduction, the resonant phenomena with eigenfrequency ratios $3/2, 4/3, 5/4$ should occur in the immediate vicinity of the innermost stable circular geodesic and the neutron star surface, at $r \geq r_{\rm ms} \sim 6\,{\rm M}_{\odot}$, while in the case of the Z-source Circinus X1, with atypical eigenfrequency ratios $3/1$ and $4/1$, the resonances should occur at larger distances $r \geq 10\,{\rm M}_{\odot}$, which are, nevertheless, still within the general relativistic region of influence of the central object. Therefore, it is certainly relevant to consider the excitation of the blob oscillations by gravitational perturbing forces, considering a forced resonance between oscillations with the radial and vertical epicyclic frequencies and the frequency of the oscillating perturbing force.[3] In the atoll sources, the duration of the observed QPO phenomena is typically $\sim 10^3$ s and it is reasonable to look for an excitation mechanism with a growth timescale of a similar order. Also, since the size of the observed X-ray fluctuations is typically around 1–10 %, the oscillation dimensionless amplitude $x_{\rm max}/r$ probably needs to reach values of $\gtrsim 10^{-3}$. As we have seen in Section 5, it looks plausible to have $x_{\rm max}/r$ for oscillations in the inner part of the disc growing to $\gtrsim 10^{-3}$ within 10^3 s as a result of gravitational perturbations coming either from neutron-star asymmetries corresponding to misaligned quadrupole moments (radial and vertical oscillations) or from a binary companion (probably only for radial oscillations).

The binary partner of the neutron star induces harmonic force oscillations in all relevant situations, i.e. throughout the range $R_{\rm A} < R < 10^3\,R_{\rm A}$ while the neutron-star asymmetries induce harmonic force oscillations for $R \gtrsim 10\,R_{\rm A}$, but anharmonic oscillations for $R \lesssim 10\,R_{\rm A}$, becoming more strongly anharmonic as the surface of the neutron star is approached. The Fourier analysis clearly shows how progressively higher harmonics appear in the spectrum when $R \to R_{\rm A}$ (see Fig. 3 for the case of a single mountain and Fig. 6 for the case of two symmetric mountains).

We conclude that the types of gravitational perturbation considered in this paper provide a plausible mechanism for inducing QPO behaviour although many details remain to be worked out, particularly regarding how the oscillations of blobs in the disc lead to the observed variations in the X-ray emission. We note, however, that directly explaining the X-ray variations is a problem common to other proposed models as well. Although the influence of the binary partner could be effective in providing the perturbations, the more intriguing possibility is that they might be provided by the neutron-star asymmetries which seem likely to be dominant for the inner parts of the disc most relevant for kilohertz QPOs. It is striking that the same magnitude for the misaligned quadrupole moment advocated elsewhere for explaining limiting pulsar periods, seems also to be effective for giving a viable mechanism for inducing QPO behaviour.

ACKNOWLEDGEMENTS

This work was supported by the Czech grants MSM 4781305903 and GAČR 202/06/0041.

[3] Of course, the restoring force could also be of magnetic origin but in that case it would be necessary to consider a complicated interaction between the magnetic field and the disc material. We postpone discussion of this to future studies including also a more detailed discussion of the disc properties. On the other hand, the gravitational perturbing forces could act to some extent independently of the detailed structure of the disc or the blob.

REFERENCES

Abramowicz, M. A., Barret, D., Bursa, M., Horák, J., Kluźniak, W., Rebusco, P. and Török, G. (2005a), A note on the slope-shift anticorrelation in the neutron star kHz QPOs data, in Hledík and Stuchlík (2005), pp. 1–9.

Abramowicz, M. A., Barret, D., Bursa, M., Horák, J., Kluźniak, W., Rebusco, P. and Török, G. (2005b), The correlations and anticorrelations in QPO data, *Astronom. Nachr.*, **326**(9), pp. 864–866.

Abramowicz, M. A. and Kluźniak, W. (2001), A precise determination of black hole spin in GRO J1655−40, *Astronomy and Astrophysics*, **374**, pp. L19–L20, arXiv: `astro-ph/0105077`, URL `http://adsabs.harvard.edu/abs/2001A\%26A...374L..19A`.

Abramowicz, M. A., Kluźniak, W., Stuchlík, Z. and Török, G. (2004), Twin peak QPOs frequencies in microquasars and Sgr A*. The resonance and other orbital models, in Hledík and Stuchlík (2004), pp. 1–23.

Abramowicz, M. A., Lanza, A., Spiegel, E. A. and Szuszkiewicz, E. (1992), Vortices on accretion disks, *Nature*, **356**, p. 41.

Alimi, J.-M. and Füzfa, A., editors (2006), *Albert Einstein Century International Conference, Paris, France, 18–22 July 2005*, volume 861, AIP, Melville, New York.

Aschenbach, B. (2004), Measuring mass and angular momentum of black holes with high-frequency quasi-periodic oscillations, *Astronomy and Astrophysics*, **425**, pp. 1075–1082.

Aschenbach, B. (2006), Mass and Angular Momentum of Black Holes: An Overlooked Effect of General Relativity Applied to the Galactic Center Black Hole Sgr A*, *Chinese Astronom. Astrophys.*, **6**, pp. 221–227, updated version of a talk given at the 2005 Frascati Workshop, Vulcano, Italy, May 23–28, arXiv: `astro-ph/0603193`.

Bakala, P., Török, G. and Stuchlík, Z. (2007), in preparation.

Bardeen, J. M. (1973), Timelike and Null Geodesics in the Kerr Metric, in C. D. Witt and B. S. D. Witt, editors, *Black Holes*, p. 215, Gordon and Breach, New York–London–Paris.

Bardeen, J. M. and Peterson, J. A. (1975), The Lense–Thirring effect and accretion disks around Kerr black holes, *Astrophys. J. Lett.*, **195**, p. L65.

Barret, D., Olive, J.-F. and Miller, M. C. (2005), An abrupt drop in the coherence of the lower kilohertz QPO in 4U 1636−536, *Monthly Notices Roy. Astronom. Soc.*, **361**, pp. 855–860.

Baym, G., Pethick, C. and Sutherland, P. (1971), The Ground State of Matter at High Densities: Equation of State and Stellar Models, *Astrophys. J.*, **170**, p. 299, URL `http://adsabs.harvard.edu/cgi-bin/nph-bib_query?bibcode=1971ApJ...170..299B&db_key=AST`.

Belloni, T., Méndez, M. and Homan, J. (2005), The distribution of kHz QPO frequencies in bright low mass X-ray binaries, *Astronomy and Astrophysics*, **437**, pp. 209–216.

Belloni, T., Méndez, M. and Sánchez-Fernández, C. (2001), The high-frequency QPOs in GRS 1915+105, *Astronomy and Astrophysics*, **372**, pp. 551–556, arXiv: `astro-ph/0104019`.

Bildsten, L. (1998), Gravitational Radiation and Rotation of Accreting Neutron Stars, *Astrophys. J.*, **501**, pp. L89–L93.

Bildsten, L. and Cutler, C. (1995), Nonradial Oscillations in Neutron Star Oceans: A Source of Quasi-periodic X-Ray Oscillations?, *Astrophys. J.*, **449**, p. 800.

Brown, E. F. and Bildsten, L. (1998), The Ocean and Crust of a Rapidly Accreting Neutron Star: Implications for Magnetic Field Evolution and Thermonuclear Flashes, *Astrophys. J.*, **496**, p. 915.

Carroll, B. W. and Ostlie, D. A. (1996), *An Introduction to Modern Astrophysics*, Addison-Wesley, Reading, Massachusetts, ISBN 0-201-54730-9.

Cutler, C. (2002), Gravitational Waves from Neutron Stars with Large Toroidal B-Fields, *Phys. Rev. D*, **66**, p. 084025.

Gil, J. and Mitra, D. (2001), Vacuum Gaps in Pulsars and PSR J2144−3933, *Astrophys. J.*, **550**, pp. 383–391.

Glendenning, N. K. (1996), *Compact Stars*, Springer, New York.

Hameury, J. M., Bonazzola, S., Heyvaerts, J. and Lasota, J. P. (1983), Magnetohydrostatics in the polar caps of the gamma-ray burst sources, *Astronomy and Astrophysics*, **128**, pp. 369–374.

Haskell, B., Andersson, N., Jones, D. and Samuelsson, L. (2007a), Is LIGO already constraining the parameters of QCD?, arXiv: `0708.2984`.

Haskell, B., Jones, D. I. and Andersson, N. (2006), Mountains on neutron stars: accreted versus non-accreted crusts, *Monthly Notices Roy. Astronom. Soc.*, **373**, pp. 1423–1439.

Haskell, B., Samuelsson, L., Glampedakis, K. and Andersson, N. (2007b), Modelling magnetically deformed neutron stars, arXiv: `0705.1780`.

Hledík, S. and Stuchlík, Z., editors (2004), *Proceedings of RAGtime 4/5: Workshops on black holes and neutron stars, Opava, 14–16/13–15 October 2002/2003*, Silesian University in Opava, Opava, ISBN 80-7248-242-4.

Hledík, S. and Stuchlík, Z., editors (2005), *Proceedings of RAGtime 6/7: Workshops on black holes and neutron stars, Opava, 16–18/18–20 September 2004/2005*, Silesian University in Opava, Opava, ISBN 80-7248-334-X.

Homan, J., van der Klis, M., Jonker, P. G., Wijnands, R., Kuulkers, E., Méndez, M. and Lewin, W. H. G. (2002), RXTE Observations of the Neutron Star Low-Mass X-Ray Binary GX 17+2: Correlated X-Ray Spectral and Timing Behavior, *Astrophys. J.*, **568**(2), pp. 878–900.

Jaroszyński, M., Abramowicz, M. A. and Paczyński, B. (1980), Supercritical accretion disks around black holes, *Acta Astronom.*, **30**, pp. 1–34.

Kato, S. (2004a), Mass and Spin of GRS 1915+105 Based on a Resonance Model of QPOs, *Publ. Astronom. Soc. Japan*, **56**(5), pp. L25–L28.

Kato, S. (2004b), Resonant Excitation of Disk Oscillations by Warps: A Model of kHz QPOs, *Publ. Astronom. Soc. Japan*, **56**(5), pp. 905–922.

Kato, S. and Fukue, J. (1980), Trapped Radial Oscillations of Gaseous Disks around a Black Hole, *Publ. Astronom. Soc. Japan*, **32**(3), pp. 377–388.

Kluźniak, W., Abramowicz, M. A., Bursa, M. and Török, G. (2007), QPOs and resonance in accretion disks, *Rev. Mexicana Astronom. Astrofís. and (Serie de Conferencias)*, **27**, pp. 18–25.

Kozłowski, M., Jaroszyński, M. and Abramowicz, M. A. (1978), The analytic theory of fluid disks orbiting the Kerr black hole, *Astronomy and Astrophysics*, **63**(1–2), pp. 209–220, URL `http://adsabs.harvard.edu/abs/1978A\%26A....63..209K`.

Landau, L. D. and Lifshitz, E. M. (1976), *Mechanics*, volume I of *Course of Theoretical Physics*, Elsevier Butterworth-Heinemann, Oxford, 3rd edition, ISBN 0-7506-2896-0.

Mannarelli, M., Rajagopal, K. and Sharma, R. (2007), The rigidity of crystalline color superconducting quark matter, arXiv: `hep-ph/0702021`.

Melatos, A. and Payne, D. J. B. (2005), Gravitational Radiation from an Accreting Millisecond Pulsar with a Magnetically Confined Mountain, *Astrophys. J.*, **623**, p. 1044, arXiv: `astro-ph/0503287`.

Novikov, I. D. and Thorne, K. S. (1973), Black hole astrophysics, in C. D. Witt and B. S. D. Witt, editors, *Black Holes*, p. 343, Gordon and Breach, New York–London–Paris.

Owen, B. J. (2005), Maximum elastic deformations of compact stars with exotic equations of state, *Phys. Rev. Lett.*, **95**, p. 211101.

Pétri, J. (2005), Forced oscillations in a hydrodynamical accretion disk and QPOs, *Astronomy and Astrophysics*.

Remillard, R. A. (2004), *AIPC*, **714**, pp. 13–20.

Remillard, R. A. (2005), X-ray spectral states and high-frequency QPOs in black hole binaries, *Astronom. Nachr.*, **326**(9), pp. 804–807, arXiv: `astro-ph/0510699`.

Remillard, R. A. and McClintock, J. E. (2006), X-Ray Properties of Black-Hole Binaries, *Annual Review of Astronomy and Astrophysics*, **44**(1), pp. 49–92, arXiv: `astro-ph/0606352`.

Rezzolla, L. (2004), A new simple model for high frequency quasiperiodic oscillations in black hole candidates, in P. Karet, F. K. Lamb and J. H. Swank, editors, *X-ray Timing 2003: Rossi and Beyond*, volume 714, p. 36, NY: American Institu of Physics, Melville.

Rezzolla, L., Yoshida, S., Maccarone, T. J. and Zanotti, O. (2003), A new simple model for high-frequency quasi-periodic oscillations in black hole candidates, *Monthly Notices Roy. Astronom. Soc.*, **344**(3), pp. L37–L41.

Shapiro, S. L. and Teukolsky, S. A. (1983), *Black Holes, White Dwarfs and Neutron Stars: The Physics of Compact Objects*, John Wiley & Sons, New York, ISBN 0-471-87316-0.

Smoluchowski, R. and Welch, D. O. (1970), Progressive deformation of the crust of pulsars, *Phys. Rev. Lett.*, **24**, pp. 1191–1192.

Stella, L. and Vietri, M. (1999), kHz Quasiperiodic Oscillations in Low-Mass X-Ray Binaries as Probes of General Relativity in the Strong-Field Regime, *Phys. Rev. Lett.*, **82**(1), pp. 17–20.

Strohmayer, T. E. (2001), Discovery of a Second High Frequency QPO from the Microquasar GRS 1915+105, *Astrophys. J.*, **554**, pp. L169–L172.

Strohmayer, T. E., Mushotzky, R. F., Winter, L., Soria, R., Uttley, P. and Cropper, M. (2007), Quasi-Periodic Variability in NGC 5408 X-1, *Astrophys. J.*, **660**, pp. 580–586, arXiv: `astro-ph/0701390`.

Strohmayer, T. E., van Horn, H. M., Ogata, S., Iyetomi, H. and Ichimaru, S. (1991), The shear modulus of the neutron star crust and nonradial oscillations of neutron stars, *Astrophys. J.*, **375**, pp. 679–686, ISSN 0004-637X.

Stuchlík, Z. and Hledík, S. (2005), Excitation of oscillations by a small inhomogeneity on the surface of a neutron star, in Hledík and Stuchlík (2005), pp. 189–208.

Stuchlík, Z., Slaný, P. and Török, G. (2004), Marginally stable thick discs with gradient inversion of orbital velocity measured in locally non-rotating frames: A mechanism for excitation of oscillations in accretion discs?, in Hledík and Stuchlík (2004), pp. 239–256.

Stuchlík, Z., Slaný, P. and Török, G. (2006), Toroidal LNRF-velocity Profiles in Thick Accretion Discs Orbiting Rapidly Rotating Kerr Black Holes, in Alimi and Füzfa (2006), pp. 778–785.

Stuchlík, Z., Slaný, P. and Török, G. (2007a), Humpy LNRF-velocity profiles in accretion discs orbiting almost extreme Kerr black holes – A possible relation to quasi-periodic oscillations, *Astronomy and Astrophysics*, **463**(3), pp. 807–816, arXiv: `astro-ph/0612439`.

Stuchlík, Z., Slaný, P. and Török, G. (2007b), Humpy LNRF-velocity profiles in accretion discs orbiting rapidly rotating Kerr black holes and a possible relation to epicyclic oscillations, in V. Karas and G. Matt, editors, *Black Holes from Stars to Galaxies – Across the Range of Masses*, volume 238 of *Proceedings of IAU Symposium*, pp. 459–460, International Astronomical Union, Cambridge University Press, Cambridge, UK, ISSN 1743-9213.

Stuchlík, Z., Slaný, P. and Török, G. (2007c), LNRF-velocity hump-induced oscillations of a Keplerian disc orbiting near-extreme Kerr black hole: A possible explanation of high-frequency QPOs in GRS 1915+105, *Astronomy and Astrophysics*, **470**(2), pp. 401–404, arXiv: `0704.1252v2`.

Stuchlík, Z., Slaný, P., Török, G. and Abramowicz, M. A. (2005), Aschenbach effect: Unexpected topology changes in motion of particles and fluids orbiting rapidly rotating Kerr black holes, *Phys. Rev. D*, **71**, p. 024037 (9), arXiv: `gr-qc/0411091`.

Stuchlík, Z., Török, G. and Bakala, P. (2007d), On a multi-resonant origin of high frequency quasiperiodic oscillations in the neutron-star X-ray binary 4U 1636−53, submitted to Astronomy and

Astrophysics, arXiv: 0704.2318.

Stuchlík, Z., Čermák, P., Török, G., Urbanec, M. and Bakala, P. (2007e), Genetic Selection of Neutron Star Structure Matching the X-Ray Observations, in N. Callaos, Q. Lesso, C. Zinn and O. Goriachkin, editors, *The 11th World Multi-Conference on Systemics, Cybernetics and Informatics: WMSCI 2007, July 8–11, Orlando, USA*, pp. 41–44, Internat. Inst. of Inf. and Syst.

Török, G. (2005a), A possible 3 : 2 orbital epicyclic resonance in QPOs frequencies of Sgr A*, *Astronomy and Astrophysics*, **440**(1), pp. 1–4, arXiv: astro-ph/0412500.

Török, G. (2005b), QPOs in microquasars and Sgr A*: measuring the black hole spin, *Astronom. Nachr.*, **326**(9), pp. 856–860, arXiv: astro-ph/0510669.

Török, G. (2007), Energy switch accross resonant points, submitted.

Török, G., Abramowicz, M. A., Bakala, P., Bursa, M., Horák, J., Kluźniak, W., Rebusco, P. and Stuchlík, Z. (2007a), On the distribution of kHz QPO frequency ratio in the atoll source 4U1635−53, *Astronomy and Astrophysics*, submitted.

Török, G., Abramowicz, M. A., Kluźniak, W. and Stuchlík, Z. (2005), The orbital resonance model for twin peak kHz quasi periodic oscillations in microquasars, *Astronomy and Astrophysics*, **436**(1), pp. 1–8, arXiv: astro-ph/0401464.

Török, G., Abramowicz, M. A., Kluźniak, W. and Stuchlík, Z. (2006), A Non-Linear Resonance Model for the Black Hole and Neutron Star QPOs: Theory Supported by Observations, in Alimi and Füzfa (2006), p. 786, arXiv: astro-ph/0603847.

Török, G., Bakala, P., Stuchlík, Z. and Čech, P. (2007b), Modelling the twin peak QPO distribution in the atoll source 4U1636−53, submitted to Acta Astronomica.

Török, G. and Barret, D. (2007), Reverse of the twin peak QPO amplitude, in preparation.

Török, G. and Stuchlík, Z. (2005a), Epicyclic frequencies of Keplerian motion in Kerr spacetimes, in Hledík and Stuchlík (2005), pp. 315–338.

Török, G. and Stuchlík, Z. (2005b), Radial and vertical epicyclic frequencies of Keplerian motion in the field of Kerr naked singularities. Comparison with the black hole case and possible instability of naked singularity accretion discs, *Astronomy and Astrophysics*, **437**(3), pp. 775–788, arXiv: astro-ph/0502127.

Török, G., Stuchlík, Z. and Bakala, P. (2007c), A remark about possible unity of the neutron star and black hole high frequency QPOs, *Central European J. Phys.*, **5**(4), pp. 457–462.

Ushomirsky, G., Cutler, C. and Bildsten, L. (2000), Deformations of Accreting Neutron Star Crusts and Gravitational Wave Emission, *Monthly Notices Roy. Astronom. Soc.*, **319**, p. 902.

van der Klis, M. (1998), Kilohertz Quasi-Periodic Oscillations in Low-Mass X-Ray Binaries, in R. Buccheri, J. van Paradijs and M. A. Alpar, editors, *The Many Faces of Neutron Stars*, p. 337, Kluwer, Dordrecht.

van der Klis, M. (2000), Millisecond Oscillations in X-ray Binaries, *Annual Review of Astronomy and Astrophysics*, **38**, pp. 717–760, arXiv: astro-ph/0001167.

Woosley, S. E. and Wallace, R. K. (1982), The thermonuclear model for gamma-ray bursts, *Astrophys. J.*, **258**, pp. 716–732.

Proceedings of *RAGtime 8/9, 15–19/19–21 September, 2006/2007, Hradec nad Moravicí, Opava, Czech Republic*
S. Hledík and Z. Stuchlík, editors, Silesian University in Opava, 2007, pp. 323–361

Orbital resonance model of QPOs in braneworld Kerr black hole spacetimes

Zdeněk Stuchlík and Andrea Kotrlová[a]

Institute of Physics, Faculty of Philosophy & Science, Silesian University in Opava,
Bezručovo nám. 13, CZ-746 01 Opava, Czech Republic
[a] andrea.kotrlova@fpf.slu.cz

ABSTRACT
Rotating black holes in the brany universe of the Randall–Sundrum type with infinite additional dimension are described by the Kerr geometry with a tidal charge b representing the interaction of the brany black hole and the bulk spacetime. We investigate the role of the tidal charge in the orbital resonance model of quasiperiodic oscillations (QPOs) in black hole systems. The orbital Keplerian frequency $\nu_{\rm K}$ and the radial and vertical epicyclic frequencies $\nu_{\rm r}$, ν_θ of the equatorial, quasicircular geodetical motion are discussed, and the local maxima of their radial profiles related to Keplerian accretion discs are given, assuming the inner edge of the disc located at loci of the innermost stable circular geodesic. The resonant conditions are given for possible direct (parametric) resonances of the oscillations with the radial and vertical epicyclic frequencies and for some trapped oscillations of the warped discs with resonant combinational frequencies involving the Keplerian and radial epicyclic frequencies. It is shown, how the tidal charge could influence matching of the observational data indicating the 3 : 2 frequency ratio observed in GRS 1915+105 microquasar with prediction of the orbital resonance model. The "magic" dimensionless black hole spin enabling presence of strong resonant phenomena at the radius, where $\nu_{\rm K} : \nu_\theta : \nu_{\rm r} = 3 : 2 : 1$, is determined in dependence on the tidal charge. Such strong resonances could be relevant even in sources with highly scattered resonant frequencies, as those expected in Sgr A*.

Keywords: Accretion – accretion disks – braneworld black hole physics – X-rays: general

1 INTRODUCTION

In recent years, one of the most promising approaches to the higher-dimensional gravity theories seem to be the string theory and M-theory describing gravity as a truly higher-dimensional interaction becoming effectively 4D at low enough energies. These theories inspired braneworld models, where the observable universe is a 3-brane (domain wall) to which the standard-model (non-gravitational) matter fields are confined, while gravity field enters the extra spatial dimensions, the size of which may be much larger than the Planck length scale $l_{\rm P} \sim 10^{-33}$ cm (Arkani-Hamed et al., 1998). The braneworld models

978-80-7248-419-5

could therefore provide an elegant solution to the hierarchy problem of the electroweak and quantum gravity scales, as these scales become to be of the same order ($\sim$ TeV) due to large scale extra dimensions (Arkani-Hamed et al., 1998). Therefore, future collider experiments can test the braneworld models quite well, including the hypothetical mini black hole production on the TeV-energy scales (Emparan et al., 2002; Dimopoulos and Landsberg, 2001). On the other hand, the braneworld models could influence astrophysically important properties of black holes, enabling observational tests of these models.

Gravity can be localized near the brane at low energies even with a non-compact, infinite size extra dimension with the warped spacetime satisfying the 5D Einstein equations with negative cosmological constant (as shown by Randall and Sundrum, 1999). Then an arbitrary energy-momentum tensor could be allowed on the brane (Shiromizu et al., 1999).

The Randall–Sundrum model gives 4D Einstein gravity in low energy limit, and the conventional potential of weak, Newtonian gravity appears on the 3-brane with high accuracy. Significant deviations from the Einstein gravity occur at very high energies, e.g., in the very early universe, and in vicinity of compact objects (see, e.g., Maartens, 2004; Germani and Maartens, 2001; Aliev and Gümrükçüoğlu, 2005). Gravitational collapse of matter trapped on the brane results in black holes mainly localized on the brane, but their horizon could be extended into the extra dimension. The high-energy effects produced by the gravitational collapse are disconnected from the outside space by the horizon, but they could have a signature on the brane, influencing properties of black holes (Maartens, 2004). There are high-energy effects of local character influencing pressure in collapsing matter, and also non-local corrections of "back-reaction" character arising from the influence of the Weyl curvature of the bulk space on the brane – the matter on the brane induces Weyl curvature in the bulk which makes influence on the structures on the brane due to the bulk graviton stresses (Maartens, 2004). The combination of high-energy (local) and bulk stress (non-local) effects alters significantly the matching problem on the brane, as compared to the 4D Einstein gravity; for spherical objects, matching no longer leads to a Schwarzschild exterior in general (Maartens, 2004; Germani and Maartens, 2001). Moreover, the Weyl stresses induced by bulk gravitons imply that the matching conditions do not have unique solution on the brane; in fact, knowledge of the 5D Weyl tensor is needed as a minimum condition for uniqueness (Germani and Maartens, 2001).[1]

Study of braneworld black holes is a rather complicated issue due to the "back-reactions" between the brany structures and the bulk space. If the brany black hole horizon extension is much smaller than the extra dimensions scale, the black hole could be considered as a higher-dimensional object and can be described by the solutions of the higher-dimensional vacuum Einstein equations (Aliev and Frolov, 2004; Frolov et al., 2003; Frolov and Stojkovic, 2003).

When the horizon radius is much greater than the length scale of extra dimension, the black hole becomes effectively 4D with a finite extension along the extra dimensions. Exact description of such black holes is not found yet generally, but some reasonable approaches were developed in the 3D braneworld of Randall and Sundrum (Emparan et al., 2000).

[1] At present, no exact 5D solution in the braneworld model is known.

There are two kinds of black hole solutions in the Randall–Sundrum braneworld model with infinite extension of the extra dimension.

One kind of these solutions looks like black string from the viewpoint of an observer in the bulk, while being described by the Schwarzschild metric for matter trapped on the brane (Chamblin et al., 2000). The generalizations to rotating black string solution (Modgil et al., 2002) and solutions with dilatonic field (Nojiri et al., 2000) were also found. However, the black string solutions have a curvature singularities at infinite extension along the extra dimension (anti-de Sitter horizon of the Randall–Sundrum braneworld). There is a proposal that the black hole strings could evolve to a localized black cigar solutions due to the classical instability near the anti-de Sitter horizon (Chamblin et al., 2000; Gregory and Laflamme, 1993), but it is not resolved at present (Horowitz and Maeda, 2001; Aliev and Gümrükçüoğlu, 2005).

Second kind of these solutions representing a promising way of generating exact localized solutions in the Randall–Sundrum braneworld models was initiated by Maartens and his coworkers (Maartens, 2004; Germani and Maartens, 2001; Dadhich et al., 2000). Assuming spherically symmetric metric induced on the 3-brane, the effective gravitational field equations on the brane could be solved, giving a Reissner–Nordström static black hole solutions endowed with a "tidal" charge parameter b (Dadhich et al., 2000) instead of the standard electric charge parameter Q^2 (Misner et al., 1973). The tidal charge reflects the effects of the Weyl curvature of the bulk space, i.e., from the 5D graviton stresses (Maartens, 2004) with bulk graviton tidal effect giving the name of the charge. Note that the tidal charge can be both positive and negative, and there are some indications that the negative tidal charge should properly represent the "back-reaction" effects of the bulk space Weyl tensor on the brane (Maartens, 2004; Dadhich et al., 2000; Sasaki et al., 2000).

In the simplest model of a spherically symmetric star with uniform density profile the high-energy and bulk graviton stress effects alter the matching conditions as compared with general relativistic case and make them unambitious since we do not know exact 5D Weyl tensor. Two different exact exterior solutions have been found, both satisfying the braneworld matching conditions and having asymptotically Schwarzschild character (Germani and Maartens, 2001). The first of these external solutions is of the known Reissner–Nordström metric form with a tidal charge characterizing the bulk graviton stress effect on the brane that is related to the density parameter of the star. The second solution is more complicated, and its metric tensor components explicitly depend on both the star density and brane tension. These two external solutions differ significantly, e.g., in the behaviour of the exterior curvature invariant (Germani and Maartens, 2001).

The exact stationary and axisymmetric solutions describing rotating black holes localized in the Randall–Sundrum braneworld were derived in Aliev and Gümrükçüoğlu (2005), having the metric tensor of the Kerr–Newman form with a tidal charge describing the 5D correction term generated by the 5D Weyl tensor stresses. The tidal charge has an "electric" character again and arises due to the 5D gravitational coupling between the brane and the bulk, reflected on the brane through the "electric" part of the bulk Weyl tensor (Aliev and Gümrükçüoğlu, 2005), in close analogy with the spherically symmetric case (Dadhich et al., 2000).

When both the tidal and electric charge are present in the brany black hole, its character is much more complex and usual Kerr–Newman form of the metric tensor is allowed only

in the approximate case of the small values of rotation parameter a, when in the linear approximation in a the metric arrives at the usual Boyer–Lindquist form describing charged and slowly rotating brany black holes (Aliev and Gümrükçüoğlu, 2005). For large enough rotational parameters, when the linear approximation is no longer valid, additional off-diagonal metric components $g_{r\phi}$, g_{rt} are relevant along with the standard $g_{\phi t}$ component due to the combined effects of the local bulk on the brane and the dragging effect of rotation, which through the "squared" energy momentum tensor on the brane distort the event horizon that becomes a stack of non-uniformly rotating null circles having different radii at fixed θ while going from the equatorial plane to the poles (Aliev and Gümrükçüoğlu, 2005). The uniformly rotating horizon is recovered for the small enough rotation parameter. In the absence of rotation, the metric tensor reduces to the Reissner–Nordström form with correction terms of local and non-local origin (Chamblin et al., 2001).

Here we restrict attention to the Kerr–Newman type of solutions describing the brany rotating black holes with no electric charge, since in astrophysically relevant situations the electric charge of the black hole must be exactly zero, or very small (Zel'dovich and Novikov, 1971; Damour et al., 1978). Then the results obtained in analysing the behaviour of test particles and photons or test fields around the Kerr–Newman black holes could be used assuming both positive and negative values of the brany tidal parameter b (used instead of the charge parameter Q^2).

It is very important to test the role of the hypothetical tidal charge, implied by the theory of multidimensional black holes in the Randall–Sundrum braneworld with non-compactified additional space dimension, in astrophysical situations, namely in the accretion processes and related optical phenomena, including the oscillatory features observed in the black hole systems. There are two complementary reasons for such studies. First, the observational data from the black hole systems (both Galactic binary systems or Sgr A* and active galactic nuclei) could restrict the allowed values of the tidal charge, giving a relevant information on the properties of the bulk spacetime and putting useful additional limits on the elementary particle physics. Second, the presence of the tidal charge could help much in detailed understanding of some possible discrepancies in the black hole parameter estimates coming from observational data that are obtained using different aspects of modelling accretion phenomena.

In fact, the black hole parameter estimates come from a variety of astrophysical observations (van der Klis, 2000, 2006; McClintock and Remillard, 2004; Remillard, 2005; Remillard and McClintock, 2006; McClintock et al., 2007). The black hole spin estimates are commonly given by the optical methods, namely by X-ray line profiles (Laor, 1991; Karas et al., 1992; Dovčiak et al., 2004; Fabian and Miniutti, 2005; Zakharov, 2003; Zakharov and Repin, 2006) and X-ray continuum spectra (McClintock et al., 2006; Middleton et al., 2006; Shafee et al., 2006), and by quasiperiodic oscillations, the frequency of which enable, in principle, the most precise spin estimates, because of high precision of the frequency measurements (Stuchlík et al., 2007b).[2]

Therefore, we discuss here in detail the orbital resonance model of QPOs, which seems to be the most promising in explaining the observational data from four microquasars

[2] But see some problems connected with the wide variety of the resonance models.

GRO J1655−40, XTE 1550−564, H 1743−322, GRS 1915+105 (Török et al., 2005; Török, 2005a,b; Stuchlík et al., 2007c) and in Sgr A* (Aschenbach, 2004; Aschenbach et al., 2004; Török, 2005a) or some extragalactic sources as NGC 5408 X-1 (Strohmayer et al., 2007).

It is well known that in astrophysically relevant situations the electric charge of a black hole becomes zero or negligible on short time scales because of its neutralization by accreting preferentially oppositely charged particles from ionized matter of the accretion disc (Zel'dovich and Novikov, 1971; Misner et al., 1973; Damour et al., 1978). Clearly, this statement remains true in the braneworld model, and that is the reason why it si enough to consider properties of brany Kerr black holes endowed with a tidal charge only. Of course, the tidal charge reflecting the non-local gravitational effects of the bulk space is non-negligible in general and it can have quite strong effect on the physical processes in vicinity of the black hole.

In Section 2, the effective gravitational field equations on the brane are introduced and briefly discussed. In Section 3, the Kerr black holes with a tidal charge, introduced by Aliev and Gümrükçüoğlu (2005), are described and their properties are briefly summarized. In Section 4, the Carter equations of motion are given, the equatorial circular geodesics are determined and properties of photon circular orbits and innermost stable orbits are discussed. Since the excitation of quasiperiodic oscillations and resonant phenomena between these oscillations could be dependent on the energy efficiency of the accretion processes in assumed thin Keplerian disc, we briefly summarize the properties of Keplerian circular orbits in the brany Kerr spacetimes. In Section 5, the radial and vertical (latitudinal) epicyclic frequencies ν_{r} and ν_θ, together with the Keplerian orbital frequency ν_{K}, are given. In Section 6, their properties are discussed, namely their radial profiles through the Keplerian accretion disc with its inner radius assumed to be located at the radius of the innermost stable circular geodesic, where the radial epicyclic frequency vanishes. In Section 7, we shortly discuss the resonance conditions for the direct resonance of the both epicyclic frequencies ($\nu_\theta : \nu_{\mathrm{r}} = 3 : 2$) assumed to be in a parametric resonance (Török et al., 2005), and the resonance of trapped oscillations assumed in warped disc as discussed by Kato (2007) $[(2\nu_{\mathrm{K}} - \nu_{\mathrm{r}}) : (\nu_{\mathrm{K}} - \nu_{\mathrm{r}}) = 3 : 2]$. In Section 8 we determine the "magic" (dimensionless) spin of brany Kerr black holes in dependence on the (dimensionless) tidal charge, enabling presence of strong resonant phenomena because of the very special frequency ratio $\nu_{\mathrm{K}} : \nu_\theta : \nu_{\mathrm{r}} = 3 : 2 : 1$; possibility of other small integer ratios of the three frequencies is briefly discussed. Concluding remarks on the resonant phenomena in strong gravity of brany black holes are presented in Section 9.

Notice that we focus our discussion on the case of the negative tidal charge, which is preferred physically because of contributing to confining the negative cosmological constant of the bulk on the gravitational field (Maartens, 2004, 2000).

2 EFFECTIVE GRAVITATIONAL FIELD EQUATIONS ON THE BRANE

Using the Gauss–Codazzi projective approach, Shiromizu et al. (1999) has defined the effective gravitational field equations on a 3-brane in a 5D bulk spacetime. Aliev and Gümrükçüoğlu (2005); Aliev and Gümrükçüoğlu (2004) has shown that an extension of the Arnowitt, Deser and Misner (ADM) formalism (Arnowitt et al., 1962) of 4D Einstein

gravitational theory to the 5D brany model is possible. The basic ideas of the 5D ADM formalism can be summarized after Aliev and Gümrükçüoğlu (2005) in the following way.

Let us assume 5D bulk spacetime endowed with the metric g_{AB} and coordinates x^A ($A = 0, 1, 2, 3, 4$) that includes a 3-brane with spacetime metric $h_{\alpha\beta}$. Introducing an arbitrary scalar function

$$Z = Z(x^A) \tag{1}$$

with $Z = \text{const}$ describing family of non-intersecting timelike hypersurfaces Σ_Z filling the bulk, we assume that the 3-brane is located at the $Z = 0$ hypersurface. We can introduce the unit spacelike normal to the brane ($Z = 0 = \text{const}$)

$$n_A = N\partial_A Z = (0, 0, 0, 0, N)\,, \qquad g_{AB}\, n^A n^B = 1\,, \tag{2}$$

where the scalar function

$$N = \left| g^{AB}\partial_A Z\, \partial_B Z \right|^{-1/2} \tag{3}$$

is called *lapse function*. Using the parametric expression of the brane surface $x^A = x^A(y^\alpha)$, a local frame of four vectors can be given in the form

$$e^A_\alpha = \frac{\partial x^A}{\partial y^\alpha}\,, \tag{4}$$

where y^α are spacetime coordinates on the brane ($\alpha = 0, 1, 2, 3$), which is orthogonal to n^A as

$$n_A\, e^A_\alpha = 0\,. \tag{5}$$

The brany spacetime is then determined by the induced metric

$$h_{\alpha\beta} = g_{AB}\, e^A_\alpha\, e^B_\beta\,, \tag{6}$$

while the bulk spacetime metric can be given in the form

$$g_{AB} = n_A n_B + h_{\alpha\beta}\, e^\alpha_A\, e^\beta_B\,. \tag{7}$$

It is crucial to introduce a spacelike "evolution vector" into the fifth dimension Z^A, given by the relation

$$Z^A\partial_A Z = 1\,, \tag{8}$$

where Z is the parameter along orbits of vector Z^A. Since Z^A is tangent to a congruence of curves intersecting the hypersurfaces $Z = \text{const}$ in the slicing of the spacetime, the evolution vector can be decomposed into normal and tangential parts

$$Z^A = Nn^A + N^\alpha e^A_\alpha\,, \tag{9}$$

with N^α being the shift vector. Then we can always define coordinate system $(y^\alpha, y^5) = (y^\alpha, Z)$ on the bulk spacetime and decompose the spacetime metric in the form

$$\mathrm{d}s^2 = g_{AB}\,\mathrm{d}x^A\mathrm{d}x^B = h_{\alpha\beta}\,\mathrm{d}y^\alpha\mathrm{d}y^\beta + 2N_\alpha\,\mathrm{d}y^\alpha\mathrm{d}Z + (N^2 + N_\alpha N^\alpha)\,\mathrm{d}Z^2\,, \tag{10}$$

corresponding to the standard ADM approach.

The brane bending in the bulk is determined by the extrinsic curvature tensor K_{AB} defined by the relation

$$\nabla_A n_B \equiv K_{AB} + n_A a_B\,, \qquad K_{AB}\,n^A = 0\,, \tag{11}$$

where ∇ denotes covariant derivative related to g_{AB}, and the 5-acceleration of the normals reads

$$a_A = n^B\,\nabla_B\,n_A\,. \tag{12}$$

The brane-projected extrinsic curvature tensor is then given by the relation

$$K_{\alpha\beta} = \nabla_{(B}n_{A)}e^A_\alpha e^B_\beta = \frac{1}{2N}\left(\partial_5 h_{\alpha\beta} - D_\alpha N_\beta - D_\beta N_\alpha\right) \tag{13}$$

with $\partial_5 = \partial/\partial Z$ and D being the covariant derivative related to the induced metric $h_{\alpha\beta}$.

The Einstein 5D equations in the bulk spacetime have the form

$${}^{(5)}G_{AB} = {}^{(5)}R_{AB} - \tfrac{1}{2}g_{AB}{}^{(5)}R = -\Lambda_5 g_{AB} + \kappa_5^2\left({}^{(5)}T_{AB} + \sqrt{\frac{h}{g}}\,\tau_{AB}\,\delta Z\right)\,, \tag{14}$$

where $\kappa_5^2 = 8\pi G_5$ (G_5 being the gravitational constant), Λ_5 is the bulk cosmological constant (assuming anti-de Sitter geometry), ${}^{(5)}T_{AB}$ is the energy-momentum tensor in the bulk, τ_{AB} is the energy-momentum tensor on the brane, h and g being metric determinants of $h_{\alpha\beta}$ and g_{AB}.

The effective Einstein gravitational equations (EGE) on the brane could then be given by using the Israel junction generalized to 5D situation. In order to realize the Israel method, the 5D Einstein equations have to be related to the intrinsic and extrinsic curvature on the brane surface according to the metric decomposition (10) and the δ-function singularity in Eq. (14) has to be related to the brany extrinsic-curvature jump on its evolving to the 5th dimension; finally the evolutionary terms has to be expressed in terms of the 4D quantities on the brane, i.e., there is matching of these terms on the brane (Aliev and Gümrükçüoğlu, 2005).

Denoting the brane tension λ and assuming the brany energy-momentum tensor in the form $\tau_{\alpha\beta} = -\lambda h_{\alpha\beta} + T_{\alpha\beta}$, the resulting Israel junction condition on the Z_2 symmetric brane reads

$$K_{\alpha\beta} = -\tfrac{1}{2}\kappa_5^2\left[T_{\alpha\beta} - \tfrac{1}{3}h_{\alpha\beta}(T - \lambda)\right] \tag{15}$$

leading to the gravitational field equations on the brane in the form (Aliev and Gümrükçüoğlu, 2005)

$$G_{\alpha\beta} = -\Lambda h_{\alpha\beta} + \kappa_4^2\,T_{\alpha\beta} + \kappa_5^4\,S_{\alpha\beta} - W_{\alpha\beta} - 3\kappa_5^2\,U_{\alpha\beta}\,. \tag{16}$$

The traceless tensor

$$W_{\alpha\beta} = A_{\alpha\beta} - \tfrac{1}{4}\, h_{\alpha\beta}\, A \tag{17}$$

is constructed from the "electric" part of the bulk Riemann tensor

$$A_{\alpha\beta} = {}^{(5)}R_{ABCD}\, n^A\, n^C\, e^B_\alpha\, e^D_\beta\,, \qquad A = h_{\alpha\beta}\, A^{\alpha\beta}\,. \tag{18}$$

The cosmological constant on the brane

$$\Lambda = \tfrac{1}{2}\left(\Lambda_5 + \tfrac{1}{6}\kappa_5^4\,\lambda^2 - \kappa_5^2\, P\right)\,, \tag{19}$$

and

$$\kappa_4^2 = \tfrac{1}{6}\,\kappa_5^4\,\lambda\,, \tag{20}$$

with

$$P = {}^{(5)}T_{AB}\, n^A\, n^B \tag{21}$$

being the normal compressive pressure term in 5D spacetime. The "squared energy-momentum" tensor is given by

$$S_{\alpha\beta} = -\tfrac{1}{4}\left[\left(T^\gamma_\alpha\, T_{\gamma\beta} - \tfrac{1}{3}T\, T_{\alpha\beta}\right) - \tfrac{1}{2}h_{\alpha\beta}\left(T_{\gamma\delta}\, T^{\gamma\delta} - \tfrac{1}{3}T^2\right)\right]\,, \tag{22}$$

while the traceless brany part of the bulk energy-momentum tensor is

$$U_{\alpha\beta} = -\tfrac{1}{3}\left({}^{(5)}T_{\alpha\beta} - \tfrac{1}{4}h_{\alpha\beta}\, h^{\gamma\delta}\, {}^{(5)}T_{\gamma\delta}\right)\,. \tag{23}$$

In the effective 4D EGE (16)–(23), $W_{\alpha\beta}$ describes non-local gravitational effect of the bulk space onto the brane and is sometimes called Weyl fluid (Shiromizu et al., 1999), while the local bulk effects on the brane are given by $S_{\alpha\beta}$, $U_{\alpha\beta}$ and P. In addition to the EGE (16)–(23), the $4+1$ decomposition of the 5D EGE (16) results also in the Hamiltonian constraint equation

$$\tfrac{1}{2}\left(R - K^2 + K_{\alpha\beta}K^{\alpha\beta}\right) = \Lambda_5 - \kappa_5^2 P\,, \tag{24}$$

and the momentum constraint equation

$$D_\alpha K^\alpha_\beta - D_\beta K = \kappa_5^2\, J_\beta\,, \tag{25}$$

where $K = K_{\alpha\beta}\, h^{\alpha\beta}$, while $J_\alpha = {}^{(5)}T_{\alpha B}\, n^B$ determines energy-momentum flux onto the brane (Aliev and Gümrükçüoğlu, 2005).

It should be stressed that the self-consistent solutions of the effective 4D EGE (16)–(23) on the brane require the knowledge of the non-local gravitational and energy-momentum terms coming from the bulk spacetime. Therefore, in general the brany field equations are not closed and evolution equations into the bulk have to be solved for the projected bulk curvature and energy-momentum tensors (Aliev and Gümrükçüoğlu, 2004). However, in particular cases the brany-equations system could be made closed assuming a special ansatz for the induced metric. In this way, both spherically symmetric and axially symmetric brany black hole spacetime has been found (Dadhich et al., 2000; Aliev and Gümrükçüoğlu, 2005). Assuming vacuum bulk and brany spacetimes, the non-local gravitational effects of the bulk could be simply given by the so called tidal charge entering the standard metric of the black hole spacetimes.

3 BRANEWORLD KERR BLACK HOLES

The rotating black holes localized on a 3-brane in the Randall–Sundrum braneworld model were derived under the assumption of stationary and axisymmetric Kerr–Schild metric on the brane and supposing empty bulk space and no matter fields on the brane ($T_{\alpha\beta} = 0$, Aliev and Gümrükçüoğlu, 2005). The effective EGE (16) then reduce to the form

$$R_{\alpha\beta} = -E_{\alpha\beta}\,, \tag{26}$$

where

$$E_{\alpha\beta} = {}^{(5)}C_{ABCD}\, n^A\, n^C\, e^B_\alpha\, e^D_\beta \tag{27}$$

is the "electric" part of the 5D Weyl tensor, used besides the $W_{\alpha\beta}$ tensor to describe the non-local gravitational effects of the bulk space onto the brane. Further, the relations

$$\Lambda_5 = -\frac{6}{l^2}\,, \qquad G_4 = \frac{G_5}{l} \tag{28}$$

can be deduced from Eqs (19) and (20), assuming zero cosmological constant on the brane ($\Lambda_4 = 0$). Here,

$$l = \frac{6}{\lambda\kappa_5^2} \tag{29}$$

is the curvature radius of the anti-de Sitter spacetimes. (Henceforth we set $G_4 = 1$.)

Using the condition $T_{\alpha\beta} = 0$ in the constraint equation (24), it is clear that the momentum constraint equation is satisfied identically, while the Hamiltonian constraint equation reads

$$R = 0\,. \tag{30}$$

This condition in the Kerr–Schild ansatz implies that the line element for the brany rotating black holes can be expressed in the standard Boyer–Lindquist coordinates in the form (Aliev and Gümrükçüoğlu, 2005)

$$\begin{aligned} \mathrm{d}s^2 = &-\left(1 - \frac{2Mr - b}{\Sigma}\right)\mathrm{d}t^2 - \frac{2a(2Mr - b)}{\Sigma}\sin^2\theta\,\mathrm{d}t\mathrm{d}\phi \\ &+ \frac{\Sigma}{\Delta}\,\mathrm{d}r^2 + \Sigma\,\mathrm{d}\theta^2 + \left(r^2 + a^2 + \frac{2Mr - b}{\Sigma}\,a^2\sin^2\theta\right)\sin^2\theta\,\mathrm{d}\phi^2\,, \end{aligned} \tag{31}$$

where

$$\Delta = r^2 + a^2 - 2Mr + b\,, \tag{32}$$

$$\Sigma = r^2 + a^2\cos^2\theta\,. \tag{33}$$

We can see that this metric looks exactly like the Kerr–Newman solution in general relativity (Misner et al., 1973), in which the square of the electric charge Q^2 is replaced by a

tidal charge parameter b (or "brany" parameter). Since the metric is asymptotically flat, by passing to the far-field regime we can interpret the parameter M as the total mass of the black hole and parameter a as the specific angular momentum (the black hole spin). The Coulomb-type nature of the tidal charge is verified by calculating the components of the tensor $E_{\alpha\beta}$ through equation (26) (Aliev and Gümrükçüoğlu, 2005).

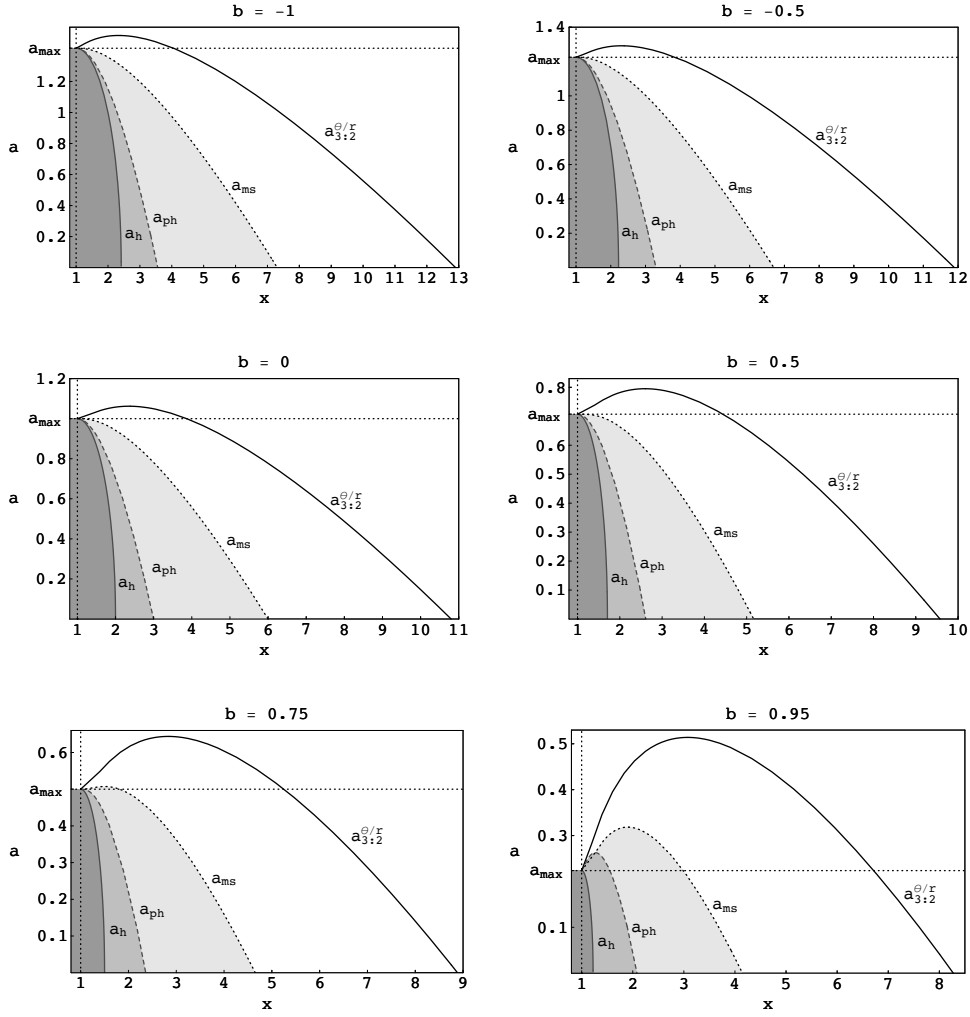

Figure 1. The behaviour of functions $a_{\rm h}$ (gray solid line), $a_{\rm ph}$ (dashed line) and $a_{\rm ms}$ (dotted line) that implicitly determine the radius of the outer event black hole horizon, the limiting photon orbit and the marginally stable circular orbit in the equatorial plane ($\theta = \pi/2$) of a rotating black hole with a fixed value of the tidal charge b. The function $a^{\theta/{\rm r}}_{3:2}$ (black solid line) represents the radii where the direct resonance $\nu_\theta : \nu_{\rm r} = 3:2$ occurs.

The event horizons of the spacetime are determined by the condition $\Delta = 0$. The radius of the outer event horizon is given by the relation

$$r_+ = M + \sqrt{M^2 - a^2 - b}\,. \tag{34}$$

The horizon structure depends on the sign of the tidal charge. We see that, in contrast to its positive values, the negative tidal charge tends to increase the horizon radius (see, e.g., Fig. 1).

The event horizon does exist provided that

$$M^2 \geq a^2 + b\,, \tag{35}$$

where the equality corresponds to the family of extreme black holes. It is clear that the positive tidal charge acts to weaken the gravitational field and we have the same horizon structure as in the usual Kerr–Newman solution. However, new interesting features arise for the negative tidal charge. For $b < 0$ and $a \to M$ it follows from equation (34) that the horizon radius

$$r_+ \to M + \sqrt{-b} > M\,; \tag{36}$$

such a situation is not allowed in the framework of general relativity. From equations (34) and (35) we can see that for $b < 0$, the extreme horizon $r_+ = M$ corresponds to a black hole with rotation parameter a greater than its mass M (e.g., for extreme black hole with $b = -M^2$ we have $a = \sqrt{2}\,M$). Thus, the bulk effects on the brane may provide a mechanism for spinning up the black hole on the brane so that its rotation parameter exceeds its mass. Such a mechanism is impossible in general relativity. Further, if the inner horizon determined by the formula

$$r_- = M - \sqrt{M^2 - a^2 - b} \tag{37}$$

turns out to be negative (it is possible for $b < 0$, again), the physical singularity ($r = 0$, $\theta = \pi/2$) is expected to be of space-like character, contrary to the case of $b > 0$, when it is of time-like character (Dadhich et al., 2000).

4 GEODESIC MOTION

Motion of a test particle of mass m is given by the standard geodesic equation

$$\frac{\mathrm{D}U^\mu}{\mathrm{d}\tau} = 0 \tag{38}$$

accompanied by the normalization condition $U_\mu U^\mu = -m^2$ and can be treated in full analogy with the Kerr case (see Carter, 1968). There are three motion constants given by the spacetime symmetry – the energy being related to the Killing vector field $\partial/\partial t$, the axial angular momentum being related to the Killing vector field $\partial/\partial\phi$, and the angular momentum constant related to the hidden symmetry of the Kerr spacetime (Carter, 1973).

The geodesic equations could then be fully separated and integrated using the Hamilton–Jacobi method.

For the motion restricted to the equatorial plane ($\theta = \pi/2$), the Carter equations take the form

$$\frac{\mathrm{d}\theta}{\mathrm{d}\lambda} = 0\,, \tag{39}$$

$$r^2\frac{\mathrm{d}r}{\mathrm{d}\lambda} = \pm\sqrt{R(r)}\,, \tag{40}$$

$$r^2\frac{\mathrm{d}\phi}{\mathrm{d}\lambda} = -(aE - L) + \frac{aP(r)}{\Delta}\,, \tag{41}$$

$$r^2\frac{\mathrm{d}t}{\mathrm{d}\lambda} = -a(aE - L) + \frac{(r^2 + a^2)P(r)}{\Delta}\,, \tag{42}$$

where

$$P(r) = E(r^2 + a^2) - La\,, \tag{43}$$

$$R(r) = P(r)^2 - \Delta\left[m^2r^2 + (aE - L)^2\right]\,. \tag{44}$$

The proper time of the particle τ is related to the affine parameter λ by $\tau = m\lambda$. The constants of motion are: energy E and axial angular momentum L of the test particle in infinity (related to the stationarity and the axial symmetry of the geometry); for the equatorial motion, the third constant of motion $Q = 0$ (Carter, 1973).

The equatorial circular orbits can most easily be determined by solving simultaneously the equations

$$R(r) = 0\,, \qquad \frac{\mathrm{d}R}{\mathrm{d}r} = 0\,. \tag{45}$$

The specific energy and the specific angular momentum of the circular motion at a given radius are then determined by the relations (Aliev and Gümrükçüoğlu, 2005; Dadhich and Kale, 1977)

$$\frac{E}{m} = \frac{r^2 - 2Mr + b \pm a\sqrt{Mr - b}}{r\left(r^2 - 3Mr + 2b \pm 2a\sqrt{Mr - b}\right)^{1/2}}\,, \tag{46}$$

$$\frac{L}{m} = \pm\frac{\sqrt{Mr - b}\left(r^2 + a^2 \mp 2a\sqrt{Mr - b}\right) \mp ab}{r\left(r^2 - 3Mr + 2b \pm 2a\sqrt{Mr - b}\right)^{1/2}}\,. \tag{47}$$

Here and in the following, the upper sign corresponds to the corotating orbits ($L > 0$), while the lower sign implies retrograde, counter-rotating ($L < 0$) motion of the particles.

From equation (46) we can see that the circular orbits can exist from infinity up to the radius of the limiting circular photon orbit, determined by the condition

$$r^2 - 3Mr + 2b \pm 2a\sqrt{Mr - b} = 0\,, \tag{48}$$

where $E/m \to \infty$ and $L/m \to \pm\infty$, but the impact parameter $B = L/E$ remains finite.

The radius of the marginally bound orbits with $E^2 = m^2$ is given by the largest root of the polynomial equation

$$Mr(4Mr - r^2 - 4b + a^2) + b(b - a^2) \pm 2a(b - 2Mr)\sqrt{Mr - b} = 0\,. \tag{49}$$

The loci of the stable circular orbits are given by the condition

$$\frac{\partial^2 R}{\partial r^2} \leq 0\,, \tag{50}$$

where the case of equality corresponds to the marginally stable circular orbits. Using the relations (46) and (47), we obtain the equation governing the marginally stable orbits in the form

$$Mr(6Mr - r^2 - 9b + 3a^2) + 4b(b - a^2) \mp 8a(Mr - b)^{3/2} = 0\,. \tag{51}$$

Notice that analogical equations of the form (48), (49) and (51) were obtained for an equatorial circular geodesic motion in the Kerr–Newman spacetime a long time ago (Aliev and Galtsov, 1981; Dadhich and Kale, 1977). It is evident (see Fig. 1) that the positive tidal charge will play the same role in its effect on the circular orbits as the electric charge in the Kerr–Newman spacetime – the radius of the circular photon orbit, as well as the radii of the innermost bound and the innermost stable circular orbits move towards the event horizon as the positive tidal charge increases for both direct and retrograde orbits, while for the negative tidal charge the distance of the radii of the limiting photon orbit, the innermost bound and the innermost stable circular orbits from the event horizon enlarge as the absolute value of b increases for both direct and retrograde motions of the particles (Aliev and Gümrükçüoğlu, 2005). Further, for the class of direct orbits, the negative tidal charge tends to increase the efficiency of an accretion disc around a maximally rotating braneworld black hole (the binding energy of a particle at the marginally stable direct orbit is given for appropriately chosen values of b in Fig. 2 (Aliev and Gümrükçüoğlu, 2005)).

In the analysis of the epicyclic frequency profiles, it is useful to relate the profiles to the photon circular geodesic and innermost stable circular geodesic radii that are relevant in discussions of properties of the accretion disc and their oscillations. Therefore, we put the limiting radii in an appropriate form.

For simplicity, we put $M = 1$ hereafter and we use dimensionless radial coordinate

$$x = r/(\mathrm{G}M/\mathrm{c}^2)\,. \tag{52}$$

The outer event horizon $x_{\mathrm{h}}(a, b)$ is then implicitly determined by the relation

$$a = a_{\mathrm{h}} \equiv \sqrt{2x - x^2 - b}\,. \tag{53}$$

Focusing our attention to the corotating orbits, we find the radius of the photon circular orbit $x_{\mathrm{ph}}(a, b)$ to be given by the relation

$$a = a_{\mathrm{ph}} \equiv \frac{x(3 - x) - 2b}{2\sqrt{x - b}}\,, \tag{54}$$

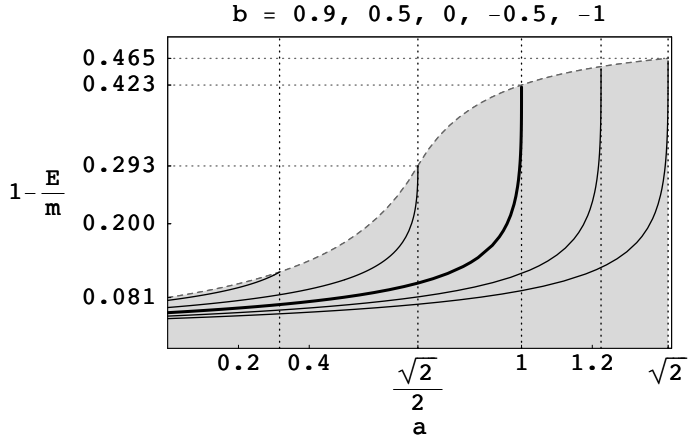

Figure 2. The binding energy per unit mass ($E_{\rm binding} = 1 - E/m$) of a particle at the marginally stable direct orbit $x = x_{\rm ms}$ as a function of the brany parameter b. The binding energy profile in thin Keplerian disc is given for appropriately chosen values of b (full lines). The dashed line corresponds to the binding energy for maximally rotating (extreme) braneworld black hole. Thick line represents the case of Kerr spacetime with $b = 0$. We can see that for extreme black hole with $b = -1$ and $a = \sqrt{2}$ the binding energy $E_{\rm binding} \simeq 46.5\,\%$, while for extreme Kerr black hole with $b = 0$, $a = 1$ we have $E_{\rm binding} \simeq 42.3\,\%$ and for extreme case of the Reissner–Nordström black hole where $b = 1$ and $a = 0$ the binding energy per unit mass of a particle at the marginally stable orbit is only $8.1\,\%$. So for the class of direct orbits, the negative tidal charge tends to increase the efficiency of an accretion disc around a maximally rotating braneworld black hole.

and the radius of the marginally stable corotating orbit $x_{\rm ms}(a, b)$ by the equation

$$a = a_{\rm ms} \equiv \frac{4(x-b)^{3/2} \mp x\sqrt{3x^2 - 2x(1+2b) + 3b}}{3x - 4b}\,; \tag{55}$$

for extreme black holes the maximum value of the black hole spin is

$$a_{\rm max} = \sqrt{1-b}\,, \tag{56}$$

thus, e.g., for $b = -1$ we have $a_{\rm max} = \sqrt{2}$.

5 EPICYCLIC OSCILLATIONS OF KEPLERIAN DISCS

It is well known that for oscillations of both thin Keplerian (Kato et al., 1998; Kluźniak and Abramowicz, 2001) and toroidal discs (Rezzolla et al., 2003) around black holes (neutron stars) the orbital Keplerian frequency $\nu_{\rm K}$ and the related radial and vertical epicyclic frequencies $\nu_{\rm r}$ and ν_θ of geodetical quasi-circular motion are relevant and observable directly or through some combinational frequencies (Török et al., 2005; Török and Stuchlík, 2005a,b; Stuchlík et al., 2007b). Of course, for extended tori, the eigenfrequencies of their oscillations are shifted from the epicyclic frequencies in dependence on the thickness of the

torus (Šrámková, 2005; Blaes et al., 2007). Similarly, due to non-linear resonant phenomena, the oscillatory eigenfrequencies could be shifted from the values corresponding to the geodetical epicyclic frequencies in dependence on the oscillatory amplitude (Landau and Lifshitz, 1976). However, it is expected that shift of this kind is observed in neutron star systems (Abramowicz et al., 2005a,b), while in microquasars, i.e., binary black hole systems, the observed frequency scatter is negligible and the geodetical epicyclic frequencies should be relevant. Here, we restrict our attention to the geodetical epicyclic oscillations of Keplerian discs in microquasars.

In the case of the Kerr black holes with the brany tidal charge b, the formulae of the test particle geodetical circular motion and its epicyclic oscillations, obtained by Aliev and Galtsov (1981) could be directly applied. We can write down the following relations for the orbital and epicyclic frequencies:

$$\nu_{\mathrm{r}}^2 = \alpha_{\mathrm{r}}\, \nu_{\mathrm{K}}^2 \,, \tag{57}$$

$$\nu_{\theta}^2 = \alpha_{\theta}\, \nu_{\mathrm{K}}^2 \,, \tag{58}$$

where the Keplerian frequency reads

$$\nu_{\mathrm{K}} = \frac{1}{2\pi}\left(\frac{\mathrm{G}M}{r_{\mathrm{G}}^3}\right)^{1/2} \frac{\sqrt{x-b}}{x^2 + a\sqrt{x-b}} = \frac{1}{2\pi}\frac{\mathrm{c}^3}{\mathrm{G}M}\frac{\sqrt{x-b}}{x^2 + a\sqrt{x-b}} \,, \tag{59}$$

and the dimensionless quantities determining the epicyclic frequencies are given by

$$\alpha_{\mathrm{r}}(x,a,b) = \frac{4\left(b - x - a^2\right)}{x^2} + \frac{8a\sqrt{x-b}}{x^2} + \frac{x(x-2) + a^2 + b}{x(x-b)} \,, \tag{60}$$

$$\alpha_{\theta}(x,a,b) = 1 + \frac{2a^2}{x^2} - \frac{2a\sqrt{x-b}}{x^2} - \frac{2a\sqrt{x-b}}{x(x-b)} + \frac{a^2}{x(x-b)} \,, \tag{61}$$

which reduce to the standard relations for quasi-circular geodesics in Kerr metric (Török and Stuchlík, 2005b) for $b = 0$.

In the limit of the Reissner–Nordström like static braneworld black hole ($a = 0$), we arrive at

$$\alpha_{\mathrm{r}}(x,b) = \frac{4(b-x)}{x^2} + \frac{x(x-2) + b}{x(x-b)} \,, \tag{62}$$

$$\alpha_{\theta}(x,b) = 1 \,, \tag{63}$$

so that $\nu_{\mathrm{K}}(x,b) = \nu_{\theta}(x,b)$ due to the spherical symmetry of the spacetime.

In the field of brany Kerr black holes ($a \neq 0$), there is (see Fig. 3)

$$\nu_{\mathrm{K}}(x,a,b) > \nu_{\theta}(x,a,b) > \nu_{\mathrm{r}}(x,a,b) \,, \tag{64}$$

however, this statement is not generally correct in the case of brany Kerr naked singularities. In the next section we show that the case when $\nu_{\theta}(x,a,b) \leq \nu_{\mathrm{r}}(x,a,b)$ is also possible.

The properties of ν_{K}, ν_{θ}, ν_{r} for Kerr black hole spacetimes are reviewed, e.g., in Kato et al. (1998) and for both Kerr black hole and Kerr naked singularity spacetimes in Török and Stuchlík (2005b). We can summarize that in Kerr spacetime with zero tidal charge ($b = 0$)

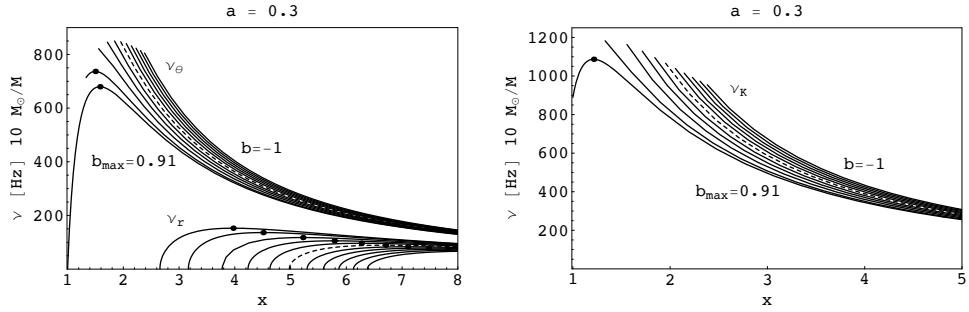

Figure 3. The behaviour of the two epicyclic frequencies ν_{r}, ν_θ (*left panel*), and Keplerian frequency ν_{K} (*right panel*) in the field of braneworld Kerr black holes with fixed value of the black hole spin $a = 0.3$ and various values of the tidal charge parameter b. The curves are spaced by 0.2 in b and they are plotted from the outer event black hole horizon x_{h}. The dashed line represents Kerr spacetime with zero tidal charge.

- the Keplerian frequency is a monotonically decreasing function of radius for the whole range of black hole rotational parameter $a \in (-1, 1)$ in astrophysically relevant radii above the photon orbit;
- for slowly rotating black holes the vertical epicyclic frequency is a monotonically decreasing function of radius in the same radial range as well; however, for rapidly rotating black holes this function has a maximum;
- the radial epicyclic frequency has a local maximum for all $a \in (-1, 1)$, and is zero at the innermost stable circular geodesic;
- for Kerr naked singularities the behaviour of the epicyclic frequencies is different; a detailed analysis (Török and Stuchlík, 2005b) shows that the vertical frequency can have two local extrema, and the radial one even three local extrema.

In the next section we discuss the behaviour of the fundamental orbital frequencies for Keplerian motion in the field of both brany Kerr black hole and brany Kerr naked singularities.

We express the frequency as $\nu\,[\mathrm{Hz}]\,10\,\mathrm{M}_\odot/M$ in every quantitative plot of frequency dependence on radial coordinate x, i.e., displayed value is the frequency relevant for a central object with a mass of $10\,\mathrm{M}_\odot$, which could be simply rescaled for another mass by just dividing the displayed value by the respective mass in units of ten solar mass.

6 PROPERTIES OF THE KEPLERIAN AND EPICYCLIC FREQUENCIES

First, it is important to find the range of relevance for the functions $\nu_{\mathrm{K}}(x, a, b)$, $\nu_\theta(x, a, b)$, $\nu_{\mathrm{r}}(x, a, b)$ above the event horizon x_{h} for black holes, and above the ring singularity located at $x = 0$ ($\theta = \pi/2$) for naked singularities.

Stable circular geodesics, relevant for the Keplerian, thin accretion discs exist for $x > x_{\mathrm{ms}}(a, b)$, where $x_{\mathrm{ms}}(a, b)$ denotes the radius of the marginally stable orbit, determined (in

an implicit form) by the relation (51), which coincides with the condition

$$\alpha_{\rm r}(x, a, b) = 0\,. \tag{65}$$

For toroidal, thick accretion discs the unstable circular geodesics can be relevant in the range $x_{\rm mb} \leq x_{\rm in} < x < x_{\rm ms}$, being stabilized by pressure gradients in the tori. The radius of the marginally bound circular geodesic $x_{\rm mb}$, implicitly determined by the equation (49), is the lower limit for the inner edge of thick discs (Kozłowski et al., 1978; Krolik and Hawley, 2002).

Clearly, the Keplerian orbital frequency is well defined up to $x = x_{\rm ph}$. However, $\nu_{\rm r}$ is well defined, if $\alpha_{\rm r} \geq 0$, i.e., at $x \geq x_{\rm ms}$, and $\nu_{\rm r} = 0$ at $x_{\rm ms}$. We can also show that for $x \geq x_{\rm ph}$, there is $\alpha_\theta \geq 0$; i.e., the vertical frequency ν_θ is well defined at $x > x_{\rm ph}$.

From Fig. 3, we can conclude that not only the both epicyclic frequencies but even the Keplerian frequency can have a maximum located above the outer event black hole horizon; this kind of behaviour is not allowed in Kerr spacetime. In the next subsection we will discuss, if the maximum could be located above the marginally stable or the limiting photon circular orbit.

6.1 Local extrema of the Keplerian frequency

Denoting by $\mathcal{X}_{\rm K}$ the local extrema of Keplerian frequency $\nu_{\rm K}$, we can give the extrema by the condition

$$\frac{\partial \nu_{\rm K}}{\partial r} = 0 \quad \Leftrightarrow \quad \frac{\partial \nu_{\rm K}}{\partial x} = 0\,, \tag{66}$$

where x is dimensionless radial coordinate (52). From (59), we find that the corresponding derivative[3] is

$$\nu'_{\rm K} = \frac{1}{2\pi}\sqrt{\frac{GM}{r_{\rm G}^3}}\,\frac{x(4b-3x)}{2\sqrt{x-b}\left(x^2+a\sqrt{x-b}\right)^2} = \frac{x(4b-3x)\nu_{\rm K}}{2(x-b)\left(x^2+a\sqrt{x-b}\right)}\,, \tag{67}$$

and relation (66) implies that Keplerian frequency has a local extremum located at

$$\mathcal{X}_{\rm K} = \tfrac{4}{3}b\,. \tag{68}$$

The second derivative at $x = \mathcal{X}_{\rm K}$

$$\nu''_{\rm K} = \frac{-162\sqrt{3}}{\sqrt{b}\left(3\sqrt{3}\,a + 16b^{3/2}\right)^2} \tag{69}$$

is always negative, thus Keplerian frequency could have one local maximum at $x = \mathcal{X}_{\rm K}$.

Generally, the maximum is located at or above the outer event black hole horizon if the condition

$$\mathcal{X}_{\rm K} \geq 1 \tag{70}$$

[3] After introducing $'$ as $\mathrm{d}/\mathrm{d}r$.

is satisfied that implies the relevant range of the tidal charge parameter

$$0.75 \leq b \leq 1 \tag{71}$$

and from relation (56) the possible values of the black hole spin are allowed from the interval

$$0 \leq a \leq 0.5\,, \tag{72}$$

where the case of a black hole with $a = 0.5$ and $b = 0.75$ corresponds to the maximally rotating (extreme) braneworld Kerr black hole with the maximum of Keplerian frequency situated exactly at the Boyer–Lindquist coordinate radius of the extreme black hole horizon $x_{\rm h} = 1$.

From relations (53) and (54) we obtain

$$a_{\rm h}(x = \mathcal{X}_{\rm K}) = \tfrac{1}{3}\sqrt{b(15 - 16b)}\,, \tag{73}$$

$$a_{\rm ph}(x = \mathcal{X}_{\rm K}) = \sqrt{3b}\left(1 - \tfrac{8}{9}b\right)\,, \tag{74}$$

which implicitly determine that the maximum of Keplerian frequency is situated at the radius coinciding with the radius of the black hole horizon $\mathcal{X}_{\rm K} = x_{\rm h}$ (73) or the circular photon orbit $\mathcal{X}_{\rm K} = x_{\rm ph}$ (74). From Eq. (55) we obtain the same relation as (74), thus

$$a_{\rm ms}(x = \mathcal{X}_{\rm K}) = a_{\rm ph}(x = \mathcal{X}_{\rm K})\,, \tag{75}$$

it means that the functions $a_{\rm ph}$ and $a_{\rm ms}$ cross each other at the radius where the Keplerian frequency has its maximum $x = \mathcal{X}_{\rm K} = 4/3b$.

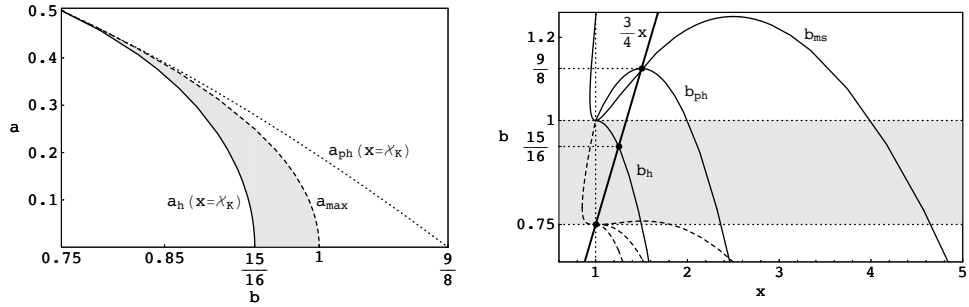

Figure 4. *Left panel:* the functions $a_{\rm h}(x = \mathcal{X}_{\rm K})$ (solid line), $a_{\rm ph}(x = \mathcal{X}_{\rm K})$ (dotted line) determining that the maximum of Keplerian frequency is situated exactly at the black hole horizon $\mathcal{X}_{\rm K} = x_{\rm h}$, at the photon orbit $\mathcal{X}_{\rm K} = x_{\rm ph}$. Dashed line represents maximum possible value of the black hole spin corresponding to the concrete value of the brany parameter b, so the area above $a_{\rm max}$ belong to naked singularities. The gray area illustrates all possible combinations of the black hole spin a and the tidal charge b for which the Keplerian frequency has its maximum located at $x_{\rm h} \leq \mathcal{X}_{\rm K} \leq x_{\rm ph}$. The *right panel* displays the functions $b_{\rm h}$, $b_{\rm ph}$ and $b_{\rm ms}$ implicitly determining the location of the black hole horizon, the limiting photon orbit and the marginally stable orbit for $a = 0$ (solid lines) and $a = 0.5$ (dashed lines). Thick line represents (in an implicit form) the maximum of Keplerian frequency $b = 3x/4$.

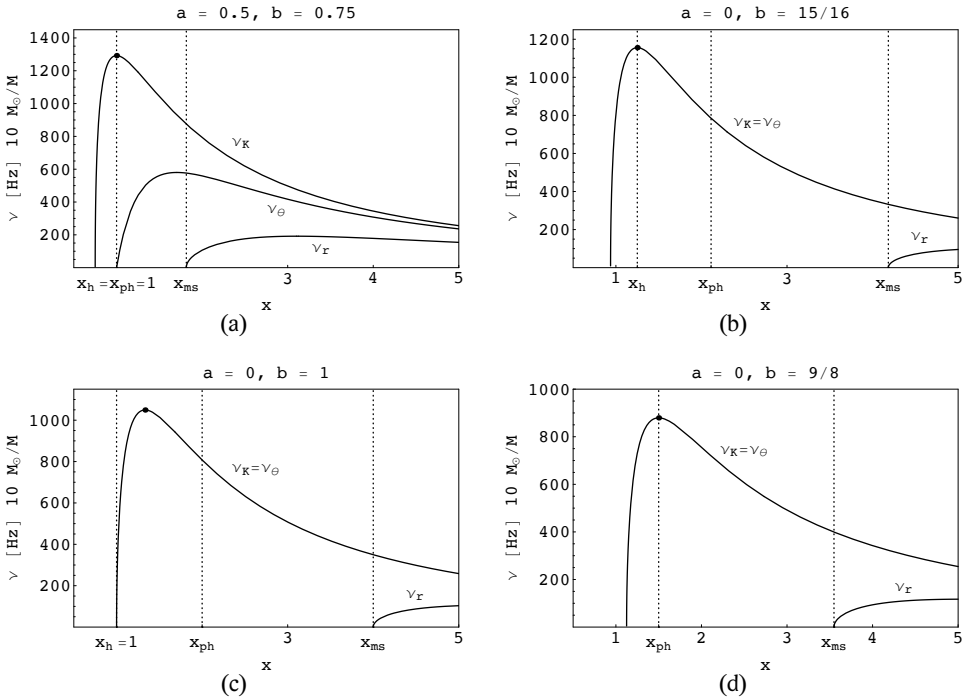

Figure 5. The Keplerian and epicyclic frequencies for various values of the black hole spin a and the tidal charge b: (a) the only case when the Keplerian frequency has its maximum located exactly at $\mathcal{X}_{\rm K} = x_{\rm h} = x_{\rm ph}$; (b)–(d) represent braneworld Reissner–Nordström spacetime where $\nu_{\rm K} = \nu_\theta$; (a), (c) correspond to the extreme black holes, (d) to naked singularity.

The functions $a_{\rm h}(x = \mathcal{X}_{\rm K})$, $a_{\rm ph}(x = \mathcal{X}_{\rm K})$ are shown in the left panel of Fig. 4. We can see that for brany Kerr black holes all possible values of the tidal charge parameter and black hole spin imply the condition

$$a_{\rm ph}(x = \mathcal{X}_{\rm K}) \geq a_{\rm max}\,, \tag{76}$$

thus the maximum of Keplerian frequency could never be located above the photon orbit $x_{\rm ph}$. Only for maximally rotating black hole with $b = 0.75$ and $a = a_{\rm max} = 0.5$, the maximum is situated exactly at the Boyer–Lindquist coordinate radius of the limiting photon orbit that merges with the radius of the black hole horizon, so $\mathcal{X}_{\rm K} = x_{\rm ph} = x_{\rm h} = 1$ (see Fig. 5).[4]

We can conclude that for brany parameter from interval (71) and black hole spin from interval (72), the Keplerian frequency has its maximum located between the black hole

[4] However, note the behaviour of extreme Kerr black hole at $x = 1$, where the same coordinate corresponds to an infinitely long throat of the proper radial distance, with different positions of the horizon and the circular photon, marginally bound and marginally stable orbits (Bardeen, 1973).

horizon and the photon circular orbit

$$x_{\rm h} \leq \mathcal{X}_{\rm K} \leq x_{\rm ph}\,. \tag{77}$$

In astrophysically relevant radii above the photon orbit $x > x_{\rm ph}$ the Keplerian frequency is a monotonically decreasing function of radius for the whole range of the brany tidal charge parameter b as in the standard Kerr spacetimes.

Notice that the function $a_{\rm ph}$ (54) has two local extrema situated at $x = 1$ and $x = \mathcal{X}_{\rm K} = 4/3b$, which for brany parameter $b > 0.75$ corresponds to the local maximum. Also the function $a_{\rm ms}$ (55) has two local extrema located at $x = 1$ and $x = 2b$, that for brany parameter $b > 0.5$ corresponds to the local maximum (this local maximum appears only for naked singularities, since $a > a_{\rm max}$). So neither the function $a_{\rm ph}$ nor $a_{\rm ms}$ are for $x > 1$ monotonically decreasing functions of radius for the whole range of the brany tidal charge parameter b as in usual Kerr spacetime. This special behaviour of $a_{\rm ph}$ and $a_{\rm ms}$ implies that for some values of the brany parameter b the loci of the photon orbit $x_{\rm ph}$ and the marginally stable orbit $x_{\rm ms}$ for extreme braneworld Kerr black holes do not merge with the black hole horizon located at $x_{\rm h} = 1$ as in Kerr spacetime and are shifted to higher radii. We have

$$x_{\rm ph} > 1 \quad \text{for} \quad b > 0.75\,, \tag{78}$$

$$x_{\rm ms} > 1 \quad \text{for} \quad b > 0.5\,. \tag{79}$$

Actually, this special behaviour of $a_{\rm ph}$ and $a_{\rm ms}$ implies that the Keplerian frequency could not have its maximum located above the photon orbit. E.g., for extreme Reissner–Nordström braneworld black hole with $a = 0$ and $b = 1$, we have $x_{\rm h} = 1$, $x_{\rm ph} = 2$, $x_{\rm ms} = 4$ and $\mathcal{X}_{\rm K} = 4/3$ (see Figs 4 and 5).

The functions $a_{\rm ph}$ and $a_{\rm ms}$ are for various values of the tidal charge b illustrated in Fig. 1.

6.2 Local extrema of epicyclic frequencies

The local extrema of the radial and vertical epicyclic frequencies $\mathcal{X}_{\rm r}$, $\mathcal{X}_\theta$ are given by the condition

$$\frac{\partial \nu_i}{\partial x} = 0 \quad \text{for} \quad \mathcal{X}_i\,, \quad \text{where} \quad i \in \{{\rm r}, \theta\}\,. \tag{80}$$

Using (57) and (58), the corresponding derivatives can be given in the form

$$\nu_i' = \sqrt{\alpha_i}\left(\nu_{\rm K}' + \frac{\alpha_i'}{2\alpha_i}\nu_{\rm K}\right), \tag{81}$$

$$\alpha_i' = \frac{\beta_i}{x^3(x-b)^{5/2}}\,, \tag{82}$$

where $\nu_{\rm K}'$ is given by (67), and

$$\begin{aligned}\beta_{\rm r}(x,a,b) = {} & -4a(3x-4b)(x-b)^2 + \sqrt{x-b} \\ & \times \left[a^2\left(6x^2 - 15xb + 8b^2\right) - \left(x^3 b - 6x^3 + 18x^2 b - 21xb^2 + 8b^3\right)\right], \end{aligned} \tag{83}$$

$$\beta_\theta(x,a,b) = a\left(x - a\sqrt{x-b} - b\right)\left(6x^2 - 9xb + 4b^2\right). \tag{84}$$

Relations (80) and (81) imply the condition determining extrema $\mathcal{X}_i(a, b)$ of the epicyclic frequencies profiles

$$\beta_i(x, a, b) = -\frac{2\nu_{\mathrm{K}}'}{\nu_{\mathrm{K}}}\, x^3 (x - b)^{5/2}\, \alpha_i(x, a, b)\,, \quad i \in \{\mathrm{r}, \theta\}\,. \tag{85}$$

We have checked that in the case of counter-rotating orbits ($a < 0$) the extrema $\mathcal{X}_\theta$ are located under the photon circular orbit and the extrema $\mathcal{X}_\mathrm{r}$ are just extensions of the $\mathcal{X}_\mathrm{r}$ for corotating case, therefore, we focus mainly on the case of corotating orbits ($a > 0$) in the next discussion.

In Figs 6 and 7 we show for various values of brany parameter b curves $\mathcal{A}_\mathrm{r}^k(x = \mathcal{X}_\mathrm{r}, b)$ ($\mathcal{A}_\theta^k(x = \mathcal{X}_\theta, b)$), $k \in \{1, 2\}$ implicitly determined by the relations (85); index k denotes different branches of the solution of (85).

The radial epicyclic frequency has one local maximum for braneworld Kerr black holes with rotational parameter restricted by

$$0 \leq a \leq a_{\max}(b)\,, \tag{86}$$

and for all possible values of brany parameter b. The local maximum is always located above the marginally stable orbit x_{ms} (see Fig. 6).

But for braneworld Kerr naked singularities with

$$b < b_{\mathrm{c}} \doteq 0.29143 \tag{87}$$

the radial epicyclic frequency has two local maxima and one local minimum for

$$a_{\max} < a < a_{\mathrm{c1(r)}}\,, \tag{88}$$

where $a_{\mathrm{c1(r)}}$ corresponds to the local maximum of $\mathcal{A}_\mathrm{r}^2(x = \mathcal{X}_\mathrm{r}, b)$, and again one local maximum for

$$a \geq a_{\mathrm{c1(r)}}\,, \tag{89}$$

as in usual Kerr naked singularity spacetime (Török and Stuchlík, 2005b). However, for some specific values of a

$$a_1 < a < a_2\,, \tag{90}$$

where a_1 we obtain from equation

$$\mathcal{A}_\mathrm{r}^1(x = \mathcal{X}_\mathrm{r}, b) = a_{\mathrm{ms}} \tag{91}$$

and a_2 from

$$\mathcal{A}_\mathrm{r}^2(x = \mathcal{X}_\mathrm{r}, b) = a_{\mathrm{ms}}\,, \tag{92}$$

the radial epicyclic frequency has one extra local minimum, because for these special values of a there exists no marginally stable orbit (given by condition (65), i.e., $\nu_\mathrm{r} = 0$), therefore the radial epicyclic frequency is for a from (90) always greater than zero.

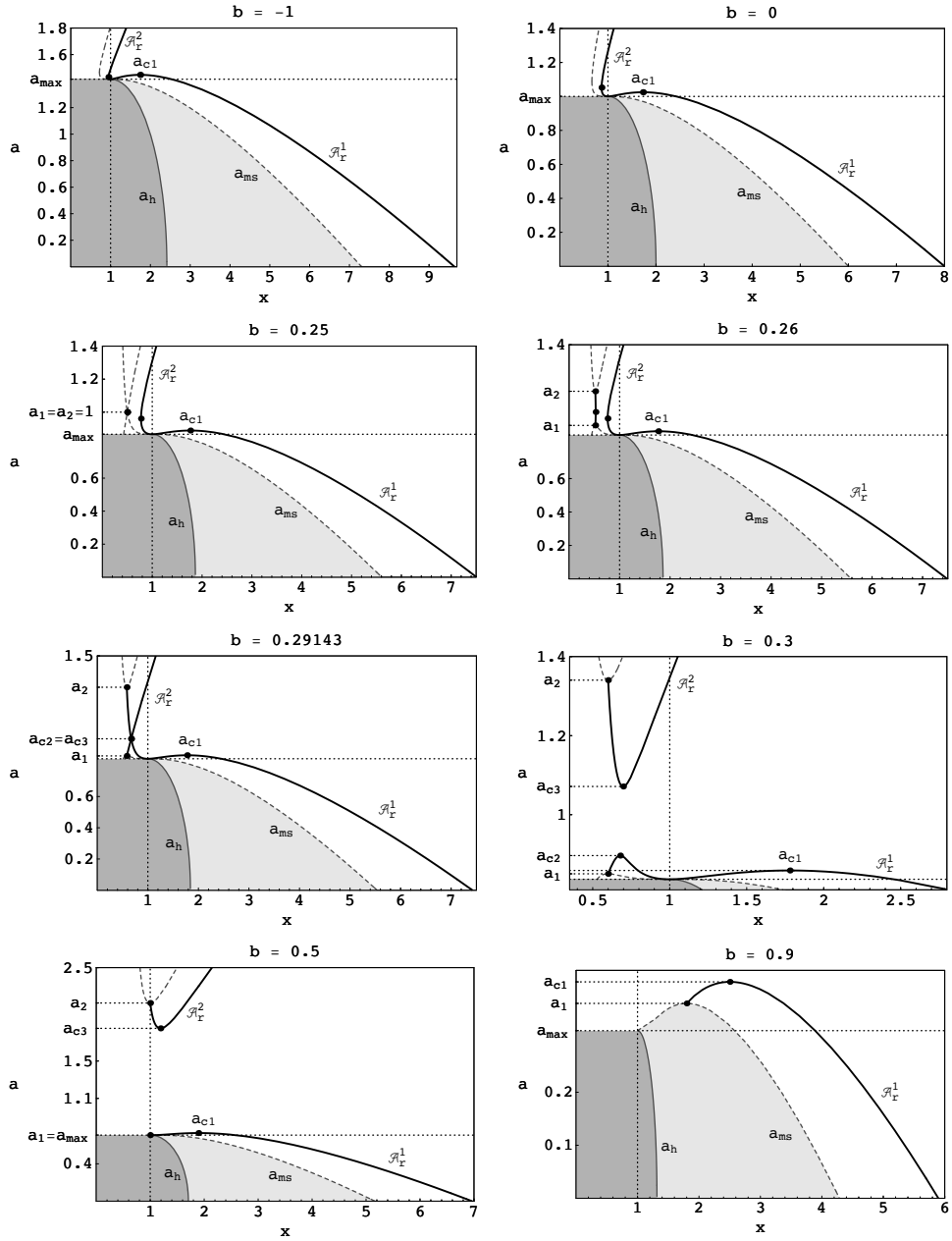

Figure 6. The functions $\mathcal{A}_r^1(x = \mathcal{X}_r, b)$, $\mathcal{A}_r^2(x = \mathcal{X}_r, b)$, implicitly determining the locations $\mathcal{X}_r$ of the radial epicyclic frequency local extrema for various values of brany parameter b.

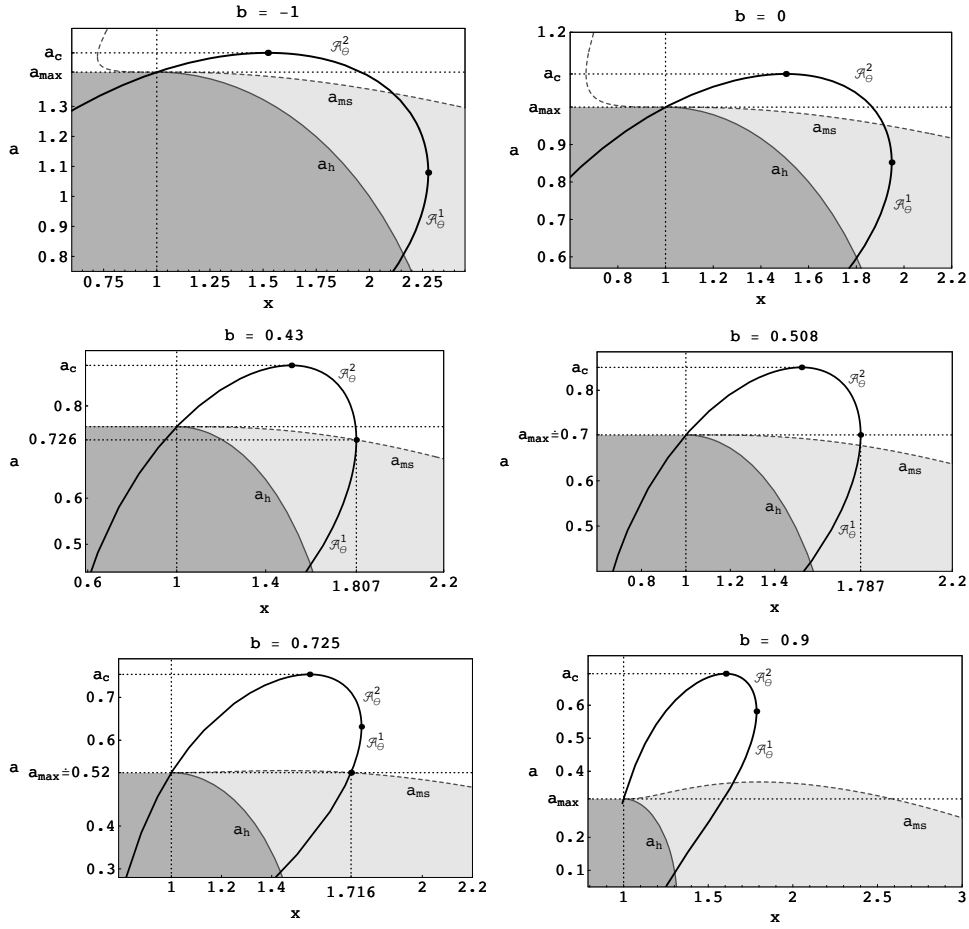

Figure 7. The functions $\mathcal{A}^1_\theta(x = \mathcal{X}_\theta, b)$, $\mathcal{A}^2_\theta(x = \mathcal{X}_\theta, b)$, implicitly determining the locations $\mathcal{X}_\theta$ of the vertical epicyclic frequency local extrema for various values of brany parameter b.

For braneworld Kerr naked singularities with $b > b_c$ the situation is more complicated, as we can see in Fig. 6. Denoting by $a_{c1(r)}$ and $a_{c2(r)}$, the local maxima of $\mathcal{A}^2_r(x = \mathcal{X}_r, b)$, and $a_{c3(r)}$ the local minimum of $\mathcal{A}^1_r(x = \mathcal{X}_r, b)$, then if

$$b_c < b < 0.5\,, \tag{93}$$

and $a_{c2(r)} > a_{c1(r)}$ ($a_{c2(r)} < a_{c1(r)}$), the radial epicyclic frequency has for $a_{max} < a \leq a_1$ two local maxima and one local minimum; for $a_1 < a < a_{c1(r)}$ ($a_1 < a < a_{c2(r)}$) two local maxima and also two local minima; for $a_{c1(r)} \leq a < a_{c2(r)}$ ($a_{c2(r)} \leq a < a_{c1(r)}$) one local maximum and one local minimum; for $a_{c2(r)} \leq a \leq a_{c3(r)}$ ($a_{c1(r)} \leq a \leq a_{c3(r)}$) the radial epicyclic frequency is a monotonically decreasing function of the radial coordinate without any extrema; for $a_{c3(r)} < a < a_2$ it has again one local maximum and one local minimum;

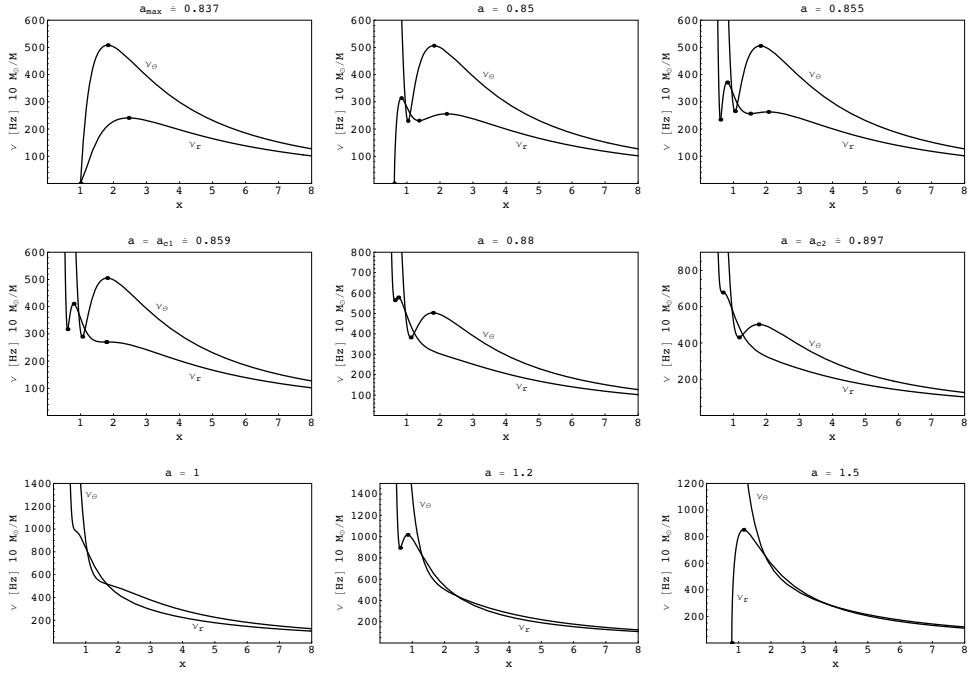

Figure 8. The behaviour of the epicyclic frequencies for $b = 0.3$ and for some representative values of rotational parameter a in braneworld Kerr naked singularity spacetimes, including the extreme braneworld Kerr black hole.

and finally for $a \geq a_2$ it has only one local maximum as in black hole spacetime (a_1 and a_2 are given by (91) and (92), the condition $a_{\rm max} < a_1 < a_{\rm c1(r)}$ is always satisfied). Notice that for $a_1 < a < a_2$, $\nu_{\rm r}$ could not be equal to zero (see Fig. 8).

If $b = 0.5$, then $a_1 = a_{\rm c2(r)} = a_{\rm max} \doteq 0.707$, and for $a_{\rm max} < a < a_{\rm c1(r)}$ the radial epicyclic frequency has one local maximum and one local minimum; for $a_{\rm c1(r)} \leq a \leq a_{\rm c3(r)}$ it is a monotonically decreasing function of the radial coordinate without any extrema; for $a_{\rm c3(r)} < a < a_2$ it has again one local maximum and one local minimum; and for $a \geq a_2$ it has only one local maximum.

In the case of braneworld Kerr naked singularities with

$$b > 0.5\,, \tag{94}$$

the behaviour of the radial epicyclic frequency is different due to the effect described in the previous section (see relation (79)). For $a_{\rm max} < a \leq a_1$, $\nu_{\rm r}$ has one local maximum; for $a_1 < a < a_{\rm c1(r)}$ it has one local maximum and one local minimum; for $a_{\rm c1(r)} \leq a \leq a_{\rm c3(r)}$ it is a monotonically decreasing function of the radial coordinate without any extrema; for $a_{\rm c3(r)} < a < a_2$ it has again one local maximum and one local minimum; and finally for $a \geq a_2$ it has only one local maximum.

The vertical epicyclic frequency has a local maximum (at $x > x_{\rm ms}$) only for rapidly rotating black holes with (see Fig. 7)

$$a_{{\rm ms}(\theta)} < a < a_{\rm max} \quad \text{and} \quad b < 0.725\,, \tag{95}$$

where $a_{{\rm ms}(\theta)}$ we obtain as a solution of equation

$$a_{\rm ms} = \mathcal{A}^k_\theta\,, \tag{96}$$

for $k = 1$ or 2. There is $a_{{\rm ms}(\theta)} = a_{\rm max}(b = 0.725) \doteq 0.524$. (For maximally rotating black hole with $b = 0.725$ and $a_{\rm max} \doteq 0.524$, the local maximum is located exactly at the radius of the marginally stable orbit, $\mathcal{X}_\theta = x_{\rm ms}$). Note that in the black hole case the local maximum of $\nu_\theta(x, a, b)$ is relevant in resonant effects for $x > x_{\rm ms}$.

For $b > 0.725$ the vertical epicyclic frequency is a monotonically decreasing function of radius for the whole range of black hole rotational parameter a.

In the braneworld Kerr naked singularity spacetimes, the function ν_θ has a local minimum and a local maximum for

$$a_{\rm max} < a < a_{{\rm c}(\theta)}\,, \tag{97}$$

and has no astrophysically relevant local extrema for

$$a \geq a_{{\rm c}(\theta)}\,. \tag{98}$$

Clearly, the behaviour of the epicyclic frequencies substantially differs for braneworld Kerr naked singularities in comparison with braneworld Kerr black holes. Examples of the behaviour of the epicyclic frequencies in Kerr naked singularity spacetimes with $b = 0.3$ are given in Fig. 8.

6.3 Ratio of epicyclic frequencies

The ratio of epicyclic frequencies ν_θ and $\nu_{\rm r}$ needs to be well defined for some models of QPOs (Abramowicz et al., 2004; Kato, 2004). It is well known (see, e.g., Kato et al., 1998) that for the Kerr black holes ($-1 \leq a \leq 1$) the inequality

$$\nu_{\rm r}(x, a) < \nu_\theta(x, a) \tag{99}$$

holds, i.e., the equation $\nu_{\rm r}(x, a) = \nu_\theta(x, a)$ does not have any real solution in the whole range of black hole rotational parameter $a \in (-1, 1)$ and

$$\frac{\nu_\theta}{\nu_{\rm r}} > 1 \tag{100}$$

for any Kerr black hole. Furthermore, this ratio is a monotonic function of radius for any fixed $a \in (-1, 1)$ (Török and Stuchlík, 2005b). These statements are valid also for any brany Kerr black hole (i.e., for b fixed and $a \leq a_{\rm max}$).

However, the situation is different for Kerr naked singularities. For $b = 0$ and $a > 1$, the epicyclic frequencies ν_θ, $\nu_{\rm r}$ can satisfy the equality condition

$$\nu_\theta(a, x) = \nu_{\rm r}(a, x) \tag{101}$$

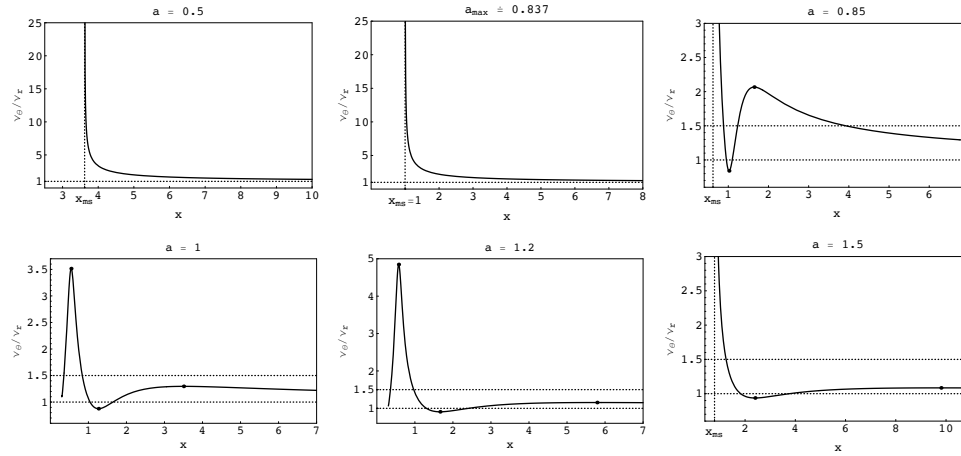

Figure 9. The behaviour of ratio $\nu_\theta/\nu_\mathrm{r}(x)$ of the epicyclic frequencies for braneworld Kerr black hole and naked singularity spacetimes with $b = 0.3$. The marginally stable orbit x_ms is denoted by a dotted vertical line (if this orbit exists at the given spacetime).

giving a strong resonant phenomenon, which occurs at the critical radius

$$x_\mathrm{sr} = a^2 \qquad (a \geq 1)\,. \tag{102}$$

This means that for any Kerr naked singularity the epicyclic frequency ratio $\nu_\theta/\nu_\mathrm{r}$ is a non-monotonic function that reaches value 1 at the point given by (102); for detailed discussion (see Török and Stuchlík, 2005b).

Furthermore, for brany Kerr naked singularities with $b > 0$ the epicyclic frequencies can satisfy even the condition (see Figs 8 and 9)

$$\nu_\theta(x, a, b) \leq \nu_\mathrm{r}(x, a, b)\,, \tag{103}$$

that is not allowed in Kerr naked singularities. For naked singularities with $b < 0$ again the relation

$$\nu_\theta(x, a, b) > \nu_\mathrm{r}(x, a, b) \tag{104}$$

is valid, as in the Kerr black hole spacetimes.

7 RESONANCE CONDITIONS

The orbital resonance models for QPOs proposed by Abramowicz and Kluźniak (2001); Abramowicz et al. (2004) are particularly based on resonance between epicyclic frequencies which are excited at a well defined resonance radius $x_{n:m}$ given by the condition

$$\frac{\nu_\theta}{\nu_\mathrm{r}}(a, b, x_{n:m}) = \frac{n}{m}\,, \tag{105}$$

where $n : m$ is (most often) $3 : 2$ in the case of *parametric resonance* (the effect itself is described by the Mathieu equation (see Landau and Lifshitz, 1976)) and arbitrary rational ratio of two small integral numbers $(1, 2, 3, \dots)$ in the case of *forced resonances*. Another, so called *"Keplerian" resonance* model, takes into account possible parametric or forced resonances between oscillations with radial epicyclic frequency $\nu_{\rm r}$ and Keplerian orbital frequency $\nu_{\rm K}$.

For a particular resonance $n : m$, the equation

$$n\nu_{\rm r} = m\nu_{\rm v}\,; \quad \nu_{\rm v} \in \{\nu_\theta, \nu_{\rm K}\} \tag{106}$$

determines the dimensionless resonance radius $x_{n:m}$ as a function of the dimensionless spin a in the case of direct resonances that can be easily extended to the resonances with combinational frequencies (Stuchlík et al., 2007b). From the known mass of the central black hole (e.g., low-mass in the case of binary systems or hi-mass in the case of supermassive black holes), the observed double peak frequencies $(\nu_{\rm upp}, \nu_{\rm down})$, and the Eqs (57)–(59), (106) imply the black hole spin, consistent with different types of resonances with the beat frequencies taken into account. This procedure was first applied to the microquasar GRO 1655−40 by Abramowicz and Kluźniak (2001), more recently to the other three microquasars (Török et al., 2005) and also to the Galaxy centre black hole Sgr A* (Török, 2005a).

The twin peak QPOs were observed in four microquasars, namely GRO 1655−40, XTE 1550−564, H 1743−322, GRS 1915+105 (Török et al., 2005). In all of the four cases, the frequency ratio of the twin peaks is very close to $3 : 2$. The very probable interpretation of observed twin peak kHz QPOs is the $3 : 2$ parametric resonance, however, generally it is not unlikely that more than one resonance could be excited in the disc at the same time (or in different times) under different internal conditions. Indeed, observations of the kHz QPOs in the microquasar GRS 1915+105, and of the QPOs in extragalactic sources NGC 4051, MCG-6-30-15 (Lachowicz et al., 2006) and NGC 5408 X−1 (Strohmayer et al., 2007), and the Galaxy centre Sgr A* (Aschenbach et al., 2004) show a variety of QPOs with frequency ratios differing from the $3 : 2$ ratio.

The resonances could be parametric or forced and of different versions according to the epicyclic (Keplerian) frequencies entering the resonance directly, or in some combinational form. In principle, for any case of the resonance model version, one can determine both the spin and mass of the black hole just from the eventually observed set of frequencies. However, the obvious difficulty would be to identify the right combination of resonances and its relation to the observed frequency set. Within the range of black hole mass allowed by observations, each set of twin peak frequencies puts limit on the black hole spin. Of course, the resonance model versions are consistent with observations, if the allowed spin ranges are overlapping each other. Clearly, two or more twin peaks then generally make the spin measurement more precise.

Here we consider the versions of the resonance model explaining the $3 : 2$ ratio taking into account both the direct and one type of simple combinational resonances.

First, we investigate radial coordinate determining position, where the ratio

$$\frac{\nu_{\rm upp}}{\nu_{\rm down}} = \frac{3}{2} \tag{107}$$

occurs for the simple case of the parametric resonance between the radial and vertical epicyclic oscillations. The resonant conditions determining implicitly the resonant radius $x_{n:m}$ must be related to the radius of the innermost stable circular geodesic $x_{\rm ms}$ giving the inner edge of Keplerian discs. Therefore, for all the relevant resonance radii, there must be $x_{n:m} \geq x_{\rm ms}$, where $x_{\rm ms}$ is implicitly given by (55).

The result is given in the way relating the dimensionless spin a and the dimensionless resonance radius x for frequency ratio $n:m = 3:2$

$$a = a^{\theta/{\rm r}}_{3:2}(x,b) \equiv \frac{1}{39x-44b}\left\{4(11x-10b)\sqrt{x-b} - \sqrt{(5x+4b)\left[39x^3-2x^2(17+22b)+43xb-4b^2\right]}\right\}. \tag{108}$$

The behaviour of function $a^{\theta/{\rm r}}_{3:2}$ representing the direct resonance $\nu_\theta : \nu_{\rm r} = 3:2$ is for various values of brany parameter b illustrated in Fig. 1. We can see that for all considered values of b the condition $x_{3:2} > x_{\rm ms}$ is always satisfied.

On the other hand, in the framework of the warp disc oscillations, the frequency of which are given by combinations of the Keplerian and epicyclic frequencies, resonant phenomena could be relevant too. Usually, the inertial-acoustic and g-mode oscillations and their resonances are relevant (Kato, 2007). We plan to give a detailed study of multi-resonant phenomena related to observable triple frequency sets in future. Here, we give as an example the study of the simple frequency relation

$$\frac{2\nu_{\rm K}-\nu_{\rm r}}{\nu_{\rm K}-\nu_{\rm r}} = \frac{3}{2}. \tag{109}$$

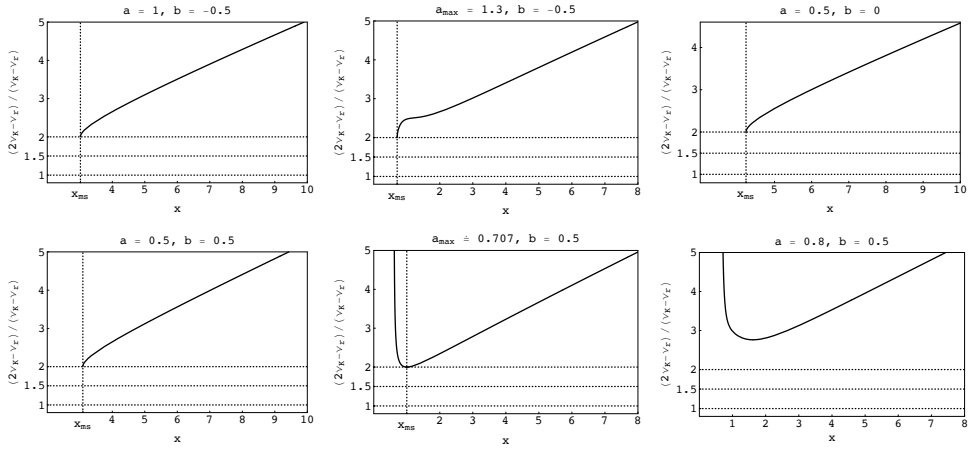

Figure 10. The behaviour of ratio $(2\nu_{\rm K}-\nu_{\rm r})/(\nu_{\rm K}-\nu_{\rm r})$ representing the resonance of trapped oscillations assumed in warped disc (Kato, 2007). The marginally stable orbit $x_{\rm ms}$ is denoted by a dotted vertical line (if this orbit exists at the given spacetime).

However, there exists no solution for this ratio in both Kerr black hole and Kerr naked singularity spacetimes for any value of brany parameter b. The lowest relevant frequency ratio is $(2\nu_{\rm K} - \nu_{\rm r}) : (\nu_{\rm K} - \nu_{\rm r}) = 2:1$ (see Fig. 10).

7.1 Application to microquasar GRS 1915+105

The frequency ratio of the upper twin peak QPOs observed in microquasar GRS 1915+105 is very close to 3:2 (Török et al., 2005):

$$\nu_{\rm upp} = (168 \pm 3)\,{\rm Hz}\,, \tag{110}$$

$$\nu_{\rm down} = (113 \pm 5)\,{\rm Hz}\,. \tag{111}$$

From the known limits on the mass of the black hole in GRS 1915+105 (McClintock and Remillard, 2004)

$$10.0\,{\rm M}_\odot < M < 18.0\,{\rm M}_\odot\,, \tag{112}$$

the observed double peak frequencies (110), (111), and the Eqs (57)–(59), (106) imply the black hole spin consistent with different types of resonances. Assuming the very probable interpretation of observed twin peak kHz QPOs in microquasar as the 3 : 2 standard parametric resonance

$$\frac{\nu_\theta}{\nu_{\rm r}}(a, b, x_{3:2}) = \frac{3}{2} \tag{113}$$

and identifying

$$\nu_{\rm upp} \equiv \nu_\theta\,, \tag{114}$$

we can express the black hole mass in the form

$$\frac{M}{{\rm M}_\odot} = \frac{1}{2\pi}\,\frac{{\rm c}^3}{{\rm GM}_\odot}\,\frac{\sqrt{x-b}}{x^2 + a\sqrt{x-b}}\,\frac{\sqrt{\alpha_\theta}}{\nu_\theta}\,, \tag{115}$$

where $a = a_{3:2}^{\theta/{\rm r}}(x, b)$ is given by the relation (108).

According to the spectral analysis of the X-ray continuum by McClintock et al. (2006), the compact primary of the binary X-ray source GRS 1915+105 is a rapidly-rotating Kerr black hole with a lower limit on its dimensionless spin of

$$a > 0.98\,. \tag{116}$$

Fig. 11 shows the predictions of the 3 : 2 parametric resonance model in the mass-spin plane. It demonstrates possible combinations of mass and black hole spin of GRS 1915+105 as they are predicted by the 3 : 2 parametric resonance model for various values of brany parameter b. We can summarize, that only for the brany parameter b from the interval

$$-0.755 \le b \le 0.03\,, \tag{117}$$

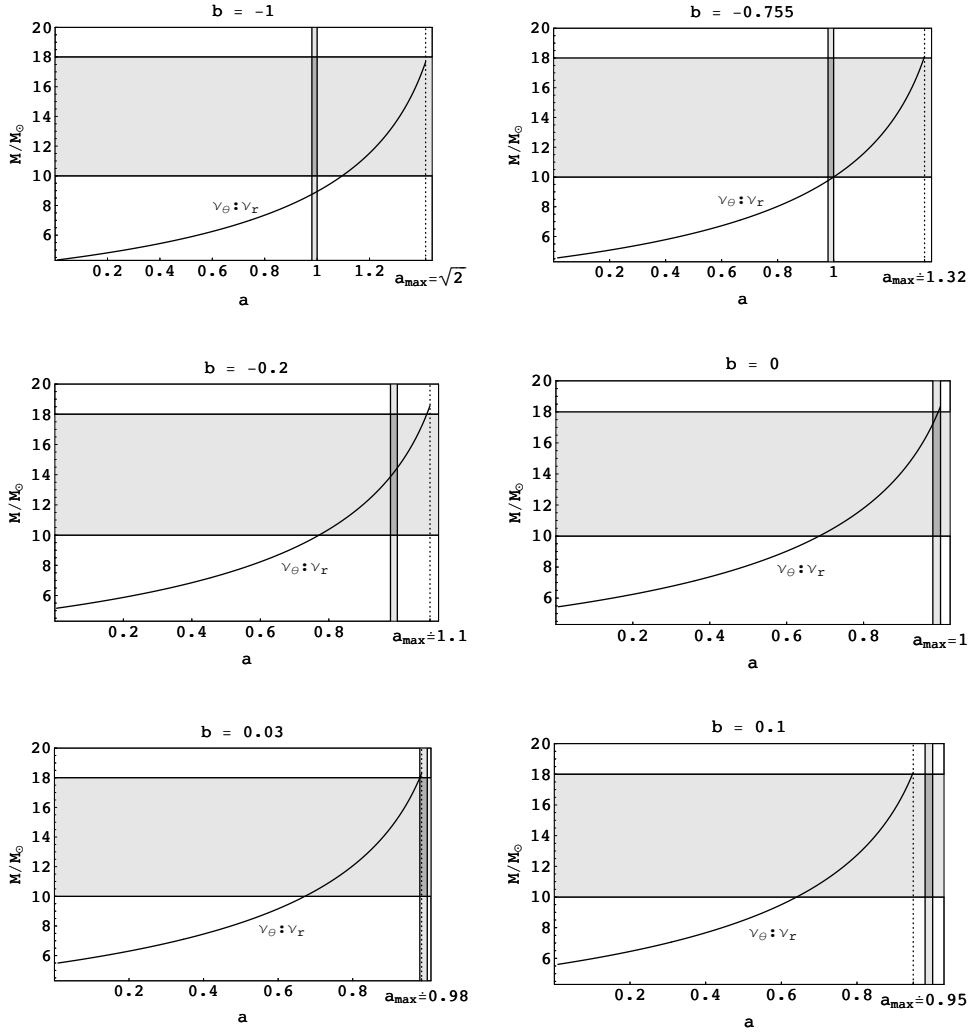

Figure 11. Possible combinations of mass and black hole spin predicted by the standard parametric resonance model ($\nu_\theta : \nu_r = 3 : 2$) for the high-frequency QPOs observed from the microquasar GRS 1915+105. Shaded regions indicate the likely ranges for the mass (inferred from optical measurements of radial curves McClintock et al., 2006)) and the dimensionless spin (inferred from the X-ray spectral data fitting McClintock and Remillard, 2004)) of GRS 1915+105.

the standard parametric resonance model matches the observational constraints.

Notice that although the spectral fitting analysis has been done by McClintock et al. (2006) very carefully, the spin estimate is valid only in Kerr spacetime. We can suppose that for braneworld Kerr black hole with non-zero brany parameter b, the spin estimates may

be shifted to higher values of a due to the influence of the brany tidal charge on the optical phenomena near a rotating black hole (Schee and Stuchlík, 2007a,b).

8 STRONG RESONANT PHENOMENA – "MAGIC" SPIN

Generally, the resonances could be excited at different radii of the accretion disc under different internal conditions; such a situation is discussed in detail by Stuchlík et al. (2007b). However, we have shown (Stuchlík et al., 2007a) that for special values of dimensionless black hole spin a strong resonant phenomena could occur when different resonances can be excited at the same radius, as cooperative phenomena between the resonances may work in such situations.

There exists a possibility of direct resonances of oscillations with all of the three orbital frequencies, characterized by a triple frequency ratio set

$$\nu_{\mathrm{K}} : \nu_{\theta} : \nu_{\mathrm{r}} = s : t : u \tag{118}$$

with $s > t > u$ being small integers. The frequency set ratio (118) can be realized only for special values of the black hole spin a. The black hole mass is then related to the magnitude of the frequencies.

Assuming two resonances $\nu_{\mathrm{K}} : \nu_{\theta} = s : t$ and $\nu_{\mathrm{K}} : \nu_{\mathrm{r}} = s : u$ occurring at the same x, we arrive to the conditions

$$\alpha_{\theta}(a, b, x) = \left(\frac{t}{s}\right)^2 , \tag{119}$$

$$\alpha_{\mathrm{r}}(a, b, x) = \left(\frac{u}{s}\right)^2 \tag{120}$$

that have to be solved simultaneously for x, a and b. The solution is given by the condition

$$a^{\theta}(x, b, t/s) = a^{\mathrm{r}}(x, b, u/s) , \tag{121}$$

where

$$a^{\theta}(x, b, t/s) = \frac{\sqrt{x - b}}{3x - 2b} \times \left\{2x - b \pm \sqrt{b^2 - 2bx\left[2 + x\left((t/s)^2 - 1\right)\right] + x^2\left[4 + 3x\left((t/s)^2 - 1\right)\right]}\right\} , \tag{122}$$

$$a^{\mathrm{r}}(x, b, u/s) = \frac{1}{3x - 4b}\left\{4(x - b)^{3/2} \pm x\sqrt{b\left[3 - 4b\,(u/s)^2\right] + x\left[7b\,(u/s)^2 - 2\,(2b + 1)\right] - 3x^2\left[(u/s)^2 - 1\right]}\right\} . \tag{123}$$

For Kerr spacetime with $b = 0$ the explicit solution determining the relevant radius for any triple frequency set ratio $s : t : u$ takes the form

$$x(s, t, u) = \frac{6s^2}{6s^2 \pm 2\sqrt{2}\sqrt{(t - u)(t + u)(3s^2 - t^2 - 2u^2)} - (t^2 + 5u^2)} . \tag{124}$$

Clearly, the condition $t^2 + 2u^2 \leq 3s^2$ is always satisfied. The corresponding black hole spin a is then determined, e.g., by Eq. (122) giving $a^\theta(x(s,t,u),t/s)$. Of course, we consider only the black hole cases when $a \leq a_{\rm max}$. This condition puts a restriction on allowed values of s, t, u.

A detailed discussion of the black holes admitting strong resonant phenomena is for small integer ($s \leq 5$) given in Stuchlík et al. (2007a). Of special interest seems to be the case of the "magic" spin, when the Keplerian and epicyclic frequencies are in the ratio $\nu_{\rm K} : \nu_\theta : \nu_{\rm r} = 3:2:1$ at the common radius $x_{3:2:1}$. In fact, this case involves rather extended structure of resonances with $\nu_{\rm K} : \nu_{\rm r} = 3:1$, $\nu_{\rm K} : \nu_\theta = 3:2$, $\nu_\theta : \nu_{\rm r} = 2:1$. Notice that in this case also the simple combinational frequencies could be in this small integer ratio as

$$\frac{\nu_{\rm K}}{\nu_\theta - \nu_{\rm r}} = \frac{3}{1}\,, \quad \frac{\nu_{\rm K}}{\nu_{\rm K} - \nu_{\rm r}} = \frac{3}{2}\,, \quad \frac{\nu_\theta}{\nu_\theta - \nu_{\rm r}} = \frac{2}{1}\,. \tag{125}$$

Of course we obtain the strongest possible resonances when the beat frequencies enter the resonance satisfying the conditions

$$\frac{\nu_\theta + \nu_{\rm r}}{\nu_{\rm K}} = \frac{3}{3} = 1\,, \quad \frac{\nu_\theta}{\nu_{\rm K} - \nu_{\rm r}} = \frac{2}{2} = 1\,, \quad \frac{\nu_{\rm r}}{\nu_{\rm K} - \nu_\theta} = 1\,, \quad \frac{\nu_\theta - \nu_{\rm r}}{\nu_{\rm r}} = 1\,. \tag{126}$$

In Kerr spacetime where $b = 0$ we obtain the "magic" spin $a_{\rm magic} = 0.983$ and the common radius $x_{3:2:1} = 2.395$ (see Fig. 12). Assuming all possible values of brany parameter b we can conclude that this special case of the "magic" spin could occur only for brany parameter from the interval

$$b_{\rm magic} \in \langle -3.258; 0.287 \rangle\,, \tag{127}$$

that implies the "magic" spin from the interval

$$a_{\rm magic} \in \langle 0.844; 2.063 \rangle\,. \tag{128}$$

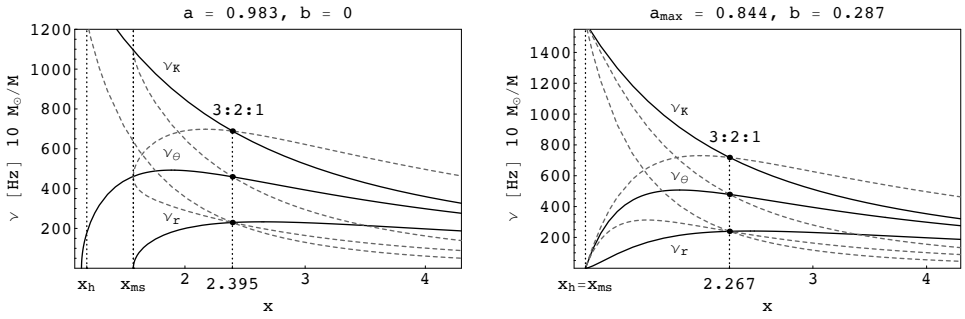

Figure 12. The special cases of the triple frequency ratio sets of the orbital frequencies $\nu_{\rm K}, \nu_\theta, \nu_{\rm r}$ (black solid lines) with the corresponding "magic" spin a and the shared resonance radius for Kerr spacetime (*left panel*) and for the extreme braneworld black hole with $b = 0.287$ (*right panel*). For completeness we present the relevant simple combinational frequencies $\nu_\theta - \nu_{\rm r}$, $\nu_\theta + \nu_{\rm r}$, $\nu_{\rm K} - \nu_\theta$, $\nu_{\rm K} - \nu_{\rm r}$ (grey dashed lines). Notice that the "magic" spin represents the only case when the combinational and direct orbital frequencies coincide at the shared resonance radius.

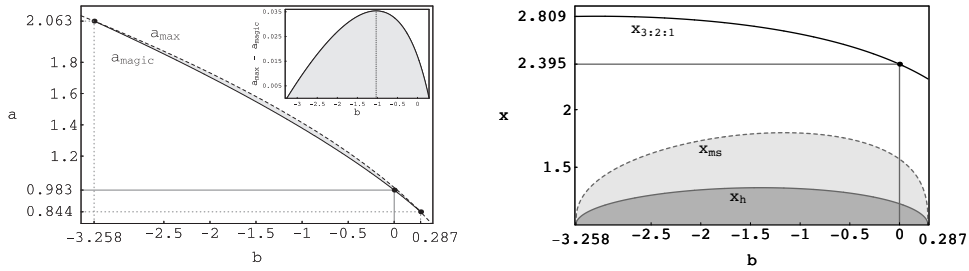

Figure 13. "Magic" black hole spin a (*left panel*) and the common radius $x_{3:2:1}$ (*right panel*) as the function of the "magic" brany parameter b, that imply the frequency ratio set $\nu_{\mathrm{K}} : \nu_{\theta} : \nu_{\mathrm{r}} = 3:2:1$ arising at the common orbit $x_{3:2:1}$. Dashed line in the *left panel* represents $a_{\max}$, corresponding to the extreme black holes. We can see that for all possible values of the "magic" brany parameter $a_{\mathrm{magic}} \to a_{\max}$. In the *right panel*, there is also shown the radius of the outer event black hole horizon x_{h} (gray solid line) and the marginally stable circular orbit x_{ms} (dashed line) of a rotating black hole carrying a given value of the "magic" brany parameter b and "magic" black hole spin a.

Only for this values of a and b we have $a \leq a_{\max}$, where $a_{\max}$ corresponds to the extreme black hole (see Fig. 13).

8.1 Sgr A* black hole parameters

The Galaxy centre source Sgr A* can serve as a proper candidate system, since three QPOs were reported (but not fully accepted by the astrophysical community) for the system (Aschenbach, 2004; Török, 2005a) with frequency ratio corresponding to the "magic" spin

$$(1/692) : (1/1130) : (1/2178) \approx 3:2:1 \tag{129}$$

and with the upper frequency being observed with a rather high error

$$\nu_{\mathrm{upp}} = (1.445 \pm 0.16)\,\mathrm{mHz}\,. \tag{130}$$

Considering a black hole with the spin comparable to the "magic" value $a \sim a_{\mathrm{magic}}$, with the frequency ratio $\nu_{\mathrm{K}} : \nu_{\theta} : \nu_{\mathrm{r}} = 3:2:1$ at the sharing radius $x_{3:2:1}$, and identifying $\nu_{\mathrm{upp}} = \nu_{\mathrm{K}}$, we obtain for all possible values of "magic" brany parameter $b_{\mathrm{magic}} \in \langle -3.258; 0.287 \rangle$ the black hole mass of Sgr A* in the interval

$$3.82 \times 10^6\,\mathrm{M}_{\odot} < M < 5.59 \times 10^6\,\mathrm{M}_{\odot}\,, \tag{131}$$

which meets the allowed range of the Sgr A* mass coming from the analysis of the orbits of stars moving within 1000 light hour of Sgr A* (Ghez et al., 2005)

$$2.8 \times 10^6\,\mathrm{M}_{\odot} < M < 4.6 \times 10^6\,\mathrm{M}_{\odot} \tag{132}$$

at its higher mass end. In all these cases, the black hole spin $a \to a_{\max}$, in agreement with the assumption that Galactic centre black hole should be fast rotating. The results are summarized in Table 1.

Table 1. Determining of the black hole spin and mass in Sgr A* with assumed observed characteristic frequency ratio set $\nu_{\rm K} : \nu_\theta : \nu_{\rm r} = 3 : 2 : 1$ at the common orbit $x_{3:2:1}$ for various values of brany parameter b; $\nu_{\rm up} = (1.445 \pm 0.16)$ mHz is used to determine the black hole mass.

$b_{\rm magic}$	$a_{\rm magic}$	$x_{\rm ms}$	$x_{3:2:1}$	$M\ [10^6\,{\rm M}_\odot]$
0.287150	0.844304	1	2.26663	4.477–5.592
0	0.983043	1.57081	2.39467	4.293–5.362
−1	1.378867	1.79706	2.65656	3.971–4.959
−2	1.705166	1.73104	2.77498	3.849–4.808
−2.969659	1.985138	1.42803	2.81093	3.819–4.769
−3.257659	2.063410	1	2.80953	3.821–4.773

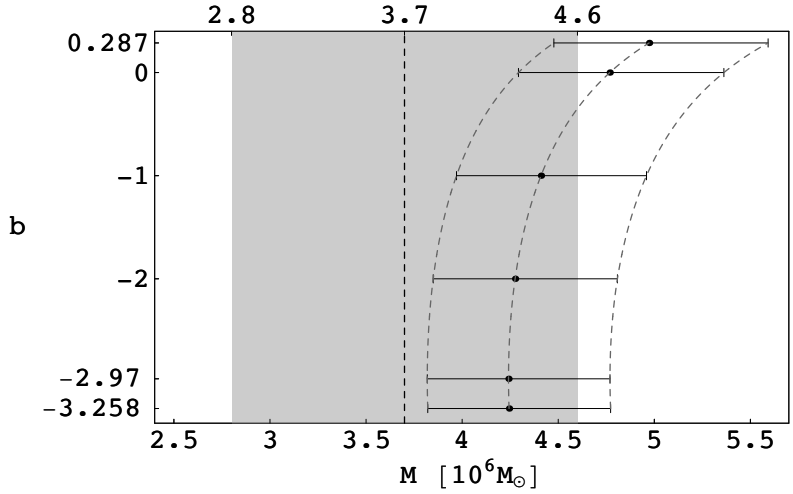

Figure 14. Mass of Sgr A*: strong resonant model with the frequency ratio $\nu_{\rm K} : \nu_\theta : \nu_{\rm r} = 3 : 2 : 1$ for various values of brany parameter b. The observational restrictions from the orbital motion of stars in vicinity of Sgr A* (Ghez et al., 2005) are illustrated here by the gray rectangle.

From Fig. 14 we can see that the best fit is obtained for the brany parameter $b \sim -2.97$ that implies "magic" spin $a_{\rm magic} \sim 1.99$ and the radius $x_{3:2:1} = 2.81$.

The model should be further tested and more precise frequency measurements are very important.

9 CONCLUSIONS

The orbital resonance model and its simple generalization to multiresonance model with strong resonances is formulated for the brany Kerr black holes, when the bulk-space influence is described by a single, brany tidal charge parameter.

In the limit of strong gravitational field, the brany parameter b can be, in principle, high in its magnitude, therefore, we put no restriction on the values of b. We describe the properties of the radial and vertical epicyclic frequencies related to the oscillatory motion in the equatorial plane of the Kerr spacetimes. While their behaviour is qualitatively similar for Kerr and brany Kerr black holes, there are strong differences in the case of naked singularities – in some range of their parameters, the vertical epicyclic frequency could be even lower than the radial one. Such a situation is impossible in standard Kerr spacetimes. Further, in the field of brany Kerr naked singularities, the structure of the radial profiles is much richer than in the standard case, namely the number of local extrema could be higher in comparison with the standard Kerr naked singularities. Further, in a special family of the brany naked singularity spacetimes, the radial epicyclic frequency has no zero point since there is no marginally stable circular geodesic in these spacetimes.

Assuming the parametric resonance acting directly between the oscillations with radial and vertical epicyclic frequency, we give the rule for the resonant radius with a given frequency ratio. The rule is tested for the uppermost twin frequencies observed in the GRS 1915+105 microquasar; and limits on the spin and brany parameters are obtained and compared with the estimates for $b = 0$, given in Török et al. (2005).[5]

In the Galaxy center source Sgr A*, three frequencies were reported that could be treated in the scope of the strong resonance model (Aschenbach, 2004, 2007; Török, 2005a,b). The model predicts an exact value of the black hole spin and puts limits on its mass. It is shown that the black hole mass estimate given by the strong resonance model is in the best agreement with the value of $M \sim 3.7 \times 10^6\,\mathrm{M}_\odot$ (Ghez et al., 2005) for negative brany parameter $b \sim -2.97$, with the "magic" spin $a \approx 1.99$.

We can conclude that the orbital resonance model can put some limits on the values of the brany parameter and could be useful in estimating influence of hypothetical external dimension to the properties of the brany universe.

ACKNOWLEDGEMENTS

This work was supported by the following Czech grants: MSM 4781305903, LC06014, GAČR 205/03/H144 and GAČR 202/06/0041. One of the authors (Z. S.) would like to express his gratitude to the Czech Committee for Collaboration with CERN for support and CERN Theory Division for perfect hospitality.

[5] However, it should be noted that whole the five frequency patterns could be explained in terms of the extended resonance model (Stuchlík et al., 2007b).

REFERENCES

Abramowicz, M. A., Barret, D., Bursa, M., Horák, J., Kluźniak, W., Rebusco, P. and Török, G. (2005a), A note on the slope-shift anticorrelation in the neutron star kHz QPOs data, in Hledík and Stuchlík (2005), pp. 1–9.

Abramowicz, M. A., Barret, D., Bursa, M., Horák, J., Kluźniak, W., Rebusco, P. and Török, G. (2005b), The correlations and anticorrelations in QPO data, *Astronom. Nachr.*, **326**(9), pp. 864–866.

Abramowicz, M. A. and Kluźniak, W. (2001), A precise determination of black hole spin in GRO J1655−40, *Astronomy and Astrophysics*, **374**, pp. L19–L20, arXiv: `astro-ph/0105077`, URL `http://adsabs.harvard.edu/abs/2001A\%26A...374L..19A`.

Abramowicz, M. A., Kluźniak, W., Stuchlík, Z. and Török, G. (2004), Twin peak QPOs frequencies in microquasars and Sgr A*. The resonance and other orbital models, in Hledík and Stuchlík (2004), pp. 1–23.

Aliev, A. N. and Frolov, V. (2004), Five Dimensional Rotating Black Hole in a Uniform Magnetic Field. The Gyromagnetic Ratio, *Phys. Rev. D*, **69**, p. 084022, arXiv: `hep-th/0401095`.

Aliev, A. N. and Galtsov, D. V. (1981), Radiation from relativistic particles in non-geodesic motion in a strong gravitational field, *Gen. Relativity Gravitation*, **13**, pp. 899–912.

Aliev, A. N. and Gümrükçüoğlu, A. E. (2004), Gravitational Field Equations on and off a 3-Brane World, *Classical Quantum Gravity*, **21**, p. 5081, arXiv: `hep-th/0407095`.

Aliev, A. N. and Gümrükçüoğlu, A. E. (2005), Charged Rotating Black Holes on a 3-Brane, *Phys. Rev. D*, **71**(10), p. 104027, arXiv: `hep-th/0502223v2`.

Arkani-Hamed, N., Dimopoulos, S. and Dvali, G. (1998), The Hierarchy Problem and New Dimensions at a Millimeter, *Phys. Lett. B*, **429**, pp. 263–272, arXiv: `hep-ph/9803315`.

Arnowitt, R., Deser, S. and Misner, C. W. (1962), The Dynamics of General Relativity, volume 7, pp. 227–265, Wiley, arXiv: `gr-qc/0405109`.

Aschenbach, B. (2004), Measuring mass and angular momentum of black holes with high-frequency quasi-periodic oscillations, *Astronomy and Astrophysics*, **425**, pp. 1075–1082, arXiv: `astro-ph/0406545`.

Aschenbach, B. (2007), Measurement of Mass and Spin of Black Holes with QPOs, *Chinese Astronom. Astrophys.*, accepted for publication, arXiv: `0710.3454`.

Aschenbach, B., Grosso, N., Porquet, D. and Predehl, P. (2004), X-ray flares reveal mass and angular momentum of the Galactic Center black hole, *Astronomy and Astrophysics*, **417**, pp. 71–78, arXiv: `astro-ph/0401589`.

Bardeen, J. M. (1973), Timelike and Null Geodesics in the Kerr Metric, in C. D. Witt and B. S. D. Witt, editors, *Black Holes*, p. 215, Gordon and Breach, New York–London–Paris.

Blaes, O. M., Šrámková, E., Abramowicz, M. A., Kluźniak, W. and Torkelsson, U. (2007), Epicyclic Oscillations of Fluid Bodies. Paper III. Newtonian Non-Slender Torus, *Astrophys. J.*, **665**, pp. 642–653, arXiv: `0706.4483`, URL `http://adsabs.harvard.edu/abs/2007ApJ...665..642B`.

Carter, B. (1968), Global Structure of the Kerr Family of Gravitational Fields, *Phys. Rev.*, **174**(5), pp. 1559–1571.

Carter, B. (1973), Black hole equilibrium states, in C. D. Witt and B. S. D. Witt, editors, *Black Holes*, pp. 57–214, Gordon and Breach, New York–London–Paris.

Chamblin, A., Hawking, S. W. and Reall, H. S. (2000), Brane-World Black Holes, *Phys. Rev. D*, **61**(6), p. 065007, arXiv: `hep-th/9909205`.

Chamblin, A., Reall, H. S., Shinkai, H. and Shiromizu, T. (2001), Charged Brane-World Black Holes, *Phys. Rev. D*, **63**(6), p. 064015, arXiv: `hep-th/0008177`.

Dadhich, N. and Kale, P. P. (1977), Equatorial circular geodesics in the Kerr–Newman geometry, *J. Math. Phys.*, **18**, pp. 1727–1728.

Dadhich, N., Maartens, R., Papadopoulos, P. and Rezania, V. (2000), Black holes on the brane, *Phys. Rev. B*, **487**, arXiv: `hep-th/0003061v3`.

Damour, T., Hanni, R. S., Ruffini, R. and Wilson, J. R. (1978), Regions of magnetic support of a plasma around a black hole, *Phys. Rev. D*, **17**(6), pp. 1518–1523.

Dimopoulos, S. and Landsberg, G. (2001), Black Holes at the Large Hadron Collider, *Phys. Rev. Lett.*, **87**(16), p. 161602.

Dovčiak, M., Karas, V., Martocchia, A., Matt, G. and Yaqoob, T. (2004), An XSPEC model to explore spectral features from black-hole sources, in Hledík and Stuchlík (2004), pp. 33–73, arXiv: `astro-ph/0407330`.

Emparan, R., Horowitz, G. T. and Myers, R. C. (2000), Black Holes Radiate Mainly on the Brane, *Phys. Rev. Lett.*, **85**(3), pp. 499–502, arXiv: `hep-th/0003118`.

Emparan, R., Masip, M. and Rattazzi, R. (2002), Cosmic Rays as Probes of Large Extra Dimensions and TeV Gravity, *Phys. Rev. D*, **65**, p. 064023, arXiv: `hep-ph/0109287`.

Fabian, A. C. and Miniutti, G. (2005), *Kerr Spacetime: Rotating Black Holes in General Relativity*, Cambridge University Press, Cambridge, eprint astro-ph/0507409 is a part of this book, arXiv: `astro-ph/0507409`.

Frolov, V. and Stojkovic, D. (2003), Quantum Radiation from a 5-Dimensional Rotating Black Hole, *Phys. Rev. D*, **67**, p. 084004, arXiv: `gr-qc/0211055`.

Frolov, V., Šnajdr, M. and Stojkovic, D. (2003), Interaction of a brane with a moving bulk black hole, *Phys. Rev. D*, **68**, p. 044002, arXiv: `gr-qc/0304083`.

Germani, C. and Maartens, R. (2001), Stars in the braneworld, *Phys. Rev. D*, **64**, p. 124010, arXiv: `hep-th/0107011`.

Ghez, A. M., Salim, S., Hornstein, S. D., Tanner, A., Lu, J. R., Morris, M., Becklin, E. E. and Duchêne, G. (2005), Stellar Orbits around the Galactic Center Black Hole, *Astrophys. J.*, **620**, pp. 744–757, arXiv: `astro-ph/0306130`.

Gregory, R. and Laflamme, R. (1993), Black Strings and p-Branes are Unstable, *Phys. Rev. Lett.*, **70**(19), pp. 2837–2840, arXiv: `hep-th/9301052`.

Hledík, S. and Stuchlík, Z., editors (2004), *Proceedings of RAGtime 4/5: Workshops on black holes and neutron stars, Opava, 14–16/13–15 October 2002/2003*, Silesian University in Opava, Opava, ISBN 80-7248-242-4.

Hledík, S. and Stuchlík, Z., editors (2005), *Proceedings of RAGtime 6/7: Workshops on black holes and neutron stars, Opava, 16–18/18–20 September 2004/2005*, Silesian University in Opava, Opava, ISBN 80-7248-334-X.

Horowitz, G. T. and Maeda, K. (2001), Fate of the Black String Instability, *Phys. Rev. Lett.*, **87**(13), p. 131301, arXiv: `hep-th/0105111`.

Karas, V., Vokrouhlický, D. and Polnarev, A. G. (1992), In the vicinity of a rotating black hole – A fast numerical code for computing observational effects, *Monthly Notices Roy. Astronom. Soc.*, **259**, pp. 569–575.

Kato, S. (2004), Resonant Excitation of Disk Oscillations by Warps: A Model of kHz QPOs, *Publ. Astronom. Soc. Japan*, **56**(5), pp. 905–922.

Kato, S. (2007), Frequency Correlations of QPOs Based on a Disk Oscillation Model in Warped Disks, *Publ. Astronom. Soc. Japan*, **59**, pp. 451–455, arXiv: `astro-ph/0701085`.

Kato, S., Fukue, J. and Mineshige, S. (1998), Black-hole accretion disks, in S. Kato, J. Fukue and S. Mineshige, editors, *Black-hole accretion disks*, Kyoto University Press, Kyoto, Japan.

Kluźniak, W. and Abramowicz, M. A. (2001), The physics of kHz QPOs – strong gravity's coupled anharmonic oscillators, submitted in Phys. Rev. Lett., arXiv: astro-ph/0105057, URL http://adsabs.harvard.edu/abs/2001astro.ph..5057K.

Kozłowski, M., Jaroszyński, M. and Abramowicz, M. A. (1978), The analytic theory of fluid disks orbiting the Kerr black hole, *Astronomy and Astrophysics*, **63**(1–2), pp. 209–220, URL http://adsabs.harvard.edu/abs/1978A\%26A....63..209K.

Krolik, J. H. and Hawley, J. F. (2002), Where Is the Inner Edge of an Accretion Disk around a Black Hole?, *Astrophys. J.*, **573**(2), pp. 754–763, arXiv: astro-ph/0203289.

Lachowicz, P., Czerny, B. and Abramowicz, M. A. (2006), Wavelet analysis of MCG-6-30-15 and NGC 4051: a possible discovery of QPOs in 2 : 1 and 3 : 2 resonance, *Monthly Notices Roy. Astronom. Soc.*, submitted, arXiv: astro-ph/0607594.

Landau, L. D. and Lifshitz, E. M. (1976), *Mechanics*, volume I of *Course of Theoretical Physics*, Elsevier Butterworth-Heinemann, Oxford, 3rd edition, ISBN 0-7506-2896-0.

Laor, A. (1991), Line profiles from a disk around a rotating black hole, *Astrophys. J.*, **376**, pp. 90–94.

Maartens, R. (2000), Cosmological dynamics on the brane, *Phys. Rev. D*, **62**, p. 084023, arXiv: hep-th/0004166.

Maartens, R. (2004), Brane-world gravity, *Living Rev. Rel.*, **7**, arXiv: gr-qc/0312059v2.

McClintock, J. E., Narayan, R. and Shafee, R. (2007), Estimating the Spins of Stellar-Mass Black Holes, in M. Livio and A. Koekemoer, editors, *Black Holes*, volume 707, Cambridge University Press, Cambridge, in press, to appear in 2008, arXiv: 0707.4492v1.

McClintock, J. E. and Remillard, R. A. (2004), Black Hole Binaries, in W. H. G. Lewin and M. van der Klis, editors, *Compact Stellar X-Ray Sources*, Cambridge University Press, Cambridge, arXiv: astro-ph/0306213.

McClintock, J. E., Shafee, R., Narayan, R., Remillard, R. A., Davis, S. W. and Li, L. (2006), The Spin of the Near-Extreme Kerr Black Hole GRS 1915+105, *Astrophys. J.*, **652**(2), pp. 518–539, arXiv: astro-ph/0606076.

Middleton, M., Done, C., Gierliński, M. and Davis, S. W. (2006), Black hole spin in GRS 1915+105, *Monthly Notices Roy. Astronom. Soc.*, **373**(3), pp. 1004–1012, arXiv: astro-ph/0601540v2.

Misner, C. W., Thorne, K. S. and Wheeler, J. A. (1973), *Gravitation*, W. H. Freeman and Co, New York, San Francisco.

Modgil, M. S., Panda, S. and Sengupta, G. (2002), Rotating Brane World Black Holes, *Modern Phys. Lett. A*, **17**, pp. 1479–1487, arXiv: hep-th/0104122.

Nojiri, S., Obregon, O., Odintsov, S. D. and Ogushi, S. (2000), Dilatonic Brane-World Black Holes, Gravity Localization and Newton's Constant, *Phys. Rev. D*, **62**(6), p. 064017, arXiv: hep-th/0003148.

Randall, L. and Sundrum, R. (1999), An Alternative to Compactification, *Phys. Rev. D*, **83**(2), pp. 4690–4693, arXiv: hep-th/9906064.

Remillard, R. A. (2005), X-ray spectral states and high-frequency QPOs in black hole binaries, *Astronom. Nachr.*, **326**(9), pp. 804–807, arXiv: astro-ph/0510699.

Remillard, R. A. and McClintock, J. E. (2006), X-Ray Properties of Black-Hole Binaries, *Annual Review of Astronomy and Astrophysics*, **44**(1), pp. 49–92, arXiv: astro-ph/0606352.

Rezzolla, L., Yoshida, S., Maccarone, T. J. and Zanotti, O. (2003), A new simple model for high-frequency quasi-periodic oscillations in black hole candidates, *Monthly Notices Roy. Astronom. Soc.*, **344**(3), pp. L37–L41.

Sasaki, M., Shiromizu, T. and Maeda, K. (2000), Gravity, stability, and energy conservation on the Randall–Sundrum brane world, *Phys. Rev. D*, **62**, p. 024008, arXiv: hep-th/9912233.

Schee, J. and Stuchlík, Z. (2007a), Optical effects in brany Kerr spacetimes, pp. 221–256, this volume.

Schee, J. and Stuchlík, Z. (2007b), Spectral line profile of radiating ring orbiting a brany Kerr black hole, pp. 209–220, this volume.

Shafee, R., McClintock, J. E., Narayan, R., Davis, S. W., Li, L.-X. and Remillard, R. A. (2006), Estimating the Spin of Stellar-Mass Black Holes via Spectral Fitting of the X-ray Continuum, *Astrophys. J.*, **636**, pp. L113–L116, arXiv: astro-ph/0508302.

Shiromizu, T., Maeda, K. and Sasaki, M. (1999), The Einstein Equations on the 3-Brane World, *Phys. Rev. D*, **62**, p. 024012, arXiv: gr-qc/9910076.

Šrámková, E. (2005), Epicyclic oscillation modes of a Newtonian, non-slender torus, *Astronom. Nachr.*, **326**(9), pp. 835–837.

Strohmayer, T. E., Mushotzky, R. F., Winter, L., Soria, R., Uttley, P. and Cropper, M. (2007), Quasi-Periodic Variability in NGC 5408 X-1, *Astrophys. J.*, **660**, pp. 580–586, arXiv: astro-ph/0701390.

Stuchlík, Z., Kotrlová, A. and Török, G. (2007a), Black holes admitting strong resonant phenomena, submitted.

Stuchlík, Z., Kotrlová, A. and Török, G. (2007b), Multi-resonance models of QPOs, pp. 363–416, this volume.

Stuchlík, Z., Slaný, P. and Török, G. (2007c), LNRF-velocity hump-induced oscillations of a Keplerian disc orbiting near-extreme Kerr black hole: A possible explanation of high-frequency QPOs in GRS 1915+105, *Astronomy and Astrophysics*, **470**(2), pp. 401–404, arXiv: 0704.1252v2.

Török, G. (2005a), A possible 3 : 2 orbital epicyclic resonance in QPO frequencies of Sgr A*, *Astronomy and Astrophysics*, **440**(1), pp. 1–4, arXiv: astro-ph/0412500.

Török, G. (2005b), QPOs in microquasars and Sgr A*: measuring the black hole spin, *Astronom. Nachr.*, **326**(9), pp. 856–860, arXiv: astro-ph/0510669.

Török, G., Abramowicz, M. A., Kluźniak, W. and Stuchlík, Z. (2005), The orbital resonance model for twin peak kHz quasi periodic oscillations in microquasars, *Astronomy and Astrophysics*, **436**(1), pp. 1–8, arXiv: astro-ph/0401464.

Török, G. and Stuchlík, Z. (2005a), Epicyclic frequencies of Keplerian motion in Kerr spacetimes, in Hledík and Stuchlík (2005), pp. 315–338.

Török, G. and Stuchlík, Z. (2005b), Radial and vertical epicyclic frequencies of Keplerian motion in the field of Kerr naked singularities. Comparison with the black hole case and possible instability of naked singularity accretion discs, *Astronomy and Astrophysics*, **437**(3), pp. 775–788, arXiv: astro-ph/0502127.

van der Klis, M. (2000), Millisecond Oscillations in X-ray Binaries, *Annual Review of Astronomy and Astrophysics*, **38**, pp. 717–760, arXiv: astro-ph/0001167.

van der Klis, M. (2006), Rapid X-ray Variability, in W. H. G. Lewin and M. van der Klis, editors, *Compact Stellar X-Ray Sources*, pp. 39–112, Cambridge University Press, Cambridge.

Zakharov, A. F. (2003), The iron K_α line as a tool for analysis of black hole characteristics, *Publ. Astronom. Observator. Belgrade*, **76**, pp. 147–162, arXiv: astro-ph/0411611.

Zakharov, A. F. and Repin, S. V. (2006), Different types of Fe K_α lines from radiating annuli near black holes, *New Astronomy*, **11**, pp. 405–410, arXiv: astro-ph/0510548.

Zel'dovich, Y. B. and Novikov, I. D. (1971), *Relativistic Astrophysics*, volume 1, University of Chicago Press, Chicago.

Proceedings of *RAGtime 8/9, 15–19/19–21 September, 2006/2007, Hradec nad Moravicí, Opava, Czech Republic*
S. Hledík and Z. Stuchlík, editors, Silesian University in Opava, 2007, pp. 363–416

Multi-resonance models of QPOs

Zdeněk Stuchlík, Andrea Kotrlová[a]
and Gabriel Török

Institute of Physics, Faculty of Philosophy & Science, Silesian University in Opava,
Bezručovo nám. 13, CZ-746 01 Opava, Czech Republic
[a] andrea.kotrlova@fpf.slu.cz

ABSTRACT
Using known frequencies of the accretion disc twin peak quasiperiodic oscillations (QPOs) and the known mass of the central black hole, the black hole dimensionless spin a can be determined, assuming a concrete version of the orbital resonance model. However, because of large range of observationally limited values of the black hole mass, its spin can be estimated with a low precision only. Higher precision of the black hole spin measurement is possible in the framework of multi-resonance model of QPOs inspired by complex high-frequency QPO patterns observed in some black hole and neutron star systems. In the simple orbital resonance models we determine the spin and mass dependence of the twin peak frequencies for non-linear resonances of oscillations with the epicyclic and Keplerian frequencies or their combinations in the case of a general rational frequency ratio $n : m$, $n > m$. In the multi-resonant model, the twin peak resonances are combined properly to give the observed frequency set. The multi-resonant model is proposed in three distinct versions. In the first one, related probably to the neutron star binary systems, more instances of one resonance occur at more specific radii. In the second case, more resonances are sharing one specific radius, allowing for "cooperative" resonant phenomena in the field of black holes with a specific value of spin. In the third ("ugly") case, more resonances occur at more specific radii; we restrict our attention to the case of two such resonant radii. For special values of the spin, only triple-set of frequencies is observed because of coincidence of some frequencies, allowing determination of the spin from the triple frequency ratio set. The spin is determined precisely, but not uniquely as the same frequency set could be relevant for more than one concrete spin and combination of resonant oscillations.

Keywords: Compact objects – X-ray variability – theory – observations

1 INTRODUCTION

Non-linear resonance between some modes of oscillations in the accretion discs around black holes can play a crucial role in exciting detectable modulations of the X-ray flux. This idea is supported by observations in four microquasars showing twin peak quasiperiodic oscillations (QPOs), the ratio of the frequency peaks is 3 : 2. Using known frequencies of

978-80-7248-419-5

the twin peaks and the known mass of the central black hole, the black-hole dimensionless spin a can be determined, assuming a concrete resonance model (Török et al., 2005). This was already done for the presently known sources and few miscellaneous resonance models, however, because of large range of observationally limited values of the black hole mass, its spin can be estimated with a low precision only. Nevertheless, at present more complex QPO structures are observed in both black hole and neutron star systems. The microquasar GRS 1915+105 reveals high-frequency QPOs appearing at four frequencies with the lower and upper pairs in the ratio close to 3 : 2 and even a fifth frequency was reported, although not confirmed. In Sgr A*, three frequencies were reported with the ratio close to 3 : 2 : 1. In the galactic nuclei MCG-6-30-15 and NGC 4051, two pairs of QPOs were reported with the ratios close to 3 : 2 and 2 : 1. In the binaries containing neutron stars, the twin peak oscillations have frequencies and their ratios highly scattered, but concentrated around ratios 3 : 2, 4 : 3, 5 : 4. A well arranged review of the observational data in black hole and neutron star systems can be found in McClintock and Remillard (2004); Remillard and McClintock (2006); van der Klis (2006).

Here, we present basic ideas of the orbital multi-resonant model that is able to explain some of the complex high-frequency QPO patterns observed in the black-hole and neutron-star systems. We shall focus on three versions of the multi-resonant model enabling relatively precise estimates of the black-hole and neutron-star spacetime parameters.

2 THE ORBITAL RESONANCE MODEL AND ITS MULTI-RESONANT VERSIONS

The standard orbital resonance model (Abramowicz and Kluźniak, 2001; Kluźniak and Abramowicz, 2001) assumes non-linear resonance of oscillations of an accretion disc orbiting a central object, considered to be a rotating black hole or a neutron star. The relevant accretion disc can be a thin disc with Keplerian angular velocity profile, or thick toroidal disc with angular velocity profile given by distribution of the specific angular momentum of the fluid. The frequency of the disc oscillations is related to the Keplerian frequency (orbital frequency of tori), or to the radial and vertical epicyclic frequencies of the circular test particle motion in the field of Kerr black holes (or the Hartle–Thorne spacetime in the case of neutron stars). The epicyclic frequencies can be relevant for both the thin, Keplerian discs with quasicircular geodetical motion and for thick, toroidal discs.

In the simplest case of the orbital resonance models involving Keplerian and epicyclic oscillations with a single resonance connected to one specific radius we are able to determine the spin and mass dependence of the twin peak frequencies for both the parametric (internal) and forced non-linear resonances of oscillations with the epicyclic and Keplerian frequencies or their combinations in the case of a general rational frequency ratio $n : m$. Both parametric and forced resonance models make clear and precise predictions about the values of observed frequencies in connection with spin and mass of the observed object. Then we can relate the spin and mass of the black hole and having the black hole mass estimate from other observations, the spin limits could be established (Kluźniak and Abramowicz, 2001; Török et al., 2005).

Details of excitation mechanisms of eventual resonances are still not fully explained, nevertheless one can imagine that not only one resonance could be excited in the accretion disc. Then there arises a possibility of higher precision of the black hole dimensionless spin measurements under assumption that the non-linear resonances are excited at different radii of the accretion disc with different frequency ratios or by an assumption of resonances sharing the same radius, as indicated by observations of the microquasar GRS 1915+105, the galactic nuclei Sgr A*, and extragalactic objects NGC 4051 and MCG-6-30-15. We can introduce a variety of multi-resonance models enabling us to explain the complex frequency patterns observed in some of the sources.

The multi-resonance models could be classified in the following way.

(A) Orbital resonance models involving Keplerian and epicyclic oscillations

(A1) More instances of one resonance occurring at more specific radii

This kind of the multi-resonance model is probably relevant in the neutron star binary systems, where data clustering of the twin peak QPOs is observed for the ratios 3 : 2, 4 : 3, 5 : 4 in six atoll sources (Török et al., 2007d; Török, 2007; Török et al., 2007b). When more resonant points corresponding to the data clustering around the rational frequency ratios is observed in a specific atoll source, e.g., the 4U 1636−53 source, the frequency ratio falls with the frequency magnitude growing, excluding thus the possibility of direct resonances of oscillations with the Keplerian or epicyclic frequencies which exhibit an inverse kind of behaviour (Stuchlík et al., 2007f; Török et al., 2007a). There is a variety of possible resonance models that could explain quite well the data fitting in such cases, however, it is important that all of these models involve combinational frequencies – for example, the total precession model involving resonance of oscillations with the Keplerian frequency and the total precession frequency given by the difference of the vertical and radial epicyclic frequencies (Stuchlík et al., 2007f), which generalizes the well know relativistic precession model (Stella and Vietri, 1999, 1998). Both the models enable a relatively precise determination of the neutron star parameters (Stuchlík et al., 2007f), especially when corrections due to the neutron star magnetic field are taken into account (Török et al., 2007a).

(A2) More resonances sharing one specific radius

This special case allows existence of strong resonant phenomena, since the Keplerian and both epicyclic frequencies are in the rational ratios in a shared radius and cooperative phenomena between different kinds of resonance could appear. Of course, such a situation is allowed for black holes with a specific spin only. The very important triple frequency set with ratios 3 : 2 : 1 is then given by the case of the "magic" spin $a = 0.983$, when the resonances share the radius $r/M = 2.395$ (Stuchlík et al., 2007b). In this magic case, the combinational frequencies give the same frequency ratios. Therefore, the combinational and the simple frequency oscillations could be in the 1 : 1 ratio, corresponding to the strongest possible resonant phenomena. In such a case, the scatter of the resonant frequencies could be the highest one, indicating a possible implication to the frequency set (probably) observed in Sgr A* (Aschenbach, 2007). The mass range is then in agreement with limits given by other observations.

(A3) More resonances occurring at more specific radii (the "ugly" case)

In general, we can expect the oscillations to be excited at two (or more) different radii of the accretion disc that enter the forced or parametric resonance in the framework of different versions of the resonance model. In such situations we are making the black hole spin estimate within two properly chosen versions of the resonance model, obtaining thus in principle more precise determinations of the spin than in the case, when only one twin peak is observed. In special cases, when a common upper (lower, mixed) frequency is observed in the two frequency pairs (i.e., only three different frequencies are observed), the triple frequency set is precisely given for specifically fixed values of the black hole spin independently of the black hole mass. Then, the spin is in principle determined precisely (within the precision of the frequency measurements), but not uniquely, as in general the same frequency set could occur for different values of the spin within different versions of the resonance model. It is clear that in such situations the black hole spin estimates coming from the spectra fitting and the line profile model could be relevant in determining the proper versions of the resonant model. When the black hole spin is found, its mass can be determined from the magnitude of the observed frequencies. For each type of both the direct and simple combinational resonances between oscillations with the epicyclic and Keplerian frequencies, the set of triple frequency ratios and the related dimensionless black hole spin are given (Stuchlík and Török, 2005). The resonances are considered up to $n = 5$ as the excitation of higher order resonances is highly improbable.

(B) Extended orbital resonance model with hump-induced oscillations

In the microquasar GRS 1915+105, a near-extreme Kerr black hole with the spin $a \sim 1$ is expected, and all the five (six) frequencies of observed QPOs can be explained in the framework of the extended resonance model with the hump-induced oscillations (Stuchlík et al., 2006, 2007e,d). In the extended resonance model, we assume forced resonance of the epicyclic oscillations with the oscillations induced by the "humpy" orbital velocity profile (related to the locally non-rotating frames) that occurs in Keplerian discs orbiting Kerr black holes with $a > 0.9953$ (see also Stuchlík et al., 2005). The humpy-induced oscillations could appear also in thick accretion discs, but the critical black hole spin is even higher than in the case of Keplerian disks. In the "humpy" extended resonance model, all the oscillations in resonance can be related to the exclusively defined "humpy radius" with extremal orbital velocity gradient within the humpy profile. The spin and mass of the black hole could then be determined with high precision. However, this model can be relevant only for near-extreme Kerr black holes with spin $a > 0.9953$. We shall not discuss this model here as its overview is presented in Stuchlík et al. (2007d).

3 DETERMINATION OF THE BLACK HOLE SPIN FROM THE RESONANCE MODEL

It is well known that the formulae for the vertical epicyclic frequency ν_θ and the radial epicyclic frequency ν_r take in the gravitational field of a rotating Kerr black hole (with the mass M and dimensionless spin a) the form (see, e.g., Aliev and Galtsov, 1981; Kato et al.,

1998; Stella and Vietri, 1999, 1998)

$$\nu_\theta^2 = \alpha_\theta\, \nu_{\rm K}^2\,, \quad \nu_r^2 = \alpha_r\, \nu_{\rm K}^2\,, \tag{1}$$

where the Keplerian frequency $\nu_{\rm K}$ and related dimensionless epicyclic frequencies are given by the formulae

$$\nu_{\rm K} = \frac{1}{2\pi}\left(\frac{GM}{r_{\rm G}^3}\right)^{1/2} (x^{3/2}+a)^{-1} = \frac{1}{2\pi}\left(\frac{c^3}{GM}\right)(x^{3/2}+a)^{-1}\,,$$

$$\alpha_\theta = 1 - 4ax^{-3/2} + 3a^2x^{-2}\,,$$

$$\alpha_r = 1 - 6x^{-1} + 8ax^{-3/2} - 3a^2x^{-2}\,.$$

Here $x = r/(GM/c^2)$ is the dimensionless radius, expressed in terms of the gravitational radius of the black hole. For a particular resonance $n:m$, the equation

$$n\nu_r = m\nu_{\rm v}\,, \quad \nu_{\rm v} \in \{\nu_\theta, \nu_{\rm K}\} \tag{2}$$

determines the dimensionless resonance radius $x_{n:m}$ as a function of the dimensionless spin a in the case of direct resonances that can be easily extended to the resonances with combinational frequencies, as discussed in detail later. The resonances could be realized as internal, parametric resonances which are determined by the Mathieu equation corresponding to conservative systems, or forced non-linear resonances with beat frequencies allowed (Landau and Lifshitz, 1976).

From the known mass of the central black hole (e.g., low-mass in the case of binary systems or hi-mass in the case of supermassive black holes), the observed double peak frequencies ($\nu_{\rm upp}$, $\nu_{\rm down}$) and the Eqs (1)–(2) imply the black hole spin, consistent with different types of resonances with the beat frequencies taken into account. This procedure was first applied to the microquasar GRO 1655−40 by Abramowicz and Kluźniak (2001), more recently to the other three microquasars (Török et al., 2005) and also to the Galaxy centre black hole Sgr A* (Török, 2005).

4 MULTIPLE RESONANCES AND RESONANCE CONDITIONS

The very probable interpretation of twin peak frequencies observed in microquasars is the 3:2 parametric resonance, however, generally it is not unlikely that more than one resonance could be excited in the disc at the same time (or in different times) under different internal conditions. Indeed, observations of the kHz QPOs in the microquasar GRS 1915+105, and of the QPOs in extragalactic sources NGC 4051, MCG-6-30-15 (Lachowicz et al., 2006) and NGC 5408 X-1 (Strohmayer et al., 2007), and the Galaxy centre Sgr A* (Aschenbach et al., 2004) show a variety of QPOs with frequency ratios differing from the 3:2 ratio.

The resonances could be parametric or forced and of different versions according to the epicyclic (Keplerian) frequencies entering the resonance directly, or in some combinational

form. In principle, for any case of the resonance model version, one can determine both the spin and mass of the black hole just from the eventually observed set of frequencies. However, the obvious difficulty would be to identify the right combination of resonances and its relation to the observed frequency set. Within the range of black hole mass allowed by observations, each set of twin peak frequencies puts limit on the black hole spin. Of course, the resonance model versions are consistent with observations, if the allowed spin ranges are overlapping each other. Clearly, two or more twin peaks then generally make the spin measurement more precise.

Here we consider the special case of two different resonances determined by a doubled ratio of natural numbers $n:m$ and $n':m'$. Such resonances are located at the corresponding radii $x_{n:m}$, $x_{n':m'}$ and characterized by observable set of frequencies resulting from the relevant resonance modes (forced or parametric). Thus, the generic relation of $n:m$ and $n':m'$ *puts restrictions on the spin of the central black hole*. It is reasonable (because of arguments mentioned above) to assume that in the black hole systems one of this excited resonances is a $3:2$ parametric (internal) resonance. However, it is more convenient to consider general frequency ratios with small integers, with order of the resonances $n+m \leq 9$ ($n'+m' \leq 9$), since only then are the resonant phenomena realistic (see Landau and Lifshitz, 1976 for details). Notice that in some sources (e.g., NGC 5408 X-1), the ratio $4:3$ occurs for the strongest QPOs (Strohmayer et al., 2007) supporting the necessity to consider the general ratios at both radii. Of course, in special cases, the resonant radii could coincide, i.e., $x_{n:m} = x_{n':m'}$.

4.1 Resonance conditions

We shall investigate radial coordinates determining positions, where the rational ratios occur for all possible versions of the resonance between the radial and vertical epicyclic and the Keplerian oscillations ($\nu_{\mathrm{K}} > \nu_\theta > \nu_r$ for $a > 0$), taking into account both the direct and simple combinational resonances. For all possible resonances of the epicyclic and Keplerian oscillations, the resonance condition is given in terms of the frequency ratio

$$p = \left(\frac{m}{n}\right)^2 .$$

All the resonant conditions determining implicitly the resonant radius $x_{n:m}$ must be related to the radius of the innermost stable circular geodesic x_{ms} giving the inner edge of Keplerian discs. Therefore, for all the relevant resonance radii, there must be $x_{n:m} \geq x_{\mathrm{ms}}$, where x_{ms} is implicitly given by

$$a = a_{\mathrm{ms}} \equiv \frac{\sqrt{x}}{3}\left(4 - \sqrt{3x-2}\right) .$$

The results are summarized in the following way relating the dimensionless spin a and the dimensionless resonance radius determined by the resonance model version and the ratio p.

4.1.1 Direct resonances

$$\text{D1.}\quad \frac{\nu_\theta}{\nu_r} = \frac{n}{m}\,, \quad a = a^{\theta/r}(x,\,p)$$
$$\equiv \tfrac{1}{3}\sqrt{x}\,(p+1)^{-1}\left\{2(p+2) - \sqrt{(1-p)\,[3x(p+1) - 2(2p+1)]}\right\}, \qquad (3)$$

$$\text{D2.}\quad \frac{\nu_{\rm K}}{\nu_r} = \frac{n}{m}\,, \quad a = a^{{\rm K}/r}(x,\,p) \equiv \frac{\sqrt{x}}{3}\left[4 - \sqrt{3x(1-p) - 2}\right],$$

$$\text{D3.}\quad \frac{\nu_{\rm K}}{\nu_\theta} = \frac{n}{m}\,, \quad a = a^{{\rm K}/\theta}(x,\,p) \equiv \frac{\sqrt{x}}{3}\left[2 \pm \sqrt{4 - 3x(1-p)}\right].$$

The results are illustrated in Fig. 1.

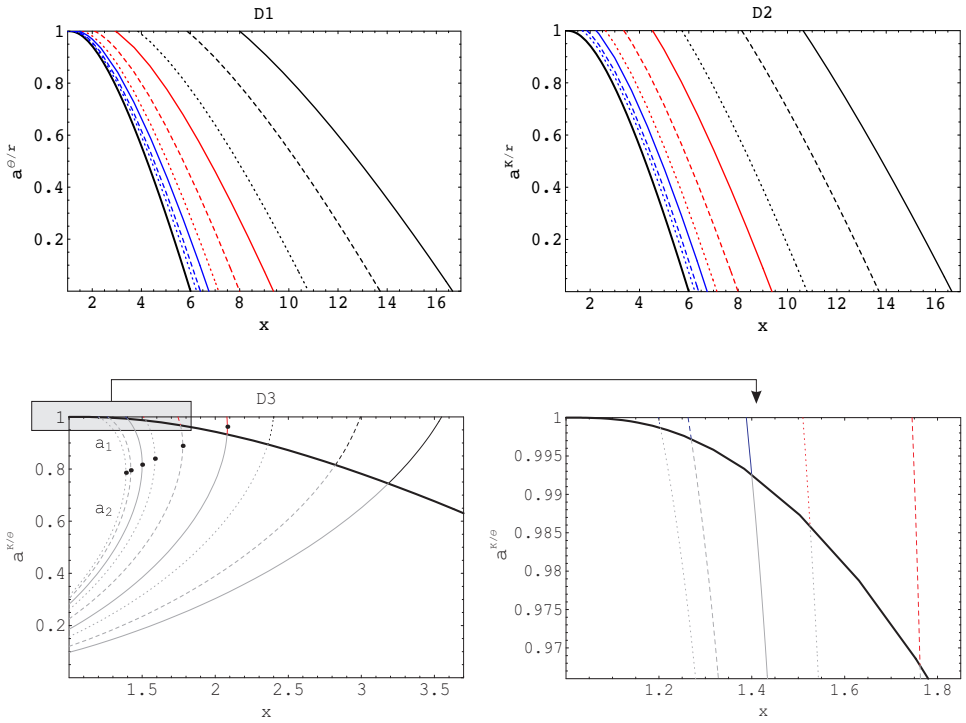

Figure 1. Direct resonances: for each version of the direct resonances the functions $a = a(x,\,p)$ are drawn for $n : m = 5 : 4$ (black solid line), $4 : 3$ (black dashed line), $3 : 2$ (black dotted line), $5 : 3$ (red solid line), $2 : 1$ (red dashed line), $5 : 2$ (red dotted line), $3 : 1$ (blue solid line), $4 : 1$ (blue dashed line), $5 : 1$ (blue dotted line). Black thick line represents $a_{\rm ms}$ which implicitly determines the radius of the marginally stable orbit $x_{\rm ms}$ giving a natural restriction on the validity of the resonance model versions involving radial epicyclic oscillations.

4.1.2 Simple combinational resonances

4.1.2.1 Combinations of ν_θ, ν_r

C1.1 $$\frac{\nu_\theta+\nu_r}{\nu_\theta}=\frac{n}{m}\,,\quad a=a^{(\theta+r)/\theta}(x,p)\equiv a^{\theta/r}(x,p^{\mathrm{I}})\,,$$
$$p^{\mathrm{I}}=\left(\frac{n-m}{m}\right)^2=\frac{\left(1-\sqrt{p}\right)^2}{p}\,,$$

C1.2 $$\frac{\nu_\theta}{\nu_\theta-\nu_r}=\frac{n}{m}\,,\quad a=a^{\theta/(\theta-r)}(x,p)\equiv a^{\theta/r}(x,p^{\mathrm{II}})\,,$$
$$p^{\mathrm{II}}=\left(\frac{n-m}{n}\right)^2=\left(1-\sqrt{p}\right)^2\,,$$

C1.3 $$\frac{\nu_\theta+\nu_r}{\nu_r}=\frac{n}{m}\,,\quad a=a^{(\theta+r)/r}(x,p)\equiv a^{\theta/r}(x,p^{\mathrm{III}})\,,$$
$$p^{\mathrm{III}}=\left(\frac{m}{n-m}\right)^2=\frac{p}{\left(\sqrt{p}-1\right)^2}\,,$$

C1.4 $$\frac{\nu_\theta-\nu_r}{\nu_r}=\frac{n}{m}\,,\quad a=a^{(\theta-r)/r}(x,p)\equiv a^{\theta/r}(x,p^{\mathrm{IV}})\,,$$
$$p^{\mathrm{IV}}=\left(\frac{m}{n+m}\right)^2=\frac{p}{\left(\sqrt{p}+1\right)^2}\,,$$

C1.5 $$\frac{\nu_r}{\nu_\theta-\nu_r}=\frac{n}{m}\,,\quad a=a^{r/(\theta-r)}(x,p)\equiv a^{\theta/r}(x,p^{\mathrm{V}})\,,$$
$$p^{\mathrm{V}}=\left(\frac{n}{n+m}\right)^2=\frac{1}{\left(\sqrt{p}+1\right)^2}\,,$$

C1.6 $$\frac{\nu_\theta+\nu_r}{\nu_\theta-\nu_r}=\frac{n}{m}\,,\quad a=a^{(\theta+r)/(\theta-r)}(x,p)\equiv a^{\theta/r}(x,p^{\mathrm{VI}})\,,$$
$$p^{\mathrm{VI}}=\left(\frac{n-m}{n+m}\right)^2=\left(\frac{\sqrt{p}-1}{\sqrt{p}+1}\right)^2\,.$$

4.1.2.2 Combinations of ν_{K}, ν_r

C2.1 $$\frac{\nu_{\mathrm{K}}+\nu_r}{\nu_{\mathrm{K}}}=\frac{n}{m}\,,\quad a=a^{(\mathrm{K}+r)/\mathrm{K}}(x,p)\equiv a^{\mathrm{K}/r}(x,p^{\mathrm{I}})\,,$$

C2.2 $$\frac{\nu_{\mathrm{K}}}{\nu_{\mathrm{K}}-\nu_r}=\frac{n}{m}\,,\quad a=a^{\mathrm{K}/(\mathrm{K}-r)}(x,p)\equiv a^{\mathrm{K}/r}(x,p^{\mathrm{II}})\,,$$

C2.3 $$\frac{\nu_{\mathrm{K}}+\nu_r}{\nu_r}=\frac{n}{m}\,,\quad a=a^{(\mathrm{K}+r)/r}(x,p)\equiv a^{\mathrm{K}/r}(x,p^{\mathrm{III}})\,,$$

C2.4 $$\frac{\nu_{\mathrm{K}}-\nu_r}{\nu_r}=\frac{n}{m}\,,\quad a=a^{(\mathrm{K}-r)/r}(x,p)\equiv a^{\mathrm{K}/r}(x,p^{\mathrm{IV}})\,,$$

C2.5 $$\frac{\nu_r}{\nu_{\mathrm{K}}-\nu_r}=\frac{n}{m}\,,\quad a=a^{r/(\mathrm{K}-r)}(x,p)\equiv a^{\mathrm{K}/r}(x,p^{\mathrm{V}})\,,$$

C2.6 $$\frac{\nu_{\mathrm{K}}+\nu_r}{\nu_{\mathrm{K}}-\nu_r}=\frac{n}{m}\,,\quad a=a^{(\mathrm{K}+r)/(\mathrm{K}-r)}(x,p)\equiv a^{\mathrm{K}/r}(x,p^{\mathrm{VI}})\,.$$

4.1.2.3 Combinations of ν_{K}, ν_θ

C3.1 $$\frac{\nu_{\mathrm{K}}+\nu_\theta}{\nu_{\mathrm{K}}}=\frac{n}{m}\,,\quad a=a^{(\mathrm{K}+\theta)/\mathrm{K}}(x,\,p)\equiv a^{\mathrm{K}/\theta}(x,\,p^{\mathrm{I}})\,,$$

C3.2 $$\frac{\nu_{\mathrm{K}}}{\nu_{\mathrm{K}}-\nu_\theta}=\frac{n}{m}\,,\quad a=a^{\mathrm{K}/(\mathrm{K}-\theta)}(x,\,p)\equiv a^{\mathrm{K}/\theta}(x,\,p^{\mathrm{II}})\,,$$

C3.3 $$\frac{\nu_{\mathrm{K}}+\nu_\theta}{\nu_\theta}=\frac{n}{m}\,,\quad a=a^{(\mathrm{K}+\theta)/\theta}(x,\,p)\equiv a^{\mathrm{K}/\theta}(x,\,p^{\mathrm{III}})\,,$$

C3.4 $$\frac{\nu_{\mathrm{K}}-\nu_\theta}{\nu_\theta}=\frac{n}{m}\,,\quad a=a^{(\mathrm{K}-\theta)/\theta}(x,\,p)\equiv a^{\mathrm{K}/\theta}(x,\,p^{\mathrm{IV}})\,,$$

C3.5 $$\frac{\nu_\theta}{\nu_{\mathrm{K}}-\nu_\theta}=\frac{n}{m}\,,\quad a=a^{\theta/(\mathrm{K}-\theta)}(x,\,p)\equiv a^{\mathrm{K}/\theta}(x,\,p^{\mathrm{V}})\,,$$

C3.6 $$\frac{\nu_{\mathrm{K}}+\nu_\theta}{\nu_{\mathrm{K}}-\nu_\theta}=\frac{n}{m}\,,\quad a=a^{(\mathrm{K}+\theta)/(\mathrm{K}-\theta)}(x,\,p)\equiv a^{\mathrm{K}/\theta}(x,\,p^{\mathrm{VI}})$$

Simple combinational resonances of the types C1, C2, C3 occur at the same radii as the direct resonances D1, D2, D3. Therefore, it is enough to relate the ratios of the simple combinational and direct resonances. The results are summarized in Tables 1 and 2.

Table 1. Combinations of ν_{v}, ν_r, $\mathrm{v}\in\{\theta,\mathrm{K}\}$.

$n:m$	ν_{v}/ν_r	Condition	$a(x,\,p)$
$\frac{\nu_{\mathrm{v}}+\nu_r}{\nu_{\mathrm{v}}}$	$\frac{m}{n-m}$	$m<n<2m$	$a^{\mathrm{v}/r}(x,\,p^{\mathrm{I}})$
$\frac{\nu_{\mathrm{v}}}{\nu_{\mathrm{v}}-\nu_r}$	$\frac{n}{n-m}$	$n>m$	$a^{\mathrm{v}/r}(x,\,p^{\mathrm{II}})$
$\frac{\nu_{\mathrm{v}}+\nu_r}{\nu_r}$	$\frac{n-m}{m}$	$n>2m$	$a^{\mathrm{v}/r}(x,\,p^{\mathrm{III}})$
$\frac{\nu_{\mathrm{v}}-\nu_r}{\nu_r}$	$\frac{n+m}{m}$	$n>m$	$a^{\mathrm{v}/r}(x,\,p^{\mathrm{IV}})$
$\frac{\nu_r}{\nu_{\mathrm{v}}-\nu_r}$	$\frac{n+m}{n}$	$n>m$	$a^{\mathrm{v}/r}(x,\,p^{\mathrm{V}})$
$\frac{\nu_{\mathrm{v}}+\nu_r}{\nu_{\mathrm{v}}-\nu_r}$	$\frac{n+m}{n-m}$	$n>m$	$a^{\mathrm{v}/r}(x,\,p^{\mathrm{VI}})$

Table 2. Combinations of ν_{K}, ν_θ.

$n:m$	$\nu_{\mathrm{K}}/\nu_\theta$	Condition	$a(x,\,p)$
$\frac{\nu_{\mathrm{K}}+\nu_\theta}{\nu_{\mathrm{K}}}$	$\frac{m}{n-m}$	$m<n<2m$	$a^{\mathrm{K}/\theta}(x,\,p^{\mathrm{I}})$
$\frac{\nu_{\mathrm{K}}}{\nu_{\mathrm{K}}-\nu_\theta}$	$\frac{n}{n-m}$	$n>m$	$a^{\mathrm{K}/\theta}(x,\,p^{\mathrm{II}})$
$\frac{\nu_{\mathrm{K}}+\nu_\theta}{\nu_\theta}$	$\frac{n-m}{m}$	$n>2m$	$a^{\mathrm{K}/\theta}(x,\,p^{\mathrm{III}})$
$\frac{\nu_{\mathrm{K}}-\nu_\theta}{\nu_\theta}$	$\frac{n+m}{m}$	$n>m$	$a^{\mathrm{K}/\theta}(x,\,p^{\mathrm{IV}})$
$\frac{\nu_\theta}{\nu_{\mathrm{K}}-\nu_\theta}$	$\frac{n+m}{n}$	$n>m$	$a^{\mathrm{K}/\theta}(x,\,p^{\mathrm{V}})$
$\frac{\nu_{\mathrm{K}}+\nu_\theta}{\nu_{\mathrm{K}}-\nu_\theta}$	$\frac{n+m}{n-m}$	$n>m$	$a^{\mathrm{K}/\theta}(x,\,p^{\mathrm{VI}})$

4.1.3 Combinations of ν_{K}, ν_θ, ν_r

We shall consider resonances of oscillations with one simple frequency taken from the three orbital frequencies and a simple combination of the other two frequencies.

CT1. $$\frac{\nu_{\mathrm{K}}}{\nu_\theta-\nu_r}=\frac{n}{m}\quad\Rightarrow\quad\frac{\nu_\theta}{\nu_r}=1+\frac{m}{n}\frac{\nu_{\mathrm{K}}}{\nu_r}\,,$$
$a^{\mathrm{K}/(\theta-r)}(x,\,p)$ is solution of the equation
$$(\alpha_\theta-\alpha_r)^2-2p(\alpha_\theta+\alpha_r)+p^2=0$$

giving the relation

$$a = a^{\mathrm{K}/(\theta-r)}(x,\, p) \equiv \sqrt{x} + \frac{1}{2\cdot 3^{5/6}} \times \left[\sqrt{\frac{A^{2/3}+B}{A^{1/3}}} - \sqrt{A^{1/3}\left(\frac{4\sqrt{3}\,p\,x^{5/2}}{\sqrt{A+A^{1/3}B}} - 1\right) - \frac{B}{A^{1/3}}}\right], \tag{4}$$

$$A = 6p^2x^5 + \sqrt{36p^4x^{10} - B^3}\,,$$

$$B = 3^{1/3}px^3\left[4 + (p-4)x\right].$$

CT2. $\dfrac{\nu_\theta}{\nu_\mathrm{K}-\nu_r} = \dfrac{n}{m} \quad\Rightarrow\quad \dfrac{\nu_\theta}{\nu_r} = \dfrac{n}{m}\left(\dfrac{\nu_\mathrm{K}}{\nu_r} - 1\right),$

$a^{\theta/(\mathrm{K}-r)}(x,\, p)$ is solution of the equation

$$p^2\alpha_\theta^2 - 2p\alpha_\theta\,(1+\alpha_r) + (1-\alpha_r)^2 = 0\,.$$

CT3. $\dfrac{\nu_r}{\nu_\mathrm{K}-\nu_\theta} = \dfrac{n}{m} \quad\Rightarrow\quad \dfrac{\nu_\theta}{\nu_r} = \dfrac{\nu_\mathrm{K}}{\nu_r} - \dfrac{m}{n},$

$a^{r/(\mathrm{K}-\theta)}(x,\, p)$ is solution of the equation

$$(1-\alpha_\theta)^2 - 2p\alpha_r\,(1+\alpha_\theta) + p^2\alpha_r^2 = 0\,.$$

CT4. $\dfrac{\nu_\theta+\nu_r}{\nu_\mathrm{K}} = \dfrac{n}{m} \quad\Rightarrow\quad \dfrac{\nu_\theta}{\nu_r} = \dfrac{n}{m}\dfrac{\nu_\mathrm{K}}{\nu_r} - 1\,,$

$a^{(\theta+r)/\mathrm{K}}(x,\, p)$ is solution of the equation

$$p^2\,(\alpha_r-\alpha_\theta)^2 - 2p\,(\alpha_r+\alpha_\theta) + 1 = 0\,.$$

The condition $m < n < 2m$ has to be satisfied.

CT5. $\dfrac{\nu_\mathrm{K}+\nu_r}{\nu_\theta} = \dfrac{n}{m} \quad\Rightarrow\quad \dfrac{\nu_\theta}{\nu_r} = \dfrac{m}{n}\left(\dfrac{\nu_\mathrm{K}}{\nu_r} + 1\right),$

$a^{(\mathrm{K}+r)/\theta}(x,\, p)$ is solution of the equation

$$(\alpha_\theta - p)^2 - 2p\alpha_r\,(\alpha_\theta+p) + p^2\alpha_r^2 = 0\,.$$

CT6. $\dfrac{\nu_\mathrm{K}+\nu_\theta}{\nu_r} = \dfrac{n}{m} \quad\Rightarrow\quad \dfrac{\nu_\theta}{\nu_r} = \dfrac{n}{m} - \dfrac{\nu_\mathrm{K}}{\nu_r},$

$a^{(\mathrm{K}+\theta)/r}(x,\, p)$ is solution of the equation

$$p^2\,(\alpha_\theta-1)^2 - 2p\alpha_r\,(\alpha_\theta+1) + \alpha_r^2 = 0\,.$$

The condition $n > 2m$ has to be satisfied.

Except the case CT1, we give the resonance condition in an implicit form, because the final relation is too complex to be written explicitly. That is the reason why we present the resonant conditions in the graphical form only (see Fig. 2). Notice that the implicit condition is polynomial of 4th order in the spin a. Only one of the possible solutions is physically relevant.

Resonances of beat frequencies (four frequencies combined from ν_K, ν_θ, ν_r) constitute family of 13th cases, e.g., the type CF1 is given by the condition $(\nu_\mathrm{K}-\nu_r):(\nu_\theta-\nu_r) = n:m$. All of these cases will be presented in Stuchlík et al. (2007c).

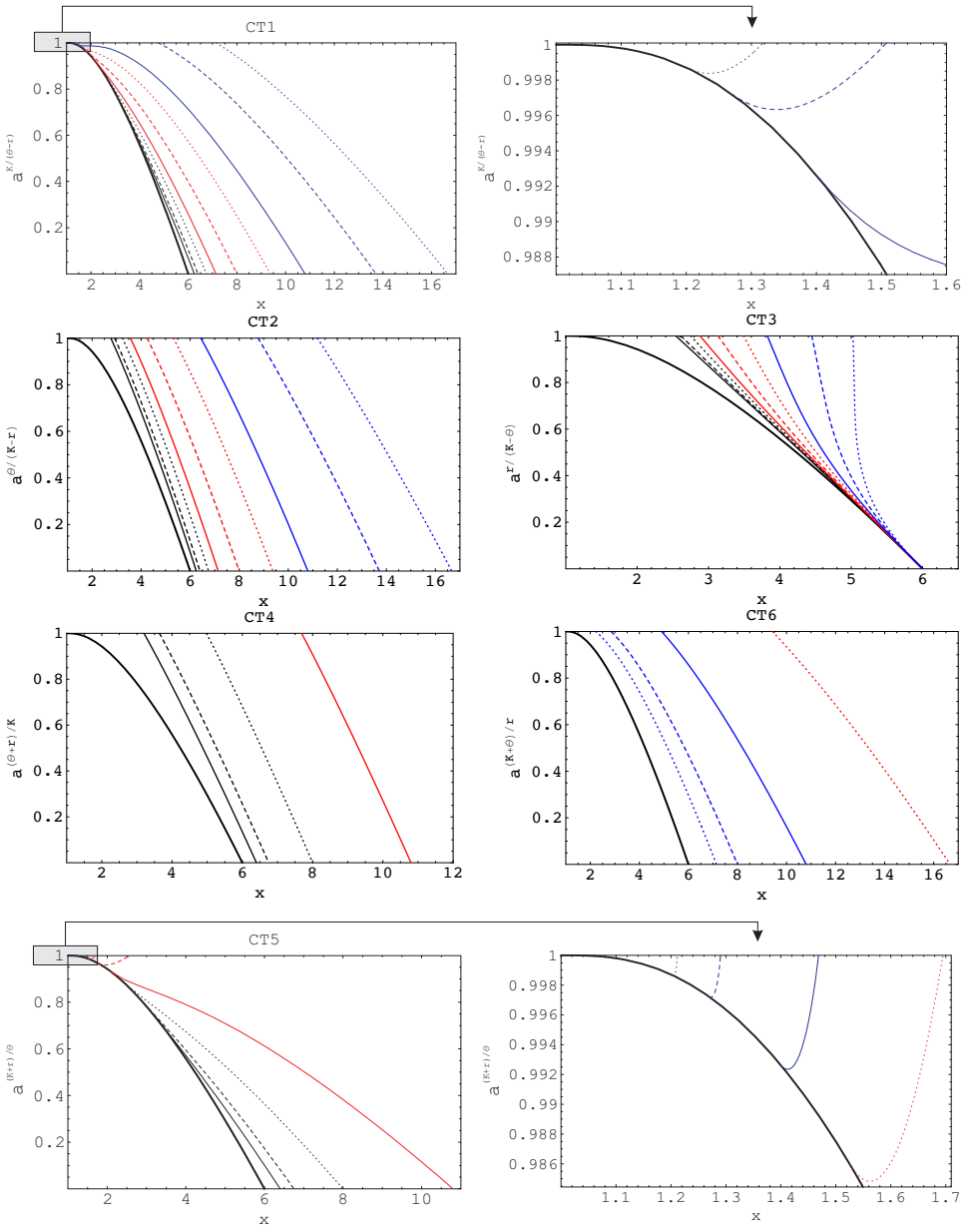

Figure 2. Simple combinational resonances: for each versions of the simple combinations of the three orbital frequencies $\nu_{\rm K}$, ν_θ, ν_r the functions $a = a(x,\, p)$ are drawn for $n : m = 5 : 4$ (black solid line), $4 : 3$ (black dashed line), $3 : 2$ (black dotted line), $5 : 3$ (red solid line), $2 : 1$ (red dashed line), $5 : 2$ (red dotted line), $3 : 1$ (blue solid line), $4 : 1$ (blue dashed line), $5 : 1$ (blue dotted line). Black thick line represents $a_{\rm ms}$ which implicitly determines the radius of the marginally stable orbit $x_{\rm ms}$.

When two twin peak QPOs are observed with frequency ratios $n : m$ and $n' : m'$, respectively, we have to find two versions of resonance that could explain both the ratios and magnitudes of the observed frequencies and, for a given range of allowed mass in the source, they must predict the same black hole spin a, or more precisely, an overlapping intervals of the spin. Therefore, it is clear that, generally, two observed twin peak QPOs could make the spin estimates more precise. Notice that two different resonances are necessary when two twin peaks are observed with the same ratios but different magnitudes.

5 CHARACTERISTIC SETS OF FREQUENCIES WITH A DUPLEX FREQUENCY

In some specific situations, for some specific values of the black hole dimensionless spin, two twin peak QPOs observed at the radii $x_{n:m}$ and $x_{n':m'}$ have the bottom, top, or mixed (the bottom at the inner radius and the top in the outer radius, or vice versa) frequencies identical. Such situations can be characterized by sets of three frequencies with ratio $s : t : u$, given by the $n : m$ and $n' : m'$ ratios, the relevant versions of the resonance, and the type of the duplex (common) frequency.

When only direct resonances of the epicyclic oscillations are allowed, the first case with "bottom identity" can be realized by the situation with two resonances having common radial epicyclic frequency, while the second case with "top identity" can be realized by the situation with two resonances having common vertical epicyclic frequency. These two possibilities are in principle allowed by the non-monotonicity of the epicyclic frequencies (1) discussed in detail in Török and Stuchlík (2005a,b). When the Keplerian oscillations and the combinational frequencies are allowed, all the mixed, bottom, and top identities are possible.

It is rather familiar piece of knowledge that the Keplerian frequency $\nu_{\mathrm{K}}(x, a)$ is a monotonically decreasing function of the radial coordinate for any value of the black hole spin. On the other hand, the radial epicyclic frequency has the global maximum for any Kerr black hole. However, also the vertical epicyclic frequency is not monotonic if the spin is sufficiently high (see, e.g., Kato et al., 1998; Perez et al., 1997). For the Kerr black-hole spacetimes, the locations $\mathcal{R}_r(a)$, $\mathcal{R}_\theta(a)$ of maxima of the epicyclic frequencies ν_r, ν_θ are implicitly given by the conditions (Török and Stuchlík, 2005a)

$$\beta_j(x, a) = \frac{1}{2}\frac{\sqrt{x}}{x^{3/2} + a}\,\alpha_j(x, a)\,, \quad \text{where } j \in \{r, \theta\}\,,$$

$$\beta_r(x, a) \equiv \frac{1}{x^2} - \frac{2a}{x^{5/2}} + \frac{a^2}{x^3}\,,$$

$$\beta_\theta(x, a) \equiv \frac{a}{x^{5/2}} - \frac{a^2}{x^3}\,.$$

For any black hole spin, the extrema of the radial epicyclic frequency $\mathcal{R}_r(a)$ must be located above the marginally stable orbit. On the other hand, the latitudinal extrema $\mathcal{R}_\theta(a)$ are located above the photon (marginally bound or marginally stable) circular orbit only if the limits on the black hole spin $a > 0.748$ $(0.852, 0.952)$ are satisfied (Török and Stuchlík, 2005b). In the Keplerian discs, with the inner boundary $x_{\mathrm{in}} \sim x_{\mathrm{ms}}$, the limiting value $a = 0.952$ is relevant.

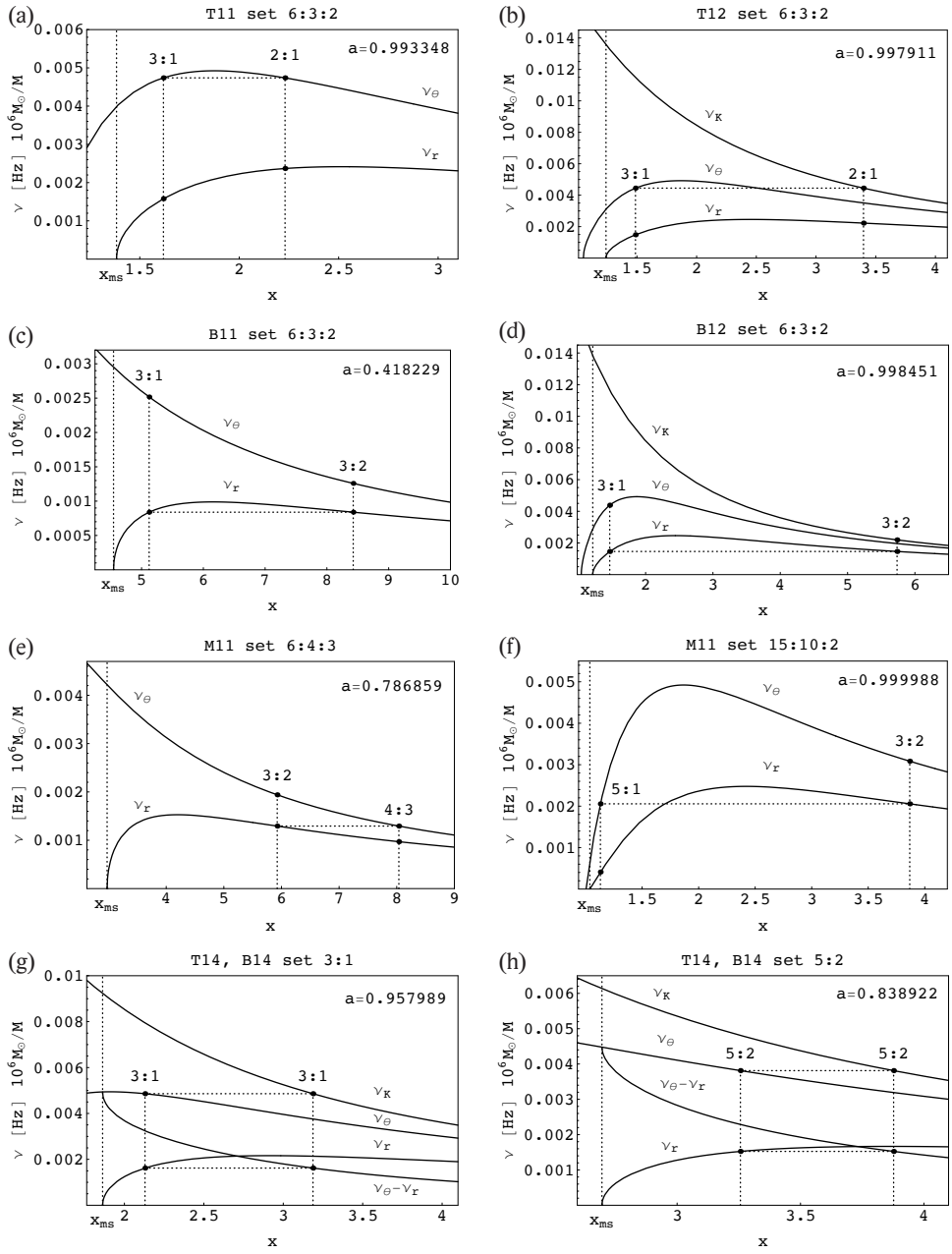

Figure 3. The typical cases of the frequency triples with top (a), (b), bottom (c), (d), and both types of mixed identities (e), (f). There are also shown two interesting exceptional cases: two frequencies with the same magnitude and the ratio 3 : 1 (g) and 5 : 2 (h) that are in resonance at two different radii.

From the point of view of the observational consequences, it is important to know, for which frequency ratios $n:m$ the resonant frequencies $\nu_\theta(a, n:m)$, considered as a function of the black hole spin a for a given frequency ratio $n:m$, has a non-monotonic character. A detailed analysis (Török and Stuchlík, 2005a) shows that $\nu_\theta(a, n:m)$ has a local maximum for $n:m > 11:5$, i.e., in physically relevant situations (n, m small enough for the resonance), it occurs for the ratios $\nu_\theta : \nu_r = 5:2, 3:1, 4:1, 5:1$. This means that while the "bottom identity" could happen for any black hole spin a, the "top identity" can arise only for $a \sim 1$ if the epicyclic oscillations are considered only.

The typical cases of the frequency triple sets with bottom, top and both types of mixed identities containing duplex frequencies are illustrated in Fig. 3.

5.1 Triple frequencies and black hole spin

Let us consider a simple situation with the "top identity" of the upper frequencies in two resonances between the radial and vertical epicyclic oscillations at two radii x_p, $x_{p'}$ with $p^{1/2} = m:n$, $p'^{1/2} = m':n'$. The condition $\nu_\theta(a, x_p) = \nu_\theta(a, x_{p'})$ is then transformed to the relation

$$\alpha_\theta^{1/2}(a, x_p)\left(x_p^{3/2} + a\right)^{-1} = \alpha_\theta^{1/2}(a, x_{p'})\left(x_{p'}^{3/2} + a\right)^{-1}$$

which uniquely determines the black hole spin a. When two different resonances are combined, we proceed in the same manner. For example, the case of "bottom identity" in the resonance between the radial and vertical epicyclic oscillations at x_p and the resonance between the Keplerian oscillations with ν_K and total precession oscillations with $\nu_\mathrm{T} = \nu_\theta - \nu_r$ at $x_{p'}$ implies the condition $\nu_r(a, x_p) = (\nu_\theta - \nu_r)(a, x_{p'})$ that leads to the relation

$$\alpha_r^{1/2}(a, x_p)\left(x_p^{3/2} + a\right)^{-1} = \left[(\alpha_\theta - \alpha_r)(a, x_{p'})\right]\left(x_{p'}^{3/2} + a\right)^{-1}$$

which uniquely determines the spin a, since in Eq. (3) (and (4)), the radii x_p and $x_{p'}$ are related to the spin a by the resonance conditions for $a^{\theta/r}(x, p)$ and $a^{\mathrm{K}/(\theta-r)}(x, p')$, respectively.

Therefore, for given types of the doubled resonances, the ratios $n:m$ and $n':m'$ determine the ratio in the triple frequency set $s:t:u$. The black hole spin a is given by the types of the two resonances and the ratios p, p', quite independently of the black hole mass M.

Since the radial and vertical epicyclic frequencies and the Keplerian frequency have the same dependence on the black hole mass M, the above given arguments hold in the same way for any kind of the three frequency set, for any of the bottom, top, or mixed frequency identity with any two resonances containing any combination of the frequencies ν_K, ν_θ, ν_r. Therefore, the triple frequency sets with the "duplex" frequencies can be used to determine the black hole spin with very high precision, independently on the uncertainties in determining the black hole mass M: of course, the parameter M can be addressed by the magnitude of the measured frequencies. Notice, however, that the relation between the black hole spin and the triple frequency ratios is not unique in general situations. For a given frequency ratio several values of a are allowed and some other methods of the spin measurement must be involved.

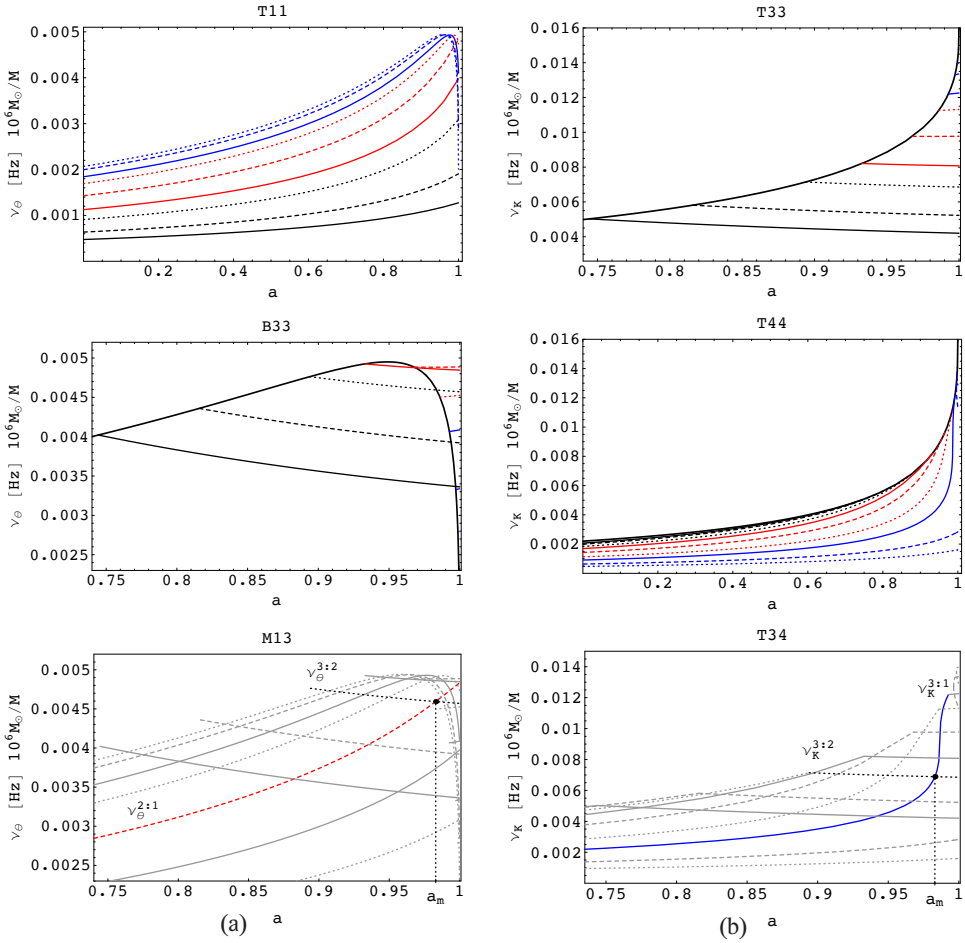

Figure 4. Determination of black hole spin for several cases of resonances. The functions $\nu_{\rm V} = \nu_{\rm V}^{n:m}(a, x_{n:m}(a))$, $\upsilon \in \{\theta, {\rm K}\}$, for: $n:m = 5:4$ (black solid line), $4:3$ (black dashed line), $3:2$ (black dotted line), $5:3$ (red solid line), $2:1$ (red dashed line), $5:2$ (red dotted line), $3:1$ (blue solid line), $4:1$ (blue dashed line), $5:1$ (blue dotted line). Black thick line in T33, T44, and B33 represents $\nu_{\rm V} = \nu_{\rm V}(a, x_{\rm ms})$ which denotes the frequency on the marginally stable orbit.

The triple frequency set ratios are directly given by the versions of resonance that occurs in the two twin peak QPOs under consideration, while the relevant spin a can be easily determined by searching for common points of the relevant frequency functions for a fixed mass M. The schemes for treating the situations with duplex frequencies are given in Figs 3 and 4. We consider here only the direct resonances, and some of the triplex simple combinational resonances. The other simple combinational resonances are directly given in Tables 3 and 4. Detailed results for all the combinational resonances will be presented in Stuchlík et al. (2007c).

Table 3. Simple combinational frequency ratios given by direct frequency ratios $n:m$, $\nu_{\rm v} \in \{\nu_\theta, \nu_{\rm K}\}$ ($\nu_{\rm v}/\nu_r > 1$).

$\frac{\nu_{\rm v}}{\nu_r}$	$\frac{\nu_{\rm v}+\nu_r}{\nu_{\rm v}}$	$\frac{\nu_{\rm v}}{\nu_{\rm v}-\nu_r}$	$\frac{\nu_{\rm v}+\nu_r}{\nu_r}$	$\frac{\nu_{\rm v}-\nu_r}{\nu_r}$	$\frac{\nu_r}{\nu_{\rm v}-\nu_r}$	$\frac{\nu_{\rm v}+\nu_r}{\nu_{\rm v}-\nu_r}$
5:**4**	9:5	5:1	9:4	–	4:1	9:1
4:**3**	7:4	4:1	7:3	–	3:1	7:1
3:**2**	5:3	3:1	5:2	–	2:1	5:1
5:**3**	8:5	5:2	8:3	–	3:2	4:1
2:**1**	3:2	2:1	3:1	–	–	3:1
5:**2**	7:5	5:3	7:2	3:2	–	7:3
3:**1**	4:3	3:2	4:1	2:1	–	2:1
4:**1**	5:4	4:3	5:1	3:1	–	5:3
5:**1**	6:5	5:4	6:1	4:1	–	3:2

Table 4. Simple combinational frequency ratios given by direct frequency ratios $n:m$ ($\nu_{\rm K}/\nu_\theta \geq 1$).

$\frac{\nu_{\rm K}}{\nu_\theta}$	$\frac{\nu_{\rm K}+\nu_\theta}{\nu_{\rm K}}$	$\frac{\nu_{\rm K}}{\nu_{\rm K}-\nu_\theta}$	$\frac{\nu_{\rm K}+\nu_\theta}{\nu_\theta}$	$\frac{\nu_{\rm K}-\nu_\theta}{\nu_\theta}$	$\frac{\nu_\theta}{\nu_{\rm K}-\nu_\theta}$	$\frac{\nu_{\rm K}+\nu_\theta}{\nu_{\rm K}-\nu_\theta}$
5:**4**	9:5	5:1	9:4	–	4:1	9:1
4:**3**	7:4	4:1	7:3	–	3:1	7:1
3:**2**	5:3	3:1	5:2	–	2:1	5:1
5:**3**	8:5	5:2	8:3	–	3:2	4:1
2:**1**	3:2	2:1	3:1	1:1	1:1	3:1
5:**2**	7:5	5:3	7:2	3:2	–	7:3
3:**1**	4:3	3:2	4:1	2:1	–	2:1
4:**1**	5:4	4:3	5:1	3:1	–	5:3
5:**1**	6:5	5:4	6:1	4:1	–	3:2

The method is illustrated in Fig. 4 for several cases of resonances. The results of detailed analysis are given in Tables 5–7. We give schemes of the direct resonances (D1–D3) and the triple combinational resonances (CT1–CT6) that cannot be deduced from the Tables of direct resonances.

For the simple combinational resonances containing only two of the three relevant frequencies, the results can be easily determined from the Tables of the direct resonances, because at a given radius x_p, where a direct resonance occurs, the combinational resonances of the two relevant frequencies occur, and the relevant ratio of the combinational resonances is given by the relations expressed explicitly for the direct resonance $\nu_\theta : \nu_r = n : m$

$$\frac{\nu_\theta + \nu_r}{\nu_r} = \frac{n+m}{m}\,, \tag{5}$$

$$\frac{\nu_\theta}{\nu_\theta - \nu_r} = \frac{n}{n-m}\,, \tag{6}$$

$$\frac{\nu_\theta - \nu_r}{\nu_r} = \frac{n-m}{m}\,, \tag{7}$$

$$\frac{\nu_\theta + \nu_r}{\nu_\theta - \nu_r} = \frac{n+m}{n-m}\,. \tag{8}$$

In the other two cases of direct resonances, the combinational resonance ratios are given in analogy to the relations (5)–(8).

In all of the simple combinational resonances occurring at the same radius as the corresponding direct resonance, the related black hole spin a remains unchanged, only the triple of the frequency ratios is different and determined by the relations for the combinational frequencies.

In presenting the final results in the Tables 5–7, we have taken into account all the ratios with $n, m = 1, 2, 3, 4, 5$. The highest resonance order considered here is $n + m = 9$, corresponding to the highest order resonances with $n : m = 5 : 4$ that are observed in some black hole systems (see Remillard and McClintock, 2006; Strohmayer et al., 2007) and in neutron star systems (see Belloni et al., 2005, 2007; Barret et al., 2005; Török, 2007).

Table 5. Top identity.

$++$	$\frac{\nu_\theta}{\nu_r}$	$\frac{\nu_K}{\nu_r}$	$\frac{\nu_K}{\nu_\theta}$	$\frac{\nu_K}{\nu_\theta - \nu_r}$	$\frac{\nu_\theta}{\nu_K - \nu_r}$
$\frac{\nu_\theta}{\nu_r}$	T11	T12	T13	T14	T15
$\frac{\nu_K}{\nu_r}$		T22	T23	T24	T25
$\frac{\nu_K}{\nu_\theta}$			T33	T34	T35
$\frac{\nu_K}{\nu_\theta - \nu_r}$				T44	T45
$\frac{\nu_\theta}{\nu_K - \nu_r}$					T55

(continued on next page)

Table 5. *(continued)*

$\nu_{\rm up}$	$\nu_{\rm middle}$	$\nu_{\rm down}$	T11 sets	a
ν_θ	$\nu_r^{3:2}$	$\nu_r^{4:1}$	**12** : 8 : 3	0.999795
ν_θ	$\nu_r^{3:2}$	$\nu_r^{5:1}$	**15** : 10 : 3	0.999159
ν_θ	$\nu_r^{5:3}$	$\nu_r^{4:1}$	**20** : 12 : 5	0.997586
ν_θ	$\nu_r^{5:3}$	$\nu_r^{5:1}$	**5** : 3 : 1	0.996344
ν_θ	$\nu_r^{2:1}$	$\nu_r^{5:2}$	**10** : 5 : 4	0.998375
ν_θ	$\nu_r^{2:1}$	$\nu_r^{3:1}$	**6** : 3 : 2	0.993348
ν_θ	$\nu_r^{2:1}$	$\nu_r^{4:1}$	**4** : 2 : 1	0.988797
ν_θ	$\nu_r^{2:1}$	$\nu_r^{5:1}$	**10** : 5 : 2	0.986815
ν_θ	$\nu_r^{5:2}$	$\nu_r^{3:1}$	**15** : 6 : 5	0.983254
ν_θ	$\nu_r^{5:2}$	$\nu_r^{4:1}$	**20** : 8 : 5	0.978128
ν_θ	$\nu_r^{5:2}$	$\nu_r^{5:1}$	**5** : 2 : 1	0.975855
ν_θ	$\nu_r^{3:1}$	$\nu_r^{4:1}$	**12** : 4 : 3	0.972240
ν_θ	$\nu_r^{3:1}$	$\nu_r^{5:1}$	**15** : 5 : 3	0.969840
ν_θ	$\nu_r^{4:1}$	$\nu_r^{5:1}$	**20** : 5 : 4	0.964070
$\nu_{\rm up}$	$\nu_{\rm middle}$	$\nu_{\rm down}$	T12 sets	a
$\nu_\theta^{3:2} = \nu_{\rm K}^{5:3}$	$\nu_r^{3:2}$	$\nu_r^{5:3}$	**15** : 10 : 9	0.986488
$\nu_\theta^{3:1} = \nu_{\rm K}^{2:1}$	$\nu_r^{2:1}$	$\nu_r^{3:1}$	**6** : 3 : 2	0.997911
$\nu_\theta^{3:1} = \nu_{\rm K}^{5:2}$	$\nu_r^{5:2}$	$\nu_r^{3:1}$	**15** : 6 : 5	0.766192
$\nu_\theta^{4:1} = \nu_{\rm K}^{5:3}$	$\nu_r^{5:3}$	$\nu_r^{4:1}$	**20** : 12 : 5	0.999855
$\nu_\theta^{4:1} = \nu_{\rm K}^{2:1}$	$\nu_r^{2:1}$	$\nu_r^{4:1}$	**4** : 2 : 1	0.993823
$\nu_\theta^{4:1} = \nu_{\rm K}^{5:2}$	$\nu_r^{5:2}$	$\nu_r^{4:1}$	**20** : 8 : 5	0.883596
$\nu_\theta^{4:1} = \nu_{\rm K}^{3:1}$	$\nu_r^{3:1}$	$\nu_r^{4:1}$	**12** : 4 : 3	0.585950
$\nu_\theta^{5:1} = \nu_{\rm K}^{3:2}$	$\nu_r^{3:2}$	$\nu_r^{5:1}$	**15** : 10 : 3	0.999943
$\nu_\theta^{5:1} = \nu_{\rm K}^{5:3}$	$\nu_r^{5:3}$	$\nu_r^{5:1}$	**5** : 3 : 1	0.999245
$\nu_\theta^{5:1} = \nu_{\rm K}^{2:1}$	$\nu_r^{2:1}$	$\nu_r^{5:1}$	**10** : 5 : 2	0.992017
$\nu_\theta^{5:1} = \nu_{\rm K}^{5:2}$	$\nu_r^{5:2}$	$\nu_r^{5:1}$	**5** : 2 : 1	0.901701
$\nu_\theta^{5:1} = \nu_{\rm K}^{3:1}$	$\nu_r^{3:1}$	$\nu_r^{5:1}$	**15** : 5 : 3	0.684098
$\nu_\theta^{5:1} = \nu_{\rm K}^{4:1}$	$\nu_r^{4:1}$	$\nu_r^{5:1}$	**20** : 5 : 4	0.277977

Table 5. *(continued)*

$\nu_{\rm up}$	$\nu_{\rm middle}$	$\nu_{\rm down}$	T13 sets	a
$\nu_\theta^{2:1} = \nu_{\rm K}^{5:4}$	$\nu_\theta^{5:4}$	$\nu_r^{2:1}$	**10** : 8 : 5	0.959149
$\nu_\theta^{5:2} = \nu_{\rm K}^{5:4}$	$\nu_\theta^{5:4}$	$\nu_r^{5:2}$	**5** : 4 : 2	0.920283
$\nu_\theta^{3:1} = \nu_{\rm K}^{5:4}$	$\nu_\theta^{5:4}$	$\nu_r^{3:1}$	**15** : 12 : 5	0.999569
				0.900496
$\nu_\theta^{4:1} = \nu_{\rm K}^{5:4}$	$\nu_\theta^{5:4}$	$\nu_r^{4:1}$	**20** : 16 : 5	0.995816
				0.881660
$\nu_\theta^{5:1} = \nu_{\rm K}^{5:4}$	$\nu_\theta^{5:4}$	$\nu_r^{5:1}$	**5** : 4 : 1	0.994044
				0.873208

$\nu_{\rm up}$	$\nu_{\rm middle}$	$\nu_{\rm down}$	T14 sets	a
$\nu_\theta^{5:3} = \nu_{\rm K}^{3:1}$	$\nu_r^{5:3}$	$(\nu_\theta - \nu_r)^{3:1}$	**15** : 9 : 5	0.768181
$\nu_\theta^{2:1} = \nu_{\rm K}^{5:2}$	$\nu_r^{2:1}$	$(\nu_\theta - \nu_r)^{5:2}$	**10** : 5 : 4	0.718139
$\nu_\theta^{2:1} = \nu_{\rm K}^{3:1}$	$\nu_r^{2:1}$	$(\nu_\theta - \nu_r)^{3:1}$	**6** : 3 : 2	0.926845
$\nu_\theta^{5:2} = \nu_{\rm K}^{2:1}$	$(\nu_\theta - \nu_r)^{2:1}$	$\nu_r^{5:2}$	**10** : 5 : 4	0.545519
$\nu_\theta^{5:2} = \nu_{\rm K}^{5:2}$	–	$\nu_r^{5:2} = (\nu_\theta - \nu_r)^{5:2}$	**5** : **2**	0.838922
$\nu_\theta^{5:2} = \nu_{\rm K}^{3:1}$	$\nu_r^{5:2}$	$(\nu_\theta - \nu_r)^{3:1}$	**15** : 6 : 5	0.953351
$\nu_\theta^{3:1} = \nu_{\rm K}^{5:3}$	$(\nu_\theta - \nu_r)^{5:3}$	$\nu_r^{3:1}$	**15** : 9 : 5	0.324388
$\nu_\theta^{3:1} = \nu_{\rm K}^{2:1}$	$(\nu_\theta - \nu_r)^{2:1}$	$\nu_r^{3:1}$	**6** : 3 : 2	0.657961
$\nu_\theta^{3:1} = \nu_{\rm K}^{5:2}$	$(\nu_\theta - \nu_r)^{5:2}$	$\nu_r^{3:1}$	**15** : 6 : 5	0.866415
$\nu_\theta^{3:1} = \nu_{\rm K}^{3:1}$	–	$\nu_r^{3:1} = (\nu_\theta - \nu_r)^{3:1}$	**3** : **1**	0.957989
$\nu_\theta^{4:1} = \nu_{\rm K}^{3:2}$	$(\nu_\theta - \nu_r)^{3:2}$	$\nu_r^{4:1}$	**12** : 8 : 3	0.303179
$\nu_\theta^{4:1} = \nu_{\rm K}^{5:3}$	$(\nu_\theta - \nu_r)^{5:3}$	$\nu_r^{4:1}$	**20** : 12 : 5	0.498556
$\nu_\theta^{4:1} = \nu_{\rm K}^{2:1}$	$(\nu_\theta - \nu_r)^{2:1}$	$\nu_r^{4:1}$	**4** : 2 : 1	0.723465
$\nu_\theta^{4:1} = \nu_{\rm K}^{5:2}$	$(\nu_\theta - \nu_r)^{5:2}$	$\nu_r^{4:1}$	**20** : 8 : 5	0.882500
$\nu_\theta^{4:1} = \nu_{\rm K}^{3:1}$	$(\nu_\theta - \nu_r)^{3:1}$	$\nu_r^{4:1}$	**12** : 4 : 3	0.959714
$\nu_\theta^{5:1} = \nu_{\rm K}^{4:3}$	$(\nu_\theta - \nu_r)^{4:3}$	$\nu_r^{5:1}$	**20** : 15 : 4	0.157838
$\nu_\theta^{5:1} = \nu_{\rm K}^{3:2}$	$(\nu_\theta - \nu_r)^{3:2}$	$\nu_r^{5:1}$	**15** : 10 : 3	0.392986
$\nu_\theta^{5:1} = \nu_{\rm K}^{5:3}$	$(\nu_\theta - \nu_r)^{5:3}$	$\nu_r^{5:1}$	**5** : 3 : 1	0.552361
$\nu_\theta^{5:1} = \nu_{\rm K}^{2:1}$	$(\nu_\theta - \nu_r)^{2:1}$	$\nu_r^{5:1}$	**10** : 5 : 2	0.744570
$\nu_\theta^{5:1} = \nu_{\rm K}^{5:2}$	$(\nu_\theta - \nu_r)^{5:2}$	$\nu_r^{5:1}$	**5** : 2 : 1	0.887578
$\nu_\theta^{5:1} = \nu_{\rm K}^{3:1}$	$(\nu_\theta - \nu_r)^{3:1}$	$\nu_r^{5:1}$	**15** : 5 : 3	0.959924
$\nu_\theta^{5:1} = \nu_{\rm K}^{4:1}$	$(\nu_\theta - \nu_r)^{4:1}$	$\nu_r^{5:1}$	**20** : 5 : 4	0.999502

Table 5. *(continued)*

ν_{up}	ν_{middle}	ν_{down}	T15 sets	a
ν_θ	$\nu_r^{5:4}$	$(\nu_{\mathrm{K}}-\nu_r)^{4:1}$	**20** : 16 : 5	0.864496
ν_θ	$\nu_r^{4:3}$	$(\nu_{\mathrm{K}}-\nu_r)^{3:1}$	**12** : 9 : 4	0.906232
ν_θ	$\nu_r^{3:2}$	$(\nu_{\mathrm{K}}-\nu_r)^{2:1}$	**6** : 4 : 3	0.948037
ν_θ	$\nu_r^{3:2}$	$(\nu_{\mathrm{K}}-\nu_r)^{5:2}$	**15** : 10 : 6	0.666292
ν_θ	$(\nu_{\mathrm{K}}-\nu_r)^{3:2}$	$\nu_r^{5:3}$	**15** : 10 : 9	0.966994
ν_θ	–	$\nu_r^{5:3}=(\nu_{\mathrm{K}}-\nu_r)^{5:3}$	**5** : **3**	0.912558
ν_θ	$\nu_r^{5:3}$	$(\nu_{\mathrm{K}}-\nu_r)^{2:1}$	**10** : 6 : 5	0.716619
ν_θ	$(\nu_{\mathrm{K}}-\nu_r)^{5:4}$	$\nu_r^{2:1}$	**10** : 8 : 5	0.917696
ν_θ	$(\nu_{\mathrm{K}}-\nu_r)^{4:3}$	$\nu_r^{2:1}$	**4** : 3 : 2	0.882162
ν_θ	$(\nu_{\mathrm{K}}-\nu_r)^{3:2}$	$\nu_r^{2:1}$	**6** : 4 : 3	0.780930
ν_θ	$(\nu_{\mathrm{K}}-\nu_r)^{5:3}$	$\nu_r^{2:1}$	**10** : 6 : 5	0.623205
ν_θ	$(\nu_{\mathrm{K}}-\nu_r)^{5:4}$	$\nu_r^{5:2}$	**5** : 4 : 2	0.771066
ν_θ	$(\nu_{\mathrm{K}}-\nu_r)^{4:3}$	$\nu_r^{5:2}$	**20** : 15 : 8	0.687766
ν_θ	$(\nu_{\mathrm{K}}-\nu_r)^{3:2}$	$\nu_r^{5:2}$	**15** : 10 : 6	0.436347
ν_θ	$(\nu_{\mathrm{K}}-\nu_r)^{5:4}$	$\nu_r^{3:1}$	**15** : 12 : 5	0.999725 0.620936
ν_θ	$(\nu_{\mathrm{K}}-\nu_r)^{4:3}$	$\nu_r^{3:1}$	**12** : 9 : 4	0.475318
ν_θ	$(\nu_{\mathrm{K}}-\nu_r)^{5:4}$	$\nu_r^{4:1}$	**20** : 16 : 5	0.996250 0.312660
ν_θ	$(\nu_{\mathrm{K}}-\nu_r)^{4:3}$	$\nu_r^{4:1}$	**4** : 3 : 1	0.997314
ν_θ	$(\nu_{\mathrm{K}}-\nu_r)^{3:2}$	$\nu_r^{4:1}$	**12** : 8 : 3	0.998678
ν_θ	$(\nu_{\mathrm{K}}-\nu_r)^{5:3}$	$\nu_r^{4:1}$	**20** : 12 : 5	0.999422
ν_θ	$(\nu_{\mathrm{K}}-\nu_r)^{5:4}$	$\nu_r^{5:1}$	**5** : 4 : 1	0.994655
ν_θ	$(\nu_{\mathrm{K}}-\nu_r)^{4:3}$	$\nu_r^{5:1}$	**20** : 15 : 4	0.995929
ν_θ	$(\nu_{\mathrm{K}}-\nu_r)^{3:2}$	$\nu_r^{5:1}$	**15** : 10 : 3	0.997628
ν_θ	$(\nu_{\mathrm{K}}-\nu_r)^{5:3}$	$\nu_r^{5:1}$	**5** : 3 : 1	0.998615
ν_θ	$(\nu_{\mathrm{K}}-\nu_r)^{2:1}$	$\nu_r^{5:1}$	**10** : 5 : 2	0.999545
ν_θ	$(\nu_{\mathrm{K}}-\nu_r)^{5:2}$	$\nu_r^{5:1}$	**5** : 2 : 1	0.999960

ν_{up}	ν_{middle}	ν_{down}	T22 sets	a
–	–	–	–	–

Table 5. *(continued)*

$\nu_{\rm up}$	$\nu_{\rm middle}$	$\nu_{\rm down}$	T23 sets	a
$\nu_{\rm K}$	$\nu_\theta^{5:4}$	$\nu_r^{2:1}$	**10** : 8 : 5	0.978822
$\nu_{\rm K}$	$\nu_\theta^{5:4}$	$\nu_r^{5:2}$	**5** : 4 : 2	0.882162
$\nu_{\rm K}$	$\nu_\theta^{4:3}$	$\nu_r^{5:2}$	**20** : 15 : 8	0.953845
$\nu_{\rm K}$	$\nu_\theta^{5:4}$	$\nu_r^{3:1}$	**15** : 12 : 5	0.835951
$\nu_{\rm K}$	$\nu_\theta^{4:3}$	$\nu_r^{3:1}$	**12** : 9 : 4	0.907924
$\nu_{\rm K}$	$\nu_\theta^{3:2}$	$\nu_r^{3:1}$	**3** : 2 : 1	0.983043
$\nu_{\rm K}$	$\nu_\theta^{5:4}$	$\nu_r^{4:1}$	**20** : 16 : 5	0.793780
$\nu_{\rm K}$	$\nu_\theta^{4:3}$	$\nu_r^{4:1}$	**4** : 3 : 1	0.865670
$\nu_{\rm K}$	$\nu_\theta^{3:2}$	$\nu_r^{4:1}$	**12** : 8 : 3	0.942454
$\nu_{\rm K}$	$\nu_\theta^{5:3}$	$\nu_r^{4:1}$	**20** : 12 : 5	0.979390
$\nu_{\rm K}$	$\nu_\theta^{5:4}$	$\nu_r^{5:1}$	**5** : 4 : 1	0.775420
$\nu_{\rm K}$	$\nu_\theta^{4:3}$	$\nu_r^{5:1}$	**20** : 15 : 4	0.847170
$\nu_{\rm K}$	$\nu_\theta^{3:2}$	$\nu_r^{5:1}$	**15** : 10 : 3	0.924540
$\nu_{\rm K}$	$\nu_\theta^{5:3}$	$\nu_r^{5:1}$	**5** : 3 : 1	0.962250
$\nu_{\rm K}$	$\nu_\theta^{2:1}$	$\nu_r^{5:1}$	**10** : 5 : 2	0.995139
$\nu_{\rm up}$	$\nu_{\rm middle}$	$\nu_{\rm down}$	T24 sets	a
$\nu_{\rm K}$	$\nu_r^{4:3}$	$(\nu_\theta - \nu_r)^{5:1}$	**20** : 15 : 4	0.849640
$\nu_{\rm K}$	$\nu_r^{3:2}$	$(\nu_\theta - \nu_r)^{4:1}$	**12** : 8 : 3	0.883497
$\nu_{\rm K}$	$\nu_r^{5:3}$	$(\nu_\theta - \nu_r)^{3:1}$	**15** : 9 : 5	0.656160
$\nu_{\rm K}$	$\nu_r^{2:1}$	$(\nu_\theta - \nu_r)^{5:2}$	**10** : 5 : 4	0.704526
$\nu_{\rm K}$	$\nu_r^{2:1}$	$(\nu_\theta - \nu_r)^{3:1}$	**6** : 3 : 2	0.912558
$\nu_{\rm K}$	$(\nu_\theta - \nu_r)^{2:1}$	$\nu_r^{5:2}$	**10** : 5 : 4	0.619190
$\nu_{\rm K}$	–	$\nu_r^{5:2} = (\nu_\theta - \nu_r)^{5:2}$	**5** : **2**	0.882162
$\nu_{\rm K}$	$\nu_r^{5:2}$	$(\nu_\theta - \nu_r)^{3:1}$	**15** : 6 : 5	0.972292
$\nu_{\rm K}$	$(\nu_\theta - \nu_r)^{5:3}$	$\nu_r^{3:1}$	**15** : 9 : 5	0.438554
$\nu_{\rm K}$	$(\nu_\theta - \nu_r)^{2:1}$	$\nu_r^{3:1}$	**6** : 3 : 2	0.771066
$\nu_{\rm K}$	$(\nu_\theta - \nu_r)^{5:2}$	$\nu_r^{3:1}$	**15** : 6 : 5	0.926708
$\nu_{\rm K}$	–	$\nu_r^{3:1} = (\nu_\theta - \nu_r)^{3:1}$	**3** : **1**	0.983043
$\nu_{\rm K}$	$(\nu_\theta - \nu_r)^{3:2}$	$\nu_r^{4:1}$	**12** : 8 : 3	0.481612
$\nu_{\rm K}$	$(\nu_\theta - \nu_r)^{5:3}$	$\nu_r^{4:1}$	**20** : 12 : 5	0.691677
$\nu_{\rm K}$	$(\nu_\theta - \nu_r)^{2:1}$	$\nu_r^{4:1}$	**4** : 2 : 1	0.865670
$\nu_{\rm K}$	$(\nu_\theta - \nu_r)^{5:2}$	$\nu_r^{4:1}$	**20** : 8 : 5	0.953294
$\nu_{\rm K}$	$(\nu_\theta - \nu_r)^{3:1}$	$\nu_r^{4:1}$	**12** : 4 : 3	0.986299
$\nu_{\rm K}$	$(\nu_\theta - \nu_r)^{4:3}$	$\nu_r^{5:1}$	**20** : 15 : 4	0.317752

Table 5. *(continued)*

ν_{K}	$(\nu_\theta - \nu_r)^{3:2}$	$\nu_r^{5:1}$	**15** : 10 : 3	0.631698
ν_{K}	$(\nu_\theta - \nu_r)^{5:3}$	$\nu_r^{5:1}$	**5** : 3 : 1	0.775420
ν_{K}	$(\nu_\theta - \nu_r)^{2:1}$	$\nu_r^{5:1}$	**10** : 5 : 2	0.898553
ν_{K}	$(\nu_\theta - \nu_r)^{5:2}$	$\nu_r^{5:1}$	**5** : 2 : 1	0.962250
ν_{K}	$(\nu_\theta - \nu_r)^{3:1}$	$\nu_r^{5:1}$	**15** : 5 : 3	0.986541

ν_{up}	ν_{middle}	ν_{down}	T25 sets	a
$\nu_{\mathrm{K}}^{3:2} = \nu_\theta^{5:2}$	$\nu_r^{3:2}$	$(\nu_{\mathrm{K}} - \nu_r)^{5:2}$	**15** : 10 : 6	0.956544
$\nu_{\mathrm{K}}^{5:3} = \nu_\theta^{2:1}$	$\nu_r^{5:3}$	$(\nu_{\mathrm{K}} - \nu_r)^{2:1}$	**10** : 6 : 5	0.884722
$\nu_{\mathrm{K}}^{2:1} = \nu_\theta^{5:4}$	$(\nu_{\mathrm{K}} - \nu_r)^{5:4}$	$\nu_r^{2:1}$	**10** : 8 : 5	0.951420
$\nu_{\mathrm{K}}^{2:1} = \nu_\theta^{4:3}$	$(\nu_{\mathrm{K}} - \nu_r)^{4:3}$	$\nu_r^{2:1}$	**4** : 3 : 2	0.913464
$\nu_{\mathrm{K}}^{2:1} = \nu_\theta^{3:2}$	$(\nu_{\mathrm{K}} - \nu_r)^{3:2}$	$\nu_r^{2:1}$	**6** : 4 : 3	0.805342
$\nu_{\mathrm{K}}^{2:1} = \nu_\theta^{5:3}$	$(\nu_{\mathrm{K}} - \nu_r)^{5:3}$	$\nu_r^{2:1}$	**10** : 6 : 5	0.638490
$\nu_{\mathrm{K}}^{5:2} = \nu_\theta^{5:4}$	$(\nu_{\mathrm{K}} - \nu_r)^{5:4}$	$\nu_r^{5:2}$	**5** : 4 : 2	0.674200
$\nu_{\mathrm{K}}^{5:2} = \nu_\theta^{4:3}$	$(\nu_{\mathrm{K}} - \nu_r)^{4:3}$	$\nu_r^{5:2}$	**20** : 15 : 8	0.590613
$\nu_{\mathrm{K}}^{5:2} = \nu_\theta^{3:2}$	$(\nu_{\mathrm{K}} - \nu_r)^{3:2}$	$\nu_r^{5:2}$	**15** : 10 : 6	0.357791
$\nu_{\mathrm{K}}^{3:1} = \nu_\theta^{5:4}$	$(\nu_{\mathrm{K}} - \nu_r)^{5:4}$	$\nu_r^{3:1}$	**15** : 12 : 5	0.458802
$\nu_{\mathrm{K}}^{3:1} = \nu_\theta^{4:3}$	$(\nu_{\mathrm{K}} - \nu_r)^{4:3}$	$\nu_r^{3:1}$	**12** : 9 : 4	0.337980
$\nu_{\mathrm{K}}^{4:1} = \nu_\theta^{5:4}$	$(\nu_{\mathrm{K}} - \nu_r)^{5:4}$	$\nu_r^{4:1}$	**20** : 16 : 5	0.169411

ν_{up}	ν_{middle}	ν_{down}	T33 sets	a
–	–	–	–	–

ν_{up}	ν_{middle}	ν_{down}	T34 sets	a
ν_{K}	$\nu_\theta^{5:4}$	$(\nu_\theta - \nu_r)^{4:3}$	**20** : 16 : 15	0.746323
ν_{K}	$\nu_\theta^{5:4}$	$(\nu_\theta - \nu_r)^{3:2}$	**15** : 12 : 10	0.757958
ν_{K}	$\nu_\theta^{5:4}$	$(\nu_\theta - \nu_r)^{5:3}$	**5** : 4 : 3	0.775420
ν_{K}	$\nu_\theta^{5:4}$	$(\nu_\theta - \nu_r)^{2:1}$	**10** : 8 : 5	0.817199
ν_{K}	$\nu_\theta^{5:4}$	$(\nu_\theta - \nu_r)^{5:2}$	**5** : 4 : 2	0.882162
ν_{K}	$\nu_\theta^{5:4}$	$(\nu_\theta - \nu_r)^{3:1}$	**15** : 12 : 5	0.942336
ν_{K}	$\nu_\theta^{4:3}$	$(\nu_\theta - \nu_r)^{3:2}$	**12** : 9 : 8	0.821125
ν_{K}	$\nu_\theta^{4:3}$	$(\nu_\theta - \nu_r)^{5:3}$	**20** : 15 : 12	0.833218
ν_{K}	$\nu_\theta^{4:3}$	$(\nu_\theta - \nu_r)^{2:1}$	**4** : 3 : 2	0.865670
ν_{K}	$\nu_\theta^{4:3}$	$(\nu_\theta - \nu_r)^{5:2}$	**20** : 15 : 8	0.918302
ν_{K}	$\nu_\theta^{4:3}$	$(\nu_\theta - \nu_r)^{3:1}$	**12** : 9 : 4	0.967289
ν_{K}	$\nu_\theta^{3:2}$	$(\nu_\theta - \nu_r)^{5:3}$	**15** : 10 : 9	0.897294
ν_{K}	$\nu_\theta^{3:2}$	$(\nu_\theta - \nu_r)^{2:1}$	**6** : 4 : 3	0.915030
ν_{K}	$\nu_\theta^{3:2}$	$(\nu_\theta - \nu_r)^{5:2}$	**15** : 10 : 6	0.949454

Table 5. *(continued)*

$\nu_{\rm K}$	$\nu_\theta^{3:2}$	$(\nu_\theta - \nu_r)^{3:1}$	**3** : 2 : 1	0.983043
$\nu_{\rm K}$	$\nu_\theta^{5:3}$	$(\nu_\theta - \nu_r)^{2:1}$	**10** : 6 : 5	0.940089
$\nu_{\rm K}$	$\nu_\theta^{5:3}$	$(\nu_\theta - \nu_r)^{5:2}$	**5** : 3 : 2	0.962250
$\nu_{\rm K}$	$\nu_\theta^{5:3}$	$(\nu_\theta - \nu_r)^{3:1}$	**15** : 9 : 5	0.986070
$\nu_{\rm K}$	$\nu_\theta^{2:1}$	$(\nu_\theta - \nu_r)^{5:2}$	**10** : 5 : 4	0.974517
$\nu_{\rm K}$	$\nu_\theta^{2:1}$	$(\nu_\theta - \nu_r)^{3:1}$	**6** : 3 : 2	0.986666
$\nu_{\rm K}$	$\nu_\theta^{5:2}$	$(\nu_\theta - \nu_r)^{3:1}$	**15** : 6 : 5	0.988762
$\nu_{\rm K}$	$\nu_\theta^{3:1}$	$(\nu_\theta - \nu_r)^{4:1}$	**12** : 4 : 3	0.996798
$\nu_{\rm K}$	$\nu_\theta^{4:1}$	$(\nu_\theta - \nu_r)^{5:1}$	**20** : 5 : 4	0.998637

$\nu_{\rm up}$	$\nu_{\rm middle}$	$\nu_{\rm down}$	T35 sets	a
–	–	–	–	–

$\nu_{\rm up}$	$\nu_{\rm middle}$	$\nu_{\rm down}$	T44 sets	a
–	–	–	–	–

$\nu_{\rm up}$	$\nu_{\rm middle}$	$\nu_{\rm down}$	T45 sets	a
$\nu_{\rm K}^{4:3} = \nu_\theta^{5:4}$	$(\nu_{\rm K} - \nu_r)^{5:4}$	$(\nu_\theta - \nu_r)^{4:3}$	**20** : 16 : 15	0.115806
$\nu_{\rm K}^{3:2} = \nu_\theta^{5:4}$	$(\nu_{\rm K} - \nu_r)^{5:4}$	$(\nu_\theta - \nu_r)^{3:2}$	**15** : 12 : 10	0.306117
$\nu_{\rm K}^{3:2} = \nu_\theta^{4:3}$	$(\nu_{\rm K} - \nu_r)^{4:3}$	$(\nu_\theta - \nu_r)^{3:2}$	**12** : 9 : 8	0.219609
$\nu_{\rm K}^{5:3} = \nu_\theta^{5:4}$	$(\nu_{\rm K} - \nu_r)^{5:4}$	$(\nu_\theta - \nu_r)^{5:3}$	**5** : 4 : 3	0.449961
$\nu_{\rm K}^{5:3} = \nu_\theta^{4:3}$	$(\nu_{\rm K} - \nu_r)^{4:3}$	$(\nu_\theta - \nu_r)^{5:3}$	**20** : 15 : 12	0.383769
$\nu_{\rm K}^{5:3} = \nu_\theta^{3:2}$	$(\nu_{\rm K} - \nu_r)^{3:2}$	$(\nu_\theta - \nu_r)^{5:3}$	**15** : 10 : 9	0.218273
$\nu_{\rm K}^{2:1} = \nu_\theta^{5:4}$	$(\nu_{\rm K} - \nu_r)^{5:4}$	$(\nu_\theta - \nu_r)^{2:1}$	**10** : 8 : 5	0.646387
$\nu_{\rm K}^{2:1} = \nu_\theta^{4:3}$	$(\nu_{\rm K} - \nu_r)^{4:3}$	$(\nu_\theta - \nu_r)^{2:1}$	**4** : 3 : 2	0.605596
$\nu_{\rm K}^{2:1} = \nu_\theta^{3:2}$	$(\nu_{\rm K} - \nu_r)^{3:2}$	$(\nu_\theta - \nu_r)^{2:1}$	**6** : 4 : 3	0.505260
$\nu_{\rm K}^{2:1} = \nu_\theta^{5:3}$	$(\nu_{\rm K} - \nu_r)^{5:3}$	$(\nu_\theta - \nu_r)^{2:1}$	**10** : 6 : 5	0.375605
$\nu_{\rm K}^{5:2} = \nu_\theta^{5:4}$	$(\nu_{\rm K} - \nu_r)^{5:4}$	$(\nu_\theta - \nu_r)^{5:2}$	**5** : 4 : 2	0.819423
$\nu_{\rm K}^{5:2} = \nu_\theta^{4:3}$	$(\nu_{\rm K} - \nu_r)^{4:3}$	$(\nu_\theta - \nu_r)^{5:2}$	**20** : 15 : 8	0.798295
$\nu_{\rm K}^{5:2} = \nu_\theta^{3:2}$	$(\nu_{\rm K} - \nu_r)^{3:2}$	$(\nu_\theta - \nu_r)^{5:2}$	**15** : 10 : 6	0.746336
$\nu_{\rm K}^{5:2} = \nu_\theta^{5:3}$	$(\nu_{\rm K} - \nu_r)^{5:3}$	$(\nu_\theta - \nu_r)^{5:2}$	**5** : 3 : 2	0.679474
$\nu_{\rm K}^{5:2} = \nu_\theta^{2:1}$	$(\nu_{\rm K} - \nu_r)^{2:1}$	$(\nu_\theta - \nu_r)^{5:2}$	**10** : 5 : 4	0.489267
$\nu_{\rm K}^{3:1} = \nu_\theta^{5:4}$	$(\nu_{\rm K} - \nu_r)^{5:4}$	$(\nu_\theta - \nu_r)^{3:1}$	**15** : 12 : 5	0.923851
$\nu_{\rm K}^{3:1} = \nu_\theta^{4:3}$	$(\nu_{\rm K} - \nu_r)^{4:3}$	$(\nu_\theta - \nu_r)^{3:1}$	**12** : 9 : 4	0.912811
$\nu_{\rm K}^{3:1} = \nu_\theta^{3:2}$	$(\nu_{\rm K} - \nu_r)^{3:2}$	$(\nu_\theta - \nu_r)^{3:1}$	**3** : 2 : 1	0.885010
$\nu_{\rm K}^{3:1} = \nu_\theta^{5:3}$	$(\nu_{\rm K} - \nu_r)^{5:3}$	$(\nu_\theta - \nu_r)^{3:1}$	**15** : 9 : 5	0.848463
$\nu_{\rm K}^{3:1} = \nu_\theta^{2:1}$	$(\nu_{\rm K} - \nu_r)^{2:1}$	$(\nu_\theta - \nu_r)^{3:1}$	**6** : 3 : 2	0.742897
$\nu_{\rm K}^{3:1} = \nu_\theta^{5:2}$	$(\nu_{\rm K} - \nu_r)^{5:2}$	$(\nu_\theta - \nu_r)^{3:1}$	**15** : 6 : 5	0.473232

Table 5. *(continued)*

$\nu_{\mathrm{K}}^{4:1} = \nu_{\theta}^{2:1}$	$(\nu_{\mathrm{K}} - \nu_r)^{2:1}$	$(\nu_\theta - \nu_r)^{4:1}$	**4** : 2 : 1	0.996164
$\nu_{\mathrm{K}}^{4:1} = \nu_{\theta}^{5:2}$	$(\nu_{\mathrm{K}} - \nu_r)^{5:2}$	$(\nu_\theta - \nu_r)^{4:1}$	**20** : 8 : 5	0.901229
$\nu_{\mathrm{K}}^{4:1} = \nu_{\theta}^{3:1}$	$(\nu_{\mathrm{K}} - \nu_r)^{3:1}$	$(\nu_\theta - \nu_r)^{4:1}$	**12** : 4 : 3	0.728900
$\nu_{\mathrm{K}}^{5:1} = \nu_{\theta}^{4:1}$	$(\nu_{\mathrm{K}} - \nu_r)^{4:1}$	$(\nu_\theta - \nu_r)^{5:1}$	**20** : 5 : 4	0.711175

ν_{up}	ν_{middle}	ν_{down}	T55 sets	a
–	–	–	–	–

Table 6. Bottom identity.

– –	$\frac{\nu_\theta}{\nu_r}$	$\frac{\nu_{\mathrm{K}}}{\nu_r}$	$\frac{\nu_{\mathrm{K}}}{\nu_\theta}$	$\frac{\nu_{\mathrm{K}}}{\nu_\theta - \nu_r}$	$\frac{\nu_\theta}{\nu_{\mathrm{K}} - \nu_r}$
$\frac{\nu_\theta}{\nu_r}$	B11	B12	B13	B14	B15
$\frac{\nu_{\mathrm{K}}}{\nu_r}$		B22	B23	B24	B25
$\frac{\nu_{\mathrm{K}}}{\nu_\theta}$			B33	B34	B35
$\frac{\nu_{\mathrm{K}}}{\nu_\theta - \nu_r}$				B44	B45
$\frac{\nu_\theta}{\nu_{\mathrm{K}} - \nu_r}$					B55

ν_{up}	ν_{middle}	ν_{down}	B11 sets	a
$\nu_\theta^{5:2}$	$\nu_\theta^{3:2}$	ν_r	5 : 3 : **2**	0.986747
$\nu_\theta^{5:2}$	$\nu_\theta^{5:3}$	ν_r	15 : 10 : **6**	0.140827
$\nu_\theta^{3:1}$	$\nu_\theta^{4:3}$	ν_r	9 : 4 : **3**	0.999171
$\nu_\theta^{3:1}$	$\nu_\theta^{3:2}$	ν_r	6 : 3 : **2**	0.418229
$\nu_\theta^{4:1}$	$\nu_\theta^{5:4}$	ν_r	16 : 5 : **4**	0.996953
$\nu_\theta^{4:1}$	$\nu_\theta^{4:3}$	ν_r	12 : 4 : **3**	0.891596
$\nu_\theta^{5:1}$	$\nu_\theta^{5:4}$	ν_r	20 : 5 : **4**	0.975970

Table 6. *(continued)*

$\nu_{\rm up}$	$\nu_{\rm middle}$	$\nu_{\rm down}$	B12 sets	a
$\nu_{\rm K}^{4:3}$	$\nu_\theta^{5:4}$	ν_r	16 : 15 : **12**	0.973553
$\nu_{\rm K}^{5:1}$	$\nu_\theta^{4:3}$	ν_r	15 : 4 : **3**	0.724899
$\nu_{\rm K}^{5:3}$	$\nu_\theta^{3:2}$	ν_r	10 : 9 : **6**	0.838559
$\nu_{\rm K}^{4:1}$	$\nu_\theta^{3:2}$	ν_r	8 : 3 : **2**	0.940033
$\nu_{\rm K}^{2:1}$	$\nu_\theta^{5:3}$	ν_r	6 : 5 : **3**	0.912558
$\nu_{\rm K}^{3:1}$	$\nu_\theta^{5:3}$	ν_r	9 : 5 : **3**	0.915450
$\nu_{\rm K}^{5:2}$	$\nu_\theta^{2:1}$	ν_r	5 : 4 : **2**	0.882162
$\nu_{\rm K}^{3:1}$	$\nu_\theta^{2:1}$	ν_r	3 : 2 : **1**	0.983043
$\nu_{\rm K}^{3:1}$	$\nu_\theta^{5:2}$	ν_r	6 : 5 : **2**	0.771066
$\nu_{\rm K}^{4:1}$	$\nu_\theta^{5:2}$	ν_r	8 : 5 : **2**	0.967440
$\nu_{\rm K}^{5:1}$	$\nu_\theta^{5:2}$	ν_r	10 : 5 : **2**	0.995139
$\nu_\theta^{3:1}$	$\nu_{\rm K}^{3:2}$	ν_r	6 : 3 : **2**	0.998451
$\nu_{\rm K}^{4:1}$	$\nu_\theta^{3:1}$	ν_r	4 : 3 : **1**	0.865670
$\nu_{\rm K}^{5:1}$	$\nu_\theta^{3:1}$	ν_r	5 : 3 : **1**	0.962250
$\nu_{\rm K}^{5:1}$	$\nu_\theta^{4:1}$	ν_r	5 : 4 : **1**	0.775420
$\nu_\theta^{4:1}$	$\nu_{\rm K}^{5:4}$	ν_r	16 : 5 : **4**	0.999967
$\nu_\theta^{4:1}$	$\nu_{\rm K}^{4:3}$	ν_r	12 : 4 : **3**	0.997358
$\nu_\theta^{5:1}$	$\nu_{\rm K}^{5:4}$	ν_r	20 : 5 : **4**	0.997787
$\nu_\theta^{5:1}$	$\nu_{\rm K}^{4:3}$	ν_r	15 : 4 : **3**	0.976490 0.767142

$\nu_{\rm up}$	$\nu_{\rm middle}$	$\nu_{\rm down}$	B13 sets	a
–	–	–	–	–

$\nu_{\rm up}$	$\nu_{\rm middle}$	$\nu_{\rm down}$	B14 sets	a
$\nu_{\rm K}^{3:1}$	$\nu_\theta^{5:4}$	$\nu_r^{5:4} = (\nu_\theta - \nu_r)^{3:1}$	12 : 5 : **4**	0.660514
$\nu_{\rm K}^{5:2}$	$\nu_\theta^{4:3}$	$\nu_r^{4:3} = (\nu_\theta - \nu_r)^{5:2}$	15 : 8 : **6**	0.262715
$\nu_{\rm K}^{3:1}$	$\nu_\theta^{4:3}$	$\nu_r^{4:3} = (\nu_\theta - \nu_r)^{3:1}$	9 : 4 : **3**	0.897551
$\nu_{\rm K}^{5:2}$	$\nu_\theta^{3:2}$	$\nu_r^{3:2} = (\nu_\theta - \nu_r)^{5:2}$	5 : 3 : **2**	0.780190
$\nu_{\rm K}^{3:1}$	$\nu_\theta^{3:2}$	$\nu_r^{3:2} = (\nu_\theta - \nu_r)^{3:1}$	6 : 3 : **2**	0.972843
$\nu_{\rm K}^{5:2}$	$\nu_\theta^{5:3}$	$\nu_r^{5:3} = (\nu_\theta - \nu_r)^{5:2}$	15 : 10 : **6**	0.863198
$\nu_{\rm K}^{3:1}$	$\nu_\theta^{5:3}$	$\nu_r^{5:3} = (\nu_\theta - \nu_r)^{3:1}$	9 : 5 : **3**	0.982104
$\nu_{\rm K}^{5:2}$	$\nu_\theta^{2:1}$	$\nu_r^{2:1} = (\nu_\theta - \nu_r)^{5:2}$	5 : 4 : **2**	0.882162
$\nu_{\rm K}^{3:1}$	$\nu_\theta^{2:1}$	$\nu_r^{2:1} = (\nu_\theta - \nu_r)^{3:1}$	3 : 2 : **1**	0.983043
$\nu_{\rm K}^{5:2} = \nu_\theta^{5:2}$	–	$\nu_r^{5:2} = (\nu_\theta - \nu_r)^{5:2}$	**5** : **2**	0.838922
$\nu_{\rm K}^{3:1}$	$\nu_\theta^{5:2}$	$\nu_r^{5:2} = (\nu_\theta - \nu_r)^{3:1}$	6 : 5 : **2**	0.974930

Table 6. *(continued)*

$\nu_\theta^{3:1}$	$\nu_{\mathrm{K}}^{5:2}$	$\nu_r^{3:1} = (\nu_\theta - \nu_r)^{5:2}$	6 : 5 : **2**	0.753467
$\nu_{\mathrm{K}}^{3:1} = \nu_\theta^{3:1}$	–	$\nu_r^{3:1} = (\nu_\theta - \nu_r)^{3:1}$	**3** : **1**	0.957989
$\nu_\theta^{4:1}$	$\nu_{\mathrm{K}}^{5:2}$	$\nu_r^{4:1} = (\nu_\theta - \nu_r)^{5:2}$	8 : 5 : **2**	0.396889
$\nu_\theta^{4:1}$	$\nu_{\mathrm{K}}^{3:1}$	$\nu_r^{4:1} = (\nu_\theta - \nu_r)^{3:1}$	4 : 3 : **1**	0.896685
$\nu_\theta^{5:1}$	$\nu_{\mathrm{K}}^{3:1}$	$\nu_r^{5:1} = (\nu_\theta - \nu_r)^{3:1}$	5 : 3 : **1**	0.777444
$\nu_\theta^{5:1}$	$\nu_{\mathrm{K}}^{4:1}$	$\nu_r^{5:1} = (\nu_\theta - \nu_r)^{4:1}$	5 : 4 : **1**	0.998146

ν_{up}	ν_{middle}	ν_{down}	B15 sets	a
$\nu_\theta^{5:2}$	$\nu_\theta^{5:4}$	$\nu_r^{5:4} = (\nu_{\mathrm{K}} - \nu_r)^{5:2}$	10 : 5 : **4**	0.733477
$\nu_\theta^{2:1}$	$\nu_\theta^{4:3}$	$\nu_r^{4:3} = (\nu_{\mathrm{K}} - \nu_r)^{2:1}$	6 : 4 : **3**	0.982619
$\nu_\theta^{5:3}$	$\nu_\theta^{3:2}$	$\nu_r^{3:2} = (\nu_{\mathrm{K}} - \nu_r)^{5:3}$	10 : 9 : **6**	0.989634
$\nu_\theta^{2:1}$	$\nu_\theta^{3:2}$	$\nu_r^{3:2} = (\nu_{\mathrm{K}} - \nu_r)^{2:1}$	4 : 3 : **2**	0.590679
$\nu_\theta^{5:3}$	–	$\nu_r^{5:3} = (\nu_{\mathrm{K}} - \nu_r)^{5:3}$	**5** : **3**	0.912558
$\nu_\theta^{2:1}$	$\nu_\theta^{5:3}$	$\nu_r^{5:3} = (\nu_{\mathrm{K}} - \nu_r)^{2:1}$	6 : 5 : **3**	0.259800
$\nu_\theta^{2:1}$	$\nu_\theta^{5:3}$	$\nu_r^{2:1} = (\nu_{\mathrm{K}} - \nu_r)^{5:3}$	6 : 5 : **3**	0.880442
$\nu_\theta^{5:2}$	$\nu_\theta^{2:1}$	$\nu_r^{5:2} = (\nu_{\mathrm{K}} - \nu_r)^{2:1}$	5 : 4 : **2**	0.271182
$\nu_\theta^{3:1}$	$\nu_\theta^{2:1}$	$\nu_r^{3:1} = (\nu_{\mathrm{K}} - \nu_r)^{2:1}$	3 : 2 : **1**	0.616894 0.999667
$\nu_\theta^{4:1}$	$\nu_\theta^{5:2}$	$\nu_r^{4:1} = (\nu_{\mathrm{K}} - \nu_r)^{5:2}$	8 : 5 : **2**	0.999244
$\nu_\theta^{5:1}$	$\nu_\theta^{5:2}$	$\nu_r^{5:1} = (\nu_{\mathrm{K}} - \nu_r)^{5:2}$	10 : 5 : **2**	0.993442 0.427764
$\nu_\theta^{5:1}$	$\nu_\theta^{3:1}$	$\nu_r^{5:1} = (\nu_{\mathrm{K}} - \nu_r)^{3:1}$	5 : 3 : **1**	0.999506

ν_{up}	ν_{middle}	ν_{down}	B22 sets	a
$\nu_{\mathrm{K}}^{5:2}$	$\nu_{\mathrm{K}}^{2:1}$	ν_r	5 : 4 : **2**	0.749094
$\nu_{\mathrm{K}}^{3:1}$	$\nu_{\mathrm{K}}^{5:3}$	ν_r	9 : 5 : **3**	0.598576
$\nu_{\mathrm{K}}^{3:1}$	$\nu_{\mathrm{K}}^{2:1}$	ν_r	3 : 2 : **1**	0.913806
$\nu_{\mathrm{K}}^{3:1}$	$\nu_{\mathrm{K}}^{5:2}$	ν_r	6 : 5 : **2**	0.999156
$\nu_{\mathrm{K}}^{4:1}$	$\nu_{\mathrm{K}}^{3:2}$	ν_r	8 : 3 : **2**	0.696084
$\nu_{\mathrm{K}}^{4:1}$	$\nu_{\mathrm{K}}^{5:3}$	ν_r	12 : 5 : **3**	0.901673
$\nu_{\mathrm{K}}^{4:1}$	$\nu_{\mathrm{K}}^{2:1}$	ν_r	4 : 2 : **1**	0.996445
$\nu_{\mathrm{K}}^{5:1}$	$\nu_{\mathrm{K}}^{4:3}$	ν_r	15 : 4 : **3**	0.468451
$\nu_{\mathrm{K}}^{5:1}$	$\nu_{\mathrm{K}}^{3:2}$	ν_r	10 : 3 : **2**	0.885647
$\nu_{\mathrm{K}}^{5:1}$	$\nu_{\mathrm{K}}^{5:3}$	ν_r	15 : 5 : **3**	0.975778

ν_{up}	ν_{middle}	ν_{down}	B23 sets	a
–	–	–	–	–

Table 6. *(continued)*

$\nu_{\rm up}$	$\nu_{\rm middle}$	$\nu_{\rm down}$	B24 sets	a
$\nu_{\rm K}^{3:1}$	$\nu_{\rm K}^{5:4}$	$\nu_r^{5:4} = (\nu_\theta - \nu_r)^{3:1}$	12 : 5 : **4**	0.495016
$\nu_{\rm K}^{5:2}$	$\nu_{\rm K}^{4:3}$	$\nu_r^{4:3} = (\nu_\theta - \nu_r)^{5:2}$	15 : 8 : **6**	0.174769
$\nu_{\rm K}^{3:1}$	$\nu_{\rm K}^{4:3}$	$\nu_r^{4:3} = (\nu_\theta - \nu_r)^{3:1}$	9 : 4 : **3**	0.775077
$\nu_{\rm K}^{5:2}$	$\nu_{\rm K}^{3:2}$	$\nu_r^{3:2} = (\nu_\theta - \nu_r)^{5:2}$	5 : 3 : **2**	0.660135
$\nu_{\rm K}^{3:1}$	$\nu_{\rm K}^{3:2}$	$\nu_r^{3:2} = (\nu_\theta - \nu_r)^{3:1}$	6 : 3 : **2**	0.926760
$\nu_{\rm K}^{5:2}$	$\nu_{\rm K}^{5:3}$	$\nu_r^{5:3} = (\nu_\theta - \nu_r)^{5:2}$	15 : 10 : **6**	0.794181
$\nu_{\rm K}^{3:1}$	$\nu_{\rm K}^{5:3}$	$\nu_r^{5:3} = (\nu_\theta - \nu_r)^{3:1}$	9 : 5 : **3**	0.963424
$\nu_{\rm K}^{5:2}$	$\nu_{\rm K}^{2:1}$	$\nu_r^{2:1} = (\nu_\theta - \nu_r)^{5:2}$	5 : 4 : **2**	0.869857
$\nu_{\rm K}^{3:1}$	$\nu_{\rm K}^{2:1}$	$\nu_r^{2:1} = (\nu_\theta - \nu_r)^{3:1}$	3 : 2 : **1**	0.980124
$\nu_{\rm K}^{5:2}$	–	$\nu_r^{5:2} = (\nu_\theta - \nu_r)^{5:2}$	**5** : **2**	0.882162
$\nu_{\rm K}^{3:1}$	$\nu_{\rm K}^{5:2}$	$\nu_r^{5:2} = (\nu_\theta - \nu_r)^{3:1}$	6 : 5 : **2**	0.983466
$\nu_{\rm K}^{3:1}$	$\nu_{\rm K}^{5:2}$	$\nu_r^{3:1} = (\nu_\theta - \nu_r)^{5:2}$	6 : 5 : **2**	0.854958
$\nu_{\rm K}^{3:1}$	–	$\nu_r^{3:1} = (\nu_\theta - \nu_r)^{3:1}$	**3** : **1**	0.983043
$\nu_{\rm K}^{4:1}$	$\nu_{\rm K}^{5:2}$	$\nu_r^{4:1} = (\nu_\theta - \nu_r)^{5:2}$	8 : 5 : **2**	0.609007
$\nu_{\rm K}^{4:1}$	$\nu_{\rm K}^{3:1}$	$\nu_r^{4:1} = (\nu_\theta - \nu_r)^{3:1}$	4 : 3 : **1**	0.976789
$\nu_{\rm K}^{5:1}$	$\nu_{\rm K}^{3:1}$	$\nu_r^{5:1} = (\nu_\theta - \nu_r)^{3:1}$	5 : 3 : **1**	0.954420

$\nu_{\rm up}$	$\nu_{\rm middle}$	$\nu_{\rm down}$	B25 sets	a
$\nu_\theta^{2:1}$	$\nu_{\rm K}^{3:2}$	$\nu_r^{3:2} = (\nu_{\rm K} - \nu_r)^{2:1}$	4 : 3 : **2**	0.885695
$\nu_\theta^{2:1}$	$\nu_{\rm K}^{5:3}$	$\nu_r^{5:3} = (\nu_{\rm K} - \nu_r)^{2:1}$	6 : 5 : **3**	0.342013
$\nu_{\rm K}^{2:1}$	$\nu_\theta^{5:3}$	$\nu_r^{2:1} = (\nu_{\rm K} - \nu_r)^{5:3}$	6 : 5 : **3**	0.912558
$\nu_{\rm K}^{5:2}$	$\nu_\theta^{3:2}$	$\nu_r^{5:2} = (\nu_{\rm K} - \nu_r)^{3:2}$	5 : 3 : **2**	0.997182
$\nu_{\rm K}^{5:2}$	$\nu_\theta^{5:3}$	$\nu_r^{5:2} = (\nu_{\rm K} - \nu_r)^{5:3}$	15 : 10 : **6**	0.880606
$\nu_{\rm K}^{5:2}$	$\nu_\theta^{2:1}$	$\nu_r^{5:2} = (\nu_{\rm K} - \nu_r)^{2:1}$	5 : 4 : **2**	0.221062
$\nu_{\rm K}^{3:1}$	$\nu_\theta^{3:2}$	$\nu_r^{3:1} = (\nu_{\rm K} - \nu_r)^{3:2}$	6 : 3 : **2**	0.997713
$\nu_{\rm K}^{3:1}$	$\nu_\theta^{5:3}$	$\nu_r^{3:1} = (\nu_{\rm K} - \nu_r)^{5:3}$	9 : 5 : **3**	0.913062
$\nu_{\rm K}^{3:1}$	$\nu_\theta^{2:1}$	$\nu_r^{3:1} = (\nu_{\rm K} - \nu_r)^{2:1}$	3 : 2 : **1**	0.475159
$\nu_{\rm K}^{4:1}$	$\nu_\theta^{5:3}$	$\nu_r^{4:1} = (\nu_{\rm K} - \nu_r)^{5:3}$	12 : 5 : **3**	0.970995
$\nu_{\rm K}^{4:1}$	$\nu_\theta^{2:1}$	$\nu_r^{4:1} = (\nu_{\rm K} - \nu_r)^{2:1}$	4 : 2 : **1**	0.759538
$\nu_{\rm K}^{5:1}$	$\nu_\theta^{5:3}$	$\nu_r^{5:1} = (\nu_{\rm K} - \nu_r)^{5:3}$	15 : 5 : **3**	0.998539
$\nu_{\rm K}^{5:1}$	$\nu_\theta^{2:1}$	$\nu_r^{5:1} = (\nu_{\rm K} - \nu_r)^{2:1}$	5 : 2 : **1**	0.885657
$\nu_{\rm K}^{5:1}$	$\nu_\theta^{5:2}$	$\nu_r^{5:1} = (\nu_{\rm K} - \nu_r)^{5:2}$	10 : 5 : **2**	0.269751

$\nu_{\rm up}$	$\nu_{\rm middle}$	$\nu_{\rm down}$	B33 sets	a
–	–	–	–	–

Table 6. *(continued)*

ν_{up}	ν_{middle}	ν_{down}	B34 sets	a
$\nu_{\mathrm{K}}^{4:3}$	$\nu_{\mathrm{K}}^{5:4}$	$\nu_{\theta}^{5:4} = (\nu_{\theta} - \nu_{r})^{4:3}$	16 : 15 : **12**	0.768456
$\nu_{\mathrm{K}}^{3:2}$	$\nu_{\mathrm{K}}^{5:4}$	$\nu_{\theta}^{5:4} = (\nu_{\theta} - \nu_{r})^{3:2}$	6 : 5 : **4**	0.814015
$\nu_{\mathrm{K}}^{5:3}$	$\nu_{\mathrm{K}}^{5:4}$	$\nu_{\theta}^{5:4} = (\nu_{\theta} - \nu_{r})^{5:3}$	20 : 15 : **12**	0.853957
$\nu_{\mathrm{K}}^{2:1}$	$\nu_{\mathrm{K}}^{5:4}$	$\nu_{\theta}^{5:4} = (\nu_{\theta} - \nu_{r})^{2:1}$	8 : 5 : **4**	0.914614
$\nu_{\mathrm{K}}^{5:2}$	$\nu_{\mathrm{K}}^{5:4}$	$\nu_{\theta}^{5:4} = (\nu_{\theta} - \nu_{r})^{5:2}$	10 : 5 : **4**	0.965747
$\nu_{\mathrm{K}}^{3:1}$	$\nu_{\mathrm{K}}^{5:4}$	$\nu_{\theta}^{5:4} = (\nu_{\theta} - \nu_{r})^{3:1}$	12 : 5 : **4**	0.986880
$\nu_{\mathrm{K}}^{3:2}$	$\nu_{\mathrm{K}}^{4:3}$	$\nu_{\theta}^{4:3} = (\nu_{\theta} - \nu_{r})^{3:2}$	9 : 8 : **6**	0.855369
$\nu_{\mathrm{K}}^{5:3}$	$\nu_{\mathrm{K}}^{4:3}$	$\nu_{\theta}^{4:3} = (\nu_{\theta} - \nu_{r})^{5:3}$	5 : 4 : **3**	0.889086
$\nu_{\mathrm{K}}^{2:1}$	$\nu_{\mathrm{K}}^{4:3}$	$\nu_{\theta}^{4:3} = (\nu_{\theta} - \nu_{r})^{2:1}$	6 : 4 : **3**	0.937852
$\nu_{\mathrm{K}}^{5:2}$	$\nu_{\mathrm{K}}^{4:3}$	$\nu_{\theta}^{4:3} = (\nu_{\theta} - \nu_{r})^{5:2}$	15 : 8 : **6**	0.975527
$\nu_{\mathrm{K}}^{3:1}$	$\nu_{\mathrm{K}}^{4:3}$	$\nu_{\theta}^{4:3} = (\nu_{\theta} - \nu_{r})^{3:1}$	9 : 4 : **3**	0.990714
$\nu_{\mathrm{K}}^{5:3}$	$\nu_{\mathrm{K}}^{3:2}$	$\nu_{\theta}^{3:2} = (\nu_{\theta} - \nu_{r})^{5:3}$	10 : 9 : **6**	0.921475
$\nu_{\mathrm{K}}^{2:1}$	$\nu_{\mathrm{K}}^{3:2}$	$\nu_{\theta}^{3:2} = (\nu_{\theta} - \nu_{r})^{2:1}$	4 : 3 : **2**	0.959385
$\nu_{\mathrm{K}}^{2:1}$	$\nu_{\mathrm{K}}^{5:3}$	$\nu_{\theta}^{5:3} = (\nu_{\theta} - \nu_{r})^{2:1}$	6 : 5 : **3**	0.967538
ν_{up}	ν_{middle}	ν_{down}	B35 sets	a
$\nu_{\mathrm{K}}^{4:1}$	$\nu_{\theta}^{5:4}$	$\nu_{\theta}^{4:1} = (\nu_{\mathrm{K}} - \nu_{r})^{5:4}$	16 : 5 : **4**	0.998070
ν_{up}	ν_{middle}	ν_{down}	B44 sets	a
–	–	–	–	–
ν_{up}	ν_{middle}	ν_{down}	B45 sets	a
$\nu_{\mathrm{K}}^{4:3}$	$\nu_{\theta}^{5:4}$	$(\nu_{\theta} - \nu_{r})^{4:3} = (\nu_{\mathrm{K}} - \nu_{r})^{5:4}$	16 : 15 : **12**	0.285641
$\nu_{\mathrm{K}}^{3:2}$	$\nu_{\theta}^{5:4}$	$(\nu_{\theta} - \nu_{r})^{3:2} = (\nu_{\mathrm{K}} - \nu_{r})^{5:4}$	6 : 5 : **4**	0.586875
$\nu_{\mathrm{K}}^{3:2}$	$\nu_{\theta}^{4:3}$	$(\nu_{\theta} - \nu_{r})^{3:2} = (\nu_{\mathrm{K}} - \nu_{r})^{4:3}$	9 : 8 : **6**	0.444214
$\nu_{\mathrm{K}}^{5:3}$	$\nu_{\theta}^{5:4}$	$(\nu_{\theta} - \nu_{r})^{5:3} = (\nu_{\mathrm{K}} - \nu_{r})^{5:4}$	20 : 15 : **12**	0.738633
$\nu_{\mathrm{K}}^{5:3}$	$\nu_{\theta}^{4:3}$	$(\nu_{\theta} - \nu_{r})^{5:3} = (\nu_{\mathrm{K}} - \nu_{r})^{4:3}$	5 : 4 : **3**	0.655638
$\nu_{\mathrm{K}}^{5:3}$	$\nu_{\theta}^{3:2}$	$(\nu_{\theta} - \nu_{r})^{5:3} = (\nu_{\mathrm{K}} - \nu_{r})^{3:2}$	10 : 9 : **6**	0.412837
$\nu_{\mathrm{K}}^{2:1}$	$\nu_{\theta}^{5:4}$	$(\nu_{\theta} - \nu_{r})^{2:1} = (\nu_{\mathrm{K}} - \nu_{r})^{5:4}$	8 : 5 : **4**	0.882635
$\nu_{\mathrm{K}}^{2:1}$	$\nu_{\theta}^{4:3}$	$(\nu_{\theta} - \nu_{r})^{2:1} = (\nu_{\mathrm{K}} - \nu_{r})^{4:3}$	6 : 4 : **3**	0.848374
$\nu_{\mathrm{K}}^{2:1}$	$\nu_{\theta}^{3:2}$	$(\nu_{\theta} - \nu_{r})^{2:1} = (\nu_{\mathrm{K}} - \nu_{r})^{3:2}$	4 : 3 : **2**	0.753126
$\nu_{\mathrm{K}}^{2:1}$	$\nu_{\theta}^{5:3}$	$(\nu_{\theta} - \nu_{r})^{2:1} = (\nu_{\mathrm{K}} - \nu_{r})^{5:3}$	6 : 5 : **3**	0.605036
$\nu_{\mathrm{K}}^{5:2}$	$\nu_{\theta}^{5:4}$	$(\nu_{\theta} - \nu_{r})^{5:2} = (\nu_{\mathrm{K}} - \nu_{r})^{5:4}$	10 : 5 : **4**	0.961586
$\nu_{\mathrm{K}}^{5:2}$	$\nu_{\theta}^{4:3}$	$(\nu_{\theta} - \nu_{r})^{5:2} = (\nu_{\mathrm{K}} - \nu_{r})^{4:3}$	15 : 8 : **6**	0.952213
$\nu_{\mathrm{K}}^{5:2}$	$\nu_{\theta}^{3:2}$	$(\nu_{\theta} - \nu_{r})^{5:2} = (\nu_{\mathrm{K}} - \nu_{r})^{3:2}$	5 : 3 : **2**	0.925224
$\nu_{\mathrm{K}}^{5:2}$	$\nu_{\theta}^{5:3}$	$(\nu_{\theta} - \nu_{r})^{5:2} = (\nu_{\mathrm{K}} - \nu_{r})^{5:3}$	15 : 10 : **6**	0.881629

Table 6. *(continued)*

$\nu_{\rm K}^{5:2}$	$\nu_\theta^{2:1}$	$(\nu_\theta-\nu_r)^{5:2}=(\nu_{\rm K}-\nu_r)^{2:1}$	5 : 4 : **2**	0.712080
$\nu_{\rm K}^{3:1}$	$\nu_\theta^{5:4}$	$(\nu_\theta-\nu_r)^{3:1}=(\nu_{\rm K}-\nu_r)^{5:4}$	12 : 5 : **4**	0.986719
$\nu_{\rm K}^{3:1}$	$\nu_\theta^{4:3}$	$(\nu_\theta-\nu_r)^{3:1}=(\nu_{\rm K}-\nu_r)^{4:3}$	9 : 4 : **3**	0.986484
$\nu_{\rm K}^{3:1}$	$\nu_\theta^{3:2}$	$(\nu_\theta-\nu_r)^{3:1}=(\nu_{\rm K}-\nu_r)^{3:2}$	6 : 3 : **2**	0.984319
$\nu_{\rm K}^{3:1}$	$\nu_\theta^{5:3}$	$(\nu_\theta-\nu_r)^{3:1}=(\nu_{\rm K}-\nu_r)^{5:3}$	9 : 5 : **3**	0.975422
$\nu_{\rm K}^{3:1}$	$\nu_\theta^{2:1}$	$(\nu_\theta-\nu_r)^{3:1}=(\nu_{\rm K}-\nu_r)^{2:1}$	3 : 2 : **1**	0.922985
$\nu_{\rm K}^{3:1}$	$\nu_\theta^{5:2}$	$(\nu_\theta-\nu_r)^{3:1}=(\nu_{\rm K}-\nu_r)^{5:2}$	6 : 5 : **2**	0.686529
$\nu_{\rm K}^{4:1}$	$\nu_\theta^{4:3}$	$(\nu_\theta-\nu_r)^{4:1}=(\nu_{\rm K}-\nu_r)^{4:3}$	12 : 4 : **3**	0.997450
$\nu_{\rm K}^{4:1}$	$\nu_\theta^{3:1}$	$(\nu_\theta-\nu_r)^{4:1}=(\nu_{\rm K}-\nu_r)^{3:1}$	4 : 3 : **1**	0.927315
$\nu_{\rm K}^{5:1}$	$\nu_\theta^{4:1}$	$(\nu_\theta-\nu_r)^{5:1}=(\nu_{\rm K}-\nu_r)^{4:1}$	5 : 4 : **1**	0.927542

$\nu_{\rm up}$	$\nu_{\rm middle}$	$\nu_{\rm down}$	B55 sets	a
–	–	–	–	–

Table 7. Middle identity.

$+\ -$	$\dfrac{\nu_\theta}{\nu_r}$	$\dfrac{\nu_{\rm K}}{\nu_r}$	$\dfrac{\nu_{\rm K}}{\nu_\theta}$	$\dfrac{\nu_{\rm K}}{\nu_\theta-\nu_r}$	$\dfrac{\nu_\theta}{\nu_{\rm K}-\nu_r}$
$\dfrac{\nu_\theta}{\nu_r}$	M11	M12	M13	M14	M15
$\dfrac{\nu_{\rm K}}{\nu_r}$	M21	M22	M23	M24	M25
$\dfrac{\nu_{\rm K}}{\nu_\theta}$	M31	M32	M33	M34	M35
$\dfrac{\nu_{\rm K}}{\nu_\theta-\nu_r}$	M41	M42	M43	M44	M45
$\dfrac{\nu_\theta}{\nu_{\rm K}-\nu_r}$	M51	M52	M53	M54	M55

$\nu_{\rm up}$	$\nu_{\rm middle}$	$\nu_{\rm down}$	M11 sets	a
$\nu_\theta^{3:2}$	$\nu_r^{3:2}=\nu_\theta^{4:3}$	$\nu_r^{4:3}$	6 : **4** : 3	0.786859
$\nu_\theta^{3:2}$	$\nu_r^{3:2}=\nu_\theta^{5:1}$	$\nu_r^{5:1}$	15 : **10** : 2	0.999988
$\nu_\theta^{5:3}$	$\nu_r^{5:3}=\nu_\theta^{5:1}$	$\nu_r^{5:1}$	25 : **15** : 3	0.999860
$\nu_\theta^{2:1}$	$\nu_r^{2:1}=\nu_\theta^{5:1}$	$\nu_r^{5:1}$	10 : **5** : 1	0.999842
$\nu_\theta^{5:2}$	$\nu_r^{5:2}=\nu_\theta^{4:3}$	$\nu_r^{4:3}$	10 : **4** : 3	0.999575
$\nu_\theta^{4:1}$	$\nu_r^{4:1}=\nu_\theta^{5:4}$	$\nu_r^{5:4}$	20 : **5** : 4	0.977966

Table 7. *(continued)*

$\nu_{\rm up}$	$\nu_{\rm middle}$	$\nu_{\rm down}$	M12 sets	a
$\nu_{\rm K}^{4:3}$	$\nu_r^{4:3} = \nu_\theta^{5:4}$	$\nu_r^{5:4}$	20 : **15** : 12	0.0560561
$\nu_{\rm K}^{5:1}$	$\nu_r^{5:1} = \nu_\theta^{5:4}$	$\nu_r^{5:4}$	25 : **5** : 4	0.622555
$\nu_{\rm K}^{5:3}$	$\nu_r^{5:3} = \nu_\theta^{4:3}$	$\nu_r^{4:3}$	20 : **12** : 9	0.878624
$\nu_{\rm K}^{3:1}$	$\nu_r^{3:1} = \nu_\theta^{4:3}$	$\nu_r^{4:3}$	12 : **4** : 3	0.353929
$\nu_{\rm K}^{4:1}$	$\nu_r^{4:1} = \nu_\theta^{4:3}$	$\nu_r^{4:3}$	16 : **4** : 3	0.907931
$\nu_{\rm K}^{5:1}$	$\nu_r^{5:1} = \nu_\theta^{4:3}$	$\nu_r^{4:3}$	20 : **4** : 3	0.986324
$\nu_{\rm K}^{2:1}$	$\nu_r^{2:1} = \nu_\theta^{5:1}$	$\nu_r^{5:1}$	10 : **5** : 1	0.999928
$\nu_{\rm K}^{5:2}$	$\nu_r^{5:2} = \nu_\theta^{5:1}$	$\nu_r^{5:1}$	25 : **10** : 2	0.999817
$\nu_{\rm K}^{3:1}$	$\nu_r^{3:1} = \nu_\theta^{5:1}$	$\nu_r^{5:1}$	15 : **5** : 1	0.999816
$\nu_{\rm K}^{4:1}$	$\nu_r^{4:1} = \nu_\theta^{5:1}$	$\nu_r^{5:1}$	20 : **5** : 1	0.999917
$\nu_{\rm K}^{5:1}$	$\nu_r^{5:1} = \nu_\theta^{5:1}$	$\nu_r^{5:1}$	25 : **5** : 1	0.999995
$\nu_{\rm up}$	$\nu_{\rm middle}$	$\nu_{\rm down}$	M13 sets	a
$\nu_{\rm K}^{5:4}$	ν_θ	$\nu_r^{5:3}$	25 : **20** : 12	0.956364
$\nu_{\rm K}^{4:3}$	ν_θ	$\nu_r^{5:3}$	20 : **15** : 9	0.996837
$\nu_{\rm K}^{5:4}$	ν_θ	$\nu_r^{2:1}$	5 : **4** : 2	0.882162
$\nu_{\rm K}^{4:3}$	ν_θ	$\nu_r^{2:1}$	8 : **6** : 3	0.935213
$\nu_{\rm K}^{3:2}$	ν_θ	$\nu_r^{2:1}$	3 : **2** : 1	0.983043
$\nu_{\rm K}^{5:4}$	ν_θ	$\nu_r^{5:2}$	25 : **20** : 8	0.828130
$\nu_{\rm K}^{4:3}$	ν_θ	$\nu_r^{5:2}$	20 : **15** : 6	0.889176
$\nu_{\rm K}^{3:2}$	ν_θ	$\nu_r^{5:2}$	15 : **10** : 4	0.949454
$\nu_{\rm K}^{5:3}$	ν_θ	$\nu_r^{5:2}$	25 : **15** : 6	0.997059 0.975619
$\nu_{\rm K}^{2:1}$	ν_θ	$\nu_r^{5:2}$	10 : **5** : 2	0.995139 0.977812
$\nu_{\rm K}^{5:4}$	ν_θ	$\nu_r^{3:1}$	15 : **12** : 4	0.800994
$\nu_{\rm K}^{4:3}$	ν_θ	$\nu_r^{3:1}$	4 : **3** : 1	0.865670
$\nu_{\rm K}^{3:2}$	ν_θ	$\nu_r^{3:1}$	9 : **6** : 2	0.931945 0.996488
$\nu_{\rm K}^{5:3}$	ν_θ	$\nu_r^{3:1}$	5 : **3** : 1	0.988678 0.962250
$\nu_{\rm K}^{2:1}$	ν_θ	$\nu_r^{3:1}$	6 : **3** : 1	0.986666
$\nu_{\rm K}^{5:2}$	ν_θ	$\nu_r^{3:1}$	15 : **6** : 2	0.997177
$\nu_{\rm K}^{5:4}$	ν_θ	$\nu_r^{4:1}$	5 : **4** : 1	0.775420 0.999388
$\nu_{\rm K}^{4:3}$	ν_θ	$\nu_r^{4:1}$	16 : **12** : 3	0.843271 0.997648

Table 7. *(continued)*

$\nu_{\rm K}^{3:2}$	ν_θ	$\nu_r^{4:1}$	6 : **4** : 1	0.915030
				0.990960
$\nu_{\rm K}^{5:3}$	ν_θ	$\nu_r^{4:1}$	20 : **12** : 3	0.980095
				0.949229
$\nu_{\rm K}^{2:1}$	ν_θ	$\nu_r^{4:1}$	8 : **4** : 1	0.978338
$\nu_{\rm K}^{5:2}$	ν_θ	$\nu_r^{4:1}$	10 : **4** : 1	0.992258
$\nu_{\rm K}^{3:1}$	ν_θ	$\nu_r^{4:1}$	12 : **4** : 1	0.996798
$\nu_{\rm K}^{4:1}$	ν_θ	$\nu_r^{4:1}$	16 : **4** : 1	0.999436
$\nu_{\rm K}^{5:4}$	ν_θ	$\nu_r^{5:1}$	25 : **20** : 4	0.764031
				0.998558
$\nu_{\rm K}^{4:3}$	ν_θ	$\nu_r^{5:1}$	20 : **15** : 3	0.833218
				0.996294
$\nu_{\rm K}^{3:2}$	ν_θ	$\nu_r^{5:1}$	15 : **10** : 2	0.907362
				0.988353
$\nu_{\rm K}^{5:3}$	ν_θ	$\nu_r^{5:1}$	25 : **15** : 3	0.976048
				0.943291
$\nu_{\rm K}^{2:1}$	ν_θ	$\nu_r^{5:1}$	10 : **5** : 1	0.974517
$\nu_{\rm K}^{5:2}$	ν_θ	$\nu_r^{5:1}$	25 : **10** : 2	0.989990
$\nu_{\rm K}^{3:1}$	ν_θ	$\nu_r^{5:1}$	15 : **5** : 1	0.995297
$\nu_{\rm K}^{4:1}$	ν_θ	$\nu_r^{5:1}$	20 : **5** : 1	0.998637
$\nu_{\rm K}^{5:1}$	ν_θ	$\nu_r^{5:1}$	25 : **5** : 1	0.999541

$\nu_{\rm up}$	$\nu_{\rm middle}$	$\nu_{\rm down}$	M14 sets	a
$\nu_{\rm K}^{5:2}$	$\nu_\theta^{5:4} = (\nu_\theta - \nu_r)^{5:2}$	$\nu_r^{5:4}$	25 : **10** : 8	0.215317
$\nu_{\rm K}^{3:1}$	$\nu_\theta^{5:4} = (\nu_\theta - \nu_r)^{3:1}$	$\nu_r^{5:4}$	15 : **5** : 4	0.862108
$\nu_{\rm K}^{5:2}$	$\nu_\theta^{4:3} = (\nu_\theta - \nu_r)^{5:2}$	$\nu_r^{4:3}$	10 : **4** : 3	0.781001
$\nu_{\rm K}^{3:1}$	$\nu_\theta^{4:3} = (\nu_\theta - \nu_r)^{3:1}$	$\nu_r^{4:3}$	12 : **4** : 3	0.967080
$\nu_{\rm K}^{2:1}$	$\nu_\theta^{3:2} = (\nu_\theta - \nu_r)^{2:1}$	$\nu_r^{3:2}$	6 : **3** : 2	0.679246
$\nu_{\rm K}^{5:2}$	$\nu_\theta^{3:2} = (\nu_\theta - \nu_r)^{5:2}$	$\nu_r^{3:2}$	15 : **6** : 4	0.943001
$\nu_{\rm K}^{3:1}$	$\nu_\theta^{3:2} = (\nu_\theta - \nu_r)^{3:1}$	$\nu_r^{3:2}$	9 : **3** : 2	0.986477
$\nu_{\rm K}^{4:1}$	$\nu_\theta^{3:2} = (\nu_\theta - \nu_r)^{4:1}$	$\nu_r^{3:2}$	12 : **3** : 2	0.996851
$\nu_{\rm K}^{5:3}$	$\nu_\theta^{5:3} = (\nu_\theta - \nu_r)^{5:3}$	$\nu_r^{5:3}$	25 : **15** : 9	0.415384
$\nu_{\rm K}^{2:1}$	$\nu_\theta^{5:3} = (\nu_\theta - \nu_r)^{2:1}$	$\nu_r^{5:3}$	10 : **5** : 3	0.862386
$\nu_{\rm K}^{5:2}$	$\nu_\theta^{5:3} = (\nu_\theta - \nu_r)^{5:2}$	$\nu_r^{5:3}$	25 : **10** : 6	0.968455
$\nu_{\rm K}^{3:1}$	$\nu_\theta^{5:3} = (\nu_\theta - \nu_r)^{3:1}$	$\nu_r^{5:3}$	15 : **5** : 3	0.989352
$\nu_{\rm K}^{3:2}$	$\nu_\theta^{2:1} = (\nu_\theta - \nu_r)^{3:2}$	$\nu_r^{2:1}$	3 : **2** : 1	0.544870
$\nu_{\rm K}^{5:3}$	$\nu_\theta^{2:1} = (\nu_\theta - \nu_r)^{5:3}$	$\nu_r^{2:1}$	10 : **6** : 3	0.795779

Table 7. *(continued)*

$\nu_{\mathrm{K}}^{2:1}$	$\nu_\theta^{2:1} = (\nu_\theta - \nu_r)^{2:1}$	$\nu_r^{2:1}$	4 : **2** : 1	0.939903
$\nu_{\mathrm{K}}^{5:4}$	$\nu_\theta^{5:2} = (\nu_\theta - \nu_r)^{5:4}$	$\nu_r^{5:2}$	25 : **20** : 8	0.128587
$\nu_{\mathrm{K}}^{4:3}$	$\nu_\theta^{5:2} = (\nu_\theta - \nu_r)^{4:3}$	$\nu_r^{5:2}$	20 : **15** : 6	0.489035
$\nu_{\mathrm{K}}^{3:2}$	$\nu_\theta^{5:2} = (\nu_\theta - \nu_r)^{3:2}$	$\nu_r^{5:2}$	15 : **10** : 4	0.781086
$\nu_{\mathrm{K}}^{5:3}$	$\nu_\theta^{5:2} = (\nu_\theta - \nu_r)^{5:3}$	$\nu_r^{5:2}$	25 : **15** : 6	0.888972
$\nu_{\mathrm{K}}^{2:1}$	$\nu_\theta^{5:2} = (\nu_\theta - \nu_r)^{2:1}$	$\nu_r^{5:2}$	10 : **5** : 2	0.964306
$\nu_{\mathrm{K}}^{5:4}$	$\nu_\theta^{3:1} = (\nu_\theta - \nu_r)^{5:4}$	$\nu_r^{3:1}$	15 : **12** : 4	0.454063
$\nu_{\mathrm{K}}^{4:3}$	$\nu_\theta^{3:1} = (\nu_\theta - \nu_r)^{4:3}$	$\nu_r^{3:1}$	4 : **3** : 1	0.655792
$\nu_{\mathrm{K}}^{3:2}$	$\nu_\theta^{3:1} = (\nu_\theta - \nu_r)^{3:2}$	$\nu_r^{3:1}$	9 : **6** : 2	0.838000
$\nu_{\mathrm{K}}^{5:3}$	$\nu_\theta^{3:1} = (\nu_\theta - \nu_r)^{5:3}$	$\nu_r^{3:1}$	5 : **3** : 1	0.912550
$\nu_{\mathrm{K}}^{5:4}$	$\nu_\theta^{4:1} = (\nu_\theta - \nu_r)^{5:4}$	$\nu_r^{4:1}$	5 : **4** : 1	0.626952
$\nu_{\mathrm{K}}^{4:3}$	$\nu_\theta^{4:1} = (\nu_\theta - \nu_r)^{4:3}$	$\nu_r^{4:1}$	16 : **12** : 3	0.749908
$\nu_{\mathrm{K}}^{3:2}$	$\nu_\theta^{4:1} = (\nu_\theta - \nu_r)^{3:2}$	$\nu_r^{4:1}$	6 : **4** : 1	0.871285
$\nu_{\mathrm{K}}^{5:3}$	$\nu_\theta^{4:1} = (\nu_\theta - \nu_r)^{5:3}$	$\nu_r^{4:1}$	20 : **12** : 3	0.925476
$\nu_{\mathrm{K}}^{5:4}$	$\nu_\theta^{5:1} = (\nu_\theta - \nu_r)^{5:4}$	$\nu_r^{5:1}$	25 : **20** : 4	0.679029
$\nu_{\mathrm{K}}^{4:3}$	$\nu_\theta^{5:1} = (\nu_\theta - \nu_r)^{4:3}$	$\nu_r^{5:1}$	20 : **15** : 3	0.778985
$\nu_{\mathrm{K}}^{3:2}$	$\nu_\theta^{5:1} = (\nu_\theta - \nu_r)^{3:2}$	$\nu_r^{5:1}$	15 : **10** : 2	0.881466
$\nu_{\mathrm{K}}^{5:3}$	$\nu_\theta^{5:1} = (\nu_\theta - \nu_r)^{5:3}$	$\nu_r^{5:1}$	25 : **15** : 3	0.929040
$\nu_{\mathrm{K}}^{4:1}$	$\nu_\theta^{5:1} = (\nu_\theta - \nu_r)^{4:1}$	$\nu_r^{5:1}$	20 : **5** : 1	0.999458
$\nu_{\mathrm{K}}^{5:1}$	$\nu_\theta^{5:1} = (\nu_\theta - \nu_r)^{5:1}$	$\nu_r^{5:1}$	25 : **5** : 1	0.999727

ν_{up}	ν_{middle}	ν_{down}	M15 sets	a
$\nu_\theta^{2:1}$	$\nu_\theta^{4:3} = (\nu_{\mathrm{K}} - \nu_r)^{2:1}$	$\nu_r^{4:3}$	8 : **4** : 3	0.529797
$\nu_\theta^{4:3}$	$\nu_\theta^{3:2} = (\nu_{\mathrm{K}} - \nu_r)^{4:3}$	$\nu_r^{3:2}$	4 : **3** : 2	0.988237
$\nu_\theta^{3:2}$	$\nu_\theta^{3:2} = (\nu_{\mathrm{K}} - \nu_r)^{3:2}$	$\nu_r^{3:2}$	9 : **6** : 4	0.838418
$\nu_\theta^{5:3}$	$\nu_\theta^{3:2} = (\nu_{\mathrm{K}} - \nu_r)^{5:3}$	$\nu_r^{3:2}$	5 : **3** : 2	0.475727
$\nu_\theta^{5:4}$	$\nu_\theta^{5:3} = (\nu_{\mathrm{K}} - \nu_r)^{5:4}$	$\nu_r^{5:3}$	25 : **20** : 12	0.915554
$\nu_\theta^{4:3}$	$\nu_\theta^{5:3} = (\nu_{\mathrm{K}} - \nu_r)^{4:3}$	$\nu_r^{5:3}$	20 : **15** : 9	0.820673
$\nu_\theta^{3:2}$	$\nu_\theta^{5:3} = (\nu_{\mathrm{K}} - \nu_r)^{3:2}$	$\nu_r^{5:3}$	15 : **10** : 6	0.409873
$\nu_\theta^{5:4}$	$\nu_\theta^{2:1} = (\nu_{\mathrm{K}} - \nu_r)^{5:4}$	$\nu_r^{2:1}$	5 : **4** : 2	0.632931
$\nu_\theta^{4:3}$	$\nu_\theta^{2:1} = (\nu_{\mathrm{K}} - \nu_r)^{4:3}$	$\nu_r^{2:1}$	8 : **6** : 3	0.282928
$\nu_\theta^{5:4}$	$\nu_\theta^{4:1} = (\nu_{\mathrm{K}} - \nu_r)^{5:4}$	$\nu_r^{4:1}$	5 : **4** : 1	0.999439
$\nu_\theta^{4:3}$	$\nu_\theta^{4:1} = (\nu_{\mathrm{K}} - \nu_r)^{4:3}$	$\nu_r^{4:1}$	16 : **12** : 3	0.999879
$\nu_\theta^{5:4}$	$\nu_\theta^{5:1} = (\nu_{\mathrm{K}} - \nu_r)^{5:4}$	$\nu_r^{5:1}$	25 : **20** : 4	0.998638
$\nu_\theta^{4:3}$	$\nu_\theta^{5:1} = (\nu_{\mathrm{K}} - \nu_r)^{4:3}$	$\nu_r^{5:1}$	20 : **15** : 3	0.999280
$\nu_\theta^{3:2}$	$\nu_\theta^{5:1} = (\nu_{\mathrm{K}} - \nu_r)^{3:2}$	$\nu_r^{5:1}$	15 : **10** : 2	0.999827

Table 7. *(continued)*

$\nu_{\rm up}$	$\nu_{\rm middle}$	$\nu_{\rm down}$	M21 sets	a
$\nu_\theta^{5:4}$	$\nu_r^{5:4} = \nu_{\rm K}^{5:4}$	$\nu_r^{5:4}$	25 : **20** : 16	0.845849
$\nu_\theta^{4:1}$	$\nu_r^{4:1} = \nu_{\rm K}^{5:4}$	$\nu_r^{5:4}$	20 : **5** : 4	0.998803
$\nu_\theta^{5:1}$	$\nu_r^{5:1} = \nu_{\rm K}^{5:4}$	$\nu_r^{5:4}$	25 : **5** : 4	0.990401 0.613804
$\nu_\theta^{4:3}$	$\nu_r^{4:3} = \nu_{\rm K}^{4:3}$	$\nu_r^{4:3}$	16 : **12** : 9	0.937003
$\nu_\theta^{3:2}$	$\nu_r^{3:2} = \nu_{\rm K}^{4:3}$	$\nu_r^{4:3}$	6 : **4** : 3	0.279224
$\nu_\theta^{3:1}$	$\nu_r^{3:1} = \nu_{\rm K}^{4:3}$	$\nu_r^{4:3}$	12 : **4** : 3	0.248602
$\nu_\theta^{5:3}$	$\nu_r^{5:3} = \nu_{\rm K}^{3:2}$	$\nu_r^{3:2}$	5 : **3** : 2	0.955769
$\nu_\theta^{2:1}$	$\nu_r^{2:1} = \nu_{\rm K}^{3:2}$	$\nu_r^{3:2}$	6 : **3** : 2	0.926504
$\nu_{\rm up}$	$\nu_{\rm middle}$	$\nu_{\rm down}$	M22 sets	a
$\nu_{\rm K}^{3:2}$	$\nu_r^{3:2} = \nu_{\rm K}^{4:3}$	$\nu_r^{4:3}$	6 : **4** : 3	0.549318
$\nu_{\rm K}^{2:1}$	$\nu_r^{2:1} = \nu_{\rm K}^{3:2}$	$\nu_r^{3:2}$	6 : **3** : 2	0.981859
$\nu_{\rm K}^{5:2}$	$\nu_r^{5:2} = \nu_{\rm K}^{3:2}$	$\nu_r^{3:2}$	15 : **6** : 4	0.921650
$\nu_{\rm K}^{3:1}$	$\nu_r^{3:1} = \nu_{\rm K}^{4:3}$	$\nu_r^{4:3}$	12 : **4** : 3	0.165341
$\nu_{\rm K}^{3:1}$	$\nu_r^{3:1} = \nu_{\rm K}^{3:2}$	$\nu_r^{3:2}$	9 : **3** : 2	0.948045
$\nu_{\rm K}^{4:1}$	$\nu_r^{4:1} = \nu_{\rm K}^{4:3}$	$\nu_r^{4:3}$	16 : **4** : 3	0.666295
$\nu_{\rm K}^{4:1}$	$\nu_r^{4:1} = \nu_{\rm K}^{3:2}$	$\nu_r^{3:2}$	12 : **3** : 2	0.993213
$\nu_{\rm K}^{5:1}$	$\nu_r^{5:1} = \nu_{\rm K}^{5:4}$	$\nu_r^{5:4}$	25 : **5** : 4	0.402260
$\nu_{\rm K}^{5:1}$	$\nu_r^{5:1} = \nu_{\rm K}^{4:3}$	$\nu_r^{4:3}$	20 : **4** : 3	0.847118
$\nu_{\rm up}$	$\nu_{\rm middle}$	$\nu_{\rm down}$	M23 sets	a
$\nu_{\rm K}^{5:4}$	$\nu_\theta^{5:4} = \nu_{\rm K}^{2:1}$	$\nu_r^{2:1}$	5 : **4** : 2	0.894644
$\nu_{\rm K}^{4:3}$	$\nu_\theta^{4:3} = \nu_{\rm K}^{2:1}$	$\nu_r^{2:1}$	8 : **6** : 3	0.952671
$\nu_{\rm K}^{5:4}$	$\nu_\theta^{5:4} = \nu_{\rm K}^{5:2}$	$\nu_r^{5:2}$	25 : **20** : 8	0.797122
$\nu_{\rm K}^{4:3}$	$\nu_\theta^{4:3} = \nu_{\rm K}^{5:2}$	$\nu_r^{5:2}$	20 : **15** : 6	0.852883
$\nu_{\rm K}^{3:2}$	$\nu_\theta^{3:2} = \nu_{\rm K}^{5:2}$	$\nu_r^{5:2}$	15 : **10** : 4	0.905219
$\nu_{\rm K}^{5:4}$	$\nu_\theta^{5:4} = \nu_{\rm K}^{3:1}$	$\nu_r^{3:1}$	15 : **12** : 4	0.751206

Table 7. *(continued)*

$\nu_{\rm up}$	$\nu_{\rm middle}$	$\nu_{\rm down}$	M24 sets	a
$\nu_{\rm K}^{5:2}$	$\nu_{\rm K}^{5:4} = (\nu_\theta - \nu_r)^{5:2}$	$\nu_r^{5:4}$	25 : **10** : 8	0.142859
$\nu_{\rm K}^{3:1}$	$\nu_{\rm K}^{5:4} = (\nu_\theta - \nu_r)^{3:1}$	$\nu_r^{5:4}$	15 : **5** : 4	0.732013
$\nu_{\rm K}^{5:2}$	$\nu_{\rm K}^{4:3} = (\nu_\theta - \nu_r)^{5:2}$	$\nu_r^{4:3}$	10 : **4** : 3	0.645676
$\nu_{\rm K}^{3:1}$	$\nu_{\rm K}^{4:3} = (\nu_\theta - \nu_r)^{3:1}$	$\nu_r^{4:3}$	12 : **4** : 3	0.907926
$\nu_{\rm K}^{2:1}$	$\nu_{\rm K}^{3:2} = (\nu_\theta - \nu_r)^{2:1}$	$\nu_r^{3:2}$	6 : **3** : 2	0.561945
$\nu_{\rm K}^{5:2}$	$\nu_{\rm K}^{3:2} = (\nu_\theta - \nu_r)^{5:2}$	$\nu_r^{3:2}$	15 : **6** : 4	0.893308
$\nu_{\rm K}^{3:1}$	$\nu_{\rm K}^{3:2} = (\nu_\theta - \nu_r)^{3:1}$	$\nu_r^{3:2}$	9 : **3** : 2	0.980201
$\nu_{\rm K}^{5:3}$	$\nu_{\rm K}^{5:3} = (\nu_\theta - \nu_r)^{5:3}$	$\nu_r^{5:3}$	25 : **15** : 9	0.345642
$\nu_{\rm K}^{2:1}$	$\nu_{\rm K}^{5:3} = (\nu_\theta - \nu_r)^{2:1}$	$\nu_r^{5:3}$	10 : **5** : 3	0.797820
$\nu_{\rm K}^{5:2}$	$\nu_{\rm K}^{5:3} = (\nu_\theta - \nu_r)^{5:2}$	$\nu_r^{5:3}$	25 : **10** : 6	0.948618
$\nu_{\rm K}^{3:1}$	$\nu_{\rm K}^{5:3} = (\nu_\theta - \nu_r)^{3:1}$	$\nu_r^{5:3}$	15 : **5** : 3	0.986477
$\nu_{\rm K}^{4:1}$	$\nu_{\rm K}^{5:3} = (\nu_\theta - \nu_r)^{4:1}$	$\nu_r^{5:3}$	20 : **5** : 3	0.997252
$\nu_{\rm K}^{3:2}$	$\nu_{\rm K}^{2:1} = (\nu_\theta - \nu_r)^{3:2}$	$\nu_r^{2:1}$	3 : **2** : 1	0.535413
$\nu_{\rm K}^{5:3}$	$\nu_{\rm K}^{2:1} = (\nu_\theta - \nu_r)^{5:3}$	$\nu_r^{2:1}$	10 : **6** : 3	0.780597
$\nu_{\rm K}^{2:1}$	$\nu_{\rm K}^{2:1} = (\nu_\theta - \nu_r)^{2:1}$	$\nu_r^{2:1}$	4 : **2** : 1	0.928219
$\nu_{\rm K}^{5:2}$	$\nu_{\rm K}^{2:1} = (\nu_\theta - \nu_r)^{5:2}$	$\nu_r^{2:1}$	5 : **2** : 1	0.981230
$\nu_{\rm K}^{5:4}$	$\nu_{\rm K}^{5:2} = (\nu_\theta - \nu_r)^{5:4}$	$\nu_r^{5:2}$	25 : **20** : 8	0.171905
$\nu_{\rm K}^{4:3}$	$\nu_{\rm K}^{5:2} = (\nu_\theta - \nu_r)^{4:3}$	$\nu_r^{5:2}$	20 : **15** : 6	0.590405
$\nu_{\rm K}^{3:2}$	$\nu_{\rm K}^{5:2} = (\nu_\theta - \nu_r)^{3:2}$	$\nu_r^{5:2}$	15 : **10** : 4	0.862325
$\nu_{\rm K}^{5:4}$	$\nu_{\rm K}^{3:1} = (\nu_\theta - \nu_r)^{5:4}$	$\nu_r^{3:1}$	15 : **12** : 4	0.671550
$\nu_{\rm up}$	$\nu_{\rm middle}$	$\nu_{\rm down}$	M25 sets	a
$\nu_\theta^{5:3}$	$\nu_{\rm K}^{3:2} = (\nu_{\rm K} - \nu_r)^{5:3}$	$\nu_r^{3:2}$	5 : **3** : 2	0.755103
$\nu_\theta^{4:3}$	$\nu_{\rm K}^{5:3} = (\nu_{\rm K} - \nu_r)^{4:3}$	$\nu_r^{5:3}$	20 : **15** : 9	0.990792
$\nu_\theta^{3:2}$	$\nu_{\rm K}^{5:3} = (\nu_{\rm K} - \nu_r)^{3:2}$	$\nu_r^{5:3}$	15 : **10** : 6	0.541631
$\nu_\theta^{5:4}$	$\nu_{\rm K}^{2:1} = (\nu_{\rm K} - \nu_r)^{5:4}$	$\nu_r^{2:1}$	5 : **4** : 2	0.649836
$\nu_\theta^{4:3}$	$\nu_{\rm K}^{2:1} = (\nu_{\rm K} - \nu_r)^{4:3}$	$\nu_r^{2:1}$	8 : **6** : 3	0.286597
$\nu_{\rm up}$	$\nu_{\rm middle}$	$\nu_{\rm down}$	M31 sets	a
–	–	–	–	–
$\nu_{\rm up}$	$\nu_{\rm middle}$	$\nu_{\rm down}$	M32 sets	a
–	–	–	–	–
$\nu_{\rm up}$	$\nu_{\rm middle}$	$\nu_{\rm down}$	M33 sets	a
–	–	–	–	–

Table 7. *(continued)*

$\nu_{\rm up}$	$\nu_{\rm middle}$	$\nu_{\rm down}$	M34 sets	a
$\nu_{\rm K}^{3:2}$	$\nu_{\rm K}^{5:4} = (\nu_\theta - \nu_r)^{3:2}$	$\nu_\theta^{5:4}$	15 : **10** : 8	0.877094
$\nu_{\rm K}^{5:3}$	$\nu_{\rm K}^{5:4} = (\nu_\theta - \nu_r)^{5:3}$	$\nu_\theta^{5:4}$	25 : **15** : 12	0.906562
$\nu_{\rm K}^{2:1}$	$\nu_{\rm K}^{5:4} = (\nu_\theta - \nu_r)^{2:1}$	$\nu_\theta^{5:4}$	10 : **5** : 4	0.948609
$\nu_{\rm K}^{5:2}$	$\nu_{\rm K}^{5:4} = (\nu_\theta - \nu_r)^{5:2}$	$\nu_\theta^{5:4}$	25 : **10** : 8	0.980682
$\nu_{\rm up}$	$\nu_{\rm middle}$	$\nu_{\rm down}$	M35 sets	a
–	–	–	–	–
$\nu_{\rm up}$	$\nu_{\rm middle}$	$\nu_{\rm down}$	M41 sets	a
$\nu_\theta^{5:3}$	$\nu_{\rm K}^{4:1} = \nu_r^{5:3}$	$(\nu_\theta - \nu_r)^{4:1}$	20 : **12** : 3	0.613540
$\nu_\theta^{2:1}$	$\nu_{\rm K}^{4:1} = \nu_r^{2:1}$	$(\nu_\theta - \nu_r)^{4:1}$	8 : **4** : 1	0.804129
$\nu_\theta^{5:2}$	$\nu_{\rm K}^{4:1} = \nu_r^{5:2}$	$(\nu_\theta - \nu_r)^{4:1}$	10 : **4** : 1	0.534484
$\nu_\theta^{4:3}$	$\nu_{\rm K}^{5:1} = \nu_r^{4:3}$	$(\nu_\theta - \nu_r)^{5:1}$	20 : **15** : 3	0.116240
$\nu_\theta^{3:1}$	$\nu_{\rm K}^{5:1} = \nu_r^{3:1}$	$(\nu_\theta - \nu_r)^{5:1}$	15 : **5** : 1	0.993761
$\nu_\theta^{4:1}$	$\nu_{\rm K}^{5:1} = \nu_r^{4:1}$	$(\nu_\theta - \nu_r)^{5:1}$	20 : **5** : 1	0.627571
$\nu_{\rm up}$	$\nu_{\rm middle}$	$\nu_{\rm down}$	M42 sets	a
$\nu_{\rm K}^{5:3}$	$\nu_{\rm K}^{4:1} = \nu_r^{5:3}$	$(\nu_\theta - \nu_r)^{4:1}$	20 : **12** : 3	0.404877
$\nu_{\rm K}^{2:1}$	$\nu_{\rm K}^{4:1} = \nu_r^{2:1}$	$(\nu_\theta - \nu_r)^{4:1}$	8 : **4** : 1	0.761539
$\nu_{\rm K}^{5:2}$	$\nu_{\rm K}^{4:1} = \nu_r^{5:2}$	$(\nu_\theta - \nu_r)^{4:1}$	10 : **4** : 1	0.770916
$\nu_{\rm K}^{4:3}$	$\nu_{\rm K}^{5:1} = \nu_r^{4:3}$	$(\nu_\theta - \nu_r)^{5:1}$	20 : **15** : 3	0.031074
$\nu_{\rm K}^{3:2}$	$\nu_{\rm K}^{5:1} = \nu_r^{3:2}$	$(\nu_\theta - \nu_r)^{5:1}$	15 : **10** : 2	0.919990
$\nu_{\rm K}^{5:1}$	$\nu_{\rm K}^{5:1} = \nu_r^{5:1}$	$(\nu_\theta - \nu_r)^{5:1}$	25 : **5** : 1	0.843250
$\nu_{\rm up}$	$\nu_{\rm middle}$	$\nu_{\rm down}$	M43 sets	a
$\nu_{\rm K}^{5:4}$	$\nu_{\rm K}^{2:1} = \nu_\theta^{5:4}$	$(\nu_\theta - \nu_r)^{2:1}$	5 : **4** : 2	0.756494
$\nu_{\rm K}^{5:4}$	$\nu_{\rm K}^{5:2} = \nu_\theta^{5:4}$	$(\nu_\theta - \nu_r)^{5:2}$	25 : **20** : 8	0.832743
$\nu_{\rm K}^{4:3}$	$\nu_{\rm K}^{5:2} = \nu_\theta^{4:3}$	$(\nu_\theta - \nu_r)^{5:2}$	20 : **15** : 6	0.866061
$\nu_{\rm K}^{3:2}$	$\nu_{\rm K}^{5:2} = \nu_\theta^{3:2}$	$(\nu_\theta - \nu_r)^{5:2}$	15 : **10** : 4	0.894083
$\nu_{\rm K}^{5:4}$	$\nu_{\rm K}^{3:1} = \nu_\theta^{5:4}$	$(\nu_\theta - \nu_r)^{3:1}$	15 : **12** : 4	0.903699
$\nu_{\rm K}^{4:3}$	$\nu_{\rm K}^{3:1} = \nu_\theta^{4:3}$	$(\nu_\theta - \nu_r)^{3:1}$	4 : **3** : 1	0.930913
$\nu_{\rm K}^{3:2}$	$\nu_{\rm K}^{3:1} = \nu_\theta^{3:2}$	$(\nu_\theta - \nu_r)^{3:1}$	9 : **6** : 2	0.952228
$\nu_{\rm K}^{5:3}$	$\nu_{\rm K}^{3:1} = \nu_\theta^{5:3}$	$(\nu_\theta - \nu_r)^{3:1}$	5 : **3** : 1	0.958675

Table 7. *(continued)*

$\nu_{\rm up}$	$\nu_{\rm middle}$	$\nu_{\rm down}$	M44 sets	a
$\nu_{\rm K}^{4:3}$	$\nu_{\rm K}^{2:1} = (\nu_\theta - \nu_r)^{4:3}$	$(\nu_\theta - \nu_r)^{2:1}$	8 : **6** : 3	0.662659
$\nu_{\rm K}^{5:2}$	$\nu_{\rm K}^{4:1} = (\nu_\theta - \nu_r)^{5:2}$	$(\nu_\theta - \nu_r)^{4:1}$	10 : **4** : 1	0.899182
$\nu_{\rm K}^{3:1}$	$\nu_{\rm K}^{4:1} = (\nu_\theta - \nu_r)^{3:1}$	$(\nu_\theta - \nu_r)^{4:1}$	12 : **4** : 1	0.985873
$\nu_{\rm K}^{5:2}$	$\nu_{\rm K}^{5:1} = (\nu_\theta - \nu_r)^{5:2}$	$(\nu_\theta - \nu_r)^{5:1}$	25 : **10** : 2	0.294779
$\nu_{\rm K}^{3:1}$	$\nu_{\rm K}^{5:1} = (\nu_\theta - \nu_r)^{3:1}$	$(\nu_\theta - \nu_r)^{5:1}$	15 : **5** : 1	0.928691
$\nu_{\rm up}$	$\nu_{\rm middle}$	$\nu_{\rm down}$	M45 sets	a
$\nu_\theta^{5:4}$	$\nu_{\rm K}^{2:1} = (\nu_{\rm K} - \nu_r)^{5:4}$	$(\nu_\theta - \nu_r)^{2:1}$	5 : **4** : 2	0.364986
$\nu_\theta^{4:3}$	$\nu_{\rm K}^{2:1} = (\nu_{\rm K} - \nu_r)^{4:3}$	$(\nu_\theta - \nu_r)^{2:1}$	8 : **6** : 3	0.137701
$\nu_\theta^{5:4}$	$\nu_{\rm K}^{5:2} = (\nu_{\rm K} - \nu_r)^{5:4}$	$(\nu_\theta - \nu_r)^{5:2}$	25 : **20** : 8	0.684415
$\nu_\theta^{4:3}$	$\nu_{\rm K}^{5:2} = (\nu_{\rm K} - \nu_r)^{4:3}$	$(\nu_\theta - \nu_r)^{5:2}$	20 : **15** : 6	0.578981
$\nu_\theta^{3:2}$	$\nu_{\rm K}^{5:2} = (\nu_{\rm K} - \nu_r)^{3:2}$	$(\nu_\theta - \nu_r)^{5:2}$	15 : **10** : 4	0.241782
$\nu_\theta^{5:4}$	$\nu_{\rm K}^{3:1} = (\nu_{\rm K} - \nu_r)^{5:4}$	$(\nu_\theta - \nu_r)^{3:1}$	15 : **12** : 4	0.851471
$\nu_\theta^{4:3}$	$\nu_{\rm K}^{3:1} = (\nu_{\rm K} - \nu_r)^{4:3}$	$(\nu_\theta - \nu_r)^{3:1}$	4 : **3** : 1	0.795501
$\nu_\theta^{3:2}$	$\nu_{\rm K}^{3:1} = (\nu_{\rm K} - \nu_r)^{3:2}$	$(\nu_\theta - \nu_r)^{3:1}$	9 : **6** : 2	0.621812
$\nu_\theta^{5:3}$	$\nu_{\rm K}^{3:1} = (\nu_{\rm K} - \nu_r)^{5:3}$	$(\nu_\theta - \nu_r)^{3:1}$	5 : **3** : 1	0.308179
$\nu_\theta^{3:2}$	$\nu_{\rm K}^{4:1} = (\nu_{\rm K} - \nu_r)^{3:2}$	$(\nu_\theta - \nu_r)^{4:1}$	6 : **4** : 1	0.956880
$\nu_\theta^{5:3}$	$\nu_{\rm K}^{4:1} = (\nu_{\rm K} - \nu_r)^{5:3}$	$(\nu_\theta - \nu_r)^{4:1}$	20 : **12** : 3	0.858169
$\nu_\theta^{2:1}$	$\nu_{\rm K}^{4:1} = (\nu_{\rm K} - \nu_r)^{2:1}$	$(\nu_\theta - \nu_r)^{4:1}$	8 : **4** : 1	0.373293
$\nu_\theta^{2:1}$	$\nu_{\rm K}^{5:1} = (\nu_{\rm K} - \nu_r)^{2:1}$	$(\nu_\theta - \nu_r)^{5:1}$	10 : **5** : 1	0.909266

Table 7. *(continued)*

$\nu_{\rm up}$	$\nu_{\rm middle}$	$\nu_{\rm down}$	M51 sets	a
$\nu_\theta^{5:3}$	$\nu_\theta^{5:2}=\nu_r^{5:3}$	$(\nu_{\rm K}-\nu_r)^{5:2}$	25 : **15** : 6	0.955966
$\nu_\theta^{2:1}$	$\nu_\theta^{5:2}=\nu_r^{2:1}$	$(\nu_{\rm K}-\nu_r)^{5:2}$	10 : **5** : 2	0.936010
$\nu_\theta^{3:2}$	$\nu_\theta^{3:1}=\nu_r^{3:2}$	$(\nu_{\rm K}-\nu_r)^{3:1}$	9 : **6** : 2	0.885275
$\nu_\theta^{5:3}$	$\nu_\theta^{3:1}=\nu_r^{5:3}$	$(\nu_{\rm K}-\nu_r)^{3:1}$	5 : **3** : 1	0.760403
$\nu_\theta^{2:1}$	$\nu_\theta^{3:1}=\nu_r^{2:1}$	$(\nu_{\rm K}-\nu_r)^{3:1}$	6 : **3** : 1	0.692253
$\nu_\theta^{5:2}$	$\nu_\theta^{3:1}=\nu_r^{5:2}$	$(\nu_{\rm K}-\nu_r)^{3:1}$	15 : **6** : 2	0.802951
$\nu_\theta^{4:3}$	$\nu_\theta^{4:1}=\nu_r^{4:3}$	$(\nu_{\rm K}-\nu_r)^{4:1}$	16 : **12** : 3	0.778856
$\nu_\theta^{3:2}$	$\nu_\theta^{4:1}=\nu_r^{3:2}$	$(\nu_{\rm K}-\nu_r)^{4:1}$	6 : **4** : 1	0.184900
$\nu_\theta^{3:1}$	$\nu_\theta^{4:1}=\nu_r^{3:1}$	$(\nu_{\rm K}-\nu_r)^{4:1}$	12 : **4** : 1	0.153782
$\nu_\theta^{4:1}$	$\nu_\theta^{4:1}=\nu_r^{4:1}$	$(\nu_{\rm K}-\nu_r)^{4:1}$	16 : **4** : 1	0.992768 0.738425
$\nu_\theta^{5:4}$	$\nu_\theta^{5:1}=\nu_r^{5:4}$	$(\nu_{\rm K}-\nu_r)^{5:1}$	25 : **20** : 4	0.704324
$\nu_\theta^{4:1}$	$\nu_\theta^{5:1}=\nu_r^{4:1}$	$(\nu_{\rm K}-\nu_r)^{5:1}$	20 : **5** : 1	0.999623
$\nu_\theta^{5:1}$	$\nu_\theta^{5:1}=\nu_r^{5:1}$	$(\nu_{\rm K}-\nu_r)^{5:1}$	25 : **5** : 1	0.995744 0.481907

$\nu_{\rm up}$	$\nu_{\rm middle}$	$\nu_{\rm down}$	M52 sets	a
$\nu_{\rm K}^{2:1}$	$\nu_\theta^{5:2}=\nu_r^{2:1}$	$(\nu_{\rm K}-\nu_r)^{5:2}$	10 : **5** : 2	0.972707
$\nu_{\rm K}^{5:2}$	$\nu_\theta^{5:2}=\nu_r^{5:2}$	$(\nu_{\rm K}-\nu_r)^{5:2}$	25 : **10** : 4	0.932020
$\nu_{\rm K}^{3:1}$	$\nu_\theta^{5:2}=\nu_r^{3:1}$	$(\nu_{\rm K}-\nu_r)^{5:2}$	15 : **5** : 2	0.949921
$\nu_{\rm K}^{4:1}$	$\nu_\theta^{5:2}=\nu_r^{4:1}$	$(\nu_{\rm K}-\nu_r)^{5:2}$	20 : **5** : 2	0.989062
$\nu_{\rm K}^{5:3}$	$\nu_\theta^{3:1}=\nu_r^{5:3}$	$(\nu_{\rm K}-\nu_r)^{3:1}$	5 : **3** : 1	0.917082
$\nu_{\rm K}^{2:1}$	$\nu_\theta^{3:1}=\nu_r^{2:1}$	$(\nu_{\rm K}-\nu_r)^{3:1}$	6 : **3** : 1	0.709136
$\nu_{\rm K}^{5:2}$	$\nu_\theta^{3:1}=\nu_r^{5:2}$	$(\nu_{\rm K}-\nu_r)^{3:1}$	15 : **6** : 2	0.717384
$\nu_{\rm K}^{3:1}$	$\nu_\theta^{3:1}=\nu_r^{3:1}$	$(\nu_{\rm K}-\nu_r)^{3:1}$	9 : **3** : 1	0.793520
$\nu_{\rm K}^{4:1}$	$\nu_\theta^{3:1}=\nu_r^{4:1}$	$(\nu_{\rm K}-\nu_r)^{3:1}$	12 : **3** : 1	0.907095
$\nu_{\rm K}^{5:1}$	$\nu_\theta^{3:1}=\nu_r^{5:1}$	$(\nu_{\rm K}-\nu_r)^{3:1}$	15 : **3** : 1	0.964119
$\nu_{\rm K}^{3:2}$	$\nu_\theta^{4:1}=\nu_r^{3:2}$	$(\nu_{\rm K}-\nu_r)^{4:1}$	6 : **4** : 1	0.273678
$\nu_{\rm K}^{3:1}$	$\nu_\theta^{4:1}=\nu_r^{3:1}$	$(\nu_{\rm K}-\nu_r)^{4:1}$	12 : **4** : 1	0.117032
$\nu_{\rm K}^{4:1}$	$\nu_\theta^{4:1}=\nu_r^{4:1}$	$(\nu_{\rm K}-\nu_r)^{4:1}$	16 : **4** : 1	0.553757
$\nu_{\rm K}^{5:1}$	$\nu_\theta^{4:1}=\nu_r^{5:1}$	$(\nu_{\rm K}-\nu_r)^{4:1}$	20 : **4** : 1	0.757588
$\nu_{\rm K}^{5:1}$	$\nu_\theta^{5:1}=\nu_r^{5:1}$	$(\nu_{\rm K}-\nu_r)^{5:1}$	25 : **5** : 1	0.340368

Table 7. *(continued)*

ν_{up}	ν_{middle}	ν_{down}	M53 sets	a
$\nu_{\mathrm{K}}^{5:4}$	ν_θ	$(\nu_{\mathrm{K}}-\nu_r)^{5:4}$	25 : **20** : 16	0.852956
$\nu_{\mathrm{K}}^{4:3}$	ν_θ	$(\nu_{\mathrm{K}}-\nu_r)^{5:4}$	20 : **15** : 12	0.953845
$\nu_{\mathrm{K}}^{5:4}$	ν_θ	$(\nu_{\mathrm{K}}-\nu_r)^{4:3}$	5 : **4** : 3	0.882162
$\nu_{\mathrm{K}}^{4:3}$	ν_θ	$(\nu_{\mathrm{K}}-\nu_r)^{4:3}$	16 : **12** : 9	0.985324
$\nu_{\mathrm{K}}^{5:4}$	ν_θ	$(\nu_{\mathrm{K}}-\nu_r)^{3:2}$	15 : **12** : 8	0.942336
ν_{up}	ν_{middle}	ν_{down}	M54 sets	a
$\nu_{\mathrm{K}}^{5:4}$	$\nu_\theta^{5:4}=(\nu_\theta-\nu_r)^{5:4}$	$(\nu_{\mathrm{K}}-\nu_r)^{5:4}$	25 : **20** : 16	0.532710
$\nu_{\mathrm{K}}^{4:3}$	$\nu_\theta^{5:4}=(\nu_\theta-\nu_r)^{4:3}$	$(\nu_{\mathrm{K}}-\nu_r)^{5:4}$	20 : **15** : 12	0.641973
$\nu_{\mathrm{K}}^{3:2}$	$\nu_\theta^{5:4}=(\nu_\theta-\nu_r)^{3:2}$	$(\nu_{\mathrm{K}}-\nu_r)^{5:4}$	15 : **10** : 8	0.777089
$\nu_{\mathrm{K}}^{5:3}$	$\nu_\theta^{5:4}=(\nu_\theta-\nu_r)^{5:3}$	$(\nu_{\mathrm{K}}-\nu_r)^{5:4}$	25 : **15** : 12	0.854595
$\nu_{\mathrm{K}}^{2:1}$	$\nu_\theta^{5:4}=(\nu_\theta-\nu_r)^{2:1}$	$(\nu_{\mathrm{K}}-\nu_r)^{5:4}$	10 : **5** : 4	0.933685
$\nu_{\mathrm{K}}^{5:2}$	$\nu_\theta^{5:4}=(\nu_\theta-\nu_r)^{5:2}$	$(\nu_{\mathrm{K}}-\nu_r)^{5:4}$	25 : **10** : 8	0.977777
$\nu_{\mathrm{K}}^{5:4}$	$\nu_\theta^{4:3}=(\nu_\theta-\nu_r)^{5:4}$	$(\nu_{\mathrm{K}}-\nu_r)^{4:3}$	5 : **4** : 3	0.463299
$\nu_{\mathrm{K}}^{4:3}$	$\nu_\theta^{4:3}=(\nu_\theta-\nu_r)^{4:3}$	$(\nu_{\mathrm{K}}-\nu_r)^{4:3}$	16 : **12** : 9	0.590528
$\nu_{\mathrm{K}}^{3:2}$	$\nu_\theta^{4:3}=(\nu_\theta-\nu_r)^{3:2}$	$(\nu_{\mathrm{K}}-\nu_r)^{4:3}$	6 : **4** : 3	0.746592
$\nu_{\mathrm{K}}^{5:3}$	$\nu_\theta^{4:3}=(\nu_\theta-\nu_r)^{5:3}$	$(\nu_{\mathrm{K}}-\nu_r)^{4:3}$	20 : **12** : 9	0.835260
$\nu_{\mathrm{K}}^{2:1}$	$\nu_\theta^{4:3}=(\nu_\theta-\nu_r)^{2:1}$	$(\nu_{\mathrm{K}}-\nu_r)^{4:3}$	8 : **4** : 3	0.924992
$\nu_{\mathrm{K}}^{5:2}$	$\nu_\theta^{4:3}=(\nu_\theta-\nu_r)^{5:2}$	$(\nu_{\mathrm{K}}-\nu_r)^{4:3}$	10 : **4** : 3	0.974537
$\nu_{\mathrm{K}}^{3:1}$	$\nu_\theta^{4:3}=(\nu_\theta-\nu_r)^{3:1}$	$(\nu_{\mathrm{K}}-\nu_r)^{4:3}$	12 : **4** : 3	0.991126
$\nu_{\mathrm{K}}^{5:4}$	$\nu_\theta^{3:2}=(\nu_\theta-\nu_r)^{5:4}$	$(\nu_{\mathrm{K}}-\nu_r)^{3:2}$	15 : **12** : 8	0.292271
$\nu_{\mathrm{K}}^{4:3}$	$\nu_\theta^{3:2}=(\nu_\theta-\nu_r)^{4:3}$	$(\nu_{\mathrm{K}}-\nu_r)^{3:2}$	4 : **3** : 2	0.465645
$\nu_{\mathrm{K}}^{3:2}$	$\nu_\theta^{3:2}=(\nu_\theta-\nu_r)^{3:2}$	$(\nu_{\mathrm{K}}-\nu_r)^{3:2}$	9 : **6** : 4	0.673939
$\nu_{\mathrm{K}}^{5:3}$	$\nu_\theta^{3:2}=(\nu_\theta-\nu_r)^{5:3}$	$(\nu_{\mathrm{K}}-\nu_r)^{3:2}$	5 : **3** : 2	0.789734
$\nu_{\mathrm{K}}^{2:1}$	$\nu_\theta^{3:2}=(\nu_\theta-\nu_r)^{2:1}$	$(\nu_{\mathrm{K}}-\nu_r)^{3:2}$	6 : **3** : 2	0.905012
$\nu_{\mathrm{K}}^{5:2}$	$\nu_\theta^{3:2}=(\nu_\theta-\nu_r)^{5:2}$	$(\nu_{\mathrm{K}}-\nu_r)^{3:2}$	15 : **6** : 4	0.968241
$\nu_{\mathrm{K}}^{3:1}$	$\nu_\theta^{3:2}=(\nu_\theta-\nu_r)^{3:1}$	$(\nu_{\mathrm{K}}-\nu_r)^{3:2}$	9 : **3** : 2	0.987798
$\nu_{\mathrm{K}}^{5:4}$	$\nu_\theta^{5:3}=(\nu_\theta-\nu_r)^{5:4}$	$(\nu_{\mathrm{K}}-\nu_r)^{5:3}$	25 : **20** : 12	0.069653
$\nu_{\mathrm{K}}^{4:3}$	$\nu_\theta^{5:3}=(\nu_\theta-\nu_r)^{4:3}$	$(\nu_{\mathrm{K}}-\nu_r)^{5:3}$	20 : **15** : 9	0.306291
$\nu_{\mathrm{K}}^{3:2}$	$\nu_\theta^{5:3}=(\nu_\theta-\nu_r)^{3:2}$	$(\nu_{\mathrm{K}}-\nu_r)^{5:3}$	15 : **10** : 6	0.583540
$\nu_{\mathrm{K}}^{5:3}$	$\nu_\theta^{5:3}=(\nu_\theta-\nu_r)^{5:3}$	$(\nu_{\mathrm{K}}-\nu_r)^{5:3}$	25 : **15** : 9	0.733910
$\nu_{\mathrm{K}}^{2:1}$	$\nu_\theta^{5:3}=(\nu_\theta-\nu_r)^{2:1}$	$(\nu_{\mathrm{K}}-\nu_r)^{5:3}$	10 : **5** : 3	0.880994
$\nu_{\mathrm{K}}^{5:2}$	$\nu_\theta^{5:3}=(\nu_\theta-\nu_r)^{5:2}$	$(\nu_{\mathrm{K}}-\nu_r)^{5:3}$	25 : **10** : 6	0.961517
$\nu_{\mathrm{K}}^{3:1}$	$\nu_\theta^{5:3}=(\nu_\theta-\nu_r)^{3:1}$	$(\nu_{\mathrm{K}}-\nu_r)^{5:3}$	15 : **5** : 3	0.986726
$\nu_{\mathrm{K}}^{3:2}$	$\nu_\theta^{2:1}=(\nu_\theta-\nu_r)^{3:2}$	$(\nu_{\mathrm{K}}-\nu_r)^{2:1}$	3 : **2** : 1	0.336030

Table 7. *(continued)*

$\nu_{\rm up}$	$\nu_{\rm middle}$	$\nu_{\rm down}$	M55 sets	a
$\nu_{\rm K}^{5:3}$	$\nu_\theta^{2:1} = (\nu_\theta - \nu_r)^{5:3}$	$(\nu_{\rm K} - \nu_r)^{2:1}$	10 : **6** : 3	0.584608
$\nu_{\rm K}^{2:1}$	$\nu_\theta^{2:1} = (\nu_\theta - \nu_r)^{2:1}$	$(\nu_{\rm K} - \nu_r)^{2:1}$	4 : **2** : 1	0.817798
$\nu_{\rm K}^{5:2}$	$\nu_\theta^{2:1} = (\nu_\theta - \nu_r)^{5:2}$	$(\nu_{\rm K} - \nu_r)^{2:1}$	5 : **2** : 1	0.943948
$\nu_{\rm K}^{3:1}$	$\nu_\theta^{2:1} = (\nu_\theta - \nu_r)^{3:1}$	$(\nu_{\rm K} - \nu_r)^{2:1}$	6 : **2** : 1	0.986208
$\nu_{\rm K}^{5:1}$	$\nu_\theta^{2:1} = (\nu_\theta - \nu_r)^{5:1}$	$(\nu_{\rm K} - \nu_r)^{2:1}$	10 : **2** : 1	0.998643
$\nu_{\rm K}^{5:3}$	$\nu_\theta^{5:2} = (\nu_\theta - \nu_r)^{5:3}$	$(\nu_{\rm K} - \nu_r)^{5:2}$	25 : **15** : 6	0.234708
$\nu_{\rm K}^{2:1}$	$\nu_\theta^{5:2} = (\nu_\theta - \nu_r)^{2:1}$	$(\nu_{\rm K} - \nu_r)^{5:2}$	10 : **5** : 2	0.673737
$\nu_{\rm K}^{5:2}$	$\nu_\theta^{5:2} = (\nu_\theta - \nu_r)^{5:2}$	$(\nu_{\rm K} - \nu_r)^{5:2}$	25 : **10** : 4	0.900086
$\nu_{\rm K}^{3:1}$	$\nu_\theta^{5:2} = (\nu_\theta - \nu_r)^{3:1}$	$(\nu_{\rm K} - \nu_r)^{5:2}$	15 : **5** : 2	0.979611
$\nu_{\rm K}^{2:1}$	$\nu_\theta^{3:1} = (\nu_\theta - \nu_r)^{2:1}$	$(\nu_{\rm K} - \nu_r)^{3:1}$	6 : **3** : 1	0.451536
$\nu_{\rm K}^{5:2}$	$\nu_\theta^{3:1} = (\nu_\theta - \nu_r)^{5:2}$	$(\nu_{\rm K} - \nu_r)^{3:1}$	15 : **6** : 2	0.827671
$\nu_{\rm K}^{3:1}$	$\nu_\theta^{3:1} = (\nu_\theta - \nu_r)^{3:1}$	$(\nu_{\rm K} - \nu_r)^{3:1}$	9 : **3** : 1	0.959038
$\nu_{\rm K}^{5:2}$	$\nu_\theta^{4:1} = (\nu_\theta - \nu_r)^{5:2}$	$(\nu_{\rm K} - \nu_r)^{4:1}$	10 : **4** : 1	0.571544
$\nu_{\rm K}^{3:1}$	$\nu_\theta^{4:1} = (\nu_\theta - \nu_r)^{3:1}$	$(\nu_{\rm K} - \nu_r)^{4:1}$	12 : **4** : 1	0.862765
$\nu_{\rm K}^{5:2}$	$\nu_\theta^{5:1} = (\nu_\theta - \nu_r)^{5:2}$	$(\nu_{\rm K} - \nu_r)^{5:1}$	25 : **10** : 2	0.121260
$\nu_{\rm K}^{3:1}$	$\nu_\theta^{5:1} = (\nu_\theta - \nu_r)^{3:1}$	$(\nu_{\rm K} - \nu_r)^{5:1}$	15 : **5** : 1	0.679004
$\nu_\theta^{5:4}$	$\nu_\theta^{5:3} = (\nu_{\rm K} - \nu_r)^{5:4}$	$(\nu_{\rm K} - \nu_r)^{5:3}$	25 : **20** : 12	0.509812 0.971209
$\nu_\theta^{5:2}$	$\nu_\theta^{5:1} = (\nu_{\rm K} - \nu_r)^{5:2}$	$(\nu_{\rm K} - \nu_r)^{5:1}$	25 : **10** : 2	0.612861

5.2 Strong resonant phenomena

The presented results show that usually the triple frequency sets fixing the black hole spin a occur at two different radii. However, there are some interesting cases when the triple frequencies occur at the same radius. Then one could expect intuitively higher probability for the resonant phenomena to arise, especially in the cases of ratios of very low integers $3:2:1, 4:3:2, 6:3:2, \ldots$ as a causally related cooperation of the resonances at the given radius should come into the game. A crucial role is expected for direct resonances of oscillations with all three orbital frequencies characterized by a triple frequency ratio set (s, t, u being small natural numbers)

$$\nu_{\mathrm{K}} : \nu_\theta : \nu_r = s : t : u \,,$$

when strong resonant phenomena are possible (Stuchlík et al., 2007b). Assuming two resonances with ratios $\nu_{\mathrm{K}} : \nu_\theta = s : t$ and $\nu_{\mathrm{K}} : \nu_r = s : u$ sharing the same radius x, we can determine the radius giving $s : t : u$ ratio from equation (Stuchlík et al., 2007b)

$$x\,(s/u, t/u) \equiv 6(s/u)^2 \Big\{ \pm 2\sqrt{2}\sqrt{(t/u-1)(t/u+1)\left[3(s/u)^2 - (t/u)^2 - 2\right]} - \left[(t/u)^2 + 5\right] + 6(s/u)^2 \Big\}^{-1} ,$$

and the related black hole spin is given by

$$a(x(s/u, t/u), u/s) \equiv \frac{\sqrt{x}}{3}\left\{4 \pm \sqrt{-2 + 3x\left[1 - (u/s)^2\right]}\right\} . \tag{9}$$

A detailed discussion of the black holes admitting strong resonant phenomena is for small integer ($s \leq 5$) given in Stuchlík et al. (2007b). Here, all the results are contained in Tables 5–7. Since $x(s, t, u)$ can be considered as a two-parameter $(s/u, t/u)$ family of solutions for the shared resonant radii, we are able to give the results of finding the strong resonance radii and the corresponding spin in Fig. 5.

Of special interest seems to be the case of the "magic" spin $a = 0.983$, when the Keplerian and epicyclic frequencies are in the ratio $\nu_{\mathrm{K}} : \nu_\theta : \nu_r = 3 : 2 : 1$ at the common radius $x_{3:2:1} = 2.3947$ (see left panel in Fig. 6). In fact, this case involves rather extended structure of resonances with $\nu_{\mathrm{K}} : \nu_r = 3:1$, $\nu_{\mathrm{K}} : \nu_\theta = 3:2$, $\nu_\theta : \nu_r = 2:1$. Notice that in this case also the simple combinational frequencies could be in this small integer ratio as

$$\frac{\nu_{\mathrm{K}}}{\nu_\theta - \nu_r} = \frac{3}{1} , \qquad \frac{\nu_{\mathrm{K}}}{\nu_{\mathrm{K}} - \nu_r} = \frac{3}{2} , \qquad \frac{\nu_\theta}{\nu_\theta - \nu_r} = \frac{2}{1} .$$

Of course we obtain the strongest possible resonances when the beat frequencies enter the resonance satisfying the conditions

$$\frac{\nu_\theta + \nu_r}{\nu_{\mathrm{K}}} = \frac{3}{3} = 1 , \qquad \frac{\nu_\theta}{\nu_{\mathrm{K}} - \nu_r} = \frac{2}{2} = 1 , \qquad \frac{\nu_r}{\nu_{\mathrm{K}} - \nu_\theta} = 1 , \qquad \frac{\nu_\theta - \nu_r}{\nu_r} = 1 .$$

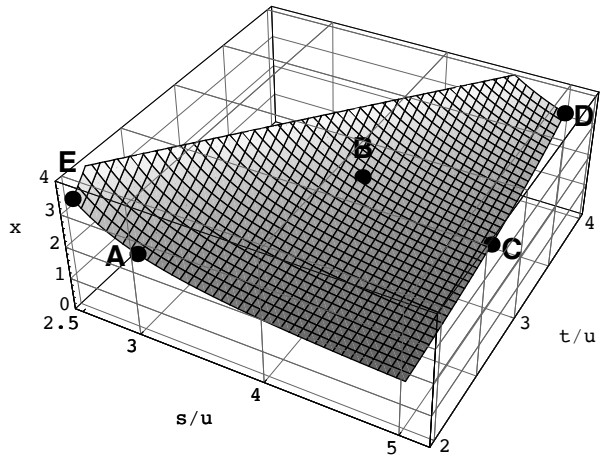

Figure 5. The function $x(s/u, t/u)$ determining the triple frequency ratio set $s:t:u$ at the same radius. The points represents the ratio: $s:t:u = 3:2:1$ (A), $4:3:1$ (B), $5:3:1$ (C), $5:4:1$ (D), $5:4:2$ (E).

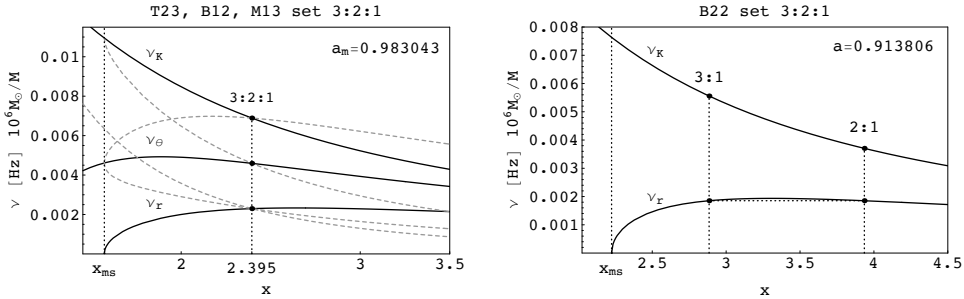

Figure 6. *Left:* The case of a "magic" spin, when the strongest resonances could occur at the same radius. For completeness we present the relevant simple combinational frequencies $\nu_\theta - \nu_r$, $\nu_\theta + \nu_r$, $\nu_\mathrm{K} - \nu_\theta$, $\nu_\mathrm{K} - \nu_r$ (grey dashed lines). Notice that the "magic" spin $a_\mathrm{m} = 0.983$ represents the only case when the combinational and direct orbital frequencies coincide at the shared resonance radius. *Right:* Another example of the characteristic set $3:2:1$ that appear at different radii; this case gives the best estimate of mass of Sgr A*.

It should be stressed that beside the case of strong resonances between oscillations with ν_K, ν_θ, ν_r sharing the same radius, the characteristic set $3:2:1$ could appear also due to resonances at different radii (see right panel in Fig. 6), namely in B22, B15, B24, B25, B45, T45, M14, M24 and M54 cases.

Another interesting exceptional case occurs, e.g., for the spin $a = 0.958$, when two frequencies with the same magnitude (and ratio) are in resonance of different origin at two different radii, see Fig. 3g.

6 DISCUSSION

The multi-resonant model of QPOs assumes that internal parametric and/or forced resonant non-linear phenomena can occur between oscillations with the vertical and radial epicyclic frequency and/or with the orbital (Keplerian) frequency and their simple combinations in both thin and thick accretion discs rotating around black holes or neutron stars. It is possible that the resonances are excited for different internal and external reasons, at different radii within the accretion discs, and two pairs (or more complex combinations) of the resonant frequencies could occur in general situations. For simplicity, we consider here two pairs of the frequencies, or their special reductions. In this case one can determine both the spin and mass of the black hole with precision higher than for individual twin peaks, but it would be rather difficult to identify the relevant combination of the resonances.

For special values of the black hole spin, the bottom (top) epicyclic frequencies could be equal at different radii, since there exist local extrema of the radial profiles of both the epicyclic frequencies in the Kerr black hole spacetimes. If Keplerian frequency or beat frequencies could also enter the resonance phenomena, top, bottom, or mixed coinciding frequencies in various versions of resonance are possible. We have shown that in such situations, the ratio of the triples of the resonance frequencies is directly related to the black hole spin, independently of the black hole mass. Such a possibility of direct measurement of the black hole spin is very important because of relatively high uncertainties in observational estimates of the black hole mass, necessary for determination of the black hole spin in general resonant phenomena (Török et al., 2005) or in black hole spin determinations based on the measurements of profiled spectral lines (Laor, 1991; Karas et al., 1992; Dovčiak et al., 2004; Fabian and Miniutti, 2005; Zakharov, 2003; Zakharov and Repin, 2006). A similar method could in principle be used in neutron star X-ray binaries, if eigenfrequencies of the resonant points related to the observed QPOs are determined.

6.1 Black holes

The relation between the tripled frequency ratios and the black hole spin is presented in Tables 5–7 reflecting all the possible cases of the bottom, top and mixed frequency identities. Of course, there could be real difficulty in choosing the proper combination of the resonance model versions in analysing data from concrete sources. Clearly, then all the relevant data have to be combined and other methods for the black hole spin measurement have to be applied, e.g., those based on the spectrum continuum (McClintock et al., 2006; Middleton et al., 2006; Shafee et al., 2006) and profiled spectral lines (Laor, 1991; Karas et al., 1992; Dovčiak et al., 2004; Fabian and Miniutti, 2005; Zakharov, 2003; Zakharov and Repin, 2006).

Even the method of triple frequency sets must be treated very carefully because of uncertainties of frequency measurement in QPOs (Remillard and McClintock, 2006). In fact, in some versions of the multi-resonance model, even a relatively high precision of the frequency measurements could imply a rather high scatter in the black hole spin. The triple frequency set method could be expected to work quite efficiently in the case of ratios of small integers, as $3:2:1$, $4:3:2$, etc. The other possible frequency sets have to be taken seriously, but the analysis must be very careful for high integers in the triple frequency sets. It is more

and more difficult to distinguish different triple frequency sets with order of the resonances growing, when uncertainties of the frequency measurements are relatively high. We expect that analysis of each concrete source will need an appropriate combination of different methods. Clearly, a detailed analysis of assumed resonance phenomena, both parametric and forced, and their excitation by both external and internal causes must be taken into consideration. Especially, the expected resonance strength and allowed range of resonant frequencies must be treated very carefully.

In fact, when the equations of motion for non-linear oscillations are solved by successive approximations, higher harmonics and combinational frequencies occur in oscillating systems corresponding to higher approximations; as the degree of approximation increases, the strength of the resonances and the resonant frequency width decrease rapidly as shown by Landau and Lifshitz (1976). Therefore, only small integers are allowed in frequency ratios in realistic resonant phenomena and observations in black hole and neutron star systems indicate that the integers $n, m \leq 5$ in agreement with the theory of non-linear oscillations.

Notice that from the point of view of the frequency analysis presented here, the same observational frequency ratios could be obtained if a combinational frequency enters the resonance and then is directly observed, or if direct (e.g., epicyclic) frequencies enter the resonance, but we observe an appropriate combinational (beat) frequency. However, detailed analysis concerning the resonance strength and resonance frequency width gives different detailed results in these two cases (Landau and Lifshitz, 1976).

In the special case of the triple frequency ratios arising in a single radius (or in its close vicinity), the resonant phenomena could occur most frequently and efficiently, as different types of oscillations that enter the resonance at a fixed radius could cooperate, while when arising in different radii they are assumed causally independent. It should be stressed that of special interest are the triple frequency ratio sets of $\nu_{\mathrm{K}} : \nu_\theta : \nu_r = s : t : u$ with s, t, u being small integers corresponding to strong resonance phenomena due to a large variety of possible cooperative resonances (see Stuchlík et al., 2007b). The most promising example of such a special situation arises for the "magic" black hole spin $a = 0.983$, when at the radius $x_{3:2:1} = 2.395$, the frequency ratio is $\nu_{\mathrm{K}} : \nu_\theta : \nu_r = 3 : 2 : 1$. Clearly, in vicinity of black holes with $a = 0.983$, the resonant phenomena should be strongest, as the order of the resonances is of the lowest possible values, and, moreover, all the resonances, including those with beat frequencies, could cooperate efficiently even for frequencies scattered from the exact resonant eigenfrequencies. In fact, we could consider the situation as corresponding to the bottom, top and mixed resonant frequency triples discussed above, but appearing at a common radius.

It is quite instructive to determine, how the frequency measurement precision could influence the black hole spin estimates in this very special case.[1] We give the range of the black hole spin for which the $3 : 2 : 1$ resonant phenomena could be relevant assuming the precision of frequency measurements in the usually reported period of 0.5–2 %. The scatter of the black hole spin related to the frequency measurement errors is shown in Fig. 7. We

[1] Notice that a similar estimate must be realized in analysing data from all sources that could be considered as realistic candidates of a system for which the triple frequency method is applicable.

Table 8. T23, $a_{\rm m} = 0.983043$: the scatter of the black hole spin related to the frequency measurement errors.

$\Delta\nu_{\rm up}$ [%]	$a_{\rm m} - \Delta$	$a_{\rm m} + \Delta$	$\approx \Delta a$ [%]
±0.5	0.980599	0.985449	±0.2
±1.0	0.978117	0.987817	±0.5
±1.5	0.975596	0.990146	±0.7
±2.0	0.973038	0.992436	±1.0

illustrate the situation for the possible versions of resonance, namely T23, T24, T34, B12, B14, B24, M13. We can see that except the case of B12, all the cases give a strong restriction on the dimensionless spin even for the 3 percent error in frequency measurements. On the other hand, for the case of B12, only the 0.5 % measurement error gives a reasonable restriction on a, while even for 1 % error, values of $a > 1$ are allowed. Clearly, if the relevant frequency curves cross in a large (small) relative angle, the spin is determined with high (low) precision. The same rule is relevant in analysing any resonance triple frequency set.

In the case of T23, the detailed results are illustrated by Table 8. We can see that the one percent error in frequency measurement implies an error of 0.005 in spin determination, while three percent frequency error implies 0.015 error in spin determination – in the latter case the period of allowed values of the spin reads $0.9678 < a_{\rm m} < 0.9969$, when the upper limit enters the region of applicability of the extended resonance model (Stuchlík et al., 2006, 2005, 2004). Non-linear resonance of the humpy oscillations and the oscillations with the orbital frequencies could explain the complex frequency sets as those observed in the microquasar GRS 1915+105 (Stuchlík et al., 2007e).

6.2 Sgr A* black hole parameters

The QPOs with frequency ratio $\sim 3:2:1$ were reported for Sgr A* (Aschenbach, 2004; Aschenbach et al., 2004; Török, 2005) and are therefore a properly simple sample to test the multi-resonant models presented here. Although the observations were not confirmed yet, and there are doubts on validity of the data as they are not fully accepted by the astrophysical community, we feel it could be important and interesting to test possible implications of the observations assuming their relevance (Aschenbach, 2007). We have shown that the observed data imply spin a and mass M of Sgr A* black hole not contradicting the mass estimated given by the star orbital motion (Ghez et al., 2005)

$$2.8 \times 10^6\,{\rm M}_\odot < M < 4.6 \times 10^6\,{\rm M}_\odot \qquad (10)$$

considering also the error given by uncertainty in distance measurement to Sgr A*, if the strong resonant model with $\nu_{\rm K} : \nu_\theta : \nu_r = 3:2:1$ is applied (Stuchlík et al., 2007b). Here, we have tested all the relevant versions of the multi-resonant orbital model. The results are summarized in Table 9, including the case of strong resonant phenomena.

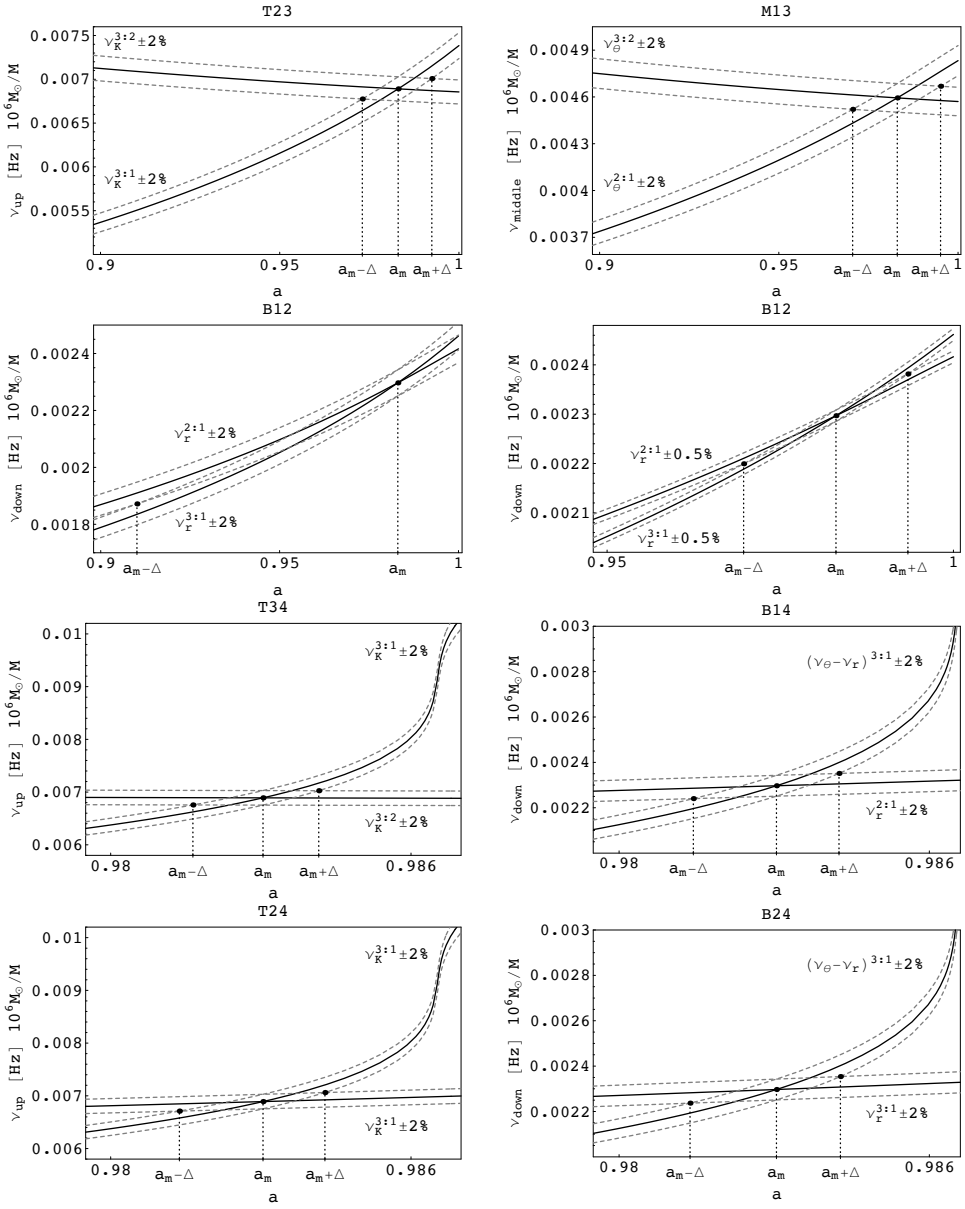

Figure 7. Spin error for the case of the "magic" spin allowing $\nu_{\rm K} : \nu_\theta : \nu_r = 3 : 2 : 1$, $a_{\rm m} = 0.983043$: the scatter of the black hole spin related to the 2% error in frequency measurements. The interval of allowed values of the spin is for T23: $a \in \langle 0.973038, 0.992436\rangle$; for M13: $a \in \langle 0.970599, 0.995125\rangle$; for T34: $a \in \langle 0.981643, 0.984157\rangle$; for B14: $a \in \langle 0.981436, 0.984253\rangle$; for T24 and B24: $a \in \langle 0.981372, 0.98428\rangle$. For the case of B12, only the 0.5% measurement error gives a reasonable restriction on black hole spin: $a \in \langle 0.969714, 0.993428\rangle$ (for 2% measurement error: $a \in \langle 0.91012, 1.01155\rangle$).

Table 9. The black hole spin and mass of Sgr A* calculated for all the relevant versions of the multi-resonant orbital model with assumed observed characteristic frequency ratio set $\nu_{\rm up} : \nu_{\rm middle} : \nu_{\rm down} = 3:2:1$; $\nu_{\rm up} = (1.445 \pm 0.16)$ mHz is used to determine the black hole mass.

$\nu_{\rm up}$	$\nu_{\rm middle}$	$\nu_{\rm down}$	a	$M\left[10^6\,{\rm M}_\odot\right]$
$\nu_{\rm K}$	$\nu_\theta^{3:2}$	$\nu_r^{3:1}$	0.983043	4.293–5.362
$\nu_{\rm K}^{3:1} = \nu_\theta^{3:2}$	$(\nu_{\rm K} - \nu_r)^{3:2}$	$(\nu_\theta - \nu_r)^{3:1}$	0.885010	2.054–2.566
$\nu_\theta^{3:1}$	$\nu_\theta^{2:1}$	$\nu_r^{3:1} = (\nu_{\rm K} - \nu_r)^{2:1}$	0.616894	1.903–2.376
$\nu_\theta^{3:1}$	$\nu_\theta^{2:1}$	$\nu_r^{3:1} = (\nu_{\rm K} - \nu_r)^{2:1}$	0.999667	2.606–3.255
$\nu_{\rm K}^{3:1}$	$\nu_{\rm K}^{2:1}$	ν_r	0.913806	3.463–4.325
$\nu_{\rm K}^{3:1}$	$\nu_{\rm K}^{2:1}$	$\nu_r^{2:1} = (\nu_\theta - \nu_r)^{3:1}$	0.980124	3.983–4.975
$\nu_{\rm K}^{3:1}$	$\nu_\theta^{2:1}$	$\nu_r^{3:1} = (\nu_{\rm K} - \nu_r)^{2:1}$	0.475159	1.733–2.165
$\nu_{\rm K}^{3:1}$	$\nu_\theta^{2:1}$	$(\nu_\theta - \nu_r)^{3:1} = (\nu_{\rm K} - \nu_r)^{2:1}$	0.922985	2.422–3.025
$\nu_{\rm K}^{3:2}$	$\nu_\theta^{2:1} = (\nu_\theta - \nu_r)^{3:2}$	$\nu_r^{2:1}$	0.544870	2.095–2.617
$\nu_{\rm K}^{3:2}$	$\nu_{\rm K}^{2:1} = (\nu_\theta - \nu_r)^{3:2}$	$\nu_r^{2:1}$	0.535413	2.065–2.580
$\nu_{\rm K}^{3:2}$	$\nu_\theta^{2:1} = (\nu_\theta - \nu_r)^{3:2}$	$(\nu_{\rm K} - \nu_r)^{2:1}$	0.336030	1.594–1.991

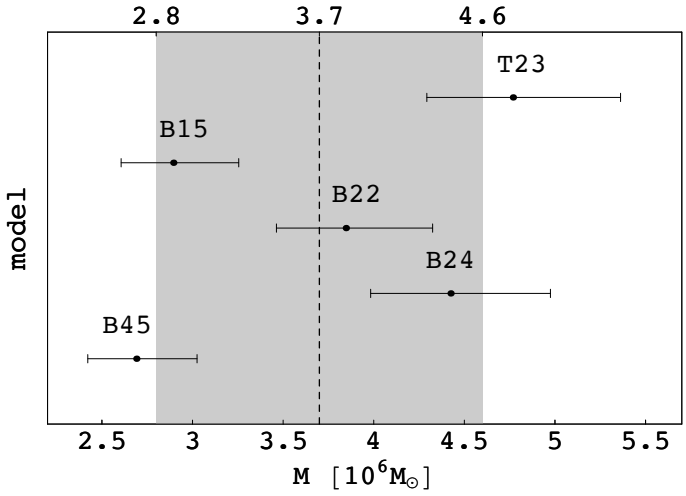

Figure 8. Mass of Sgr A*: five versions of multi-resonance model that are compatible with mass estimates given by the star orbital motion (Ghez et al., 2005), illustrated here by the gray rectangle.

We can see (Fig. 8) that from all of the theoretically allowed versions, only five versions is compatible with observational restrictions from the orbital motion of stars in vicinity of Sgr A*. In all the allowed cases, the black hole spin $a > 0.9$, in agreement with the assumption that Galactic centre black hole should be fast rotating. The best fit is obtained for the spin $a = 0.913806$, and mass $M \in (3.463\text{–}4.325) \times 10^6\,\mathrm{M}_\odot$, with resonances $\nu_\mathrm{K} : \nu_r = 3:1$, $\nu_\mathrm{K} : \nu_r = 2:1$, having a common bottom frequency. For $a = 0.914$, the estimated mass $M \sim 3.9 \times 10^6\,\mathrm{M}_\odot$ is close to the orbital motion estimation $M \sim 3.7 \times 10^6\,\mathrm{M}_\odot$, while in the other four acceptable cases, the difference is much greater, e.g., the strong resonances for the "magic" spin imply $M \sim 4.8 \times 10^6\,\mathrm{M}_\odot$. The model should be further tested and more precise frequency measurements are very important. We have to compare these results to those of the other methods of black hole spin measurement. For Sgr A*, the relativistic precession of the nearby star orbits is very promising (Kraniotis, 2005, 2007).

6.3 Neutron stars

In principle, our method could be applied to the neutron star systems. Recent analysis of QPOs observed in X-ray sources with neutron stars (Török et al., 2007c; Stuchlík et al., 2007f; Belloni et al., 2007; Török, 2007) indicates that two (several) resonances could appear in the neutron star systems. However, the situation is more complex than in the twin peak QPOs observed in black hole systems, where the observed resonant frequencies are quite well fixed in the resonance points.[2] In the neutron star systems, the twin peak frequencies are widely scattered around the resonance point with the frequency ratio usually being close to 3 : 2. The scatter of the twin peak frequencies is correlated and approximated by linear fits (Abramowicz et al., 2005) $\nu_t = A\nu_b + B$, and an anticorrelation of the parameters A, B was predicted by the resonance theory and indicated from observational data related to twelve atoll neutron star X-ray binary systems (Abramowicz et al., 2005). However, in the studies of QPOs phenomena in neutron star sources, the spacetime structure is usually not addressed, or the Schwarzschild spacetime is assumed in the models. We believe that for a deeper understanding of the QPOs phenomenon, especially with relation to the orbital multi-resonance model, the neutron stars have to be represented by the Hartle–Thorne metric relating both the rotation and quadrupole moment of the star (Hartle and Thorne, 1968).

Recent analysis of the neutron star source 4U 1636−53 indicates resonance at two resonance points, namely with frequency ratios 3 : 2, and 5 : 4 (Török et al., 2007c; Stuchlík et al., 2007f; Belloni et al., 2007; Török, 2007); moreover, two resonance points with the same ratios seem to be indicated by analysis of the source 4U 1608−52 (Török, 2007). This means that the QPO frequency linear fits and the anticorrelation data (Abramowicz et al., 2005) related to the 3 : 2 frequency ratio are not quite consistent, being, in the case of at least two sources, contaminated with the data connected to the 5 : 4 resonance. Moreover, there is an indication (Török, 2007) that in other two of the twelve sources (4U 1820−30 and 4U 1735−44), the resonance point is given by the ratio 4 : 3, rather than 3 : 2.

[2] We believe that the fundamental difference reflects the presence of the surface structures and internal magnetic field of neutron stars.

In the case of the source 4U 1636−53, both the resonance points can be related to the same version of the simple combinational resonance. The best possibilities correspond to the total precession resonance model with $\nu_{\rm K} : (\nu_\theta - \nu_r)$ (Török et al., 2007c; Stuchlík et al., 2007f), or to the relativistic precession model with $\nu_{\rm K} : (\nu_{\rm K} - \nu_r)$ (Stella and Vietri, 1999, 1998). The models give qualitatively good agreement with the observed data, but the quantitatively good fitting is possible with inclusion of the neutron star magnetic field influence onto the epicyclic frequencies (Török et al., 2007a).

Recent data, at least for the source 4U 1636−53, indicate very convincingly that the resonance points are both very close to the innermost stable circular geodesics of the Hartle–Thorne spacetime, representing the inner edge of the accretion disc. Therefore, it is quite natural to expect that the resonant oscillations could be forced by some inhomogeneities on the surface of the neutron star. In fact, it is shown (Stuchlík et al., 2007a) that in close vicinity of the neutron star surface, the influence of "mountains" related to the deformations of the neutron star can be very strong, and the excitation of the forced oscillations can be efficient enough.

The resonance points, corresponding to the resonance eigenfrequencies, can be determined as the intersection points of the resonance frequency curve with the lines giving the frequency (integer) ratios. However, there exists an independent and natural method which probably could work in determining observationally the resonance points as the eigenfrequencies of the oscillations in resonance. This method is based on the energy reverse effect discovered by Török (2007); Török et al. (2007d); Török and Stuchlík (2005a), which shows that in the neutron star atoll sources the energy of the quasiperiodic oscillations in the upper and lower frequencies is equal just when the frequency ratio is equal to the exact ratio of small integers, i.e., to the ratio of the resonance eigenfrequencies, while the energy differs when the frequency ratio is different. The energy reverse effect is in agreement with the resonance theory (Horák, 2004), therefore, it is probably reasonable to assume that the frequency of oscillations at the energy reverse point determines eigenfrequencies of the resonance. Of course, one should expect that for a properly chosen resonance curve, both methods will give close results.

In such a way, we are able to study the resonance model in the neutron star systems in a complete way, similarly to the case of the black hole systems. It should be stressed that the results relating the frequency sets and the black hole dimensionless spin are derived for the Kerr spacetimes. Therefore, in the neutron star systems they could be applied in situations when their spacetime is represented by the Kerr geometry with precision high enough, i.e., when the Hartle–Thorne metric parameters are sufficiently close to the special values corresponding to the Kerr geometry.

7 CONCLUSIONS

The triple frequency set method determines the black hole (neutron star) spin with very high precision, but it could work only incidentally, for special values of the spin. However, it is worth to make a detailed scan of all the observational data for the black hole systems in order to look for some candidate systems, since any success in precise determination of the spin could help very much in determining other physical parameters of the system

and to understand a wide scale of astrophysical phenomena.[3] For example, as a possible candidate for such a system could be considered even the black hole system in the Galactic centre Sgr A*, where frequencies with the ratio 3 : 2 : 1 were reported (Aschenbach et al., 2004; Török, 2005), although not confirmed later, making Sgr A* a candidate for a black hole with spin close to the "magic" value $a = 0.983$. However, a better fit is probably related to the spin $a = 0.914$, when the predicted mass $M \sim 3.9 \times 10^6\,\mathrm{M}_\odot$ is very close to the star orbital motion estimate $M \sim 3.7 \times 10^6\,\mathrm{M}_\odot$. Another black hole candidate system for the triple frequency set analysis could be considered in the source NGC 5408 X-1 because of the reported triple of observed frequencies (Strohmayer et al., 2007), for application of extended resonance model see Slaný and Stuchlík (2007).

In Tables 5–7 we present a detailed guide across all the possible triple frequency sets and related values of the black hole spin a, shown for all the possible double combinations of both the direct and simple combinational resonances with the order of individual resonances limited by $n \leq 5$ allowed by recent observations. The presented Table guide includes also the special cases, when the resonances occur at the same radius implying expectation of resonant phenomena in some strong form because of anticipated causally related cooperative effects (see Stuchlík et al., 2007b), or some degenerate cases when the same pair of frequencies appears at different radii. It is clear that comparison of observational data with the guide Tables must be done extremely carefully, as different resonances can give the same triple frequency ratio set and black hole spin. The resonant frequency width and resonance strength, which differ in different versions of the resonant phenomena and depend strongly on the order of the resonance (see Landau and Lifshitz, 1976), have to be considered in detailed analysis of any realistic candidate black hole (or neutron star) system. We expect a relatively realistic possibility to study systems exhibiting low integer ratios in observed triple frequency sets, as 3 : 2 : 1, 4 : 2 : 1, 5 : 4 : 2, 6 : 4 : 3, etc., when scatter of the observed frequencies and their ratios could enable estimates of the order of the resonance involved and determination of its type through the detailed analysis of the resonant phenomena and their comparison with observational data. In systems where the observed frequency ratio sets involve high integers, we have to expect difficulties in differing between theoretical frequency sets with very close ratios.

The efficiency of the black hole spin determination by using the triple frequency set ratios grows strongly with growing precision of the frequency measurements. Therefore, in the case of measurements of very high precision, the method could work even for the frequency sets ratio of high integers, because in resonances of high order the frequencies in the resonance must be tuned very fine in order to let the resonance to work (Landau and Lifshitz, 1976).

On the other hand, in neutron star atoll sources (in six cases studied recently) the observed QPO data could be well fitted by one frequency relation, given by the relativistic precession model or the total precession model, which can explain coupling of twin peak QPOs nearby the small integer frequency ratios 3 : 2, 4 : 3, 5 : 4 by resonant phenom-

[3] In the neutron star atoll sources, the fitting of the observational data by the total precession frequency relations crossing the resonance points enables very precise determination of the neutron star Hartle–Thorne metric parameters M, j, q. On the other hand, this precision of spacetime parameters measurement implies strong restrictions on validity of acceptable equations of state (Stuchlík et al., 2007g,f; Urbanec et al., 2007).

ena (Török et al., 2007c; Stuchlík et al., 2007f; Bakala et al., 2007). However, the frequency fits probably must be slightly corrected by the influence of the neutron star magnetic field on the epicyclic frequencies (Török et al., 2007a). The orbital resonance model and its multi-resonant versions assume equatorial disc structures and their oscillations with frequencies related to the epicyclic frequencies of the equatorial circular orbits. However, it was shown quite recently (Kovář et al., 2007) that halo orbits (i.e., bound orbits concentrated around stable off-equatorial circular orbits) could exist in vicinity of both neutron stars and black holes due to the presence of magnetic fields related to the neutron stars or accretion discs around the neutron stars or black holes. The oscillatory motion related to the halo orbits with epicyclic frequencies related to the off-equatorial circular orbits can, in principle, also explain some of the QPOs oscillations observed in the neutron star or black hole binary systems (Stuchlík and Kovář, 2007).

We can conclude that the multi-resonant model of QPOs based on the orbital motion is capable to explain a wide range of QPO phenomena observed in both black hole and neutron star X-ray binary systems or in supermassive galactic centre (Sgr A*) and intermediate (NGC 5408 X-1) black holes systems. However, it seems that some basic properties of resonant phenomena in black hole and neutron star systems differ, probably because of presence of the surface effect in the neutron star systems. The data analysis indicates that in neutron star systems probably one frequency relation, given by the relativistic precession or the total precession model, could explain data clustering around the resonant points with ratios 3 : 2, 4 : 3, 5 : 4 observed in the six atoll sources investigated recently. In the black hole systems, the QPO data indicate presence of different versions of the multi-resonance model in concrete sources. We can speculate that the strong resonant phenomena allowed in black hole systems with special values of dimensionless spin could be observationally preferred because of wide range of (possibly) cooperating resonant phenomena. One of candidates for such a system seems to be the central black hole in Sgr A*. In any case, a lot of observational and theoretical research is necessary for deeper understanding to the resonant phenomena indicated in black hole system.

ACKNOWLEDGEMENTS

This work was supported by the Czech grants MSM 4781305903, LC06014 and GAČR 205/03/H144.

REFERENCES

Abramowicz, M. A., Barret, D., Bursa, M., Horák, J., Kluźniak, W., Rebusco, P. and Török, G. (2005), A note on the slope-shift anticorrelation in the neutron star kHz QPOs data, in Hledík and Stuchlík (2005), pp. 1–9.

Abramowicz, M. A. and Kluźniak, W. (2001), A precise determination of black hole spin in GRO J1655−40, *Astronomy and Astrophysics*, **374**, pp. L19–L20, arXiv: `astro-ph/0105077`, URL `http://adsabs.harvard.edu/abs/2001A\%26A...374L..19A`.

Aliev, A. N. and Galtsov, D. V. (1981), Radiation from relativistic particles in non-geodesic motion in a strong gravitational field, *Gen. Relativity Gravitation*, **13**, pp. 899–912.

Aschenbach, B. (2004), Measuring mass and angular momentum of black holes with high-frequency quasi-periodic oscillations, *Astronomy and Astrophysics*, **425**, pp. 1075–1082, arXiv: astro-ph/0406545.

Aschenbach, B. (2007), Measurement of Mass and Spin of Black Holes with QPOs, *Chinese Astronom. Astrophys.*, accepted for publication, arXiv: 0710.3454.

Aschenbach, B., Grosso, N., Porquet, D. and Predehl, P. (2004), X-ray flares reveal mass and angular momentum of the Galactic Center black hole, *Astronomy and Astrophysics*, **417**, pp. 71–78, arXiv: astro-ph/0401589.

Bakala, P., Šrámková, E., Stuchlík, Z. and Török, G. (2007), Dipole magnetic field on a Schwarzschild background and related epicyclic frequencies, pp. 1–10, this volume.

Barret, D., Olive, J.-F. and Miller, M. C. (2005), An abrupt drop in the coherence of the lower kilohertz QPO in 4U 1636−536, *Monthly Notices Roy. Astronom. Soc.*, **361**, pp. 855–860.

Belloni, T., Méndez, M. and Homan, J. (2005), The distribution of kHz QPO frequencies in bright low mass X-ray binaries, *Astronomy and Astrophysics*, **437**, pp. 209–216.

Belloni, T., Méndez, M. and Homan, J. (2007), On the kHz QPO frequency correlations in bright neutron star X-ray binaries, *Monthly Notices Roy. Astronom. Soc.*, **376**(3), pp. 1133–1138, arXiv: astro-ph/0702157.

Dovčiak, M., Karas, V., Martocchia, A., Matt, G. and Yaqoob, T. (2004), An XSPEC model to explore spectral features from black-hole sources, in Hledík and Stuchlík (2004), pp. 33–73, arXiv: astro-ph/0407330.

Fabian, A. C. and Miniutti, G. (2005), *Kerr Spacetime: Rotating Black Holes in General Relativity*, Cambridge University Press, Cambridge, eprint astro-ph/0507409 is a part of this book, arXiv: astro-ph/0507409.

Ghez, A. M., Salim, S., Hornstein, S. D., Tanner, A., Lu, J. R., Morris, M., Becklin, E. E. and Duchêne, G. (2005), Stellar Orbits around the Galactic Center Black Hole, *Astrophys. J.*, **620**, pp. 744–757, arXiv: astro-ph/0306130.

Hartle, J. B. and Thorne, K. (1968), Slowly rotating relativistic stars II. Model for neutron stars and supermassive stars, *Astrophys. J.*, **153**, pp. 807–834.

Hledík, S. and Stuchlík, Z., editors (2004), *Proceedings of RAGtime 4/5: Workshops on black holes and neutron stars, Opava, 14–16/13–15 October 2002/2003*, Silesian University in Opava, Opava, ISBN 80-7248-242-4.

Hledík, S. and Stuchlík, Z., editors (2005), *Proceedings of RAGtime 6/7: Workshops on black holes and neutron stars, Opava, 16–18/18–20 September 2004/2005*, Silesian University in Opava, Opava, ISBN 80-7248-334-X.

Horák, J. (2004), General aspects of nonlinear resonance 3 : 2 in QPO context, in Hledík and Stuchlík (2004), pp. 91–110, arXiv: astro-ph/0408092.

Karas, V., Vokrouhlický, D. and Polnarev, A. G. (1992), In the vicinity of a rotating black hole – A fast numerical code for computing observational effects, *Monthly Notices Roy. Astronom. Soc.*, **259**, pp. 569–575.

Kato, S., Fukue, J. and Mineshige, S. (1998), Black-hole accretion disks, in S. Kato, J. Fukue and S. Mineshige, editors, *Black-hole accretion disks*, Kyoto University Press, Kyoto, Japan.

Kluźniak, W. and Abramowicz, M. A. (2001), Strong-field gravity and orbital resonance in black holes and neutron stars – kHz quasi-periodic oscillations (QPO), *Acta Phys. Polon. B*, **32**, pp. 3605–3612.

Kovář, J., Stuchlík, Z. and Karas, V. (2007), On existence of halo orbits in Kerr–Newman spacetimes, pp. 125–138, this volume.

Kraniotis, G. V. (2005), Frame dragging and bending of light in Kerr and Kerr–(anti-)de Sitter spacetimes, *Classical Quantum Gravity*, **22**, pp. 4391–4424, arXiv: gr-qc/0507056.

Kraniotis, G. V. (2007), Periapsis and gravitomagnetic precessions of stellar orbits in Kerr and Kerr–de Sitter black hole spacetimes, *Classical Quantum Gravity*, **24**, pp. 1775–1808, arXiv: gr-qc/0602056.

Lachowicz, P., Czerny, B. and Abramowicz, M. A. (2006), Wavelet analysis of MCG-6-30-15 and NGC 4051: a possible discovery of QPOs in 2 : 1 and 3 : 2 resonance, *Monthly Notices Roy. Astronom. Soc.*, submitted, arXiv: astro-ph/0607594.

Landau, L. D. and Lifshitz, E. M. (1976), *Mechanics*, volume I of *Course of Theoretical Physics*, Elsevier Butterworth-Heinemann, Oxford, 3rd edition, ISBN 0-7506-2896-0.

Laor, A. (1991), Line profiles from a disk around a rotating black hole, *Astrophys. J.*, **376**, pp. 90–94.

McClintock, J. E. and Remillard, R. A. (2004), Black Hole Binaries, in W. H. G. Lewin and M. van der Klis, editors, *Compact Stellar X-Ray Sources*, Cambridge University Press, Cambridge, arXiv: astro-ph/0306213.

McClintock, J. E., Shafee, R., Narayan, R., Remillard, R. A., Davis, S. W. and Li, L. (2006), The Spin of the Near-Extreme Kerr Black Hole GRS 1915+105, *Astrophys. J.*, **652**(2), pp. 518–539, arXiv: astro-ph/0606076.

Middleton, M., Done, C., Gierliński, M. and Davis, S. W. (2006), Black hole spin in GRS 1915+105, *Monthly Notices Roy. Astronom. Soc.*, **373**(3), pp. 1004–1012, arXiv: astro-ph/0601540v2.

Perez, C. A., Silbertgleit, A. S., Wagoner, R. V. and Lehr, D. E. (1997), Relativistic Diskoseismology. I. Analytical Results for "Gravity Modes", *Astrophys. J.*, **476**(2), pp. 589–604, URL http://www.journals.uchicago.edu/doi/abs/10.1086/303658.

Remillard, R. A. and McClintock, J. E. (2006), X-Ray Properties of Black-Hole Binaries, *Annual Review of Astronomy and Astrophysics*, **44**(1), pp. 49–92, arXiv: astro-ph/0606352.

Shafee, R., McClintock, J. E., Narayan, R., Davis, S. W., Li, L.-X. and Remillard, R. A. (2006), Estimating the Spin of Stellar-Mass Black Holes via Spectral Fitting of the X-ray Continuum, *Astrophys. J.*, **636**, pp. L113–L116, arXiv: astro-ph/0508302.

Slaný, P. and Stuchlík, Z. (2007), Extended orbital resonance model applied to QPOs observed in three near-extreme Kerr black hole candidate systems, pp. 257–265, this volume.

Stella, L. and Vietri, M. (1998), Lense–Thirring Precession and Quasi-periodic Oscillations in Low-Mass X-Ray Binaries, *Astrophys. J. Lett.*, **492**, pp. L59–L62, arXiv: astro-ph/9709085.

Stella, L. and Vietri, M. (1999), kHz Quasiperiodic Oscillations in Low-Mass X-Ray Binaries as Probes of General Relativity in the Strong-Field Regime, *Phys. Rev. Lett.*, **82**(1), pp. 17–20.

Strohmayer, T. E., Mushotzky, R. F., Winter, L., Soria, R., Uttley, P. and Cropper, M. (2007), Quasi-Periodic Variability in NGC 5408 X-1, *Astrophys. J.*, **660**, pp. 580–586, arXiv: astro-ph/0701390.

Stuchlík, Z., Konar, S., Miller, J. C. and Hledík, S. (2007a), Excitation of oscillations in accretion discs orbiting compact objects, pp. 293–322, this volume.

Stuchlík, Z., Kotrlová, A. and Török, G. (2007b), Black holes admitting strong resonant phenomena, submitted.

Stuchlík, Z., Kotrlová, A. and Török, G. (2007c), Multi-resonance model of QPOs: possible high precession determination of black hole spin, in preparation.

Stuchlík, Z. and Kovář, J. (2007), Epicyclic oscillations related to off-equatorial circular orbits, in preparation.

Stuchlík, Z., Slaný, P. and Török, G. (2004), Marginally stable thick discs with gradient inversion of orbital velocity measured in locally non-rotating frames: A mechanism for excitation of oscillations

in accretion discs?, in Hledík and Stuchlík (2004), pp. 239–256.

Stuchlík, Z., Slaný, P. and Török, G. (2006), Humpy LNRF-velocity profiles in accretion discs orbiting nearly extreme Kerr black holes. A possible relation to QPOs, *Astronomy and Astrophysics*, accepted for publication, arXiv: `astro-ph/0612439`.

Stuchlík, Z., Slaný, P. and Török, G. (2007d), Extended orbital resonance model with hump-induced oscillations, pp. 449–467, this volume.

Stuchlík, Z., Slaný, P. and Török, G. (2007e), LNRF-velocity hump-induced oscillations of a Keplerian disc orbiting near-extreme Kerr black hole: A possible explanation of high-frequency QPOs in GRS 1915+105, *Astronomy and Astrophysics*, **470**(2), pp. 401–404, arXiv: `0704.1252v2`.

Stuchlík, Z., Slaný, P., Török, G. and Abramowicz, M. A. (2005), The Aschenbach effect: unexpected topology changes in motion of particles and fluids orbiting rapidly rotating Kerr black holes, *Phys. Rev. D*, **71**, p. 024037 (9), arXiv: `gr-qc/0411091`.

Stuchlík, Z. and Török, G. (2005), On the possibility of precise determination of black hole spin in the framework of resonance models, in Hledík and Stuchlík (2005), pp. 253–263.

Stuchlík, Z., Török, G. and Bakala, P. (2007f), On a multi-resonant origin of high frequency quasiperiodic oscillations in the neutron-star X-ray binary 4U 1636−53, submitted to Astronomy and Astrophysics, arXiv: `0704.2318`.

Stuchlík, Z., Čermák, P., Török, G., Urbanec, M. and Bakala, P. (2007g), Genetic Selection of Neutron Star Structure Matching the X-Ray Observations, in N. Callaos, Q. Lesso, C. Zinn and O. Goriachkin, editors, *The 11th World Multi-Conference on Systemics, Cybernetics and Informatics: WMSCI 2007, July 8–11, Orlando, USA*, pp. 41–44, Internat. Inst. of Inf. and Syst.

Török, G. (2005), A possible 3 : 2 orbital epicyclic resonance in QPOs frequencies of Sgr A*, *Astronomy and Astrophysics*, **440**(1), pp. 1–4.

Török, G. (2007), Reverse of twin peak QPO amplitude relationship in six atoll sources.

Török, G., Abramowicz, M. A., Kluźniak, W. and Stuchlík, Z. (2005), The orbital resonance model for twin peak kHz quasi periodic oscillations in microquasars, *Astronomy and Astrophysics*, **436**(1), pp. 1–8, arXiv: `astro-ph/0401464`.

Török, G., Bakala, P., Stuchlík, Z. and Šrámková, E. (2007a), On a multi-resonant origin of high frequency QPOs in the atoll source 4U 1636−53, pp. 489–499, this volume, URL `http://xmm.esac.esa.int/external/xmm_science/workshops/2007_science/presentations/P2.6.pdf`.

Török, G., Bakala, P., Stuchlík, Z. and Čech, P. (2007b), Modelling the twin peak QPO distribution in the atoll source 4U 1636−53, pp. 479–488, this volume.

Török, G. and Stuchlík, Z. (2005a), Epicyclic frequencies of Keplerian motion in Kerr spacetimes, in Hledík and Stuchlík (2005), pp. 315–338.

Török, G. and Stuchlík, Z. (2005b), Radial and vertical epicyclic frequencies of Keplerian motion in the field of Kerr naked singularities. Comparison with the black hole case and possible instability of naked singularity accretion discs, *Astronomy and Astrophysics*, **437**(3), pp. 775–788, arXiv: `astro-ph/0502127`.

Török, G., Stuchlík, Z. and Bakala, P. (2007c), A remark about possible unity of the neutron star and black hole high frequency QPOs, *Central European J. Phys.*, **5**(4), pp. 457–462.

Török, G., Stuchlík, Z. and Čermák, P. (2007d), Reverse of twin peak kHz QPO inter relationship in the six atoll sources, pp. 511–522, this volume.

Urbanec, M., Stuchlík, Z., Török, G., Bakala, P. and Čermák, P. (2007), Neutron star equation of state and QPO observations, pp. 523–531, this volume.

van der Klis, M. (2006), Rapid X-ray Variability, in W. H. G. Lewin and M. van der Klis, editors, *Compact Stellar X-Ray Sources*, pp. 39–112, Cambridge University Press, Cambridge.

Zakharov, A. F. (2003), The iron K_α line as a tool for analysis of black hole characteristics, *Publ. Astronom. Observator. Belgrade*, **76**, pp. 147–162, arXiv: `astro-ph/0411611`.

Zakharov, A. F. and Repin, S. V. (2006), Different types of Fe K_α lines from radiating annuli near black holes, *New Astronomy*, **11**, pp. 405–410, arXiv: `astro-ph/0510548`.

Proceedings of *RAGtime 8/9, 15–19/19–21 September, 2006/2007, Hradec nad Moravicí, Opava, Czech Republic*
S. Hledík and Z. Stuchlík, editors, Silesian University in Opava, 2007, pp. 417–431

Properties of pseudo-Newtonian gravitational potential in Schwarzschild–de Sitter spacetimes

Zdeněk Stuchlík and Jiří Kovář[a]

Institute of Physics, Faculty of Philosophy & Science, Silesian University in Opava,
Bezručovo nám. 13, CZ-746 01 Opava, Czech Republic
[a] Jiri.Kovar@fpf.slu.cz

ABSTRACT
We introduce the gravitational potential for the pseudo-Newtonian description of the gravitational field around static and spherically symmetric black holes in the universe with the repulsive cosmological constant, described in terms of the general relativistic approach by the Schwarzschild–de Sitter geometry. In order to demonstrate the accuracy of the pseudo-Newtonian approach and its possible applications, we construct the effective potential for a test particle motion and compare its behaviour with its general relativistic counterpart. Our results indicate that the pseudo-Newtonian potential could be useful in applications of developed Newtonian theories of accretion disks in astrophysically interesting situations in large galactic structures for spacetimes with the cosmological parameter $y = \Lambda M^2/3 \leq 10^{-6}$.

1 INTRODUCTION

Recent cosmological observations of distant supernova Ia type explosions indicate an accelerating universe; starting at the cosmological redshift $z \sim 1$ (Spergel et al., 2003) the accelerated expansion should be generated by some appropriate form of the so-called dark energy. Moreover, these results are in an accord with detailed observations of the anisotropies of the microwave cosmic background radiation indicating that the energy content of the dark energy represents $\sim 73\,\%$ of the energy content in the observable universe; the sum of energy densities is very close to the critical energy density corresponding to an almost parabolic universe as given by a large variety of cosmological tests indicating a concordance inflationary cosmological model (Bahcall et al., 1999; Wang et al., 2000). There is a variety of possible candidates for the dark energy. All of the related models have the equation of state with parameter $w = p/\rho$ varying during the cosmological expansion.

Nevertheless, the recent observational data indicate that the allowed equation of state is very close to the case of a repulsive cosmological constant $\Lambda > 0$ with $\rho_\Lambda \sim 0.73\rho_{\rm crit}$ (Spergel et al., 2003). Therefore, it is quite important to consider the influence of $\Lambda > 0$ quite seriously.

We have tested possible effects of $\Lambda > 0$ in astrophysical situations (Stuchlík, 2005), investigating namely the properties of black-hole solutions of Einstein equations for the

978-80-7248-419-5

test particle motion in Schwarzschild–de Sitter (SdS, Stuchlík and Hledík, 1999) and Kerr–de Sitter (KdS, Stuchlík and Slaný, 2004) spacetimes and the test perfect fluid in SdS (Stuchlík et al., 2000) and KdS (Slaný and Stuchlík, 2005) spacetimes. Further, the test particle and fluid properties were treated also in the framework of the optical reference geometry (Kovář and Stuchlík, 2006, 2007) allowing introduction of inertial forces in the intuitively natural Newtonian way (Abramowicz et al., 1988, 1995).

It should be stressed that all of the relevant effects of $\Lambda > 0$ on the black-hole structure are quite well expressed in the SdS spacetimes, since the rotational effects of the black hole spin are concentrated into the region in the close vicinity of the black-hole horizon, where the influence of $\Lambda > 0$ can be abandoned for realistic values of the black hole mass and the relict cosmological constant (Stuchlík, 2005). Of course, the efficiency of the accretion processes is controlled by the rotational effects in the innermost parts of the disc, where the KdS spacetime structure is relevant (Stuchlík, 2005). For near-extreme black holes the efficiency takes large values ~ 0.4 as compared with the SdS spacetimes where the efficiency ~ 0.059. Therefore, in studying the large scale properties of disc structures, investigation of the SdS spacetime is quite sufficient (only the accretion efficiency has to be given by the KdS spacetime structure, governing the innermost parts of the disc).

For this reason, it is worth to realize more detailed studies of the disc structures around supermassive black holes reflecting the influence of the repulsive cosmological constant. There is one especially important problem that could be hardly solved in the framework of full general relativistic approach, namely influence of $\Lambda > 0$ on the structure of self-graviting disc. We expect that the pseudo-Newtonian approach could be successful. For those purposes, we introduce here a pseudo-Newtonian potential of the SdS spacetimes that could enable us to use directly standard techniques developed in the framework of Newtonian physics.

By using the standard Newtonian quantities and formulas for the central gravitational field with the gravitational potential ψ_{N} replaced by the pseudo-Newtonian potential ψ, we are able to include the repulsive cosmological constant and some relativistic effects into account and use the standard Newtonian routines. In a central gravitational field, we manage in the standard way with the orbital velocity v, angular velocity Ω, and with the angular momentum l_{c} per "free" particle mass given by the relations

$$v = \left(r\frac{\mathrm{d}\psi}{\mathrm{d}r}\right)^{1/2}, \quad \Omega = \left(\frac{1}{r}\frac{\mathrm{d}\psi}{\mathrm{d}r}\right)^{1/2}, \quad l_{\mathrm{c}} = \left(r^3\frac{\mathrm{d}\psi}{\mathrm{d}r}\right)^{1/2} \tag{1}$$

in the case of circular motion.

Defining the pseudo-Newtonian potential for the SdS spacetime, we have to reflect properly both the gravitational attraction of the black hole and the repulsive effects of the cosmological constant. In comparison with the well known Paczyński–Wiita potential $\psi_{\mathrm{PW}} = 1/(r - 2GM/c^2)$ (Paczyński and Wiita, 1980) describing with high precision properties of Schwarzschild black holes (related to accretion processes) that has naturally defined behaviour at infinity, in the SdS spacetimes, we have to find a proper reference point that could in a well defined way serve in a similar sense as infinity in asymptotically flat spacetimes. It is shown (Stuchlík and Hledík, 1999; Hledík, 2002; Stuchlík, 2002) that such a role could be attributed to the so-called static radius, where the gravitational attraction

of the black hole acting on matter is exactly balanced by the cosmic repulsion, i.e., test particles feel no force, similarly to asymptotic infinity in flat spacetimes. Concentrating on the properties of the stationary configurations in the SdS spacetimes, the static radius is appropriately chosen; we do not reflect here properties of the spacetime near the cosmological horizon of the SdS spacetimes, nevertheless, the pseudo-Newtonian potential we are using here reflects the basic spacetime property near the cosmological horizon, since it diverges there.

In the pseudo-Newtonian potential we properly fix position of the marginally stable orbit, marginally bound orbit, the static radius, and the energy at these radii in agreement with the exact general relativistic values.

2 THE BACKGROUND AND GRAVITATIONAL POTENTIAL

In the standard Schwarzschild coordinates (t, r, θ, ϕ), and the geometric system of units $(c = G = 1)$, the SdS spacetimes are determined by the line element (Stuchlík and Hledík, 1999)

$$\mathrm{d}s^2 = -\left(1 - \frac{2M}{r} - \frac{\Lambda r^2}{3}\right)\mathrm{d}t^2 + \left(1 - \frac{2M}{r} - \frac{\Lambda r^2}{3}\right)^{-1}\mathrm{d}r^2 + r^2(\mathrm{d}\theta^2 + \sin^2\theta\,\mathrm{d}\phi^2)\,, \quad (2)$$

where M is the mass parameter of the spacetimes. It is useful to introduce the dimensionless parameter $y = \Lambda M^2/3$ and use dimensionless coordinates $t \to t/M, r \to r/M$, which is equivalent to putting $M = 1$.

The pseudo-singularities of the line element, i.e., black-hole and cosmological horizons, are given by the relation $g_{tt} = 1 - 2/r - yr^2 = 0$, thus by solutions of the equation

$$y = y_{\mathrm{h}} \equiv \frac{r-2}{r^3}\,, \quad (3)$$

which can be expressed in the form

$$r_{\mathrm{h}} = \frac{2}{\sqrt{3y}}\cos\frac{\pi + \xi}{3}\,, \quad (4)$$

$$r_{\mathrm{c}} = \frac{2}{\sqrt{3y}}\cos\frac{\pi - \xi}{3}\,, \quad (5)$$

where $\xi = \cos^{-1}(3\sqrt{3y})$. Both the horizons exist for $0 < y < y_{\mathrm{crit}} = 1/27$, separating the spacetimes into two dynamic regions and one static region. For $y = 1/27$, both the horizons coalesce at the radius of the so-called static radius[1]

$$r = r_{\mathrm{s}} \equiv y^{-1/3}\,, \quad (6)$$

taking the value $r_{\mathrm{s}} = 3$ in this case. For $y > 1/27$, the horizons disappear and the SdS spacetimes become dynamic naked-singularity spacetimes (see Fig. 1).

[1] At the static radius the gravitational attraction of the central object is just balanced by the cosmic repulsion. The gravitational force, defined in the general relativistic framework of the optical reference geometry (Stuchlík and Hledík, 1999; Hledík, 2002; Stuchlík, 2002), disappears there.

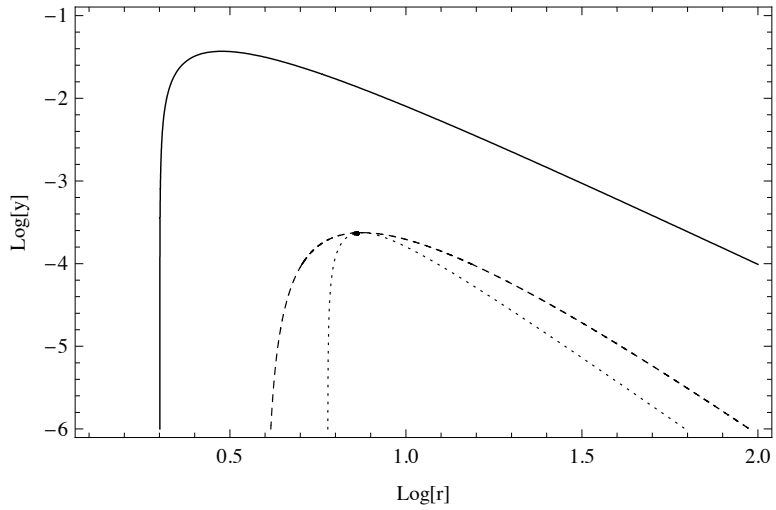

Figure 1. Functions $y_{\rm h}(r)$ (solid) determining the radii of horizons, $y_{\rm mb}$ (dashed) determining the marginally bound orbits, and $y_{\rm ms}(r)$ (dotted) determining the marginally stable circular orbits. The regions above the solid curve correspond to the dynamic parts of the SdS spacetimes determined by fixed value of y.

According to the standard way (Mukhopadhyay, 2002; Mukhopadhyay and Misra, 2003), the pseudo-Newtonian gravitational potential can be defined by replacing the Newtonian angular momentum per particle mass in the Newtonian definition of the potential[2] with the general relativistic angular momentum per rest mass and energy per rest mass ratio $l = L/E$, which plays the role of the pseudo-Newtonian angular momentum per free particle mass, i.e.,

$$\psi = \int \frac{L^2}{E^2 r^3}\,{\rm d}r\,. \tag{7}$$

Considering now the circular geodesic motion at the radii corresponding to the extrema of the relativistic effective potential (Stuchlík and Hledík, 1999)

$$V_{\rm eff}(r;\,L,\,y) = \left[\left(1-\frac{2}{r}-yr^2\right)\left(1+\frac{L^2}{r^2}\right)\right]^{1/2}\,, \tag{8}$$

[2] In the Newtonian physics, the gravitational potential for the central field can be defined by the relation $\partial_r \psi_{\rm N} = -G_r/m = l_{\rm N}^2/r^3$, where G_r is the gravitational force radial component and $l_{\rm N} = L_{\rm N}/m$ is the angular momentum per free particle mass.

and the related relativistic constants of motion (Stuchlík and Hledík, 1999)

$$L_{\rm c}(r;y) \equiv \left[r(1-yr^3)\right]^{1/2}\left(1-\frac{3}{r}\right)^{-1/2}, \tag{9}$$

$$E_{\rm c}(r;y) \equiv \left(1-\frac{2}{r}-yr^2\right)\left(1-\frac{3}{r}\right)^{-1/2}, \tag{10}$$

the gravitational potential (7) can be written in the form

$$\psi = \frac{r}{2(2-r+r^3y)} + K\,, \tag{11}$$

where K is the integrating constant. Note that this method works quite well in spherically symmetric, non-rotating spacetimes. However, it is much more complicated task to find in a proper way a pseudo-Newtonian potential in rotating (e.g., Kerr or KdS) spacetimes, because of a non-trivial influence of the dragging of inertial frames.

By using the condition $\psi(r = r_{\rm s}) = 0$ relating the potential at the static radius to the "starting point" corresponding to infinity in asymptotically flat spacetime, we obtain the potential in the form

$$\psi(r;y) = \frac{r^3y - 3ry^{1/3} + 2}{2(1-3y^{1/3})(2-r+r^3y)} \tag{12}$$

illustrated in Fig. 2.

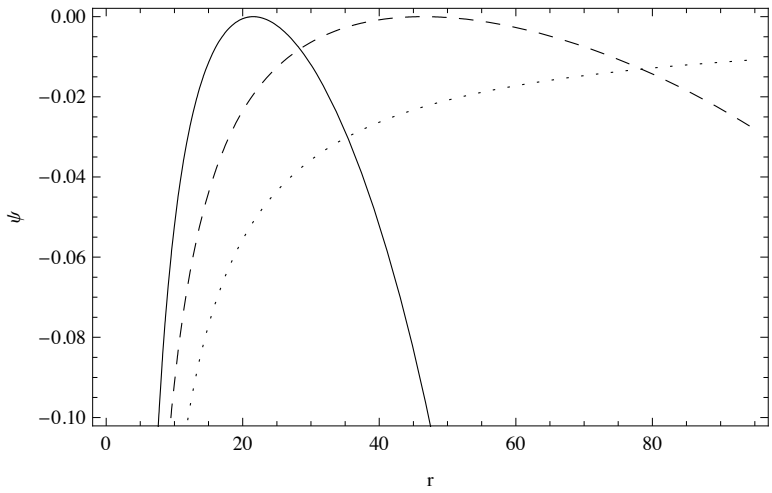

Figure 2. Pseudo-Newtonian gravitational potential $\psi(r;y)$ for three fixed values of the cosmological parameter $y = 0$ (dotted), $y = 10^{-5}$ (dashed) and $y = 10^{-4}$ (solid).

3 TEST PARTICLE MOTION

In the case of central gravitational fields a test particle motion is confined to central planes and we can choose the equatorial plane. Following the Newtonian physics, the radial equation of the Keplerian equatorial motion can be written in the form

$$\frac{1}{2}\left(\frac{\mathrm{d}r}{\mathrm{d}t}\right)^2 = e + v_{\mathrm{eff}}\,, \tag{13}$$

where e is the common Newtonian energy per particle mass (energy) and v_{eff} is the pseudo-Newtonian effective potential per particle mass (effective potential) defined by the relation

$$v_{\mathrm{eff}}(r; l, y) = \psi(r; y) + \frac{l^2}{2r^2}\,, \tag{14}$$

whereas $\psi(r; y)$ is the pseudo-Newtonian gravitational potential (12) and l is the pseudo-Newtonian angular momentum per particle mass (angular momentum) defined in Section 2. The circular (Keplerian) orbits are then determined by the extrema of the effective potential, i.e., by the condition $\partial_r v_{\mathrm{eff}} = 0$. The solution is given by the relation for the pseudo-Newtonian angular momentum at a given radius, and takes the form

$$l^2 = l_{\mathrm{c}}^2(r; y) \equiv \frac{r^3(1 - r^3 y)}{(2 - r + r^3 y)^2}\,. \tag{15}$$

The corresponding energy of particles on the circular orbits is given by the relation

$$e_{\mathrm{c}}(r; y) \equiv v_{\mathrm{eff}}(r; l = l_{\mathrm{c}}, y) = \frac{1}{2(1 - 3y^{1/3})} - \frac{r(r-3)}{2(2 - r + r^3 y)^2}\,. \tag{16}$$

3.1 Marginally stable and bound orbits

Behaviour of the pseudo-Newtonian effective potential $v_{\mathrm{eff}}(r; l, y)$ qualitatively follows the behaviour of its general relativistic counterpart $V_{\mathrm{eff}}(r; L, y)$ as shown in Fig. 3.

We demonstrate this statement by a detailed investigation of the behaviour of the functions $l_{\mathrm{c}}^2(r; y)$, governing the extrema of the potential $v_{\mathrm{eff}}(r; l, y)$, and the energies (the effective potential extrema) of the related circular orbits $e_{\mathrm{c}}(r; y)$, given by Eqs (15) and (16), and their general relativistic counterparts $L_{\mathrm{c}}^2(r; y)$ and $E_{\mathrm{c}}(r; y)$, given by Eqs (9) and (10).

The functions $l_{\mathrm{c}}^2(r; y)$ and $e_{\mathrm{c}}(r; y)$ diverge at the radius of the black-hole horizon r_{h} and vanish at the static radius, while $L_{\mathrm{c}}^2(r; y)$ and $E_{\mathrm{c}}(r; y)$ diverge at the radius of the photon circular orbit, $L_{\mathrm{c}}^2(r; y)$ vanishes at the static radius, and $E_{\mathrm{c}}(r; y)$ does not (see Figs 4 and 5).

Note that the energy $E_{\mathrm{c}}(r = r_{\mathrm{s}}; y) = (1 - 3y^{1/3}) \equiv E_{\mathrm{s}}(y)$ corresponds to the rest energy of particles. Thus, the pseudo-Newtonian approach implies that the existence of the circular orbits is limited by the static radius from above, in accord with the full relativistic approach, and by the black-hole horizon from below, in contrast to the relativistic approach, where the lower limit is given by the photon orbit. Of course, this is caused by the fact that we do not obtain the photon circular orbit in the pseudo-Newtonian approach.[3]

[3] The same situation occurs for the standard Paczyński–Wiita pseudo-Newtonian potential defined for the Schwarzschild spacetimes (Paczyński and Wiita, 1980).

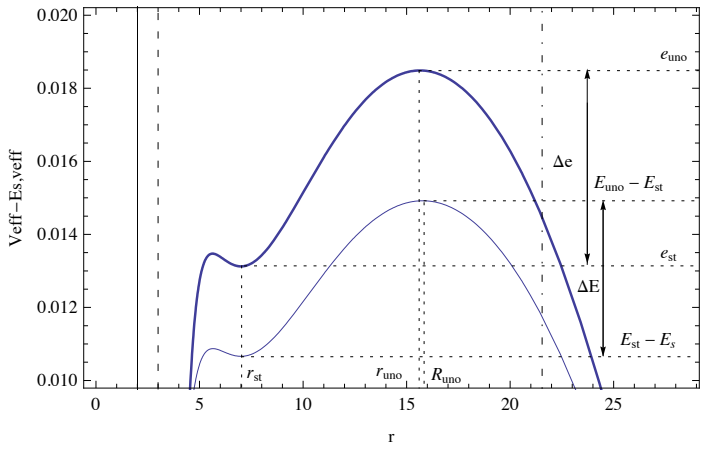

Figure 3. Pseudo-Newtonian $v_{\rm eff}(r; l, y)$ (thick) and relativistic $(V_{\rm eff}(r; L, y) - E_{\rm s}(y))$ (thin) effective potentials in SdS spacetime with $y = 10^{-4}$, corresponding to test particle motion with the pseudo-Newtonian and relativistic angular momenta $l^2 = l_{\rm c}^2(r = 7) = 13.4$ and $L^2 = L_{\rm c}^2(r = 7) = 11.8$, i.e., both determining the stable circular orbits at the radius $r_{\rm st} = 7$ (for the energy and radius notation see the text below).

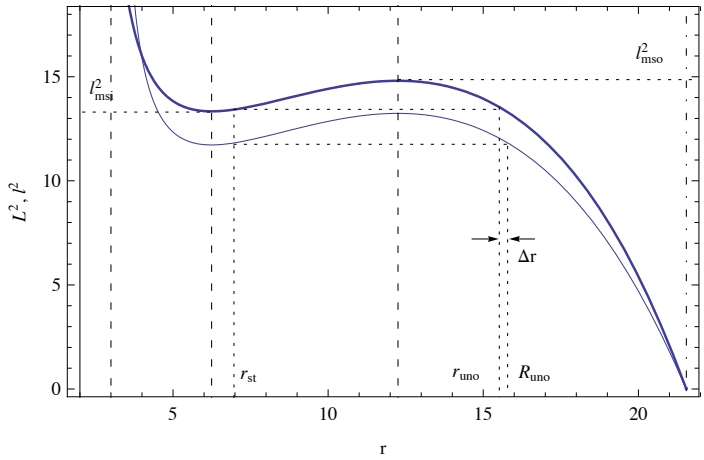

Figure 4. Radial profiles of the pseudo-Newtonian $l_{\rm c}^2(r; y)$ (thick) and relativistic $L_{\rm c}^2(r; y)$ angular momenta determining circular geodesics in SdS spacetime with $y = 10^{-4}$. The momenta determine the extrema of the potentials $v_{\rm eff}(r; l, y)$ and $V_{\rm eff}(r; L, y)$ (see Fig. 3). We show an example of typical behaviour of the angular momenta, each with two extrema. The solid vertical line denotes the radius of black-hole horizon, the dashed vertical lines denote the radius of photon circular orbit ($r = 3$) and the radii of marginally stable orbits determined by the extrema of the angular momenta profile. The dashed-dotted vertical line denotes the static radius. The dotted lines suggest determination of the difference Δr in positions of the outer unstable circular orbits $r_{\rm uno}$ and $R_{\rm uno}$, defined in the pseudo-Newtonian and relativistic ways, for coalescing value of the stable circular orbit at $r_{\rm st} = 7$.

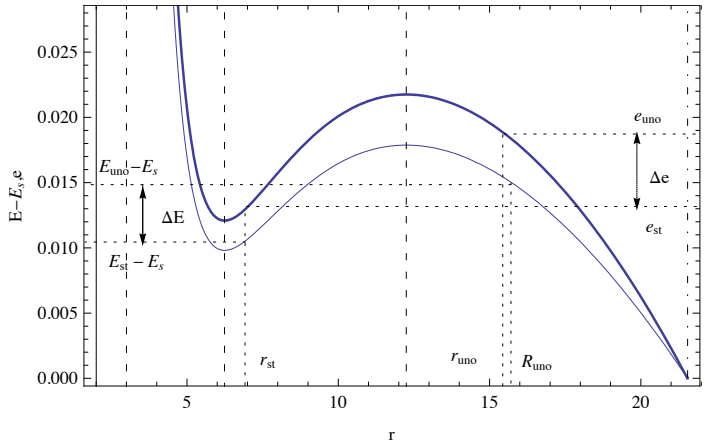

Figure 5. Pseudo-Newtonian $e_c(r; y)$ (thick) and relativistic $E_c(r; y) - E_s(y)$ energy ($y = 10^{-4}$). The dotted lines demonstrate determination of the energy difference (potential barrier) Δe (ΔE) between the outer unstable orbit at r_{uno} (R_{uno}), and central stable orbits at r_{st} ($R_{st} = r_{st}$) (for the dashed-dotted and dashed vertical lines meaning see Fig. 4).

As in the general relativistic approach, the stable circular orbits, determined by the minima of the effective potential $v_{eff}(r; l, y)$, satisfy the condition $\partial_r l_c^2(r; y) > 0$ and the unstable circular orbits, determined by the maxima of $v_{eff}(r; l, y)$, satisfy the condition $\partial_r l_c^2(r; y) < 0$.

Marginally inner and outer stable circular orbits are determined by extrema $l_{msi}^2(y)$ and $l_{mso}^2(y)$ of the function $l_c^2(r; y)$, located at the radii given by solutions of the equation

$$y = y_{ms}(r) \equiv \frac{r-6}{r^3(4r-15)}\,, \tag{17}$$

just as in the fully general relativistic approach, because loci of the extrema of the functions $l_c^2(r; y)$ and $L_c^2(r; y)$ coincide. The stable circular orbits are then limited by the condition $4yr^4 - 15yr^3 - r + 6 \leq 0$. The function $y_{ms}(r)$ vanishes at $r = 6$, corresponding to the marginally stable circular orbit in the Schwarzschild spacetime, diverges at $r = 0$ and at $r = 15/4$, and has minimum at $r = 3$, where $y_{ms}(r = 3) = 1/27$. The function is irrelevant at the range $0 < r < 15/4$ where $y_{ms}(r) > 1/27$. The physically relevant part of $y_{ms}(r)$ is located at $r \geq 6$. Its maximum is located at $r_{ms,e} = 15/2$ and the corresponding maximum is $y_{ms}(r = r_{ms,e}) = 12/15^4 \equiv y_{ms,e}$ (see Fig. 1).

This value of $y = y_{ms,e} \doteq 0.000237$ represents limiting value of y for the SdS spacetimes admitting existence of stable geodesics, i.e., existence of accretion discs. The behaviour of the effective potential determining the innermost and outermost stable circular orbits is illustrated in Fig. 6.

The marginally bound circular orbits, i.e., two unstable circular orbits with the same energy and appropriately chosen angular momentum, located at the radii r_{mbi} and r_{mbo}, are

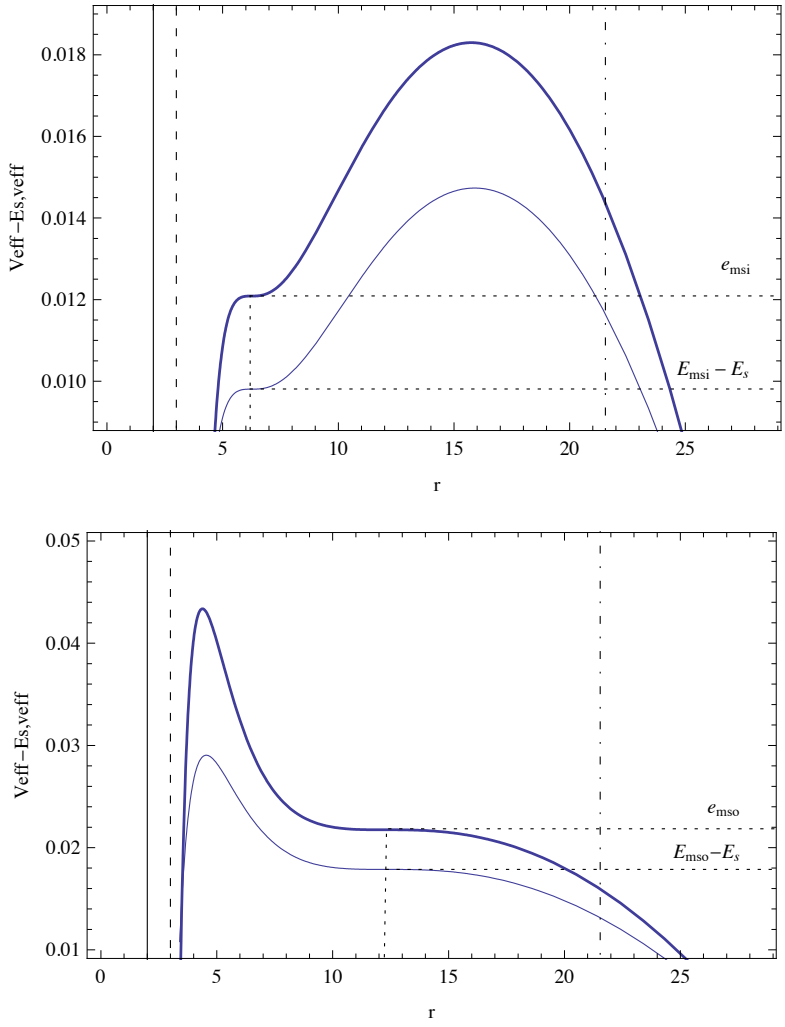

Figure 6. Marginally stable circular orbits. Pseudo-Newtonian $v_{\rm eff}(r; l, y)$ (thick) and relativistic $V_{\rm eff}(r; L, y) - E_{\rm s}(y)$ effective potentials for $y = 10^{-4}$, and $l^2 = l^2_{\rm c}(r = 6.2) = 13.3$ and $L^2 = L^2_{\rm c}(r = 6.2) = 11.7$ (*upper figure*); $l^2 = l^2_{\rm c}(r = 12.3) = 14.8$ and $L^2 = L^2_{\rm c}(r = 12.3) = 13.2$ (*lower figure*). The inflex points of the effective potentials determine the marginally stable circular orbits with the energies $e_{\rm msi}$, $e_{\rm mso}$, and $E_{\rm msi} - E_{\rm s}$, $E_{\rm mso} - E_{\rm s}$.

determined by the condition (see Fig. 7)

$$e_{\rm c}(r = r_{\rm mbi}; y) = e_{\rm c}(r = r_{\rm mbo}; y) \equiv e_{\rm mb}(y)\,. \tag{18}$$

The radii $r_{\rm mbi}$, $r_{\rm mbo}$ and the corresponding value $e_{\rm mb}(y)$ can be found by using the following numerical procedure. The unstable circular orbits become the marginally bound

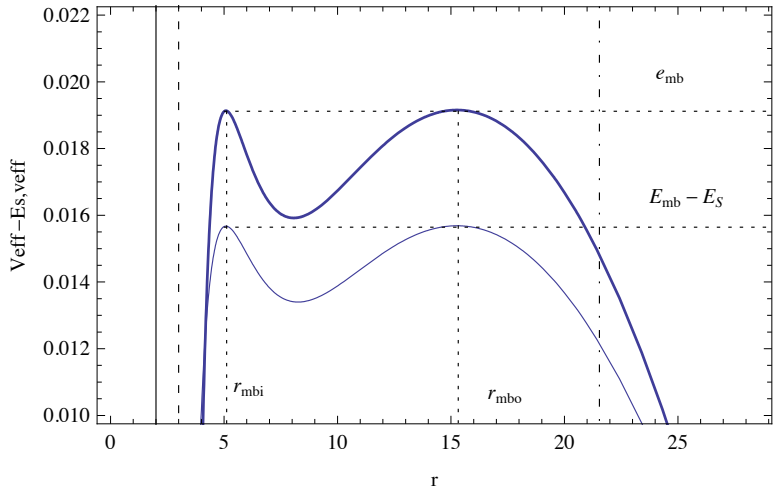

Figure 7. Marginally bound circular orbits. Pseudo-Newtonian $v_{\rm eff}(r; l, y)$ (thick) and relativistic $V_{\rm eff}(r; L, y) - E_{\rm s}(y)$ effective potentials for $y = 10^{-4}$, $l^2 = l^2_{\rm c}(r = 15.3) = 13.7$ and $L^2 = L^2_{\rm c}(r = 15.3) = 12.2$. The circular orbits corresponding to the potential extrema $e_{\rm emb}$ and $E_{\rm mb} - E_{\rm s}$ determine the marginally bound circular orbits at the radii $r_{\rm mbi}$ and $r_{\rm mbo}$, having the same value for both the pseudo-Newtonian and relativistic cases.

orbits for the particular choice of $l^2_{\rm c}(r; y) = l^2_{\rm mb}(y)$. Thus the radii of such orbits can be determined from Eq. (15), choosing the proper two roots, now the functions of $l^2_{\rm c}$ and y. By using condition (18), we immediately obtain $l^2_{\rm mb}(y)$ and by using the relation (15) again, the searched radii $r_{\rm mbi}(y)$, $r_{\rm mbo}(y)$, and also the function $y_{\rm mb}(r)$ governing these radii (see Fig. 1). The general relativistic formulas imply the same results, because

$$e_{\rm c}(r; y) = \tfrac{1}{2}\left[E^{-2}_{\rm s}(y) - E^{-2}_{\rm c}(r; y)\right], \tag{19}$$

and for fixed values of r, corresponding to $r_{\rm mbi}$ and $r_{\rm mbo}$, there is $E_{\rm c}(r = r_{\rm mbi}) = E_{\rm c}(r = r_{\rm mbo})$, and thus $e_{\rm c}(r = r_{\rm mbi}) = e_{\rm c}(r = r_{\rm mbo})$.

3.2 Potential barriers

For values of the cosmological parameter y allowing existence of the stable circular orbits, i.e., $0 < y < y_{\rm ms,e}$, the functions $l^2_{\rm c}(r; y)$ and $L^2_{\rm c}(r; y)$ have two extrema governed by the function $y_{\rm ms}(r)$ (see Fig. 4). These extrema correspond to the innermost and outermost stable circular geodesics with $l^2 = l^2_{\rm msi}$ and $l^2 = l^2_{\rm mso}$, and $L^2 = L^2_{\rm msi}$ and $L^2 = L^2_{\rm mso}$, respectively, which determine extension and accretion efficiency of thin, Keplerian discs. The marginally stable perfect fluid configuration with $l^2(r, \theta) = \text{const}$ and $l^2 \in (l^2_{\rm msi}, l^2_{\rm mso})$ are determined by intersections of $l^2 = \text{const}$ and $l^2_{\rm c}(r, y)$ curve that determine the centre and edges of the fluid configuration (Stuchlík et al., 2000). Therefore we realize a detailed comparison of the potentials $v_{\rm eff}(r; l, y)$ and $V_{\rm eff}(r; L, y)$, concentrating on the

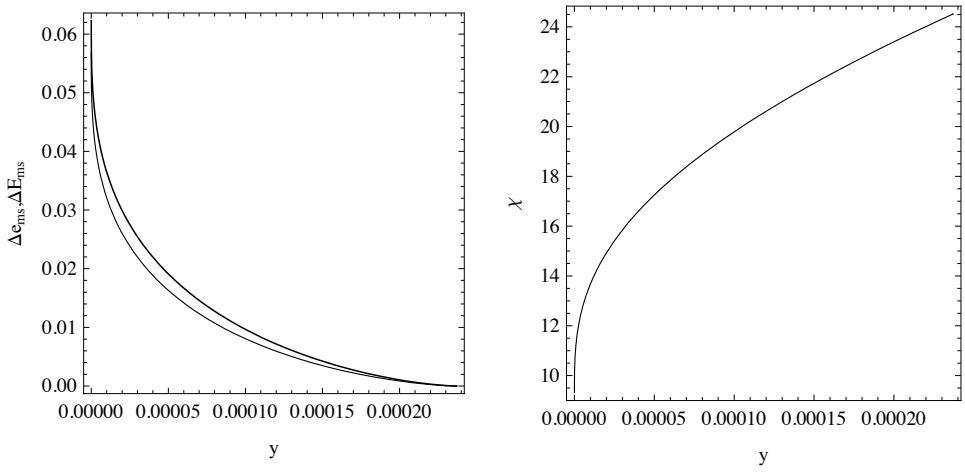

Figure 8. *Left:* Efficiency of the Keplerian discs accretion determined in the pseudo-Newtonian $\Delta e_{\rm ms}(y)$ (thick) and relativistic $\Delta E_{\rm ms}(y)$ ways. *Right:* Characteristic quantity χ describing the inaccuracy in the determination of the Keplerian accretion efficiency as a function of the cosmological parameter.

differences in positions of the inner, central and outer circular orbits (determined in the pseudo-Newtonian and relativistic ways), and the differences in the corresponding values of both the potentials.

We start with analyzing the pseudo-Newtonian and relativistic energy differences between the outer and inner marginally stable circular orbits, which determine efficiency of the accretion processes in Keplerian discs

$$\Delta e_{\rm ms}(y) = e_{\rm mso}(y) - e_{\rm msi}(y)\,, \tag{20}$$

$$\Delta E_{\rm ms}(y) = E_{\rm mso}(y) - E_{\rm msi}(y)\,. \tag{21}$$

The energy differences $\Delta e_{\rm ms}(y)$ and $\Delta E_{\rm ms}(y)$ are compared in Fig. 8. Clearly, for astrophysically relevant values of $y < 10^{-15}$, the pseudo-Newtonian and relativistic efficiencies are very close. The differences of the pseudo-Newtonian and relativistic efficiency, can be characterized by the quantity

$$\chi = \frac{\Delta e_{\rm ms} - \Delta E_{\rm ms}}{\Delta E_{\rm ms}}\, 100\,\%\,, \tag{22}$$

the dependence of which on the cosmological parameter is illustrated in Fig. 8. In the limit of $y \to 0$, i.e., in the Schwarzschild spacetimes, there is $\Delta e_{\rm ms} = 0.0625$, $\Delta E_{\rm ms} = 0.0572$ and $\chi \sim 10\,\%$, and these values hold for the astrophysically relevant values of y.

Further, it is of astrophysical relevance to compare dependence of the pseudo-Newtonian and relativistic characteristics of marginally stable discs with uniform distribution of angular momentum $l^2(r,\theta) = \text{const}$. Assuming a fixed radius of stable circular orbit corres-

ponding to the disc centre, we can determine and compare the outer edge of the disc and the potential energy well for the matter of the disc.

By fixing a value of the radius of stable circular orbit $r = r_{\rm st}$, and calculating the corresponding values of both the pseudo-Newtonian and relativistic angular momenta $l_{\rm c}^2(r = r_{\rm st}; y)$ and $L_{\rm c}^2(r = r_{\rm st}; y)$ (see Fig. 4), we can determine the radii of the corresponding outer unstable circular geodesics (edge of the disc) $r_{\rm uno}(r_{\rm st}; y)$ (calculated by using $l_{\rm c}^2$) and $R_{\rm uno}(r_{\rm st}; y)$ (calculated by using $L_{\rm c}^2$), and their difference

$$\Delta r_{\rm uno}(r_{\rm st}; y) = r_{\rm uno}(r_{\rm st}; y) - R_{\rm uno}(r_{\rm st}; y)\,. \tag{23}$$

The inaccuracies in the pseudo-Newtonian determination of the positions of the outer unstable orbit, in dependence on the position of the stable central circular orbit, can be characterized by the quantity

$$\xi = \frac{\Delta r_{\rm uno}}{R_{\rm uno} - r_{\rm st}}\, 100\,\%\,. \tag{24}$$

We can also calculate the pseudo-Newtonian energies at the radius of the stable circular orbit and at the related outer unstable orbit, i.e., $e_{\rm c}(r = r_{\rm st}; y) \equiv e_{\rm st}(r_{\rm st}; y)$ and $e_{\rm c}(r = r_{\rm uno}; y) \equiv e_{\rm uno}(r_{\rm st}; y)$, and their difference (potential barrier)

$$\Delta e(r_{\rm st}; y) = e_{\rm uno}(r_{\rm st}; y) - e_{\rm st}(r_{\rm st}; y)\,. \tag{25}$$

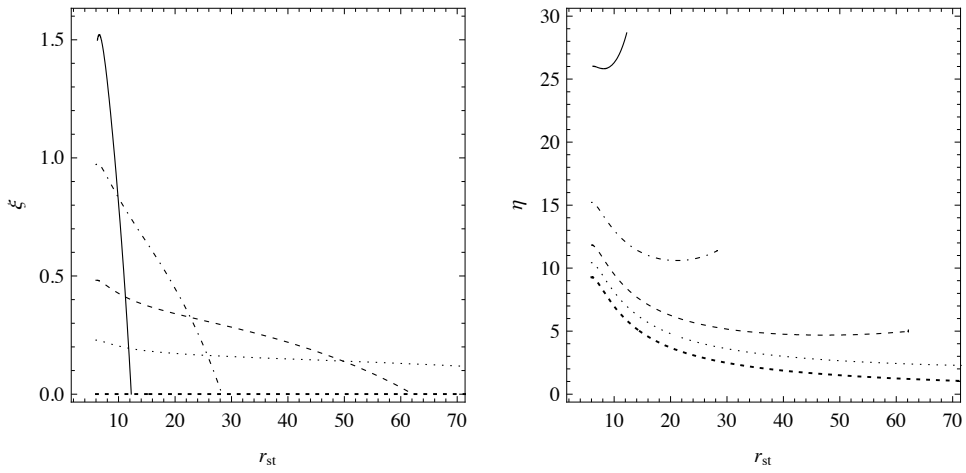

Figure 9. *Left:* Characteristic quantity ξ describing the inaccuracies in the pseudo-Newtonian determination of the positions of the outer unstable orbit; *Right:* Characteristic quantity η describing the inaccuracies in the pseudo-Newtonian determination of the potential barrier between the outer unstable and central stable circular orbits, for $y = 10^{-4}$ (solid), $y = 10^{-5}$ (dashed-dotted) $y = 10^{-6}$ (dashed) $y = 10^{-7}$ (dotted) $y = 0$ (thick dotted).

The same can be done in the relativistic case, i.e., we calculate the energies $E_c(r = r_{st}; y) \equiv e_{st}(r_{st}; y)$ and $E_c(r = R_{uno}; y) \equiv E_{uno}(r_{st}; y)$, and their difference (potential barrier)

$$\Delta E(r_{st}; y) = E_{uno}(r_{st}; y) - E_{st}(r_{st}; y) . \tag{26}$$

The inaccuracies in the pseudo-Newtonian determination of such a potential barrier, in dependence on the position of the stable central circular orbit, can be characterized by the quantity

$$\eta = \frac{\Delta e - \Delta E}{\Delta E} 100\,\% . \tag{27}$$

Dependencies of both the characteristic quantities ξ and η are given in Fig. 9 for selected values of y. Clearly, the precision is high for both ξ and η, when $y < 10^{-6}$. Note that for $y \to 0$, the positions of unstable circular orbits $r_{uno} \to \infty$, $R_{uno} \to \infty$, and $\xi \to 0$. In fact, it is irrelevant to study ξ for $y = 0$, because there are no outer unstable orbits in the Schwarzschild spacetime. On the other hand, there is $e_{uno} \to 0$ and $E_{uno} \to 1$ for $y \to 0$, $r_{uno} \to \infty$ and $r_{uno} \to \infty$. Thus, in the case $y = 0$, η describes the differences in the pseudo-Newtonian and relativistic determinations of the potential barrier between the stable orbit and infinity.

4 CONCLUSIONS

We have shown that the gravitational field of the spherically symmetric and static black hole in the universe with a positive cosmological constant, described by the Schwarzschild–de Sitter solution of Einstein's equations, can be alternatively described with a relatively high precision by using appropriately defined pseudo-Newtonian gravitational potential.

The presented gravitational potential satisfies important conditions. It admits existence of the static radius, diverges at horizons, and it gives marginally stable and bound orbits at radii exactly equal to those given in the relativistic expressions. The energy difference of these orbits is close to the relativistic relations.

We have tested the potential correctness by comparing some pseudo-Newtonian results concerning the test particle geodetical motion with the general relativistic ones. We have been interested in astrophysically relevant situations. Thus, we have chosen range of the cosmological parameter ($0 < y \leq 0.000237$), allowing the existence of stable circular geodesics, i.e., existence of accretion discs. The differences in the pseudo-Newtonian and relativistic calculations of the accretion processes efficiency have been also studied, whereas the related inaccuracies of the pseudo-Newtonian efficiency determination are less then 15 % for $y \leq 10^{-5}$.

Moreover, assuming the central circular orbit position fixed, we have compared results of the pseudo-Newtonian and relativistic calculations of the outer unstable circular orbits positions, and the related energy differences (potential barriers) between the central stable and outer unstable orbits. The comparisons suggest that within a certain inaccuracy (less than 1 % in the case of the radii determination, and less than 15 % in the case of the potential barriers determination, for $y \leq 10^{-5}$), the obtained pseudo-Newtonian results are in a good

agreement with the relativistic ones. As for the the potential barriers, we can state that the differences between the results of both the approaches tend to be smaller for y decreasing.

Note that in principle we could characterize differences between the positions of the inner unstable orbits determined in the pseudo-Newtonian and relativistic ways, and between the related potential barriers. We could also study the differences between the positions of the inner unstable circular orbits or central stable orbits, determined in both the ways, and the differences between the related potential barriers when fixing the positions of the outer unstable orbit, etc. We have not proceeded these comparisons representing, in a way, alternatives of the presented ones. We prepare a detailed study of the application of the pseudo-Newtonian potential on the perfect fluid dynamics, which is in accordance with our intention to study accretion processes and the properties of accretion discs in dependence on the parameter y in the pseudo-Newtonian way (Stuchlík and Kovář, 2008).

ACKNOWLEDGEMENTS

This work was supported by the Czech grants MSM 4781305903 and GAČR 202/06/0041. One of the authors (Z. S.) would like to express his gratitude to the Czech Committee for Collaboration with CERN for support and CERN Theory Division for perfect hospitality.

REFERENCES

Abramowicz, M. A., Carter, B. and Lasota, J. (1988), Optical reference geometry for stationary and static dynamics, *Gen. Relativity Gravitation*, **20**, p. 1173.

Abramowicz, M. A., Nurowski, P. and Wex, N. (1995), Optical reference geometry for stationary and axially symmetric spacetimes, *Classical Quantum Gravity*, **12**(6), pp. 1467–1472, URL `http://www.iop.org/EJ/abstract/0264-9381/12/6/012`.

Bahcall, N., Ostriker, J. P., Perlmutter, S. and Steinhardt, P. J. (1999), The cosmic triangle: Revealing the state of the universe, *Science*, **284**, pp. 1481–1488.

Hledík, S. (2002), Optical geometry, inertial forces, and embedding diagrams, in Semerák et al. (2002), pp. 161–192.

Kovář, J. and Stuchlík, Z. (2006), Forces in Kerr space-times with a repulsive cosmological constant, *Internat. J. Modern Phys. A*, **21**, pp. 4869–4897, arXiv: `gr-qc/0611152`.

Kovář, J. and Stuchlík, Z. (2007), Optical reference geometry and inertial forces in Kerr–de Sitter spacetimes, *Classical Quantum Gravity*, **24**, pp. 565–594.

Mukhopadhyay, B. (2002), Description of Pseudo-Newtonian Potential for the Relativistic Accretion Disks around Kerr Black Holes, *Astrophys. J.*, **581**, p. 427.

Mukhopadhyay, B. and Misra, R. (2003), Pseudo-Newtonian Potentials to Describe the Temporal Effects on Relativistic Accretion Disks around Rotating Black Holes and Neutron Stars, *Astrophys. J.*, **582**, p. 347.

Paczyński, B. and Wiita, P. J. (1980), Thick accretion disks and supercritical luminosities, *Astronomy and Astrophysics*, **88**(1–2), pp. 23–31, URL `http://adsabs.harvard.edu/abs/1980A\%26A...88...23P`.

Semerák, O., Podolský, J. and Žofka, M., editors (2002), *Gravitation: Following the Prague Inspiration (A Volume in Celebration of the 60th Birthday of Jiří Bičák)*, World Scientific, New Jersey, London, Singapore, Hong Kong, ISBN 981-238-093-0.

Slaný, P. and Stuchlík, Z. (2005), Relativistic thick discs in the Kerr–de Sitter backgrounds, *Classical Quantum Gravity*, **22**, pp. 3623–3651, URL `http://www.iop.org/EJ/abstract/-search=44947255.2/0264-9381/22/17/019`.

Spergel, D. N., Verde, L., Peiris, H. V., Komatsu, E., Nolta, M. R., Bennett, C. L., Halpern, M., Hinshaw, G., Jarosik, N., Kogut, A., Limon, M., Meyer, S. S., Page, L., Tucker, G. S., Weiland, J. L., Wollack, E., Wright, E. L. and Turolla, R. (2003), First Year Wilkinson Microwave Anisotropy Probe (WMAP) Observations: Determination of Cosmological Parameters, *Astrophys. J. Suppl.*, **148**, p. 175, arXiv: `astro-ph/0302209`.

Stuchlík, Z. (2002), The role of a repulsive cosmological constant in astrophysical processes, in Semerák et al. (2002), pp. 27–83.

Stuchlík, Z. (2005), Influence of the Relict Cosmological Constant on Accretion Discs, *Modern Phys. Lett. A*, **20**(8), pp. 561–575.

Stuchlík, Z. and Hledík, S. (1999), Some properties of the Schwarzschild–de Sitter and Schwarzschild–anti-de Sitter spacetimes, *Phys. Rev. D*, **60**(4), p. 044006 (15 pages).

Stuchlík, Z. and Kovář, J. (2008), Pseudo-Newtonian gravitational potential for modelling of accretion processes in Schwarzschild-de Sitter spacetimes, in preparation.

Stuchlík, Z. and Slaný, P. (2004), Equatorial circular orbits in the Kerr–de Sitter spacetimes, *Phys. Rev. D*, **69**, p. 064001, ISSN 1094-1622, arXiv: `gr-qc/0307049`.

Stuchlík, Z., Slaný, P. and Hledík, S. (2000), Equilibrium configurations of perfect fluid orbiting Schwarzschild–de Sitter black holes, *Astronomy and Astrophysics*, **363**(2), pp. 425–439, ISSN 0004-6361 (printed version), 1432-0746 (parallel-to-print version), URL `http://adsabs.harvard.edu/abs/2000A\%26A...363..425S`.

Wang, L., Caldwell, R. R., Ostriker, J. P. and Steinhardt, P. J. (2000), Cosmic concordance and quintessence, *Astrophys. J.*, **530**(1), pp. 17–35, URL `http://www.journals.uchicago.edu/doi/abs/10.1086/308331`.

Proceedings of *RAGtime 8/9, 15–19/19–21 September, 2006/2007, Hradec nad Moravicí, Opava, Czech Republic*
S. Hledík and Z. Stuchlík, editors, Silesian University in Opava, 2007, pp. 433–447

Equilibrium configurations of perfect fluid in Reissner–Nordström–de Sitter spacetimes

Zdeněk Stuchlík, Hana Kučáková and Petr Slaný

Institute of Physics, Faculty of Philosophy & Science, Silesian University in Opava,
Bezručovo nám. 13, CZ-746 01 Opava, Czech Republic

ABSTRACT
Marginally stable perfect fluid tori with uniform distribution of specific angular momentum are determined in the Reissner–Nordström–de Sitter black-hole and naked-singularity spacetimes. Perfect fluid toroidal configurations are allowed only in the spacetimes admitting existence of stable circular geodesics. The configurations with equipotential surfaces crossing itself in a cusp allow accretion (inner cusp) and/or excretion (outer cusp) of matter from the toroidal configuration. The classification of the Reissner–Nordström–de Sitter spacetimes according to the properties of the marginally stable tori is given.

1 INTRODUCTION

Many observations suggest that the energy sources in quasars and active galactic nuclei are accretion discs orbiting massive black-holes. However, despite the cosmic censorship hypothesis (Penrose, 1969) that is not probed yet, existence of naked singularities related to the black hole solutions of the Einstein equations is not excluded (see, e.g., de Felice and Yunqiang, 2001) and is still worth of consideration.

The accretion discs could be geometrically thin with low accretion rates and negligible pressure, characterized by quasicircular geodetical motion, or geometrically thick with high accretion rates and relevant pressure gradients that could be, in the basic approximation, determined by equipotential surfaces of test perfect fluid orbiting the central object (Abramowicz, 1998).

The presence of a repulsive cosmological constant (dark, or vacuum, energy) $\Lambda_0 \sim 10^{-56}\,\mathrm{cm}^{-2}$ indicated by wide range of cosmological tests (Spergel et al., 2003) could influence significantly the properties of the accretion discs (Stuchlík, 2005), as shown both for the Schwarzschild–de Sitter (SdS) spacetimes (Stuchlík and Hledík, 1999; Stuchlík et al., 2000) and Kerr–de Sitter (KdS) spacetimes (Stuchlík and Slaný, 2004; Slaný and Stuchlík, 2005).

Geodetical motion and related thick accretion disc properties in the Reissner–Nordström–de Sitter (RNdS) spacetimes were studied in Stuchlík and Hledík (2002). Since some characteristics of the geodetical motion in RNdS spacetimes differ from those in SdS and KdS spacetimes, we shall study here properties of equilibrium tori in the RNdS spacetimes.

978-80-7248-419-5

Recall that Reissner–Nordström–(anti-)de Sitter (RN(a)dS) black-hole spacetimes and some RNdS black-hole spacetimes a region containing stable circular geodesics exists, which allows accretion processes in the disk regime. On the other hand, around some naked singularities even two separated regions with stable circular geodesics exist. The inner region is limited from below by particles with zero angular momentum that are located in stable equilibrium positions (Stuchlík and Hledík, 2002).

The hydrodynamical structure of perfect fluid orbiting RNdS black holes (and naked-singularities) is investigated for configurations with uniform distribution of angular momentum density. In the black-hole and the naked-singularity backgrounds admitting the existence of stable circular geodesics, closed equipotential surfaces with a cusp, allowing the existence of toroidal accretion disks, can exist (Stuchlík et al., 2000).

It is well known that at low accretion rates the pressure is negligible, and the accretion disk is geometrically thin. Its basic properties are determined by the circular geodesic motion in the black-hole (naked-singularity) background (Novikov and Thorne, 1973). At high accretion rates, the pressure is relevant, and the accretion disk must be geometrically thick (Abramowicz et al., 1988). Its basic properties are determined by equipotential surfaces of test perfect fluid (i.e., perfect fluid that does not alter the black-hole geometry) rotating in the black-hole (naked-singularity) background.

The accretion is possible, if a toroidal equilibrium configuration of the test fluid containing a critical, self-crossing equipotential surface can exist in the background. The cusp of this equipotential surface corresponds to the inner edge of the disk, and the accretion inflow of matter into the black hole is possible due to a mechanical non-equilibrium process, i.e., because of matter slightly overcoming the critical equipotential surface. The pressure gradients push the inner edge of the thick disks under the radius $r_{\rm ms}$, which corresponds to marginally stable circular geodesic (Kozłowski et al., 1978; Abramowicz et al., 1978).

The simplest, but quite illustrative case of the equipotential surfaces of the test fluid can be constructed for the configurations with uniform distribution of the angular momentum density. This case is fully governed by the geometry of the spacetime, however, it contains all the characteristic features of more complex cases of the rotation of the fluid (Jaroszyński et al., 1980). Moreover, this case is also very important physically since it corresponds to marginally stable equilibrium configurations (Seguin, 1975).

2 PROPERTIES OF THE REISSNER–NORDSTRÖM–(ANTI-)DE SITTER SPACETIMES

In the standard Schwarzschild coordinates (t, r, θ, ϕ), and the geometrical units ($c = G = 1$), the RNdS ($\Lambda > 0$), and RN(a)dS ($\Lambda < 0$) spacetimes are given by the line element (Stuchlík and Hledík, 2002)

$$\begin{aligned} \mathrm{d}s^2 = &-\left(1 - \frac{2M}{r} + \frac{Q^2}{r^2} - \frac{\Lambda}{3}r^2\right)\mathrm{d}t^2 \\ &+ \left(1 - \frac{2M}{r} + \frac{Q^2}{r^2} - \frac{\Lambda}{3}r^2\right)^{-1}\mathrm{d}r^2 + r^2(\mathrm{d}\theta^2 + \sin^2\theta\,\mathrm{d}\phi^2)\,, \end{aligned} \tag{1}$$

and the related electromagnetic field is given by the four-potential

$$A_\mu = \frac{Q}{r}\,\delta^t{}_\mu\,.$$

Here, M denotes mass and Q denotes electric charge of the spacetimes. However, it is convenient to introduce a dimensionless cosmological parameter

$$y \equiv \tfrac{1}{3}\Lambda M^2\,,$$

a dimensionless charge parameter

$$e \equiv \frac{Q}{M}\,,$$

and dimensionless coordinates $t \to t/M, r \to r/M$. It is equivalent to putting $M = 1$.

3 GEODETICAL MOTION

Motion of uncharged test particles and photons is governed by the geodetical structure of the spacetime. The geodesic equation reads

$$\frac{\mathrm{D}p^\mu}{\mathrm{d}\lambda} = 0\,,$$

where $p^\mu \equiv \mathrm{d}x^\mu/\mathrm{d}\lambda$ is the four-momentum of a test particle (photon) and λ is the affine parameter related to the proper time τ of a test particle by $\tau = \lambda/m$.

It follows from the central symmetry of the geometry Eq. (1) that the geodetical motion is allowed in the central planes only. Due to existence of the time Killing vector field $\xi_{(t)} = \partial/\partial t$ and the axial Killing vector field $\xi_{(\phi)} = \partial/\partial\phi$, two constants of the motion must exist, being the projections of the four-momentum onto the Killing vectors (Stuchlík and Hledík, 2002):

$$p_t = g_{t\mu}p^\mu = -\tilde{E}\,,$$
$$p_\phi = g_{\phi\mu}p^\mu = \Phi\,.$$

In the spacetimes with $\Lambda \neq 0$, the constants of motion $\tilde{E}$ and Φ cannot be interpreted as energy and axial component of the angular momentum at infinity since the geometry is not asymptotically flat.

It is convenient to introduce specific energy E, specific axial angular momentum L and impact parameter ℓ by the relations

$$E = \frac{\tilde{E}}{m}\,, \qquad L = \frac{\Phi}{m}\,, \qquad \ell = \frac{\Phi}{\tilde{E}}\,.$$

Choosing the plane of the motion to be the equatorial plane ($\theta = \pi/2$ being constant along the geodesic), we find that the motion of test particles ($m \neq 0$) can be determined by an "effective potential" of the radial motion

$$V_{\mathrm{eff}}^2(r; L, y, e) \equiv \left(1 - \frac{2}{r} + \frac{e^2}{r^2} - yr^2\right)\left(1 + \frac{L^2}{r^2}\right)\,.$$

Since

$$\left(u^r\right)^2 = \left(\frac{\mathrm{d}r}{\mathrm{d}\tau}\right)^2 = E^2 - V_{\mathrm{eff}}^2(r; L, y, e)\,,$$

the motion is allowed where

$$E^2 \geq V_{\mathrm{eff}}^2(r; L, y, e)\,,$$

and the turning points of the radial motion are determined by the condition

$$E^2 = V_{\mathrm{eff}}^2(r; L, y, e)\,.$$

The radial motion of photons ($m = 0$) is determined by a "generalized effective potential" $\ell_{\mathrm{ph}}^2(r; y, e)$ related to the impact parameter ℓ. The motion is allowed, if

$$\ell^2 \leq \ell_{\mathrm{ph}}^2(r; y, e) \equiv \frac{r^4}{r^2 - 2r + e^2 - yr^4}\,,$$

the condition $\ell^2 = \ell_{\mathrm{ph}}^2(r; y, e)$ gives the turning points of the radial motion (Stuchlík and Hledík, 2002).

The special case of $e = 0$ has been extensively discussed in Stuchlík and Hledík (1999). Therefore, we concentrate our discussion on the case $e^2 > 0$. The effective potentials $V_{\mathrm{eff}}^2(r; L, y, e)$ and $\ell_{\mathrm{ph}}^2(r; y, e)$ define turning points of the radial motion at the static regions of the RN(a)dS spacetimes. (At the dynamic regions, where the inequalities $V_{\mathrm{eff}}^2(r; L, y, e) < 0$ and $\ell_{\mathrm{ph}}^2(r; y, e) < 0$ hold, there are no turning points of the radial motion.) Effective potential V_{eff}^2 is zero at the horizons, while ℓ^2 diverges there. At $r = 0$, $V_{\mathrm{eff}}^2 \to +\infty$, while $\ell_{\mathrm{ph}}^2 = 0$. Circular orbits of uncharged test particles correspond to local extrema of the effective potential ($\partial V_{\mathrm{eff}}/\partial r = 0$). Maxima ($\partial^2 V_{\mathrm{eff}}/\partial r^2 < 0$) determine circular orbits unstable with respect to radial perturbations, minima ($\partial^2 V_{\mathrm{eff}}/\partial r^2 > 0$) determine stable circular orbits. The specific energy and specific angular momentum of particles on a circular orbit, at a given r, are determined by the relations (Stuchlík and Hledík, 2002)

$$E_{\mathrm{c}}(r; y, e) = \frac{1 - 2/r + e^2/r^2 - yr^2}{\left(1 - 3/r + 2e^2/r^2\right)^{1/2}}\,, \qquad L_{\mathrm{c}}(r; y, e) = \left(\frac{r - e^2 - yr^4}{1 - 3/r + 2e^2/r^2}\right)^{1/2}\,.$$

(The minus sign for L_{c} is equivalent to the plus sign in spherically symmetric spacetimes.)

4 BOYER'S CONDITION FOR EQUILIBRIUM CONFIGURATIONS OF TEST PERFECT FLUID

We consider test perfect fluid rotating in the ϕ direction. Its four velocity vector field U^μ has, therefore, only two non-zero components

$$U^\mu = (U^t, 0, 0, U^\phi)\,,$$

which can be functions of the coordinates r, θ. The stress-energy tensor of the perfect fluid is

$$T^{\mu}{}_{\nu} = (p + \epsilon)U^{\mu}U_{\nu} + p\,\delta^{\mu}{}_{\nu}\,,$$

where ϵ and p denote the total energy density and the pressure of the fluid. The rotating fluid can be characterized by the vector fields of the angular velocity Ω, and the angular momentum per unit mass (angular momentum density) ℓ, defined by

$$\Omega = \frac{U^{\phi}}{U^{t}}\,, \quad \ell = -\frac{U_{\phi}}{U_{t}}\,.$$

Projecting the energy conservation law $T^{\mu\nu}{}_{;\nu} = 0$ onto the hypersurface orthogonal to the four velocity U^{μ} by the projection tensor $h_{\mu\nu} = g_{\mu\nu} + U_{\mu}U_{\nu}$, we obtain the relativistic Euler equation in the form (Stuchlík et al., 2000)

$$\frac{\partial_{\mu} p}{p + \epsilon} = -\partial_{\mu}(\ln U_{t}) + \frac{\Omega\,\partial_{\mu}\ell}{1 - \Omega\ell}\,,$$

where

$$(U_{t})^{2} = \frac{g_{t\phi}^{2} - g_{tt}\,g_{\phi\phi}}{g_{\phi\phi} + 2\ell g_{t\phi} + \ell^{2} g_{tt}}\,.$$

The solution of the relativistic Euler equation can be given by Boyer's condition determining the surfaces of constant pressure through the "equipotential surfaces" of the potential $W(r, \theta)$ by the relations (Abramowicz et al., 1978)

$$\int_{0}^{p} \frac{\mathrm{d}p}{p + \epsilon} = W_{\mathrm{in}} - W\,, \tag{2}$$

$$W_{\mathrm{in}} - W = \ln(U_{t})_{\mathrm{in}} - \ln(U_{t}) + \int_{\ell_{\mathrm{in}}}^{\ell} \frac{\Omega\,\mathrm{d}\ell}{1 - \Omega\ell}\,; \tag{3}$$

the subscript "in" refers to the inner edge of the disk. The equipotential surfaces are determined by the condition

$$W(r, \theta) = \mathrm{const}\,,$$

and in a given spacetime can be found from Eq. (3), if a rotation law $\Omega = \Omega(\ell)$ is given. The surfaces of constant pressure $p(r, \theta) = \mathrm{const}$ are given by Eq. (2).

5 EQUIPOTENTIAL SURFACES OF THE MARGINALLY STABLE CONFIGURATIONS

Equilibrium configurations of test perfect fluid rotating around an axis of rotation ($\theta = 0$) in a given spacetime are determined by the equipotential surfaces, where the gravitational and inertial forces are just compensated by the pressure gradient (Stuchlík et al., 2000).

The equipotential surfaces can be closed or open. Moreover, there is a special class of critical, self-crossing surfaces (with a cusp), which can be either closed or open. The closed equipotential surfaces determine stationary equilibrium configurations. The fluid can fill any closed surface – at the surface of the equilibrium configuration pressure vanish, but its gradient is non-zero (Kozłowski et al., 1978). The critical, self-crossing closed equipotential surfaces $W_{\rm cusp}$ are important in the theory of thick accretion disks, because accretion onto the black hole through the cusp of the equipotential surface located in the equatorial plane is possible due to the Paczyński mechanism.

According to Paczyński, the accretion into the black hole is driven through the vicinity of the cusp due to a little overcoming of the critical equipotential surface, $W = W_{\rm cusp}$, by the surface of the disk. The accretion is thus driven by a violation of the hydrostatic equilibrium, rather than by viscosity of the accreting matter (Kozłowski et al., 1978).

All characteristic properties of the equipotential surfaces for a general rotation law are reflected by the equipotential surfaces of the simplest configurations with uniform distribution of the angular momentum density ℓ (Jaroszyński et al., 1980). Moreover, these configurations are very important astrophysically, being marginally stable (Seguin, 1975). Under the condition

$$\ell(r,\theta) = \text{const}\,,$$

holding in the rotating fluid, a simple relation for the equipotential surfaces follows from Eq. (3):

$$W(r,\theta) = \ln U_t(r,\theta)\,,$$

with $U_t(r,\theta)$ being determined by $\ell = \text{const}$, and the metric coefficients only.

The equipotential surfaces are described by the formula $\theta = \theta(r)$, given by the differential equation (Stuchlík et al., 2000)

$$\frac{\mathrm{d}\theta}{\mathrm{d}r} = -\frac{\partial p/\partial r}{\partial p/\partial\theta}\,,$$

which for the configurations with $\ell = \text{const}$ reduces to

$$\frac{\mathrm{d}\theta}{\mathrm{d}r} = -\frac{\partial U_t/\partial r}{\partial U_t/\partial\theta}\,.$$

The equipotential surfaces are given by the formula

$$W(r;\theta,y,e) = \ln\frac{(1-2/r+e^2/r^2-yr^2)^{1/2}r\sin\theta}{\left[r^2\sin^2\theta-(1-2/r+e^2/r^2-yr^2)\ell^2\right]^{1/2}}\,.$$

The best insight into the nature of the $\ell = \text{const}$ configurations can be obtained by the examination of the behaviour of the potential $W(r,\theta)$ in the equatorial plane ($\theta = \pi/2$). The condition of the local extrema of the potential $W(r,\theta=\pi/2,y,e)$ is identical with the condition of vanishing of the pressure gradient ($\partial U_t/\partial r = 0$, $\partial U_t/\partial\theta = 0$). The extrema of $W(r,\theta=\pi/2,y,e)$ correspond to the points, where the fluid moves along a circular geodesic (Stuchlík et al., 2000).

6 CLASSIFICATION OF THE REISSNER–NORDSTRÖM–DE SITTER SPACETIMES

Seven types of the RNdS spacetimes with qualitatively different behaviour of the effective potential of the geodetical motion (and the circular orbits) exist. The description of the types of the Reissner–Nordström (RN) spacetimes with a positive cosmological constant ($y > 0$) according to the properties of the circular geodesics can be given in the following way (Stuchlík and Hledík, 2002):

dS-BH-1 One region of circular geodesics at $r > r_{\mathrm{ph}+}$ with unstable then stable and finally unstable geodesics (for radius growing).[1]

dS-BH-2 One region of circular geodesics at $r > r_{\mathrm{ph}+}$ with unstable geodesics only.

dS-NS-1 Two regions of circular geodesics, the inner region consists of stable geodesics only, the outer one contains subsequently unstable, then stable and finally unstable circular geodesics.

dS-NS-2 Two regions of circular orbits, the inner one consist of stable orbits, the outer one of unstable orbits.

dS-NS-3 One region of circular orbits, subsequently with stable, unstable, then stable and finally unstable orbits.

dS-NS-4 One region of circular orbits with stable and then unstable orbits.

dS-NS-5 No circular orbits allowed.

7 PROPERTIES OF EQUILIBRIUM CONFIGURATIONS OF PERFECT FLUID

We shall discuss the perfect fluid configurations in the framework of the RNdS spacetime classification due to circular geodesic properties. Of course, only the spacetimes admitting existence of stable circular geodesics are taken into account, since the equilibrium configurations are allowed only in these spacetimes (Stuchlík and Hledík, 2002).

The behaviour of the potential $W(r, \theta = \pi/2)$, and corresponding equipotential surfaces (meridional sections) are given, according to the values of $\ell = \mathrm{const}$, and illustrated by representative sequences of figures. The radial coordinate is expressed in units of M. The cusps of the toroidal disks correspond to the local maxima of $W(r, \theta = \pi/2)$, the central rings correspond to their local minima.

7.1 dS-BH-1 ($M = 1, e = 0.5, y = 10^{-6}$)

(1) Open surfaces only, no disks are possible, surface with the outer cusp exists ($\ell = 3.00$);

(2) an infinitesimally thin, unstable ring exists ($\ell = 3.55378053$);

(3) closed surfaces exist, many equilibrium configurations without cusps are possible, one with the inner cusp ($\ell = 3.75$);

[1] Type dS-BH-1 means asymptotically de Sitter black-hole spacetime of type 1; in the following, the notation has to be read in an analogous way.

(4) there is an equipotential surface with both the inner and outer cusps, the mechanical non-equilibrium causes an inflow into the black hole, and an outflow from the disk, with the same efficiency ($\ell = 3.8136425$);

(5) accretion into the black-hole is impossible, the outflow from the disk is possible ($\ell = 4.00$);

(6) the potential diverges, the inner cusp disappears ($\ell = 4.96797564$);

(7) the closed equipotential surfaces still exist, one with the outer cusp ($\ell = 6.00$);

(8) an infinitesimally thin, unstable ring exists (the centre, and the outer cusp coalesce) ($\ell = 7.11001349$);

(9) open equipotential surfaces exist only, there is no cusp in this case ($\ell = 10.00$).

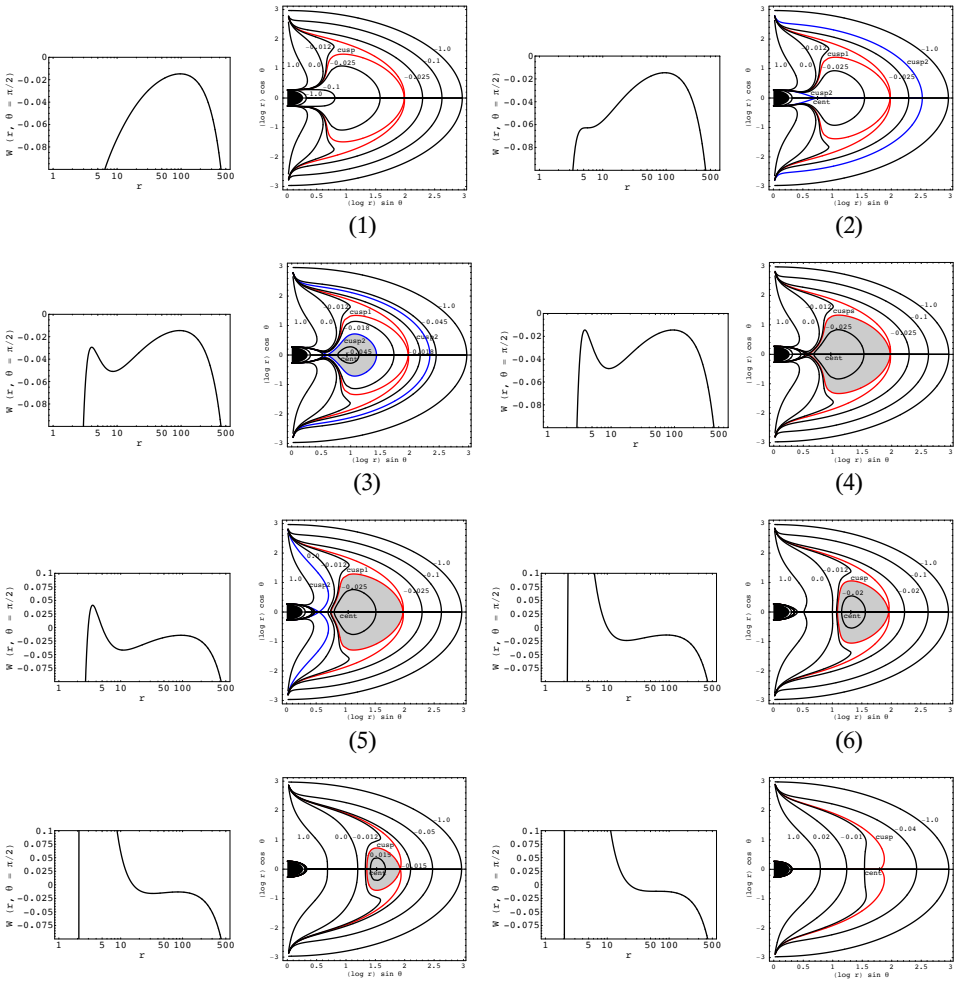

(1) (2) (3) (4) (5) (6) (7) (8)

(plots continued on the next page)

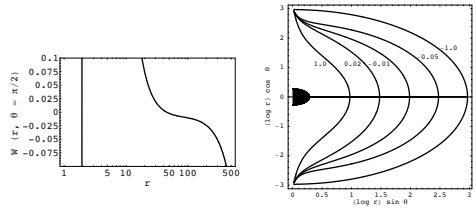

(9)

7.2 dS-NS-1 ($M = 1, e = 1.02, y = 0.00001$)

(1) Closed surfaces exist, one with the outer cusp, equilibrium configurations are possible ($\ell = 2.00$);

(2) the second closed surface with the cusp, and the centre of the second disk appear, the inner disk (1) is inside the outer one (2) ($\ell = 3.04327472$);

(3) two closed surfaces with a cusp exist, the inner disk is still inside the outer one ($\ell = 3.15$);

(4) closed surface with two cusps exists, two disks meet in one cusp, the flow between disk 1 and disk 2, and the outflow from disk 2 are possible ($\ell = 3.2226824$);

(5) the disks are separated, the outflow from disk 1 into disk 2 only, and the outflow from disk 2 are possible ($\ell = 3.55$);

(6) the cusp 1 disappears, the potential diverges, two separated disks still exist ($\ell = 3.91484803$);

(7) like in the previous case, the flow between disk 1 and disk 2 is impossible, the outflow from disk 2 is possible ($\ell = 4.40$);

(8) disk 1 exists, so does an infinitesimally thin, unstable ring exists (region 2) ($\ell = 4.9486708$);

(9) disk 1 exists only, there are no surfaces with a cusp ($\ell = 5.15$);

(10) disk 1 is infinitesimally thin ($\ell = 5.39574484$);

(11) no disks, open equipotential surfaces only ($\ell = 6.00$).

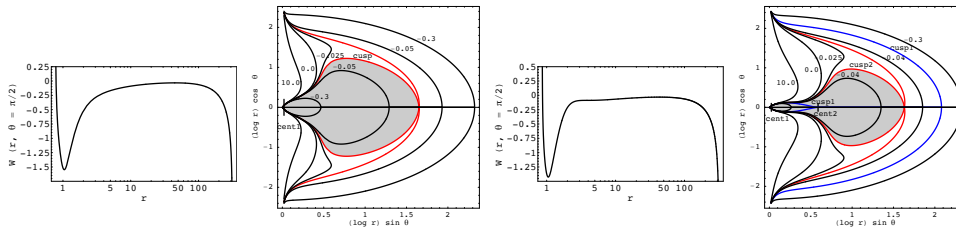

(1) (2)

(plots continued on the next page)

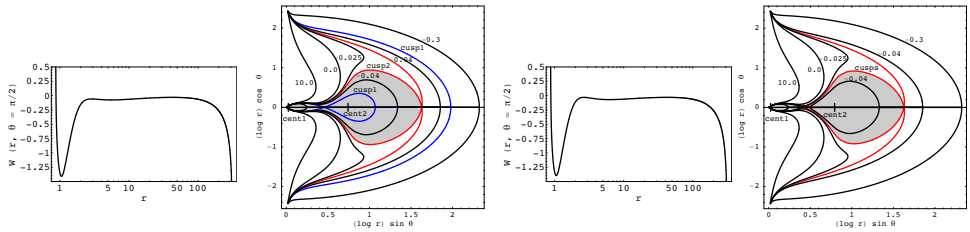

(3) (4)

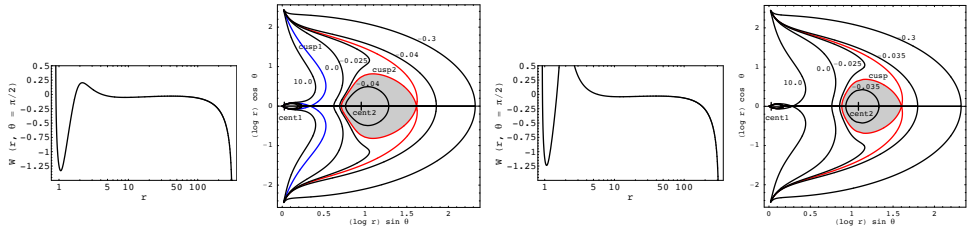

(5) (6)

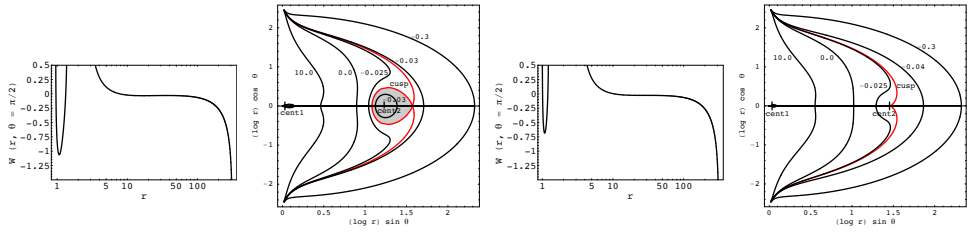

(7) (8)

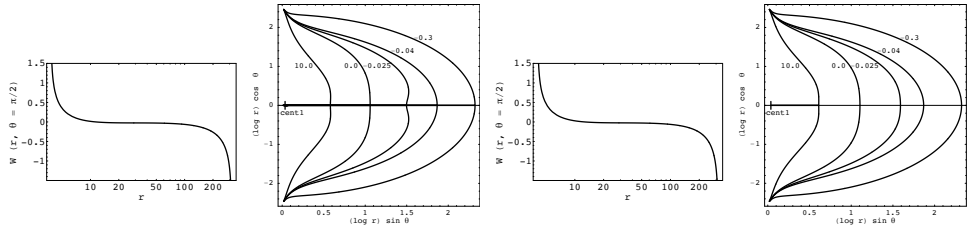

(9) (10)

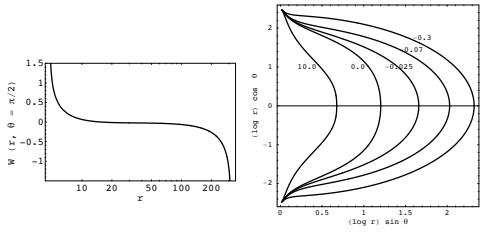

(11)

7.3 dS-NS-2 ($M = 1, e = 1.02, y = 0.01$)

(1) There are only one centre and one disk in this case, closed equipotential surfaces exist, one with the cusp, the outflow from the disk is possible ($\ell = 4.00$);

(2) the potential diverges, the cusp disappears, equilibrium configurations are possible (closed surfaces exist), but the outflow from the disk is impossible ($\ell = 4.25403109$);

(3) the situation is similar to the previous case ($\ell = 5.00$);

(4) the disk is infinitesimally thin ($\ell = 6.40740525$);

(5) no disk is possible, open equipotential surfaces only ($\ell = 7.00$).

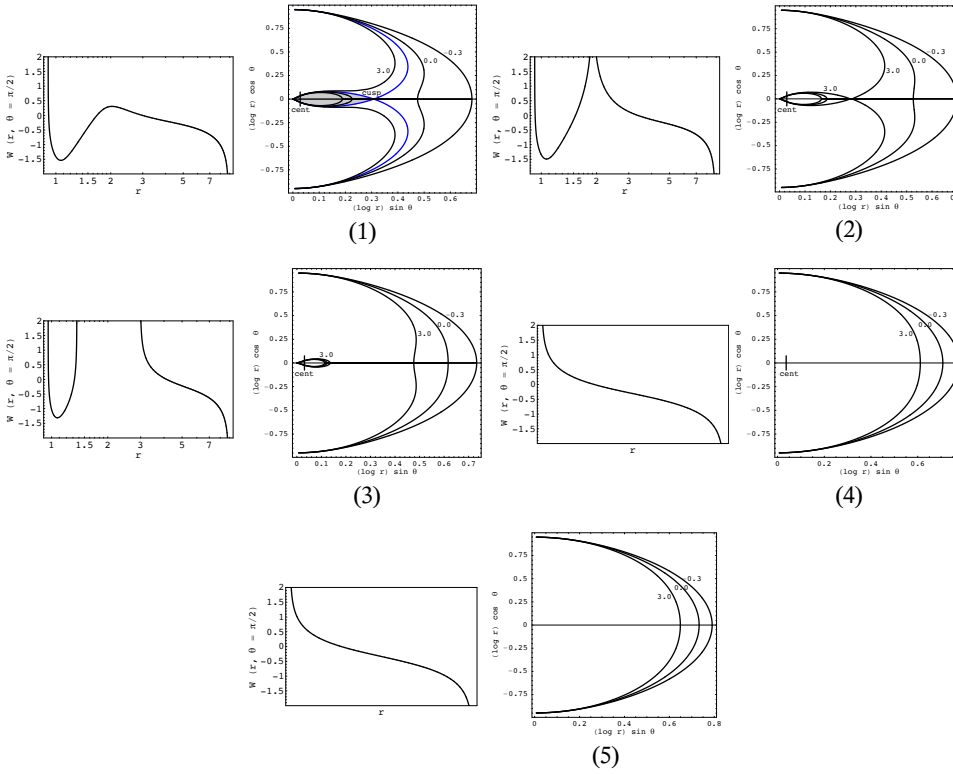

7.4 dS-NS-3 ($M = 1, e = 1.07, y = 0.0001$)

(1) Closed surfaces exist, one with the outer cusp, equilibrium configurations are possible ($\ell = 2.50$);

(2) the second closed surface with the cusp, and the centre of the second disk appear, the inner disk (1) is inside the outer one (2) ($\ell = 2.93723342$);

(3) two closed surfaces with a cusp exist, the inner disk is still inside the outer one ($\ell = 3.00$);

(4) closed surface with two cusps exists, two disks meet in one cusp, the flow between disk 1 and disk 2, and the outflow from disk 2 are possible ($\ell = 3.0411677$);

(5) the disks are separated, the outflow from disk 1 into disk 2 only, and the outflow from disk 2 are possible ($\ell = 3.20$);

(6) an infinitesimally thin, unstable ring exists (region 1), also disk 2 ($\ell = 3.42331737$);

(7) one cusp, and disk 2 exist only, the outflow from disk 2 is possible ($\ell = 3.50$);

(8) an infinitesimally thin, unstable ring exists (region 2) ($\ell = 3.59008126$);

(9) no disk, no cusp, open equipotential surfaces only ($\ell = 3.80$).

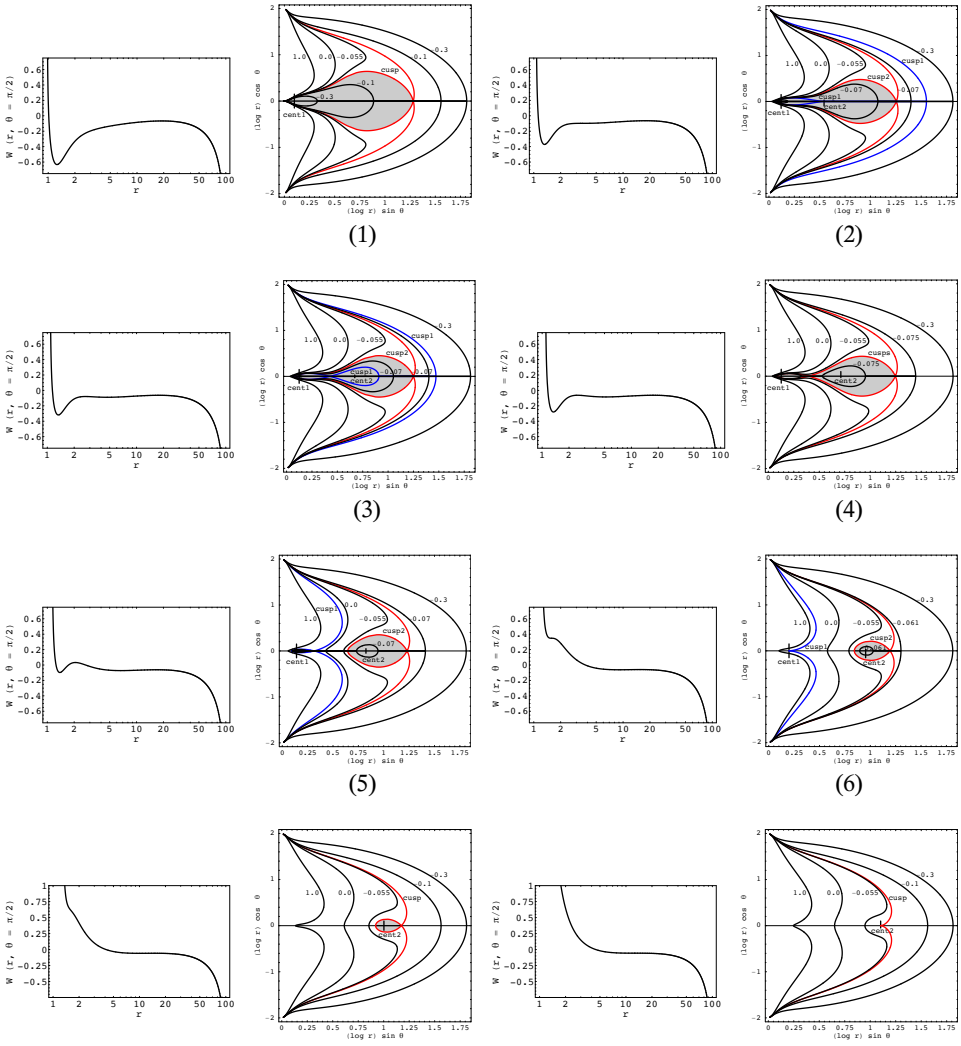

(plots continued on the next page)

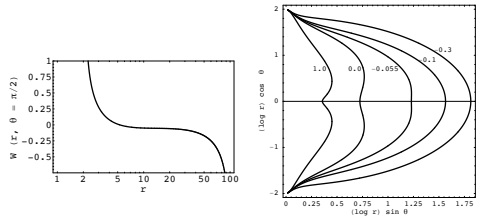

(9)

7.5 dS-NS-4 ($M = 1, e = 1.07, y = 0.01$)

(1) There are only one centre and one disk in this case, closed equipotential surfaces exist, one with the cusp, the outflow from the disk is possible ($\ell = 3.00$);

(2) an infinitesimally thin, unstable ring exists ($\ell = 3.63788074$);

(3) no disk is possible, no cusp, open equipotential surfaces exist only ($\ell = 3.80$).

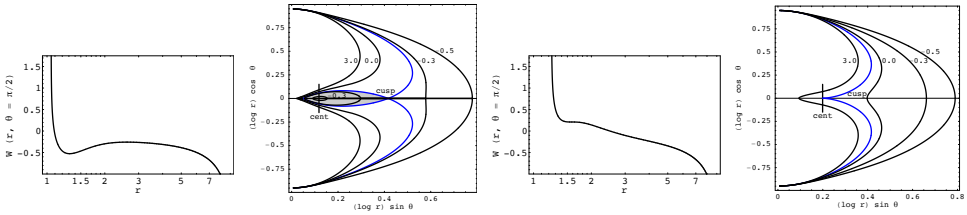

(1) (2)

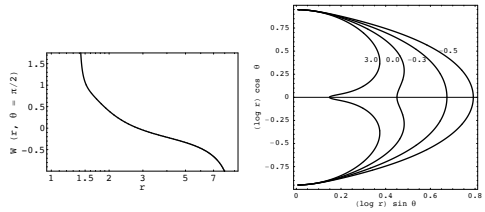

(3)

8 CONCLUSIONS

The RNdS spacetimes can be separated into seven types of spacetimes with qualitatively different character of the geodetical motion. In five of them toroidal disks can exist, because in these spacetimes stable circular orbits exist.

The presence of an outer cusp of toroidal disks nearby the static radius which enables outflow of mass and angular momentum from the accretion disks by the Paczyński mechanism, i.e., due to a violation of the hydrostatic equilibrium. This is the same mechanism that drives the accretion into the black hole through the inner cusp (Stuchlík et al., 2000).

The motion above the outer horizon of black-hole backgrounds has the same character as in the SdS spacetimes for asymptotically de Sitter spacetimes. There is only one static radius in these spacetimes. No static radius is possible under the inner black-hole horizon, no circular geodesics are possible there.

The motion in the naked-singularity backgrounds has similar character as the motion in the field of RN naked singularities. However, in the case of RNdS, two static radii can exist, while the RN naked singularities contain one static radius only. The outer static radius appears due to the effect of the repulsive cosmological constant. Stable circular orbits exist in all of the naked-singularity spacetimes. There are even two separated regions of stable circular geodesics in some cases. The inner one is limited by the inner static radius from bellow, where particles with zero angular momentum (in stable equilibrium positions) are located. In the asymptotically de Sitter naked-singularity spacetimes, two regions of stable circular orbits can exist, if $e^2 < 275/216$, and $y < 0.00174$ (Stuchlík and Hledík, 2002). Then two separated tori are possible in these spacetimes.

ACKNOWLEDGEMENTS

This work was supported by the Czech grant MSM 4781305903 and by the Czech Ministry of Education under the project LC06014.

REFERENCES

Abramowicz, M. A. (1998), Physics of black hole accretion, in M. A. Abramowicz, G. Björnsson and J. E. Pringle, editors, *Theory of Black Hole Accretion Disks*, pp. 50–60, Cambridge University Press, Cambridge.

Abramowicz, M. A., Carter, B. and Lasota, J. (1988), Optical reference geometry for stationary and static dynamics, *Gen. Relativity Gravitation*, **20**, p. 1173.

Abramowicz, M. A., Jaroszyński, M. and Sikora, M. (1978), Relativistic accreting disks, *Astronomy and Astrophysics*, **63**(1–2), pp. 221–224, URL `http://adsabs.harvard.edu/abs/1978A\%26A....63..221A`.

de Felice, F. and Yunqiang, Y. (2001), Turning a black hole into a naked singularity, *Classical Quantum Gravity*, **18**, pp. 1235–1244.

Jaroszyński, M., Abramowicz, M. A. and Paczyński, B. (1980), Supercritical accretion disks around black holes, *Acta Astronom.*, **30**, pp. 1–34.

Kozłowski, M., Jaroszyński, M. and Abramowicz, M. A. (1978), The analytic theory of fluid disks orbiting the Kerr black hole, *Astronomy and Astrophysics*, **63**(1–2), pp. 209–220, URL `http://adsabs.harvard.edu/abs/1978A\%26A....63..209K`.

Novikov, I. D. and Thorne, K. S. (1973), Black hole astrophysics, in C. D. Witt and B. S. D. Witt, editors, *Black Holes*, p. 343, Gordon and Breach, New York–London–Paris.

Penrose, R. (1969), Gravitational collapse: The role of general relativity, *Nuovo Cimento B*, **1**(special number), pp. 252–276.

Seguin, F. H. (1975), *Astrophys. J.*, **197**, p. 745.

Slaný, P. and Stuchlík, Z. (2005), Relativistic thick discs in the Kerr–de Sitter backgrounds, *Classical Quantum Gravity*, **22**, pp. 3623–3651, URL `http://www.iop.org/EJ/abstract/-search=44947255.2/0264-9381/22/17/019`.

Spergel, D. N., Verde, L., Peiris, H. V., Komatsu, E., Nolta, M. R., Bennett, C. L., Halpern, M., Hinshaw, G., Jarosik, N., Kogut, A., Limon, M., Meyer, S. S., Page, L., Tucker, G. S., Weiland, J. L., Wollack, E., Wright, E. L. and Turolla, R. (2003), First Year Wilkinson Microwave Anisotropy Probe (WMAP) Observations: Determination of Cosmological Parameters, *Astrophys. J. Suppl.*, **148**, p. 175, arXiv: `astro-ph/0302209`.

Stuchlík, Z. (2005), Influence of the Relict Cosmological Constant on Accretion Discs, *Modern Phys. Lett. A*, **20**(8), pp. 561–575.

Stuchlík, Z. and Hledík, S. (1999), Some properties of the Schwarzschild–de Sitter and Schwarzschild–anti-de Sitter spacetimes, *Phys. Rev. D*, **60**(4), p. 044006 (15 pages).

Stuchlík, Z. and Hledík, S. (2002), Properties of the Reissner–Nordström spacetimes with a nonzero cosmological constant, *Acta Phys. Slovaca*, **52**(5), pp. 363–407, ISSN 0323-0465/02, erratum notice can be found at `http://www.acta.sav.sk/acta02/no6/`, URL `http://www.acta.sav.sk/acta02/no5/`.

Stuchlík, Z. and Slaný, P. (2004), Equatorial circular orbits in the Kerr–de Sitter spacetimes, *Phys. Rev. D*, **69**, p. 064001, ISSN 1094-1622, arXiv: `gr-qc/0307049`.

Stuchlík, Z., Slaný, P. and Hledík, S. (2000), Equilibrium configurations of perfect fluid orbiting Schwarzschild–de Sitter black holes, *Astronomy and Astrophysics*, **363**(2), pp. 425–439, ISSN 0004-6361 (printed version), 1432-0746 (parallel-to-print version), URL `http://adsabs.harvard.edu/abs/2000A\%26A...363..425S`.

Proceedings of *RAGtime 8/9, 15–19/19–21 September, 2006/2007, Hradec nad Moravicí, Opava, Czech Republic*
S. Hledík and Z. Stuchlík, editors, Silesian University in Opava, 2007, pp. 449–467

Extended orbital resonance model with hump-induced oscillations

Zdeněk Stuchlík[a], Petr Slaný and Gabriel Török

Institute of Physics, Faculty of Philosophy & Science, Silesian University in Opava,
Bezručovo nám. 13, CZ-746 01 Opava, Czech Republic
[a] zdenek.stuchlik@fpf.slu.cz

ABSTRACT
Change of sign of the LNRF-velocity gradient has been found for accretion discs orbiting rapidly rotating Kerr black holes with spin $a > 0.9953$ for Keplerian discs and $a > 0.99979$ for marginally stable thick discs. Such a "humpy" LNRF-velocity profiles occur just above the marginally stable circular geodesic and could be related to oscillations of accretion discs. The frequency of such "hump"-induced oscillations can be identified with the maximal rate of change of the orbital velocity within the "humpy" profile. Therefore, we introduce an extended orbital resonance model (EXORM) of quasiperiodic oscillations (QPOs) assuming non-linear resonant phenomena between oscillations with the orbital epicyclic frequencies and the humpy frequency defined in a fully general relativistic way. The EXORM is developed for both Keplerian discs and perfect-fluid tori where the approximation of oscillations with epicyclic frequencies is acceptable. Clearly, the EXORM could be applied to the near-extreme Kerr black hole systems exhibiting relatively complex QPO frequency patterns. Assuming a Keplerian disc, it can be shown that in the framework of the EXORM, all the QPOs observed in the microquasar GRS 1915+105 could be explained, while it is not possible in the case of QPOs observed in the Galactic Centre source Sgr A*.

Keywords: Black hole physics – accretion, accretion disks – relativity

1 INTRODUCTION

High frequency (kHz) twin peak quasi-periodic oscillations (QPOs) with frequency ratios 3 : 2 (and sometimes 3:1) are observed in microquasars (see, e.g., van der Klis, 2000; McClintock and Remillard, 2004; Remillard, 2005). In the Galactic Centre black hole Sgr A*, Genzel et al. (2003) measured a clear periodicity of 1020 sec in variability during a flaring event. This period is in the range of Keplerian orbital periods at a few gravitational radii from a black hole with mass $M \sim 3.6 \times 10^6\,\mathrm{M}_\odot$ estimated for Sgr A* (Ghez et al., 2005; Weinberg et al., 2005). More recently, Aschenbach et al. (2004); Aschenbach (2004, 2006) reported three QPO periodicities at 692 sec, 1130 sec and 2178 sec that correspond to frequency ratios $(1/692) : (1/1130) : (1/2178) \sim 3 : 2 : 1$. These observational data are not quite convincing (see, e.g., Abramowicz et al., 2004), but surely deserve attention (Aschenbach, 2007).

978-80-7248-419-5

Detailed analysis of the variable X-ray black-hole binary system (microquasar) GRS 1915+105 reveals high-frequency QPOs appearing at five frequencies, namely $\nu_1 = (27 \pm 1)$ Hz (Belloni et al., 2001), $\nu_2 = (41 \pm 1)$ Hz, $\nu_3 = (67 \pm 1)$ Hz (Morgan et al., 1997; Strohmayer, 2001), and $\nu_4 = (113 \pm 5)$ Hz, $\nu_5 = (167 \pm 5)$ Hz (Remillard and McClintock, 2006). In this range of their errors, both upper pairs are close to the frequency ratio 3 : 2 suggesting the possible existence of resonant phenomena in the system. Observations of oscillations with these frequencies have different qualities, but in all five cases the data are quite convincing (see McClintock and Remillard, 2004; Remillard and McClintock, 2006).

Several models have been developed to explain the kHz QPO frequencies, and it is usually preferred that these oscillations are related to the orbital motion near the inner edge of an accretion disc. In particular, two ideas based on the strong-gravity properties have been proposed. While Stella and Vietri (1998, 1999) introduced the "Relativistic Precession Model" considering that the kHz QPOs directly manifest the modes of a slightly perturbed (and therefore epicyclic) relativistic motion of blobs in the inner parts of the accretion disc, Kluźniak and Abramowicz (2001) propose models based on non-linear oscillations of an accretion disc that assume resonant interaction between orbital and/or epicyclic modes. In a different context, the possibility of resonant coupling between the epicyclic modes of motion in the Kerr spacetime was also mentioned in the early work of Aliev and Galtsov (1981). The radial and vertical epicyclic oscillations could be related to both the thin Keplerian discs (Abramowicz et al., 2003; Kato, 2001) and the thick, toroidal accretion discs (Rezzolla et al., 2003). In particular, the observations of high frequency twin peak QPOs with the 3 : 2 frequency ratio in microquasars can be explained by the parametric resonance between the radial and vertical epicyclic oscillations, $\nu_{\rm v} : \nu_{\rm r} \sim 3 : 2$. This hypothesis, under the assumption of geodesic oscillations (i.e., for thin discs), puts strong limit on the mass-spin relation for the central black hole in microquasars (Török et al., 2005; Török, 2005; Török et al., 2006).

Aschenbach (2004, 2006, 2007) discovered that two changes of sign of the radial gradient of the Keplerian orbital velocity as measured in the locally non-rotating frame (LNRF, Bardeen et al., 1972) occur in the equatorial plane of Kerr black holes with $a > 0.9953$. Stuchlík et al. (2005) have found that the gradient sign change in the LNRF-velocity profiles occurs also for non-geodesic motion with uniform distribution of the specific angular momentum $\ell(r, \theta) = \text{const}$ (i.e., in marginally stable thick discs) around extremely rapid Kerr black holes with $a > 0.99979$.[1] The global character of the phenomenon is given in terms of topology changes of the von Zeipel surfaces (equivalent to equivelocity surfaces in the tori with $\ell(r, \theta) = \text{const}$). Toroidal von Zeipel surfaces exist around the circle corresponding to the minimum of the equatorial LNRF-velocity profile, indicating possibility of development of some instabilities in that part of the marginally stable disc with positive gradient of the orbital velocity in LNRF (Stuchlík et al., 2004, 2005, 2006a,b, 2007a,b,c,d).

The positive radial gradient of orbital LNRF-velocity around black holes with $a > 0.9953$ seems to be a physically interesting phenomenon, even if a direct mechanism relating this

[1] Note that the assumption of uniform distribution of the specific angular momentum can be relevant at least at the inner parts of the thick disc and that matter in the disc follows nearly geodesic circular orbits nearby the center of the disc and in the vicinity of its inner edge determined by the cusp of its critical equipotential surface (see Abramowicz et al., 1978).

phenomenon to triggering the oscillations, and subsequent linking of the oscillations to the excitation of radial (and vertical) epicyclic oscillations, is unknown. Therefore, an extended orbital resonance model (EXORM) has been developed, with hypothetical hump-induced oscillations assumed to enter a non-linear resonance with the radial or vertical epicyclic oscillations (Stuchlík et al., 2007b). It should be stressed that due to the non-linear resonance, combinational frequencies are allowed to be observable.

In the EXORM, the frequency of the hump-induced oscillations is related to the maximal positive radial gradient of the LNRF-velocity in the "humpy" velocity profile in the general relativistic, coordinate-independent form. Further, since the gradient is defined locally, being connected to the LNRF, it has to be transformed into the form related to distant stationary observers, giving observationally relevant "humpy" frequency $\nu_{\rm h}$. Then the "humpy" and epicyclic frequencies could be estimated at the radius of definition of the "humpy" frequency.

In the case of Keplerian discs, the epicyclic resonance radii $r_{3:1}$ and $r_{4:1}$ (with $\nu_{\rm v} : \nu_{\rm r} = 3:1, 4:1$) are located in vicinity of the "humpy" radius $r_{\rm h}$ where efficient triggering of oscillations with frequencies $\sim \nu_{\rm h}$ could be expected. Asymptotically (for $1-a < 10^{-4}$) the ratio of the epicyclic and Keplerian frequencies and the humpy frequency is nearly constant, i.e., almost independent of a, being for the radial epicyclic frequency $\nu_{\rm r} : \nu_{\rm h} \sim 3:2$. In the case of thick discs, the situation is more complex due to dependence on distribution of the specific angular momentum ℓ determining the disc properties. For $1-a < 10^{-6}$, the frequency ratios of the humpy frequency and the orbital and epicyclic frequencies are again nearly constant and independent of both a and ℓ being for the radial epicyclic frequency $\nu_{\rm r} : \nu_{\rm h} \sim 4:1$. In the limiting case of very slender tori ($\ell \sim \ell_{\rm ms}$) the epicyclic resonance radius $r_{4:1} \sim r_{\rm h}$ for all the relevant interval of $1-a < 2\times 10^{-4}$.

In Section 2, we briefly summarize properties of the Aschenbach effect for Keplerian thin discs, and $\ell = {\rm const}$ thick discs. In Section 3, the extended resonance model is introduced, i.e., the critical "humpy" frequency, connected to the LNRF-velocity positive gradient in the humpy profiles, is given in the physically relevant, coordinate independent form for the both Keplerian and $\ell = {\rm const}$ discs. At the radius of its definition, the humpy frequency is compared to the radial and vertical epicyclic frequency and the orbital frequency. In Section 4, fitting of the observed frequencies in the GRS 1915+105 microquasar in the framework of the EXORM is summarized, while it is demonstrated that the data reported for Sgr A* could not be probably fitted by EXORM. In Section 5, concluding remarks are presented.

2 LNRF-VELOCITY PROFILES OF ACCRETION DISCS

The locally non-rotating frames (LNRF) are given by the tetrad of 1-forms (Bardeen et al., 1972)

$$\begin{aligned} \boldsymbol{e}^{(t)} &= \left(\frac{\Sigma\Delta}{A}\right)^{1/2} \boldsymbol{d}t\,, \quad \boldsymbol{e}^{(\varphi)} = \left(\frac{A}{\Sigma}\right)^{1/2} \sin\theta\,(\boldsymbol{d}\varphi - \omega\,\boldsymbol{d}t)\,, \\ \boldsymbol{e}^{(r)} &= \left(\frac{\Sigma}{\Delta}\right)^{1/2} \boldsymbol{d}r\,, \qquad \boldsymbol{e}^{(\theta)} = \Sigma^{1/2}\,\boldsymbol{d}\theta\,, \end{aligned} \tag{1}$$

where

$$\omega = -\frac{g_{t\varphi}}{g_{\varphi\varphi}} = \frac{2ar}{A} \tag{2}$$

is the angular velocity of the LNRF relative to distant observers.

In the Kerr spacetimes with the rotational parameter assumed to be $a > 0$, the relevant metric coefficients in the standard Boyer–Lindquist coordinates read:

$$g_{tt} = -\frac{\Delta - a^2 \sin^2\theta}{\Sigma}\,,\ g_{t\varphi} = -\frac{2ar\sin^2\theta}{\Sigma}\,,\ g_{\varphi\varphi} = \frac{A\sin^2\theta}{\Sigma}\,,\ g_{rr} = \frac{\Sigma}{\Delta}\,,\ g_{\theta\theta} = \Sigma\,, \tag{3}$$

where

$$\Delta = r^2 - 2r + a^2\,, \quad \Sigma = r^2 + a^2\cos^2\theta\,, \quad A = (r^2+a^2)^2 - \Delta a^2\sin^2\theta\,. \tag{4}$$

The geometrical units, $c = G = 1$, together with putting the mass of the black hole $M = 1$, are used in order to obtain completely dimensionless formulae hereafter.

For matter orbiting a Kerr black hole with a 4-velocity U^μ and angular velocity profile $\Omega(r,\theta)$, the azimuthal component of its 3-velocity in the LNRF reads

$$\mathcal{V}^{(\varphi)} = \frac{U^\mu e^{(\varphi)}_\mu}{U^\nu e^{(t)}_\nu} = \frac{A\sin\theta}{\Sigma\sqrt{\Delta}}\,(\Omega - \omega)\,. \tag{5}$$

2.1 Keplerian thin discs

In thin discs matter follows nearly circular geodetical orbits characterized by the Keplerian distributions of the angular velocity and the specific angular momentum (in the equatorial plane, $\theta = \pi/2$)

$$\Omega = \Omega_{\rm K}(r;a) \equiv \frac{1}{(r^{3/2}+a)}\,, \qquad \ell = \ell_{\rm K}(r;a) \equiv \frac{r^2 - 2ar^{1/2} + a^2}{r^{3/2} - 2r^{1/2} + a}\,. \tag{6}$$

The azimuthal component of the Keplerian 3-velocity in the LNRF reads

$$\mathcal{V}^{(\varphi)}_{\rm K}(r;a) = \frac{(r^2+a^2)^2 - a^2\Delta - 2ar(r^{3/2}+a)}{r^2(r^{3/2}+a)\sqrt{\Delta}} \tag{7}$$

and formally diverges for $r \to r_+ = 1 + \sqrt{1-a^2}$, where the black-hole event horizon is located. Its radial gradient is given by

$$\frac{\partial \mathcal{V}^{(\varphi)}_{\rm K}}{\partial r} = -\frac{r^5 + a^4(3r+2) - 2a^3 r^{1/2}(3r+1) - 2a^2r^2(2r-5) + 2ar^{5/2}(5r-9)}{2\Delta^{3/2}\sqrt{r}\,(r^{3/2}+a)^2}\,. \tag{8}$$

As shown by Aschenbach (2004, 2006), the velocity profile has two changes of the gradient sign (where $\partial\mathcal{V}^{(\varphi)}/\partial r = 0$) in the field of rapidly rotating Kerr black holes with $a > a_{\rm c(K)} \doteq 0.9953$.

2.2 Marginally stable tori

Perfect-fluid stationary and axisymmetric toroidal discs are characterized by the 4-velocity field $U^\mu = (U^t, 0, 0, U^\varphi)$ with $U^t = U^t(r,\theta)$, $U^\varphi = U^\varphi(r,\theta)$, and by distribution of the specific angular momentum $\ell = -U_\varphi/U_t$. The angular velocity of orbiting matter, $\Omega = U^\varphi/U^t$, is then related to ℓ by the formula

$$\Omega = -\frac{\ell g_{tt} + g_{t\varphi}}{\ell g_{t\varphi} + g_{\varphi\varphi}}\,. \tag{9}$$

The marginally stable tori are characterized by uniform distribution of the specific angular momentum

$$\ell = \ell(r,\theta) = \text{const}\,, \tag{10}$$

and are fully determined by the spacetime structure through equipotential surfaces of the potential $W = W(r,\theta)$ defined by the relations (Abramowicz et al., 1978)

$$W - W_{\text{in}} = \ln\frac{U_t}{(U_t)_{\text{in}}}\,, \qquad (U_t)^2 = \frac{g_{t\varphi}^2 - g_{tt}g_{\varphi\varphi}}{g_{tt}\ell^2 + 2g_{t\varphi}\ell + g_{\varphi\varphi}}\,; \tag{11}$$

the subscript "in" refers to the inner edge of the disc. The LNRF orbital velocity of the torus is given by

$$\mathcal{V}_{\text{T}}^{(\varphi)} = \frac{A(\Delta - a^2\sin^2\theta) + 4a^2r^2\sin^2\theta}{\Sigma\sqrt{\Delta}\,(A - 2a\ell r)\sin\theta}\,\ell\,. \tag{12}$$

For marginally stable tori it is enough to consider the motion in the equatorial plane, $\theta = \pi/2$. Formally, this velocity vanishes for $r \to \infty$ and $r \to r_+$, i.e., there must be a change of its radial gradient for any values of the parameters a and ℓ, contrary to the case of Keplerian discs. The radial gradient of the equatorial LNRF velocity of $\ell = \text{const}$ tori reads

$$\frac{\partial\mathcal{V}_{\text{T}}^{(\varphi)}}{\partial r} = \left\{\frac{[\Delta + (r-1)r][r(r^2+a^2) - 2a(\ell - a)]}{[r(r^2+a^2) - 2a(\ell-a)]^2\sqrt{\Delta}} - \frac{r(3r^2+a^2)\Delta}{[r(r^2+a^2) - 2a(\ell-a)]^2\sqrt{\Delta}}\right\}\ell\,, \tag{13}$$

so it changes its orientation at radii determined for a given ℓ by the condition

$$\ell = \ell_{\text{ex}}(r;a) \equiv a + \frac{r^2[(r^2+a^2)(r-1) - 2r\Delta]}{2a[\Delta + r(r-1)]}. \tag{14}$$

For both thick tori and Keplerian discs we have to consider the limit on the disc extension given by the innermost stable orbit. For Keplerian discs this is the marginally stable geodetical orbit, $r_{\text{in}} \approx r_{\text{ms}}$, while for thick tori this is an unstable circular geodesic kept stable by pressure gradients and located between the marginally bound and the marginally stable geodetical orbits, $r_{\text{mb}} \lesssim r_{\text{in}} \lesssim r_{\text{ms}}$, with the radius being determined by the specific angular

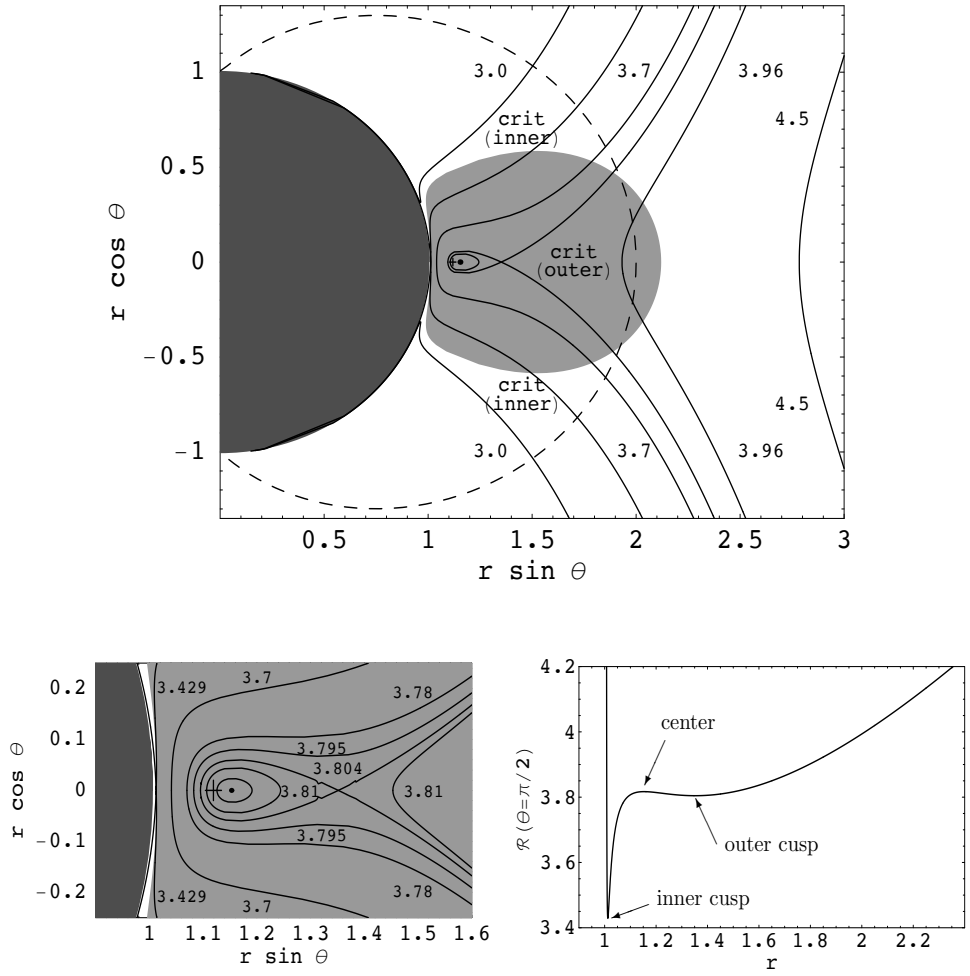

Figure 1. Von Zeipel surfaces (meridional sections). For $a > a_{\mathrm{c(T)}}$ and ℓ appropriately chosen, two surfaces with a cusp, or one surface with both the cusps, together with closed (toroidal) surfaces, exist, being located always inside the ergosphere (dashed surface) of a given spacetime. Both the outer cusp and the central ring of closed surfaces are located inside the toroidal equilibrium configurations corresponding to marginally stable thick discs (light-gray region; its shape is determined by the critical self-crossing *equipotential surface* of the potential $W(r, \theta)$. The cross (+) denotes the centre of the torus. Dark region corresponds to the black hole. Figures illustrating all possible configurations of the von Zeipel surfaces are presented in Stuchlík et al. (2005). Here we present the figure plotted for the parameters $a = 0.99998$, $\ell = 2.0065$. Critical value of the von Zeipel radius corresponding to the inner and the outer self-crossing surface is $\mathcal{R}_{\mathrm{c(in)}} \doteq 3.429$ and $\mathcal{R}_{\mathrm{c(out)}} \doteq 3.804$, respectively, the central ring of toroidal surfaces corresponds to the value $\mathcal{R}_{\mathrm{center}} \doteq 3.817$. Interesting region containing both the cusps and the toroidal surfaces is plotted in detail at the left lower figure. Right lower figure shows the behaviour of the von Zeipel radius in the equatorial plane. (Taken from Stuchlík et al., 2007b)

momentum $\ell = \text{const} \in (l_{\rm ms}, l_{\rm mb})$ through the equation $\ell = \ell_{\rm K}(r; a)$; $\ell_{\rm ms}$ ($\ell_{\rm mb}$) denotes specific angular momentum of the circular marginally stable (marginally bound) geodesic.

Detailed discussion of Stuchlík et al. (2005) shows that two physically relevant changes of sign of $\partial \mathcal{V}_{\rm T}^{(\varphi)}/\partial r$ in the tori occur for Kerr black holes with the rotational parameter $a > a_{\rm c(T)} \doteq 0.99979$. The interval of relevant values of the specific angular momentum $\ell \in (\ell_{\rm ms}(a), \ell_{\rm ex(max)}(a))$, where $\ell_{\rm ex(max)}(a)$ corresponds to the local maximum of the function (14), grows with a growing up to the critical value of $a_{\rm c(mb)} \doteq 0.99998$. For $a > a_{\rm c(mb)}$, the interval of relevant values of $\ell \in (\ell_{\rm ms}(a), \ell_{\rm mb}(a))$ is narrowing with the rotational parameter growing up to $a = 1$, which corresponds to a singular case where $\ell_{\rm ms}(a = 1) = \ell_{\rm mb}(a = 1) = 2$. Notice that the situation becomes to be singular only in terms of the specific angular momentum; it is shown (see Bardeen et al., 1972) that for $a = 1$ both the total energy E and the axial angular momentum L differ at $r_{\rm ms}$ and $r_{\rm mb}$, respectively, but their combination, $\ell \equiv L/E$, giving the specific angular momentum, coincides at these radii.

A physically reasonable global quantity characterizing rotating fluid configurations in terms of the LNRF orbital velocity is so-called von Zeipel radius defined by the relation

$$\mathcal{R} \equiv \frac{\ell}{\mathcal{V}_{\rm LNRF}^{(\varphi)}} = (1 - \omega\ell)\,\tilde{\varrho}\,, \tag{15}$$

which generalizes in another way as compared with (Abramowicz et al., 1995) the Schwarzschildian definition of the gyration radius $\tilde{\varrho}$ (Abramowicz et al., 1993). Note that, except for the Schwarzschild case $a = 0$, the von Zeipel surfaces, defined as the surfaces of $\mathcal{R}(r, \theta; a, \ell) = \text{const}$, *do not coincide* with those introduced by Kozłowski et al. (1978) as the surfaces of constant ℓ/Ω (see Stuchlík et al., 2005 for more details).

In the case of marginally stable tori the von Zeipel surfaces $\mathcal{R} = \text{const}$ coincide with the equivelocity surfaces $\mathcal{V}^{(\varphi)}(r, \theta; a, \ell) = \mathcal{V}_{\rm T}^{(\varphi)} = \text{const}$. Topology of the von Zeipel surfaces can be directly determined by the behaviour of the von Zeipel radius in the equatorial plane

$$\mathcal{R}(r, \theta = \pi/2; a, \ell) = \frac{r(r^2 + a^2) - 2a(\ell - a)}{r\sqrt{\Delta}}\,. \tag{16}$$

The local minima of the function (16) determine loci of the cusps of the von Zeipel surfaces, while its local maximum (if it exists) determines a circle around which closed toroidally shaped von Zeipel surfaces are concentrated (see Fig. 1). Notice that the inner cusp is always physically irrelevant being located outside of the toroidal configuration of perfect fluid. Behaviour of the von Zeipel surfaces nearby the centre and the inner edge of the thick discs orbiting Kerr black holes with $a > a_{\rm c(T)} \doteq 0.99979$, i.e., the existence of the von Zeipel surface with toroidal topology, suggests possible generation of instabilities in both the vertical and radial direction.

In terms of the redefined rotational parameter $(1 - a)$, the "humpy" profile of the LNRF orbital velocity of marginally stable thick discs occurs for discs orbiting Kerr black holes with $1 - a < 1 - a_{\rm c(T)} \doteq 2.1 \times 10^{-4}$, which is more than one order lower than the value $1 - a_{\rm c(K)} \doteq 4.7 \times 10^{-3}$ found by Aschenbach (2004) for the Keplerian thin discs. Moreover, in the thick discs, the velocity difference $\Delta\mathcal{V}_{\rm T}^{(\varphi)}$ is smaller but comparable with those in the thin discs. In fact, for $a \to 1$, the velocity difference in the thick discs $\Delta\mathcal{V}_{\rm T}^{(\varphi)} \approx 0.02$, while for the Keplerian discs it goes even up to $\Delta\mathcal{V}_{\rm K}^{(\varphi)} \approx 0.07$ (Stuchlík et al., 2007d).

3 EXTENDED ORBITAL RESONANCE MODEL

The orbital resonance model assumes non-linear parametric and forced resonances of oscillations with the orbital (Keplerian) and radial or vertical epicyclic frequencies, or their combinations. Here, we extend this model by introducing hypothetical additional oscillations, induced by the hump in the LNRF-velocity profile of accretion discs of both Keplerian and toroidal character, that are supposed to be in a non-linear resonance with orbital or epicyclic oscillations.

In Kerr spacetimes, the frequencies of the radial and latitudinal (vertical) epicyclic oscillations related to an equatorial Keplerian circular orbit at a given r are determined by the formulae (see, e.g., Aliev and Galtsov, 1981)

$$\nu_{\mathrm{r}}^2 = \nu_{\mathrm{K}}^2(1 - 6r^{-1} + 8ar^{-3/2} - 3a^2r^{-2})\,, \tag{17}$$

$$\nu_{\mathrm{v}}^2 \equiv \nu_{\theta}^2 = \nu_{\mathrm{K}}^2(1 - 4ar^{-3/2} + 3a^2r^{-2})\,, \tag{18}$$

where the Keplerian frequency $\nu_{\mathrm{K}} = \Omega_{\mathrm{K}}/2\pi$. A detailed analysis of properties of the epicyclic frequencies can be found in Török and Stuchlík (2005a,b). The epicyclic oscillations with the frequencies ν_{r}, ν_{v} can be related to both the thin Keplerian discs (Abramowicz and Kluźniak, 2001; Kato, 2004) and thick, toroidal discs (Rezzolla et al., 2003).

According to Aschenbach (2004, 2006), the non-monotonicity of the LNRF-velocity profile of accretion discs could excite oscillations with characteristic frequency that has to be related to the maximum gradient in the "humpy" part of the accretion discs velocity profile.

Although there is no detailed idea on the mechanism generating the hump-induced oscillations, it is clear that the Aschenbach proposal of defining the characteristic frequency deserves attention. It should be stressed, however, that a detailed analysis of the instability could reveal a difference between the characteristic frequency and the actual observable one, as the latter should be associated with the fastest growing unstable mode. In any case, the humpy frequency represents an upper limit on the frequencies of the hump-induced oscillations, as it is given by maximum of the LNRF-velocity gradient in the humpy part of the velocity profile.

At the present state of the EXORM, we assume that the characteristic humpy frequency is a typical frequency of oscillations induced by the conjectured "humpy instability," and that the humpy oscillations could excite oscillations with the epicyclic frequencies or some combinational frequencies, if appropriate conditions for a forced resonance are satisfied in vicinity of the radius where the humpy oscillations occur (Stuchlík et al., 2007d).

The fully general relativistic definition of the critical frequency for a possible excitation of oscillations in the disc is given by the relations

$$\nu_{\mathrm{crit}}^{\tilde{R}} = \left.\frac{\partial \mathcal{V}^{(\varphi)}}{\partial \tilde{R}}\right|_{\max}, \qquad \mathrm{d}\tilde{R} = \sqrt{g_{rr}}\,\mathrm{d}r = \sqrt{\frac{\Sigma}{\Delta}}\,\mathrm{d}r\,, \tag{19}$$

where $\mathcal{V}^{(\varphi)} = \mathcal{V}_{\mathrm{K}}^{(\varphi)}(r; a)$ in thin Keplerian discs, and $\mathcal{V}^{(\varphi)} = \mathcal{V}_{\mathrm{T}}^{(\varphi)}(r; l, a)$ in marginally stable thick discs and $\tilde{R}$ is the physically relevant, coordinate independent proper radial distance. Such a locally defined frequency, confined naturally to the observers orbiting the black hole with the LNRF, should be further related to distant stationary observers by the

formula (taken at the BL coordinate r corresponding to $(\partial \mathcal{V}^{(\varphi)}/\partial \tilde{R})_{\max}$)

$$\nu_{\rm h} = \nu_{\infty}^{\tilde{R}} = \sqrt{-(g_{tt} + 2\omega g_{t\varphi} + \omega^2 g_{\varphi\varphi})}\, \nu_{\rm crit}^{\tilde{R}}\,. \tag{20}$$

We call such a coordinate-independent and, in principle, observable frequency the "humpy frequency," as it is related to the humpy profile of $\mathcal{V}^{(\varphi)}$, and denote it $\nu_{\rm h}$. It should be stressed that the physically relevant humpy frequency $\nu_{\rm h} = \nu_{\infty}^{\tilde{R}}$, connected to observations by distant observers and exactly defined by Eqs (19) and (20), represents an upper limit on characteristic frequencies of oscillations induced by the hump of the LNRF-velocity profile, and the realistic humpy frequencies, as observed by distant observers, can be expected close to but smaller than $\nu_{\infty}^{\tilde{R}}$. Further, we denote $r_{\rm h}$ the BL radius of definition of the humpy oscillations frequency, where $\partial \mathcal{V}^{(\varphi)}/\partial \tilde{R} = (\partial \mathcal{V}^{(\varphi)}/\partial \tilde{R})_{\max}$.

In the case of the Keplerian discs we obtain the "humpy frequency" to be given by the relation

$$\begin{aligned}\nu_{\rm h} =& \frac{-r_{\rm h}^5 - a^4(3r_{\rm h}+2) + 2a^3 r_{\rm h}^{1/2}(3r_{\rm h}+1) - 2a^2 r_{\rm h}^2(2r_{\rm h}-5) + 2a r_{\rm h}^{5/2}(5r_{\rm h}-9)}{2\Delta_{\rm h} r_{\rm h}^2\,(r_{\rm h}^{3/2}+a)^2} \\ &\times \sqrt{r_{\rm h} - 2 - \frac{4a^2}{r_{\rm h}(r_{\rm h}^2+a^2)+2a^2}}\,,\end{aligned} \tag{21}$$

where $\Delta_{\rm h} = r_{\rm h}^2 - 2r_{\rm h} + a^2$. The BL radius $r_{\rm h}$ where the positive gradient of the velocity profile in terms of the proper radial distance reaches its maximum, so-called "humpy radius," is given by the condition

$$\frac{\partial}{\partial r}\left(\frac{\partial \mathcal{V}^{(\varphi)}}{\partial \tilde{r}}\right) = 0 \tag{22}$$

leading to the equation

$$\begin{aligned}&3a^7(r+2) + a^6\sqrt{r}(21r^2+18r-4) - a^5 r(33r^2+10r+20) \\ &\quad + a^4 r\sqrt{r}(45r^3 - 62r^2 - 68r + 16) - a^3 r^3(83r^2 - 122r - 60) \\ &\quad + a^2 r^4\sqrt{r}(27r^2 - 130r + 136) - 9a r^5(7r^2 - 26r + 24) \\ &\quad + r^7\sqrt{r}(3r-2) = 0\,,\end{aligned} \tag{23}$$

which must be solved numerically. The spin dependence of the humpy radius and the related humpy frequency is illustrated in Fig. 2. The humpy radius $r_{\rm h}$ falls monotonically with increasing spin a, while the humpy frequency $\nu_{\rm h}$ has a maximum for $a = 0.9998$, where $\nu_{\rm h(max)} = 607\ (\mathrm{M}_\odot/M)$ Hz, and it tends to $\nu_{\rm h(}a\to 1{\rm)} = 588\ (\mathrm{M}_\odot/M)$ Hz.

The ratios of the humpy frequency and the orbital and epicyclic frequencies at the humpy radius were determined in Stuchlík et al. (2007b) revealing almost spin-independent asymptotic behaviour for $a \to 1$ represented closely by the ratios of integer numbers, $\nu_{\rm K} : \nu_{\rm v} : \nu_{\rm r} : \nu_{\rm h} \sim 46 : 11 : 3 : 2$, which imply a possibility of resonant phenomena between the hump-induced and orbital or epicyclic oscillations. For Keplerian discs, the ratios of the epicyclic frequencies and the humpy frequency are given in the dependence on the black-hole spin in Fig. 3.

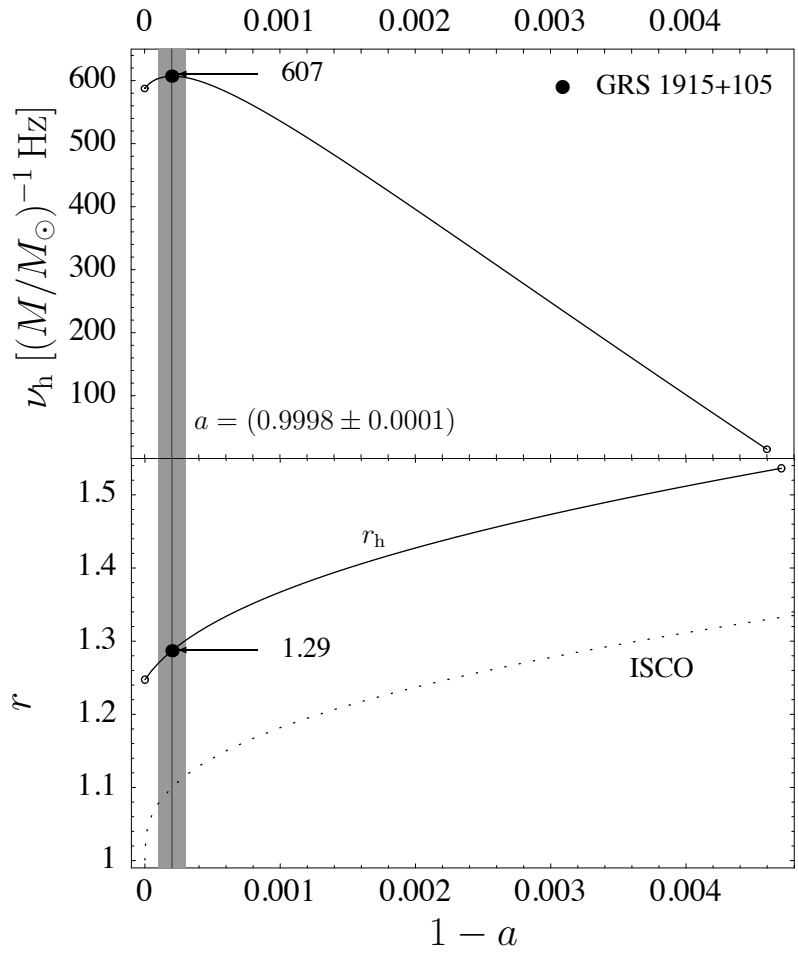

Figure 2. Spin-dependence of the humpy frequency $\nu_{\rm h}$ and the humpy radius $r_{\rm h}$ that is compared with the Boyer–Lindquist radius of the innermost stable circular orbit. (Taken from Stuchlík et al., 2007d)

The marginally stable tori have a structure that depends on the value of the specific angular momentum $\ell \in (\ell_{\rm ms}, \ell_{\rm mb})$. The oscillations of slender tori ($\ell \approx \ell_{\rm ms}$) have frequencies equal to the epicyclic frequencies relevant for test particle motion, but the frequencies of non-slender tori are different, as shown for pseudo-Newtonian tori (Šrámková, 2005; Blaes et al., 2007) and expected for tori in the strong gravitational field of Kerr black holes. Therefore, comparison of the humpy frequencies and the epicyclic frequencies is relevant for the slender tori only.

The humpy frequency is defined for all $a > 0.99979$ and all $\ell \in (\ell_{\rm ms}, \ell_{\rm mb})$, see Fig. 4. It is important that in the field of Kerr black holes with $1 - a < 10^{-8}$, there is $\nu_{\rm h}(a, \ell) \simeq 150\,{\rm Hz}\,(M/{\rm M}_\odot)^{-1}$ independently of a and ℓ (Stuchlík et al., 2007b). Further, the physically

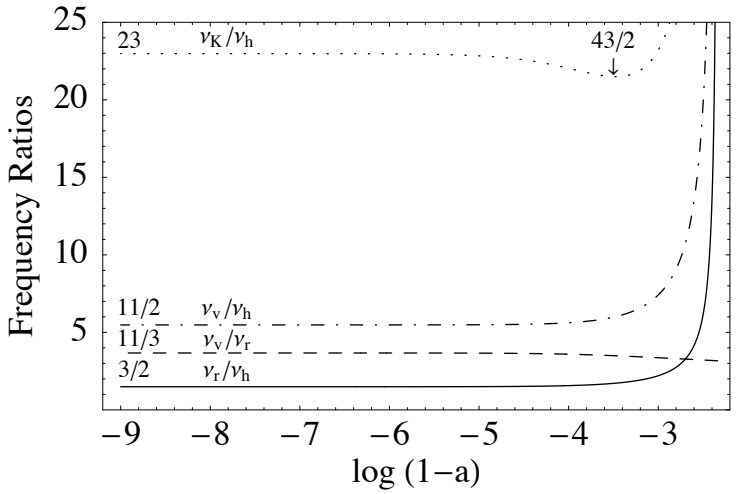

Figure 3. Spin dependence of the ratios of the radial (ν_r) and vertical (ν_v) epicyclic frequencies, and the Keplerian frequency (ν_K) to the thin-disc humpy frequency related to distant observers (ν_h). All the frequency ratios are asymptotically (for $1 - a < 10^{-4}$) constant. There si $\nu_K : \nu_v : \nu_r : \nu_h \sim 46 : 11 : 3 : 2$. Therefore, we can expect some resonant phenomena on the ratio of $\nu_r : \nu_h \sim 3 : 2$, and $\nu_K : \nu_v \sim 4$ that could be both correlated. (Taken from Stuchlík et al., 2007b)

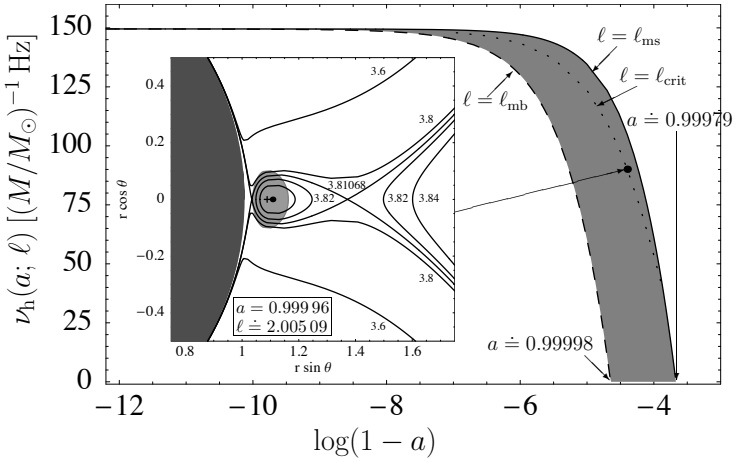

Figure 4. Interval of humpy frequencies for the marginally stable thick discs with $\ell \in (\ell_{ms}, \ell_{mb})$ as a function of the black-hole spin a. For $a \to 1$, the interval is narrowing and asymptotically reaching the value of 150 Hz $(M/M_\odot)^{-1}$. Dotted curve corresponds to the humpy frequencies of marginally stable slender tori with $\ell = \ell_{crit}$, for which the critical von Zeipel surface contains two cusps (as it is demonstrated for one special case in the left panel of the figure; the torus is given by the light-gray region).

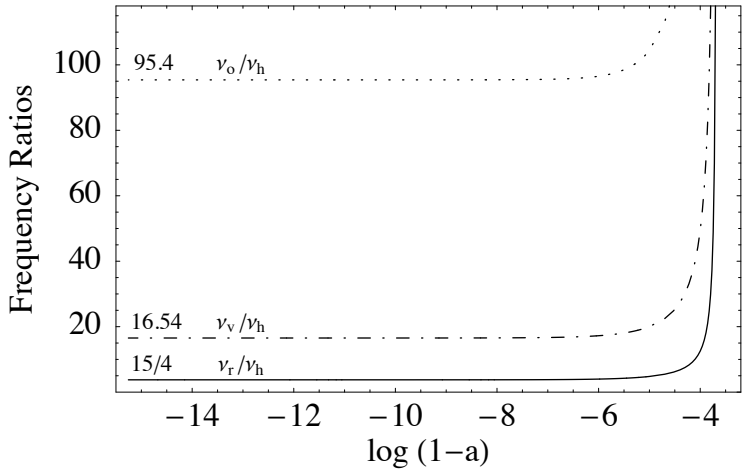

Figure 5. Spin dependence of the ratios of the radial (ν_r) and vertical (ν_v) epicyclic frequencies, and the orbital frequency (ν_o) of the marginally stable $\ell = \ell_{ms}$ disc to the thick-disc humpy frequency related to distant observers (ν_h). All the frequency ratios are asymptotically (for $1-a < 10^{-6}$) almost constant. (Taken from Stuchlík et al., 2007b)

important case of tori admitting evolution of toroidal von Zeipel surfaces with the critical surface self-crossing in both the inner and the outer cusps is allowed at $\ell = \ell_{crit}$, where $\ell_{crit} \gtrsim \ell_{ms}$ only slightly differs from ℓ_{ms}, i.e., such tori can be slender, see Fig. 4. The ratios of ν_r/ν_h, ν_v/ν_h and ν_o/ν_h are given for the tori with $\ell \approx \ell_{ms}$ in Fig. 5. Their asymptotical values, valid for $1 - a < 10^{-6}$, are independent of both a and ℓ.

Of course, in realistic situations the hump-induced oscillation mechanism could work at the vicinity of r_h, with slightly different frequencies; we should take into account that the shift of the radius, where the mechanism works, shifts both the locally measured (LNRF) frequency (Eq. (19)) and the frequency related to distant observers (Eq. (20)). The zones of radii, where the critical frequency $\nu^{\tilde{R}}_{crit}$ differs up to 1 %, 10 % and 20 % of its maximal value (given by $(\partial \mathcal{V}^{(\varphi)}/\partial \tilde{R})_{max}$) for thin (Keplerian) discs or 1 %, 5 % and 10 % of its maximum for marginally stable discs with $\ell = \ell_{ms}$, are given in Fig. 6. We can see (Fig. 6) that the resonant epicyclic frequencies radii $r_{3:1}$ and $r_{4:1}$ are located within the zone of the hump-induced oscillation mechanism in both thin discs and marginally stable tori.

In Keplerian discs the sign changes of the radial gradient of the orbital velocity in LNRF occur nearby the $r = r_{3:1}$ orbit (with $\nu_v : \nu_r = 3 : 1$), while in the vicinity of the $r = r_{3:2}$ orbit (with $\nu_v : \nu_r = 3 : 2$), $\partial \mathcal{V}^{(\varphi)}/\partial r < 0$ for all values of a for both Keplerian discs and marginally stable tori with all allowed values of ℓ. The parametric resonance, which is the strongest one for the ratio of the epicyclic frequencies $\nu_v : \nu_r = 3:2$, can occur at the $r = r_{3:2}$ orbit, while its effect is much smaller at the radius $r = r_{3:1}$, as noticed by Abramowicz et al. (2003). Nevertheless, the forced resonance may take place at the $r_{3:1}$ orbit. Notice that the forced resonance at $r = r_{3:1}$ can generally result in observed QPOs frequencies with $3 : 2$ ratio due to the beat frequencies allowed for the forced resonance as shown in Abramowicz

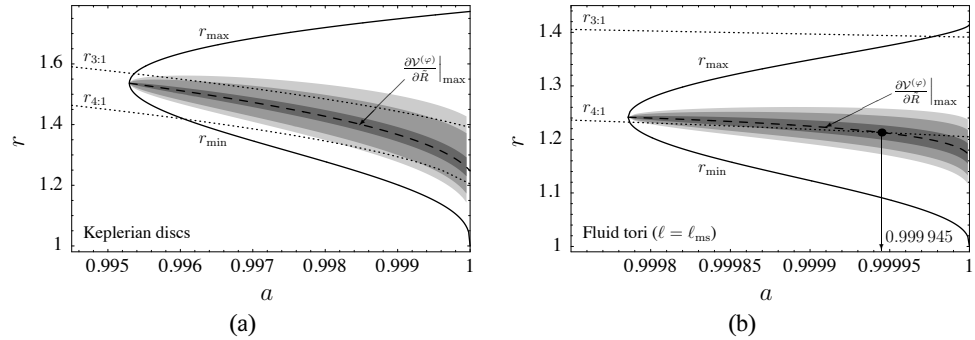

Figure 6. Positions of local extrema of $\mathcal{V}^{(\varphi)}$ (in BL coordinates) for Keplerian discs (a) and marginally stable discs with $\ell = \ell_{\rm ms}$ (b) together with the locations of resonant orbits $r_{3:1}$ and $r_{4:1}$ (where the resonance between the vertical and radial epicyclic oscillations takes place) in dependence on the rotational parameter a of the black hole. Dashed curve corresponds to the maximum positive values of the LNRF orbital velocity gradient in terms of the proper radial distance where the critical frequency $\nu^{\tilde{R}}_{\rm crit}$ is defined, boundaries of shaded regions correspond to orbits where the velocity gradient giving the characteristic frequency, $\partial \mathcal{V}^{(\varphi)}/\partial \tilde{R}$, reaches (a) 99 %, 90 %, 80 % and (b) 99 %, 95 %, 90 % of its maximum. (Taken from Stuchlík et al., 2007b)

et al. (2004). But the forced resonance at $r_{3:1}$ between the epicyclic frequencies, induced by the humpy profile of $\mathcal{V}^{(\varphi)}$, seems to be irrelevant in the case of microquasars, since all observed frequencies lead to the values of the rotational parameter $a < a_{\rm c(K)}$, as shown by Török et al. (2005).

4 APPLICATION OF THE EXTENDED RESONANCE MODEL

The extended orbital resonance model with hump-induced oscillations can be applied only to black hole systems containing a near-extreme Kerr black hole candidates. One of the most promising of such systems seems to be the microquasar GRS 1915+105, where the extremely high spin $a \sim 1$ was predicted by continuous spectra fitting method (McClintock et al., 2006). Another promising candidate for the near-extreme Kerr black hole could be considered the Galaxy Centre Sgr A*. In fact, all the QPO frequencies observed in GRS 1915+105 microquasar could be explained in the framework of the EXORM (Stuchlík et al., 2007d; Slaný and Stuchlík, 2007). Therefore, we briefly summarize these results, and then we consider the case of Sgr A*, assuming relevance of all the three frequencies reported by Aschenbach (Aschenbach, 2004, 2007).

4.1 GRS 1915+105

Assuming mass $M = 14.8\,{\rm M}_\odot$ and dimensionless spin $a = 0.9998$ for the GRS 1915+105 Kerr black hole (see Stuchlík et al., 2007d; Slaný and Stuchlík, 2007 for details), the EXORM predicts the following pattern of observable frequencies composed from the

humpy and epicyclic frequencies and their combinations

$$\nu_1 \sim (\nu_r - \nu_h) = (26 \pm 2)\,\mathrm{Hz}\,, \tag{24}$$

$$\nu_h \equiv \nu_2 = (41 \pm 1)\,\mathrm{Hz}\,, \tag{25}$$

$$\nu_r \equiv \nu_3 = (67 \pm 1)\,\mathrm{Hz}\,, \tag{26}$$

$$\nu_4 \sim (\nu_r + \nu_h) = (108 \pm 2)\,\mathrm{Hz}\,, \tag{27}$$

$$\nu_5 \sim (\nu_v - \nu_r) = (0.17 \pm 0.01)\,\mathrm{kHz}\,. \tag{28}$$

The corresponding humpy radius is $r_h = 1.29$. At such a radius, the vertical epicyclic frequency of a particle orbiting the Kerr black hole with the mass and spin given above reaches the value $\nu_v = (0.23 \pm 0.01)$ kHz that enters the highest (combinational) frequency.

4.2 Sgr A*

There are three frequencies related to the Sgr A* QPOs (Aschenbach, 2004; Török, 2005):

$$\nu_u = 1.445\,\mathrm{mHz}\,, \quad \nu_m = 0.885\,\mathrm{mHz}\,, \quad \nu_l = 0.459\,\mathrm{mHz}\,. \tag{29}$$

These frequencies come in the rational ratio $\nu_u : \nu_m : \nu_l \sim 3 : 2 : 1$. Assuming EXORM with the humpy and radial epicyclic frequency and their combinational frequencies, we can distinguish three different cases of the resonant phenomena explaining the observed frequencies.

$\nu_r : \nu_h \sim 3:2$

The observed frequency pattern is given by $\nu_u = \nu_r$, $\nu_m = \nu_h$, $\nu_l = \nu_r - \nu_h$. The value of the spin, given by the frequency ratio, and the humpy frequency are then given by (compare Figs 2 and 3)

$$a_{3:2} = 0.999984\,, \qquad \nu_{h(3:2)} = 590\,\frac{\mathrm{M}_\odot}{M}\,\mathrm{Hz}\,. \tag{30}$$

Using the condition $\nu_m = \nu_h$, we obtain mass of the black hole to be

$$M = 0.667 \times 10^6\,\mathrm{M}_\odot\,. \tag{31}$$

(Note that in this case we have chosen – see Fig. 3 – the value of the spin at the region where the frequency ratio $\nu_r : \nu_h$ starts to be close to the asymptotical value of $\sim 3:2$.)

$\nu_r : \nu_h \sim 2:1$

The observed frequency pattern is given by $\nu_u = \nu_r + \nu_h$, $\nu_m = \nu_r$, $\nu_l = \nu_h$. The value of the spin and the humpy frequency are then given by (compare Figs 2 and 3)

$$a_{2:1} = 0.99925\,, \qquad \nu_{h(2:1)} = 567\,\frac{\mathrm{M}_\odot}{M}\,\mathrm{Hz}\,. \tag{32}$$

Using the condition $\nu_l = \nu_h$, we obtain mass of the black hole to be

$$M = 1.235 \times 10^6\,\mathrm{M}_\odot\,. \tag{33}$$

$\nu_r : \nu_h \sim 3:1$

The observed frequency pattern is given by $\nu_u = \nu_r$, $\nu_m = \nu_r - \nu_h$, $\nu_l = \nu_h$. The value of the spin and the humpy frequency are given by (Figs 2 and 3)

$$a_{3:1} = 0.999984\,, \qquad \nu_{h(3:1)} = 425\,\frac{M_\odot}{M}\,\mathrm{Hz}\,. \tag{34}$$

Using the condition $\nu_l = \nu_h$, we obtain mass of the black hole to be

$$M = 0.926 \times 10^6\,M_\odot\,. \tag{35}$$

However, by analysing data of the orbits of stars moving within 1000 light hours of the Sgr A* black hole, its mass is estimated to be $M \sim 3.6 \times 10^6\,M_\odot$, and the error of the estimate is given by (Ghez et al., 2005; Weinberg et al., 2005)

$$2.8 \times 10^6\,M_\odot < M < 4.6 \times 10^6\,M_\odot. \tag{36}$$

Clearly, the Sgr A* black hole mass predicted by the three simple variants of the EXORM are all completely out of the mass estimates given by relatively precise star-orbit measurements. Therefore, we can conclude that the EXORM cannot be applied to explain the QPOs observed in the Sgr A* black hole candidate. Although we expect a fast rotating black hole in the Galaxy Centre, it is probably not a near-extreme Kerr black hole that sites in Sgr A*.

5 CONCLUDING REMARKS

The extended orbital resonance model with the hypothetical humpy oscillations could be related to the QPO resonant phenomena in both thin Keplerian discs and marginally stable tori orbiting near-extreme Kerr black holes. The non-linear resonance is assumed between oscillations with the humpy frequency and the radial or vertical epicyclic frequency. Both parametric and forced resonance phenomena are possible, therefore, the combinational frequencies are allowed too. Generally, more than two observable oscillations are predicted.

The EXORM can successfully explain all five QPO frequencies observed in the microquasar GRS 1915+105 (Stuchlík et al., 2007d), where a near-extreme black hole with $a \sim 1$ is predicted by spectral X-ray continuum fitting (McClintock et al., 2006). Although Middleton et al. (2006) refer to a substantially lower, intermediate value of the black-hole spin, $a \sim 0.7$, to which the EXORM cannot be applied, the recent analysis by Narayan et al. (2007) and McClintock et al. (2007) demonstrated convincingly that the near-extreme black hole is more probable there, making the predictions of the EXORM still well viable. This model is successfully applied to explain QPOs observed also in the case of the other microquasar XTE J1650−500, and in the near-extreme intermediate-mass Kerr black hole candidate in the system NGC 5408 X-1 (Slaný and Stuchlík, 2007).

On the other hand, the EXORM is not able to explain, in any of its variants, the QPOs observed in the Sgr A* source, i.e., in the Galactic Centre Kerr black hole. The differences in the black hole mass estimated by the EXORM and by analysing the star orbits in vicinity of the black hole are too high to believe that some more exact QPOs measurements could give a solution of this discrepancy. On the other hand, it is worth to note that the Sgr A* QPOs,

if true, could be explained within the multiresonance model based on the assumption of strong resonances of oscillation with the orbital and both epicyclic frequencies (Stuchlík et al., 2007a). The spin estimated in this case is ~ 0.983, corresponding to a fast rotating, but not near-extreme Kerr black hole.

We can conclude that the EXORM could be considered as a promising model of QPOs in near-extreme Kerr black holes systems, where the oscillations occur in the innermost parts of the accretion disc. The model enables very precise measurements of the black hole parameters, in particular, of the black hole spin since its value is given (usually) by the frequency ratio of the humpy frequency and the radial epicyclic frequency. However, the predictions of the EXORM have to be confronted to the black hole parameter estimates coming from other methods, as those based on the optical phenomena in strong gravitational fields, e.g., the spectral X-ray continuum fitting, the profiled spectral (Fe-K) lines fitting, time delay methods, or by methods based on the orbital motion analysis. The present situation seems to be rather controversial, however, we believe that in future, with developing both the theoretical models and observational techniques, we could be able to understand the accretion phenomena in much deeper detail as compared to the present understanding.

ACKNOWLEDGEMENTS

This work was supported by the Czech grant MSM 4781305903 and by the GAČR grant 202/06/0041 (Z. S.).

REFERENCES

Abramowicz, M. A., Jaroszyński, M. and Sikora, M. (1978), Relativistic accreting disks, *Astronomy and Astrophysics*, **63**(1–2), pp. 221–224, URL `http://adsabs.harvard.edu/abs/1978A\%26A....63..221A`.

Abramowicz, M. A., Karas, V., Kluźniak, W., Lee, W. and Rebusco, P. (2003), Non-Linear Resonance in Nearly Geodesic Motion in Low-Mass X-Ray Binaries, *Publ. Astronom. Soc. Japan*, **55**(2), pp. 467–471, URL `http://pasj.asj.or.jp/v55/n2/550214/550214-frame.html`.

Abramowicz, M. A. and Kluźniak, W. (2001), A precise determination of black hole spin in GRO J1655−40, *Astronomy and Astrophysics Lett.*, **374**, pp. L19–L21.

Abramowicz, M. A., Kluźniak, W., Stuchlík, Z. and Török, G. (2004), Twin peak QPOs frequencies in microquasars and Sgr A*. The resonance and other orbital models, in Hledík and Stuchlík (2004), pp. 1–23.

Abramowicz, M. A., Miller, J. and Stuchlík, Z. (1993), Concept of radius of gyration in general relativity, *Phys. Rev. D*, **47**(4), pp. 1440–1447, ISSN 1089-4918, URL `http://link.aps.org/abstract/PRD/v47/p1440`.

Abramowicz, M. A., Nurowski, P. and Wex, N. (1995), Optical reference geometry for stationary and axially symmetric spacetimes, *Classical Quantum Gravity*, **12**(6), pp. 1467–1472, URL `http://www.iop.org/EJ/abstract/0264-9381/12/6/012`.

Aliev, A. N. and Galtsov, D. V. (1981), Radiation from relativistic particles in non-geodesic motion in a strong gravitational field, *Gen. Relativity Gravitation*, **13**, pp. 899–912.

Aschenbach, B. (2004), Measuring mass and angular momentum of black holes with high-frequency quasi-periodic oscillations, *Astronomy and Astrophysics*, **425**, pp. 1075–1082, arXiv: astro-ph/0406545.

Aschenbach, B. (2006), Mass and Angular Momentum of Black Holes: An Overlooked Effect of General Relativity Applied to the Galactic Center Black Hole SgrA*, *Chinese Astronom. Astrophys.*, **6**, pp. 221–227, updated version of a talk given at the 2005 Frascati Workshop, Vulcano, Italy, May 23–28, arXiv: astro-ph/0603193.

Aschenbach, B. (2007), Measurement of Mass and Spin of Black Holes with QPOs, *Chinese Astronom. Astrophys.*, accepted for publication, arXiv: 0710.3454.

Aschenbach, B., Grosso, N., Porquet, D. and Predehl, P. (2004), X-ray flares reveal mass and angular momentum of the Galactic Center black hole, *Astronomy and Astrophysics*, **417**, pp. 71–78, arXiv: astro-ph/0401589.

Bardeen, J. M., Press, W. H. and Teukolsky, S. A. (1972), Rotating black holes: locally nonrotating frames, energy extraction, and scalar synchrotron radiation, *Astrophys. J.*, **178**, pp. 347–369.

Belloni, T., Méndez, M. and Sánchez-Fernández, C. (2001), The high-frequency QPOs in GRS 1915+105, *Astronomy and Astrophysics*, **372**, pp. 551–556, arXiv: astro-ph/0104019.

Blaes, O. M., Šrámková, E., Abramowicz, M. A., Kluźniak, W. and Torkelsson, U. (2007), Epicyclic Oscillations of Fluid Bodies. Paper III. Newtonian Non-Slender Torus, *Astrophys. J.*, **665**, pp. 642–653, arXiv: 0706.4483, URL http://adsabs.harvard.edu/abs/2007ApJ...665..642B.

Genzel, R., Schödel, R., Ott, T., Eckart, A., Alexander, T., Lacombe, F., Rouan, D. and Aschenbach, B. (2003), Near-infrared flares from accreting gas around the supermassive black hole at the Galactic Centre, *Nature*, **425**, pp. 934–937, arXiv: astro-ph/0310821.

Ghez, A. M., Salim, S., Hornstein, S. D., Tanner, A., Lu, J. R., Morris, M., Becklin, E. E. and Duchêne, G. (2005), Stellar Orbits around the Galactic Center Black Hole, *Astrophys. J.*, **620**, pp. 744–757, arXiv: astro-ph/0306130.

Hledík, S. and Stuchlík, Z., editors (2004), *Proceedings of RAGtime 4/5: Workshops on black holes and neutron stars, Opava, 14–16/13–15 October 2002/2003*, Silesian University in Opava, Opava, ISBN 80-7248-242-4.

Kato, S. (2001), Trapping of Non-Axisymmetric g-Mode Oscillations in Thin Relativistic Disks and kHz QPOs, *Publ. Astronom. Soc. Japan*, **53**, pp. L37–L39.

Kato, S. (2004), Mass and Spin of GRS 1915+105 Based on a Resonance Model of QPOs, *Publ. Astronom. Soc. Japan*, **56**(5), pp. L25–L28.

Kluźniak, W. and Abramowicz, M. A. (2001), Strong-field gravity and orbital resonance in black holes and neutron stars – kHz quasi-periodic oscillations (QPO), *Acta Phys. Polon. B*, **32**, pp. 3605–3612.

Kozłowski, M., Jaroszyński, M. and Abramowicz, M. A. (1978), The analytic theory of fluid disks orbiting the Kerr black hole, *Astronomy and Astrophysics*, **63**(1–2), pp. 209–220, URL http://adsabs.harvard.edu/abs/1978A\%26A....63..209K.

McClintock, J. E., Narayan, R. and Shafee, R. (2007), Estimating the Spins of Stellar-Mass Black Holes, in M. Livio and A. Koekemoer, editors, *Black Holes*, volume 707, Cambridge University Press, Cambridge, in press, to appear in 2008, arXiv: 0707.4492v1.

McClintock, J. E. and Remillard, R. A. (2004), Black Hole Binaries, in W. H. G. Lewin and M. van der Klis, editors, *Compact Stellar X-Ray Sources*, Cambridge University Press, Cambridge, arXiv: astro-ph/0306213.

McClintock, J. E., Shafee, R., Narayan, R., Remillard, R. A., Davis, S. W. and Li, L. (2006), The Spin of the Near-Extreme Kerr Black Hole GRS 1915+105, *Astrophys. J.*, **652**(2), pp. 518–539, arXiv: astro-ph/0606076.

Middleton, M., Done, C., Gierliński, M. and Davis, S. W. (2006), Black hole spin in GRS 1915+105, *Monthly Notices Roy. Astronom. Soc.*, **373**(3), pp. 1004–1012, arXiv: astro-ph/0601540v2.

Morgan, E. H., Remillard, R. A. and Greiner, J. (1997), RXTE Observation of GRS 19115+105, *Astrophys. J.*, **482**, pp. 993–1010.

Narayan, R., McClintock, J. E. and Shafee, R. (2007), Estimating the Spins of Stellar-Mass Black Holes by Fitting Their Continuum Spectra, in Y. F. Yuan, X. D. Li and D. Lai, editors, *Astrophysics of Compact Objects*, AIP, to appear, arXiv: 0710.4073v1.

Remillard, R. A. (2005), X-ray spectral states and high-frequency QPOs in black hole binaries, *Astronom. Nachr.*, **326**(9), pp. 804–807, arXiv: astro-ph/0510699.

Remillard, R. A. and McClintock, J. E. (2006), X-Ray Properties of Black-Hole Binaries, *Annual Review of Astronomy and Astrophysics*, **44**(1), pp. 49–92, arXiv: astro-ph/0606352.

Rezzolla, L., Yoshida, S., Maccarone, T. J. and Zanotti, O. (2003), A new simple model for high-frequency quasi-periodic oscillations in black hole candidates, *Monthly Notices Roy. Astronom. Soc.*, **344**(3), pp. L37–L41.

Slaný, P. and Stuchlík, Z. (2007), Extended orbital resonance model applied to QPOs observed in three near-extreme Kerr black hole candidate systems, pp. 257–265, this volume.

Šrámková, E. (2005), Epicyclic oscillation modes of a Newtonian, non-slender torus, *Astronom. Nachr.*, **326**(9), pp. 835–837.

Stella, L. and Vietri, M. (1998), Lense–Thirring Precession and Quasi-periodic Oscillations in Low-Mass X-Ray Binaries, *Astrophys. J. Lett.*, **492**, pp. L59–L62, arXiv: astro-ph/9709085.

Stella, L. and Vietri, M. (1999), kHz Quasiperiodic Oscillations in Low-Mass X-Ray Binaries as Probes of General Relativity in the Strong-Field Regime, *Phys. Rev. Lett.*, **82**(1), pp. 17–20.

Strohmayer, T. E. (2001), Discovery of a Second High Frequency QPO from the Microquasar GRS 1915+105, *Astrophys. J.*, **554**, pp. L169–L172.

Stuchlík, Z., Kotrlová, A. and Török, G. (2007a), Multi-resonance models of QPOs, pp. 363–416, this volume.

Stuchlík, Z., Slaný, P. and Török, G. (2004), Marginally stable thick discs with gradient inversion of orbital velocity measured in locally non-rotating frames: A mechanism for excitation of oscillations in accretion discs?, in Hledík and Stuchlík (2004), pp. 239–256.

Stuchlík, Z., Slaný, P. and Török, G. (2006a), Humpy LNRF-velocity profiles in accretion discs orbiting rapidly rotating Kerr black holes: a possible relation to QPOs, in T. Belloni, editor, *Proceedings of the Sixth Microquasar Workshop – Microquasars and Beyond: From Binaries To Galaxies, Como, Italy, 18–22 September, 2006*, p. PoS(MQW6)095, Como, Italy, URL http://pos.sissa.it/archive/conferences/033/095/MQW6_095.pdf.

Stuchlík, Z., Slaný, P. and Török, G. (2006b), Toroidal LNRF-velocity Profiles in Thick Accretion Discs Orbiting Rapidly Rotating Kerr Black Holes, in J.-M. Alimi and A. Füzfa, editors, *Albert Einstein Century International Conference, Paris, France, 18–22 July 2005*, volume 861, pp. 778–785, AIP, Melville, New York.

Stuchlík, Z., Slaný, P. and Török, G. (2007b), Humpy LNRF-velocity profiles in accretion discs orbiting almost extreme Kerr black holes – A possible relation to quasi-periodic oscillations, *Astronomy and Astrophysics*, **463**(3), pp. 807–816, arXiv: astro-ph/0612439.

Stuchlík, Z., Slaný, P. and Török, G. (2007c), Humpy LNRF-velocity profiles in accretion discs orbiting rapidly rotating Kerr black holes and a possible relation to epicyclic oscillations, in V. Karas and G. Matt, editors, *Black Holes from Stars to Galaxies – Across the Range of Masses*, volume 238 of *Proceedings of IAU Symposium*, pp. 459–460, International Astronomical Union, Cambridge University Press, Cambridge, UK, ISSN 1743-9213.

Stuchlík, Z., Slaný, P. and Török, G. (2007d), LNRF-velocity hump-induced oscillations of a Keplerian disc orbiting near-extreme Kerr black hole: A possible explanation of high-frequency QPOs in GRS 1915+105, *Astronomy and Astrophysics*, **470**(2), pp. 401–404, arXiv: 0704.1252v2.

Stuchlík, Z., Slaný, P., Török, G. and Abramowicz, M. A. (2005), The Aschenbach effect: unexpected topology changes in motion of particles and fluids orbiting rapidly rotating Kerr black holes, *Phys. Rev. D*, **71**, p. 024037 (9), arXiv: gr-qc/0411091.

Török, G. (2005), QPOs in microquasars and Sgr A*: measuring the black hole spin, *Astronom. Nachr.*, **326**(9), pp. 856–860, arXiv: astro-ph/0510669.

Török, G., Abramowicz, M. A., Kluźniak, W. and Stuchlík, Z. (2005), The orbital resonance model for twin peak kHz quasi periodic oscillations in microquasars, *Astronomy and Astrophysics*, **436**(1), pp. 1–8, arXiv: astro-ph/0401464.

Török, G., Abramowicz, M. A., Kluźniak, W. and Stuchlík, Z. (2006), A non-linear resonance model for the black hole and neutron star QPOs: theory supported by observations, to appear in Proceedings of the Albert Einstein Century International Conference, arXiv: astro-ph/0603847.

Török, G. and Stuchlík, Z. (2005a), Epicyclic frequencies of Keplerian motion in Kerr spacetimes, in S. Hledík and Z. Stuchlík, editors, *Proceedings of RAGtime 6/7: Workshops on black holes and neutron stars, Opava, 16–18/18–20 September 2004/2005*, pp. 315–338, Silesian University in Opava, Opava, ISBN 80-7248-334-X.

Török, G. and Stuchlík, Z. (2005b), Radial and vertical epicyclic frequencies of Keplerian motion in the field of Kerr naked singularities. Comparison with the black hole case and possible instability of naked singularity accretion discs, *Astronomy and Astrophysics*, **437**(3), pp. 775–788, arXiv: astro-ph/0502127.

van der Klis, M. (2000), Millisecond Oscillations in X-ray Binaries, *Annual Review of Astronomy and Astrophysics*, **38**, pp. 717–760, arXiv: astro-ph/0001167.

Weinberg, N. N., Milosavljević, M. and Ghez, A. M. (2005), Astrometric Monitoring of Stellar Orbits at the Galactic Center with a Next Generation Large Telescope, in P. K. Seidelmann and A. K. B. Monet, editors, *Astrometry in the Age of the Next Generation of Large Telescopes*, volume 338 of *ASP Conf. Series*, p. 252, ASP, arXiv: astro-ph/0512621v2.

Proceedings of *RAGtime 8/9, 15–19/19–21 September, 2006/2007, Hradec nad Moravicí, Opava, Czech Republic*
S. Hledík and Z. Stuchlík, editors, Silesian University in Opava, 2007, pp. 469–477

Long-duration gamma-ray bursts: SPH simulations with microphysics

Paul Taylor

Department of Astrophysics, Oxford University, Denys Wilkinson Building
Keble Road, Oxford OX1 3RH, United Kingdom
ptaylor@astro.ox.ac.uk

ABSTRACT
While they occur, gamma-ray bursts are nearly as bright as the visible universe. We briefly discuss the observational constraints on the macrophysical properties of the long-duration variety, and what we infer to be the relevant microphysics for their evolution. Finally, we present simulations of the early stages of long-duration gamma-ray bursts (LGRBs), starting from a physical progenitor and using smoothed particle hydrodynamics. We show that self-gravitating disks formed around black holes during stellar core-collapse are hydrodynamically unstable to forming spiral structure which facillitates LGRB production.

Keywords: Gamma-ray bursts – supernovae Ic – collapsar – accretion disk – hydrodynamic instabilities – Toomre criterion – smoothed particle hydrodynamics – neutrino cooling

1 INTRODUCTION

Even by astrophysical standards, gamma-ray bursts (GRBs) are extreme phenomena: though stellar-sized in origin, they are some of the brightest events in the universe, releasing up to $\approx 10^{51}$–10^{52} erg in a few seconds, and they have been observed out to a redshift distance of $z = 6.29$, or roughly 12.7 billion lightyears. Yet they are also a relatively recent discovery, first reported by Klebesadel et al. (1973), and our understanding of these bursts has had to both increase and adapt swifly during these few intervening decades.

The first 16 GRB detections were recorded by the Cold War era Vela satellites, designed to detect high-energy photons from nuclear test explosions on Earth. Since then, thousands have been catalogued, and valuable information has been gained from subsequent observations spanning the electromagnetic spectrum – perhaps one day to be augmented by gravitational wave data as well. Even so, we still have far from a complete picture of what makes GRBs, from their progenitor(s) to their source of energy. Here, we present a model whose basic form is provided by observational constraints and by some theoretical arguments in order to explain one class of GRBs. We first review in an "evolutionary" fashion the macrophysics of GRBs and the self-consistent requirements imposed upon any model. Once we believe ourselves to be on firm, theoretical ground, we then discuss the numerical

978-80-7248-419-5

implementation of relevant microphysics. Finally, we present our initial simulations and results for producing a GRB.

2 OBSERVATIONAL BACKGROUND AND CONSTRAINTS

As mentioned, GRBs were first reported in the 1970s. As an increasing number of detections were made, they were determined to be distributed isotropically across the sky, and to be of cosmic origin (redshift distance $z \geq 0.0085$). Initial estimates of the total energy released by GRBs based on typical distances to sources were extraordinarily large, $\approx 10^{53}$–10^{54} erg. These were quickly scaled down by orders of magnitude by the assumption that observed gamma-rays were released in relativistic jets, as evinced by achromatic breaks in observed lightcurves (e.g., Rhoads, 1997).

Observations of temporal duration and spectral hardness ratios led to the classification of two types of burst: short (SGRBs, < 2 s) and long (LGRBs, > 2 s), each with distinct progenitor scenarios. Here, we focus on the latter case of LGRBs, which have all been observed at $z \geq 1$. A recent a3nd major breakthrough for the understanding of these events came with their observed association with rather energetic core-collapse (Type Ic) supernovae (SNe): first, with GRB980425 and SN1998bw (Galama et al., 1998), and then with GRB030329 and SN2003dh (Stanek et al., 2003). Subsequent studies of host galaxies have shown that LGRBs tend to occur in low-metallicity star forming regions (SFRs, Le Floc'h et al., 2003; Conselice et al., 2005). Therefore, the emergent picture of a LGRB was that of a massive (short-lived), stellar progenitor collapsing in on itself, which led to the adoption of the "Collapsar" model (Woosley, 1993) originally used in explaining core-collapse SNe; very briefly, the scenario assumes the production of a jet from a disk-black hole system formed in a collapsing star.

There are a number of important constraints placed upon the collapsar progenitor and its early evolution. Firstly, the progenitor must be massive ($> 25\,M_\odot$ for a single-star), in accordance with the large remnant masses ($2.9\,M_\odot$ for SN1998bw) and associated SNe kinetic energies (related to the amount of nickel produced), $\sim 2 \times 10^{52}$ erg; some astronomers created a high-energy extension of SNe, calling GRB-related events hypernovae (HNe), though further associations have not necessarily borne this out. Also, the progenitor must not possess an envelope, as the SNe Ic spectra necessarily contained neither H nor He lines. The lack of an envelope further assists jet propagation – its energy is not dissipated into kinetic energy (the "baryon massloading problem").

In order to form a disk, we require the progenitor to have rapid rotation, so that the entire star does not collapse directly into a black hole (BH) but instead becomes centrifugally balanced around a compact central object formed by the core, such as a neutron star (NS), which accretes material; disk-BH systems are common in astrophysics (quasars, X-ray binaries, etc.) and tend to produce collimated outflows aligned along or near the rotation axis; such systems are also typically very efficient in converting the energy of infalling matter into outgoing radiation. This rotation requirement is also consistent with the observed polarisation of the associated SNe/HNe (Mazzali et al., 2005). Any centrifugally supported disk must have enough specific angular momentum to remain outside the BH innermost stable circular orbit (ISCO), which, for a $2\,M_\odot$ BH, is given by $j_{\rm ISCO} \geq 2 \times 10^{16}\,{\rm cm^2\,s^{-1}}$.

Also, we expect a stable disk-BH system to exist for approximately the duration of the burst, up to the order of 1000 s (which also requires the disk to be at least a sizeable fraction of the mass of the central BH at any given time, even if it gains material from the continually infalling star).

Finally, while the exact mechanism for producing the jets of gamma-rays is uncertain, most models, such as the Blandford–Znajek mechanism (Blandford and Znajek, 1977) or neutrino annihilation (Paczyński, 1990; Popham et al., 1999), require high accretion rates, ~ 0.01–$0.1\,\mathrm{M}_\odot\,\mathrm{s}^{-1}$, onto the central BH. Assuming that the system contains sufficient angular momentum to form a centrifugally balanced disk in the first place, it becomes a formidable challenge to transfer that angular momentum outwards through the disk efficiently to meet the necessary accretion rates.

We shall not go into detail on the subject here, but, very briefly, we meet the first three requirements by utilising a pre-collapse progenitor evolved from the merger of two helium stars (more details below). The remnant object possesses enough mass; most importantly, the merging process is able to eject the H and He envelopes from the system during a common-envelope phase, as well as to retain sufficient angular momentum to form a centrifugally balanced disk (which are nearly mutually exclusive goals for realistic single-star progenitors, where losing an envelope results in losing angular momentum). The high BH accretion rate remains the crucial requirement for this model to meet.

We note that much of the matter in the collapsing star will be quite hot and dense, and that it will be shocked to higher temperatures ($T > 10^{10}\,\mathrm{K} \sim 0.1\,\mathrm{MeV}$) and densities ($\rho > 10^9\,\mathrm{g\,cm}^{-3}$) as it settles into the equatorial plane. Also, the disk/central object mass ratio is quite large compared to most astrophysical systems. Such self-gravitating disks are susceptible to local clumping and in particular globally unstable to forming structures such as spiral arms, which are quite efficient at transferring angular momentum outwards and matter inwards. A hydrodynamically unstable disk would provide a fully self-consistent model for forming LGRBs, and we provide preliminary results in support of this scenario below.

3 DISK STABILITY AND MICROPHYSICS

In studying galaxies, Toomre (1964) provided a useful dimensionless parameter, Q_T, for characterising the hydrodynamic stability of a (galactic) disk against forming clumps or spiral arms, since called the Toomre parameter:

$$Q_\mathrm{T} = \frac{\kappa c_\mathrm{s}}{\pi G \Sigma}\,, \tag{1}$$

where κ is the epicyclic frequency (Ω for a Keplerian case); c_s, the local sound speed; G, the gravitational constant; Σ, the surface density of the disk; and $Q_\mathrm{T} \gtrsim 1$ describes global stability. This parameter has been successfully applied to other disk-like systems, notably proto-stellar and planetary disk studies (e.g., Pickett et al., 2000), and also to analytical models of GRB disks by Panaitescu et al. (2001). The parameter compares the stabilising effects of rotation (centrifugal support) and large sound speed (essentially, a higher thermal pressure resisting compression and clumping), to the destabilising effects of self-gravity (larger Σ and, locally, ρ) and cooling (so that thermal support against clumping is reduced).

In the case of disks formed in collapsars, the dense material is optically thick to radiation but is in a regime of T-ρ phase space where cooling *via* neutrino emission is important by such processes as pair annihilation, the photoneutrino process and plasmon decay, given respectively by

$$\mathrm{e}^+ + \mathrm{e}^- \rightarrow \nu_\mathrm{e} + \bar{\nu}_\mathrm{e}\,, \tag{2}$$

$$\mathrm{e}^\pm + \gamma \rightarrow \mathrm{e}^\pm + \nu_\mathrm{e} + \bar{\nu}_\mathrm{e}\,, \tag{3}$$

and

$$\gamma_\mathrm{phot} \rightarrow \nu + \bar{\nu}\,, \tag{4}$$

where e^+ are positrons; e^-, electrons; γ, photons; $\nu_{(\mathrm{e})}$, (electron-)neutrinos; and $\bar{\nu}_{(\mathrm{e})}$, (electron-)antineutrinos. Such cooling is quite rapid, efficient and destabilising to collapsar disks.

4 SIMULATING WITH SPH

We now test the self-consistency of the collapsar model described above by using an adapted version of the smoothed particle hydrodynamics (SPH) code, GADGET (Springel, 2005). Briefly, SPH approximates a continuous fluid with discrete particles, interpolating (and hence smoothing) values of the fluid equations. Generally, SPH is good for modelling systems with large and changing density ranges, such as we expect for the collapsar. GADGET, in particular, is a versatile code used for simulating stellar to galactic to cosmological scales, and it is easy to implement additional physics (*i.e.*, to accompany the hydrodynamics and gravitation), such as cooling via neutrino emission and interaction with a NS/BH central object. We discuss further expansions of the code in Section 5.

Here, we simulate the 3D evolution of a collapsing progenitor, the formation and evolution of a disk-BH system, and the development of spiral structure which facilitates angular momentum transfer and rapid accretion. The collapsar progenitor comes from the (1D) resultant of the merger of two He stars ($8 + 8\,\mathrm{M}_\odot$), evolved until the point of core collapse by Fryer and Heger (2005). We map the 1D model into a 3D star made of concentric shells, each with constant angular velocity. We begin our simulation at approximately 2 s after core-collapse, when a proto-NS has formed from the homologous core, and an outgoing, spherical rarefaction wave leads to the infall of further layers of the progenitor.

Following Colgate et al. (1993); Fryer (2006), we assume that around the central proto-NS a hot, convective envelope has formed which, at radius $r \approx 1 \times 10^7$ cm, balances the ram pressure of the infalling star with $\dot{M}$/shell rates approximating those in similar scenarios in Fryer (2006). We evolve the system in time, representing a neutron star by a single, hydrodynamical body in the centre, which accretes matter and maintains a mass-radius relation given by static proto-NS models of Nicotra (2006). At a maximum NS mass ($= 1.9602\,\mathrm{M}_\odot$, for this model) the central object becomes a BH, modelled as a free boundary which accretes matter at the ISCO for a Schwarzschild BH, $R_\mathrm{ISCO} = 6\,\mathrm{G}M/\mathrm{c}^2$. The outer boundary condition of the simulation mimics continued infall, *i.e.*, the outermost

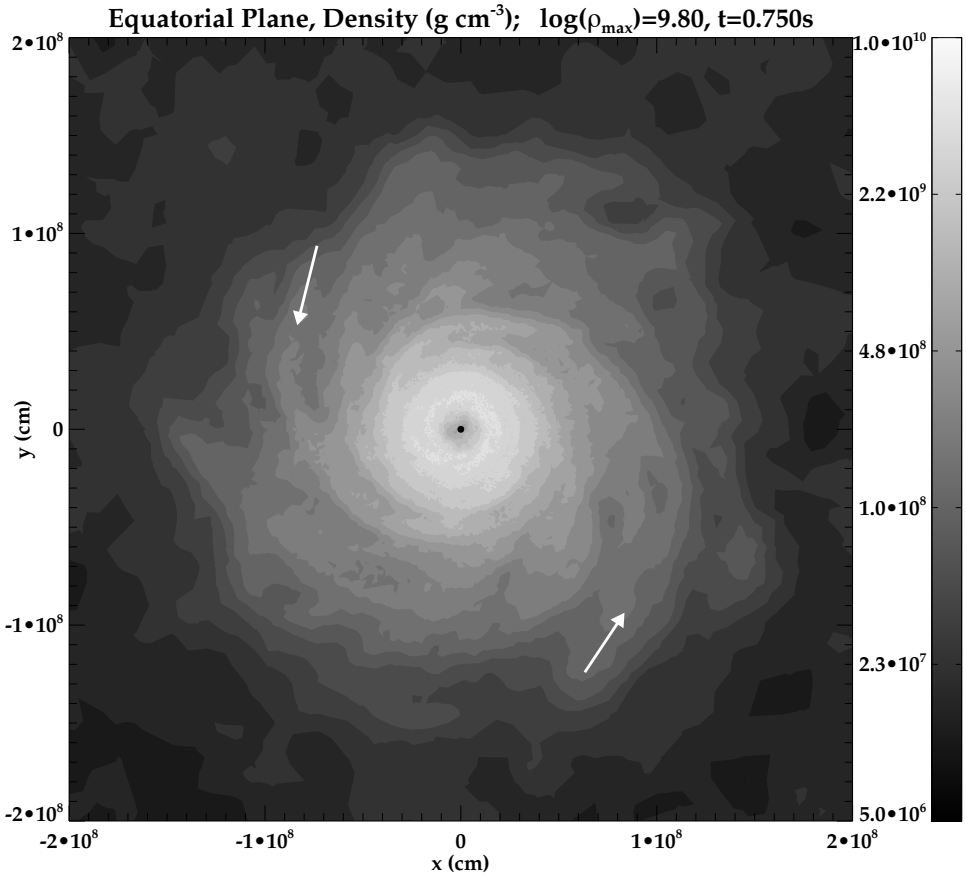

Figure 1. Mass density contours of a thin slice of the inner collapsar region in the equatorial plane. Arrows indicate high-density spiral arms.

boundary of SPH particles moves inwards but remains at a radius much greater than the evolving accretion disk. We utilise a polytropic equation of state for the gas, with $\gamma = 4/3$.

In Figs 1 and 2, we show the mass density and entropy (per baryon), respectively, of the central region of the collapsar at $t = 750\,\mathrm{ms}$ after the beginning of the simulation. By this point, the original central NS has just accreted enough mass to become a BH $\approx 2\,\mathrm{M}_\odot$. The disk/BH mass ratio is $\approx 1/10$ (defining the "disk" as material near the equatorial plane with density $\rho > 10^8\,\mathrm{g\,cm^{-3}}$), and the minimum value of the stability parameter in the disk is $Q_\mathrm{T} = 1.3$; indeed, the superimposed arrows show two spiral arms rotating anti-clockwise, stretching outward from the central BH (shown as black dot, real size of boundary, R_ISCO). The spirals are characterised by increased density and decreased entropy compared to matter at similar radii; the latter effect reflects the efficient cooling by neutrinos which carries away both energy and entropy from these regions heated by compression.

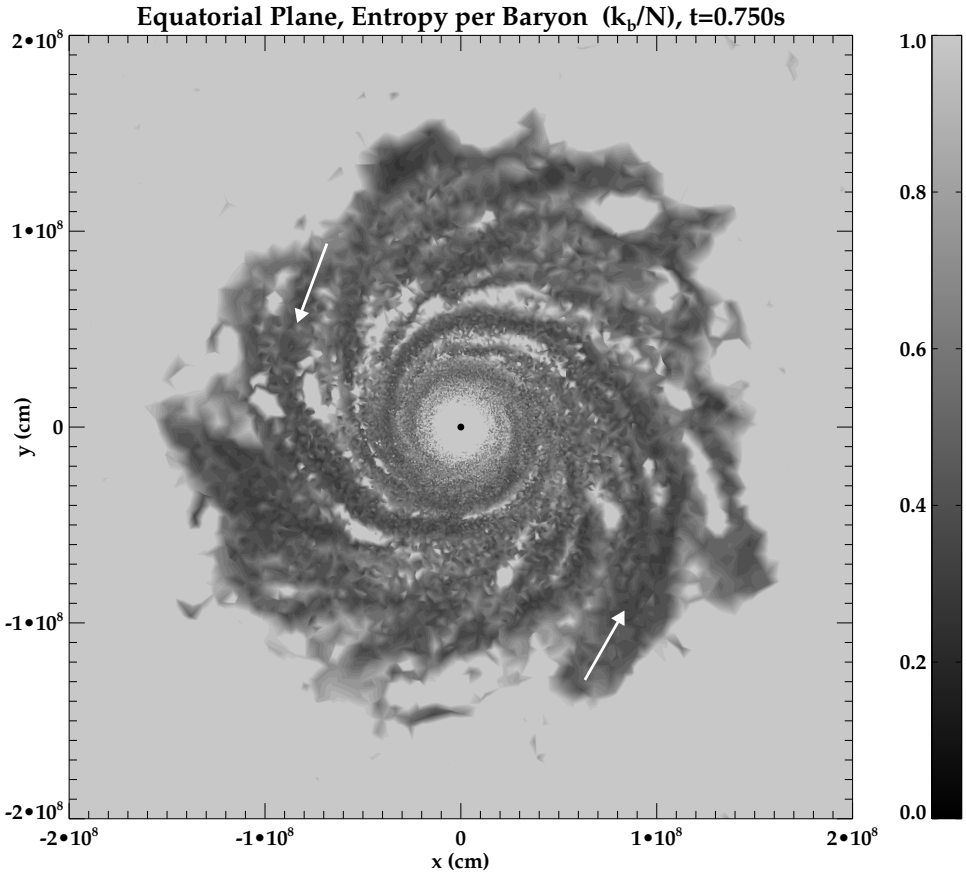

Figure 2. Entropy per baryon contours of a thin slice of the inner collapsar region in the equatorial plane. Arrows indicate spiral arms with low entropy (from neutrino cooling), which shock surrounding material to high entropy and facilitate the inward radial motion of material.

Furthermore, the spiral arms shock surrounding material to noticeably higher entropy, a process which also facilitates inward accretion of material. Values of the accretion rate onto the central BH fall within the range, 0.04–0.08 $M_\odot\ s^{-1}$.

5 CONCLUSIONS

We have shown, using a "real" progenitor, that collapsars can form circum-BH disks hydrodynamically unstable to the formation of spiral arms, and that the resulting spiral structure provides a mechanism for meeting the requirements of the early stages of a LGRB (as we currently understand them). The spiral instability develops in the disk on the short dynamical timescales established in the system by the rapid rotation of the inner disk region. The

high accretion rates onto the BH from the disk match those required theoretically to fuel relativistic jets.

Here, we have only considered hydrodynamics and the important role of microphysics enacted as cooling by neutrino production. We have not included magnetic effects, the most relevant being the possible presence of the magnetic rotation instability (MRI), which provides another mechanism for transferring angular momentum outward in disks. Other groups have begun to implement ideal magnetohydrodynamics into disk simulations, which assumes a fluid of infinite conductivity, but we have chosen the opposite extreme; we plan to estimate the susceptibility of forming relevant magnetic fields in future work.

This simulation is wholly Newtonian, both in the self-gravity of the disk matter and in the attraction of the central NS/BH source. While this approximation may be valid throughout most of the disk outside the central region, we also plan to investigate the inclusion of general relativistic effects in future simulations; given the rapid rotation in the system, we assume the central NS and subsequent BH should possess interestingly large angular momenta. In SPH studies of SGRBs, simulations of merging neutron stars have approximated relativistic effects using conformal flatness (Oechslin et al., 2002), and we plan to implement a similar scheme for our single BH. We expect this to alter the accretion dynamics slightly, by changing the behaviour of the inner boundary, but probably not disturbing the global dynamics of the disk and spiral structures.

Finally, resolution is an important issue for numerical modelling; these simulations commenced with $\approx 5 \times 10^5$ particles to represent a collapsing star; we plan to increase the number of particles (and hence, the resolution) by at least an order of magnitude in further studies, to minimise any computational effects of coarse graining. This will be particularly relevant at the inner boundary, where we require the smoothing lengths of individual particles to be much smaller than the radius of the central object in order to avoid numerical artifacts in accretion.

ACKNOWLEDGEMENTS

The author appreciates the assistance of his thesis supervisors, Profs. John Miller and Philipp Podsiadlowski, during this ongoing research and also that of New College for providing financial support to attend this conference.

REFERENCES

Blandford, R. D. and Znajek, R. L. (1977), Electromagnetic extraction of energy from Kerr black holes, *Monthly Notices Roy. Astronom. Soc.*, **179**, pp. 433–456, URL `http://adsabs.harvard.edu/abs/1977MNRAS.179..433B`.

Colgate, S. A., Herant, M. and Benz, W. (1993), Neutron star accretion and the neutrino fireball, *Phys. Rep.*, **227**, pp. 157–174, URL `http://adsabs.harvard.edu/abs/1993PhR...227..157C`.

Conselice, C. J., Vreeswijk, P. M., Fruchter, A. S., Levan, A., Kouveliotou, C., Fynbo, J. P. U., Gorosabel, J., Tanvir, N. R. and Thorsett, S. E. (2005), Gamma-Ray Burst-Selected High-Redshift Galaxies: Comparison to Field Galaxy Populations to $z \sim 3$, *Astrophys. J.*, **633**, pp. 29–40, arXiv: `astro-ph/0508197`, URL `http://adsabs.harvard.edu/abs/2005ApJ...633...29C`.

Fryer, C. L. (2006), Fallback in stellar collapse, *New Astronomy Reviews*, **50**, pp. 492–495, URL http://adsabs.harvard.edu/abs/2006NewAR..50..492F.

Fryer, C. L. and Heger, A. (2005), Binary Merger Progenitors for Gamma-Ray Bursts and Hypernovae, *Astrophys. J.*, **623**, pp. 302–313, arXiv: astro-ph/0412024, URL http://adsabs.harvard.edu/abs/2005ApJ...623..302F.

Galama, T. J., Vreeswijk, P. M., van Paradijs, J., Kouveliotou, C., Augusteijn, T., Böhnhardt, H., Brewer, J. P., Doublier, V., Gonzalez, J.-F., Leibundgut, B., Lidman, C., Hainaut, O. R., Patat, F., Heise, J., in't Zand, J., urley, K. H., Groot, P. J., Strom, R. G., Mazzali, P. A., Iwamoto, K., Nomoto, K., Umeda, H., Nakamura, T., Young, T. R., Suzuki, T., Shigeyama, T., Koshut, T., Kippen, M., Robinson, C., de Wildt, P., Wijers, R. A. M. J., Tanvir, N., Greiner, J., Pian, E., Palazzi, E., Frontera, F., Masetti, N., Nicastro, L., Feroci, M., Costa, E., Piro, L., Peterson, B. A., Tinney, C., Boyle, B., Cannon, R., Stathakis, R., Sadler, E., Begam, M. C. and Ianna, P. (1998), An unusual supernova in the error box of the γ-ray burst of 25 April 1998, *Nature*, **395**, pp. 670–672, arXiv: astro-ph/9806175, URL http://adsabs.harvard.edu/abs/1998Natur.395..670G.

Klebesadel, R. W., Strong, I. B. and Olson, R. A. (1973), Observations of Gamma-Ray Bursts of Cosmic Origin, *Astrophys. J. Lett.*, **182**, p. L85, URL http://adsabs.harvard.edu/abs/1973ApJ...182L..85K.

Le Floc'h, E., Duc, P.-A., Mirabel, I. F., Sanders, D. B., Bosch, G., Diaz, R. J., Donzelli, C. J., Rodrigues, I., Courvoisier, T. J.-L., Greiner, J., Mereghetti, S., Melnick, J., Maza, J. and D.Minniti (2003), Are the hosts of gamma-ray bursts sub-luminous and blue galaxies?, *Astronomy and Astrophysics*, **400**, pp. 499–510, arXiv: astro-ph/0301149, URL http://adsabs.harvard.edu/abs/2003A\%26A...400..499L.

Mazzali, P. A., Kawabata, K. S., Maeda, K., Nomoto, K., Filippenko, A. V., Ramirez-Ruiz, E., Benetti, S., Pian, E., Deng, J., Tominaga, N., Ohyama, Y., Iye, M., Foley, R. J., Matheson, T., Wang, L. and Gal-Yam, A. (2005), An Asymmetric Energetic Type Ic Supernova Viewed Off-Axis, and a Link to Gamma Ray Bursts, *Science*, **308**, pp. 1284–1287, arXiv: astro-ph/0505199, URL http://adsabs.harvard.edu/abs/2005Sci...308.1284M.

Nicotra, O. E. (2006), Structure of protoneutron stars within a static approach, arXiv: nucl-th/0607055, URL http://adsabs.harvard.edu/abs/2006nucl.th...7055N.

Oechslin, R., Rosswog, S. and Thielemann, F.-K. (2002), Conformally flat smoothed particle hydrodynamics application to neutron star mergers, *Phys. Rev. D*, **65**(10), p. 103005, arXiv: gr-qc/0111005, URL http://adsabs.harvard.edu/abs/2002PhRvD..65j3005O.

Paczyński, B. (1990), Super-Eddington winds from neutron stars, *Astrophys. J.*, **363**, pp. 218–226, URL http://adsabs.harvard.edu/abs/1990ApJ...363..218P.

Panaitescu, A., Kumar, P. and Narayan, R. (2001), Observational Prospects for Afterglows of Short-Duration Gamma-Ray Bursts, *Astrophys. J. Lett.*, **561**, pp. L171–L174, arXiv: astro-ph/0108132, URL http://adsabs.harvard.edu/abs/2001ApJ...561L.171P.

Pickett, B. K., Durisen, R. H., Cassen, P. and Mejia, A. C. (2000), Protostellar Disk Instabilities and the Formation of Substellar Companions, *Astrophys. J. Lett.*, **540**, pp. L95–L98, URL http://adsabs.harvard.edu/abs/2000ApJ...540L..95P.

Popham, R., Woosley, S. E. and Fryer, C. (1999), Hyperaccreting Black Holes and Gamma-Ray Bursts, *Astrophys. J.*, **518**, pp. 356–374, arXiv: astro-ph/9807028, URL http://adsabs.harvard.edu/abs/1999ApJ...518..356P.

Rhoads, J. E. (1997), How to Tell a Jet from a Balloon: A Proposed Test for Beaming in Gamma-Ray Bursts, *Astrophys. J. Lett.*, **487**, p. 1, arXiv: astro-ph/9705163, URL http://adsabs.harvard.edu/abs/1997ApJ...487L...1R.

Springel, V. (2005), The cosmological simulation code GADGET-2, *Monthly Notices Roy. Astronom. Soc.*, **364**, pp. 1105–1134, arXiv: astro-ph/0505010, URL http://adsabs.harvard.edu/abs/2005MNRAS.364.1105S.

Stanek, K. Z., Matheson, T., Garnavich, P. M., Martini, P., Berlind, P., Caldwell, N., Challis, P., Brown, W. R., Schild, R., Krisciunas, K., Calkins, M. L., Lee, J. C., Hathi, N., Jansen, R. A., Windhorst, R., Echevarria, L., Eisenstein, D. J., Pindor, B., Olszewski, E. W., Harding, P., Holland, S. T. and Bersier, D. (2003), Spectroscopic Discovery of the Supernova 2003dh Associated with GRB 030329, *Astrophys. J. Lett.*, **591**, pp. L17–L20, arXiv: astro-ph/0304173, URL http://adsabs.harvard.edu/abs/2003ApJ...591L..17S.

Toomre, A. (1964), On the gravitational stability of a disk of stars, *Astrophys. J.*, **139**, pp. 1217–1238, URL http://adsabs.harvard.edu/abs/1964ApJ...139.1217T.

Woosley, S. E. (1993), Gamma-ray bursts from stellar mass accretion disks around black holes, *Astrophys. J.*, **405**, pp. 273–277, URL http://adsabs.harvard.edu/abs/1993ApJ...405..273W.

Proceedings of *RAGtime 8/9, 15–19/19–21 September, 2006/2007, Hradec nad Moravicí, Opava, Czech Republic*
S. Hledík and Z. Stuchlík, editors, Silesian University in Opava, 2007, pp. 479–488

Modelling the twin peak QPO distribution in the atoll source 4U 1636−53

Gabriel Török[a], Pavel Bakala, Zdeněk Stuchlík and Petr Čech

Institute of Physics, Faculty of Philosophy & Science, Silesian University in Opava, Bezručovo nám. 13, CZ-746 01 Opava, Czech Republic
[a] terek@volny.cz

ABSTRACT
Relation between the lower and upper frequency mode of twin peak quasiperiodic oscilations observed in neutron star X-ray binaries is qualitatively well fitted by the frequency relation following from the relativistic precession model. Assuming this model with no preferred radius and the probability of a twin QPO excitation being uniform across the inner edge of an accretion disc, we compare the expected and observed twin peak QPO distribution in the case of atoll source 4U 1636−53. We find these two distributions highly incompatible.We also find that the observed distribution roughly corresponds to the expected one if an additional consideration of preferred resonant orbits is included. We notice that our findings are relevant for some disc-oscillation QPO models as well.

Keywords: X-rays: binaries – accretion: accretion disks – stars: neutron

1 INTRODUCTION

Several models have been outlined to explain observations of the kHz quasiperiodic oscilations (QPOs) in the X-ray fluxes from neutron-star binary systems, and it is mostly preferred that their origin is related to orbital motion near the inner edge of an accretion disc (see van der Klis, 2006; Lamb, 2003; Lamb and Boutloukos, 2007 for a recent review). It is often argued that relation between the lower and upper QPO frequency mode ($\nu_{\rm L}$, $\nu_{\rm U}$) is qualitatively well fitted by the frequency relation implied by the particular relativistic preccesion model (Stella and Vietri, 1999). Sources roughly follow the relation given by the model for central compact object mass $M \sim 2\,{\rm M}_\odot$ (Belloni et al., 2007b).

In this paper we examine the twin QPO distribution given by the relativistic preccesion model (in next the RP model) and compare it with those observed in the case of atoll source 4U 1636−53. We also discuss a model including preferred orbits.

978-80-7248-419-5

2 APPLIED OBSERVATIONAL DATA AND THEIR PARAMETRIZATION

The data we examine are taken from the study of Barret et al. (2005) and follow from the shift-add procedure through continuous segments of observation (see Méndez et al., 1998; Barret et al., 2005 for details). We seek over data corresponding to nine years of 4U 1636−53 monitoring by RXTE for all detected twin peak QPOs, i.e., for simultaneous detections of the lower and upper kHz QPO oscillations.

Note that we choose the twin peak QPO occurences as there is no apparent link between distributions of the individual QPO modes (see Bulik, 2005; Török et al., 2007b). We take into account only detections of oscillations above 500 Hz with quality factor (defined as the QPO centroid frequency over the full-width of the peak at its half-maximum) $Q \geq 3$ and significance (defined as the integral of the Lorentzian fitting the peak in PDS divided by its error) $S \geq 3$.

For the purposes of our study we parametrize the twin peak QPO occurences by their frequency ratio

$$R \equiv \frac{\nu_{\rm U}}{\nu_{\rm L}} \,. \tag{1}$$

As discussed in the next section this choice makes our discussion less dependent on the concrete properties of the central compact object in 4U 1636−53. It also avoids possible confusion of the linear parametrization with a parametrization of an individual QPO mode distribution. Further advantage of this choice in the relation to resonant QPO models is discussed in Section 3.2.

3 MODELLING DISTRIBUTION

In the RP model (Stella and Vietri, 1999) the kHz QPOs represent a manifestation of the modes of a relativistic epicyclic motion of blobs in the inner parts of accretion disc. The motion of a hot spot (radiating blob) is assumed to be nearly geodesic. Observed lower QPO oscillation frequency is then related to the relativistic precession of the orbiting hot spot while the upper QPO oscillation is associated directly to its Keplerian frequency

$$\nu_{\rm l}(r) = \nu_{\rm P} = \nu_{\rm K}(r) - \nu_{\rm r}(r) \,, \quad \nu_{\rm U}(r) = \nu_{\rm K}(r) \,, \tag{2}$$

where $\nu_{\rm K}$, $\nu_{\rm r}$, ν_θ are Keplerian and radial or vertical epicyclic frequencies of the geodesic motion and $\nu_{\rm P}$ is the periastron precession frequency.

In a given axially symmetric spacetime, the relevant angular velocities of the azimuthal, radial and vertical "quasielliptic" orbital motion reads in the spherical coordinates r, θ, ϕ (see, e.g., Abramowicz et al., 2003a),[1]

$$\Omega_{\rm K} = u^\phi / u^t \,, \tag{3}$$

$$\omega_i^2 = \frac{(g_{tt} + \Omega_{\rm K} + g_{t\phi})^2}{2 g_{ii}} \left(\frac{\partial^2 U}{\partial i^2} \right)_\ell \,, \tag{4}$$

[1] Henceforth we already use the geometrical units ($c = G = 1$, $M = GM^*/c^2, r = r^*, t = ct^*$), where the asterisk denote the standard units.

with $g_{\mu\nu}$ being components of the metric tensor, and U being the *effective potential* for the equatorial geodetical motion given by the standard relation

$$U(r,\theta,\ell) \equiv g^{tt} - 2\ell g^{t\phi} + \ell^2 g^{\phi\phi} ,$$

where ℓ denotes the specific angular momentum of the orbiting test particle

$$\ell = -\frac{u_\phi}{u_t} ;$$

for a Keplerian motion $\ell = \ell_{\rm K}(r,\theta)$. In the following we suppose the external neutron star spacetime described by the Hartle–Thorne metric (Hartle and Thorne, 1968) which represents the solution of vacuum Einstein field equations for the exterior of rigidly and relatively slowly rotating, stationary and axially symmetric body. The components $g_{\mu\nu}$, $\mu,\nu \in \{t,r,\theta,\phi\}$ of relevant metric tensor together with explicit formulae (3), (4) derived in Abramowicz et al. (2003a) are given in the Appendix A.

3.1 Distribution model I

Let us assume that there is no preferred radius in the RP model and the probability of a QPO excitation is uniform distributed across the inner part of the accretion disc. Then after a sufficient integration time the number of QPO excitations (and detections) $\mathrm{d}n(r)$ should be equal for any given radius r when related to the unit length in the radial direction

$$\frac{\mathrm{d}n}{\mathrm{d}\tilde{r}} = \text{const} , \quad \mathrm{d}\tilde{r} = \sqrt{g_{rr}}\,\mathrm{d}r , \tag{5}$$

where $\tilde{r}$ denotes a proper distance in the radial direction in the equatorial plane of the disc.

Considering mass M, angular momentum j and quadrupole moment q of the central compact object, one may find from relations (1), (2) and (5) a QPO distribution $\mathrm{d}n/\mathrm{d}R$ which is illustrated in Fig. 1.[2]

3.1.1 Properties of central compact object and implied distribution

Because the parameters M, j and q of the central compact object in 4U 1636−53 are not known, similarly to the other QPO sources, i.e., Barret et al. (2005), we produce an averaged distribution (in next the mean distribution) $\mathrm{d}n/\mathrm{d}R$ for a family of sources. The family we consider is characterized by parameters $M \in (1.2\mathrm{M}_\odot, 2.2\mathrm{M}_\odot)$, $j \in (0, 0.14)$ and $q \in (j^2, 6j^2)$ with a Gaussian distribution on a 2σ level for each interval

$$p(x_i) = \frac{w}{\sigma\sqrt{2\pi}} \exp\left[-\frac{(x_i - \bar{x}_i)^2}{2\sigma^2}\right] ,$$

where $\{M, j, q\} \ni x_i \in (\bar{x}_i \pm \Delta x_i)$ and $2\sigma = \Delta x$.

[2] Strictly speaking, the density $\mathrm{d}n/\mathrm{d}R$ is a function of j and q, independent of M – frequencies (2) scale with $1/M$, nevertheless, the mass still play a role for finite distributions if observational restrictions are connected to the QPO frequency.

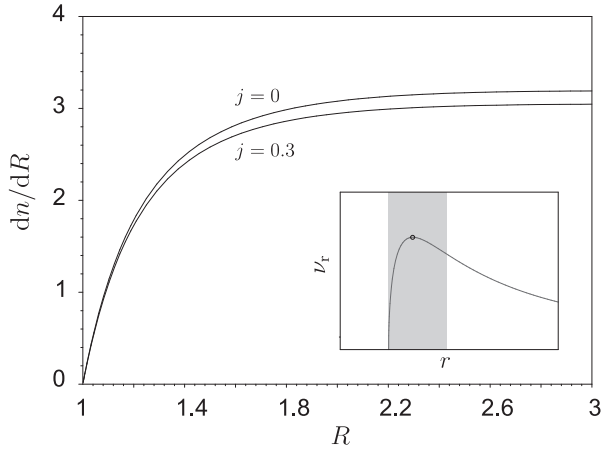

Figure 1. The distribution function $\mathrm{d}n/\mathrm{d}R$ for two representative values of the angular momentum j and Kerr limit of quadrupole moment $q = j^2$. Shadow in the inserted figure roughly indicates relevant part of the accretion disc.

For hundred sources we produce ~ 200 datapoints per each source corresponding to a constant density $\mathrm{d}n/\mathrm{d}\tilde{r}$ in the region located between the radius corresponding to the maximum of radial epicyclic frequency and a marginally stable orbit.[3] We also discard any datapoints below $\nu_{\mathrm{L}} = 500$ Hz in order to obtain results comparable with our observational data as these are restricted by the same limit. To mimic an observational error we blur the implied frequencies with the 3 % Gaussian error on a 2σ level of confidence.

We find that the variations of individual distributions to the mean are rather small which follows from the partial $1/M$ scaling of the orbital frequencies (2) and from small influence of the low neutron star angular momentum to the frequency ratio R (see Fig. 1). Within the considered radial range the ratio R is a monotonic and decreasing function of the radial coordinate, changing from $R = 1$ to $R \sim 2$.[4] Maximum variations $\Delta R(j, q) = R(r_{\max}, 0, 0) - R(r_{\max}, j, q)$ at the maximum of the radial epicyclic frequency within the examined interval of the angular momentum do not exceed $\Delta R \sim 0.02$.

The mean distribution therefore rather well represents all the considered combinations (M, j, q). The mean distribution is shown in Fig. 2a together with the "Schwarzschild" distribution ($j = 0$ and $q = 0$). Fig. 2b provides a comparison to the observational data.

[3] The considered radial interval agrees with rough observational constraints to the model (see, e.g., Belloni et al., 2007b).

[4] The value $R = 1$ represents rather *asymptotic* number corresponding to the marginally stable circular orbit. Notice also that for the Schwarzschild spacetime the value at the maximum of radial epicyclic frequency reads exactly $R = 2$ and slowly decreases with the increasing angular momentum j (see, e.g., Török and Stuchlík, 2005).

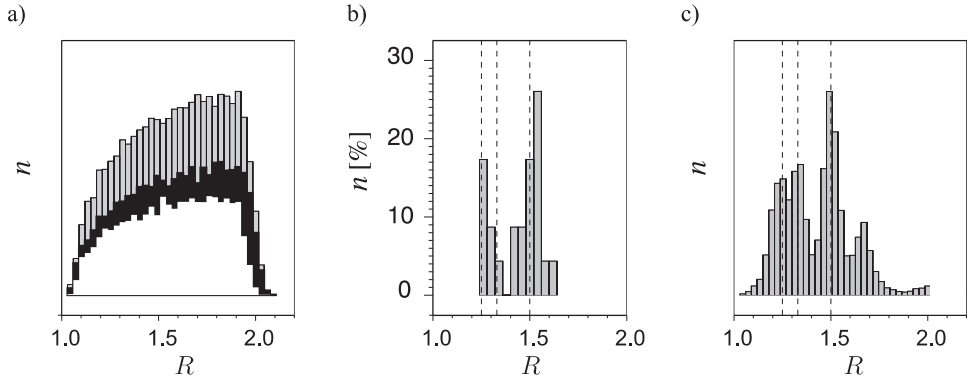

Figure 2. (a) The twin peak QPO distribution implied by RP model with no preferred orbits (model I). Colours correspond to: Grey – averaged distribution, black – "Schwarzschild" distribution ($j = 0,\ q = 0$), white – $j = 0.3, q = 0.09$). Vertical axes scale is arbitrary for a given distribution. (b) The observed twin peak QPO distribution. (c) The distribution model II (see the main text).

3.2 Distribution model II

One can easily recognize from Fig. 2 that the constructed distribution (in next the model I) significantly differs from the empirical one. We apply the Kolmogorov–Smirnov (KS) test (Press et al., 1997) to quantify this statement. In terms of the test, the probability that the constructed and the observed distributions come from the same parent distribution is $p_{\rm KS} \sim 10^{-5}$ for any parameters $M,\ j, q$ from the considered intervals.

The unsatisfactory result presented above is connected to the conclusions of the studies of kHz QPO ratio distribution in the neutron star sources (Abramowicz et al., 2003b; Belloni et al., 2005, 2007a; Török et al., 2007b) – the ratio distribution tends to cluster close to ratio of small natural numbers.

It was proposed that the clustering can be connected to different instances of one orbital resonance (Török et al., 2007b) involving modes formally identical or similar to the modes (2). In such a case it is impossible to model the underlying distribution without a precise knowledge of the physical mechanism. Nevertheless, in Fig. 2c we show a modified version (model II) of the simulated distributional model I, satisfying the following restrictions:

- The datapoints are created only close to the "resonant" radii with the ratio $R = k/l$, where $k, l \in \{1, 2, 3, 4, 5, 6\}$.
- The distribution of datapoints around the resonant radii is implied by the Cauchy–Lorentz distribution in the ratio R

$$p(R) = w_{k/l}\,\frac{\lambda_{k/l}/\pi}{(R - k/l)^2 + \lambda_{k/l}^2}\,.$$

- The weights $w_{k/l}$ of individual Lorentzians are normalized as

$$\sum w_{k/l} = 1\,, \quad w_{k/l} \sim 1/j^2\,, \tag{6}$$

where j is the higher number from the two k, l. The width of the Lorentzians is arbitrarily given as $\lambda = 0.013R$ so there is $\sim 97\,\%$ of datapoints relevant to the Lorentzians in the interval $R \in (1, 2)$.
- All the other properties are the same as in the case of model I.

The *distribution guess* (model II) above includes preference of orbits with the Keplerian and periastron frequency being in resonant ratios, and its detailed properties are rather arbitrary. Its comparison with observation gives the KS probability $p_{\rm KS} \sim 40\,\%$ within the considered range of central compact object parameters.

4 CONCLUSIONS

The observational data we use correspond to all the RXTE observations of 4U 1636+53 till 2005 proceeded by the shift-add technique through continuous segments of observation. The part of data displaying significant twin peak QPOs is restricted to about 20 hours of observation represented in our study by 23 datapoints corresponding to the individual continuous observations. It is needed for a further study to proceed this data by other methods in order to obtain more detailed view of the distribution. However, in terms of the RP model the 23 significant datapoints we use represent[5] the statistics of $\sim 10^7$ individual hot spots averaged in well defined way which allows us to conclude that

- *The twin peak QPO distribution obtained from the relativistic precession (RP) model under the consideration of the QPO excitation probability being uniform across the inner part of the accretion disc is highly incompatible with that given by observational data.* This result is independent of the choice of reasonable sample of intervals of parameters M, j, q.[6] Because of the shape of resulting histograms (Figs 1 and 2a) the result is also independent of the exact delimitation of the radial disc region (which we consider between a maximum of the radial epicyclic frequency and the marginally stable circular orbit).
- On the other hand the arbitrary consideration of preferred "resonant" radii implies a twin peak QPO distribution showing similarities to the observational one.[7]

Finally we notice that several QPO models (hot spot- or disc oscillations-like) introduce frequency relations which are qualitatively and also quantitatively similar to those implied by the relativistic precession model. Moreover, in the limit of the Schwarzschild spacetime these relations coincide (Horák et al., 2007; Török et al., 2007b; Stuchlík et al., 2007). Our discussion of quantitative distribution of observations is thus roughly relevant also for those models, including the model considering the radial $m = 1$ and vertical $m = 2$ disc-oscillation modes.

---

5 Under the assumption of the hot spot lifetime being equal to few orbits.

6 For completeness, we check also for "extreme values" like $j \sim 0.3$.

7 It has been recently noticed (Török et al., 2007a) that the distribution can be well described (KS probability $\sim$ 98 %) by a sum of two Lorentzians having the centroids at $R = 1.51$ and 1.28. Nevertheless the eventual relevance of (exactly) these frequency ratios to a QPO model is not clear at present.

ACKNOWLEDGEMENTS

We thank Jiří Horák for useful discussions and suggestions. The authors are supported by the Czech grants MSM 4781305903, LC06014, and GAČR 202/06/0041.

REFERENCES

Abramowicz, M. A., Almergren, G. J. E., Kluźniak, W. and Thampan, A. V. (2003a), The Hartle–Thorne circular geodesics, submitted inClassical Quantum Gravity, arXiv: `gr-qc/0312070`.

Abramowicz, M. A., Bulik, T., Bursa, M. and Kluźniak, W. (2003b), Evidence for a 2 : 3 resonance in Sco X-1 kHz QPOs, *Astronomy and Astrophysics Lett.*, **404**, pp. L21–L24, arXiv: `astro-ph/0206490v2`.

Barret, D., Olive, J.-F. and Miller, M. C. (2005), An abrupt drop in the coherence of the lower kilohertz QPO in 4U 1636−536, *Monthly Notices Roy. Astronom. Soc.*, **361**, pp. 855–860.

Belloni, T., Homan, J., Motta, S., Ratti, E. and Méndez, M. (2007a), RossiXTE monitoring of 4U 1636−53: I. Long-term evolution and kHz Quasi-Periodic Oscillations, *Monthly Notices Roy. Astronom. Soc.*, **379**, pp. 247–252, arXiv: `0705.0793`.

Belloni, T., Méndez, M. and Homan, J. (2005), The distribution of kHz QPO frequencies in bright low mass X-ray binaries, *Astronomy and Astrophysics*, **437**, pp. 209–216.

Belloni, T., Méndez, M. and Homan, J. (2007b), On the kHz QPO frequency correlations in bright neutron star X-ray binaries, *Monthly Notices Roy. Astronom. Soc.*, **376**(3), pp. 1133–1138, arXiv: `astro-ph/0702157`.

Bulik, T. (2005), The statistics of Sco X-1 kHZ QPOs, *Astronom. Nachr.*, **326**(9), pp. 861–863.

Hartle, J. B. and Thorne, K. (1968), Slowly rotating relativistic stars II. Model for neutron stars and supermassive stars, *Astrophys. J.*, **153**, pp. 807–834.

Horák, J., Bakala, P., Stuchlík, Z. and Török, G. (2007), in preparation.

Lamb, F. K. (2003), High Frequency QPOs in Neutron Stars and Black Holes: Probing Dense Matter and Strong Gravitational Fields, in E. P. J. van den Heuvel, L. Kaper, E. Roi and R. A. M. J. Wijers, editors, *From X-Ray Binaries to Gamma-ray Bursts, proceedings of a symposium held in memory of Jan van Paradijs*, volume 308 of *ASP Conference*, pp. 221–250, Banff, AB, Canada, arXiv: `0705.0030v1`.

Lamb, F. K. and Boutloukos, S. (2007), Accreting Neutron Stars in Low-Mass X-Ray Binary Systems, in E. F. Milone, D. A. Leahy and D. Hobill, editors, *Short-Period Binary Stars: Observations, Analyses, and Results*, volume 352 of *Astrophysics and Space Science Library*, Springer, Dordrecht, arXiv: `0705.0155v2`.

Méndez, M., van der Klis, M., Wijnands, R., Ford, E. C., van Paradijs, J. and Vaughan, B. A. (1998), Kilohertz Quasi-periodic Oscillation Peak Separation Is not Constant in the Atoll Source 4U 1608−52, *Astrophys. J. Lett.*, **505**, pp. L23–L26.

Press, W. H., Teukolsky, S. A., Vetterling, W. T. and Flannery, B. P. (1997), *Numerical Recipes in C: The Art of Scientific Computing*, Cambridge University Press, Cambridge, 2nd edition, ISBN 0-521-43108-5, URL `http://www.nr.com/`.

Stella, L. and Vietri, M. (1999), kHz Quasiperiodic Oscillations in Low-Mass X-Ray Binaries as Probes of General Relativity in the Strong-Field Regime, *Phys. Rev. Lett.*, **82**(1), pp. 17–20.

Stuchlík, Z., Török, G. and Bakala, P. (2007), On a multi-resonant origin of high frequency quasiperiodic oscillations in the neutron-star X-ray binary 4U 1636−53, submitted to Astronomy and Astrophysics, arXiv: `0704.2318`.

Török, G., Abramowicz, M. A., Bakala, P., Bursa, M., Horák, J., Kluźniak, W., Rebusco, P. and Stuchlík, Z. (2007a), On the distribution of kHz QPO frequency ratio in the atoll source 4U1635−53, *Astronomy and Astrophysics*, submitted.

Török, G. and Stuchlík, Z. (2005), Radial and vertical epicyclic frequencies of Keplerian motion in the field of Kerr naked singularities. Comparison with the black hole case and possible instability of naked singularity accretion discs, *Astronomy and Astrophysics*, **437**(3), pp. 775–788, arXiv: `astro-ph/0502127`.

Török, G., Stuchlík, Z. and Bakala, P. (2007b), A remark about possible unity of the neutron star and black hole high frequency QPOs, *Central European J. Phys.*, **5**(4), pp. 457–462.

van der Klis, M. (2006), Rapid X-ray Variability, in W. H. G. Lewin and M. van der Klis, editors, *Compact Stellar X-Ray Sources*, pp. 39–112, Cambridge University Press, Cambridge.

APPENDIX A: FORMULAE FOR ORBITAL GEODESIC FREQUENCIES IN THE HARTLE–THORNE METRIC

Components of the metric tensor

$$\mathrm{d}s^2 = g_{tt}\,\mathrm{d}t^2 + g_{rr}\,\mathrm{d}r^2 + g_{\theta\theta}\,\mathrm{d}\theta^2 + g_{\phi\phi}\,\mathrm{d}\phi^2 + g_{\phi t}\,\mathrm{d}\phi\mathrm{d}t + g_{t\phi}\,\mathrm{d}t\mathrm{d}\phi\,,$$

are given as

$$\begin{aligned}
g_{tt} &= +(1-2M/r)\left(1 + j^2 {F_1}^t + q {F_2}^t\right),\\
g_{rr} &= -(1-2M/r)^{-1}\left(1 + j^2 {F_1}^r - q {F_2}^r\right),\\
g_{\theta\theta} &= -r^2\left(1 + j^2 {F_1}^\theta + q {F_2}^\theta\right),\\
g_{\phi\phi} &= -r^2\sin^2\theta\left(1 + j^2 {F_1}^\phi + q {F_2}^\phi\right),\\
g_{t\phi} &= -2(M^2/r)\, j \sin^2\theta\,,
\end{aligned}$$

where

$$\begin{aligned}
{F_1}^t &= [8Mr^4(r-2M)]^{-1}[u^2(48M^6 - 8M^5 r - 24M^4 r^2 - 30M^3 r^3 - 60M^2 r^4\\
&\quad + 135Mr^5 - 45r^6) + (r-M)(16M^5 + 8M^4 r - 10M^2 r^3 - 30Mr^4 + 15r^5)]\\
&\quad + A_1(r)\,,\\
{F_2}^t &= [8Mr\,(r-2M)]^{-1}\,[5(3u^2-1)(r-M)(2M^2 + 6Mr - 3r^2)] - G_1(r)\,,\\
{F_1}^r &= [8Mr^4\,(r-2M)]^{-1}[(G_2 - 72M^5 r) - 3u^2(G_2 - 56M^5 r)] - G_1(r)\,,\\
{F_2}^r &= {F_2}^t\,,\\
{F_1}^\theta &= (8Mr^4)^{-1}(1-3u^2)(16M^5 + 8M^4 r - 10M^2 r^3 + 15Mr^4 + 15r^5) + G_3(r)\,,\\
{F_2}^\theta &= (8Mr)^{-1}[5(1-3u^2)(2M^2 - 3Mr - 3r^2)] - G_3(r)\,,\\
{F_1}^\phi &= {F_1}^\phi\,,\\
{F_2}^\phi &= {F_2}^\phi\,,
\end{aligned}$$

and

$$G_1 = \frac{15r(r-2M)(1-3u^2)}{16M^2}\ln\frac{r}{r-2M}\,,$$
$$G_2 = \frac{15(r^2-2M^2)(3u^2-1)}{16M^2}\ln\frac{r}{r-2M}\,,$$
$$G_3 = 80M^6 + 8M^4r^2 + 10M^3r^3 + 20M^2r^4 - 45Mr^5 + 15r^6\,,$$
$$u = \cos\theta\,.$$

The angular velocity for corotating circular particle orbits reads

$$\Omega_{\rm K} = \frac{u^\phi}{u^t} = \frac{M^{1/2}}{r^{3/2}}\left[1 - j\,\frac{M^{3/2}}{r^{3/2}} + j^2 F_1{}^{\Omega}(r) + q F_2{}^{\Omega}(r)\right],$$

where

$$F_1{}^{\Omega}(r) = (48M^7 - 80M^6r + 4M^5r^2 - 18M^4r^3 + 40M^3r^4 + 10M^2r^5 + 15Mr^6 - 15r^7)[16M^2(r-2M)r^4]^{-1} + H(r)\,,$$
$$F_2{}^{\Omega}(r) = \frac{5(6M^4 - 8M^3r - 2M^2r^2 - 3Mr^3 + 3r^4)}{16M^2(r-2M)r} - H(r)\,,$$
$$H(r) = \frac{15(r^3-2M^3)}{32M^3}\ln\frac{r}{r-2M}\,.$$

The epicyclic frequencies of circular geodesic motion are given by formulae

$$\omega_r^2 = \frac{M(r-6M)}{r^4}\left[1 + jH_1(r) - j^2H_2(r) - qH_3(r)\right],$$
$$\omega_\theta^2 = \frac{M}{r^3}\left[1 - jI_1(r) + j^2I_2(r) + qI_3(r)\right],$$

where

$$H_1(r) = \frac{6M^{3/2}(r+2M)}{r^{3/2}(r-6M)}\,,$$
$$H_2(r) = [8M^2r^4(r-2M)(r-6M)]^{-1}(384M^8 - 720M^7r - 112M^6r^2 - 76M^5r^3 - 138M^4r^4 - 130M^3r^5 + 635M^2r^6 - 375Mr^7 + 60r^8) + J(r)\,,$$
$$H_3(r) = \frac{5(48M^5 + 30M^4r + 26M^3r^2 - 127M^2r^3 + 75Mr^4 - 12r^5)}{8M^2r(r-2M)(r-6M)} - J(r)\,,$$

$$I_1(r) = \frac{6M^{3/2}}{r^{3/2}}\,,$$
$$I_2(r) = [8M^2r^4(r-2M)]^{-1}(48M^7 - 224M^6r + 28M^5r^2 + 6M^4r^3 - 170M^3r^4 + 295M^2r^5 - 165Mr^6 + 30r^7) - K(r)\,,$$
$$I_3(r) = \frac{5(6M^4 + 34M^3r - 59M^2r^2 + 33Mr^3 - 6r^4)}{8M^2r(r-2M)} + K(r)\,,$$

with

$$J(r) = \frac{15r(r-2M)(2M^2+13Mr-4r^2)}{16M^3(r-6M)} \ln\frac{r}{r-2M},$$

$$K(r) = \frac{15(2r-M)(r-2M)^2}{16M^3} \ln\frac{r}{r-2M}.$$

For completeness, the relation determining the marginally stable circular geodesic reads

$$r_{\rm ms} = 6M\left[1 - j\frac{2}{3}\sqrt{\frac{2}{3}} + j^2\left(\frac{251647}{2592} - 240\ln\frac{3}{2}\right) + q\left(-\frac{9325}{96} + 240\ln\frac{3}{2}\right)\right].$$

Proceedings of *RAGtime 8/9, 15–19/19–21 September, 2006/2007, Hradec nad Moravicí, Opava, Czech Republic*
S. Hledík and Z. Stuchlík, editors, Silesian University in Opava, 2007, pp. 489–499

On a multi-resonant origin of high frequency QPOs in the atoll source 4U 1636−53

Gabriel Török[a], Pavel Bakala, Zdeněk Stuchlík and Eva Šrámková

Institute of Physics, Faculty of Philosophy & Science, Silesian University in Opava, Bezručovo nám. 13, CZ-746 01 Opava, Czech Republic
[a] terek@volny.cz

ABSTRACT
The kHz quasiperiodic oscillations (QPOs) observed in low-mass X-ray neutron star binaries are most likely connected to the orbital motion in the accretion disc and show datapoint clustering of frequency ratio between the upper and lower QPOs in small natural numbers. It is shown for the atoll source 4U 1636−53 that using the Hartle–Thorne metric to describe the neutron star spacetime, the data clustered around the frequency ratios 3/2 and 5/4 could be fitted by three models (Relativistic Precession, Vertical Precession and Total Precession) involving the hot spot orbital motion with Keplerian, radial epicyclic and vertical epicyclic frequencies. We demonstrate that with taking into account the hotspots interaction with the neutron star magnetic field the discussed three models can provide good fits implying reasonable values of the neutron star mass and angular momentum. Therefore the hypothesis of more instances of one orbital resonance has the potential to explain the kHz QPO nature in the source 4U 1636−53.

Keywords: X-ray – neutron stars – binaries – accretion discs – QPOs

1 INTRODUCTION

General belief dominating in the astrophysical community links the observed neutron star kHz QPOs to the orbital motion near the inner edge of an accretion disc.

The ratio between frequencies of the upper and lower observed twin peak QPO cluster close to ratios of small natural numbers, most often close to the 3/2 value, but the other rational ratios 5/4 and 4/3 occur in some sources as well. The class of QPOs orbital resonance models considers a resonance between Keplerian and epicyclic frequencies of the geodesic motion.

978-80-7248-419-5

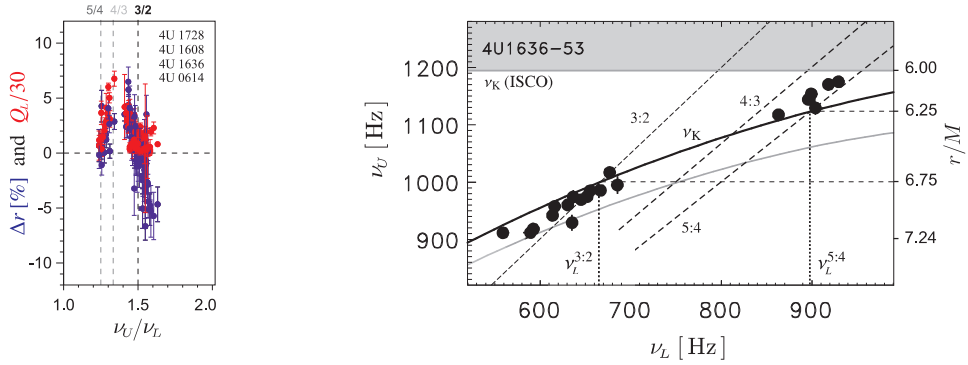

Figure 1. *Left, from Stuchlík et al. (2007); Horák et al. (2007):* The twin QPO rms amplitude difference together with the lower frequency quality factor as a function of the frequency ratio. It has been recently shown (Horák et al., 2007) that such a behaviour may result from the resonant energy exchange between two time-dependent eigenfrequency modes. *Right, from Stuchlík et al. (2007); Horák et al. (2007):* The frequency correlation in the atoll source 4U 1636−53. Curve $\nu_{\rm K}$ determines the upper QPO frequency following from the relativistic precession model (Stella and Vietri, 1999) under the consideration of the gravitational field described by the Schwarzschild metric with the central mass $M = 1.84\,{\rm M}_\odot$, the grey curve denotes the same relation but for $M = 2\,{\rm M}_\odot$, i.e., the trend reported by Belloni et al. (2007b). Note that the actual (observed) frequencies of the resonance are allowed to differ from given resonant eigenfrequencies (Landau and Lifshitz, 1976; Abramowicz et al., 2005).

The results of several studies (Belloni et al., 2005; Barret et al., 2005, 2006; Abramowicz et al., 2005; Méndez, 2006; Barret et al., 2006) indicate that for a given source the upper and lower QPO frequency can be traced through the whole observed range of frequencies but the probability to detect both QPOs *simultaneously* increases when the frequency ratio is close to the ratio of small natural numbers, namely $3/2$, $4/3$ and $5/4$ in the case of six atoll sources (Stuchlík et al., 2007). In Fig. 1 we show correlation corresponding to the occurences of twin peaks for the atoll source 4U 1636−53 taken from Abramowicz et al. (2005), method A in the paper. This correlation was obtained by the shift-add (Méndez et al., 1998) fitting of continuos segments of observations from all the at available RXTE data (see Barret et al., 2005, 2006; Abramowicz et al., 2005 for details). We stress that contrary to the studies considering separated single QPO distributions, e.g., the recent paper of Belloni et al. (2007a), the twin peak QPO distribution examined here includes only simultaneous significant detections of both QPO frequencies (i.e., the detections of both the peaks above 2.5σ significance having quality factor higher than 3). These two approaches in counting the number of occurences are different, but both legal being dependend on the reason (and assumptions) of the counting.

In the sense described above, the atoll source 4U 1636−53 shows twin peak clustering around two distinct values ($3/2$ and $5/4$) of the frequency ratio. The same frequency ratios correspond to the change in sign of the twin peak QPO amplitude difference, suggesting existence of a resonant energy overflow (Stuchlík et al., 2007; Horák et al., 2007). We

explore the idea of Török et al. (2007) that the two clusters may follow from different instances of one orbital resonance.

2 ORBITAL FREQUENCIES OF GEODESIC MOTION CLOSE TO ROTATING NEUTRON STARS

The correct treatment of an orbital motion close to (rotating) neutron stars requires the general relativistic approach. For a given axially symetric spacetime the angular velocities of the azimuthal, radial and vertical "quasielliptic" orbital motion read (see, e.g., Abramowicz et al., 2003a)

$$\Omega_{\rm K} = u^{\phi}/u^{t}\,, \qquad \omega_i^2 = \frac{\left(g_{tt} + \Omega_{\pm}\, g_{t\phi}\right)^2}{g_{ii}} \left(\frac{\partial^2 U}{\partial i^2}\right)_{\ell}\,, \tag{1}$$

where $g_{\mu\nu}$ are components of the line element, $i \in (r, \theta)$ and U is an *effective potential* $U(r, \theta, \ell) \equiv g^{tt} - 2\ell g^{t\phi} + \ell^2 g^{\phi\phi}$, with ℓ denoting the specific angular momentum of the orbiting test particle $\ell = -u_{\phi}/u_t$. In the following we consider Keplerian motion and $l = l_{\rm K}(r, \theta)$. Due to the inequality between the azimuthal and radial frequency, the eccentric orbits waltz at the *periastron precession frequency* $\nu_{\rm P}$ and in addition the orbits tilted relative to the equatorial plane of the spinning central mass wobble at the *nodal (often called Lense–Thirring) precession frequency* (e.g. Misner et al., 1973)

$$\nu_{\rm LT} = \nu_{\rm K} - \nu_{\theta}\,, \qquad \nu_{\rm P} = \nu_{\rm K} - \nu_{\rm r}\,.$$

Both the declination of the quasi-ellipse plane and position of the periastron then reach the initial state simultaneously in the period characterized by the *total precession frequency*

$$\nu_{\rm T} = \nu_{\rm P} - \nu_{\rm LT} = \nu_{\theta} - \nu_{\rm r}\,.$$

We consider the external neutron star spacetime described by the Hartle–Thorne metric (Hartle and Thorne, 1968), which represents the solution of vacuum Einstein field equations for the exterior of rigidly and relatively slowly rotating, stationary and axially symmetric body, and the explicit form of Eq. (1) derived by Abramowicz et al. (2003a).

3 TESTING THE HYPOTHESIS OF A RESONANCE BETWEEN TWO TIME-DEPENDENT EIGENFREQUENCY MODES

3.1 Frequency identification

Usually the $n : m$ orbital resonant models assuming a non-linear resonance between Keplerian and/or epicyclic frequencies (see, e.g., Abramowicz et al., 2004) identify the resonant eigenfrequencies $\nu_{\rm L}^0$, $\nu_{\rm U}^0$ as

$$\nu_{\rm L}^0 = \nu_{\rm r}(r_{n:m})\,, \quad \nu_{\rm U}^0 = \nu_{\rm v}(r_{n:m}) \quad \nu_{\rm v} \in [\nu_{\theta},\ \nu_{\rm K}]\,, \qquad \frac{\nu_{\rm v}(r_{n:m})}{\nu_{\rm r}(r_{n:m})} = \frac{n}{m}\,. \tag{2}$$

where n, m are small natural numbers and $r_{n:m}$ is the generic resonant radius.

In the case of a considerably weak forced or parametric non-linear resonance (Landau and Lifshitz, 1976), the upper and lower observed QPO frequencies $\nu_{\rm L}$ and $\nu_{\rm U}$ are related to the resonant eigenfrequencies either directly $\nu_{\rm L} \doteq \nu_{\rm L}^0$, $\nu_{\rm U} \doteq \nu_{\rm U}^0$, or as their linear combinations $\nu_{\rm L} \doteq \alpha\nu_{\rm L}^0$, $\nu_{\rm U} \doteq \beta\nu_{\rm U}^0$, where α and β are small integral numbers.

In general case of a system in a non-linear resonance, the observed frequencies differ from resonance eigenfrequencies by a frequency corrections proportional to the square of small dimensionless amplitudes (Landau and Lifshitz, 1976). It was shown by Abramowicz et al. (2003b) that a resonance characterized by one pair of eigenfrequencies may reproduce the whole range of frequencies observed in a neutron star source. Later Abramowicz et al. (2005) considered the idea of one eigenfrequency pair (so called resonant point in the frequency-frequency plane) common for a set of neutron star sources. It was found that the coefficients of linear fits well approximating individual sources are anticorrelated, in good accord with the non-linear resonance and the hypothesis of one eigenfrequency-pair. On the other hand this approach, incorporating certain difficulties (e.g., the extremely large extension of the observed frequency range), is not proved yet, and some observational facts like the multi-peaked ratio distribution suggest that more then one resonant points may be responsible for the almost linear observed frequency correlation (Stuchlík et al., 2007).

In next we focus on the hypothesis of more resonant points corresponding to different instances of one orbital resonance and suppose that the observed frequencies are close to the resonance eigenfrequencies, i.e., that the observed frequency correlation follows the generic relation between resonant eigenfrequencies,

$$\nu_{\rm L} \sim \nu_{\rm L}^0\,, \quad \nu_{\rm U} \sim \nu_{\rm U}^0\,. \tag{3}$$

We checked in the Hartle–Thorne spacetimes that the ratio between the Keplerian (or vertical epicyclic) frequency and radial epicyclic frequency monotonically increases with decreasing radius r whereas the Keplerian (vertical epicyclic) frequency increases (Stuchlík et al., 2007). In other words, for the models given by Eq. (2) considering resonance between Keplerian (vertical epicyclic) frequency and radial epicyclic frequency satisfying relation (3), the ratio of observed frequencies should increase with increasing QPO frequency, but that is opposite to what is observed.

However, such relations are not the only possible in the framework of resonance models, and in Bursa (2004) so called vertical precession resonance introduced in order to match the spin estimated from fits of the X-ray spectral continua for the microquasar GRO J1655−40 was discussed. The resonance should occur between the vertical epicyclic frequency and the periastron precession frequency fulfilling the relation (Bursa, 2004)

$$\nu_{\rm L}^0(r) = \nu_{\rm P}(r) = \nu_{\rm K}(r) - \nu_{\rm r}(r)\,, \quad \nu_{\rm U}^0(r) = \nu_\theta(r)\,, \qquad \text{“Bursa”} \tag{4}$$

for a particular choice of the resonant radius r defined by the condition $\nu_{\rm u} = 3/2\nu_{\rm l}$.

As noticed in Török et al. (2007), for the Schwarzschild spacetime the relations (4) coincide with those following from the Relativistic Precession model (Stella and Vietri, 1999):

$$\nu_{\rm L}^0(r) = \nu_{\rm P}(r) = \nu_{\rm K}(r) - \nu_{\rm r}(r)\,, \quad \nu_{\rm U}^0(r) = \nu_{\rm K}(r)\,. \qquad \text{“Stella”} \tag{5}$$

Opposite to the relations (2), the two relationships (4), (5) as well as the other two relationships (Stuchlík et al., 2007)

$$\nu_{\rm L}^0(r) = \nu_\theta(r) - \nu_{\rm r}(r)\,, \quad \nu_{\rm U}^0(r) = \nu_\theta(r) \qquad \text{“Total precession I”;}$$
$$\nu_{\rm L}^0(r) = \nu_{\rm T}(r) = \nu_\theta(r) - \nu_{\rm r}\,, \quad \nu_{\rm U}^0(r) = \nu_{\rm K}(r) \qquad \text{“Total precession II”}$$

imply increase of $\nu_{\rm U}^0$ for increasing $\nu_{\rm L}^0$. We fit the QPO frequencies observed in 4U 1636−53 by the four different frequency relationships presented above testing the hypothesis that an appropriate resonance formula may be responsible for all the observed datapoints.

3.2 Matching the data

In order to obtain a rough scan we calculated the above frequency relations in the Hartle–Thorne metric for the range of the mass $M \in 1$–$4\,{\rm M}_\odot$, the internal angular momentum $j \in 0$–0.5 and a physically meaningful quadrupole momentum q with a step equivalent to the thousand points in all three quantities, i.e., for 3-dimensional maps each having 10^9 points. Then, for each pair (M, j), we keep the value of the quadrupole momentum q which gives the lowest χ^2 with respect to the observed datapoints. For the Schwarzschild spacetime ($q = j = 0$), when relations giving all the considered models merge, the best fit is reached for the mass $M \doteq 1.77\,{\rm M}_\odot$, with a $\chi^2 \doteq 400 \sim 20$ d.o.f.

Having a rough clue given by these maps we searched for local χ^2 minima using the Marquardt–Levenberg non-linear least squares method (Marquardt, 1963). The map for the relation “Stella” coinciding with the prediction given by Relativistic Precession model of Stella & Vietri and its representative fit are shown in Figs 2 and 3.

As previously realized, the relation “Stella” match the observational data most likely for relatively high angular momentum close to $j \sim 0.5$ and the central mass $M \sim 2.4$–$2.8\,{\rm M}_\odot$, reaching (not very satisfactory) $\chi^2 \sim 15$ d.o.f.. Unfortunately, the detailed analysis shown

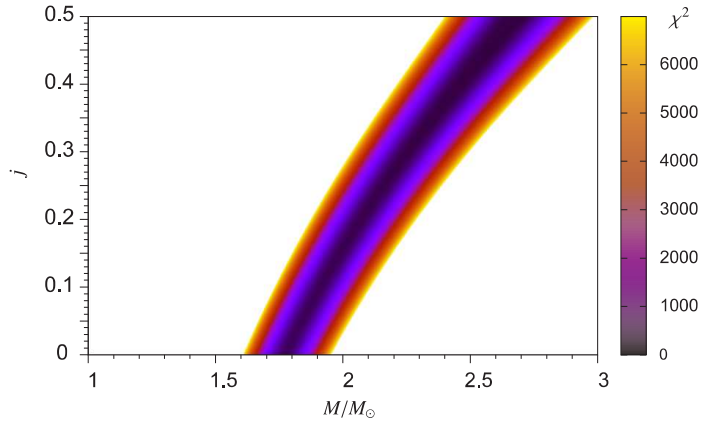

Figure 2. Map of χ^2 (inverse quality measure) of the fits by relation “Stella.”

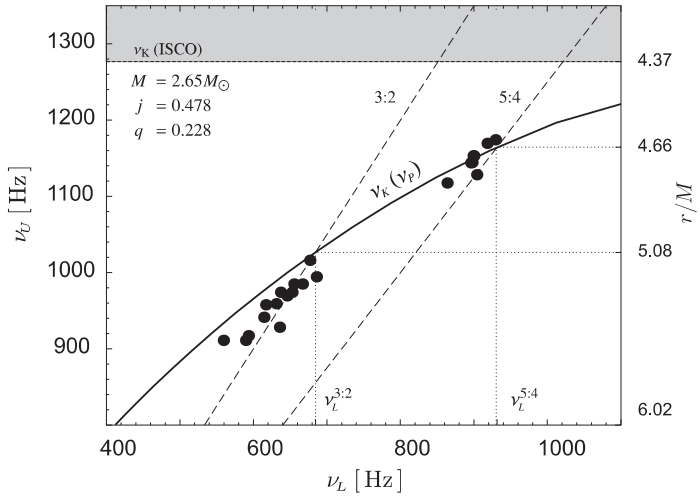

Figure 3. The best fit reached by relation "Stella."

that the other three relations do not provide better results, although the mass estimates could be lower in comparison with the estimate given by Relativistic Precession model.

4 DISCUSSION

The discussed geodesic relations provide fits which are in good qualitative agreement with general trend observed in the neutron star kHz QPO data (see Belloni et al., 2007b). Nevertheless, no one of this relations provides really good fits (we checked for the other five atoll sources that trends are the same as for 4U 1636−53). Moreover, the best fits require rather unrealistic values of mass and angular momentum with respect to the present knowledge of the neutron star equation of state (Glendenning, 1997) as tested in Urbanec et al. (2007). This is, of course, fundamental problem for any model considering the presented geodesic frequency relations, and not only for their resonant interpretation.

To check whether some non-geodesic influence can resolve the problem given above we consider assumption that the effective frequency of radial oscillations may be lowered, e.g., by the radiation blob interaction with the accretion disk or with the neutron star magnetic field (of course, in such a case all the frequencies would be modified by dependent corrections, nevertheless, in the case of the magnetic field it was shown by Aliev and Galtsov (2006); Bakala et al. (2007) that corrections to radial epicyclic frequency should be the strongest one). Then, in the lowest order approximation, the effective frequency of radial oscillations may be written as

$$\tilde{\nu}_{\mathrm{r}} = \nu_{\mathrm{r}}(1 - k)\,,$$

where k is a small constant.

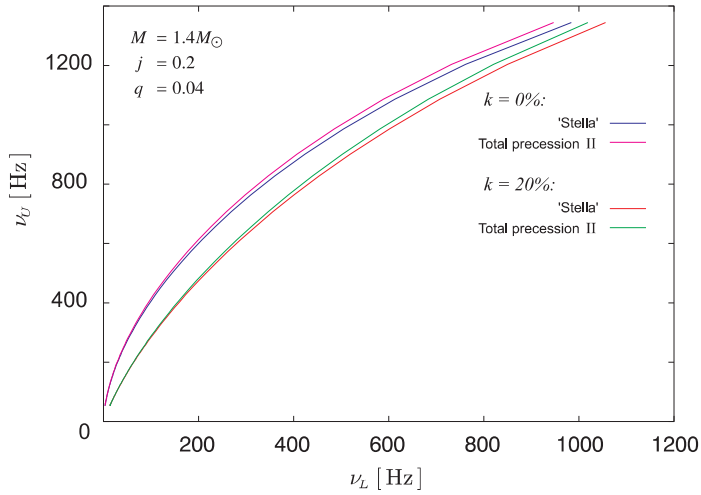

Figure 4. Behaviour of frequency-frequency plot implied by the relation "Stella" vs. those implied by the "Total Precession II" for the case of $\tilde{\nu}_{\rm r} = \nu_{\rm r}$ and $\tilde{\nu}_{\rm r} = 0.8\nu_{\rm r}$.

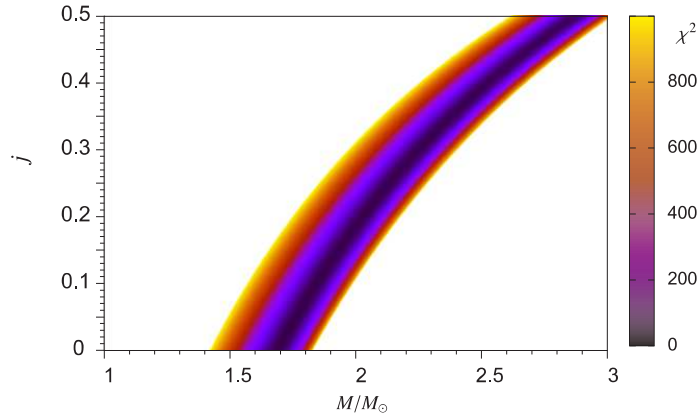

Figure 5. The map of χ^2 reached by the relation "Total precession II" for $k \in (0, 0.2)$.

In Figs 4 and 5 we show the qualitative behaviour of the frequency-frequency plot implied by the relation "Stella" vs. the one implied by the "Total Precession relation II." In the frequency relation $\tilde{\nu}_{\rm r}$ is used instead of $\nu_{\rm r}$.

Because the discussed frequencies of the Keplerian orbital motion scale roughly as $1/M$, the relations given by the "Total Precession" imply lower frequencies in terms of the frequency-frequency plot that should require lower mass in comparison with the Relativistic Precession model in order to fit the same datapoints. In general, the mass is

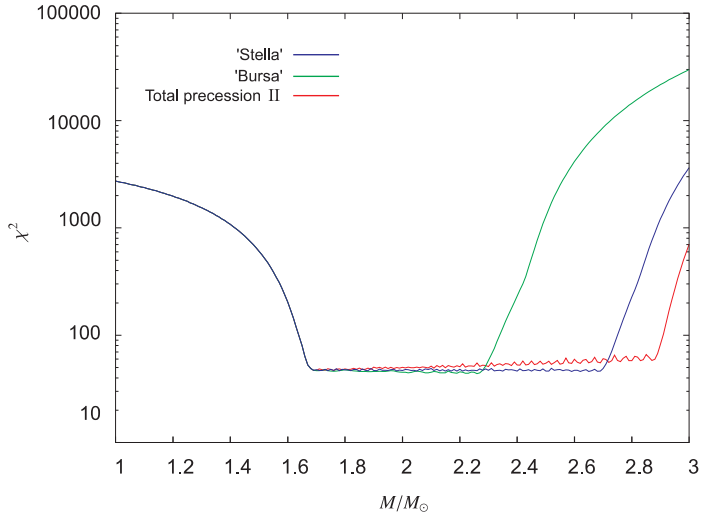

Figure 6. χ^2 (inverse quality measure) of the fits by the Relativistic Precession frequency relation with $\tilde{\nu}_{\rm r}$ used instead of $\nu_{\rm r}$. For a given combination M, j, the coefficient k is chosen as the best one from the interval 0–20 %. A correction of the result presented in Stuchlík et al. (2007)

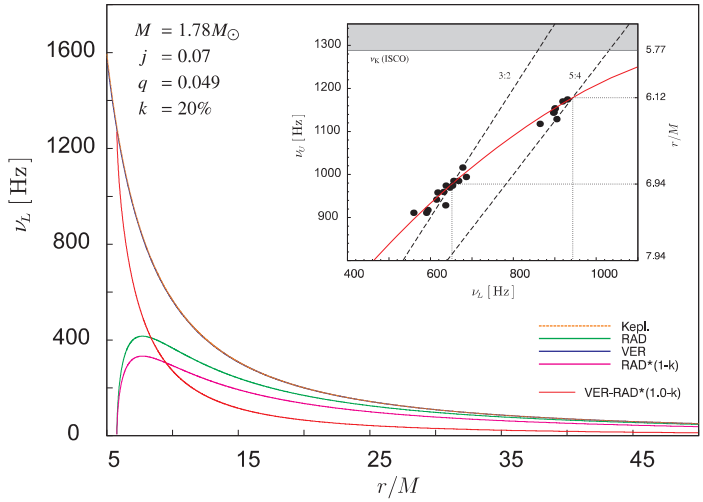

Figure 7. The representative low angular momentum fit for the "Total Precession II" relation. A correction of the result presented in Stuchlík et al. (2007).

lower when the vertical epicyclic frequency is included instead of the Keplerian one in the frequency relation. The same holds for substitution of $\nu_{\rm r}$ by $\tilde{\nu}_{\rm r}$.

Having this motivation and assuming lowering of both the χ^2 of fits and related neutron-star mass, we repeated the fitting procedure described above using the frequency $\tilde{\nu}_{\rm r}$ instead

of ν_r for all four discussed relationships. The resulting quality of fits is shown in the Figs 6 and 7 for the three most convenient frequency relations together with a representative fit.

5 CONCLUSIONS

The modified frequency relations with $\tilde{\nu}_r$ provide the best fits having $\chi^2 \sim 2$–5 d.o.f. when the coefficient k is in the interval 5–20 %. The mass required for a reasonable χ^2 value is then in the interval 1.6–1.8 $M_\odot$ and the relevant angular momentum $j \sim 0.05$–0.2. For a fixed angular momentum, the frequency relations corresponding to the Total Precession implies slightly lower mass than those including Relativistic Precession.

We stress that the Total Precession frequency corresponds to similar effect as the relativistic precession frequency but when considering a resonance, this may naturally include all the three fundamental precessions: Keplerian, periastron, and Lense–Thirring. For the perfect free particle motion, if the Keplerian and total precession frequency form rational fractions, the trajectory is self-repeating (i.e., closed, Stuchlík et al., 2007).

The debate above touching the blob QPO interpretation requires further research including realistic consideration of the frequency corrections. In addition the proposed multi-resonance may also occur not between the considered hot spot modes but between similar disc oscillations modes as well, which deserves attention too.

The observational facts like the ratio clustering and rms amplitudes difference behaviour, together with the fact that the discussed frequency relations can provide good fits conditioned by reasonable values of the neutron star mass and angular momentum, indicates that the hypothesis of more instances of one orbital resonance has the potential to explain the neutron star kHz QPO nature.

ACKNOWLEDGEMENTS

This work was supported by the Czech grants MSM 4781305903 (Z. S., G. T.) and LC06014 (P. B., E. S.). The authors (G. T., P. B., E. S.) would like to thank the fishermen community in Derítő-Tó, Tata, Hungary for a royal hospitality and inspiring atmosphere for the research.

REFERENCES

Abramowicz, M. A., Almergren, G. J. E., Kluźniak, W. and Thampan, A. V. (2003a), The Hartle–Thorne circular geodesics, submitted inClassical Quantum Gravity, arXiv: `gr-qc/0312070`.

Abramowicz, M. A., Barret, D., Bursa, M., Horák, J., Kluźniak, W., Rebusco, P. and Török, G. (2005), A note on the slope-shift anticorrelation in the neutron star kHz QPOs data, in S. Hledík and Z. Stuchlík, editors, *Proceedings of RAGtime 6/7: Workshops on black holes and neutron stars, Opava, 16–18/18–20 September 2004/2005*, pp. 1–9, Silesian University in Opava, Opava, ISBN 80-7248-334-X.

Abramowicz, M. A., Karas, V., Kluźniak, W., Lee, W. and Rebusco, P. (2003b), Non-Linear Resonance in Nearly Geodesic Motion in Low-Mass X-Ray Binaries, *Publ. Astronom. Soc. Japan*, **55**(2), pp. 467–471, URL `http://pasj.asj.or.jp/v55/n2/550214/550214-frame.html`.

Abramowicz, M. A., Kluźniak, W., Stuchlík, Z. and Török, G. (2004), Twin peak QPOs frequencies in microquasars and Sgr A*. The resonance and other orbital models, in Hledík and Stuchlík (2004), pp. 1–23.

Aliev, A. N. and Galtsov, D. V. (2006), Epicyclic Frequencies and Resonant Phenomena Near Black Holes: The Current Status, to appear in Eleventh Marcel Grossmann Proceedings.

Bakala, P., Šrámková, E., Stuchlík, Z. and Török, G. (2007), Dipole magnetic field on a Schwarzschild background and related epicyclic frequencies, pp. 1–10, this volume.

Barret, D., Olive, J. and Miller, M. C. (2006), The coherence of kilohertz quasi-periodic oscillations in the X-rays from accreting neutron stars, *Monthly Notices Roy. Astronom. Soc.*, **370**, pp. 1140–1146.

Barret, D., Olive, J.-F. and Miller, M. C. (2005), An abrupt drop in the coherence of the lower kilohertz QPO in 4U 1636−536, *Monthly Notices Roy. Astronom. Soc.*, **361**, pp. 855–860.

Belloni, T., Homan, J., Motta, S., Ratti, E. and Méndez, M. (2007a), RossiXTE monitoring of 4U 1636−53: I. Long-term evolution and kHz Quasi-Periodic Oscillations, *Monthly Notices Roy. Astronom. Soc.*, **379**, pp. 247–252, arXiv: 0705.0793.

Belloni, T., Méndez, M. and Homan, J. (2005), The distribution of kHz QPO frequencies in bright low mass X-ray binaries, *Astronomy and Astrophysics*, **437**, pp. 209–216.

Belloni, T., Méndez, M. and Homan, J. (2007b), On the kHz QPO frequency correlations in bright neutron star X-ray binaries, *Monthly Notices Roy. Astronom. Soc.*, **376**(3), pp. 1133–1138, arXiv: astro-ph/0702157.

Bursa, M. (2004), Variability of accreting sources at very high time resulution, in Hledík and Stuchlík (2004), pp. 25–32.

Glendenning, N. K. (1997), *Compact Stars: Nuclear Physics, Particle Physics, and General Relativity*, Springer-Verlag, New York.

Hartle, J. B. and Thorne, K. (1968), Slowly rotating relativistic stars II. Model for neutron stars and supermassive stars, *Astrophys. J.*, **153**, pp. 807–834.

Hledík, S. and Stuchlík, Z., editors (2004), *Proceedings of RAGtime 4/5: Workshops on black holes and neutron stars, Opava, 14–16/13–15 October 2002/2003*, Silesian University in Opava, Opava, ISBN 80-7248-242-4.

Horák, J., Abramowicz, M. A., Rebusco, P. and Török, G. (2007), Evidence of internal resonance in neutron stars kilohertz QPOs, in preparation.

Landau, L. D. and Lifshitz, E. M. (1976), *Mechanics*, volume I of *Course of Theoretical Physics*, Elsevier Butterworth-Heinemann, Oxford, 3rd edition, ISBN 0-7506-2896-0.

Marquardt, D. W. (1963), An Algorithm for Least-Squares Estimation of Nonlinear Parameters, *J. Soc. Indust. App. Math.*, **11**, pp. 431–441.

Méndez, M. (2006), On the maximum amplitude and coherence of the kilohertz quasi-periodic oscillations in low-mass X-ray binaries, *Monthly Notices Roy. Astronom. Soc.*, **371**(4), pp. 1925–1938.

Méndez, M., van der Klis, M., Wijnands, R., Ford, E. C., van Paradijs, J. and Vaughan, B. A. (1998), Kilohertz Quasi-periodic Oscillation Peak Separation Is not Constant in the Atoll Source 4U 1608−52, *Astrophys. J. Lett.*, **505**, pp. L23–L26.

Misner, C. W., Thorne, K. S. and Wheeler, J. A. (1973), *Gravitation*, W. H. Freeman and Co, New York, San Francisco.

Stella, L. and Vietri, M. (1999), kHz Quasiperiodic Oscillations in Low-Mass X-Ray Binaries as Probes of General Relativity in the Strong-Field Regime, *Phys. Rev. Lett.*, **82**(1), pp. 17–20.

Stuchlík, Z., Török, G. and Bakala, P. (2007), On a multi-resonant origin of high frequency quasiperiodic oscillations in the neutron-star X-ray binary 4U 1636−53, submitted to Astronomy and Astrophysics, arXiv: 0704.2318.

Török, G., Stuchlík, Z. and Bakala, P. (2007), A remark about possible unity of the neutron star and black hole high frequency QPOs, *Central European J. Phys.*, **5**(4), pp. 457–462.

Urbanec, M., Stuchlík, Z., Török, G., Bakala, P. and Čermák, P. (2007), Neutron star equation of state and QPO observations, pp. 523–531, this volume.

Proceedings of *RAGtime 8/9, 15–19/19–21 September, 2006/2007, Hradec nad Moravicí, Opava, Czech Republic*
S. Hledík and Z. Stuchlík, editors, Silesian University in Opava, 2007, pp. 501–510

On mutual relation of kHz QPOs

Gabriel Török,[1,a] Michal Bursa,[2] Jiří Horák,[2] Zdeněk Stuchlík[1] and Pavel Bakala[1]

[1] Institute of Physics, Faculty of Philosophy & Science, Silesian University in Opava, Bezručovo nám. 13, CZ-746 01 Opava, Czech Republic
[2] Astronomical Institute, Czech Academy of Sciences, Boční II 1401/1a, CZ-141 31 Praha 4, Czech Republic
[a] terek@volny.cz

ABSTRACT
We further investigate the issue of clustering of kHz QPO frequency ratios in neutron star low mass X-ray binaries. In this note we report on the recent analysis of occurrences and properties of kHz QPOs in the source 4U 1636−53. Assuming that kHz QPOs occur in pairs whose frequencies are linearly correlated, we find a prominent frequency (or a narrow frequency region) that separates upper and lower QPO observations. The two QPO modes are then simultaneously detected mainly in the vicinity of this transition points. We show that this can be understood in terms of correlations of QPO properties with frequency, such as quality factor and rms amplitude. We find that rms amplitudes and quality factors of both QPOs nearly equal at the transition point. In addition, the QPO frequencies are nearly commensurable there. We investigate also five other atoll sources obtaining similar results.

Keywords: X-rays: binaries – stars: neutron – accretion, accretion disks

1 INTRODUCION

A long discussion has been devoted to the issue of distributions of kHz QPO in neutron-star low mass X-ray binaries (LMXB). The first work in the subject was by Abramowicz et al. (2003) who examined simultaneous detections of the upper and lower QPOs in the Z-source Sco X-1. The authors show that that the ratios of the lower and upper QPOs frequencies cluster most often close to the value $\nu_{\rm U}/\nu_{\rm L} = 3/2$. Recently, Török et al. (2007a) have examined occurrence of the twin QPOs in the atoll source 4U 1636−53 applying the same methodology as Abramowicz et al. (2003). They found that the distribution of the frequency ratios of two simultaneously detected QPOs peaks near 3/2 and 4/3.

A preference of the commensurable frequency ratios data of kHz QPOs has been systematically checked by a group of Belloni and his collaborators. Belloni et al. (2005) have re-examined the ratio distribution in Sco X-1 and later in a larger sample comprising four atoll sources including 4U 1636 (Belloni et al., 2005). They argued that such clustering does not provide any useful information because frequencies of the two QPOs are correlated and

978-80-7248-419-5

the distribution of the ratio of two correlated quantities is completely determined by the distribution of one of them. Keeping this argument, a recent study of Belloni et al. (2007) based on systematic eighteen month observation of 4U 1636−53 concludes that there is no preferred frequency ratio.

In our view the disagreement in results of groups of Abramowicz et al and Belloni et al comes from a confusion between the observed frequency distribution (the one, which can be recovered from observed data) and the intrinsic distribution (the "invisible" one really produced by the source). While Abramowicz et al. (2003) examine the frequency ratios of the actually observed QPO pairs, analyses of Belloni et al. (2005, 2007) study primarily distributions of frequencies of a single QPO and they make implications for the distribution of the other, often invisible, QPO.

The incompatibility of the two observational single frequency distributions and that of the double peak detections in 4U 1636−53 has been recently clearly demonstrated by Török et al. (2007a). Assuming that kHz QPOs are intrinsically occurs in pairs whose frequencies are linearly correlated, Török et al. (2007b) concluded that the observational upper an lower QPO distributions are nearly complementary and find some prominent frequencies (or a narrow frequency regions) that separate upper and lower QPO observations. The existence of this prominent frequencies is most likely implied by QPO quality factor and rms amplitude correlations.

2 THE LOWER VS. UPPER KHZ QPO DISTRIBUTION

In Figs 1a and 1c, we show frequency histograms of continuous observations from the study of Belloni et al. (2007). This study is based on large systematic eighteen-months observational campaign resulting in the sample of 305 comparable continuous observations. The authors found only three observations in which both QPOs were detected simultaneously. We plot their data with the upper and lower QPO frequency being drawn in accord with the observational frequency correlation ($\nu_{\rm U} = 0.701\,\nu_{\rm L} + 520$ Hz; Abramowicz et al., 2005). It is clear from the figure that the two distributions of lower and upper kHz QPO observations are nearly complementary, i.e. the lower QPO mode is mainly seen above the $3/2$ point, while the upper QPO mode is seen mainly below it.

We conclude this section with a finding that when only one (lower or upper) QPO peak is detected, it almost always occur above or below, respectively, the critical frequency corresponding to the $3/2$ ratio. When both peaks are detected simultaneously, they seem to occur either close to $3/2$ or $5/4$ ratio.

3 PROPERTIES OF OSCILLATION MODES

In the process of finding QPOs, the important properties are the quality factor Q of peaks (defined as the QPO centroid frequency over the peak full-width at its half-maximum) and their fractional root-mean-squared amplitudes r (a measure for the signal amplitude given as a fraction of the total source flux that is proportional to the root mean square of the peak power contribution to the power spectrum PDS). Shape of a peak in the PDS is most often fitted by a Lorentzian. Only peaks that are sufficiently significant and have $Q > 2$ are

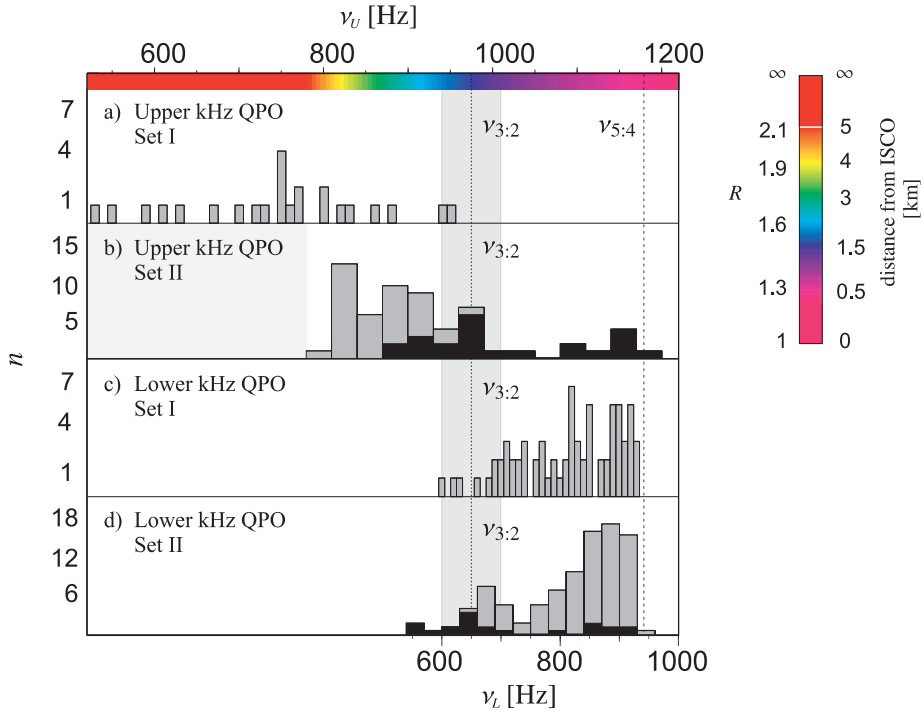

Figure 1. Distribution of the frequencies identified as the lower resp. upper kHz QPO. Frequency values are averaged per observation. Set I: from Belloni et al. (2007). Set II: from Török et al. (2007a), after Barret et al. (2005). The frequency axes are drawn with respect to the observed frequency correlation ($\nu_U = 0.701\nu_L + 520$ Hz; Abramowicz et al., 2005). The dashed vertical line corresponds to the frequency at which the correlation passes the 3/2 ratio, surrounding shaded area denotes an arbitrary scatter of 5% in frequency ratio with the observational uncertainty. We use the distributions from the original papers without any additional rebinning. The upper QPO frequency range investigated in Set I extends to lower values than in Set II because of a different sensitivity of the analysis, which is marked by shadow area in the left part of the panel (b). The black filled folds in Set II correspond to simultaneous observations of the second QPO in pair. Note that the two sets represent two different analysis of data observed in different epochs. Both sets display the same cut-off close to $\nu_L \sim 650$ Hz. The color-scale indicates frequency ratio and its eventual correspondence to the distance from Innermost-Stable-Circular-Orbit if the relativistic precession model is considered (see Török et al., 2007c for details).

considered as a QPO. The significance S is given by the relation between the integral area of a Lorentzian in PDS and its error. For a particular detection it depends on the source countrate and observational conditions and it is proportional to r and Q as $S \propto r^2\sqrt{Q/\nu}$. Usually, $S \geq 2$–4 is being used as the low threshold limit for detections.[1]

[1] The standard process of the QPO determining is in detail described in van der Klis (1989).

Barret et al. (2005) (see also Méndez, 2006) have shown that both quality factors and rms amplitudes are determined mainly by frequency of QPO, i.e., $Q = Q(\nu)$, $r = r(\nu)$. Moreover, their profiles greatly differ between lower and upper QPO modes. The quality factor of the upper QPO is usually small and tends to stay at a constant level

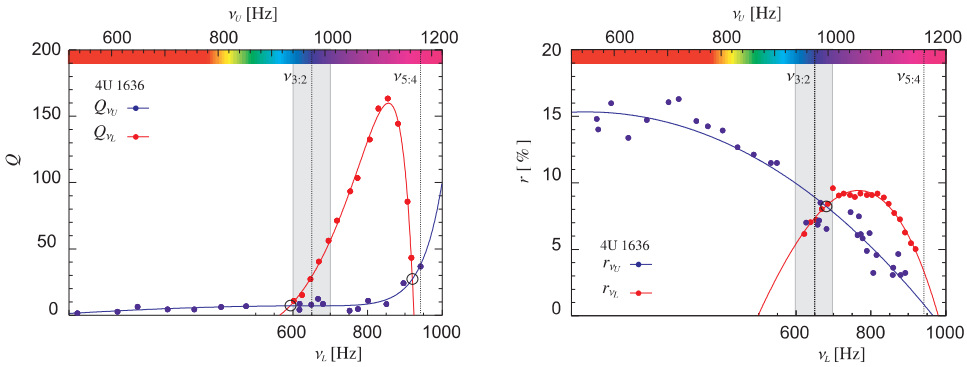

Figure 2. *Left:* Quality factor behaviour in 4U 1636−53. *Right:* rms amplitude behaviour. Data in both panels come from the study of Barret et al. (2005). Continuous curves are obtained from interpolation by several exponentials (see, e.g., Török, 2007).

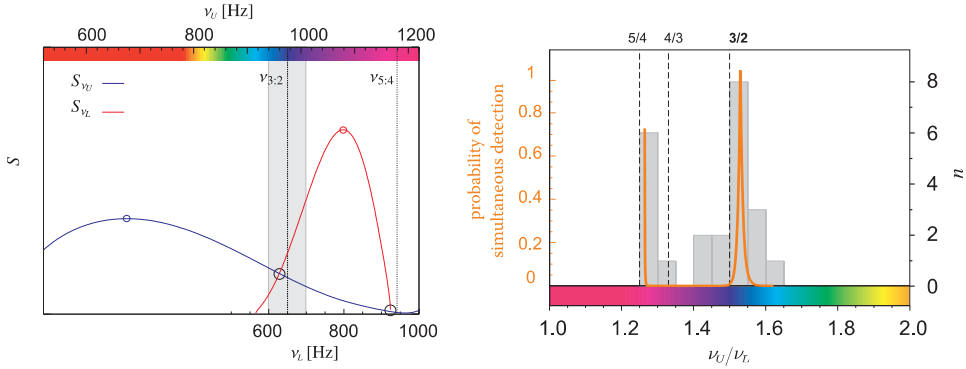

Figure 3. *Left:* The QPO significance as implied by the rms amplitude and quality factor behaviour. The continuous curves from Fig. 2 were considered. Note that the question how close to the 3/2 and 5/4 frequency ratio are the intersections in Q, r and S requires a further observational (but also theoretical) study. *Right:* At frequencies, where the expected significances of the upper and lower QPO modes equal, there is the highest chance that if one mode can be detected the other could be detected as well. The probability of the simultaneous detection should be therefore roughly proportional to $e^{-1}|\Delta S|$. This function is plotted over the histogram of twin peak distribution in frequency ratios (same data are used as in Fig. 1b,d). Note the function $e^{-1}|\Delta S|$ express the relative share between twin and single detections. Its relation to absolute numbers is non-trivial and depends on the intrinsical frequency distribution (which could be, e.g., uniform), on the source countrate and measurement conditions. The agreement between position of peaks then suggests that the observed ratio clustering is mostly related to the QPO amplitude and quality factor correlations.

around $Q_{\rm U} \sim 10$, in contrast with the lower QPO quality factor that improves with frequency and can reach up to $Q_{\rm L} \sim 200$ before a sharp drop of coherence at high frequencies. Amplitudes of upper QPO generally decrease with frequency, while the lower QPO amplitudes show first an increase and then start to decay too.

Figure 2 shows the behaviour of amplitudes and quality factors of individual QPO modes in 4U 1636−53 and how they change with frequencies. Note that both of the two properties are becoming similar as the frequency approaches points corresponding to $3/2$ or $5/4$ ratio (see in this context also Török, 2007). Both quantities are becoming similar as the frequency approaches points corresponding to $3/2$ or $5/4$ ratio (see in this context also Török, 2007). The left panel of Fig. 3 shows the profiles of lower and upper QPO significance as inferred from the behavior of r and Q. Obviously, close to $3/2$ or $5/4$ points, the QPO significances are comparable, while they are much different elsewhere. The upper QPO mode is usually more significant left from the $3/2$ point (at lower frequencies), while the lower QPO mode dominates right from that point.

Different profiles of significance have interesting implications for detections of both QPOs. At frequencies, where the expected significances equal, there is the highest chance that if one mode can be detected, the other could be detected as well. The probability of simultaneous detection (normalized with respect to probability of total lower and upper QPO detections) should be therefore roughly proportional to $\exp(-|\Delta S|)$, where ΔS is the difference of significances. Figure 3 (right) shows the calculated probability of simultaneous detection. For reference, the histogram of simultaneous observations of both QPOs is plotted too. The clustering of frequency ratios close to $3/2$ in the data is in this view determined by the behavior of rms amplitudes and quality factors and namely related to the fact that these quantities become equal close to that frequency ratio. In the same view, the special importance of the $3/2$ point (and also $5/4$, etc.) lies in the fact that around this point QPO modes exchange dominance (cf. Török, 2007; Török et al., 2007c).

4 FIVE OTHER ATOLL SOURCES

We apply similar approach to five other atoll sources, namely 4U 1728−34, 4U 1608−52, 4U 0614+09, 4U 1820−30 and 4U 1735−44. We use the approximated profiles of amplitudes and quality factors derived by Török et al. (2007c). The results are shown in Figs 4 and 5.

5 DISCUSSION

The complementarity in the lower and upper QPO distributions, shown in Section 2, can now be easily understood as a direct consequence of changing significance due to varying QPO properties Q and r. The (two) significances shown in Fig. 3 (left) exhibit the same relations as the (two) distributions from Fig. 1.

It is likely that if QPOs are produced in a source, they are always produced in pairs, but often only one mode of the pair gains enough power to be actually observed. Around the special points $3/2$ and $5/4$, where significances are comparable, there is a great chance that if one mode can be detected the other could be detected as well (Fig. 3, left), because both

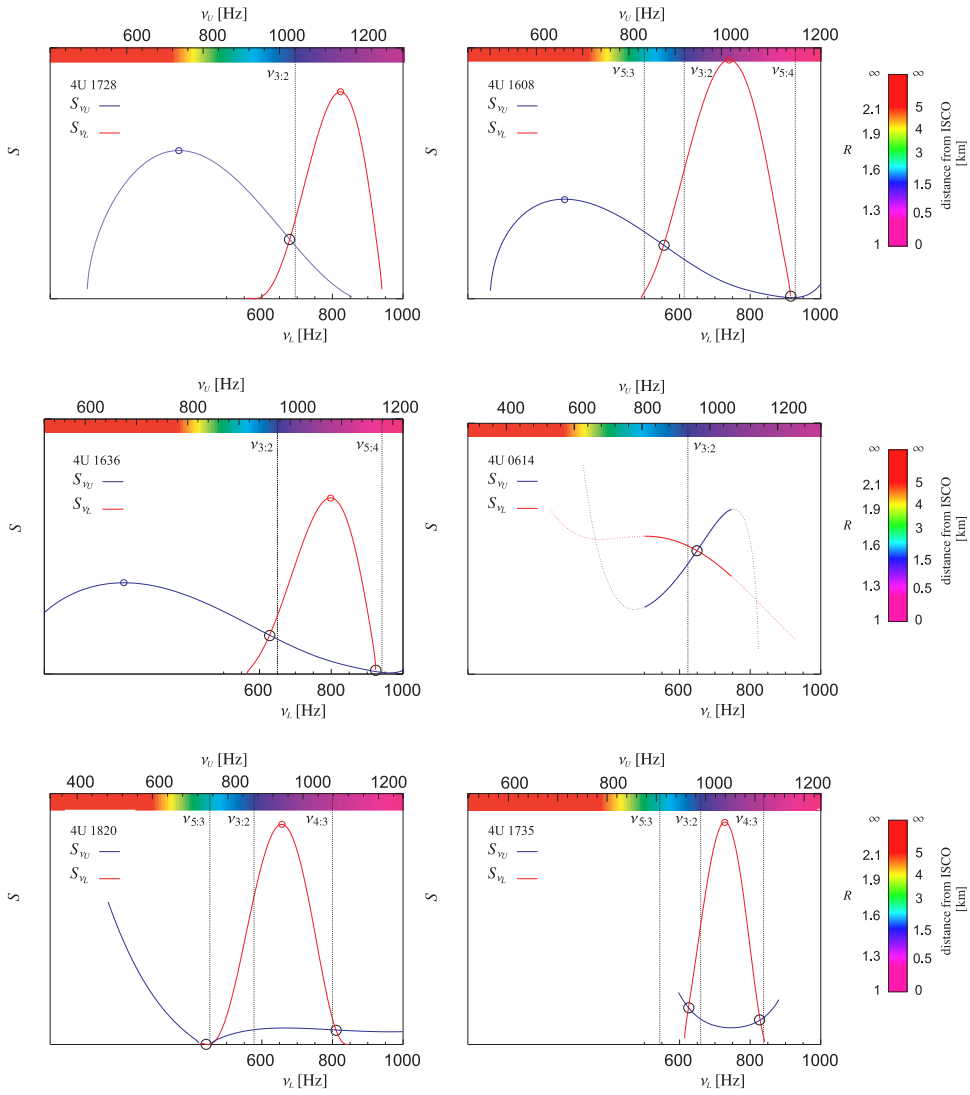

Figure 4. The QPO significancy as implied by the rms amplitude and quality factor behaviour. The continuous curves from Figs 2 and 3 in Török et al. (2007c) were considered. In the case of 4U 0614 only parts of curves corresponding to the frequency range $\nu_L \sim 500$–800 Hz are reliable. The shape of dotted parts is mostly given only by two distant datapoints.

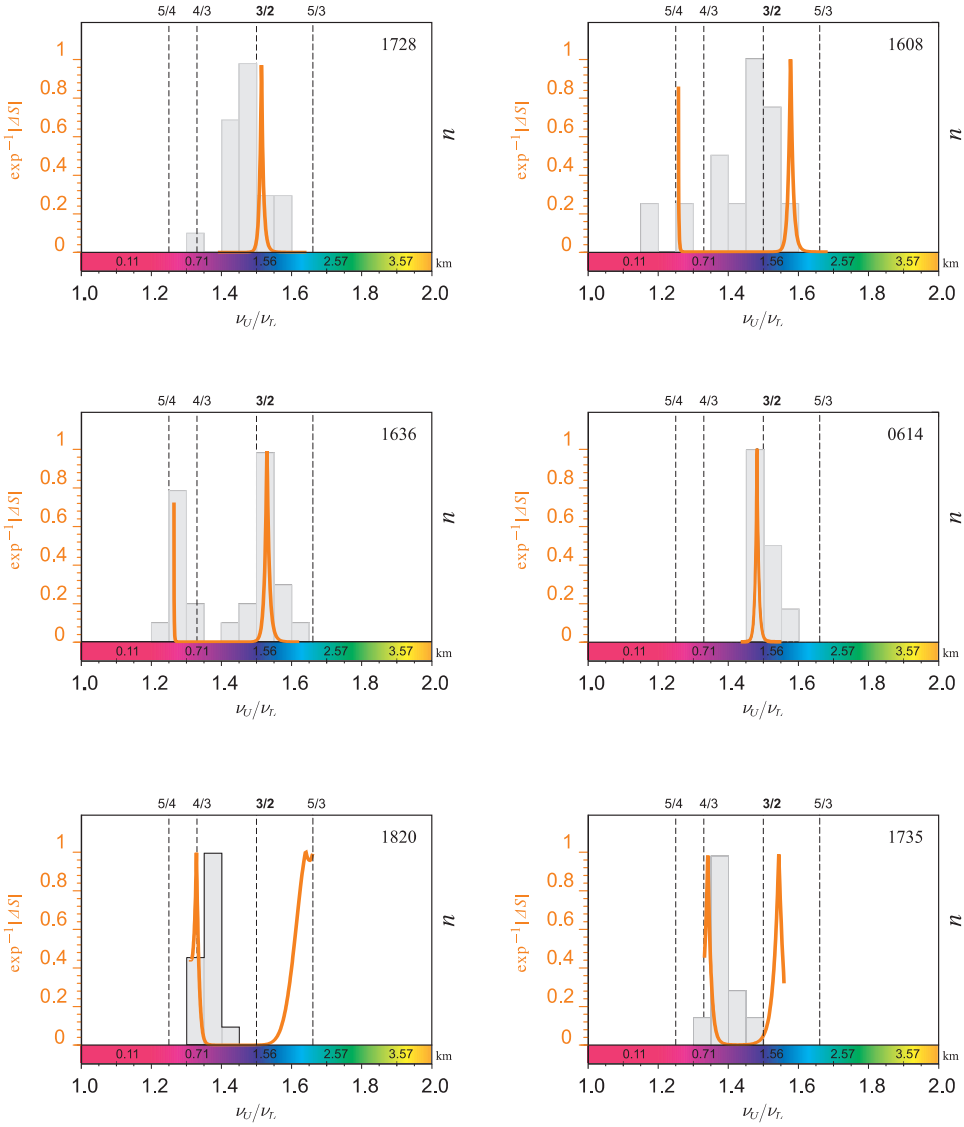

Figure 5. Functions $\exp(-\Delta S)$ as follow from Fig. 4. Grey folds indicate the *total* twin peak QPO distribution in the source, based on the available RXTE data used in Török et al. (2007c).

peaks have nearly the same properties. Indeed, this is exactly what is observed and has been laboured or challenged many times (Abramowicz et al., 2003; Belloni et al., 2005; Bulik, 2005; Yin et al., 2005; Belloni et al., 2007) that pairs of QPOs cluster close to the $3/2$ and some other small rational number ratios.

Figure 3 (right) illustrates the reasons for the clustering of pairs. At frequencies, where the expected significances of the upper and lower QPO modes equal, there is the highest chance that if one mode can be detected, the other could be detected as well. The probability of the simultaneous detection should be therefore roughly proportional to $\mathrm{e}^{-1}|\Delta S|$, where ΔS is the difference of significances.

We have been able to find the same effect at work in the case of several other atoll sources (Figs 4 and 5), which further supports our arguments.

From time to time, the conditions at the source become such that both QPOs can be detected simultaneously regardless of their frequency, because of their high brightness. These events allows us not only to see QPO pairs close to the critical point, but sporadically also all the way along the frequency–frequency correlation line. The relative number of twin QPO occurences far from critical points is however low with respect to number of significant detections of the only one peak.

The clustering of frequency ratios close to $3/2$ is in this view determined by the behaviour of rms amplitudes and quality factors and namely by the fact that these quantities become equal close to that frequency ratio. In the same view, the special importance of the $3/2$ point (and also $5/4$, etc.) lies in the fact that around this point QPO modes exchange dominance (cf. Török, 2007; Török et al., 2007c).

6 CONCLUSIONS

We have compared the frequency distributions of individually detected lower and upper QPOs in 4U 1636−53 and pointed out that there is a narrow transition region, where the occurrence of QPOs is changed. On one side of the transition point (at low frequencies) upper QPO mode is most often detected, while on the other side (at high frequencies) the lower QPO mode occurs mostly. The position of the critical point is close to the $3/2$ point in frequency ratios.

We show that this transition can be understood as a consequence of correlations of QPO rms amplitudes and quality factors with frequency. The qualitative difference in the distributions of observed lower and upper QPOs is given by intrinsic changes of the oscillator properties resulting in the varying significance of peaks. We demonstrate that at frequencies, where the both QPO modes have comparable properties, there is a high probability of detecting both peaks of a twin pair simultaneously. Comparing with the observed twin QPO distribution, we found a precise match with our prediction.

We therefore conclude that there is a fundamental difference between observed and intrinsic distribution of kilohertz QPOs over frequencies, because the observed distribution is affected by actual properties of the two oscillators. Even if the intrinsic distributions of both modes were uniform in frequencies, there would be a non-trivial profile of observed distributions and clustering of double-peak detections around certain points.

This note is based mainly on the detailed analysis of a single atoll source 4U 1636−53. We have also checked five other atoll sources (six in total), and we find similar results in all cases. The problem is worth to be investigated in further details, nevertheless it seems the above 4U 1636−53 results have a general validity:

Figures 4 and 5 suggest that while both upper and lower oscillations are produced across a large range of frequencies, the probability of twin peak QPO detection is for a given source increased (or enhanced), where the freqency ratio is close to ratio of small integers (5/4, 4/3, 3/2, 5/3). The special importance of these points seem not to be so much in that clustering, but it comes from the very fact that one mode is dumped and the other excited whenever the QPO pair cross them – both modes have similar properties there, so that both can be seen in all probability at once.

ACKNOWLEDGEMENTS

We thank M. Abramowicz, W. Kluźniak and M. Méndez for several discussions on the subject. Especially, we are thankful to D. Barret for ideas and comments. P. B. a G. T. would like to thank the fishermen community in Derítő-Tó, Tata, Hungary for a royal hospitality and inspiring atmosphere for the research. M. B., J. H. and G. T. also thank to the hospitality of Yukawa Institute of Theoretical Physics (Kyoto, Japan). The authors are supported by the Czech grants MSM 4781305903 and LC06014.

REFERENCES

Abramowicz, M. A., Barret, D., Bursa, M., Horák, J., Kluźniak, W., Rebusco, P. and Török, G. (2005), The correlations and anticorrelations in QPO data, *Astronom. Nachr.*, **326**(9), pp. 864–866.

Abramowicz, M. A., Bulik, T., Bursa, M. and Kluźniak, W. (2003), Evidence for a 2 : 3 resonance in Sco X-1 kHz QPOs, *Astronomy and Astrophysics Lett.*, **404**, pp. L21–L24, arXiv: `astro-ph/0206490v2`.

Barret, D., Olive, J.-F. and Miller, M. C. (2005), An abrupt drop in the coherence of the lower kilohertz QPO in 4U 1636−536, *Monthly Notices Roy. Astronom. Soc.*, **361**, pp. 855–860.

Belloni, T., Homan, J., Motta, S., Ratti, E. and Méndez, M. (2007), RossiXTE monitoring of 4U 1636−53: I. Long-term evolution and kHz Quasi-Periodic Oscillations, *Monthly Notices Roy. Astronom. Soc.*, **379**, pp. 247–252, arXiv: `0705.0793`.

Belloni, T., Méndez, M. and Homan, J. (2005), The distribution of kHz QPO frequencies in bright low mass X-ray binaries, *Astronomy and Astrophysics*, **437**, pp. 209–216.

Bulik, T. (2005), The statistics of Sco X-1 kHZ QPOs, *Astronom. Nachr.*, **326**(9), pp. 861–863.

Méndez, M. (2006), On the maximum amplitude and coherence of the kilohertz quasi-periodic oscillations in low-mass X-ray binaries, *Monthly Notices Roy. Astronom. Soc.*, **371**(4), pp. 1925–1938.

Török, G. (2007), Reverse of twin peak QPO amplitude relationship in six atoll sources.

Török, G., Abramowicz, M. A., Bakala, P., Bursa, M., Horák, J., Kluźniak, W., Rebusco, P. and Stuchlík, Z. (2007a), On the distribution of kHz QPO frequency ratio in the atoll source 4U1635−53, *Astronomy and Astrophysics*, submitted.

Török, G., Barret, D., Bursa, M. and Horák, J. (2007b), in preparation.

Török, G., Stuchlík, Z. and Čermák, P. (2007c), Reverse of twin peak kHz QPO inter relationship in the six atoll sources, pp. 511–522, this volume.

van der Klis, M. (1989), Fourier techniques in X-ray timing, in H. Ögelman and E. P. J. van den Heuvel, editors, *Timing Neutron Stars*, p. 27, URL `http://adsabs.harvard.edu/abs/1989tns..conf...27V`.

Yin, H., Zhang, C., Zhao, Y., Song, L. and Zhang, F. (2005), A Study on the Correlations between the Twin kHz QPO Frequencies in Sco X-1, *Chinese Astronom. Astrophys.*, **5**(6), pp. 595–600.

Proceedings of *RAGtime 8/9, 15–19/19–21 September, 2006/2007, Hradec nad Moravicí, Opava, Czech Republic*
S. Hledík and Z. Stuchlík, editors, Silesian University in Opava, 2007, pp. 511–522

Reverse of twin peak kHz QPO interrelationship in the six atoll sources

Gabriel Török[a], Zdeněk Stuchlík and Petr Čermák

Institute of Physics, Faculty of Philosophy & Science, Silesian University in Opava,
Bezručovo nám. 13, CZ-746 01 Opava, Czech Republic
[a] terek@volny.cz

ABSTRACT
Several models have been outlined to explain the (upper and lower) kilohertz quasi-periodic oscillations (QPOs) detected in many accreting neutron star X-ray binaries. When facing the theory to observation, rather limited attention has been payed to the *mutual* relations between the (correlated) QPO amplitudes and quality factors till now. In this paper we report on recent results on these relations. For six neutron star atoll sources (namely 4U 1728−34, 4U 1608−52, 4U 1636−53, 4U 0614+09, 4U 1820−30 and 4U 1735−44) spanning wide range of frequencies we investigate whether the relationship between the rms amplitudes and quality factors of the observed kHz QPO modes $\nu_{\rm L}$, $\nu_{\rm U}$ display features that could have a significant meaning in terms of the proposed QPO models.We find for all the six sources that after the twin kHz QPOs pass a point (or the narrow interval) where their ratio R equals ~ 1.5 the lower/upper oscillation becomes stronger/weaker than other one with increasing QPO frequency. Existence of a similar effect close to $R = 1.33$ or $R = 1.25$ is also indicated. Moreover, for increasing QPO frequency, shortly after passing $3/2$ ratio, the difference between QPO amplitudes as well as lower QPO quality factor reaches its maxima on a narrow frequency interval where lower QPO is much stronger than the upper one. This interval lies between frequencies corresponding to $3/2$ and $4/3$ (or $5/4$) frequency ratio. This finding implies restrictions to the orbital QPO models (both hot spot- and disc oscillations- like) and also to QPO modulation mechanism. In a wider context, our results may indicate the existence of an energy overflow between the upper and lower QPO mode when their ratio is close to ratio of small integral numbers.

Keywords: X-rays: binaries – stars: neutron – accretion, accretion disks

1 INTRODUCTION

Number of black hole and neutron star sources in low mass X-ray binaries show quasi-periodic oscillations (QPOs) in their observed X-ray fluxes, i.e., peaks in the Fourier variability power density spectra (hereafter PDS). Frequencies of some QPOs are in the kHz range that corresponds to frequencies of orbital motion close to central compact object. A representative high frequency QPO observation shows two peaks in the kHz

978-80-7248-419-5

(i.e., $\sim$ (200–1500) Hz) part of PDS. These so-called twin peak QPOs with the lower and upper frequency $\nu_{\rm L}$ and $\nu_{\rm U}$ often arise simultaneuosly in case of the neutron star sources,[1] while the black hole QPO peaks are rather detected from different observations (see van der Klis, 2006 for a well-arranged review on the QPO problematic). In contrast to the black hole kHz QPOs with fixed frequencies often having a 3 : 2 ratio, the neutron star kHz twin (and single) peak QPOs span a large frequency range following nearly linear frequency-frequency relation specific for a given source (Psaltis et al., 1998; Belloni et al., 2005; Abramowicz et al., 2005a; Bursa, 2006).

Several models have been outlined to explain observations of the neutron star kHz QPOs, and it is mostly preferred that their origin is related to orbital motion near an inner edge of an accretion disc.[2]

Among others, two often discussed models based on the strong gravity properties have been proposed. Stella and Vietri (1998, 1999) introduced the "Relativistic Precession Model" in which the kHz QPOs represent a direct manifestation of modes of a relativistic epicyclic motion of blobs in the inner parts of the accretion disc. In this model the lower and upper kHz QPO frequencies are identified with the Keplerian and periastron precession frequency.

Kluźniak and Abramowicz (2001) proposed models based on *non-linear accretion disc oscillations* that relate the lower and upper kHz QPO frequency to the disc oscillation modes, which are in the basic version of the model given by the epicyclic frequencies of a test particle orbital motion.

1.1 Strength of signal

Because of the expected links to the orbital motion, most discussions of the neutron star kHz QPOs have for a long time been concentrated mainly on the frequencies, frequency-frequency relations and the frequency evolution.

The other QPO properties, namely its *quality factor Q* (defined as a QPO centroid frequency over a full-width of the peak at its half-maximum) and a *fractional root-mean-squared amplitude r* (a measure of the signal amplitude given as a fraction of the total source flux that is proportional to the root mean square of the peak power contribution to the power spectrum), have been studied as well, but have not drug such a general attention. In the past few years both the quality factor and rms amplitude have been studied systematically for several sources, and possible consequences for various QPO models have been outlined (see, e.g., Méndez, 2006; Barret et al., 2006 for further information and references).

Some consequences of the quality factor behaviour have already been discussed for several QPO models including the resonance model (see Barret et al., 2005a), but the rms amplitude measurements have not been considered in this context so far. In fact most of the consideration has been attracted to the quality factor and rms amplitudes as separated frequency functions. Rather limited attention has been payed to the *mutual relations* between

[1] Note however that detections of just a single peak are not rare (see, e.g., Barret et al., 2005b; Méndez, 2006).

[2] See van der Klis (2006); Lamb and Boutloukos (2007) for a recent review.

the (correlated) QPO amplitudes and quality factors. In next we report on recent findings on these relations.

2 SIX ATOLL SOURCES DATA

In general, many of very sensitive X-ray timing methods unfortunately do not follow properties of both QPOs simultaneously but bring high amount of information connected to large range of frequencies.

In order to take advantage of this methods we focus in next on the six atoll sources (namely 4U 1728−34, 4U 1608−52, 4U 1636−53, 4U 0614+09, 4U 1820−30 and 4U 1735−44) spanning wide range of frequencies which have been well investigated in past years. We profit from the existing studies and use for next proceeding the published results on rms amplitude and quality factor correlations from the large collection made out by Méndez (2006). Main references to original papers are as follows: 4U 1728 (Méndez et al., 2001), 4U 1608 (Méndez et al., 2001), 4U 1636 (Barret et al., 2005b), 4U 0614 (van Straaten et al., 2002), 4U 1820 (Barret et al., 2006), 4U 1735 (Barret et al., 2006).

We interpolate the amplitude data for each source using the best fits for both amplitudes by a sum of three exponentials

$$r_i = \sum_{j=1}^{3} P_{i,j}^{(0)} \left[\exp\left(P_{i,j}^{(1)} + \nu_i P_{i,j}^{(2)} \right) + P_{i,j}^{(3)} \right], \quad i \in \{\mathrm{U}, \mathrm{L}\}.$$

We interpolate in the same way also quality factor data except we use four exponentials instead of three

$$Q_i = \sum_{j=1}^{4} O_{i,j}^{(0)} \left[\exp\left(O_{i,j}^{(1)} + \nu_i O_{i,j}^{(2)} \right) + O_{i,j}^{(3)} \right], \quad i \in \{\mathrm{U}, \mathrm{L}\}.$$

As noticed in several studies, the frequency correlations in the six sources which we discuss in this paper are well fitted by linear relations (Abramowicz et al., 2005b; Belloni et al., 2005; Bursa, 2006; Zhang et al., 2006). We therefore use this property to relate the above correlations, i.e., in next we expect that frequency correlations are linear in the range above $\nu_{\mathrm{L}} = 500$ Hz and follow relations found in Abramowicz et al. (2005b,a).

The results we obtained for interpolated rms amplitudes and quality factors are shown in Figs 1 and 2.

3 AMPLITUDE DIFFERENCE

It follows from Figs 1 and 2 that the amplitudes of both oscillations (and not so clearly also their quality factors) are comparable on a frequency range which is rather narrow with respect to the total frequency range spanned by the six sources. Moreover, we noticed that for all six sources the QPO properties are comparable in range corresponding to the ~ 1.5 frequency ratio (we mark this frequency among others in the above figures).

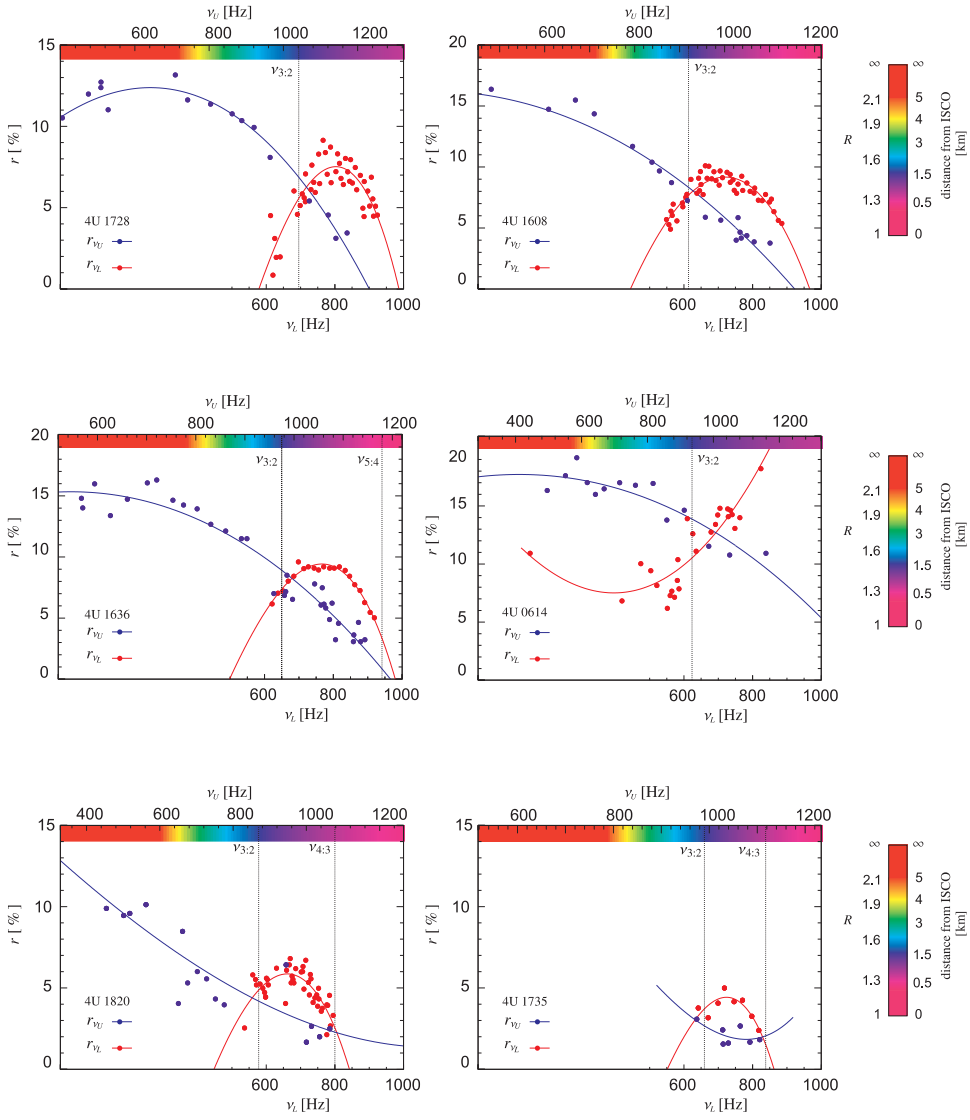

Figure 1. Amplitudes of the lower and upper oscillation plotted vs. both QPO frequencies. The colour scale indicates frequency ratio (and possibly also a distance of the QPO excitation radius from the *Innermost-Stable-Circular-Orbit* as discussed in the Section 6). Note that while the frequency ratio is well determined in the range above $\nu_L \sim 500$ Hz, the ratio possibly corresponding to QPO detections below $\nu_U(\nu_L \sim 500\,\text{Hz})$ (i.e., above $R \gtrsim 1.7$) is highly uncertain. In this range the lower QPOs are in this six atoll sources usually not detected or their detections are not very clear (Barret et al., 2005b), although there are some exceptions (Zhang et al., 2006).

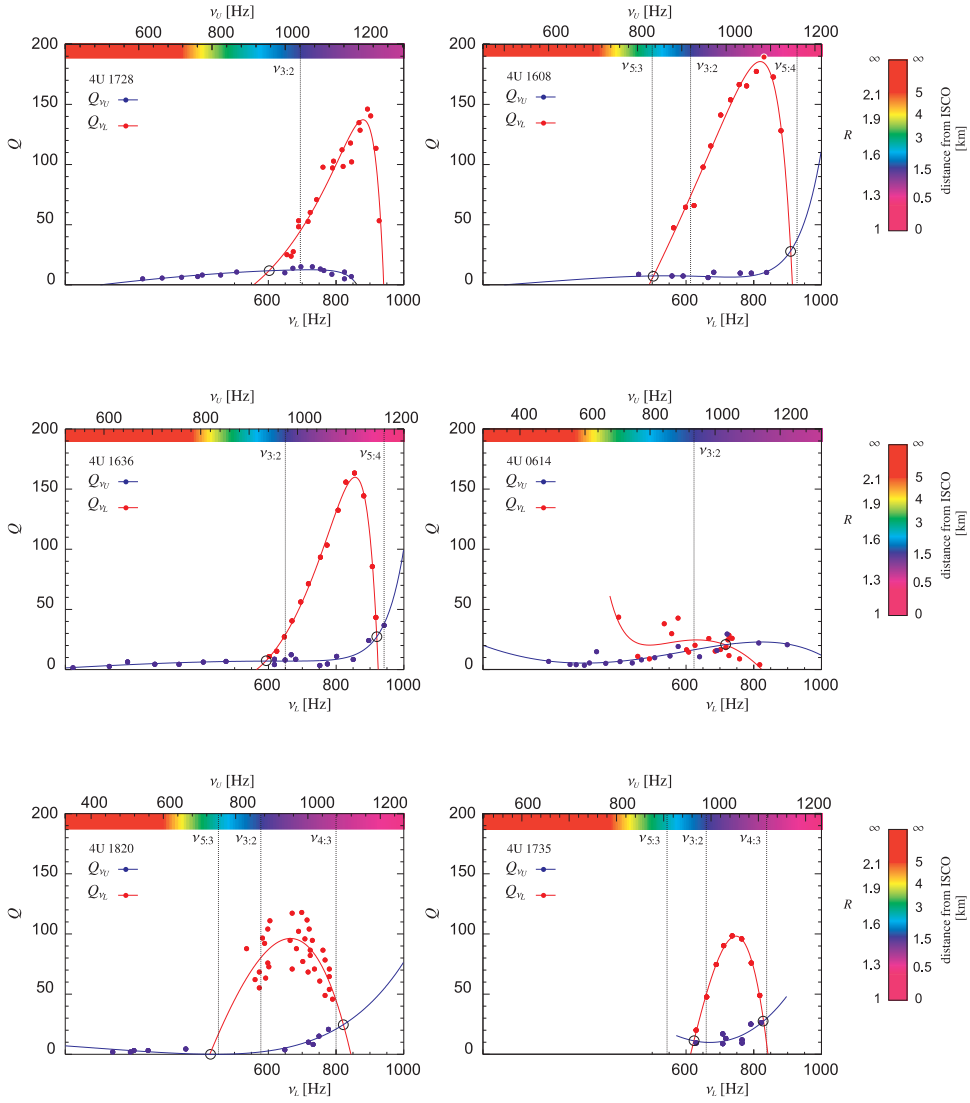

Figure 2. Quality factor of the lower and upper oscillation plotted vs. both QPO frequencies. The very fact that the QPOs detected below $\nu_{\rm U} \Leftrightarrow \nu_{\rm L} \sim 500$ Hz are well identified to be the upper oscillations results from studies of the lower and upper QPO phenomenology which differ in many aspects (see van der Klis, 2004; Barret et al., 2005b; Belloni et al., 2007). Even if the (undetected) lower QPO were still present and only weak (having low r and q), the ratio corresponding to the upper QPO oscillations would strongly depend on frequency relation which could be easily the power-law instead of linear relation (Zhang et al., 2006e.g.,).

In the following, in order to investigate findings given above in detail, we characterize an actual excess between the strength of the upper and lower observed kHz frequency oscillation by the quantity Δr. It is defined as a difference between the lower and upper frequency rms amplitudes r_{L}, r_{U} corresponding to the same upper (lower) QPO frequency,

$$\Delta r = r_{\mathrm{L}} - r_{\mathrm{U}} \,. \tag{1}$$

Under assumption that frequencies of the two oscillations and also their properties always follow the same correlation, Δr should correspond to a difference $r_{\mathrm{L}} - r_{\mathrm{U}}$ measured within a twin peak QPO observation.

3.1 Parametrization

Some orbital QPO models, like that of Stella and Vietri, relate a given observed QPO frequency (or a frequency pair) to a specific radial position inside the accretion disc. These models often express the observable frequencies ν_{L}, ν_{U} as a combination of frequencies characteristic for a geodesic orbital motion.

Frequencies of the geodesic motion at a given orbit scale inversely with mass M of the central compact object when the angular momentum j and quadrupole moment q are fixed and one can write

$$\nu_i = M^{-1}\, \nu_{\mathrm{K}}(j,q,r) \left[1\alpha_{i,\mathrm{K}} + \kappa_r(j,q,r)\alpha_{i,r} + \kappa_\theta(j,q,r)\alpha_{i,\theta}\right] , \tag{2}$$

where $i \in \{\mathrm{U}, \mathrm{L}\}$, κ_r and κ_θ stand for the radial and vertical epicyclic dimensionless frequencies, and $\alpha_{i,j}$ are real coefficients. Because of this the ratio of observable frequencies is not a function of the mass M of the central compact object. In relation to kinematics of a test particle geodesic motion and in relation to a propagation of disc oscillation modes, the ratio of two functions of the type (2) provides a better direct indication of the orbital position inside of the inner part of the accretion disc than the usual radial coordinate. For instance a function $\nu_{\mathrm{K}}/(\nu_{\mathrm{K}} - \nu_{\mathrm{r}})$ equals 1 at the marginally stable circular orbit for any angular momentum j and a relative change of this function with j at the position of maximum of the radial epicyclic frequency is about $10\times$ lower than relevant relative change of the radial coordinate (Török et al., 2007).

Therefore, for the above class of the QPO models, the ratio $R = \nu_{\mathrm{U}}/\nu_{\mathrm{L}}$ represents a measure of the radial position corresponding to a QPO excitation, fully independent of the central compact object mass M, and in a less direct sense also nearly independent of its j and q parameters. The frequency ratio R has a genuine importance for the resonant QPO model too.

Hence, for the amplitude difference we use in next parametrization with the frequency ratio,

$$\Delta r = \Delta r(R) \,.$$

4 AMPLITUDES DIFFERENCE MEASURED DIRECTLY FROM TWIN QPO OBSERVATIONS

In this Section, based on the recently submitted paper, we investigate amplitude difference behaviour as found directly from simultaneous twin QPO observations. Such a way of analysis use potentially much lower amount of PDS for investigation than the methods resulting to the data we use above. On the other hand, where applicable, it should provide better sensitivity and view to the amplitude difference behaviour with respect to the uncertainties in the observational correlations between frequencies of the two QPOs and their properties.

Following Barret et al. (2005b, 2006) we use all (up to the end of 2004) public archival RXTE data for the examined six atoll sources. We consider segments of temporally continuous collection of data from a single pointing. For each segment an average PDS is produced.

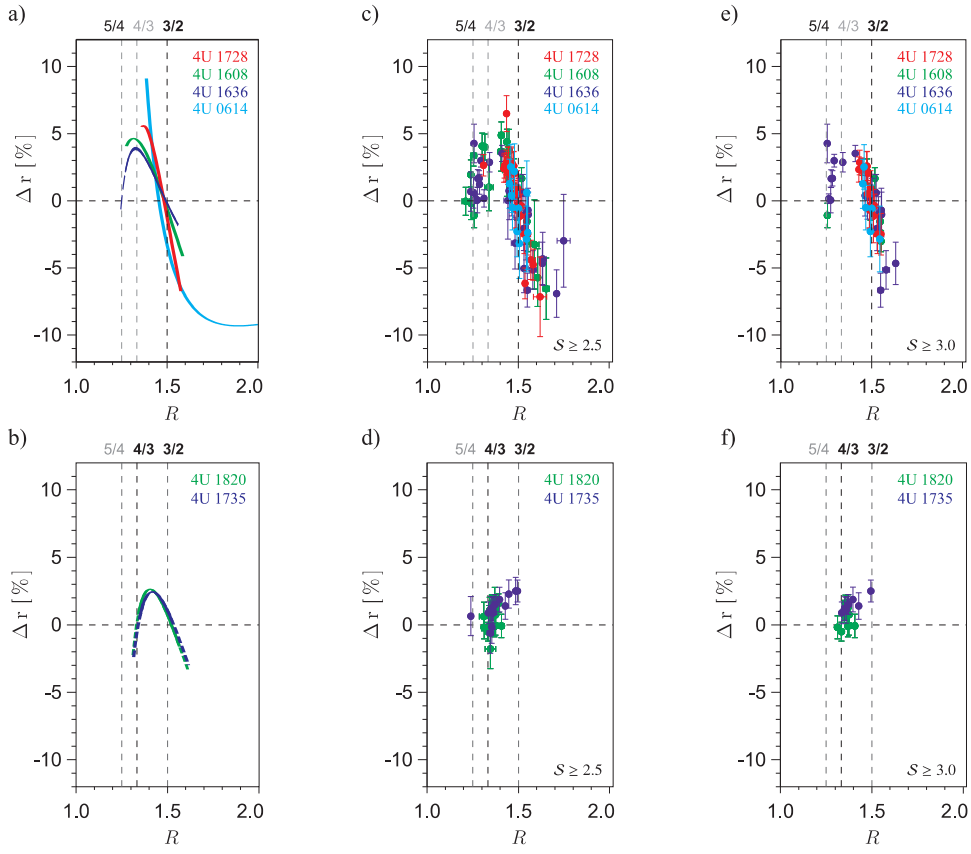

Figure 3. Difference of the rms amplitudes Δr vs. the frequency ratio R. (a), (b) The interpolation of published data (i.e., Set I). Dashed parts of curves correspond to an extrapolation. (c), (d) From the analysis of continuous data segment (i.e., Set II), only datapoints with significancy higher than 2.5σ are considered. (e), (f) The same, but with significancy threshold higher than 3σ.

The PDS is searched for a QPO using a scanning technique which looks for peak excesses above the Poisson counting noise level (see Boirin et al., 2000). To minimize the effects of a long term frequency drift, the QPO frequencies are estimated on the shortest statistically permitted timescales, applying a recursive search algorithm. In case of presence of two QPO peaks in the segment averaged PDS, the peak with the highest *significance S* (defined as an integral of the Lorentzian fitting of the peak divided by its error) is considered for a further tracking. All PDS are then shifted to the reference one. The obtained PDS is then searched for final QPOs. For a further analysis wee keep the resulting peaks detected above 500 Hz with $Q \geq 3$ and above $S \geq 3\sigma$ (respectively 2.5σ, see the caption in Fig. 3). Because of the purpose of our study we are interested especially in segments where the two QPO peaks are detected simultaneously. For such segments we calculate the rms amplitudes for both of the peaks.

The above procedure allows us to determine in coherent way the discrete mean values of the amplitude difference Δr corresponding to the individual continuous segments of observations, i.e., to the simultaneous significant observations of both QPOs. In next we refer to this data as to the Set II and consequently refer to the data from interpolated published results as to the Set I.

We plot the continuous functions $\Delta r(R)$ resulting from interpolation functions (i.e., Set I) as well as discrete values corresponding to individual continuous segments of observations in Fig. 3.

5 BEHAVIOUR OF FUNCTION $\Delta r(R)$

It is visible from Fig. 3 that for all six sources the upper and lower QPO amplitudes equal when the correlation passes a "zero" point close to $R = 1.5$. More precisely, for all six sources the interpolated curves cross zero within the interval $R = 1.5 \pm 3\,\%$.

The curves we display in the figure are plotted for the consistently mapped interval of the frequency ratio $\sim$ (1.25–1.6). There is a strong indication that the trends we display are valid for the whole available range of R (see Fig. 2). The $1.5 \pm 3\,\%$ range represents therefore at least about 10% subinterval of the actually analyzed range of data.

In addition to 4U 1636, comparing Figs 3(a) and (c), one may conclude that also in case of 4U 1608 there exists a second such point that appears close to $R = 1.25$. Moreover data of 4U 1735 and 4U 1820 sources display the existence of the second "zero" point as well, but here it appears close to $R = 1.33$.

In Table 1 we give a summary of the Δr roots.

6 DISCUSSION AND CONCLUSIONS

For the six sources (4U 1728−34, 4U 1608−52, 4U 1636−53, 4U 0614+09, 4U 1820−30 and 4U 1735−44), the upper and lower QPO amplitudes equal when the correlation function passes a "zero" point most likely located in the interval $R = 1.5 \pm 3\,\%$.[3]

[3] This range corresponds to the interval spanned by the individual mean values of Δr.

Table 1. Roots R_1, R_2 of functions $\Delta r(R)$. Displayed errors correspond to a unit variation of χ^2.

Source	Set I		Set II	
	$R_1(\Delta r = 0)$	$R_2(\Delta r = 0)$	$R_1(\Delta r = 0)$	$R_2(\Delta r = 0)$
1728	1.48 ± 0.01	–	1.50 ± 0.01	–
1608	1.48 ± 0.01	–	1.52 ± 0.02	1.26 ± 0.01
1636	1.49 ± 0.01	1.25 ± 0.01	1.52 ± 0.02	1.26 ± 0.01
614	1.45 ± 0.01	–	1.48 ± 0.01	–
1820	1.52 ± 0.01	1.33 ± 0.01	–	1.34 ± 0.01
1735	1.53 ± 0.02	1.34 ± 0.01	–	1.35 ± 0.02

For four sources (1608, 1636, 1820, 1735) and marginally also for 1728 there is an evidence for the existence of another such point (close to $R = 1.33$ or 1.25).

Moreover, we notice in the Figs 1, 2 and 3 that for increasing QPO frequency, shortly after passing 3/2 ratio, *the difference between QPO amplitudes as well as lower QPO quality factor reaches its maxima on a narrow frequency interval where lower QPO is much stronger than the upper one*.

Within the framework of the QPO resonance models, one should notice that the amplitude difference behaviour, together with the behaviour of quality factor, may indicate existence of an energy overflow between the lower and upper QPO mode typical for nonlinear resonances (e.g., Horák and Karas, 2006). In this context it is also rather apparent that the "zero" points are *close* to the 3/2 and 4/3 or 5/4 value (which we denote by dashed vertical lines in Fig. 3). Nevertheless, in order to take this indicia as a serious evidence, a model giving a detailed explanation of the effect is highly required.

Within the scope of the other orbital QPO models there should be an explanation why the zero points appear. For instance in case of the relativistic precession model, one can solve Eq. (2) for a particular form of expressions $\nu_{\rm K}$ and $\nu_{\rm r}$ in the Schwarzschild geometry with respect to radial coordinate, obtaining (e.g., Török et al., 2007) the relation $r = 6R^2/(2R - 1)$. According to this formula, the $R = 1.5$ frequency ratio would correspond to an orbital radius $r = 6.75\,M$ which is about 14 kilometres for a neutron star with "canonic" mass $M = 1.4\,{\rm M}_\odot$. The $\pm 3\,\%$ interval in R would be projected onto only about $\pm 1.5\,\%$ interval in r, i.e., onto $r \sim \pm 0.1\,M \doteq \pm 200$ m. We illustrate this "to a T" in the Fig. 4 which also gives a scale for the Figs 1 and 2. It is then a question not only why the observed amplitudes corresponding to oscillations at this radius equal, but also why they equal for six sources at the same radius with a scatter less than 250 m.[4,5]

[4] The equality of the observed amplitudes would imply also the equality of the intrinsical amplitudes if the (questionable) modulation mechanism works in the same way for both oscillations.

[5] For the observationally relevant illustration we use absolute units of metres, and express the distance for the canonic mass $M = 1.4\,{\rm M}_\odot$ and $q = j^2 = 0$. For a scatter in mass the absolute interval in radius can be substantially higher, but our value 200 m is still relevant after a normalization.

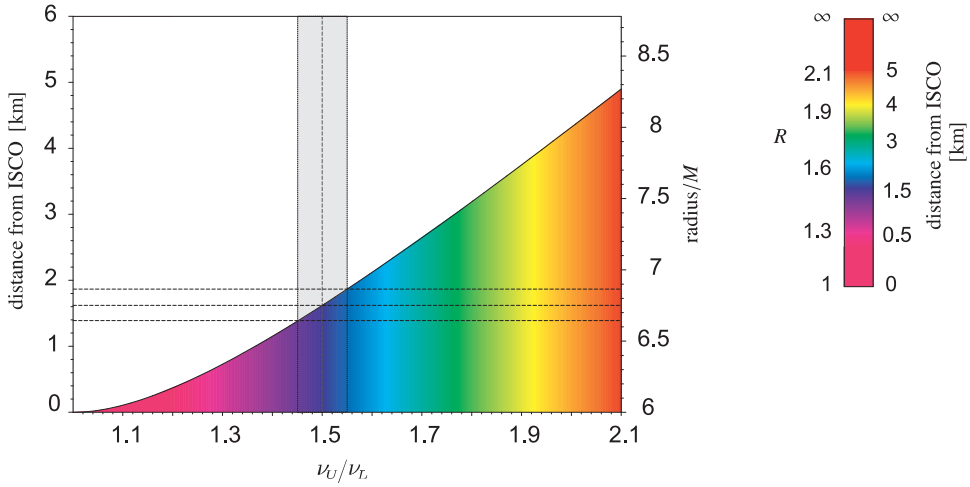

Figure 4. Relation between observed kHz QPO frequency ratio and QPO excitation distance from the *Innermost-Stable-Circular-Orbit* following from the model of Stella and Vietri as derived for Schwarzschild spacetimes and $M = 1.4\,\mathrm{M}_\odot$. Region corresponding to a 3 % scatter in R is denoted. Colour scale relating distance and QPO frequency ratio (and frequency) established in this way is included into Figs 1 and 2.

An analogical question connected to orbital regions associated to equivalent amplitudes of the observed oscillations arises for several orbital QPO models, and requires a selfconsistent explanation within the framework of a given model. The same consideration is not touching only the hot-spot-like QPO models, but also models that identify the QPOs as radius dependent disc-oscillation modes.

Full statistical analysis and an exact delimitation of the individual positions of "zero" points and their consistence with the ratio of small natural numbers namely with a $3/2$ ratio demands a further consequent observational (and theoretical) study.

We can, however, conlude that the very existence of "zero" points and the apparent similarity in the amplitude difference behaviour, especially in case of 1735 and 1820 showing nearly identical "energy conservation," represent a strong challenge for any QPO model.

ACKNOWLEDGEMENTS

We thank Didier Barret for all personal, scientific, and technical help, and for providing with the data and analysis software on which builds the Section 4. We also thank to Marek Abramowicz, Włodek Kluźniak, Jiří Horák, Michal Bursa, Pavel Bakala and Eva Šrámková for several discussions. The work has been supported by the Czech grants MSM 4781305903 and LC06014.

REFERENCES

Abramowicz, M. A., Barret, D., Bursa, M., Horák, J., Kluźniak, W., Rebusco, P. and Török, G. (2005a), A note on the slope-shift anticorrelation in the neutron star kHz QPOs data, in S. Hledík and Z. Stuchlík, editors, *Proceedings of RAGtime 6/7: Workshops on black holes and neutron stars, Opava, 16–18/18–20 September 2004/2005*, pp. 1–9, Silesian University in Opava, Opava, ISBN 80-7248-334-X.

Abramowicz, M. A., Barret, D., Bursa, M., Horák, J., Kluźniak, W., Rebusco, P. and Török, G. (2005b), The correlations and anticorrelations in QPO data, *Astronom. Nachr.*, **326**(9), pp. 864–866.

Barret, D., Kluźniak, W., Olive, J., Paltani, S. and Skinner, G. K. (2005a), On the high coherence of kHz quasi-periodic oscillations, *Monthly Notices Roy. Astronom. Soc.*, **357**(4), pp. 1288–1294.

Barret, D., Olive, J. and Miller, M. C. (2006), The coherence of kilohertz quasi-periodic oscillations in the X-rays from accreting neutron stars, *Monthly Notices Roy. Astronom. Soc.*, **370**, pp. 1140–1146.

Barret, D., Olive, J.-F. and Miller, M. C. (2005b), An abrupt drop in the coherence of the lower kilohertz QPO in 4U 1636−536, *Monthly Notices Roy. Astronom. Soc.*, **361**, pp. 855–860.

Belloni, T., Homan, J., Motta, S., Ratti, E. and Méndez, M. (2007), RossiXTE monitoring of 4U 1636−53: I. Long-term evolution and kHz Quasi-Periodic Oscillations, *Monthly Notices Roy. Astronom. Soc.*, **379**, pp. 247–252, arXiv: `0705.0793`.

Belloni, T., Méndez, M. and Homan, J. (2005), The distribution of kHz QPO frequencies in bright low mass X-ray binaries, *Astronomy and Astrophysics*, **437**, pp. 209–216.

Boirin, L., Barret, D., Olive, J., Bloser, P. F. and Grindlay, J. E. (2000), Low and High Frequency Quasi-Periodic Oscillations in 4U 1915−05, arXiv: `astro-ph/0007071`.

Bursa, M. (2006), Ph.D. thesis, Astronomical Institute, Charles University in Prague.

Horák, J. and Karas, V. (2006), Twin-peak quasiperiodic oscillations as an internal resonance, *Astronomy and Astrophysics*, **451**(2), pp. 377–386.

Kluźniak, W. and Abramowicz, M. A. (2001), The physics of kHz QPOs – strong gravity's coupled anharmonic oscillators, submitted in Phys. Rev. Lett., arXiv: `astro-ph/0105057`, URL `http://adsabs.harvard.edu/abs/2001astro.ph..5057K`.

Lamb, F. K. and Boutloukos, S. (2007), Accreting Neutron Stars in Low-Mass X-Ray Binary Systems, in E. F. Milone, D. A. Leahy and D. Hobill, editors, *Short-Period Binary Stars: Observations, Analyses, and Results*, volume 352 of *Astrophysics and Space Science Library*, Springer, Dordrecht, arXiv: `0705.0155v2`.

Méndez, M. (2006), On the maximum amplitude and coherence of the kilohertz quasi-periodic oscillations in low-mass X-ray binaries, *Monthly Notices Roy. Astronom. Soc.*, **371**(4), pp. 1925–1938.

Méndez, M., van der Klis, M. and Ford, E. C. (2001), The Amplitude of the Kilohertz Quasi-periodic Oscillations in 4U 1728−34, 4U 1608−52, and Aquila X-1, as a Function of X-Ray Intensity, *Astrophys. J.*, **561**(2), pp. 1016–1026.

Psaltis, D., Mendez, M., Wijnands, R., Homan, J., Jonker, P. G., van der Klis, M., Lamb, F. K., Kuulkers, E., van Paradijs, J. and Lewin, W. H. G. (1998), The Beat-Frequency Interpretation of Kilohertz Quasi-periodic Oscillations in Neutron Star Low-Mass X-Ray Binaries, *Astrophys. J. Lett.*, **501**, p. L95, arXiv: `astro-ph/9805084`.

Stella, L. and Vietri, M. (1998), Lense–Thirring Precession and Quasi-periodic Oscillations in Low-Mass X-Ray Binaries, *Astrophys. J. Lett.*, **492**, pp. L59–L62, arXiv: `astro-ph/9709085`.

Stella, L. and Vietri, M. (1999), kHz Quasiperiodic Oscillations in Low-Mass X-Ray Binaries as Probes of General Relativity in the Strong-Field Regime, *Phys. Rev. Lett.*, **82**(1), pp. 17–20.

Török, G., Stuchlík, Z., Čermák, P. and Bakala, P. (2007), in preparation.

van der Klis, M. (2004), A review of rapid X-ray variability in X-ray binaries, arXiv: `astro-ph/0410551v1`.

van der Klis, M. (2006), Rapid X-ray Variability, in W. H. G. Lewin and M. van der Klis, editors, *Compact Stellar X-Ray Sources*, pp. 39–112, Cambridge University Press, Cambridge.

van Straaten, S., van der Klis, M., Di Salvo, T. and Belloni, T. (2002), A Multi-Lorentzian Timing Study of the Atoll Sources 4U 0614+09 and 4U 1728−34, *Astrophys. J.*, **568**(2), pp. 912–930.

Zhang, C. M., Yin, H. X., Zhao, Y. H., Zhang, F. and Song, L. M. (2006), The correlations between the twin kHz QPO frequencies of LMXBs, *Monthly Notices Roy. Astronom. Soc.*, **366**, p. 1373, arXiv: `astro-ph/0601318`.

Proceedings of *RAGtime 8/9, 15–19/19–21 September, 2006/2007, Hradec nad Moravicí, Opava, Czech Republic*
S. Hledík and Z. Stuchlík, editors, Silesian University in Opava, 2007, pp. 523–531

Neutron star equation of state and QPO observations

Martin Urbanec[1], Zdeněk Stuchlík[1], Gabriel Török[1], Pavel Bakala[1] and Petr Čermák[2]

[1]Institute of Physics, Faculty of Philosophy & Science, Silesian University in Opava, Bezručovo nám. 13, CZ-746 01 Opava, Czech Republic
[2]Institute of Computer Science, Faculty of Philosophy & Science, Silesian University in Opava, Bezručovo nám. 13, CZ-746 01 Opava, Czech Republic

ABSTRACT
Assuming a resonant origin of the twin peak quasiperiodic oscillations observed in the X-ray neutron star binary systems, we apply a genetic algorithm method for selection of neutron star models. It was suggested that pairs of kilohertz peaks in the X-ray Fourier power density spectra of some neutron stars reflect a non-linear resonance between two modes of accretion disk oscillations. We investigate this concept for a specific neutron star source. Each neutron star model is characterized by the equation of state (EOS), rotation frequency Ω and central energy density ρ_c. These determine the spacetime structure governing geodesic motion and position dependent radial and vertical epicyclic oscillations related to the stable circular geodesics. Particular kinds of resonances (KR) between the oscillations with epicyclic frequencies, or the frequencies derived from them, can take place at special positions assigned ambiguously to the spacetime structure. The pairs of resonant eigenfrequencies relevant to those positions are therefore fully given by KR, ρ_c, Ω, EOS and can be compared to the observationally determined pairs of eigenfrequencies in order to eliminate the unsatisfactory sets (KR, ρ_c, Ω, EOS). For the elimination we use the advanced genetic algorithm. Genetic algorithm comes out from the method of natural selection when subjects with the best adaptation to assigned conditions have most chances to survive. The chosen genetic algorithm with sexual reproduction contains one chromosome with restricted lifetime, uniform crossing and genes of type $3/3/5$. For encryption of physical description (KR, ρ_c, Ω, EOS) into the chromosome we use the Gray code. As a fitness function we use correspondence between the observed and calculated pairs of eigenfrequencies.

Keywords: Neutron stars – genetic algorithm – X-ray variability – theory – observations

1 INTRODUCTION

Recently developed observational techniques provide good quality data from observations of quasiperiodic oscillations (QPOs) in black hole and neutron star sources (Stuchlík et al.,

978-80-7248-419-5

2007a; Török et al., 2007b). It is shown that in the case of some neutron star atoll sources (e.g., 4U1636−53, Barret et al., 2006) the data can be well fitted by the so called multi-resonant total precession model (Stuchlík et al., 2007a). The fits give high precision values of the neutron star spacetime parameters; in addition, in some cases the rotation frequency of the neutron star is determined almost exactly from the QPO independent measurements. This enables us to put some limits on equations of state (EOS) describing the neutron star interior. Here we focus our attention on the EOS given by the Skyrmion interaction that are very well tuned to the data given by the nuclear physics (Říkovská Stone et al., 2003). Using the genetic algorithm method, which appears to be very fast and efficient, we select the acceptable EOS from 27 types of the Skyrmion EOS selected by other methods (Říkovská Stone et al., 2003), concentrating on the source data observed in 4U 1636−53. For the other five atoll sources (4U 1608−52, 4U 1728−34, 4U 0614+09, 4U 1820−30 and 4U 1735−444), the method gives similar results.

2 FITTING THE QPO DATA

The results of recent studies of neutron star QPOs indicate that for a given source the upper and lower QPO frequency can be traced through the whole range of observed frequencies but the probability to detect both QPOs simultaneously increases when the frequency ratio is close to ratio of small natural numbers (namely $3/2$, $4/3$, $5/4$ in the case of atoll sources studied recently (Stuchlík et al., 2007a; Török et al., 2007a,b). Therefore, the multi-resonant orbital model based on the oscillations with Keplerian ($\nu_{\rm K}$) and epicyclic vertical (ν_θ) or radial ($\nu_{\rm r}$) frequencies was used to explain the observed data (Stuchlík et al., 2007a). They are calculated assuming the spacetime given by the Hartle–Thorne metric (Hartle and Thorne, 1968; Chandrasekhar and Miller, 1974; Miller, 1977). The fitting procedure has shown that the best results are obtained using the total precession model, where in all the sources the upper frequency $\nu_{\rm u} = \nu_{\rm K}$ and the lower frequency $\nu_{\rm l} = \nu_{\rm T} = \nu_\theta - \nu_{\rm r}$ (Stuchlík et al., 2007a). We concentrate here on the case of 4U 1636−53, when the mass and dimensionless spin of the neutron star are fitted to values ($\chi^2 + 1$ precision) in the range

$$M = 1.77 \pm 0.07\,, \quad j = 0.051 \pm 0.044\,, \tag{1}$$

$$M = 1.84 \pm 0.07\,, \quad j = 0.101 \pm 0.044\,. \tag{2}$$

This interval of allowed values of M and j will be used to test the EOS for the neutron star in the 4U 1636−53 source.

3 THE NEUTRON STAR STRUCTURE

In neutron stars, the strong gravity (i.e., Einstein's gravitational equations) must be relevant for the structure equations. The spacetime geometry is assumed to be stationary and axisymmetric, the perturbative approach of Hartle and Thorne (1968) is used. To calculate model of a rotating neutron star, one has to start with the static non-rotating configuration.

The line element in standard Schwarzschild coordinates (t, r, θ, ϕ) is given by

$$\mathrm{d}s^2 = -\mathrm{e}^{\nu}\,\mathrm{d}t^2 + [1 - 2m(r)/r]^{-1}\,\mathrm{d}r^2 + r^2[\mathrm{d}\theta^2 + \sin^2\theta\,(\mathrm{d}\phi - \omega\,\mathrm{d}t)^2]\,, \tag{3}$$

where ν is function of r only and $m(r)$ is the mass inside a sphere of radius r

$$m(r) = 4\pi \int_0^r \rho(r_1) r_1^2 \, \mathrm{d}r_1 \,. \tag{4}$$

To calculate model of non-rotating, unperturbed star one has to integrate TOV equation of hydrostatic equilibrium

$$\frac{\mathrm{d}P}{\mathrm{d}r} = -\frac{Gm(r)\rho}{r^2} \frac{(1 + P/\rho c^2)\left[1 + 4\pi r^3 P/m(r)c^2\right]}{1 - 2Gm(r)/rc^2} \,. \tag{5}$$

The integration is done outward from the centre (for given values of central energy density ρ_c) up to surface (where pressure P vanishes). One obtains the global properties of non-rotating neutron star as its mass M, radius R and the internal characteristic profiles of metric coefficients, pressure, energy density and number density of baryons expressed as functions of the radial coordinate.

The rotational effect is, in the linear approximation, given by the Hartle–Thorne metric (Hartle and Thorne, 1968)

$$\begin{aligned} \mathrm{d}s^2 = &- \mathrm{e}^{\nu} \left[1 + 2(h_0 + h_2 P_2)\right] \mathrm{d}t^2 + \frac{1 + 2(m_0 + m_2 P_2)/(r - 2M)}{1 - 2M/r} \, \mathrm{d}r^2 \\ &+ r^2 \left[1 + 2(v_2 - h_2) P_2\right] \left[\mathrm{d}\theta^2 + \sin^2\theta \, (\mathrm{d}\phi - \omega \, \mathrm{d}t)^2\right] , \end{aligned} \tag{6}$$

where $P_2 = P_2(\cos\theta) = (3\cos^2\theta - 1)/2$ is the Legendre polynomial of 2nd order, ω is the angular velocity of the local inertial frame, which is related to star's angular velocity Ω, and h_0, h_2, m_0, m_2 are functions of r and are all proportional to Ω^2.The angular velocity ω can be found by solving equation

$$\frac{1}{r^4} \frac{\mathrm{d}}{\mathrm{d}r} \left(r^4 j \frac{\mathrm{d}\tilde{\omega}}{\mathrm{d}r} \right) + \frac{4}{r} \frac{\mathrm{d}j}{\mathrm{d}r} \tilde{\omega} = 0 \,, \tag{7}$$

where

$$j(r) = \mathrm{e}^{-\nu(r)/2} [1 - 2m(r)/r]^{1/2} \,. \tag{8}$$

One integrates Eq. (7) outward from the centre for arbitrarily chosen $\tilde{\omega}_\mathrm{c}$ with boundary condition $\mathrm{d}\omega/\mathrm{d}r = 0$. At the surface one can calculate the angular momentum J and frequency of rotation Ω corresponding to $\tilde{\omega}_\mathrm{c}$ from the relation

$$\Omega_\mathrm{new} = \tilde{\omega}(R) + \frac{2J}{R^3} \,. \tag{9}$$

We take frequency of rotation Ω as an input parameter; thus, after integrating Eq. (7), we rescale the frequency $\tilde{\omega}$ in order to obtain the proper value of Ω by

$$\tilde{\omega}_{\mathrm{new}(r)} = \tilde{\omega}_{\mathrm{old}(r)} \frac{\Omega_\mathrm{new}}{\Omega_\mathrm{old}} \,. \tag{10}$$

The angular momentum is given by the relation

$$J = \frac{1}{6}R^4\left(\frac{\mathrm{d}\tilde{\omega}}{\mathrm{d}r}\right)_{r=R} . \tag{11}$$

After finishing this procedure one could calculate mass and pressure perturbation factors m_0, p_0 and h_0 from equations

$$\frac{\mathrm{d}m_0}{\mathrm{d}r} = 4\pi r^2\frac{\mathrm{d}\rho}{\mathrm{d}P}(\rho+P)p_0 + \frac{1}{12}j^2r^4\left(\frac{\mathrm{d}\tilde{\omega}}{\mathrm{d}r}\right)^2 - \frac{1}{3}r^3\frac{\mathrm{d}j^2}{\mathrm{d}r}\tilde{\omega}^2 , \tag{12}$$

$$\frac{\mathrm{d}p_0}{\mathrm{d}r} = -\frac{m_0(1+8\pi r^2P)}{(r-2m)^2} - \frac{4\pi(\rho+P)r^2p_0}{r-2m} + \frac{1}{12}\frac{r^4j^2}{r-2m}\left(\frac{\mathrm{d}\tilde{\omega}}{\mathrm{d}r}\right)^2 + \frac{1}{3}\frac{\mathrm{d}}{\mathrm{d}r}\left(\frac{r^3j^2\tilde{\omega}^2}{r-2m}\right) , \tag{13}$$

$$\frac{\mathrm{d}h_0}{\mathrm{d}r} = -\frac{\mathrm{d}}{\mathrm{d}r}\delta p_0 + \frac{1}{3}\frac{\mathrm{d}}{\mathrm{d}r}(r^2\mathrm{e}^{-2\lambda_0}\tilde{\omega}^2) . \tag{14}$$

The boundary condition requires that m_0 and h_0 vanish at the centre of the star. In (Miller, 1977), the series expansions of the m_0 and h_0 terms were calculated near the centre. These expansions has to be used while calculating the model numerically. The mass of the rotating object is given by

$$M(R) = M_0(R) + m_0(R) + J^2/R^3 . \tag{15}$$

After integrating the monopole equations, one could integrate quadrupole equations to obtain quadrupole momentum and shape of the object. Quadrupole perturbation factor $v_2 = h_2 + k_2$ is given by solution of the equation

$$\frac{\mathrm{d}v_2}{\mathrm{d}r} = -2\frac{\mathrm{d}v_0}{\mathrm{d}r}h_2 + \left(\frac{1}{r}+\frac{\mathrm{d}v_0}{\mathrm{d}r}\right)\left[\frac{1}{6}r^4j^2\left(\frac{\mathrm{d}\tilde{\omega}}{\mathrm{d}r}\right)^2 - \frac{1}{3}r^3\tilde{\omega}^2\frac{\mathrm{d}j^2}{\mathrm{d}r}\right] \tag{16}$$

and h_2 is given by

$$\begin{aligned}\frac{\mathrm{d}h_2}{\mathrm{d}r} = &-\frac{2v_2}{r(r-2m(r))\,\mathrm{d}v_0/\mathrm{d}r} \\ &+\left\{-2\frac{\mathrm{d}v_0}{\mathrm{d}r} + \frac{r}{2(r-2m(r))\,\mathrm{d}v_0/\mathrm{d}r}\left[8\pi(\rho+p) - \frac{4m(r)}{r}\right]\right\}h_2 \\ &+\frac{1}{6}\left[r\frac{\mathrm{d}v_0}{\mathrm{d}r} - \frac{1}{2(r-2m(r))\,\mathrm{d}v_0/\mathrm{d}r}\right]r^3j^2\left(\frac{\mathrm{d}\tilde{\omega}}{\mathrm{d}r}\right)^2 \\ &-\frac{1}{3}\left[r\frac{\mathrm{d}v_0}{\mathrm{d}r} + \frac{1}{2(r-2m(r))\,\mathrm{d}v_0/\mathrm{d}r}\right]r^2\tilde{\omega}^2\frac{\mathrm{d}j^2}{\mathrm{d}r} .\end{aligned} \tag{17}$$

One solves these two equations with the following boundary conditions at $r = 0$:

$$h_2^{(\mathrm{P})} \to ar^2 , \quad h_2^{(\mathrm{C})} \to Br^2 , \quad v_2^{(\mathrm{P})} \to br^4 , \quad v_2^{(\mathrm{C})} \to -\tfrac{2}{3}\pi(\rho_c+3p_c)Br^4 . \tag{18}$$

Index (P) denotes particular solution and index (C) denotes complementary function which is a solution of the equations homogeneous to Eqs (16), (17); constants a and b are related by

$$b + \tfrac{2}{3}\pi(\rho_c + 3p_c)a = \tfrac{2}{3}\pi(\rho_c + 3p_c)j_c^2 \,. \tag{19}$$

Outside the neutron star, where $\rho = P = 0$, $j = 1$, the functions h_2 and v_2 are given by the relations

$$h_2 = J^2\left(\frac{1}{M_0 r^3} + \frac{1}{r^4}\right) + K\,Q_2^2\left(\frac{r}{M_0} - 1\right) , \tag{20}$$

$$v_2 = -\frac{J^2}{r^4} + K\frac{2M_0}{[r(r-2M_0)]^{1/2}}\,Q_2^1\left(\frac{r}{M_0} - 1\right) . \tag{21}$$

The integration is done for arbitrarily chosen value of a; the general solution is given as a sum of the particular solution and the complementary function

$$h_2 = h_2^{(\mathrm{P})} + Ah_2^{(\mathrm{C})} , \quad v_2 = v_2^{(\mathrm{P})} + Av_2^{(\mathrm{C})} . \tag{22}$$

Constants A and K can be found by solving the set of two equations. The quadrupole momentum is given by the relation

$$Q = \tfrac{8}{5}K M^3 + J^2/M \,. \tag{23}$$

In the next approximation, the quadrupole moment $q = Q/M^3$ of the star is introduced. The fitting procedure shows that $q \sim j^2$ (Stuchlík et al., 2007a) where $j = J/M^2$. Therefore, the spacetime could be considered quasi-Kerr and the Kerr metric and related formula of the orbital motion could be used.

4 SKYRMION INTERACTIONS AND RELATED EOS

The effective Skyrmion interaction implies a variety of parametrizations in the framework of mean-field theory. All give similar agreement with experimentally established nuclear ground states at the saturation density n_0, but they imply varying behaviour of both symmetric and asymmetric nuclear matter when density grows (up to $3n_0$).

The general form of the effective Skyrme interaction implies total binding energy of nuclei as the integral of an energy density functional $\mathcal{H}$, determined as a function of nine empirical parameters $t_0, t_1, t_2, t_3, x_0, x_1, x_2, x_3$ and α in the form (Říkovská Stone et al., 2003)

$$\mathcal{H} = \mathcal{K} + \mathcal{H}_0 + \mathcal{H}_3 + \mathcal{H}_{\mathrm{eff}} \,, \tag{24}$$

where the kinetic term $\mathcal{K} = (\hbar/2m)\tau$, is given by the kinetic densities $\tau = \tau_n + \tau_p$, with τ being the total density, τ_n (τ_p) being the neutron (proton) density. The other terms are given by the relations

$$\begin{aligned}
\mathcal{H}_0 &= \tfrac{1}{4}t_0\left[(2+x_0)n^2 - (2x_0+1)(n_p^2 + n_n^2)\right] \\
\mathcal{H}_3 &= \tfrac{1}{24}t_3 n^\alpha\left[(2+x_3)n^2 - (2x_3+1)(n_p^2 + n_n^2)\right] \\
\mathcal{H}_{\mathrm{eff}} &= \tfrac{1}{8}\left[t_1(2+x_1) + t_2(2+x_2)\right]\tau_n + \tfrac{1}{8}\left[t_2(2x_2+1) - t_1(2x_1+1)\right](\tau_p n_p + \tau_n n_n) \,.
\end{aligned} \tag{25}$$

The pressure is then given by

$$P(n_{\rm b}, I) = n_{\rm b}^2 \frac{\partial \varepsilon}{\partial n_{\rm b}}\,, \tag{26}$$

where ε is the binding energy per particle and $I = (N-Z)/A$ denotes asymmetry of nuclear matter.

In (Říkovská Stone et al., 2003), 87 different Skyrme parametrizations were restricted to 27, using limits implied by the spherically symmetric models of neutron stars and by experimentally tested properties of nuclear matter. Here, we shall test acceptability of nine of these 27 Skyrme parametrizations to the limits put by the QPO measurements, using axisymmetric models in first approximation with respect to the star rotation.

5 DETERMINATION OF NEUTRON STAR STRUCTURE USING GENETIC ALGORITHM

Genetic algorithm (GA) arises from the method of natural selection, where subjects with best adaptation to assigned conditions have highest chance to survive (Goldberg, 1989). GA takes into account the following natural mechanism – mutation and lifetime limit restricting risk of degradation, which is kept in local extreme from optimization viewpoint. GA has iteration character. GA doesn't work with separate result in particular iterations, but with population. In each iteration GA works with several results (generally a lot of results, with standard value being of hundreds), which are included in the population trying to ensure appearance of still better results via genetic operations with these results. Generally, the GA scheme is given in the form

$$\mathrm{GA} = (N, P, f, \Theta, \Omega, \Psi, \tau)\,, \tag{27}$$

where P is population containing N elements, Θ is parent selection operator which selects u elements from P. Evaluation for each chromosome is performed by the fitness function f, whereas

$$f : S_i \leftarrow R\,, \quad i = 1, \ldots, N\,. \tag{28}$$

Genetic operators included in Ω are, namely, crossover operator $\Omega_{\rm C}$, mutation operator $\Omega_{\rm M}$ and other problem-oriented or implementation-oriented specific operators, which all together generate v offsprings from u parents. Ψ is deletion operator, which removes v selected elements from actual population $P(t)$; v elements is added into the new population $P(t+1)$, τ is the stop-criterion. Parent selection operator Θ and genetic operators Ω have stochastic character, deletion operator Ψ is generally deterministic.

We have selected GA with sexual reproduction containing one chromosome with restricted lifetime parameter, 5 iterations. The crossover operator is selected with uniform crossing, using genes of type 3/3/5. We used the Gray code in order to encrypt parameters to chromosomes, which is useful by reason of bypassing so-called Hamming barrier (see Stuchlík et al., 2007b for details).

Chromosomes are compound of genes; each gene presents 1 bit value. However, genes contain more than 1 bit (using the redundancy encrypt). Bit values inside a gene are mapped onto outside value of gene (0 or 1) via specific map function, in which border between 0 and 1 is not crisp, but there exists so-called "shade zone," where value carried by the gene is determined randomly (Čermák, 2006; Čermák and Chmiel, 2004). We pressed the number of members in each generation to 400 and iterate 40 generations. We define two tasks of selecting neutron star structure. The first one determines ρ_c, Ω with preset EOS where fitness function f is χ^2 (Stuchlík et al., 2007a,b). (It is important to say here that at present the fitness function is tabulated.) The second one determines the EOS, ρ_c, Ω with using fitness function χ^2. Both tasks put limits on the EOS under consideration. Overcoming those limits implies removing the corresponding chromosomes by setting value of fitness function to the maximum value (10^{200}). For a given EOS, the allowed neutron star structure is provided by the GA described above and the fitness function χ^2. The chromosome structure is given by two values, central density and rotation frequency. Interval of central density we choose from 0.4×10^{15} to 3.3×10^{15}.

In the first task, partition of the central density is set to 4096 (12 bits). Interval of rotation frequency is set from 50 to 8000 and the partition to 8192 (13 bits). Table 1 shows determination of the central density (in units of 10^{15} g cm^{-3}) and the rotation frequency for the given number of EOS.

Because the resulting frequencies do not fit the observed rotation frequency interval (Lamb, 2003), and also the fitness function has too many local minima with exactly the same value for different combinations of ρ_C, Ω and the same EOS, we make determ-

Table 1. Fitness function and corresponding parameters for all tested EOS, with $\Omega \in (50; 8000)$.

EOS type	ρ_c	Ω	Fitness
0-SkT5	2.1244	964.17	56.556
1-SkO′	1.5575	979.70	56.686
2-SkO	1.3987	711.85	56.601
3-SLy4	1.4896	1373.71	57.292
4-GS	1.1225	743.89	57.223
5-SkI2	1.1185	1241.72	57.688
6-SkI5	0.9359	791.43	57.059
7-SGI	1.0170	986.49	57.028
8-SV	0.7889	590.55	56.393

Table 2. Global minimum for $\Omega \in (1827.21; 1828.03)$.

Ω_{min}	Ω_{max}	Fitness	EOS	ρ_c	Ω
1827.21	1828.03	57.542	1	1.79021	1827.66

ination of values mentioned before, but we set – in accord with observation – the range of rotation frequencies from 1827.21 to 1828.03 with partition 64 (6 bit).

Clearly, for selecting the most convenient EOS we need referenced χ^2 value as the global minimum χ^2 over all EOS. Thus we make second task, determination of the best resulting neutron star structure over all used EOS (see Table 2 for the result). The corresponding EOS value is given by zero based EOS number (4 bits).

6 CONCLUSIONS

Analysis of QPO's in neutron star atoll sources in the framework of Hartle–Thorne geometry gives very detailed data (neutron star parameters as mass, spin and quadrupole moment) that could be quite well used for constraining the wide scale of allowed EOS by determining the structure of neutron stars from the complex set of structural differential equations. The testing by standard procedures is a long-time consuming procedure. Here, we show in the case of the atoll source 4U 1636−53 that the genetic algorithm method could make the proper selection in a wide sample of EOS of Skyrmion type in a very efficient and short way (with same precision and the time consumed for the GA about 30 minutes, being by orders shorter than the time consumed by the standard methods).

We expect that the method based on genetic algorithm allows much stronger tests, while including the quadrupole moment calculated directly without using the quasi-Kerr approximation $q \sim j^2$. Further, we have to expect that the neutron star parameters, estimated by the QPO data while assuming geodetical epicyclic oscillations given directly by the spacetime parameters, could be to some extent shifted, because of the influence of the neutron star magnetic field onto the frequency of the epicyclic oscillations in the inner part of the accretion disc near the neutron star surface, where generation of QPOs is assumed (Bakala et al., 2007).

ACKNOWLEDGEMENTS

This work was supported by Czech grants MSM 4781305903 (Z. S., P. Č. and G. T.) and LC06014 (M. U. and P. B.).

REFERENCES

Bakala, P., Šrámková, E., Stuchlík, Z. and Török, G. (2007), Dipole magnetic field on a Schwarzschild background and related epicyclic frequencies, pp. 1–10, this volume.

Barret, D., Olive, J.-F. and Miller, M. C. (2006), Drop of coherence of the lower kilo-Hz QPO in neutron stars: Is there a link with the innermost stable circular orbit?, *Astronom. Nachr.*, **326**(6), pp. 808–811.

Chandrasekhar, S. and Miller, J. C. (1974), On slowly rotating homogeneous masses in general relativity, *Monthly Notices Roy. Astronom. Soc.*, **167**, pp. 63–79.

Goldberg, D. E. (1989), *Genetic Algorithms in Search, Optimization, and Machine Learning*, Addison-Wesley, Reading, MA, ISBN 0-201-15767-5.

Hartle, J. B. and Thorne, K. (1968), Slowly rotating relativistic stars II. Model for neutron stars and supermassive stars, *Astrophys. J.*, **153**, pp. 807–834.

Lamb, F. K. (2003), High Frequency QPOs in Neutron Stars and Black Holes: Probing Dense Matter and Strong Gravitational Fields, in E. P. J. van den Heuvel, L. Kaper, E. Roi and R. A. M. J. Wijers, editors, *From X-Ray Binaries to Gamma-ray Bursts, proceedings of a symposium held in memory of Jan van Paradijs*, volume 308 of *ASP Conference*, pp. 221–250, Banff, AB, Canada, arXiv: 0705.0030v1.

Miller, J. C. (1977), Quasi-stationary gravitational collapse of slowly rotating bodies in general relativity, *Monthly Notices Roy. Astronom. Soc.*, **179**, pp. 483–498.

Stuchlík, Z., Török, G. and Bakala, P. (2007a), On a multi-resonant origin of high frequency quasiperiodic oscillations in the neutron-star X-ray binary 4U 1636−53, submitted to Astronomy and Astrophysics, arXiv: 0704.2318.

Stuchlík, Z., Čermák, P., Török, G., Urbanec, M. and Bakala, P. (2007b), Genetic Selection of Neutron Star Structure Matching the X-Ray Observations, in N. Callaos, Q. Lesso, C. Zinn and O. Goriachkin, editors, *The 11th World Multi-Conference on Systemics, Cybernetics and Informatics: WMSCI 2007, July 8–11, Orlando, USA*, pp. 41–44, Internat. Inst. of Inf. and Syst.

Török, G., Abramowicz, M. A., Bakala, P., Bursa, M., Horák, J., Kluźniak, W., Rebusco, P. and Stuchlík, Z. (2007a), On the distribution of kHz QPO frequency ratio in the atoll source 4U1635−53, *Astronomy and Astrophysics*, submitted.

Török, G., Stuchlík, Z. and Bakala, P. (2007b), A remark about possible unity of the neutron star and black hole high frequency QPOs, *Central European J. Phys.*, **5**(4), pp. 457–462.

Čermák, P. (2006), Parameters optimization of fuzzy-neural model using GA, *Internat. J. Comput. Intelligence Theory and Practice*, **1**, pp. 23–30.

Čermák, P. and Chmiel, P. (2004), Parameters optimization of fuzzy-neural dynamic models, in S. Dick, L. Kurgan, P. Musilek, W. Pedrycz and M. Reformat, editors, *23rd International Conference of the North American Fuzzy Information Processing Society*, pp. 762–767, IEEE & NAFIPS, Banff, AB, Canada, ISBN 0-7803-8377-X, IEEE Cat. No. 04TH8736C.

Říkovská Stone, J., Miller, J. C., Koncewicz, R., Stevenson, P. D. and Strayer, M. R. (2003), Nuclear matter and neutron-star properties calculated with the Skyrme interaction, *Phys. Rev. C*, **68**, pp. 034324–1–034324–16.

Title: **Proceedings of RAGtime 8/9: Workshops on black holes and neutron stars, 15–19/19–21 September 2006/2007, Hradec nad Moravicí, Opava, Czech Republic**

Published by: Silesian University in Opava
Faculty of Philosophy and Science
Institute of Physics
Bezručovo nám. 13
CZ-746 01 Opava
Czech Republic

Editors: S. Hledík and Z. Stuchlík

Cover design: Otakar Karlas

1st edition

Printed by BITTISK s.r.o., Opava, Czech Republic

Published in December 2007

ISBN 978-80-7248-419-5

Typeset in LaTeX

Název: **Proceedings of RAGtime 8/9: Workshops on black holes and neutron stars, 15–19/19–21 September 2006/2007, Hradec nad Moravicí, Opava, Czech Republic**

Nakladatel: Slezská univerzita v Opavě
Filozoficko-přírodovědecká fakulta
Ústav fyziky
Bezručovo nám. 13
CZ-746 01 Opava
Česká republika

Editoři: S. Hledík a Z. Stuchlík

Obálka: Otakar Karlas

První vydání

Tisk: BITTISK s.r.o., Opava, Česká republika

Vydáno v prosinci 2007

ISBN 978-80-7248-419-5

Vysázeno systémem LaTeX